18th International Conference on Sustainable Energy Technologies

20-22 August 2019 - Kuala Lumpur - Malaysia

Sustainable Energy Towards the New Revolution

Conference Proceedings Volume 2

Proceedings of the

18th International Conference on Sustainable Energy Technologies

SET 2019

20-22 August 2019
Kuala Lumpur, Malaysia

Volume 2

Edited by

Professor Saffa Riffat, Dr Yuehong Su,
Professor Norli Ismail and Dr Mardiana Idayu Ahmad

SET 2019 Admin Support
Department of Architecture and the Built Environment
Faculty of Engineering, University of Nottingham

Reference to a conference paper:

To cite a paper published in these conference proceedings, please substitute the highlighted sections of the reference below with the details of the article you are referring to:

Author(s) Surname, Author(s) Initial(s), 2019. 'Title of paper'. In Riffat, Su, Ismail, Ahmad. ed., **Sustainable Energy Towards the New Revolution**: Proceedings of the 18th International Conference on Sustainable Energy Technologies, 20-22 August 2019, Kuala Lumpur, Malaysia. University of Nottingham: Buildings, Energy & Environment Research Group. Volume X, pp XX-XX. Available from: nottingham-repository.worktribe.com/ [Last access date].

ISBN-13: 9780853583318

Version: 10.02.2020

Foreword

The 18th International Conference on Sustainable Energy Technologies was a significant international academic event in the domain of world sustainable energy technologies with a theme of '*Sustainable Energy Towards the New Revolution'*. The conference aimed to provide a forum for the exchange of latest technical information, the dissemination of up-to-date research results, and the presentation of major topics including sustainable energy, low carbon technologies, eco-cities, energy security and environmental policy.

Held from August 20th – 22nd 2019 in Kuala Lumpur, Malaysia, the conference was a collaboration between the World Society of Sustainable Energy Technologies (WSSET), the Universiti Sains Malaysia and University of Nottingham. World-renowned experts and scholars in the area, representatives of prominent enterprises and universities attended to discuss new developments and achievements in the field, as well as promoting academic exchange, application of scientific results, university-industry collaboration and government-industry collaboration.

The papers contained in these proceedings focus on topics such as Energy Storage for the Age of Renewables; Research, Innovation and Commercialisation in Sustainable Energy Technologies; Integrating Planning & Policy, Architecture, Engineering & Economics; Energy and Environment; Engineering Thermo-physics; and Systemic Change for Cities.

About 230 delegates from 30 countries attended SET2019; nearly 400 abstracts were received and 190 papers have been published in the conference proceedings. The proceedings have therefore been divided into three volumes. I hope you enjoy as much as I did the breadth of work you will find in these proceedings.

We would like to thank all participating authors for their contributions to both the conference and to the publishing of this book. We are also indebted to our international scientific committee for their advice and seemingly endless review of papers. We would also like to thank unreservedly Celia Berry, Zeny Amante-Roberts, Dr Mardiana Idayu Ahmad and Professor Dr Norli Ismail for their tireless efforts in making SET2019 one of the most successful conferences we have held. Also a huge thanks to our sponsors First Solar, PCM Products Ltd and Professor Terry Payne.

Professor Saffa Riffat
Chair in Sustainable Energy Technologies
President of the World Society of Sustainable Energy Technologies
Fellow of the European Academy of Sciences
SET 2019 Chairman

CONTENTS

Paper Number **Title** **Page**

#128: Theoretical analysis of energy recovery from food waste based on an integrated gasification and Stirling engine system

Jialing CHEN[1], Xian LI [2], Yanjun DAI[3]*, Chi-Hwa WANG[4]

[1] Institution of Refrigeration and Cryogenics, Shanghai Jiao Tong University, Shanghai 200240, China
gillianchen@sjtu.edu.cn
[2] NUS Environmental Research Institute, National University of Singapore, Singapore 138602
erilx@nus.edu.sg
[3] Institution of Refrigeration and Cryogenics, Shanghai Jiao Tong University, Shanghai 200240, China
*Corresponding author: yjdai@sjtu.edu.cn
[4] Department of Chemical and Biomolecular Engineering, National University of Singapore, Singapore 117585
chewch@nus.edu.sg

The high cost of food waste treatment by the traditional method and the hygiene problems caused by the accumulation make the reduction and energy regeneration of food waste locally necessary. In this paper, a combined gasification and CHP unit using Stirling engine system is modelled and evaluated. The process is aimed to treat the food waste from the canteen in the campus of Shanghai Jiao Tong University. After pre-treatment, the water content of food waste from the canteens at SJTU is less than 17%. By establishing a steady-state chemical reaction equilibrium model, the characteristics and yield of syngas from food waste through gasification process are analysed. When the equivalence ratio of gasification is 0.294, the results show that CO accounts for 18.4% and H2 accounts for 22.6% in syngas, and the higher heating value is 5.61 MJ/m^3. The syngas is fed to a Stirling engine for power generation. The Stirling engine has low requirements of feedstock and is suitable for distributed waste to energy systems. By providing with 1175kg/d of food waste during peak days, the maximum energy output of the system is 131.7kW, and the overall efficiency of the system is $\eta_{all} = 44.5\%$, with 21.6kW electricity and 110.1kW heat in hot water.

Keywords: *food waste; gasification; Stirling engine; syngas*

1. INTRODUCTION

Approximately 8 tonnes of food waste were generated at Shanghai Jiao Tong University (SJTU). The amount of food waste is expected to further increase in future. Food waste has been transported to landfill and deposited after drying at campus. When buried in landfill, food waste decomposes to form methane, a greenhouse gas, and leachate that is harmful to land.

Comparing the anaerobic digestion (AD) process with gasification, the latter can deal with indigestible cellulose and lignin which cannot be completed digested in AD, so the remaining waste will be less. Gasification also has the advantage of faster processing speeds and smaller equipment size. Compared with incineration processes, the gasification process can significantly decrease the emission of CO_2 and NO_x.

Compared with ICE, the Stirling engine has an independent combustion chamber, the cylinder structure is relatively simple, and fuel with low calorific value and high impurity content can be used, which is less affected by tar and carbon deposition. The amount of air and fuel mixture can be controlled more accurately, so emissions from incomplete combustion will be greatly reduced. For a system of 1.5 MW biomass chemical energy, the electric power ranges from 20.57 kW to 103.40 kW and heat power ranges from 1128.54 to 880.27 kW in a self-sufficient, biomass based district heating system integrated with a Stirling engine and biomass gasification (Skorek-Osikowska, 2017).

In this paper, a Stirling engine is driven by an auto-thermal gasifier, and the dried food waste from canteens at SJTU was used as the feedstock of gasification. Syngas produced from gasification was predicted using a 0-D kinetic model. A Chemkin model was used to predict the combustion of syngas. The performance of the Stirling engine and the power generation and heat recovery from the whole system was discussed.

2. SYSTEM DESCRIPTION

An integrated gasification and Stirling engine system is depicted in Figure 1. The system is composed of two main subsystems in which a Stirling engine is driven by an auto-thermal gasifier. The food waste is fed to the gasifier after smashing and drying. Syngas produced by the gasifier flows through a gas-to-water heat exchanger to heat water. After dust elimination by a cyclone, syngas is burned in a combustion chamber. The exhaust gas drives the Stirling engine to generate power, and the cooling fluid also produces heat through a water-to-water heat exchanger HE-2. The exhaust gas at the outlet of the Stirling engine has a high temperature, and the rest heat is collected through the gas-to-water heat exchanger HE-3. The exhaust gas is discharged into the atmosphere after post-treatment. The production of the whole system is electricity, hot water, exhaust gas and a small number of ash.

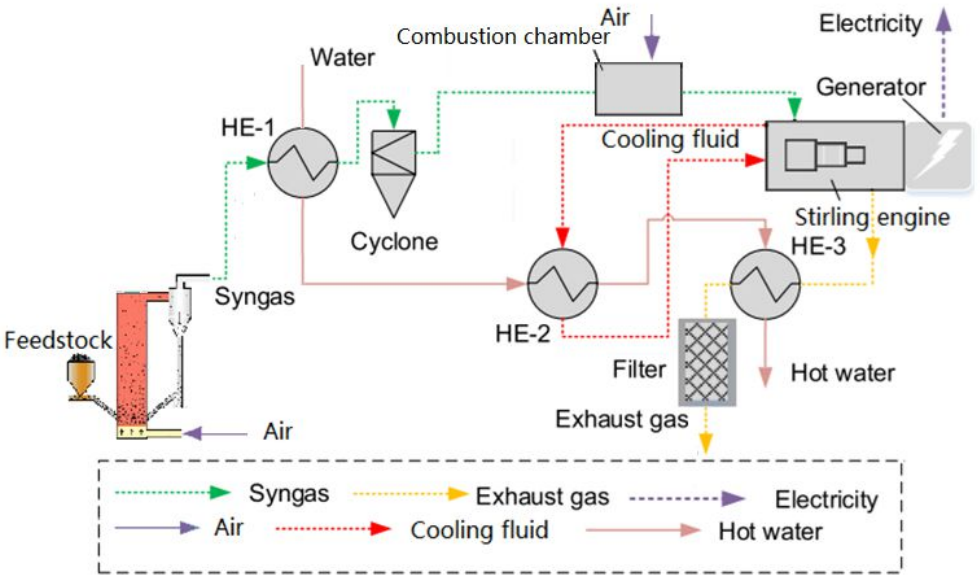

Figure 1: An integrated gasification and Stirling engine system

3. MATERIALS AND METHODS

3.1. Feedstock

The dried food waste from Shanghai Jiao Tong University is fed into the gasifier. The analysis of feedstock is shown in Table 1.

Table 1: Analysis of feedstock

Parameters	Value
C (wt %)	50.65
H (wt %)	8.18
O (wt %)	35.03
N (wt %)	2.34
S (wt %)	0.20
Moisture (wt %)	17
Ash (wt %)	7.8
Chemical composition	$CH_{1.938}O_{0.5187}$

Equation 1: (Channiwala, 2002)

$$HHV_f = 0.3491F_C - 1.1783F_H - 0.1034F_O - 0.0151F_N + 0.1005F_S - 0.0211F_A$$

Where:

- HHV_f = higher heating value of feedstock, MJ/kg
- F_C、F_H、F_O、F_N、F_S、F_A : the mass fraction of element C、H、O、N、S and ash

3.2. Gasifier

Since the content of other elements except C, H, and O is extremely small, the influence of other elements is ignored, and the reaction of nitrogen is not considered. The chemical reaction equation can be expressed as follows:

Equation 2: (Sharma Shweta, 2016)

$$CH_x\ O_y + m\left(O_2 + 3.76N_2\right) + wH_2O \rightarrow n_{H_2}H_2 + n_{CO}CO + n_{CO_2}CO_2 + n_{H_2O}\ H_2O + n_{CH_4}CH_4 + 3.76mN_2$$

The performance of gasification is cold gas efficiency, which can be calculated as follows:

Equation 3:

$$\eta_{CG} = \frac{\dot{V}_s \mathrm{HHV}_s}{\dot{m}_f HHV_f + \dot{Q}_{in}}$$

Where:

- $\dot{V}_s$ = volume flow rate of syngas, Nm^3/s
- $\dot{m}_f$ = mass flow rate of feedstock, kg/s
- HHV_s = higher heating value of syngas, MJ/Nm^3
- HHV_f = higher heating value of feedstock, MJ/kg
- $\dot{Q}_{in}$ = other heat flux into the gasification, i.e. hot air, steam and solar

3.3. Combustion chamber

The simulations of adiabatic combustion temperature in the combustion chamber were carried out using the premixed laminar burner-stabilized flame reactor module in the Chemkin Pro Package (Smith *et al*).

Equation 4: $$t_y = \varphi t_{ad}$$

Where:

- t_y = actual combustion temperature, °C
- t_{ad} = adiabatic combustion temperature, °C
- φ = combustion temperature correction factor

3.4. Stirling engine

The Stirling engine is driven by temperature difference. Electric power generated by the Stirling engine can be calculated as:

Equation 5: $$\dot{Q}_{SE} = \eta_{el,SE}\dot{Q}_S$$

Where:

- $\eta_{el,SE}$ = electricity efficiency of Stirling engine

Equation 6: $$\eta_{el,SE} = -2\cdot10^{-8}\Delta T_{SE}{}^2 - 5\cdot10^{-5}\Delta T_{SE} + 0.2921$$ *(Bartela, 2017)*

Where:

- ΔT_{SE}= degree of cooling of exhaust gas in Stirling engine, •

Heat recovered from the cooling fluid of Stirling engine can be calculate as:

Equation 7: $$\dot{Q}_{SE} = \eta_{q,SE}\dot{Q}_S$$

Where:

- $\eta_{q,SE}$= heat recovery efficiency from Stirling engine
- $\dot{Q}_S$= heat transferred to Stirling engine from exhaust gas, kW

Heat recovered from the whole system is:

Equation 8: $$\dot{Q} = \dot{Q}_1 + \dot{Q}_{SE} + \dot{Q}_3$$ [7]

Where:

- $\dot{Q}_1$= heat recovered from gas-to-water heat exchanger HE-1, kW
- $\dot{Q}_{SE}$ = heat recovered from Stirling engine, kW

- $\dot{Q}_3$ = heat recovered from gas-to-water heat exchanger HE-3, kW

4. RESULTS AND DISCUSSION

4.1. Syngas

The temperature of feedstock is 25°C and that of the inlet air is 28°C. This paper studies the effects of equivalence ratio on food waste gasification. By simulation, the mole fractions of different components in the syngas are shown in Figure 2. With an increase of the equivalence ratio (ER) from 0.07 to 0.4, the mole fraction of nitrogen increases significantly from 25.1% to 49.4% 2. It is the main cause of the decrease of the higher heating value of syngas from 9.44 MJ/Nm^3 to 4.64 MJ/ Nm^3. The mole fraction of hydrogen increases when the equivalence ratio is low (ER<0.15) and then decreases. The mole fraction of carbon monoxide mainly increases with the increases but starts to decrease when the equivalence is over 0.36. The mole fraction of carbon maintains relatively constant between 6.6% and 12.2%. The mole fraction of methane drops fast with the equivalence ratio increasing, and the methane in syngas is near 0 when the equivalence ratio is over 0.38 (Figure 2).

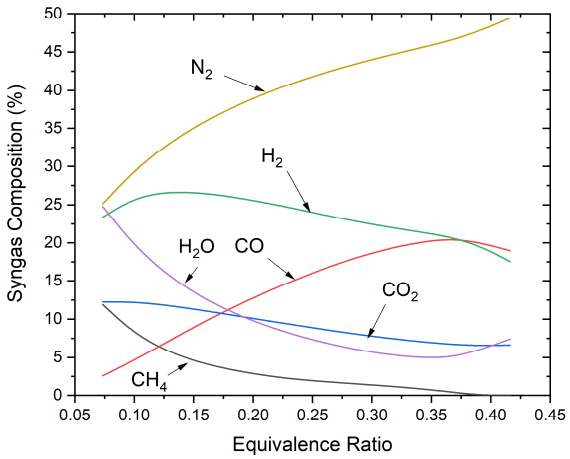

Figure 2: Mole fraction of syngas composition as a function of equivalence ratio of gasification

As the gasification is an exothermic reaction, the reaction temperature of gasification increases with the equivalence ratio, which is shown in Figure 3. When the equivalence is over 0.37, the hydrogen production begins to decrease with the increase of air inflow. Similarly, when the equivalence is over 0.39, the carbon monoxide productions begins to decrease in the same time. As a result, the cold gas efficiency is in peak, reaching 83.9%, when ER=0.37.

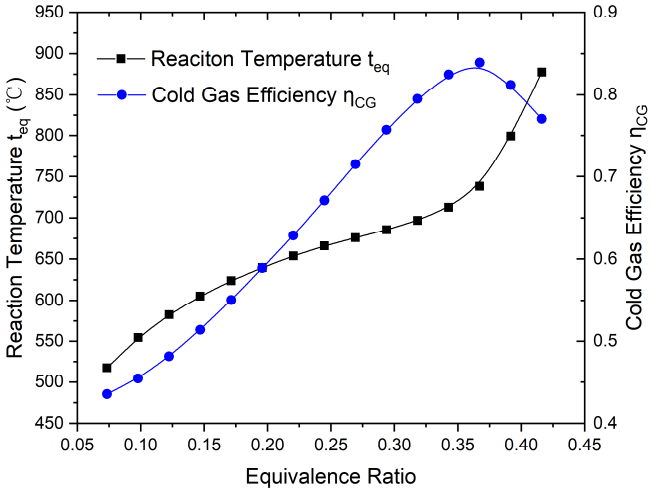

Figure 3: Reaction temperature and cold gas efficiency as a function of equivalence ratio of gasification

3.1. Combustion chamber

The gas temperature at the inlet of the combustion chamber is 150°C. Assuming that the syngas is completely burned in the combustion chamber and there is no heat dissipation, we can get the adiabatic combustion temperature of syngas as Figure 4. As is known when calculating the syngas composition, with the increase of equivalence ratio of gasification, the heating value of syngas decreases, so the adiabatic combustion temperature has a whole trend of decrease. However, the adiabatic combustion temperature stays steady from 1538°C to 1545°C when the equivalence ratio of gasification is between 0.20 and 0.34. When combustion temperature correction factor $\varphi = 0.75$, the actual combustion temperature varies from 1154°C to 1157°C.

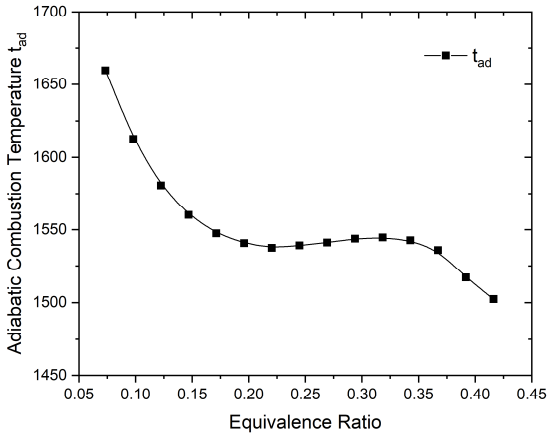

Figure 4: Adiabatic combustion temperature of syngas in the chamber as a function of equivalence ratio of gasification

3.2. Power generation and heat recovery

Since the degree of cooling of exhaust gas in the Stirling engine is an important influencing factor of power generation of the Stirling engine, this paper researches the effects of degrees of cooling in the Stirling engine ΔT_{SE} from 100°C to 600°C on the overall power generation and heat recovery. Efficiency of electricity generation in the engine decreases from 28.7% to 25.5% when ΔT_{SE} increases from 100°C to 600°C. Efficiencies of gas-to-water exchangers are 70% and heat recovery efficiency from the engine $\eta_{q,SE} = 45\%$. Taking the equivalence ratio of gasification as 0.294, the mass of food waste needed to be handled during peak days is 1175kg/d.

As Figure 5 shows, the power generation of the system increases from 5.3 kW to 25.6 kW but the increasing speed drops when ΔT_{SE} increases from 100°C to 600°C. Meanwhile, the heat recovery from the whole system decrease from 125.9 kW to 105.4 kW.

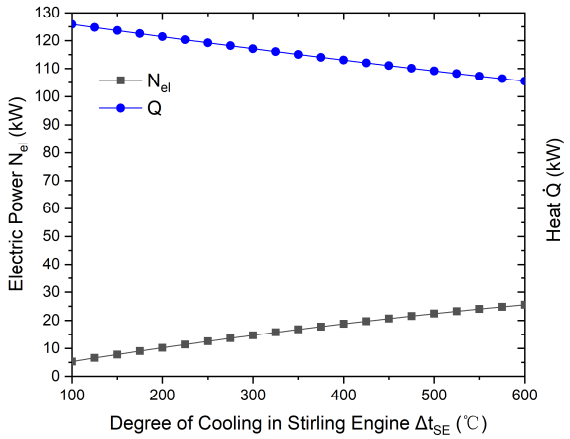

Figure 5: Electric power and heat output of the system as a function of degree of cooling of exhaust gas in Stirling engine

Meanwhile, as Figure 6 shows, the efficiency of electricity of the whole system η_{el} increases from 1.8% to 8.6% when ΔT_{SE} increases from 100°C to 600°C, and the efficiency of heat generation of the whole system η_q decreases from 42.6% to 35.7%. The overall efficiency of the whole system has a slight increase at first and then decreases a little. When the degree of cooling of exhaust gas in the Stirling engine $\Delta T_{SE} = 375℃$, the overall efficiency of the system η_{all} is at the peak, 44.5%. When the electricity efficiency of Stirling engine $\eta_{el,SE} = 26.3\%$, the efficiency of electricity of the whole system $\eta_{el} = 7.3\%$ and the efficiency of heat generation of the whole system $\eta_q = 37.2\%$. Therefore, the maximum energy output of the system is 131.7kW, with 21.6kW electricity and 110.1kW heat in hot water.

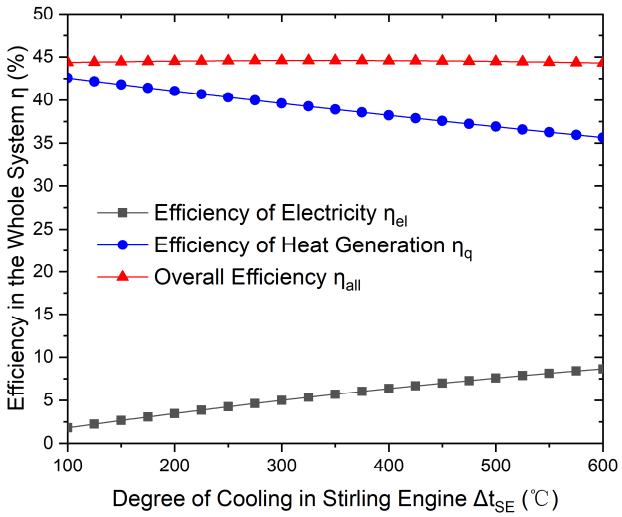

Figure 6: Efficiency of electricity, efficiency of heat generation and overall efficiency of the whole system as a function of degree of cooling of exhaust gas in Stirling engine

5. CONCLUSIONS

In this paper, the dried food waste from canteens at SJTU was used as the feedstock for gasification. Different syngas compositions, reaction temperatures and cold gas efficiencies were compared under different equivalence ratios. A Chemkin model was used to predict the combustion of syngas and the performance of the Stirling engine and power generation and heat recovery from the whole system was discussed. The main findings were as follows:

1) The cold gas efficiency of gasification reached the peak, 83.9%, when the equivalence ratio was 0.37;
2) The combustion temperature has a trend to decrease when the equivalence ratio of gasification increases, but stays steady when ER=0.20~0.34;
3) Taking the equivalence ratio of gasification as 0.294, the maximum energy output of the system is 131.7kW and the overall efficiency of the system $\eta_{all} = 44.5\%$, with 21.6kW electricity and 110.1kW heat in hot water.

6. ACKNOWLEDGEMENT

This research programme is funded by the National Research Foundation (NRF), Prime Minister's Office, Singapore under its Campus for Research Excellence and Technological Enterprise(CREATE) programme. Grant Number R- 706-001-102-281, National University of Singapore.

7. REFERENCES

Bartela Ł, Kotowicz J, Dubiel K. Ekonomiczna ocena zasadności zastosowania silnika Stirlinga w układzie kogeneracyjnym opartym na zgazowaniu biomasy. Rynek Energii 2017; 129(2):80-7 [In Polish].

Channiwala SA, Parikh PP. A unified correlation for estimating HHV of solid, liquid and gaseous fuels. Fuel 2002; 81: 1051-63.

Sharma Shweta, Sheth Pratik N. Air-steam biomass gasification: Experiments, modeling and simulation. Energy Conversion and Management 2016; 110: 307-318.

Skorek-Osikowska Anna, Kotowicz Janusz, Uchman Wojciech. Thermodynamic assessment of the operation of a self-sufficient, biomass based district heating system integrated with a Stirling engine and biomass gasification. Energy 2017; 141: 1764-1778.

Smith GP, Golden DM, Frenklach M, Moriarty NW, Eiteneer B, Goldenberg M, et al., GRI 3.0, available at http://www.me.berkeley.edu/gri_mech/.

#132: Experimental study on dehumidification performance of vermiculite-based desiccant

Ziwei CHEN[1], Mariana Velasco CARRASCO[2], Saffa RIFFAT[3]

[1]Department of Architecture and Built Environment, Faculty of Engineering, University of Nottingham, University Park, Nottingham NG7 2RD UK, Ziwei.chen1@nottingham.ac.uk
[2]Department of Architecture and Built Environment, Faculty of Engineering, University of Nottingham, University Park, Nottingham NG7 2RD UK, ezxmv@nottingham.ac.uk
[3]Department of Architecture and Built Environment, Faculty of Engineering, University of Nottingham, University Park, Nottingham NG7 2RD UK, saffa.riffat@nottingham.ac.uk

High moisture content of indoor air can have serious health implications for occupants. Conventionally, dehumidification in buildings is realised by mechanical vapour compression, while desiccant materials with a high attraction for water vapour show promise for environmentally-friendly indoor air conditioning without overcooling or reheating problems. For dehumidification, solid desiccant materials rely on the adsorption of vapour molecules onto the surface to retain moisture, which is different from the liquid desiccant materials which absorb water molecules into the solution. Solid desiccant materials are of great importance to the solid desiccant-based system because the material characteristics affects the system performance markedly. Vermiculite as a natural and safe material has a long history of use in gardening and commercial horticultural, having great absorptive capabilities because of the concertina-like structure. However, few studies have been presented regarding its application for built environment and dehumidification performance for indoor humidity control. Composite desiccant materials are receiving wide attention owing to their improved property for dehumidification and regeneration. In this study, two vermiculite-based composite desiccants have been synthesised, with vermiculite used as a host matrix and $CaCl_2$, $MgSO_4$ as hygroscopic salts. Experimental tests have been conducted under various operating conditions using an advanced environmental chamber to simulate a hot and humid indoor environment. The experimental results demonstrate the feasibility of using vermiculite-based desiccants for indoor humidity control. Compared with silica gel-CaCl2, improved dehumidification performance is achieved by the vermiculite-based composite desiccants.

Keywords: solid desiccant; composite desiccant; dehumidification; humidity control, building applications

1. INTRODUCTION

Air dehumidification plays an important role in achieving indoor thermal comfort, especially in hot and humid climates. Various dehumidification technologies have been developed for use in the built environment, for example cooling coil, solid and liquid desiccant dehumidification and electrochemical dehumidification (Zhang, 2008). Mechanical vapour compression has been widely adopted to meet indoor cooling and dehumidification demands; this method cools air to dew point temperature to provide dehumidification and consumes more energy to reheat supply air to the desired temperature (Xiao et al., 2011). The drawbacks of conventional mechanical vapour compression also have other concerns, such as leakage, bacterial breeding, and fungi due to water condensation on the surface of the cooling coil. Alternatively, the desiccant-based technology provides an energy-efficient and cost-effective solution for indoor dehumidification. Desiccants such as hygroscopic substances are featured with strong affinity for water vapour and can be classified into solid and liquid desiccants depending on physical state. Comparatively, the solid desiccants are safer and more economical to utilise for dehumidification, relying on the adsorption of vapour molecules onto their surface to retain moisture (Yang et al., 2015). In recent years, a variety of new solid desiccants has been developed with improvements in water/vapour adsorption capability, regeneration ability, durability and stability (Pallav, 2018), for instance porous physical adsorbent and composite desiccant on the basis of two different desiccant materials. Figure 1 presents the detailed classification of the available solid desiccant materials based on the review of the literature (Zheng et al., 2014, Sultan et al., 2015, Jani et al., 2016, Rambhad et al., 2016, Wu et al., 2018, Pallav, 2018, Jani et al., 2015, Henninger et al., 2009).

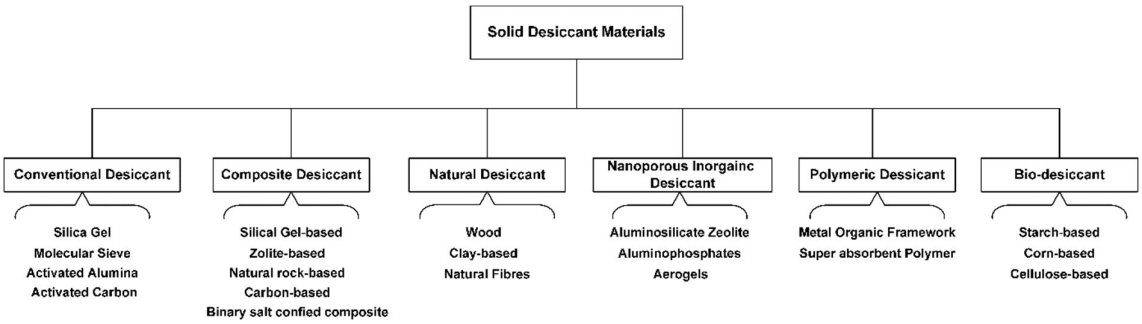

Figure 1: Classification of solid desiccant materials

Silica gel is the most common solid desiccant, being chemical inert, toxic-free, long life, low abrasion, low cost and having great feasibility under different conditions. The characteristics of silica gel and its applications have been widely explored both experimentally and theoretically. It has been stated in literature (Barbé et al., 2012) that silica gel is suitable for dehumidification at high relative humidity condition (e.g. 60-90%RH) at an indoor temperature range of 21 to 32℃. However, its high regeneration temperature (100-120℃) limits building applications. To address this shortcoming, a variety of composite desiccant materials have been developed by combining silica gel with other solid or liquid desiccants such as lithium chloride (Yu et al., 2014), calcium chloride (Wu et al., 2007) and strontium bromide (Courbon et al., 2017). Chen et al. (2015) developed a composite material using silica gel and two different types of polymers for dehumidification and an improvement of 41% in the sorption capacity compared with pure silica gel was observed. Because of the improved performance, various combinations of desiccant and salts have been investigated and composite desiccants are typically available in silica-based, mesoporous silicate-based and carbon-based. The dehumidification performance of composite desiccant materials depends greatly on the host and immersed salts which implies the importance of an optimal selection of the component materials and optimisation of material composition.

In terms of salts used for composite materials, the common types include halides, nitrates, sulphates of alkali and alkali earth metal that adsorb weakly on the surface of host material (Gordeeva and Aristov, 2012). Salts could offer an additional contribution to the sorption capability of the composite material compared to a single solid desiccant material. Instead of impregnating a single hygroscopic salt, more attention has been paid to applying salt mixtures into host materials for enhanced sorption ability. Alternatively, natural mineral clays can be another option as the host due to the material availability and low cost. Vermiculite is a natural, inorganic and non-toxic mineral that has been widely accepted from the building industry to gardening. Owing to the features of lightweight, chemically non-reactive, fire resistant and odourless, vermiculite has been a popular candidate for composite materials, especially for thermochemical storage applications. The macro-porous structure and high specific surface area make vermiculite perfect for salt impregnation to eliminate the deliquescence problem of salts. For instance, Zhang et al. (2016) assessed the thermochemical characterisation of vermiculite-$SrBr_2$. Casey et al. (2017) investigated the performance of nano-composite energy storage absorbents vermiculite-$CaCl_2$ and vermiculite-$CaCl_2$-$LiNO_3$ for domestic scale thermal energy storage. Jarimi et al. (2017) discussed nano-composite materials using $MgCl_2$-$MgSO_4$, $CaCl_2$-LiCl and $MgSO_4$-$CaCl_2$ salts mixtures impregnated into vermiculite. Their characterisation analysis demonstrated that the vermiculite-based composite materials are promising candidates for thermochemical heat storage systems compared to composite materials with individual salts. They also

suggested that vermiculite is appealing for building applications, because of low costs (e.g. $0.21-0.4/kg) and low regeneration temperature in the range of 50-80°C. On the other hand, Kumar and Yadav (2017) synthesised a composite desiccant using vermiculite, $CaCl_2$ and sawdust for fresh water production. Based on their experimental results, the composite material demonstrates great capabilities of adsorption and desorption.

In terms of indoor dehumidification application, vermiculite-based composite desiccant materials have not been widely adopted and evaluated. In this study, the feasibility of vermiculite-based composite desiccants for indoor dehumidification is evaluated through experimental work. Dehumidification performance of vermiculite-$CaCl_2$-$MgSO_4$ and vermiculite-$CaCl_2$ are also compared with that of silica gel and silica gel-$CaCl_2$.

2. COMPOSITE MATERIAL SYNTHESIS

In this study, two vermiculite-based composite desiccant materials (vermiculite-$CaCl_2$ and vermiculite-$CaCl_2$-$MgSO_4$) has been synthesised by impregnating hygroscopic salts $CaCl_2$ and $MgSO_4$ to the host material vermiculite. In addition, the composite desiccant material silica gel-$CaCl_2$ has been also produced for comparison.

2.1. Material selection and characteristics

Vermiculite is present as a lightweight filler and the thermophysical properties of vermiculite is listed in Table 1.

Table 1: Thermophysical properties of vermiculite (Aydin et al., 2015)

	Specific Heat	Specific Surface area	Porosity	Sorption Ability (water)
Vermiculite	1.08 kJ/kg.K	80-10 m^2/g	2.8 cm^3/g	0.03 kg.kg

Silica gel is an amorphous form of silicon dioxide and is presented as porous beads or granules. It absorbs water vapour up to 40% of its dry mass through physical adsorption into its internal pores without any chemical reaction (Zendehboudi et al., 2018). The salts used in this study are highly hygroscopic $CaCl_2$ and $MgSO_4$, which are deliquescent and dissolve without proper containment within a host matrix (Jarimi et al., 2017). The deliquescence relative humidity values of $CaCl_2$ and $MgSO_4$ are 28.1% and 92% at 25℃ respectively (Rumble et al., 2018). $CaCl_2$ has been regarded as a promising salt regarding sorption rate, heat storage capacity, hydrothermal performance and cyclic capability. On the other hand, $MgSO_4$ has high energy storage density and fast sorption kinetics. Using $CaCl_2$-$MgSO_4$ impregnated into vermiculite contributes to a lower regeneration temperature of the composite desiccant material, which is feasible for building application.

2.2. Material synthesis

Five steps have been followed to prepare the composite desiccant based on the method pioneered by Aristov et al. (1996). For mixtures of salt solutions of $CaCl_2$-$MgSO_4$, saturated solution of $CaCl_2$ and $MgSO_4$ were mixed with a mixing ratio of 2:1.

1. Weigh the required amount of vermiculite and fully dry the vermiculite using an oven to remove water;
2. Prepare saturated salt solution;
3. Mix the saturated salt solution with the host material vermiculite by adding the solution into the vermiculite in a container and constant stir as the salt solution soaks into the pores of vermiculite;
4. Ensure the vermiculite is uniformly impregnated by the salts by visual check whether a fully wetted transition takes place;
5. Dry the wetted composite material by placing into an oven to evaporate the water for full dehydration and ensure the salts are confined within the vermiculite.

In addition, silica gel- $CaCl_2$ composite adsorbent was produced by impregnating calcium chloride into the pore volumes of the host silica gel which mainly comprises the preparation of the aqueous of calcium chloride and the immersion of the silica gel in the solution. Aqueous $CaCl_2$ solution was prepared with mass concentration of 50% and was kept under ambient temperature for few hours for stabilisation and preventing crystallisation. The silica gel was prepared in a tank and the tank was placed in a water bath with a constant temperature of 90°C. Then the prepared aqueous solution was added to the tank, so that the silica gel soaked into the solution. Grains of microporous host silica gel were immersed thereafter in the solution and kept for 24-36 hours to allow the $CaCl_2$ solution to penetrate and fill all the pore volumes. Then, the composite desiccant was taken out from the tank and washed with water to avoid calcium chloride on the surface of the composite desiccant. After washing away the salt, the composite desiccants were placed inside an oven for drying under 80°C. During the drying process, the composite adsorbents were being taken out and weighed from time to time until their weight losses were found negligibly small.

Scanning Electron Microscope (SEM) was also used to visualise the morphology and microstructure of the produced composite desiccant. It can also be used to check whether hygroscopic salts are binding uniformly inside the matrix of the host material for better mass and heat transfer performance. An energy dispersive X-ray microanalysis (EDX) system was adopted, which is Philips (FEI) XL30 SEM. Figure 2 presents the SEM photos of vermiculite, vermiculite-$CaCl_2$, vermiculite-$CaCl_2$-$MgSO_4$ and silica gel-$CaCl_2$. As seen from Figure 2a, raw vermiculite has thin lamellas that provide sufficient surface area for accommodating a great quantity of salts. It can be noted in Figure 2b and 2c, unique structures have been formed on the vermiculite surface by impregnating salts.

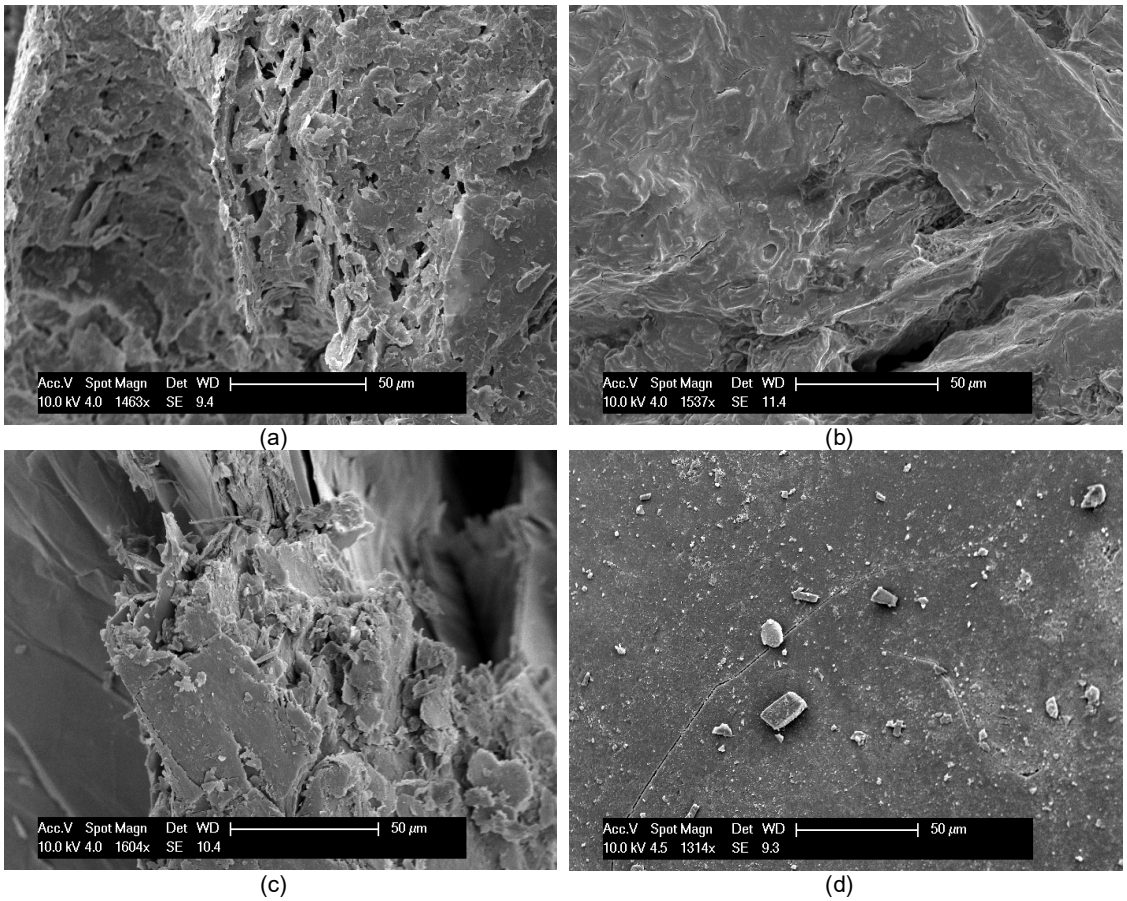

Figure 2: SEM photos of (a) vermiculite, (b) vermiculite-$CaCl_2$, (c) vermiculite-$CaCl_2$-$MgSO_4$ and (d) silica gel-$CaCl_2$

3. EXPERIMENTAL SET-UP

Experimental tests have been conducted in the Marmont Laboratory, University of Nottingham, UK. In order to test the dehumidification performance of the composite desiccant materials, a desiccant box has been designed and built, as seen in Figure 3. For testing, the composite desiccant material is placed on the wire mesh trays inside the desiccant box, so that it could dehumidify the passing moist air effectively. The inlet of desiccant box is connected to the environmental chamber, which is capable of providing air flow under different conditions.

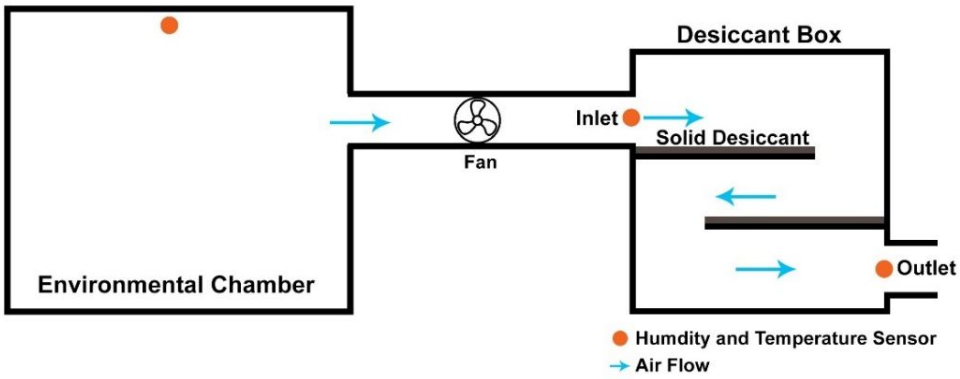

Figure 3: Schematic graph of the desiccant test rig

The main measurement instruments with their respective accuracies are listed in Table 1. A K-type thermocouple is used to measure the ambient temperature. Sensirion humidity and temperature sensors are installed at the air inlet and outlet of the desiccant box and corresponding air velocity is obtained by a Testo anemometer.

Table 1: Specifications of measurement instruments

Device	Measurement Range	Accuracy
RS K-type thermocouple probe	0-1100ºC	±0.75%
Sensirion EK-H4 humidity sensor	-40 to +125 ºC 0-100% RH	±0.75% ±2%
Testo thermo-anemometer 405i	0-30 m/s	±5%

Thermophysical properties of the moist air are determined based on the measured air temperature and relative humidity by referring to equations 1-3 (Tsilingiris, 2008)

Equation 1: $$P_s = 12.062 - \frac{4039.558}{T+235.379}$$

Equation 2: $$\%RH = \frac{P_w}{P_s} \times 100$$

Equation 3: $$\omega = 0.62198 \frac{P_w}{P_{A-P_w}}$$

Where:

- P_s = Saturated vapour pressure (bar)
- RH = Air relative humidity (%)
- P_w = Partial pressure of water vapour in the air (Pa)
- ω = Air humidity ratio (kg/kg$_{dryair}$)
- P_A = Atmospheric pressure of moist air (Pa)

In this study, the dehumidification performance is mainly assessed by moisture removal, which represents the change in the air humidity ratio across the desiccant box (i.e. $\omega_{inlet} - \omega_{outlet}$).

4. RESULTS AND DISCUSSION

Experimental tests have been conducted under different conditions which has been realised by varying the supply conditions of environmental chamber.

4.1. Dehumidification performance of vermiculite-$CaCl_2$

Tests have been conducted to evaluate the feasibility of Vermiculite-$CaCl_2$ for indoor dehumidification performance in hot and humid regions. Figure 4 shows experimental results under inlet conditions with temperature ranging from 26-28℃ and relative humidity 60-70%. The results show that Vermiculite-$CaCl_2$ is capable of absorbing moisture from the air to achieve dehumidification demand. It can also be seen that the test conditions affects the dehumidification performance of Vermiculite-$CaCl_2$ as higher moisture removal is observed at a hotter humid condition.

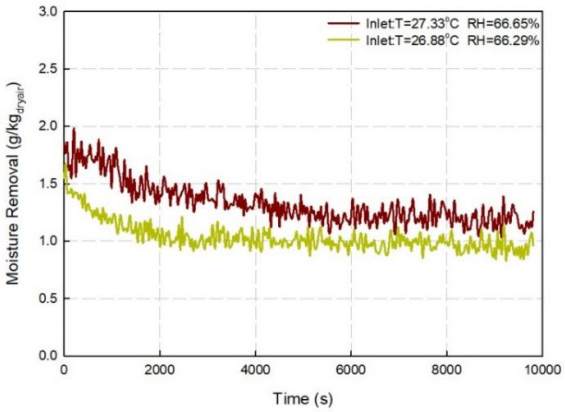

Figure 4: Moisture removal by Vermiculite-$CaCl_2$

4.2. Dehumidification performance of vermiculite-$CaCl_2$-$MgSO_4$

To investigate the feasibility of Vermiculite-$CaCl_2$-$MgSO_4$ for indoor dehumidification performance in hot and humid regions, tests have been carried out under different humidity conditions. The inlet condition supplied by the environmental chamber varies from 27-32°C and relative humidity 60-80%. Figure 5 presents the results of moisture removal performance during testing period. It can be noted that the composite desiccant material is feasible for dehumidification as moisture in the air can be effectively absorbed. Compared to the results of Vermiculite-$CaCl_2$, better dehumidification performance is obtained by Vermiculite-$CaCl_2$-$MgSO_4$. Due to the limited amount of composite materials used for testing, the moisture removal reduces gradually with time as desiccants may become saturated by absorbing moisture from the air. The dehumidification performance varies with the operating conditions, but the difference is not very significantly as seen in Figure 5.

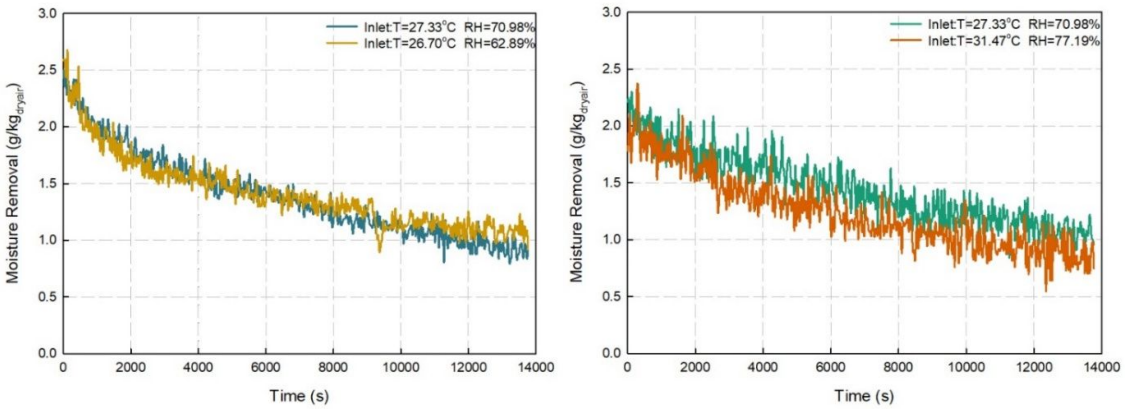

Figure 5: Moisture removal by Vermiculite-$CaCl_2$-$MgSO_4$

4.3. Comparison with Silica gel and Silica gel-$CaCl_2$

In order to compare the dehumidification performance of Vermiculite-$CaCl_2$ and Vermiculite-$CaCl_2$-$MgSO_4$ with silica gel and silica gel-$CaCl_2$, tests have been implemented for silica gel and silica gel-$CaCl_2$ under hot and humid conditions. Figure 6 demonstrates the moisture removal of silica gel and silica gel-$CaCl_2$ respectively. Comparatively, higher moisture removal can be archived by both Vermiculite-$CaCl_2$ and Vermiculite-$CaCl_2$-$MgSO_4$ under similar hot and humid condition, which indicates better dehumidification performance can be realised by using vermiculite-based composite desiccant.

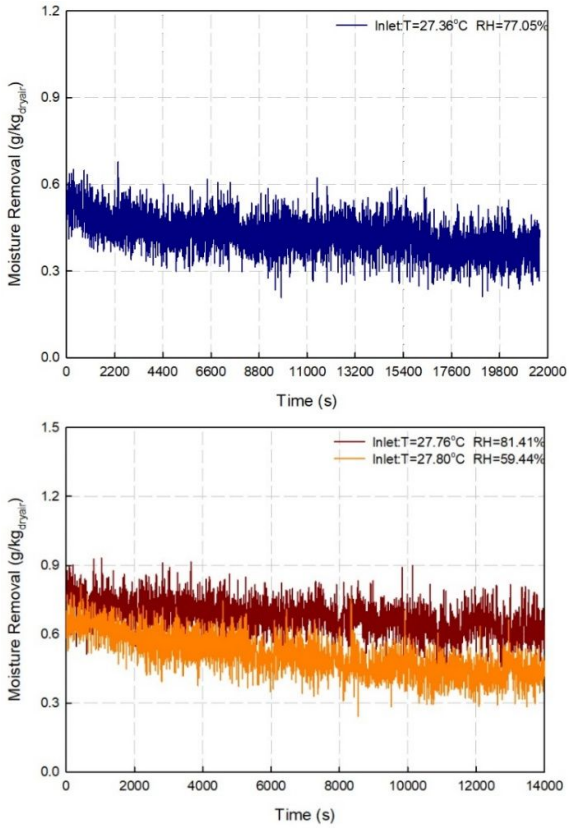

Figure 6: Moisture removal by silica gel (left) and silica gel-$CaCl_2$ (right)

Another performance evaluation metric can be used for comparison is the dehumidification effectiveness (i.e Equation 4), which is defined as the percentage of moisture removed in the desiccant box.

Equation 4: $$\varepsilon = \frac{\omega_{inlet} - \omega_{outlet}}{\omega_{inlet}}$$

Where:

- $\omega_{inlet} - \omega_{outlet}$ = air humidity ratio difference at inlet and outlet of desiccant box (kg/kg$_{dryair}$)
- ε = Dehumidification effectiveness

The highest dehumidification effectiveness of the Vermiculite-$CaCl_2$-$MgSO_4$ is 18.10%, while for Vermiculite-$CaCl_2$ is 12.73%, 6.58% for silica gel-$CaCl_2$ and 4.16% for silica gel.

5. CONCLUSION

In this study, the feasibility of using vermiculite-based composite material as desiccants for indoor dehumidification was assessed. Two different vermiculite-based composite desiccants (Vermiculite-$CaCl_2$ and Vermiculite-$CaCl_2$-$MgSO_4$) were produced and tests were conducted to investigate the dehumidification performance under different humid conditions. The experimental results reveal that the economical vermiculite-based composite desiccant materials can be an alternative option for indoor dehumidification humid regions. Compared to the dehumidification performance of silica gel and silica gel- $CaCl_2$, better dehumidification performance was observed for both Vermiculite-$CaCl_2$ and Vermiculite-$CaCl_2$-$MgSO_4$. Further investigations on different vermiculite-based composite desiccant materials under a variety of operating conditions are recommended for future work and the regeneration capacity can be evaluated for building application.

6. REFERENCES

Aristov, Y. I., Tokarev, M. M., Cacciola, G. & Restuccia, G. 1996. Selective water sorbents for multiple applications, 1. CaCl2 confined in mesopores of silica gel: Sorption properties. Reaction Kinetics and Catalysis Letters, 59, 325-333.

Aydin, D., Casey, S. P. & Riffat, S. 2015. The latest advancements on thermochemical heat storage systems. Renewable and Sustainable Energy Reviews, 41, 356-367.

Barbé, B., Gillet, P., Beelaert, G., Fransen, K. & Jacobs, J. 2012. Assessment of desiccants and their instructions for use in rapid diagnostic tests. Malaria Journal, 11, 326.

Casey, S. P., Aydin, D., Elvins, J. & Riffat, S. 2017. Salt impregnated desiccant matrices for 'open' thermochemical energy conversion and storage – Improving energy density utilisation through hygrodynamic & thermodynamic reactor design. Energy Conversion and Management, 142, 426-440.

Chen, C.-H., Hsu, C.-Y., Chen, C.-C. & Chen, S.-L. 2015. Silica gel polymer composite desiccants for air conditioning systems. Energy and Buildings, 101, 122-132.

Courbon, E., D'ans, P., Permyakova, A., Skrylnyk, O., Steunou, N., Degrez, M. & Frère, M. 2017. A new composite sorbent based on SrBr2 and silica gel for solar energy storage application with high energy storage density and stability. Applied Energy, 190, 1184-1194.

Gordeeva, L. G. & Aristov, Y. I. 2012. Composites 'salt inside porous matrix' for adsorption heat transformation: a current state-of-the-art and new trends. International Journal of Low-Carbon Technologies, 7, 288-302.

Henninger, S. K., Habib, H. A. & Janiak, C. 2009. MOFs as Adsorbents for Low Temperature Heating and Cooling Applications. Journal of the American Chemical Society, 131, 2776-2777.

Jani, D. B., Mishra, M. & Sahoo, P. K. 2016. Solid desiccant air conditioning – A state of the art review. Renewable and Sustainable Energy Reviews, 60, 1451-1469.

Jani, J. B., Rajput, V. P. & Shukla, M. 2015. A Review on Performance Anyalysis of Different Desiccant Materials for a Desiccant Cooling System. International Journal of Advance Research in Engineering, Science & Technology, 2, 2394-2444.

Jarimi, H., Aydin, D., Zhang, Y., Ding, Y., Ramadan, O., Chen, X., Dodo, A., Utlu, Z. & Riffat, S. 2017. Materials characterization of innovative composite materials for solar-driven thermochemical heat storage (THS) suitable for building application. International Journal of Low-Carbon Technologies, 13, 30-42.

Kumar, M. & Yadav, A. 2017. Composite desiccant material "CaCl2/Vermiculite/Saw wood": a new material for fresh water production from atmospheric air. Applied Water Science, 7, 2103-2111.

Pallav, G. 2018. Advanced Desiccants for HVAC System: A Review. International Journal of Engineering Technology Science and Research, 5, 221-224.

Rambhad, K. S., Walke, P. V. & Tidke, D. J. 2016. Solid desiccant dehumidification and regeneration methods—A review. Renewable and Sustainable Energy Reviews, 59, 73-83.

Rumble, J. R., Lide, D. R. & Bruno, T. J. 2018. CRC handbook of chemistry and physics : a ready-reference book of chemical and physical data.

Sultan, M., El-Sharkawy, I. I., Miyazaki, T., Saha, B. B. & Koyama, S. 2015. An overview of solid desiccant dehumidification and air conditioning systems. Renewable and Sustainable Energy Reviews, 46, 16-29.

Tsilingiris, P. T. 2008. Thermophysical and transport properties of humid air at temperature range between 0 and 100 °C. Energy Conversion and Management, 49, 1098-1110.

Wu, H., Wang, S. & Zhu, D. 2007. Effects of impregnating variables on dynamic sorption characteristics and storage properties of composite sorbent for solar heat storage. Solar Energy, 81, 864-871.

Wu, X. N., Ge, T. S., Dai, Y. J. & Wang, R. Z. 2018. Review on substrate of solid desiccant dehumidification system. Renewable and Sustainable Energy Reviews, 82, 3236-3249.

Xiao, F., Ge, G. & Niu, X. 2011. Control performance of a dedicated outdoor air system adopting liquid desiccant dehumidification. Applied Energy, 88, 143-149.

Yang, Y., Rana, D. & Lan, C. Q. 2015. Development of solid super desiccants based on a polymeric superabsorbent hydrogel composite. RSC Advances, 5, 59583-59590.

Yu, N., Wang, R. Z., Lu, Z. S. & Wang, L. W. 2014. Development and characterization of silica gel–LiCl composite sorbents for thermal energy storage. Chemical Engineering Science, 111, 73-84.

Zendehboudi, A., Angrisani, G. & Li, X. 2018. Parametric studies of silica gel and molecular sieve desiccant wheels: Experimental and modeling approaches. International Communications in Heat and Mass Transfer, 91, 176-186.

Zhang, L.-Z. 2008. Total Heat Recovery : Heat and Moisture Recovery from Ventilation Air, New York, NY, USA, Nova Science Publishers, Inc.

Zhang, Y. N., Wang, R. Z., Zhao, Y. J., Li, T. X., Riffat, S. B. & Wajid, N. M. 2016. Development and thermochemical characterizations of vermiculite/SrBr2 composite sorbents for low-temperature heat storage. Energy, 115, 120-128.

Zheng, X., Ge, T. S. & Wang, R. Z. 2014. Recent progress on desiccant materials for solid desiccant cooling systems. Energy, 74, 280-294.

#134: A novel heat storage system with solar ammonia water resorption heat pump cycle based on concentration difference

Peng CHU[1,*], Teng JIA[2,*], Yanjun DAI[3,*]

Institute of Refrigeration and Cryogenics, Shanghai Jiao Tong University, 800 Dongchuan Road, Shanghai, and Engineering Research Center of Solar Power and Refrigeration, MOE, China
[1]dr.chu@sjtu.edu.cn
[2]hitjiateng@sjtu.edu.cn
[3]yjdai@sjtu.edu.cn

With energy consumption for heating areas increasing, the application of solar energy has become more and more widespread in recent years. However, shortages due to discontinuity and weak guarantee rates are the main limitations of solar energy. The aim of this study is to define and validate a new heat storage system with an ammonia water resorption heat pump based on concentration difference, which would improve the utilisation range and time of solar energy in heating areas. The system can be divided into two parts: one is for heat storage in day time, while the other part is working for heating at night. A theoretic model is established and analysed based on thermodynamics and properties of ammonia water. The results of the simulation show that the coupled working pressure ranges (the high pressure and low pressure of the system) are determined by the given temperature of the absorbers and generators in the cycle. With optimising the pairs of the pressure in the given condition (the high/low pressure generator/ absorber of 90°C, 45°C, 40°C and 5°C), an acceptable pair of working pressure is carried out (1.5Mpa/0.48Mpa), and the coefficient of performance (COP) could reach about 1.51, while the energy storage density (ESD) could also reach about 54kwh/m^3.

Keywords: heat storage; concentration difference; ammonia water; resorption heat pump

1. INTRODUCTION

Due to the instability and intermittent nature of solar radiation, energy storage systems are usually required in solar air conditioning systems to achieve continuous and stable operation and to prolong the working hours of solar air conditioners. At present, solar energy storage systems mainly have three forms: sensible heat storage, phase change energy storage and thermochemical energy storage (Ibrahim *et al,* 2017; Mohamed *et al*, 2017). Currently, sensible heat storage and phase change energy storage is the most researched, and the most extensive application of sensible heat storage in practical engineering is also the most mature (Zhang *et al,* 2016). Due to the shortcomings of low energy storage density and heat loss in sensible heat storage (Dincer, 2002), related scholars have, in recent years, begun to research thermochemical energy storage technology with higher energy density and smaller heat loss (Cot-Gores *et al,* 2012; Deshmukh *et al,* 2017). They have also summarised the current research progress on the mechanism, classification, cycle and materials of solar energy absorption and adsorption energy storage systems.

Wilbur *et al.* (Wilbur & Mitchell, 1975) analysed the performance of the storage system of two storage tanks and found that the size of cooling tower shrunk in concentration difference cooling storage system to that in a normal system. Ibrahim (Ibrahim *et al,* 2017) also conducted a theoretical study on the characteristics of the solar-driven lithium bromide solution concentration difference cooling storage system with two solution tanks, and analysed the effects of cooling storage temperature and pressure on performance. The results showed that the system coefficient of performance (COP) is 0.69 and the energy storage density can reach 119.6 kWh/m^3 in a complete cooling charging and discharging cycle.

Han (Han *et al,* 2017) proposed a novel heat-driven ammonia water energy storage system. It is found that the generator inlet temperature and inlet concentration have a positive effect on ESD, while the effect of ambient temperature could be neglected. Additionally, the maximum ESD could reach 523 MJ/m^3 when the generator temperature and inlet concentration are 180°C and 0.7 kg/kg respectively.

In this paper, a novel heat storage system is proposed and a mathematical model is established to validate the feasibility of the system. Then, a series of indices are proposed to evaluate the performance of the system. Finally, some parameters are analysed to seek the impact on the system performance.

2. SYSTEM DESCRIPTION

The schematic diagram of the energy storage system is shown in Figure 1. The system consists of the following components: high pressure generator (HPG), high pressure absorber (HPA), low pressure generator (LPG), low pressure absorber (LPA), solution heat exchanger (SHX), solution pump (SP), the throttle valve (TV), solution mixing tank (SMT), strong solution tank (SST), weak solution tank (WST) and pipelines. The whole system has two modes: energy charging mode and energy discharging mode, and the detail working principle of the system is described as follows.

The energy charging mode: shown in Figure 1(a). The initial solution flows from point 0 to point 4 through the heat exchangers and the solution pump. In this stage, the concentration of the solution keeps constant, while the temperature gets higher. Then the solution is separated to two flows to flow into the HPG and HPA. In HPG, the ammonia solution is heated by the heat source (such as solar energy), and generates high pressure vapour as well as weak solution. After that, the weak solution would flow into the weak solution tank and be stored, while the high pressure vapour flows into the HPA and then is absorbed by the solution flows from point 6. Finally, the concentrated solution generated from HPA flows into the strong solution tank. In this process, the concentration difference between the two solution tanks is produced.

The energy discharging mode: shown in Figure 1(b). The concentrated and diluted solution generated in energy storage mode flows from the solution tanks to LPA and LPG, respectively. In LPG, the solution gains heat from ambient air and generates low pressure vapour and diluted solution in state 13. After flowing into LPA, the low pressure vapour is absorbed by the weak solution from WST. In this process, the LPA releases heat to the supply water, which is used for floor heating in winter. Finally, the solution at point 13 and point 14 get mixed in SMT, and then flows through heat exchanger and solution pump into the SST.

It is remarkable that in this system the temperature of the heat source is not so strict, which means that the system could work steadily in a quite loose temperature range. Therefore, even when the solar energy is considered inadequate in winter or cloudy weather, the system could couple the solar collectors well.

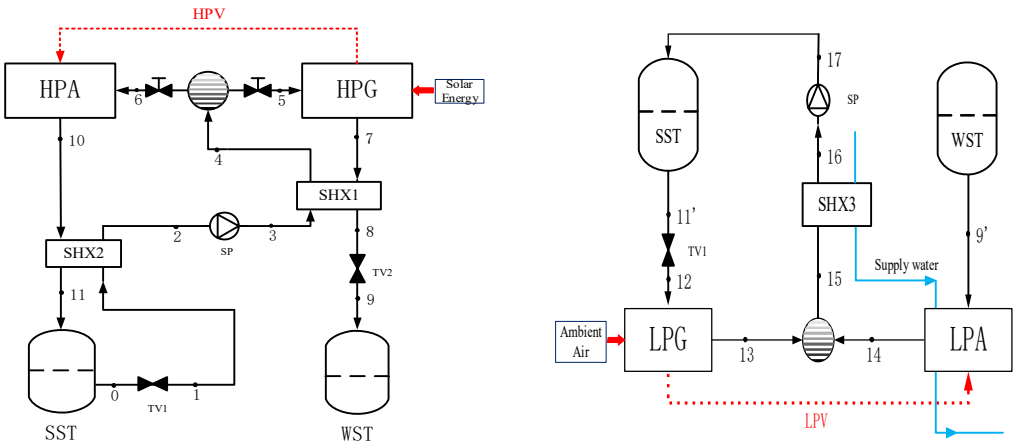

(a) *Energy charging mode* (b) *Energy discharging mode*

Figure 1: Schematic diagram of the system

3. MATHEMATICAL MODEL

To evaluate the feasibility and performance of system, a numerical model is built and analysed in Matlab (2017b), while the thermodynamic properties of the ammonia water are obtained with Refprop9.1.

3.1. Simplification assumptions

By consulting the results presented in previous literature, analysing the dynamic impact of the ammonia water on the system would not only make the whole model more complicated, but would also have little meaning (Jia & Dai, 2018). In this paper, the mathematical model of the system is conducted based on thermodynamic analysis. To simplify the model, some reasonable assumptions are made as below:

1) The system runs under steady state;
2) Pressure drops and heat loss along the pipelines and main components are neglected;
3) The output solutions of the HPG, HPA, LPG and LPA are saturated;
4) The solution flowing through the throttle valve is an adiabatic process;
5) The solution flowing through the solution pump and mixing in the SMT are all adiabatic processes.
6) The energy charging mode runs six hours per day, which the energy discharging mode runs 12 hours per day.

3.2. Balance equation of each component

The main components of the system include: HPG, HPA, LPG, LPA, solution pumps, solution heat exchangers, throttle valves, solution mixed tank, solution separated tank, strong solution tank and weak solution tank. Each component can be regarded as a CV (control volume) with energy transfer and mass transfer. Then a series of equations can be obtained according to the mass and energy conservation equations:

Equation 1: Conservation of mass:

$$\sum_i m_{out} - \sum_i m_{in} = 0$$

Where:

- m = mass flow of the solution or vapour (kg/s)

Equation 2: Conservation of NH_3:

$$\sum_i \left(m_{out}\ x_{out}\right) - \sum_i \left(m_{in}\ x_{in}\right) = 0$$

Where:

- x = concentration of the solution or vapour

Equation 3: Conservation of energy:

$$\left(\sum_i \left(m_{out}\ h_{out}\right)-\sum_i \left(m_{in}\ h_{in}\right)\right)+\left(\sum_i Q_{out}-\sum_i Q_{in}\right)+\left(\sum_i W_{out}-\sum_i W_{in}\right)=0$$

Where:

- $h=$ enthalpy of the solution or vapour (J)
- $Q=$ heat flow exchanged of the component (J/s)
- $W=$ work flow exchanged of the component (J/s)

Apply the Equation 2 in the component LPG and LPA, we can get:

Equation 4: ammonia conservation in LPG:

$$m_{13}\ x_{13}+m_{v2}\ x_{v2}-m_{12}\ x_{12}=0$$

Equation 5: ammonia conservation in LPA:

$$m_{14}\ x_{14}-m_{v2}\ x_{v2}-m_{9'}\ x_{9'}=0$$

3.3. Solution process of the model

With the assumptions in section 3.1, we can get that the mass flow and concentration in generators are related to those in absorbers. Then we can get the circulation ratio f and coefficient k of the LPG, LPA, HPG and HPA:

Equation 6: circulation ratio f of HPG:

$$f_1=\frac{m_5}{m_{v1}}=\frac{x_{v1}-x_7}{x_{15}-x_7}$$

Equation 7: coefficient k of HPA:

$$k_1=\frac{m_{10}}{m_{v1}}=\frac{x_{v1}-x_{15}}{x_{10}-x_{15}}$$

Equation 8: circulation ratio f of LPG:

$$f_2=\frac{m_{12}}{m_{v2}}=\frac{x_{v2}-x_{13}}{x_{12}-x_{13}}$$

Equation 9: coefficient k of LPA:

$$k_2=\frac{m_{14}}{m_{v2}}=\frac{x_{v2}-x_9}{x_{14}-x_9}$$

The main parameters can be obtained in Table 1.

Table 1: Main parameters in each component

State points	Mass flow rate	Pressure
1	m7+m10	P_L
2	m1	P_L
3	m1	P_H
4	m1	P_H
5	f1*mv1	P_H
6	(k1-1)*mv1	P_H
7	(f1-1)*mv1	P_H
8	(f1-1)*mv1	P_H
9	(f1-1)*mv1	P_L
10	k1*mv1	P_H
11	k1*mv1	P_H
12	f2*mv2	P_L
13	(f2-1)*mv2	P_L
14	mv2*k2	P_L
HPV	2*f2*mv2/k1	P_H
LPV	1	P_L

Then the results can be obtained by following the computational flowchart in Figure 2 after multiple iterations.

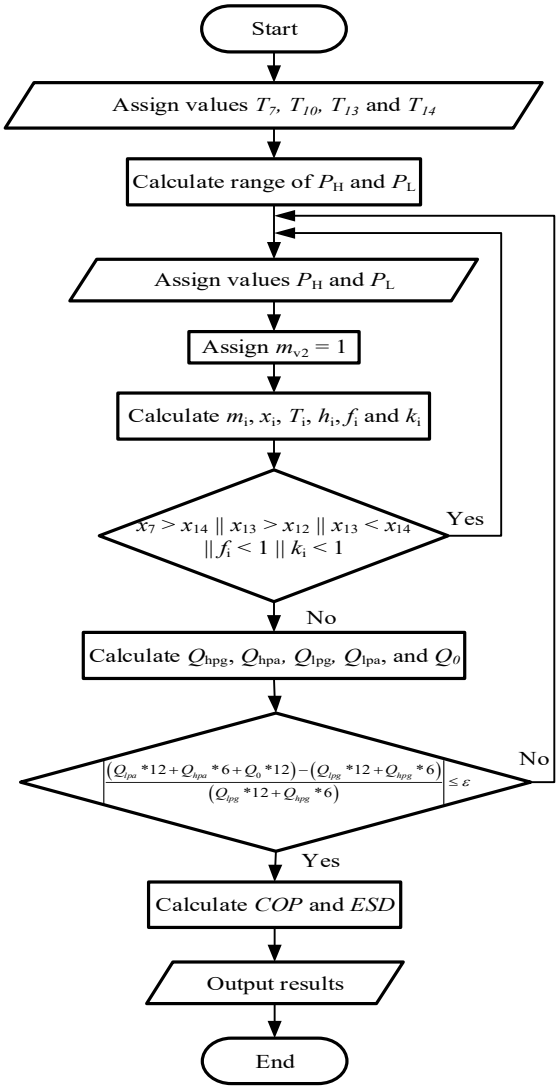

Figure 2: The computational flowchart of the mathematical model

3.4. Performance indices

In this paper, performance of the energy storage system is evaluated in terms of the coefficient of performance (COP) and the energy storage density (ESD) of the system

Equation 10: COP of the system:

$$COP = \frac{Q_{hpa} + 2Q_{lpa} + 2Q_0}{Q_{hpg}}$$

Where:

Q_0 = the heat flow exchanged between the supply water and the two-phase flow solution (J/s)

Equation 11: ESD of the system:

$$ESD = \frac{12\left(Q_{lpa} + Q_0\right)}{1000V}$$

Where:

$V =$ the total volume of the solution tanks (m^3)

4. RESULTS AND DISCUSSION

The performance of the system in terms of feasible P_H/P_L pairs, heat source temperature, COP and ESD are investigated as following:

4.1. Feasible P_H/P_L pairs

The feasible P_H/P_L pairs are calculated as Figure 3 under the initial conditions in Table 2.

Table 2: Initial working conditions

Parameters	Values (°C)
HPG outlet temperature T7	90
HPA outlet temperature T10	40
LPG outlet temperature T13	5
LPA outlet temperature T14	35

As is shown in Figure 3, the minimum P_H and P_L of the system under the given conditions are respectively 0.1 MPa and 0.54Mpa, which the maximum P_H of the system could reach 1.52MPa. In addition, for given high pressure P_H values, the range of P_L extends with the increase of the P_H value. The reason for this phenomenon is that the concentration of ammonia solution flows out of HPG and HPA increases with the high pressure, which results that the LPG and LPA could work in a wider P_L condition. Furthermore, it is remarkable that the feasible P_H /P_L pairs are only obtained in the given conditions in Table 2. If the initial condition changes, the ranges of the pressures should be calculated again.

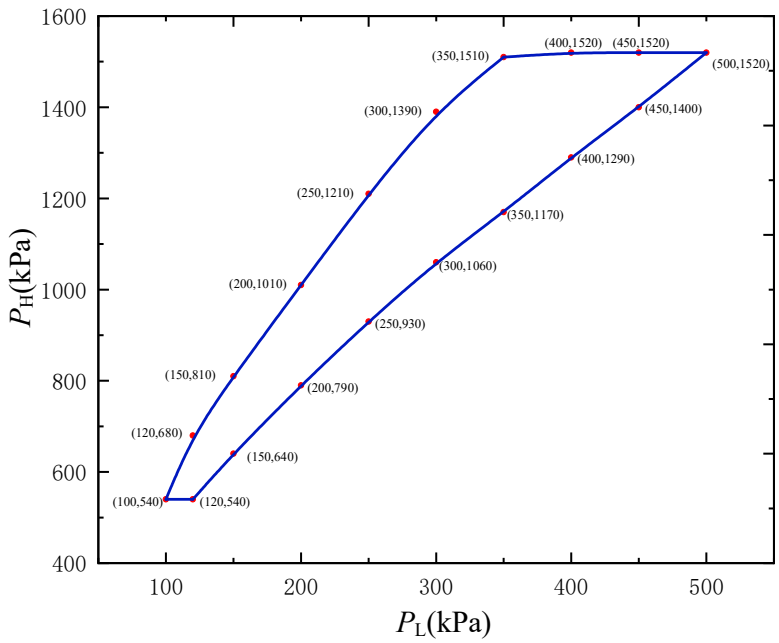

Figure 3: Feasible P_H/P_L pairs

4.2. Influence of P_H/P_L on COP and ESD

By consulting the results in section 4.1, a series of pressure ranges are chosen to evaluate the impact on system COP and ESD, and the results are shown in Figure 4 and Figure 5. In Figure 4, the curve shows the relationship between COP/ ESD and the low working pressure of the system, when the high working temperature is set as 1.45 MPa while the other conditions are the same as Table 2. From Figure 4, we can get that the ESD of the system

increases with the increasing low working pressure, and the system ESD could reach about 50 kWh/m^3. Similarly, the ESD of the system rises with the pressure at the beginning. But when the pressure reaches about 0.4 MPa, the system COP begins to drop when the pressure increases continually, and the maximum COP of the system is about 1.4 under the given condition.

In Figure 5, it is shown that the relationship between high working pressure and COP/ESD of the system under the condition P_L = 0.45 MPa. From the figure, we could obtain that the COP increases with the pressure, and the COP could reach about 1.48 finally. The ESD of the system increases with the pressure when the pressure is lower than 1.42 MPa, but after that it drops significantly with increasing pressure and the maximum ESD of the system is about 48.5 kWh/m^3. Therefore, to realise better system performance, it is important to choose a suitable pair of working temperatures.

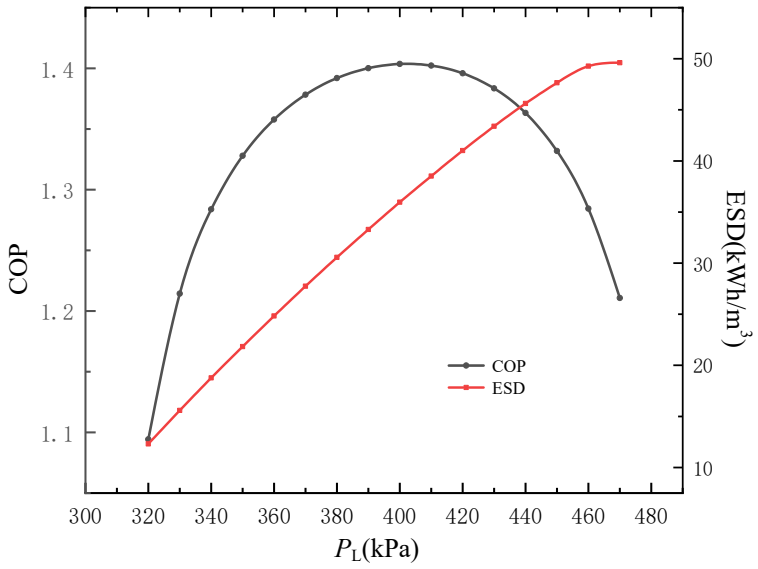

Figure 4: Effect of P_L on COP and ESD (P_H = 1450kPa)

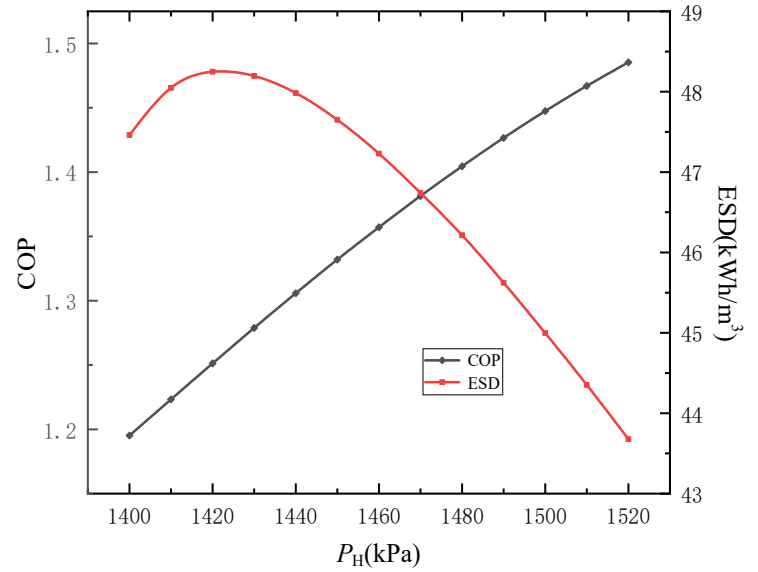

Figure 5: Effect of P_H on COP and ESD (P_L = 450kPa)

4.3. Influence of heat source temperature on COP and ESD

Due to the temperature limitations of solar energy collectors in winter, the heat source temperature is of great importance to drive the system. In this part, the relationship between the system performance and the heat source temperature is investigated. The initial conditions are the same as that in Table 2, and the P_H and P_L are 1.45 MPa and 0.40 MPa, respectively. The impact of heat source temperature on system performance is shown in Figure 6. From the results, the ESD of the system increases with the temperature, and finally reaches about 105 kWh/m^3. As for system COP, the increasing trend with the temperature is significant before 92°C, after that the COP almost keeps constant or slightly decreases with the temperature. On the one hand, to realise higher energy storage density, higher driven temperature is necessary, on the other hand, we should also recognise that higher heat source temperature may be hard to realise with solar energy, and the system COP also has less demand on very high temperature.

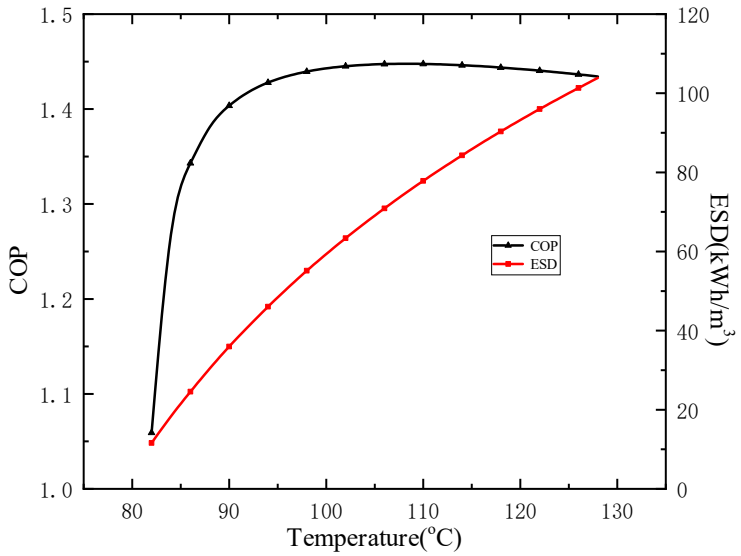

Figure 6: Effect of heat source temperature on COP and ESD (P_H = 1450kPa, P_L=400kPa)

5. CONCLUSION

In this paper, a novel energy storage system with ammonia water resorption heat pump based on concentration difference is investigated. To evaluate the performance of the system, a mathematical model has been established based on thermodynamics theorem, energy and mass conservation equations. The main results are:

(1) Under the given conditions, the range of high working pressure is from 0.54 MPa to 1.52 MPa, while the range of low pressure is from 0.1 MPa to 0.5 MPa corresponding with the high working pressure.
(2) The ESD increases with low working pressure, and the COP increases with the pressure at the beginning, but then drops after a certain point, while the phenomenon in that with high working pressure is in contrast.
(3) Both the system ESD and COP increase with the heat source temperature, but when the temperature is higher than 92°C, the COP keeps almost constant. So simply enhancing the heat source temperature to a large degree may have little influence on system performance.
(4) The minimum heat source temperature demand under the given conditions could reach 82°C, which could extend the use of solar energy usage.

6. ACKNOWLEDGEMENT

The authors acknowledge the support of the National Science Foundation of China, under contract No. 51736006.

7. REFERENCES

Cot-Gores, J., Castell, A. & Cabeza, L. F. (2012) Thermochemical energy storage and conversion: A-state-of-the-art review of the experimental research under practical conditions. *Renewable and Sustainable Energy Reviews*, 16(7), 5207-5224.

Deshmukh, H., Maiya, M. P. & Murthy, S. S. (2017) Study of sorption based energy storage system with silica gel for heating application. *Applied Thermal Engineering*, 111, 1640-1646.

Dincer, I. (2002) On thermal energy storage systems and applications in buildings. *Energy and buildings*, 34(4), 377-388.

Han, B.-C., Cheng, W.-L., Li, Y.-Y. & Nian, Y.-L. (2017) Thermodynamic analysis of heat driven Combined Cooling Heating and Power system (CCHP) with energy storage for long distance transmission. *Energy Conversion and Management*, 154, 102-117.

Ibrahim, N. I., Al-Sulaiman, F. A., Rahman, S., Yilbas, B. S. & Sahin, A. Z. (2017) Heat transfer enhancement of phase change materials for thermal energy storage applications: A critical review. *Renewable and Sustainable Energy Reviews*, 74, 26-50.

Jia, T. & Dai, Y. (2018) Development of a novel unbalanced ammonia-water absorption-resorption heat pump cycle for space heating. *Energy*, 161, 251-265.

Mohamed, S. A., Al-Sulaiman, F. A., Ibrahim, N. I., Zahir, M. H., Al-Ahmed, A., Saidur, R., Yılbaş, B. S. & Sahin, A. Z. (2017) A review on current status and challenges of inorganic phase change materials for thermal energy storage systems. *Renewable and Sustainable Energy Reviews*, 70, 1072-1089.

Wilbur, P. J. & Mitchell, C. E. (1975) Solar absorption air conditioning alternatives. *Solar Energy*, 17(3), 193-199.

Zhang, H., Baeyens, J., Caceres, G., Degreve, J. & Lv, Y. (2016) Thermal energy storage: Recent developments and practical aspects. *Progress in Energy and Combustion Science*, 53, 1-40.

#138: Simulation of a micro channel separate heat pipe (MCSHP) under low airflow rate

Sikai ZOU, Quan ZHANG*, Chang YUE, Sheng DU

College of Civil Engineering, Hunan University, Changsha, Hunan 410082, China
**Corresponding Author: quanzhang@hnu.edu.cn*

Water-cooled micro channel separate heat pipe (MCSHP) is an efficient cooling technology for data centres. To optimise the design of MCSHP, some numerical models have been proposed. However, the matched air-side and refrigerant side heat transfer correlations of evaporators in these numerical models were suitable to predict the heat transfer performance of separate heat pipe where the Reynolds number is higher than 75; they are unsuited to predict the heat transfer performance of MCSHP under partial load and low airflow rate. In this study, a steady-state numerical model with a combination of ε-NTU methods was developed. The existed air-side heat transfer correlations of louvered fin heat exchanger and refrigerant side two-phase heat transfer correlations of micro channel heat exchanger were tested in the model under different airflow rates with the optimal refrigerant filling ratio. The mean absolute deviation between the selected model and experiment was less than 10%. By using this model, the thermal performance under partial heating load and airflow rate were analysed. The simulation results show that the MCSHP has superior start-up performance to ensure the data centre thermal safety under low airflow rates (200m3/h-1500m3/h) and partial heating load rates (19.2%-51.1%). The developed model can be used to improve the controllability and energy-saving performance of MCSHP.

Keywords: numerical model; micro channel separate heat pipe; heat transfer; correlation

1. INTRODUCTION

As a powerful engine for industrial intellectualisation, the number and scale of data centres are increasing rapidly. The energy consumption of data centres accounts for 1.3% of the world's energy consumption (Ebrahimi, 2014). In order to ensure thermal safety, the energy consumption of data centre cooling system accounts for 30% to 50% of the total energy consumption (Ham, 2015; Ling, 2018). As one of the most widely used data centre cooling system, Computer Room Air Conditioner (CRAC) has some shortcomings: (1) local hot spots due to airflow mal-distribution; (2) low utilisation of natural cold source due to sensible heat transfer. Researchers have explored some more efficient cooling systems, such as micro channel separate heat pipe (MCSHP) due to being closer to the servers. The MCSHP is a kind of loop thermosyphon consisting of four sectors: a micro channel exchanger as the evaporator, a coolant distribution unit (CDU) as the condenser, and two connecting pipes between them (Ling, 2016). The evaporator of MCSHP is located on the backplate of the rack, cooling servers by refrigerant two-phase flow boiling heat transfer. By shortening air supply distance and latent heat transfer, this cooling method improves the efficiency of the cooling system. Due to those advantages, some researchers have carried out more insightful research on the heat transfer characteristics of MCSHP (Ling, 2016; Ding, 2016; Ling, 2016; Ding, 2017). The results show that the MCSHP has a better utilisation rate of natural cold source than CRACs.

Unlike the CRACs, loop thermosyphon has no pump drive, which reduces energy consumption of the cooling system. Therefore, design of the evaporator and condenser exchanger is the main determinant of the heat transfer performance of loop thermosyphon. In order to optimise the structure design, some researchers have established numerical heat transfer models of loop thermosyphon with the airflow rate ranged from 1500 m^3/h to 6000 m^3/h (Zhang, 2015; Ling, 2015; Ling, 2017). According to recent research (China Data Center Annual Research Report on Cooling Technology Development 2017), the average utilisation rate of data centres is only 50.61%, compared with 29.01% for large scale data centres in China. To save energy, fans of the evaporator will adjust the airflow rate according to the exhaust airflow temperature. The decrease of airflow rate will affect the air-side heat transfer coefficient of the evaporator (Ling, 2016), and the air-side Reynolds number would be below 75, which exceeds the prediction range of the existing air-side correlations of the louvered fin heat exchangers (Chang, 1997; Kim, 2002; Dong, 2007; Kim, 2008). Meanwhile, it has been pointed out that the partial heating load will affect the start-up and heat transfer performance of heat pipe systems (Hong, 2015; Maydanik, 2017). At present, the existing refrigerant side heat transfer correlations mostly fitted by the data obtained from normal operating mechanical refrigeration systems and their applicability to MCSHP under partial heating loads needs further study.

This paper aims to establish a steady-state numerical model of a water cooled MCSHP under low airflow rate (<1500 m3/h) and partial heating load with the optimal refrigerant filling ratio. In order to accurately predict the heat transfer performance, ε-NTU method with suitable correlations is used for the calculation of the micro channel heat exchanger of evaporator and the plate heat exchanger of CDU. The simulation results and experimental results are compared and verified. Finally, the thermal performance under partial heating load and airflow rate were analysed.

2. EXPERIMENTAL METHODS

2.1. Experimental setup

In order to determine the optimal refrigerant filling ratio and thermal performance of MCSHP under low airflow rate, the experiments were carried out in an enthalpy difference laboratory. The schematic diagram is shown in Figure 1. The heating load was simulated by indoor airflow provided by the enthalpy difference laboratory, the temperature and humidity of indoor air were set at 35°C and 45%, respectively, which are the hot aisle temperature and humidity regulated by Code for design of data centres (Code for design of data centres GB50174-2017). The hot air was driven by eight exhaust fans to transfer the heat to the evaporator on backplate of the rack, and was cooled by phase heat transfer of refrigerant inside the evaporator. Then vaporised refrigerant entered the CDU through the vapor pipe, and was condensed by heat transfer with chilled water. The CDU of MCSHP was cooled by 12°C chilled water supplied by a 30kW chiller, the chilled water flow rate was regulated by a variable frequency pump. Finally, condensed refrigerant went back to the evaporator and entered the next circulation by gravity. The structure parameters of MCSHP are shown in Table. 1. The exhaust airflow from the rack was collected by the containment, and airflow rate was measured by the airflow measuring system of the enthalpy difference laboratory using air enthalpy difference method. The rated airflow rate of those exhaust fans is 1800 m^3/h. During the test, the airflow rate can be adjusted by controlling power of exhaust fans. Refrigerant temperatures and pressures at the inlet and outlet of evaporator and condenser ①-④ were measured by PT100 platinum resistors and AKS32 pressure transmitters. Chilled water temperatures at the inlet and outlet of condenser ⑤-⑥ were also measured by PT100 platinum resistors. Indoor, rack inlet and outlet air temperatures and humidity ⑦-⑨ were measured by enthalpy difference laboratory.

Table 1: The structure parameters of MCSHP.

Structure parameters	Value	Structure parameters	Value
Liquid/Vapor pipe diameter (mm)	25	Louver pitch P_l(mm)	1
Liquid inlet diameter (mm)	16	Number of flat tube N_t	30
Vapor outlet diameter (mm)	19	Number of row N_r	1
Transverse flat tube pitch P_f (mm)	8	Number of micro channel in flat tube	19
Micro channel pitch P_m (mm)	0.4	Plate length, L_c (mm)	466
Flat tube height H_t (mm)	2	Plate width, P_w (mm)	111
Flat tube width F_w (mm)	25.4	Area of the plate, A_c (m^2)	0.079
Flat Tube distance L (mm)	1580	Plate thickness, δ_c (mm)	0.4
Fin pitch F_p (mm)	2	Angle of the corrugation, β (°)	30
Fin thickness δ_f (mm)	0.105	Corrugation amplitude, b_c (mm)	2.4
Fin width B_f (mm)	25	Plate pitch, P_p (mm)	2.8
Fin width H_f (mm)	8	Number of plates	20
Louver angle θ (°)	30	Number of plates effective in heat transfer, N_c	18
Louver length L_l (mm)	7		

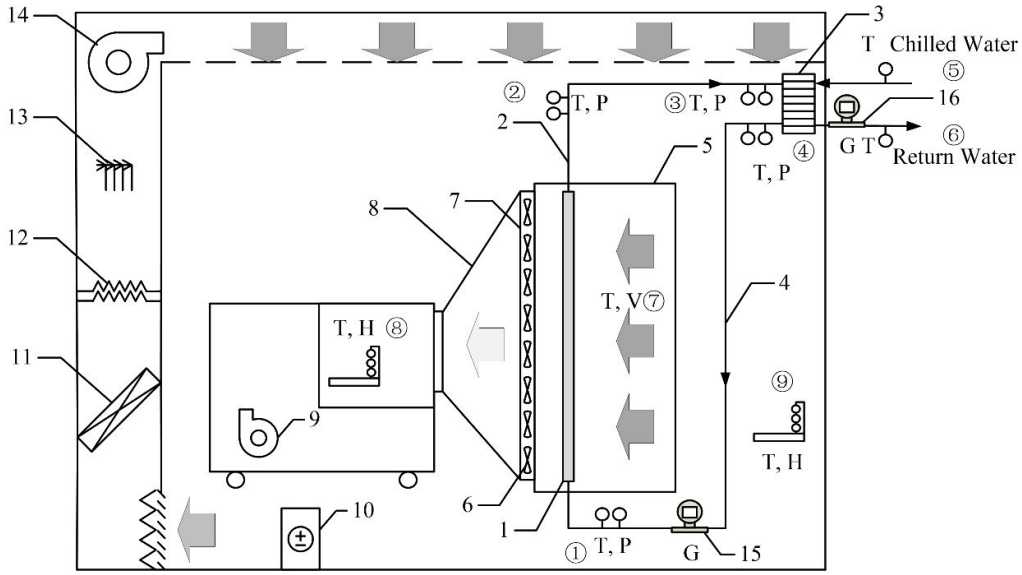

T-Temperature
P-Pressure
H-Humidity
V-Airflow rate
1.Micro channel evaporator
2. Vapor pipe
3. CDU
4. Liquid pipe
5. Rack
6. Exhaust fan
7. Backplate
8. Airflow containment
9. Speed adjusting fan
10. Heater
11. Evaporator
12. Heater
13. Humidifier
14. Fan
15. Coriolis type meter
16. Magnetic flow meter

Figure 1: Schematic diagram of a MCSHP and testing facility.

2.2. Tests and results

Before thermal characteristics test of the MCSHP, the optimal filling ratio should be determined. It has been reported that filling ratio is a main factor that determines the thermal performance of the MCSHP, and the optimal filling ratio is independent of the variation of airflow rate (Ling, 2016). The test conditions are shown in Table 2.

The airflow rate was constant at 1800m^3/h during the filling ratio test, and the filling charge increased from 0.6kg to 1.8kg, with each increase of 0.2kg, corresponding to the filling ratio from 27% to 84%. Figure 2 shows the cooling capacity of MCSHP under various filling ratios. The cooling capacity is calculated as in Equation 1. The results show that the cooling capacity of MCSHP increased with the filling ratio and reaches the maximum value when the filling ratio reached 65%. With the further increased of filling ratio, the cooling capacity of MCSHP began to decrease. It indicates that the optimal filling ratio of tested MCSHP is 65%.

Equation 1: $$Q = m_w(h_{w,out} - h_{w,in})$$

Where:

- Q = cooling capacity of MCSHP (W)
- m_w = chilled water mass velocity (kg/s)
- $h_{w,in}$ enthalpy of the chilled water inlet (kJ/kg)
- $h_{w,out}$ = enthalpy of the chilled water outlet (kJ/kg)

Then the thermal performance of MCSHP with an optimal filling ratio was tested under 600 m^3/h -1800m^3/h. The air-side heat transfer coefficient decreased with the decrease of airflow rate, which resulting in the cooling capacity of the heat pipe decreases. Under 600 m^3/h airflow rate, the heat transfer capacity of MCSHP was 3642W, which was 51.1% lower than that of normal airflow (1800 m^3/h).

Table 2: Test conditions.

	Range
Filling charge (kg)	0.6, 0.8, 1, 1.2, 1.4, 1.6, 1.8
Indoor air temperature (•)	35
Indoor air humidity (%)	55
Chilled water temperature (•)	12
Chilled water flow rate (m^3/h)	1.71
Airflow rate (m^3/h)	600, 800,1000, 1200, 1400, 1600, 1800

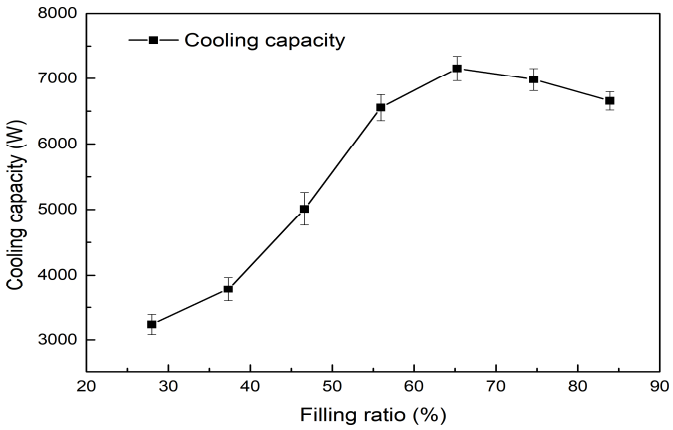

Figure 2: Cooling capacity under different refrigerant filling ratios.

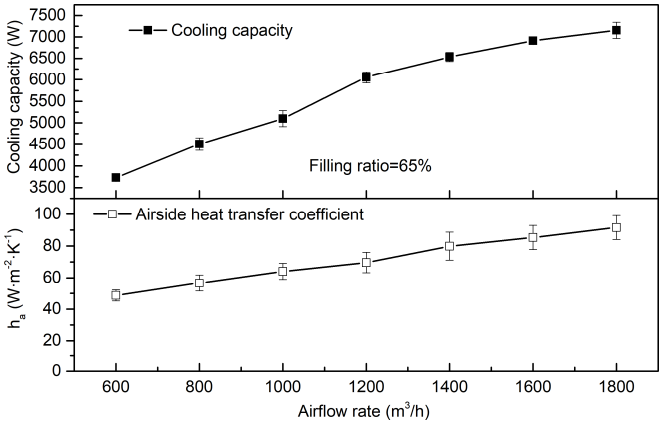

Figure 3: Cooling capacity and air-side heat transfer coefficient under low flow rate.

7. SIMULATION MODELS

The simulation model of a MCSHP comprise three modules: a micro channel evaporator, a water cooled condenser, and connection tubes. The models of evaporator and condenser used a finite volume method to predict the total cooling capacity, air-side heat transfer coefficient and pressure drop, and refrigerant mass flow rate, heat transfer coefficient and pressure. Each flow channel of working fluid inside the evaporator and condenser were divided into 100 segments. The heat transfer coefficient and outlet temperatures of refrigerant and other working fluids was calculated by ε-NTU method (Kim, 2002). The refrigerant thermodynamic properties were acquired from the NIST Refrigerant Database REFPROP (Lemmon, 2002). The working fluids along the system cycle abides by momentum (pressure), energy (enthalpy) and mass conservation, as follows:

Equation 2: $$\int \mathrm{d}p = 0$$

Equation 3: $$\int \mathrm{d}h = 0$$

Equation 4: $$\int \mathrm{d}m = \sum m_i$$

Where:

- p = pressure of the working fluid (Pa)
- h = enthalpy of the working fluid (kJ/kg)
- m, m_i = mass flow rate of the refrigerant (kg/h)

Figure 4 illustrates the flow chart of the simulation model of the MCSHP. As shown in Figure 4, the refrigerant mass flow rate, enthalpy and pressure are unknown therefore three iterations are needed for simulation of the MCSHP. Two heat transfer rates are needed to be supposed and two iterations are needed in one control volume. The heat transfer coefficient and pressure drop of working fluids are calculated by correlations in Table 3.

Table 3: Heat transfer and pressure drop correlations for simulation.

Working fluid	Item		Correlation
Refrigerant	Single phase	Heat transfer coefficient	Churchill,1977
		Pressure drop	Gnielinski,1975
	Evaporator two-phase	Heat transfer coefficient	Gungor and Winterton,1987
			Sun, 2009
			Shah, 1982
			Kandlikar, 1990
			Lee and Lee, 2001
			Chen, 1966
		Pressure drop	Friedel, 1979
	Condensation two-phase	Heat transfer coefficient	Han, 2003
		Pressure drop	Shah, 1988
	Connection tubes	Pressure drop	Coleman, 2004
Air-side		Heat transfer coefficient	Dong, 2007
			Kim, 2002
			Chang, 1997
			Kim, 2008
		Pressure drop	Kim, 2008
Water side		Heat transfer coefficient	Dittus, 1985

The following assumptions were made for constructing this model:

(1) the refrigerant, air and water in the evaporator and condenser have a one-dimensional homogeneous flow;
(2) the airflow is evenly distributed among the micro channel exchanger;
(3) the refrigerant flow rate, temperature and pressure are evenly distributed in every channel of evaporator and condenser;
(4) the axial heat transfers and heat dissipation of working fluids are neglected.

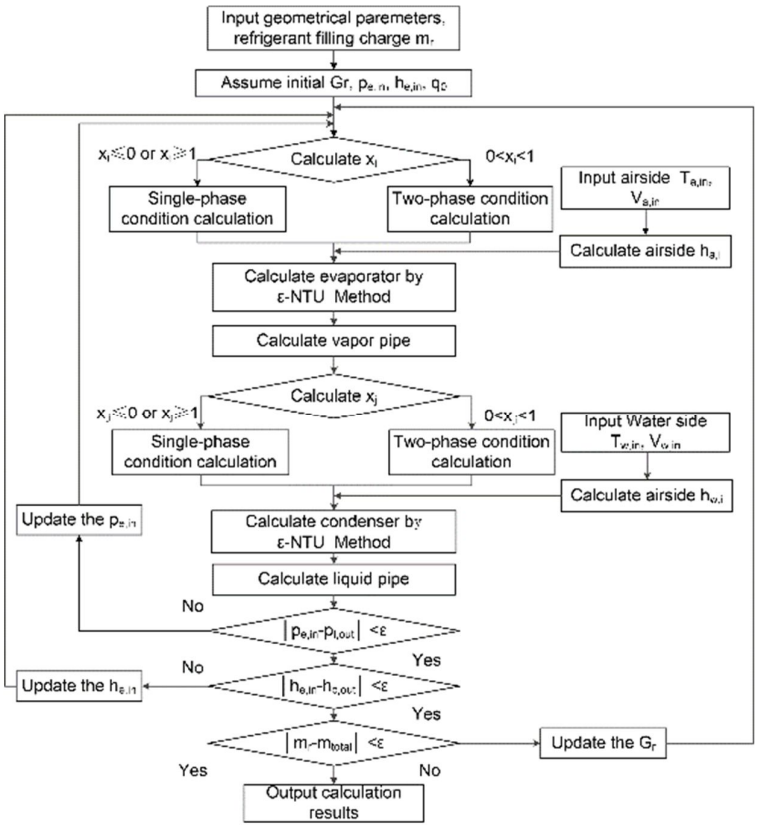

Figure 4: Flow chart of the MCSHP modelling.

3.1. Evaporator model and heat transfer correlations selecting

In the evaporator model, airside and refrigerant side heat transfer coefficient of each segment were calculated by heat transfer correlations using ε-NTU method. Therefore, the applied correlations with insufficient prediction accuracy will lead to inaccurate prediction of evaporator model and reduce the calculation accuracy of other modules. The following heat transfer correlations have been widely used to predict the air-side heat transfer coefficient of micro channel heat exchangers: Chang (1997); Kim (2002); Dong (2007) and Kim (2008). Figure 5 describes the experimental results and the prediction results of these correlations under low airflow and Reynolds number. Compared with the experimental data, Kim correlation (2002) predicted best with a mean absolute deviation (MAD) of 9.62%, according to Equation 5. While other correlations unpredicted the experimental results, and their MADs are more than 30%. Thus, Kim (2002) correlation was selected to calculated the air-side heat transfer coefficient of MCSHP.

Equation 5:

$$\mathrm{MAD} = \frac{1}{N}\frac{\left|h_{\mathrm{pred}} - h_{\mathrm{exp}}\right|}{h_{\mathrm{exp}}}$$

Where :

- h_{pred} = heat transfer coefficient calculated by heat transfer correlation
- h_{exp} = heat transfer coefficient obtained by experiments

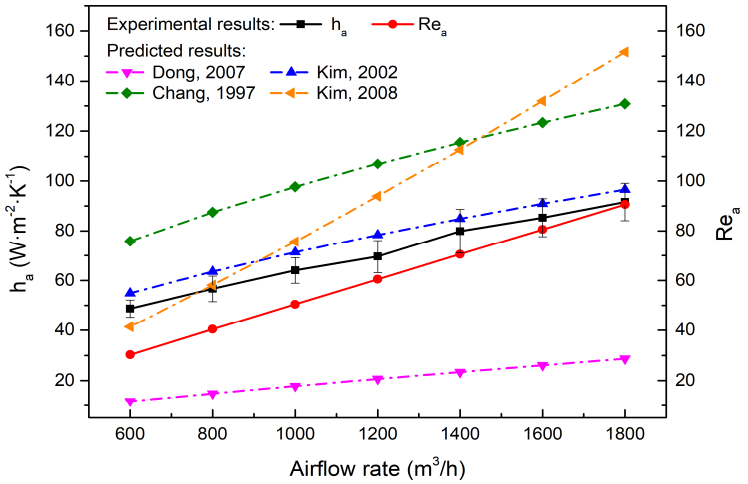

Figure 5: Experimental and predicted air-side heat transfer coefficients under low flow rate.

The correlations used for the heat transfer and pressure drop calculation are summarised in Table 3. The existing two-phase boiling heat transfer correlations were fitted from the experimental data obtained by the mechanical refrigeration system. Compared with the mechanical cooling system, the decrease of airflow rate will not just lead to the decrease of wall heat flux, but to the decrease of mass flow rate. Thus, the suitability of existing correlations in the micro channel evaporator of the MCSHP is unclear. During the development of the evaporator model, six two-phase boiling heat transfer correlations (Chen, 1966; Gungor, 1987; Kandlikar, 1990; Lee, 2001; Sun, 2009; Shah, 1982) suitable for microchannel heat exchangers are adopted.

3.2. Condenser model

In the plate heat exchanger model, water side and refrigerant side heat transfer coefficient of each segment were calculated by heat transfer correlations using ε-NTU method. When the refrigerant was in single phase, the refrigerant heat transfer coefficient was calculated by Gnielinski (Gnielinski, 1975) correlation. Han (Han, 2003) correlation was used to predict the refrigerant heat transfer coefficient in two phase region and the water side heat transfer coefficient was calculated by Dittus (Dittus, 1985) correlation.

3.3. Connection tube model

In connection tube model, the vapor pipe, liquid pipe and collecting pipe in the MCSHP were considered adiabatic, so the refrigerant flow inside them was treated as isoenthalpy flow. The pressure drop was calculated by Equation 6-10. Coleman (Coleman, 2004) correlation is used to calculate the compact pressure drop at the collecting pipe.

Equation 6: $$\Delta p_{f,r} = \left(\lambda_f l + \sum \xi_f\right)\frac{\rho_r u_r^2}{2g}$$

Equation 7: $$\Delta p_g = \rho_r g \Delta H$$

Equation 8: $$C_c = 1 - \frac{1-\sigma_c}{2.08(1-\sigma_c)+0.5371}$$

Equation 9: $$\Delta p_c = \frac{(2.26G_r)^2}{2\rho_r}\left[\left(1-\sigma_c^2 C_c^2\right) - 2C_c(1-C_c)\right]$$

Equation 10: $$\Delta p_{total} = \Delta p_{f,r} + \Delta p_g + \Delta p_c$$

Where:

- $\Delta p_{f,r}$ = friction pressure drop (Pa)
- Δp_g = gravity pressure drop (Pa)
- Δp_c = compact pressure drop (Pa)
- λ_f = frictional resistance coefficient
- ξ_f = local resistance coefficient
- ρ_r = refrigerant density (kg/m^3)
- u_r = refrigerant mass velocity (m/s)

- G_r = refrigerant mass flux (kg/m^2•s)
- ΔH = height difference of the tube inlet and outlet (m)
- σ_c = ratio of microchannel cross-sectional area to collector cross-sectional area
- C_c = compact coefficient, g is the gravitational acceleration (m/s^2)

8. RESULTS AND DISCUSSION

4.1. Model verification

The model was established in Matlab R2016a. Figure 6 shows the comparison of the cooling capacity between experimental results and predictions under different airflow rates by using six existing correlations. As the figure shows, Gungor, Kandlikar and Shah correlations had good prediction results with MADs of less than 5%. The MAD of the predicted results by using Lee correlation was 9.4%. The prediction results by using Chen and Sun correlations were lower than the cooling capacities of the experimental database with MADs of more than 10%. The comparison shows that two strictly empirical correlations (Kandlikar, 1990; Shah, 1982) and one superposition correlations (Gungor, 1987) showed good prediction accuracy for cooling capacities of the micro channel evaporator under low airflow rate and partial heating load.

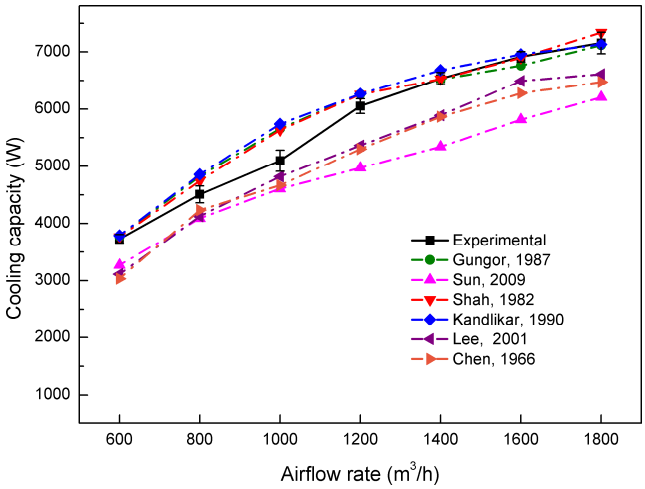

Figure 6: Comparison of the cooling capacity between calculated and experimental results by six two-phase heat transfer correlations.

The prediction results of heat transfer correlations on evaporator outlet temperature were also verified, those parameters would affect the prediction accuracy of the evaporator wall temperatures, the refrigerant temperature and pressure in other components. The results of four heat transfer correlations with higher prediction accuracy are compared in Figure 7. According to the (ESA HP standard first issue PSS-49), when the maximum temperature difference of the refrigerant in the evaporator is higher than 5°C, this phenomenon is considered to dry out. The temperature difference between the inlet and outlet of the evaporator predicted by Gungor and Kandlikar correlations were higher than the experimental data, and dry out was wrongly predicted under the airflow rate larger than 1400m^3/h. Shah correlation showed good prediction accuracy of evaporator outlet temperature under the airflow rate lower than 1200 m^3/h, and its MAD was 6.2%, which is similar to Lee correlation (MAD=4.5%).

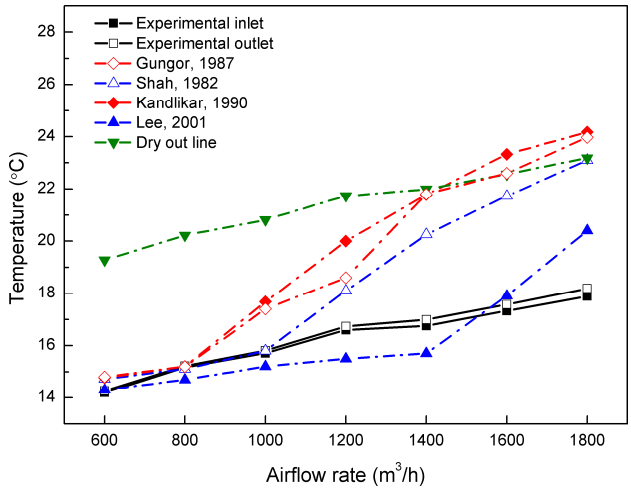

Figure 7: Comparison of the refrigerant outlet temperature between calculated and experimental results by heat transfer correlations.

As the starter engine of MCSHP, the prediction accuracy of mass flow rate in evaporator would affect the calculation results of heat transfer performance and pressure drop of other parts. Prediction results of four correlations agreed well with the experimental data; their MADs were all lower than 6% as shown in Figure 8. Lee correlation showed the best predicted with the MAD of 2.7%.

Overall, cooling capacity, refrigerant evaporator outlet temperature and mass flow rate calculated by the Shah correlation provided the best agreement with the experimental results. The Shah correlation will be used in the evaporator model of the MCSHP.

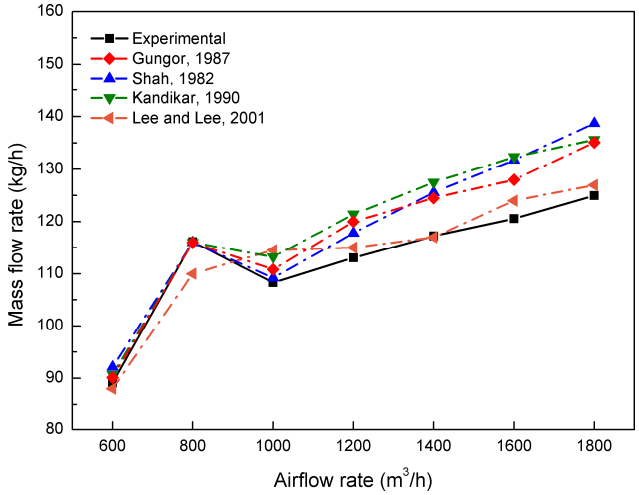

Figure 8: Comparison of the mass flow rate between calculated and experimental results by heat transfer correlations.

4.2 Analysis and discussion

Figure 9 shows the cooling capacity and airflow outlet temperature of the MCSHP under low airflow rate (200m^3/h -600m^3/h). The cooling capacity of MCSHP decreased gradually with the decreasing airflow rate. Under 200 m^3/h airflow rate, the cooling capacity was 1368W, which was 19.2% of the cooling capacity of MCSHP under 1800 m^3/h airflow rate. The outlet airflow temperature of the evaporator was 13.5°C, which was lower than the exhaust temperature specified in (Code for design of data centres GB50174-2017). The simulation results show that the MCSHP has superior start-up performance to meet the data centre cooling requirements under low airflow rate and partial low heating load rate (19.2%-51.1%).

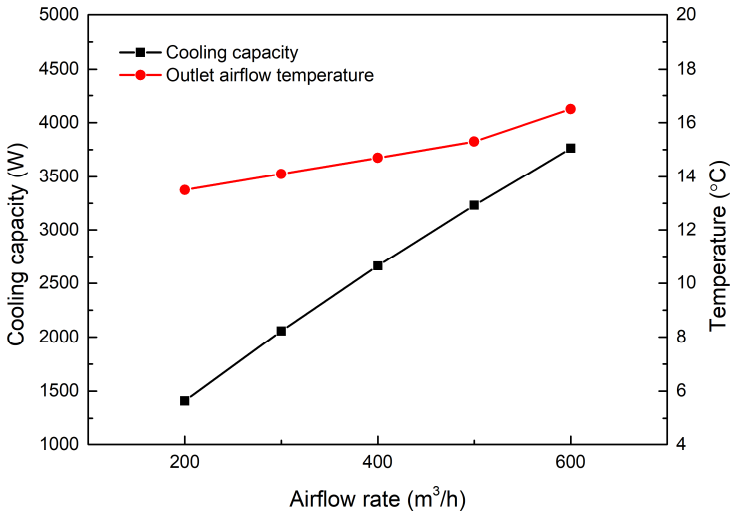

Figure 9: Cooling capacity and outlet airflow temperature under low airflow rate: 200m³/h -600m³/h.

9. CONCLUSION

In this study, a steady-state numerical model of a water cooled MCSHP with the optimal refrigerant filling ratio was developed using ε-NTU method under low flow rate and partial heating load. Finite volume method was used to establish evaporator and the condenser models and integrate to simulate the system of the MCSHP. Four air-side heat transfer correlations and six boiling heat transfer correlations were selected by comparing the predicted results with the experimental results. Kim and Bullard correlation provides the most accurate prediction of air-side heat transfer coefficient with the MAD of 9.62%. The MAD between the cooling capacity, refrigerant evaporator outlet temperature and mass flow rate predicted by the developed model using Shah correlation and experiment results were 3.3%, 6.2% and 4.7% under low airflow rate. The verification result showed that developed numerical model can provide accurate prediction for heat transfer performance of MCSHP under low flow rate. The thermal performance under partial heating load and airflow rate were simulated and analysed by the developed model. Due to the superior start-up performance, MCSHP can ensure the data centre thermal safety under low airflow rate (200m³/h-1500m³/h) and partial heating load rate (19.2%-51.1%). The developed model can be used to improve the controllability and energy-saving performance of MCSHP.

10. REFERENCES

Chang, Y. J., & Wang, C. C.. (1997). A generalized heat transfer correlation for iouver fin geometry. *International Journal of Heat & Mass Transfer*, 40(3), 533-544.

Chen, & J., C., (1966). Correlation for boiling heat transfer to saturated fluids in convective flow. *Ind.eng.chem.proc.des.dev*, 5(3), 322-329.

China Data Center Annual Research Report on Cooling Technology Development 2017 (2018), Beijing: China Architecture & Building Press.

Churchill S W.. (1977). Comprehensive Correlating Equations for Heat, Mass and Momentum Transfer in Fully Developed Flow in Smooth Tubes. *Industrial & Engineering Chemistry Fundamentals*, 16(1), 109–116.

COLEMAN, J.. (2004). An experimentally validated model for two-phase sudden contraction pressure drop in microchannel tube headers. *Heat Transfer Engineering*, 25(3), 9.

Ding, T., He, Z. G., Hao, T., & Li, Z. . (2016). Application of separated heat pipe system in data center cooling. *Applied Thermal Engineering*, 109(109), 207-216.

Ding, T., Cao, H. W., He, Z. G., & Li, Z.. (2017). Experiment research on influence factors of the separated heat pipe system, especially the filling ratio and freon types. *Applied Thermal Engineering*, 118, 357-364.

Dong, J., Chen, J., Chen, Z., Zhang, W., & Zhou, Y.. (2007). Heat transfer and pressure drop correlations for the multi-louvered fin compact heat exchangers. *Energy Conversion and Management*, 48(5), 1506-1515.

Dittus, F. W., & Boelter, L. M. K.. (1985). Heat transfer in automobile radiators of the tubular type. *International Communications in Heat and Mass Transfer*, 12(1), 3-22.

Ebrahimi, K., Jones, G. F. , & Fleischer, A. S.. (2014). A review of data center cooling technology, operating conditions and the corresponding low-grade waste heat recovery opportunities. *Renewable and Sustainable Energy Reviews*, 31(2), 622-638.

Friedel, L.. (1979) Improved friction pressure drop correlation for horizontal and vertical two-phase pipe flow. European: Two-Phase Flow Group Meeting, Paper E, vol. 2.

Gnielinski V.. (1975). New equations for heat and mass transfer in the turbulent flow in pipes and channels. *International Chemical Engineering*, 16(2), 359-368

Gungor K.E., Winterton R.H.S.. (1987) Simplified general correlation for saturated flow boiling and comparison with data. *Chemical Engineering Research and Design*, 65(2), 148-156.

Han, D., Lee, K., Kim, Y.. (2003). The characteristics of condensation in brazed plate heat exchangers with different chevron angles. *J. Korean Phys. Soc.* 43 (1), 66–73.

Ham, S. W., Kim, M. H., Choi, B. N., & Jeong, J. W.. (2015). Simplified server model to simulate data center cooling energy consumption. *Energy and Buildings*, 86, 328-339.

Heat Pipe Qualification Requirements. (1983). Paris: ESA PSS-49 Issues 2.

Kim, M. H., & Bullard, C. W.. (2002). Air-side thermal hydraulic performance of multi-louvered fin aluminum heat exchangers. *International Journal of Refrigeration*, 25(3), 390-400.

Kim, N. H., & Cho, J. P.. (2008). Air-side performance of louver-finned flat aluminum heat exchangers at a low velocity region. *Heat and Mass Transfer*, 44(9), 1127-1139

Lee, H. J., & Lee, S. Y.. (2001). Heat transfer correlation for boiling flows in small rectangular horizontal channels with low aspect ratios. *International Journal of Multiphase Flow*, 27(12), 2043-2062.

Lemmon E.W., Huber M.L., McLinden M.O.. (2002). NIST reference fluid thermodynamic and transport properties–REFPROP.

Ling, L., Zhang, Q., Yu, Y., & Liao, S.. (2015). Study on thermal performance of micro-channel separate heat pipe for telecommunication stations: Experiment and simulation, *International Journal of Refrigeration*, 59, 198-209.

Ling, L., Zhang, Q., Yu, Y., Liao, S., & Sha, Z.. (2016). Experimental study on the thermal characteristics of micro channel separate heat pipe respect to different filling ratio. Applied Thermal Engineering, 102, 375-382.

Ling, L., Zhang, Q., Yu, Y., & Liao, S.. (2016). Experimental investigation on the thermal performance of water cooled multi-split heat pipe system (mshps) for space cooling in modular data centers. *Applied Thermal Engineering*, 107, 591-601.

Ling, L., Zhang, Q., Yu, Y., Wu, Y., Liao, S., & Sha, Z.. (2017). Simulation of a micro channel separate heat pipe (mcshp) under low heat flux and low mass flux. *Applied Thermal Engineering*, 119, 25-33.

Ling, L., Zhang, Q., Yu, Y., Ma, X., & Liao, S.. (2018). Energy saving analysis of the cooling plant using lake water source base on the optimized control strategy with set points change. *Applied Thermal Engineering*, 130, 1440-1449.

Maydanik Yu.F., Vershinin S.V., Chernysheva M. A.. (2017). Experimental study of an ammonia loop heat pipe with a flat diskshaped evaporator using a bimetal wall, *Applied Thermal Engineering*, 126, 643-652.

Ministry of housing and urban-rural development of the People's Republic of China, General administration of quality supervision, inspection and quarantine of the People's Republic of China. Code for design of data centers (GB50174-2017). (2017). Beijing: China planning Publishing House.

Shah R. K., Focke W. W.. (1988). Plate heat exchangers and their design theory. Washington: Heat Transfer Equipment Design, 227–254.

Shah M. M.. (1982). Chart correlation for saturated boiling heat transfer: equations and further study. *ASHRAE Trans*, 88, 185–196.

Sun, L., & Mishima, K.. (2009). An evaluation of prediction methods for saturated flow boiling heat transfer in mini-channels. *International Journal of Heat and Mass Transfer*, 52(23-24), 5323-5329.

Yang, S., Tao, W.. (2006). Heat Transfer, fourth ed. Beijing: Heiger Education Press.

Zhang, H., Shao, S., Xu, H., Zou, H., Tang, M., & Tian, C.. (2015). Numerical investigation on integrated system of mechanical refrigeration and thermosyphon for free cooling of data centers. *International Journal of Refrigeration*, 60, 9-18.

Zhang, H., Shao, S. , Xu, H., Zou, H., & Tian, C.. (2015). Integrated system of mechanical refrigeration and thermosyphon for free cooling of data centers. *Applied Thermal Engineering*, 75, 185-192.

#139: Numerical study of concentrated photovoltaic system indirect cooling using water and phase change material

Hosam NASEF[1,2], Sameh NADA[1,3], Hamdy HASSAN[1,4]

[1] *Department of Energy Resources Engineering, Egypt-Japan University of Science and Technology (E-JUST), P.O. Box 179, New Borg El-Arab City 21934, Alexandria, Egypt, hosam.nasef@ejust.edu.eg*
[2] *Department of Mechanical Power Engineering, Faculty of Engineering, Tanta University, Tanta 31511, Egypt, hosam.nasef@f-eng.tanta.edu.eg*
[3] *Department of Mechanical Engineering, Benha Faculty of Engineering, Benha University, Benha, Egypt., samehnadar@yahoo.com*
[4] *Department of Mechanical Engineering, Faculty of Engineering, Assuit University, Assuit, Egypt., hamdyaboali@yahoo.com*

In the present theoretical study, an indirect cooling of a concentrated photovoltaic (CPV) system with phase change material (PCM) is carried out by using a new integration. The integration is based on using a heat transfer medium/fluid to transfer the dissipated heat from the CPV system to the PCM. The new system allows separating the PCM away from CPV which reduces the consumed power for the tracking system and avoids increasing the overall thermal resistance of the CPV-PCM direct integrated system. The study is carried out using PCM plates in parallel configuration and water at different flow velocities as heat transfer medium. A complete mathematical model including the heat transfer through the PV, heat transfer medium, and PCM plates is presented and solved by using ANSYS-FLUENT software. The results indicated that this indirect technique in cooling the CPV system by using the heat transfer medium and PCM is more performant compared to conventional heat sink PCM. Additionally, the CPV cell temperature decreases with increasing the flow velocity of the heat transfer medium. The temperature of the cell does not exceed 78°C and PCM maximum temperature is kept below the limit of degradation temperature.

Keywords: integrative passive-active cooling system; concentrated photovoltaic cells; thermal regulation; phase change material

1. INTRODUCTION

Regulating the temperature of solar cell is very important to protect it from temporary loss in power or permanent damage due material degradation (Royne et al., 2005). A well-designed solar cell cooling system should consider many aspects such as: maximum temperature of the cell, uniform temperature distribution along the cell, system durability and capacity. Different cooling techniques could be adapted which depend mainly on PV generation, concentration technology and weather condition

Passive cooling systems using metal fins (Theodore, 2011) are suitable for single PV cell because the heat sink could be extend in all direction without limitations (Royne et al., 2005). Other complex systems contain natural circulation cycle (Royne, 2005) or involving phase change materials (PCMs) as a heat sink (Shokouhmand and Kamkari, 2013) which is examined successfully for PV temperature regulating (Hasan et al., 2010; Nada et al., 2018; Nada and El-Nagar, 2018). The melting process of PCM is examined numerically with CPV systems to investigate the effect of inclination angles (Emam et al., 2017).

However, active cooling systems using air, water or other heat transfer fluid in an open or a closed loop is the most effective method for high concentration ratio (CR) more than 10 CR. Two phase flow in microchannel heat sink which is considered an effective active cooling technique, was practically investigated to regulate the temperature of CPV system (Radwan et al., 2019). The immersion of PV panels in dielectric fluid was successfully investigated experimentally (Liu et al., 2011) to cool it from both sides.

The blending between both of active and passive cooling technology is considered a good path to cross the limitations of each techniques individually. PCM heat sink and forced flow of water jacket was modelled (Emam and Ahmed, 2018a) to with CPV system. The main barrier to increase the CR of their design was the maximum operating temperature of the PCM at which the material loss its original properties permanently and become non-functional. The performance of a tracking-integrated concentrating photovoltaic-thermal (CPV-T) system with immersed encapsulated PCM spheres had been experimentally examined. Results showed that compared with the CPV-T system that only water cooled, the average increases of the electrical, thermal, and overall efficiencies for the CPV-T system with PCM cooling are more than 10%, 5%, and 15%, respectively (Su et al., 2018).

From the previous literature review and to the authors' best knowledge, it is clear that all previous studies used the PCM in CPV cooling, the CPV system was in direct contact with the PCM. This direct contact technique of cooling has limited the cooling capacity of the PV because of the limited contact space and its limitation by the phase change temperature of the PCM. So, in the present study, an indirect cooling of the CPV with PCM is carried out using a new integration technique. The integration is based on using a heat transfer medium between the PCM and the CPV which transfers the dissipated heat from the CPV to the PCM. The advantages of this proposed technique are (i) it solves the limitation of the contact area between the PCM and the CPV, and (ii) solves the limitation of the PCM melting degradation temperatures in case of direct contact technique. In the present work, a new system of cooling and thermal regulation of CPV cell is conducted using a closed loop of cooling water integrated with a battery of PCMs enclosure to thermally regulate the cooling water temperature which used to cool the CPV system. The current design allows higher contact area and temperature difference between the CPV and the heat transfer fluid which mean the possibility to allow the system to work on high concentration ratio and achieve higher thermal efficiency of the system. The stored heat in PCM enclosures can be taken back during the charging process for any other applications such as heating systems or water desalination planets.

2. PHYSICAL MODEL

In the current work, the performance of low concentrated photovoltaics cell (CPV) with concentration ratio (CR) of 10 is investigated. The CPV is cooled by water in a direct contact back channel. The circulated water passes through a battery/tank containing aluminum-capsulated Phase Change Material (PCM) panels of type RT 35HC. The PCM panels regulates the water temperature before it goes back to the Panel. The performance of the CPV with direct contact PCM-heat sink is also investigated in the current study under the same operating and design conditions to compare the results of both systems. Figure 1 shows a schematic diagram of this PCM-cooling water loop integrated technique.

As shown in Figure 1, the physical model consists of CPV section, PCMs battery/tank system and circulating pump and piping system. The CPV section consists of the PV cell integrated from the back with the cooling channel where the water passes through it to cool the cell. The PV panel consists of the cell covered from both sides by the EVA layers. The cell with the EVA layer covered from the top by the glass layer and from the back by TPT layer. The TPT layer is in direct contact with the water-cooling channel and the glass layer is subjected to the sun simulator. The CPV is mounted with an inclination angle of 30° corresponding to the latitude angle of Alexandria, (Egyptian city) to maximize the received solar radiation. The PV module optical and thermophysical properties of the materials used in this study are given in Table 1.

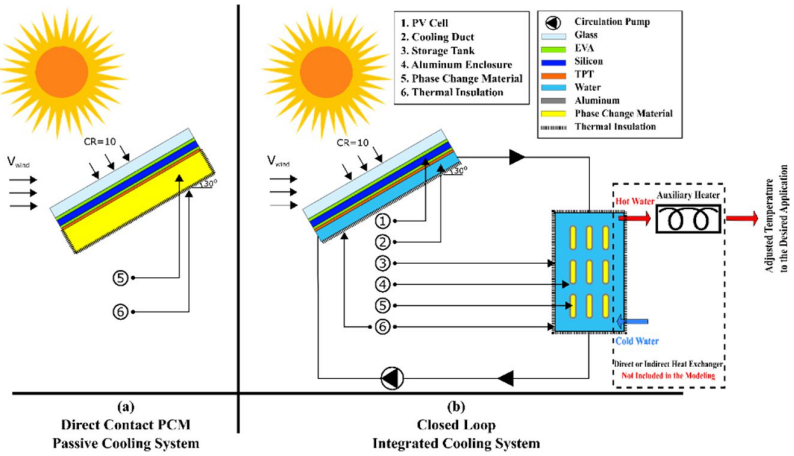

Figure 1: 2D Physical Model for both a) Direct Contact PCM and b) Closed loop integrated cooling systems

Table 1: The PV module optical and thermophysical properties of the used materials (Zhou et al., 2015)

Material	α	R	τ	ε	ρ (kg/m3)	κ (W/mK)	C_p (J/kg K)	t (mm)
Glass	0.04	0.04	0.92	0.85	2450	2	500	3.2
EVA	0.08	0.02	0.9	–	950	0.311	2090	0.5
Cell	0.9	0.08	0.02	–	2330	130	677	0.2
TPT	0.128	0.86	0.012	0.9	1200	0.15	1250	0.3

The Storage tank has height of 200 mm and a width of 50 mm The PCM battery section consists of nine PCM panels enclosed in a tank. The capsulated PCM panel/plate is of dimensions 50 mm (length) x 5 mm (thickness).with internal vertical and horizontal spacing of 5 mm. The capsulated PCM panels is covered with an aluminium shell of 0.5 mm thickness. The PCM type inside the capsulated panels is RT 35HC. The volume of the PCM inside either in the direct contact PCM or all encapsulated panels in the integrated cooling system is $2.2017*10^{-3}$ m^3 per unit width with packing factor, the ratio between the volume of PCM and the water in the storage tank, of 22.37%. The cooling duct behind the CPV cell in the closed loop cooling system is 5 mm width. The thermophysical properties of the PCM and the aluminium shell are given in Table 2.

Table 2: PCM and aluminium thermophysical properties.

Thermophysical properties	PCM RT35HC ("Rubitherm," 2015)	Aluminium (Kamkari and Groulx, 2018)
Thermal conductivity. (W/mK) (Solid / Liquid)	0.2 / 0.2	211 / –
Density (kg/m3) (Solid / Liquid)	880 (at 25 °C) / 770 (at 40 °C)	2675 / –
Specific heat capacity. (kJ/kg K) (Solid /Liquid)	2 / 2	0.903 / –
Melting temperature (range) (°C)	34 – 36 (main peak: 35)	–
Heat of fusion (kJ/kg)	240	–
Volumetric expansion, ΔV (1/kg) %	12	–

Four circulation volume flowrates of cooling fluid have been used $5*10^{-5}$,$10*10^{-5}$, $15*10^{-5}$ and $20*10^{-5}$ m^3/s per unit width which generate four circulation velocities of the heat transfer fluid in the cooling duct in the closed loop cooling system 0.01, 0.02, 0.03 and 0.04 m/s. The effects of these flowrates on melting process of the PCM and CPV cell are investigated. A pump and piping system are used to circulate the heat transfer fluid between the CPV section and the PCM battery section. The heat transfer fluid used in the circuit is pure water due to its availability, high heat capacity and heat transfer and suitability for direct use for different applications.

3. MATHEMATICAL MODEL

3.1. Photovoltaic layers

The main mode of the heat transfer between the PV layers is transient conduction which is expressed by the heat transfer diffusion equation (Radwan and Ahmed, 2017). The solar cell electric efficiency is calculated from (Xu and Kleinstreuer, 2014). The power productivity per unit width of the solar cell can be given by the following relation (Kant et al., 2016). While the fluid flow and heat transfer through the phase change material are governed by the

conservation equations which are computed based on (Brent et al., 1988; Emam and Ahmed, 2018b). The average solar cell temperature, stored thermal energy, and thermal efficiency of the CPV-PCM system over the period from the initial time (t_i) to the complete melting time(t_m) are calculated based on (Emam and Ahmed, 2018b):

3.2. Boundary and initial conditions

The convective heat transfer coefficient from the glass cover to the atmosphere due to the wind effect (Ahmed and Radwan, 2017) and the radiation heat transfer coefficients between the glass cover and the sky are estimated by the correlation (Rejeb et al., 2015). Adiabatic boundary conditions are applied for all outer walls of the system except for the specified surfaces of the CPV.

3.3. Properties of heat transfer fluid

Pure Water is used as heat transfer fluid (HTF) due to its availability and suitability for direct use for different applications. The thermophysical properties of the pure water as functions of temperature are used during modeling based on the developed polynomial expressions of (Jayakumar et al., 2008).

4. MATHEMATICAL MODEL SOLUTION

In the current investigation, two comprehensive models were developed and solved numerically in two dimension model considering all components have the same unit depth by using the commercial software ANSYS FLUENT 17.2. The first model is the integration between thermal model for CPV layers, closed loop water and melting-solidification thermo fluid model for PCM. The coupled PRESTO and second-order upwind schemes were adapted to solve and model the governing equations. The second developed model for comparison is direct coupling between thermal model for CPV layers and melting-solidification thermo fluid model for PCM. The SIMPLE, PRESTO and second-order upwind schemes were used to solve and model the governing equations at each time step.

4.1. Mesh and time dependence study

A mesh independent test has been carried out for the integrated cooling system, it is found that 1173517 grids is suitable after testing grid number of 380742, 494282 , 577781, 698407 , 876321, 1173517, 1457431, 2120040 and 3103207 with error of 11.129 %, 10.260 %, 1.660 %, 7.550%, 1.101 %, 0.731 %, 0.915 %, 0.181 %, and 0 % based on maximum number of grids. A time step independency test was carried out to choose the best time step for the model calculations. The time step of 0.2 second is used after testing 0.1, 0.2, 0.3 and 0.5 second with error of 0 %, 0.3656 %, 0.4566 %, 12.379 %, 0.4566 % and 8.2492 %, based on minimum value of time step, to make balance between solution accuracy and computational cost. For the case of conventional direct contact PCM cooling system, the model is performed with 101655 elements with maximum grid size of 0.2 mm and time step of 0.2 second based on a model of the same configuration (Rabie et al., 2019). For both models, the error was kept below 10^{-4} for continuity and momentum equations and below 10^{-6} for energy equation.

4.2. Model validation

The validation of the numerical results is conducted by comparing the predicted results and the corresponding experimental and numerical results. The direct contact PCM model is validated with (Kamkari and Shokouhmand, 2014) by comparing the liquid fraction of PCM domain with one wall under a constant temperature kept at 70°C of the present model results with the experimental data of (Kamkari and Shokouhmand, 2014). Figure 2 (a) shows this comparison for the variation of liquid fraction percentage. This figure shows that the comparison with (Kamkari and Shokouhmand, 2014) demonstrates a good agreement between the current predicted results and the experiments.

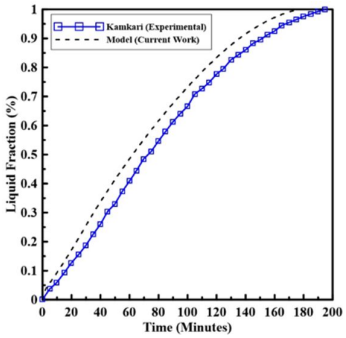

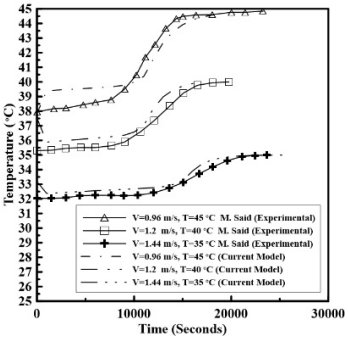

(a) Liquid fraction (Kamkari and Shokouhmand, 2014) *(b) Outlet HTF temperature (Said and Hassan, 2018)*

Figure 2: Validation for the variation of liquid fraction and temperature with time

The second model of the present study (model of the heat transfer between the PCM and the PV) is validated with the comparison with Said and Hassan (Said and Hassan, 2018) by comparing the predicted outlet temperature HTF of different inlet velocities and temperatures which is going out from PCM-cooled duct with the experimental results of (Said and Hassan, 2018). To conduct this comparison, the model was run under the same conditions of (Said and Hassan, 2018). As shown in Figure 2 (b), the comparison shows a good agreement between the present model and experiments which represent the coupling between HTF and PCM enclosure.

5. RESULTS AND DISCUSSIONS

The system is initialised with an initial temperature T_{in} = 33 ^{O}C and the PCM is in the solid state. For the glass surface of CPV is considered under free convection boundary conditions with h= 9.89 W/m^2 K due to a wind speed of 1 m/s and T_{amb} = 33 ^{O}C. The CPV is studied at an inclination angle 30^{O} and the glass surface is considered at a constant concentration ratio of CR=10 sun of a constant sun solar intensity of 1000 W/m^2. The model was run for different velocities of the HTF. The model in case of the PCM tanks at direct contact of the CPV back surface was also run at the same conditions for the sake of comparison. The study was carried out to express the system performance including the silicon layer and glass surface local temperature, the PV power output, the efficiency of the CPV and the monitoring of the PCM melting process by tracing the liquid fraction of each PCM enclosure. In this section, the results of thermal behaviour and performance of the proposed integrated system and the direct contact CPV-PCM system are discussed, evaluated and compared. Moreover, the effects of the velocity of HTF on the thermal behaviour and performance of the proposed system are also presented, discussed and evaluated.

5.1. Effect of heat transfer fluid circulation velocity

In the following section, the effect of the HTF velocity on the temperature levels of the CPV cells and on its performance (efficiency and net output power) are investigated.

Figure 3 shows the effects of HTF velocity on the transient average temperature of the solar cell for Water-PCM integrated system. It is clear that the silicon temperature has a general upward trend over the entire time for all cases. For four circulation velocities, the average silicon temperature sharply grows to 70°C on the first two minutes and stays at this value without variation for another five minutes. After that, the silicon temperature slightly increases to the end of the time to a value around 85°C. The disappearance of the constant temperature in the interval 2-7 min in case of high velocities can be attributed to the high heat transfer coefficient and high flow rate which rapidly increase the fluid temperature at the inlet of the cell water channel. Comparing the temperatures histories at 0.01 to 0.04 m/s, it is noticed that, around the 17th minute, there is an exchange point of the cell temperature levels between 0.01 to 0.04 m/s cases; where the temperature level of the silicon layer in case of 0.04 m/s is lower than that of case 0.01 m/s before the 17th minute because the convection heat transfer is high due to the high HTF velocity. But after the 17th minute, the silicon temperature in case of 0.04 m/s increases to become higher than the 0.01 m/s case. This can be attributed to the level of the HTF temperature which increases in case of 0.04 m/s to become higher than that of case 0.01 m/s This means that, increasing the HTF velocity has a positive impact on the cell temperature before the 17th minute and has a negative impact after this time because the heat storage capacity of the PCM is constant which is consumed faster in case of 0.04m/s than in case of 0.01 m/s.

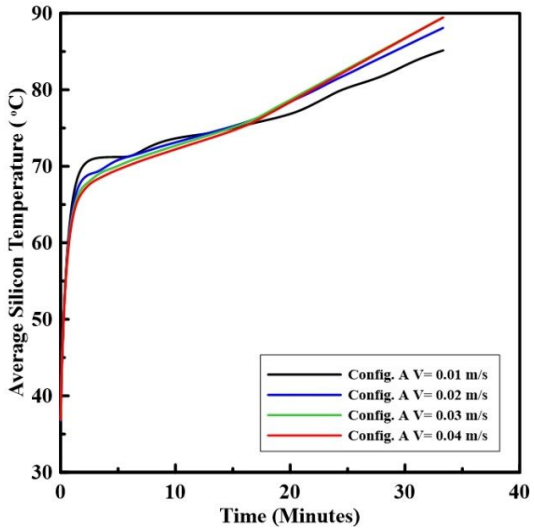

Figure 3: Evolution of the average silicon temperature at different velocities with time

Figure 4 represents the effect of the HTF velocity on the efficiency of the solar cell and the generated net power per unit width. As shown in the figure for all studied HTF velocities and types, the efficiency profile has a general downward trend over the simulation time. For all cases, the efficiency drops sharply to 12% in the first 2 minutes then continues decreasing gradually to reach about 11% at the end of the simulation time. The figure also shows that, before the 17th minute, the efficiency in case of 0.04 m/s velocity is higher than that of case 0.01 m/s and the reverse occurs after the 17th minute where the efficiency of 0.01 m/s case becomes higher than that of 0.04 m/s. This can be attributed to the cell temperature levels of the two velocities before and after the 17th minute as discussed early in Figure 3. It is remarkable that the efficiency curves also have an exchange point at the 17th minute due to the reverse relation between silicon efficiency and its working temperature. On the other hand, for all studied cases, the net power has a decreasing trend along the entire period of modelling. The figure shows that the net power falls suddenly to be around 150 W/m in the first two minutes then gradually decreases to nearly 136 W/m for all cases, respectively., The figure also shows that before the 17th minute, the net power in case of 0.04 m/s is higher than that of 0.01 m/s and the opposite is true after the 17th minute. This trend can be attributed to the trend of the cell temperature at the different velocities as described in Figure 3.

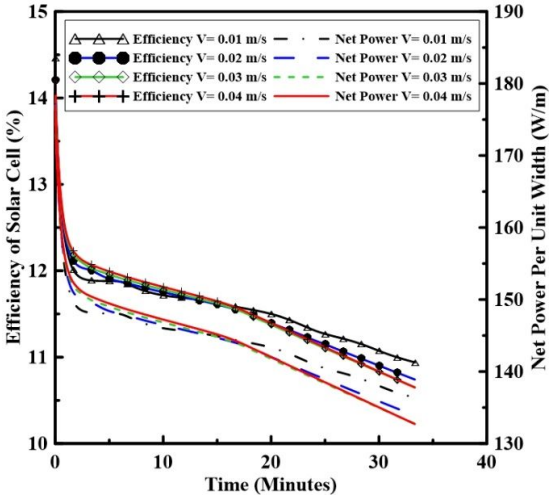

Figure 4: Effects of HTF velocity on the solar cell efficiency

Figure 5 (a) shows the variation of the liquid fraction percentage during the simulation period for different HTF velocities. It is clear that all cases have a general upward trend over the melting time. There is a constant start at zero value for two minutes for all cases, then the curves gradually increase to the value of 100% liquid between 16 and 21 minutes for cases of 0.04 to 0.01 m/s, respectively. Then all liquid fractions stay constant at a value of 100% to the end of modelling time. The figure also shows that after the 7th minute of starting the process, the liquid fraction in case of 0.04 m/s is always higher than that of case 0.01 m/s and a complete melting in case of 0.04 occurs before the case of 0.01 m/s. This can be attributed to the higher heat transfer coefficient and higher HTF mass flow

rate which accelerate the melting process. While Figure 5 (b) shows maximum temperature of PCM during simulation for the case of direct contact (DC) PCM and the case of PCM integrated with HTF with different circulation velocities, The results shows that .DC PCM model exceeds the allowable working temperature of the selected PCM which is 70°C according to the manufacturer ("Rubitherm," 2015), while for the model of PCM integrated with HTF the maximum working temperature do not exceeds the maximum working temperature and stayed below 58°C during the modelling. The water as a HTF regulate the distribution of the heat energy with convection.

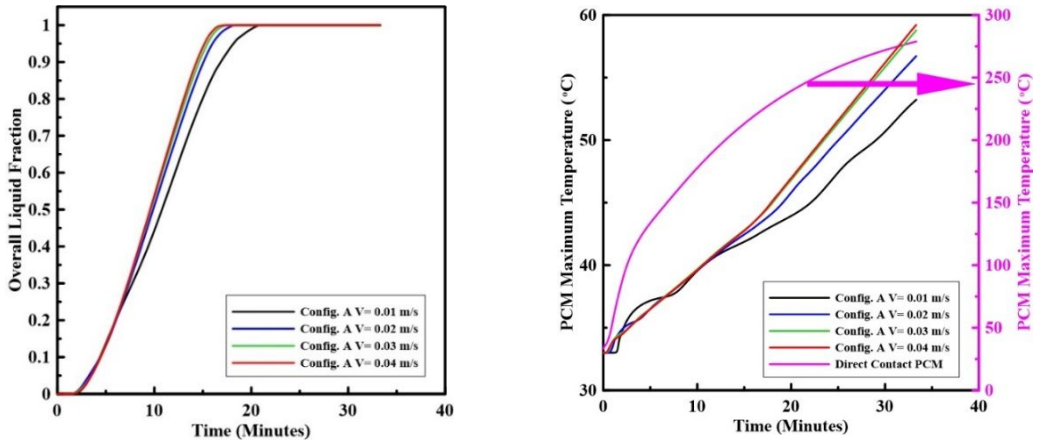

(a) Overall Liquid Fraction *(b) PCM maximum temperature*

Figure 5: Variation of Overall Liquid Fraction and PCM maximum temperature with time at Different Velocities

Figure 6 illustrates the melting process of different HTF velocities. It is clear that the melting process for the closed loop system finishes after 16th to 21st minutes for the different velocities of HTF while this process takes about 33 minutes to be completed for the case of DC PCM. It is remarkable that for all the combined systems, the first group of the PCM enclosures starts and finishes the melting process early before the second and the third group of the PCM enclosures. This can be attributed to that this group is the first group that meets the hot fluid coming from the CPV cell. The subsequent group meets this fluid at lower temperature where it was cooled by the downstream group of the PCM. The figure also shows that the melting process in case of 0.04 m/s is faster than other cases.

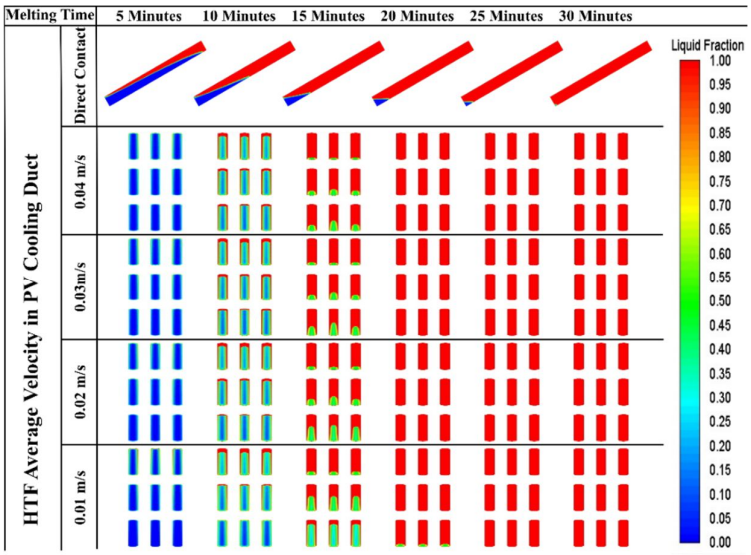

Figure 6: Liquid fraction for different velocities after 5, 10, 15, 20, 25 and 30 minutes

Figure 7 shows the difference between maximum and minimum temperature along the silicon layer for different circulation velocities. It is obvious that the temperature is more homogenous over the cell for higher circulation velocity while the opposite is right for lower velocity. Low values of solar cell temperature uniformity cause the thermal stresses and electrical resistance to decrease which enhance the performance of the CPV system and increase the lifetime of the system.

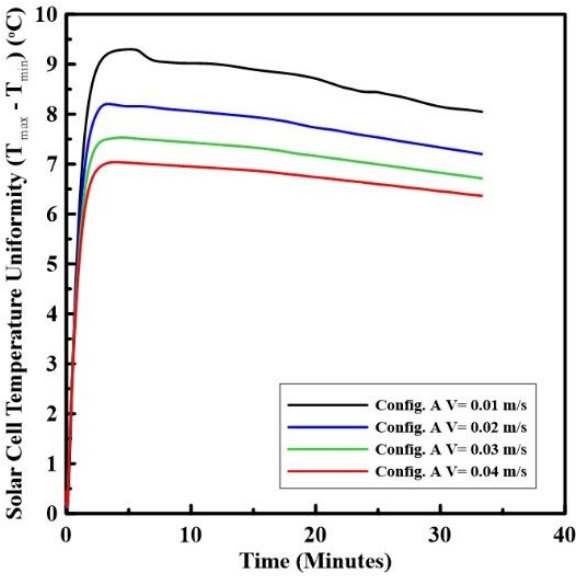

Figure 7: Variation of solar cell temperature uniformity with time for different circulation velocity

Figure 8 shows temperature distribution along the length of the cell for both glass and silicon layer for different circulation velocities. It is obvious that the temperature of glass layer is slightly lower than the silicon layer for each case because the effect of cooling by convection to the ambient. The glass temperature can be further cooled by passing the cooling fluid in front of the glass surface which will affect directly on the performance of the CPV system.

Figure 9 shows the evolution of the average temperature silicon layer for different circulation velocity after 5 to 30 minutes with 5 minutes time step. It can be concluded that using variable circulation velocity can enhance the performance of the CPV system and take the advantage of positive effects of both high and low velocities. Low circulation velocity can be selected at the beginning of system cooling until complete melting of PCM, after that it is recommended to increase the circulation velocity to increase the heat transfer coefficient to maintain the temperature of CPV system at lower values.

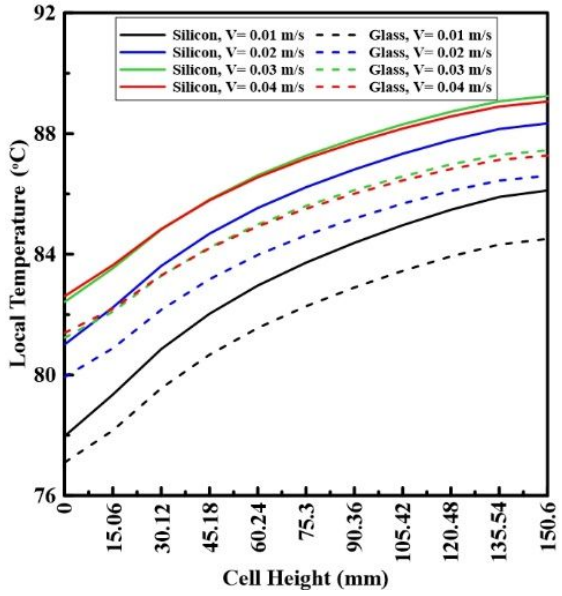

Figure 8: Local temperature of glass and silicon layer along the cell length after 30 minutes

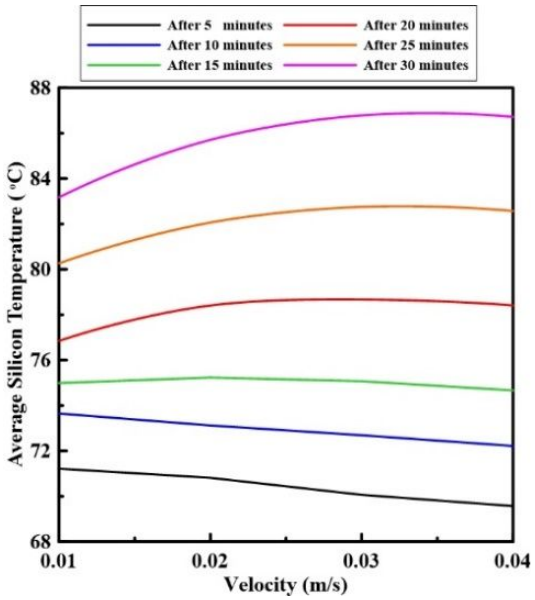

Figure 9: Variation of average temperature of silicon layer with different circulation velocity after different modelling time step

6. CONCLUSIONS

The new integrated CPV cooling system proves its reliability for regulating CPV cell temperature and store heat energy in PCM as thermal battery for other applications. Changing the volume flowrate increase the performance of the system to the point which consume all PCM charging capacity which could be extent by increasing the volume of PCM. The following can be determined from the obtained outcomes:

- The presented integrated cooling system can regulate the temperature of the CPV system and keep PCM in the limit of operating temperatures which cannot be obtained by DC PCM.
- Increasing the circulation velocity from 0.01 to 0.04 m/s increases the performance of the system until completely melting then the performance decreases for high velocities.
- Increasing the circulation velocity from 0.01 to 0.04 m/s increases the temperature regularity of the cell which decreases thermal stresses and enhances electric performance of the system.
- It is recommended to cool the CPV system from both sides because the glass temperature is still high.
- Using variable circulation volume flowrates which create different heat transfer coefficients can regulate the temperature of the CPV system better than single circulation flowrate by creating balance between the CPV system temperatures and discharging time of PCM.

7. ACKNOWLEDGEMENT

The work described in the current paper is financially supported by the Egyptian government through the Ministry of Higher Education (MoHE-Egypt). The authors would as well like to acknowledge the Egypt-Japan University of Science and Technology (E-JUST) for offering the facilities and tools.

8. REFERENCES

Ahmed, M., Radwan, A., 2017. Performance evaluation of new modified low-concentrator polycrystalline silicon photovoltaic/thermal systems. Energy Conversion and Management 149, 593–607. https://doi.org/10.1016/j.enconman.2017.07.057

Brent, A.D., Voller, V.R., Reid, K.J., 1988. Enthalpy-porosity technique for modeling convection-diffusion phase change: Application to the melting of a pure metal. Numerical Heat Transfer 13, 297–318. https://doi.org/10.1080/10407788808913615

Emam, M., Ahmed, M., 2018a. Performance analysis of a new concentrator photovoltaic system integrated with phase change material and water jacket. Solar Energy 173, 1158–1172. https://doi.org/10.1016/j.solener.2018.08.069

Emam, M., Ahmed, M., 2018b. Cooling concentrator photovoltaic systems using various configurations of phase-change material heat sinks. Energy Conversion and Management 158, 298–314. https://doi.org/10.1016/j.enconman.2017.12.077

Emam, M., Ookawara, S., Ahmed, M., Ookawara, S., Ahmed, M., 2017. Performance study and analysis of an inclined concentrated photovoltaic-phase change material system. Solar Energy 150, 229–245. https://doi.org/10.1016/j.solener.2017.04.050

Hasan, A., McCormack, S.J., Huang, M.J., Norton, B., 2010. Evaluation of phase change materials for thermal regulation enhancement of building integrated photovoltaics. Solar Energy 84, 1601–1612. https://doi.org/10.1016/j.solener.2010.06.010

Jayakumar, J.S., Mahajani, S.M., Mandal, J.C., Vijayan, P.K., Bhoi, R., 2008. Experimental and CFD estimation of heat transfer in helically coiled heat exchangers. Chemical Engineering Research and Design 86, 221–232. https://doi.org/10.1016/j.cherd.2007.10.021

Kamkari, B., Groulx, D., 2018. Experimental investigation of melting behaviour of phase change material in finned rectangular enclosures under different inclination angles, Experimental Thermal and Fluid Science. https://doi.org/10.1016/j.expthermflusci.2018.04.007

Kamkari, B., Shokouhmand, H., 2014. Experimental investigation of phase change material melting in rectangular enclosures with horizontal partial fins. International Journal of Heat and Mass Transfer 78, 839–851. https://doi.org/10.1016/j.ijheatmasstransfer.2014.07.056

Kant, K., Shukla, A., Sharma, A., Biwole, P.H., 2016. Heat transfer studies of photovoltaic panel coupled with phase change material. Solar Energy 140, 151–161. https://doi.org/10.1016/j.solener.2016.11.006

Liu, L., Zhu, L., Wang, Y., Huang, Q., Sun, Y., Yin, Z., 2011. Heat dissipation performance of silicon solar cells by direct dielectric liquid immersion under intensified illuminations. Solar Energy 85, 922–930. https://doi.org/10.1016/j.solener.2011.02.007

Nada, S.A., El-Nagar, D.H., 2018. Possibility of using PCMs in temperature control and performance enhancements of free stand and building integrated PV modules. Renewable Energy 127, 630–641. https://doi.org/10.1016/j.renene.2018.05.010

Nada, S.A., El-Nagar, D.H., Hussein, H.M.S., 2018. Improving the thermal regulation and efficiency enhancement of PCM-Integrated PV modules using nano particles. Energy Conversion and Management 166, 735–743. https://doi.org/10.1016/j.enconman.2018.04.035

Rabie, R., Emam, M., Ookawara, S., Ahmed, M., 2019. Thermal management of concentrator photovoltaic systems using new configurations of phase change material heat sinks. Solar Energy 183, 632–652. https://doi.org/10.1016/j.solener.2019.03.061

Radwan, A., Ahmed, M., 2017. The influence of microchannel heat sink configurations on the performance of low concentrator photovoltaic systems. Applied Energy 206, 594–611. https://doi.org/10.1016/j.apenergy.2017.08.202

Radwan, A., Ookawara, S., Ahmed, M., 2019. Thermal management of concentrator photovoltaic systems using two-phase flow boiling in double-layer microchannel heat sinks. Applied Energy 241, 404–419. https://doi.org/10.1016/j.apenergy.2019.03.017

Rejeb, O., Dhaou, H., Jemni, A., 2015. A numerical investigation of a photovoltaic thermal (PV/T) collector. Renewable Energy 77, 43–50. https://doi.org/10.1016/j.renene.2014.12.012

Royne, A., 2005. Cooling devices for densely packed, high concentration PV arrays. The University of Sydney.

Royne, A., Dey, C.J., Mills, D.R., 2005. Cooling of photovoltaic cells under concentrated illumination: A critical review. Solar Energy Materials and Solar Cells 86, 451–483. https://doi.org/10.1016/j.solmat.2004.09.003

Rubitherm, 2015. URL https://www.rubitherm.eu

Said, M.A., Hassan, H., 2018. Parametric study on the effect of using cold thermal storage energy of phase change material on the performance of air-conditioning unit. Applied Energy 230, 1380–1402. https://doi.org/10.1016/j.apenergy.2018.09.048

Shokouhmand, H., Kamkari, B., 2013. Experimental investigation on melting heat transfer characteristics of lauric acid in a rectangular thermal storage unit. Experimental Thermal and Fluid Science 50, 201–212. https://doi.org/10.1016/j.expthermflusci.2013.06.010

Su, Y., Zhang, Y., Shu, L., 2018. Experimental study of using phase change material cooling in a solar tracking concentrated photovoltaic-thermal system. Solar Energy 159, 777–785. https://doi.org/10.1016/j.solener.2017.11.045

Theodore, L., 2011. Heat transfer applications for the practicing engineer (series: essential engineering calculations series), Recherche.

Xu, Z., Kleinstreuer, C., 2014. Concentration photovoltaic-thermal energy co-generation system using nanofluids for cooling and heating. Energy Conversion and Management 87, 504–512. https://doi.org/10.1016/j.enconman.2014.07.047

Zhou, J., Yi, Q., Wang, Y., Ye, Z., 2015. Temperature distribution of photovoltaic module based on finite element simulation. Solar Energy 111, 97–103. https://doi.org/10.1016/j.solener.2014.10.040

#142: Performance analysis of a fresh air dehumidification system using heat pump with desiccant coated heat exchanger

Shaowei CHAI[1], Yao ZHAO[2], Tianshu GE[3], Yanjun DAI[4]

[1] *Institute of Refrigeration and Cryogenics, Shanghai Jiao Tong University, 800 Dongchuan Road, Shanghai, & MOE Engineering Research Center of Solar Power & Refrigeration, China, shwchai@sjtu.edu.cn*
[2] *Institute of Refrigeration and Cryogenics, Shanghai Jiao Tong University, 800 Dongchuan Road, Shanghai, & MOE Engineering Research Center of Solar Power & Refrigeration, China, zhaoyao420@sjtu.edu.cn*
[3] *Institute of Refrigeration and Cryogenics, Shanghai Jiao Tong University, 800 Dongchuan Road, Shanghai, & MOE Engineering Research Center of Solar Power & Refrigeration, China, baby_wo @sjtu.edu.cn*
[4] *Institute of Refrigeration and Cryogenics, Shanghai Jiao Tong University, 800 Dongchuan Road, Shanghai, & MOE Engineering Research Center of Solar Power & Refrigeration, China, yjdai@sjtu.edu.cn*

With the increasing attention on indoor air quality, the use of fresh air conditioning systems has become more widespread in recent years. However, the dew point dehumidification method of conventional air conditioning systems results in high energy consumption because the temperature of the air needs to be reduced below the dew point temperature. The aim of this study is to evaluate the performance of a fresh air dehumidification system using a heat pump with desiccant-coated heat exchanger for of moisture removal and coefficient of performance (COP) in typical hot-humid outdoor conditions in Shanghai. The key equipment of the system is desiccant coated heat exchanger (DCHE), which is fabricated by a conventional fin-tube heat exchanger with desiccant materials coated on the fin surface. Cold capacity provided by a heat pump is used during the dehumidification process so that the harmful effect of adsorption heat could be overcome and the efficiency of dehumidification could be improved due to the DCHE. The waste heat caused by the heat pump is used to regenerate the desiccant material. The experiment results show that the average moisture removal of the system is 4.67 g/kgDA and the COP is 5.20. Higher moisture removal could be achieved in the optimised system at a lower air flow rate with a slight reduction on COP. The COP of the dehumidification system is higher than conventional air-conditioner due to the dehumidification of the desiccant.

Keywords: dehumidification; fresh air; heat pump; desiccant coated heat exchanger; COP

1. INTRODUCTION

Thermal comfort can be improved for people living in hot and humid climates, especially in summer, by using air conditioning. However, indoor air quality (IAQ) and the impact on energy consumption are of key concern: the return air to indoors is treated to cool and dehumidify before re-entering the room to reduce energy consumption, but this may lead to a poor IAQ due to indoor pollutants (Yu et al., 2009). In addition, modern buildings often adopt airtight windows to have ensure soundproofing which causes a low fresh air exchange rate of about 0.3 to 0.5 times per hour (Hsieh, Chuang, Hou, & Huang, 2018). Using a fresh air system for air conditioning is an effective method to improve IAQ, however, the expense of energy consumption may increase with the higher heat and humidity load of fresh air in summer (Dongmei, Shiming, Zhongping, & Ming-yin, 2013).

Air conditioning systems are one of the largest energy consumers in the construction industry, accounting for 20% to 50% of total energy consumption in developed countries (Vakiloroaya, Samali, Fakhar, & Pishghadam, 2014). Air conditioning loads could be divided into two components, namely the sensible heat load and the latent heat load, with the latent heat load usually accounting for 20% to 40% of the total air conditioning loads. In a conventional vapor compression cycle, the latent heat load of moisture content is reduced by decreasing the temperature of the air below the dew point temperature. The air temperature may be too low for the air to be supplied directly back indoors, so the reheat coil is used to increase the temperature of the air resulting in additional energy consumption and low efficiency. In recent years, desiccant coated heat exchangers (DCHE) have been proposed by researchers (Ge et al., 2010) to enhance the performance of dehumidification systems. Experimental results show that the DCHE overcomes well the harmful effect of adsorption heat in desiccant dehumidification process, and good dehumidification performance can be achieved under given conditions (Sun et al., 2017). Zhao et al. (2016) studied a solar driven dehumidification system using DCHE with heat recovery. Results show the electrical *COP* can reach 13.83 due to the use of solar energy and heat recovery. However, the instability of solar energy is a disadvantage to the continuous operation of the system.

In this paper, a fresh air dehumidification system using a heat pump with a DCHE is presented. A series of experiments are conducted to study the performance of the system and the factors that affect the performance on typical ambient condition of Shanghai.

2. DESCRIPTION OF EXPERIMENTAL SET-UP

2.1. Desiccant coated heat exchanger (DCHE)

As a novel humidity processing device, DCHE is fabricated by a conventional fin-tube heat exchanger with desiccant materials coated on the fin surface. The schematic diagram of DCHE during dehumidification process and regeneration process is shown in Figure 1. In order to overcome the harmful adsorption heat generated by desiccant moisture adsorption during dehumidification process, cooling water flows through tubes to remove the adsorption heat to keep a high efficiency of dehumidification. During regeneration process, hot air flows through the surface of the fins of the DCHE to provide heat capacity to regenerate desiccant (during regeneration process, cooling water does not flow) so that desiccant regains moisture absorption capacity. The structural parameters of DCHEs used in the experiment system and the photo of the DCHE are presented in Table 1 and Figure 2, respectively.

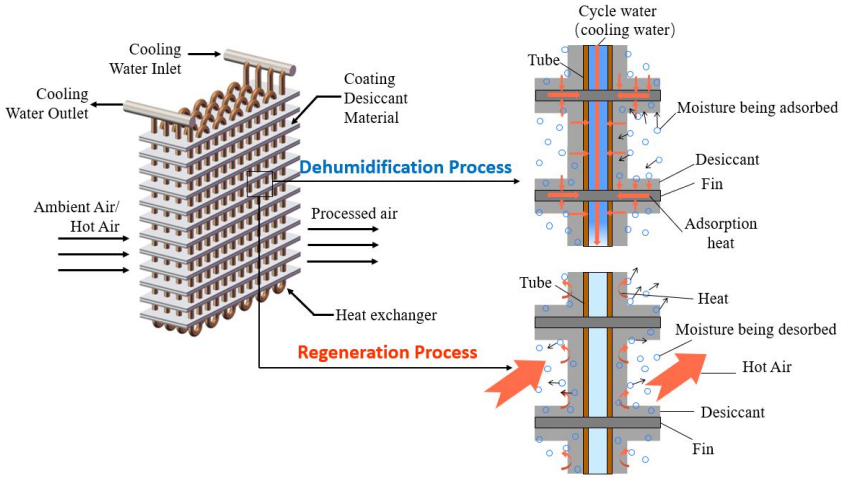

Figure 1: Schematic diagram of DCHE during dehumidification process and regeneration process

Table 1: Structural parameters of DCHE.

Component	Parameters
Structural size (mm)	340×340×88
Mass (kg)	7.627
Thickness of the fin (mm)	0.15
Spacing of the fin (mm)	2
Outer diameter of the tube (mm)	9.87
Glue quantity (kg)	1.843

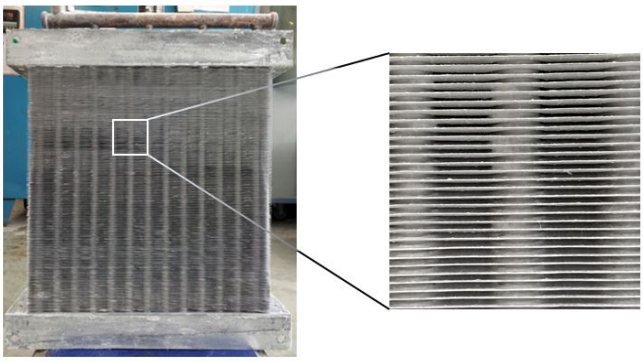

Figure 2: Photo of the DCHE

2.2. Experimental system description

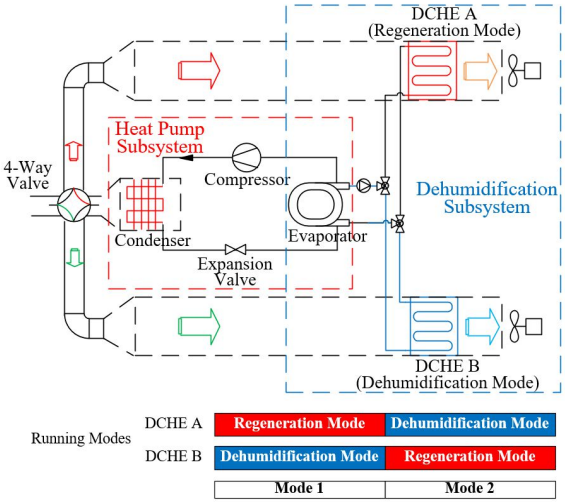

Figure 3: Schematic diagram and running modes of the fresh air desiccant dehumidification system

The schematic diagram of the studied fresh air desiccant dehumidification system is shown in Figure 3. The system could be divided into two subsystems which are connected by air ducts and water pipes. The first subsystem is a conventional vapour compression heat pump subsystem consisting of compressor, evaporator, condenser and expansion valve by which hot air and cooling water could be provided. The refrigerant used in the heat pump subsystem is R134a and a compressor with a rated power of 450W is used. The cooling water provided by evaporator can be pumped to DCHE A or DCHE B through a 3-way water valves, and the ambient air can flow through DCHE B or DCHE A by 4-way air valve after being heated by the condenser. The second subsystem is a dehumidification subsystem which consists of two identical DCHEs, a 4-way air valve, air ducts, fans and other fittings. Two DCHEs are placed on opposite sides of the four-way valve and the motor of the 4-way air valve can be switched repeatedly between 0 and 90 degrees. The two air ducts are isolated from each other because of the blade of 4-way air valve. With the switch of blade between 0 to 90 degrees, the dehumidification system can operate in two running modes without the switch between evaporator and condenser in the heat pump subsystem: during

mode 1, DCHE A is regenerated by hot air so that the desiccant can regain moisture absorption capacity; at the same time, DCHE B is in dehumidification process with harmful adsorption heat overcome by cooling water flowing through the tube of DCHE. During mode 2, DCHE A is in dehumidification process while DCHE B is in regeneration process. Fan is installed at the ends of the air ducts respectively so that air can be drawn pass through the DCHEs. With mode 1 and mode 2 switching, the dehumidification system can achieve continuous dehumidification. In addition, the desiccant is used to treat the latent heat load of the process air so the temperature of the air does not need to be lowered below the dew point temperature, which could increase the evaporation temperature of the heat pump subsystem and improve system performance.

2.3. Measurements and data acquisition

Temperature, relative humidity and process air flowrate of inlet and outlet air were measured in the experiment. Air temperature and humidity sensors with accuracy of±0.3°C and ±2%RH were employed to test the temperature and relative humidity of inlet and outlet air. Air flow rates can be calculated by the area of air ducts and the velocity of process air, which was measured by a hot-wire anemometer with accuracy of±0.004m/s. Temperature and flowrate of cooling water was measured as well. PT 100 temperature sensors with accuracy of±0.1°C were used to measure the temperature of cooling water and water meters with accuracy of ±1.0% were employed to test the water flow rate. In addition, the electric power of all electrical appliances including compressor, fans and water pump, etc. was measured by a power meter with accuracy of ±1.0%. All these measurement data were collected into a computer by a data acquisition instrument Agilent 34972A. The main parameters of the measuring devices in the experiment are shown in Table 2.

Table 2: Parameters of test instrumentation

Parameter	Sensor	Accuracy	Range
Air temperature	Temperature sensor	±0.3°C	-30-70°C
Relative humidity	Relative humidity sensor	±2%RH	0-100%
Air flowrate	Hot-wire anemometer	±0.004m/s	0-5m/s
Water temperature	PT 100	±0.1°C	0-200°C
Water flowrate	Water meter	±1.0%	0-999m^3
Total electric power	Power meter	±1.0%	0-6600W

3. METHODOLOGY

3.1. Mathematical model

The fresh air dehumidification system consisted of the heat pump subsystem and the dehumidification subsystem. The performance of the heat pump subsystem was calculated by the Program Solkane 9.0. A mathematical model of DCHE during dehumidification process was developed by mass and energy conservation to predict the dehumidification system performance. The following assumptions were considered to simplify the calculation: (1) The process of the dehumidification system was at steady state; (2) Molecules of desiccant material were evenly distributed in the heat exchanger surface; (3) Heat transfer consistence of the copper tube was negligible and its temperature was assumed to be equal to that of the desiccant material; (4) Heat conduction as well as the mass diffusion within both air stream and desiccant material was negligible.

The energy conservation equation of DCHE is given as:

Equation 1: Energy conservation equation

$$c_w \dot{m}_w \left(T_{w,out} - T_{w,in}\right) = \dot{m}_a (h_{a,in} - h_{a,out})$$

Where:

- c_w = the specific heat capacity of water, kJ/(kg · K)
- $\dot{m}_w, \dot{m}_a$ = the mass flow of water and process air, kg/s
- $T_{w,in}, T_{w,out}$ = the inlet and outlet temperature of water, °C
- $h_{a,in}, h_{a,out}$ = the inlet and outlet enthalpy of the process air, kJ/kg

The mass conservation equation is given as:

Equation 2: Mass conservation equation

$$\dot{m}_a (d_{a,in} - d_{a,out})\tau = m_{desi} W$$

Where:

- $d_{a,in}, d_{a,out}$ = the inlet and out humidity ratio of the process air, g/kgDA
- τ = the time of dehumidification process, s
- m_{desi} = the mass of desiccant coated on the DCHE, g
- W = the amount of moisture adsorption by desiccant, g

The amount of moisture adsorption by desiccant silica gel is calculated by the sorption isotherm, which is obtained by Micromeritics gas adsorption analyser (ASAP2020) as shown below.

Equation 3: Fitting equation of desiccant

$$W = 0.62731\,x^3 - 0.60991\,x^2 + 0.2468\,x + 0.00418 \quad (0 < x < 0.77, R^2 = 0.9944)$$

$$W = -153.60301\,x^3 + 403.12453\,x^2 - 347.68326\,x + 98.96314 \quad (0.77 \leqslant x < 1, R^2 = 0.9984)$$

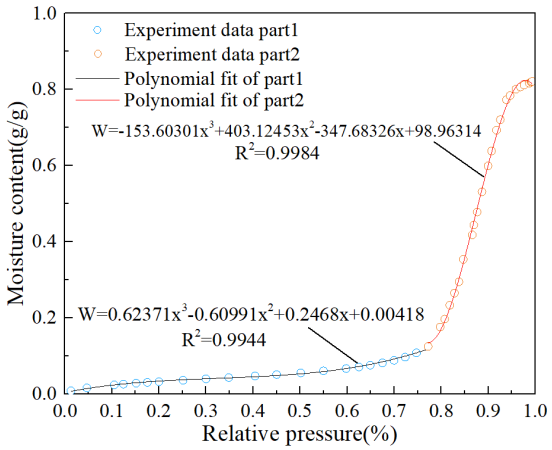

Figure 4: The sorption isotherm of desiccant silica gel

Some supplementary equations for calculating the enthalpy and humidity related parameters are as follows:

Equation 4: Inlet enthalpy

$$h_{a,in} = 1.005\,t_{a,in} + d_{a,in}(2501 + 1.86\,t_{a,in})$$

Equation 5: Outlet enthalpy

$$h_{a,out} = 1.005\,t_{a,out} + d_{a,out}(2501 + 1.86\,t_{a,out})$$

Equation 6: Saturation pressure of water vapour

$$P_{qb} = \frac{2}{15}\exp\left(18.5916 - \frac{3991.11}{t + 233.84}\right)$$

Equation 7: Relationship between humidity ratio and water vapour pressure

$$d = 0.622\frac{P_q}{B - P_q}$$

Equation 8: Relative pressure

$$x = \frac{P_q}{P_{qb}}$$

Where:

- $t_{a,in}, t_{a,out}$ = the inlet and outlet temperature of the process air, °C
- P_{qb}, P_q = the saturation pressure and water vapor pressure of process air, Pa
- B = atmospheric pressure (101325Pa)
- X = relative pressure

3.2. Performance indices

In this paper, performance of the fresh air dehumidification system is evaluated in terms of instant moisture removal Δd_{DE} , as listed in equation (1), average moisture removal $\Delta d_{DE,avg}$, as listed in equation (2), and coefficient of performance (*COP*) of system, as listed in equation (3). The instant moisture removal Δd_{DE} , g/kgDA, is defined by the difference of humidity ratio of inlet and outlet air:

Equation 9: Instant moisture removal

$$\Delta d_{DE} = d_{a,in} - d_{a,out}$$

In a cycle period, average moisture removal $\Delta d_{DE,avg}$, g/kgDA, is more appropriate to describe the dehumidification ability of system because of the variations of desiccant and system status, which is defined in equation (2).

Equation 10: Average moisture removal

$$\Delta d_{DE,avg} = \frac{\sum_0^\tau \Delta d_{DE}}{\tau}$$

In order to investigate the overall efficiency of the system, coefficient of performance of the system is shown in equation (3), which is defined as the ratio between enthalpy change of inlet and outlet air and electric power consumed including compressor, water pumps and fans, et al.

Equation 11: Coefficient of performance of the system

$$COP = \frac{Q}{P_e} = \frac{\dot{m}_a \left(h_{a,in} - h_{a,out}\right)}{P_e}$$

Where:

P_e = the electric power consumed including compressor and water pump, kW

4. RESULTS AND DISCUSSION

The fresh air dehumidification system was experimentally tested in conditions of typical ambient air during the summer in Shanghai, China. The dynamic performance of outlet air of the DCHE was recorded to show the supply air status. Also, the performance of the system including average moisture removal and coefficient of performance (*COP*) was tested.

4.1. Dynamic performance analysis

Dynamic performance of the fresh air dehumidification system in terms of outlet air condition was experimentally tested in this part. In the experiment, the operation parameters were as follows: the average temperature and relative humidity of inlet air were 29.8°C and 60.29%, respectively, and the humidity ratio was 15.97 g/kgDA. Air flow rate was 400 m^3/h, namely velocity of inlet air was 0.96 m/s according to the area of ducts. The average temperatures of cooling water during dehumidification process was 19.7°C and the average temperature of heated air in regeneration process was 45.9°C. The operation cycle time is 20 minutes.

Outlet air temperature and humidity ratio of one cycle time including dehumidification process and regeneration process are shown in Figure 5. The cooling water temperature and regeneration air temperature are shown in Figure 4 as well in order to describe the utilisation of cooling capacity and heat capacity. In the experiment, the dehumidification process of one DCHE could be divided into two parts: in the first part (0-180s), a rapid decrease of outlet air humidity ratio occurs because the cooling water flows into the DCHE rapidly and the high absorption potential of the desiccant caused by previous half cycle of regeneration. However, the temperature of the outlet air is still higher than the ambient temperature due to the effect of high temperature regeneration in the previous half cycle. In addition, fluctuations occur due to the heat capacity caused by the previous half cycle of heated air regeneration. During this part, the instant maximum moisture removal of the dehumidification occurs, which is 7.41 g/kgDA, and at this moment, the outlet air humidity ratio is 8.56 g/kgDA. In the second part (180-600s), with cooling water flowing into DCHE continuously, the temperature of outlet air gradually decreases below 25°C, while the humidity ratio increases slowly because the desiccant approaches saturation gradually but is still less than the ambient humidity ratio. After the desiccant is approaches saturation, the DCHE switches to the regeneration

process by 4-way air valve and 3-way water valves switching. The regeneration process could be divided into two parts: in the first part (600-840s), the outlet air temperature and humidity ratio increased sharply with heated air flowing through the DCHE after 4-way air valve switching. In the second part (840-1200s), the outlet air temperature continued to rise, while the outlet air humidity ratio decreased slightly because the desiccant gradually totally releases the water vapor adsorbed during the dehumidification process. During the dehumidification process, average outlet air temperature and humidity ratio are 27.7°C and 9.91 g/kgDA, respectively. Meanwhile, average moisture removal during the dehumidification process is 6.31 g/kgDA, while average moisture released is 6.38 g/kgDA during the regeneration process.

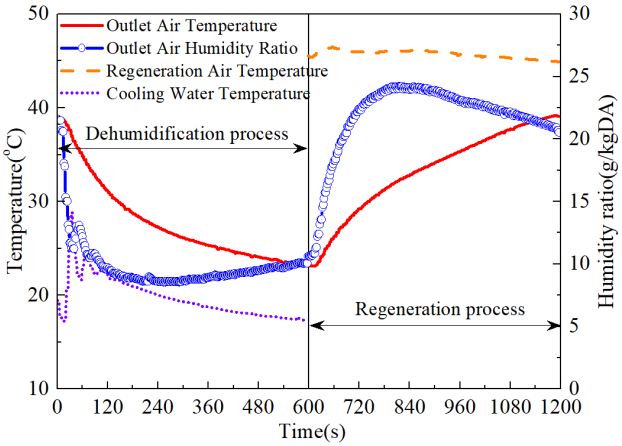

Figure 5: Dynamic performance of the fresh air dehumidification system

4.2. Dehumidification performance of system

In this part, experimental tests of the fresh air dehumidification system were conducted on the Shanghai typical summer conditions (temperature is 28.2°C - 30.1°C, humidity ratio is 15.7 g/kgDA to 16.1 g/kgDA) with different cycle times and air flowrates. The results are shown in Figure 6. Moisture removal and *COP* of system increases first and then decreases with the increase of cycle time. When the cycle is 20 minutes, meaning 10 minutes in dehumidification mode and 10 minutes in regeneration mode, the dehumidification system reaches the most moisture removal 4.67 g/kgDA and the best *COP* 5.20. In a dehumidification cycle, at the beginning of dehumidification process, *COP* was high because the large moisture removal adsorbed by desiccant and *COP* reduced with the decrease of moisture removal adsorbed by desiccant as the process progressed. Therefore, the average *COP* of the dehumidification system decreased with the increase of cycle time within a certain range. However, when the cycle time was too short, the average *COP* of the system reduced because of the loss cooling capacity caused by switching. The best cycle time of the dehumidification system was 20 minutes. Change in *COP* of system with the increase of air flowrate has similar results. With the increase of air flowrate from 400 m^3/h to 650 m^3/h, the average *COP* of the system increased from 4.42 to 5.20, and decreased to 5.08 with the increase of air flowrate from 650 m^3/h to 900 m^3/h. However, the average moisture removal decreased from 6.31 g/kgDA to 3.35 g/kgDA with the increase of air flowrate from 400 m^3/h to 900 m^3/h because the contact time between the process air and the desiccant decreased with the increase of air flowrate.

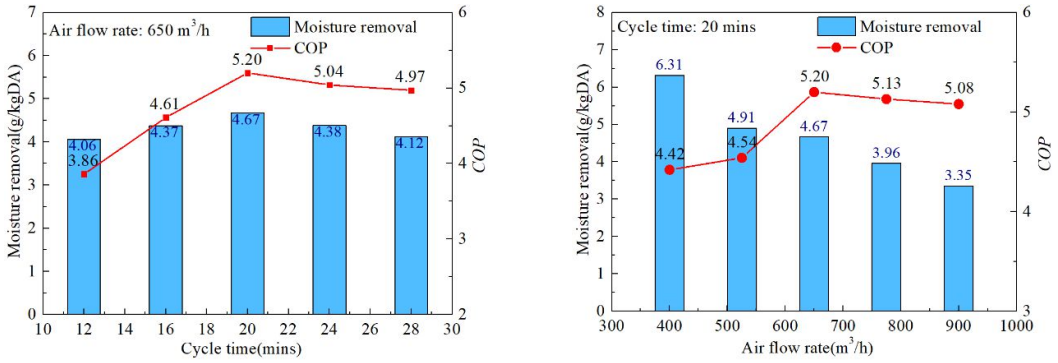

Figure 6: Influence of cycle time and air flowrate on performance of system

4.3. Optimisation for the system

For desiccant, isothermal dehumidification is a better dehumidification process. However, in the system, in order to achieve isothermal dehumidification, the air flowrate was increased to cause a higher evaporation temperature, so that the mass transfer driving force was insufficient during the dehumidification process, which caused the moisture removal to be low. The humidity ratio of supply air did not reach the supply air requirement of less than 10 g/kgDA, although the system *COP* was higher. In this part, the system was optimised for operation at a smaller air flowrate (250m^3/h to 450m^3/h) under both ARI Humidity and ARI Summer conditions to increase the moisture removal to meet the air supply requirements. The results, which are shown in Figure 7, indicate that the moisture removal decreased from 10.49 g/kgDA to 5.54 g/kgDA while COP increase from 4.41 to 4.85 with the increase of air flowrate from 250 m^3/h to 450 m^3/h on the ARI Humidity condition. The outlet air humidity ratio could reduce below 10 g/kgDA as the air flowrate is in 250 m^3/h to 400 m^3/h. Similarly, on the ARI Summer condition, the moisture removal decreased from 7.81 g/kgDA to 3.04 g/kgDA while *COP* increase from 4.07 to 4.43 with the increase of air flowrate from 250 m^3/h to 450 m^3/h. The dehumidification system shows a better performance on the humidity condition. According to calculations, the COP of a conventional heat pump system that could achieve the same moisture removal under ideal rated conditions is also shown in Figure 7. The conventional heat pump system uses the method of condensing to dehumidification, which is to reduce the temperature of the air below the dew point temperature. Therefore, the larger the moisture required, the lower the evaporation temperature of the system, which leads to a reduction in the COP of the conventional heat pump system. This novel fresh air dehumidification system used desiccant to treat the latent heat load, which increased the evaporation temperature of the heat pump subsystem and increased the COP of the system. Compared with the traditional heat pump system, the dehumidification system had a COP increase of about 15% to 55%.

Table. 3 ARI Humidity and ARI Summer conditions

	Temperature (°C)	Relative humidity (%)	Humidity ratio (g/kgDA)
ARI Humidity	30	60	16.1
ARI Summer	35	40	14.3

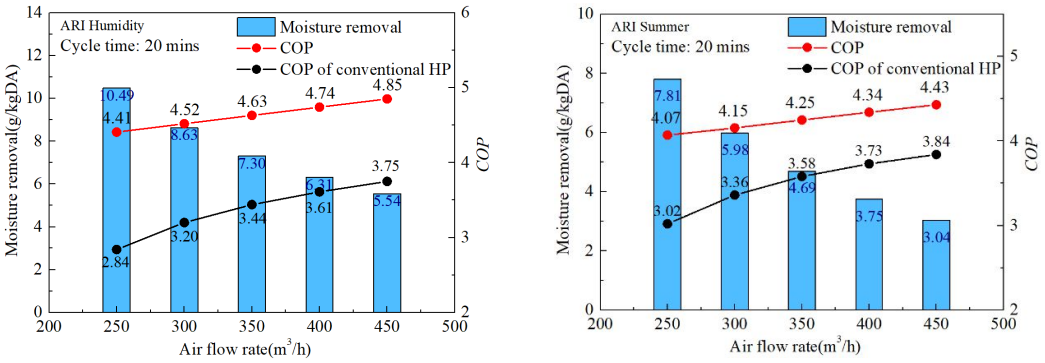

Figure 7: Influence of air flowrate on performance of optimised system on ARI Humidity and ARI Summer conditions

5. CONCLUSION

In this paper, a fresh air dehumidification system using heat pump with desiccant coated heat exchanger (DCHE) was presented. A series of experiments were conducted on typical ambient condition of Shanghai to study the performance including moisture removal and COP of the system and the factors that affect the performance. In this research, the fresh air dehumidification system could achieve isothermal dehumidification by inter cooling based the desiccant coated heat exchanger. The average moisture removal is 4.67 g/kgDA and the average COP of system is 5.20 on the condition that the cycle time is 20 minutes and air flowrate is 650 m^3/h. The cycle time and air flowrate are two factors that affect the performance of the dehumidification system. Higher moisture removal could be achieved in the optimised system at lower air flowrate with a slight reduce on COP. The dehumidification shows a better performance on humidity conditions.

6. ACKNOWLEDGEMENT

This research work is funded by the National Natural Science Foundation of China (No. 51961165110).

7. REFERENCES

Dongmei, P., Shiming, D., Zhongping, L., & Ming-yin, C. 2013. Air-conditioning for sleeping environments in tropics and/or sub-tropics – A review. Energy, 51: 18-26.

Ge, T. S., Dai, Y. J., Wang, R. Z., & Peng, Z. Z. 2010. Experimental comparison and analysis on silica gel and polymer coated fin-tube heat exchangers. Energy, 35(7): 2893-2900.

Hsieh, Y.-Y., Chuang, Y.-H., Hou, T.-F., & Huang, B.-J. 2018. A study of heat-pump fresh air exchanger. Applied Thermal Engineering, 132: 708-718.

Sun, X. Y., Dai, Y. J., Ge, T. S., Zhao, Y., & Wang, R. Z. 2017. Comparison of performance characteristics of desiccant coated air-water heat exchanger with conventional air-water heat exchanger – Experimental and analytical investigation. Energy, 137: 399-411.

Vakiloroaya, V., Samali, B., Fakhar, A., & Pishghadam, K. 2014. A review of different strategies for HVAC energy saving. Energy Conversion and Management, 77: 738-754.

Yu, B. F., Hu, Z. B., Liu, M., Yang, H. L., Kong, Q. X., & Liu, Y. H. 2009. Review of research on air-conditioning systems and indoor air quality control for human health. International Journal of Refrigeration, 32(1): 3-20.

Zhao, Y., Dai, Y. J., Ge, T. S., Wang, H. H., & Wang, R. Z. 2016. A high performance desiccant dehumidification unit using solid desiccant coated heat exchanger with heat recovery. Energy and Buildings, 116: 583-592.

#143: Research on effective utilisation of solar thermal energy by solar energy bench

Takashi YOSHIKAWA

Kindai University Technical College, 7-1 Kasugaoka Nabari-shi MIE 518-0459 Japan, yoshikawa@kuc.ac.jp

This study looks at the effective utilisation of thermal energy especially in a small power domain. In previous studies, the author has clarified the effectiveness of using thermal energy applications for HEMS (Home Energy Management System). In this HEMS, sensor network nodes were used which required an average power of several hundred micro Watts to continue working. We set a challenge to utilise the energy of the temperature difference between the human body and circumference and successfully achieved in excess of an average 100uW power. Now we are interested in gathering more power from solar thermal energy. The first stage involved developing a solar energy bench. The solar energy bench design was based on the solar cooker for gathering solar thermal energy and was focused as the thermal energy raising the temperature of the dumped water used for heat retention. The warming surface of the thermoelectric element was exposed in hot water to solar energy and the opposite surface of the element was attached to the heat sink and exposed in the cooling side. In the first trial, we obtained an electrical energy of almost 0.2mW which was very small compared to estimates. The first prototype had many problems: heat insulation mechanism; heat collecting mechanism; heat transfer mechanism and especially around the heat dissipation mechanism. Subsequently, the revised model introduced a water cooling mechanism on the cooling surface. In the revised solar energy bench, successful results were achieved. The obtained power was over 3mW which is sufficient to keep the sensor network system working. The consideration about the power generating characteristics between air cooling mechanism and water cooling mechanism will be discussed.

Keywords: thermal energy, solar energy, thermoelectric element, energy harvesting

1. INTRODUCTION

Nowadays, there is a movement towards power saving due to environmental problems such as global warming and lack of power resources, and one of the effective methods of saving energy is HEMS (Home Energy Management System). HEMS is a system based on sensing, communicating and controlling the energy consumption of life at home, and it is estimated to have the potential energy saving of 10% to 20%. Japan's government is establishing a HEMS project, and the goal announced by the Ministry of Economy was that HEMS must be spread to all households (50 million households) by 2030 (Yoshikawa, 2017). Although HEMS is considered to be the best method of solving energy problems, it has still not been disseminated widely. This is due to three problems: one is the restriction of location freedom, another is the high initial cost, and finally the low interest shown by individuals for domestic energy saving. Therefore a novel HEMS is proposed which is operated with a sensor network eliminating the problems mentioned above. The biggest challenge in HEMS with sensor networks is securing the power for each sensor network node to keep working. HEMS with sensor networks provide relief, safety and comfort, and the power required is defined by many categories depending on the type of application provided. This study considers a HEMS that uses 20uW power as the first step. A supply of about 100uW on average is necessary to obtain 20uW of usable power (Yoshikawa, 2012). In order to secure the power required by the sensor node, we are looking to harvest energy from human body heat, room illumination, walking vibration and so on. In previous research, the author has shown that 100uW of power can be secured in a house (Yoshikawa & Awai, 2012).

For this study, we have examined the energy harvesting methods applied outdoors and solar power is the most commonly used natural energy power generation. Solar power generation is a convenient method as power is obtained simply by installing a flat panel, but some problems have arisen as follows:

(1) The natural landscape is marred with an array of huge panels;
(2) Ecosystems may be destroyed;
(3) Land does not develop naturally;
(4) Many panels are discarded after 20 years of life, and recycling is expensive;
(5) Some panels contain toxic substances such as Cd and Pb.

Although there are such problems, solar power is currently considered to be the core of new energy. Therefore, this study focused on the use of solar thermal energy, which has a long wavelength, rather than the light energy of the sun. When thermal energy is converted into electrical energy, generated power using thermoelectric elements is performed in a room temperature range, but it has been shown that power generation efficiency is lower than that of photovoltaic power generation. Here, we aim to generate power of mW class to operate the communication terminal of the sensor network described above, not the large power represented by Mega solar. We defined the "solar energy bench" that enables anyone to easily collect the power required for the operation of the sensor network node with solar thermal energy, and started developing this solar energy bench. The concept is defined that solar aperture area is smaller than $1m^2$ and that power generation is possible by being set into the living environment, specifically, locations considered were gardens, rooves, parks, etc.

2. TEMPERATURE DIFFERENCE POWER GENERATION FOR INDOORS

Previous research has experimented with temperature differential power generation in various indoor scenes. The results are described in the experiments of low temperature range (20°C to 40°C) and high temperature range (about 100°C)

2.1. Human body power generation

We have used a Peltier element for the temperature differential power generator which was attached to human skin on its heating surface and attached to the heatsink on its cooling surface. Usually, the human body is constantly around 37°C. The generating power was measured to account for various room temperatures and, to consider human movement, we have also considered the situation when various convection was applied. The experimental landscape is shown in Figure 1 and the results are shown in Figure 2. The Room temperature was selected as 5°C, 10°C, and 30°C corresponding to the Japanese seasons of winter, spring and autumn, and summer respectively. Convection is selected as 0m/s, 0.3m/s, 1.2m/s, respectively corresponding to the quiet state, a momentary hand action, and swinging. Room temperature and convection is controlled by the incubator and PC fan respectively (Yoshikawa, 2015).

The generated power is evaluated as the value of open voltage multiplying short current divided by 4 using I-V property based on the data measured by the source meter. Relating to the temperature difference, winter is the season for greatest power generation, the power is three times larger comparing to the generating power in summer. Relating to the existence of the convection, the generated power at 1.2m/s convection is five times larger

comparing to the generated power when convection is not applied. As the result of this experiment, more than 100uW power generation is warranted during all seasons. And the results show the convection works effectively for power generation. But these results show we can't draw out the sufficient ability of the thermoelectric element because the theoretical value of the generating power must be larger than those results (ref.3.2).

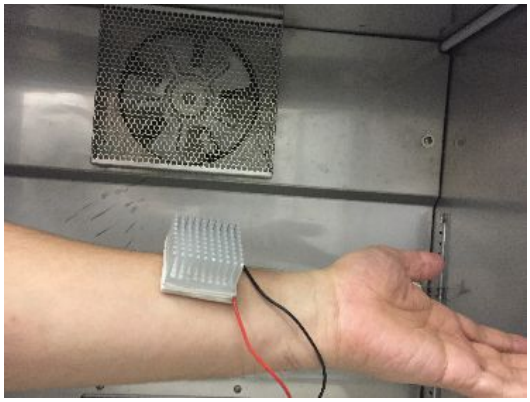

Thermoelectric element (4cm square)

Figure 1: Experiment Landscape

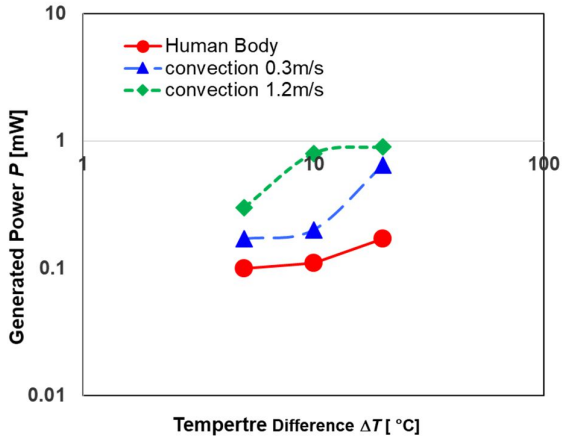

Figure 2: Human skin power generation results

2.2. Hot water tank power generation

As well as previous experiment, we have evaluated the temperature differential power generation in higher temperature region. The surface temperature of hot water tank in the waste incinerator arrives at 100°C. Thermoelectric elements were attached to the outer surface of a hot water tank, as shown in Figure 3, inserting the high thermal conductive silicon sheet.

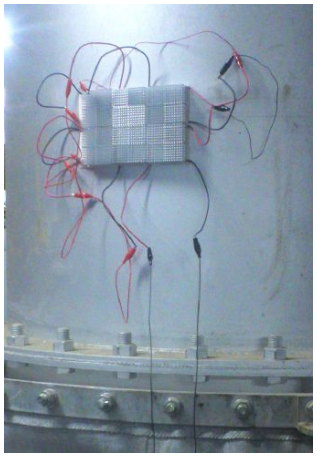

Figure 3: Water tank thermal power generation

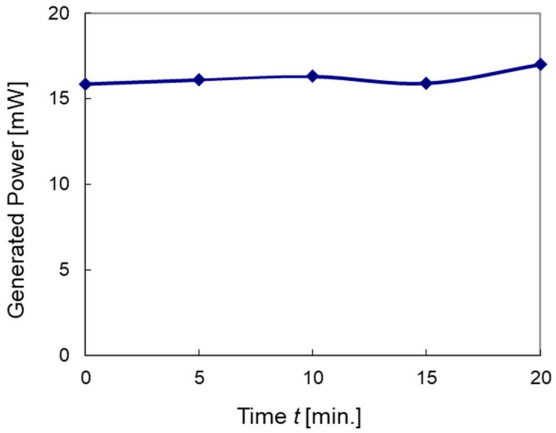

Figure 4: Hot water tank power generation result

The generated power was around 16mW which is 100 times larger than the power by human body power generation under the condition that the temperature difference is 3 times larger and the number of thermoelectric element is 14 times larger comparing to the human body power generation. Considering 4cm square conversion as the same area of human body power generation, generated power is calculated as 1.2mW. Referring to the theoretical consideration, generated power is proportional to the square of the difference of temperature. The estimated power referring to the body generated power as 160uW results in 1.44mW which is comparable to the experimented result 1.2mW, showing that we can't draw out the sufficient ability of the thermoelectric element as well as human body experiment.

3. CONSIDERATION FOR THE DECREASE IN GENERATING POWER

We considered that the decrease in generated power may be due to the lack of temperature difference between the two surfaces of the thermoelectric element. Therefore, the validity of the hypothesis was verified by numerical calculation, and the difference from the theoretical value was clarified by experiments.

3.1. Numerical simulation for consideration for the decrease in generating power

As shown in the measurement results of the 2nd section, in the previous temperature difference power generation experiments, the amount of power generation was lower than theoretical value of the thermoelectric elements. In order to investigate the cause, numerical analysis was conducted using program code FEMAP on the transient characteristics of the temperature around the thermoelectric element when one surface of the thermoelectric element is heated and the other surface with heat sink is immersed in air.

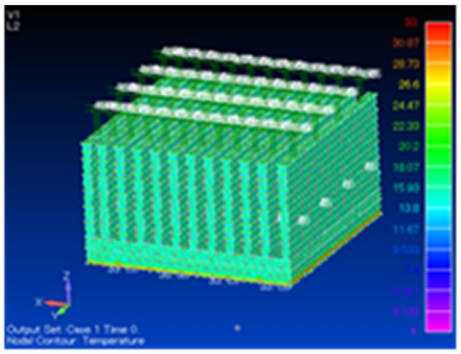

Figure 5: Calculation Model for Heat transmission

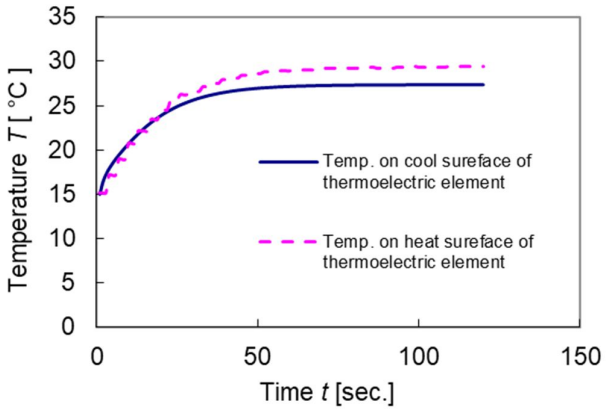

Figure 6: Calculated result of Temperature transition

In this calculation, the temperature characteristic is shown when the temperature of the temperature controller is 30°C with respect to the room temperature of 15°C. When the heat sink is not attached, the temperature difference between the heated surface and the exposed surface is almost 0°C (overlapping with solid line in Figure 6), and the temperature difference of 3°C between cool surface and heat surface can be finally secured by attaching the heat sink. This result shows the effect of being able to give a temperature difference by attaching a heat sink. On the other hand it means even if a heat sink is attached, the temperature difference between two surfaces of the thermoelectric elements is far below to the value originally intended to give as a temperature difference. It is considered that this is due to the convection of air from the heat source and the heat conduction through the thermoelectric element itself. It is considered that it is necessary to actively cool the cooling surface using external power source in order to draw out the ability of the thermoelectric element itself, but in view of the fact that the original our purpose is to extract the weak electric power, we can't use external energy. So we thought about introducing a cooling mechanism that immerses the cooling surface in water. In order to verify the effect, comparative experiments of air cooling system and water cooling system were conducted.

3.2. Experimental data in air cooling and water cooling referring to the theoretical value

We measured the difference in the amount of power generation in terms of heat radiation surface with air-cooled and water-cooled. The temperature of the temperature control table was changed by 5°C from 20°C up to 40°C, and the open end voltage and the short circuit current of the thermoelectric element were measured, and the maximum output power is calculated by the product of the open end voltage and the short circuit current and dividing by 4. In the measurement of a short circuit current, we have used shunt resistance. The experimental scene in the air cooling and water cooling system is shown in Figure 7.

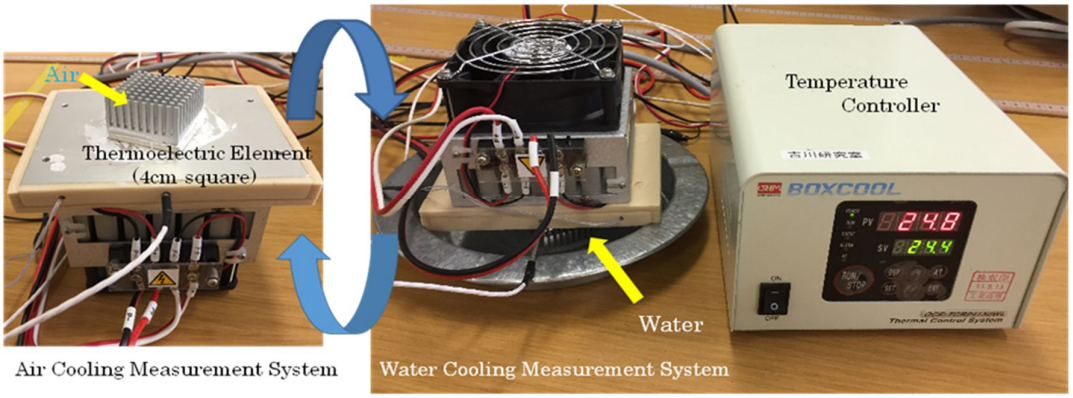

Figure 7: Landscape of Temperature Different Power Generation Measurement for Air Cooling and Water Cooling

Next the theoretical consideration is shown. The generating power is decided by the product of thermal conductive energy and thermoelectric element efficiency. Thermoelectric power is derived by following Equation 1.

Equation 1: Thermoelectric element efficiency

$$\eta = \frac{T_H - T_C}{T_H} \frac{\sqrt{1+ZT}-1}{\sqrt{1+ZT}+\frac{T_C}{T_H}}$$

Where:

- T_H, T_L= Higher Temperature [K], Lower Temperature [K]
- ZT= Figure of Merit for Thermoelectric element

The thermal conductive power is derived by Equation 2.

Equation 2: Thermal Conductive Power $Q[W] = 1.163\, S\, \lambda\, \Delta T / b$

Where:

- S, = Area of Thermoelectric Element
- λ = Thermal conductivity of Thermoelectric Element
- b = Thickness of Thermoelectric Element
- ΔT= Difference of Temperature between both surface of Thermoelectric Element

In the case of ZT=1, η is calculated as $0.0005\,\Delta T$ and using S=0.0016[m^2], b=0.005[m], λ=0.25 [kcal/mh°C], generated power P by thermoelectric element is calculated by multiplying η and Q and is shown as following Equation 3.

Equation 3: Generated Power by Thermoelectric Element $P[mW] = 0.0456\, \Delta T^2$

Here we show the results of fundamental air cooling and water cooling measurement, human body measurement, hot tank measurement, and theoretical calculation in Figure 8. Figure 8 shows that there are double decades power difference between air cooling and water cooling. And the experimental results of human body power generation and hot tank power generation are closely related to the air cooling fundamental measurement results. Of cause when we apply the convection, the generated power is approaching to the water cooling one. Here we have to pay attention that the generating power by water cooing system is closely to the theoretical value. It means the water cooling system is quite effective method for the energy harvesting.

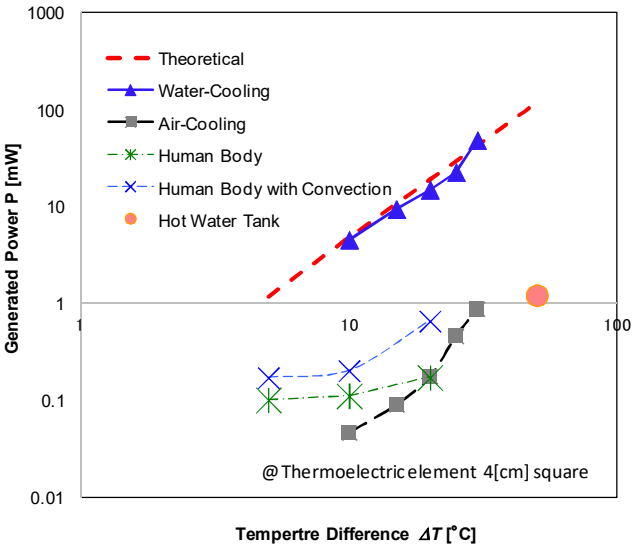

Figure 8: Generated power measured results for many kinds of application referring to the theoretical value.

4. SOLAR ENERGY BENCH DEVELOPMENT

For the reasons described in the background and through the previous experiments, we have started to study outdoor temperature differential power generation replacing the indoor applications. It is most effective to use the energy that is poured from the sun as a way to get heat outdoors. When considering the use of solar heat, the first step is to collect solar heat efficiently in a specified area. Next is to store the gathered heat for a long time. Solar Cooker is mentioned as the most compatible technology in the first step. There are various methods such as parabola type and box type for solar cooker, but in our application, we have tried to make both type of solar cooker and measured the generated power by them. The appearances of both solar cookers are shown in Figure 9 and the experimental results are shown in Figure 10.

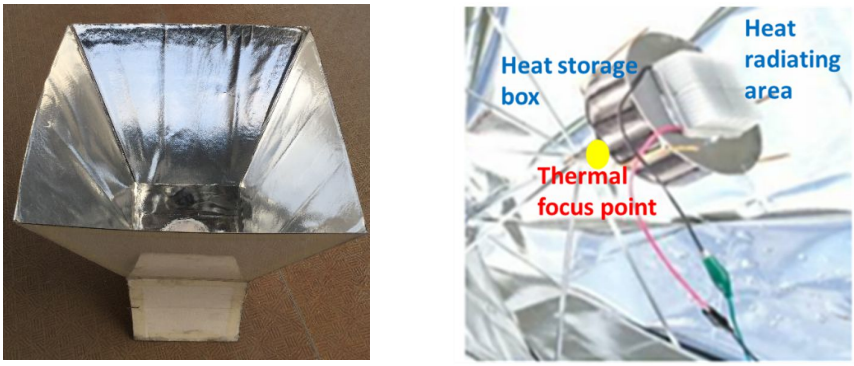

Solar aperture: 38[cm] square *Solar aperture: 80[cm] diameter*

Figure 9: Solar cooker type temperature differential power generator (Left: box type, Right: parabola type)

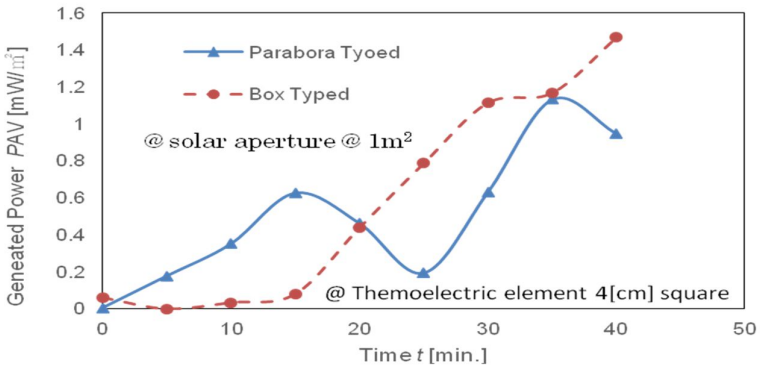

Figure 10: Solar cooker type temperature differential power generator (Left: box type, Right: parabola type)

These experiments are performed under the sun, and gathered heat energy is converted into electrical energy by thermoelectric element (4cm square). The generated power of both solar thermal power generator arrived at 1.2 [mW] based on the normalised solar aperture as 1[m^2]. The parabola type power generator has unstable power generation characteristics because the thermal focus point is narrow and almost all of the parts are exposed to the atmosphere so the wind blows around the heat storage box and the heat radiating area (around the heatsink).

This first prototype mentioned above has many problems for stable and effective power generation, so we have made the revised one. Main revised points are shown as following.

(1) The heat capacity of the heat storage container is too large, so the temperature has not risen in it.
(2) The heat dissipation mechanism for cooling surface was not working well.
(3) Both the heat receiving part and the heat radiating part were easily affected by the wind.
(4) It was too large to handle.
(5) As for the parabola type one, it was difficult to create the structure without becoming complicated.

The revised solar energy bench and its details are shown in Figure 11. First of all, miniaturisation has been realised. For one thing, we have designed the light collection cross section to the necessary minimum size. Furthermore, in the height direction, the focal length is shortened and the light collection efficiency is increased by using two matching lenses. The use of a lens is not only for downsizing but also serves to shield the heat storage unit from the outside air. Next, in order to improve the heat retention characteristics, the heat storage portion is thermally insulated by a heat retention material. Furthermore, it is the most important point that heat dissipation efficiency is improved by using a water cooling mechanism in which the heat sink on the low temperature surface is immersed in water.

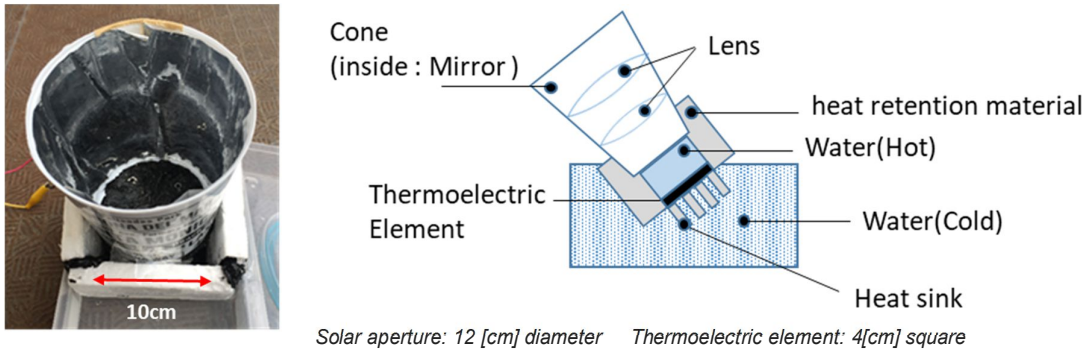

Figure 11: Overview of revised solar energy bench

4.1. Solar energy bench design concept

We have to consider for two points, one is saturation temperature, and the other is effective duration for power generation. Saturation temperature is decided by the balance between solar power as the input, denoted by *P*s, and heat radiation or heat transmitting through the heat retention material as the output denoted by *O*, shown in Figure 12.

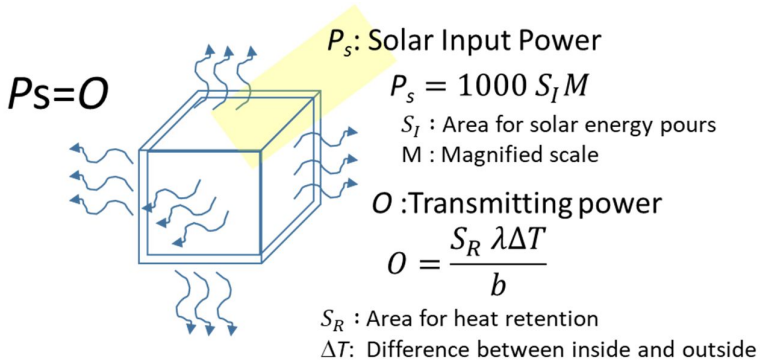

Figure 12: Explanation diagram for the derivation of the saturated temperature in the inner water tank

Duration for power generation is decided by the time constant for the whole system. In this system volume of the water in inner water tank is dominant. When we change the volume of water, time constant τ is changed as τ_1, τ_2, τ_3 and the temperature on the tank is changed shown in Figure 13. As the result, duration for power generation is decided by the volume of water tank and the proper time constant must be selected referring to the daylight hours. In this case we have chosen the value as 60 [cm^3] considering to the compensation by heat retention material.

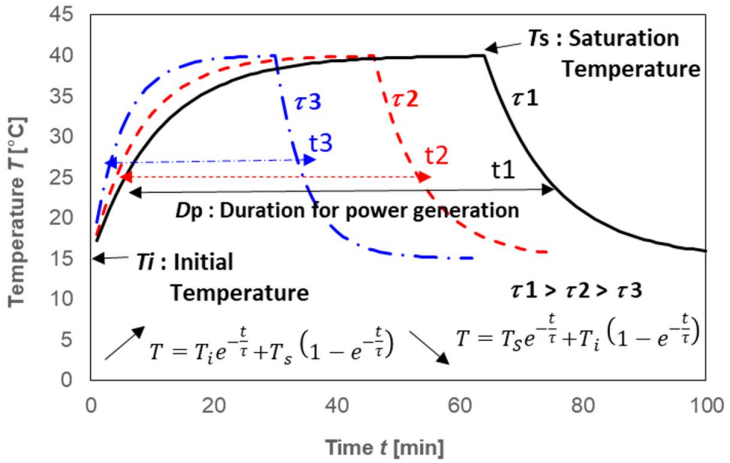

Figure 13: Explanation figure of duration for power generation dependency on time constant

As explained above, the cone size is decided referring to the demanded solar power input as well as water tank volume. We have made revised solar energy bench based on the five items I have shown and measured the characteristics of it. The measurement was performed on sunny day afternoon in December. The time duration of experiment is about two hours and the measurement is made for each five minutes. The result is shown in Figure 14 with the experimented result of first prototype solar energy bench (Box type). The generated power by revised one is much larger than the first prototype although revised one has very small aperture area just as one tenth of the area of first prototype. In this measurement we have calculated the maximum output power which is derived by multiplying output voltage and short circuit current divided by four. At the same time we have measured the temperature of inner (hot) and outer (cool) water. The difference of the temperature between inner and outer water is about 10°C. Referring to the theoretical consideration, we can get about 4.6mW but we could get only 3.7mW which was slightly smaller than that. We suppose that reason coming from the difference of temperature between the thermoelectric element surface and water. As the result, we could get the good results getting more than 3mW for a long time by revised solar energy bench. This result shows solar energy bench can be used for working of sensor network node because the average power for whole day is estimated about 100uW.

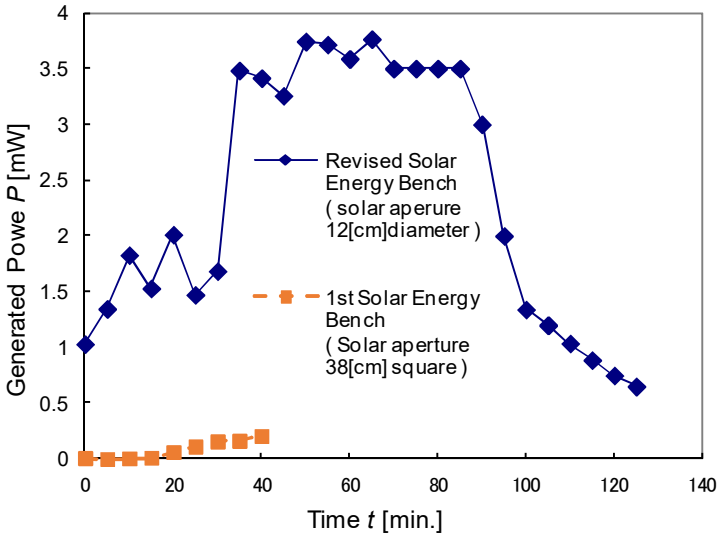

Figure 14: Measurement results for power generation of revised solar energy bench

5. CONCLUSION

We have researched energy harvesting as an energy source to operate small wireless terminals for HEMS applications until now. As the next step, we have started research on using a small communication terminal in outdoors, assuming an outdoor sensing application. When considering outdoor energy harvesting, it is most effective to use the energy pouring from the sun. Solar power is currently the most popular method of power generation using solar energy, but solar power has the problems such that the efficiency of power generation is decreased when there is no strong light or unstable energy supply, so we have started considering the use of the solar heat energy for outdoor application as an alternative method. We have experienced that there exist a seriously problem that we can't obtain enough power using the thermoelectric element comparing to the theoretical value from the background of researching various temperature difference power generation in HEMS until now. The factor was assumed that the temperature difference between the two surfaces of the thermoelectric element was not sufficiently secured, and numerical calculations and power generation experiments specialised for only the power generation part were performed. The factor is that the temperature difference between both surfaces of the thermoelectric element with the heat sink attaching to the heat radiation surface is estimated very small with a value of a few tens of percent corresponding to the temperature difference we want to apply and the generated power is measured as the value of several percent comparing to the value when radiation surface is immersed in the water. Then we have made the prototype of water cooling solar energy bench and evaluated. As the results we could get more than twenty times generating power than air cooling conventional one. The generating maximum power is over 3mW and the average power is over 2mW for two hours. This means that about 100uW of power can be obtained on average in one day by the small volume as 0.015 [m^3] (25 [cm] cube containing water reservoir) solar energy bench. We can conclude our solar energy bench can be used for power source of small sensor network terminal.

6. REFERENCES

Yoshikawa T, 2012, "Novel Concept for HEMS Apparatus", Elsevier Science Direct 2012 Energy Procedia 14, pp.1273-1279.

Yoshikawa T, Awai I, 2012, "A Novel Design for HEMS consisting of Sensor Network Nodes with Energy Harvesting and Wireless Power Transmission", AIEM(Advances in Industrial Engineering and Management), Vol.2, No.1, PP.11-15.

Yoshikawa T, 2015, "Many Kinds of Energy Source in Our Surroundings at Home", Springer Proceedings in Energy on ENEFM 2014, PP.307-312.

Yoshikawa T, 2017, "Novel Concept "HEMS E Project" Challenge", ATLANTIS PRESS, Advances in Intelligent Systems Research (AISR), Vol.145, PP.233-237.

#147: An innovative hollow fibre-based dehumidification–cooling system for residential building retrofits: experiments and case study

Ke QU[1], Xiangjie CHEN[2], Saffa RIFFAT[3]

[1] University of Nottingham, University Park, Nottingham, NG7 2RD, United Kingdom, ezxkq@nottingham.ac.uk
[2] University of Nottingham, University Park, Nottingham, NG7 2RD, United Kingdom, ezzxc1@nottingham.ac.uk
[3] University of Nottingham, University Park, Nottingham, NG7 2RD, United Kingdom, Lazsbr@nottingham.ac.uk

Building retrofitting is an important method to reduce energy consumption; however, considering the post-retrofit building performance of traditional energy efficient interventions, the issue of indoor air quality, such as humidity and sanitation, is often complained about by occupants. Therefore, independent controls for humidity and temperature in air conditioning systems needs to be further improved using advanced technologies to improve comfort levels in order to increase the retrofit rate of residential buildings. This paper presents an innovative hollow fibre-based dehumidification-cooling system with pre-cooling solution for residential building retrofits, with the aim of realising an accurate humidity control with less energy consumption compared to commercial heat pump-based air conditioners. The proposed concept for a cooling and dehumidification system is a two-step process by applying hollow fibre system, which consists a liquid desiccant dehumidification cycle, and a water evaporative cooling cycle. The experiment results show that the maximum overall cooling and dehumidification COP reached 4.36 with outlet air temperature of 27.6°C and humidity of 70.7%, when the inlet air has a temperature of 40°C and humidity of 80%, under the condition of pre-cooling degree of 0.3. Besides, the maximum dehumidification COP, and cooling COP reaches 7.10 and 9.04 respectively, with pre-cooling degree of 0.5, under the NTU value of 4.5. Moreover, an Italian residential building used as a case study to investigate the energy saving performance with the dehumidification and cooling performance under the hot and humid summer in Mediterranean area from May to September. The simulation results illustrates that approximately 84% reduction of the cooling energy consumption achieved (from 5.99 kWh/m2 to 0.96 kWh/m2) and 63% of comfort hours increased (from 4301 hours to 7031 hours), which is under humidity control section between 40% and 60% and temperature control section between 20°C and 22°C, if compared with a traditional commercial split air conditioner.

Keywords: building retrofit; hot-humid area; hollow fibre; liquid dehumidification; evaporative cooling

1. INTRODUCTION

Air conditioning systems are recognised as an indispensable method of improving human beings' thermal comfort and living conditions since the early twentieth century. With growing concerns about the greenhouse gas emissions, the aggravating primary energy shortage and increasing energy demand, the energy consumption of buildings is at a critical stage, accounting for 40% of energy demand in Europe (LRg., W., 2006). According to the EU Directive (Directive 2010/31/EU, 2010) in Europe, 6% of office, commercial and industry buildings are air-conditioned, with a total volume of 20 million cubic meters. In hot and humid climatic conditions, air conditioning systems account for more than 50% of the total building energy consumption (Pérez-Lombard, 2008; Lior, 2012). The current widely-used vapour compression system plays a dominant role in the market. However, vapour compression systems have the disadvantages of intensive energy consumption and low performance in hot and humid climate. Moreover, the possible leakage of high GWP refrigerants will lead to the depletion of the ozone Layer, which further contributes to the global warming and other associated environmental and social changes. Hence, the development of more energy efficient and environmentally benign cooling systems remains a subject of much scientific research. In the past few decades, evaporative cooling system have received much attention from researchers due to the fact that it is more environmentally friendly (use of the water as working fluids), simple in structure configuration, and uses less primary energy. Direct evaporative cooling systems work under the following principle: the incoming hot and humid air gets into direct contact with the circulating water causing the evaporation of the water and the air temperature will reduce accordingly. Subsequently, the evaporated water in the form of vapour will be absorbed by the air leading to the humidity increase of the outlet air. As the key element in desiccant cooling systems, desiccant is a material that has a significant capacity of holding water. With the advantages of light weight, corrosion resistant and no liquid droplet carryover (Chen, 2016a; Chen, 2016b), hollow fibres have been considered as alternatives to porous media or metallic materials for the manufacturing of dehumidifiers. However, work conducted by researchers (Huang, 2012; Huang, 2016; Zhang, 2012; Zhang, 2014; Zhang, 2016) have mainly focussed on theoretical modelling such as using free surface model (Zhang, 2012) with LiCl or CaCl2 as the liquid desiccant. The application of aqueous potassium formate (KCOOH) solution as the liquid desiccant in polymer hollow fibre integrated liquid desiccant cooling system has never been analysed by researchers (Zhang, 2012; Huang, 2012). This paper presents a novel two-stage dehumidification and cooling system which is based on the integration of a pre-cooled liquid desiccant dehumidification process and a pre-cooled water-cooling process. The system performance is analysed with laboratory testing and serves as the input information to the simulation model. A residential building case study in Italy is implemented by applying the innovative retrofit technology to demonstrate the performance with the novel two-stage dehumidification and cooling system.

2. PROPOSED INNOVATIVE CONCEPT AND SYSTEM SCHEMATIC

The proposed concept for evaporative cooling and dehumidification system is a two-step process, which is assembled with independent solution cycles. The first is a liquid desiccant dehumidification process and the second is a water-cooling process. The experiments were conducted in the laboratory of the Department of Architecture and Built Environment, University of Nottingham. The schematic diagram is shown in Figure 1. The proposed system comprised of two polyvinylidene fluoride (PVDF) hollow fibre units, air tunnels, solution pumps, and circulation pumps, a fan, two solution tanks, two heat exchangers, one regenerator, and one boiler. There were two similar core polymer hollow fibre modules with the dimension of the cross-section diameter of 0.2m and the height of 0.5m. The hollow fibre modules used polyvinylidene fluoride (PVDF) material (manufactured by ZENA Ltd.) consisting of 5000 fibres which had an outside diameter of 1.6mm and inside diameter of 1.4mm, an effective pore size of 0.5μm and a porosity of 50%. The flow meters were installed to control the solution flow rate inside the fibres.

In this experiment, the fan imported hot and humid air from the environment chamber and flowed direct across the first hollow fibre module. The strong potassium formate solution flowed inside the hollow fibres from top to bottom by gravity allowing moisture to transport on the external fibre surface by the difference of the water vapour pressure between the intake humid air and the liquid solution inside the fibres, which can reduce the humidity of the intake air. Meanwhile, the pre-cooling solution can also induce the heat conduction from the external hot air to the solution, which reduced part of the intake air temperature. Therefore, the intake air at point 1 with hot and humid status was processed into point 2 with hot and dehumidified status. At the same time, the weak solution out of the hollow fibre module flowed into the regeneration unit where most of the liquid water inside the weak solution evaporates, thus the solution is once more strengthened. The hot strong solution was pre-cooled by heat exchange with cold water.

Then, the hot and dehumidified air cross-flowed the second hollow fibre module from point 3, making contact with the cool surface of the external hollow fibres, and through to the outlet at point 4 with cooled and dehumidified air. The cool water flowed through the inside of the hollow fibres, absorbing the heat from the passing air by heat conduction, reducing the temperature of the air passing through, with the air keeping an almost constant relative humidity. The water was cooled in a heat exchanger, and pumped back to the cold water tank.

In conclusion, from the perspective of the heat and mass transfer, the air conditioning process can be separated into two steps. In the first step, the hot and humid air was dehumidified by the liquid desiccant strong solution, and

the pre-cooled solution can increase the dehumidification efficiency. At the same time, the air was also pre-cooled. In the second step, the pre-cooled and dehumidified air experience further cooling to be a desired cooled and dehumidified air, which satisfy the requirement of the indoor comfort environment.

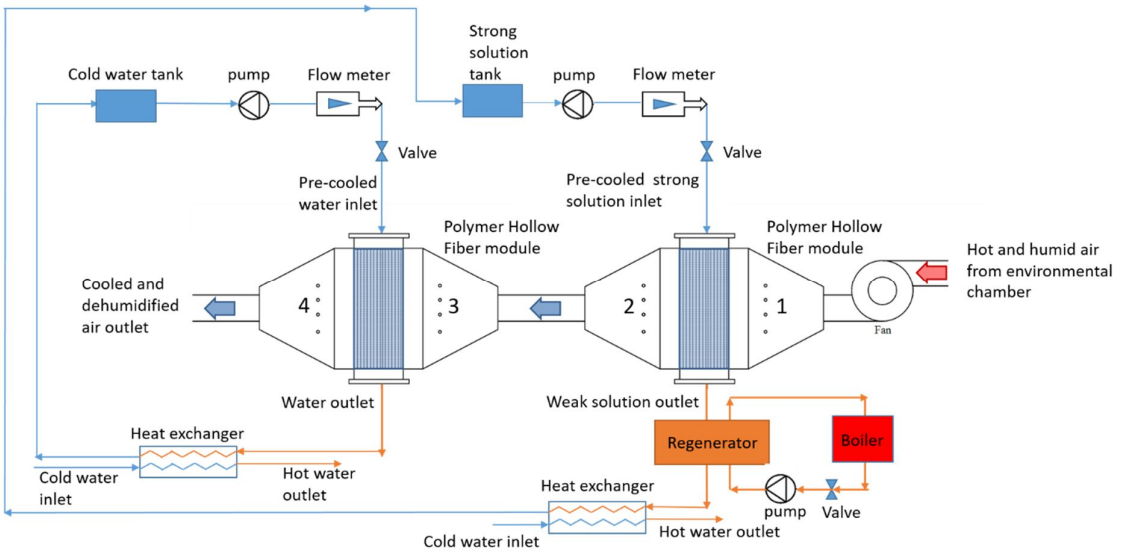

Figure 1: Schematic diagram of the innovative system

3. SYSTEM PERFORMANCE ASSESSMENT

3.1. Assessment standard

Air side moisture remove rate (MMR)

Air side moisture remove rate (MRR) indicates the dehumidification capacity, which is in the unit of kg/s. It depends on the both the dehumidification efficiency and the air mass flow rate, which can be calculated by the following equation:

Equation 1: $$MMR = \dot{m}_a * (\omega_{a,in} - \omega_{a,out})$$

Air side cooling capacity (Q_c)

The air side effectiveness cannot reflect the heat transfer ability correctly in the hollow fibre units. Because the heat transfer effectiveness is applied in the unit of heat exchanger without mass transfer. However, in the hollow fibre units, there are conjugate heat and mass transfer phenomenon. Therefore, it is important to use the cooling capacity to evaluate the real cooling ability, which can be calculated by the following equation:

Equation 2: $$Q_c = \dot{m}_a * (h_{a,in} - h_{a,out})$$

Air side pre-cooling degree (PCD)

One of the purposes of this study is to find the impact of the pre-cooling solution on the dehumidification and cooling effectiveness. Therefore, to better describe the degree of pre-cooling action and compare with varied inlet situation, the non-dimensional parameter pre-cooling degree (PCD) is defined as the ratio of the actual inlet temperature difference with pre-cooling action and the maximum temperature difference without pre-cooling action, which can be calculated with the following equation:

Equation 3: $$d_{pc} = \frac{(T_{sol,out} - T_{sol,in})_{with\ pre-cooling}}{(T_{sol,out} - T_{sol,in})_{without\ pre-cooling}}$$

3.2. Combination process

The combination of the desiccant dehumidification and water-cooling process is described in Figure 2, with process line from 1 to 2' and 2' to 4, respectively, which is compared with the conventional air conditioning process (line: 1-2-3-4) in the psychometric chart. It is obvious that the process from 1 to 2' is mainly with the function of the dehumidification, and the process from 2' to 4 is mainly with the function of the cooling. The outside air inlet temperature and humidity is 30℃ and 70%, respectively, which does not provide thermal comfortable for the occupants. The first process stage with pre-cooled 15℃ liquid desiccant can adjust the inlet air to the state of 24.7℃ and 61% (as shown in Table 1). Besides, the second stage with pure water cooling, decreases the temperature of the air from 24.7℃ to 19.8℃, while maintaining relative humidity. Compared with the conventional air conditioning process, 26% of primary energy saving is reached by applying the novel two-stage air conditioning process.

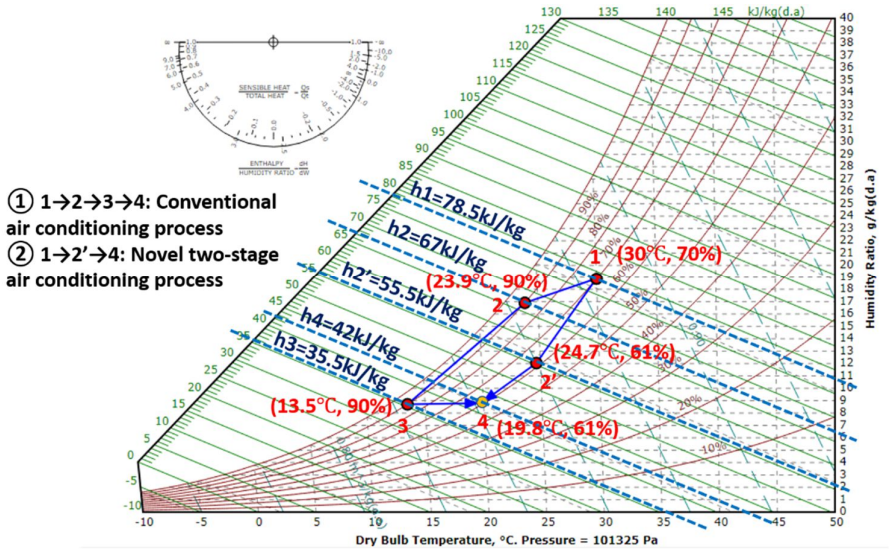

Figure 2: Comparison of conventional and novel air conditioning process in psychometric chat

Table 1: Performance of combination of two-stage dehumidification and cooling process

No	Initial condition		First stage				Second stage				overall performance		
	$T_{initial}$	$RH_{initial}$	$T_{sol,in,1}$	d_{pc}	$T_{out,1}$	$RH_{out,1}$	$T_{sol,in,2}$	d_{pc}	$T_{out,2}$	$RH_{out,2}$	MMR	Q_c	EER
1	30	70	21.3	0.09	25.39	65.73	17.5	0.10	21.14	65.66	1.02	434	3.65
2	30	70	13	0.35	23.44	56.71	16.1	0.17	19.65	56.81	1.40	701	4.27
3	30	72	15	0.30	24.53	61.97	18	0.08	20.79	60.85	1.24	611	3.73
4	30	70	15	0.30	24.70	61.00	16.6	0.26	19.80	61.00	1.33	640	3.90
5	30	75	14.2	0.27	25.01	66.53	17.2	0.12	21.39	67.29	1.25	560	3.41
6	40	75	21	0.22	32.80	71.70	20.1	0.19	24.48	70.65	2.43	1407	4.00
7	40	80	23.2	0.17	34.50	70.60	19.7	0.3	27.6	70.70	2.76	1534	4.36

4. CASE STUDY

4.1. Site introduction

In this research, a demonstration site case study was chosen located in a housing estate in the Martellago commune, the Province of Venice, the Italian region of Veneto to illustrate the system's performance of the two-stage humidification-cooling process. It is at a latitude of 45°33′N and longitude of 12°10′E and the location of the demo site in geographical are illustrated in the Figure 3 with different map scale.

Figure 3: Location of case study demo site

The research building is a semi-detached multifamily house, which is occupied by four people (two families), which was constructed in 1960s with a total of 158m^2 space area. Figure 4 illustrates the ground floor plan with one of the families. The ground floor living room is demonstrated in Figure 4 as the research object, which will be simulated with applying the technology to adjust the humidity and temperature in the living room. The ground floor has a totally floor area of 80m^2. The previous cooling system is a portable air conditioner with air-to-air heat pump, which was mounted in 2007, and has a maximum cooling capacity of 2.4 kW. From the technical view, the overall energy efficiency rate (EER) is approximately 2.5 with maximum air flow rate of 300m^3/h.

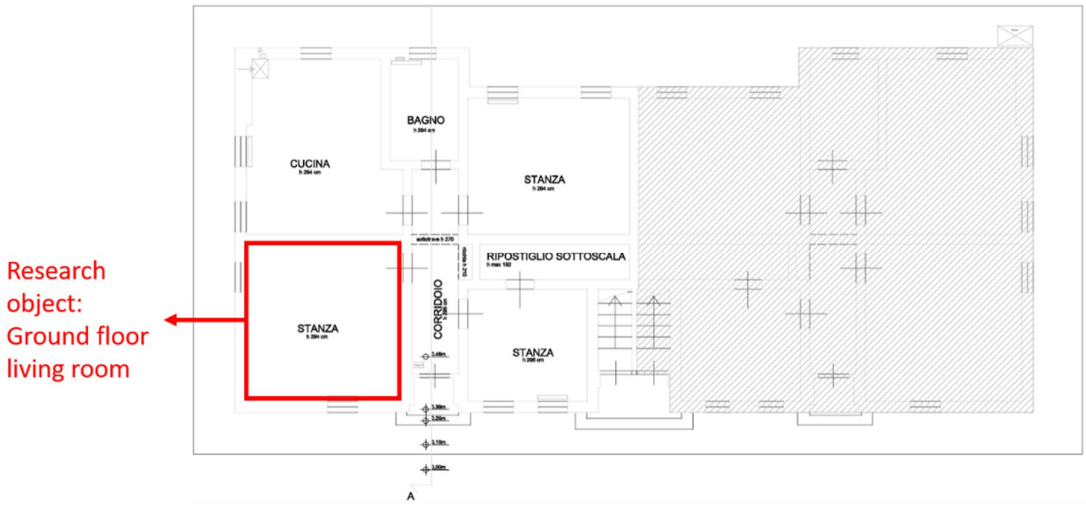

Figure 4: Ground floor plan and research room object

The weather of the demo site is Mediterranean climate with hot and humidified character, especially in summer. Figure 5 illustrates the state frequency of each hour in the summer from 1st of June to 30th of September with high frequency of humidified air more than 75% in average, which makes the occupiers feel damp and unpleasant. Besides, there are still a large number of the hourly temperature higher than 24℃ with relative humidity higher than 70%, which makes the occupants feel hot and damp. Therefore, to improve the indoor comfort level especially in summer, the dehumidifier and the cooler must be applied as an energy efficient retrofit intervention, which also helps to increase the building retrofit rate of residential building section of EU.

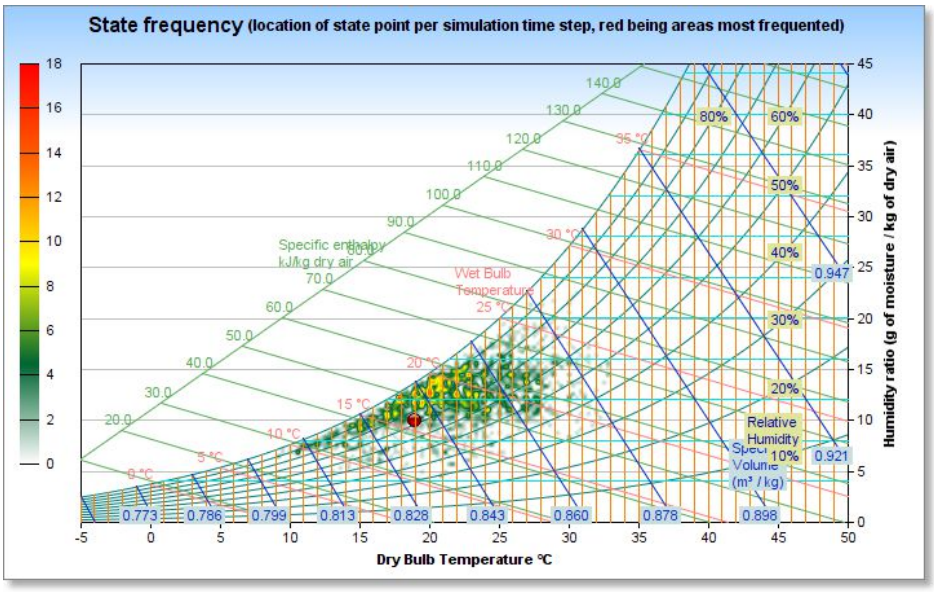

Figure 5: Frequency of hourly air state in psychrometric chart (red being area are the most frequented)

4.2. Methodology

This research used experiments and integrated simulation methodology, which integrates the basic performance coefficient from the laboratory experiment as the technical data and inputs the performance data to the building energy model in the Integrated Environmental Solutions Virtual Environment (IESVE) software. The aim of the study is to work out the post-retrofit building performance including energy consumption and comfort level related to the retrofit with the two-stage dehumidification and cooling system.

Table 2 summarises the system's performance with four key indicators including sensible heat effectiveness in the first stage (liquid dehumidification process), sensible heat effectiveness in the second stage (water cooling process), moisture removal rate in the first stage (liquid dehumidification process), moisture removal rate in the second stage (water cooling process). Besides, the four key indicators are demonstrated with pre-cooling degree varied from 0.1 to 0.5, which is based on average summer season ground water temperature (calculated between June to September), as is shown in Table 3 with relative different ground water depth. It is obvious that with the increase of the ground water depth, the average ground water temperature decreases from 19.37℃ at 0.5m depth to 16℃ at 4m depth. Moreover, Energy efficient rates (EER) with varied pre-cooling degree and ground water depth are summarised in Table 4, which is calculated according to the experimental performance of the two-stage dehumidification and cooling process. It is obvious that the system EER increases with a higher pre-cooling degree, and decreases with a deeper of the ground water depth, which indicates the highest EER of 7.98 with 0.5 degree of pre-cooling and 0.5m of ground water depth. And the lowest EER occurred with 2.38 when there is 0.1 degree of pre-cooling and 4m ground water depth.

Table 2: System performance with varied pre-cooling degree

dpc	εsen,1	εsen,2	MMR1	MMR2
0.1	29.00%	56.80%	0.45	0.45
0.2	36.84%	43.64%	0.79	0.66
0.3	33.77%	46.29%	0.89	0.53
0.4	34.43%	42.49%	0.91	0.8
0.5	35.00%	38.44%	1.09	0.89

Table 3: Ground water temperature in varied ground depth

Ground water depth	0.5m	2m	4m
Ground water temperature	19.37℃	17.83℃	16.00℃

Table 4: Energy efficient rates (EER) with varied pre-cooling degree and ground depth

System EER		Ground water depth		
		0.5m	2m	4m
Pre-cooling degree (dpc)	0.1	2.61	2.47	2.38
	0.2	4.24	3.72	3.40
	0.3	5.05	4.34	3.90
	0.4	6.47	5.44	4.79
	0.5	7.98	6.60	4.83

Table 5 defines the indoor comfort level with different temperature and relative humidity levels, with 7 categories of temperature ranges and 6 categories of relative humidity, which can be simply divided into three attitudes, including unpleasant, acceptable, and comfortable. The comfortable zone is defined as the temperature varied between 20°C and 22°C with relative humidity varied between 40% and 60%. The acceptable zone is defined as the temperature varied between 18°C and 24°C with relative humidity varied between 30% and 70%. Besides, any point of air state exceeding the acceptable zone will make people feel unpleasant. Therefore, this paper will apply the definition of the comfortable degree to make an assessment on the indoor thermal environment of the simulated post-retrofit building performance.

Table 5: Comfortable level definition of temperature and relative humidity

T		RH	
<18	Cold, unpleasant	>80%	damp, unpleasant
18-19	Cold, acceptable	70%-80%	slightly damp, unpleasant
19-20	Slightly cold, acceptable	60%-70%	Slightly damp, acceptable
20-21	Comfortable, pleasant	50%-60%	Comfortable, pleasant
21-22		40%-50%	
22-23	Slightly warm, acceptable	30%-40%	slightly dry, acceptable
23-24	Warm, acceptable	<30%	dry, unpleasant
>24	Hot, unpleasant		

4.3. Results

Integrating the two-stage system performance acquired in the experiments with the IESVE building energy model, results estimation of the post-retrofit indoor environment state are carried out under varied working conditions. Post-retrofit performance with thermal comfort and energy section are analysed with definition of different comfort degrees.

Figure 6 indicates the hourly hydrothermal state before and after retrofit. As shown in the figure, the baseline points before retrofit are mainly concentrated in the hot and humid area with temperature higher than 24℃ and relative humidity higher than 70%. Compared with the baseline, the post-retrofit results of three system working conditions under 4m-0.5dpc, 2m-0.5dpc, and 0.5m-0.5dpc are more concentrated in the acceptable zone. Working condition of 2m-0.5dpc, and 0.5m-0.5dpc are more attractive due to its' location in the comfortable zone.

Figure 7 and Figure 8 look into details of thermal satisfied hours and thermal comfort percentage according to occupants' perception. It is found that the thermal comfort hours under working condition of 0.5m and 2m ground water depth are much better than at 4m ground water depth, due to the low ground water temperature with an average of 16℃ in summer, which make the processed air temperature lower than the comfortable level. Besides, the highest 2475 comfortable hours occurred with the condition of 0.5m ground water depth and 0.1 pre-cooling degree, which accounts for 85% of the overall assessed hours. Under 0.5m ground water depth, the thermal comfort varied from 67% to 85%, which is slightly higher than the condition of 2m ground water source, with the thermal comfort varied from 56% to 79%. The worst performance occurred in the working condition of 4m ground water depth with only 3% to 31% of thermal comfort proportion, because most of the comfort states are transferred into acceptable states under low ground water temperature.

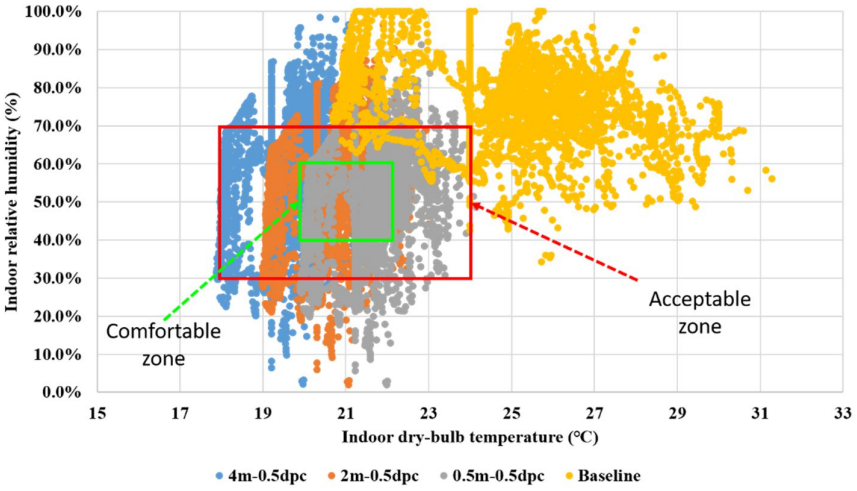

Figure 6: Hourly hydrothermal state before and after retrofit

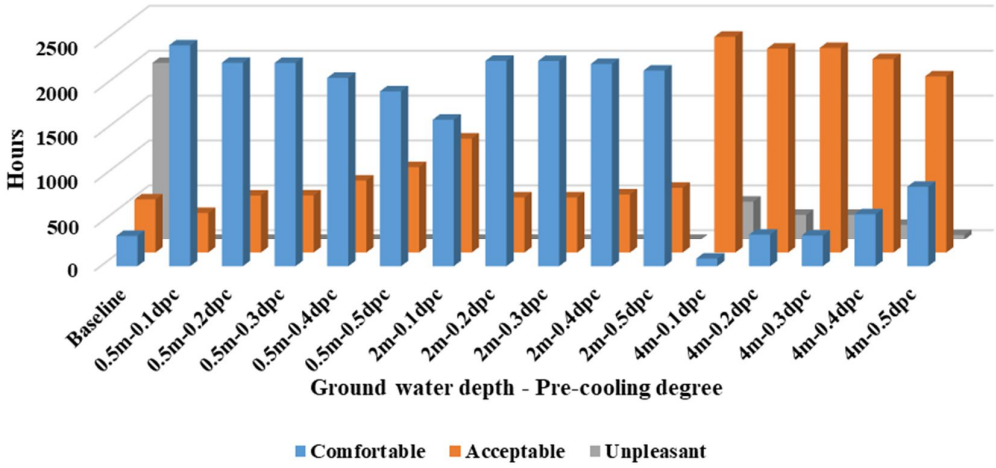

Figure 7: Thermal satisfied hours

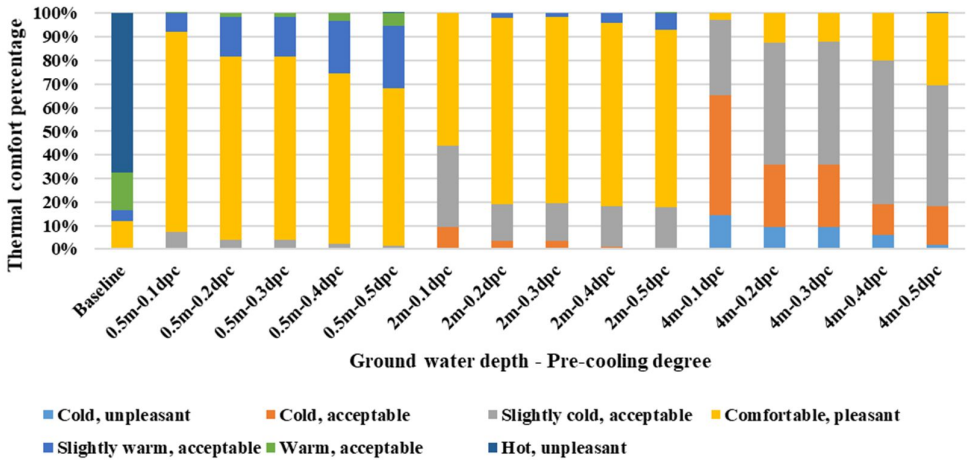

Figure 8: Thermal comfort percentage according to occupants' perception

Figure 9 and Figure 10 have a deep understanding on the humidity satisfied hours and humidity comfort percentages according to occupants' perception. It is found that humidity comfort hours under working conditions of 0.5m and 2m ground water depth are much better than at 4m ground water depth, due to the ground water temperature with an average of 16• in summer is lower than the dew point, which induced a very high relative humidity with condensation of the moist air. Besides, the highest 2531 unpleasant hours occurred with the condition of 4m ground water depth and 0.1 pre-cooling degree, which accounts for 86% of the overall assessed hours. Under 0.5m ground water depth, the humidity comfort varied from 12% to 53%, which is slightly higher than the condition of 2m ground water depth with the thermal comfort varied from 9% to 47%. Moreover, humidity results show that with increasing of pre-cooling degree, the comfortable and acceptable hours are also increase in the same trend.

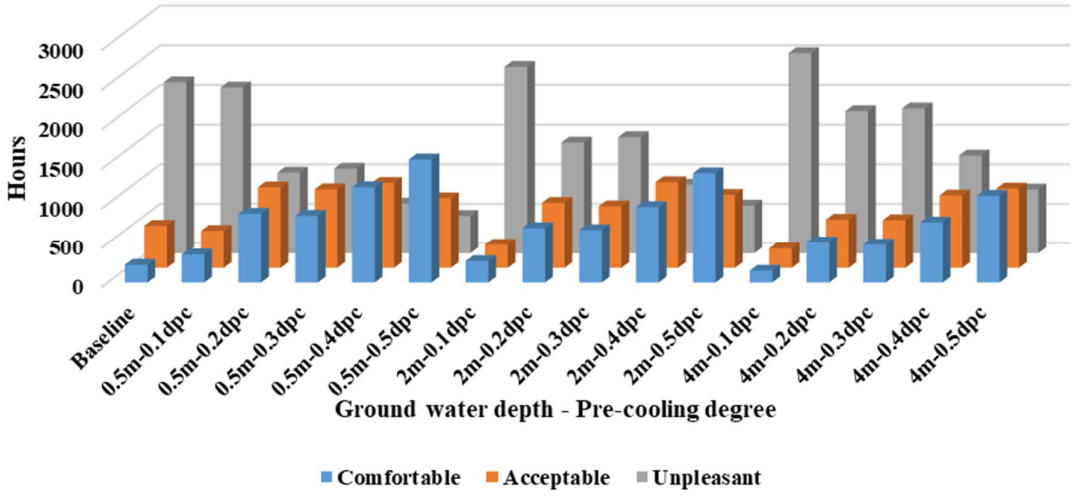

Figure 9: Humidity satisfied hours

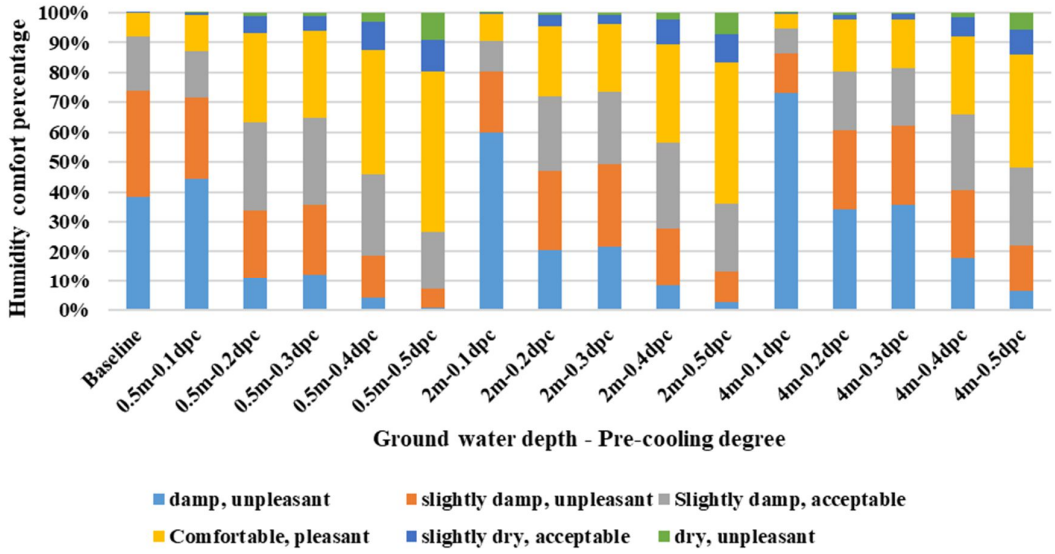

Figure 10: Humidity comfort percentage according to occupants' perception

Two recommendations with high energy efficiency are summarised in Table 6, which is compared with the baseline. As is shown in the table, the baseline has approximately 12% of thermal comfort rate, and 7.7% of humidity comfort rate, which shows that most of the time in the summer is unpleasant for the local residents. Applying the innovative two-stage dehumidification and cooling system, the comfort rate increased to 67.0% and 74.9% under working conditions of 0.5m and 2m ground water depth and the same 0.5 degree of pre-cooling. Besides, the relative humidity comfort rate increased to 53.4% and 47.4% under the relative conditions. Moreover, compared to the primary energy consumption of the cooling section of around 5.99 kWh/m2 in the baseline, the proposed system

achieved 84% reduction to 0.96kWh/m^2 and 79% reduction to 1.25kWh/m^2, under working conditions of 0.5m-0.5dpc, and 2m-0.5pdc, respectively.

Table 6 Recommendations and post-retrofit energy performance

	Temperature comfortable hours	Comfortable rate	Relative humidity comfortable hours	Comfortable rate	System EER	Primary energy consumption (kWh/m2)	Energy reduction rate
Baseline	352	12.0%	225	7.7%	2.5	5.99	
0.5m-0.5dpc	1962	67.0%	1563	53.4%	7.98	0.96	84%
2m-0.5pdc	2194	74.9%	1389	47.4%	6.60	1.25	79%

5. CONCLUSION

This paper proposed a novel two-stage dehumidification and cooling system which is based on the integration of a pre-cooled liquid desiccant dehumidification process and a pre-cooled water-cooling process. In the laboratory test, the combined system has the energy efficiency rate varied from 3.41 to 4.36 under varied test conditions, with maximum cooling capacity of 1534W, and maximum moisture removal rate of 2.76 kg/s. Moreover, a demo site case study was chosen to demonstrate the system performance of the two-stage humidification-cooling process, located in a housing estate in Martellago, Italy. With air regularly at a relative humidity of more than 75%, and temperature higher than 24°C, the occupiers feel damp and unpleasant. Therefore, to improve the indoor comfort level especially in summer, the two-stage dehumidifier and cooler is applied as an energy efficient retrofit intervention in the 60s' residential buildings. Integrating the two-stage system performance acquired in the experiments with the IESVE building energy model, results estimation of the post-retrofit indoor environment state are carried out under varied working conditions. Two recommendations with high energy efficiency are suggested. Applying the innovative two-stage dehumidification and cooling system, the comfort rate increased to 67.0% and 74.9% under working conditions of 0.5m and 2m ground water depth and the same 0.5 degree of pre-cooling. Besides, the relative humidity comfort rate increased to 53.4% and 47.4% under the relative conditions. Moreover, compared to the primary energy consumption of the cooling section of around 5.99 kWh/m^2 in the baseline, the proposed system achieved 84% reduction to 0.96kWh/m^2 and 79% reduction to 1.25kWh/m^2, under working conditions of 0.5m-0.5dpc, and 2m-0.5pdc, respectively.

6. REFERENCES

Chen, X., et al., Recent research developments in polymer heat exchangers – A review. Renewable and Sustainable Energy Reviews, 2016a. 60: p. 1367-1386.

Chen, X., et al., Experimental investigations of polymer hollow fibre heat exchangers for building heat recovery application. Energy and Buildings, 2016b. 125: p. 99-108.

Directive 2010/31/EU of 19 May 2010 on the energy performance of buildings. European Commission 2010/31/EU (EPBD), 2010.Pérez-Lombard, L., J. Ortiz, and C. Pout, A review on buildings energy consumption information. Energy and Buildings, 2008. 40(3): p. 394-398.

Huang, S.-M., et al., Fluid flow and heat mass transfer in membrane parallel-plates channels used for liquid desiccant air dehumidification. International Journal of Heat and Mass Transfer, 2012. 55(9): p. 2571-2580.

Huang, S.-M., Z. Zhong, and M. Yang, Conjugate heat and mass transfer in an internally-cooled membrane-based liquid desiccant dehumidifier (IMLDD). Journal of Membrane Science, 2016. 508: p. 73-83.

Lior, N., Sustainable energy development (May 2011) with some game-changers. Energy, 2012. 40(1): p. 3-18.

LRg., W., La consommation énergétique de nos bâtiments, un enjeu crucial pour l'avenir. http://energie.wallonie.be. 2006.

Zhang, L.-Z., et al., Conjugate heat and mass transfer in a hollow fiber membrane module for liquid desiccant air dehumidification: A free surface model approach. International Journal of Heat and Mass Transfer, 2012. 55(13–14): p. 3789-3799.

Zhang, L.-Z. and N. Zhang, A heat pump driven and hollow fiber membrane-based liquid desiccant air dehumidification system: Modelling and experimental validation. Energy, 2014. 65: p. 441-451.

Zhang, N., S.-Y. Yin, and L.-Z. Zhang, Performance study of a heat pump driven and hollow fiber membrane-based two-stage liquid desiccant air dehumidification system. Applied Energy, 2016. 179: p. 727-737.

#149: Thermal management of concentrator photovoltaics using various passive cooling configurations

Ramy RABIE[1]*, Mohamed EMAM[2], Ahmed ELWARADANY[1], Shinichi OOKAWARA[1,3], Mahmoud AHMED[1]

*[1]Department of Energy Resources Engineering Egypt-Japan University of Science and Technology, Egypt – *Corresponding author: Ramy.rabie@ejust.edu.eg*
[2] Department of Mechanical Engineering, Faculty of Engineering Shoubra, Benha University, Egypt
[3] Department of Chemical Science and Engineering, Tokyo Institute of Technology, Japan

Concentrator photovoltaics is a promising technique for enhancing the utilisation of solar energy while decreasing the system cost. Employing the concentrator photovoltaics allows the replacement of expensive solar cell area with lower-in-cost lenses or mirrors. However, concentrating the solar radiation on solar cell leads to a dramatic rise in its temperature, and reduction in its efficiency and lifetime. Passive cooling is considered in this work as it is noiseless, and no maintenance or power is required to keep it working. The effect of attaching fins along with phase change material (PCM) to the back of the solar cell under concentrated radiation on the thermal management of concentrator photovoltaics is numerically investigated. In addition, uncooled concentrator photovoltaics, concentrator photovoltaics integrated with metal sheet heat spreader and Concentrator photovoltaics attached to horizontal fins are examined with the aim of comparing with fins filled with PCM case. The solar cell temperature, as well as liquid fraction of phase change material, are the key judging parameters. The results show that adding the PCM to fins can effectively enhance the thermal regulation of the concentrator photovoltaics compared to other methods, permitting a further increase of the concentration ratio and allowing for waste heat recovery from the system. However, the phase change material thermal regulation time is limited and determined by the amount of phase change material used as the wax is acting as a thermal insulator after it fully melts.

Keywords: Phase change material – concentrator photovoltaics – passive cooling – energy storage

1. INTRODUCTION

Solar energy is almost the perfect choice to replace regular non-renewable energy resources; in particular, it is free, eco-friendly and it is abundant. Using photovoltaics allows the direct transformation of solar irradiance to electric energy with relatively high efficiency ranges from 10% to 40% according to its type and working conditions (Philipps *et al*., 2015). However, the wide utilisation of photovoltaics as the main source energy is restricted due to its high capital cost, low energy density and instability of energy production. Recently, concentrator photovoltaics (CPV) have been considered as a promising technique to decrease the solar energy system cost, increase its efficiency and recover the waste heat. The key advantages of CPV are that it permits the replacement of expensive solar cell area with lower cost lenses or mirrors. Consequently, it enables the use of high efficiency advanced solar cells such as multi-junction solar cells with a conversion efficiency of about 46%.

The conversion efficiency of solar cells does not exceed 46% and the rest of the irradiance is transformed to thermal energy. The rise of solar cell temperature reduces its efficiency while thermal stress dramatically decreases its lifetime and may damage it completely if the temperature exceeds a certain level. Subsequently, a proper cooling method should be used to keep the viability of the CPV. Zhou *et al*. (2015) have developed a three-dimensional finite model to simulate the effect of the temperature distribution on the solar cell efficiency and this concluded that increasing the solar irradiance on the cell enhances the productivity but increases the solar cell temperature and reduces the system efficiency. Additionally, it is reported that the solar cell has the higher temperature through the PV module and increasing wind speed significantly decreases its temperature.

In this work, passive cooling is considered as it is noiseless, and no maintenance or power is required to keep it working. Different types of passive cooling can be utilised including phase change material (PCM), heat pipes and fins as a heat spreader. Emam and Ahmed (2016) studied numerically the effect of integrating phase change material with a CPV system for different inclination angles under concentration ratios (CR) of 5 and 20. They reported that adding PCM to CPV can reduce the solar cell temperature to about 53°C at CR of 5. Furthermore, the inclination angle has a huge effect on the cooling capability of PCM. Manikandan *et al.* (2019) examined numerically the cooling of horizontal concentrated photovoltaics with fins only and by increasing the 3mm PCM fins by 0.75mm they reported that the solar cell efficiency increased by about 15% by using fins with PCM. Huang, Eames and Norton (2006) investigated the effect of adding fins filled with PCM RT25 and reported approximately 30°C reduction in cell temperature compared to the regular flat aluminium sheet.

As shown in the literature, there is not enough work assisting the effect of filling fins with PCM. The current study investigates the effect of adding PCM to CPV cooled with aluminium fins of different lengths. The study conducted under low concentration ratio (CR) of 8 at negative inclination angle to mimic the case using Fresnel lens concentrator.

2. PHYSICAL MODEL

In the current study, 3 different configurations have been studied. The first is PV layers attached to aluminium plates (0 fins) to simulate uncooled condition. The thermal, physical and optical properties of the layers are shown in Table 1. In the second setup, 45 aluminium fins heat sink were attached to the back of PV layers and subjected to forced convection, with fin lengths of 30 mm, 45 mm and 60 mm. The third setup integrates PCM with the fins by filling the fin cavities with paraffin wax from Rubitherm Company with a melting temperature of 35°C (RT35HC).

Table 1: The optical and thermophysical properties of Photovoltaics layers and fins.

Material	Specific heat (J/kg K)	Thermal conductivity (W /m K)	Density (kg/m^3)	Layer thickness (mm)	Absorptivity	Reflectivity	Transmissivity	Emissivity
Glass	500	2	2450	3	0.04	0.04	0.92	0.85
Silicon (cell)	677	148	2330	0.2	0.9	0.08	0.02	-
EVA	2090	0.311	950	0.5	0.08	0.02	0.9	-
TPT	1250	0.15	1200	0.3	0.128	0.86	0.012	0.9
Aluminium	903	211	2675	5	-	-	-	-

The PCM used for cooling CPV should have a high fusion heat so that it can store more energy for an extended period of time. In addition, the PCM melting temperature must be selected carefully to suit the ambient temperature since lower melting temperatures lead to better PV efficiency but it will not fully solidify at night. Moreover, the heat will flow from the surroundings to the PCM instead of following from the PCM to the surroundings. Paraffin wax RT35HC has been selected due to its proper melting temperature (Emam, Ookawara and Ahmed, 2019), high latent heat and thermal stability. Table 2 shows the thermophysical properties of the selected RT35HC PCM materials.

Table 2 : The thermophysical properties of materials (Huang *et al.*, 2008)

Thermo-physical properties	RT35(PCM)
Melting point, (°C)	35.8
Heat of fusion, (kJ/kg)	191
Thermal conductivity Solid, (W/ m K) Liquid, (W/ m K)	 0.2 0.2
Density Solid, (kg/m^3) Liquid, (kg/m^3)	 880 760
Specific heat capacity Solid, (J/ kg K) Liquid, (J/ kg K)	 2100 2400
Thermal expansion coefficient, (K^{-1})	0.0091
Kinematic viscosity (mm^2/s)	3.3

The three setups are subjected to uniform concentrated solar irradiance. The uncooled setup and cooled fins setup are investigated under different concentration ratios (CR) from 1 sun to 10 suns and the fin-PCM cooled setup is subjected CRs of 5 and 8 suns. The schematic drawing of the 2-dimensional model with all dimensions and boundary conditions is illustrated in Figure 1. It could be seen that the PV is considered to have of 5 different layers starting with 3mm thick glass on the top followed the solar cell encapsulated between two ethylene vinyl acetate (EVA) layers and finally a Tedlar (TPT) layer at the attached to the back of the module. Figure 2 shows the third setup schematic diagram where the cavities between fins are filled with PCM and thin 0.5mm aluminium sheet is added to the back of PCM to protect and hold it.

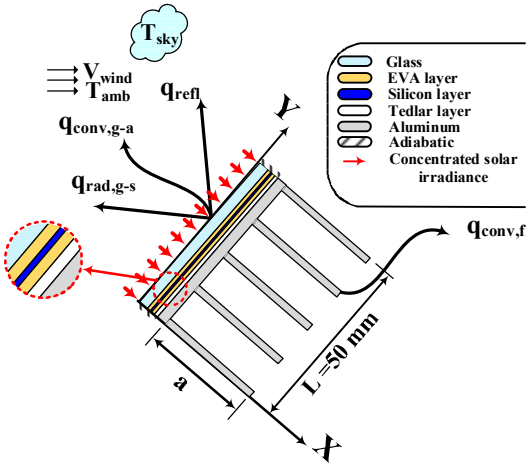

Figure 1: Passive cooling using fins only.

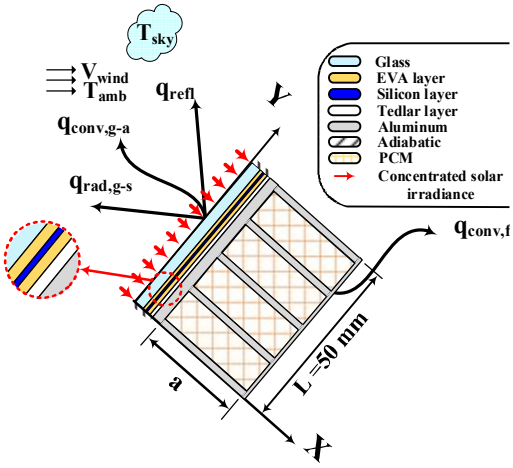

Figure 2: Passive cooling using fins filled with PCM.

3. METHODOLOGY

A comprehensive 2-dimensional model including the full photovoltaics layers, fins and PCM was developed using Ansys 19.1. The model had the ability to predict the CPV local and average temperature in addition to the liquid fraction for the phase change material. The optical and physical properties of photovoltaic layers were assumed to isotropic and independent of the temperature. In addition, the thermal contact resistance were not considered (Radwan and Ahmed, 2017). The heat was transferred through the PV layers and the fins through conduction according to heat transfer diffusion equation as follows:

Equation 1:

$$\rho_i C_{p,i} \frac{\partial T_i(x,y)}{\partial t} = k_i \left(\frac{\partial^2 T_i(x,y)}{\partial x^2} + \frac{\partial^2 T_i(x,y)}{\partial y^2}\right) + q_i \quad where \quad i = 1,2,..,n$$

Where:

- $C_{p,I}$ = the specific heat capacity (J/kg)
- ρ_i = the density (kg/m^3)
- K_i = the thermal conductivity (W/ m K)
- $T_i(x, y)$ = the temperature (K)
- q_i = internal heat generation (W/m^3)

Cell the absorbed solar irradiance through the EVA, glass and can be referred to as source term calculated using Equation 2. The source term is substituted as internal heat generation in Equation 1 (Zhou et al., 2015) .

Equation 2:

$$q_i = \frac{(1-\eta_e)\times G(t)\times \alpha_i \times \tau_i \times A_i}{V_i}$$

Where:

- q_i = internal heat generation per unit volume in layer i (W/m^3)
- η_e = the electric efficiency of the solar cell – value is set to zero for the other layers
- G(t) = the solar irradiance on the PV (W/m^2)
- α_i = the absorptivity of the layer i
- A_i = the layer i area (m^2)
- V_i = the layer i volume (m^3)

During the study, the PCM was assumed to be Newtonian, incompressible and unsteady. The phase transition of PCM was modelled using a melting solidification model in Ansys which employed the enthalpy-porosity technique to determine the existence of liquid or solid phase by means of liquid fraction quantity (λ). Proper source terms Sx and Sy (Darcy's law damping terms) were added to the momentum equation to compensate for the change of the flow velocity during the PCM phase transition. These source terms tend to have very high value in solid phase and their value decreases by increasing the liquid fraction. Variation of the PCM density was estimated by Boussinesq approximation to apply the thermal bouncy effect in molten PCM causing natural convection currents. The governing equation for PCM transition process can be written as follows (Brent, Voller and Reid, 1988; Pal and Joshi, 2001).

Equation 3: Continuity equation

$$\frac{\partial u}{\partial x}+\frac{\partial v}{\partial y}=0$$

Where:

- u = the velocity in x direction (m/s)
- y = *the velocity in y direction* (m/s)

Equation 4: Momentum equations

$$\frac{\partial u}{\partial t}+u\frac{\partial u}{\partial x}+v\frac{\partial u}{\partial y}=-\frac{1}{\rho}\frac{\partial P}{\partial x}+\frac{\mu}{\rho}\left(\frac{\partial^2 u}{\partial x^2}+\frac{\partial^2 u}{\partial y^2}\right)+g\beta\left(T-T_{ref}\right)\cos\theta+S_x$$

$$\frac{\partial v}{\partial t}+u\frac{\partial v}{\partial x}+v\frac{\partial v}{\partial y}=-\frac{1}{\rho}\frac{\partial P}{\partial y}+\frac{\mu}{\rho}\left(\frac{\partial^2 v}{\partial x^2}+\frac{\partial^2 v}{\partial y^2}\right)+g\beta\left(T-T_{ref}\right)\sin\theta+S_y$$

Where:

- u = the velocity in x direction (m/s)
- y = *the velocity in y direction* (m/s)
- ρ_i = the density (kg/m^3)
- μ = the dynamic viscosity (Pa.s)
- g = gravitational acceleration (m^2/s)
- β = thermal expansion coefficient (1/K)
- Θ = inclination angle
- S_x = Darcy's law damping in x direction
- S_y = Darcy's law damping in y direction

Equation 5: Energy Equation for molten PCM

$$\frac{\partial H}{\partial t}+u\frac{\partial H}{\partial x}+v\frac{\partial H}{\partial y}=\frac{\partial}{\partial x}\left(\alpha_l\frac{\partial H}{\partial x}\right)+\frac{\partial}{\partial y}\left(\alpha_l\frac{\partial H}{\partial y}\right)$$

Where:

- u = the velocity in x direction (m/s)
- y = the velocity in y direction (m/s)
- α_l = Thermal diffusivity of molten PCM *(m^2/s)*
- H =Total enthalpy *(J/kg)*

Equation 5: Energy Equation for solid PCM

$$\frac{\partial H}{\partial t}=\frac{\partial}{\partial x}\left(\alpha_s\frac{\partial H}{\partial x}\right)+\frac{\partial}{\partial y}\left(\alpha_s\frac{\partial H}{\partial y}\right)$$

Where:

- α_s = Thermal diffusivity of solid PCM *(m^2/s)*
- H = Total enthalpy *(J/kg)*

The system was initiated at an ambient temperature of 25°C. The upper layer of PV (glass) was subjected to forced convection and radiation with the sky temperature while all the aluminium parts were subjected to forced convection only. Sky temperature was assumed to be 6 degrees less than the ambient temperature (S P Sukhatme, 1996) and the forced convection heat transfer coefficient was taken to be 10 W/m^2.K, equivalent to a wind speed of about 1 m/s according to Notton's law (Notton *et al.*, 2005).

The computational domain was meshed quadrantally with a mesh size of 0.25mm and the time step is set to 0.2 seconds. The mesh size, as well as the time step was carefully selected according to a mesh and time step independence test with consideration to average cell temperature and PCM liquid fraction. The model was validated by comparing predicted liquid fraction development with time and fixed point transient temperature with the experimental results obtained by Kamkari and Shokouhmand (2014). Kamakari's experimental consisted of 125mm high PCM tanks filled with 50mm lauric acid; one wall of the tank was maintained at a constant temperature of 70°C. A good agreement with experimental results is shown in Figure 3.

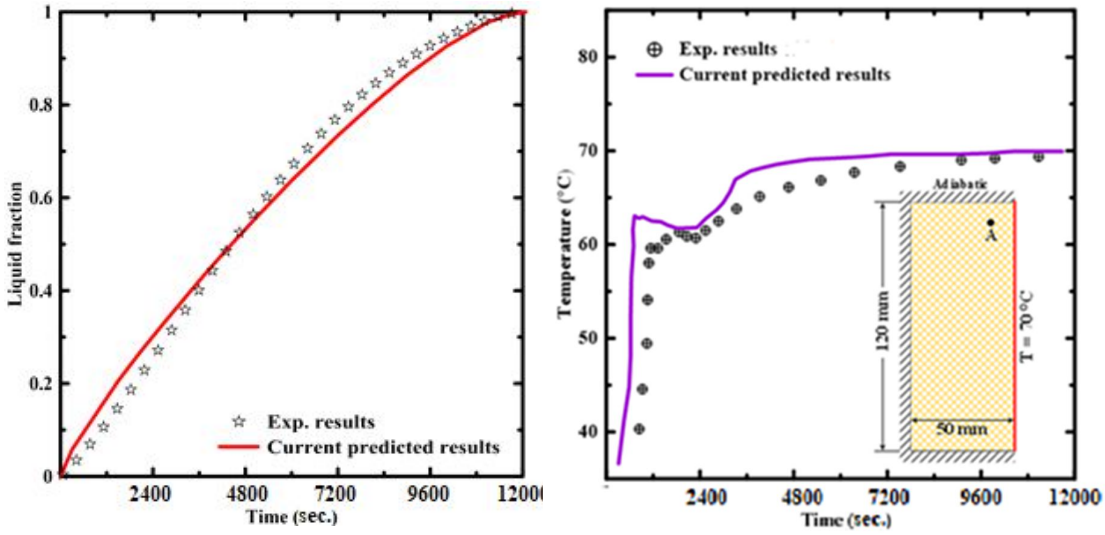

(a) (b)

Figure 3: validation with Kalamkari's experimental results a) liquid fraction , b) transient time

4. RESULTS AND DISCUSSION

In this section, the results obtained from the three setups are compared in terms of solar cell average temperature. The solar cell temperature was known to be the key parameter in the performance of the solar cell where every 1-

degree rise in the cell temperature reduces its efficiency by 0.4–0.5% (Jun Huang, 2011). Additionally, an increase in the solar cell temperature significantly reduces its lifespan.

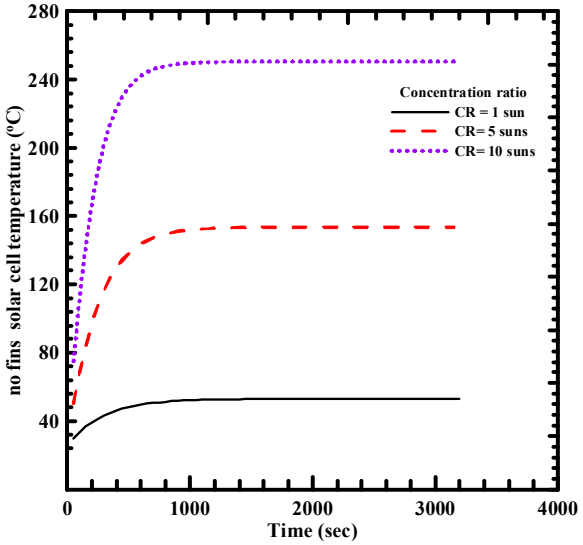

Figure 4: Transient solar cell temperature for the uncooled setup (0 fins)

Figure 4 shows the variation in solar cell average temperature against time under 3 different concentrations for no-fins setup. Increasing the concentration ratio to 5 suns led to a significant rise in the solar cell temperature of about 148°C within 14 minutes. Doubling the concentration ratio to 10 suns thrust the solar cell temperature to exceed 245°C in less than 10 minutes. Adding fins resulted in an excessive reduction in the solar cell temperature under concentrated irradiance as a result of increasing forced convection heat transfer area as shown in Figure 5. The maximum operating temperature for PV module is 85°C and a further increase in the temperature may lead to cell permanent damage as the EVA layer begins to decompose (Radwan and Ahmed, 2017). Figure 5 shows the steady state solar temperature for the uncooled setup and for PV integrated with fins with different length of 30mm, 45mm and 60mm. Based on Figure 5, in the case of the no-fins setup, the CR was limited to 2 suns to fit typical PV module operating temperature, adding fins with 30mm length allowed an increase in the concentration ratio to 6 suns while fins with 45mm and 60mm increased the CR limit to 7 suns.

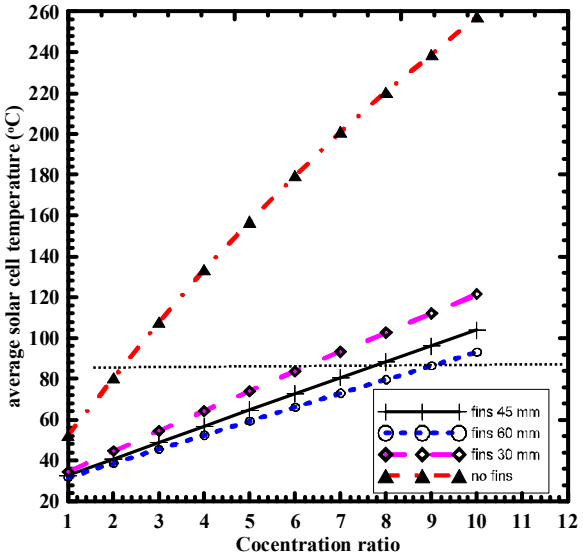

Figure 5: steady state average solar cell temperature

Although adding fins only as a passive cooling technique showed a good improvement in the thermal management of CPV and kept it within the operating temperature limit of up to CR8, but the CPV suffered from an extensive

reduction in solar cell efficiency due to huge excessive temperature difference from the nominal PV working temperature. Filling the fins with PCM resulted in a vast reduction of solar cell temperature for a period. Figure 6 shows a comparison between a transient average solar cell with a PCM of different fin lengths under CR5 of 5 suns, as shown using PCM of melting temperature maintained the solar cell at an average temperature of 48°C during melting instead of 74°C, 65°C and 60°C for fins length of 30mm, 45mm and 50mm respectively. Increasing the CR to 8 suns showed the same trend where the PCM sustained the solar cell average temperature at 56°C keeping it far away from its maximum operating condition compared to 101°C, 87°C and 79°C for fins length of 30mm, 45mm and 50mm respectively.

Despite the great improvement of the solar cell temperature, this did not last for long; once the PCM had fully melted, the solar cell temperature rose dramatically, exceeding the PV module working temperature. Figure 7 shows the liquid fraction development with time for 3 fin lengths under CR of 5 suns and 8 suns, the maximum melting time for 60mm fins at CR 5 is 4000 seconds. Low thermal conductivity of PCM can explain this dramatic rise in cell temperature. During the phase transition of PCM, almost all the received heat is absorbed in the form of latent heat at melting range temperature but once the PCM fully melts, the absorbed heat rise the PCM temperature. In addition, the low thermal conductivity of PCM prevents the fins wall from transferring heat to the atmosphere. Consequently, the molten PCM acted as insulation for the fins.

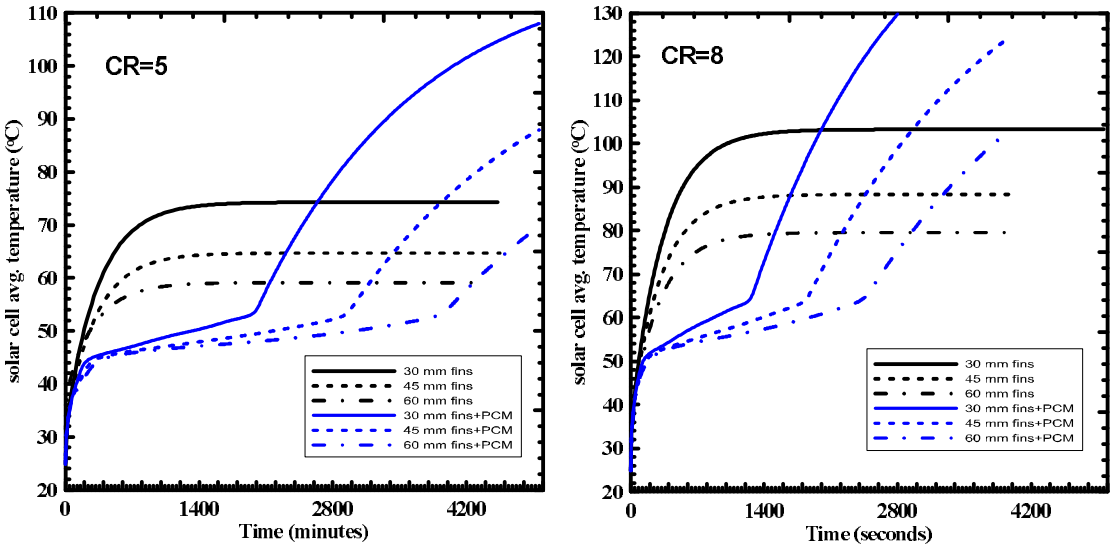

Figure 6 : average solar cell temperature a) under CR= 5 suns , b) under CR=8 suns

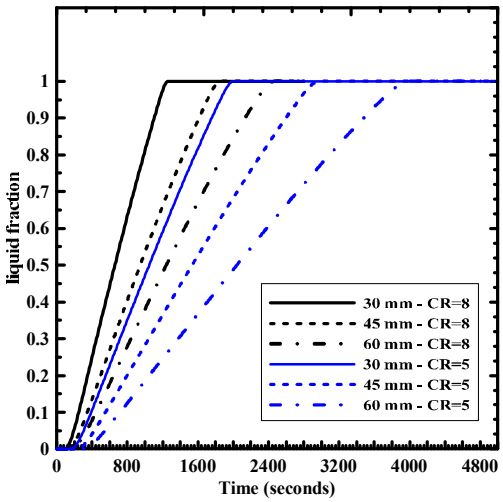

Figure 6 : Liquid fraction of PCM

5. CONCLUSION

Fins are an effective passive cooling technique for low concentration photovoltaics up to 4 suns. Filling fins with phase change material effectively reduces the solar cell average temperature by up to 45°C and allows for an increase in the concentration ratio up to 8 suns. The thermal regulation period of PCM is limited by the mass of PCM added. Once the PCM fully melts, the PCM acts as an insulator for the fins and the cell temperature rises rapidly. Further research concerning the optimisation of PCM mass and enhancing PCM thermal conductivity is recommended.

6. REFERENCES

Brent, A. D., Voller, V. R. and Reid, K. J. (1988) 'Enthalpy-porosity technique for modeling convection-diffusion phase change: application to the melting of a pure metal', *Numerical Heat Transfer*. Taylor & Francis, 13(3), pp. 297–318. doi: 10.1080/10407788808913615.

Emam M., Ahmed M., and O. S. (2016) 'Performance Enhancement of Concentrated Photovoltaic System Using Phase-Change Material', in *Proceedings of the ASME 2016 10th International Conference on Energy Sustainability*. Charlotte: ASME, p. V001T08A006. doi: 10.1115/ES2016-59641.

Emam, M., Ookawara, S. and Ahmed, M. (2019) 'Thermal management of electronic devices and concentrator photovoltaic systems using phase change material heat sinks: Experimental investigations', *Renewable Energy*. Elsevier Ltd. doi: 10.1016/j.renene.2019.03.151.

Huang, M. J. *et al.* (2008) 'The Effect of Phase Change Material Crystalline Segregation on the Building Integrated Photovoltaic System Thermal Performance', 35, pp. 1338–1343.

Huang, M. J., Eames, P. C. and Norton, B. (2006) 'Phase change materials for limiting temperature rise in building integrated photovoltaics', *Solar Energy*, 80(9), pp. 1121–1130. doi: 10.1016/j.solener.2005.10.006.

Jun Huang, M. (2011) 'The effect of using two PCMs on the thermal regulation performance of BIPV systems', *Solar Energy Materials and Solar Cells*. Elsevier, 95(3), pp. 957–963. doi: 10.1016/j.solmat.2010.11.032.

Kamkari, B. and Shokouhmand, H. (2014) 'Experimental investigation of phase change material melting in rectangular enclosures with horizontal partial fins', *International Journal of Heat and Mass Transfer*. Elsevier Ltd, 78, pp. 839–851. doi: 10.1016/j.ijheatmasstransfer.2014.07.056.

Manikandan, S. *et al.* (2019) 'Thermal Management of Low Concentrated Photovoltaic Module With Phase Change Material', *Journal of Cleaner Production*. Elsevier B.V. doi: 10.1016/j.jclepro.2019.02.086.

Notton, G. *et al.* (2005) 'Modelling of a double-glass photovoltaic module using finite differences', *Applied Thermal Engineering*. Pergamon, 25(17–18), pp. 2854–2877. doi: 10.1016/J.APPLTHERMALENG.2005.02.008.

Pal, D. and Joshi, Y. K. (2001) 'Melting in a side heated tall enclosure by a uniformly dissipating heat source', *International Journal of Heat and Mass Transfer*, 44(2), pp. 375–387. doi: 10.1016/s0017-9310(00)00116-2.

Philipps, S. P. *et al.* (2015) 'Current Status of Concentrator Photovoltaic (CPV) Technology', *National Renewable Energy Laboratory*, pp. 1–25. doi: http://www.ise.fraunhofer.de/en/publications/veroeffentlichungen-pdf-dateien-en/studien-und-konzeptpapiere/current-status-of-concentrator-photovoltaic-cpv-technology.pdf.

Radwan, A. and Ahmed, M. (2017) 'The influence of microchannel heat sink configurations on the performance of low concentrator photovoltaic systems', *Applied Energy*, 206(August), pp. 594–611. doi: 10.1016/j.apenergy.2017.08.202.

S P Sukhatme, J. K. N. (1996) *Solar Energy - S P Sukhatme, McGraw Hill*. Available at: https://books.google.com.eg/books?id=QUNODwAAQBAJ&printsec=frontcover&hl=ar&source=gbs_ge_summary_r&cad=0#v=onepage&q&f=false.

Zhou, J. *et al.* (2015) 'Temperature distribution of photovoltaic module based on finite element simulation', *Solar Energy*. Elsevier Ltd, 111, pp. 97–103. doi: 10.1016/j.solener.2014.10.040.

#151: A low energy thermally driven seawater desalination by direct spray method

An Experimental Study

Raid ALROWAIS[1], Muhammad BURHAN[2], Muhammad Wakil SHAHZAD[3], Doskhan YBYRAIYMKUL[4], Q. CHEN, Kim Choon NG[5]

Water Desalination and Reuse Center (WDRC), King Abdullah University of Science and Technology (KAUST)
[1]raid.alrowais@kaust.edu.sa
[2]Muhammad.burhan@kaust.edu.sa
[3]Muhammad.shahzad@kaust.edu.sa
[4]Doskhan.ybyraiymkul@kaust.edu.sa
[5]kimchoon.ng@kaust.edu.sa

Thermal desalination processes, such as the multi-stage flashing (MSF) and the multi-effect distillation (MED), played a dominant role in seawater desalination within GCC countries, due to its high efficiency, low maintenance and ability to operate in higher silt and salt concentrations However, these desalination plants are prone to having high capital cost at >US$2000 per m3, almost two-fold higher than the membrane-based plants. The authors proposed a tubeless direct-spray of seawater into an empty chamber of saturated states where the excess enthalpy, between the differential pressures and temperatures of feed to those in the flashed chamber, is allowed to flash into vapour under low vacuum. Being devoid of tube-based heat transfer resistances, the initial CAPEX will be much lower, typically <US$800 per m3. Moreover, it can handle feed of high salt concentration without the fear of scaling within the flashed vessel. To boost the flashing phenomenon, an injection of micro-vapour bubbles (MVB) was incorporated into the seawater feed prior to its injection via the nozzles. The MVB embedded feed has the potential to increase the flashed rates by two-fold due to the higher surface area of vapour bubbles at the point of flashing.

Keywords: Direct spray seawater desalination; micro-vapour bubbles enhancement; thermally-driven desalination

1. INTRODUCTION

Thermally-driven seawater desalination methods have played a dominant role in the Gulf Co-operation Countries (GCC) due to its ability to handle severe seawater feed conditions, namely the high dissolved salt concentrations of feed up to 45,000 ppm (Cl^- 55%, Na^+ 30.6%, SO^{2-}_4 7.7%, Mg^{2+} 3.7%, Ca^{2+} 1.2%, K^+ 1.1%, Other 0.7%.), as well as the fluctuating silt contents from shallower depths (Ng *et al.*, 2017; Shahzad, 2019; Ouda, 2015; Shahzad, 2015). About 65% of the total desalination capacity in these economies is attributed to either the multi-stage flashing (MSFs) or the multi-effect distillation (MEDs) methods. The robust operational characteristics and the low maintenance cost of thermal techniques have led to longer plant life. In some instances, the actual operation of plants were stretched beyond design life span by as much as 10 years. However, the main disadvantage of MSFs and the MEDs plants is the higher initial capital cost (CAPEX) when compared with the membrane-based reverse osmosis (RO). A typical CAPEX of thermally-driven plants may vary from US$1800-2200 per m^3.day whilst the seawater RO (SWRO) plants have a lower CAPEX of less than US$1200/$m^3$.day.

Despite the higher CAPEX of the thermally-driven plants, the unit cost of potable water produced is lower due to better energy efficiency (Ouda, 2015; Shahzad, 2015). Recent studies of energy efficacy reported in all practical desalination methods that the consumption of primary energy revealed a higher figure of merit of MEDs up to 2-3 percentages points. When expressed in the universal performance ratio, defined as UPR = 2360/ (3.6*$kWh_{\_pe}/m^3$), typically UPR of MEDs are greater than 110 whilst the SWRO plants have lower UPR values, typically 100 to 105. Despite these marginal differences in the energy efficacy, it is noted from these reports that all practical seawater desalination methods are relatively inefficient. When compared to the thermodynamic limit (TL) for seawater desalination, all desalination available hitherto are far from the ideal limit, i.e., the $UPR_{\_TL}$ is 828; The TL corresponds to a specific primary energy consumption defined by Gibbs energy for dissolved salts separation of 0.78 kWh_{pe}/m^3 at 3.5% salt concentration and a water temperature of 25°C. These existing desalination methods are merely 10 to 13% of the TL. Another point to note is that the lower unit cost of water from MSFs and MEDs methods are a consequence of lower OPEX costs, particularly the effects of less scaling or fouling degradation in the plants and less percentages of electricity consumption vis-a-vis to SWRO plants.

2. DIRECT SPRAY SEAWATER DESALINATION

Conventional MSF and MED stages have dense tube density to provide the required heat transfer area, either for evaporative or condensing applications in the derivation of vapour or liquid. The material used in these tubes are usually of cuprous nickel (10% Ni) or titanium to with stand the corrosive nature of brine (3.4 to 5% by weight). To overcome the relatively high initial capital cost (CAPEX) of thermally driven desalination plants, we propose a direct spray method of the seawater feed into a partial vacuum chambers where the latter chambers are maintained at a lower saturated conditions of pressures and temperature. The relative difference in the thermodynamic states to the designed stages enables the exploitation of the excess enthalpy of the brine as it emerges from the spray nozzles.

Being tubeless in the vessels, the direct spray of externally heated seawater (typically up to 65°C at the top-brine stage) has two distinct advantages: Firstly, initial design cost of the evaporator and condenser vessels are greatly reduced, typically in terms of unit cubic meter of distillate per day, its CAPEX can be less than US$700/$m^3$.day. Secondly, the spray of brine into an empty chamber of each stage can mitigate the scale formation as there are virtually no dry spots within the chambers. Consequently, the direct depressurization of the liquid brine in the nozzles resulted in the formation of liquid droplets. The corresponding excess water enthalpy held by the droplets, as they emerged from the nozzles would result in the “vapour flashing” phenomenon, i.e., water vapour evaporates from the surfaces of liquid droplets, reducing its diameter as the droplets travelled down the trajectory paths.

The generated vapour in the evaporators then migrates across to the adjacent condenser chambers. Being set at a few degrees lower in vapour temperature within each evaporator to condenser pair, the favourable temperature gradient, the vapour condenses onto the cooler surfaces of distillate or potable water droplets which is drawn from the subsequent lower stages. In this paper, two sets of experiments were organized: (i) the tests with RO or potable water to validate the suitability of direct spray evaporative effects and (ii) the tests with intake seawater feed from the Red Sea. Appropriate measures of insulation were taken to minimize the leak leaks or heat infiltration from the ambient. For convenience, an electric heater of nominal heating rate of 1.5 kW is used for temperature control for the feed to the top brine stage.

3. THE EXPERIMENTAL SETUP AND WORKING PRINCIPLE

A lab-scale direct-spray seawater desalination system has been constructed in the laboratory of King Abdullah University of Science and Technology (KAUST). It comprises three major components, namely, 1) evaporator, 2) condenser, and 3) other supporting components such as the spray nozzles, in-line feed heaters, water pumps, vacuum pump, distillate tank and heat exchangers. Figure 1 shows the schematic of the experimental setup with an inter-connecting pipe for vapour transfer from evaporator to condenser chambers whilst Figure 2 illustrates the

(direct spray seawater desalination) DSSD facility at KAUST. The top of the evaporator is partitioned to contain the seawater feed at a desired pressure (P) and temperature (T). Water droplets are formed when the seawater feed passes through the nozzle. Owing to the pressure (hence local saturation temperature) difference, there is an accumulation of liquid enthalpy in the water droplets, resulting in evaporation or flashing of the seawater from the surface of droplets, and causing the separation of dissolved salts to give potable water. The water vapour produced in the evaporator is drawn to the adjacent condenser chamber through a connecting pipe due to pressure difference created by spraying of cooler water in latter chamber. The combined distillate exits the condenser to a weighing scale for recording of the distillate flow rates.

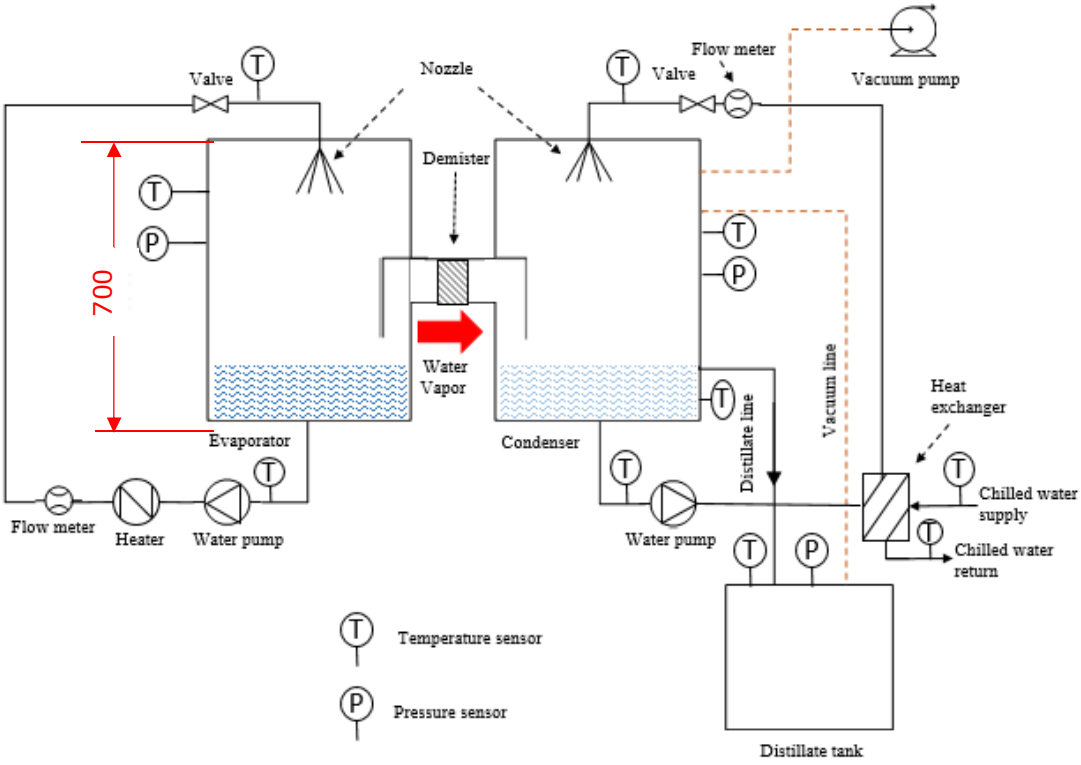

Figure 1: A schematic of the evaporator-condenser pair for direct spray seawater desalination (DSSD)

Figure 2: A pictorial view of the DSSD facility at KAUST

4. RESULTS AND DISCUSSION

Seawater heated, to a pre-set feed water temperature typically from 35 to 65 Celsius, is sprayed to the evaporator to effect the flashing phenomena. The advantage of using a low-temperature feed is because they are available in abundance from renewable solar energy or exhaust of processes. The injected seawater matches the pressure needed by nozzles operating at two or more bar, producing water droplets of diameters less than 40μm. The fine droplets enhances the flashing effect and water vapour is generated from the surfaces of droplets. Figure 3 shows a pictorial view of the water droplet jet in a 120° cone jet whilst the droplet sizes distribution are shown in Figure 4. A similar type of water jet droplets is used within the condenser chamber. Water vapour produced from the evaporator migrates across to an adjacent similar condenser vessel where concomitantly a jet of potable water is sprayed. The cooler surfaces of the water droplets permit vapour to condense, producing a stream of distillate which is then collected. Experiments of the direct spray desalination are conducted across a range of seawater water feed temperatures, starting from 35°C to 55°C in step of 5K. Such a low temperature range can be readily obtained from either the waste/exhaust heat or the renewable solar sources. The second parameter of control in the direct spray experiments is the temperature difference across the evaporator and the condenser. A total of 3 temperature differential ranges were conducted, namely (i) 3-5K, (ii) 5-7K, and (iii) 7-9K. Together with the feed temperatures, these parameters determines the rate of flashing in the vessels. The nozzle requires a feed water pressure of 2 bar at a flow rate of 2.5 l/min. To avoid clogging from suspended particles in the feed, a 5 micro filter is used prior to the inlet to the nozzle.

Table 1 depicts the distillate production rates expressed in L/min.m^{3,} and depending of the feed water temperatures and the degree of temperatures differences across evaporator-condenser, up to 9.28 L/min.m^3 of distillate production were obtained. The maximum distillate production rate is about 3% of the supplied excess enthalpy supplied from the feed spray which is in agreement to the available literature (Miyatake, 1981a; Miyatake, 1981b; Wellmann, 2015; Chen, 2016a; El-Fiqi, 2007; Mutair, 2009; Mutair, 2010; Muthunayagam, 2005; Miyatake, 1985; Ikegami, 2006; Chen, 2016b; Chen, 2018; Chen, 2017; Darwish *et al.*, 1976; Gopalakrishna, 1987; Balaji, 2016). A comparison with seawater tests shows that there is a reduction of distillate production up to 10%, due mainly to the effects of salinity and the boiling point elevation up to 2K, as shown in Figure 5.

Table 1. A summary of the distillate flow rates in L per minute per unit volume of evaporator (L/(hr.m^3)

Feed Water Temperature (°C)	$^{**}\Delta T_{Evap\text{-}Cond}$ = (3 - 5) K	$\Delta T_{Evap\text{-}Cond}$ = (5 - 7) K	$\Delta T_{Evap\text{-}Cond}$ = (7 - 9) K
40	2.38	3.02	4.26
50	3.14	5.09	7.13
60	6.34	8.02	9.28

$^{**}\Delta T_{E\text{-}C}$ = ΔT_vapour (Evaporator to Condenser), and diameter of vessel = 0.32 m, high = 0.70 m

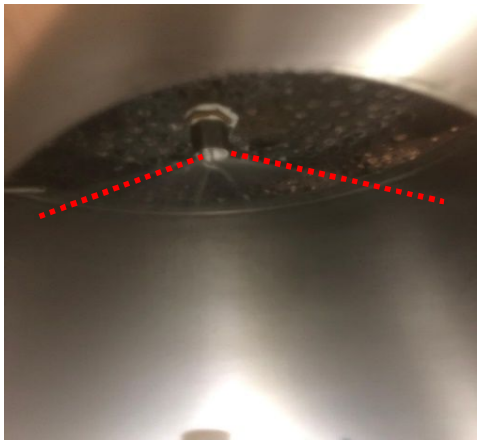

Figure 3: A picture of the water spray jet with fine distribution of water droplets covering an angle of 120 degrees.

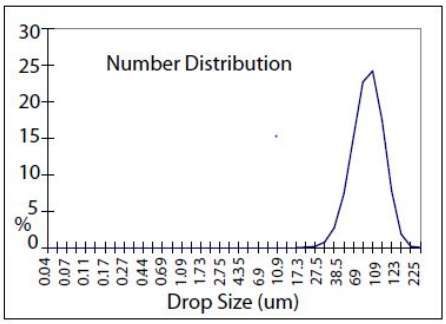

Figure 4: The typical distribution of droplet diameters versus percentages of droplets.

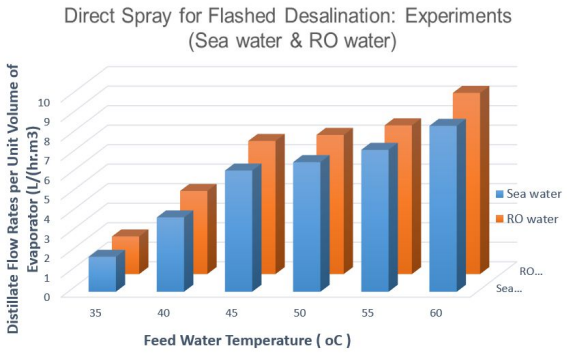

Figure 5: A comparison of seawater and RO water in a DSSD experiments at the same boundary conditions.

The pump in the direct spray consumed about 400 $W_{elec.}$ delivering 2 *l*/min at a mano-metric head of 30 m to the nozzles. The heat input to the evaporator feed varies from 260 W to 1200 W across a waste heat or solar thermal heated exchanger. Depending on the feed temperatures and the temperature differences between evaporator and condenser vessels, the distillate production rates are determined. Experiments indicated that the highest distillate production realm occurs at the boundaries of both mentioned parameters, and the limiting region is dictated by the scaling limits of seawater. For a fair comparison, both types of derived energy (electricity and thermal energy) are converted to the primary energy input using the relevant conversion factors as reported recently (Shahzad, 2019). As shown in Table 2, the universal performance ratio (UPR) of direct contact flashing distillation varies from 20 to 98 which compares well with the conventional seawater methods, namely about 90 for SWROs, and 105 for the MEDs.

Table 2: Universal performance ratio for the direct-spray evaporative desalination method is depicted. The energy efficacy, expressed in terms of the primary energy, is the same as the conventional commercial methods of literature. However, the capital cost needed is far less than the conventional methods.

	Temperature difference (DT) across heater		RO water				Seawater			
Feed Temp. (oC)	(RO)	(SW)	Distillate (m3/h)	**Total Primary energy consump-tion (W)	kWh_pe/m3	UPR	Distillate (m3/h)	**Total Primary energy consumption (W)	kWh_pe/m3	UPR
35	3.75	1.87	0.02527	814.84	31.24	20.68	0.0242	807.40	33.38	19.36
40	5.47	3.29	0.04446	821.64	14.27	45.27	0.0515	813.02	15.79	40.92
45	6.99	6.49	0.08770	827.66	8.98	71.94	0.0839	825.68	9.84	65.67
50	7.19	8.69	0.11743	828.45	8.60	75.14	0.0897	834.38	9.30	69.48
55	8.3	8.53	0.11527	832.84	8.09	79.88	0.0982	833.75	8.49	76.13
60	8.04	8.54	0.11540	831.81	6.63	97.41	0.1149	833.79	7.26	89.01

*** The conversion factors of electricity and thermal heat sources are 1/0.5 and 1/35.33, respectively [2]. The UPR is defined as UPR=2326 / (3.6*kWh_pe /m3). The primary energy consumption of a desalination method is given by {(kWh_elec*1/0.5) + kWh_thermal / 35.53)} where the derived energies are converted to the primary energy by their respective exergy based conversion factors (Shahzad, 2019).*

5. CONCLUSION

In summary, a direct-contact spray desalination experiments have been successfully conducted at assorted parameters and the two major factors that has significant impact to the production of distillate are the temperature of feed spray and the temperature differential across the evaporator and condenser chambers. It is observed that the optima for distillate yield resides at the boundary corner of the operational regime, that is, it occurs at the highest feed source temperatures and the highest temperature potential available at the evaporator and condenser. From the experiments, the highest rate of distillate production can be achieved per cubic meter of chamber volume, with 65ºC feed and a temperature difference between evaporator-condenser pair of 9K, is about 9.5 l/h.m3. In the single stage design, the energy efficacy of the direct spray evaporative desalination process can achieve a universal performance ratio (UPR) of 97 which is comparable to all existing desalination efficacy level. With multi-effect designs, however, an optimal combination of the number of stages can be inserted at an optimal DT in each evaporator-condenser pair, exploiting synergistically the feed enthalpy to achieve a two-fold increase in the UPR vis-à-vis the exiting desalination methods available hitherto.

6. REFERENCES

Balaji, D. "Experimental study on the effect of feed water nozzles on non-equilibrium temperature difference and flash evaporation in a single-stage evaporator and an investigation of effect of process parameters on the liquid flashing in a LTTD desalination process." *Desalination and Water Treatment* 57.56 (2016): 27152-27168.

Chen, Q., Li, Y and Chua, KJ. "On the thermodynamic analysis of a novel low-grade heat driven desalination system." *Energy Conversion and Management* 128 (2016a): 145-159.

Chen, Q., et al. "Development of a model for spray evaporation based on droplet analysis." Desalination 399 (2016b): 69-77.

Chen, Q., et al. "On the second law analysis of a multi-stage spray-assisted low-temperature desalination system." *Energy conversion and management* 148 (2017): 1306-1316.

Chen, Q., Li, Y and Chua, KJ. "Experimental and mathematical study of the spray flash evaporation phenomena." *Applied Thermal Engineering* 130 (2018): 598-610.

Darwish, MA., Serageldin, SG. and Eldessouky. HT. "Flashing in desalination units." *Desalination*19.1-3 (1976): 93-101

El-Fiqi, AK., et al. "Flash evaporation in a superheated water liquid jet." Desalination 206.1-3 (2007): 311-321.

Gopalakrishna, S., Purushothaman VM., and Lior, N. "An experimental study of flash evaporation from liquid pools." *Desalination* 65 (1987): 139-151.

Ikegami, Y, et al. "Experimental study on a spray flash desalination (influence of the direction of injection)." *Desalination* 194.1-3 (2006): 81-89.

Miyatake, O, et al. "An experimental study of spray flash evaporation." Desalination 36.2 (1981a): 113-128.

Miyatake, O, et al. "Effect of liquid temperature on spray flash evaporation." Desalination 37.3 (1981b): 351-366

Miyatake, O, Tomimura, T. and Ide, Y. "Enhancement of spray flash evaporation by means of the injection of bubble nuclei." *Journal of solar energy engineering*107.2 (1985): 176-182.

Mutair, S, and Ikegami, Y. "Experimental study on flash evaporation from superheated water jets: Influencing factors and formulation of correlation." *International Journal of Heat and Mass Transfer* 52.23-24 (2009): 5643-5651.

Mutair, S. and Yasuyuki, I.. "Experimental investigation on the characteristics of flash evaporation from superheated water jets for desalination." *Desalination* 251.1-3 (2010): 103-111.

Muthunayagam, AE., Ramamurthi, K. and Paden, JR. "Modelling and experiments on vaporization of saline water at low temperatures and reduced pressures." *Applied Thermal Engineering* 25.5-6 (2005): 941-952.

Ng, KC., Shahzad, MW., Son, HS. and Hamed, OA. An Exergy Approach to Efficiency Evaluation of Desalination, Applied Physics Letters 110 (2017) 184101. doi: 10.1063/1.4982628.

Ouda, O.K.M. "Domestic water demand in Saudi Arabia: Assessment of desalinated water as strategic supply source." *Desalination and Water Treatment* 56.11 (2015): 2824-2834

Shahzad, MW, et al. "An experimental investigation on MEDAD hybrid desalination cycle." *Applied energy* 148 (2015): 273-281

Shahzad, MW., Burhan M. and Ng, KC. A Standard Primary Energy Approach for Comparing Desalination Processes, Nature Clean Water 1 (2019) 1-7. DOI: 10.1038/s41545-018-0028-4.

Wellmann, J, et al. "Modeling an innovative low-temperature desalination system with integrated cogeneration in a concentrating solar power plant." Desalination and Water Treatment 55.12 (2015): 3163-3171.

#153: 3D study for the effect of using micro heat sink with parallel microchannels on the performance of thermoelectric generators (TEG) in waste heat recovery application

Ayman ELDESOUKEY[1, 2], Hamdy HASSAN[1, 3], Shinichi OOKAWARA[1, 4]

[1]*Egypt-Japan University of Science and Technology (E-JUST), Alexandria, Egypt, Egypt, ayman.eldesoukey@ejust.edu.eg*
[2]*Mechanical Engineering Department, Faculty of Engineering, Kafrelsheikh University, Egypt,*
[3]*Mechanical Engineering Department, Faculty of Engineering, Assiut University, Egypt Egypt, hamdy.aboali@ejust.edu.eg*
[4]*Department of Chemical Science and Engineering, Tokyo Institute of Technology, Japan Japan, sokawara@chemeng.titech.ac.jp*

Recently waste heat recovery has an important presence into our daily applications. Thermoelectric generators present a possible way to harvest waste heat and make a contribution to energy sustainability. In this study a thermoelectric generator module employed along the chimney which is used to collect the waste heat recovered from the combustion flue gases of almost 330°C. In order to enhance the thermoelectric generator performance, a water-cooled micro heat sink is integrated to the system. A CFD Numerical model using ANSYS-Fluent was used to predict the flow field and heat transfer through the micro heat sink. Additionally, by using the Fluent User Defined Functions (UDF) the thermoelectric generator performance was also predicted where the thermal-electrical fields solved simultaneously. The results showed the effect of applying parallel microchannels and the effect of changing the flow characteristics on the output power of the thermoelectric generators. The proposed system efficiency increasingly improved with the applying of microchannel heat sink. The effect of applying multiple micro heat sink configurations are also presented. The results corroborate previous experimental and theoretical studies.

Keywords: waste heat recovery system; microchannels; teg; thermoelectric generators; energy sustainability

1. INTRODUCTION

Energy sustainability has become one of the most pressing issue we face in our daily activities. Consuming fossil fuels with the effect of combustion products affects directly on environment and strategic storage of it. One of the most effective methods to sustain our energy consumption is by applying waste heat recovery methods to most fossil fuel applications. Thermoelectric generators (TEG) is one waste heat recovery method that can convert heat directly into electricity with no need for combustion processes or moving parts; simply a solid-state energy conversion device. Many researchers have studied the performance of TEG when applied to exhaust gases from combustion chimneys (Champier, 2017). Most studies focus mainly on TEG materials development and composition but the thermal management of the hot and cold sides of the TEG module has significant importance on improving the TEG system energy production (Rezania *et al*., 2013). In the case of power generation, there are a few important studies that were carried out using based, the thermal resistance of the system and developing analytic models to predict the performance of micro heat sinks and TEG (Yazawa and Shakouri, 2011). Chen, Rosendahl & Condra (2011), Rezania *et al.* (2013) and Eldesoukey & Hassan (2019) proposed a three-dimensional TEG model and the thermoelectric processes of Thomson Peltier, and Seebeck effects were integrated with Joule heat source terms by applying a finite volume method numerical model solved by a computational fluid dynamics simulator (ANSYS FLUENT).

For the thermoelectric generators modules, by increasing the convective surface area, high density of heat dissipation provided at the two-sided module, microscale heat transfer systems can enhance the thermal coupling to the hot and cold surfaces (Kandlikar and King, 2013). Therefore, the challenge is to design an effective heat exchanger within microelectronic dimension restrictions (Kandlikar and King, 2013). Microscale single-phase heat transfer has been widely used in industrial and scientific applications (Rezania and Rosendahl, 2012). Using microchannel heat sinks provides low weight and compact energy systems, compared to the traditional macroscale heat sinks, and increases modularity. In contrast to macrochannels, a reduced flow rate in the microchannel heat sink is enough to maintain the same average temperature difference between the hot and cold sides of the TEGs. Using microchannel heat sinks also increases the Nusselt number in the channels (Sajid, Hassan and Rahman, 2017).

Research has indicated that, based on equal hydraulic diameter and equal Reynolds number, heat sinks with rectangular channels had less thermal resistance but required more pumping power than heat sinks with circular channels. In this work, the thermal effect of the TEG on conventional channel, MiniChannel and parallel microchannel heat sink and the thermal reaction between them are considered. Based on the operating conditions of a commercial TEG module, the three-dimensional governing equations for fluid flow and heat transfer in addition to thermal and electrical fields of the TEG module were solved instantly in the laminar flow regime by using FVM and the commercial computational fluid dynamic (CFD) solver, ANSYS FLUENT by applying User Defined Functions (UDF).

Considering the maximum temperature limitation for Bi2Te3 material as negative (n) and positive (p) legs, the thermal performance of the flow was studied along the three heat sinks with isothermal hot surface of the TEG and a wide range of pressure drops (Reynolds number). By considering the maximum temperature limitation for Bi2Te3 material (600 K) in this work was applied.

2. MATHEMATICAL MODEL

The physical model of the present case study is composed of 3D TEG with dimensions (40mm *40mm) mounted on a chimney wall that provides constant temperature at the hot side of the TEG of 600 K while the cold side is cold by Parallel Microchannel heat exchanger consisting of eight channels with 4 mm width and a height of 150 microns as shown in Figure 1. The mathematical model of the present physical model includes the mathematical model of the TEG and the mathematical model of the case study of the TEG mounted on the chimney wall. The mathematical model is constructed at steady state conditions of the TEG and the studied case. In this model, the TEG materials properties such as the thermal conductivity, Seebeck coefficient, and electrical resistivity, etc. and fluid properties are temperature dependent.

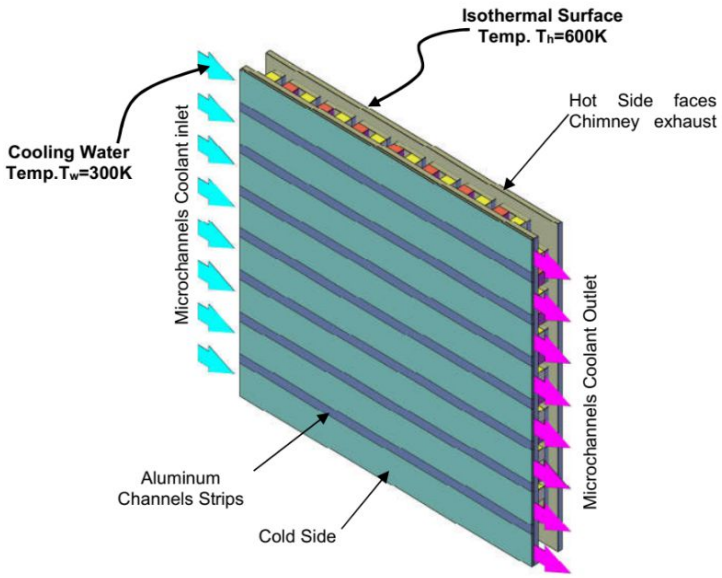

Figure 1: Physical model of the case study

2.1. TEG Model

Simplified models of the TEGs are not enough to accurately predict the detailed performance of the practical TEG systems with multidimensional construction. Also, they cannot precisely transfer non-uniform heat flow or temperature distributions boundary conditions to the thermoelectric model (Jang, Tsai and Wu, 2013). So, in this work, a 3D complete model of the TEG is presented coupling the electrical TEG model, and the thermal TEG model as follow:

Equation 1: the electric field governing equation inside a control volume for solid regions related to the thermoelectric phenomenon.

$$\vec{\nabla}\phi = -\alpha\vec{\nabla}T - \frac{\vec{j}}{\sigma}$$

Where:

- $\vec{\nabla}\phi$ = electrical Potential gradient, V/m
- α = Seebeck Coefficient, V/K
- $\vec{\nabla}T$ = Temperature gradient, K/m
- σ = electric Conductivity, Siemens/m
- $\vec{j}$ = current density vector, Amp/m^2

Equation 2: The electric potential (EP) equation in the solid regions. $\vec{\nabla}\cdot\left[\sigma\vec{\nabla}\phi\right] + S_e = 0$

Where:

- S_e = Electric Potential Source Term, Amp/m^3

Equation 3: The current density expression from Equation 3. $\vec{j} = -\sigma\vec{\nabla}\phi - \sigma\alpha\vec{\nabla}T$

$$j_x = -\sigma\frac{\partial\phi}{\partial x} - \sigma\alpha\frac{\partial T}{\partial x}, \qquad j_y = -\sigma\frac{\partial\phi}{\partial y} - \sigma\alpha\frac{\partial T}{\partial y}, \qquad j_z = -\sigma\frac{\partial\phi}{\partial z} - \sigma\alpha\frac{\partial T}{\partial z}$$

Where:

- j_x, j_y, j_z = components of the current density vector

Equation 4: The dot product for both sides of equation (3) with the operator $\vec{\nabla}$. $\vec{\nabla}\cdot\vec{j} = -\vec{\nabla}\cdot\left[\sigma\vec{\nabla}\phi\right] - \vec{\nabla}\cdot\left[\sigma\alpha\vec{\nabla}T\right]$

Equation 5: The conservation of current density at steady state. $\vec{\nabla}\cdot\vec{j} = 0$

Equation 6: The Combination of Equation 4 and 5.

$$\vec{\nabla} \cdot [\sigma \vec{\nabla} \phi] + \vec{\nabla} \cdot [\sigma \alpha \vec{\nabla} T] = 0$$

Equation 7: The electrical source term S_e represented from Equation 2 and 6.

$$S_e = \vec{\nabla} \cdot [\sigma \alpha \vec{\nabla} T]$$

Equation 8: The three-dimensional Cartesian form of the electrical source term S_e.

$$S_e = \frac{d(\sigma\alpha)}{dT}\left[\left(\frac{\partial T}{\partial x}\right)^2 + \left(\frac{\partial T}{\partial y}\right)^2 + \left(\frac{\partial T}{\partial z}\right)^2\right] + \sigma\alpha\left[\frac{\partial^2 T}{\partial x^2} + \frac{\partial^2 T}{\partial y^2} + \frac{\partial^2 T}{\partial z^2}\right]$$

Equation 9: The heat energy equation for no translation or rotation motion of the solid zones.

$$\vec{\nabla} \cdot [k \vec{\nabla} T] + S_h = (\rho_m c_p)\frac{\partial T}{\partial t}$$

Where:

- k = thermal conductivity coefficient, W/m.K
- S_h = Energy Equation Source Term, W/m^3
- ρ_m= mass density, kg/m3
- c_p = specific heat, J/kg.K
- t = time, s

Equation 10: The general energy equation by adding the Thomson heat and Joule heating terms for thermoelectric phenomenon at steady state.

$$\vec{\nabla} \cdot \vec{q} = -\vec{\nabla} \cdot [k \vec{\nabla} T] = \rho_m C_p \frac{\partial T}{\partial t} + \frac{|\vec{j}|^2}{\sigma} - \left[T \frac{d\alpha}{dT} \vec{j}\right] \cdot \vec{\nabla} T$$

Where:

- $\vec{q}$ = heat flux vector, W/m2
- $\frac{j^2}{\sigma}$ = the volumetric Joule heating term, W'm^3
- $\left[T \frac{d\alpha}{dT} \vec{j}\right] \cdot \vec{\nabla} T$ = Thomson heat term, W/m^3

Equation 11: At steady state; the energy equation used by ANSYS Fluent can be expressed by.

$$\vec{\nabla} \cdot [k \vec{\nabla} T] + S_h = 0$$

Equation 12: Therefore, from the Equations (10) and (11), the source term Sh can be expressed as follow.

$$S_h = -\left[T \frac{d\alpha}{dT} \vec{j}\right] \cdot \vec{\nabla} T + \frac{|\vec{j}|^2}{\sigma}$$

Equation 13: Equation (12) in three-dimensional Cartesian form, the heat source term is expressed by.

$$S_h = T \frac{d\alpha}{dT}\left[j_x \frac{\partial T}{\partial x} + j_y \frac{\partial T}{\partial y} + j_z \frac{\partial T}{\partial z}\right] + \left[\frac{j_x^2 + j_y^2 + j_z^2}{\sigma}\right]$$

As, $\frac{d(\sigma\alpha)}{dT}$ and $\frac{d\alpha}{dT}$ can be easily determined from temperature dependent material properties. The first derivatives of temperature and electric potential in x,y,z directions in the previous equations can be determined using gradient UDF Macros of the Fluent for temperature and electric potential gradient respectively.

For the problem of the second derivative inside Fluent solver, Used Defined Scalars (UDS) is used to adapt these equations for the Fluent solver as shown in Equation 14.

Equation 14: Substitution of temperature gradient components in terms of UDS.

$$\frac{\partial T}{\partial x} = \mathrm{UDS0}, \quad \frac{\partial T}{\partial y} = \mathrm{UDS1}\,, \quad \frac{\partial T}{\partial z} = UDS2$$

Equation 15: The source terms S_e as a function of UDS from Equations 8 and 14 :

$$S_e = \frac{d(\sigma\alpha)}{dT}[(\mathrm{UDS0})^2 + (\mathrm{UDS1})^2 + (\mathrm{UDS2})^2] + \sigma\alpha\left[\frac{\partial \mathrm{UDS0}}{\partial x} + \frac{\partial \mathrm{UDS1}}{\partial x} + \frac{\partial \mathrm{UDS2}}{\partial x}\right]$$

For the coupling of the energy equation output data and the potential equation, individual components of the electric current density can be accessed and stored in User Defined Memory UDM and to be used by Fluent solver.

Equation 16: Memorising of current density as function of UDM.

$$j_x = \mathrm{UDM0}, \qquad j_y = \mathrm{UDM1}, \qquad j_z = \mathrm{UDM2}$$

In addition to the benefit of coupling the energy and potential equations with this method, it reduces the computational time due to reducing the required memory size per iteration.

Also, the source term S_h is expressed by:

Equation 17: The source terms S_h as a function of UDS and UDM from Equations 13 and 16

$$S_h = T\frac{d\alpha}{dT}[\mathrm{UDM0} * \mathrm{UDS0} + \mathrm{UDM1} * \mathrm{UDS1} + \mathrm{UDM2} * \mathrm{UDS2}] + \frac{1}{\sigma}[\mathrm{UDM0}^2 + \mathrm{UDM1}^2 + \mathrm{UDM2}^2]$$

2.2. Heat Transfer Model

For the cooling water flow inside the microchannels, the conservation of mass, momentum, and energy equations are used and solved by conventional conservation laminar flow equations as noted in (Soliman and Hassan, 2018).

Equation 18: Conservation of mass for cooling water. $$\vec{\nabla}.(\rho\vec{V}) = 0$$

Equation 19: Conservation of momentum for cooling water. $$\vec{\nabla}.(\rho\vec{V}\,\vec{V}) = -\vec{\nabla}\,P + \vec{\nabla}.(\mu\,\nabla\vec{V}\,)$$

Equation 20: Conservation of energy for cooling water. $$\vec{V}.\vec{\nabla}(\rho C_w T_w) = \nabla.(k_w\vec{\nabla}T_w)$$

Equation 21: The convection heat transfer coefficient for the wind obtained by(Notton et al., 2005): $h_{wind} = 5.82 + 4.07v$

Where:

- ρ = water density, kg/m^3
- $\vec{V}$ = water flow velocity vector, m/s
- P = water flow pressure, Pa
- μ = water dynamic viscosity,Pa.s
- C_w = water specific heat, kJ/kg.K
- T_w = Water Temperature, K
- k_w = Water thermal conductivity,W/m.K

3. NUMERICAL SOLUTION

The previous governing equations with the boundary conditions and the programmed UDF integrated inside ANSYS-Fluent are solved numerically by the commercial ANSYS-FLUENT18 software. The physical model geometry was created by using DESIGN MODELER software and the grid of the model is carried out using MESHING software and all are used in ANSYS Workbench. A mesh independent test is performed to select the best number of meshes for the numerical solution of the previous mathematical models. Figure 2 shows the variation of the output power from the TEG with a different number of elements. The power is calculated based on the TEG cold surface temperature of 300 K and hot surface temperature 600 K. Figure 2 indicates that after the number of elements reaches over 10^6, the output power is virtually constant. The number of elements 1,100,084 is chosen and it is found enough for the model in the present study, adequate to satisfy the convergence criteria for the numerical solution of the different mathematical equations and saves computation efforts without loss in solution accuracy.

3.1. Model validation

The validation of the present model is carried out by using the numerical and experimental results of Chen *et al.* (Chen, Rosendahl and Condra, 2011) for the same operating conditions. The TEG used is the same thermoelectric module used by Chen where its cold side is fixed at a temperature (T_{cold}) of 303 K, and its hot side is set at temperature (T_{hot}) changing from 340 K to 430 K. All the parameters and configurations and input data are taken as the same as the Chen model. Figure 3 shows a comparison of the present model results and the numerical and experimental results of Chen et al. (2011) for the output power of the TEG with change the value. Moreover, the same comparison between the current model results and the results for Chen for the TEG electric current is shown in Figure 4. Figures 3 and 4 show good agreement between the current model results and the experimental and numerical results of Chenet *et al*. (2011). The validation also indicates that the present numerical results agree very well with Chen's experimental results rather than his numerical results for the output power and electric current of the of the TEG. This means that the current numerical solution gives more accuracy and reliability in calculations and more adequate interface dealing with the electric and thermal field parameters. Figure 6a shows the

temperature distribution through the TEG legs for T_{hot}=600K, T_{cold}=300K and load resistance =3.4 Ω. The temperature distribution on the TEG legs for the same conditions of Figure 6a is shown in Figure 5b. Figure 5a illustrates well the ability of the present mathematical model of the TEG to present temperature distribution through the TEG legs in a three-dimensional form. Figure 5b also indicates the decrease of the temperature through the TEG legs from the hot side to the cold side

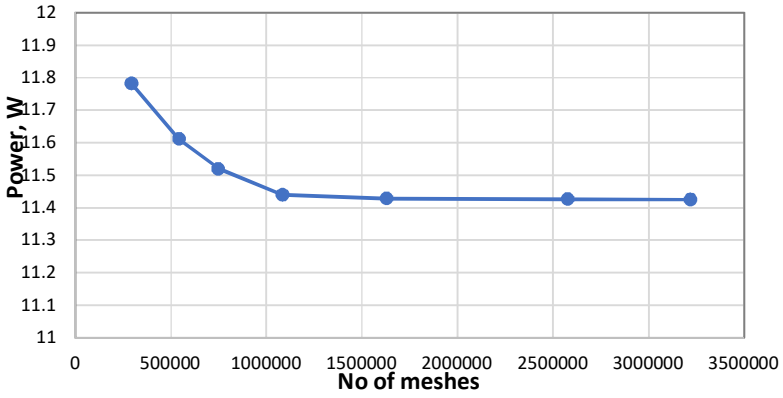

Figure 2: Variation of the TEG power output at different numbers of meshes

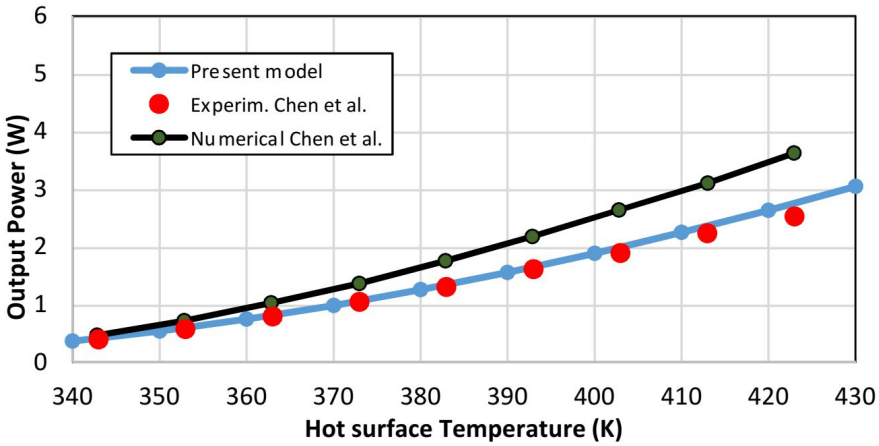

.Figure 3: Comparison of the output power of the present TEG model results and Chen, Rosendahl and Condra (2011) results

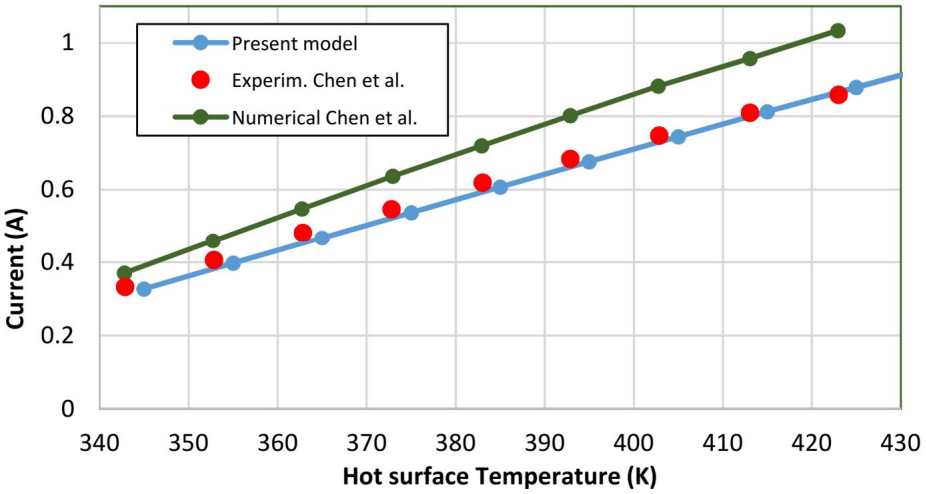

Figure 4: Comparison of the electric current of the present TEG model results and Chen et al. (2011) results

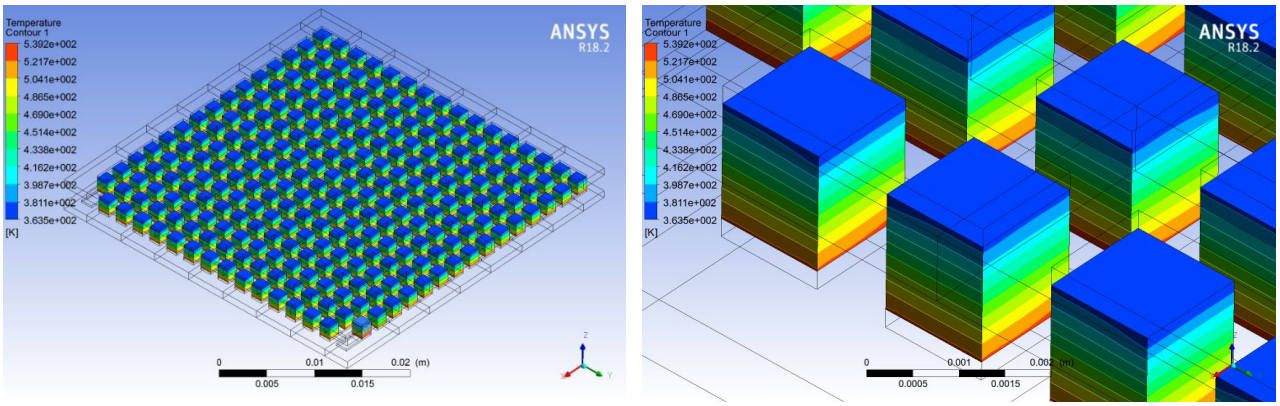

(a) *(b)*

Figure 5: a) Temperature distribution for the present TEG module's n-p legs at Th=600K, Tc=300K and REL=3.4 Ω

b): Detailed temperature contours for the TEG legs

3.2. System Configurations

The current study based on three configurations shown in Figure 6 classified as per the smallest dimension of the channel as mentioned in Kandlikar and King (2013) which are as follow: Configuration 1 (G1) and configuration 2 (G2) consist of conventional and mini heat sink with width 40 mm and single channel with 10 mm and 3 mm respectively; where configuration 3 (G3) consists of micro heat sink with eight microchannels of width 4 mm and height of 150 microns with strips between them of 1.14 mm width. All the three configurations use water at 300 K as a coolant. The boundary conditions for the three configuration are the same where the flow is to be a laminar flow and the inlet velocity is uniform at the inlet. The top of the channels is affected by heat transfer coefficient due to wind speed while the side surfaces of the TEG is set to be adiabatic

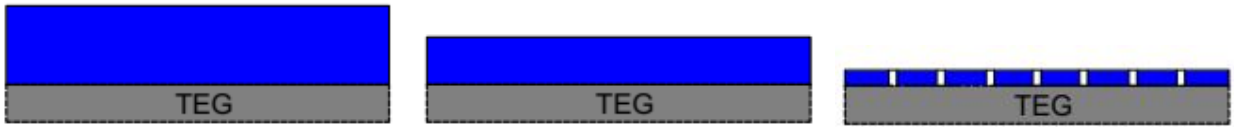

Configuration (1) - G1
(Conventional-Channel)

Configuration (2) - G2
(Mini-Channel)

Configuration (3) - G3
(Micro-Channels)

Figure 6: Geometrical configurations for cooling TEG module by three different heat sinks

4. RESULTS AND DISCUSSION

The chimney is used in many industrial applications where the flow gases temperature inside the chimney maintain the hot side of constant temperature of T_{hot} = 600 K. The TEG is an effective way to recover the heat loss from the chimney and transfer it directly into useful electrical energy as illustrated previously. The used TEG in this study is a commercial module consists of 127 couples, the entire module dimensions are 40mm×40mm ×3mm where each n-leg or p-leg has dimensions of 1.4mm×1.4mm×1.6mm as shown in Figure 7. The thermophysical properties of the used TEG are illustrated in table1 which are temperature dependent.

Figure 8 show the total power delivered by the TEG module for three configurations of TEG cooling system which are Parallel Microchannels G3 and configurations of single conventional and mini channel (G2 and G2) of the same width 40mm and with different channel heights of 10 and 3mm respectively for the same Reynold number laminar flow range of (20-300). The results show that by the using of parallel microchannel heat sink as in G3 gives more total power produced from the TEG module while G2 for the mini-channel gives more than G1 for the conventional-Channel. The percentage of the produced power for G3 is almost 200% of that produced of G2 and 250% compared by that produced by G1 at the same Reynold number (Re=300).

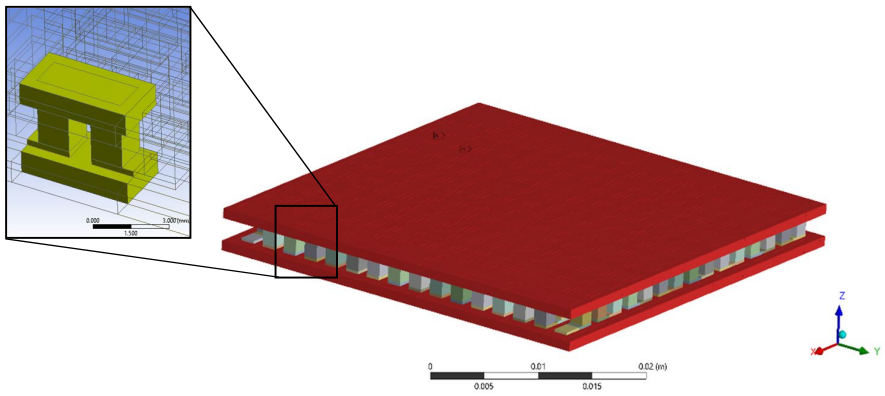

Figure 7: Geometry of the used TEG module with the basic unit built in of the n-p couple

Table 1: Thermophysical Properties of the TEG legs (n-p) types

Property	Description
α_p	$= (5.921376\times10^{-13})T^3-(3.274207\times10^{-9})T^2+(2.422355\times10^{-6})T-2.743842\times10^{-4}$
α_n	$= (1.291689\times10^{-13})T^3+(1.074408\times10^{-9})T^2-(9.271759\times10^{-7})T+8.95888\times10^{-6}$
ρ_p	$= (2.248899\times10^{-14})T^3-(1.250867\times10^{-10})T^2+(1.388189\times10^{-7})T-2.244786\times10^{-5}$
ρ_n	$= (-1.24614\times10^{-14})T^3-(6.429015\times10^{-11})T^2+(9.103036\times10^{-8})T-1.049646\times10^{-5}$
k_n (W/m.K)	$= (-1.592653\times10^{-8)}T^3+(2.905845\times10^{-5})T^2-(1.58323\times10^{-2})T+3.727526$
k_p (W/m.K)	$= (1.251606\times10^{-7})T^3-(1.242845\times10^{-4})T^2+(3.873788\times10^{-2})T-2.362707$

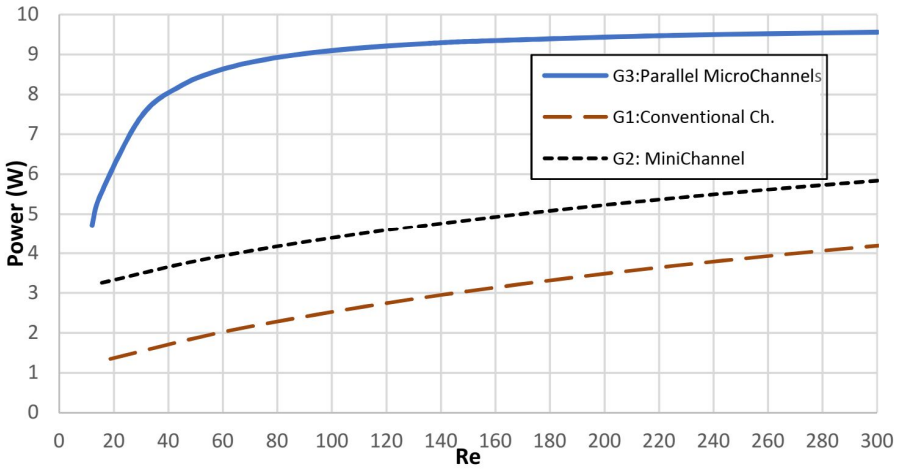

Figure 8: Total produced power for water cooled configurations

Although the G3 gives much more produced power, also it consumes much more pumping power as the friction loss is greater in micro channels than in conventional or mini channel as shown in Figure 9. Pluming power consumption for the G3 is greater than that for G1 and G2 by almost 1.2×10^5 times. By realising the fact that the working fluid is flowing at a very low Re within laminar flow ranges for 20-300 Re the consumed power is found to be almost 0.6 W for Re=300 where for G1 and G2 is almost none compared to produced power from these configurations. The results show that at certain Re values the net output power will decrease with the increase of the fluid flow velocity as the friction will rise and the temperature difference will remain almost constant. While for G1 and G2 the friction remains very low relative to the produced power.

Figure 10 shows that the key parameter to increase the output power of the TEG module is that the cold side temperature of the TEG where the results shows that G3 give the lowest T_{cold} of all Re number ranges which lead

the micro channel configuration on the top of the three configurations producing power at low laminar flow characteristics.

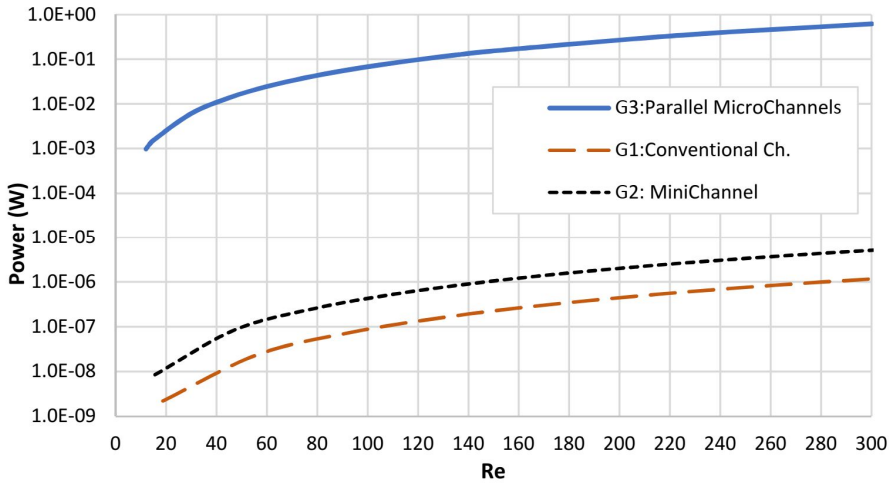

Figure 9: Pumping power for water cooled configurations

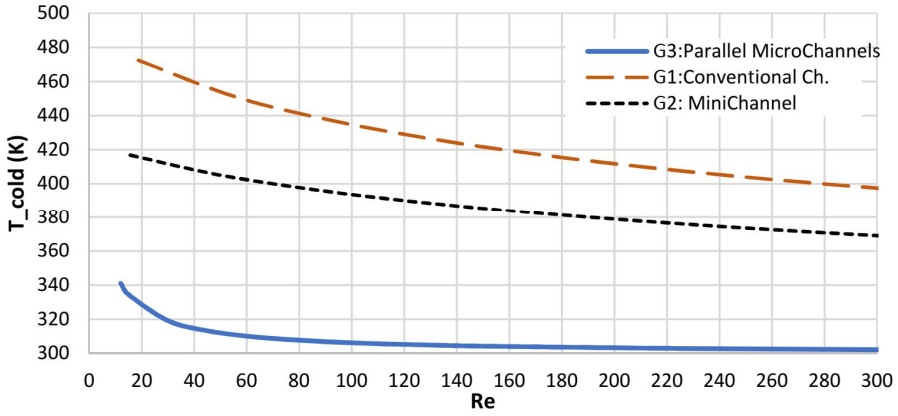

Figure 10: TEG cold side average temperature

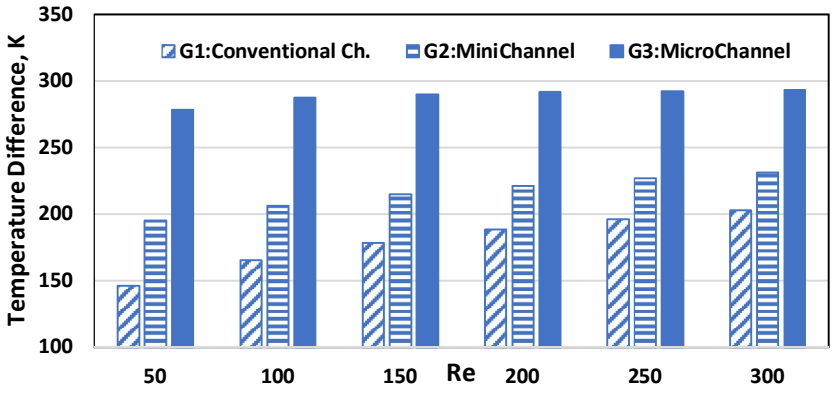

Figure 11: Temperature difference between the hot and cold sides of the TEG module at different flow conditions

The difference in cooling effect between the three geometrical configurations of the heat sink can be easily noticed from Figures 10 and 11 where the temperature difference between the hot and cold sides of the TEG module is

presented at different Re values. This identifies that G3 has the most significant cooling effect by almost 90% and 42% increasing from G1 and G2 respectively at Re=50 where that increment decreases by increasing Re values. These results ensure the results obtained from Figure 8 where the difference in output produced power is related directly on the temperature difference of the TEG sides and it appears that at Re=50 the temperature difference increment ratios of 90% and 42% resulted in 340% and 120% in produced power between G3 and the other two configurations. When the increment ratio decreases, the output power ratio decreases also, which confirms that improving the cooling effect thus directly affecting the temperature difference has an important role in improving power produced from TEG systems.

5. CONCLUSION

In summary, the cooling of the TEG module has a significant importance in producing power generated. Cooling by conventional, mini and micro channels were applied to the TEG module. Using microchannels in the heat sink raised the power produced by almost 340% of that produced from conventional and 120% for the MiniChannel heat sink. Pumping power increases by increasing the flow velocity but under laminar flow conditions for all configurations it can be neglected. Using microchannel heat sinks provides low weight and compact energy systems, compared to the traditional macroscale heat sinks which needs more focus in future research to optimise it with larger scale TEG system.

6. REFERENCES

Champier, D. (2017) 'Thermoelectric generators: A review of applications', *Energy Conversion and Management*. Elsevier Ltd, 140, pp. 167–181. doi: 10.1016/j.enconman.2017.02.070.

Chen, M., Rosendahl, L. A. and Condra, T. (2011) 'A three-dimensional numerical model of thermoelectric generators in fluid power systems', *International Journal of Heat and Mass Transfer*. Elsevier Ltd, 54(1–3), pp. 345–355. doi: 10.1016/j.ijheatmasstransfer.2010.08.024.

Eldesoukey, A. and Hassan, H. (2019) '3D model of thermoelectric generator (TEG) case study: Effect of flow regime on the TEG performance', *Energy Conversion and Management*, 180, pp. 231–239. doi: 10.1016/j.enconman.2018.10.104.

Jang, J. Y., Tsai, Y. C. and Wu, C. W. (2013) 'A study of 3-D numerical simulation and comparison with experimental results on turbulent flow of venting flue gas using thermoelectric generator modules and plate fin heat sink', *Energy*. Elsevier Ltd, 53, pp. 270–281. doi: 10.1016/j.energy.2013.03.010.

Kandlikar, S. G. and King, M. R. (2013) *Introduction*. Second Edition, *Heat Transfer and Fluid Flow in Minichannels and Microchannels*. Second Edition. Elsevier Ltd. doi: 10.1016/B978-0-08-098346-2.00001-6.

Notton, G. *et al.* (2005) 'Modelling of a double-glass photovoltaic module using finite differences', *Applied Thermal Engineering*, 25(17–18), pp. 2854–2877. doi: 10.1016/j.applthermaleng.2005.02.008.

Rezania, A. *et al.* (2013) 'Co-optimized design of microchannel heat exchangers and thermoelectric generators', *International Journal of Thermal Sciences*. Elsevier Masson SAS, 72, pp. 73–81. doi: 10.1016/j.ijthermalsci.2013.05.002.

Rezania, A. and Rosendahl, L. A. (2012) 'Thermal effect of a thermoelectric generator on parallel microchannel heat sink', *Energy*. Elsevier Ltd, 37(1), pp. 220–227. doi: 10.1016/j.energy.2011.11.043.

Sajid, M., Hassan, I. and Rahman, A. (2017) 'An overview of cooling of thermoelectric devices', *Renewable and Sustainable Energy Reviews*. Elsevier Ltd, 78(April), pp. 15–22. doi: 10.1016/j.rser.2017.04.098.

Soliman, A. M. A. and Hassan, H. (2018) '3D study on the performance of cooling technique composed of heat spreader and microchannels for cooling the solar cells', *Energy Conversion and Management*. Elsevier, 170(May), pp. 1–18. doi: 10.1016/j.enconman.2018.05.075.

Yazawa, K. and Shakouri, A. (2011) 'Cost-efficiency trade-off and the design of thermoelectric power generators', *Environmental Science and Technology*, 45(17), pp. 7548–7553. doi: 10.1021/es2005418.

#154: Withering of tea leaves using heat. A pipe heat exchanger utilising low-temperature geothermal energy

Yohanes GUNAWAN, Nandy PUTRA[1*], Imansyah Ibnu HAKIM, Dinni AGUSTINA

Applied Heat Transfer Laboratory, Department of Mechanical Engineering, Universitas Indonesia, 16424 Depok, Jawa Barat, Indonesia,
**Corresponding author: nandyputra@eng.ui.ac.id*

The volume of Indonesian tea exports to the European Union (EU) decreased by 43% in 2014 because of the EU setting a maximum residue limit of anthraquinone (AQ) for tea as 0.02 mg/kg. The content of AQ in tea leaves increases during the process of the withering and drying, especially when there is incomplete combustion of firewood, the energy source for withering and drying of tea leaves. This study aims to develop and test a new concept for the direct use of low-temperature geothermal energy with a heat pipe heat exchanger (HPHE) for the withering of tea leaves as a solution for energy sources free from AQ. The geothermal fluid simulators used water heated by a 9000W heater and flowed by a pump. The HPHE consisted of 42 heat pipes and 181 fins. The heat pipe was 700mm long with an outer diameter of 10mm; the fluid in the heat pipe worked using water with a filling ratio of 50%. Each fin was made of aluminum with a thickness of 0.105mm and a size of 76mm × 345mm. The results show that the effectiveness of the HPHE varied from 66% to 79.59%. For 100g of fresh tea leaves, the heating energy produced ranges from 15.21W to 45.07W, meaning it can wither tea leaves from 80% to 54% of the wet base (w.b.) in a time varying from 11h 56m to only 49.6 minutes. The Page mathematical model is the best model to represent the behaviour of the tea leaves with this HPHE system. The use of an HPHE is a new concept for the direct use of low-temperature geothermal energy for the withering of tea leaves, which is acceptable and feasible to use as renewable energy in the tea-making industry and as a substitute for fossil fuels.

Keywords: heat pipe heat exchanger, low temperature geothermal energy, anthraquinone, tea leaves, withering, drying

1. INTRODUCTION

Tea contains antioxidants which are very useful for the body. These antioxidants can help in protecting against various diseases, including heart disease and reducing the risk of cancer (Chacko et al., 2010, Suliburska et al., 2012). Tea is a healthy drink that is extremely well-known worldwide. Indonesia is one of the most abundant tea-producing and exporting countries globally. The tea export destinations of Indonesia include Australia, Africa, Middle East, USA, Canada, Russia, Asia, and the EU.

However, aside from the importance of consuming tea, there is some concern in the processing of fresh leaves. The most crucial stage in tea processing is withering and drying, which uses firewood as the heat source (Azapagic et al., 2016). Because this involves the process of burning solid fuels (fuel wood, biomass), the probability of incomplete combustion is extremely high. An incomplete combustion process produces polycyclic aromatic hydrocarbons (PAHs), which if distributed can increase the anthraquinone (AQ) residue in the tea leaves (Pincemaille et al., 2014, Adisa et al., 2015, Abd El-Aty et al., 2014). If the content is excessive, AQ can be highly dangerous for human health.

To protect consumer health, through the regulation of commission no. 1146/2014, the EU has set the maximum limit of residual AQ for tea as 0.02 mg/kg. Based on the research conducted by Putra et al., it was concluded that some teas from Indonesia contained AQ exceeding the threshold set by the EU (Putra et al., 2017a). The regulation caused the tea export from Indonesia to the EU to decrease from a volume of 17,000 tons in 2013 to 10,000 tons in 2014, i.e. a decrease of 43% (International Tea Committee, 2016).

The increase in AQ content occurs during the process of withering and drying of the leaves (Wang et al., 2018), especially when there is incomplete combustion of the firewood which is used as the energy source. This research discusses approaches and other sources of energy for this process. Regarding this issue, the standard solution until now is the use of industrial diesel oil (IDO) (Vidanagama and Lokupitiya, 2018). However, the problems with this are that the use of IDO is highly dependent on the oil prices, which affects the production costs, and that as this energy use increases, the rate of global warming also increases.

Indonesia is rich in geothermal resources, with a total potential of approximately 28,617 MW, spread throughout the country (Nasruddin et al., 2016). Sources of low-temperature geothermal energy that are located at shallow depths are mostly found in the area of the geothermal resources of Indonesia (Prasetya et al., 2017, Pikra et al., 2015). Therefore, the potential for using it directly for the withering and drying of agricultural and plantation commodities is high (Afuar et al., 2016, Zlatanović et al., 2013).

Research related to the utilisation of geothermal energy for drying has been carried out by Afuar et al. (2016). They designed a tomato drying system using heat exchangers. In the tomato drying process, water content must be reduced from 95.7% to 26% and it requires a drying air temperature of 50–70°C. Drying 1 ton of tomatoes per day requires 7 kg/s of geothermal water. Prasetya et al. (2017) identified the manifestation of geothermal energy at a rate of 3 kg/s and temperature of 87°C flowing into a multilevel system consisting of several applications (Prasetya et al., 2017). The three applications chosen were cacao drying, egg hatching incubation machines, and a new tourism site called geothermal therapy. From the technical and economic aspects, it is highly advantageous to perform the improvement and optimisation of the direct use of geothermal energy.

Until now, the direct use of geothermal energy has commonly been performed by either withdrawing geothermal fluids (specifically by a pump), or flowing (based on the difference in the soil height). Regardless of providing electricity or ground height difference, the use of pumps and pipe production is highly susceptible to scaling and corrosion because the geothermal fluid has a high silica content and corrosive properties (Franco and Vaccaro, 2013, Pambudi et al., 2015). The application of a heat pipe to capture the geothermal energy without withdrawing and draining the fluid is one solution to this problem.

The application of a heat pipe as a heat exchanger is already well tested for several applications, such as battery cooling, passive nuclear cooling, electric motor cooling, and air conditioning in rooms (Putra et al., 2016, Kusuma et al., 2017, Putra et al., 2017b). Kerrigan et al. designed heat pipe radiators to utilise low-temperature geothermal energy (Kerrigan et al., 2011). Radiators that use heat pipes have numerous advantages compared to conventional radiator panels, where the power panels can reduce the thermal mass significantly. In their next study, Kerrigan et al. modified the number of heat pipes and number of fins used and the results were significantly improved; the power density increase could reduce the thermal mass (Kerrigan et al., 2013). The use of heat pipes for melting ice and snow applications utilising heat from within the earth has also been conducted with satisfactory results (Zorn et al, 2015).

A new concept is needed to use low-temperature geothermal energy directly for the withering and drying of agricultural and plantation commodities, without employing pumps or different heights for the withdrawal of liquid

fluids. This paper proposes using a heat pipe heat exchanger (HPHE). To provide a solution to the problem of AQ, the commodity chosen in this study is tea leaves.

Research related to the drying characteristics of tea leaves has been carried out by several previous researchers. Ghodake et al. (2006) carried out the characterisation of the 25 varieties of tea harvested from the tea garden of Kharagpur, India. Data analysis uses the approach of 2 models from Henderson-Pabis and Page. The energy source was an electric heater. The Page model provides a better prediction of the characteristics of the tea leaf at temperatures higher than 35°C. Panchariya et al. (2002) developed a drying tool model suitable for drying black tea, investigating the effects of temperature and air velocity on the model coefficients that can describe the drying characteristics of black tea. The energy source for drying black tea was an electric heater that can be adjusted to the temperature as desired. The results show that the Lewis model is adequate in describing the drying behaviour of one layer of black tea particles. Dutta et al. (Dutta and Baruah, 2014) used fire from biomass gasification as an energy source for drying tea. The investigation of a thin layer of drying of fermented tea (Camellia sinensis) kinetics was conducted at air temperatures of 80, 90,100, 110°C with the speed of each drying air 0.50; 0.65; 0.75 m/s. The modified Page model provides better predictions regarding the drying kinetic of black tea thin layers followed by the Lewis model.

The main objectives of this study are as follows: (1) the development of suitable test equipment for the withering of tea leaves using an HPHE for withdrawing heat from geothermal energy; (2) investigating the effect of temperature and hot air velocity on the velocity and identification of suitable mathematical models which can describe the characteristics of Indonesian tea drying and drying when using the HPHE; (3) determining the energy needed to remove moisture from tea leaves when using the HPHE system by a thermodynamic analysis. A limitation of this study is that qualitative results, such as the taste and aroma of tea after the withering and drying process with this system, have not been discussed here. Based on our literature survey, research related to the application of heat pipes for the withering or drying of tea leaves has not been conducted previously.

2. MATERIALS AND METHODS

2.1. Experimental Design

In this study, the HPHE consisted of 42 heat pipes in a staggered arrangement and 181 fins. The heat pipe was made from copper with the wick in the form of sintered copper; the fluid used was water with a filling ratio of 50%. The heat pipe had a 700mm length and 10mm outer diameter. The adiabatic area was wrapped in glass wool and polyurethane, serving as its thermal insulation system. Each fin was made from aluminium with a thickness of 0.105mm and size area of 76mm x 345mm. The lengths of the condenser, adiabatic, and evaporator areas for the HPHE were 350mm, 100mm and 250mm, respectively. The dimensions of the HPHE and fins can be seen in Figure 1.

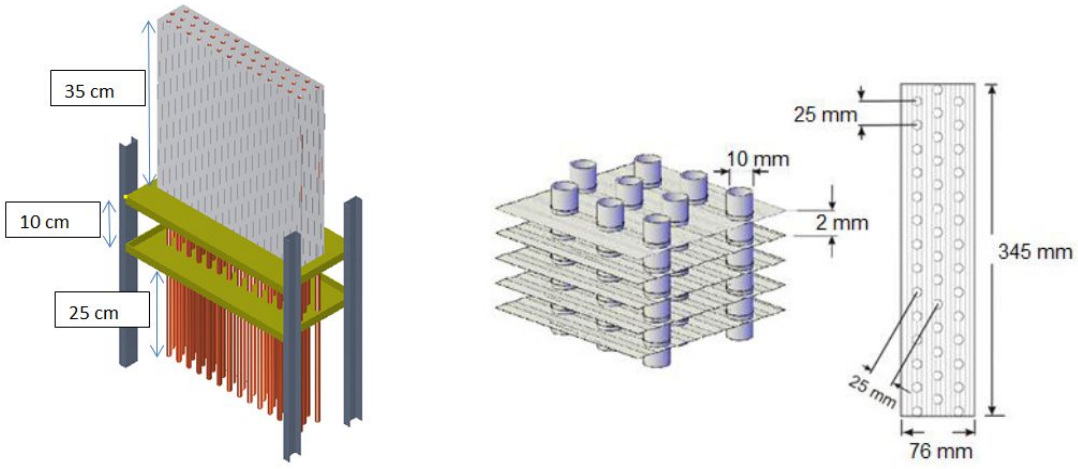

Figure 1: Sizes of the (a) HPHE and (b) Fins

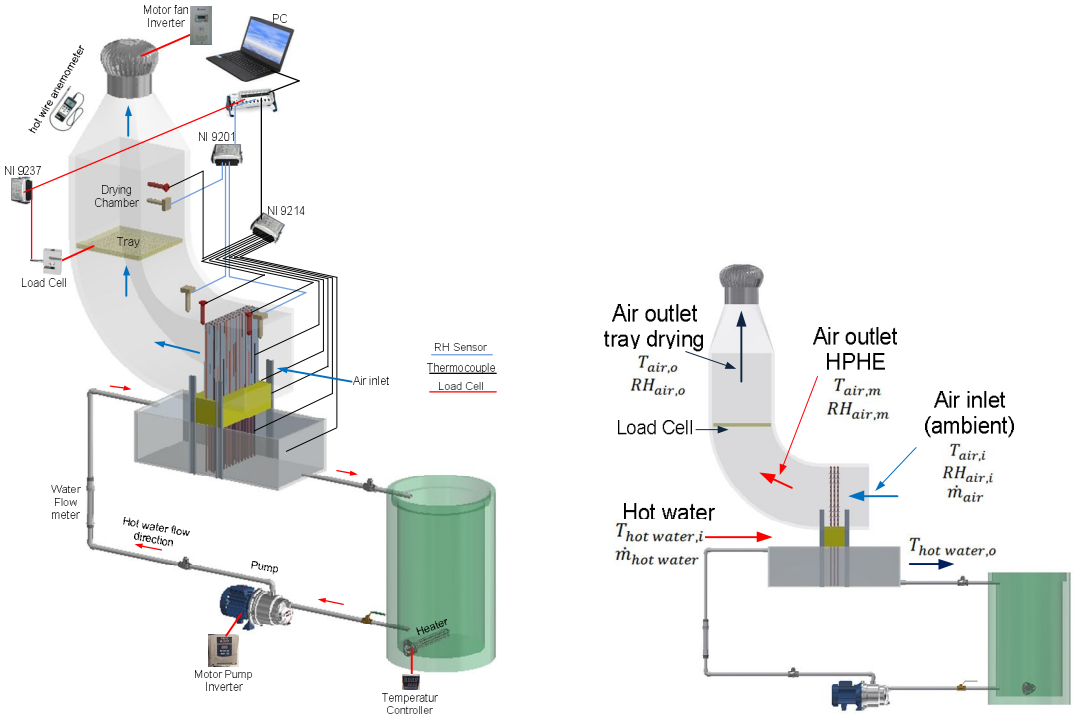

Figure 2: (a) Schematic of the experimental withering set-up; (b) Positions of the measuring instruments

Geothermal fluids were simulated with heated water with a heating capacity of 9000W to achieve temperatures from 40 to 80°C with a maximum flow of 18 L/min. Hot water flowed into a water bath in which the evaporator area of the HPHE was submerged. Hot water flowed with a pump which was connected to an inverter so that the flow of hot water could be controlled according to the variations in testing. Air for the withering and drying was ambient air and flowed with a fan, which was connected to the inverter so that the air flow could also be adjusted. The ambient air which entered the system became hot after passing through the HPHE condenser area. The heat used to heat the air was taken from the hot water that flowed in the evaporator part of the HPHE. The heated air was used to wither or dry the commodity placed on the tray. The tray was connected to the load cell so that the weight of the product could be measured in real time during testing. All the equipment was then assembled in the experimental set-up shown in Figure 2 (a).

The sensors used, and their placements, can be seen in Figure 2 (b). Type K thermocouples were connected to the cDAQ NI-9214 module, and the relative humidity sensor used THD-D Autonics type connected to NI-cDAQ 9201. For the measurement of hot water flow, a thermocouple was placed in the hot water area entering the evaporator HPHE (T water, i); the hot water area exited the evaporator HPHE (T water, o). To measure the airflow, thermocouples and relative humidity sensors were installed on the side of the ambient air entering the HPHE condenser area (T air, i; air RH, i); one side of the hot air exited the HPHE condenser area (T air, m; RH air, m), and the other side of the hot air exited from the drying tray area (T air, o; RH air, o). A load cell of capacity 1000 g measured the tea weight in the drying tray connected to the NI-cDAQ 9237 module. The tray area was 360 x 360 mm^2. The data acquisition (DAQ) module sent a signal to a computer with installed LabView software; hence, all the signals from the sensors could be recorded in real time.

A portable hot wire Lutron AM-4204 measured the airflow in the ducting. The hot water flow was measured using a Dwyer Flowmeter installed after the water pump. All the HPHE units, air ducting, water tanks, hot water pipes, and all the measuring instruments used were arranged in one unit, as can be seen in Figure 3 (a).

(a) (b)

Figure 3: (a) Final assembly of the tea withering testing equipment; (b) Tea commodities in the drying tray, size 36 cm x 36 cm

2.2. Experimental procedure

The fresh tea leaves used in this study were tea picked from plantations in the Gunung Mas Tea Plantation area, PTPN VIII located in Bogor, Indonesia. Before being placed into the drying tray, the tea leaves were measured initially for their moisture content. The water content measurements were performed by applying 1980 AOAC standards and ISO 712 (Association of Official Analytical Chemists, 1980; International Organization for Standardization, 1985).

The experiment was conducted from 18.30 WIB to 07.00 WIB. The goal was to obtain a relatively constant temperature and RH ambient. The variables considered were the drying air temperature and air velocity. Considering the temperature range and amount of geothermal water available in several locations in Indonesia and the actual temperature of the withering tea leaves, the heater in the water bath was set at water temperatures of 40, 50, and 60°C (Pikra et al., 2015, Prasetya et al., 2017, Ghodake et al., 2006). The flow of hot water was set to a value of 18 L/s, which was used in previous studies for an optimal hot water flow (Imansyah Ibnu Hakim et al., 2019).

Airspeed was chosen from the research of Panchariya et al., and set as a part of the independent variables at 0.2, 0.4, and 0.6 m/s (P.C. Panchariya et al., 2002). A steady state was reached after the apparatus was run for approximately 1 h. After the temperature was stable and air velocity was at the specified value, 100 g of tea leaves was placed on the tray, and the experiment was conducted for 4 h for each test variation. Figure 3 (b) shows the condition of the tea leaves on the tray in the ducting. The 100-gram tea weight was chosen because it was adjusted to the tray dimensions and according to a similar study by Panchariya et al. (P.C. Panchariya et al., 2002).

2.3. Analysis of data experiment

The performance of the HPHE can be indicated by the values of its effectiveness and heat recovery. For the value of its effectiveness, according to El-Baky et al. (Abd El-Baky and Mohamed, 2007) with the assumptions that there was no condensation on the freshwater flow and the specific heat which passed through the evaporator and condenser is constant, the equation is

Equation 1: Effectiveness (%)

$$\varepsilon = \frac{T_{air,i} - T_{air,m}}{T_{hot\ water,i} - T_{air,i}}$$

Where:

- $T_{air,i}$ = Temperature of air inlet HPHE in condenser area (°C)
- $T_{air,m}$ = Temperature of air outlet HPHE in condenser area (°C)
- $T_{hot\ water,i}$ = Temperature of hot water inlet HPHE in evaporator area (°C)

The thin-layer drying model illustrating the drying phenomenon of these materials mainly falls into three categories: theoretical, semi-theoretical, and empirical. The semi-theoretical model is generally derived by simplifying the general solution of the second Fick law or modifying a simplified model, which is applicable in the range of temperature, relative humidity, air flow velocity, and water content. Among the drying models of semi-theoretical thin layers, the Henderson and Pabis models, Page model, Lewis model, and modified Page model are widely used for the process of tearing or drying of tea leaves (Ghodake et al., 2006, P.C. Panchariya et al., 2002, Dutta and Baruah, 2014). The mathematical model equations are presented in Table 1. In this analysis, the value of the

equilibrium moisture content (M_e) is considered to have a value of 0, because the relative humidity fluctuated and the value was relatively small compared to M_o and M (Purnomo and Indarti, 2018).

Table 1: Mathematical models for the process of withering and drying of tea leaves

No	Model Name	Equation of Moisture Ratio (MR)
1	Henderson and Pabis	$MR = \frac{M - M_e}{M_o - M_e} = A_o\, exp(-k_o t)$
2	Page	$MR = \frac{M - M_e}{M_o - M_e} = exp(-k_o t^n)$
3	Lewis	$MR = \frac{M - M_e}{M_o - M_e} = exp(-k_o t)$
4	Page Modified	$MR = \frac{M - M_e}{M_o - M_e} = exp(-k_o t)^n$

Where:

- M = moisture content of tea leaves % (d.b.)
- M_e = equilibrium moisture content % (d.b.)
- M_o = initial moisture content % (d.b.)
- k_o = drying rate constant (h^{-1})
- t = time (h)
- A_o = model coefficient
- n = exponent

2.4. Withering Model Validation

The curve of the withering/drying of the tea leaves is matched to the experimental data using two different equations. χ^2, E_{RMS}, E_{MB}, and R^2 are used as the main criteria for selecting the best equation to account for the variations in the drying curve of the tea leaf samples and determine the most suitable model. The lower the above-mentioned criteria, the better the match. The statistical values can be calculated as follows (Ghodake et al., 2006):

Equation 2: $\chi\ square$

$$\chi^2 = \frac{\sum_{i=1}^{N}\left(MR_{exp,i} - MR_{pre,i}\right)^2}{N - n}$$

Equation 3: Mean Square Error

$$E_{RMS} = \sqrt{\frac{\sum_{i=1}^{N}\left(MR_{pre,i} - MR_{exp,i}\right)^2}{N}}$$

Equation 4: Mean Bias Error

$$E_{MB} = \left[\frac{1}{N}\sum_{i=1}^{N}\left(MR_{pre,i} - MR_{exp,i}\right)\right]$$

Equation 5: Coefficient of Determination

$$R^2 = 1 - \frac{\sum_{i=1}^{N}\left(MR_{exp,i} - MR_{pre,i}\right)^2}{\sum_{i=1}^{N}\left(MR_{exp,i} - MR_{expmean}\right)^2}$$

Where:

- $MR_{exp,\,i}$ = *i*-th experimental moisture ratio
- $MR_{pre,\,i}$ = *i* -th predicted moisture ratio
- $MR_{exp,\,mean}$ = mean value of the experimental moisture ratio
- N = number of observations

3. RESULT AND DISCUSSION

3.1. Temperature and relative humidity profile

The experiment was conducted and the temperature profiles of the hot water entering the HPHE, hot water exiting the HPHE, air entering the HPHE (ambient), air exiting the HPHE, and air exiting the drying tray can be seen in Figure 4 (a). The entering water was set at a temperature of 50°C, with variations in the air velocity set at speeds of 0.2, 0.4, and 0.6 m/s. It took approximately 1 hour from when the hot air heater was turned on until it was found to remain stable at 50°C.

When the variation in the flow velocity was 0.2 m/s, the hot water temperature of the HPHE exit was nearly 49.9°C, or the temperature difference was approximately 0.1°C. This shows that the HPHE evaporator can absorb heat from the incoming hot water and then transfer it into the side of the HPHE condenser, which can increase the air temperature by 9.1°C. When variation in the flow velocity was 0.4 m/s, the hot water temperature of the HPHE exit was approximately 49.8°C, or the temperature difference was nearly 0.2°C. In comparison, the difference in temperature of the intake air and HPHE exit on the side of the condenser was approximately 9.32°C. When the flow velocity of air was 0.6 m/s, the hot water temperature of the HPHE exit was near 49.7°C, or the temperature difference was approximately 0.3°C. In contrast, the difference in the temperature of the air intake and exit of the HPHE on the condenser side was nearly 9.35°C. This occurs because on increasing the air stream velocity, more energy can be absorbed from the hot water. This phenomenon shows that the HPHE works appropriately. However, on opposing the gusts of air, the temperature of the air coming out of the HPHE decreased. This is because the air contact time with the HPHE is reduced by changing the air velocity (Hassan, 2013).

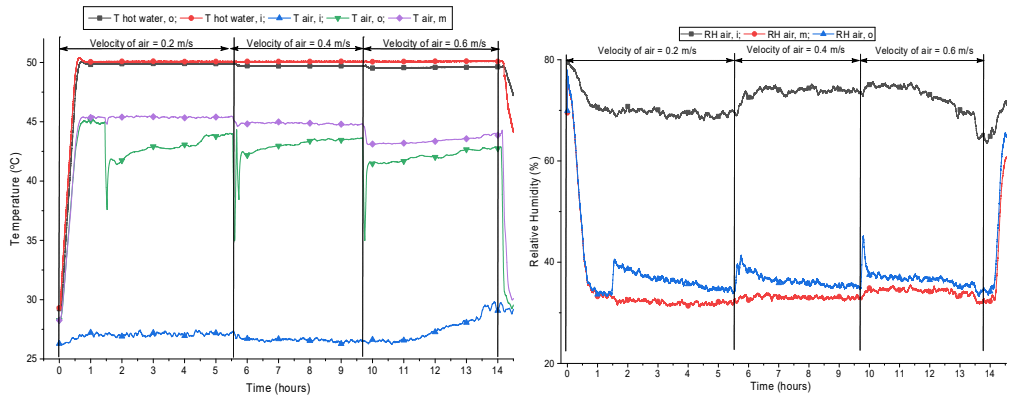

Figure 4: (a) Temperature profile; (b) Profiles of the relative humidity of air for various airspeed variations (0.2, 0.4, and 0.6 m/s) at a temperature and hot water flow rate of 50°C and 18 L/min, respectively

Figure 4 (b) shows the value of the relative humidity of the air entering and leaving the HPHE system and air coming out of the drying tray. It can be seen that the humidity of the air exiting the HPHE decreases because the air temperature rises after passing through the HPHE system, which results in some of the moisture in the air being evaporated. In addition, an increase in the air temperature will also increase the steam saturation pressure, resulting in a decrease in the value of the relative humidity.

The air humidity in the HPHE system in this experiment was not conditioned, so that the relative humidity of the air exiting the HPHE system also depended on the amount of ambient air RH. The average decrease in the relative humidity in the HPHE condenser was from 71.92% to 33.09%. Besides being affected by the temperature, the decrease in the relative humidity of the air exiting the HPHE was also affected by the speed of the air entering the HPHE. A higher velocity of air entering the HPHE reduces the heat transfer duration; hence decreasing the amount of heat absorbed (Hassan, 2013, Danielewicz et al., 2014). This is because the mass convection coefficient is a function of Reynold's number and the relative humidity (Zhang et al., 2007)

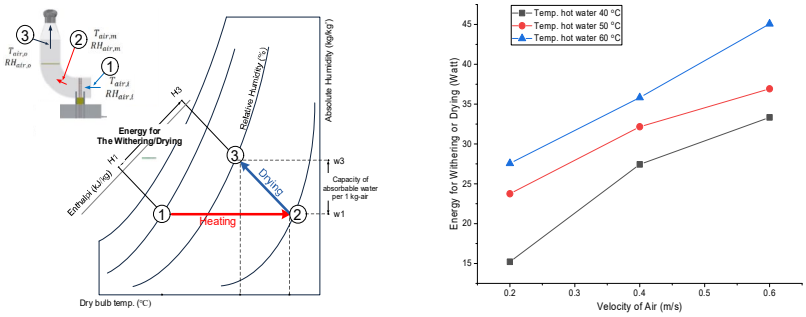

Figure 5: (a) Process of heating and drying on the Psychrometric chart (ideal); (b) Energy for the Withering base on the Psychrometric Chart

From Figure 4 (b), it can also be seen that immediately after the tea leaves were placed in the drying tray, the relative humidity of the air exiting the drying tray rose drastically and then decreased the withering time. This shows

that shortly after the tea leaves are placed in the tray, much of the water vapour on the tea leaves was removed, and subsequently, it decreased. The decrease in the water vapour on the tea leaves was caused by the hot air from the condenser side of the HPHE blowing the vapour out of the system.

By knowing the initial and final water contents in the tea (w.b.), the amount of water vapour that is successfully removed by this system can be calculated using the principle of mass equilibrium. The amount of water vapour that is successfully removed during the test is also validated with the results of the weighing of the weight of the tea leaves at the end of the test. The process of withering the tea leaves using the HPHE can be seen in the psychometric chart in Figure 5 (a). From this process, the air properties for each test: absolute humidity, temperature, and specific air volume in each process (point 1 to 3) can be seen. Thus, the amount of drying/withering energy from the HPHE system in this study can be seen in Figure 5 (b).

The energy for the withering increased with increasing air velocity, meaning the process of withering the tea leaves became fast. This is based on Figures 4 (a) and 4 (b), where the differences in the temperature and relative humidity on the exit side of the HPHE and drying tray become increasingly smaller with the increasing speed of the drying air. This also applies to the increase in temperature, which will accelerate the process of the withering/drying.

3.2. HPHE effectiveness

The performance of the HPHE system can be seen from the value of its effectiveness. From Figure 6 (a), it can be noted that the highest effectiveness of the HPHE occurred at a variation in the air velocity of 0.2 m/s with a hot water temperature and flow of 60°C and 18 L/min, respectively. In comparison, the least effectiveness occurred at a variation in the air velocity of 0.6 m/s with the hot water temperature and flow of 40°C and 18 L/min, respectively.

The higher the temperature of the hot water flow, the higher the heat capacity that can be transferred by the HPHE. With the increase in the temperature of the hot water received by the HPHE evaporator, the latent heat of the working fluid in the heat pipe was rapidly achieved. This means the evaporation of the heat transfer to the condenser in the heat pipe (under the saturation condition of the evaporator) also occurred more rapidly. The latent heat of the working fluid had a major impact on the rate of heat transfer from the evaporator to the condenser so that the heat pipe performance also increased. The trend of the characteristic values of the effectiveness is consistent with the results of research conducted by Putra et al. (Nandy Putra, 2017).

Figure 6 (b) shows the difference in the temperature of the intake and exit air of the HPHE ($\Delta Tc = T_{air,o} - T_{air,i}$). It can be seen that the increase in the temperature of the hot water received by the evaporator of the HPHE increased the value of ΔTc. However, increasing the speed of the air flow reduced the value of ΔTc. Because the convection heat transfer coefficient (h) is a function of the fluid velocity, when the air velocity increases, the convection coefficient of the heat transfer of the HPHE condenser section will also increase. The HPHE system has the ability to transfer heat at a fixed optimum value. When the heat value (q) released in the HPHE condenser section remains constant, the convection heat transfer coefficient value increases because the air velocity increases. With a fixed area of heat (A) heat transfer, according to the convection heat transfer equation: $q = h.A.\Delta T_C$, the value of ΔTc will decrease.

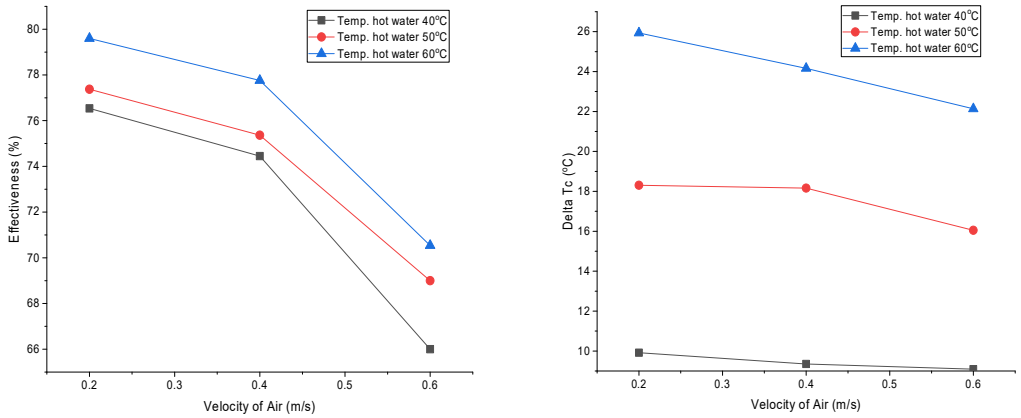

Figure 6: (a) Effectiveness of Each Test Variation; (b) Amount of Δ Tc for each test variation.

3.3. Withering Model

The measured moisture content of the tea leaves before being placed into the drying tray is approximately 80% of the wet base (w.b.). The trend of the decrease in the moisture ratio (MR) is used as an indicator to determine the duration of the withering process to achieve the expected water content of the tea leaves. For the tea leaves withering process, the expected target of moisture in the tea leaves is 56% (w.b.) (Ghodake et al., 2006). Figure 7 (a) presents the comparison of the MR value patterns of all the test variations. The higher the hot water temperature used for the withering process and higher the speed of the drying air, the faster is the drying process.

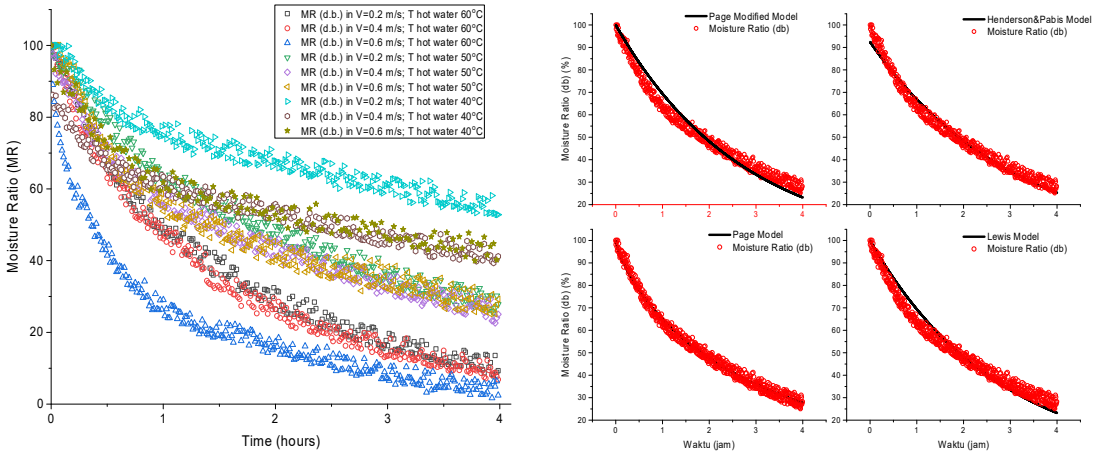

Figure 7: (a) Comparison of the Moisture Ratio Curve (MR) for tea commodities for all variations in this test; (b) Fitting of experimental results with mathematical models at air speeds of 0.2 m/s, speed and flow temperature of hot water = 18 litres / minute, 50°C.

The results of the fitting of the MR experiment and four mathematical models can be seen in Figure 7 (b). The summary of the results of this analysis is that the Page model consistently provides larger R^2 in comparison to the other three models. In the research conducted by Panchariya et al., the values of R^2, χ^2, and Emb received for the mathematical model for the withering/drying of tea leaves were above 0.93 and below 9.0 x 10^{-4} and 0.018, respectively (P.C. Panchariya et al., 2002). The Page model also consistently provides root mean square error (ERMS) values, i.e. a low mean bias error (Emb) compared to the Lewis model, modified Page model, and Henderson–Pabis model. Therefore, from this study, it can be concluded that the Page model is the best model to represent the withering behaviour of the tea leaves. On selecting the Page model to be used to describe the process of tea drift, for 100 gram tea leaves, the time to reduce the tea water content in various research variations can be estimated, the results of which are given in Table 2.

Table 2: Tea leaves withering time estimation

Temperature of Hot Water (°C)	Velocity of Air (m/s)	The Air Temperature Exits from the HPHE (°C)	Time to Withering of the Tea Leaf from Moisture Content of 80% to 56% (wb)
40	0.2	37.53	11 hours 55 minute
	0.4	37.33	8 hours 25 minute
	0.6	36.15	7 hours 2 minute
50	0.2	45.39	3 hours 30 minute
	0.4	44.85	3 hours 15 minute
	0.6	43.38	3 hours 9 minute
60	0.2	52.39	1 hours 52 minute
	0.4	51.84	1 hours 41 minute
	0.6	49.96	49 minute

4. CONCLUSION

A new concept for the withering and drying of tea leaves is successfully built and tested under various withering conditions. It is adapted to the operating conditions in the tea industry, and uses low-temperature geothermal energy sources. The effectiveness of the HPHE increases with increasing temperature of the hot water, but decreases with increasing air velocity entering the system. The effectiveness of the HPHE varies from 66% to 79.59%. For 100 g of fresh tea leaves, the heating energy produced varies from 15.21 to 45.07 W, so it can wither the tea leaves from 80% (w.b.) to 54% (w.b.) in 11 h 56 m to 49.6 m. The Page mathematical model is the best model to represent the withering behaviour of the tea leaves with the HPHE system.

The use of the HPHE in the direct utilisation of low-temperature geothermal energy for the withering of tea leaves is acceptable and feasible to be used, specifically in the application of renewable energy in the tea-making industry and for the substitution of fossil fuels. Further research is needed to optimise the drying conditions in the tea industry for its upscaling business.

5. ACKNOWLEDGEMENT

The author would like to thank Directorate of Research and Community Engagements Universitas Indonesia (DRPM UI) for funding this research project under the Q1Q2 Program 2019, no. NKB-0315/UN2.R3.1/HKP05.00/2019, and Research and Development Center for Electricity, New, Renewable Energy and Energy Conservation Technology (P3tek KEBTKE), Ministry of Energy and Mineral Resources (KESDM) Republic Indonesia for the scholarship awarded to the first author.

6. REFERENCES

Abd El-Aty, A. M., Choi, J.-H., Rahman, M. M., Kim, S.-W., Tosun, A. & Shim, J.-H. 2014. Residues and contaminants in tea and tea infusions: a review. *Food Additives & Contaminants: Part A,* 31**,** 1794-1804.

Abd El-Baky, M. A. & Mohamed, M. M. 2007. Heat pipe heat exchanger for heat recovery in air conditioning. *Applied Thermal Engineering,* 27**,** 795-801.

Adisa, A., Jimenez, A., Woodham, C., Anthony, K., Nguyen, T. & Saleh, M. A. 2015. Determination of polycyclic aromatic hydrocarbons in dry tea. *Journal of Environmental Science and Health, Part B,* 50**,** 552-559.

Afuar, W., Sibarani, B., Abdurrahman, G. & Hendrarsakti, J. 2016. Design of Tomato Drying System by Utilizing Brine Geothermal. *IOP Conference Series: Earth and Environmental Science,* 42**,** 012020.

Association of Official Analytical Chemists. 1980. AOAC. *Official methods of analysis (13th ed).* Washington, DC.

Azapagic, A., Bore, J., Cheserek, B., Kamunya, S. & Elbehri, A. 2016. The global warming potential of production and consumption of Kenyan tea. *Journal of Cleaner Production,* 112**,** 4031-4040.

Chacko, S. M., Thambi, P. T., Kuttan, R. & Nishigaki, I. 2010. Beneficial effects of green tea: A literature review. *Chinese Medicine,* 5**,** 13.

Danielewicz, J., Sayegh, M. A., Śniechowska, B., Szulgowska-Zgrzywa, M. & Jouhara, H. 2014. Experimental and analytical performance investigation of air to air two phase closed thermosyphon based heat exchangers. *Energy,* 77**,** 82-87.

Dutta, P. P. & Baruah, D. C. 2014. Drying modelling and experimentation of Assam black tea (Camellia sinensis) with producer gas as a fuel. *Applied Thermal Engineering,* 63**,** 495-502.

Franco, A. & Vaccaro, M. 2013. On the use of heat pipe principle for the exploitation of medium–low temperature geothermal resources. *Applied Thermal Engineering,* 59**,** 189-199.

Ghodake, H. M., Goswami, T. K. & Chakraverty, A. 2006. Mathematical Modeling of Withering Characteristics of Tea Leaves. *Drying Technology,* 24**,** 159-164.

Hassan, M. A. M. 2013. Investigation of Performance of Heat Pipe as Heat Exchanger Using Alternative Refrigerants. *Journal of Energy Engineering,* 139**,** 18-24.

Imansyah Ibnu Hakim, Nandy Putra & Gunawan, Y. 2019. Experimental Study for Heat Pipe Applications on Low Enthalpy Geothermal Energy Utilization or Agricultural Products Dryers. *Journal of Advanced Research in Fluid Mechanics and Thermal Sciences*.

International Organization for Standardization. 1985. ISO 712:1985. *Cereal and Cereal-Product Determination of Moisture Content (Routine Reference Method)*

International Tea Committee, 2016. Monthly Statistical Summary

Kerrigan, K., Jouhara, H., O'donnell, G.E. & Robinson, A.J. 2011. Heat pipe-based radiator for low grade geothermal energy conversion in domestic space heating. *Simulation Modelling Practice and Theory,* 19**,** 1154-1163.

Kerrigan, K., Jouhara, H., O'donnell, G. E. & Robinson, A. J. 2013. A naturally aspirated convector for domestic heating application with low water temperature sources. *Energy and Buildings,* 67**,** 187-194.

Kusuma, M. H., Putra, N., Antariksawan, A. R., Susyadi & Imawan, F. A. 2017. Investigation of the Thermal Performance of a Vertical Two-Phase Closed Thermosyphon as a Passive Cooling System for a Nuclear Reactor Spent Fuel Storage Pool. *Nuclear Engineering and Technology,* 49**,** 476-483.

Nandy Putra, T.A., Adi Winarta 2017. Experimental Study of Heat Pipe Heat Exchanger in Hospital HVAC System for Energy Conservation. *International Journal on Advance Science Engineering Information Technology,* 7.

Nasruddin, Idrus Alhamid, M., Daud, Y., Surachman, A., Sugiyono, A., Aditya, H. B. & Mahlia, T. M. I. 2016. Potential of geothermal energy for electricity generation in Indonesia: A review. *Renewable and Sustainable Energy Reviews,* 53**,** 733-740.

P.C. Panchariya, D. Popovic & Sharma, A. L. 2002. Thin-layer modelling of black tea drying process. *Journal of Food Engineering,* 52**,** 349–357.

Pambudi, N.A., Itoi, R., Yamashiro, R., Css Syah Alam, B.Y., Tusara, L., Jalilinasrabady, S. & Khasani, J. 2015. The behavior of silica in geothermal brine from Dieng geothermal power plant, Indonesia. *Geothermics,* 54**,** 109-114.

Pikra, G., Rohmah, N., Pramana, R. I. & Purwanto, A. J. 2015. The Electricity Power Potency Estimation from Hot Spring in Indonesia with Temperature 70-80°C Using Organic Rankine Cycle. *Energy Procedia,* 68**,** 12-21.

Pincemaille, J., Schummer, C., Heinen, E. & Moris, G. 2014. Determination of polycyclic aromatic hydrocarbons in smoked and non-smoked black teas and tea infusions. *Food Chemistry,* 145**,** 807-813.

Prasetya, N., Umra Lubis, D. E., Raharjo, D., Saptadji, N. M. & Pratama, H. B. 2017. Smart geo-energy village development by using cascade direct use of geothermal energy in Bonjol, West Sumatera. *IOP Conference Series: Earth and Environmental Science,* 103**,** 012004.

Purnomo, C. W. & Indarti, S. 2018. Modification of Indirect Solar Dryer for Simplicia Production. *IOP Conference Series: Earth and Environmental Science,* 120**,** 012026.

Putra, D. P., Bakhtiar, A. & Hajatri, P. 2017a. Development and Validation of Analysis Method For Anthraquinone by liquid Chromatography Tandem Mass Spectrometry. *Jurnal Sains dan Teknologi Farmasi; Vol 19 No Supl1 (2017): Vol 19 Supplement 1, December 2017*.

Putra, N., Ariantara, B. & Pamungkas, R. A. 2016. Experimental investigation on performance of lithium-ion battery thermal management system using flat plate loop heat pipe for electric vehicle application. *Applied Thermal Engineering,* 99**,** 784-789.

Putra, N. S. D., Anggoro, T. & Winarta, A. 2017b. Experimental Study of Heat Pipe Heat Exchanger in Hospital HVAC System for Energy Conservation. *International Journal on Advanced Science, Engineering and Information Technology,* 7**,** 871.

Sulibursk a, J., Bogdanski, P., Szulinska, M., Stepien, M., Pupek-Musialik, D. & Jablecka, A. 2012. Effects of Green Tea Supplementation on Elements, Total Antioxidants, Lipids, and Glucose Values in the Serum of Obese Patients. *Biological Trace Element Research,* 149**,** 315-322.

Vidanagama, J. & Lokupitiya, E. 2018. Energy usage and greenhouse gas emissions associated with tea and rubber manufacturing processes in Sri Lanka. *Environmental Development,* 26**,** 43-54.

Wang, X., Zhou, L., Luo, F., Zhang, X., Sun, H., Yang, M., Lou, Z. & Chen, Z. 2018. 9,10-Anthraquinone deposit in tea plantation might be one of the reasons for contamination in tea. *Food Chem,* 244**,** 254-259.

Zorn, R., Steger, H., & Kölbel, T. De-Icing and Snow Melting System with Innovative Heat Pipe Technology. Proceedings World Geothermal Congress, 2015 Melbourne, Australia.

Zhang, J., Gupta, A. & Baker, J. 2007. Effect of Relative Humidity on the Prediction of Natural Convection Heat Transfer Coefficients. *Heat Transfer Engineering,* 28**,** 335-342.

Zlatanović, I., Komatina, M. & Antonijević, D. 2013. Low-temperature convective drying of apple cubes. *Applied Thermal Engineering,* 53**,** 114-123.

#157: ZnO-PTAA potential hybrid hetero-junction for transparent renewable energy device

A transparent optoelectronic device

Bablu K GHOSH[1]*, ABDUL I.A. RANI[1], Ismail SAAD[1], Khairul A. MOHMAD[2]

[1]*Electrical and Electronic Engineering, Faculty of Engineering, Universiti Malaysia Sabah, Kota-kinabalu 88400, Sabah, Malaysia,*
**Corresponding author: ghoshbab@ums.edu.my*
[2]*Faculty of Electrical and Electronic Engineering, Universiti Tun Hossein Onn Malaysia 86400 Parit Raja, Batu Pahat, Johor, Malaysia*

Cost effective transparent renewable energy technology shows promise in helping to fulfill future micro- and nano-segment energy demands. The application of transparent renewable energy devices could be substantial built in to housing and other transparent sub-systems. Organic devices have a higher breakdown and greater open circuit voltage whereas inorganic devices have low breakdown voltage and greater thermal saturation. Current disputes can be standardised by a combination of both. The effect of organic-inorganic hybrid hetero-junctions band barrier on leakage current and subsequent current density have been investigated for prospective green applications. Instead of the commonly used p-type PEDOT:PSS highly conductive and thermally stable PTAA organic material was employed in this study. PTAA is deposited on RF sputtered inorganic ZnO/ITO materials by a spin-coating method at a thickness of 100 and 60nm for 1000 and 2000 rpm growth sequence respectively. Different temperature annealed materials heterointerface J-V characterisation are accomplished. The band barrier and annealing temperature show marked variations on leakage current, and current density are investigated. Grain size, barrier height and leakage current relationships were realised from this study. Greater grain size shows higher barrier height however, leakage current were found to be reduced at the greater grain size. Simulated hetero-structure and corresponding optoelectrical properties were characterised by using general purpose photovoltaic device model (GPVDM). PTAA as p-type emitter materials, its transparent properties were found promising in absorbing particular energy bands paramount for the climate change scenario. Annealing temperature and growth properties were shown to improve conversion performance of electrical energy.

Keywords: ZnO, PTAA, optoelectronic, renewable energy, band barrier, annealing

1. INTRODUCTION

Cost effective renewable energy technology is essential to satisfy future micro and nano stage energy demands. Organic solar cells (OSC) and detectors are new technologies which have a better inclination in converting light into electrical energy. Despite first being proven seventy years ago, it is only recently that it is shown to be feasible in energy applications (Kim, 2017; Bulovic, 2017; Dang, 2011; Zhang, 2018). In recent studies, OSC as a blended and bulk hetero-junction (BHJ) solar cells have displayed their distinguishing features in terms of open circuit voltage (Voc) and fill factor (FF) (Rani, 2018). Due to easy processing and lower cost, inorganic (metal oxide) - organic hybrid technology is flourishing in optoelectronic fields. Organic devices possess a higher breakdown voltage and its excitonic nature shows greater open circuit voltage. In contrast, inorganic devices have low breakdown voltage and the greater thermal saturation current is standardised by a combination of organic-inorganic materials in hybrid HJ. As a fundamental energy conversion device, its transparent range of applications with optimum conversion efficiency and stability are crucial (Bulovic, 2017). A recent comprehensive review has realised that diverse metal oxides interface engineering materials are vital for band barriers and carrier transport to enhance efficiency and stability (Ghosh, 2019). High temperature processed inorganic emitter design on Si is costly and non-transparency is not suitable for transparent devices. In contrast to well-known Si hybrid hetero-junction (HJ) or diverse emitters on Si as energy conversion device (Chen, 2006; Ghosh, 2018), ZnO-based materials are advantageous in optoelectronics device designs (Özgür,2005). The ZnO nanostructure with a greater band edge which creates a substantial amount of barrier height to minimise energy loss. The organic layer thickness, conductivity and n-type ZnO resistivity are critical parameters to administer device performance. Nevertheless, Si HJ minimum barrier is supposed to enhance reverse saturation current that ultimately reduces Voc and short circuit current density (Js). In contrast to Si-Si directional covalent bonding, II-VI ZnO material bonding is flexible to accommodate a hetero-structure (HS) with minimum interface defects; as a result less thermal current leakage is expected. The II-VI materials' greater flexibility is accommodated by dissimilar materials on light-matter interaction. The inter-band transition has greater columbic interaction due to electrons possessing a greater binding effect in the conduction band thus stabilising the bound exciton or having greater binding potential with the PTAA materials. This binding potential once greater than thermalisation energy $K_{\beta}T$ thus, stabilises against thermal effect and it shows greater open circuit voltage, Voc (Ghosh, 2019).

Carrier transport stuffs are crucial to improving device's optoelectronic properties. Organic materials carrier transport purpose, p-type conductivity problem is resolved by the introduction of organic hole transport materials (HTM**)** and it has opened up research interest in the transparent optoelectronic field. Previously all inorganic transparent photo detectors (Tsai, 2011), solar photovoltaic devices (Patel, 2017) fabrication and performance have been analysed. The p-NiO/n-ZnO materials interface barrier energy analysis has shown greater electron barrier energy in comparison to the hole barrier energy. It has certainly huge scope for carrier recombination. The barrier effect is significant to minimise the junction leakage current at high temperature and high breakdown voltage. In our study replacement of traditionally used P3HT or PEDOT:PSS by highly conductive and thermal stable PTAA (Poly-triarylamine) polymer of band edge greater than PEDOT:PSS (Khadka, 2017) was expected to perform well. Inherently ZnO of n-type conductivity has lowest resistivity (Tsai, 2011), p-type PTAA with better interface properties can minimise energy loss. PTAA has good chemical potential to stabilise excitonic properties thus improving Voc (Khadka, 2017). It may possibly be due to higher barrier potential leading to less carrier recombination loss. The electronic properties are related to quantum energy states of hetero interface. The materials fabrication process and physical conditions are significant to control crystallinity. Hence, grain size and leakage current for diverse barrier energy at the hetero-interface may differ. Active layer proper thickness, growth parameters, related grain size effect on leakage current and optical properties on electrical performance have yet to be precisely studied. Thermal stress and interface physical properties are highly correlated. In this respect PTAA is highly stable even at elevated temperature. It was anticipated to increase p-type carrier conduction as a result optoelectric properties were expected to be enhanced. Loss mechanism and barrier interrelation in organic materials for energy conversion is so complex in comparison to inorganic materials. In this study inter-band transition scenario barrier effect was investigated.

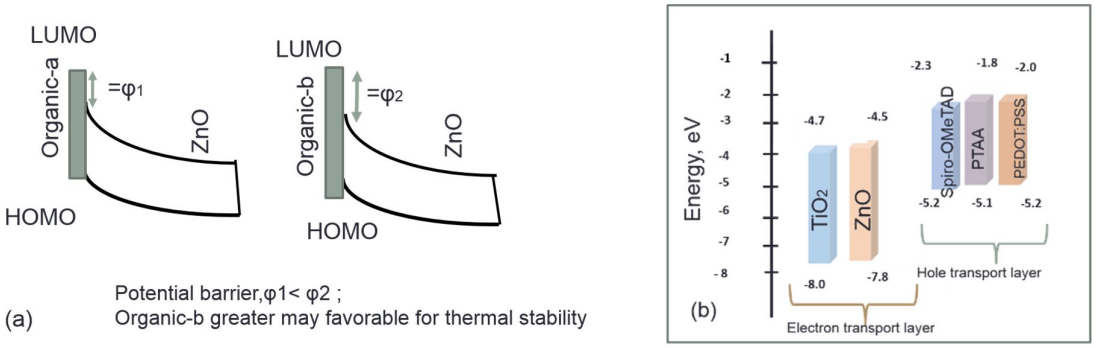

Figure 1: Schematic hybrid PN junction (a); ZnO and PTAA energy level compare to others (b)

The ZnO band barrier effect on interface property and how it acts to reduce energy loss will be studied. It is anticipated that current density would be enhanced by minimising leakage current in PTAA/ ZnO HS and to reduce energy loss thus optoelectronic energy conversion would be enhanced.

2. METHODOLOGY

2.1. Growth process

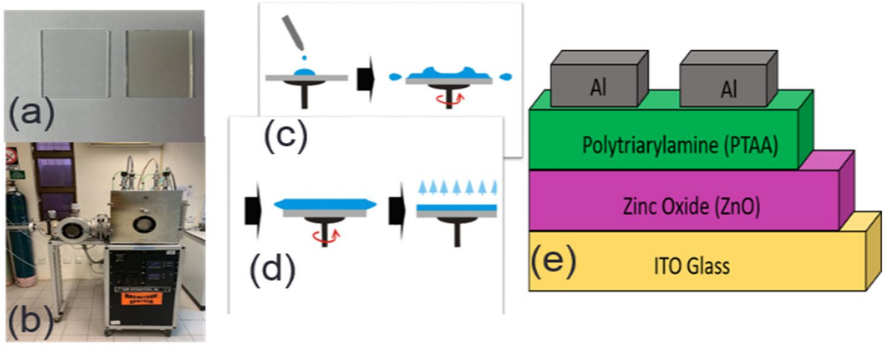

Figure 2: Substrate (glass and ITO) (a), RF sputtering (b), PTAA deposition (c), annealing (d), and schematic design (e)

ZnO/PTAA films were deposited onto ITO by radio frequency (RF) sputtering and spin coating method. ZnO was initially deposited on ITO using RF spattering. The RF power is kept at 100 W with the mixture of Argon (Ar) and Nitorgen (N_2) gas at flow rate of 8 sccm at room temperature. ZnO film thickness of ~300 nm for 40 minutes deposition. To achieve wurtzite structure, ZnO film is annealed at 400°C for an hour. Then it was loaded to the organic chamber for spin coated PTAA deposition. PTAA (Lumtec) is initially dissolved and soaked in chloroform for 12 hours to obtain 1% wt polymer mixture. It is deposited on the sputtered ZnO layer spin coating speed 1000 and 2000 RPM. PTAA layer was deposited at ~100 nm and ~60 nm for 1000 and 2000 RPM respectively. Eventually the device is annealed with different temperature from 100°C to 150°C. RF sputtering stoichiometry and growth rate of spin coating method are perceived some difficulties. Surface properties at highs temperature >130°C are shown to be slightly degraded.

2.2. Characterisations

All transparent devices have a lot of potential in UV detection and energy conversion even during the day / night cycle. After different temperature thermal annealing, optical and interface (current density-voltage, J-V) analysis was performed by real measurements to explore the prospects for energy conversion. From XRD analysis, grain size was measured and its relation with leakage current and barrier height (numerically calculated) were found. The general purpose photovoltaic device model (GPVDM) software was used for HS model design and its interface assessment.

3. RESULT AND DISCUSSION

ZnO as higher band edge materials precise HS and band barrier are realised from software design as shown in Figure 3. Different thicknesses of the configuration energy absorption and dissimilar materials hetero-surface abrupt energy level are revealed.

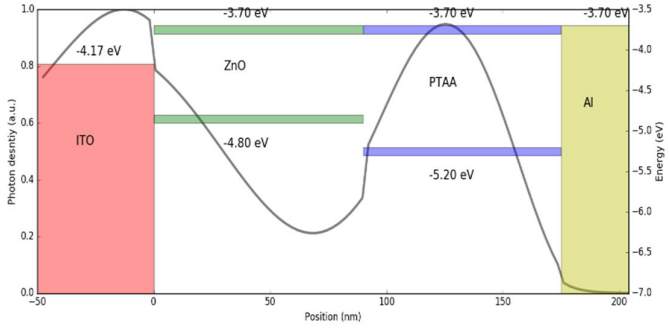

Figure 3: Carrier accumulation due to abrupt interface band barrier (simulation data)

Interface carrier generation and separation is dominated by the PTAA photo physical properties. Figure 4 shows the interface barrier related photon distribution in PTAA-ZnO materials deposited on ITO. Simulation based interface results found that the greater barrier ended with precise interface and marked photon distribution. It is typical in HJ organic solar cell.

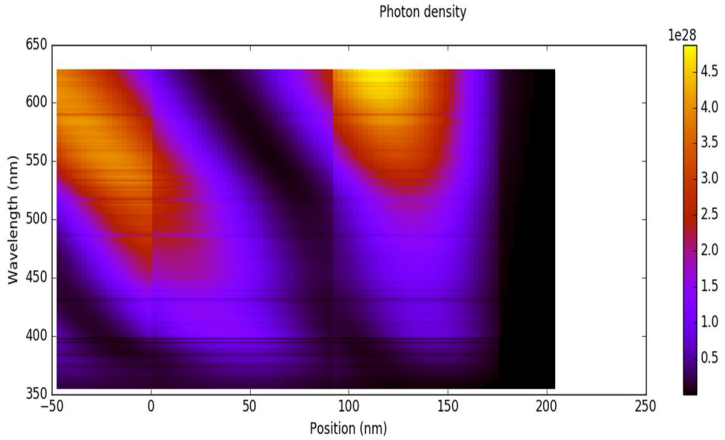

Figure 4: Barrier related energy variance and photon distribution (simulation data)

For physical interface properties analysis, leakage current is potentially dependent on annealing temperatures. Lower melting temperature of PTAA leads to reduced annealing temperatures. Leakage current density of the deposited PTAA layer at 1000 rpm and J-V are shown below in Figure 5. The figure shows the analytical leakage current properties of materials under different annealing temperatures. Irrespective of band barrier, annealing temperature effect can be understood from the leakage current related semi-log current versus voltage analysis in the range of -4 to +4 V. Certain anomalies are found though its proper cause is not yet understood.

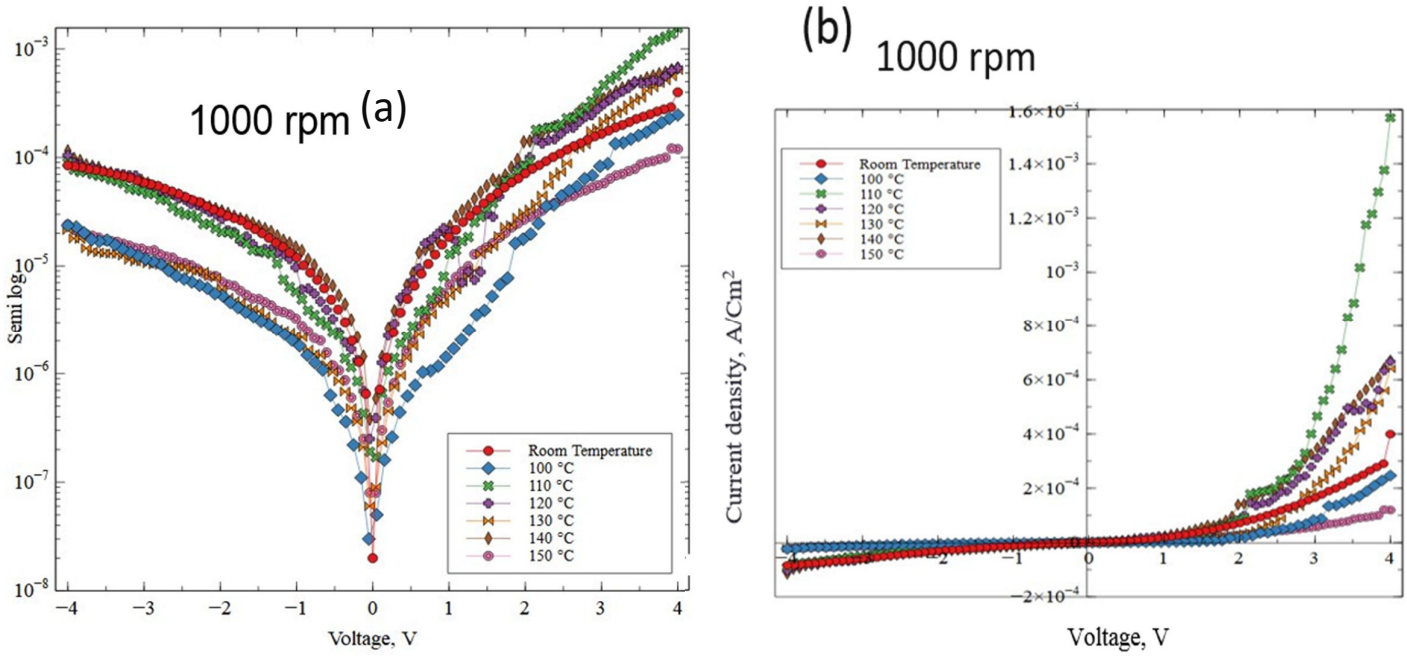

Figure 5: Thermal annealing effect on leakage current (a) and active layer current density by J-V analysis (b)

Compared to room temperature, high temperature annealing was expected to improve grain properties or HS interface quality. As a result less electrical loss was shown in Figure 5 (a). Figure 5 (b) illustrates proper annealing temperatures that resemble better crystalline quality and current density at 110°C. Above this temperature interface or surface property starts to deteriorate although lessening of current density at high annealing temperature is not yet clear. It may relate to the PTAA physical properties with temperature since the ZnO melting temperature is very high. The crystalline quality or band barrier may be concerned with the trade-off between Voc and Js. Annealing of the active layer possibly supports improving the crystalline quality thus reducing carrier recombination and improving carrier transport properties.

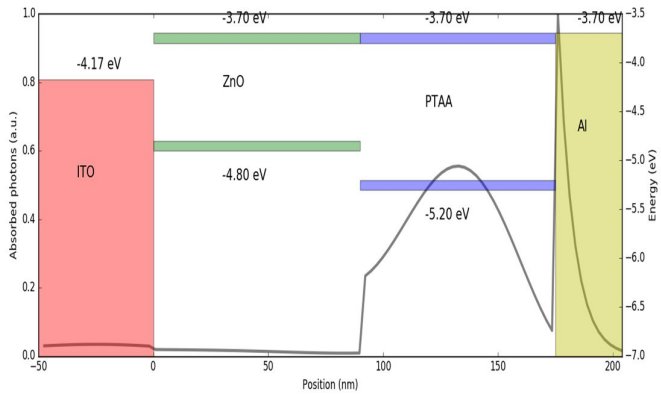

Figure. 6: Absorption trend in the active materials (simulation data)

The software based absorption analysis was done similar to the structure. The absorption spectrum minimal energy absorption in ITO and ZnO layer was faced towards the optical source. Absorption in the active PTAA materials was seen, however very sharp absorption close to the metallic contact area was possibly due to carrier accumulation at the contact area as shown below in Figure 6. This is one reason for limited conversion efficiency due to improper ohmic contract of p-type layer. However, the current density and leakage current variation with different growth and annealing situations were studied. It could be a step ahead to optoelectric energy transfer in transparent conductive layer for transparent optoelectric device studies.

Figure 7 shows the variation of barrier height with grain size for diverse annealing temperature at 1000 and 2000 rpm growth rate.

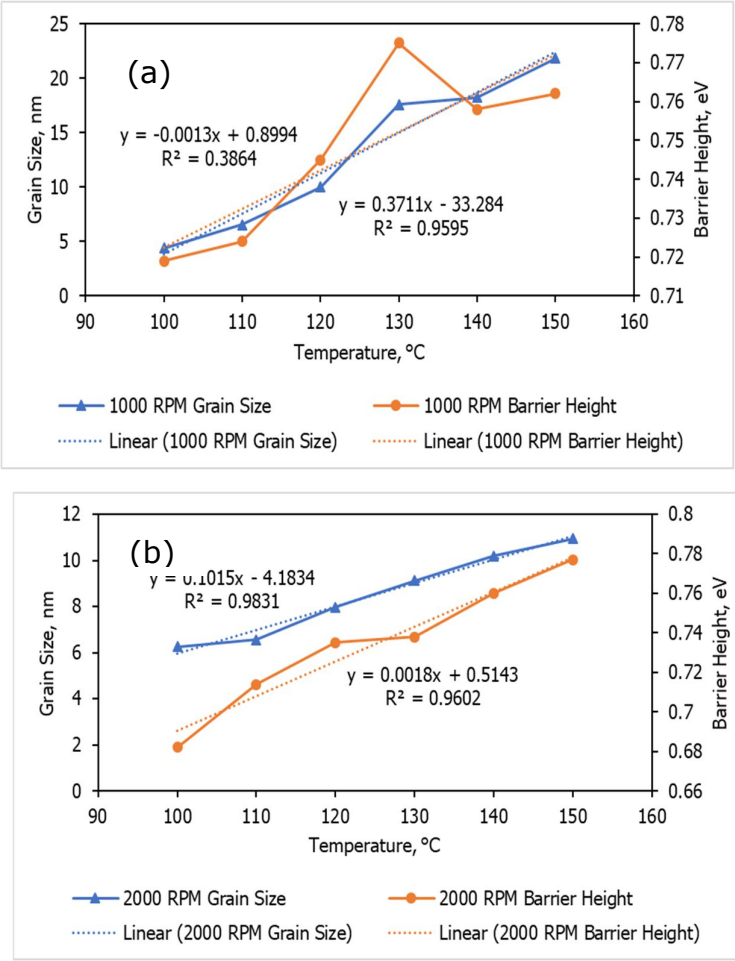

Figure. 7: Interface barrier height variation with annealing temperature for 1000 rpm (a) and 2000 rpm (b) growth rate

The trend of variation of barrier height was almost linear with grain size but higher temperature anomalies between them may be due to thermal effect. PTAA was deposited in 2000rpm, the variation of barrier height reference to grain size is shown to be very precise for the entire range of annealing temperature. Compared to 1000rpm growth, 2000 rpm thin film was found to be more consistent.

From the grain size and barrier height relationship, it is difficult to find carrier properties of hybrid hetero-structure. Barrier height seems to be related to the photo-physical status of active materials in which hetero-junction or interface area is significant. The interface barrier is shown to be dependent on grain size and annealing temperature. Thus, the relationship of leakage current with barrier height for different growth rate were carried out. The barrier height is quantum level energy barrier relating to materials excitonic interaction with temperature, physical properties and growth parameters. Figure 8 shows the grain size relation with leakage current. Uniform variation of barrier height with annealing temperature is observed for 2000 rpm as shown in Figure 8 (b). In this aspect growth conditions and its diversity effect on organic materials were found. It may be related to leakage current and energy loss.

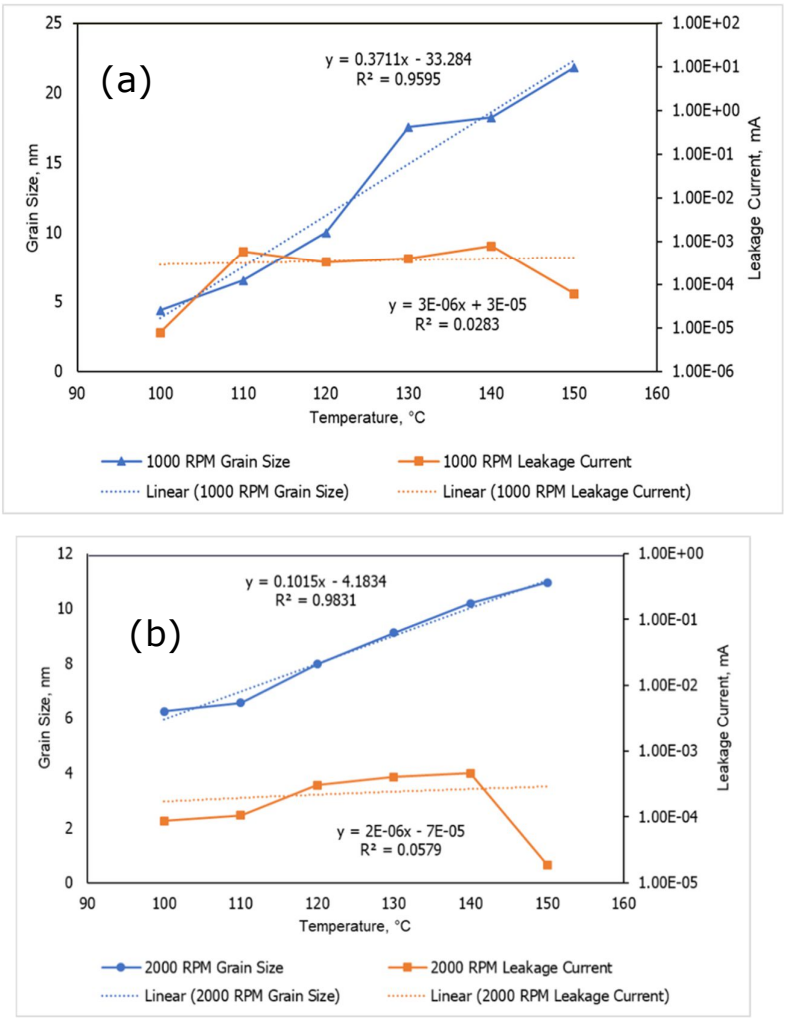

Figure. 8: Variation of leakage current with grain size at 1000 rpm (a) and 2000 rpm (b) growth rate of PTAA.

The leakage current of 1000 and 2000rpm growth rate of PTAA were shown to have very similar trends with grain size variation. At low temperature and low grain size, it seems to be lower however, it remains almost steady with increasing temperature and grain size. Eventually at the highest grain size and barrier height it drops towards low level. It may be due to an improvement of interface properties at the greater grain size which supports greater barrier heights. From the analysis it was revealed that barrier height and grain size are influential in controlling leakage current or PTAA/ZnO hetero-junction energy loss. Though greater barrier height resembles relatively high series resistance however, particular band absorption by this device with greater barrier height may be beneficial for applications in the climate change scenario.

4. CONCLUSION

The electrical performance of p-type PTAA/ n-type ZnO transparent hybrid HJ device optoelectric energy conversion was studied. Different growth strategies and annealing temperature were considered as contributing factors to mark variations of interface quality or barrier effect. Thus diverse leakage current and current density were observed at dissimilar growth conditions. Minimum leakage current at greater grain size and higher barrier height were observed. Although Al contact is significant for fabricating cheaper devices however, Al metal contact's may support accumulate carrier, thus sudden energy absorption at the interface was observed. The Al work function relation to p-type PTAA materials LUMO either, depends on PTAA carrier concentration, or annealing conditions and are not yet understood. The effect of annealing temperature on optical absorption and PTAA carrier concentration impact are essential to be studied further.

5. ACKNOWLEDGEMENT

This work was supported partially by the Fundamental Research Grant Scheme (FRGS) funded by the Ministry of Education, Malaysia under. Grant No K086" and UMS grant GUG0183-2/2017.

6. REFERENCES

Bulovic, V. and Lunt, R.R., Massachusetts Institute of Technology, 2017. *Transparent photovoltaic cells*. U.S. Patent 9,728,735.

Chen, C.H. and Shih, I., 2006. Hybrid organic on inorganic semiconductor heterojunction. *Journal of Materials Science: Materials* in *Electronics*, *17*(12), pp.1047-1053

Dang, M.T., Hirsch, L. and Wantz, G., 2011. P3HT: PCBM, best seller in polymer *photovoltaic* research. *Advanced Materials*, *23*(31), pp.3597-3602.

Ghosh, B.K., Khairul, A.M., Afishah, A., Saad, I., Rani, A.I.A. and Ghosh, S.K., 2018. Analysis of emitter layer diverse effects on electrical performance for prospective Si hybrid solar cell. CEAT 2018; Kuala Lumpur; Malaysia, IET Conference Publications Vol. 2018, Issue CP749, 2018

Ghosh BK, Biswas TK, 2019; Emerging solar cell energy trade-off: Interface engineering materials impact on stability and efficiency progression, *Int J, Engrgy Res*. 43(5) 1670-88; https://doi.org/10.1002/er.4298

Khadka, D.B., Shirai, Y., Yanagida, M., Ryan, J.W. and Miyano, K., 2017. Exploring the effects of interfacial carrier transport layers on device performance and optoelectronic properties of planar perovskite solar cells. *Journal of Materials*

Kim, H.S., Yadav, P., Patel, M., Kim, J., Pandey, K., Lim, D. and Jeong, C., 2017. Transparent Cu4O3/ZnO heterojunction photoelectric devices. *Superlattices and Microstructures*, *112*, pp.262-268.

Özgür, Ü., Alivov, Y.I., Liu, C., Teke, A., Reshchikov, M., Doğan, S., Avrutin, V.C.S.J., Cho, S.J. and Morkoç, H., 2005. A comprehensive review of ZnO materials and devices. *Journal of applied physics*, *98*(4), p.11.

Patel, M., Kim, H.S., Kim, J., Yun, J.H., Kim, S.J., Choi, E.H. and Park, H.H., 2017. Excitonic metal oxide heterojunction (NiO/ZnO) solar cells for all-transparent module integration. *Solar Energy Materials and Solar Cells*, *170*, pp.246-253.

Rani, A.I.A., Mohamad, K.A., Ghosh, B.K., Saad, I., Ibrahim, P., Alias, A. and Rahman, A.A., 2018. Electrical stimulation of different photoactive layer thickness on organic heterojunction solar cell. CEAT 2018; Kuala Lumpur; Malaysia; IET Conference Publications.Vol.2018, Issue CP749, 2018

Tsai, S.Y., Hon, M.H. and Lu, Y.M., 2011. Fabrication of transparent p-NiO/n-ZnO heterojunction devices for ultraviole photodetectors. *Solid-State Electronics*, *63*(1), pp.37-41.

Zhang, Y., Kan, B., Sun, Y., Wang, Y., Xia, R., Ke, X., Yi, Y.Q.Q., Li, C., Yip, H.L., Wan, X. and Cao, Y., 2018. Non fullerene Tandem Organic Solar Cells with High Performance of 14.11%. *Advanced Materials*, p.1707508.*Chemistry C*, *5*(34), pp.8819-8827.

#158: Performance estimation of membrane-based dehumidification using heat exchanger analogy approaches

Gilbong LEE[1], Beomjoon LEE[2], Chul Woo ROH[3], Bong Soo CHOI[4], Eunseok WANG[5], Ho-Sang RA[6], Junhyun CHO[7], Young-Jin BAIK[8], Young-Soo LEE[9], Hyungki SHIN[10]

Thermal Energy Systems Laboratory, Korea Institute of Energy Research, Republic of Korea
[1]giblee@kier.re.kr; [2]beomjoon.lee@kier.re.kr; [3]chulwoo.rho@kier.re.kr
[4]cbs@kier.re.kr; [5]eswang@kier.re.k; [6]hsra@kier.re.kr; [7]jhcho@kier.re.kr
[8]twinjin@kire.re.kr; [9]yslee@kier.re.kr; [10]hkeewind@kier.re.kr

The DOE's 2014 reports evaluated membrane heat pumps technology as one of the most promising alternatives to conventional vapour compression methods. The vapour compression methods maintain evaporator temperature lower than dew points to deal with the latent heat load which generally occupies 20-30% of total cooling load. In membrane heat pump systems, only the water vapour transfers and there is no phase change. This migration is caused by the difference in vapour pressure before and after the membrane. A vacuum pump or blower is used to make the pressure difference. However, there is no methodology for predicting dehumidification performance of membranes when it is used as a part of cooling system. In this study, with the assumption that there is a similarity between heat transfer and moisture pervaporation, the performance indexes of the membrane were derived using well-known heat exchanger method, ε-NTU models. The performance estimations were conducted for two representative system layouts – bypass layout and vacuum layout. Simple relations between design parameters were suggested, and these would give design guides for researchers

Keywords: membrane; dehumidification; ε-NTU method; heat exchanger analogy

1. INTRODUCTION

Since the release of the Department of Energy's (DEO) Building Technologies Office's report, "Energy savings potential and RD&D Opportunities for Non-vapor-compression HVAC technologies" in 2014, membrane heat pump technology has received a lot of interest. As its title implies, the main goal of the report is to analyse alternative technologies to the vapour compression cycle which is one of the most commonly used technologies in the residential and commercial heating, ventilation, and air conditioning (HVAC) applications. Research, development and deployment recommendations were presented in the report based on technical potential, development status, and non-energy benefits of each technology candidate. Figure 1 is the prime results of the DOE's report. Technical energy saving potential was suggested for various candidate technologies such as "thermoelastic", "evaporative liquid desiccant", "membrane heat pump", "ground-coupled solid desiccant system", and so on. From Figure 1, membrane heat pump seems to have high energy saving potential for domestic and commercial air-conditioning sector.

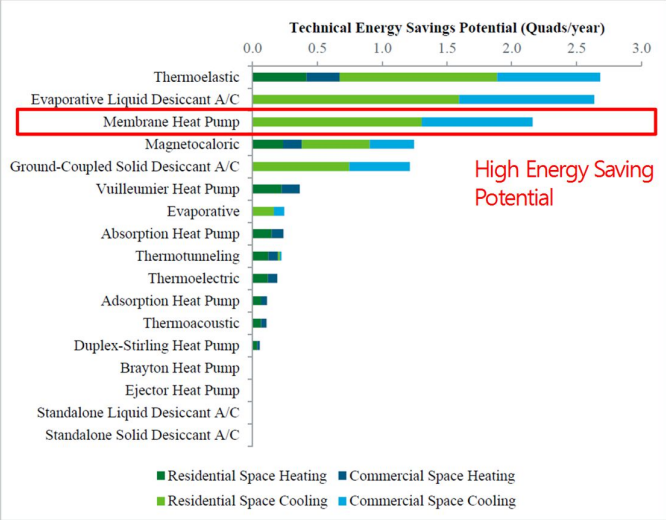

Figure 1: Comparison of technical energy savings potential (Quads/year)

Latent cooling load generally occupies 20-30% of total cooling load. The vapour compression cycle deals with latent cooling load by maintaining evaporator temperature lower than dew points. Since low evaporator temperature increases compressor work and decreases system efficiency, much research has been conducted to treat latent load more effectively. When certain treatments are applied to the surface of the membrane, air-borne water vapour can be selectively transferred through the membrane. Figure 2(a) shows this water vapour transport process. In this situation, the side where dehumidification occurs is generally referred to as the feed side, and the side where water vapours are added is the permeate side. Unlike in the adsorption cycle or absorption cycle, water vapour can be moved without phase change. The migration is driven by the difference in water vapour pressure between the front and back sides of the membrane.

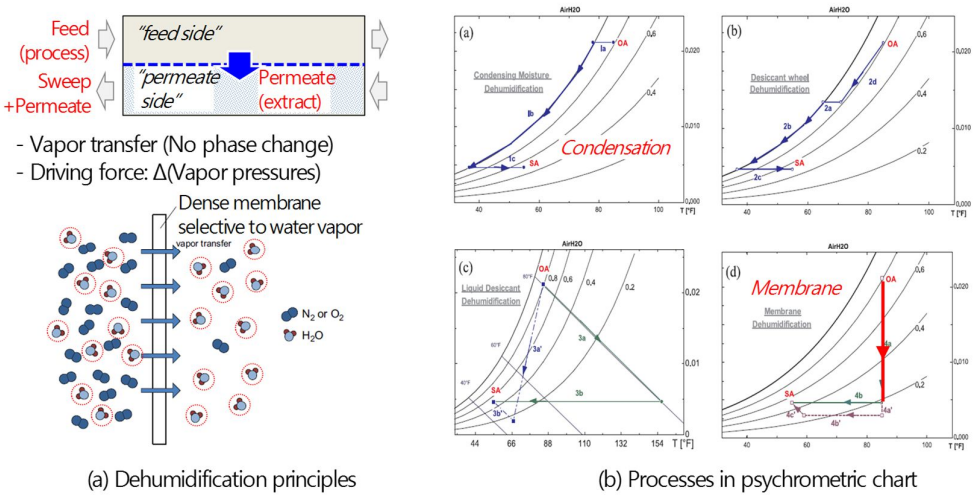

Figure 2: Dehumidification of membrane heat pump

Figure 2(b) shows various dehumidification processes on the psychrometric chart. In order to dehumidify the air conditioner, we currently use the method of condensing and reheating as described in graph (a). On the other hand, the membrane decreases vapour concentration without changing the temperature. Therefore air moves in a vertical direction as shown in graph (d).

This dehumidification by membrane is the core part of the membrane heat pump system. However for the design of the heat pump, there is currently no guide for the expected value of dehumidification performance of membrane in HVAC applications. This is due to the fact that we still do not have enough information on membrane dehumidification applications in the system level. Guidance is very helpful in the early stages of system design, therefore simple expressions for performance of membrane dehumidification are suggested in this study based on heat exchanger analogy approach.

2. MEMBRANE-BASED HEAT PUMP SYSTEM DESIGN

Figure 3 shows three representative system layouts for membrane heat pump applications (Woods, 2014). First, as shown in Figure 3(a), humid air can be dehumidified by making the permeate side as the water vapour dominant state and keeping its pressure lower than the water vapour pressure of feed side. Since water vapour pressure of air is around 10 kPa, a vacuum pump is generally used to make the pressure of the permeate side lower than the feed side water vapour pressure in layout 1.

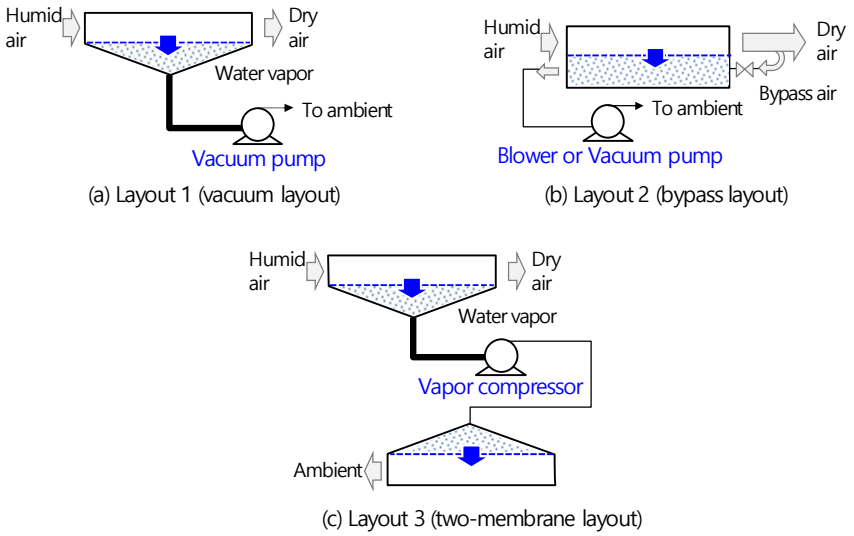

Figure 3: Membrane heat pump system layouts (Woods, 2014)

However, vacuum pumps require a huge amount of power because of the extremely high pressure ratio. As a way to reduce power consumption, a bypass layout is suggested where some of the outlet air of the feed side is extracted as shown in Figure 3(b): its pressure is reduced, and then the extracted/low pressure air is supplied to the permeate side for the dehumidification of feed air. A ring blower can be used to supply bypass air and lower the pressure. In this case, a higher flow rate may be required. Another approach to reduce power consumption is to use two membranes as shown in Figure 3(c). This layout is similar to layout 1 as the permeate side is water vapour dominant. Layout 3 transfers vapour to the outside air by making the discharge pressure higher than the water vapour pressure by using a compressor. To realise this method, a low pressure vapour compressor is needed.

3. SIMPLE ANALYSIS APPROACH

3.1. Test of membrane dehumidification and concept to performance limits

As a solution to plume abatement and the water reduction of cooling towers, membrane module technology was considered in our project. The basic structure of the membrane of interest was hollow fibre, illustrated in Figure 4, which is currently commercialised in water purification and hemodialysis. Although hollow fibres are widely used in the market for the purpose of filtering, pore size is not suitable for gas separation. A special surface treatment was applied to allow hollow fibres to transfer water vapour selectively. Another research team is developing the surface treatment technology using nanoparticles as shown in the centre of Figure 4. Through this, selectivity and permeability can be obtained.

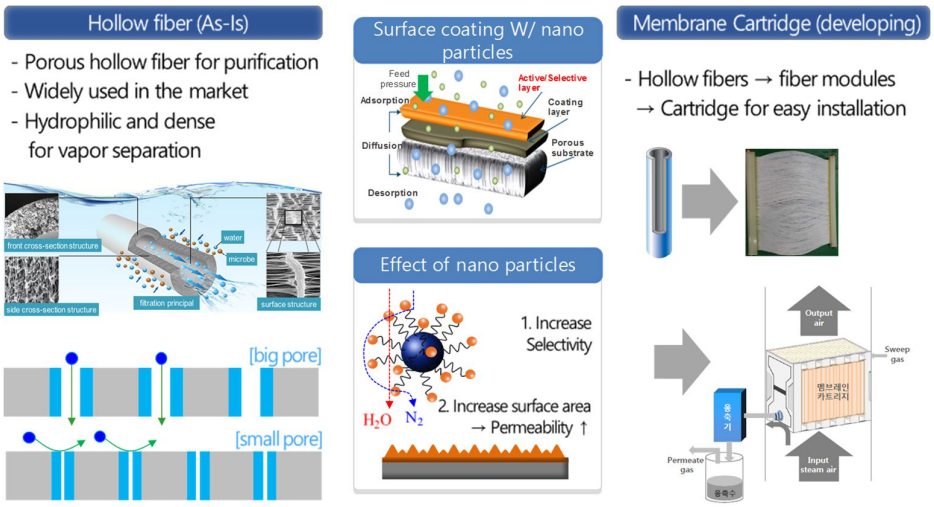

Figure 4: Hollow fibre membrane

Tests were conducted to evaluate the dehumidification performance in the cooling tower prototype. Since the membranes were developed with operating pressures of around 0.6 bar, a ring blower was used as a fluid driving machine. Figure 5(a) shows the test results of absolute and relative humidity of the feed side and the retentate side in the unit test. In the system test, there was a significant difference in air properties of the feed side which was not noticed while there was increased humidity ratio in the permeate side (Figure 5(b)).

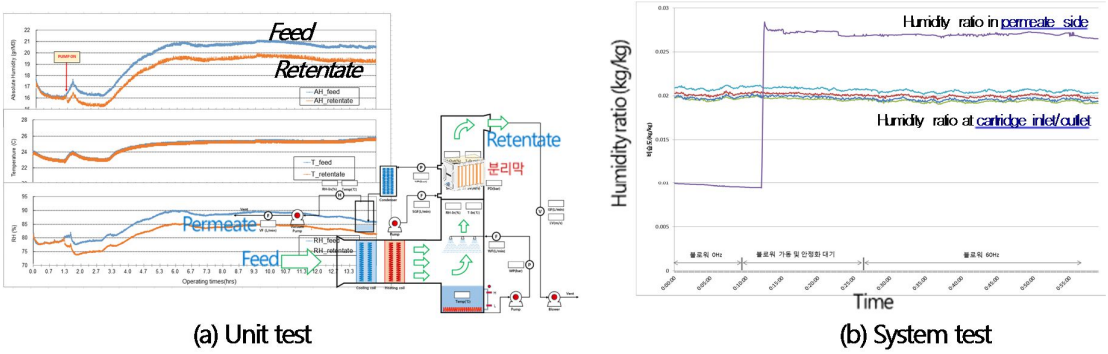

Figure 5: Dehumidification performance test

As a step of validation on the test results, simple analysis on theoretical limits of performance was performed. The operating conditions were as follows; the feed flow rate was 2000 CMH, the permeate flow rate was 200 CMH, and the operating pressure was 0.6 bar. The following assumptions were adopted: 1) The system layout is bypass type; 2) The entire system is isothermal because there is no phase change; 3) Since dry air flow rate is much higher than water vapour, volume flow rates of both feed and permeate are assumed constant.

The most ideal situation for the dehumidification is when the pressure of the permeate outlet becomes equal to the pressure of the feed inlet. Then, the inlet and outlet relative humidity ratios of the feed side can be expressed with pressure ratio r_p (permeate/feed) and volume flow rate ratio C_r (permeate/feed) as the following equation in Figure 6. As the smaller r_p becomes and the larger C_r becomes, the smaller the outlet humidity is obtained. In the tests, the C_r was 0.1 and r_p was 0.6. Then the ideal expectation of dehumidification becomes about 4%. Considering performance degradation in actual application, expectation might be reduced to 2-3%, which may explain why there was no significant changes in the outlet of feed air.

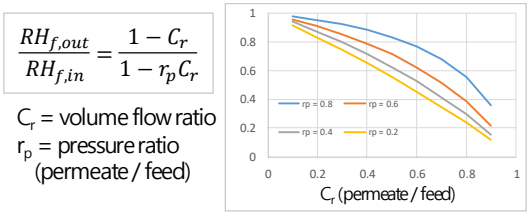

Figure 6: relative humidity ratios of the inlet and outlet

3.2. Simple analysis approach for bypass layout

Next, this concept was extended to extract simple expressions for more general situations of bypass layout. Assumptions were as followings.

- Because there is no phase change, the whole control volume is considered to be under isothermal process. By using gas equation, the density of water vapour becomes proportional to water vapour pressure.
- Since the dry air pressure is higher than the water pressure in the bypass method, the volume flow is considered constant in both feed and permeate.
- The water vapour transfer is proportional to the differential pressure and the transfer coefficient U is considered constant.

The water vapour movement of the bypass layout and the governing equations are illustrated in Figure 7. The equations are similar to those of the counter flow heat exchanger where temperatures correspond to water pressures.

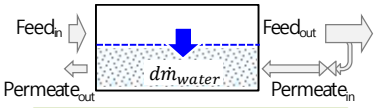

$$d\dot{m}_{water} = U \cdot p\left(P_f - P_p\right) dx$$

$$C_1 \dot{Q}_p \frac{dP_p}{dx} = U \cdot p(P_f - P_p)$$

$$C_1 \dot{Q}_p \left(P_{p,out} - P_{p,in}\right) = C_1 \dot{Q}_f (P_{f,in} - P_{f,out})$$

Figure 7: Water vapour transfer and governing equations

The well-known ε-NTU equations of the counter flow heat exchanger is presented in Figure 8(a). By applying them, simple analysis equations becomes like Figure 8(b). NTU for dehumidification is expressed with the volume flow of the permeate side, gas constant R, temperature of water, and the total surface area A. The efficiency equation can be expressed in the similar way where C_r is the flow rate of permeate and feed. Finally the pressure ratio (or relative humidity ratio) of the inlet and outlet of the feed side is expressed for bypass layout in terms of efficiency, pressure ratio, and flow rate.

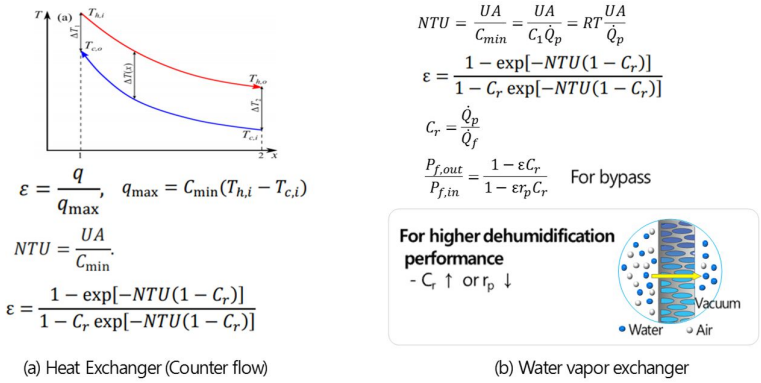

Figure 8: Simple analysis for bypass layout applying heat transfer ε-NTU method

3.3. Simple analysis approach for vacuum layout

The key difference from the bypass layout is that the permeate volume flow is greatly affected by the water vapour transferred. Therefore constant volume flow assumptions becomes invalid in the vacuum layout. For simple analysis, similar procedures were conducted with the following assumptions.

- Since there is no phase change, the assumption of isothermal is still valid.
- The mass value of the gas is proportional to the pressure. Also the constant volumetric flow assumption is still valid in the feed side.
- There is only water vapour on the permeate side.
- The vapour transfer may increase the pressure or increase the volumetric flow rate. However the pressure in the flow direction should not increase. Therefore the vapour pressure at the permeate side is assumed to be constant.

With these assumptions, the performance of the feed and permeate sides were analysed. In the case of the feed side, the volume flow of the feed is constant and the vapour pressure of the permeate is constant. Then the outlet pressure of the feed is expressed with an exponential foam in following equations:

$$C_1 \dot{Q}_f \frac{dP_f}{dx} = -U \cdot p(P_f - P_w)$$

$$\ln \frac{P_f - P_w}{P_{f,in} - P_w} = -\frac{U \cdot p}{C_1 \dot{Q}_f} x$$

$$\ln \frac{P_{f,out} - P_w}{P_{f,in} - P_w} = -\frac{U \cdot A}{C_1 \dot{Q}_f}$$

$$P_{f,out} = P_w + (P_{f,in} - P_w) \exp\left(-\frac{U \cdot A}{C_1 \dot{Q}_f}\right)$$

In the case of the permeate side, the outlet flow is an unknown value. Whether total mass balance between feed and permeate is used or differential equation of mass transfer is used, the permeate outlet flow is expressed with the feed flow rate as follows:

$$\frac{d\dot{Q}_p}{dx} = \frac{U \cdot p}{C_1} (P_f - P_w)/P_w$$

$$\dot{Q}_w = \frac{(P_f - P_w)}{P_w} \left(1 - \exp\left(-\frac{U \cdot A}{C_1 \dot{Q}_f}\right)\right) \dot{Q}_f$$

When the heat capacity ratio is 0, the efficiency of heat exchanger becomes "ε = 1-exp(-NTU)". Because of the assumption of no dry air flow on the permeate side, simple equations become:

$$NTU = \frac{U \cdot A}{C_1 \dot{Q}_f}$$

$$\varepsilon = 1 - \exp(-NTU)$$

Let $P_{fout} = A \cdot P_{fin}$
and $Q_w = C_r \cdot Q_{fin}$

$$C_r = \frac{(1-A)\varepsilon}{\varepsilon - (1-A)}$$

Where:

- C_r = Capacity ratio between fluid devices
  - Feed side: Axial fan, sirocco fan, etc.
  - Permeate side: Vacuum pump
- ε = Membrane exchanger efficiency
- (1-A) = dehumidification expectation

NTU is expressed with feed side flow rate.

3.4. Summary of simple analysis for membrane dehumidification

Table 1 summarises the results of the bypass layout and vacuum layout. In terms of system design, Cr, ε, and (1-A) are the main design parameters; Cr is the capacity ratio between fluid devices (such as fan and vacuum pumps); ε is the efficiency of membrane exchanger; (1-A) is the expected value of dehumidification. Therefore, the last equations would be the starting points in designing dehumidification system with membrane technology.

Table 1: Summary of simple analysis approach

Bypass layout	Vacuum layout
$NTU = \frac{UA}{C_{min}} = \frac{UA}{C_1 \dot{Q}_p} = RT\frac{UA}{\dot{Q}_p}$	$NTU = \frac{U \cdot A}{C_1 \dot{Q}_f}$
$\varepsilon = \frac{1 - \exp(-NTU(1-C_r))}{1 - C_r \exp(-NTU(1-C_r))}$	$\varepsilon = 1 - \exp(-NTU)$
$1 - A = \frac{\varepsilon C_r (1 - r_p)}{1 - \varepsilon r_p C_r}$	$C_r = \frac{(1-A)\varepsilon}{\varepsilon - (1-A)}$

4. CONCLUSION

In this study, simple dehumidification performance expressions for bypass layout and vacuum layout were derived using a heat exchanger analogy approach. The simple expressions for dehumidification performance of ring blower and vacuum pump layouts are suggested with the main design parameters; Cr, ε, and (1-A). Every HVAC system needs fluid driving devices and each fluid driving device has its own performance data provided by manufacturers. If the detailed performance data of fluid driving devices are applied, then performance expectation and guidelines might be provided in the initial stage of membrane heat pump system design.

5. ACKNOWLEDGEMENT

This work was jointly supported by the National Research Council of Science & Technology (NST) grant by the Korea government (MSIP) (No. CRC-15-07-KIER) and the Energy Efficiency & Resources Core Technology Program of the Korea Institute of Energy Technology Evaluation and Planning (KETEP), granted financial resource from the Ministry of Trade, Industry & Energy, Republic of Korea (No. 2017010000850).

6. REFERENCES

Energy Efficiency & Renewable Energy, 2014, Energy Savings Potential and RD&D Opportunities for Non-Vapor-Compression HVAC Technologies: DOE. DOE/EE-1021.

Woods, J., 2014, Membrane processes for heating, ventilation, and air conditioning. *Renewable and Sustainable Energy Reviews*, 33, 290-304.

Qu, M., Abdelazia, O., Gao, Z., Yin, Ho., 2018. Isothermal membrane-based air dehumidification: A comprehensive review. *Renewable and Sustainable Energy Reviews*, 82, 4060-4069.

#159: Experiments on the effects of outdoor air-based methods for water saving and plume abatement of cooling tower

Gilbong LEE[1], Beomjoon LEE[2], Chul Woo ROH[3], Bong Soo CHOI[4], Eunseok WANG[5], Ho-Sang RA[6], Junhyun CHO[7], Jongjae CHO[8], Hyungki SHIN[9], Jong Won CHOI[10]

Thermal Energy Systems Laboratory, Korea Institute of Energy Research, Republic of Korea,
[1]giblee@kier.re.kr; [2]beomjoon.lee@kier.re.kr; [3]chulwoo.rho@kier.re.kr;
[4]cbs@kier.re.kr; [5]eswang@kier.re.k; [6]hsra@kier.re.kr; [7]jhcho@kier.re.kr
[8]jjcturbine@kier.re.kr; [9]hkeewind@kier.re.kr; [10]jwchoi@kier.re.kr

Cooling towers are widely used for commercial, industrial and power plant cooling purposes. In Korea, coal-fired power plants and nuclear power plants are generally located on the coast, while most combined-power plants are located inland and use cooling towers to condense steam. The number of power plants operating will change according to the government energy policies and in the future, it is expected that the need for cooling towers for inland power plants will increase. Since power plants are massive water consuming facilities, methods for saving water in cooling towers should be considered. Also, in industrial facilities, the plume, which often occurs when relative humidity is high, constantly raises social conflicts between residents and manufactures. However, similar technologies can be applied to water saving and plume abatement. In this study, we first investigated the performance of the condensing module using outside air to reduce the relative humidity of exit air (outdoor-air-condensing method). This module has the advantage that a cooling heat source is not necessary but an excessive increase of fan air volume is required, and the structure for water recovery could become complicated. The application of a membrane module which selectively transfers water vapour was also investigated (membrane dehumidification method). The results showed excessive energy disadvantage to generate pressure differences. Since the membrane method considered requires a high bypass airflow for higher dehumidification, it also has a disadvantage similar to that of the outdoor air module. Finally the dehumidification / regeneration module (heat pump method) was examined and this method gave the best performance in water saving and plume abatement.

Keywords: cooling tower; water saving; plume abatement; outdoor air condensing

1. INTRODUCTION

Reduction of water consumption in cooling towers can be achieved through recovering evaporated water vapour or dealing with a portion of the cooling load with a dry cooling system (Lindahl, 2010). In this study, an outdoor-air-condensing method, membrane dehumidification method and heat-pump method were tested for recovering evaporated water vapour. The first method condenses the nearly saturated wet air by outdoor air of relatively low temperature. The second method dehumidifies cooling tower exit air by selectively transferring water vapour through a membrane (Woods, 2014). The last method condenses water vapour and reheats wet air by combining a heat pump cycle. Each method is applied as an individual module which is placed at the top of a conventional cooling tower (Figure 1). With this modular approach, it is possible to separately apply modifications of each module.

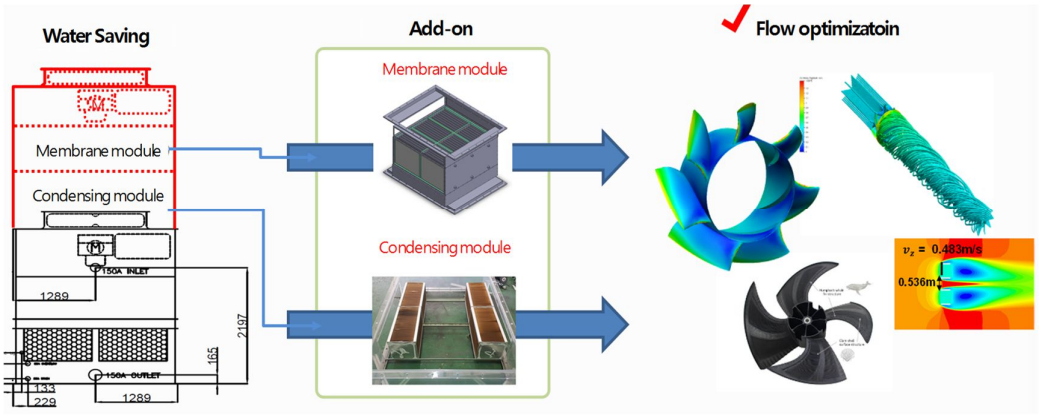

Figure 1: Approach to implement water-saving module on a cooling tower

2. CONDENSING MODULE USING OUTDOOR AIR (OUTDOOR-AIR-CONDENSING METHOD)

To select initial design parameters for a condensing module using outdoor air, a simulation tool for water condensing in the module was developed by a co-working institute, Sogang University. Considering the results of the simulation, the size and layout of condensing module was determined as shown in Figure 2. This module was installed in the prototype (Figure 3) and the performance tests were conducted.

The modules were placed both below and above the water spraying nozzles. When they were in the lower position, the whole surface of condensing nozzles were continuously wetted by the water droplets from the spray nozzles. The wetted surfaces showed low heat transfer performance and the water condensing rate was 1-5% of water consumption. When modules were in the higher position, parts of the surfaces were wetted and had improved heat transfer performance. The water condensing rate was increased up to 8%. Figure 4 shows the water condensing rate of the modules. When two heat exchangers (pitch 4.5mm and pitch 5.0mm) were used, the condensing rate showed lower condensing rates than the one heat exchanger case (pitch 5.0mm). This was due to the increase of flow resistance being too high to compensate for the increase of the heat transfer area. The best performance case was pitch 5.0mm and 3,000 CMH air intake case which was similar to the results from the simulation.

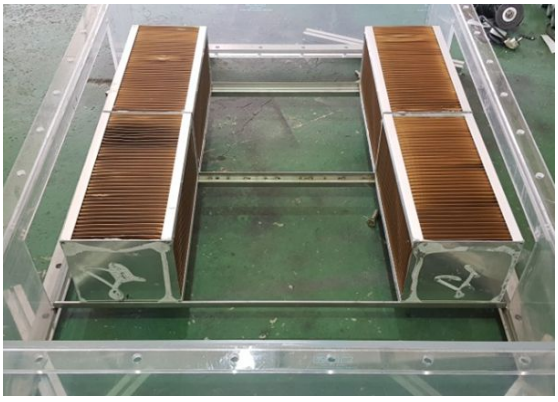

Figure 2: Structure and layout of condensing module using outdoor air

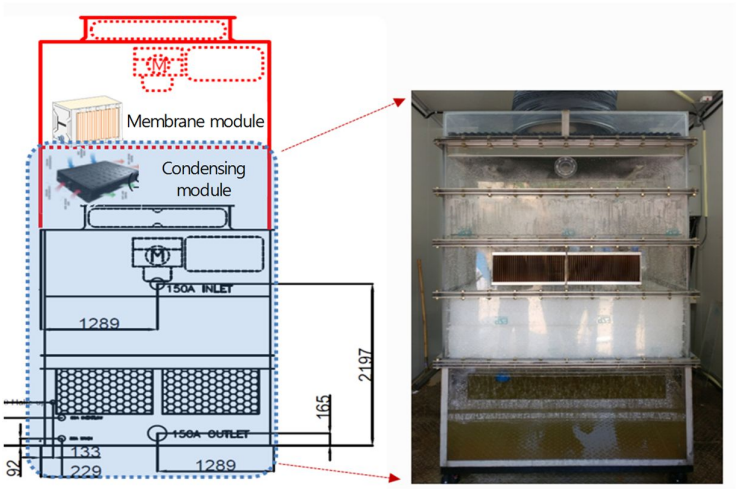

Figure 3: Installation of condensing module in the cooling tower prototype

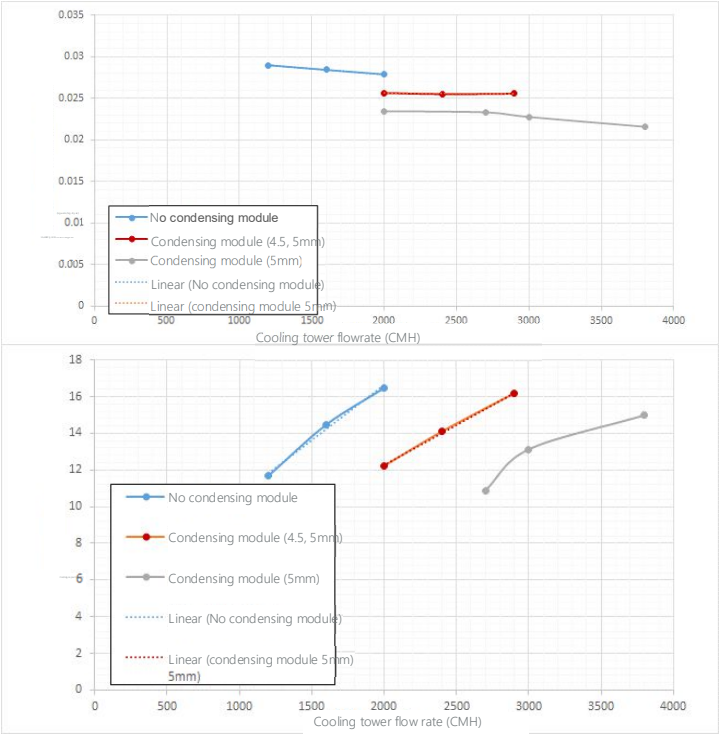

Figure 4: Test results of condensing module using outdoor air

3. MEMBRANE MODULE (MEMBRANE DEHUMIDIFICATION METHOD)

The membrane module was designed based on the operation conditions shown in Figure 5. The condensing module and membrane module were placed in the prototype (Figure 6). Lower back pressure is needed to generate a pressure difference between the front and back surfaces of the membrane. A ring blower was used in this study because the reference working pressure of the membrane was 0.7 bar. Figure 7 shows trends of humidity ratio before and after the ring blower operation. Due to the selective transferring characteristics, the humidity ratio in the extracted side of membrane (permeate side) increased more than 2.5 times that of the feed side, which perfectly represents the membrane's selectivity.

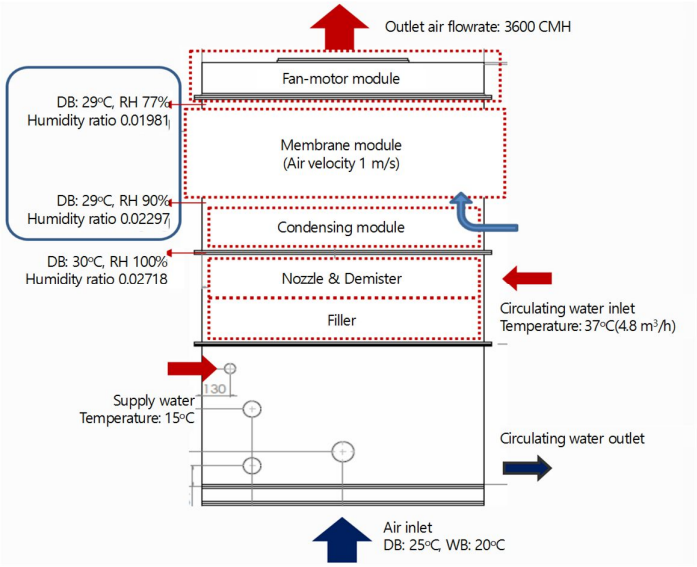

Figure 5: Operation conditions for membrane module design

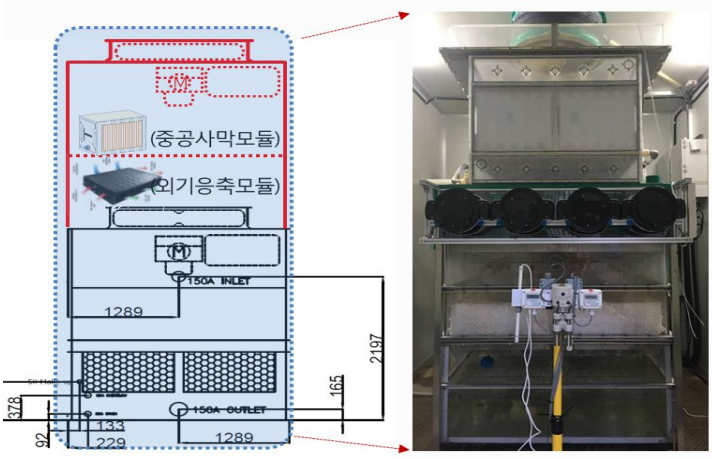

Figure 6: Prototype with condensing module and membrane module

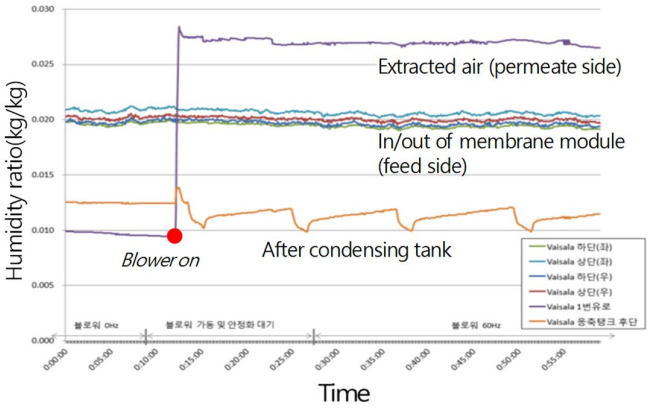

Figure 7: Humidity ratio trends of membrane module

To measure water extraction through the membrane, the extracted air was cooled down by a chiller and the amount of condensing water was measured. The rate was about 20% of the cooling tower water consumption. Considering the fact that the humidity ratio was increased from 0.010 to 0.026, the net portion of membrane for water saving

was estimated to be 12% of total consumption. When both modules were used, total 26% of consumed water was recovered (Figure 8). The contributions of modules were 12% for the membrane module and 14% for the condensing module.

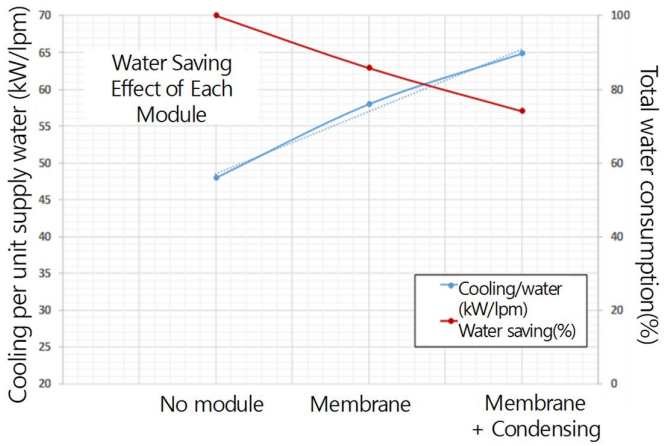

Figure 8: Overall water saving results of proto type

4. DEHUMIDIFICATION / REGENERATION MODULE (HEAT PUMP METHOD)

The hot and humid air leaving a cooling tower would become a white plume when the outdoor temperature is low (Tyagi *et al,* 2012). This white plume is not environmentally harmful, however, there have been a lot of complaints raised against white plume, and thus plume abatement has become an important factor around cooling towers in Korea. Similar technologies can be applied to water saving and plume abatement except that additional heating is preferred for plume abatement. To achieve both, a heat pump cycle application to the cooling tower was tested. A preliminary duct test which simulated the cooling tower operation presented in Figure 9 was carried out. Relative humidity of 75% and 95%, dry bulb temperature of 36°C and an air flow rate of 1,000 m^3/h were the test conditions. Air-to-water heat exchangers were used for both dehumidification and regeneration processes.

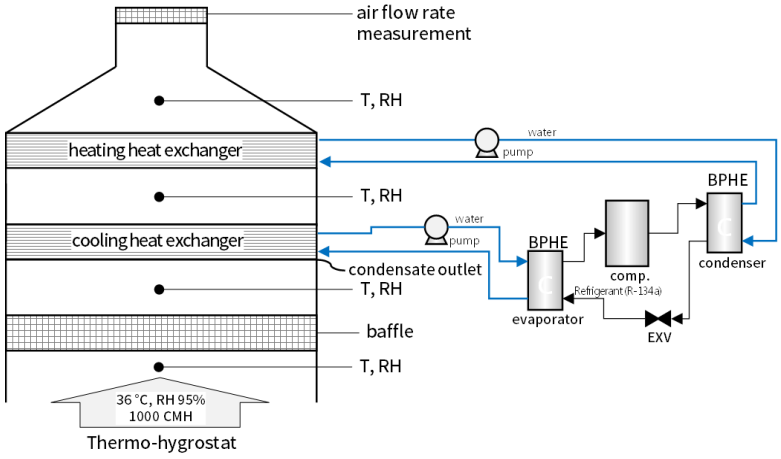

Figure 9: Schematic diagram of dehumidification /regeneration module and heat pump system

When the supply temperature of water from the heat pump for dehumidification was 24°C and the supply temperature for regeneration was 61°C, the air leaving the cooling tower became 51°C DB, RH 31% with inlet condition of 36°C DB, RH 95%. The water recovering rate was 28.5% (cooling tower water consumption: 10.5 g/s, water recovering: 3.0 g/s, air flowrate: 1,000 CMH). Figure 10 shows the inlet and outlet air status of dehumidification / regeneration module. It was expected that the cooling tower would be safe from plume generation even when the outdoor condition is 0°C, RH 95%.

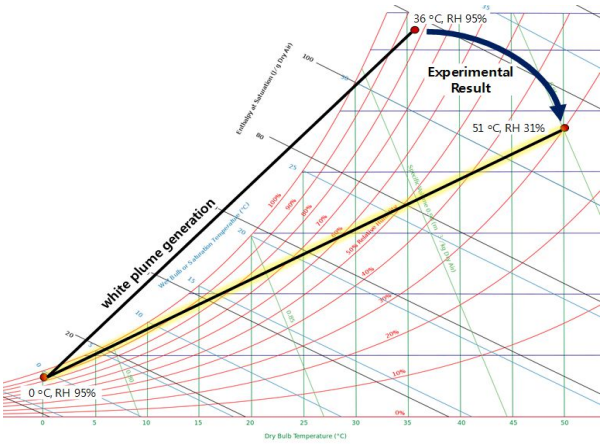

Figure 10: Inlet and outlet air status of dehumidification / regeneration module in the psychrometric chart

5. CONCLUSION

In this study, water saving in a cooling tower was investigated through recovering evaporated water vapour. An outdoor-air-condensing method, membrane dehumidification method and heat-pump method were tested and the effects are provided as a ratio to water consumption without any module. In the test with both the outdoor-air-condensing method and membrane dehumidification method, it was expected that a total of 26% water consumption would be recovered. The contribution of each water recovery method was analysed as 12% for the membrane method and 14% for the outdoor-air-condensing method. A performance evaluation of heat pump based dehumidification (water reduction) / regeneration (plume prevention) module was carried out. The water reduction effect was analysed under cooling tower discharge air conditions of 36ºC, RH (relative humidity) 95% and RH 75%, and a flow rate of 1000 m^3/h. The water recovered by the heat pump evaporator was about 3.0 g / s which corresponded to 28.5% of the cooling tower water consumption. For plume prevention, the results would guarantee that the cooling tower is safe from plume even when outdoor condition is 0°C, RH 95%.

6. ACKNOWLEDGEMENT

This work was jointly supported by the National Research Council of Science & Technology (NST) grant by the Korea government (MSIP) (No. CRC-15-07-KIER) and the Energy Efficiency & Resources Core Technology Program of the Korea Institute of Energy Technology Evaluation and Planning (KETEP), granted financial resource from the Ministry of Trade, Industry & Energy, Republic of Korea (No. 2017010000850).

7. REFERENCES

Lindahl, P., Mortensen, K., 2010. Cooling Technology Institute Annual Conference/Plume abatement-the next generation. Houston, Texas: Cooling Technology Institute.

Woods, J., 2014, Membrane processes for heating, ventilation, and air conditioning. *Renewable and Sustainable Energy Reviews*, 33, 290-304.

Tyagi, S.K., Pandey, A.K., Pant, P.C., Tyagi, V.V., 2012, Formation, potential and abatement of plume from wet cooling towers: A review. *Renewable and Sustainable Energy Reviews*, 16, 3409-3429.

#160: Experimental studies of wood particles combustion in an intensive air flow

Denis SVISHCHEV[1], Maria KOZLOVA[2], Pavel RALNIKOV[3]

[1]*Laboratory of Thermodynamics, Melentiev Energy Systems Institute, SB RAS, 130 Lermontov Street, Irkutsk 664033, Russia, denis.svishchev@gmail.com*
[2]*Laboratory of Thermodynamics, Melentiev Energy Systems Institute, SB RAS, 130 Lermontov Street, Irkutsk 664033, Russia, mari.kozlova.95@mail.ru*
[3]*Ural Federal University (UrFU), 19 Mir Street, Yekaterinburg 620002, Russia, ral-pavel@mail.ru*

Wood fuel gasification in the downdraft process is characterised by specific modes. In comparison with traditional modes, these do not have a pyrolysis zone in the fuel bed that precedes the fuel oxidation zone. Fuel is supplied into the oxidising zone without charring, where it reacts with the intensive cold air flow from tuyeres. This study aims to simulate conversion of particles in the gasifier close to the tuyeres. For this purpose the particles are burned in the muffle furnace space and the ceramic channel simulating the presence of other bed particles at a first approximation.

Burning of particles in the furnace space allowed determining different mechanisms of their combustion. A two-stage process is observed in the range of tuyere velocities below 20 m s-1 and at its first stage the volatiles escape from the particle and burn. At the tuyere velocities above 125 m s-1 combustion of particles is realised primarily as a single-stage process. The intensive air flow reaches the fuel particle surface and initiates combustion of the surface charcoal layer. In this case the stages of devolatilisation and char residue combustion run concurrently.

The combustion velocity of particles in the heated muffle furnace space increases steadily with the air flow rate (in the studied range). The combustion velocity of particles in the ceramic channel increases first and then decreases with the growing air velocity in the tuyere. These regularities are explained by the cooling effect of the air flow on the particles. Presumably, this cooling effect can be observed while gasifying the fuel bed, which leads to decrease in the cold gas efficiency and increase in the tar concentration in the producer gas. At air velocity above 95 m s -1, fragmentation of fuel particles commences. A layer of charcoal formed at an initial stage of burning heats up in the intensive air flow and is separated from the particle surface.

Keywords: wood biomass; single particle combustion; gasification mechanism; particle fragmentation

1. INTRODUCTION

During solid fuel gasification different conditions for the reaction of solid particles with gaseous oxidiser are created. At gasification in a fixed bed a gasifying agent reacts mainly with charred fuel rather than with raw fuel (Reed, 1998). Processes in the fluidised beds are characteristics by intensive mixing of fuel particles. Gas velocity in the oxidising zone is about 0.5-2.5 m s^{-1} for the bubbling fluidised bed, and 4-6 m s^{-1} for the circulating fluidised bed (Basu, 2006). Gas velocity at entrained flow gasification is 15-30 m s^{-1}, but fuel particles 20-80 μm in size in these conditions move with the flow (Gräbner, 2014). Relative velocity of solid and gaseous media turns out to be comparatively low.

This paper investigates the process of unstratified downdraft gasification that is characterised by the lack of pyrolysis zone in the bed (Svishchev, 2019a). Raw fuel that has not been subjected to thermal impact reacts with an intensive tuyere air flow whose velocity from each tuyere reaches 10-40 m s^{-1}. The described conversion conditions make this process is different from other gasification processes.

For studying the mechanism of unstratified process we developed a technique and a rig for testing the combustion of single particles in different conditions. Transition from a bed to an individual particle simplifies the experiment and procedures for obtaining the experimental data. The main drawback of tests with a single particle is a lack of surrounding particles that form the bed. It is worthwhile assuming that surrounding particles considerably enhance the combustion rate of one another due to high turbulent constituent of heat and mass exchange processes. For example, during graphite particle combustion in the fluidised bed, the Sherwood number increased drastically with growth of inert material particles size (Hayhurst, 2002).

The single particles combustion mechanism includes the stages of the release and combustion of volatiles (homogeneous process) and the combustion of a char residue (heterogeneous process). Depending on the combustion conditions these stages can proceed sequentially or overlap each other.

Howard and Essenhigh have established a significant overlap of the stages of homogeneous and heterogeneous combustion of polyfractional pulverised coal. When about 95% of volatiles were released, about 50% of the char residue reacted simultaneously (Howard, 1967). Accounting for the coal fractional composition in the mathematical model allowed the authors to establish a significant overlap of stages for particles less than 15 μm, from 15 to 65 μm a slight overlap and staged combustion for particles larger than 65 microns. Tufano et al. clarified later the data from Howard and Essenhigh. Detailed kinetic modelling indicated the overlapping of the stages of combustion of volatiles and char residue even for coal particles of 100 μm in size (Tufano, 2019).

For fuels with a high yield of volatiles, such as biomass, staged combustion is typical, even for relatively small particles 53–75 μm in size (Zhang, 2019) and 0–100 μm (Ye, 2019). However, spectral analysis of the radiation of burning biomass particles with a size of 224-250 μm reveals a slight overlap of the stages of homogeneous and heterogeneous combustion (Weng, 2019).

For large particles of biomass mainly staged combustion is characteristic. Remacha et al. found that the volatile flux from the particle surface was an order of magnitude higher than the oxygen flux diffusing to the particle surface (Remacha, 2018). The volatile flux protects the solid surface of the particle from oxidation by oxygen. However, Manson et al. noted that the overlap of the stages caused by the asymmetric heating up of the particle when the char residue began to react on one side, while the volatiles were still released on the other side (Mason, 2015).

The paper presents results of studying the combustion of large single wood particles. The process parameters were varied during the experiment, and a ceramic channel was used for creating the conditions for conversion of an individual particle similar to conditions for particles conversion in the bed.

2. A METHOD FOR STUDYING THE PARTICLES COMBUSTION

For studying the particles combustion in an intensive air flow we proposed and tested our own method (Svishchev, 2019b). Following this method, a sample was placed into the heated space of a furnace and blown over by air from a stationary tuyere (Figure 1). The temperature of the air entering the tuyere was about room temperature (20-22°C). The sample was held by a thermocouple with an open junction. The sample can be burnt out completely or removed from the furnace after desired period of time measured from the moment the particle was placed in the furnace. Burning particles are quenched in the quenching chamber. After the tests the volume of particles, their weight and shape were measured.

Particles of similar initial sizes and weight, prepared from the same wood piece (pine tree) were used for tests. They were 12±0.1 mm cubical shape particles weighing 671±11 mg.

Sample exposure in the furnace for different period of time allowed simulation of time-dependent change of mass, volume and shape of a particle that was averaged by multiple samples. For charred particles the structure of internal layers and their ultimate composition can be identified. This method for samples testing allows visual observation of the burning process and measurement of particles temperature using a thermocouple.

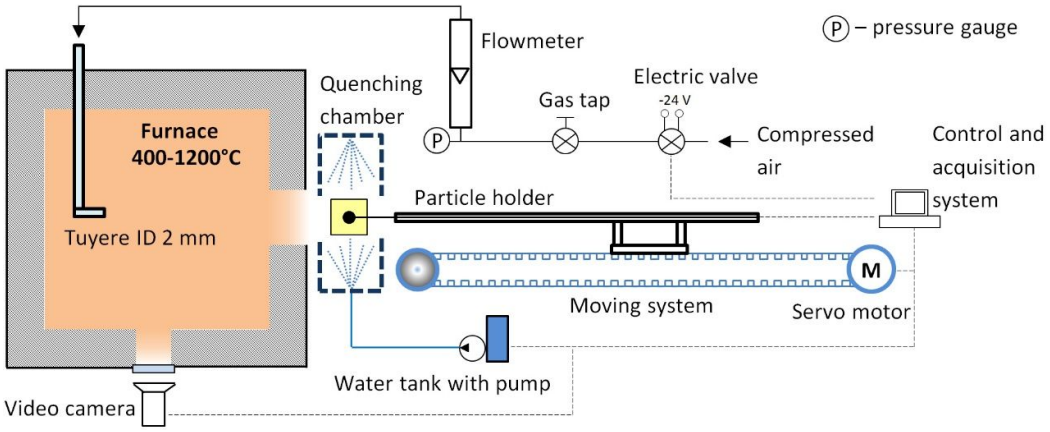

Figure 1: A schematic diagram of a rig for burning single fuel particles (Svishchev, 2019b)

In the first series of experiments the particles were burnt completely. In the course of the experiments we studied the impact of such parameters as furnace temperature, and air velocity in the tuyere. Three heating temperatures were used: 800, 1000 and 1200°C. The value of 1000°C corresponds to the range of temperatures achieved by the fuel bed in the experiments with the quartz reactor (Svishchev, 2019a). Different air flow rates were tested for each furnace temperature. Air flow velocity in the tuyere varied from 10 to 125 m s^{-1}. The number of parallel samples in the experiment was from 3 to 5.

In the second series of experiments a ceramic channel was placed into the furnace (Figure 2) that simulated environment of bed particles. It was made of a ceramic tube and was placed in the furnace on a fireclay brick support. An inner diameter of a channel was 20.5 mm, and clearance between particles edge and an internal wall of the channel was 1.8 mm.

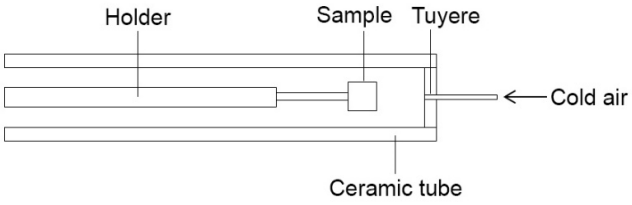

Figure 2: Schematic diagram of a ceramic channel

Heating temperature during the experiments was 600 and 800°C. Air velocity in the tuyere varied from 10 to 125 m s^{-1}. In some experiments the samples were burnt out completely up to the moment of particle tear-off from a holder by an air flow, or partially. In the latter case the burning particles were removed and then quenched following the developed procedure.

3. RESULTS AND DISCUSSION

3.1. Mechanisms of particles combustion in the air flow

Combustion of single wooden particles follows three possible mechanisms depending on the air blow velocity. The first mechanism was realised at an air blow velocity of 20 m s^{-1} and lower. It was characterised by stage-wise nature. After the particle ignition, a flame of burning volatiles was formed around it (Figure 3a). This flame obstructs air penetration to the particle surface and prevents oxidation of a charcoal layer. A front side of a particle remains cold and there was no flame near it.

Volatiles are released and burnt at the first stage. A flame envelope was torn off from the particle surface when the temperature in its centre was as high as 330-350°C (Figure 3b). The flame base was located at the rear surface of

a particle. After termination of intensive release of volatiles the carbon residue of a particle started to incandesce, and a stage of carbon residue combustion commenced (Figure 3c).

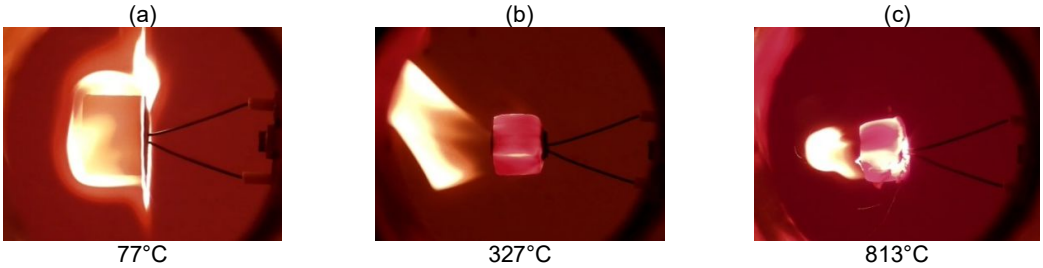

Figure 3: Stages of particle combustion at a muffle temperature of 800°C and air flow velocity of 20m s^{-1}. Temperatures under the pictures are readings of thermocouple in the centre of a particle. Air was fed by a tuyere shown in the pictures on the right

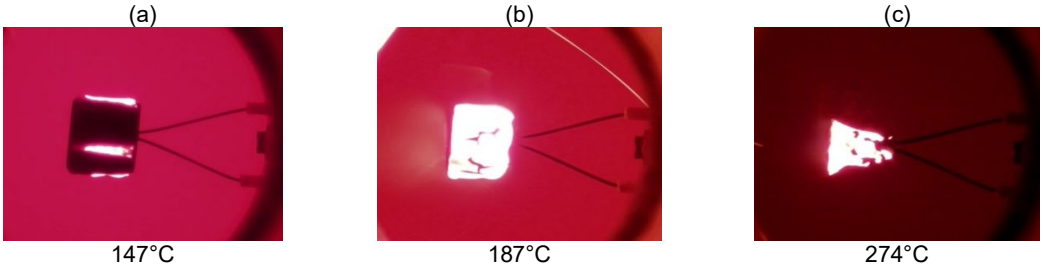

Figure 4: Particle combustion at a furnace temperature of 800°C and air flow velocity of 125 m s^{-1}. Figures below the pictures are temperatures in the centre of a particle

A one-stage mechanism of particle combustion occurred at air velocity in the tuyere above 125m s^{-1}. At the initial stage of particle combustion its front edges and corners started incandescing, which evidences burning of a charcoal layer in these places (Figure 4a). Flame during burning was not observed. Incandescent areas gradually embraced the entire particle, but not its rear plane (Figure 4b). The particle centre remained relatively cold. Its temperature was about 190-200°C, which was not sufficient for the wood to be intensively decomposed. The centre of the particle was heated to the temperature of pyrolysis commencement only when the burning front came to it directly (Figure 4c). In a single-stage mechanism of combustion the stages of volatiles released and of charcoal residue burning occurred simultaneously.

In the range of air flow velocities from 20 to 125 m s^{-1} a mixed combustion mechanism occurred. With the growing velocity of air blow a two-stage conversion gradually changed over to a single-stage one. It is worthwhile mentioning that the temperature impact on the ranges in which some or other type of combustion mechanism occurred was not observed. This impact was most probably irrelevant.

There are flame-photometry methods for identification of tar concentration in the producer gas (Moersch, 2000). Intensity of flame glow in a certain subspectrum happened to be proportional to the tar content in the burnt gas. With the air blow velocity growth and with transition from a two-stage mechanism of conversion to one-stage mechanism, the yellow colour of flame gradually faded. It can be assumed that the amount of tar coming to the flame envelope was reduced due to its decomposition during filtration through a red-hot charcoal layer. This conclusion is hypothetical and needs confirmation.

3.2. Experiments on particles combustion in the heated ceramic channel

Air velocity increase (from 10 to 20 m s^{-1} at a temperature in the channel of 600°C, and from 10 to 40 m s^{-1} at 800°C) first reduced particle combustion time and increased combustion process intensity (Figure 5). Further increase of air blow velocity gave the opposite effect, i.e. it led to combustion time increase. This regularity was conditioned by particles cooling by an intensive cold air flow. At a channel temperature of 600°C and at air blow velocity of 120 m s^{-1} the particle did not ignite, but charred (Figure 5a).

Time of samples combustion in the furnace at the air velocity increased from 20 to 125 m s^{-1} steadily reduced. Differences between dynamics of particles combustion in the furnace and that in the channel can be explained by different temperature of air forwarded to the particle surface. Hot air from the free space of a furnace can be captured by cold air flow coming from a tuyere. Temperature of the air coming to the particle in this case would be higher than temperature of the tuyere air. When a ceramic channel was used, hot air from the furnace space was

not ejected (Figure 2). It can be assumed that in the experiments with the channel the air coming to the sample had lower temperature than air in the experiments without a channel.

At the air velocity of 20 m s^{-1} and temperature of 800°C, specific mode of particles combustion in the channel occurs. Volatiles escaped from the sample inflame and form a 'buzzing' flame with strong whirling around the particle. At the same process parameters, at the initial stage of combustion the sample combustion in the free space of a furnace was accompanied by formation of 'calm' flame around the particle.

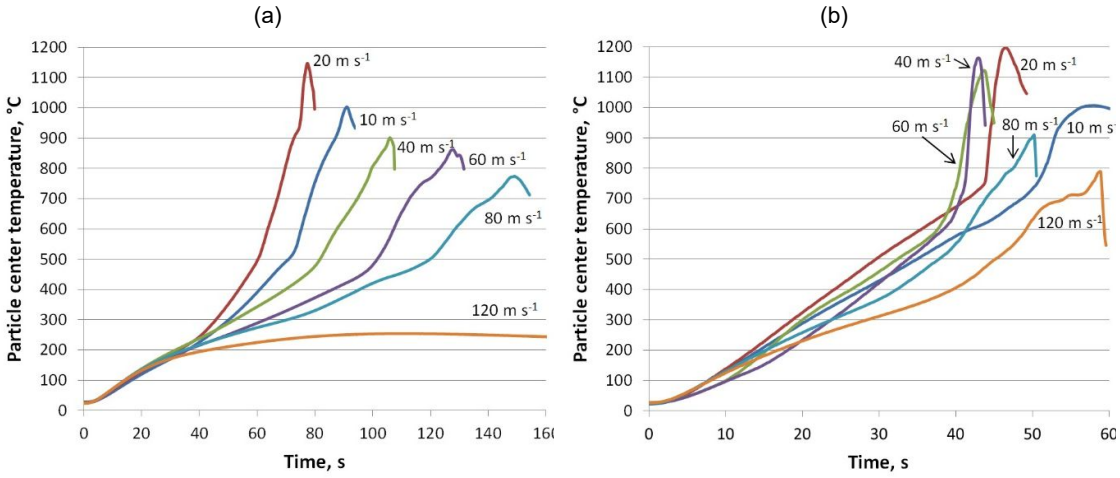

Figure 5: Change in the particle centre temperature versus time at different velocity of tuyere air blow. Experiments with the use of a ceramic channel heated up to 600°C (a) and 800°C (b)

Temperature of the air coming to the sample in the experiments with free space in the furnace was higher than in the experiments with a ceramic channel. Despite such temperature differences the dynamics of particles combustion as a function of time in some experiments was practically identical. Nature of changes in the weight of residue for samples tested in the channel of a furnace at the air flow velocity of 20 m s^{-1} was comparable (Figure 6). The general nature of changes in the weight of particles residue can be explained based on two assumptions. First, air temperature had no notable impact on this mode of particles combustion; and second, flame whirling in the channel intensified heat exchange processes and balances lower temperature of the air fed to the sample.

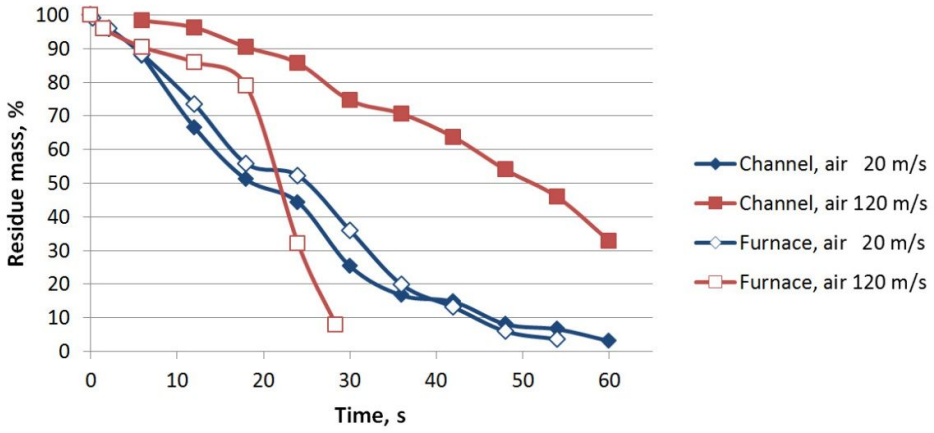

Figure 6: Change in the particle residue weight versus time. Channel and furnace temperature was 800°C

At a channel temperature of 600°C and air velocity above 40m s^{-1} a low-temperature mode of particles combustion was observed. This mode creates conditions for smouldering combustion of a char layer formed on the sample surface. Smouldering combustion commences on the rear side of particles and slowly goes over to lateral sides. The front plane was not subjected to carbonisation. Released volatiles mixed with cold air and did not ignite. A holder was strongly tarred in the course of this process.

The effect of single particles cooling by tuyere air allows us to make a hypothesis on the nature of fuel gasification in the downdraft gasification process. Some results reported in literature evidence continuous growth of combustible components content in the gas with air flow rate increasing (Yamazaki, 2005), or growth followed by a fall in the areas of high air flow rates (Dogru, 2002). The fall can be explained by cooling of particles of the bed in the vicinity of tuyeres. Cooling can also affect the degree of volatiles conversion that are formed from the fuel in this particular area and may cause high concentration of tar in the producer gas. Tar was not a desirable product of gasification.

3.3. Particles fragmentation during combustion

Destruction of fuel particles into smaller ones is referred to as fragmentation. This phenomenon occurs in the process of fuel combustion, gasification and pyrolysis (Caposciutti, 2019; Cui, 2016). There are two types of fragmentation. Primary fragmentation is destruction of particles at stages of fuel drying and devolatilisation (Litun, 2018). It is due to mechanical stresses between different points of the same particle with different temperature, and due to destructive effects of pressure of gas-vapour formed during pyrolysis. Secondary fragmentation occurs at a stage of charcoal residues conversion and is conditioned by the particles porosity growth (Costa, 2015).

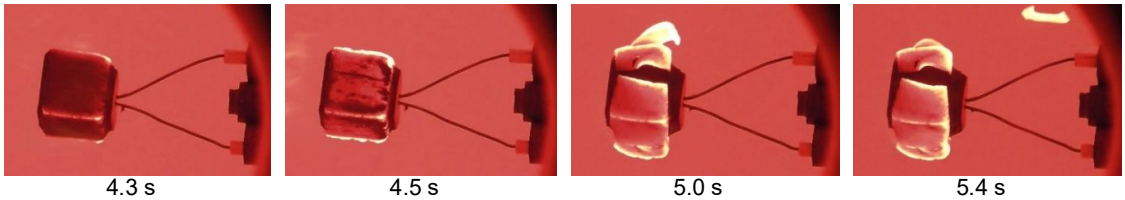

Figure 7: Particle fragmentation and preceding stages. Time elapsed after sample placing into the furnace was given under the photos. On the right of photos a part of a holder was seen

In a number of experiments we observed the following mechanism of burning particles fragmentation (Figure 7). First, within several seconds after placing a sample into the furnace it carbonised. Then the outer layer of charcoal starts reacting with the air flow and rapidly incandesced (Figure 7, 4.5 s). The incandesced charcoal layer was separated from the particle surface (Figure 7, 5.0 s). The major share of separated fragments remained fixed to the particle and burned near its surface, but some fragments were separated and flew to the furnace space. In Figure 7, 5.4 s the separated fragment can be seen in the top right-hand part of the photo. Particle fragmentation was probably due to the following two causes: at rapid heating of the surface layer of charcoal an intensive pyrolysis commenced in the underlying layers of a particle. Gaseous products formed putting pressure on the surface layer. During heating this layer expanded, which facilitated its separation from the particle. Existence of a similar mixed mechanism of fragmentation was mentioned earlier in literature (Litun, 2018).

Fragmentation, to a certain extent, is a stochastic phenomenon and probability of its occurrence can conveniently be estimated by fragmentation event rate (Sreekanth, 2014). This parameter was calculated as a ratio between fragmentation events and a total number of parallel samples tested under specified conditions. The number of parallel samples in the experiment was from 3 to 5. From the standpoint of statistics this number was not large, therefore, estimation of fragmentation event rate was rather approximate.

Fragmentation event rate to a great extent depended on the velocity of air coming to the particle from a tuyere, and to a lesser extent - on the furnace temperature (Table 1). At the air flow velocity of up to 50 m s^{-1} the fragmentation occurred rather seldom and its event rate practically vanished. Starting from 60 m s^{-1} the fragmentation events rate grew, and in the range of 95-125 m s^{-1} it was observed in the major share of particles. Strong dependence of fragmentation event rate on the air velocity was consistent with the mechanism of process occurrence proposed above. At high air velocity it intensively reacted with the charcoal layer on the particle surface. Rapid heating of this layer accelerated particle pyrolysis and created temperature stresses in the charcoal layer.

Table 1: Fragmentation event rate (%) as a function of tuyere air velocity and furnace temperature

T furnace, °C	Air flow in the tuyere, m s^{-1}					
	20	40	50	60	95	125
800	0	0	0	0	100	80
1000	0	0	0	50	100	100
1200	0	0	0	0	100	100

Fragmentation phenomenon is not desirable in the process of fuel combustion and gasification. It facilitates formation of small charcoal particles and their removal from the bed with ash, which reduces efficiency of fuel conversion and aggravates the problems of solid residue utilisation afterwards (Patuzzi, 2016).

4. CONCLUSION

During tests of single fuel particles in the experiments on the rig, different mechanisms of their combustion were observed. In the range of tuyere air velocity below 20 m s^{-1}, a two-stage process occurred. Volatiles were released from the particle and burned at the initial stage of this process. Charcoal residue burned at the second stage of the process. At the air velocity above 125 m s^{-1} a one-stage mechanism of single particles combustion prevailed. Intensive air flow reached the fuel particle surface and caused burning of a surface layer of charcoal. Stages of volatiles released from fuel and of char residue combustion occurred simultaneously.

When particles burned in the heated muffle space, the rate of their combustion grew with the air flow velocity growth (in the studied range). Rate of particles combustion in the ceramic channel first grew than reduced with the air flow velocity growth in the tuyere. These regularities were due to the cooling effect of the air flow. Hypothetically this cooling effect can be observed during fuel bed gasification as well, that would reduce the gasification efficiency and raise tar concentration in the producer gas.

Specific combustion conditions of particles in the channel were observed during the experiment, when burning volatiles formed a 'buzzing' flame with strong whirling around the particle. This whirling was assumed to intensify the heat exchange process which, in turn, balanced relatively lower temperature of the coming air than that of the burning sample in the furnace space.

At the tuyere air velocity above 60-95 m s^{-1} the fragmentation of fuel particles commenced. A surface layer of charcoal formed on the particle surface started to react intensively with the air oxygen, which caused its rapid heating and separation from the particle.

5. ACKNOWLEDGEMENT

The reported study was funded by RFBR within Research Project № 18-38-00774 and by Siberian Branch of the Russian Academy of Sciences (Fundamental Research Program, Scientific Project III.17.1.2, registration number AAAA-A17-117030310448-0, Melentiev Energy Systems Institute).

6. REFERENCES

Basu, P., 2006. Combustion and gasification in fluidized beds. FL: CRC Press.

Caposciutti, G., Almuina-Villar, H., Dieguez-Alonso, A., Gruber, T., Kelz, J., Desideri, U., Hochenauer, C., Scharler, R., Anca-Couce, A., 2019. Experimental investigation on biomass shrinking and swelling behaviour: Particles pyrolysis and wood logs combustion. Biomass and Bioenergy, 123, 1–13.

Cui, T., Xu, J., Fan, W., Chang, Q., Yu, G., Wang, F., 2016. Experimental study on fragmental behavior of coals and biomasses during rapid pyrolysis. Bioresource Technology, 222, 439–47.

Costa, F.F., Costa, M., 2015. Particle fragmentation of raw and torrefied biomass during combustion in a drop tube furnace. Fuel, 159, 530–37.

Dogru, M., Howarth, C.R., Akay, G., Keskinler, B., Malik, A.A., 2002. Gasification of hazelnut shells in a downdraft gasifier. Energy, 27, 415–27.

Gräbner, M., 2015. Industrial Coal Gasification Technologies Covering Baseline and High-Ash Coal. Singapore: Wiley.

Hayhurst, A.N., Parmar, M.S. 2002. Measurement of the mass transfer coefficient and Sherwood number for carbon spheres burning in a bubbling fluidized bed. Combustion and Flame, 130 (4), 361-75.

Howard, J.B., Essenhigh, R.H., 1967. Mechanism of solid-partical combustion with simultaneous gas-phase volatiles combustion. Symposium (International) on Combustion 11, 399–408.

Litun, D.S., Ryabov, G.A., 2018. Modern State and Topical Issues of Studying Solid Fuel Particle Primary Fragmentation Processes as Applied to Biomass Combustion and Gasification in Fluidized and Dense Bed (Review). Thermal Engineering, 65, 875–84.

Mason, P.E., Darvell, L.I., Jones, J.M., Pourkashanian, M., Williams, A., 2015. Single particle flame-combustion studies on solid biomass fuels. Fuel 151, 21–30.

Moersch, O., Spliethoff, H., Hein, K.R.G. 2000. Tar quantification with a new online analyzing method. Biomass and Bioenergy, 18 (1), 79-86.

Patuzzi, F., Prando, D., Vakalis, S., Rizzo, A.M., Chiaramonti, D., Tirler, W., Mimmo, T., Gasparella, A., Baratieri, M., 2016. Small-scale biomass gasification CHP systems: Comparative performance assessment and monitoring experiences in South Tyrol (Italy). Energy, 112, 285–93.

Reed, T.B., 1998. Handbook of biomass downdraft gasifier engine systems. 2nd ed. Golden Colorado: Biomass Energy Foundation Press.

Remacha, M.P., Jiménez, S., Ballester, J., 2018. Devolatilization of millimeter-sized biomass particles at high temperatures and heating rates. Part 2: Modeling and validation for thermally-thin and -thick regimes. Fuel 234, 707–722.

Sreekanth, M., 2014. Primary Fragmentation of Wood in a Fluidized Bed Combustor - An Experimental Investigation. Int. J. Innovation Sci. Res, 9(2), 502-10.

Svishchev, D.A., Kozlov, A.N., Penzik, M.V., 2019a. Unstratified Downdraft Gasification: Conditions for Pyrolysis Zone Existence. Energy Procedia, 158, 649–54.

Svishchev, D.A., Kozlova, M.A., Ralnikov, P.A., 2019b. A method of studying thermochemical conversion of single biomass particles in an intense air flow. J. Phys.: Conf. Ser. 1261, 012036.

Tufano, G.L., Stein, O.T., Kronenburg, A., Gentile, G., Stagni, A., Frassoldati, A., Faravelli, T., Kempf, A.M., Vascellari, M., Hasse, C., 2019. Fully-resolved simulations of coal particle combustion using a detailed multi-step approach for heterogeneous kinetics. Fuel 240, 75–83.

Weng, W., Costa, M., Aldén, M., Li, Z., 2019. Single particle ignition and combustion of pulverized pine wood, wheat straw, rice husk and grape pomace. Proceedings of the Combustion Institute 37, 2663–2671.

Yamazaki, T., Kozu, H., Yamagata, S., Murao, N., Ohta, S., Shiya, S., Ohba, T., 2005. Effect of superficial velocity on tar from downdraft gasification of biomass. Energy & Fuels, 19, 1186–91.

Ye, B., Zhang, R., Cao, J., Lei, K., Liu, D., 2019. The study of co-combustion characteristics of coal and microalgae by single particle combustion and TGA methods. Journal of the Energy Institute S1743967119303927.

Zhang, Y., Zhao, J., Ma, Z., Yang, F., Cheng, F., 2019. Effect of oxygen concentration on oxy-fuel combustion characteristic and interactions of coal gangue and pine sawdust. Waste Management 87, 288–294.

#162: Electromagnetic vibration energy harvester designs for low-powered technology applications

Muhammad Faruq FOONG[1], Chung Ket THEIN[2], Yun Ii GO[3]

[1] School of Engineering and Physical Sciences, Heriot-Watt University, No. 1, Jalan Venna P5/2, Precinct 5, 62200, Malaysia, m.foong@hw.ac.uk
[2] School of Engineering and Physical Sciences, Heriot-Watt University, No. 1, Jalan Venna P5/2, Precinct 5, 62200, Malaysia, ckthein@gmail.com
[3] School of Engineering and Physical Sciences, Heriot-Watt University, No. 1, Jalan Venna P5/2, Precinct 5, 62200, Malaysia, y.go@hw.ac.uk

Energy harvested from ambient sources is generally low and unable to sustain high-powered devices. However, with the current advancement in renewable energies, low-powered technologies are heading towards a more green and sustainable source of energy. One of the most promising source of renewable energy is ambient vibrations, and hence comes the concept of vibration energy harvesting. The primary goal in vibration energy harvesting research is to produce a harvester capable of generating a high voltage and power output. Generally, sufficient voltage is required for AC to DC conversion, whereas adequate power is necessary to sustain an electronic device. This study analyse and compares the performance of three different cantilever-based electromagnetic vibration energy harvester designs for low frequency and low base acceleration applications. The three designs consist of a conventional Single-degree-of-freedom (SDOF) design, an Anti-phase design and a Two-degree-of-freedom (2DOF) design. The mathematical model for all three designs were derived based on the Euler-Bernoulli beam theory, Coulomb's friction law and Faraday's law of electromagnetic induction. Based on this model, the voltage and power output of all three designs under optimum load resistance condition were analytical determined. Two different frequency tuning methods were applied in where the first method involves geometrical frequency tuning by changing the thickness of the cantilever beams and the second method is mass frequency tuning by increasing the mass of a proof mass placed at the free end of the beam. Results showed that under the first tuning method, all three designs produced sufficient voltage for AC to DC conversion. However, the Anti-phase design produced a significantly higher power output and power density than the other two designs. The second tuning method resulted in a significant increase in power output and power density as compared to the first tuning method. However, the voltage generated was lower and in some instances, insufficient for AC to DC conversion. Nevertheless, the 2DOF design produced the highest power output and power density at lower natural frequencies.

Keywords: electromagnetic vibration energy harvesting; voltage; AC to DC conversion; power; frequency tuning

1. INTRODUCTION

Approaching the vision of Industry 4.0, the demand for small powered electronics such as wireless sensors have drastically increased over the past decade. Normally, these electronics are powered by a small lithium battery. While the battery itself has a low energy consumption, the life cycle assessment of these batteries demonstrated a 736.35 kg CO_{2eq} carbon footprint (Liang *et al.,* 2017). Additionally, the use of batteries may not be practical for electronics placed in remote areas where accessibility is limited. Therefore, methods of extracting energy from the ambient surroundings have been developed as a mean for providing a sustainable and green source of power. One of the most promising source of green energy comes from mechanical vibrations.

The concept of vibration energy harvesting was first introduced in the late 90's by William and Yates (1996). Vibration energy harvesting involves amplifying ambient vibrations at resonance and converting it into electrical power through different means, with the two most common conversion method being piezoelectric transducer and electromagnetic induction. These two methods generally result in similar power densities (Arroyo *et al.,* 2012). However, piezoelectric transduction generates more voltage whereas electromagnetic induction has a higher current. Ambient vibrations can range from 1.0 Hz to 200.0 Hz. However, most public structures exhibit a fundamental natural frequency of less than 10.0 Hz (Rhimi and Lajnef, 2012). Additionally, the acceleration level of ambient vibrations are very low and are usually less than 1.0 g-level (9.8 ms^{-2}) (Ab Rahman and Kok, 2011). This makes vibration energy harvesting applications limited to low-powered devices due to its small power output. One of its practical uses involves powering wireless sensor nodes for monitoring purposes (Li *et al.,* 2019; Bradai *et al.,* 2018).

Many designs have been proposed over the past decade in an attempt to enhance the performance of a vibration energy harvester. Qi *et al.* (2017) and Zhu *et al.* (2013) proposed a different arrangement of the Halbach array to increase the power output of an electromagnetic vibration energy harvester. Klein and Zuo (2017) attempted to improve the performance of an electromagnetic vibration energy harvester through velocity amplification. Thein *et al.* (2015) performed a finite element optimisation to determine the optimum topology for a piezoelectric vibration energy harvester that would result in the maximum power output. These designs mainly consist of a vibrating cantilever beam or a vibrating mass on a spring. Erturk and Inman (2007) showed that under unloaded conditions, the cantilever beam design can reach a 1.6 times higher amplitude than mass and spring system.

This paper analyses and compares the performance of three different cantilever-based electromagnetic vibration energy harvester designs between a fundamental natural frequency range of 5.0 Hz to 10.0 Hz and an acceleration level of 0.1 g-level. The first design is the common single-degree-of-freedom (SDOF) cantilever beam configuration. The second design applies the concept of relative velocity and anti-phase vibration to maximise the power output of the harvester. This design was proposed by Foong *et al.* (2019). Finally, the third design is a two-degree-of-freedom design, modified from the first design by including a spring. Two different frequency tuning methods were applied and the maximum root-mean-squared (RMS) voltage, average power outputs and power densities of all three designs were analysed and discussed.

2. GOVERNING EQUATIONS

This section describes the governing equations used to perform the analytical analysis for the three designs. The first design will be referred to as the SDOF design, and the second and third design designated as the Anti-phase design and 2DOF design. The cross section of cantilever beams used in practical applications close resemble the Euler-Bernoulli beam theory (Sun *et al.,* 2013). The mechanism of an electromagnetic vibration energy harvester is based on the principle of electromagnetic induction. Faraday's law of electromagnetic induction states that voltage is induced in a conductor when the conductor experiences a change in the surrounding magnetic flux. The rate of change of magnetic flux depends on the velocity of the conductor passing through a magnetic field relative to source of the magnetic field. The higher the relative velocity of the conductor, the larger the induced voltage.

2.1. Voltage and power output equation for an electromagnetic circuit

Consider the following electromagnetic circuit configuration:

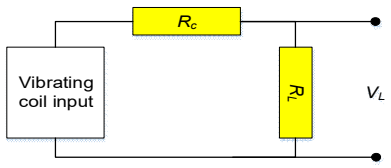

Figure 1: Electromagnetic circuit configuration.

Here, R_C and R_L in Figure 1 refers to the coil resistance and load resistance and V_L is the voltage generated across the load resistance. The RMS voltage generated can be defined as

Equation 1: RMS peak voltage output of an electromagnetic vibration energy harvester.

$$V_L = \frac{1}{\sqrt{2}} NBL_C f v_r \frac{R_L}{R_L + R_C}$$

Where N is the number of turn of coil, B is the average magnetic flux strength of the magnets, L_c is the effective length of the coil, f is the coil fill factor and v_r is the relative velocity of the coil. The average power output at the load resistance, P_L, can then be calculated by

Equation 2: Average peak power output of an electromagnetic vibration energy harvester.

$$P_L = \frac{V_L^2}{R_L}$$

Much of the past research has demonstrated the existence of an optimum load resistance which would result in maximum power. This value can easily be determined by plotting P_L against R_L and identifying the load resistance value that corresponds to the maximum power output. Equations 1 and 2 demonstrate that the only mechanical contribution towards the power output of an electromagnetic harvester is the relative velocity of the coil.

2.2. Equation of motion for SDOF design

Figure 2 illustrates the setup of the SDOF design and its schematic representation. The SDOF works by simply vibrating a roll of conductor coil between two pairs of magnets, resulting in a change in the magnet's magnetic flux and hence inducing voltage. In this design, the magnets are relatively stationary with the base.

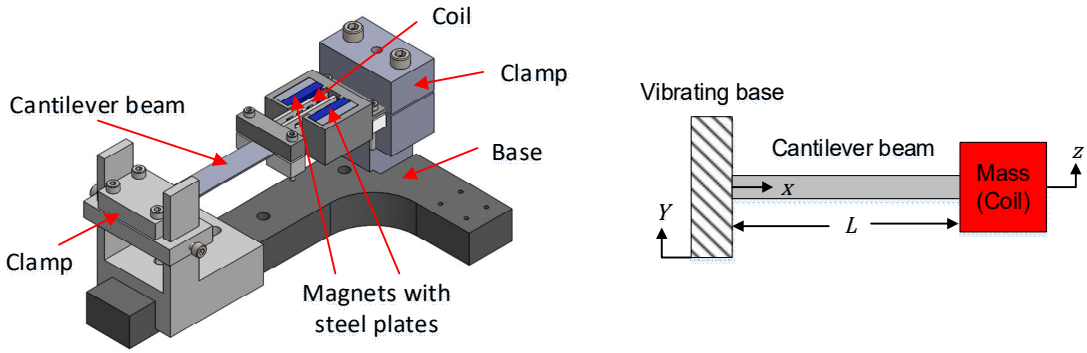

Figure 2: SDOF Design and side view schematic representation.

Consider the case of a clamp-free cantilever with a proof mass loaded at its free end and subjected to a harmonic base excitation motion at its clamped end. Based on Figure 2, the vertical motion of the beam at position x along the length of the beam and time t can be described by

Equation 3: Vertical displacement of cantilever beam under harmonic base excitation.

$$z_{abs}(x,t) = z(x,t) + Ye^{i\omega t}$$

Where z_{abs} is the absolute vertical displacement of the beam, z is the vertical displacement of the beam relative to the base, Y is the vertical displacement of the harmonic base input and ω is the driving frequency of the base. Using the method of separation of variables, the steady-state response of $z(x,t)$ can be defined as (Kim *et al.*, 2010)

Equation 4: Evaluation of relative displacement using method of separation of variables.

$$z(x,t) = \sum_{n=1}^{\infty} \varphi_n(x)\eta_n(t)$$

Where $\phi_n(x)$ is the beam eigenfunction and $\eta_n(t)$ is the response function. The subscript n in Equation 4 corresponds to the mode number of the beam ($n = 1,2,3 \ldots$). These two terms can be described by the following equations:

Equation 5: Eigenfunction of clamp-free cantilever beam.

$$\varphi_n(x) = C_n\left[\cosh\frac{\lambda_n}{L}x - \cos\frac{\lambda_n}{L}x - D_n\left(\sinh\frac{\lambda_n}{L}x - \sin\frac{\lambda_n}{L}x\right)\right]$$

Equation 6: Response function of SDOF vibrating system.

$$\eta_n(t) = \frac{\omega^2 Y e^{i\omega t} F_n}{\omega_n^2 - \omega^2 + i2\varsigma_n\omega_n\omega}$$

Where L is the length of the cantilever beam, ς_n is the modal damping ratio and C_n, λ_n, D_n and F_n are constants derived from the inertial terms and boundary conditions of the beam and proof mass. ω_n is the modal natural frequency of the beam and can be determined from Equation 7.

Equation 7: Modal natural frequency of clamp-free cantilever beam with proof mass.

$$\omega_n = \lambda_n^2\sqrt{\frac{Eh^2}{12\rho L^4}}$$

Where h and ρ are the respective thickness and density of the cantilever beam. Substituting Equations 5 and 6 into Equation 4 and considering the steady-state amplitude (peak displacement) at first mode resonance where $n=1$, $\omega = \omega_1$ and $Ye^{i\omega t} = Y$ results in

Equation 8: Steady-state amplitude of cantilever beam at first mode resonance.

$$z(x) = \frac{Y\varphi_1(x)F_1}{2\varsigma_1}$$

For an electromagnetic vibration energy harvester, ς_1 is equal to the sum of contribution from the mechanical damping, ς_m, and the electromagnetic damping, ς_e (Ooi and Gilbert, 2015). The mechanical damping ratio of cantilever beams can be estimated using the critically damped stress method proposed by Foong et al. (2019)

Equation 9: Prediction of the mechanical damping ratio for cantilever beams.

$$\varsigma_m = Q(2\sigma_i)^R + S$$

$$\sigma_i = \frac{E}{2}hY\left(\frac{\lambda_1}{L}\right)^2 C_1F_1$$

Where Q, R and $S$are constants determined from experiment and σ_i is defined as the maximum stress of the beam under critically damped condition ($\varsigma_m = 1$). The electromagnetic damping can be estimated by

Equation 10: Electromagnetic damping ratio prediction.

$$\varsigma_e = \frac{(NBL_Cf)^2}{2m_e\omega_1(R_C + R_L)}$$

Where m_e is the effective mass of the beam and proof mass system. Equation 8 is valid for $0 \le x \le L$. Normally, the relative velocity of the coil needs to be evaluated based on the amplitude at the centre of the coil, which is located at $x > L$. To evaluate the amplitude when x is larger than L, the following equation must be considered

Equation 11: Evaluation of steady state amplitude for $x > L$.

$$z(x > L) = \frac{YF_1}{2\varsigma_1}\left[\varphi_1(L) + (x - L)\varphi_1'(L)\right]$$

Where $\varphi_1'(x)$ is the derivative of $\varphi_1(x)$ with respect to x. Since the magnets are relatively stationary with the base, the relative peak velocity of the coil, v_r^P, at first mode resonance is defined as

Equation 12: Relative peak velocity of coil at first mode resonance for SDOF design.

$$v_r^P = z\omega_1$$

2.3. Equation of motion for Anti-phase design

The aim of the Anti-phase design was to increase the induced voltage generated in the coil by increasing the relative velocity between the coil and the magnets. Referring to Figure 3, as the main beam vibrates, the two support beams with the attached coils would vibrate in the opposite direction to the main beam due to the displacement gradient of the main beam. This motion is often regarded as an anti-phase motion. When coupled with two regular SDOF cantilever beams with attached magnets, the relative velocity between the coil and the magnet increases since the magnets vibrates in the same direction as the main beam, which is anti-phase to the coil. Nevertheless, the volume consumed by this design is larger than the SDOF design.

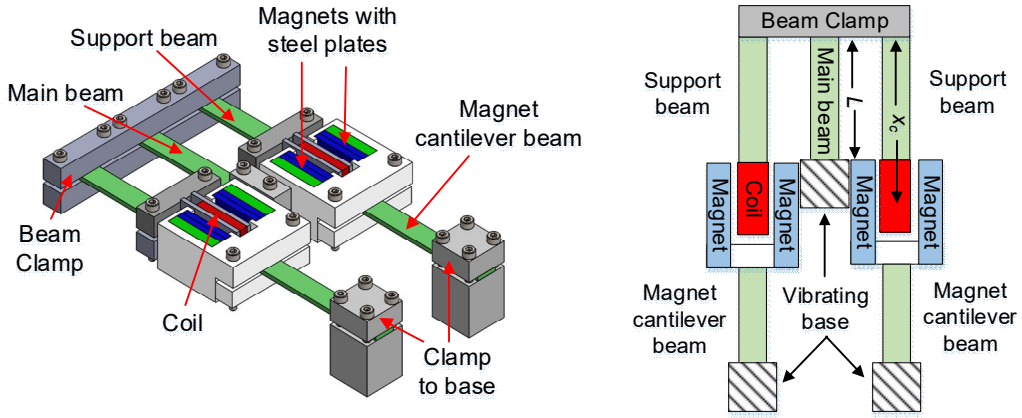

Figure 3: Anti-phase design and top view schematic representation.

Generally, the equation of motion for the SDOF design is applicable for the main beam and the magnet cantilever beams in the anti-phase design, provided that F_1 is greater than 0. However, it is only valid for the first mode vibration. Assuming that the vibration of the support beams are negligible, the amplitude at the centre of the coil, z_c , can be determined by:

Equation 13: Amplitude at the centre of coil for Anti-phase design.

$$z_c = \frac{YF_1}{2\zeta_1}\left[\varphi_1(L) + x_c\varphi_1'(L)\right]$$

Where L here refers to the length of the main beam and x_c is the horizontal distance from $x = L$ to the centre of the coil. Since the design consist of a pair of coil and magnets on each support beam, the electromagnetic damping of the system is doubled. In this design, the magnet cantilever beams can act as an isolated system from the main beam, making it possible for the magnet cantilever beams to have a different fundamental natural frequency than the main and support beams. However, Foong *et al.* (2019) reported that maximum power is achieved when the natural frequency of the magnet cantilever beams and the support beams are equal. Under this said condition, the relative peak velocity of the coil for the anti-phase design is equal to

Equation 14: Relative peak velocity of coil at first mode resonance for Anti-phase design.

$$v_r^p = (z_m - z_c)\omega_1$$

Where z_m is the amplitude of the magnets which can be determined from the SDOF equations. It is worth to mention that the design would only produce favourable output if the coil can achieve significant amplitude when compared to the magnets.

2.4. Equation of motion for 2DOF design

The 2DOF design in Figure 4 is similar to the SDOF design in terms of harvester setup and volume space. However, a spring was introduced to the base of the cantilever beam in order to amplify the amplitude of the system. To simplify analysis, the 2DOF design was modelled as a spring-mass system consisting of two springs, two masses and two dampers. m_1, k_1 and c_1 in Figure 4 corresponds to the mass of clamp and guiderail, stiffness of spring and damping of spring respectively, whereas m_2, k_2 and c_2 are the effective mass, effective stiffness and damping of the cantilever beam and coil. In the actual design, a mechanical guiderail (HIWIN MGW9C model) was attached to the spring to ensure vertical motion. This would undeniably introduce friction into the system as seen

in the spring mass representation in Figure 4, denoted by F_R. Although the friction force of mechanical sliders tend to be generally small (HIWIN, 2012), it cannot be ignored when solving for low base acceleration level cases.

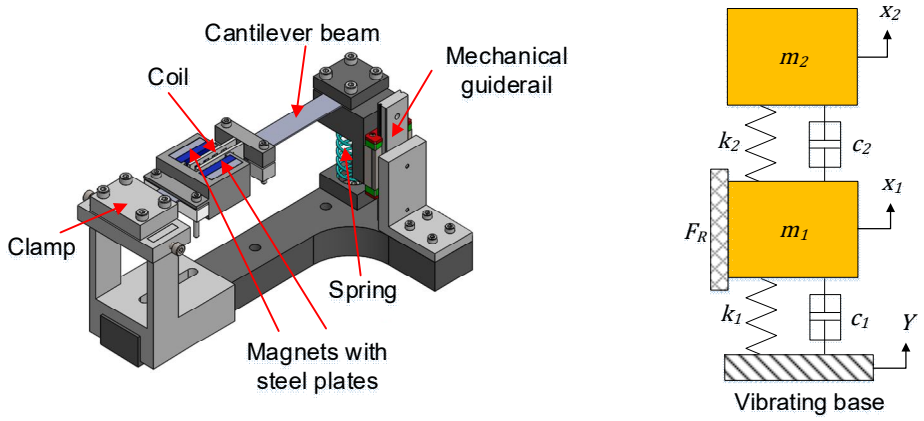

Figure 4: 2DOF design and spring mass model representation.

Assuming a massless spring, a sinusoidal base input and the Coulomb friction model, the governing equations for a 2DOF system with a single friction contact surface is

Equation 15: Governing equations for 2DOF design under sinusoidal base excitation.

$$m_1\ddot{x}_1 + c_1\dot{x}_1 + k_1x_1 + c_2\left(\dot{x}_2 - \dot{x}_1\right) + k_2\left(x_1 - x_2\right) = k_1Y\sin\left(\omega t\right) - F_R$$

$$m_2\ddot{x}_2 - c_2\left(\dot{x}_2 - \dot{x}_1\right) - k_2\left(x_1 - x_2\right) = 0$$

Where Y is the amplitude of the sinusoidal base input. The damping constants, c_1 and c_2, can be related to its corresponding damping ratio by

Equation 16: Relationship between damping constants and damping ratio.

$$c_1 = 2\varsigma_1\sqrt{k_1m_1}$$

$$c_2 = 2\varsigma_2\sqrt{k_2m_2}$$

Where ς_1 and ς_2 here correspond to the damping ratio of c_1 and c_2. Note that ς_2 is inclusive of the mechanical damping of the beam and the electromagnetic damping. Equation 15 can be solved by considering the following steady-state solutions

Equation 17: Form of steady-state solutions for 2DOF design.

$$x_1\left(t\right) = A_1\sin\left(\omega t\right) + B_1\cos\left(\omega t\right)$$

$$x_2\left(t\right) = A_2\sin\left(\omega t\right) + B_2\cos\left(\omega t\right)$$

Where A_1, B_1, A_2 and B_2 are constants which can be determined by substituting Equation 17 into equation 15 and equating the sine and cosine terms. Applying the trigonometrical identities, the steady-state amplitudes, X_1 and X_2, of the 2DOF design can be calculated as

Equation 18: Steady-state amplitudes for 2DOF design.

$$X_1 = \sqrt{A_1^2 + B_1^2}$$

$$X_2 = \sqrt{A_2^2 + B_2^2}$$

The steady-state amplitude of the coil would correspond to X_2. Similar to the case for the SDOF design, the relative peak velocity of the coil at the fundamental resonance mode is

Equation 19: Relative peak velocity of coil at first mode resonance for 2DOF design.

$$v_r^P = x_2\omega_1$$

Overall, Equations 12, 14 and 18 can be substituted into Equations 1 and 2 to determine the maximum RMS voltage and maximum average power output of each design under first mode resonance.

3. RESULTS AND DISCUSSION

In this section, the power output of all three harvester designs were analysed and compared. Two different frequency tuning methods were considered, namely geometrical tuning and mass tuning. For the geometrical tuning method, the length and width of all cantilever beams (including main beam, support beams and magnet cantilever beams) in all designs were set equal at 65.0mm and 10.0mm respectively. The thickness of the beams however were adjusted to meet the fundamental natural frequency range of 5.0 Hz to 10.0 Hz. For the mass tuning method, the same beam length and width were used, and the thickness of the beams was fixed at 2.0mm. Instead, a cube mass measuring 20mm x 20mm x 20mm was placed on the coil (SDOF and 2DOF designs) and the main beam (Anti-phase design). The natural frequency of the designs were then tuned by varying the density of this cube mass. All cantilever beams were made from glass fibre. A base input of 0.1 g-level was applied to all analysis.

The same magnets and coil were used in all three designs. To estimate the average strength of the magnetic flux acting on the coil, the magnets were simulated using CST Studio 2017 finite element software as seen in Figure 5. The magnet arrangement in Figure 5 consist of eight neodymium magnets measuring 25.0mm x 10.0mm x 3.0mm, horizontally spaced at 14.0mm apart and vertically spaced at 3.0mm apart. The poles of the magnets are inscribed on the magnets in Figure 5, with N and S referring to the north and south poles respectively. Two steel plates measuring 25.0mm x 48.0mm x 5.0mm were placed behind the magnets. The purpose of these steel plates was to concentrate the magnetic field in the region of the coil. The red outlines in Figure 5 designate the area covered by the coil, with each outline measuring 4.0mm x 10.8mm.

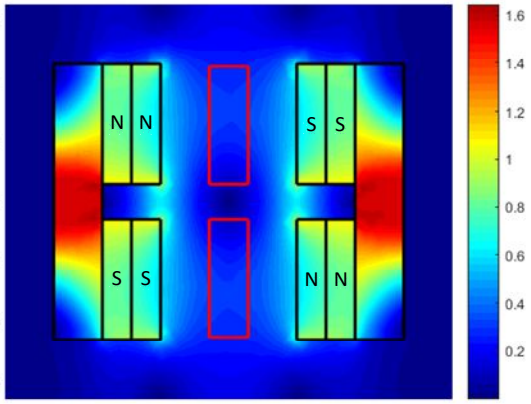

Figure 5: Finite element simulation of the magnet arrangement.

The average magnetic field strength was determined to be 0.26 T. The mechanical properties of the cantilever beam and the specifications of the coil and spring (2DOF design) are tabulated in Table 1. These properties were obtained and measured from available assets in the lab.

Table 1: Specification of cantilever beam material and coil.

Cantilever beam		Coil		Spring	
Material	Glass Fibre	N	490	k (Nm^{-1})	1017.8
E (GPa)	25	L_s (mm)	50	ς_1	0.08
ρ (kgm^{-3})	1850	f	0.65	h_s (mm)	40
Q (Pa^{-1})	3.476 x 10^{-9}	R_c (Ω)	9.3		
R	1				
S	2.019 x 10^{-3}				

Where h_s refers to the height of the spring. One of the main concerns in vibration energy harvesting is volume occupied by the harvester. Generally, it is desirable for a harvester to produce a high power output within a small volume space. Therefore, the performance of a harvester is usually measured in terms of its power density, P_D, which is quantified as the ratio of the harvester's maximum power output to its occupied practical volume. In this

paper, a cuboid profile was assumed for the volume. The width and length of each designs are tabulated in Table 2, whereas the height of the volume was defined as a function of the maximum vibrating amplitude at first mode resonance, a_1 . To allow a fair comparison, only one side of the anti-phase power output and half of its total volume was considered.

Table 2: Practical volume for SDOF, anti-phase and 2DOF designs.

Volume dimensions	SDOF	Anti-phase	2DOF
Length (mm)	123	178	123
Width (mm)	44	52	44
Height (mm)	$2a_1+18$	$2a_1+23$	a_1+h_s+9

All analysis conducted was under the condition of optimum load resistance to maximise the power output. Figure 6 shows the comparison between the maximum RMS voltage and maximum average power output for all three designs under geometrical frequency tuning.

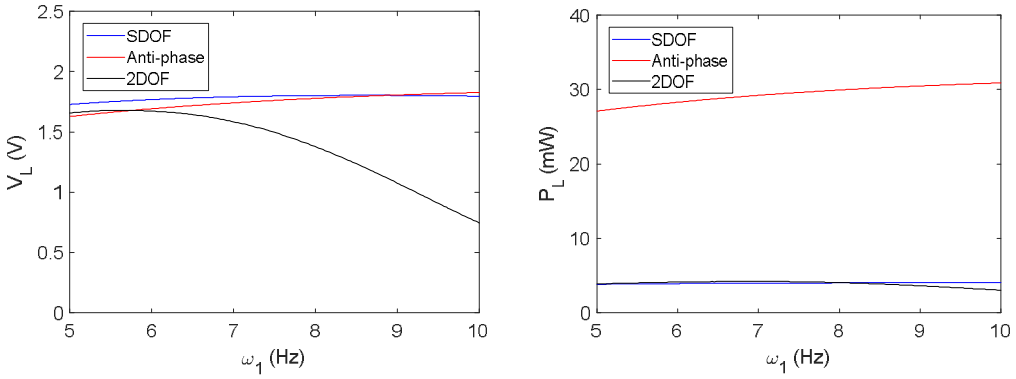

Figure 6: Comparison between the maximum RMS voltage and maximum average power of all three designs using the geometrical frequency tuning method.

Figure 6 shows that the SDOF and Anti-phase designs display an increasing trend in voltage output against frequency whereas the 2DOF design shows the opposite. The voltage outputs of the SDOF and 2DOF design are almost similar, whereas the 2DOF design demonstrated a lower voltage output than the two designs for frequencies higher than 5.9 Hz. Normally, a high voltage output is desired as the AC voltage from the vibrating coil must be converted into DC output prior to application. A standard full bridge rectifier made up of four of Schottky diodes which has a typical threshold voltage of 0.3 V (Yilmaz et al., 2014) would consume 0.6 V per cycle. This means that under geometrical tuning, all designs are capable of AC to DC conversion within the frequency range, although the 2DOF design would result in a low DC voltage output at higher frequencies. In terms of power output, the Anti-phase design displayed an approximately 7.5 times higher power than the other two designs, while the 2DOF design demonstrated a somewhat similar power output to the SDOF design. Based on Equation 2, this suggest that the optimum load resistance of the SDOF design is significantly higher than the other two designs. Figure 7 illustrates the same comparison as Figure 6, but under the mass frequency tuning method instead.

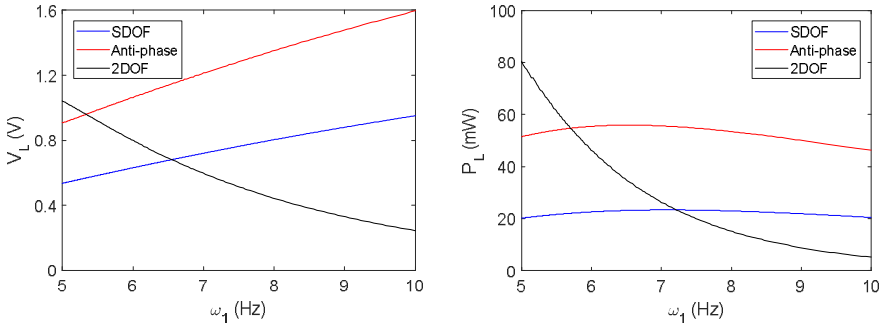

Figure 7: Comparison between the maximum RMS voltage and maximum average power output of all three designs using the mass frequency tuning method.

The mass frequency tuning method resulted in a significant increase in power output for all three designs as compared to the observations made in Figure 6. This is consistent with the observations made by Foong et al. (2019) in terms of power output. However, this method also caused a substantial drop in voltage output at lower frequencies. This means that AC to DC conversion would not be possible for the SDOF design at frequencies lower than 5.7 Hz and the 2DOF design at frequencies higher than 7.0 Hz if the same diodes were considered. Nevertheless, below 5.7 Hz, the 2DOF design generated a larger power output than the other two designs. The reduction in voltage and the increase in power output suggest that the mass frequency tuning method result in a lower optimum load resistance value than the geometrical frequency tuning method. Figure 8 shows the comparison between the power densities of all three designs under both frequency tuning methods.

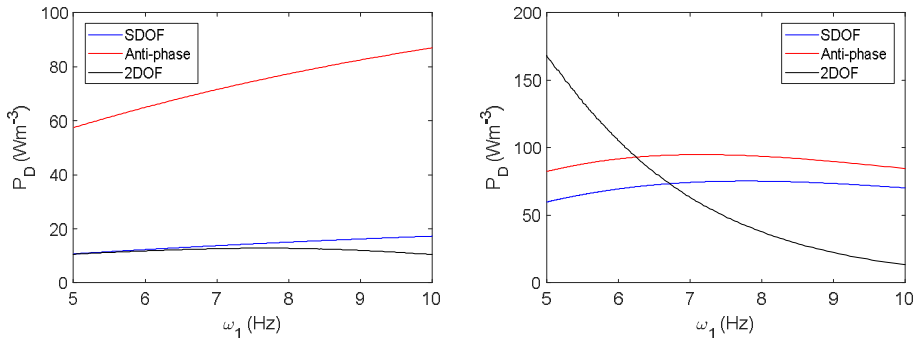

Figure 8: Comparison between the power and power density of all three designs using the geometrical frequency tuning method (left) and the mass frequency tuning method (right).

The power densities of all three designs are observed to be higher when their natural frequencies are tuned by the mass frequency tuning method, corresponding to the increase in power output. Despite having an approximately 35.0% larger practical volume, the Anti-phase design was observed to have a higher power density than the SDOF design under both tuning methods. This shows that the Anti-phase design performs better than the SDOF design regardless of how the natural frequency of harvester was tuned. Under the geometrical frequency tuning method, the 2DOF design demonstrated the worst power density. However, the performance of the 2DOF design became superior to the other two designs at lower frequencies when its natural frequency was tuned by the mass frequency tuning method.

4. CONCLUSION

The performance of three different cantilever-based electromagnetic vibration energy harvesters for low frequency and low base acceleration applications have been analysed. The natural frequency of the designs was tuned using two different tuning methods and the voltage and power output of the designs under optimum load resistance condition were analysed. When tuned using the geometrical frequency tuning method, all three designs displayed sufficient voltage generation for AC to DC conversion. However, the Anti-phase design demonstrated a significantly larger power output and power density when compared with the other two designs, despite having a larger practical volume. Under the mass frequency tuning method, a substantial increase in power output and power density were observed in all three design as compared to the geometrical frequency tuning method. However, the voltage output in all three designs also dropped, causing the voltage generated by the SDOF and 2DOF designs to be insufficient for AC to DC conversion within a certain frequency range. Nevertheless, the 2DOF design displayed the highest power output and power density at natural frequencies below 5.7 Hz. Overall, the geometrical frequency tuning methods resulted in a higher voltage output and under this method, the Anti-phase design displayed the best performance. On the other hand, the mass frequency tuning method resulted in a larger power output and power density, in which the 2DOF design displayed the most promising result at lower frequencies. Future works involve experimental verification of the analysis performed here and design optimisation.

5. REFERENCES

Ab Rahman, M.F., and Kok S.L., 2011. IEEE Student Conference on Research and Development/Investigation of useful ambient vibration sources for the application of energy harvesting. Cyberjaya, Malaysia: IEEE.

Aroyyo, E., Badel, A., Famosa, F., Wu Y., and Qiu J., 2012. Comparison of electromagnetic and piezoelectric vibration energy harvesters: Model and experiments. *Sensors and Actuators A*, 183, 148-156.

Bradai, S., Naifar, S., Viehweger, C., and Kanoun, O., 2017. ICoEV/ Electromagnetic Vibration Energy Harvesting for Railway Applications, Sofia, Bulgaria: EDP Sciences.

Erturk, A., and Inman, D.J., 2008. On Mechanical Modeling of Cantilevered Piezoelectric Vibration Energy Harvesters. *Journal of Intelligent Material Systems and Structures*, 19, 1311-1325.

Foong, F.M., Thein, C.K., and Yurchenko, D., 2019. On mechanical damping of cantilever beam-based electromagnetic resonators. *Mechanical Systems and Signal Processing*, 119, 120-137.

Foong, F.M., Thein, C.K., Ooi, B.L., and Yurchenko, D., 2019. Increased power output of an electromagnetic vibration energy harvester through anti-phase resonance. *Mechanical Systems and Signal Processing*, 116, 129-145.

Kim, M., Hoegen, M., Dugundji, J., and Wardle, B.L., 2010. Modeling and experimental verification of proof mass effects on vibration energy harvester performance. Smart Materials and Structures, 19, 045023.

Klein, J., and Zuo, L., (2017). A velocity-amplified electromagnetic energy harvester for small amplitude vibration. *Smart Materials and Structures*, 26, 095057.

Liang, Y., Sua, J., Xia, B., Yu, Y., Ji, D., Sun, Y., Cui, C., and Zhu, J., 2017. Life cycle assessment of lithium-ion batteries for greenhouse gas emissions, *Resources, Conservation and Recycling,* 117 285–293.

Li, K., He, X., Wang, X., and Jiang, S., 2019. A Nonlinear Electromagnetic Energy Harvesting System for Self-Powered Wireless Sensor Nodes, *Journal of Sensor and Actuator Networks*, 8, 18.

Ooi, B.L., and Gilbert, J.M., 2014. Design of wideband vibration-based electromagnetic generator by means of dual-resonator, *Sensors and Actuators A*, 213, 9-18.

Qiu, J., Liu, X., Hu, Z., Chang, Q., Gao, Y., Yang, J., Wen, J., Tang, X., and Hu, W., 2017. Multi-directional electromagnetic vibration energy harvester using circular Halbach array, *AIP Advances*, 7, 056672.

Rhimi, M., and Lajnef R., 2012. Tunable Energy Harvesting from Ambient Vibrations in Civil Structures. *Journal of Energy Engineering*, 138(4), 185-193.

Sun, W., Liu, Y., Li, H., and Pan, D., 2013. Determination of the response distributions of cantilever beam under sinusoidal base excitation. *Journal of Physics: Conference Series*, 448, 012010.

Thein, C.K., and Liu, J.S., Numerical modeling of shape and topology optimisation of a piezoelectric cantilever beam in an energy-harvesting sensor. *Engineering with Computers*, 33, 137–148.

Williams C.B., and Yates R.B., 1996. Analysis of a micro-electric generator for microsystems. *Sensors and Actuators A*, 52, 8-11.

Yilmaz, M., Tunkar, B.A, Park, S., Elrayes, K., Mahmoud, M.A.E., Abdel-Rahman, E., and Yavuz M., 2014. High-efficiency passive full wave rectification for electromagnetic harvesters, *Journal of Applied Physics*, 116(3), 134902.

Zhu, D., Beeby, S., Tudor, J., and Harris, Nick., 2013. Increasing output power of electromagnetic vibration energy harvesters using improved Halbach arrays. *Sensors and Actuators A*, 203, 11-19.

#163: A comparative study on fuel properties of diesel-biodiesel-ethanol blends

Sachin Muralee KRISHNA[1], P. Abdul SALAM[2]

Energy Program, Department of Energy, Environment and Climate Change, Asian Institute of Technology, Pathumthani 12120, Thailand
[1]sachin@w2e.co.th
[2]salam@ait.ac.th

This paper presents the results of a comparative study conducted on fuel properties of optimal diesel-biodiesel-ethanol (DBE) blends. A nonlinear optimisation model formulated for DBE blending process with key fuel properties as constraints and solved using the Lingo optimisation software. The model established ideal blending ratio for DBE ternary fuel by maximising the net heating value (LHV) while meeting multiple fuel property constraints. Applicable fuel mixing rules were extrapolated from previous literatures for anticipating the properties of the ternary fuel blends. The model is executed at different scenarios by simultaneously varying the ethanol content in the blend and blending ratios were estimated. Further, the ternary fuel blends were prepared, and key fuel properties viz., density, cloud point, pour point, acid value, water content, calorific value, kinematic viscosity, oxidation stability and copper corrosion values were tested according to ASTM test methods and the results are discussed. All DBE blends with anhydrous ethanol was found to be completely stable while fuel blends with hydrous ethanol showed phase separation. Biodiesel acted as a good emulsifier with increase in its content in the blend, rectifying the phase separation problems caused by higher ethanol content in the blends. Ethanol had higher effect on DBE blends calorific value. The cloud point temperature did not to follow the Kay's mixing rule precisely. All DBE blends found to satisfy the Thailand fuel standard for pour point with values less than 9°C. The density of fuel blends followed Kay's mixing rule with minimum deviation. The density values of all BDE blends were within the range of 0.840 - 0.855 kg/m^3, satisfying the Thailand fuel standard as well as the premium fuel quality standards. The acid value of DBE blends increased by roughly 3% - 7% for each 10% of biodiesel added volumetrically. All the blends found to have the acid value less than the ASTM limit of 0.3mg.KOH/g.

Keywords: biodiesel; blend ratio; diesel; ethanol; optimisation

1. INTRODUCTION

Researchers have identified that the use of biofuels as a substitute for petroleum products can address future energy crisis /deficiency issues and pave way for global sustainable development. The major fuels alternatives currently under commercial development are biodiesel and ethanol, because of their bulk availability and similarity in properties with fossil fuels.

Biodiesel has fuel properties similar to that of petroleum diesel, making it a promising substitute fuel alone or as a blend (Lin & Lin, 2006). However, two major drawbacks exist with bio-diesel/ diesel-biodiesel blends as they exhibit poor performance in cold flow properties (cloud point and pour point) and kinematic viscosity. The higher viscosity of biodiesel leads to difficulties in atomising to smaller droplets and delivering to the engine at lower temperature (Lin & Lin, 2006). Thus use of biodiesel in existing automobiles have been found to require significant engine modification. Ethanol is also considered as a potential alternate fuel for diesel, but the blended fuel shows phase separation over a wide range of temperatures due to its polar nature and excess water content (Kwanchareon et al., 2007). Recent studies have identified biodiesel's ability to act as a good emulsifier for diesel-ethanol blends and can produce a stable fuel blend meeting diesel fuel properties, if mixed under appropriate ratio (Hussan et al., 2013).

A majority of the works on diesel-biodiesel-ethanol (DBE) blends have been focused on experimental characterisation of the blended fuel properties and evaluation of engine performance. Hussan et al. (2013) modified the key fuel properties of palm biodiesel by blending it with ethanol and diesel. The chemical properties of biodiesel was customised by ethanol and an optimal formulation was derived mathematically. But the study only considered kinematic viscosity as a formulation constraint in estimating optimal blend ratio. Lin et al. (2013) studied the DBE blending process developing a nonlinear optimisation model. The model established optimal DBE blends to improve system profitability by considering economic constraints such as production cost, market demand, and fuel prices along with fuel property constraints such as kinematic viscosity, density, lower heating value, cloud point, cetane number, fuel stability and sulphur content. The author also highlighted that the multifuel blend ratio will directly affect scheduling decisions and outcomes of the process control in petroleum refinery system.

In this study the fuel properties of DBE blends are evaluated. Optimal recipes for DBE blends were estimated theoretically by developing a non-linear optimisation model for DBE blending process. Further the ternary fuel blends are prepared according to refinery blending process and corresponding ASTM test methods were conducted.

2. MATERIALS AND METHODS

The experimental investigation of emulsion stability and fuel properties of the DBE blends at estimated blending ratios are carried out. Following, the emulsification characteristics and fuel properties are analysed, including blends preparation, homogeneity, and emulsion stability tests.

2.1. Raw Materials

Hydrous and anhydrous ethanol with 95% and 99.9% purity are obtained from Thai Liqueur distillery. The base high sulphur diesel (base HSD) from Bangchak Petroleum Plc. Ltd and palm oil biodiesel (POME) from Bangchak Biofuels Plc. Ltd and B Grimm Green Power Pvt. Ltd (see Figure 1).

Figure 1: (1) Palm oil biodiesel, (2) Base HSD and (3) Anhydrous ethanol

2.2. DBE blend preparation

The diesel biodiesel and ethanol are mixed to a homogeneous mixture via inline blending following refinery fuel blending method. The final blends were kept in a glass vial with a screw cap to observe their physical appearance. Twelve DBE fuel samples were prepared according to the recipes obtained from optimisation studies.

The laboratory tests were then carried out following ASTM test standards (See Table 1) to determine the essential fuels properties. The experiments were conducted in the Renewable Energy Laboratory of National Metal and Material Technology Center (MTEC), a member of National Science and Technology Development Agency (NSTDA), Thailand. The experiments were carried out under controlled temperature and humidity to ensure accurate results.

Table 1: DBE Blends quality testing and equipment

No	Fuel Property	Test Apparatus	Test Method
1.	Density	Automatic density meter DMA-4500, Anton Paar (Austria)	ASTM D-4052
2.	Cloud point	ISL, CPP 5Gs automatic cloud point pour point analyser, Chemical House & Lab Instrument Co.,Ltd. (Thailand)	ASTM D-2500
3.	Pour point	ISL, CPP 5Gs automatic cloud point pour point analyser, Chemical House & Lab Instrument Co.,Ltd. (Thailand)	ASTM D-97
4.	Acid value	Tirando 809 Potentiometric Titrator, Metrohm (Switzerland)	ASTM D-664
5.	Water content	KF 831 Karl Fischer Coulometer, Metrohm (Switzerland)	ASTM D-6304
6.	Calorific value (LHV)	bomb calorimeter model LECO-350 (LECO Corporation, USA)	ASTM D-240
7.	Kinematic viscosity	MiniAV single bath kinematic viscometer (Cannon Instrument Company, USA)	ASTM D-445
8.	Oxidation stability	Rancimat model 743, Metrohm (Switzerland)	EN 14112
9.	Copper strip corrosion	Copper strip corrosion bath	ASTM D-130

3. EXPERIMENTAL ANALYSIS

The experimental investigation of emulsion stability and fuel properties of the DBE blends at estimated blending ratios are carried out. Then the emulsification characteristics and fuel properties are analysed, including blend preparation, homogeneity, and emulsion stability tests.

3.1. Homogeneity and emulsification characteristics of DBE blends

Each DBE blend was provided with a batch number from 1 to 12 according to the blending ratios. Visual observation was carried out to analyse the homogeneity of the blends and effect on the emulsion stability. It was observed that the increase in biodiesel content delivers the blend a darker coloration (Figure 2).

Figure 2: Homogeneity analysis of DBE blends

All DBE blends exhibited excellent emulsion stability without separation. The batches 1 to 12 were analysed and physically there was no agglomeration of liquid droplets or sediment layer occurring in the blends. Biodiesel in the DBE blends acted as an emulsifier by increasing the stability of emulsions as they possess both hydrophilic and hydrophobic properties. The volumetric ratios of each component and the homogeneity test results are provided in Table 2.

Table 2: Homogeneity test of DBE blends at proposed blend ratios

Batch No	Fuel Blend	Components (%.Vol)			Phase Description
		D	B	E	
1	DBEOpt-95	95	0	5	Homogeneous blend
2	DBEOpt-78	78	17	5	Homogeneous blend
3	DBE90	90	5	5	Homogeneous blend
4	DBE85	85	10	5	Homogeneous blend
5	DBE80	80	15	5	Homogeneous blend
6	DBE75	75	20	5	Homogeneous blend
7	DBE70	70	25	5	Homogeneous blend
8	DBE65	65	30	5	Homogeneous blend
9	DB-E6	72	22	6	Homogeneous blend
10	DB-E7	65	28	7	Homogeneous blend
11	DB-E8	58	34	8	Homogeneous blend
12	DB-E9	49	42	9	Homogeneous blend

The stability of DBE blends was found to increase with increasing amount of biodiesel in the blend. A proportionately higher amount of emulsifier or biodiesel was required to stabilise the emulsions for even a minor addition of ethanol in the blend. In this study, it was also observed that the water content in ethanol if exceeding 1% created a tendency to phase separation of the fuel blend. The biodiesel content in the blend acted as a binding layer between diesel and ethanol. The surfactant property of biodiesel transformed ethanol's water content by forming a microemulsion between the water and organic phases. The arrangement in biodiesel's amphiphilic structure strengthened the basic linking among the different blending fuel (Méndez et al., 2006). The overall results confirmed that biodiesel itself can properly perform as an emulsifier at ambient temperature conditions when the amount of ethanol is less than 10% and hydrous ethanol is not suitable for fuel purposes.

3.2. Fuel characteristics

Calorific value: The net calorific value of each fuel blend is determined using Bomb Calorimeter LECO-AC350 (Figure 3) following ASTM D-240 test method. The calorific value of fuel is the quantity of heat energy discharged amid the combustion of unit quantity of fuel. One of the main factor that decides the calorific value of final blend is the water content in the base fuel. Regular diesel (45.6 MJ/kg) possess the highest calorific value among the three base fuels, while ethanol has the lowest (27.5 MJ/kg).

Figure 3: Leco AC-350 bomb calorimeter, Renewable Energy Lab, MTEC

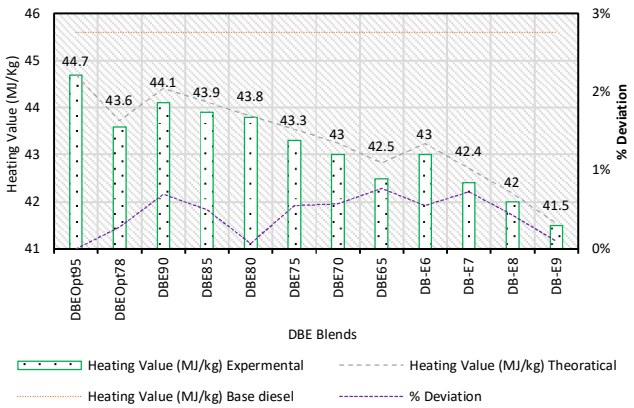

Figure 4: Comparison of experimental and predicted calorific value of DBE blends

DBEOpt95 blend with 95% base diesel and 5% ethanol was observed to have the highest calorific value of 44.7 MJ/kg by limiting the constraints to Thailand fuel standards. While considering premium fuel quality limits, DBEopt78 showed the maximum value of 43.6 MJ/kg in comparison with other DBE blends. All the test results observed to follow Kay's mixing rule with minimum deviation from the predicted results (from Figure 4). The addition of bio-fuels showed a considerable effect on lowering the heating value of DBE blends especially because of the water con-tent in it. A decrease of approximately 10% in heating value was observed while using the DB-E9 blend. The overall experiment results showed that all DBE blends have an acceptable energy content with all values higher than that of biodiesel. However, high ethanol content blends are not recommended for existing heavy-duty diesel engines.

Cloud Point (CP) and Pour Point (PP): The cloud point and pour point of DBE blends are measured as per ASTM D-2500 and ASTM D-97 standard methods using ISL, CPP 5Gs automatic cloud point, pour point analyser manufactured by Chemical House & Lab Instrument Co., Ltd (Thailand) (see Fig.5). The pour point and cloud point are the lowest and highest temperature values used for characterising the cold flow properties of fuels. Here, in the cold flow properties scenario ethanol excels by showing very low cloud and pour point temperatures, whereas diesel and biodiesel fall behind exhibiting poor values. Even though CP and PP fuel properties are not given much emphasise in Thailand due to the year round tropical climate, an experimental analysis is carried out to know more about variation in cold flow properties of ethanol contained fuels.

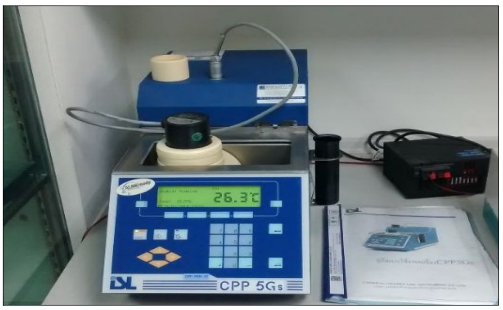

Figure 5: ISL, CPP 5Gs automatic cloud point, pour point analyser, Renewable Energy Lab, MTEC

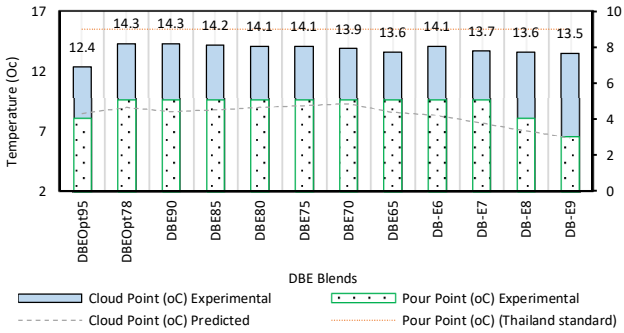

Figure 6: Experimental and predicted cloud points and pour points of DBE blends

It was found that ethanol has an immense effect on maintaining the cold flow properties of DBE blends without raising even with increasing content of biodiesel in the blend. Moreover, an addition of 1% ethanol in the blend helped in balancing the incremental effect on Cloud Point and Pour Point temperatures caused by 6% of biodiesel (DB-E7 to DB-E8) (see Figure 6). Even though all DBE blends resulted in higher cloud point than regular diesel, the results were found to be better than equivalent diesel-biodiesel blends. The experimental results precisely showed that the cloud point temperature of DBE blends doesn't follow Kay's mixing rule (no linear relationship).

Density: In this study, the specific gravity and density of DBE blends were measured by density meter DMA-4500 manufactured by Anton Paar (Austria) meeting ASTM D4052 standard (Figure 7). The density obtained for DBE blends chosen for the study showed similar results with minimum deviation, with-in the range of 0.840 - 0.855 kg/m^3, which is suitable for the premium fuel quality standard as per ASTM D4042. Also, the experimental results were observed to follow Kay's mixing rule with minimum error. The density of blends decreased with increasing ethanol content attributing to the fact that ethanol low density, lowers the final density of the blends following a linear relation. Also, a similar effect was found with biodiesel, resulting in higher tendency for increasing fuel density with biodiesel content.

Oxidation stability: Oxidation stability one key fuel property that should be given most importance as is it the measure of long-term stability and fuel quality. Especially for DBE blends, as it contains biodiesel and ethanol which have higher tendency to become unstable, more concern should be given for this fuel property. Oxidation of fuel mostly occurs when the fuel gets contact with higher temperature air or oxidative metals continuously. The Metrohm 743 Rancimat meter is used to determine the oxidation stability of the DBE blends following EN 14214 method, given in Figure 9.

Figure 7: Anton Paar density meter DMA-4500, Renewable Energy Lab, MTEC

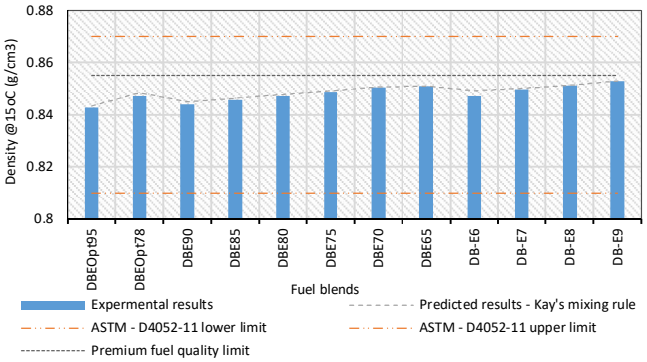

Figure 8: Comparison results of experimental and predicted values of DBE blend density

Figure 9: Oxidation stability analyser, Renewable energy lab, MTEC

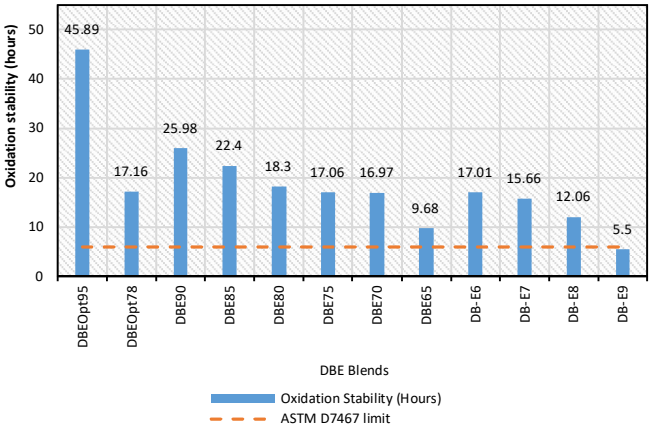

Figure 10: Oxidation stability of DBE blends

The fuel samples were tested as per Rancimat instrument method by heating up to 110 °C. The test results are shown in Figure10. The results show the induction period (IP) of POME is 22.3h and for commercial diesel is 130.6h which is significantly higher. While for ethanol due to the very low flash point (78°C) the induction period was not able to determine. As the amount of diesel increases in the blends, the stability shows better results. But the addition of even a small amount of ethanol showed an immense drop in DBE blends oxidation stability. This can be due to the reduction of unsaturated components and amount of oxygen. Oxidation of biofuels is also affected by storage time and condition, the pressure of the air, heat, and trace of metal and exposure to light (Barrufet & Setiadarma, 2003). So, this could be the reason for lower oxidation stability of DBE blends. However, except for DB-E9, all other DBE blends found to satisfy the ASTM limit with higher than 6 hour induction time.

Copper strip corrosion: Copper strip corrosion is the imperative variable in deciding the quality of fuel. This property estimates how much harm or damage the fuel causes to the fuel and engine system components made of copper alloys (brass). A copper corrosion bath (see Figure 11) is used for measuring the copper strip corrosion value. The copper strip is kept in contact with DBE blends at 50°C for 3 hours and then compared with the ASTM standard for Copper strip corrosion.

The experimental results for copper strip corrosion for base fuels and DBE blends are given in Table 3. All DBE blends found to have a corrosion value of 1b after comparison with ASTM standard. The ASTM D130 states that for fuels the copper strip corrosion should not exceed 3b and Thailand fuel standard limit for diesel is 1b. The copper strip corrosion also relates to the acid number of fuels. As observed from the acid value results, it is due to the higher acid number of biodiesel that resulted in higher corrosion value for DBE blends than diesel. The experimental results showed that all DBE blends have a copper strip corrosion value of 1b, which satisfies both ASTM and Thailand fuel standards.

Figure 11: Copper strip corrosion bath, Renewable energy lab, MTEC

Table 3: Copper strip corrosion test result

Parameters	Type of fuel				Standard ASTM D130
	D	B	E	DBE Blends	
Copper strip corrosion	1a	1b	1a	1b	Less than 3b

Water content: The water content is measured using Karl Fisher Coulometer given in Figure 12 following ASTM D6304 method. The experimental results are given in Figure 13. Among all the tested samples DB-E9 found to have the highest water content. Also, all DBE blends observed to follow increasing trend in water content with increase in biofuel content in the blend, especially ethanol. Storage time and oxidation stability are some of the reasons for the above-mentioned increasing trend. In the case of biodiesel and ethanol contained fuels, the water content generally increases with storage time and initiation oxidation instability governed by the peroxide chain mechanism. Also, the decomposition of unsaturated fatty acids can extend formation of hydroperoxides, the primary oxidation products which can result in the increase of water content in DBE blends. The ASTM D2709 standard states that water content in fuels should not exceed 2000ppm. All DBE blends are found to have water content values within the limits, satisfying the standard.

Figure 12: Metrohm, KF 831 Karl Fischer Coulometer, Renewable energy lab, MTEC

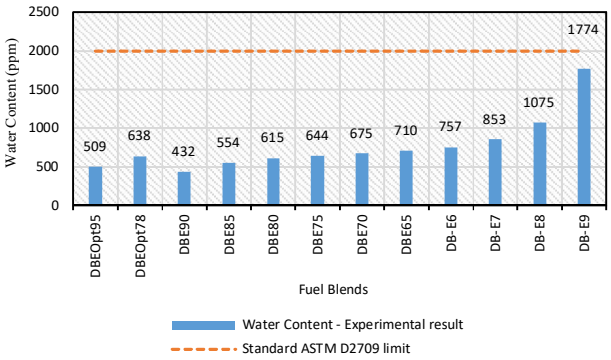

Figure 13: Water content in DBE blends

4. CONCLUSION

The DBE blended fuel characteristics such as stability, properties are tested and the following conclusions are drawn:

- All DBE blends with anhydrous ethanol were found to be completely stable while fuel blends with hydrous ethanol showed phase separation;
- Biodiesel was observed to act as a good emulsifier with increase in its content in the blend, rectifying the phase separation problems caused by higher ethanol content in the blends;
- All DBE were found to have an acceptable energy content, with the lowest for DB-E9 (9% lower than base HSD);
- The cloud point temperature was found not to follow Kay's mixing rule;
- The density of fuel blends was found to follow Kay's mixing rule with minimum deviation;
- The acid values of DBE blends were found to increase by a maximum 7% for each 10% of biodiesel added volumetrically;
- The addition of even a small amount of ethanol showed an immense drop in DBE blends oxidation stability. DBEOpt95 showed the highest induction time of 46 hours while DB-E9 showed lowest, 5.5 Hours. Except DB-E9, all other DBE blends found to satisfy the ASTM limit with higher than 6 hours induction time;
- All DBE blends have a copper strip corrosion value of 1b, which satisfies both ASTM and Thailand fuel standards;

- The DBE blends were observed to have an increasing water content as the biofuel content was increased in the blend, especially ethanol. Still, all the blends were found to have the water content values with the ASTM limit of 0.2% (2000ppm).

5. REFERENCES

Barrufet, M. A., & Setiadarma, A. 2003. Reliable heavy oil–solvent viscosity mixing rules for viscosities up to 450 K, oil–solvent viscosity ratios up to 4 × 105, and any solvent proportion. *Fluid Phase Equilibria*, 213(1–2): 65–79.

Hussan, M. J., Hassan, M. H., Kalam, M. A., & Memon, L. A. 2013. Tailoring key fuel properties of diesel–biodiesel–ethanol blends for diesel engine. *Journal of Cleaner Production*, 51: 118–125.

Kwanchareon, P., Luengnaruemitchai, A., & Jai-In, S. 2007. Solubility of a diesel–biodiesel–ethanol blend, its fuel properties, and its emission characteristics from diesel engine. *Fuel*, 86(7–8): 1053–1061.

Lin, C.-Y., & Lin, H.-A. 2006. Diesel engine performance and emission characteristics of biodiesel produced by the peroxidation process. *Fuel*, 85(3): 298–305.

Lin, J., Gaustad, G., & Trabold, T. A. 2013. Profit and policy implications of producing biodiesel–ethanol–diesel fuel blends to specification. *Applied Energy*, 104: 936–944.

Méndez, C. A., Grossmann, I. E., Harjunkoski, I., & Kaboré, P. 2006. A simultaneous optimization approach for off-line blending and scheduling of oil-refinery operations. *Computers & Chemical Engineering*, 30(4): 614–634.

#164: Development of a wet electrostatic precipitator for subway platform particles collection

Jin Han KIM[1], Jun Su PARK[2], Gil Bong LEE[3], Young Soo LEE[4], Kye Jung LEE[5], Jong Won CHOI[6]

[1]Korea Institute of Energy, Daejeon Korea, kjh0314@kier.re.kr
[2]Korea Institute of Energy, Daejeon Korea, junsu0622@kier.re.kr
[3]Korea Institute of Energy, Daejeon Korea, giblee@kier.re.kr
[4]Korea Institute of Energy, Daejeon Korea, yslee@kier.re.kr
[5]Korea Institute of Energy, Daejeon Korea, kjlee@kier.re.kr
[6]Korea Institute of Energy, Daejeon Korea, jwchoi@kier.re.kr

Recently, many researchers have paid a lot of attention to growing concentrations of ultrafine particles in the atmosphere. In particular, it has been reported that the air quality in indoor public places such as subway platforms, underground markets and indoor parking lots are even 3-5 times worse than the in-flowing air from outside due to the stationary air surroundings. Here, we designed and developed the electrospray-driven wet electrostatic precipitator to effectively collect Sub-1 um particles on a subway platform. The electrospray is one of the most attractive spray techniques to produce very fine and highly charged water droplets from high intensity electrical potential between two oppositely charged electrodes. The particles (PM10, PM2.5 and PM1.0) collection performance was investigated experimentally for different water supply and applied voltages at the conditions of inlet dust load of 160-200 mg/m3, air flowrate of 5.5 m3/min and inlet air velocity of 1.0 m/s. Through measuring the particle concentrations at both inlet and outlet ports by the optical particle sizer (OPS), we calculated the maximum collection efficiency as 99.8%, 98% and 86.7% for PM10, PM2.5 and PM1.0, respectively.

Keywords: subway platform; ultrafine particle; electrospray; wet electrostatic precipitator; collection efficiency

1. INTRODUCTION

Recently, many researchers have shown interest in decreasing concentrations of ultrafine particles in the atmosphere. This ultrafine dust causes respiratory conditions in humans, so people are increasingly interested and worried about ultrafine dust. Therefore most countries are changing their perception of the environment and tightening discipline for clean air by tightening pollution emission standards. In 2015, the Ministry of Environment set the standard for PM2.5 as the emission standard, as well as the total airborne particulate matter dust (TPS) concentration, at 25 $\mu g/m^3$ (the yearly average) (Kim and Kang, 2014: p621). In addition to reducing ultrafine dust from power plants, incinerators and construction sites, research on technology to remove ultrafine dust from underground railways, automobiles and roads is actively being carried out. Among them, subway stations are rich with sub-1μm ultrafine dust at high concentrations due to friction between the wheels and tracks of trains entering the platform. In order to remove dust within this range at high efficiency, wetting methods using water can be introduced since it is of a size that is not affected by conventional inertia, diffusion, or static electricity (Najafabadi et al., 2014: p415) Thus, in this study, a modular electrospray precipitator was developed, incorporating electrostatic spraying technology, which sprays a very small amount of water by high voltage. Borra *et al.* developed a precipitator with a modular design to provide flexible scalability for processing capacity. Within each module, 30 stainless steel nozzles can be installed into one water tube; every 10 nozzle is directed towards two electrodes and lower side (Borra *et al.,* 2004: p1319). The performance of ultrafine dust reduction was studied by changing the voltage applied to the nozzles, the strength of wind and the amount of water required through the modular electrospray precipitator.

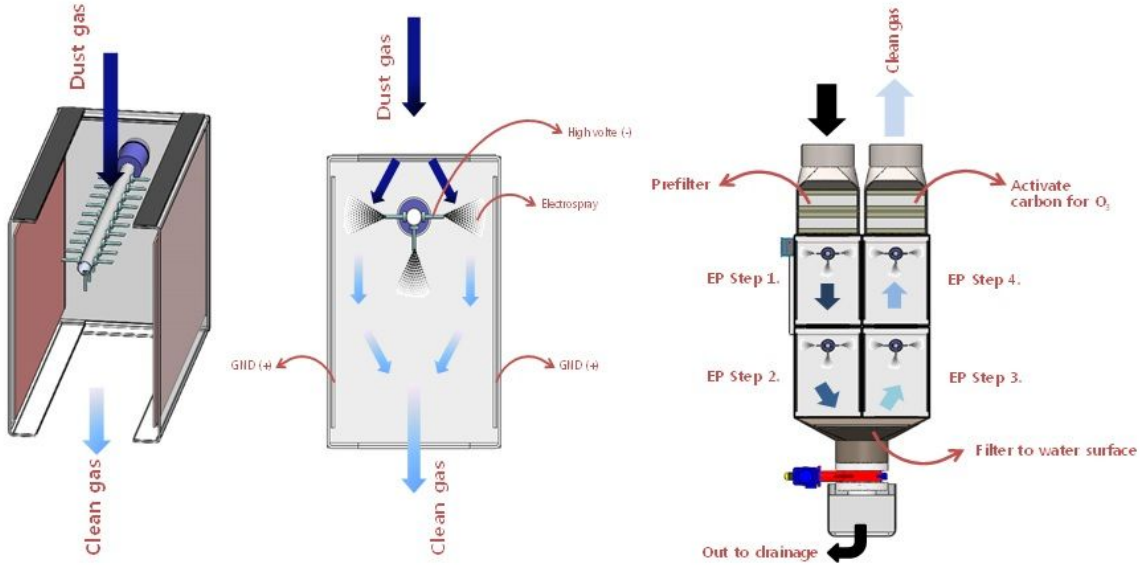

Figure 1: Single module precipitator (left), dirty gas inflow and spray view of water (middle), schematic diagram of the entire system of electrospray precipitator (right)

2. MAIN SUBJECT

2.1. Research method

Figure 1 shows the mechanism of aggregation within one module and the principle of aggregation of clams passing through four modules. When the concentration of incoming dust was increased or the need to deal with faster flow-rate crushed gases, the design of the system is such that it can be scaled by simply increasing the number of modules. Figure 2 is a prototype photograph of a modular electrospray precipitator, designed with a structure capable of inserting 10 nozzles each in the left, right and gravity directions of a 3/8 *inch* stainless steel nozzle into each module and then spraying fine water volumes toward a stainless steel electrode plate facing a nozzle facing left and right. The acrylic chamber under the stainless steel electrode at the bottom was used to collect the fine dust slurry and transfer it to a separate wastewater treatment facility. The electrical conductivity of tap water used in the experiment was measured at about 240 $\mu S/cm$. Ball flow meters, non-metallic diaphragm pump and air compressor were used to control the high voltage water to the desired flow rate. Insulation with stainless steel tube and surrounding areas was made using Teflon, polycarbonate (PC) which can be electrically insulated up to 65 *kV*. The high voltage power unit had a maximum corona current of 3 *mA* which can be measured at a maximum voltage of 50 *kV*; the negative electrode was connected to each water supply line in the module, and the ground was then

increased to the stainless steel electrode plate. The concentration of fine dust was measured by using the optical particle sizer (TSI, TSI3300) by fixing the supply dust concentration to 160-200 *mg/m*^{3} through the dust supply using hopper and screw, and by varying the flow rate of air into the precipitator and the voltage of the high voltage device.

Figure 2: Prototype of the modular electrospray precipitator

2.2. Experimental result

To test the performance of this modular electrospray precipitator, the inlet dust concentration with the air flowrate of 5.5 *CMM* was supplied at 160-200 *mg/m3*. The water flowrates in two water tubes at the top of the precipitator module was set at 0.3 and 0.5 *LPM* respectively. Finally, the applied voltage was varied at 0, 20, 30 and 40 *kV*. We calculated the collection efficiency of PM10, PM2.5 and PM1.0 through the information on the dust concentration using the optical particle sizer (OPS) at the inlet and outlet. Figure 3a shows the collection efficiency in electro- spraying water with the flowrate of 0.3 *LPM*. The linear increase of the collection efficiency per PM according to the applied voltage and the smaller the particle size, the greater the slope of the efficiency increase due to the applied voltage (Lopez-Herrera et al., 2004). As shown in Figure 3b, we also observed the collection efficiency in supplying the water of 0.5 *LPM,* which also increases with the applied voltage. The collection efficiency of PM2.5 was measured similarly for both 0.3 *LPM* and 0.5 *LPM*, however the removal efficiency for PM1.0 was observed slightly higher for 0.3 *LPM*, which is attributed that the lower water flowrate produced the smaller and the larger number of water droplets in electro-spraying mode.

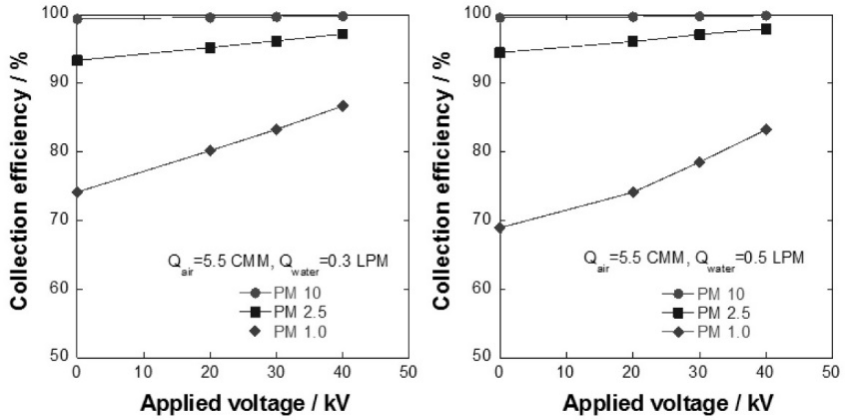

Figure 3: Collection efficiency increases with the applied voltage when 0.3 LPM (3a), 0.5 LPM (3b) of water is sprayed on the top modules

The smaller droplets can increase the probability of collision between water and dust (Kim et al., 2012). Table 1 summarises the collection efficiency of ultrafine dust from PM10, PM2.5 and PM1.0 using electrospray precipitator consisting of four modules. The dust insertion concentration was 160-200 *mg/m*^{3}, the air flowrate of 5.5 *CMM*, and the two lower modules were sprayed with 1.5 *LPM* of water for cleaning only without any separately applied voltage, it changed the flow rate of water to the top modules and shows the collection efficiency when applying an applied voltage of 40 *kV*. The PM collection efficiency for each water flowrate was calculated as 99.8%, 98% and 86.7% for PM10, PM2.5 and PM1.0 at 0.3 *LPM* also 99.8%, 97.2% and 83.3% at 0.5 *LPM*. We also investigated the relative humidity variation at the inlet and outlet of the electrospray precipitator, which is summarised in (Table 1) (Wang and You, 2013). The results give us information that the higher voltage produced the smaller water droplets and thus the air became more humid.

Table1: The PM elimination efficiency for each water flowrate at air flow rate of 5.5 CMM and applied voltage of 40 kV

		Electrospray (0.3 LPM, 40 kV)		Electrospray (0.5 LPM, 40 kV)		Explanation
		EP in	EP out	EP in	EP out	
Concentration (mg/m^3)	PM10	204.32	0.475	160.72	0.243	
	PM2.5	13.20	0.372	10.60	0.216	
	PM1.0	0.50	0.066	0.38	0.064	
Collection efficiency (%)	**PM10**	**99.8**		**99.8**		
	PM2.5	**98.0**		**97.2**		
	PM1.0	**86.7**		**83.3**		
Relative humidity at 20°C	20 kV	37.7	57.2	45.1	59.8	
	30 kV	40.3	57.6	44.9	60.7	
	40 kV	40.3	57.8	44.6	60.8	
Size fraction (%)	PM10	100	100	100	100	When PM 10 is 100%, percentage of each section
	PM2.5	6.5	78.3	6.6	88.9	
	PM1.0	0.2	13.9	0.2	26.3	

3. CONCLUSION

In this study, experimental studies were conducted to recognise the performance of ultrafine dust reduction in each operation condition of a modular electrospray precipitator using tap water with an electrical conductivity of 240 *μS/cm*. For the performance test of a modular electrospray precipitator, the wind flowrate was 5.5 *CMM* and the applied voltage was fixed at 40 *kV* and measured by the change in water supply of the top module. This was calculated at 99.8%, 98% and 86.7% for PM10, PM2.5 and PM1.0, respectively at the top module water flowrate of 0.3 *LPM*, and 99.8%, 97.2% and 83.3% for PM10, PM2.5 and PM1.0, respectively at the top module water flow rate of 0.5 *LPM*. The modular electrospray precipitator developed was a modular type electro-spray precipitator with the potential for large scalability depending on the desired treatment capacity. It was judged that it positively acted to improve air quality such as subways, underground shopping malls, and underground parking lots as it had the advantage of reducing the number of modules even in small areas.

4. ACKNOWLEDGEMENT

This research was conducted under framework of the research and development program of the Korea Institute of Energy Research (KIER) (B9-3219).

5. REFERENCES

Kim, J., Kang, D. 2014, Fine, ultrafine, and yellow dust: emerging health problems in Korea, *J Korean Med Sci*, 29, pp. 621-622

Najafabadi et al., 2014, Effects of gepmetric parameters and electric indexes on performance of a vertical wet electrostatic precipitator, *J. Electrost.*, Vol. 72, pp. 402-411.

Borra et al., 2004, Electro-hydrodynamic atomization of water stabilised by glow discharge-operating range and droplet properties, *J. Aerosol Sci.*, Vol. 35, pp. 1313-1332.

Lopez-Herrera et al., 2004, An experimental study of the electro-spraying of water in air at atmospheric pressure, *J. Amer. Soc. Mass Spectrom.*, Vol. 15, pp. 253-259.

Kim, J., Yoo, H., Hwang, Y. and Kim, H. 2012, Removal of particulate matter in a tubular wet electrostatic precipitator using as water collection electrode, *The Scientific World Journal*, Vol. 2012, pp. 1-6.

Wang, X., You, C. 2013, Effect of humidity on negative corona discharge of electrostatic precipitators, *IEEE*, Vol. 20, pp. 1720-1726.

#165: Visualisation study on the droplet size variation in water electrospray

Jun Su PARK[1], Jin Han KIM[2], Young Joo LEE[3], Young Min WOO[4], Jin Young JANG[5], Kye Jung LEE[6], Jong Won CHOI[7]

[1] Korea Institute of Energy, Daejeon Korea, junsu0622@kier.re.kr
[2] Korea Institute of Energy, Daejeon Korea, kjh0314@kier.re.kr
[3] Korea Institute of Energy, Daejeon Korea, lyj3380@kier.re.kr
[4] Korea Institute of Energy, Daejeon Korea, ywoo@kier.re.kr
[5] Korea Institute of Energy, Daejeon Korea, jy.jang@kier.re.kr
[6] Korea Institute of Energy, Daejeon Korea, kjlee@kier.re.kr
[7] Korea Institute of Energy, Daejeon Korea, jwchoi@kier.re.kr

The electrospray is one of the most attractive spray techniques to produce very fine and highly charged water droplets conically shaped. It uses highly concentrated free charges from high intensity electrical potential between two oppositely charged electrodes. In this paper, we investigated the flow motion and the water droplet size variation for different operating conditions such as flowrate, velocity, applied voltage, nozzle size, and electrode distance. From visualisation works, we analysed the most influencing parameter to the flow motion and droplet size, aiming at its application in various industries such as coatings, pharmaceuticals, or particle precipitation. In particular, we focused on its application to trap ultrafine particles since the negatively charged droplets can draw the positively charged ultrafine particle and agglomerate them. Experimental results show that the water droplet size increased as the flowrate, speed, nozzle diameter increased and as the applied voltage decreased.

Keywords: electrospray; visualisation; water, droplet; ultrafine particle

1. INTRODUCTION

Recently, researchers have paid a lot of attention to electrospray technologies and their application to ultrafine particle removal since it is attractive when applied to dust collection devices because of low initial cost, rapid response, low energy consumption and low water need (Choi, 2017). Electrospray refers to a technique to spray out highly charged fine liquid droplets; applying a high voltage to a liquid solution forming a high electric field between a narrow nozzle and the plate (Kim, 2018). As seen in Figure 1, the fine liquid droplets are scattered from a confined nozzle tip by the repulsive force among the charged droplets.

In more detail, when an insufficiently high voltage is applied to the liquid solution, the repulsive force in the liquid flowing inside the nozzle is also low, and thus the droplet does not form a spray motion. In contrast, if the repulsive force is higher than the surface tension of the liquid, the voltage is applied to the liquid solution and the spraying mode starts due to the high repulsive force (Park, 1994). Previous research has found that the droplet size depends on the liquid property, flowrate, nozzle geometry and electric field strength (Kim, 2012). This work was based on the nozzle size of less than 100 micrometer in diameter using either water or alcohol solution, and the measured droplet size was reported to range from 0.1 to 10 micrometer. However, such a small droplet size may not be appropriate for collecting the fine particles inside a flue gas due to easy evaporation tendency. Hence, we decided to investigate the electrospray motion in larger nozzles than 100 micrometer (Rulison, 1994), with sizes set at 0.5 and 1.0 mm in this study to capture the fine particles. Unfortunately, the droplet size prediction and motion variation have been neither reported nor well established to date. As a first step in this study, we visually investigated the water droplet size variation for different operating conditions such as voltage, flow rate, velocity, electrode distance (electrical field strength) and nozzle diameter (Borra, 2004, Najafabadi, 2014).

Figure 1: Electrospray mechanism

2. METHODS

We prepared the visualisation setup for the electrospray using a single stainless steel needle as shown in Figure 2. A constant flow rate was adjusted to a needle using a syringe pump, and the liquid solution used in this study was distilled (DI) water with an electrical conductivity of 0.5 μS/cm and a resistance of 2 MΩ·cm.

Visualisation studies were carried out under various voltages from 25 to 45 kV (Choi, 2017), flow rates from 5 to 20 ml/min, velocities from 0.25 to 1.0 mm/s, nozzle-plate distance from 50 to 125 mm (Lopez-Herrera, 2004), and nozzle diameter of 0.45 and 0.65 mm in order to observe the droplet size variation. In this study, droplets between 20 and 980 μm in diameter were observed. As mentioned, the smaller liquid droplet may be more desirable to collect fine particles, however the droplet size that is too small is easily evaporated or exhausted out together with flue gas when installed to an actual dust collector. Therefore, in this study we chose the needle size for the electrospray of 0.45 and 0.65 mm.

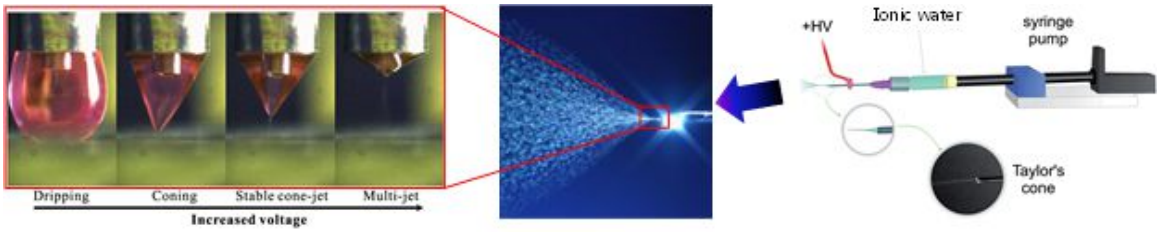

Figure 2: Pictures of electrosprayed water droplets with increasing the voltage

To get a still image of spraying droplets, we employed DSLR camera (Cannon 5D MARK2) and super high speed strobe light (LED). In a laboratory with a dark environment, we set the shutter speed as 2 s and instantly applied the light during 5 μs, which gave us a very similar image to a high speed camera. To our knowledge, this may be the first trial to capture the instant spraying image. After gathering the images, they were analysed using Adobe's Photoshop program. The high-voltage power supply used in the experiment was designed to allow the maximum voltage of 50 kV and the maximum current of 2.5 mA. Positive potential was connected to a stainless steel plate and the negative potential was done to the needle connector as shown in Figure 3.

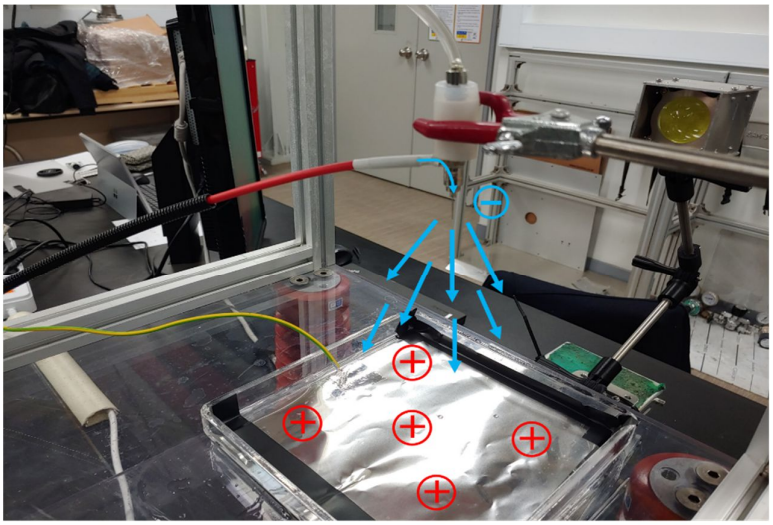

Figure 3: Experiment device

Before setting the maximum voltage, we gradually increased the negative voltage and observed the maximum allowable limit to avoid an insulation breakage (spark-over) between the nozzle tip and the plate, which was 45 kV in this study.

2.1. Experimental results

Influence of electrode distance

As the electrode distance increased, the droplet size was varied according to the flow rate (see Figure 4). At the same electrode distance, the droplet size increased as the flow rate increased. The reason for this was that as the amount of the droplet increased, the voltage exceeded the allowable limit. For the same reason, as the electrode distance increased, the droplet size increased. Therefore, a minimum flow rate and short electrode distance were required to maintain a fine liquid droplet.

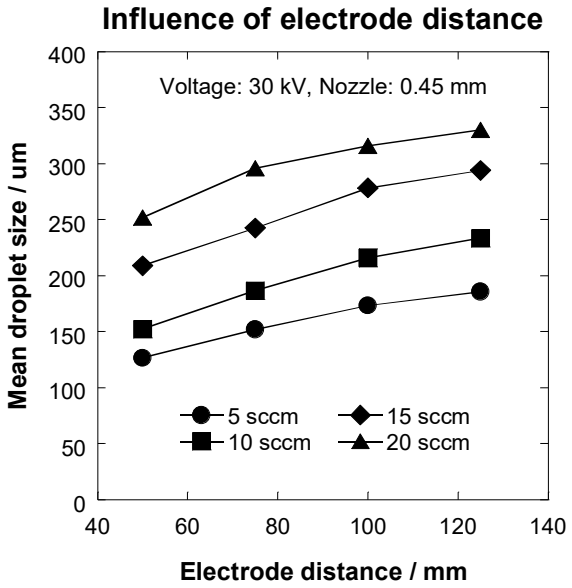

Figure 4: Influence of electrode distance

Influence of applied voltage under the same water flow rate

As shown in Figure 5, droplet changes were observed by increasing the voltage at the same flow rate condition. As with the results shown in the preceding Figure 4, at low voltages, the droplet remained large due to the allowable number of permissible limits. However, as the voltage increased, the size of the droplet decreased because the allowable number of liquid droplet increased. As the voltage increased, it was possible to make a condition to generate a lot of fine liquid droplets. However, it should be reflected in the design conditions considering the increase of operation cost and stability of the equipment.

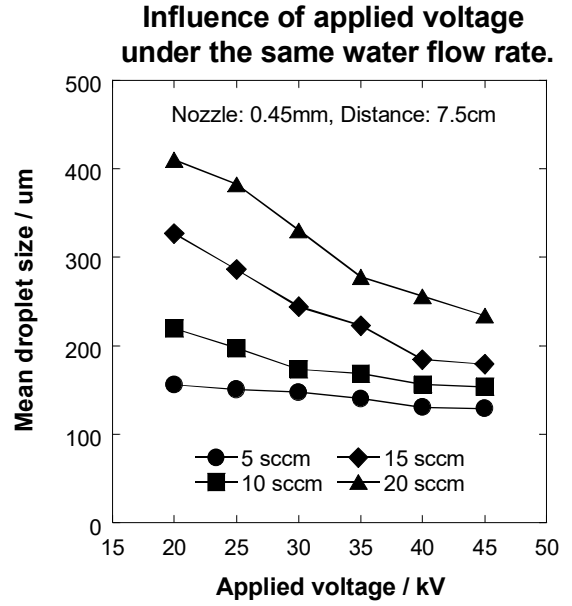

Figure 5: Influence of applied voltage under the same water flow rate.

Influence of applied voltage under the same water velocity

Figure 6 shows the variation of the droplet by changing the water velocity under the same operating conditions as the experimental method shown in Fig 5. As the nozzle inner diameter was reduced from 0.65 to 0.45 mm, the water velocity increased from 5 to 0.25 mm/sec. The increased water velocity directly affected the size of the droplet, which was about 40% smaller than the water velocity of 5 mm/sec. These results show that as the particle size of the nozzle decreased, the flow velocity increased and the allowable number of voltage acted strongly.

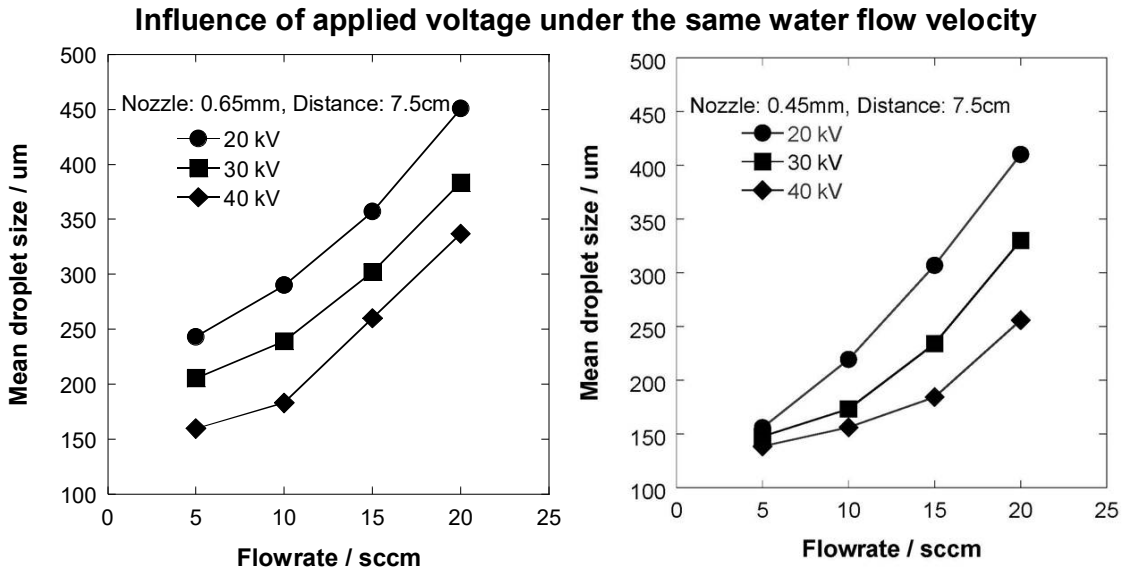

Figure 6: Influence of applied voltage under the same water velocity.

Influence of water velocity

The water velocity was increased from 0.25 to 1.0 mm/s in order to investigate the influence of droplet size and water velocity (Figure 7). At a voltage of 45kV, the droplet size decreased as the flow rate increased to 0.75 mm/s. However, if the flow rate was increased to 1.0 mm/s, the water droplet increased again, because the water velocity had exceeded the limit of repulsion. That is, as the voltage and the water velocity increased, the droplet size may decrease. However, when the repulsive force reaches the limit line, the water droplets combined with each other to form a large droplet.

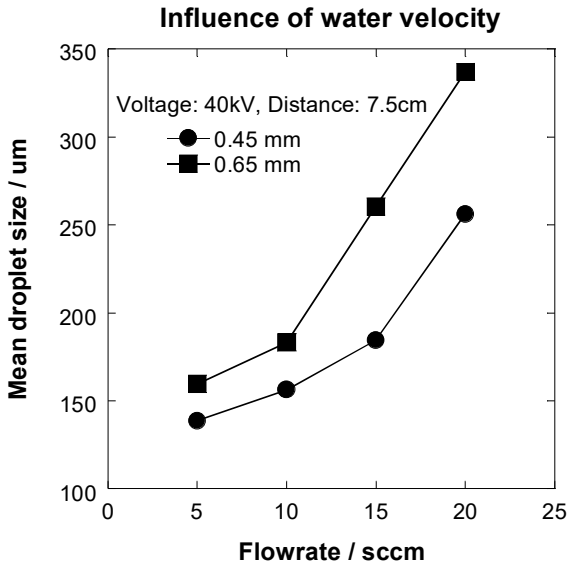

Figure 7: Influence of nozzle diameter.

3. CONCLUSION

In this study, we conducted the visualisation study on the electrospray using distilled water. Through various experimental conditions such as voltage, flow rate, velocity, electrode distance and nozzle inner diameter, we observed the droplet size variation and spray pattern. The droplet size was smaller when the applied voltage was higher, the electrode distance was closer, the flowrate was smaller, the velocity was lower, and the nozzle size was smaller, all of which were related to the repulsive force of water molecules passing through such a narrow needle. When a relatively large droplet was found, it can be understood that a sufficient amount of negative charge cannot be charged, so that it was possible to generate a fine droplet by reducing the flow rate or adjusting the inner

diameter of the nozzle. It was also found that when the inner diameter of the nozzle was relatively small, droplets become finer. Using a needle with a narrow inner diameter, it was possible to generate finer droplets with the same amount of flow and voltage. The liquid column length at bottom of the nozzle was not influenced by the electrode distance but by flowrate dominantly, which can give helpful information to design the dust collector to prevent the spark-over.

In recent years, electrospray technology, which was mainly used in the coating field before, has recently been attracting attention in the dust collecting industry due to its great benefit of low initial investment cost, low energy use and small amount of water. We speculate that the effective removal of ultrafine dust by fine water particles from the electrospray can effectively solve the air pollution problem in the near future (Choi, 2017).

4. ACKNOWLEDGEMENT

This research was conducted under framework of the research and development program of the Korea Institute of Energy Research (KIER) (B9-2451-12).

5. REFERENCES

Rulison, A. et al., 1994, Synthesis of yttria powders by electrospray pyrolysis, Journal of the American

Ceramic Society., Vol. 77, U.S.A., pp. 3244-3250.

Choi, J.W., 2017, Development of modular electrospray electrostatic precipitator for ultrafine particles removal, Air-Condi. Ref. Eng., Korea, pp. 262-267.

Choi, J.W. et al., 2017, Fine Water Droplet Generation via Electrospary and its Application to Wet Cyclone, Soc. Air Condi. Ref. Eng., Korea, pp. 1108-1113.

Choi, J.W. et al., 2017, Experimental study on the fine particles removal with the electrospray induced electrostatic precipitator, Korean Society for Energy., Korea, pp. 260.

Borra, J. et al., 2004., Electrohydrodynamic atomization of water stabilised by glow discharge-operating range and droplet properties., J. Aerosol Sci., Vol. 35., pp. 1313–1332, 2004.

Kim, J. et al., 2018, Study on the fine particles removal performance of the electrospray driven swirling electrostatic, Air-Condi. Ref. Eng., Korea, pp. 262-267.

Kim, J. et al., 2012, Removal of particulate matter in a tubular wet electrostatic precipitator using as water collection electrode, Sci. World Journal., Vol. 2012, Korea, pp. 1-6.

Lopez-Herrera, J. et al., 2004, An experimental study of the electrospraying of water in air at atmospheric pressure, J. Amer. Soc. Mass Spectrom., U.S.A, Vol. 15, pp. 253–259.

Najafabadi, M. et al., 2014, Effects of geometric parameters and electric indexes on performance of a vertical wet electrostatic precipitator, J. Electrost., Vol. 72, pp. 402-411.

Park, S.J. et al., 1994, Particle Trajectory Visualization in Electrostatic Precipitator, Trans. Korean Soc. Mech. Eng. B, Vol. 18, No.12, Korea, pp. 3270~3275.

#167: Thermal properties of phase change material from coconut oil and graphene as energy storage for building applications

Lulu SAFIRA[1], Nandy PUTRA[1*], Eny KUSRINI[2]

*[1] Department of Mechanical Engineering, Faculty of Engineering, Universitas Indonesia, 16424 Depok, West Java, Indonesia, *Corresponding author: nandyputra@eng.ui.ac.id*
[2]Department of Chemical Engineering, Faculty of Engineering, Universitas Indonesia, 16424 Depok, West Java, Indonesia

The aim of this study is to investigate the thermal properties of phase change material (PCM) from coconut oil as energy storage for building applications. Coconut oil is classified as organic PCM from fatty acids made from renewable feedstock. However, low thermal conductivity becomes one of the major drawbacks of organic PCMs and needs to be improved. Graphene can be an effective material to enhance the thermal performance of organic PCMs. In this study, we used coconut oil that has a latent heat capacity of 114.6 J/g and a melting point of 17.38ºC. PCMs were prepared by sonicating coconut oil into graphene, as supporting material. The mass fractions were 0 wt%, 0.1 wt%, 0.2 wt%, 0.3 wt%, 0.4 wt%, 0.5 wt%, respectively. The thermal conductivity test was performed using KD2 Thermal Properties Analyzer under different ambient temperatures of 5ºC, 10ºC, 15ºC, 20ºC, and 25ºC simulated with circulating thermostatic bath. Latent heat, melting point, the freezing point were determined through DSC testing. Thermal stability was determined using TGA testing. While morphology and chemical structure were examined using TEM and FT-IR, respectively. From this study, the effect of graphene addition to coconut oil indicates fluctuating increase where the highest improvement was seen in 0.3 wt% sample at 20ºC. Latent heat was decreased by 11% due to molecular movements within the PCM. However, TGA analysis revealed that the composite PCMs showed good thermal durability in building temperature ranges.

Keywords: phase change material, coconut oil, graphene, energy storage, sonication

1. INTRODUCTION

Thermal energy storage (TES) has become one of the solutions to overcome energy demands, mainly in urban area due to the excessive use of air conditioning system in the building. Techniques of thermal energy can be done through sensible heat, latent heat, thermo-chemical heat, or a combination of those techniques (Alva, Lin and Fang, 2018). Latent heat energy storage is considered to be the most effective to store and release a significant amount of heat with an inconsiderable amount of temperature fluctuation (Zhou, Zhao and Tian, 2012). The material used in latent heat energy storage is called phase change material or PCM, for short. In building applications, the PCM is used to enhance the thermal comfort by reducing the frequency of internal temperature swings so that the desired indoor air temperature can be achieved for a longer period (Sharma *et al.*, 2013).

PCM can be obtained from inorganic, organic, and eutectic materials. Inorganic PCMs include salt hydrates, metals and alloys which have high thermal conductivity and good latent heat capacity, but corrosive to metallic components, causes supercooling due to poor nucleating ability, and poses a number of engineering problems. Organic PCMs include paraffins and non-paraffins. Paraffins have been widely used for its large latent heat capacity, non-corrosive, and large temperature range. Non-paraffins came from numerous materials with varied properties which include fatty acids, esters, glycol, and alcohol. Compared to paraffins, fatty acids have a higher latent heat of fusion value (Sharma *et al.*, 2009; Pielichowska and Pielichowski, 2014). Coconut oil contains fatty acids, mostly lauric acid (Bouaid *et al.*, 2017) which makes it a considerable organic PCMs, especially in Indonesia as one of the producers of coconut oil. Saleel et al. (2019) reported that coconut oil could reduce the internal temperature of a car cabin up to 17 ºC of temperature reduction (Saleel, Mujeebu and Algarni, 2019). Wonorahardjo et al. (2018) demonstrated the performance of coconut oil as a potential TES in tropical countries, such as Indonesia, in which the coconut oil is capable of decreasing indoor air temperature per unit of air volume, measured through an experiment conducted in a thermal chamber (Wonorahardjo *et al.*, 2018).

However, the major drawback of organic PCMs is a low thermal conductivity, which reduces the rate of the heat transfer process and the rate of heat storage. To enhance it, incorporating carbon-based nanomaterials is considered to be an effective method for its low density, stability and good dispersion ability compared to metal-based material (Qureshi, Ali and Khushnood, 2018). From all carbon-based nanomaterials, graphene is one of the nanomaterials that is effective to improve the thermal properties of PCMs, especially the thermal conductivity. Zou et al. (2018) compared PCM added with CNT and graphene for lithium-ion power battery application. The result was that PCM with graphene has higher thermal conductivity than PCM with CNT (Zou *et al.*, 2018). Fan et al. (2013) also compared the effect of graphene, multi-walled carbon nanotubes, and the carbon nanofibres addition of paraffin, where graphene improved the thermal conductivity for almost 170% on 5 wt% mass fraction (Fan *et al.*, 2013).

Therefore, this study focused on analysing the thermal properties of coconut oil as PCM with the graphene of different mass fractions incorporated to the PCM. The morphology and chemical structure were tested using TEM and FTIR, respectively. Thermal properties analysed in this study include thermal conductivity, heat storage performance, and thermal durability using KD2 Thermal Properties Analyzer, DSC, and TGA.

2. METHODOLOGY

2.1. Material

In this study, coconut oil as the phase change material were obtained from the Department of the Chemical Engineering University of Indonesia, where the latent heat is 114.6 J/g and has a melting point of 17.38ºC. The graphene was a commercial product purchased from XG Sciences, Inc. with physical and chemical properties shown in Table 1. Figure 1 displays graphene and coconut oil samples.

Table 1: Properties of graphene.

Property	Value
Appearance	Black powder
Bulk density (g/cc)	0.2 – 0.4
Relative gravity (g/cc)	2.0 – 2.25
Specific surface area (m^2/g)	300
Width (µm)	Less than 2
Thickness (nm)	Less than 2
Thermal conductivity (W/mK)	Parallel to the surface: 3000
Density (g/cm^2)	2.2
Carbon content	>99%

Figure 1: Graphene (left) and Coconut oil (right).

2.2. Preparation of the coconut oil/graphene phase change material

The PCM composites were prepared by mixing graphene at different mass fractions of 0.1, 0.2, 0.3, 0.4, 0.5 wt% into coconut oil. Figure 2 shows the scheme for sample preparation steps. Coconut oil and graphene were stirred with magnetic stirrer for 30 min and ultrasonicated for 20 min.

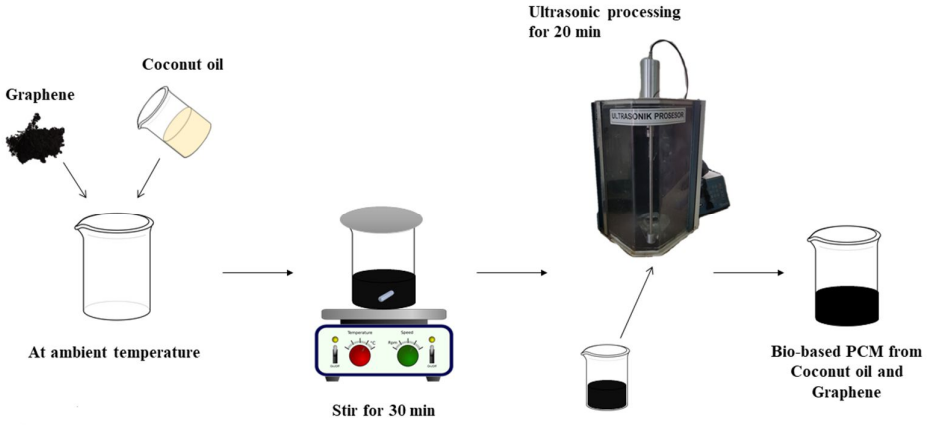

Figure 2: PCM composite preparation by ultrasonic processing.

2.3. Characterisation and properties test method

Various test methods were applied to the PCM composites to determine their properties, both structural and thermal. The morphology of PCM samples was observed with Transmission Electron Microscopy (TEM, FEI TECNAI G2 20S-Twin). Fourier-transform infrared spectroscopy (FTIR, PerkinElmer FTIR Spectrometer Spectrum Two) was used to confirm the change of chemical groups within pure coconut oil and coconut oil added with graphene.

The thermal properties of samples, such as melting and freezing temperature, as well as latent heat were measured using Differential Scanning Calorimetry (DSC, TA Instruments DSC Q20). The measurement was performed with 5ºC/min for each heating and cooling process. The samples were heated from -20ºC to 40ºC, hold for 2 min, and cooled from 40ºC to -20ºC. Latent heat of fusion and freezing of the samples were determined by numerical integration of the area under peaks that represent the solid-solid and the solid-liquid phase transitions (Jeong *et al.*, 2013). Thermal conductivity was measured using a thermal conductivity meter (KD2, Decagon Device Inc.) with an accuracy of ± 5% and its scale ranges from 0.02 to 2 $Wm^{-1}K^{-1}$. This device was also used in previous research to measure the thermal conductivity of other PCM materials, such as paraffin RT22 HC (Putra *et al.*, 2017), paraffin wax (Saydam and Duan, 2019), and palmitic acid (Sari and Karaipekli, 2009). Thermogravimetric analysis (TGA, PerkinElmer TGA 4000) was carried out to determine decomposition temperature and to test the thermal stability in building application's temperature range. The measurement was operated from 30ºC to 600ºC with a heating rate of 5ºC/min.

3. RESULT AND DISCUSSION

3.1. Morphological and chemical structure

The morphology of PCM composites was observed with transmission electron microscopy. TEM images in Figure 3 shows rolled and folded thin sheet structure of graphene and indicated well-ordered graphene layers. The length of graphene is <50 nm and the diameter ranged from 0.2 to 0.5 µm if unfolded. The nanosize of graphene made it easier to be dispersed in coconut oil and it is exhibited in the TEM images that the graphene is well-dispersed in the coconut oil.

The chemical structure of PCM composites was analysed with Fourier-transform infrared. It should be noted that coconut oil contains fatty acids and it is expected that graphene addition would not affect the fatty acids and esters in the coconut oil. Figure 4 exhibits similar peaks between pure coconut oil and the composites. The spectrum of PCM samples displays specific absorption peaks at 2955 cm^{-1} and 2850 cm^{-1} which were caused by $-CH_3$ groups. Other peaks were seen at 1742 cm^{-1} caused by C=O from fatty acids in coconut oil, and at 1153 cm^{-1} and 1110 cm^{-1} caused by vibrations from the C-O bond in the coconut oil. These results indicate that there is no chemical reaction occurred between the coconut oil and graphene. Therefore, based on the TEM images and FTIR spectroscopy that PCM from coconut oil with graphene forms a good compatibility.

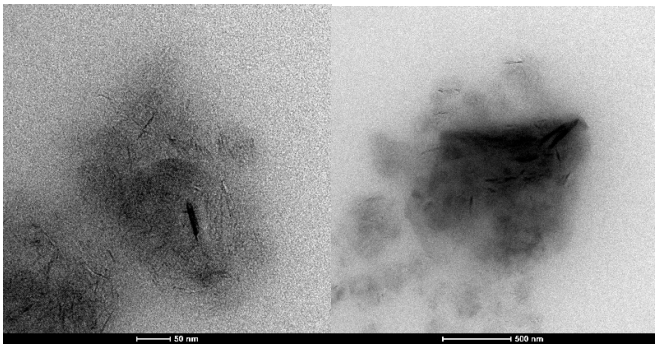

Figure 3: TEM images of composite PCM.

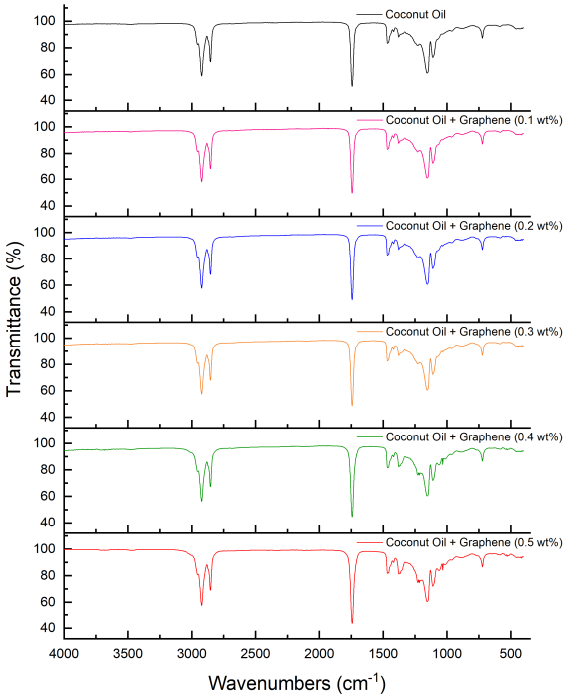

Figure 4: FT-IR result.

3.2. Thermal conductivity

The thermal conductivity of PCM composites and coconut oil PCM are presented in Figure 5 and Table 2. The measurement was done under various temperature conditions to observe whether there is any effect on thermal conductivity due to sedimentation and nanoparticle movement during solid phase at 5ºC to 15ºC and liquid phase at 20ºC to 25ºC. The measurement temperatures were simulated using the circulating thermostatic bath.

The results showed a fluctuating increase due to sedimentation and agglomeration of graphene that only a few fractions of graphene that were dispersed into coconut oil were scattered which slightly improving the thermal conductivity. The highest increase was shown in 0.3 wt% mass fraction at 20ºC where the thermal conductivity obtained was 0.357 W m^{-1} $ºC^{-1}$ or 69% from the coconut oil PCM. It can be seen as well that the results in liquid state that occurred in 25ºC showed smaller increase compared to the results in other conditions which can be caused by the movements of graphene particles in liquid that made them unable to be scattered by the sensor. In conclusion, graphene addition can be a solution to improve the thermal conductivity of coconut oil PCM. However, continuous or excessive addition of graphene will not increase the thermal conductivity more effectively due to particle sedimentation and movement.

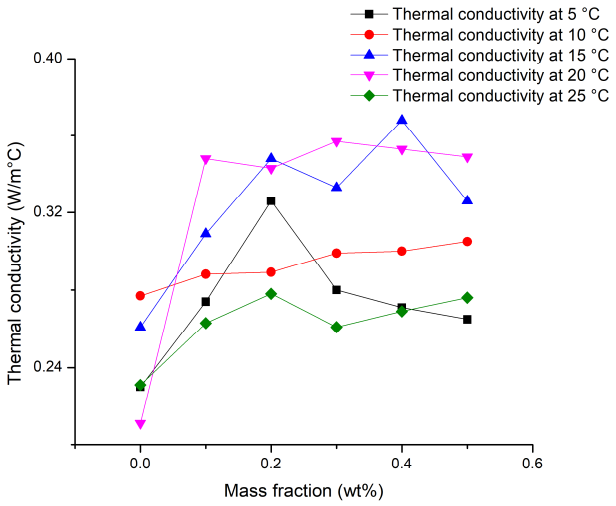

Figure 5: Thermal conductivity of PCM samples in various temperatures.

Table 2: Thermal conductivity measurement results.

T (°C)	Thermal conductivity (W/m°C)					
	Coconut oil	Coconut oil + Graphene 0.1 wt%	Coconut oil + Graphene 0.2 wt%	Coconut oil + Graphene 0.3 wt%	Coconut oil + Graphene 0.4 wt%	Coconut oil + Graphene 0.5 wt%
5	0.23	0.274	0.326	0.28	0.271	0.265
10	0.277	0.288	0.289	0.299	0.3	0.305
15	0.261	0.309	0.348	0.333	0.368	0.326
20	0.211	0.348	0.343	0.357	0.353	0.349
25	0.16	0.18	0.187	0.192	0.193	0.242

3.3. Thermal energy storage performance

DSC measurement was carried out to provide data for melting temperature, freezing temperature, latent heat and heat capacity. The DSC curves displayed in Figure 6 shows that each curve has one peak for heating processes and another one for cooling processes. In Table 3, it is shown that graphene addition gave a fluctuating result on the melting temperature of coconut oil PCM but increased the freezing temperature although by varying increments.

For latent heat of fusion is shown to be decreasing, except for 0.1 wt% sample in which the value raised to 150 J/g but the latent heat of freezing for all samples were increased. These results can be explained by interfacial liquid layering, Brownian movements, and particle clustering (Zabalegui, Lokapur and Lee, 2014).

Heat capacity was determined using Equation 1 and data from DSC measurement.

Equation 1: Heat capacity.

$$Cp = \frac{\Delta Q}{m\Delta T}$$

Where:

- Cp = heat capacity of samples (J/°C)
- ΔQ = heat flow rate (J/s)
- m = sample mass (kg)
- ΔT = heating rate (°C/s)

Figure 7 displays the results of heat capacity calculations. It is seen that graphene addition increased the heat capacity of coconut oil PCM during solid state. In liquid state also exhibited an increase of heat capacity, except for 0.1 wt% which showed a decrease. In conclusion, it can be said that graphene can increase the heat per mass unit needed to raise the temperature or in another words, the capacity of heat that can be stored during sensible process.

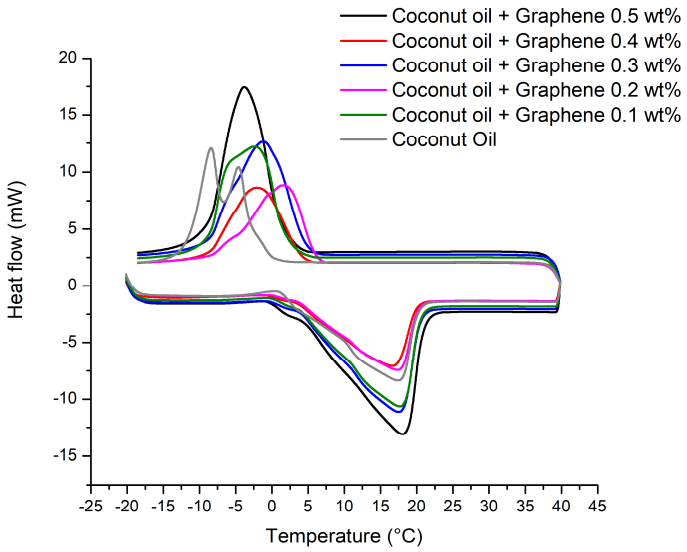

Figure 6: DSC curves of coconut oil PCM and composite PCMs.

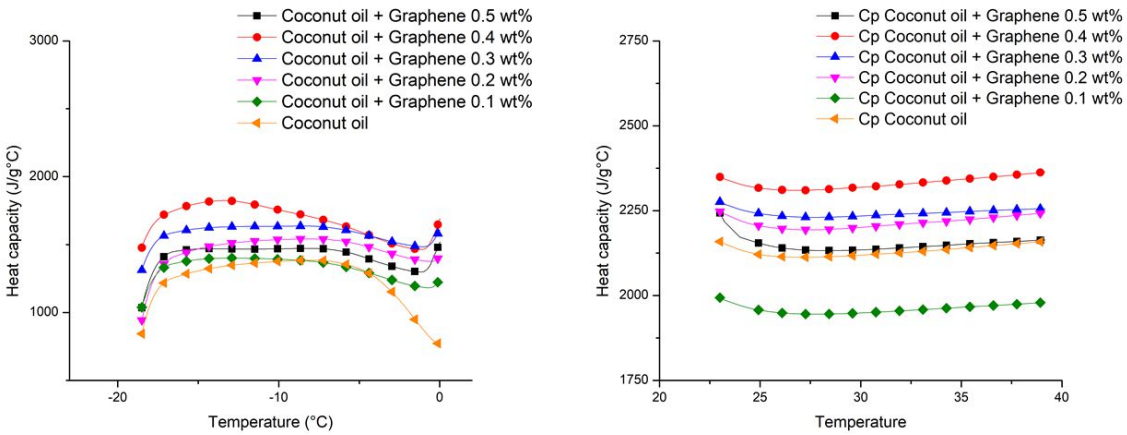

Figure 7: Heat capacity of coconut oil PCM and composite PCMs during solid state (left) and liquid state (right).

Table 3: Thermal storage properties of coconut oil PCM and composite PCMs.

Sample	Heating			Cooling		
	Tm (°C)	Onset (°C)	ΔH (J/g)	Tf (°C)	Onset (°C)	ΔH (J/g)
Coconut oil	17.38	5.32	114.6	-8.4	-6.13	94.61
Coconut oil + Graphene 0.1 wt%	17.49	4.89	150	-1.91	1.84	139.5
Coconut oil + Graphene 0.2 wt%	17.39	4.56	103.1	2	6.02	98.71
Coconut oil + Graphene 0.3 wt%	17.29	4.35	102	-0.61	4.66	98.02
Coconut oil + Graphene 0.4 wt%	16.65	2.72	103	-1.84	4.11	98.81
Coconut oil + Graphene 0.5 wt%	17.73	2.91	106	-3.18	1.37	100.7

3.4. Thermogravimetric analysis

TGA was carried out to investigate the thermal durability of composite PCMs. Based on the derivative weight curves in Figure 8, all samples were degraded in one step. For coconut oil, the peak occurred at 411.39ºC. From Table 4, it is shown that composite PCMs exhibited higher peaks than that of coconut oil. The peak of composite PCM increased by almost 10%. The thermal resistance properties that graphene brought to the PCM composites can be explained by the barrier effect in which graphene played a role in preventing heat from extraneous surroundings from being distributed in the PCM and impeding the evolution of volatile decomposition products (Pielichowska *et al.*, 2016). All degradation process occurred at above 400ºC and thus, it can be concluded that the prepared PCMs are thermally stable and resistant to thermal degradation in building temperature ranges.

Table 4: Peak of Derivative Weight of PCM samples.

Sample	Peak of Derivative Weight (°C)
Coconut oil	411.39
Coconut oil + Graphene 0.1 wt%	452.33
Coconut oil + Graphene 0.2 wt%	441.5
Coconut oil + Graphene 0.3 wt%	444.00
Coconut oil + Graphene 0.4 wt%	410.67
Coconut oil + Graphene 0.5 wt%	445.00

4. CONCLUSION

Coconut oil PCM loaded with various mass fractions of graphene were prepared through an ultrasonication process to investigate the thermal properties of PCMs as a thermal energy storage alternative in order to overcome the rising of energy demands. Through TEM analysis, graphene was shown to be well-dispersed in the coconut oil PCM. Fatty acids and esters in the coconut oil as important compounds of organic PCMs were not reacted with graphene, thus forming a good compatibility. Thermal conductivity measurement with KD2 Thermal Properties Analyzer showed that graphene loading gave a fluctuating improvement to the thermal conductivity of PCM, where the highest increase was shown in the measurement of 0.3 wt% sample in 20ºC, by 69%. However, graphene loading caused a reduction of latent heat and increased the heat capacity of PCM samples, which could be explained by Brownian motion and interfacial liquid layering. According to the TGA curves, all samples exhibited thermal durability at room temperature. Composite PCMs would experience thermal degradation at above 400ºC. Therefore, coconut oil as PCM with graphene loading can be considered as thermal energy storage in low temperature, particularly building applications.

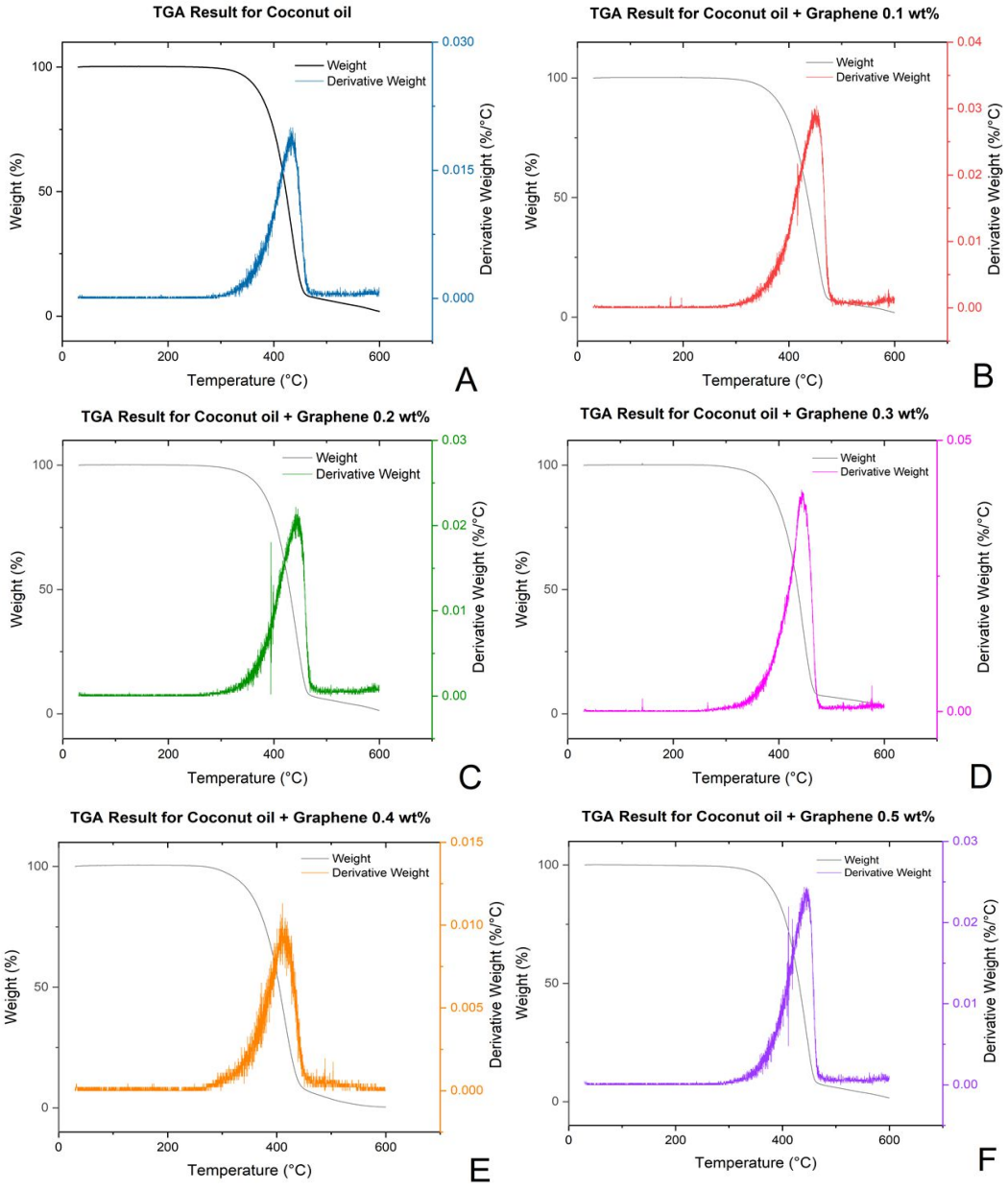

Figure 8: TGA curves of samples.

5. REFERENCES

Alva, G., Lin, Y. and Fang, G. (2018) 'An overview of thermal energy storage systems', *Energy*. Elsevier Ltd, 144, pp. 341–378. doi: 10.1016/j.energy.2017.12.037.

Bouaid, A. *et al.* (2017) 'Enzymatic butanolysis of coconut oil. Biorefinery approach', *Fuel*. Elsevier Ltd, 209, pp. 141–149. doi: 10.1016/j.fuel.2017.07.040.

Fan, L. W. *et al.* (2013) 'Effects of various carbon nanofillers on the thermal conductivity and energy storage properties of paraffin-based nanocomposite phase change materials', *Applied Energy*, 110, pp. 163–172. doi: 10.1016/j.apenergy.2013.04.043.

Jeong, S. G. *et al.* (2013) 'Improvement of the thermal properties of Bio-based PCM using exfoliated graphite nanoplatelets', *Solar Energy Materials and Solar Cells*. Elsevier, 117, pp. 87–92. doi: 10.1016/j.solmat.2013.05.038.

Pielichowska, K. *et al*. (2016) 'The influence of chain extender on properties of polyurethane-based phase change materials modified with graphene', *Applied Energy*, 162, pp. 1024–1033. doi: 10.1016/j.apenergy.2015.10.174.

Pielichowska, K. and Pielichowski, K. (2014) 'Phase change materials for thermal energy storage', *Progress in Materials Science*. Elsevier Ltd, 65, pp. 67–123. doi: 10.1016/j.pmatsci.2014.03.005.

Putra, N. *et al.* (2017) 'Characterization of the thermal stability of RT 22 HC/graphene using a thermal cycle method based on thermoelectric methods', *Applied Thermal Engineering*. Elsevier Ltd, 124, pp. 62–70. doi: 10.1016/j.applthermaleng.2017.06.009.

Qureshi, Z. A., Ali, H. M. and Khushnood, S. (2018) 'Recent advances on thermal conductivity enhancement of phase change materials for energy storage system: A review', *International Journal of Heat and Mass Transfer*. Elsevier Ltd, 127, pp. 838–856. doi: 10.1016/j.ijheatmasstransfer.2018.08.049.

Saleel, C. A., Mujeebu, M. A. and Algarni, S. (2019) 'Coconut oil as phase change material to maintain thermal comfort in passenger vehicles: An experimental analysis', *Journal of Thermal Analysis and Calorimetry*. Springer International Publishing, 136(2), pp. 629–636. doi: 10.1007/s10973-018-7676-y.

Sari, A. and Karaipekli, A. (2009) 'Preparation, thermal properties and thermal reliability of palmitic acid/expanded graphite composite as form-stable PCM for thermal energy storage', *Solar Energy Materials and Solar Cells*, 93(5), pp. 571–576. doi: 10.1016/j.solmat.2008.11.057.

Saydam, V. and Duan, X. (2019) 'Dispersing different nanoparticles in paraffin wax as enhanced phase change materials: A study on the stability issue', *Journal of Thermal Analysis and Calorimetry*. Springer International Publishing, 135(2), pp. 1135–1144. doi: 10.1007/s10973-018-7484-4.

Sharma, A. *et al*. (2009) 'Review on thermal energy storage with phase change materials and applications', *Renewable and Sustainable Energy Reviews*, 13(2), pp. 318–345. doi: 10.1016/j.rser.2007.10.005.

Sharma, A. *et al.* (2013) 'Development of phase change materials for building applications', *Energy and Buildings*. Elsevier B.V., 64, pp. 403–407. doi: 10.1016/j.enbuild.2013.05.029.

Wonorahardjo, S. *et al.* (2018) 'Potential of Thermal Energy Storage Using Coconut Oil for Air Temperature Control', *Buildings*, 8(8), p. 95. doi: 10.3390/buildings8080095.

Zabalegui, A., Lokapur, D. and Lee, H. (2014) 'Nanofluid PCMs for thermal energy storage: Latent heat reduction mechanisms and a numerical study of effective thermal storage performance', *International Journal of Heat and Mass Transfer*. Elsevier Ltd, 78, pp. 1145–1154. doi: 10.1016/j.ijheatmasstransfer.2014.07.051.

Zhou, D., Zhao, C. Y. and Tian, Y. (2012) 'Review on thermal energy storage with phase change materials (PCMs) in building applications', *Applied Energy*. Elsevier Ltd, 92, pp. 593–605. doi: 10.1016/j.apenergy.2011.08.025.

Zou, D. *et al.* (2018) 'Thermal performance enhancement of composite phase change materials (PCM) using graphene and carbon nanotubes as additives for the potential application in lithium-ion power battery', *International Journal of Heat and Mass Transfer*. Elsevier Ltd, 120, pp. 33–41. doi: 10.1016/j.ijheatmasstransfer.2017.12.024.

#168: Performance analysis of a solid desiccant enhanced indirect evaporative cooling system

Seung JIN OH[1], Kim CHOON NG[2], Wongee CHUN[3]

[1]*Clean Innovation Technology Group, Korea Institute of Industrial Technology (KITECH),102 Jejudaehak-ro, Jeju Special Self-Governing Province, 63243 South Korea, ohs8680@kitech.re.kr*
[2]*Biological and Environmental Science and Engineering Division, King Abdullah University of Science & Technology, Thuwal, 23900 Kingdom of Saudi Arabia, kimchoon.ng@kaust.edu.sa*
[3]*Department of Nuclear and Energy Engineering, Jeju National University,102 Jejudaehak-ro, Jeju Special Self-Governing Province, 63243 South Korea, wgchun@jejunu.ac.kr*

This study proposes a disruptive cooling technology that thermodynamically hybridises two different cooling devices namely, a solid desiccant dehumidifier (SDD) and an indirect evaporative cooler (IEC) in order to enhance the performance IEC for all-weather conditions. Unlike conventional rotary desiccant wheels, the solid desiccant dehumidifier incorporates with desiccant coated heat exchangers to improve moisture removal capacity of desiccant by cooling the adsorption heat of desiccant. The indirect evaporative cooler operates based on M-cycle, which creates sensible cooling effect without the change of moisture level. In the proposed cooling system, the sensible and latent of the air are to be de-coupled. The latent cooling load, which is 25 to 45% of the total cooling load in most weather, is first removed by adsorption of vapour using desiccant coated heat exchangers. The saturated adsorbent is then regenerated by using either low-temperature waste heat from industry and/or renewable energy such as solar energy and geothermal energy. With the de-coupling of the latent cooling, the remaining sensible cooling load is removed by the indirect evaporative process where water is evaporated by the purged air from the dry channel, flowing over water-film surfaces in the wet channel. A numerical simulation has been carried out so as to compare the performance of the cooling system in terms of cooling capacity and dew-point effectiveness with a single IEC. The experimental data obtained from the previous research was employed as the inlet conditions for IEC. Key results revealed that the proposed SDDIECproduced higher cooling capacity, as well as higher dew-point effectiveness under the same operating conditions.

Keywords: desiccant coated heat exchanger; indirect evaporative cooler; de-coupled cooling load; dew-point effectiveness; coefficient of performance

1. INTRODUCTION

Although the air conditioning system has transformed the lives of humans in terms of work efficiency in commercial, residential and industrial buildings for all weather conditions, these improvements have, unfortunately, been accompanied by negative effects, such as the emissions of greenhouse gases (GHG) such as CO2, either directly via refrigerant emissions and indirectly through electricity generation by burning fossil fuels (Shahzad *et al.*, 2017, 2018; 'International Energy Agency, The future of Cooling', 2018). Moreover, the global energy demand for space cooling has been projected to triple in next three decades, requiring new electricity capacity equivalent to the sum of the present capacities of U.S., Europe and Japan combined. Of the 2.8 billion people living today in the hotter and humid regions of the world, only 8 to 10% currently possess air conditioning (AC) units. As the annual income and living standards improve in these developing countries, with higher cooling degree days (CDD), the demand for AC is expected to rise sharply. Consequently, the share of AC consumption to the total electricity generation of affected countries will eventually emerge as the second-largest consumer of global electricity, after the normally expected industrial sector, by 2050 (Izquierdo *et al.*, 2011; La *et al.*, 2012; Waite *et al.*, 2017; 'International Energy Agency, The future of Cooling', 2018).

Recently, there are research groups working in the improvement solutions for efficiency improvement of air-conditioning system (Disawas and Wongwises, 2004; Minh, Hewitt and Eames, 2006; Qureshi and Zubair, 2013; Park *et al.*, 2015; Lee *et al.*, 2016; Choi *et al.*, 2017). However, they have managed only marginal reduction in the kW/RT for cooling because the solutions were mostly based on the conventional cooling cycles. The treatment of outdoor moist air is commonly performed in fin-tube heat exchangers or simply known as the air-handling units (AHUs), usually are supplied with chilled water (a cooling medium):- Both the latent and sensible cooling of return air are treated simultaneously at the AHUs which is circulated with chilled water at 5.5 to 6^{o}C. The low chilled water temperature is needed so that moist air flowing adjacent to the fin surfaces attains a dew-point temperature for vapour molecules to condense. In such a space cooling method, the treatment of the moist and return air can be performed at a finite rate but at the expense of high electricity consumption of around 0.85 to 1.2 kW/RT. Any improvement in either the refrigerant compressors (piston-cylinders, scrolls, screws, and roto-dynamic blades) as well as the heat exchangers or the refrigerants can only yield a marginal reduction in the kW/RT of less than 5%. The main reason for the lack of improvement in cooling efficiency is that these technologies have reached their physical limits constrained by the processes, materials and thermodynamic design of cycles

In this paper, we proposes a disruptive cooling technology that thermodynamically hybridises two different cooling devices namely, a solid desiccant dehumidifier (SDD) and an indirect evaporative cooler (IEC) in order to enhance the performance IEC for all-weather conditions. A numerical simulation has been carried out so as to compare the performance of the proposed cooling system with a single IEC in terms of total cooling capacity and dew-point. The experimental data obtained from the previous research was employed as the inlet conditions for IEC.

2. DESCRIPTION OF THE SOLID DESICCANT ENHANCED INDIRECT EVAPORATIVE COOLER

Figure 1 shows the representation of a solid desiccant enhanced indirect evaporative cooler (SDDIEC) for all weather conditions and depicts its operational process on psychrometric chart. The underlying principle of SSDIEC lies on the concept of decoupling technique where latent cooling load is handled separately from sensible cooling. The latent cooling load, which accounts for 25 to 45% of the total cooling load in most weather conditions, is first removed by adsorption of vapour using adsorbents such as silica gel (process 1- 2). The saturated adsorbent is then regenerated by using either low temperature waste heat from exhaust of processes in industry or renewables such as solar energy and geothermal energy. As a consequence of decoupling of the latent cooling, the remaining sensible cooling load is removed by IEC where water is evaporated by air flowing over water film surfaces (2-1). A single IEC comprises two air channels and three air streams, namely, the supply air that is dehumidified by SDD, the working air that flows in the wet channel, and the product air that is cooled down by the working air. The thin impervious membranes with high orthogonal heat transfer is employed to demarcate wet and dry channels, causing decrease in its dry-bulb air temperature. The air stream in the dry channel exchanges its heat with the interface of the cooled impervious membranes, causing decrease in its temperature while keeping humidity level constant due to the dry channel flow. As the performance of the system is depending upon the evaporating potential of the purged dry air that is flowing over the moist felt, the air must contain lower moisture content for better performance. For the most countries, however, the outdoor air is always humid in summer season, reaching its saturating limit in certain time of the day. The IEC alone cannot perform properly and therefore, the SDD system is introduced prior to the IEC in order to remove the moisture content of the outdoor air.

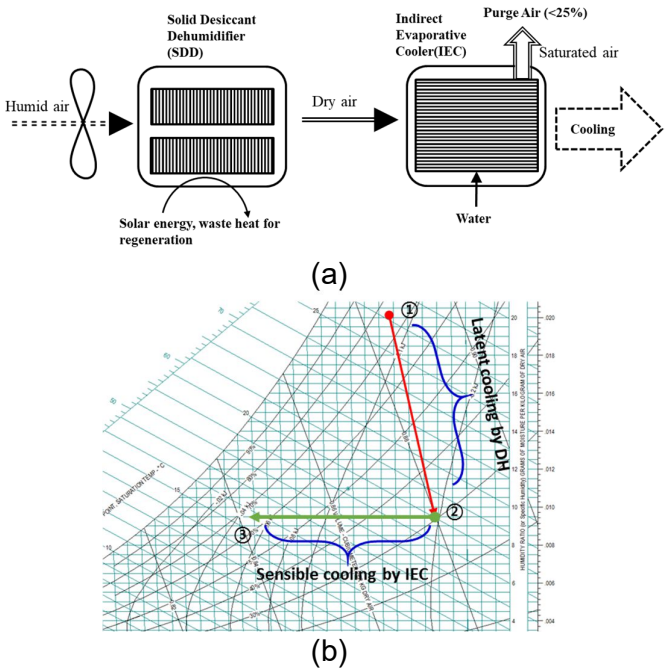

Figure 1: The conceptual design of the solid desiccant enhanced indirect evaporative cooler (a) and its psychrometric process (b)

3. NUMERICAL MODEL FOR IEC

The mathematical model was established to examine the performance of the counter-flow indirect evaporative cooler (IEC) with pre-conditioned process air. The differential control volume consists of half the height of the dry and wet channels, the separating plate, and the water film. To simplify the heat and mass transfer processes, the following assumptions were made:

(1) The air streams in both the dry and wet channels are at steady state for the heat and mass transfer analysis.
(2) Air flow is laminar and fully developed, and heat and mass transfer coefficients are constant.
(3) Heat losses to the surroundings are negligible (adiabatic condition).
(4) The wet surfaces are saturated locally with the water film.
(5) The air velocity and temperature distributions are 1-D with respect to its axial direction.

The dry air channel involves sensible cooling by forced convective heat transfer, leading the change of the enthalpy of the supply air flowing through the channel. The energy balance of air flowing in the dry channel is given by

Equation 1: The energy balance of air flowing in the dry channel.

$$\mathrm{k_a}\frac{d^2T_{da}}{dx^2} = u_{da}rho_{da}c_{p,a}\frac{dT_{da}}{dx} + \frac{h_d}{\overline{H}}(T_{da} - T_p)$$

Where:

- $c_{p,a}$ = specific heat of air-water vapour mixture and it is defined as

Equation 2: The specific heat of air-water vapour mixture.

$$\mathrm{c_{p,a}} = c_{p,a} + \omega c_{p,v}$$

The first term on the left-hand side of Equation (1) represents the longitudinal heat conduction in the air. The second term denotes the energy variation due to the bulk airflow in the longitudinal direction. The term on the right-hand side of equation indicates the convective heat transfer between the air and the plate surface. As both sensible and latent cooling effects are involved in the wet channel, heat and mass transfer mechanisms are considered between the air and water film layer, and it is given as follows

Equation 3: The energy balance of air flowing in the wet channel.

$$k_a \frac{d^2 T_{wa}}{dx^2} = -u_{wa}\rho_{wa}c_{p,wa}\frac{dT_{wa}}{dx} + \frac{h_w}{\bar{H}}(T_{wa} - T_f) + \frac{h_m \rho_{da}}{\bar{H}}[\omega_{sat}(T_f) - \omega_v]c_{p,v}(T_{wa} - T_f)$$

The mass transfer takes place only at the wetted surface, powered by the driving force of vapour partial pressure difference, and its mass exchange is written as

Equation 4: The mass balance of water vapour in the wet channel.

$$\frac{\rho_{da} D_v d^2\omega_v}{dx^2} = \rho_{da} u_{wa}\frac{d\omega_v}{dx} + h_m \bar{H}\rho_{da}(\omega_{v,sat}(T_f) - \omega_v)$$

whilst the energy balances for the water film and the impervious layer are given as

Equation 5: The energy balance of water film.

$$k_f \frac{d^2 T_f}{dx^2} = -\frac{h_w(T_{wa} - T_f)}{\delta_f} - k_f \frac{T_p - T_f}{\delta_f^2} + \frac{h_{fg} h_m \rho_{da}[\omega_{sat}(T_f) - \omega]}{\delta_f}$$

Equation 6: The energy balance of impervious layer.

$$k_p \frac{d^2 T_p}{dx^2} = -\frac{h_d(T_{da} - T_p)}{\delta_p} - k_p \frac{T_p - T_f}{\delta_p^2}$$

In this study, we compared the performance of SDIEC with IEC in terms of total cooling capacity of product air and dew-point effectiveness, which can be calculated by the following formulas:

Equation 7: The total cooling capacity of product air.

$$\dot{Q}_t = \dot{m}_{sa}[i_{in}(T_{da,in}, \omega_{in}) - i_{out}(T_{da,out}, \omega_{in})$$

Equation 8: Dew-point effectiveness.

$$\varepsilon_{dp} = \frac{T_{da,in} - T_{sa}}{T_{da,in} - T_{dp}(T_{da,in})}$$

where the enthalpy of moist air is determined by both the dry air and the water vapour,

Equation 9: The enthalpy of moist air.

$$i = i_a + \omega i_v = c_{p,a} T_{da} + \omega(c_{pv} T_{da} + i_0)$$

$\dot{m}_{sa}$ is the mass flow rate of the supply air, which is determined by the purge ratio. $\dot{m}_{da}$ is the mass flow rate of the air flowing in the dry channel (primary air), which is the sum of the mass flow of working air and the supply air.

Table 1 shows the experimental results of the solid desiccant dehumidifier (SDD) that was investigated for its performance in the previous research (Oh *et al.*, 2017). For IEC, T_{in} and ω_{in} are applied for the inlet condition while for SDIEC, T_{out} and ω_{out} are applied for its inlet condition.

Table 1: Experimental results of the solid desiccant dehumidification system (Oh *et al.*, 2017).

T_{in}[°C]	ω_{in}[g_{vapour}/$kg_{dry\ air}$](%RH)	T_{out}[°C]	ω_{out}[g_{vapour}/$kg_{dry\ air}$](%RH)
30	17.3(65%)	31.7	11.4(39%)
30	20.0(75%)	31.9	12.4(42%)
30	21.4(80%)	32.2	13.2(44%)
34	27.1(80%)	36.4	15.9(42%)
28	19.0(80%)	30.1	11.2(42%)

The mesh grid size is set at 1.0 mm when solving the differential equations. For instance, 1.0 m channel has 1000 cell elements. The governing equations (from Equation (1) to Equation (6)) are solved using the solver (bvp4c) for coupled-nonlinear ordinary differential equations in MATLAB environment.

4. RESULTS AND DISCUSSIONS

Based on the mathematical models, comparative analyses were carried out to identify the differences between the IEC and SDIEC. The SDIEC comprises of a solid desiccant dehumidifier (SDD) and a counter-flow indirect evaporative cooler (IEC). Unlike the IEC, moist air gets dehumidified as it flows through SDD. The dehumidified air then enters the IEC for sensible cooling. Figure 2 depicts the temperature profiles of the product air and the working air for both systems under different inlet air conditions. The red dotted line is the product air in the dry channel of IEC and the blue dotted line indicates the corresponding working air along the wet channel. Whereas the red solid line is the product air in the dry channel of SDDIEC and the blue solid line indicates the corresponding working air. It is clearly observed that SDDIEC produces the product air of lower temperature than IEC for all the inlet air conditions although the inlet air temperature is slightly higher. This is because the dehumidified air has more potential for water film to evaporate to the working air in the wet channel. In the case of SDDIEC, the lowest temperature was observed to be 18.4°C when the inlet temperature was 28°C and the inlet humidity ratio was 19g/kg. The inlet humidity ratio dropped up to 11.2 g/kg after the solid descant dehumidifier. On the other hand, the largest temperature drop of 11.3 K was achieved when the inlet temperature was 30°C and the inlet humidity was 20g/Kg, where the humidity ratio dropped to 12.4g/kg though the SDD.

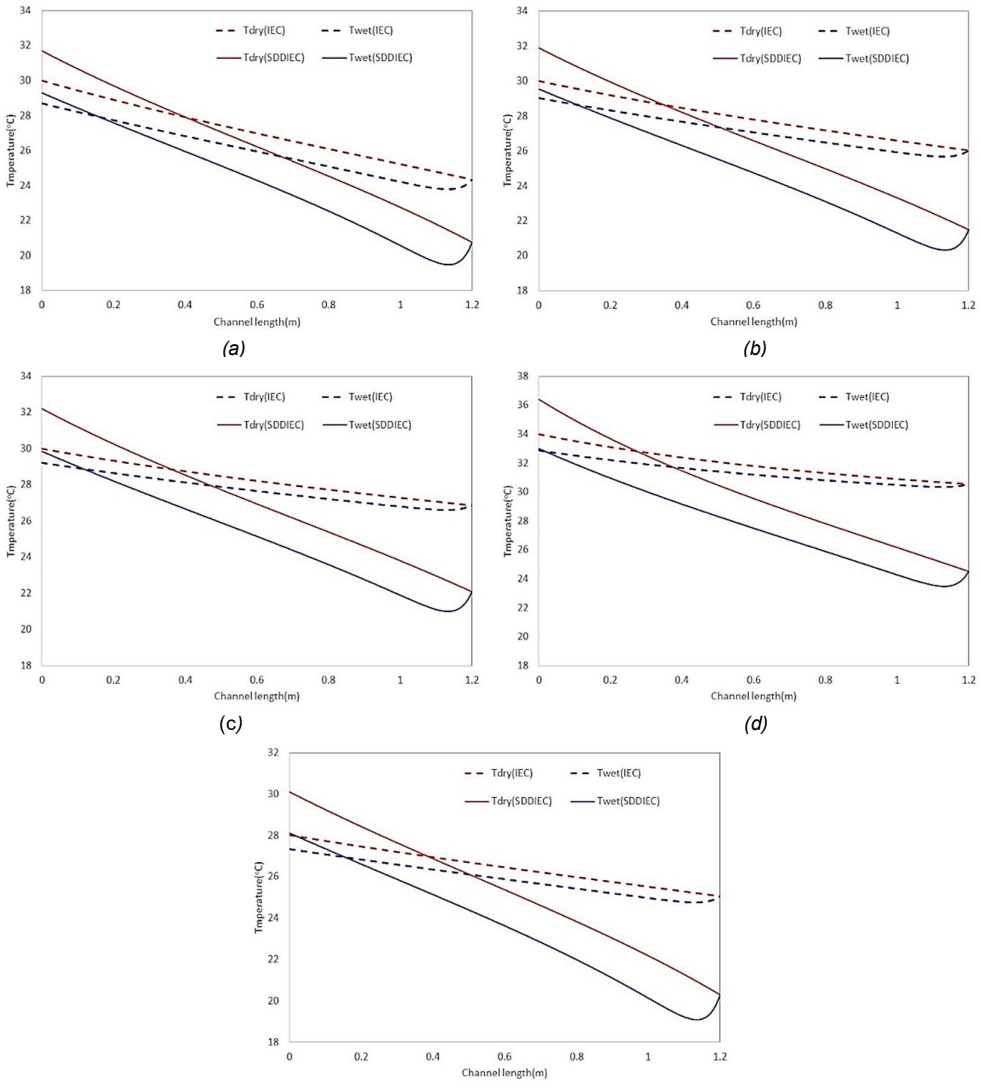

Figure 2: Comparisons of temperature between IEC and SDDIEC under different inlet air conditions: (a)T_{in}=30°C and ω_{in}=17.3 g/kg, (b)T_{in}=30°C and ω_{in} =20.0 g/kg, (c)T_{in}=30°C and ω_{in} =21.4 g/kg, (d)T_{in}=34°C and ω_{in} =27.1 g/kg, (e)T_{in}=28°C and ω_{in}=19.0 g/

Figure 3 shows the cooling capacity and the dew-point efficiency of both systems under different air conditions. It is observed that the total cooling capacities of SDIEC are superior to those of IEC for all the air conditions. The maximum cooling capacity of SDIEC was observed to be 46.9W under the inlet air temperature of 34°C and the inlet omega of 27.1g/kg, which is 10.6 times higher than IEC. It can be seen that the dew-point effectiveness of SDDIEC goes beyond 1.0 while those of IEC maintain below 1.0. This is mainly attributed to the dehumidification effect of SDD. The dew-point temperature depends on the humidity ratio, and it is considered the lowest allowable temperature under the inlet air condition. In SDDIEC, however, the humidity ratio gradually drops during dehumidification process of SDD. Hence, the lowest allowable temperature drops and the dew-point effectiveness increases above 1.0.

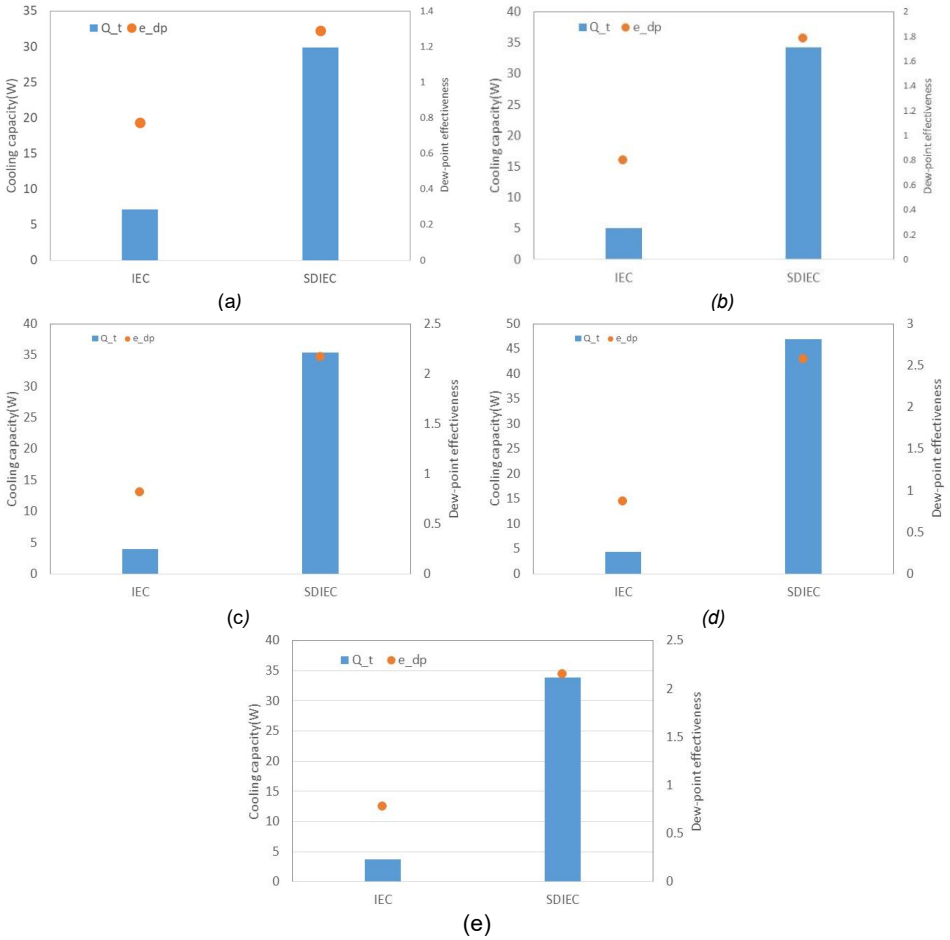

Figure 2: Comparisons of total cooling capacity and dew-point effectiveness between IEC and SDDIEC under different conditions: (a) T_{in}=30°C and ω_{in}=17.3 g/kg, (b) T_{in}=30°C and ω_{in} =20.0 g/kg, (c) T_{in}=30°C and ω_{in} =21.4 g/kg, (d) T_{in}=34°C and ω_{in} =27.1 g/kg, (e) T_{in}=28°C and ω_{in}=19.0 g/

5. CONCLUSION

In this paper, we proposes a disruptive cooling technology that thermodynamically hybridises two different cooling devices namely, a solid desiccant dehumidifier (SDD) and an indirect evaporative cooler (IEC) in order to enhance the performance IEC for all-weather conditions. A numerical simulation has been carried out so as to compare the performance of the proposed cooling system with a single IEC in terms of total cooling capacity and dew-point. The experimental data obtained from the previous research was employed as the inlet conditions for IEC. . The key findings from this study include:

(1) SDDIEC produces the product air of lower temperature than IEC for all the inlet air conditions although the inlet air temperature is slightly higher. This is because the dehumidified air has more potential for water film to evaporate to the working air in the wet channel.
(2) In the case of SDDIEC, the lowest temperature was observed to be 18.4°C when the inlet temperature was 28°C and the inlet humidity ratio was 19g/kg. The inlet humidity ratio dropped up to 11.2 g/kg after the solid descant dehumidifier. On the other hand, the largest temperature drop of 11.3 K was achieved when the

inlet temperature was 30°C and the inlet humidity was 20g/Kg, where the humidity ratio dropped to 12.4g/kg though the SDD.

(3) The total cooling capacities of SDIEC are superior to those of IEC for all the air conditions. The maximum cooling capacity of SDIEC was observed to be 46.9W under the inlet air temperature of 34°C and the inlet omega of 27.1g/kg, which is 10.6 times higher than IEC.

(4) The dew-point effectiveness of SDDIEC goes beyond 1.0 while those of IEC maintain below 1.0. This is mainly attributed to the dehumidification effect of SDD. The dew-point temperature depends on the humidity ratio, and it is considered the lowest allowable temperature under the inlet air condition. In SDDIEC, however, the humidity ratio gradually drops during dehumidification process of SDD. Hence, the lowest allowable temperature drops and the dew-point effectiveness increases above 1.0.

6. REFERENCES

Choi, S. *et al.* (2017) 'Life cycle climate performance evaluation (LCCP) on cooling and heating systems in South Korea', *Applied Thermal Engineering*. Elsevier Ltd, 120, pp. 88–98. doi: 10.1016/j.applthermaleng.2017.03.105.

Disawas, S. and Wongwises, S. (2004) 'Experimental investigation on the performance of the refrigeration cycle using a two-phase ejector as an expansion device', *International Journal of Refrigeration*, 27(6), pp. 587–594. doi: 10.1016/j.ijrefrig.2004.04.002.

'International Energy Agency, The future of Cooling' (2018).

Izquierdo, M. *et al.* (2011) 'Air conditioning in the region of Madrid, Spain: An approach to electricity consumption, economics and CO2 emissions', *Energy*, 36(3), pp. 1630–1639. doi: 10.1016/j.energy.2010.12.068.

La, D. *et al.* (2012) 'Development of a novel rotary desiccant cooling cycle with isothermal dehumidification and regenerative evaporative cooling using thermodynamic analysis method', *Energy*, 44(1), pp. 778–791. doi: 10.1016/j.energy.2012.05.016.

Lee, H. *et al.* (2016) 'Évaluation du LCCP de diverses options de cycle à compression de vapeur et de frigorigènes à faible GWP', *International Journal of Refrigeration*. Elsevier Ltd, 70, pp. 128–137. doi: 10.1016/j.ijrefrig.2016.07.003.

Minh, N., Hewitt, N. and Eames, P. (2006) 'Improved Vapour Compression Refrigeration Cycles: Literature Review and Their Application to Heat Pumps', *International Refrigeration and Air Conditioning Conference at Purdue*, pp. 1–8. Available at: http://docs.lib.purdue.edu/cgi/viewcontent.cgi?article=1794&context=iracc.

Oh, S. J. *et al.* (2017) 'Evaluation of a dehumidifier with adsorbent coated heat exchangers for tropical climate operations', *Energy*, 137, pp. 441–448. doi: 10.1016/j.energy.2017.02.169.

Park, C. *et al.* (2015) 'Recent advances in vapor compression cycle technologies', *International Journal of Refrigeration*. Elsevier Ltd, 60, pp. 118–134. doi: 10.1016/j.ijrefrig.2015.08.005.

Qureshi, B. A. and Zubair, S. M. (2013) 'Mechanical sub-cooling vapor compression systems: Current status and future directions', *International Journal of Refrigeration*. Elsevier Ltd and IIR, 36(8), pp. 2097–2110. doi: 10.1016/j.ijrefrig.2013.07.026.

Shahzad, M. W. *et al.* (2017) 'Energy-water-environment nexus underpinning future desalination sustainability', *Desalination*, 413, pp. 52–64. doi: 10.1016/j.desal.2017.03.009.

Shahzad, M. W. *et al.* (2018) 'A multi evaporator desalination system operated with thermocline energy for future sustainability', *Desalination*, 435, pp. 268–277. doi: 10.1016/j.desal.2017.04.013.

Waite, M. *et al.* (2017) 'Global trends in urban electricity demands for cooling and heating', *Energy*, 127, pp. 786–802. doi: 10.1016/j.energy.2017.03.095.

#169: Energy-efficient control of indoor thermal environment by occupants positioning and comfort range recognition using smart bracelet

Hong Jie CHEN[1], Fulin WANG[2*], Rui YAN[3], Lige ZHAO[4]

[1]*Beijing Key Laboratory of Indoor Air Quality Evaluation and Control, Department of Building Science, School of Architecture, Tsinghua University, Beijing 100084, China, sti70409@gmail.com*
[2*]*Beijing Key Laboratory of Indoor Air Quality Evaluation and Control, Department of Building Science, School of Architecture, Tsinghua University, Beijing 100084, China, flwang@tsinghua.edu.cn*
[3]*Beijing Key Laboratory of Indoor Air Quality Evaluation and Control, Department of Building Science, School of Architecture, Tsinghua University, Beijing 100084, China, yanruiqq135@163.com*
[4]*Beijing Key Laboratory of Indoor Air Quality Evaluation and Control, Department of Building Science, School of Architecture, Tsinghua University, Beijing 100084, China, 709825022@qq.com*

Nowadays, wearable devices are increasingly worn by people which they provide a good opportunity to use such devices to improve indoor thermal environment control. This paper proposed an energy-efficient control method for the indoor thermal environment by occupants positioning and comfort range recognition using a smart bracelet. The smart bracelet measures people's skin temperatures continuously, which is used to on-line learn room occupants' thermal comfort ranges and recognise the thermal comfort states. The smart bracelet is also used to identify the trajectory and position of an object by the value of acceleration data provided by the inertial sensor. Then the positioning information and thermal comfort state information are used to achieve locally personalised thermal environment control, which could be both energy efficient and thermally comfortable. Experiments were conducted to verify the performance of the proposed control method. Experiment results show that the proposed control method has advantages in reducing user's complaints of thermal discomfort and consumes 12.6% less energy than the traditional control method of giving temperature set-points by room occupants.

Keywords: Indoor thermal environment control; skin temperature; thermal comfort; positioning; energy saving

1. INTRODUCTION

There is a great need to reduce energy used for indoor thermal environment control whilst improving indoor environmental comfort levels. Many papers have focussed on thermal comfort, but very few of them study the personalised and localised control strategy of thermal environment. If the indoor thermal environment can be controlled locally according to personalised thermal sensation and occupant positioning instead of generalised space heating/cooling, energy consumption for space heating/cooling might be reduced.

Therefore we propose a control method based on thermal sensation prediction using temperature measured by a smart bracelet. Firstly, the positioning methods are investigated and the positioning technologies suitable for indoor thermal environment control are determined. Secondly, in order to verify that the proposed control method has the advantages in reducing user's thermal discomfort complaints and having better energy efficiency, comparison experiments were conducted between the proposed control method and the control method based on thermal sensation expression. The indoor thermal environment control method based on thermal sensation expression has more advantages in decreasing energy consumption than the traditional set-point-based control method (Wang et al. 2015). By combining thermal sensation prediction with positioning system, the indoor thermal environment can be controlled individually, locally, more comfortable, and more energy efficiently.

2. METHODOLOGY

2.1. Methodology of the positioning

There are many indoor positioning methods, which are used in different scenarios. The algorithms of positioning are investigated to find out the positioning algorithms suitable for indoor thermal environment control.

1). Cell of Origin (COO) / Proximity Detection / Connectivity Based Positioning:
Simple positioning method for applications with low accuracy requirements. Examples include sensors that detect physical contact, automatic identification systems and mobile wireless positioning systems.

2). Centroid Determination:

Determination of Centroid location involves consideration of multiple beacon positions within the detection range and simple positioning of the beacon at the Centroid, or determine the position of the weighted center of mass, where the weight is set according to the RSSI value, distance or uncertainty of each beacon.

3). Lateration/Trilateration/Multilateration:
All three terms refer to location determination of distance measurement. Usually 2D / 3D position is obtained by redundant calculation from the distance measurement of two or more nearby nodes.

4). Polar Point Method/Range-Bearing Positioning:
The Polar Point Method uses the distance and Angle measurements of the same station to determine the coordinates of nearby stations. This method is useful because it only needs to be measured from a station (assuming the direction is also known). Pole location can be conveniently determined for geodetic survey.

5). Fingerprinting (FP)/Scene Analysis/Pattern Matching:
The standard number of fingerprint libraries (FP) is radio frequency RSSI, but FP can also be used for acoustic processing through the visual aspect of sound or image. Fingerprints usually consist of two phases. First is the off-line calibration phase, which empirically sets or analyses the calculation to establish the fingerprint. The former is to accept a series of signal points from fixed stations and input them into the database; the second stage is the operation stage, the current point to be measured in the database to find the best matching point. In the second case the analytical model generation is used to avoid precise calibration measurements. Therefore, the signal propagation model can be used to calculate the signal strength reference value.

6). Dead reckoning:
The main sensor is inertial navigation. The precise position can be inferred by the method of position prediction, but it is susceptible to subtle errors and the error will accumulate over time (Foxlin 2005, Yang et al 2017).

7). Map Matching (MM):
A Map Matching algorithm (also known as Map Measurement) combines current location data with spatial map data to identify the correct link on which a pedestrian (or vehicle) is traveling, while improving position accuracy. The use of maps is an economical option for installing additional hardware. MM technology includes topology analysis, pattern recognition or hierarchical fuzzy reasoning algorithm and other advanced technology.

The commonly indoor positioning technology which is the integration of mapping technology and information technology using in daily life. The upper mentioned positioning methods can be divided into two categories (Trany et al, 2019). First, Infrastructure-based: The positioning sources provide sufficient positioning accuracy for common applications when network devices are pre-installed in buildings, such as Pseudolite, WIFI, RFID, UWB (Ultra-Wide Band), Infrared, Ultrasonic, LIFI (Light Fidelity), Bluetooth, etc. Second, Infrastructure-free: Requires no external facility support with the advantages of autonomy, such as Computer vision, IMU (Inertial Measurement Unit), magnetic and so on.

In addition, with the rapid development of Micro-electromechanical Systems (MEMS) technology, a variety of sensors (such as gyroscopes, accelerometers, magnetometers and barometers, etc.) are constantly reduced in size and cost, so they are widely used in various types of mobile intelligent terminal equipment. However, since it is not easy to accurately obtain the pedestrian step size and heading information in the PDR (Pedestrian Dead Reckoning) algorithm, and the current position calculation is dependent on the historical position information of the target, the positioning result will contain cumulative error, resulting in poor positioning accuracy over a long period of time (Wang and Liu 2015). The Bluetooth Low Energy (BLE) fingerprint positioning technology has the advantages of low power consumption, low cost, long-term high precision, etc., but the Received Signal Strength Indicator (RSSI) jitter caused by multi-path interference will seriously affect the accuracy of BLE fingerprint positioning (Lee and Min 2017). At the same time, due to the small coverage of a single BLE anchor, the adaptability of the system is not strong.

As a summary, the precision, stability, cost and difficulty of indoor positioning methods former mentioned are compared by Table 1. The advantages and disadvantages of indoor positioning methods are listed in Table 2.

By comparing the positioning methods available, the smart bracelet is selected to make a positioning system and combine with the air conditioning control system to achieve personalised indoor thermal comfort control. According to the existing technology products, we use Bluetooth and MENS algorithm to realise. First, based on the algorithm of positioning using smart bracelet, personal location can be recognised. Second, personalised thermal comfort range of each individual can be identified using on-learning algorithm. Third, the test bed is constructed using the positioning and personalised thermal comfort control algorithm and experiments are conducted to verify the performances of the developed control system. The following sections introduce the personalised thermal comfort control algorithm and experiment results.

Table 1: Comparison of indoor positioning method

	Precision	Stability	Cost	Difficulty
Pseudolite	cm	medium	high	medium
WiFi	Fingerprint-3m	medium	low	low
RFID	5m	medium	medium	low
UWB	15cm	High penetrating power	high	high
Infrared	5m	low	high	medium
Ultrasonic	cm	medium	medium	low
LiFi	cm	medium	low	medium
Bluetooth	Fingerprint-2m	medium	low	low
Computer vision	camera way-cm/others-m	medium disturb by light	high	high
IMU	Depending on the device	high	low	medium
magnetic	2m	disturb by environment	low	high

Table 2: Comparison of indoor positioning advantage and disadvantage

	Advantage	Disadvantage
WiFi	Recognise identity No additional equipment Low cost, simple algorithm	Influence the effectiveness of positioning Users may cause error recognition when they join other WIFI
RFID	Fast communication rate Small antenna size	No communication with other equipment
UWB	Low transmit power Strong penetration ability	Interfere with other communication systems Construction is complex and expensive
Infrared	The recognition method is simple and accurate	Transmission distance is short Penetration is very poor
LiFi	High speed	Easily distracted by lights
Bluetooth	Low power consumption. Popular	Not stable Greatly disturbed by the noise signal.
Computer vision	Identity can be recognised high accuracy	Multiple cameras are needed from all angles High cost Privacy issues Large amount of graphics computation
IMU	Location is not influenced by signal intensity.	Used as an auxiliary Motion can influence the accuracy of calculation.

2.2. Methodology of thermal sensation prediction control

After the room occupant's location is identified by the positioning method former mentioned, the next step is to control the local thermal environment where the occupant locates to achieve personalised thermal comfort. The personalised thermal environment control is achieved based on the predicted thermal sensation, which is recognised by the temperature of skin through a smart bracelet with a temperature sensor. The reason why using the bracelet as the temperature measurement method is that it is easily available and easy to combine with control system. Accordingly, the indoor environment control system measured by smart bracelet is developed, including the following steps:

1) Set the initial value of comfortable skin temperature comfort range according to literature recommendation.
2) Occupants wear their own smart wristband to measure the skin temperature, and then do the ordinary work in the room.
3) The computer keeps collecting the data of the occupants' skin temperature, and occupants can submit their hot/cold thermal complaints through their own Human Machine Interface (HMI), e.g., an APP on their smartphone, when they feel thermally uncomfortable.
4) Each occupant's comfortable skin temperature range can be updated through on-line learning algorithm.
5) According to real-time measure of skin temperature and one's comfortable skin temperature range, a fuzzy control logic is used to predict each occupant's thermal state.
6) Determine the thermal state of each occupant and decide the thermal state of group occupant.
7) Adjust the indoor air temperature and set point according to the group thermal state.
8) Use the Proportional-Integral-Differential (PID) controller to tune the room temperature by changing the output of air-conditioners.

Regarding the space with multiple occupants, the space temperature setting is decided according to the intersection of the comfort ranges of all occupants. If there is no intersection of all the comfort ranges, the intersection of the major comfort ranges is used.

3. EXPERIMENT

The comparison experiment of the control based on the thermal sensation prediction control method using the temperature measured by smart bracelet and the control based on thermal sensation expression (Wang et al. 2017) are carried out according to the experimental procedure shown in Figure 1 and Figure 2 respectively. During the experiment, three subjects entered the experimental room, started normal office activities, and complained when they felt cold or hot with the HMI on the smart phones.

The difference between the two experiments is whether the subjects had the smart bracelet or not. The duration of each experimental unit was 4 hours and in total 10 experiments were conducted for one subject group. After each experiment unit, each subject was required to fill in a questionnaire to evaluation the thermal sensation, thermal comfort level, and satisfaction level during the experiment.

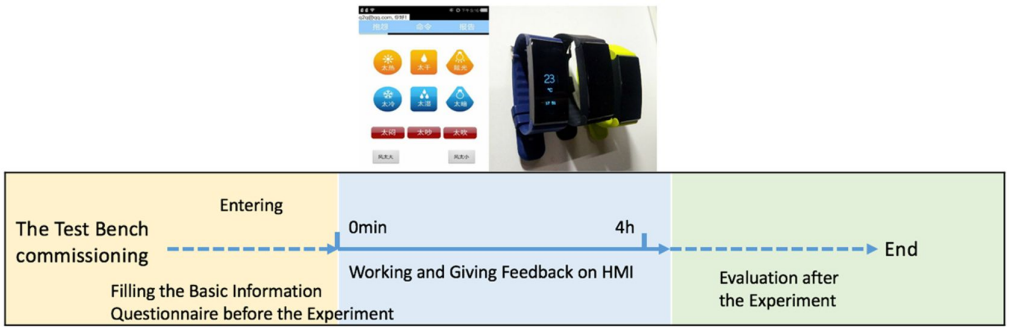

Figure 1: Experiment procedure of control based on thermal sensation prediction using smart bracelet

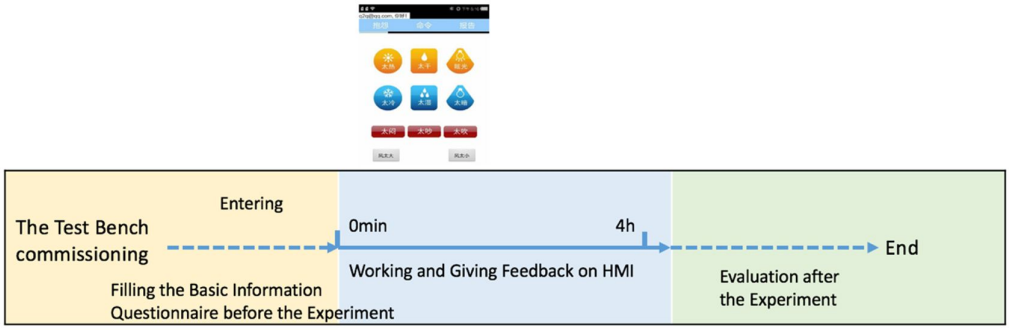

Figure 2: Experiment procedure of control based on thermal sensation expression

Two groups of six subjects from the students of Tsinghua University were recruited to conduct the comparative experiment. Their basic information is showed in Table 3. The experiment subjects are discussed below.

Table 3: Basic Information of Subjects for Experiment

Subject No.	Gender	Age	Height/cm	Weight/kg	Years in Beijing/year
1	Female	22	175	70	>3
2	Female	22	155	46	>3
3	Male	21	180	65	>3
4	Female	19	160	45	1-3
5	Female	21	158	55	1-3
6	Male	18	180	80	<1

Thermal sensation prediction

The typical experiment results of one experiment unit of the control based on the thermal sensation prediction using the temperature measured by smart bracelet is shown in Figure 3.

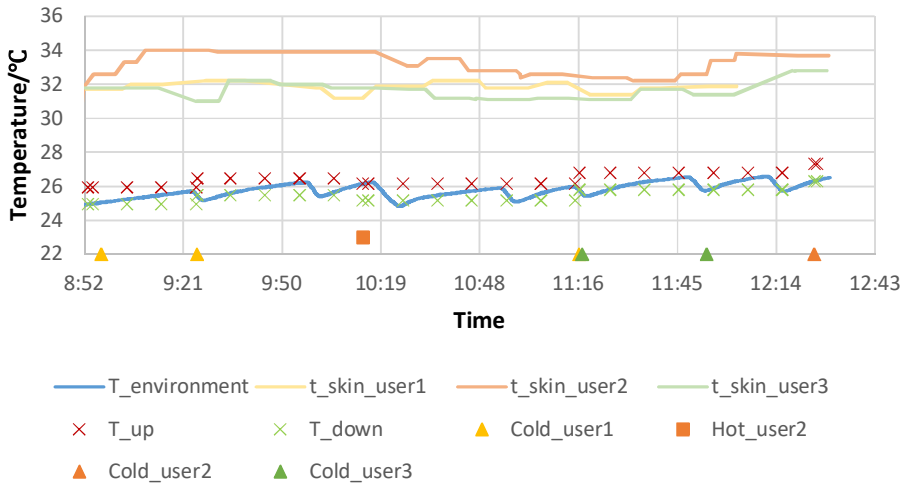

Figure 3: Typical experiment results of one experiment unit of the control based on the thermal sensation prediction

Thermal sensation expression

The typical experiment results of one experiment unit of the control based on the thermal sensation express through HMI is shown in Figure 4.

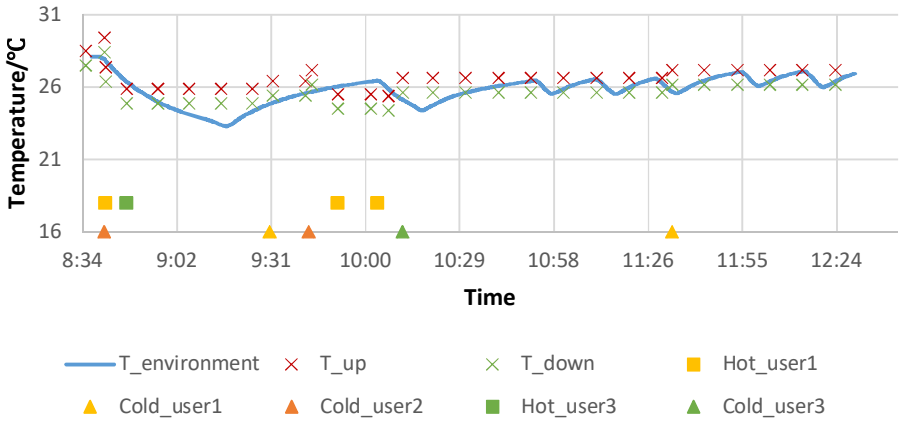

Figure 4: Typical experiment results of one experiment unit of the control based on the thermal sensation express through HMI

Comparison of energy consumption between the two control methods

The main energy consumption for indoor thermal environment control is related to the air conditioning system. Therefore, the energy consumptions of the two indoor thermal environment control methods are compared by the following equations.

Equation 1: Energy consumption of air-conditioning system. $$P = P_{rating} \times RE(t_{in}, t_{out})$$

Where:

P_{rating}: Rated power consumption of air-conditioning system, kW

$RE(t_{in}, t_{out})$: Relative power consumption to rated power consumption at the indoor temperature t_{in} and outdoor temperature t_{out} , kW

The relative power consumption to rated power consumption at the indoor temperature t_{in} and outdoor temperature t_{out} is fitted using the air-conditioner's specification data. The fitted relative power consumption is shown in Equation 2.

Equation 2: Relative power consumption to rated power consumption. $RE = (0.0113t_{in} + 0.0965) \times (0.0409t_{out} + 1.1042)$

Using the upper mentioned equations, the calculated energy consumption of the control based on thermal sensation prediction is slightly lower than the power consumption of the control based on thermal sensation expression. The power consumption of the air conditioning system based on the thermal sensation prediction is 1.6% lower than the air conditioner system based on the thermal sensation expression control. The former study has showed the control based on thermal sensation expression can save energy consumption by 11% compared with the traditional control method based on the set point given by room occupants (Wang et al 2015). Therefore, compared with the traditional control method, the proposed control method can save energy by 12.6%.

Discussion

The results described upper is based on the experiment results of 6 subjects. The subject number is not large enough to prove the results are statistically reliable. The experiments are undergoing. Further results will be added in the future experiments.

4. CONCLUSION

Among all the indoor positioning methods, BLE also known as beacon positioning can achieve the accuracy of 2 meters. Therefore, occupants' location information provided by a smart bracelet with BLE is very suitable for the enhanced air-conditioning system control. However, BLE signals are not always available or dramatically decreased by exist mental decoration material. If MEMS inertial sensors are fused with BLE, the positioning information will still satisfy the requirement in a short time when BLE signals are abnormal. Thermal sensation prediction system combines Bluetooth with MEMS position system in the smart bracelet is the new innovation in air-conditioner control method to achieve energy-efficient thermal environment. Comparison experiment show that the control based on personalised thermal comfort prediction can save 12.6% of energy consumption compared with the traditional control method based on the set point given by room occupants. These preliminary results proved that the control based on personalised thermal comfort prediction is the key to save energy in the field of indoor thermal environment control and achieve better comfort and satisfaction of room occupants.

5. ACKNOWLEDGEMENT

This research is supported by National Key R&D Program of China, Research and Demonstration of Key Technology of Net-Zero Energy Building (Project Number 2016YFE0102300) and Innovative Research Groups of the National Natural Science Foundation of China (Grant number 51521005).

6. REFERENCES

Foxlin E, 2005, Pedestrian tracking with shoe-mounted inertial sensors, IEEE Computer Graphics and Applications, 25(6), 38–46.

Huy Trany, Abhishek Mukherjiy, Nirupama Bulusu, Santosh Pandeyy,2019. Improving Infrastructure-based Indoor Positioning Systems with Device Motion Detection, IEEE International Conference on Pervasive Computing and Communications (PerCom 2019), Kyoto, Japan.

Lee K, Nam Y, Min S D, 2017. An indoor localization solution using Bluetooth RSSI and multiple sensors on a smartphone. Multimedia Tools & Applications, 77(10), 12635–12654.

Li X, Wang J, Liu C, 2015. A Bluetooth/PDR Integration Algorithm for an Indoor Positioning System. Sensors, 15, 24862-24885.

Yang W, Xiu C, Zhang J M, et al, 2017. A novel 3D pedestrian navigation method for a multiple Sensors-Based Foot-Mounted inertial system, Sensors, 17, 2695.

Wang F, Chen Z, Jiang Y, et al, 2015. Study on Indoor Thermal Environment Control Based on Thermal Sensation, HVAC, 45(10), 72-75. (in Chinese)

Wang F, Han D, Sun Z, et al, 2017. Review of indoor thermal environment automatic control methods. HVAC, 47(12),1-7. (in Chinese)

#173: Effect of SiO_2 dopant on thermal energy density, morphology and crystal structure of $CaCO_3$/CaO heat storage system

Azhar Abbas KHOSA, Chang Ying ZHAO*

Institute of Engineering Thermophysics, School of Mechanical Engineering, Shanghai Jiao Tong University (SJTU), Shanghai 200240, China
**Corresponding author: changying.zhao@sjtu.edu.cn*

Calcium carbonate demonstrates huge potential to be a part of thermal storage applications. Its decarbonation at high temperatures makes it favourite for integration in concentrated solar power plants for their smooth operation. In this paper, silicon dioxide (SiO_2) has been doped into $CaCO_3$ at different loadings and the thermal energy density of all the samples was determined. Afterwards the effect of dopant on the heat storage process and heat storage efficiency of the developed thermochemical composite were investigated. The enthalpy of reaction and the specific heat capacity were analysed in order to predict the heat storage capacity. Cyclic tests were performed to determine the reusability of the material. The samples were tested non-isothermally at different heating rates to get the thermogravimetric data for analysis. It was found that the loading of dopant helped to increase the rate of decarbonation reaction, thereby making the heat storage process efficient as compared with pure $CaCO_3$. It was observed that the large quantity (15% and 30%) of dopant had introduced a new phase of Ca_3SiO_5 during the decomposition of $CaCO_3$. In addition, volumetric as well as gravimetric energy storage densities decreased with the increase in amount of dopant.

Keywords: thermochemical heat storage; catalysis; non-isothermal methods

1. INTRODUCTION

One of the major applications of thermal energy storage (TES) systems is to regulate the intermittent operation of renewable energy systems. The currently known TES systems are thermochemical, sensible and latent (Gil, Medrano et al., 2010; Medrano, Gil et al., 2010). However, two TES systems (sensible and latent) have a common drawback that they cannot be installed in applications where long-term (seasonal) energy storage is required (Pan and Zhao, 2017). Furthermore, latent and sensible heat storage systems have lower energy storage density as compared to thermochemical system. For example, the heat storage density of latent systems ranges in between 100-500 kJ/kg, whereas for a thermochemical system, it is between 1000-3000 kJ/kg. Therefore, thermochemical heat storage systems are emerging across the globe due to higher energy storage density of materials and long-term (seasonal) storage capacity. Nevertheless, technologically thermochemical systems are less mature and their system design is complex (Ervin, Chung et al., 1974; Tamme, 2011).

Thermochemical systems require a chemical material for storing and extracting heat. Yan et al. (2015) described many criteria for choosing a suitable material, as for instance: (1) Reactions with high reversibility, moderate temperature, no by-products and high enthalpy. (2) Easily separable and stable reaction products for storing purposes. (3) Products and reactants should be non-explosive, non-toxic, non-flammable and non-corrosive. (4) Material should be cheap and abundant. The commonly known high temperature reaction pairs for thermochemical systems are MgH_2/Mg, $CaO/CaCO_3$, CoO/Co_3O_4, $Ca(OH)_2/CaO$, NH_3/H_2 and CH_4 (Chen, Jin et al., 2018). From the previously mentioned reaction pairs, calcium hydro-oxide and calcium carbonate are preferred because they are economical, readily available and highly safe. Moreover, no by-products are formed during the reaction, and their energy storage densities are comparatively higher than the rest of the mentioned materials as for $Ca(OH)_2$ and $CaCO_3$ it is 0.39 and 0.49 kWh/kg, respectively (Pardo, Deydier et al., 2014). As $CaCO_3/CaO$ pair requires a high reaction temperature (890 °C); so it can be employed in high temperature applications like concentrated solar power plants. $CaCO_3$ has shown many preferences, its reaction enthalpy is high (177.8 kJ/mol); it produces gaseous CO_2 and powdered CaO which is normally stable at room temperature; furthermore, the heat energy can be stored for a long time (Ervin, 1977). The chemical equation for the reaction is as follows.

Equation 1: Chemical equation of $CaCO_3$

$$CaCO_3 + 177.8\ kJ/mol \leftrightharpoons CaO + CO_2$$

Carbonation and decarbonation processes of $CaCO_3$ are crucial for its use in thermochemical systems. Many investigations have been performed to improve the system by focusing on those factors that affect the reactivity, such as residence time (Perejón, Miranda-Pizarro et al,. 2016), particle size (N'Tsoukpoe, Restuccia et al., 2014), temperature (Lee, Jang et al., 2012) and atmosphere (Duelli, Charitos et al., 2015). Additionally, for performance improvement inert materials were introduced to parent material in order to increase the reactivity of solid particles. For example, an inert material SiO_2 was doped in $CaCO_3$ that affected the decomposition reaction mechanism of the material. This process followed the one-dimensional diffusion model instead of contracting sphere model (in case of pure $CaCO_3$); and as a result activation energy was reduced from 187 kJ/mol to 155 kJ/mol (Shui, Yue et al., 2002). Since silica is a heat receptor and its particles create defects in the crystalline morphology of $CaCO_3$. In another study, SiO_2 was coated on $CaCO_3$ with different weight percentages (0.25%, 1% and 2%). Results showed that lower percentages (0.25% and 1%) caused a decrease in the activation energy of the material. However, higher percentages caused an increase in activation energy because silica particles prohibit the diffusion of CO_2 (Kumar, Maiti et al., 2016). It was reported elsewhere that doping of SiO_2 with more than 5% can cause an increase in activation energy, while 5% was suggested as the optimal loading of SiO_2 because this helped to decrease the activation energy by 40 kJ/mol (Chen, Jin et al., 2018). While for facilitating the calcination at moderate temperatures and lower pressures of CO_2, $CaCO_3$ was thermally pre-treated and coated with nano-silica which consequently aided to avoid the sintering of CaO particles (Valverde, Barea-López et al., 2017). On the other hand, Coating $CaCO_3$ with AlOOH changed the decarbonation mechanism to one-dimensional (D1) model from contracting area (R2) and the activation energy condensed to 90 kJ/mol (Jin, Yu et al., 2009). Doping CeO_2 in CaO helped in achieving the faster carbonation of CaO and the activation energy reduced to 40 kJ/mol from 107 kJ/mol (Yanase, Maeda et al., 2017).

In addition to all above-mentioned parameters, a reaction pair is required to withstand a number of cycles of synthesis and decomposition reactions before it can be used in an actual system. Barker (Barker, 1973) performed 40 cycles of decomposition and carbonation on $CaCO_3$ at 866°C and reported that decomposition to CaO was complete but the reactivity of CaO with CO_2 decreased after each cycle. Hydration technique was applied on $CaCO_3$ to increase its reversibility, which resulted in an improvement of 35-40% than the unhydrated $CaCO_3$. Nevertheless, the conditions to achieve this process are hindrance in its industrial applications that are low temperature and high pressure (Erans, Manovic et al., 2016). A much better technique was introduced by researchers through doping of TiO_2 (Wang, Zhu et al., 2013) and Li_2SO_4 (Lu and Wu, 2016) in $CaCO_3$ to increase its cyclic stability at high temperatures, the dopants prevented the sintering of CaO particles at high temperature and allowed it to react with more CO_2. Different forms of $CaCO_3$ e.g. dolomite, limestone and marble were studied and it was found that reactivity of CaO produced by dolomite did not decrease because of the presence of MgO that acted as inert material and helped CO_2 to diffuse more into smaller pores and react with more CaO particles (Benitez-Guerrero,

Sarrion et al., 2017). It was observed in another study that the sintering of CaO particles can be avoided by adding $Ca_3Al_2O_6$ during carbonation reaction and CO_2 can react more with CaO particles by diffusion (Jing, Li et al., 2017). Chen et al. (Chen, Zhang et al., 2016) achieved storage conversion of 0.79 over 50 cycles for a CaO to MgO ratio of 10:1 and storage conversion was 0.76 for CaO to MnO_2 ratio of 50:1. Therefore, it can be deduced that to enhance the cyclic stability and reversibility of $CaCO_3$/CaO reaction pair, doping of inert material is a possible and applicable option.

In most of the studies presented above researchers attempted different methods to increase the reversibility of the reaction by increasing the diffusion of CO_2 and decreasing the sintering of CaO particles. The focus was to maintain the cyclic stability of the material at high temperatures for use in practical applications by inserting inert materials such as SiO_2, AlOOH, CeO_2, $Ca_3Al_2O_6$, TiO_2, Li_2SO_4 and MgO. Chen et al. (Chen, Jin et al., 2018) has studied the effect of SiO_2 doping on thermodynamic properties of the $CaCO_3$. The studies using SiO_2 as dopant have not determined the thermal energy densities (volumetric and gravimetric) (Shui, Yue et al., 2002; Valverde, Perejón et al., 2012; Kumar, Maiti et al., 2016; Valverde, Barea-López et al., 2017; Chen, Jin et al., 2018). The studies were conducted by doping with small amounts of dopants and an optimal amount has been suggested. According to reference (Wang, Lee et al., 2008) SiO_2 and $CaCO_3$ can react with each other at 800°C. In this study, we have analysed the effect of large amount of dopant on the heat storage properties of material. It was observed that whether any other phase appeared after the addition of large amount of dopant or not. Heat storage efficiency as well as heat storage capacity of the materials was studied. The durability of the material was examined by performing repeated cycles of tests. Additionally, volumetric and gravimetric thermal energy densities of all the prepared samples are determined.

2. MATERIALS AND METHODOLOGY

2.1. Materials

$CaCO_3$ and SiO_2 (99.5% purity with particle size of 15 nm) were purchased from Sinopharm Chemical Reagent Company Limited and Aladdin Industrial Corporation, respectively. The proximate analysis of $CaCO_3$ is listed in Table 1. For the preparation of SiO_2/$CaCO_3$ thermal composite three different concentrations of SiO_2 (5%, 15% and 30%) were employed. Both pure and doped (by silicon dioxide) samples of calcium carbonate were analysed through simultaneous temperature analyser (STA8000 of PerkinElmer). At first, the required amount of $CaCO_3$ was dissolved in water (30 ml) followed by addition of SiO_2, the temperature of solution was maintained at 60°C for 15 min under constant mechanical stirring. Afterwards, the slurry was dried at 120°C for 5 hours and pulverised to get a fine powder. The prepared powder samples were heated non-isothermally up to 900°C by using three different heating rates of 5, 10 and 15°C/min, and 650°C was selected as the initial temperature because the decarbonation starts after this temperature. After approaching the maximum temperature (900°C), the samples were heated constantly for 10 min to allow complete decomposition of material. Argon gas with high purity (99.999%) was introduced as purge gas and the flow rate was 50 ml/min.

Table 1: Content of impurities present in the commercial $CaCO_3$.

Impurities in $CaCO_3$	Quantity (%)
Chloride	≤0.002
Sulphate	≤0.01
Alkalinity(as OH-)	≤0.25
Heavy metals(as Pb)	≤0.001
Sodium	≤0.1
Magnesium	≤0.05
Potassium	≤0.005
Iron	≤0.001
Barium	≤0.02
Strontium	≤0.05
Substances insoluble in hydrochloric acid	≤0.01

2.2. Cyclic tests

All prepared samples were tested in STA to obtain cyclic stability analysis. The sample size was maintained between 9.5±0.5 mg. During calcination process, samples were heated at a rate of 50°C/min in an inert atmosphere of Argon gas (99.999%) at 800°C for 10 minutes. Carbonation process was carried out for 10 min in highly pure carbon dioxide environment where samples were cooled down to 600°C at a rate of 50°C/min. The flow rates of Ar and CO_2 were 50 ml/min and 100 ml/min, respectively. After the completion of first cycle of decomposition and synthesis of $CaCO_3$, the process was repeated by heating the samples from 600°C to 800°C for decarbonation and the goal of 15 cycles was achieved in the same way.

2.3. Thermodynamic properties

Specific heat capacity of the pure and SiO_2 doped CaO and $CaCO_3$ materials was determined using the differential scanning calorimeter (DSC 8000 from the PerkinElmer). The weight of the samples was kept same (11.5±0.5) for analysis. Pure samples and samples doped with 15% SiO_2 were analysed and step-scan method was employed to heat up the samples to 400°C from 50°C with the heating rate of 10°C/min. Nitrogen (99.999%) was used as purge gas and the flow rate was set at 20 ml/min.

2.4. Morphology and crystal structure

The materials were analysed at room temperature for the identification of phases and crystalline structure using XRD from Da Vinci modelled D8 ADVANCE. SEM analysis of the samples was performed by JSM-7800F that helped to figure out the grain size, microstructure and surface morphology of the material. For more clarity about the chemical composition of the prepared samples, infrared radiations were passed through the material using Fourier Transform technique using NICOLET 6700 FT-IR by Thermo Scientific and the results are presented in Figure 1.

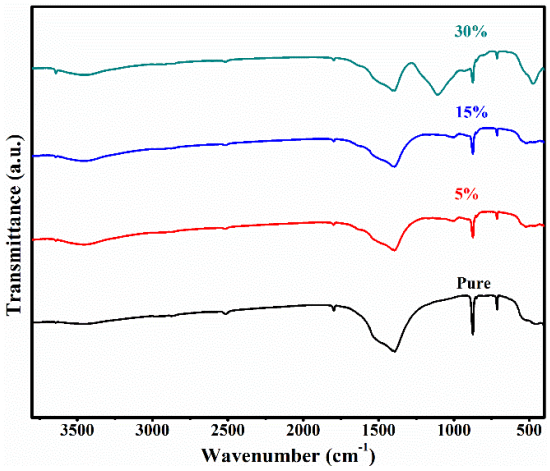

Figure 1: FT-IR analysis of all the prepared samples after mixing the materials

3. RESULTS AND DISCUSSION

3.1. Structural analysis

For better understanding the phases and crystal lattice of the pure and composite samples of $CaCO_3$, they were analysed by adopting XRD. The samples were analysed before heating at decomposition temperature and the diffraction patterns of all the SiO_2 doped samples were in accordance with the pure $CaCO_3$ as presented in the Figure 2a. The same was observed when XRD results were imported to the Jade 6.5 software and compared with the peaks available in the software. The structural phases and the planes obtained from XRD were in accordance with the JCPDS card number 05-0586. Hence, it was clear that all the peaks were in line with the pure phase this indicated that no secondary phase appeared in the samples during the mixing process. Chen et al. (Chen, Jin et al. 2018) used the ball milling method for mixing and did not find any other secondary phase after mixing. The reflection planes of $CaCO_3$ doped with SiO_2 crystal phase are clearly indexed in Figure 2a. The SiO_2 acted as a heat receptor and helped to enhance the heat absorbing properties of the parent material by causing cracks in the crystal lattice of the $CaCO_3$.

XRD patterns of calcined samples are presented in Figure 2b. The clear decomposition of all the samples was observed in the form of CaO (JCPDS card number 48-1467). Additionally, other minor secondary phase Ca_3SiO_5 (JCPDS card number 31-0301) was also observed in 15% and 30 % doped SiO_2 samples, this is well matched with Wang et al. (Wang and Lee 2009). Samples with the high amount of dopant depicted another phase (Ca_3SiO_5); the new phase was stable and it does not affect the performance of the material. Even it helps in the reversibility of the reaction at much lower temperatures (Wang, Lee et al. 2008, Wang and Lee 2009). The same effect was observed during the cycling test performed on the samples. The samples with Ca_3SiO_5 depicted a remarkable performance and their reversibility to carbonate was easier and faster.

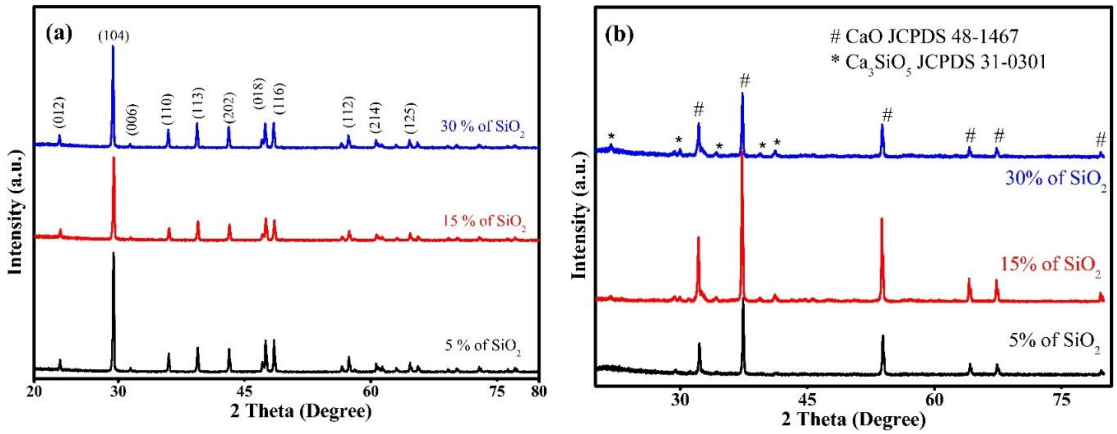

Figure 2: XRD structural analysis of $CaCO_3$ doped with different concentration of SiO_2 (a) before decomposition (b) after decomposition.

3.2. SEM analysis

The composite samples prepared by physical mixing technique were analysed with the help of SEM to better visualise and understand the morphology and particle shape of material. It was observed that after doping with different concentrations of SiO_2 surface morphology was spread with more pores depiction (Figure 3). While Figure 3c leads to the fact that particles are closely packed for higher percentage such as 30%. The rectangular particle shape was observed as a whole and the similar morphology was reported by Kumar et al. (Kumar, Maiti et al. 2016). Henceforth, it was concluded that after mixing with physical method the shape and morphology of the parent material remained same even it was doped with SiO_2.

The SEM images of samples after decarbonation are shown in Figure 4. The micrographs indicate that SiO_2 improved the porosity of the samples and the material did not sinter during the decomposition. This helped the whole sample to decompose quickly and the extraction of CO_2 produced more pores. Hence, after calcination the porous structure was observed in the SEM analysis.

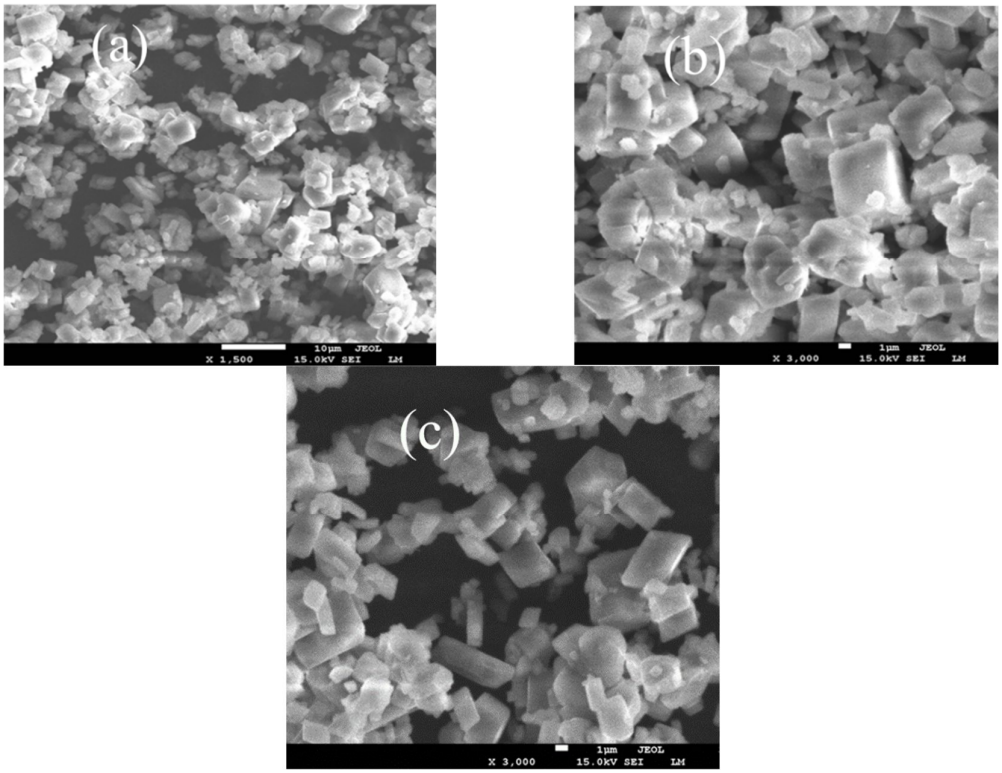

Figure 3: Surface morphology of $CaCO_3$ doped SiO_2 (a) 5 % SiO_2 (b) 15 % SiO_2 and (c) 30 % SiO_2 before decomposition.

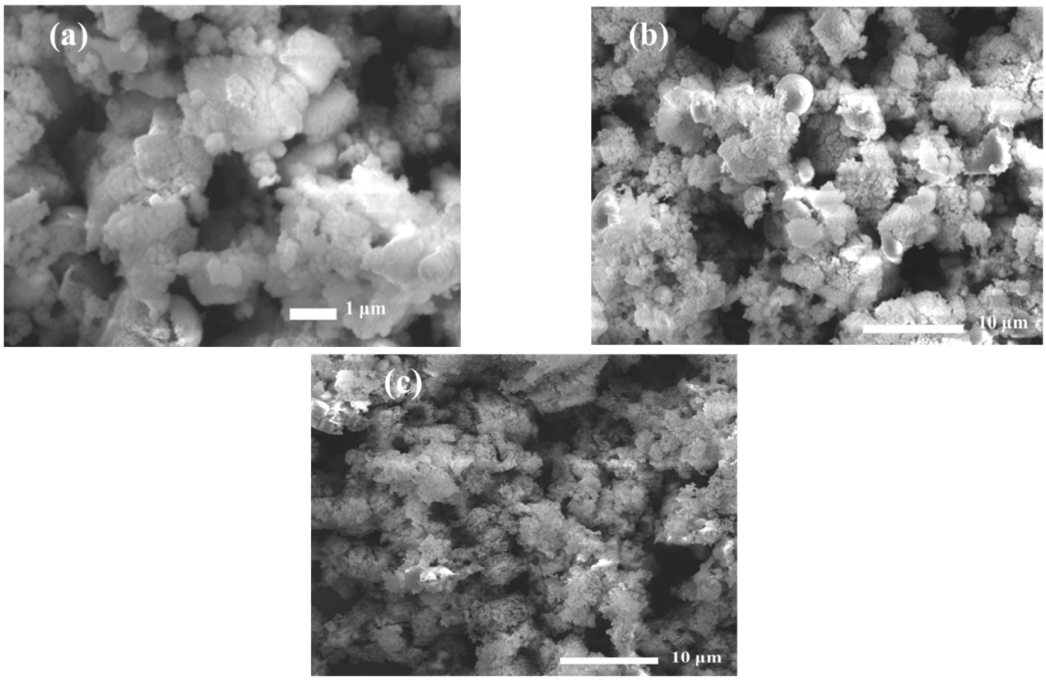

Figure 4: Surface morphology of $CaCO_3$ doped SiO_2 (a) 5 % SiO_2 (b) 15 % SiO_2 and (c) 30 % SiO_2 after decomposition.

3.3. Thermal energy density

Thermal energy density was of two types, one whose unit was based on volume is named as volumetric thermal energy density e_v [J/mL] and the other related to mass of the substance is known as gravimetric thermal energy density e_g [J/g]. These terms are calculated using the following equations.

Equation 2: Volumetric thermal energy density

$$e_v = \frac{-\Delta H \rho (100 - \varepsilon)}{M_{CaCO3} + M_{SiO2}} \div 100$$

Equation 3: Gravimetric thermal energy density

$$e_g = \frac{-\Delta H}{M_{CaCO3} + M_{SiO2}}$$

Where $-\Delta H$, M, ρ and ε are reaction enthalpy [J/mol], molecular mass [g/mol], density [g/mL] and porosity [%] of the samples, respectively. $-\Delta H$ was calculated for each sample using thermogravimetric data. Gravimetric method was used to compute the porosity of each prepared sample and density was determined by measuring mass of the samples with known volumes. Molar masses of $CaCO_3$ and SiO_2 are 100.09 and 60.08, respectively. Table 2 provides the information about the volumetric and gravimetric thermal energy densities of each sample under consideration.

Table 2: Volumetric and gravimetric thermal energy densities of each sample under analysis

Sample	$-\Delta H$ [J/mol]	ρ [g/mL]	ε [%]	e_v [J/mL]	e_g [J/g]
Pure $CaCO_3$	94609.07	0.59	44.44	311.09	945.24
$CaCO_3$+5% SiO_2	121663.5	0.42	51.22	155.35	759.59
$CaCO_3$+15% SiO_2	79431.51	0.30	44.64	83.24	495.92
$CaCO_3$+30% SiO_2	54433.77	0.28	41.67	54.75	339.85

From table 2 it is clear that both the thermal energy storage densities are decreasing as the amount of dopant was gradually increasing. This maybe because of lower density of SiO_2 that was used as dopant in the samples.

3.4. Effect of SiO_2 doping on the $CaCO_3$

To analyse the endothermic decarbonation reaction, the pure $CaCO_3$, and the prepared thermal composites (5%, 15%, 30% SiO_2@$CaCO_3$) were heated at 10 °C/min and the obtained results are shown in Figure 5. It was found that with the increase in amount of SiO_2 doping, the percentage weight loss of the samples decreased quickly and

this indicated that reaction rate became faster. Decomposition reaction of $CaCO_3$ was followed by weight loss because CO_2 was emitted when material was heated above 800 °C and CaO was formed, hence increase or decrease in weight loss was related to the reaction rate. Therefore, if the weight loss was slow it means that the rate of decomposition reaction was slow, and vice versa. In Figure 5, it can be noted that for the heating rates of 5 and 10°C/min, the high reaction rate was observed by the sample with highest (30%) loading of SiO_2 (Figures 5 a & b). On the other hand, sample with lowest (5%) quantity of SiO_2 was showing the highest reaction rate (Figure 5 c). Overall from Figure 5, it is observed that SiO_2 doped samples are decomposing very quickly than pure $CaCO_3$; this means SiO_2 has affected the decarbonation rate of the material. Decomposition reaction rate was related to the heat storage efficiency in a sense that heat was stored when material starts decomposing. If the decomposition was complete and there was no sintering of material, this indicates, the heat storage efficiency was increased. Henceforth, it was observed that by adding SiO_2 in $CaCO_3$, during decarbonation reaction CaO particles did not sinter and allowed the complete decomposition of $CaCO_3$, this was exhibited by the reaction rate of doped samples.

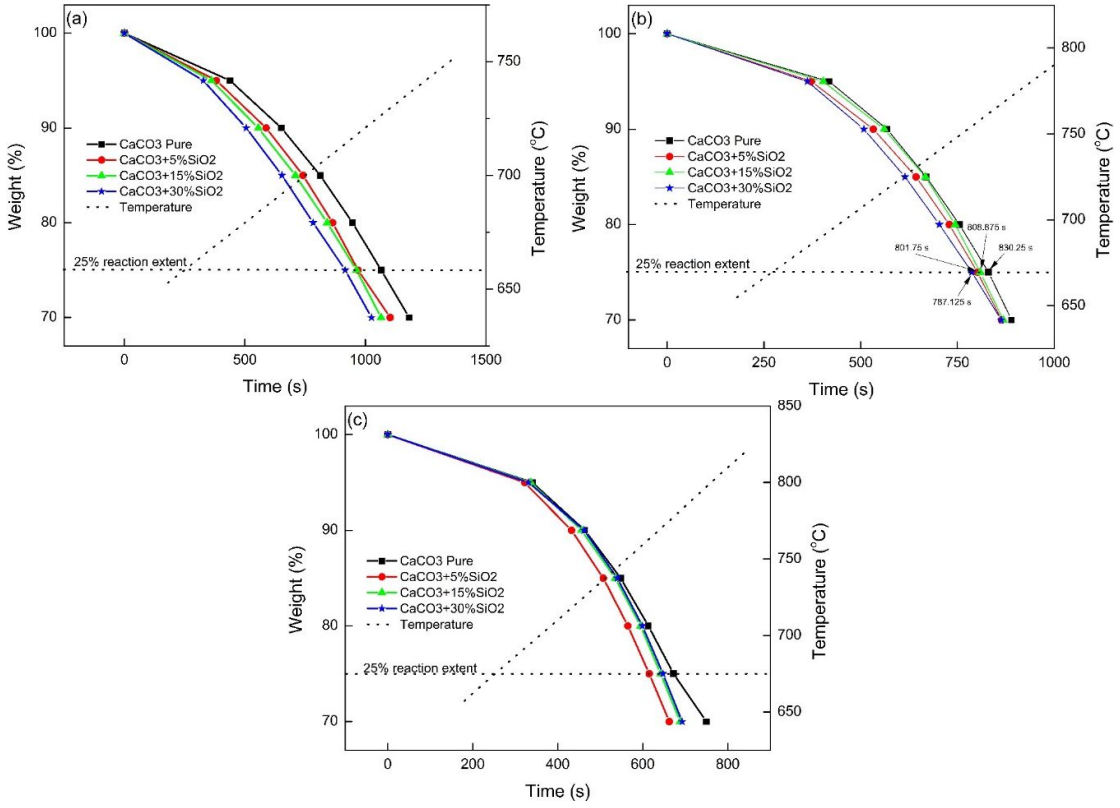

Figure 5: Decrease in weight percentage by non-isothermal heating at (a) 5 °C/min (b) 10 °C/min and (c) 15 °C/min. The weight loss was related to the rate of reaction.

In order to evaluate the heat storage capacity of pure $CaCO_3$ and $CaCO_3/SiO_2$ thermal composites, the specific heat capacity and enthalpy of reaction were determined. Therefore, to observe the heat storage capacity of these two samples we heated both the samples from 650 °C to 900°C at heating rate of 5°C/min. Values for the enthalpy of the reaction are provided in table 2. From the information in table 2, it is clear that addition of 5% SiO_2 in the $CaCO_3$ increased the enthalpy of the reaction. However, higher amounts of SiO_2 decreased the enthalpy of the reaction because of the formation of Ca_3SiO_5. This reaction enthalpy is representing the decomposition of $CaCO_3$ and synthesis of Ca_3SiO_5.

Specific heat capacity of the pure and silicon dioxide doped calcium oxide and calcium carbonate samples was determined to analyse the effect of doping on the heat storage capacity of the calcium carbonate. The specific heat capacity of the doped material was a little higher than the pure $CaCO_3$, as shown in Figure 6a. In contrast, the specific heat capacity of the pure CaO was little lower than the CaO doped with SiO_2, as shown in Figure 6b. Nevertheless, the overall trend for both the samples of two materials (CaO and $CaCO_3$) was same. It was observed that SiO_2 had very small effect on the specific heat capacity and reaction enthalpy of the $CaCO_3$. Therefore, it can be stated that the heat storage capacity of the $CaCO_3$ was reduced a little after doping with SiO_2.

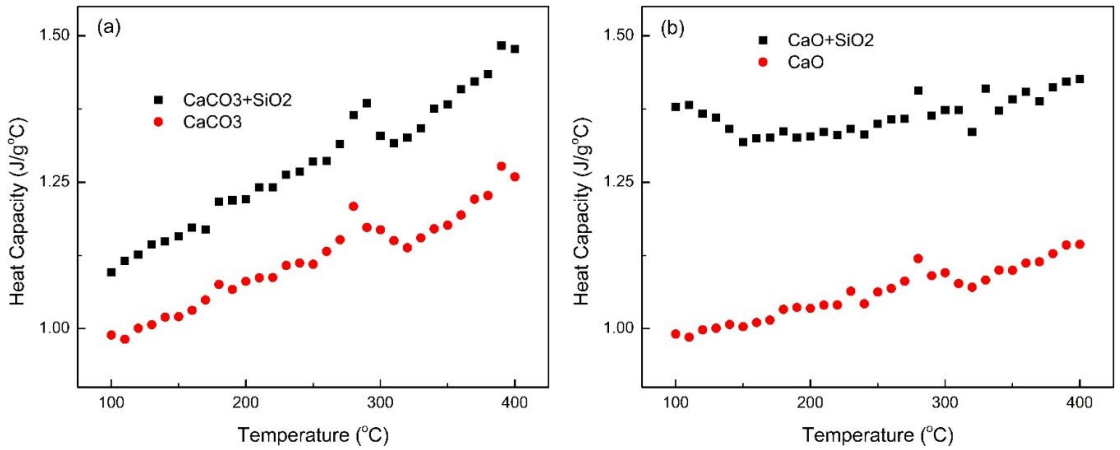

Figure 6: Specific heat capacity of (a) pure and SiO_2 doped $CaCO_3$ (b) pure and SiO_2 doped CaO. Specific heat capacity of the material helps to understand the heat storage capacity.

3.5. Cyclic Stability and Material Performance

For accessing the performance and durability of a thermochemical material over repeated cycles, cyclic tests are conducted. The decomposition of the material was allowed on 800°C for 10 min and the carbonation was performed at 600°C for the same time by changing the gas from Ar to CO_2. The same process was repeated to achieve the 15 cycles of decarbonation and carbonation of $CaCO_3$ as shown in the Figure 7. It was observed that conversion to carbonate was decreasing rapidly up to seventh cycle in pure $CaCO_3$ and the samples doped with SiO_2. After that, the reactivity of CaO was stabilising slowly and moves towards a persistent value after the completion of 15th cycle. For 15% doped sample the value of the cyclic conversion was not stable, it started to stabilise over 7 cycles but after 3 cycles it again started decreasing remarkably and reached a value of 0.48. 5% doped $CaCO_3$ sample performed well as compared to other samples and achieved a value of 0.62 for cyclic conversion. The overall performance of 5% doped sample was much better and this value of doping can be used for thermochemical heat storage systems using $CaCO_3$. The loss in cyclic use of material can be explained by the loss in pores available in CaO. The reaction between metal oxide and CO_2 gas was kind of surface reaction in the start and the further reaction was diffusion controlled and depends upon pore availability and diffusion of CO_2 in the material. Nevertheless, the newly formed carbonate layer provides resistance against diffusion of CO_2 for further reaction and the reaction rate becomes slow. As the reaction was happening continuously, so the particles gradually start sintering and hence cause reduction in the durability of the material. The same was described by Barker (Barker 1973). At the end of 15 cycles, the material doped with 5% SiO_2 was depicting good durability than pure sample. It means that the storage conversion of the sample poorly doped with SiO_2 after so many cycles was improved. The improvement was observed because the inert material reduced the sintering and accumulation of CaO grains because of a Zener pinning force, which resists the migration of particle boundary. Hence doping of SiO_2 improved the cyclic durability of the material by reducing the accumulation of the CaO particles and providing more pores for diffusion of CO_2.

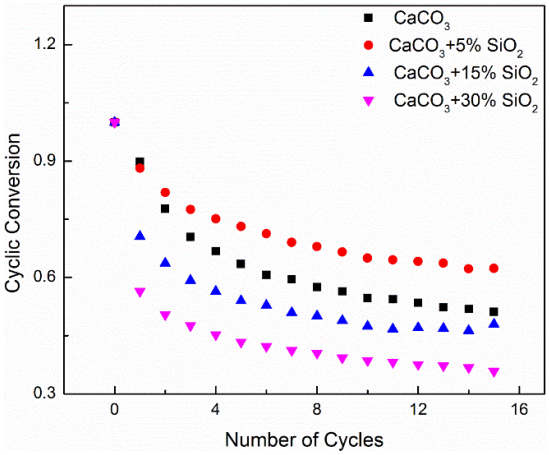

Figure 7: Cyclic conversion of pure and doped samples

4. CONCLUSION

The SiO_2 was doped in $CaCO_3$ to improve the heat storage efficiency of $CaCO_3$. The heat storage capacity of the as-prepared thermal composite was analysed as well. All the prepared composite samples were analysed to determine their volumetric as well as gravimetric thermal energy storage densities. We then analysed what happens when a large amount of dopant was used, either a new phase appeared in the parent material (calcium carbonate) or not. The durability of the samples over 15 cycles was also studied. The conclusions are as follows:

- The high thermal conductivity of SiO_2 caused an increase in the specific heat capacity of the composite material. Overall, the heat storage capacity decreased slightly after doping with SiO_2. On the other hand, during the exothermic carbonation of the oxide, enthalpy of the reaction was high because of enhanced heat transfer between gas-solid molecules.
- The dopant material lowered the thermal energy density of the pure material. The reason maybe the less density of the dopant. Volumetric and gravimetric energy density of the pure sample are 311.09 J/mL and 945.24 J/g, respectively. While the sample doped with 30% SiO_2 showed the same properties as 54.75 J/mL and 339.85 J/g, respectively.
- The doping of SiO_2 in the $CaCO_3$ increased the decarbonation reaction rate of the calcium carbonate. The increase in reaction rate was due to the fact that the SiO_2 added in the material helped in the quick removal of calcium oxide (CaO), this caused fast decomposition of $CaCO_3$, thereby increasing the decomposition rate of $CaCO_3$.
- The performance of samples with different percentages of dopant varied with rate of heating. As, it was observed for lower heating rates, samples with higher loadings performed well and their rate of reaction was high. In contrast, for high heating rates, doping samples with modest SiO_2 showed better results.
- It was observed for samples with 15% and 30% doping of SiO_2 that the CaO produced during decarbonation reaction reacted with SiO_2 and produced Ca_3SiO_5 that introduced a new phase in the calcined material. This was observed in the XRD analysis of the calcined material. Based on this, it was concluded that small quantity of dopant acted as inert material (coating material) and the large quantity took part in the reaction and produced a different product. The new phase was stable and it did not affect the performance of the material.

SiO_2 as dopant has advantages, as it is cheap and available in abundance as compared to other inert materials analysed by other researchers. $CaCO_3$ and SiO_2 composite has better performance based on facts: time to store energy is reduced, cyclic stability is improved and capacity to store energy is enhanced. Henceforth, these facts lead to the conclusion that the composite is long lasting, effective and inexpensive. It is also promising for its use in regeneration of industrial waste heat and in the regular operation of renewable energy.

5. ACKNOWLEDGEMENT

The National Natural Science Foundation of China (Grant No. 51706130) supports this work. The authors are thankful to the Foundation and acknowledge its support.

6. REFERENCES

Barker, R. (1973). "The reversibility of the reaction CaCO3⇄ CaO+ CO2." Journal of Chemical Technology and Biotechnology **23**(10): 733-742.

Benitez-Guerrero, M., B. Sarrion, A. Perejon, P. E. Sanchez-Jimenez, L. A. Perez-Maqueda and J. Manuel Valverde (2017). "Large-scale high-temperature solar energy storage using natural minerals." Solar Energy Materials and Solar Cells **168**: 14-21.

Chen, H., P. Zhang, Y. Duan and C. Zhao (2016). "Reactivity enhancement of calcium based sorbents by doped with metal oxides through the sol–gel process." Applied Energy **162**: 390-400.

Chen, X., X. Jin, Z. Liu, X. Ling and Y. Wang (2018). "Experimental investigation on the CaO/CaCO3 thermochemical energy storage with SiO2 doping." Energy **155**: 128-138.

Duelli, G., A. Charitos, M. E. Diego, E. Stavroulakis, H. Dieter and G. Scheffknecht (2015). "Investigations at a 10kWth calcium looping dual fluidized bed facility: Limestone calcination and CO2 capture under high CO2 and water vapor atmosphere." International Journal of Greenhouse Gas Control **33**: 103-112.

Erans, M., V. Manovic and E. J. Anthony (2016). "Calcium looping sorbents for CO2 capture." Applied Energy **180**: 722-742.

Ervin, G. (1977). "Solar heat storage using chemical reactions." Journal of solid state chemistry **22**(1): 51-61.

Ervin, G., D. Chung and T. Springer (1974). "A study of the use of inorganic oxides for solar energy storage for heating and cooling of Buidings." Final Report, June **1**.

Gil, A., M. Medrano, I. Martorell, A. Lázaro, P. Dolado, B. Zalba and L. F. Cabeza (2010). "State of the art on high temperature thermal energy storage for power generation. Part 1—Concepts, materials and modellization." Renewable and Sustainable Energy Reviews **14**(1): 31-55.

Jin, D., X. Yu, L. Yue and L. Wang (2009). "Decomposition kinetics study of AlOOH coated calcium carbonate." Materials Chemistry and Physics **115**(1): 418-422.

Jing, J.-y., T.-y. Li, X.-w. Zhang, S.-d. Wang, J. Feng, W. A. Turmel and W.-y. Li (2017). "Enhanced CO2 sorption performance of CaO/Ca3Al2O6 sorbents and its sintering-resistance mechanism." Applied Energy **199**: 225-233.

Kumar, D., S. C. Maiti and C. Ghoroi (2016). "Decomposition kinetics of CaCO3 dry coated with nano-silica." Thermochimica Acta **624**: 35-46.

Lee, M. g., Y. N. Jang, K. w. Ryu, W. Kim and J.-H. Bang (2012). "Mineral carbonation of flue gas desulfurization gypsum for CO2 sequestration." Energy **47**(1): 370-377.

Lu, S. and S. Wu (2016). "Calcination–carbonation durability of nano CaCO3 doped with Li2SO4." Chemical Engineering Journal **294**: 22-29.

Medrano, M., A. Gil, I. Martorell, X. Potau and L. F. Cabeza (2010). "State of the art on high-temperature thermal energy storage for power generation. Part 2—Case studies." Renewable and Sustainable Energy Reviews **14**(1): 56-72.

N'Tsoukpoe, K. E., G. Restuccia, T. Schmidt and X. Py (2014). "The size of sorbents in low pressure sorption or thermochemical energy storage processes." Energy **77**: 983-998.

Pan, Z. H. and C. Y. Zhao (2017). "Gas–solid thermochemical heat storage reactors for high-temperature applications." Energy **130**: 155-173.

Pardo, P., A. Deydier, Z. Anxionnaz-Minvielle, S. Rougé, M. Cabassud and P. Cognet (2014). "A review on high temperature thermochemical heat energy storage." Renewable and Sustainable Energy Reviews **32**: 591-610.

Perejón, A., J. Miranda-Pizarro, L. A. Pérez-Maqueda and J. M. Valverde (2016). "On the relevant role of solids residence time on their CO2 capture performance in the Calcium Looping technology." Energy **113**: 160-171.

Shui, M., L. Yue, Y. Hua and Z. Xu (2002). "The decomposition kinetics of the SiO2 coated nano-scale calcium carbonate." Thermochimica Acta **386**(1): 43-49.

Tamme, R. (2011). Thermal energy storage for industrial applications. Presentation: storage for industrial applications IEA workshop.

Valverde, J., A. Perejón and L. A. Perez-Maqueda (2012). "Enhancement of fast CO2 capture by a nano-SiO2/CaO composite at Ca-looping conditions." Environmental science & technology **46**(11): 6401-6408.

Valverde, J. M., M. Barea-López, A. Perejón, P. E. Sánchez-Jiménez and L. A. Pérez-Maqueda (2017). "Effect of Thermal Pretreatment and Nanosilica Addition on Limestone Performance at Calcium-Looping Conditions for Thermochemical Energy Storage of Concentrated Solar Power." Energy & Fuels **31**(4): 4226-4236.

Wang, M. and C.-G. Lee (2009). "Absorption of CO2 on CaSiO3 at high temperatures." Energy Conversion and Management **50**(3): 636-638.

Wang, M., C.-G. Lee and C.-K. Ryu (2008). Absorption of CO2 on CaSiO3. The 2008 Annual Meeting, Citeseer.

Wang, Y., Y. Zhu and S. Wu (2013). "A new nano CaO-based CO2 adsorbent prepared using an adsorption phase technique." Chemical Engineering Journal **218**: 39-45.

Yan, T., R. Wang, T. Li, L. Wang and I. T. Fred (2015). "A review of promising candidate reactions for chemical heat storage." Renewable and Sustainable Energy Reviews **43**: 13-31.

Yanase, I., T. Maeda and H. Kobayashi (2017). "The effect of addition of a large amount of CeO2 on the CO2 adsorption properties of CaO powder." Chemical Engineering Journal **327**: 548-554.

#176: Aqueous phase reforming of sorbitol over Calcium doped Nickel based catalysts supported on Gadolinium

Mohd Hafiz MOHD NOR[1], Ain SYUHADA[2], Mariam AMEEN[3], Aqsha Aqsha[4], Mohammad Tazli AZIZAN[5]

Department of Chemical Engineering, Universiti Teknologi PETRONAS, 32610 Seri Iskandar, Perak,
[1]mhafiznor95@gmail.com
[2]syuhada.faatah95@gmail.com
[3]mariam.ameenkk@gmail.com
[4]aqsha@utp.edu.my
[5]tazliazizan@utp.edu.my

Aqueous phase reforming (APR) is the most promising technology to produce hydrogen and value-added chemicals. The use of different supports of the catalysts has produced different products during APR reaction. Gd_2O_3, support has gained interest due to its ability to improve the catalyst surface reactivity and reduce coke formation during the reaction. In this research, Ni based catalysts supported on Gd_2O_3 and doped with different percentage of Ca (0, 3, 5 and 7 wt.%) were synthesised by a wet impregnation method. The catalysts were subjected to several characterisation technique such TGA, XRD, FESEM and BET analysis. Then, the performance of the catalysts was studied for APR of sorbitol. The TGA results showed that the calcination temperature of the catalysts was at 500°C. The XRD results show that all the three compound, NiO, CaO and Gd_2O_3 were present in the catalysts and the peak shows decreased in Gd_2O_3 peak intensity with increasing Ca compositions. The FESEM images of the catalysts show the agglomeration of the metal catalyst which was increasing with Ca addition. The BET analysis indicated that Ca percentage below 5% provides positive impact on Ni surface area and dispersion, which indicated better performance of the catalysts during the reaction. The liquid products obtained from the APR reaction were analysed using HPLC analysis. The results show the presence of pentanediol, 1,4-butanediol, 1-propanol and ethylene glycol in the liquid products. It was also observed that low Ca percentage prefers formation of C5-C4 products through decarbonylation whereas high Ca percentage favours the formation of C3-C2 carbon through retro-aldol condensation reactions.

Keywords: aqueous phase reforming; sorbitol; nickel; calcium; gadolinium; wet impregnation

1. INTRODUCTION

Over recent years, extensive research and effort have been made to investigate the production of bulk chemicals using renewable sources in preference to petrochemicals which are becoming more expensive with diminishing availability as it uses hydrocarbon feedstock (Hermann & Patel, 2007). Aqueous phase reforming (APR) of biomass is the most promising technology to fulfil this need. APR reaction occurs at operating temperatures of 200-250°C and pressures of 15-50 bar which is near to the oxygenated hydrocarbon's bubble point (Chheda et al., 2007). This process has low energy requirements through suppression of evaporation of water (Davda et al., 2005). Low energy requirement leads to low operating costs and using a renewable energy, biomass, as its feedstock demonstrates the advantages of APR over other technologies.

Sorbitol ($C_6H_{14}O_6$) is a sugar alcohol produces through hydrolytic hydrogenation of glucose. It is commonly used in manufacturing processes such as pharmaceutical aid and for numerous research purposes sorbitol has gained the interest of researchers for APR reaction to produce value added products. Its current production is estimated to be 1.2 million tons per year. Sorbitol has C:O ratio of 1:1 which shows that it is thermodynamically ideal for a reaction at relatively lower temperature compared to the other structures with the same amount of carbon, for a single step catalytic process and water-shift gas reaction (Davda et al., 2005).

Ni-based catalysts are utilised for the cheaper price and comparable performance compared to the well-known Pt-based catalyst enabling a high carbon conversion in APR process. However, Van Haasterecht et al. (2016) stated that the use of nickel alone for APR reaction will easily cause catalysts deactivation, therefore the catalyst should be doped with metal such as Ca and Mo and required support to enhance the thermal stability of the catalysts. Although no extensive research has been done on gadolinium (Gd) in APR reaction, its performance in electrochemical processes has been proved to enhance surface reactivity, higher specific surface area and longer catalyst life. Ca as a promoter further increases the stability, activity and interaction between the metal catalyst and its support (Hou et al., 2003).

Radzi et al. (2018) studied APR of sorbitol using Ca doped Ni based catalysts supported on Al_2O_3. The results obtained show that catalysts supported on Al_2O_3 favours hydrogenolysis reaction where ethylene glycol was produced as one of the liquid products for all the catalysts tested with sorbitol conversion of 69-78%.

Figure 1 shows the major reaction pathways identified during APR of sorbitol by utilising different catalysts (Li & Huber, 2010).

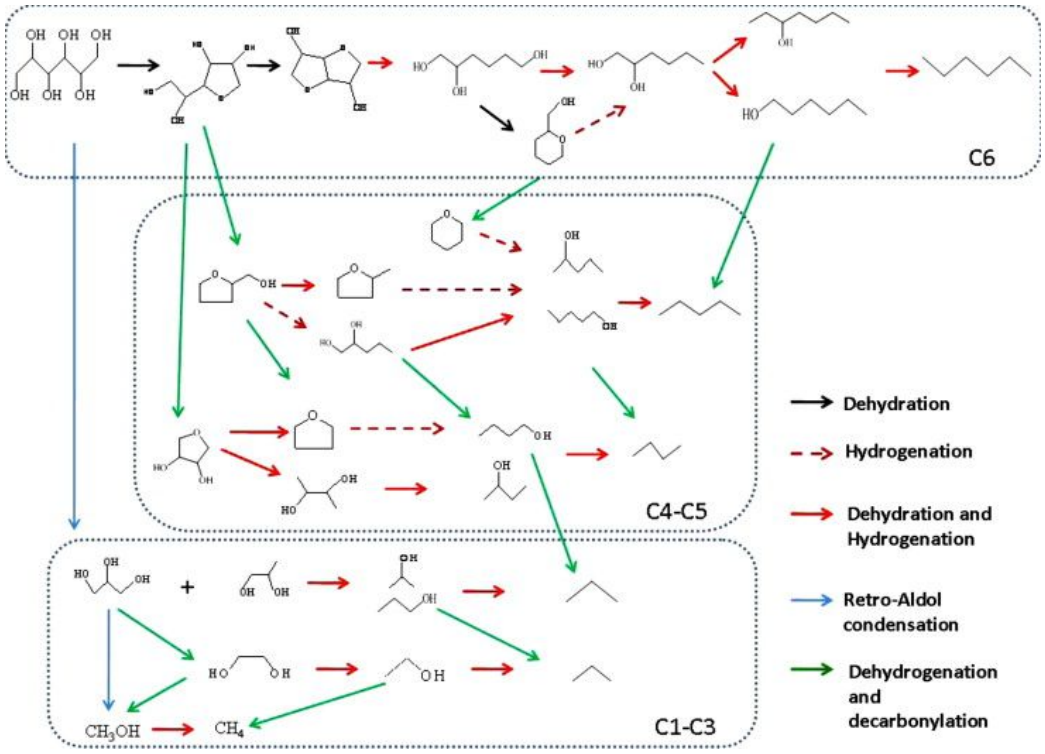

Figure 1: Possible reaction pathways during APR of sorbitol at 518K (Li & Huber, 2010)

Hydrogen was first removed from sorbitol through hydrogenation and deoxygenation steps. Conversion of sorbitol into less oxygenated derivates through sequential dehydration and hydrogenation reactions yield five or less carbon atom compounds. Products with C4-C5 resulted from the decarbonylation process in which CO was removed to produce CO_2. Breaking of the sorbitol's skeleton occurs through retro-aldol condensation reactions, which makes the formation of polyols with C4-C3 possible carbon atom. This product can undergo further breakdown to form linear alcohols and ketones through dehydration and hydrogenation reactions and eventually the formation of light alkanes.

The aim of this research was to study the physicochemical properties of Ni based catalysts supported on Gd_2O_3 doped with different compositions of Ca (3,5 and 7%) using several characterisation techniques such as XRD, FESEM and BET as well as to identify the liquid products produced from APR of sorbitol using the synthesised catalysts.

2. METHODOLOGY

2.1. Catalyst synthesising

Nickel nitrate hexahydrate ($Ni(NO_3)_2.6H_2O$) and calcium chloride dihydrate ($CaCl_2.2H_2O$) were dissolved in deionised water separately for each formulation and mixed together. Then, gadolinium oxide (Gd_2O_3) support was added into the aqueous mixture of $Ni(NO_3)_2.6H_2O$ and $CaCl_2.2H_2O$ and stirred at room temperature for 4 hours and 400 round per minute (RPM). The catalysts were then dried at 110°C for 24 hours to remove the water and calcined at 500°C for 4 hours to further remove the volatile components in the catalyst. The synthesised catalysts were denoted as X% Ca - 10% Ni/Gd_2O_3 (where X=0, 3, 5 and 7).

2.2. Catalyst characterisation

The XRD patterns were obtain using X' Pert3 Powder & Empyrean, PANalytical diffractometer equipped with a Cu Kα radiation source (λ=1.5406Å) in the 2θ range of 20°-80° in continuous mode with exposure time of 1800s and step size of 0.02°/step. The morphology of the catalysts was determined using Field Emission Scanning Electron Microscopy (FESEM) technique performed using VPFESEM, Zeiss Supra 55VP operating at an accelerating voltage of 5kV. Nitrogen(N_2) gas desorption-adsorption isotherm were determined at -196°C by using micromeritics ASAP 2020 after degassing at 300°C for 4 hours. Specific surface area of the catalysts was determine using Brunauer-Emmett-Teller (BET) method while pore volume and pore size of the catalysts were determined using BJH method.

2.3. Catalyst screening

The APR of sorbitol was conducted using PREMEX Autoclave High Pressure Reactor MED 778. Firstly, 2.0 g of catalyst was activated at 290°C under flow of hydrogen at 4 bar for 4 hours. Then, 0.05 mol of sorbitol solution was poured into the reactor. The reaction was run at 230°C with flow of nitrogen gas 20 bar and 450 RPM for 1 hour. After completed the reaction, the liquid product was collected and further analysed using High Performance Liquid Chromatography (HPLC) using external standard calibration curve.

3. RESULTS AND DISCUSSION

3.1. TGA

TGA was done to determine the calcination temperature of each sample. TGA was done to investigate the weight loss of the sample, thermal behaviour as well as the structural destruction when treated through calcination. The TGA results in Figure 1 represents the decrease in weight of the catalyst and the derivative weight which indicated the weight loss per time against temperature. The weight loss plotted showed decrement in the weight until it reaches around 500°C where the weight loss started to become constant. The derivative weight indicates that there were at least two significant peaks around the same temperature range in each sample analysis. The first peak was detected between 27°C and 160°C when removal of water and physiosorbed water was expected. Meanwhile, the second peak occurred between 240°C and 470°C when the nickel nitrate underwent decomposition into nickel oxide as recorded (Coronado et al., 2017).The other detected peaks which were not within the range might be due to the uneven nickel distribution on the support. Thus, the suitable calcination temperature for the samples is 500°C where the weight loss and derivative weight started to stabilise which corresponds to the research by Charisiou et al. (2019). The addition of calcium was shown to have no significant impact towards the calcination temperature.

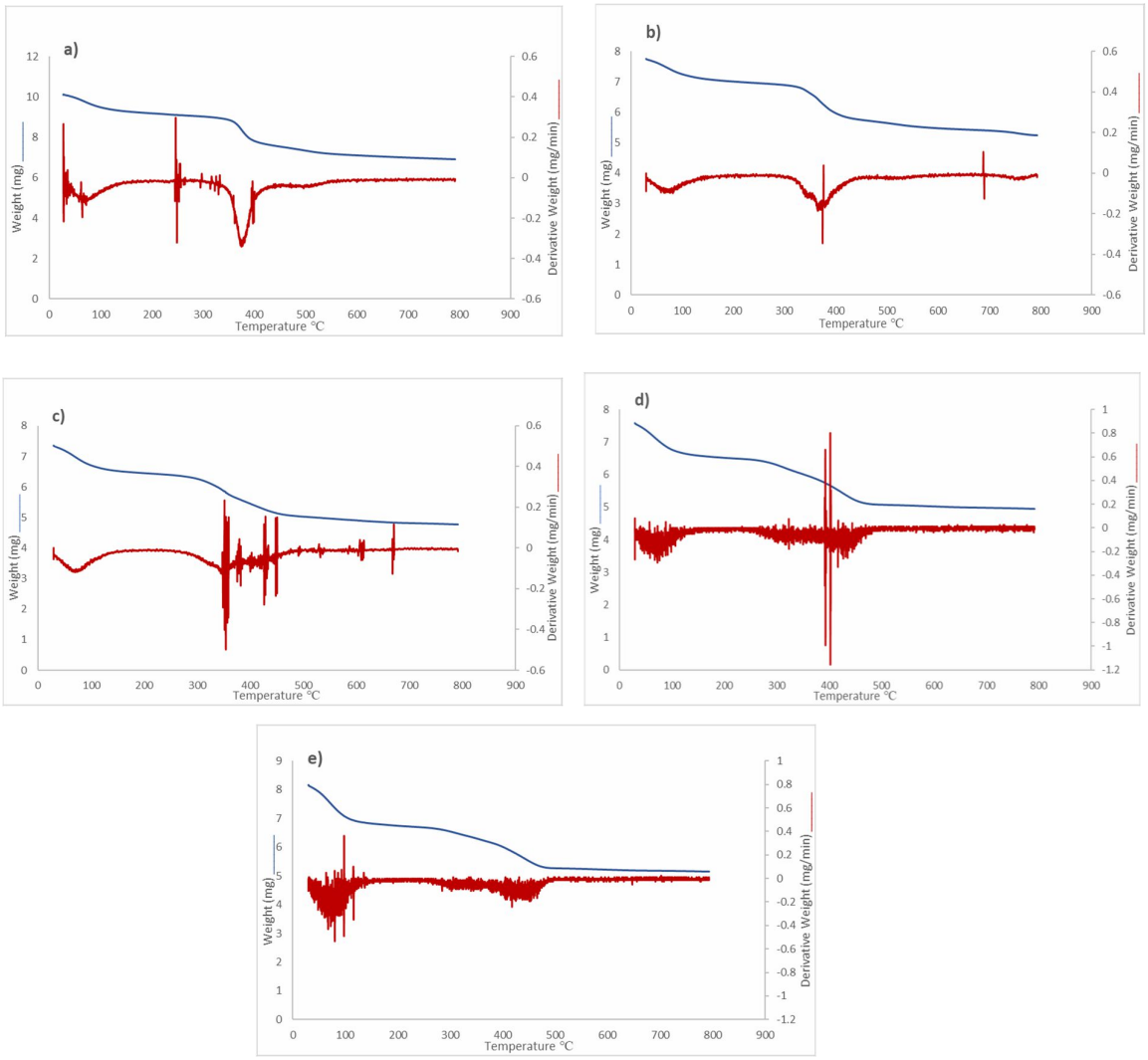

Figure 2: TGA patterns for (a) 10%Ni/Gd_2O_3; (b) 0.5%Ca-10%Ni/Gd_2O_3; (c) 3%Ca-10%Ni/Gd_2O_3; (d) 5%Ca-10%Ni/Gd_2O_3 and (e) 7%Ca-10%Ni/Gd_2O_3 catalysts.

3.2. XRD

Figure 3 shows the XRD patterns of pattern of a)10%Ni/Gd_2O_3; b)3%Ca-10%Ni/Gd_2O_3, c) 5%Ca-10%Ni/Gd_2O_3 and d) 7%Ca-10%Ni/Gd_2O_3 synthesised by wet impregnation method. The diffraction peaks of Gd_2O_3 for all the catalysts were observed at 2θ of 20.08 ,28.55 ,33.08 ,35.15, 39.01, 42.59, 47.50,49.05, 52.09, 56.37 ,57.74, 59.08, 63.13,76.69, 79.14 (JCPDS card no. #43-1014) which indicate the presence of Gd_2O_3 nanoparticles in cubic phase. The sharp and high intensity peaks observed for all the catalysts indicate that the catalysts have high crystallinity (Jiang et al., 2016). Meanwhile, the NiO peaks were observed at 2θ=37º, 43º and 63º (JCPDS card no. #47-1049) which corresponds to the formation of NiO cubic nanostructure (El-Kemary et al., 2013). The diffraction peaks of CaO were observed at 2θ=32º, 37º and 54º (JCPDS card no. #82-1690) which also indicate the presence of CaO cubic nanostructure (Imtiaz et al., 2013)]. The effect of Ca doping can be observed by comparing the XRD patterns of the catalysts. It was observed that, the doping of Ca onto the Ni /Gd_2O_3 from 3% to 7% significantly reduce the peak intensity of the Gd_2O_3.

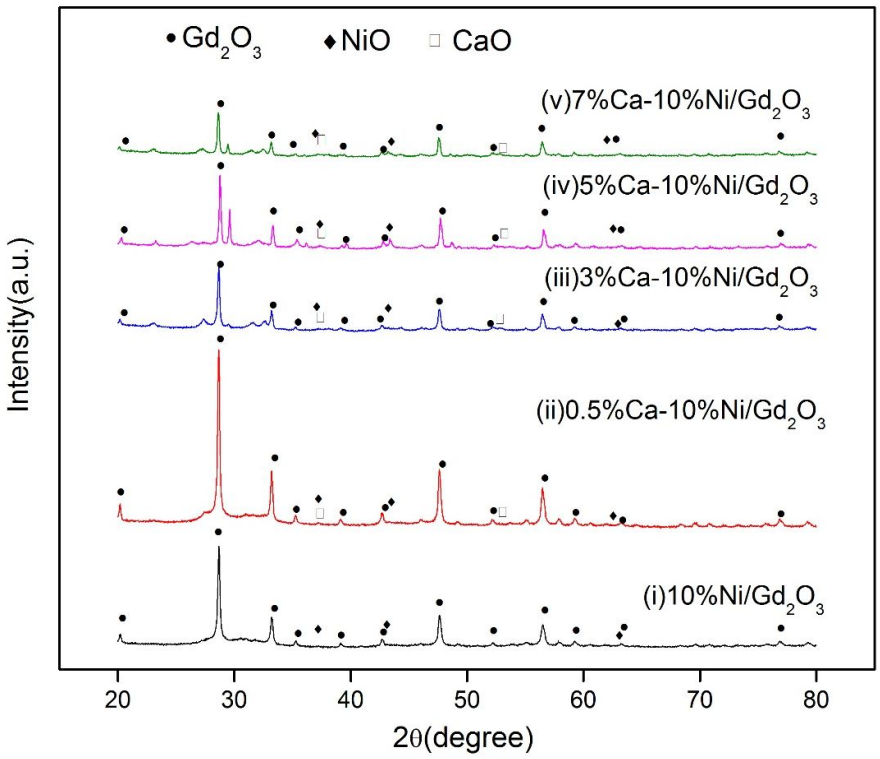

Figure 3: XRD patterns of the synthesised catalysts

3.3. FESEM Analysis

Based on FESEM images in Figure 4(i), similar cubic crystal structure for both NiO and CaO as confirmed by the XRD analysis made it difficult to distinguish both elements on the support using FESEM. It can be observed that the sample clearly had cubic morphology however, there were defects in the structure such as the formation of flake-type structure (Tamrakar et al., 2017). FESEM images shown the complex surface structure of the catalysts as the percentage of Ca doping increase. EDX spectra of the catalysts in Figure 4(ii) shown that there was particle agglomeration occurred within the catalysts and the agglomeration increases as the percentage of Ca doping increase.

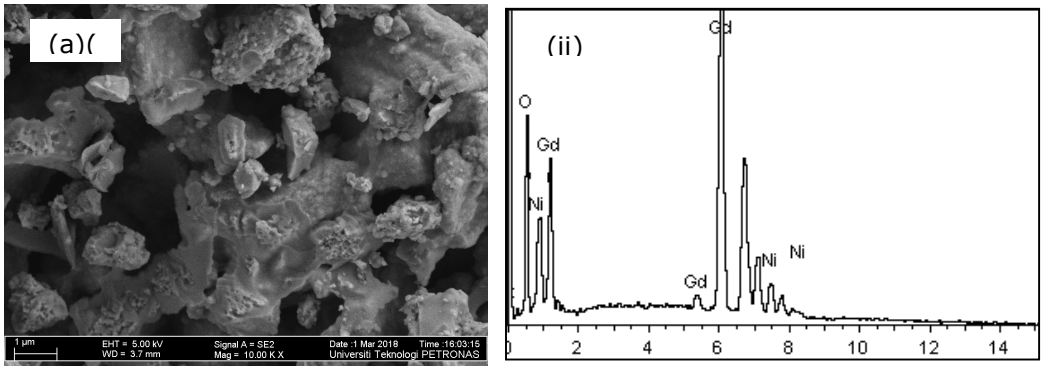

Figure 4: (i) FESEM images and (ii) EDX spectra of (a)10%Ni/Gd₂O₃;

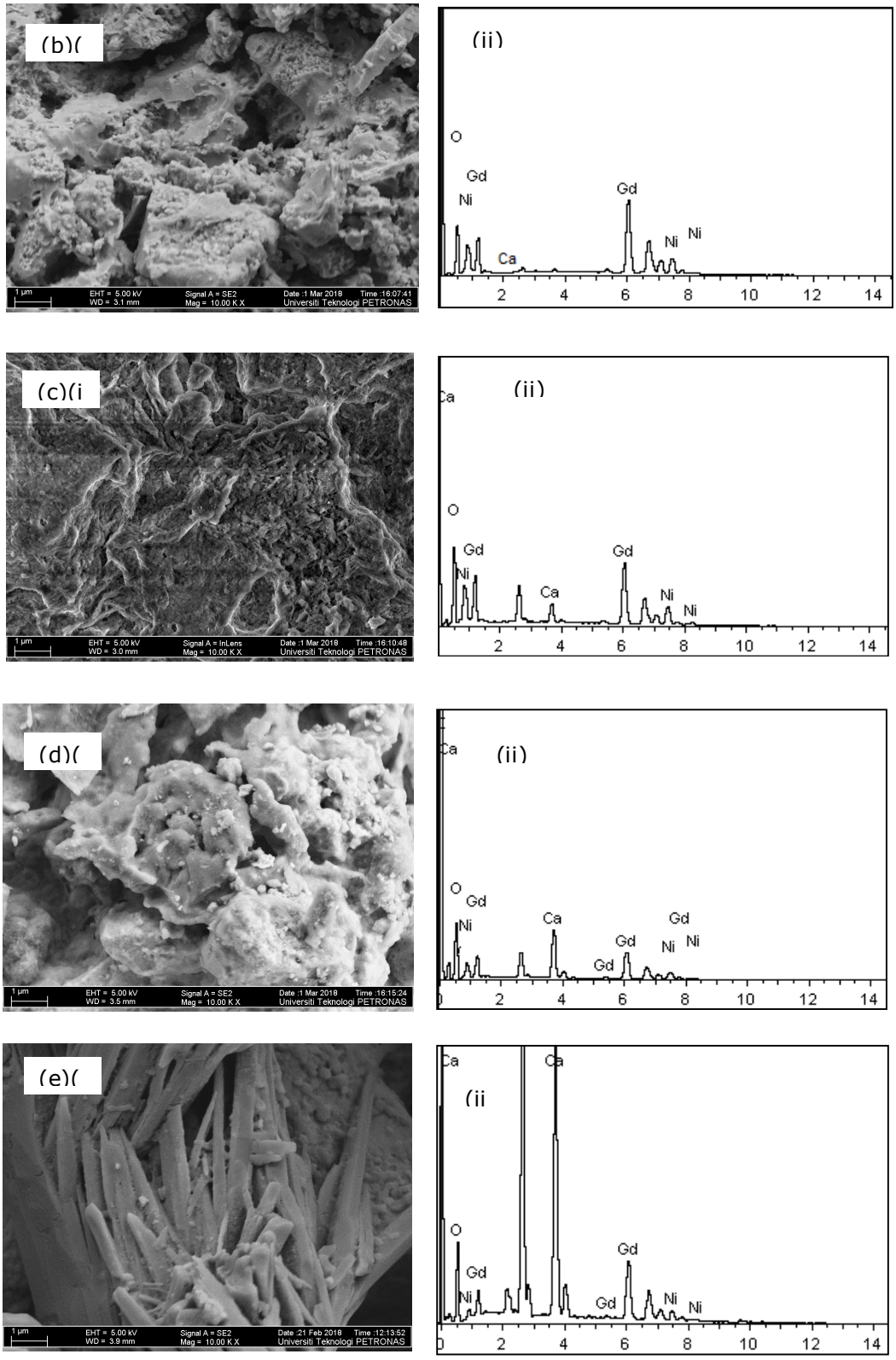

Figure 4: (i) FESEM images and (ii) EDX spectra of (a) 10%Ni/Gd_2O_3; (b) 0.5%Ca-10%Ni/Gd_2O_3; (c) 3%Ca-10%Ni/Gd_2O_3, (d) 5%Ca-10%Ni/Gd_2O_3 and (e) 7%Ca-10%Ni/Gd_2O_3 catalysts.

3.4. BET Analysis

The specific surface area, pore volume and pore size of the catalysts are shown in Table 1. The specific surface area was calculated using BET equation while pore volume and pore size were calculated using BJH method. The specific surface area of 10% Ni /Gd_2O_3, 0.5%Ca-10%Ni /Gd_2O_3, 3%Ca-10%Ni /Gd_2O_3, 5%Ca-10%Ni /Gd_2O_3 and 7%Ca10% Ni /Gd_2O_3 were reported as 9.13 m^2/g, 9.99m^2/g, 11.95m^2/g and 4.27m^2/g respectively. It was observed that the specific surface area of the catalysts slightly increased as the Ca composition increase from 3% and 5% respectively but decrease as the Ca composition increased to 7%. These results correspond to the research conducted by Koo et al. (2015) which showed that the surface area of the catalysts remained in a small range for Ca/Ni ratio (wt.%) less than 0.5. However, it has a notable reduction when the Ca/Ni ratio is beyond 0.5 due to the agglomeration of Ni particles caused by the excess Ca. Thus, the addition of Ca less than 0.5 Ca/Ni ratio brought positive effect as in decreasing Ni crystallite size, increasing the dispersion of Ni and able to prevent sintering of Ni particles (Hou et al., 2003). However, the common trend observed for pore volume and pore size shows that pore volume and pore size decreased as metal composition increased (Koo et al., 2015). The results obtained for pore volume and pore size agreed with the reported trend. This was due to the blockage of Gd_2O_3 pores by Ca ad Ni.

Table 1: BET surface area, pore volume and pore size of the synthesised catalysts.

Catalyst	BET Surface Area (m2/g)	Pore Volume (cm3/g)	Pore Size (nm)
10% Ni /Gd2O3	9.13	0.043	17.31
0.5% Ca-10% Ni /Gd2O3	4.41	0.024	22.12
3% Ca - 10% Ni /Gd2O3	9.99	0.027	10.91
5% Ca - 10% Ni /Gd2O3	11.95	0.024	7.00
7% Ca - 10% Ni /Gd2O3	4.27	0.015	6.90

Figure 5 shows the N_2 adsorption-desorption isotherms of (a) 10% Ni/Gd_2O_3, (b)3%Ca-10%Ni/Gd_2O_3, (c)5%Ca 10%Ni/Gd_2O_3 and (d)7%Ca10%Ni/Gd_2O_3 catalysts. The isotherms of the catalysts were similar to typical type IV curves which corresponding to mesoporous structure of 2 to 50 nm (Mulewa et al., 2017).

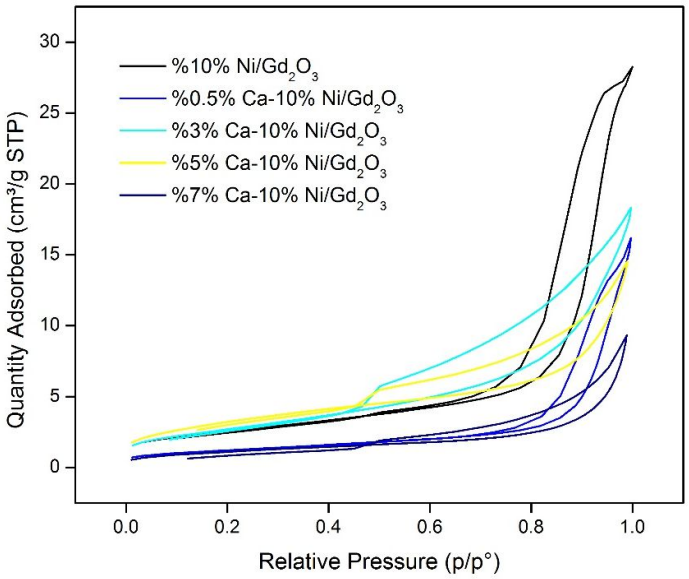

Figure 5: N_2 adsorption-desorption isotherm of the synthesised catalysts.

3.5. Analysis of product

The liquid products obtained were analysed using HPLC and compared with the external standard calibration curve. Based on the results obtained, four significant chemicals were identified for APR of sorbitol using the synthesised catalysts as tabulated in Table 2. The results shown that the concentration of pentanediol and 1,4-butanediol increased as the percentage of Ca doping increased from 0% to 3%, however as the percentage of Ca doping increased from 5% to 7%, there is no peak detected for 1,4-butanediol in the product. Therefore, this indicate that 10wt% Ni/Gd_2O_3 catalysts with less than 3% Ca doping favour decarbonylation reactions. Meanwhile, at 5% and

7% Ca doping, 1-propanol and ethylene glycol were detected, indicating that the catalysts favour retro-aldol condensation reaction and C-C cleavage to form C2 compound. These results are in line with the work conducted by Li and Huber (2010) which proved that during APR of sorbitol, pentanediol and 1,4-butanediol were produced through decarbonylation reactions where sorbitol was converted into derivatives containing less C5-C4 carbon atoms, whereas 1-propanol and ethylene glycol was achieved through the retro-aldol condensation reactions leading to the formation of polyols with C4- C3 carbon atoms and can be further converted to linear ketones or alcohols through dehydration and hydrogenation process.

Table 2: Production of liquid products for APR of glycerol using the synthesised catalysts.

Catalyst	Concentration (M)			
	Pentanediol	1,4-Butanediol	1-Propanol	Ethylene Glycol
10% Ni/Gd_2O_3	0.001249	0.0001685	-	-
0.5% Ca -10% Ni/Gd_2O_3	0.001652	0.0002067	-	-
3% Ca - 10% Ni/Gd_2O_3	0.001274	0.0002438	-	-
5% Ca - 10% Ni/Gd_2O_3	0.001984	-	0.0002821	0.0004950
7% Ca - 10% Ni/Gd_2O_3	0.002233	-	0.0002283	0.0016891

4. CONCLUSION

The XRD analysis showed the presence of all the peaks NiO, CaO and Gd_2O_3 and the decrease in peak intensity of Gd_2O_3 with high Ca percentage indicating that higher Ca made the support less crystalline. The TGA results show that the calcination temperature of the catalysts was at 500°C where at this temperature the weight loss and derivative weight loss of the catalysts started to become constant. The FESEM images of the catalysts shows that there is agglomeration of the metal catalyst which was increasing with Ca addition. The BET analysis indicated that Ca percentage below 5% provided positive impact on Ni surface area and dispersion indicating better performance. The N_2 adsorption-desorption isotherms of the catalysts were similar to Type IV indicating that the catalysts were in mesoporous structure of 2 to 50 nm. Based on the HPLC analysis of the liquid products, it can be deduced that low Ca amount prefer formation of C5-C4 products through decarbonylation reactions. Whereas high Ca amount prefers the formation of C3-C2 carbon through retro-aldol condensation reactions meaning Ca percentage can be varied if one desired shorter or longer carbon chain compounds.

5. REFERENCES

Charisiou, N. D., Papageridis, K. N., Tzounis, L., Sebastian, V., Hinder, S. J., Baker, M. A., AlKetbi, M., Polychronopoulou, K. & Goula, M. A. 2019. Ni supported on CaO-MgO-Al2O3 as a highly selective and stable catalyst for H2 production via the glycerol steam reforming reaction. International Journal of Hydrogen Energy, 44, 256-273.

Chheda, J. N., Huber, G. W. & Dumesic, J. A. 2007. Liquid-phase catalytic processing of biomass-derived oxygenated hydrocarbons to fuels and chemicals. Angewandte Chemie International Edition, 46, 7164-7183.

Coronado, I., Stekrova, M., García Moreno, L., Reinikainen, M., Simell, P., Karinen, R. & Lehtonen, J. 2017. Aqueous-phase reforming of methanol over nickel-based catalysts for hydrogen production. Biomass and Bioenergy, 106, 29-37.

Davda, R., Shabaker, J., Huber, G., Cortright, R. & Dumesic, J. A. 2005. A review of catalytic issues and process conditions for renewable hydrogen and alkanes by aqueous-phase reforming of oxygenated hydrocarbons over supported metal catalysts. Applied Catalysis B: Environmental, 56, 171-186.

El-Kemary, M., Nagy, N. & El-Mehasseb, I. 2013. Nickel oxide nanoparticles: Synthesis and spectral studies of interactions with glucose. Materials Science in Semiconductor Processing, 16, 1747-1752.

Hermann, B. G. & Patel, M. 2007. Today's and tomorrow's bio-based bulk chemicals from white biotechnology. Applied biochemistry and biotechnology, 136, 361-388.

Hou, Z., Yokota, O., Tanaka, T. & Yashima, T. 2003. Characterization of Ca-promoted Ni/α-Al2O3 catalyst for CH4 reforming with CO2. Applied Catalysis A: General, 253, 381-387.

Imtiaz, A., Farrukh, M. A., Khaleeq-ur-Rahman, M. & Adnan, R. 2013. Micelle-assisted synthesis of Al2O3· CaO nanocatalyst: optical properties and their applications in photodegradation of 2, 4, 6-trinitrophenol. The Scientific World Journal, 2013.

Jiang, X., Yu, L., Yao, C., Zhang, F., Zhang, J. & Li, C. 2016. Synthesis and characterization of Gd2O3 hollow microspheres using a template-directed method. Materials, 9, 323.

Koo, K. Y., Lee, J. H., Jung, U. H., Kim, S. H. & Yoon, W. L. 2015. Combined H2O and CO2 reforming of coke oven gas over Ca-promoted Ni/MgAl2O4 catalyst for direct reduced iron production. Fuel, 153, 303-309.

Li, N. & Huber, G. W. 2010. Aqueous-phase hydrodeoxygenation of sorbitol with Pt/SiO2–Al2O3: Identification of reaction intermediates. Journal of Catalysis, 270, 48-59.

Mulewa, W., Tahir, M. & Amin, N. A. S. 2017. MMT-supported Ni/TiO2 nanocomposite for low temperature ethanol steam reforming toward hydrogen production. Chemical Engineering Journal, 326, 956-969.

Radzi, M. R. M., Azizan, M. T., Daud, N., Topek, M. A. & Abidin, S. Z. 2018. Aqueous phase reforming of sorbitol over Ca doped Ni/Al2O3 for value-added chemicals production. Materials Today-Proceedings, 5, 21728-21736.

Tamrakar, R. K., Bisen, D. & Upadhyay, K. 2017. Change in thermoluminescence behaviour of cubic Gd2O3: Yb3+ phosphors with successive increase in Yb3+ ion concentrations. Radiation Physics and Chemistry, 130, 321-334.

Van Haasterecht, T., Swart, M., De Jong, K. P. & Bitter, J. H. 2016. Effect of initial nickel particle size on stability of nickel catalysts for aqueous phase reforming. Journal of Energy Chemistry, 25, 289-296.

#177: Research on the effect of different materials on solar-driven interfacial water evaporation

Yun Sheng ZHAO[1], Hong Feng ZHENG[2], Zhi Yong ZHAO[3], Xing Long MA[4]

[1]School of Mechanical Engineering, Beijing Institute of Technology, Beijing 100081, China, 1070213940@qq.com
[2]School of Mechanical Engineering, Beijing Institute of Technology, Beijing 100081, China, hongfeizh@bit.edu.cn
[3]School of Mechanical Engineering, Beijing Institute of Technology, Beijing 100081, China, 18811323258@163.com
[4]School of Mechanical Engineering, Beijing Institute of Technology, Beijing 100081, China, baalxmxl@yeah.net

At present, conventional solar desalination systems are high cost, high thermal resistance and low system efficiency. For solving these problems, a new device has been designed using light to directly heat seawater to produce freshwater and the influence and enhancement of different porous materials on the solar-driven desalination process was studied. The results show that when the solar irradiation was 2500 W/m^2, the water production of the system with porous carbon fibres on PVA sponge was the highest 12.43 g/h and that of the system with capillary glass tube was the lowest at 2.25 g/h. The efficiency of black sponge, black gauze, transparent capillary and carbon fibre felt systems were 34.3%, 44.7 %, 9.2% and 50% respectively. The results show that the hydrophilicity of the material, the ability to absorb light and the porous structure greatly influenced the evaporation process.

. Keywords: solar-driven steam generation; desalination; interfacial water evaporation

1. INTRODUCTION

With the global population growth and increase in consumption of resources, the shortage of freshwater is becoming an increasingly serious problem worldwide. With energy shortages and pursuit of sustainable development, the traditional seawater desalination technology is no longer applicable. Solar desalination is a good option to solve these problems. However, current solar desalination systems have lower efficiency and higher water production costs than that of traditional industrial desalination systems. In order to solve the shortcomings of traditional solar desalination, people have begun to use sunlight to heat seawater directly. This method can combine the concentrator, receiver, heat storage and pipeline into a concentrated system. Therefore, this new desalination system has low transfer resistance, low cost and high efficiency. However, in this process, improving the utilisation rate of seawater to light and increasing the evaporation rate of seawater are major difficulties.

In order to solve these problems, some research on solar-driven interfacial water evaporation desalination has been carried out. Zhou (Zhou et al., 2016) proposed a method to enhance the evaporation process in solar desalination by using plasma materials, which proved that this nanoparticle structure can enhance the evaporation process by 60%. Xue (Xue et al., 2017) used carbonised wood as the solar absorber, placing wood on the surface of water and testing its evaporation rate. In this experiment, solar-thermal efficiency of ~72% under a solar intensity was achieved. However, the two systems mentioned above only demonstrate the evaporation process and not the condensation process so desalination was not achieved. Ahsan (Ahsan and Fukuhara, 2010, Ahsan et al., 2010) studied the heat and mass transfer performance of a tube solar concentrator with direct concentrating evaporation. Omara, Chaouchi and Singh (Omara and Eltawil, 2013, Chaouchi et al., 2007, Singh et al., 1996) studied the desalination unit of seawater by using parabolic focusing and traditional disc distillator respectively. Zeng (Zeng et al., 2011) studied the enhancement of the evaporation process of seawater by putting magnetic absorbent particles in seawater and preliminary experimental results were given. Rajvanshi (Rajvanshi, 1981) studied the evaporation process by adding pigments or black charcoal to seawater and proved that the freshwater yield could be increased by 25-30% under the same conditions.

However, the fabrication of interface materials is very expensive and complicated and most solar-driven interfacial water evaporation systems only have the evaporation process with no condensation. So the objective of this paper was to design a new solar desalination system with both evaporation and condensation processes and to explore the performance of the solar desalination system with four low cost and easily accessible thermal porous materials as the basis of the experiment. Additionally, the effect of different materials on solar-driven interfacial water evaporation were studied.

2. THE STRUCTURE AND WORK PRINCIPLE OF THE SYSTEM

In order to accelerate the condensation of the system and better observe the evaporation in the system, a solar-driven interfacial water evaporation system was designed as shown in Figure 1. The system mainly consisted of the following parts: solar simulator, transparent glass cover, insulation layer, the cooling chamber, porous material, fresh water collection tank. The working principle of the system can be explained as follows: the solar simulator transmitted light through the transparent glass cover and eventually formed a circular spot on the surface of porous thermal material which was hydrophilic and had a high light absorption rate. The porous thermal material heated up and, with the mass of seawater in the porous materials being relatively small, the seawater in the porous materials heated up quickly and easily to produce vapour. The vapour leaving the surface of the porous thermal material entered the dehumidifier and condensed into freshwater on the low-temperature outside wall of the cooling chamber. Under the action of gravity, freshwater converged into the groove at the bottom of the dehumidifier and then flowed into the freshwater collection tank.

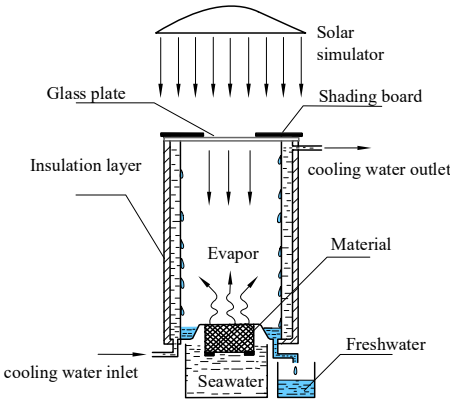

Figure 1: The structural sketch of the of solar-driven interfacial water evaporation system

3. ANALYSIS OF HEAT AND MASS TRANSFER FOR THE SYSTEM

To further study the heat-exchanging and water production situation of the system, the mathematical modelling of the process was achieved by applying mass and energy balances for the system. In order to facilitate the analysis of the energy of the system the following assumptions were considered.

(1) The moist air in the dehumidifier was saturated and its temperature was uniform in the dehumidifier.

(2) The local heat and mass transfer coefficients were uniform throughout the module;

(3) The heat preservation effect of the device was perfect and the heat loss in the system was negligible.

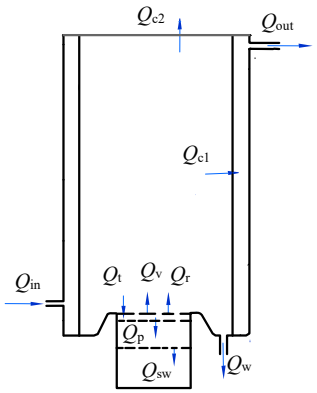

Figure 2: The heat and mass transfer mode in the first stage humidifier and dehumidifier.

Sunlight entered the system through the glass plate and the thermal porous hydrophilic material obtained solar energy Q_t. The seawater and the porous material were heated and their temperatures increased. The vapour broke away from the surface of thermal porous material and entered the dehumidifier. The energy carried by the vapour was Q_v. Radiation (Q_r) existed between the surface of porous material and the glass plate and some energy (Q_p) entered the porous material by heat conduction. Based on the energy conservation, this process is shown in Equation 1.

Equation 1:

$$Q_t = Q_v + Q_r + Q_p + m_{sw1} c_{sp} \frac{dT_{sw1}}{d\tau}$$

Equation 2:

$$AI\tau\alpha = m_e h_{fg} + \frac{\sigma A \left(T_{sw1}^4 - T_g^4\right)}{\frac{1}{\varepsilon_1} + \frac{1}{\varepsilon_2} - 1} + \lambda \frac{T_{sw1} - T_p}{\delta} + m_{sw1} c_{sp} \frac{dT_{sw1}}{dt}$$

Where:

I = solar irradiance;A =area of the thermal porous material; τ= transmittance of the glass plate;
A = absorptivity of the surface of thermal porous material; m_e = mass of the vapour;
h_{fg} = latent heat of the water; σ= Stefan-Boltzmann constant; δ = thickness of the thermal porous material;
T_{sw1} = temperature of the seawater on the surface of the porous material;
T_g = temperature of the glass plate; ε_1=the emissivity of the surface of the porous material；ε_2 = emissivity of the glass plate；
λ = thermal conductivity of the thermal porous material; m_{sw1} = mass of seawater on the surface of the porous material. c_{sp} = the specific heat capacity of the seawater. t = the exposure time.

When the vapour entered the dehumidifier, the moist air in the dehumidifier exchanged heat with the glass plate and cooling wall respectively. Taking the dehumidifier as the research object, the energy equilibrium equation occurring in the dehumidifier is described as shown in Equation 3:

Equation 3:

$$Q_v + Q_r = Q_{c2} + Q_{c1} + Q_w$$

Equation 4:

$$m_e h_{fg} + \frac{\sigma A \left(T_{sw1}^4 - T_g^4\right)}{\frac{1}{\varepsilon_1} + \frac{1}{\varepsilon_2} - 1} = A\, h_g \left(T_a - T_g\right) + A_c h_c \left(T_a - T_m\right) + Q_w$$

In addition, because the outer wall of the cooling chamber was wrapped with thermal insulation material, it was considered that the cooling chamber was insulated from the external environment. Based on the energy conservation, the rise in the cooling water temperature can be obtained by the following formula:

Equation 5:

$$Q_{c1} = m_c c_p (T_{out} - T_{in})$$

In addition, for evaluating energy efficiency of the desalination system with porous material, the steady state energy efficiency is as follows:

Equation 6

$$\eta = \frac{m_e h_{fg}}{AI\Delta t}$$

4. THE RESULT AND ANALYSIS OF THE EXPERIMENT

4.1. Equipment of experiment and four thermal porous materials

To study the effect of different thermal porous materials on solar-driven interfacial water evaporation desalination, some thermal porous materials were tested using the device, shown in Figure 3. The porous material was put in to a hollow cylinder with a height of 50mm and a diameter of 75mm, and the dehumidifier was a hollow cylinder chamber with a height of 250mm and a diameter of 120mm. The main instruments and parameters used in the experiment are shown in Table 1.

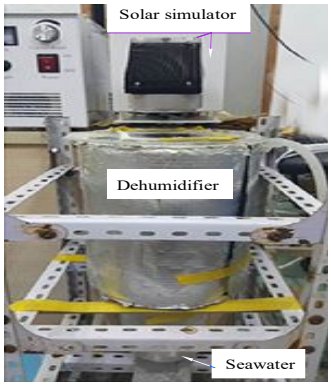

Figure 3: The multi-stage desalination experimental setup

Table 1: Specification of the different measuring devices

Instrument	Range	Accuracy
solar simulator (TRM-PD)	0-3kW	/
Solar Radiation Recorder (TRM-2)	/	±0.5%
Temperature recorder (JLS-XMT)	0-300℃	±1%
CCD camera	-10-400℃	±2 ℃
Electronic scale	0-200g	±0.01%

In order to study the hydrophilicity of the thermal porous material, the absorption of light, the function of the water unit and the durability and accessibility of the porous material, the following four types of porous materials were selected (shown in Figure 4): carbon fibre on PVA sponge; black ink-dyed gauze on PVA sponge; black ink-dyed

PVA (polyvinyl alcohol) sponge; and capillary glass tube. Among them, the PVA (polyvinyl alcohol) high density sponge made by polyvinyl alcohol not only had better hydrophilicity but also had lower thermal conductivity which can prevent heat loss. Carbon fibre was activated carbon fibre containing nano-pore size on its surface, which can increase specific surface area. The black gauze was obtained by dyeing gauze with black ink (carbon black). The diameter of the capillary glass tube was 0.9 - 1.1mm. The capillary water absorption was the direct reflection of capillary effect. Because of the difference of cohesion and adhesion, liquid overcomes the gravitational pull and rises or falls.

(a) carbon fibre on the PVA sponge

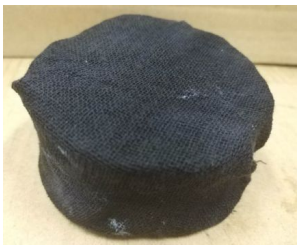

(b) black ink-dyed gauze on the PVA sponge

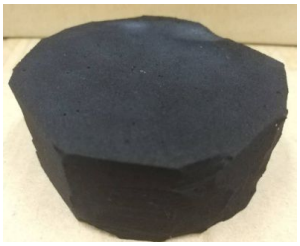

(c) the black ink-dyed PVA sponge

(d) capillary glass tube

Figure 4: The structures of four porous materials

The irradiance on the surface of porous materials was not uniform, so in order to calculate the total surface irradiance accurately, we used the method proposed by Ulmer to measure total irradiance on the surface of porous materials. Experiments on measuring flux density in a parabolic solar concentrator conducted by Ulmer conclude that an equation for calibrating irradiation by measuring grey-value on images of light spot on a Lambertian target shot through CCD sensor (Ulmer et al., 2002) as follows:

$$I=F_c \, \mathrm{GV} \qquad \textit{Equation 7}$$

By adjusting the current, the solar simulator illuminated the surface of porous materials as shown in Figure 5. Based on Equation 7, the average irradiance on the surface of the thermal porous material was 2500 W/m^2.

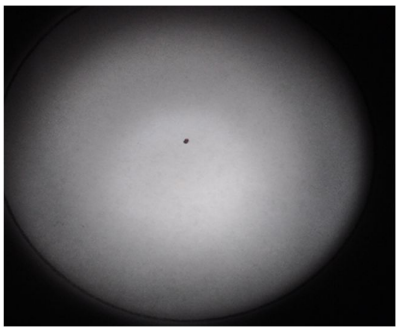

(a) Image of light spot taken from digital camera

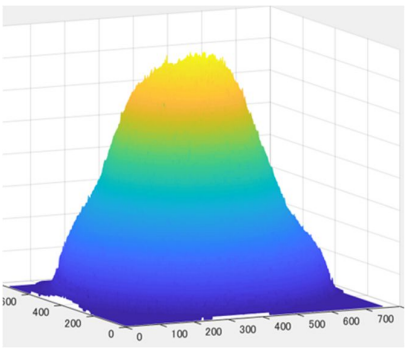

(b) Portrait view of irradiation map calibrated from intensity value

Figure 5: Irradiation on the surface of the thermal porous materials

4.2. The results of the experiment and analysis

During the experiment, water yield was measured every half hour. The variation of water production and temperature with time for four kinds of porous materials under average irradiation intensity of 2500 W/m^2 were recorded.

As can be seen from Figure 6, the freshwater production of the system with the black ink-dyed PVA (polyvinyl alcohol) sponge increased with time. Figure 7 shows that the temperature of each part of the system was stable after running for 1 hour. However, it can be seen from Figure 6 that the water production rate of the system was almost stable after 2 hours of operation. The reason was that at first, a large number of water droplets condense on the wall of evaporation system and did not drop into freshwater collecting tank. When the system reached stable water production, the water production rate of the system with black ink-dyed PVA sponge material was 8.24 g/h. When the initial temperature of seawater T_{sw1} was 21.6°C and the evaporation surface temperature was about 50.6°C, the energy efficiency (η) of the system was 34.3% on the basis of Equation 6.

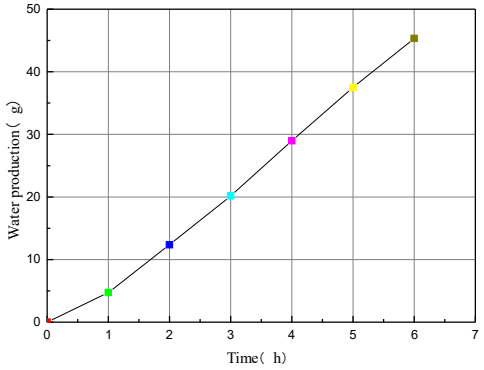

Figure 6: Variation of the water production with time for the black ink-dyed PVA (polyvinyl alcohol) sponge

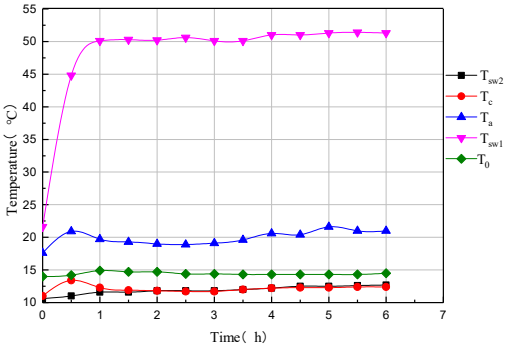

Figure 7: Variation of temperatures with time for the black ink-dyed PVA (polyvinyl alcohol) sponge

Figure 8 shows the variation of water production of system with time when the thermal porous material was the black ink-dyed gauze on the surface of the PVA sponge. The trend of water production was similar to that of the black ink-dyed PVA sponge system. The average water yield was 11.06 g/h. When the initial temperature of seawater was 24°C, the evaporation surface temperature of porous materials was 70.9°C. The efficiency of the system was 44.7% on the basis of Equation 6

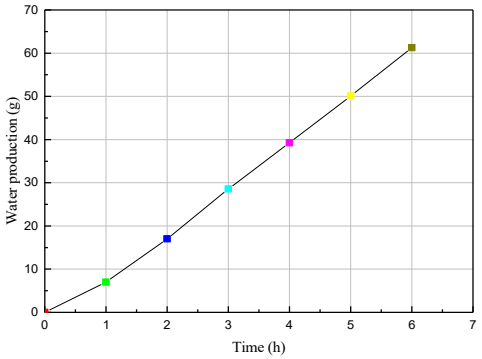

Figure 8: Variation of the water production with time for the black ink-dyed gauze on the PVA sponge

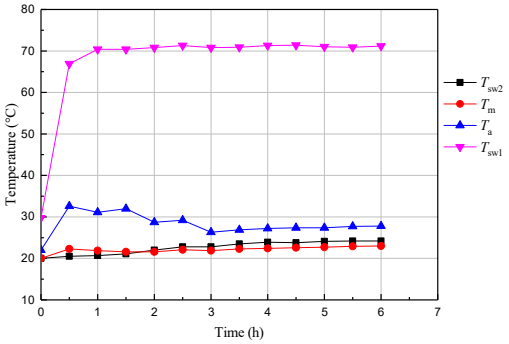

Figure 9: Variation of temperatures with time for the black ink-dyed gauze on the PVA sponge

Compared with black ink-dyed sponge, the temperature of the gauze system rose faster and the water temperature on the surface of the black ink-dyed gauze was higher. It suggests that the black gauze can absorb more light energy and was conducive to evaporation causing significant improvement in evaporation. This was because the water absorption of the gauze was different from that of the sponge. The gauze absorbs water and evaporates by the interaction of molecules in the fibre. Each fibre in the gauze was equivalent to a capillary making the water divide into smaller heated units. Additionally, seawater in the gauze had small contact area with the sponge which can reduce heat loss of convection and conduction so the system with the black ink-dyed gauze on the PVA sponge had more water production than that of black PVA sponge.

The performance of the desalination system with glass capillary system is shown in Figures 10 and 11. The trend was similar to that of the previous two porous materials: water production rate for the glass capillary was 2.25 g/h. The initial temperature of seawater was 24.7°C; the latent heat of water was 2352J/g at 62.2°C; and the efficiency of the system was 9.2% on the basis of Equation 6.

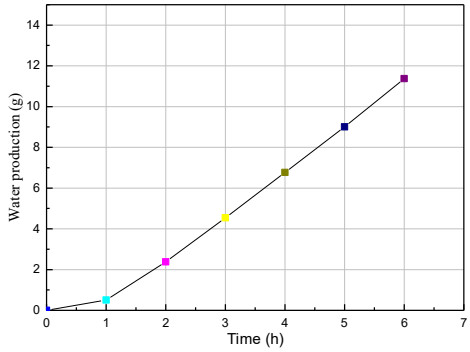

Figure 10: Variation of the water production with time for capillary glass tube

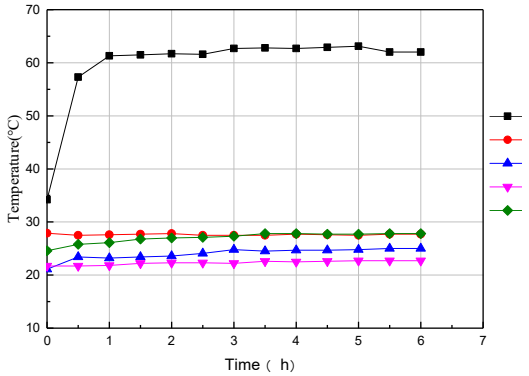

Figure 11: Variation of temperatures with time for capillary glass tube

The surface temperature of the glass capillaries was higher than that of the black sponge, but the water yield of the capillaries was significantly lower. This was because, although the glass capillary was transparent, when multiple capillaries were combined, the light irradiating on the capillary was refracted by the capillary and most of it was absorbed by it. Also, the specific heat capacity of the glass tube was low, so the temperature of seawater on the surface of the glass capillary was very high. Glass capillary with a diameter of 0.9 - 1.1mm was used in the experiment and, because of capillary effect, seawater will move upward along the capillary, but there was still a distance between the stable liquid level and the outlet of the capillary, which makes it difficult for the vapour generated in the capillary to flow out from the capillary resulting in less water production and low evaporation efficiency of the system.

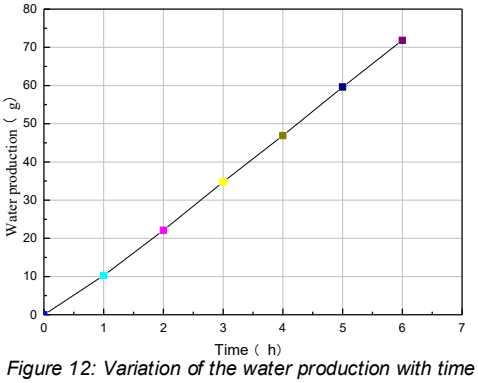

Figure 12: Variation of the water production with time for carbon fibre on the PVA sponge

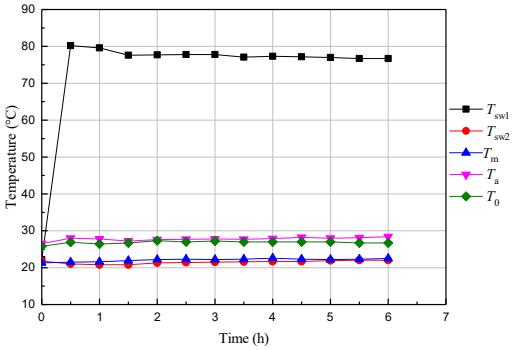

Figure 13: Variation of temperatures with time for carbon fibre on the PVA sponge

Figure 12 shows the variation of water production with time in the system of carbon fibre felt on the surface of the sponge. The trend was similar to that of the previous systems. When the system reached stable conditions, the average water yield was 12.43 g/h. The initial temperature of seawater was 21.8°C while the vaporisation heat of water was 2314 J/g at 77.5°C. The efficiency of the system was 50% based on Equation 7.

From the experimental data, it can be seen that the surface temperature of carbon fibre felt was higher than that of gauze, and the water yield of carbon fibre system was higher. This shows that carbon fibre felt had a higher light absorption rate. In addition, the aperture of carbon fibre felt was nanometer size, which made bulk water divide into small units of water and easier to heat. Additionally, the surface tension of water decreased when in smaller units, and thus easier to evaporate. Finally, it allowed the generated water vapour leave the fine holes of carbon fibre felt more easily, so the activation effect was very good. The rate of water production was relatively high.

5. CONCLUSION

In this paper, a solar desalination system for solar-driven interfacial water evaporation was designed and the performance of the system and effects of different porous materials on solar-driven interfacial water evaporation were studied. The conclusions obtained are as follows:

(1) The experimental results show that with the solar irradiance at 2500W/m2, the water yield of the black sponge system was 8.24 g/h and the efficiency of the system was 34.3%. The water yield of black gauze system was 11.06 g/h and the system efficiency was 44.7%. The water yield of the transparent capillary system was 2.25 g/h, the system efficiency was 9.2%, and the water yield of the carbon fibre felt system was 12.43 g/h, and the system efficiency was 50%.

(2) Among the four kinds of porous materials, carbon fibre felt was the most conducive to evaporation. The results show that light absorption capacity, pore size and hydrophilicity of the thermal porous material have a great effect on the solar-driven evaporation. A good thermal porous material used for solar-driven interface evaporation can greatly increase evaporation efficiency.

6. REFERENCES

Ahsan, A. & Fukuhara, T. 2010. Mass and heat transfer model of Tubular Solar Still. *Solar Energy,* 84**,** 1147-1156.

Ahsan, A., Islam, K. M. S., Fukuhara, T. & Ghazali, A. H. 2010. Experimental study on evaporation, condensation and production of a new Tubular Solar Still. *Desalination,* 260**,** 172-179.

Chaouchi, B., Zrelli, A. & Gabsi, S. 2007. Desalination of brackish water by means of a parabolic solar concentrator. *Desalination,* 217**,** 118-126.

Omara, Z. M. & Eltawil, M. A. 2013. Hybrid of solar dish concentrator, new boiler and simple solar collector for brackish water desalination. *Desalination,* 326**,** 62-68.

Rajvanshi, A. K. 1981. Effect of Various Dyes on Solar Distillation. *Solar Energy,* 27**,** 51-65.

Singh, S. K., Bhatnagar, V. P. & Tiwari, G. N. 1996. Design parameters for concentrator assisted solar distillation system. *Energy Conversion and Management,* 37**,** 247-252.

Ulmer, S., Reinalter, W., Heller, P., Lüpfert, E. & Martinez, D. 2002. Beam characterization and improvement with a flux mapping system for dish concentrators. Journal of Solar Energy Engineering. 1 (SED2002-1064), 3

Xue, G. B., Liu, K., Chen, Q., Yang, P. H., Li, J., Ding, T. P., Duan, J. J., Qi, B. & Zhou, J. 2017. Robust and Low-Cost Flame-Treated Wood for High-Performance Solar Steam Generation. *Acs Applied Materials & Interfaces,* 9**,** 15052-15057.

Zeng, Y., Yao, J. F., Horri, B. A., Wang, K., Wu, Y. Z., Li, D. & Wang, H. T. 2011. Solar evaporation enhancement using floating light-absorbing magnetic particles. *Energy & Environmental Science,* 4**,** 4074-4078.

Zhou, L., Tan, Y. L., Wang, J. Y., Xu, W. C., Yuan, Y., Cai, W. S., Zhu, S. N. & Zhu, J. 2016. 3D self-assembly of aluminium nanoparticles for plasmon-enhanced solar desalination. *Nature Photonics,* 10**,** 393-+.

#182: Characterisation of hydrochar produced by hydrothermal carbonisation of organic sludge

Wei WANG[1], Wen-Hua CHEN[2], Ming-Feng JANG[3]

[1] Chemistry Division, Institute of Nuclear Energy Research, Taiwan, nbaisgood3456@iner.gov.tw
[2] Chemistry Division, Institute of Nuclear Energy Research, Taiwan, wenhua@iner.gov.tw
[3] Chemistry Division, Institute of Nuclear Energy Research, Taiwan, mfjang@iner.gov.tw

Owing to increasing environmental concerns and concepts of sustainable development, sludge management has become an important issue recently. The energy efficient and economic feasible measure for sludge management is urgently required and hydrothermal carbonisation (HTC) has been regarded as one promising method. In this study hydrothermal carbonisation was used to convert organic sludge (OS) into the solid carbonaceous product (hydrochar) under various reaction temperature (T=180-240 °C) and residence time (t=60-240 min). The obtained hydrochar was analysed by elemental analysis, proximate analysis, SEM, FTIR, and BET to investigate the effect of reaction parameters on the hydrochar properties. Results are followed by discussions on potential applications of the obtained hydrochar. Obvious reduction of H/C and O/C ratio after HTC was observed based on the Van Krevelen diagram and FTIR analysis, revealing that dehydration and decarboxylation occur during the HTC process. The reaction temperature was regarded as the dominant parameter affecting hydrochar characteristic compared to residence time. The severity factor (log Ro) at the range from 4.13 to 5.90 showed good linear relationship with the ash content, volatile matter (VM), N content and H/C ratio of hydrochar, indicating that the severity factor could serve as a useful indicator analysing the hydrochar property. Although the surface area and porosity were improved by HTC, subsequent modification and activation should be needed to broaden the application field. Owing to the characteristic of high ash content, hydrochar derived from organic sludge might not be feasible for fuel use. Instead, the precursor of the activated carbon and low-cost adsorbent might be the potential applications, while further works is needed to verify the feasibility.

Keywords: hydrothermal carbonisation, organic sludge, hydrochar, severity factor

1. INTRODUCTION

As the environmental concerns and concepts of sustainable development increase, sludge management has gradually become an important issue discussed worldwide currently. Sludge is viewed as the residue derived from the wastewater treatment process and it mainly contains inorganic material and extracellular polymeric substances (EPS), wherein EPS primarily composed of proteins and polysaccharides. Because of large volume, high moisture content, poor dewaterability, fouling odour problems, and presence of pathogens, appropriate sludge management and utilisation are needed not only to reduce cost and handling difficulty but also to avoid harmful effect on the environment and human being. The processes for sludge management typically include preliminary treatment, stabilisation, conditioning, dewatering, followed by final treatments such as storage, landfilling, and agriculture use (Zhang *et al*. 2017). Traditionally landfilling, land application, and incineration are mainly used as a final treatment for sludge management, but these methods become unsuitable now owing to increasing environmental concerns and legislative forces. Thermal processes included pyrolysis, gasification, and combustion are regarded as alternative methods for sludge management recently due to the advantage of volume reduction and increasing dewaterability of treated sludge during the process. However, the pre-drying step is necessary for the processes mentioned above because of the restriction on feedstock moisture, which makes them become less energy efficient due to the intensive energy requirement of the pre-drying step.

Hydrothermal carbonisation (HTC) with operating temperatures of 180-250°C and pressure of 2-10 MPa is regarded as a thermal process converting organic feedstock into the solid carbonaceous product (hydrochar). The process water, liquid by-product of the HTC process, could also be used to synthesise chemicals, produce biogas, and recycle to HTC reactor for further reaction. Typically, the reaction mechanisms of hydrothermal carbonisation mainly include hydrolysis, dehydration, decarboxylation, aromatisation, and condensation polymerisation (Funke and Ziegler, 2010). As water is used as reaction medium and acts as a catalyst during HTC process, the pre-drying step is unnecessary in HTC, indicating that HTC is more energy efficient than other thermal processes such as pyrolysis, gasification, and combustion. Recently hydrothermal carbonisation has received considerable attention and it has been viewed as one promising method for treating feedstock with high moisture content such as sewage sludge or solid digestate (Libra *et al*. 2011). Additionally, hydrothermal carbonisation has a higher yield of solid carbonaceous product (45-70%) than conventional thermal processes (with pyrolysis yield=25-35% and gasification yield=10%, respectively) because of milder reaction condition (Kambo and Dutta, 2015), suggesting that it has better efficiency toward carbon utilisation as higher solid recovery.

To date, there has been an increase in research investigating the hydrothermal carbonisation for sludge management and utilisation. Nevertheless, the works are not as abundant as that for the lignocellulosic biomass and still limited. Moreover, the hydrochar property would be varied with the type of feedstock in use, further affecting the subsequent applications and the value of the obtained hydrochar. Currently, the applications of hydrochar mainly involve soil amelioration, solid fuel, adsorbents, and high added-value products such as the capacitor. Restated, char characteristic dominantly determines the applications and the added-value of hydrochar, which would further influence the economic feasibility of HTC process for sludge management. This emphasises the importance and necessity of fundamental characterisation toward hydrochar property.

In this study, hydrothermal carbonisation was carried out to convert organic sludge into hydrochar, and the obtained hydrochar under different HTC condition were examined. The schematic diagram illustrating the research process is shown in Figure 1. The main purposes of this work were (1) to explore the physical and chemical properties of hydrochar derived from organic sludge; (2) to investigate the effect of reaction temperature and residence time on hydrochar properties; (3) to evaluate the potential applications of sludge-derived hydrochar based on the obtained results.

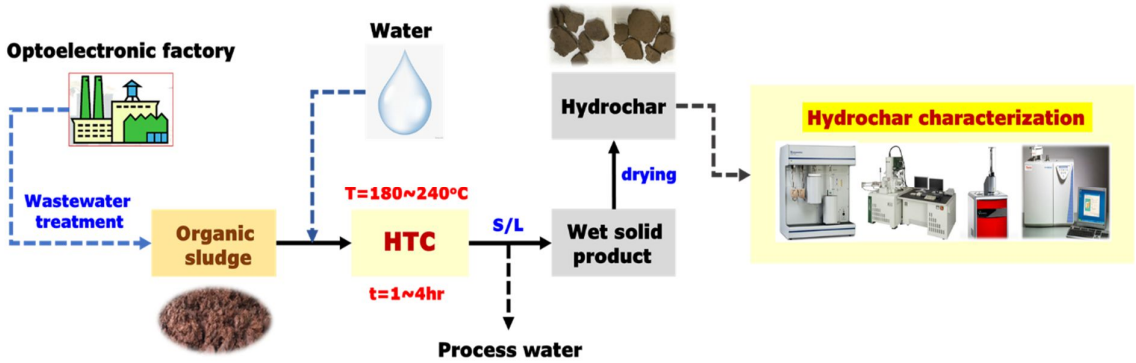

Figure 1: The schematic diagram of research process

2. MATERIAL AND METHODS

2.1. Organic Sludge

Organic sludge (OS) with initial moisture content of 90% was collected from the wastewater treatment plant of an optoelectronic factory located in Taiwan and stored at 4°C refrigerator before used. The sludge was dried at 105°C for 24 hours in the oven and ground to powder before analysis.

2.2. Hydrothermal Carbonisation

The hydrothermal carbonisation (HTC) reaction was carried out in the 2L-stirred pressure reactor (Model 4530; Parr Instrument Co., USA) with the material of CS Alloy 20Cb3. Two sets of experimental conditions: (1) fixed residence time (60 min) with varied reaction temperature (180-240°C); (2) fixed reaction temperature (200°C) with different residence time (60-240 min), were used to investigate the effect of time and temperature in HTC process. Briefly, 300 g raw organic sludge with an equal weight of water were stirred homogeneously and then transferred into the reactor. After that, the reactor was sealed and purged with N_2 gas three times to create oxygen-free circumstance, keeping the carbon inside the sludge from reacting with oxygen. After the purge step was complete, the reactor was pressurised to 150 psi using N_2 gas, heated up to the target temperature (T=180-240°C), and maintained for predetermined residence time (t=60-240 min) when the target temperature was reached. During the HTC process, the agitator was kept stirring at 150 rpm to ensure homogeneity of the mixture. When the reaction was finished, the pressure inside the reactor was released and the reactor was cooled down rapidly by water bath. Subsequently, the mixtures inside the reactor were taken out as soon as the room temperature and atmospheric pressure were reached. The solid carbonaceous products in the mixture were collected by vacuum filtration, followed by oven-drying at 105°C for 24 hr to get hydrochar product. The hydrochar of each reaction was weighed independently to calculate the yield and stored in a sealed container for further characterisation.

2.3. Analytical Methods

The hydrochar yield was calculated by the weight ratio of the recovery hydrochar to the dry sludge. The moisture of the sample was calculated by weight difference after oven-drying. The ultimate analysis of the hydrochar and raw sludge was determined by the elemental analyser (Elementar Vario ELIII, Germany). For proximate analysis, the ash content (Ash) was evaluated by NREL/TP-510-42622 method, while the volatile matter (VM) content was determined based on Chinese National Standards method (GB/T 212-2008), where one gram of sample was burned at 900°C for seven minutes in a muffle furnace. The fixed carbon (FC) content was calculated as:

Equation 1: Fixed carbon (FC) % =100% -VM % - Ash %

The higher heating value (HHV) was determined by the formula proposed by Channiwala and Parikh (Channiwala and Parikh, 2002):

Equation 2: HHV (MJ/kG) = 0.3491C+1.1783H+0.1005S+0.1034O-0:015N-0.021A

Where:

C = carbon
H = hydrogen
S = sulphur
O = oxygen
N = nitrogen
A = ash content (wt.% dry basis)

The hydrochar morphology was analysed by Scanning electron microscopy (SEM) microphotographs, obtained with a JSM-7100F. The surface functional groups of the sample were analysed by the Fourier transform infrared (FTIR) spectroscopy recorded on a Spectrum 100 spectrometer (PerkinElmer Inc, USA), where the samples were scanned from 4000 cm^{-1} to 400 cm^{-1} with a resolution of 4 cm^{-1}. The porous structure, specific surface area, and total pore volume were determined by means of N_2 adsorption-desorption isotherms at 77 K using an ASAP 2020 instrument. Surface areas were calculated by Brunauer–Emmett–Teller (BET) method.

3. RESULTS AND DISCUSSION

3.1. Ultimate and proximate analysis

The elemental analysis, proximate analysis, and yield were summarised in Table 1. For ultimate analysis, the percentages of C, H, N, and O initially in OS were 31.70%, 5.50%, 5.41%, and 24.42%, respectively. The H, N, O content in hydrochar decreased obviously after hydrothermal carbonisation, which attributed to the loss of

functional groups containing H, N, and O during the process. Generally, the mechanisms of hydrothermal carbonisation include hydrolysis, dehydration, decarboxylation, aromatisation, and condensation polymerisation. The decrease of the H content herein was mainly attributed to the phenomenon of the dehydration during HTC. Besides, the H content decreased apparently as reaction temperature increased but changed insignificantly with increasing residence time, suggesting that reaction temperature is the dominant parameter for dehydration. On the other hand, the content of C decreased from 31.70% to 24.22~27.36% after HTC process unexpectedly and declined with increasing temperature. This result was not consistent with the finding in Areeprasert *et al*. (2014), where the C content increased after HTC and elevated with increasing temperature. One possible reason is that the feedstock in use for HTC is different and the variation in feedstock composition may affect the reaction pathways, further resulting in different hydrochar composition (Wang *et al*. 2018). The reduction in C content implies that some carbon may transfer into the liquid part or convert into the gas phase during HTC process. In addition, the C content in hydrochar increased slightly with increasing time but declined obviously with increasing temperature, suggesting that temperature is the dominant parameter affecting the carbonisation process and longer reaction time may be needed for deeper carbonisation.

For the proximate analysis, the variation of volatile matter (VM) and ash content were mainly discussed. Typically the volatile matter is composed of carbon, hydrogen and trace amount of nitrogen. As shown in the results the volatile matter (VM) declined obviously from 59.71% to 34.05 - 44.27% after HTC. The decrease of volatile matter (VM) could be supported by the result of elemental analysis above, where the C, H, N content decreased after the reaction. On the other hand, the ash content of organic sludge was high (31.95%) and elevated to 48.57% - 57.88% with increasing reaction temperature and time after HTC process. In general, the ash content of sludge and its derived hydrochar are expectedly high, which has been reported before (Tay *et al*. 2001). The phenomenon of ash enrichment in hydrochar after HTC suggests that organic components were transferred into the liquid phase, while dissolved inorganic salts precipitated on the hydrochar during HTC (Zhang *et al*. 2014).

The atomic ratio of H/C versus O/C for organic sludge and derived hydrochar were shown in the Van Krevelen Diagram (Figure 2). The Van Krevelen Diagram was used to investigate the coalition effect of hydrothermal carbonisation. The initial ratios of H/C and O/C in organic sludge were 2.08 and 0.58 respectively. As shown in Figure 2, the obvious reduction in H/C and O/C ratio was observed after HTC process, where H/C declined to 1.58 - 1.76 and O/C decreased to 0.33~0.45, respectively. The H/C and O/C reduction indicates the phenomena of carbonisation, attributing to the mechanism of dehydration and decarboxylation during hydrothermal carbonisation (Funke and Ziegler, 2010). Generally, the lower value of H/C and O/C ratio suggest deeper carbonisation effect toward hydrochar. In this study, the lowest value of the above ratio was still far away from the traditional coal such as sub-bituminous, bituminous and anthracite. This may imply that the degree of carbonisation may not be enough for sludge derived hydrochar being used for fuel application.

Table 1: Characteristics and properties of hydrochar and organic sludge

sample	OS	180-60	200-60	220-60	240-60	200-120	200-240
Ultimate analysis							
C (%)	31.70	27.36	26.91	26.44	24.22	27.07	27.17
N (%)	5.41	2.91	2.61	2.21	1.89	2.44	2.35
S (%)	1.02	0.67	0.67	0.62	0.54	0.74	0.95
H (%)	5.50	4.02	3.75	3.55	3.19	3.71	3.73
Oa (%)	24.42	16.47	14.85	12.57	12.28	12.89	11.85
Atomic H/C	2.08	1.76	1.67	1.61	1.58	1.64	1.65
Atomic O/C	0.58	0.45	0.41	0.36	0.38	0.36	0.33
Proximate analysis							
FC (%)	8.34	7.16	7.41	8.87	8.07	9.31	9.31
VM (%)	59.71	44.27	41.39	36.52	34.05	37.53	36.72
Ash (%)	31.95	48.57	51.20	54.61	57.88	53.16	53.97
HHV (MJ/kg)	14.37	11.59	11.23	11.00	9.75	11.41	11.58
Yield (%)	-	60.82	56.99	55.29	50.87	57.09	57.54

Abbreviation: OS, organic sludge; FC, fixed carbon; VM, volatile matter; HHV, higher heating value; 180-60, represents hydrochar obtained from 180°C, 60 min.

[a] calculated by difference.

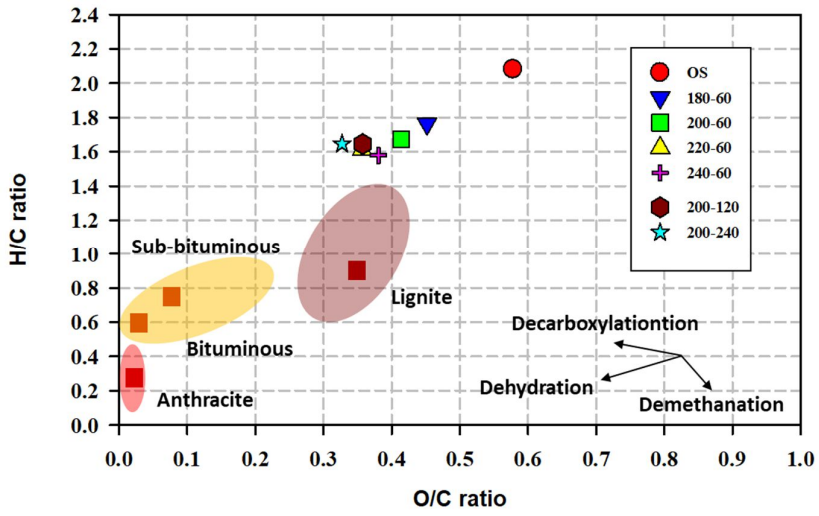

Figure 2: The Van Krevelen diagram

3.2. Solid yield and higher heating value (HHV)

To investigate the solid recovery of the HTC process, the hydrochar yield was determined. In the case of N-rich biomass such as sludge, the mechanism of hydrochar production during hydrothermal carbonisation can be categorised into two parts: (1) polymerisation of dissolved compounds. The soluble compounds in biomass like carbohydrate and protein would be firstly dissolved and hydrolysed into small molecules such as sugar and protein, subsequently converting to hydrochar by dehydration and polymerisation. (2) Solid-solid conversion. Non-soluble parts in biomass would transfer into hydrochar by HTC reaction including decarboxylation and condensation (Wang *et al*. 2018). As shown in Table 1, the yield decreased from 60.8% to 50.9% as temperature elevated from 180°C to 240°C, but increased slightly (57.0% to 57.5%) as the residence time became four times longer (60min to 240min) at 200°C. Based on the above mechanisms, the results imply that reaction temperature is the dominant parameter affecting the hydrochar yield compared to residence time, and considerable amounts of soluble compounds in feedstock would dissolve to the liquid part rather than retain in the solid phase during the process. Besides, high temperature should not be favourable for getting good yield during HTC. In addition, because it possibly takes time for dissolved compounds converting into solid char by dehydration and polymerisation, the longer residence time may be needed for further polymerisation to achieve the higher hydrochar yield.

To explore the fuel characteristic of sludge-derived hydrochar, higher heating value (HHV) was evaluated. The HHV of hydrochar ranged from 9.75 MJ/kg to 11.59 MJ/kg, which were lower than the original sludge (14.37 MJ/kg) (Table 1). The low heating value of hydrochar attributes to high ash content and lower carbon content. Considering the result from the Van Krevelen diagram, and the potential problem of slagging and fouling during char combustion due to high ash content using sludge-derived hydrochar for fuel application may not be economically feasible.

3.3. Relation between hydrochar characteristic and severity factor

To further investigate the combined effect of reaction temperature and time on the properties of the sludge-derived hydrochar, the reaction ordinate, Ro was introduced here. The reaction ordinate (Ro) was defined by Overend *et al*. (1987) and was originally used to evaluate hydrolytic depolymerisation processes (Overend and Chornet, 1987), while it was recently used to assess the condition toward hydrothermal reaction: The reaction ordinate (Ro) is defined as follow:

Equation 3: $Ro = t \cdot \exp(T-100 / 14.75)$

Where:

T = reaction temperature in °C
t = residence time in min

To illustrate the relation between reaction severity and selected experimental data, the severity factor (log Ro) was often used by many types of research. Besides, hydrochar characteristic correlated with the severity factor (log Ro) has also been reported, where the energy content of hydrochar was presented as a function of severity factor

(Hoekman *et al*. 2017). In this work, the hydrochar properties were analysed in term of log Ro by a linear regression method, and the properties with good regression results toward severity factor were shown in Figure 3. Obviously, the ash content increased with increasing severity factor, while the volatile matter (VM), N content and H/C ratio of hydrochar showed a converse trend. Additionally, there was a good linear relationship between log Ro and the above hydrochar properties when the log Ro was at range from 4.13 to 5.90. This may indicate that the severity factor (log Ro) could serve as a useful indicator to predict the hydrochar characteristic.

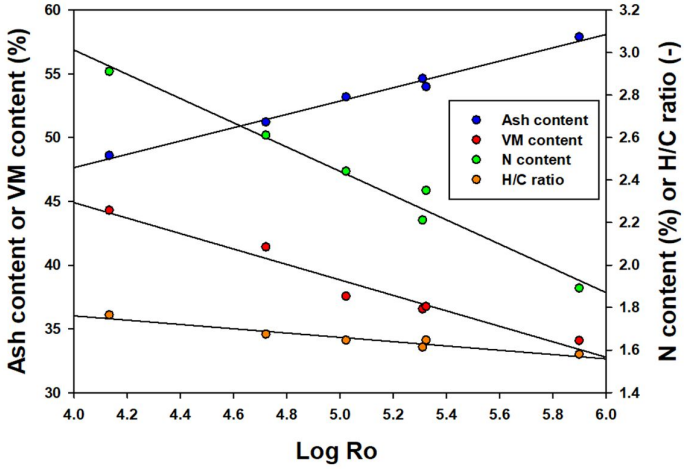

Figure 3: The relationship between hydrochar properties and HTC reaction severity (with ash content R^2=0.9882; volatile matter R^2=0.9598; N content R^2=0.9786; and H/C ratio R^2=0.9317, respectively)

3.4. Surface morphology

The SEM images were used to analyse the surface morphology of organic sludge and sludge-derived hydrochar, which were shown in Figure 4. The surface morphology of sludge changed significantly after HTC process, and the fragmentation of hydrochar and the number of derived grains increased significantly as the reaction severity raised. This revealed that the flocs and cellular tissues in sludge were broken because of gas volatilisation and chemical bond scission during the HTC process. The derived grains may result from the agglomeration of denatured protein in extracellular polymeric substances (EPS) or the sintering of the inorganic material because of thermal treatment. Furthermore, the sphere-like aggregates were observed at high reaction temperature (240°C). Based on the finding of Sevilla *et al*. (2009), we speculate that these sphere-like aggregates consisting of hydrophobic aromatic structure and hydrophilic shell may attribute to the HTC reaction of polysaccharide in the organic sludge (Sevilla and Fuertes, 2009). This observation may suggest that the occurrence of aromatisation and polymerisation in HTC require high reaction temperature.

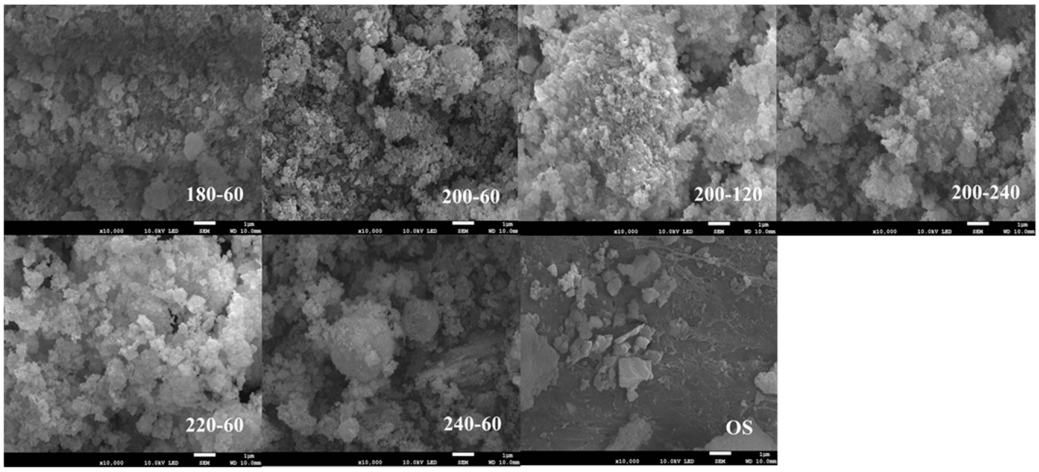

Figure 4: SEM images of organic sludge and hydrochar derived from different HTC conditions (OS: organic sludge; 180-60 represents hydrochar obtained from 180°C, 60 min.)

3.5. FTIR Spectra

Figure 5 represents the FTIR spectra of organic sludge and hydrochar with different HTC operating parameters. The obvious difference was observed after HTC showing that the surface functional groups changed during the process. Results and discussions were summarised as follow:

(1) The board band appearing at 3282cm^{-1} was associated with OH vibration in the hydroxyl group. According to the results, the intensity of the peak for hydrochar was less than that of the organic sludge, revealing that dehydration occurred during HTC. Further, the intensity of the peak became less as the temperature increased while the time effect seemed not so obviously. This may imply that dehydration is mainly influenced by temperature rather than time, which is in line with the discussion for H content reduction in section 3.1 (Peng *et al*. 2016).
(2) The band at 2800-3000cm^{-1} was attributed to aliphatic carbon -CHx stretching vibration corresponding to the alkyl aromatic structure. There was no obvious change at peak 2925 cm^{-1} and 2850 cm^{-1}, attributing to the asymmetric and symmetric -C-H stretching of the methylene groups, respectively (de Oliveira Silva *et al*. 2012).
(3) The band around 1645cm^{-1} was originated by ketone and amide group while the band at 1540 cm^{-1} attributed to C=O asymmetric stretching in the carboxylic group (Lin *et al*. 2012). Evident attenuation in peak intensity was observed at 1645cm^{-1} and 1540 cm^{-1}, implying that the decarboxylation occurred during HTC process. Still, the temperature effect seems so dominantly compared to that of the time.
(4) The peak around 1037 cm^{-1} referred to -Si-O stretching indicating the presence of SiO_2 (Yuan *et al.* 2011). Prominent growth of peak after HTC and steady increase of peak intensity with rising temperature was observed, suggesting that mineral compounds in sludge were retained in hydrochar during HTC. This result is consistent with the phenomena of ash enrichment after HTC, based on the proximate analysis in section 3.1. Still, the operating temperature seems to play an important role in determining ash content in hydrochar.

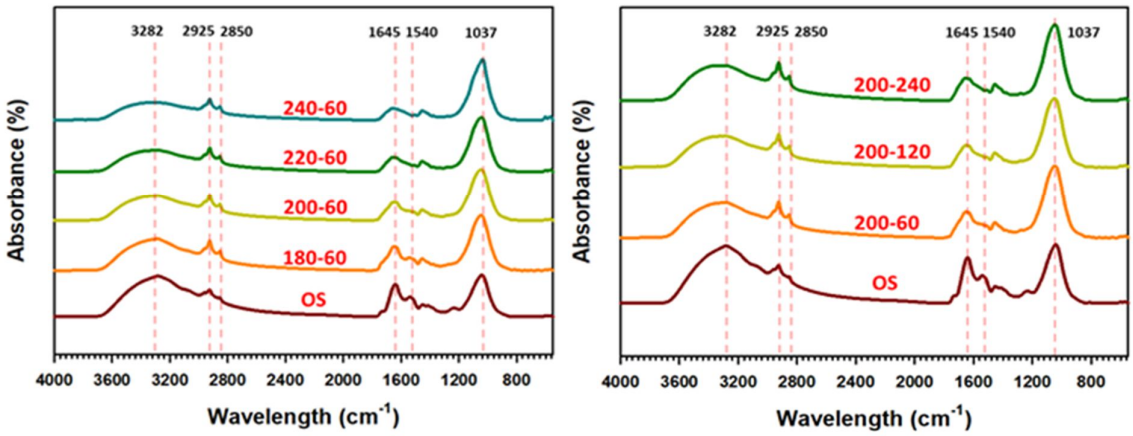

Figure 5: FT-IR spectra of organic sludge (OS) and hydrochar under various HTC conditions (left:T=180,200,220,240 °C; t=60 min; right: T=200 °C; t=60,120,240 min)

3.6. BET surface area and porosity

The adsorption isotherm plot was presented in Figures 6a and 6b. The adsorption isotherm of organic sludge could be classified as Type IV isotherms generally provided by the mesoporous adsorbent. Besides, apparent hysteresis loops were observed for the sludge sample, while this type of hysteresis loops has been observed with certain silicas and it is associated with capillary condensation and pore blocking. This probably suggests that organic sludge may contain considerable amounts of silica, which may also be supported by the observation of high ash content in the sludge. On the other hand, the adsorption isotherm of hydrochar could be viewed as Type II isotherms. Typically, macro-porous or nonporous adsorbent provided Type II isotherms indicating unrestricted monolayer-multilayer adsorption (Thommes *et al*. 2015). Based on the results, these imply that the structure of organic sludge was changed after HTC because of a series of reaction including hydrolysis, dehydration, decarboxylation, polymerisation, and aromatisation. Table 2 summarised the BET surface area (S_{BET}), total pore volume (V_t), and average pore size of sludge and hydrochar under various HTC conditions. The sludge-derived hydrochar had S_{BET} ranged from 26.48 to 35.43 m^2/g, V_t ranged from 0.24 to 0.30 cm^3/g, and average pore size ranged from 32.85 to 39.23 nm, respectively. Although the HTC enhanced the surface area by 2-3 times and improved the pore volume, the surface characteristic and porosity of hydrochar was still poor, implying that subsequent activation or modification should be needed for the further high added-value application.

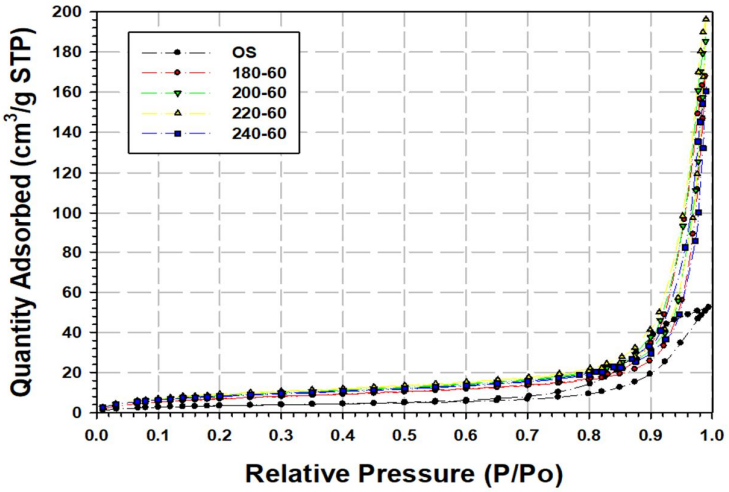

Figure 6a: The adsorption isotherm of organic sludge (OS) and hydrochar under various HTC conditions (T=180 , 200, 220, 240°C; t = 60 min)

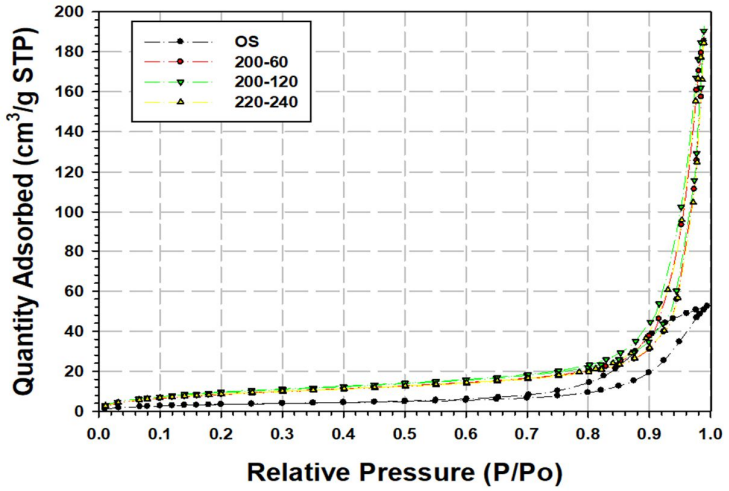

Figure 6b: The adsorption isotherm of organic sludge (OS) and hydrochar under various HTC conditions (T=200°C; t=60, 120, 240 min)

Table 2: Surface area and porosity of hydrochar and organic sludge

Sample	BET Surface Area (S_{BET}) (m^2/g)	Total Pore Volume (V_t) (cm^3/g)	Average Pore Size (nm)
OS	12.6126	0.0811	25.7269
180-60	26.4859	0.2598	39.2307
200-60	32.0941	0.2868	35.7432
220-60	33.5844	0.3035	36.1536
240-60	30.2606	0.2484	32.8476
200-120	35.4296	0.2953	33.2593
200-240	32.0872	0.2853	35.5687

Abbreviation: OS, organic sludge; 180-60, represents hydrochar obtained from 180°C, 60 min.

3.7. Discussions on potential application of sludge-derived hydrochar

The potential applications of hydrochar mainly include the capacitor, solid fuel, and low-cost adsorbent. Based on the results in this work, the sludge-derived hydrochars may not be feasible for solid fuel toward energy production, due to the low degree of carbonisation and low heating value resulting from the high ash content and low carbon content of hydrochar. High ash content in hydochar is also not favourable for combustion because of slagging and fouling problems reducing the fuel efficiency. Typically, the ash content ranged from 5 - 10% and the heating value larger than 17 - 19 MJ/kg are required for hydrochar as a solid fuel.

On the other hand, attributing to low surface area and poor porosity, sludge-derived hydrochars are not suggested for direct use in the capacitor. Instead, further activation should be required. Recently there has been an increased interest in using hydrochar as precursors of activated carbon, owing to the low degree of condensation and high density of oxygen-containing functional group in hydrochar, which are beneficial for the following activation. The activated carbons with high surface area using hydrochar as precursors have been reported by many studies, showing that hydrochar has chance to become high-value-added products under appropriate activation. For instance, Correa *et al*. (2017) showed that the hydrochar derived from biogas digestate could serve as a useful precursor for producing activated carbon with good surface property. The surface areas were elevated from 8~14 m^2/g (hydrochar) to 930–1351 m^2/g (activated carbon) via KOH activation, although the surface areas were rather low compared to other KOH activated carbons due to the high ash content in hydrochar. One interesting result was that the ash content decreased from 25.6~38.7% (hydrochar) to 6.17~7.95% (activated carbon) after KOH activation and the following acid washing step. The phenomena of ash declination might attribute to the reaction between potassium (K) and clay material inside the hydrochar, which formed the potassium- containing compounds during activation. These compounds would be further removed by the subsequent washing step, resulting in the decrease of ash content (Correa *et al.* 2017). This may also suggest that KOH activation could be one potential method to reduce the ash content in hydrochar, elevating the potential of subsequent applications. In general, the market value of the hydrochar depends on its subsequent application. The hydrochar is typically between 130 and 200 €/ton. However; the market value could be increased up to 500~1,500 €/ton via appropriate activation and modification (Lucia *et al.* 2016).

Even though hydrochar has poor surface characteristic and porosity, some works reported that it could serve as low-cost adsorbent well such as heavy metal removal agent. For example, Alatalo *et al.* (2013) used sludge-derived hydrochar (S_{BET} =9.1~18m^2, V_t = 0.04-0.09 cm^3/g) as an adsorbent for heavy metal adsorption, which showed a good effect for Pb removal. Koottatep *et al.* (2017) found that sludge-derived hydrochar with KOH modification (S_{BET} =4.41m^2, V_t = 0.04-0.049 cm^3/g) had better performance toward Cu removal than commercial activated carbon. This suggests that the surface characteristic and porosity may not be the only factor affecting the efficiency of the heavy metal adsorption, whereas functional groups could play an important role during adsorption. In summary, because of high ash content, hydrochar derived from organic sludge might not be suitable for fuel use, whereas precursors of activated carbon and low-cost adsorbent could be the potential applications.

4. CONCLUSION

In summary, compared to the residence time, the reaction temperature was regarded as the dominant parameter affecting sludge-derived hydrochar characteristic. Obvious dehydration and decarboxylation were observed after HTC based on the Van Krevelen Diagram and FTIR analysis. Additionally, the severity factor (log Ro) could serve as a useful indicator in describing hydrochar properties. Because of high ash content and low heating value, the hydrochar obtained from organic sludge may not be suitable for fuel use. Besides, Subsequent activation and modification should be needed for the application toward high added-value product such as capacitor owing to low surface area and poor porosity of the hydrochar. The precursor of the activated carbon and low-cost adsorbent might be the potential applications for the hydrochar derived from organic sludge. However, further work should be required to investigate the feasibility for applying sludge-derived hydrochar toward these potential applications. To further explore and elevate the potential value of sludge-derived hydrochar, future works would mainly include: (1) Using sludge derived hydrochar as precursors to exploit suitable KOH activation process efficiently improving the surface properties. (2) Conducting Cu^{2+}, Pb^{2+}adsorption test to evaluate the feasibility of using sludge derived hydrochar as low-cost adsorbent toward heavy metal removal.

5. REFERENCES

Alatalo, S.-M., E. Repo, E. Mäkilä, J. Salonen, E. Vakkilainen and M. Sillanpää (2013). "Adsorption behavior of hydrothermally treated municipal sludge & pulp and paper industry sludge." Bioresource Technology **147**: 71-76.

Areeprasert, C., P. Zhao, D. Ma, Y. Shen and K. Yoshikawa (2014). "Alternative solid fuel production from paper sludge employing hydrothermal treatment." Energy and Fuels **28**(2): 1198-1206.

Channiwala, S. and P. Parikh (2002). "A unified correlation for estimating HHV of solid, liquid and gaseous fuels." Fuel **81**(8): 1051-1063.

Correa, C. R., M. Bernardo, R. P. Ribeiro, I. A. Esteves and A. Kruse (2017). "Evaluation of hydrothermal carbonization as a preliminary step for the production of functional materials from biogas digestate." Journal of Analytical and Applied Pyrolysis 124: 461-474.

De Oliveira Silva, J., G. R. Filho, C. da Silva Meireles, S. D. Ribeiro, J. G. Vieira, C. V. da Silva and D. A. Cerqueira (2012). "Thermal analysis and FTIR studies of sewage sludge produced in treatment plants. The case of sludge in the city of Uberlândia-MG, Brazil." Thermochimica Acta **528**: 72-75.

Funke, A. and F. Ziegler (2010). "Hydrothermal carbonization of biomass: a summary and discussion of chemical mechanisms for process engineering." Biofuels, Bioproducts and Biorefining **4**(2): 160-177.

Hoekman, S. K., A. Broch, L. Felix and W. Farthing (2017). "Hydrothermal carbonization (HTC) of loblolly pine using a continuous, reactive twin-screw extruder." Energy Conversion and Management **134**: 247-259.

Kambo, H. S. and A. Dutta (2015). "A comparative review of biochar and hydrochar in terms of production, physico-chemical properties and applications." Renewable and Sustainable Energy Reviews **45**: 359-378.

Koottatep, T., K. Fakkaew, N. Tajai and C. Polprasert (2017). "Isotherm models and kinetics of copper adsorption by using hydrochar produced from hydrothermal carbonization of faecal sludge." Journal of Water, Sanitation and Hygiene for Development **7**(1): 102-110.

Lin, Y., D. Wang and T. Wang (2012). "Ethanol production from pulp & paper sludge and monosodium glutamate waste liquor by simultaneous saccharification and fermentation in batch condition." Chemical engineering journal **191**: 31-37.

Lucia Doyle, Barbara de mena, Michael Renz, Marisa Hernandez (2016). Industrial Scale Hydrothermal Carbonization: new applications for wet biomass waste.

Overend, R. P. and E. Chornet (1987). "Fractionation of lignocellulosics by steam-aqueous pretreatments." Philosophical Transactions of the Royal Society of London. Series A, Mathematical and Physical Sciences **321**(1561): 523-536.

Sevilla, M. and A. B. Fuertes (2009). "Chemical and structural properties of carbonaceous products obtained by hydrothermal carbonization of saccharides." Chemistry–A European Journal **15**(16): 4195-4203.

Thommes, M., K. Kaneko, A. V. Neimark, J. P. Olivier, F. Rodriguez-Reinoso, J. Rouquerol and K. S. Sing (2015). "Physisorption of gases, with special reference to the evaluation of surface area and pore size distribution (IUPAC Technical Report)." Pure and Applied Chemistry **87**(9-10): 1051-1069.

Wang, T., Y. Zhai, Y. Zhu, C. Li and G. Zeng (2018). "A review of the hydrothermal carbonization of biomass waste for hydrochar formation: Process conditions, fundamentals, and physicochemical properties." Renewable and Sustainable Energy Reviews **90**: 223-247.

Yuan, J.-H., R.-K. Xu and H. Zhang (2011). "The forms of alkalis in the biochar produced from crop residues at different temperatures." Bioresource Technology **102**(3): 3488-3497.

Zhang, Q., J. Hu, D.-J. Lee, Y. Chang and Y.-J. Lee (2017). "Sludge treatment: Current research trends." Bioresource technology **243**: 1159-1172.

#184: Performance evaluation of multi-stage indirect evaporative cooling systems

Xin CUI[1]*, Weichao YAN[1], Liwen JIN[1], Xiangzhao MENG[1], Kian Jon CHUA[2,3]

[1] *Institute of Building Environment and Sustainable Technology, School of Human Settlements and Civil Engineering, Xi'an Jiaotong University, Xi'an, Shaanxi 710049, China, *Corresponding author: cuixin@xjtu.edu.cn*

[2] *Department of Mechanical Engineering, National University of Singapore, 9 Engineering Drive 1, 117576, Singapore, mpeckje@nus.edu.sg*

[3] *Engineering Science Programme, National University of Singapore, 9 Engineering Drive 1, 117575, Singapore*

This study analysed the performance of multi-stage indirect evaporative cooling systems under two operational modes. A series of indirect evaporative coolers (IECs) were operated in a tandem arrangement. A mathematical model was established to investigate the theoretical performance of the multi-stage IEC. The model was validated by comparing the predicted air treatment conditions with experimental data acquired from literature. The calculated results show that the multi-stage arrangement is capable of improving the cooling performance and reducing the outlet air temperature. In addition, the Mode-2 IEC generally provided the product air with a lower outlet temperature compared with the Mode-1 IEC. On the other hand, the multi-stage IEC displayed a higher pressure drop resulting in a larger consumption of fan power. The cooling effectiveness, the pressure drop, and the cooling capacity are determined for the IEC with different stages. The calculation of Performance Evaluation Criteria (PEC) showed that the improvement of cooling effectiveness was achieved by sacrificing the cooling capacity for the multi-stage arrangement. It is inferred from the simulation results that the appropriate maximum stage was three-stage and two-stage for mode-1 and mode-2 IEC respectively.

Keywords: air-conditioning; indirect evaporative cooling; heat exchanger; heat and mass transfer; numerical simulation

1. INTRODUCTION

As an energy-efficient cooling techniques, the indirect evaporative cooling (IEC) system is getting increased attention (Cuce and Riffat, 2016). The key feature of IEC is the principle that the water evaporation process absorbs a large amount of latent heat (Caliskan et al., 2011). As a result, the IEC system consumes systematically less energy compared to the conventional mechanical compression system (Duan et al., 2012).

The IEC is gaining growing attention among researchers due to its energy saving and simplicity of operation (Chua et al., 2013). To assess the air treatment performance of IEC, a comprehensive analysis of the heat and mass transfer process is essential. Kim et al. (2017) conducted an experimental study to evaluate two types of cross flow IECs. Comino et al. (2018) proposed correlations based on experimental data and introduced a simplified mathematical model. The theoretical minimum temperature for a conventional IEC is the wet-bulb temperature. To produce cool air with a lower outlet temperature, recent research has proposed different designs for further enhancement of the cooling effectiveness (Cui et al., 2015; Sadighi Dizaji et al., 2018). Chen et al. (2018) investigated the control schemes used in IEC. Woods and Kozubal (2013) investigated a liquid desiccant enhanced IEC with a plate type counter-flow regenerative configuration. Pandelidis et al. (2017) compared the cooling effectiveness of three advanced IECs, pointing out that the combined cross-regenerative counter flow arrangement was able to achieve the highest overall cooling performance.

Based on the development of previous advanced designs on IEC, it is worth noting that the utilisation of multi-stage IEC system is able to improve the cooling effectiveness (Gadalla and Saghafifar, 2016). In addition, the multi-stage IEC system generates a higher pressure drop resulting in an increased energy consumption (Moshari and Heidarinejad, 2017). It can be inferred that the improvement of cooling effectiveness is achieved with sacrificing the cooling capacity and power consumption for the multi-stage configuration. Therefore, it is necessary to establish a performance evaluation method to understand the appropriate design for multi-stage IEC by considering the key criteria, such as the cooling effectiveness, the pressure drop, and the cooling capacity. However, the combined effect due to these influential parameters in a multi-stage IEC system has not been evaluated comprehensively in the existing literature. Therefore, the present study aims to address this issue by introducing the performance evaluation criteria to predict the simultaneous impact of the cooling effectiveness, the pressure drop, and the cooling capacity of multi-stage IEC operating in different modes.

In this article, two operation schemes of multi-stage IEC system are first introduced, followed by the development of a mathematical model. The validated model is then employed to analyse the performance evaluation criteria for the multi-stage IEC.

2. MATHEMATICAL FORMULATION

The multi-stage IEC system is schematically illustrated in Figure 1. A series of IECs are operated in a tandem arrangement. Two modes of IEC are evaluated in the present study. The Mode-1 IEC is a conventional counter-flow unit, while the Mode-2 IEC employs a regenerative M-cycle arrangement.

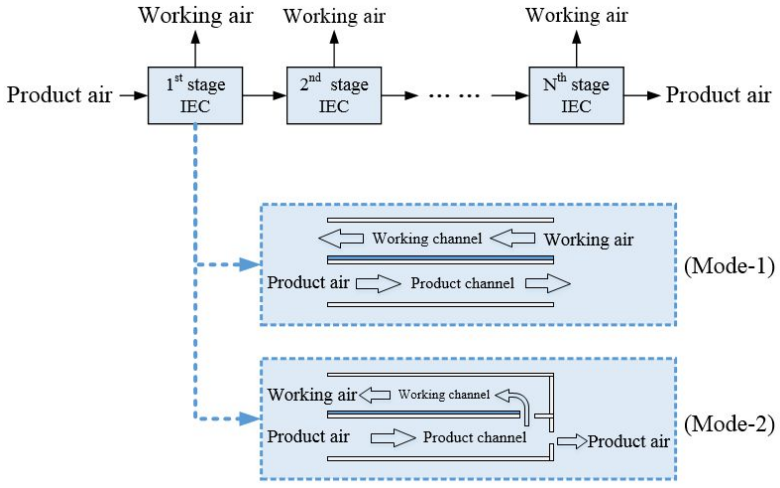

Figure 1: Schematic illustration of multi-stage IEC system operating in two modes.

2.1. Numerical model

A two-dimensional model was developed to investigate the heat and mass transfer performance of the IEC. The key governing equations are expressed as follows.

Equation 1: The continuity equation:

$$\frac{\partial u_a}{\partial x} + \frac{\partial v_a}{\partial y} = 0$$

Where:

- u_a = air velocity in x direction [m/s]
- v_a = air velocity in y direction [m/s]

Equation 2: The momentum conservation equation:

$$u_a \frac{\partial u_a}{\partial x} + v_a \frac{\partial u_a}{\partial y} = -\frac{1}{\rho_a}\frac{dp}{dx} + \nu_a \frac{\partial^2 u_a}{\partial y^2}$$

Where:

- ρ = air density [kg/m^3]
- p = pressure [kPa]

Equation 3: The energy conservation equation:

$$\frac{\partial}{\partial x}(u_a T_a) + \frac{\partial}{\partial y}(v_a T_a) = \alpha_a \frac{\partial^2 T_a}{\partial y^2}$$

Where:

- T_a = air temperature [°C]

Equation 4: The equation of species diffusion for the moist air:

$$u_a \frac{\partial c_a}{\partial x} + v_a \frac{\partial c_a}{\partial y} = D_a \frac{\partial^2 c_a}{\partial y^2}$$

Where:

- c_a = water vapor molar concentration [mol/m^3]

2.2. Performance evaluation

The wet-bulb effectiveness (WBE) and dew point effectiveness (DPE) are two common parameters for evaluating the cooling effectiveness.

Equation 5:

$$\varepsilon_{wb} = \frac{(T_{1,in} - T_{1,out})}{(T_{1,in} - T_{1,in,wb})}$$

Equation 6:

$$\varepsilon_{wb} = \frac{(T_{1,in} - T_{1,out})}{(T_{1,in} - T_{1,in,wb})}$$

The combined influence of cooling effectiveness, pressure drop, and the cooling capacity can be evaluated by the following parameters of Performance Evaluation Criteria (PEC):

Equation 7:

$$\mathrm{PEC1} = \frac{\varepsilon_{new,multi-stage}/\varepsilon_{new,one-stage}}{\Delta p_{multi-stage}/\Delta p_{one-stage}}$$

Equation 8:

$$\mathrm{PEC2} = \frac{Q_{multi-stage}/Q_{one-stage}}{\Delta p_{multi-stage}/\Delta p_{one-stage}}$$

3. RESULTS AND DISCUSSION

The numerical model is first validated by investigating the air treatment process of the IEC. Thereafter, the performance evaluation criteria can be analysed based on the validated model by considering the performance of the multi-stage configuration.

3.1. Model validation

The model's accuracy was validated by comparing the predicted temperature profile in the IEC against experimental data acquired from literature (Hsu et al., 1989). Hsu et al. [48] conducted an experimental study on a counter-flow regenerative IEC. The simulation was carried out under the same operating conditions compared with the experiments. Figure 2 shows the validation of the model by comparing the dry bulb temperature profile of the IEC. It can be inferred from the figure that the numerical model presented a good agreement with an average discrepancy of 6%. Therefore, the model is considered as an accurate approach to study the air treatment conditions of the IEC.

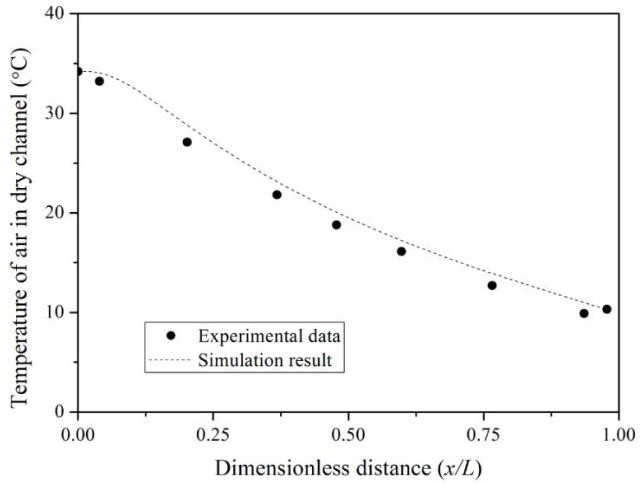

Figure 2: Comparison of air temperature profiles for a counter-flow regenerative IEC.

3.2. Cooling performance

The cooling effectiveness of the IEC has been investigated in two operating modes as shown in Figure 3. The temperature and humidity ratio of the intake air is maintained at 30°C and 10 g/kg, respectively. Therefore, the air is assumed at a wet-bulb temperature of 19.5°C and a dew point temperature of 14.1°C.

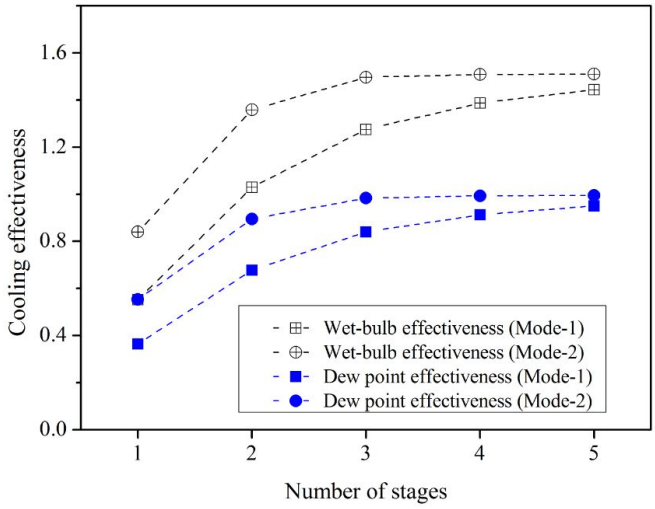

Figure 3: Cooling effectiveness for multi-stage IEC

The wet-bulb effectiveness of the one-stage IEC in Mode-1 is 40%-60%. By employing a multi-stage configuration, the product air temperature can be further reduced as a result of the pre-cooling in the prior stage. The result indicates that the multi-stage arrangement is capable of improving the cooling performance and reducing the outlet temperature. The mode-2 IEC generally shows a higher cooling effectiveness compared with the mode-1 IEC. In addition, the cooling effectiveness of the mode-2 IEC presents a small variation after the second stage. For example, the dew point effectiveness of mode-2 IEC increases from 0.55 to 0.89 by adopting a two-stage IEC, while it ranges from 0.98 to 0.99 by increase the stage number from 2 to 5.

3.3. Performance evaluation

The multi-stage IEC is able to improve the cooling effectiveness. On the other hand, the multi-stage IEC consumes more energy power due to a higher pressure drop. In addition, the cooling capacity may be reduced for a multi-stage IEC due to a reduced product air flow rate. Therefore, it is essential to consider the Performance Evaluation Criteria (PEC) for investigating the simultaneous impact of the cooling effectiveness, the pressure drop, and the cooling capacity.

The PEC1 indicates the combined effects of the cooling effectiveness and the pressure drop, while the PEC2 reflects the relationship between the cooling capacity and the pressure drop. The value of the PEC is calculated by comparing the performance of the multi-stage IEC with that of one-stage unit.

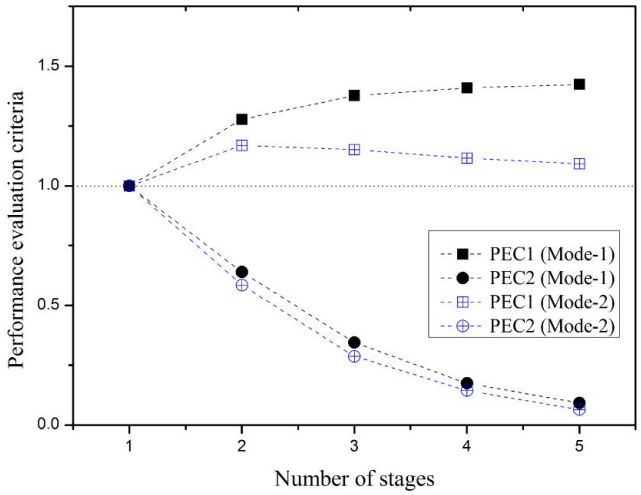

Figure 4: Performance evaluation criteria for multi-stage IEC.

Figure 4 illustrates the performance evaluation criteria for multi-stage IEC. Based on the expression of the PEC, the PEC value higher than unity demonstrates that the usage of multi-stage IEC leads to a better performance compared with a single-stage IEC. For mode-1, the PEC1 is improved slightly when the number of stage is larger than three. For mode-2, the PEC1 reaches a maximum value for a two-stage IEC, while the PEC1 drops with the increase of stages. The PEC2 decreases for multi-stage application. It may be attributed to the fact that the enhancement of cooling effectiveness is realised by sacrificing the cooling capacity.

4. CONCLUSION

The multi-stage IEC system has been analysed under two operation modes. Theoretical study has been conducted to evaluate the performance based on a validated mathematical model. The values of performance evaluation criteria were calculated by considering the combined impact of several key parameters. or mode-1, the number of stages is suggested to be not more than three, since the value of PEC1 shows a slightly improvement after the 3rd stage. For mode-2, the maximum stage is suggested to be 2-stage IEC as the PEC1 reaches a maximum value at the 2nd stage.

5. REFERENCES

Caliskan, H., Dincer, I., Hepbasli, A., 2011. Exergetic and sustainability performance comparison of novel and conventional air cooling systems for building applications. Energy and Buildings 43, 1461–1472.

Chen, Y., Yan, H., Yang, H., 2018. Comparative study of on-off control and novel high-low control of regenerative indirect evaporative cooler (RIEC). Applied Energy 225, 233–243.

Chua, K.J., Chou, S.K., Yang, W.M., Yan, J., 2013. Achieving better energy-efficient air conditioning – A review of technologies and strategies. Applied Energy 104, 87–104.

Comino, F., Milani, S., De Antonellis, S., Joppolo, C.M., Ruiz de Adana, M., 2018. Simplified performance correlation of an indirect evaporative cooling system: Development and validation. International Journal of Refrigeration 88, 307–317.

Cuce, P.M., Riffat, S., 2016. A state of the art review of evaporative cooling systems for building applications. Renewable and Sustainable Energy Reviews 54, 1240–1249.

Cui, X., Chua, K.J., Islam, M.R., Ng, K.C., 2015. Performance evaluation of an indirect pre-cooling evaporative heat exchanger operating in hot and humid climate. Energy Conversion and Management 102, 140–150.

Duan, Z., Zhan, C., Zhang, X., Mustafa, M., Zhao, X., Alimohammadisagvand, B., Hasan, A., 2012. Indirect evaporative cooling: Past, present and future potentials. Renewable and Sustainable Energy Reviews 16, 6823–6850.

Gadalla, M., Saghafifar, M., 2016. Performance assessment and transient optimization of air precooling in multi-stage solid desiccant air conditioning systems. Energy Conversion and Management 119, 187–202.

Hsu, S.T., Lavan, Z., Worek, W.M., 1989. Optimization of wet-surface heat exchanger. Energy 14, 757–770.

Kim, H.J., Ham, S.W., Yoon, D.S., Jeong, J.W., 2017. Cooling performance measurement of two cross-flow indirect evaporative coolers in general and regenerative operation modes. Applied Energy 195, 268–277.

Moshari, S., Heidarinejad, G., 2017. Analytical estimation of pressure drop in indirect evaporative coolers for power reduction. Energy and Buildings 150, 149–162.

Pandelidis, D., Anisimov, S., Rajski, K., Brychcy, E., Sidorczyk, M., 2017. Performance comparison of the advanced indirect evaporative air coolers. Energy 135, 138–152.

Sadighi Dizaji, H., Hu, E.J., Chen, L., 2018. A comprehensive review of the Maisotsenko-cycle based air conditioning systems. Energy 156, 725–749.

Woods, J., Kozubal, E., 2013. A desiccant-enhanced evaporative air conditioner: Numerical model and experiments. Energy Conversion and Management 65, 208–220.

#185: Adaption of agriculture photovoltaic technology for Papua New Guinea rural household energy supply and farmland preservation

Wen LIU[1], Fangxin ZHANG[2], Xinyu ZHANG[3], Jan INGENHOFF[4], Ora RENAGI[5], Nicholas LAMBRACHE[6], Rena LOVO[7], Dapsy OLATONA[8]

[1]Institute of Advanced Technology, University of Science and Technology of China (USTC); Solar Energy Research Center, Hubei University of Technology (HBUT), China, wenliu@ustc.edu.cn
[2]Institute of Advanced Technology, USTC; Solar Energy Research Center, HBUT, China, fangxinzhang@ustc.edu.cn
[3]Institute of Advanced Technology, USTC; Solar Energy Research Center, HBUT, China, zhangxinyu94@qq.com
[4]Institute of Advanced Technology, USTC; Solar Energy Research Center, HBUT, China, jan.ingenhoff@ustciat.cn
[5]Department of Applied Physics, Papua New Guinea University of Technology (UniTech), Lae, Morobe Province, PNG. ora.renagi@pnguot.ac.pg
[6]Department of Mechanical Engineering, UniTech, PNG. nicholas.lambrache@pnguot.ac.pg
[7]Department of Applied Physics, UniTech, PNG. seri.2018@pnguot.ac.pg
[8]Sustainable Energy Research Institute, Department of Applied Physics, UniTech, PNG. dapsy.olatona@pnguot.ac.pg

Agriculture Photovoltaic (APV) is a relatively young discipline; the concept was first proposed in 1984. The core ideas of APV are developed further in this study in a manner that allows (on one and the same farmland) the cultivation of crops and vegetables as well as simultaneously generating electricity using specially designed APV-CPV solar panels. In this collaborative dual-purpose Energy/Agricultural Land-Conservation study, the authors report significant improvement achieved in Agricultural Photovoltaic (APV) Technology by Wen Liu and his team from the Institute of Advanced Technology in Hefei, Anhui China. In particular, the study provides a detailed analyses of how the technology can be tailored to block out harmful radiation from farm crops, provide renewable electricity and thereby improve the living standards of the rural and small island populations of Papua New Guinea (PNG is a Pacific Island nation, North of Australia). The aim is to free the country from fossil fuel dependency, reduce Carbon dioxide (CO_2) emission and contribute to the global action against climate change in line with the PNG Government National Energy Policy covering 2018 to 2050 as well as the United Nations energy goals.

Keywords: agricultural photovoltaic, renewable electricity, climate change

1. INTRODUCTION

The atmosphere, oceans and land masses of the earth absorb (per year) approximately 3.8 million exajoules (EJ) from the sun's radiation (exa = 10^{18}). So, the sun can provide in one hour the current world usage of energy within one year. The amount of solar energy reaching the surface in one year is about twice as much as will ever be obtained from all non-renewable resources on earth like coal, oil, natural gas, and mined uranium combined. Thus, solar energy is and remains the main and most powerful renewable energy source we can leverage on earth. Approximately just 0.1% of that vast amount of sun energy per year is captured in biomass by Photosynthesis (Smil, 2006).

There is no doubt that life on earth depends on the sun being key to securing the food chain and providing energy for photosynthesis allowing plants and vegetable to grow. Mankind has cultivated crops by developing agriculture thousands of years ago. Various improvements have been implemented over the centuries and modern agriculture is leveraging technologies from the internet of things (IoT) and sophisticated harvesting methods. However, those modern techniques require electricity. Although being able to provide it by the power grid, consideration has been undertaken as to how to combine agriculture and power supply. This was the birth of agriculture photovoltaic, which allows crop growing and electricity generation on the same land.

Papua New Guinea (PNG), shown in Figure 1 (Perry-Castaneda, 2013), is a developing country in the Pacific Region (North of Australia) where the combination of agriculture, arable land preservation and power supply is of paramount importance to the government and the livelihood of its vast rural population.

Figure 1: Location map of PNG (inset)[i]

In 2018, the PNG government introduced an ambitious National Energy Policy to satisfy 70% of electric power needs of its population by 2030. By 2050, the policy proposes that renewable energy be utilised to satisfy the energy needs of the entire population (Basil, 2018). According to the World Bank and other statistical organisations, only about 14% of the citizens of PNG live in large cities and only about 13% of the population is connected to the fossil fuel-dependent national grid. This suggests that about 80% live in rural towns and island villages without electricity (PNG National Energy Policy Group, 2018). Therefore, it is reasonable to suggest that in order to meet the energy goal set by the PNG government, the energy demand of rural dwellers must be met. Solar energy supply by conventional flat solar panels would have been a natural choice. However, solar farms require a large amount of flat idle land which, due to the natural hilly terrains of rural PNG, does not exist. 1 kW of conventional solar panels requires approximately 100 square foot, or 10 square metres of land.

The competition for land in PNG is further exacerbated by the fact that a large portion of rural land of PNG is oil, gas and mineral rich. The interest of government and international mining companies consequently puts more pressure on the scarcity and availability of land for large scale rural farming. Due to these and other land usage issues, the rural population of PNG relies heavily on subsistence farming whereby each household grows their own staple crops in small parcels of land (called gardens) immediately adjacent to their homes.

While the rural population can feed itself by practicing subsistence farming, they remain largely cash-poor because they are unable to generate a regular income except for the occasional sale (at the local market) of surplus farm and garden produce.

The subsistence farming culture of rural PNG women and the modest energy requirement of the typical PNG 'rural household' (estimated as 160 – 240W by the Sustainable Energy Research Institute (SERI) at the Papua New Guinea University of Technology) makes the country predestined for agriculture photovoltaic (APV). The authors' previous study showed that APV-CPV innovation is particularly suited to PNG solar 'insolation' conditions and has the potential to improve the cultivation, growth and crop yield of certain vegetables, fruits and food crops that would otherwise be affected negatively if exposed to the normal daily hot sunshine. Pilot demonstration installations with 2 or 3 APV-CPV panels installed over the garden of selected households over a period of two years would reconfirm this assertion under PNG climate conditions.

In this paper we present two very new technologies in the area of agriculture photovoltaic and explore the possibility and concepts, how those technologies can be implemented in Papua New Guinea to help farmers in small villages improve their standard of living by getting access to electricity and simultaneously improved the yields of crops by protecting the plants from harmful radiation and allow artificial irrigation. We discuss in detail the status quo of agriculture in Papua New Guinea and what can be done to improve the current situation.

2. AGRICULTURE PHOTOVOLTAIC

Agriculture Photovoltaic is a relatively young discipline and the concept was first proposed in the year of 1984. The core idea is to allow farmland to simultaneously grow crops and generate electricity from solar panels. In Figure 1a, we see that the concept of agriculture photovoltaics merges smoothly and harmonises into the interconnection between consumer's energy usage and storage, energy purchasing agreements with local residential and industrial estates and energy provision to the power grid distribution system from operators (Obergfell, 2015). There are currently two solutions, the first type of APV is a geometrical splitting mode and can be found in China, Japan, Italy and Germany; The problem is that there is either no light or uneven light on the farmland, consequently the actual lighting time is shortened resulting in critically affected crop yield and quality. This has become more and more serious, especially in areas where the land is already relatively scarce. The second type is an intensity-splitting mode using thin film translucent solar cells, such as copper indium selenium cells or cadmium telluride cells, which claim to be semi-transparent (Zhang F., 2018). But the common thin film solar cells have typically high absorption rates in the photosynthesis active spectrum of plants and therefore basically block the necessary plant light. Consequently, the quality of thin film solar cell technology is poor and additionally the photosynthesis of plants becomes quite limited. Solar panels block the sunlight and thus on common solar farms, there is not only a lack of plant growth beneath the solar panels but also a tendency towards desertification of the land. On the other hand, too much sun light can be also harmful for the plants, and blocking IR and FIR as well as UV light would be beneficial for the health of the plants.

Figure 1a: basic principle of APV, Fraunhofer Institute ISE; 1b: current solution for agriculture photovoltaics by implementing mosaic type of structures carrying solar panels high above the farmland

2.1. The CPV - APV system

CPV-APV stands for concentration photovoltaic – agriculture photovoltaic. The basic principle of the CPV-APV system is shown in Figure 2. It allows red and blue wavelengths to be transmitted for plant growth while all other wavelengths are reflected on to concentrator solar cells for solar power generation. The layout of the APV-CPV system follows design concepts of concentration photovoltaic and thermal systems (CPVT). A parabolic glass panel collects the sun light and reflects it on solar cells located in the range of its parabolic focal point. The modification is that a bended glass panel covered with a special dichroitic polymer film is used allowing the transmission of red and blue light, which are the essential wavelength for plant growth (Zhang Z., 2018). As a result, simultaneous plant growth and electricity generation becomes possible on one and the same land area.

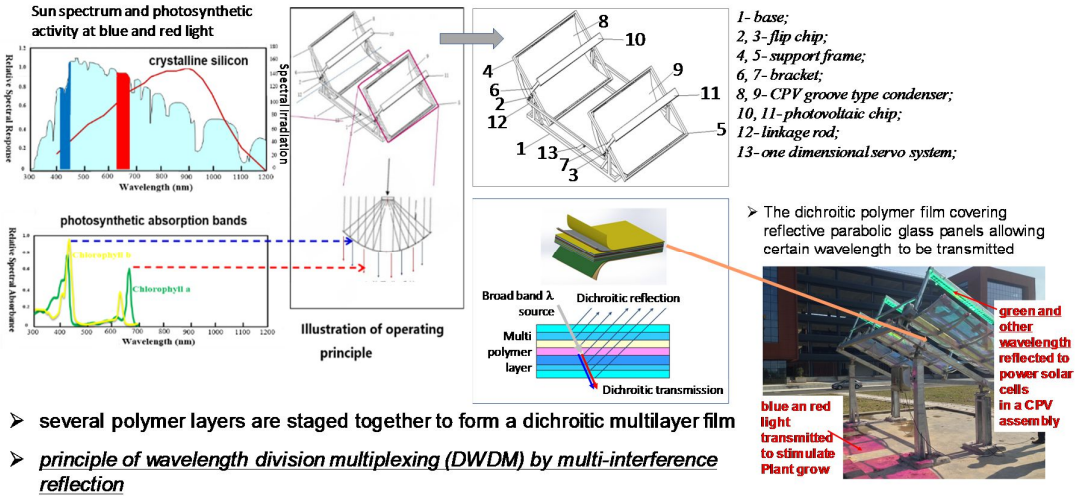

Figure 2: basic principle of CPV-APV: red and blue wavelengths are transmitted for plant growth; all other wavelengths are reflected on concentrator solar cells for solar power generation

2.2. The TGPV system

TGPV stand for tender glossy photovoltaic. By inserting a patterned glass in the middle of two conventional solar photovoltaic panels, a uniform lighting environment is available for plants. The structure of the patterned glass, shown in Figure 3, allows the sunlight to be evenly distributed beneath both the glass panel and the solar cell panels. The light transmittance decreases with the narrower widths but increases with large widths (Zhang F., 2018). It can be adjusted accordingly to the illumination demand of the crop varieties beneath.

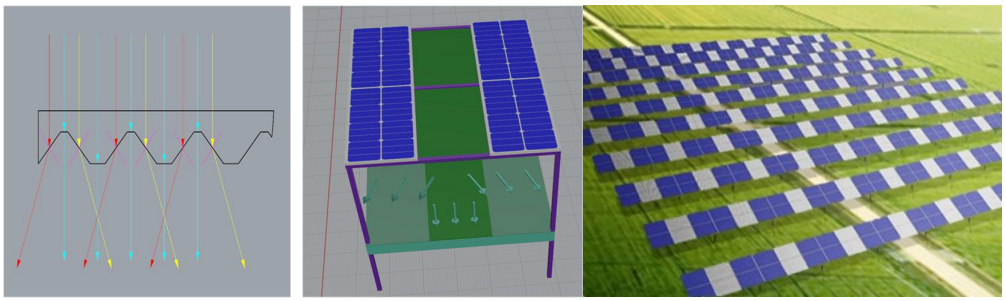

Figure 3: basic principle of TGPV: By inserting a patterned glass in the middle of two conventional solar photovoltaic panels, the uniform lighting environment is realised for plants.

Compared with the existing APV technologies, the beneficial effect of this new scheme is that the light splitter is realised through the trough glass, and the sun can be evenly distributed beneath the two sides and the middle trough glass area. The present invention can control the proportion of the light transmittance by adjusting the proportion of the area of the trough glass splitter, allowing it to change the light intensity for the crops beneath the solar photovoltaic modules in the range of 35% and 65%. The invention also effectively helps to reduce the water evaporation of the agricultural land, avoiding lack of water during droughts. It is of great significance to improve agricultural strength in deprived areas.

The CPV-APV and the TGPV systems have been implemented in China on a test field as shown below in Figure 4 and Figure 5. Various crops such as broccoli, spinach and lettuce have been grown under both systems and the crop yield were investigated and compared with those on free farmland with direct sun irradiation. Currently supplementary test sides are established in other areas in China and test areas in Costa Rica are under discussion.

In large scale, the capital costs to install such agrophotovoltaic systems are at approximately 1.5 US$ per Watt for the CPV-APV system and approximately 0.3 US$ per Watt for the TGPV system. Given the average electricity consumption per capita in PNG of approx. 441 KWh / year, one needs about an 1100-Watt system for a 5 people household. Thus, costs are 1650 US$ for the CPV-APV system and 330 U$ for the TGPV system. Electricity costs in PNG are at 0.77 Kina per KWh (~0.23 US$), so the return of investment (RoI) lies at approximately three years for the CPV-APV system and approximately one year for the TGPV system (effectively this time is shorter

considering the land use underneath the agrophotovoltaic systems cultivating crops contributing to income). Looking at costs and RoI, one certainly needs to consider the low-income wages of about 1,000 Kina per month (~300 US$) in the province of Morobe, one of the main industrial areas in PNG. Thus, investment subsidies from the PNG government would be preferred.

Figure 4: Photo of the Fuyang City CPV-APV project (Anhui Province)

Figure 5: Photo of the Fuyang City TGPV project (Anhui Province)

3. AGRICULTURE IN PAPUA NEW GUINEA

According to the World Bank, just 18 percent of Papua New Guineans live in urban areas, so farming would seem to make sense as an economic lifeline. Looking at the specific situation in Papua New Guinea we get the statistics as illustrated in the following tables (World Bank Group, 2017): Table 1 shows, that Papua New Guinea has a population of 8.2 million people and a total land area of 114.37 million acres. Just 2.3% of that land total land area are cultivated land (2.52 million acres), from which 2.2% (1.72 million acres) are for permanent crop and 0.7% (0.8 million acres) are suitable for arable land cultivating recurring crops. The amount of other non-cultivated land in Papua New Guinea is very large at 97.8% (111.85 million acres).

Table 1: Cultivated and arable land in Papua New Guinea

Population [2017]	cultivated land (arable + permanent crop)	arable land	other / non cultivated land	total country land area	cultivated land of total country land area	arable land of total country land area	other / non cultivated land of total country land area
[Million]	[acre]	[acre]	[acre]	[acre]	[%]	[%]	[%]
8,251,162	2,516,023	800,620	111,854,055	114,370,078	2.20	0.70	97.80

We can see that the amount of cultivated land in Papua New Guinea for permanent crops is small and the amount of arable land even smaller. Agriculture photovoltaic therefore makes sense as a means to preserving valuable arable land in Papua New Guinea. The sun radiation in Papua New Guinea is so strong that certain crops cannot grow well. Those crops may need a long time to grow but intense sunlight is only good for short lifetime crops. Furthermore, for a lot of vegetables and many fruits, cutting the radiation intensity by half is beneficial and may deliver totally different yields.

Table 2 shows the total agricultural land (land including all cultivated land, arable land and land which possibly could be converted into cultivated or arable land) in Papua New Guinea which is very limited at just 2.6% of the total land area. Since 84.6% of that total agricultural land in Papua New Guinea is already being cultivated, the percentage of Papua New Guinea's total land area which could be converted into additional cultivated land stands at 0.4% (about 0.46 million acres); very small compared to many other countries, and a strong reason to promote agriculture photovoltaic in Papua New Guinea. The New Agriculturist notes that the nation of the land is very mountainous, leaving generally just 25 percent of its land suitable for agriculture.

Table 2: Agricultural land in Papua New Guinea

total country land area	total land area which is called agricultural land from total country land	cultivated land from available agriculture land	land possibly to increase arable land per country	part of world agriculture land possibly to increase arable land per country	land possibly to convert into / increase to arable land
[acre]	[%]	[%]	[%]	[%]	[acre]
114,370,078	2.60	84.61	0.40	0.001243	457,595

As shown in Table 3, the population density in Papua New Guinea is about 13.86 acre per capita and the percentage of cultivated land per capita is just 0.305%. The percentage of arable land per capita is even less at 0.097% which is far below the average western standard of 0.5% arable land per capita to secure a healthy life style.

Table 3: Agriculture Papua New Guinea– data per capita

Population [2017]	total country land area	total land per capita population density	cultivated land (arable + permanent crop)	cultivated land per capita	arable land per capita	electricity comsumption per capita (2017)
[Million]	[acre]	[acre]	[acre]	[%]	[%]	[KWh]/year]
8,251,162	114,370,078	13.861	2,516,023	0.305	0.097	441

The yearly electricity consumption in Papua New Guinea of about 3639 GWh is shown in Table 4. This would require covering a land area of about 9,097 acres with solar panels, which is just 0.01 of the total land areas of Papua New Guinea but 1.14% of the arable land area. Papua New Guinea has no significant solar photovoltaic capacity installed to date.

Table 4: Electricity consumption in Papua New Guinea and solar energy provision

total country land area	electricity consumption	yearly average sunshine -> [hour/year]	A 1 MW solar plant how much can it produce per country (80% efficiency)	land to cover with solar cells to cover electricity consumption generation weighted (average sunshine hour / year)	necessary total country land area to cover with solar cells to accommodate electricity consumption	necessary arable land to cover with solar cells to accommodate electricity consumption
[acre]	[GWh]/year]	[hours/year]	[GWh]	[acre]	[%]	[%]
114,370,078	3,639	2000.00	1.600	9,097	0.01	1.14

Papua New Guinea has the perfect climate for solar, and this is the key to achieving an ambitious government plan to bring electricity to the 70 per cent of Papua New Guineans by 2030, according to Rick Hooper, Chief Executive Officer of Sydney-based solar company, Barefoot Power.. Costs to light up remote areas of Papua New Guinea would cost about 1.819 million US$, which represents about 11% of Papua New Guinea's GDP (16.58 million US$) as shown in Table 5.

Table 5: Solar energy in Papua New Guinea and necessary investment

installed Solar PV capacity by country	yearly average sunshine -> [hour/year]	land area covered by installed solar cells	installed Solar PV plant costs by country	costs to cover all electricity by solar PV per country (US$)	percent of necessary costs to cover all by solar spent already	GDP (nominal)	costs to cover all electricity by solar PV relative to GDP	remaining costs to cover all electricity by solar PV relative to GDP
[MW]	[hours/year]	[acre]	[Million US$]	[Million US$]	[%]	[Million US$]	[%]	[%]
-	2000.00	-	-	1,819	-	16,576	10.98	10.98

Figure 6: Agriculture and Photovoltaic in Papua New Guinea are currently still very rudimentary

4. ANALYSES OF HOW THE TECHNOLOGY MIGHT IMPROVE THE LIVING STANDARDS OF THE RURAL AND SMALL ISLAND POPULATIONS OF PAPUA NEW GUINEA

Almost 85 percent of the country's approximately eight million people live in rural areas including remote highland areas and far-flung islands. These areas remain difficult and costly to provide basic services and develop infrastructure, including electricity, telecommunications and roads. For example, the capital, Port Moresby is not linked by road to any of the other major population centres, except for Kerema, the capital of Gulf Province, and many villages in the highlands can only be reached by light aircraft or on foot. The Solar Energy Association of Papua New Guinea (SEAP) has been founded to increase the capacity, sustain the development and protect the viability and long-term growth of the solar energy industry (Sailesh, 2015).

An outstanding agrophotovoltaic project was undertaken in Germany on the Demeter farm at the Bodensee Lake where crop yield and electricity production were investigated for over a year. The project was led by the Fraunhofer Institute for Solar Energy Systems ISE and it was called “Agrophotovoltaic – Resource Efficient Land Use” (APV-Resola)” Elevated high above the field, solar panels provided the opportunity for electricity generation and farmers could work beneath on the farmland as schematically shown in Figure 7. The project covered one third of a hectare. The results of harvesting solar energy and crops can be found in the project summary published in May 2019 (APV-Resola, 2019).

The results from this pilot project were very successful, as it could demonstrate that agrophotovoltaic is delivering comparable results to regular solar roof systems for electricity generation. The elevated solar panels on the farmland represent in a certain way a rooftop for the farmers. The crop production is sufficiently high and can be profitably sold on the market observed Stephan Schindele, project manager of agrophotovoltaics at Fraunhofer ISE. Agrophotovoltaics (APV) has the potential to open new space that is urgently needed for the PV expansion in Germany. As stated by Prof. Hans-Martin Henning, Institute Director of Fraunhofer, ISE APV can mitigate the conflicting interests between agriculture and open space PV systems for viable land. The results from the first harvest were, for the most part, promising. The crop yield of clover grass under the PV array was only 5.3 percent less than the reference plot. The yield losses for potatoes, wheat and celeriac were between 18 to 19 percent according to Prof. Petera Högy, agricultural expert at the University of Hohenheim. From the perspective of agricultural science, agrophotovoltaics is a promising solution for increasing both the land use efficiency and the share of renewable energy provided by the agricultural sector said Prof. Iris Lewandowski, Head of the Department of Bio based Products and Energy Crops, University of Hohenheim.

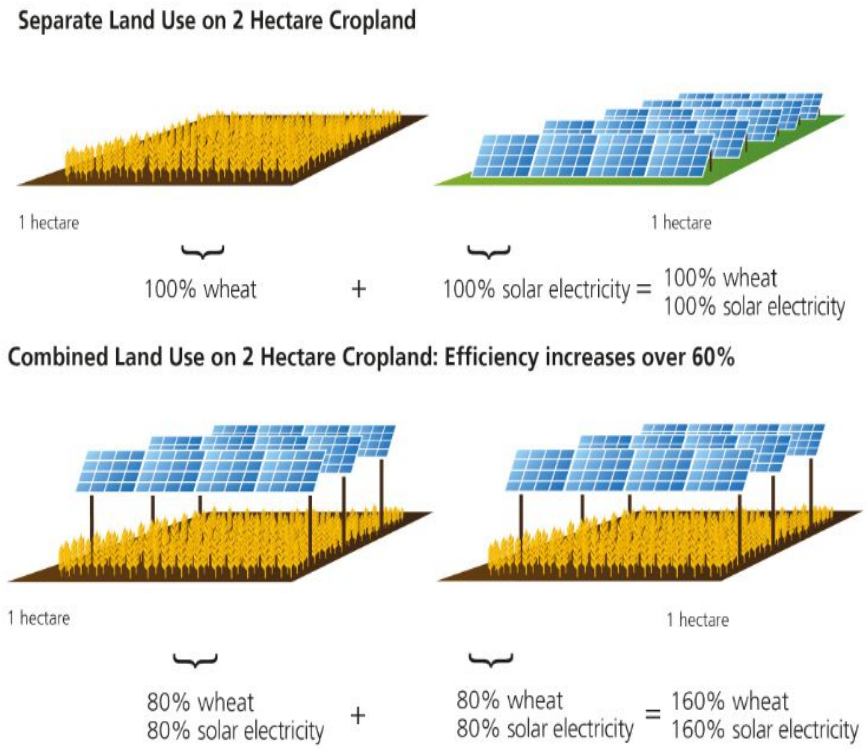

Figure 7: The dual use of agricultural land increases the land use efficiency by 60 percent ©Fraunhofer ISE

Such test systems using elevated solar panels can be even further improved by implementing the novel technologies CPV-APV and TGPV as presented in this paper. To implement such test systems in Papua New Guinea as an ideal country for solar technology would allow to further investigate the market readiness and other sectors such as differently sized systems. The technical integration could be explored and improved, for example, for wheat, potatoes, celeriac and clover grass. For the TGPV system, the south-west orientation and the layout of the solar panels and the rippled glass plates can be tailored to ensure that crops are exposed to uniform solar radiation. For the CPV-APV system, the dual tracking system could be judged towards its reliability aspects in real weather condition with wind and rain fall. All experts agree that it is important to gather more experience over the next few years and analyse other crops in various countries.

Because 80% of sun power is reflected by this new APV system, water evaporation will be reduced and thus irrigation water on farms can be reduced by more than half. This would be another significant advantage for many countries like Israel, Saudi Arabia, as well as Northern China and North West provinces. As shown in Figure 8 dual-channel optical film could be suitable for photosynthesis of visible light transmission and it can be widely used in plastic greenhouse covering film and in China's existing 50 million vegetable greenhouses. Benefits include heat insulation, filtering out the infrared band and other thermal effects of strong light; enhancing plant growth and environmental conditions of workers; saving water and reducing evaporation of water. This could also help in the preservation of desert surface water and to control deserts. It could block special spectrum to prevent UV and insect pests. Light transmittance, because of its anti-ultraviolet characteristics, can effectively improve the light transmittance and increase the effective illumination in the greenhouse (Liu, 2017).

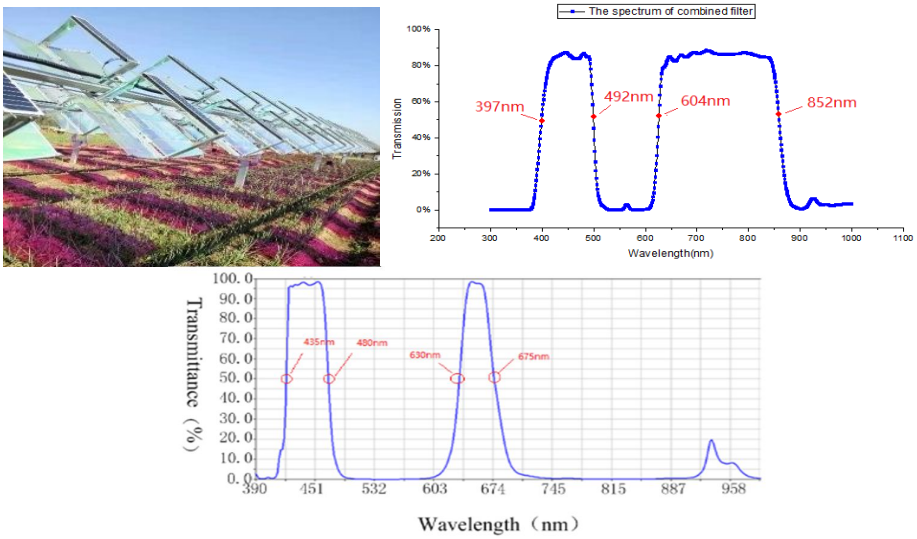

Figure 8: Shielding the farmland from harmful UV and IR radiation

Results from the tests in Fuyang city, shown in Figures 4 and 5, are demonstrated in Table 6, Figure 9 and Table 7, clearly showing the success of agriculture photovoltaic and the CPV-APV and TGPV system in particularly. The crops grow either equally as well as in free fields or even better. A variety of vegetables shown in the following table have been harvested under the two different systems, CPV-APV and TGPV. The yield in kg/price is very competitive to other farming sides and additionally electricity production in the range of 20K to 100k KWh / hectare was obtained. This demonstrates a great success and results will be even better in Papua New Guinea with a much stronger sun and more sunshine hours per year.

Table 6: In summer the results may differ because of the positive heat shielding effect pf the APV system

Type	Weight (kg/Piece)	Plant height (mm)	Root length (cm)
Under APV	0.7[a]	48.6[a]	23.8[a]
Under TGPV	0.67[a]	51.2[a]	29.4[a]
Open-air	0.74[a]	53.2[a]	25.2[a]

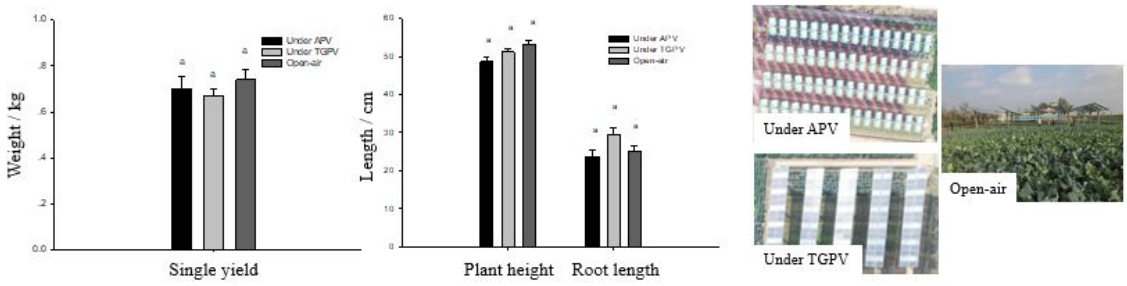

Figure 9: Different letters indicate statistically significant differences (Tukey's honest significant difference test at P < 0.05, the differences between some of the means are statistically significant, < 5% risk of concluding that a difference exists when there is no actual difference

Table 7: Fuyang, China (N32°53', E115°48'), Experimental time: 6 September - 20 November 2018 (55 days)

Type	Varieties	Planting numbers (per Hectare)	Single yield (kg/Piece)	Total yield (kg / Hectare)	Autumn power generation (KW·h /Hectare)
CPV-APV	Broccoli	34,500	0.7	24,150	21,000
	Cauliflower	34,500	1.2	41,400	
TGPV	Broccoli	34,500	0.67	23,115	105,000
	Cauliflower	34,500	1.15	39,675	
Open air	Broccoli	34,500	0.74	25,530	0
	Cauliflower	34,500	1.3	44,850	

Both systems, the CPV-APV and the TGPV, can be used to facilitate artificial irrigation in Papua New Guinea. The pumps used for the transport of the water can utilise the electricity produced above the field by the photovoltaic systems, the electricity feeds an electric motor driving the pump. Most of the traditional pump systems work with a diesel engine or with the local power grid. However, these two modes of operation present disadvantages compared to solar pumps. In many rural areas, especially in developing and emerging countries, access to the electricity grid is not always guaranteed. In these cases, farmers cannot rely on the traditional irrigation system. Thus, using an independent and alternative energy system can be a solution for the farmer to secure a safe power source and for the public grid to avoid saturation (Uddin, 2012).

Figure 11: Solar-powered irrigation: a solution to water management

5. SUMMARY AND CONCLUSION

While a couple years ago agriculture photovoltaic was still an exotic topic, it is now a well-accepted direction to harvest solar energy and crops on the same land. Simultaneous photovoltaic and photosynthesis is possible as demonstrated by many pilot projects around the world. In this paper two improved versions of agrophotovoltaic were demonstrated, one based on concentration photovoltaic and one on diffraction photovoltaic. Both systems were successfully tested in terms of yield for electricity generation and crops and were compared with existing solutions demonstrating their superiority. For both system electricity is provided in a cost competitive way compared to regular solar panels and the CPV-APV system blocks the land from harmful UV and IR radiation reducing the water evaporation form the ground. In recent years, photovoltaic agriculture has had a rapid development in China due to powerful support policies, flourishing controlled environmental agriculture, policy-oriented rural electrification and promising electric machinery for greenhouses. Therefore, photovoltaic agriculture provides new opportunities for China's photovoltaic industry, not only to solve the dilemma of overcapacity for China's photovoltaic industry effectively, but also to accelerate the development of modern agriculture in China (Xue, 2017). In Germany agrophotovoltaic systems have been tested for over a year and very positive results have been demonstrated. In the future, village-level photovoltaic agricultural power stations could gradually become the main form of photovoltaic power stations, and may even be the only form of photovoltaic power station. Agriculture in Papua New Guinea is the main source of income for many villagers where electricity provision is below 10%. We discuss statistical numbers for geographical and economic situations in Papua New Guinea and envisage the possibilities and potential to implement the novel agrophotovoltaic systems in Papua New Guinea. The benefits to improve living standards, to protect farm land from harmful UV and IR radiation, improve crop yield and income of farmers and provide possibilities for artificial irrigation are promising. Finally, we discussed capital costs and the return of investment to installing agrophotovoltaic systems in Papua New Guinea.

6. ACKNOWLEDGEMENT

This work was supported by the Major Project of Science and Technology of Anhui Province under grant 16030701093. PNG collaborators acknowledge the support of the Sustainable Energy Research Institute (SERI)

7. REFERENCES

APV-Resola, 2019, “Abschlusskonferenz”, Agenda: APV-Konferenz Berlin / Germany

Basil, S.H. 2018, March PNG Energy Policy, Port Moresby, Papua New Guinea

Bourke, R.M., 2009 “History of agriculture in Papua New Guinea in Food and Agriculture in Papua New Guinea” ANU Press, Some LIT to statistics in PNG

Husain, A.A.F., Hasan, W.Z.W., Shafie, S., Hamidon, M.N., Padney, S.S., 2018 “A review of transparent solar photovoltaic technologies” Renewable and Sustainable Energy Reviews 94 779–791

Liu, L., Guan, C., Zhang F., Li M., Lv, H., Liu, Y., Yao, P., Ingenhoff, J., 2017 “A Novel Application for Concentrator Photovoltaic in the Field of Agriculture Photovoltaics” AIP Conference Proceedings, Volume 1881, Issue 1, 10.1063/1.5001446

National Energy Policy Working Group, PNG, 2018, PNG National Energy Policy 2018-2028: Harnessing Energy for Life, Port Moresby: Papua New Guinea, https://tradingeconomics.com/Papua-New-Guinea and https://www.lightingglobal.org/Papua-New-Guinea

Obergfell, T., Schindele, S., Goetzberger, A., Reise, C., 2015 “Agrophotovoltaic – Agricultural production below optimized elevated photovoltaic systems” Fraunhofer Institute for Solar Energy Systems ISE, Freiburg in Germany

Perry C., 2013 Library Map Collection, University of Texas. Courtesy of IRENA special publication, www.irena.org

Samanta, S., Aiau, SS., 2015 “Spatial Analysis of Renewable Energy in Papua New Guinea through Remote Sensing and GIS”, International Journal of Geosciences, 6, 853-862

Smil, V., 2006 “Energy: A Beginner's Guide” Oneworld Publications ISBN 9781851684526

Sowei, J., Allen, B., “Papua New Guinea“, 2003 Publisher: United Nations University Press, Tokyo.Editors: Helen Parsons, Harold Brookfield

The World Bank, 2015, “Connecting the Unconnected in Rural Papua New Guinea” feature story http://www.worldbank.org/en/news/feature/2015/09/29/connecting-the-unconnected-in-papua-new-guinea

Uddin, J., Reza Taslim, S.M., Qader, N., Uddin, J., Islam, T., Kim, J-M. “Automated Irrigation System Using Solar Power” 2012 7th International Conference on Electrical and Computer Engineering, Dhaka, Bangladesh

World Bank Group, 2017 Food and Agriculture Organization, electronic files and web site, https://data.worldbank.org/indicator/AG.LND.AGRI.ZS

Xue, J., 2017, “Photovoltaic agriculture - New opportunity for photovoltaic applications in China” Renewable and Sustainable Energy Reviews 73, 1–9

Zhang, F., Li, M., Zhang, X., Zhang, Z., Wang, T. Liu, W., Ingenhoff, J., 2018 “The status and breakthrough of agricultural photovoltaic” 17th International Conference on Sustainable Energy Technologies, SET proceedings volume 3, 209, page 52 - 60

Zhang, Z., Zhang, F., Li, M., Liu, L., Lv, H., Liu, Y., Yao, P., Liu, W., Ou, Q., Liu, W., Ingenhoff,J., 2018 “Progress in agriculture photovoltaic leveraging CPV” AIP Conference Proceedings 2012, 110006

#187: Difficulties of passive design in Shanghai climate and what we can learn from local dwellings

A study from Feng Xian folk houses

Hongzhi MO[1], Xiaozhe LIU[2], Ruyi RUI[3] Haisong WANG[4]

[1]Faculty of Architecture, Shanghai University, 99 Shangda Rd; Head Secretary, Committee of Country Construction, the Architectural Society of Shanghai. mo@t.shu.edu.cn
[2]Faculty of Architecture, Shanghai University, 99 Shangda Rd, liu201972@qq.com
[3]Faculty of Architecture, Shanghai University, 99 Shangda Rd, ruiruyi@qq.com
[4]Faculty of Architecture, Shanghai University, 99 Shangda Rd, hay@shu.edu.cn

No sunshine in winter and extremely hot & humid in summer is the typical Shanghai climate condition, which together makes it especially difficult to build with passive design. According to a recent field survey, there are around 11K individual villages in the Shanghai region, some of them still keep their original building form for the past 100 years. These local dwellings still provide a relatively good internal environment for the local residents.

Following our recent detailed survey and drawing on these heritage dwellings (more than 100 houses located in Feng Xian, Pudong), this paper focuses on what we can learn from the traditional wisdom in passive design and its aesthetics to adapt to the Shanghai climate. Also, Shanghai climate data is analysed to support these findings.

Keywords: Feng Xian; local dwellings; passive design; folk house

1. INTRODUCTION

More than 80% of the area within Shanghai territory is agricultural land (Shanghai Government, 2018). These countryside areas of Shanghai are usually forgotten as part of Shanghai, even though it has a much longer history from before Shanghai city come into being in the late colonial period. Some existing dwellings can traced back to 1800s.

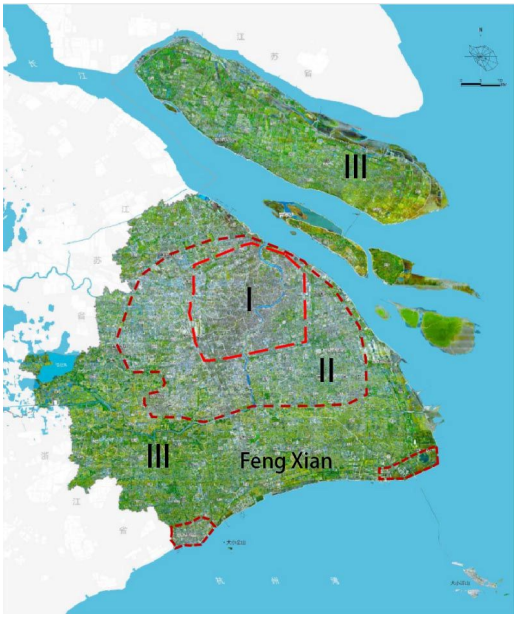

Figure 1: Countryside area in Shanghai. (I: Downtown – city area; II: uptown- mixture of city and countryside area; III Countryside). Feng Xian is the country side we are discussing in this paper.

Shanghai – its culture and the city itself (Figure 1, zone I) - was mainly formed in the 1900s by migrants from Jiangsu and Zhejiang province, and also foreigners in the late colonial era (Shanghai Statistical Yearbook, 2017). But the countryside of Shanghai (Figure 1, zone III) has a different story. Although there is little distance between the countryside surrounding Shanghai city and the city itself, there are indigenous people living there making a living by agricultural and fishing as they have for hundreds of years long before the modern Shanghai come into being. Their culture was uninfluenced by the process of modernisation of Shanghai, and they even kept their own accent (or rather a different dialect) until now, which is totally different from that in Shanghai and Jiangsu, Zhejiang resident's accents. More than 11,000 micro-villages remain in the countryside of Shanghai (Bureau of Master Planning, 2018). Although not many, there are still traditional residential housing standing untouched. They were built by the people living there for generations and uninfluenced by foreign technology. Recently we undertook a field survey and mapped all historical residential building in Feng Xian in order to study the local wisdom of understanding climate conditions and how residents utilise the climate in their housing with passive design. There were some interesting findings.

2. SHANGHAI CLIMATE CONDITION AND PASSIVE DESIGN STRATEGY

Shanghai has a subtropical maritime monsoon climate. The main climatic characteristics are: warm spring, hot summer, cool autumn, cold winter, moderate rainfall throughout the year with even seasonal distribution. Generally speaking, it is mild and moist, with four distinct seasons. The highest temperature in Shanghai is in July and August. In recent years, the summer in Shanghai has been getting hotter and hotter. Annually, there are usually ten hot days above 35°C. The coldest days are from late January to early February, usually during the Spring Festival (Figure 2a) (Shanghai Met Office, 2018). Although the number of continuously cold days is small (generally no more than 3 days), Shanghai is a no-heating facilities zone, and with humidity being very high in winter, the body sensation is uncomfortably cold. June and July usually experience continuous rain without any sunshine.

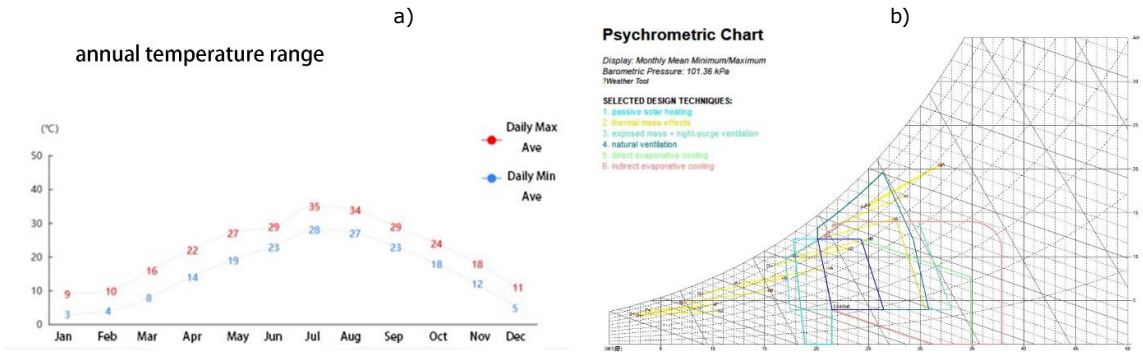

Figure 2: a) annual temperature range of Feng Xian (Shanghai Met Office, 2018). b) Psychrometric Chart with passive design feasibility overlay (weather date analysed by Ecotect Weather tool)

According to the climate condition and through the psychrometric Chart (Figure 2b), the seasonal temperature range is not extreme, but Shanghai is not one of China's winter heating zones meaning that almost all building do not provide heating in winter. It is obvious on the psychrometric chart that moisture levels are very high throughout the year. High levels of moisture in Shanghai make the winter feel much colder than the dry bulb temperature conveys. Much worse, usually through the entire winter, the region is covered with thick cloud and even efficient direct solar irradiation cannot provide enough energy, making passive solar design in winter even more desperate. During a hot summer, wind is not strong enough to provide sufficient cross ventilation, and very high moisture (usual summer sunny days experience 70-90% moisture all the time) make any evaporation cooling strategy ineffective. This kind of climate condition is the typical characteristic along the south bank of the Yangtze River covering many cities along the Yangtze River, and it is the most difficult area in China for passive design. It is the architect's biggest nightmare for passive design in this area.

3. LOCAL DWELLINGS' AESTHETIC AND WHAT WE CAN LEARN FROM THEM

Despite the difficulty in passive design in Feng Xian, it is surprising to discover that local dwellings have some wise ideas for passive design and during our stay interviewing the residents, our team experienced very good internal thermal comfort levels. Local residents were very proud of the thermal performance of their traditional buildings. They still love to stay in these houses, although they did have some complaints, but only about building material failure, not about thermal comfort. Some locals complained about bad experiences moving to newly built residential apartments with bad thermal comfort. Some of the design methodologies of how to adapt housing to the environment and the aesthetic of the local dwellings are shown in Figure 3.

Figure 3: the local dwellings in Feng Xian. After over a hundred years, these building are still in good working condition and provide good thermal performance

3.1. Building Materials

Roof

Roof is the most unique recognisable aesthetic part of Chinese traditional buildings. In Feng Xian, as far as the typhoon is concerned, the usual light-weight roof such as straw or light-weight panel roof, is not commonly seen because it cannot survive a direct hit by typhoon.

A roof should have good water resistance, be able to withstand a typhoon, and have good thermal performance. Traditional local dwellings all had a robust and relatively heavy weight roof. The Chinese style of grey tiles was the most commonly used in this area for local dwellings. Grey tiles are made of clay in a sintering process. In order to

make an anti-typhoon roof in Feng Xian, the roof is the most important building part for residents. From bottom to top, it is constructed by rafter-purline-wood panel-lime-tile (Figure 4a). Alone the east coast of China, local dwellings use more lime to connect roof tiles together at the same time making the roof look heavier than the roofs in central parts of China.

Local dwellings prepare especially thick layers of lime using chopped hemp rope to add more weight and more cohesiveness to the tiles. Central areas of China without the typhoon threat use less lime to attach tiles to construct a lighter roof (MA Zhan-yong et al., 2015), with lime barely covering all the spaces under the tiles. But in Feng Xian, the lime layer is much thicker and all spaces between tiles and the roof panel are filled. The structure of the roof make it heavy enough with no vacuum effect from heavy wind to blow/inhale the tiles to move under a heavy wind load.

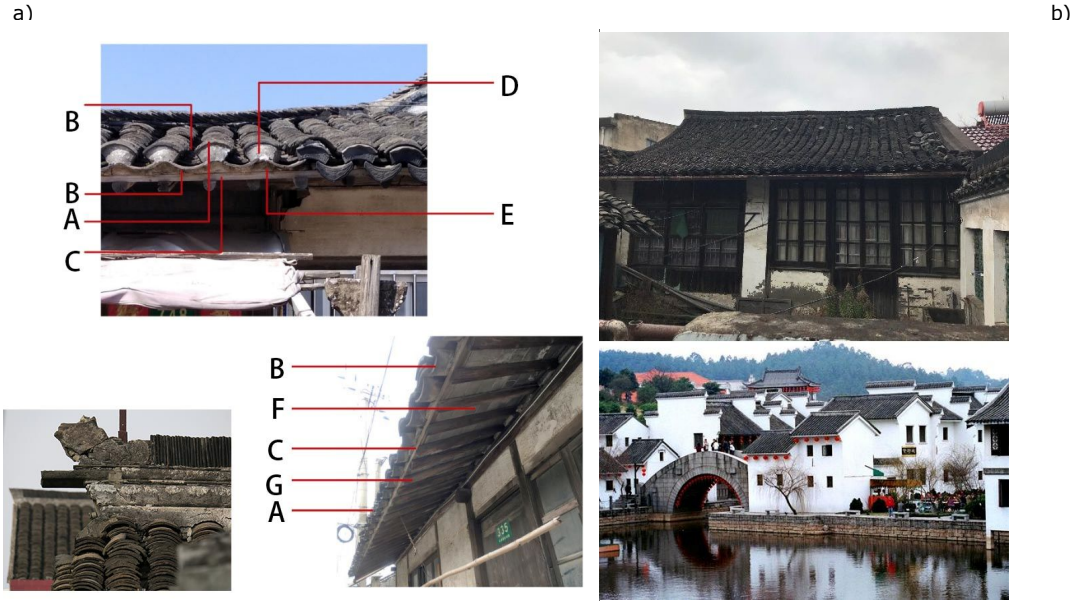

Figure 4: a) typical roof pattern in Feng Xian: (A) clay tile(cover); (B)clay tile(seated/reversed); (C)wood purline; (D)cover tile lime; (E)seat tile lime; (F)wood roof panel; (G) wood rafter; b) Difference in the roof and facade of south of the Yangtze River and Feng Xian dwellings

The local roof characteristics made Feng Xian dwellings look very different from that of traditional dwellings in regions south of the Yangtze River forming a unique aesthetic: the roof is more curved and covers a bigger area then others (Figure 4b). In the meanwhile, the heavier roof also acts as better thermal insulation material. As it is thicker, it made the summer sun more difficult to reach the room. The top image in Figure 4b shows a typical Feng Xian house, and below is a typical village south of the Yangtze River. As illustrated, most Feng Xian dwellings are single storey houses and most of those south of the Yangtze River are usually 2-3 floors high.

Most of houses south of the Yangtze River usually use the top floor as a thermal damper, to cut off summer heat from the sun to transfer to lower floors (Ding Jun-qing, 2008). In most of the traditional houses, the internal space of the top floor is rarely decorated and is without furniture, is only used as storage space and occasionally as a guest room. It is a pretty low cost efficient solution for a passive design, even though the residents still complain about over-heating in summer. But in Feng Xian, the collective wisdom is used to solve the problem cost efficiently, with a thicker roof, more robust in adverse climates with better thermal performance, and without the necessity to build another floor for thermal damper. Also the roofs last longer, requiring only minor maintenance around every 20 years compared to the south Yantze River houses which need maintainance every 10 years.

Wall

Wall structure is another essential part in thermal performance. It is a compromise to balance heat in/out, heat storage and cost to make the best solution. In Feng Xian, most local dwellings choose the rowlock brick wall (Figure 5) for the envelope structure. Although it is brick – a relatively heavy material – due to the cavity inside, it is still light-weight. As the winter temperature is not very low in Shanghai, local residents consider thermal insulation to be more important than heat preservation. Rowlock walls with the airspace within serves very well as thermal insulation to prevent external heat getting into internal rooms. Also lighter walls reduced foundation cost. As in the south Yangtze River region, no heating is provided so people tend to accept a lower temperature comfort zone.

Figure 5: rowlock wall in Feng Xian is the local choice for residential buildings even today.

Local people will put on more clothes against a moist and cold winter. This is still how local people get by in the winter. Thermal performance of the facade in winter is less important around Shanghai than in summer. Unlike current building energy efficiency codes, most residential housing in Shanghai region, including Nongtang (the narrow alleyways of old Shanghai), all use this kind of rowlock wall. According to our interviews with the residents living in these dwellings, they all reported a cool summer and warm winter when staying in these houses, very satisfied with the internal thermal comfort performance.

Floor

Figure 6: typical floor materials

Feng Xian traditional dwellings mostly use grey brick tiles or lime-earth-broken brick concrete as a flooring material (Figure 6). Without a basement, the floor is laid directly on top of rammed earth. Although very traditional materials, it is helpful in reducing internal summer temperature. Groundwater levels in Shanghai are very high meaning that these porous materials can encourage moisture to reach the surface. In sunny summer days, moisture levels can be as low as 60% in the hottest afternoon which can assist with the evaporation cooling effect to reduce internal temperature. These materials are also very low cost.

3.2. Building layout

In Feng Xian, the wind direction in summer is mostly SSE, and in winter, mostly is WWN. From our survey of more than 10 villages, all the dwellings faced the same direction: south and around 5-10 degrees offset to the east. Most buildings had either a Kwan-Yin shape gable wall (Figure 7, the wave shaped wall) or a horse-head gable wall (Figure 7, the right wall).

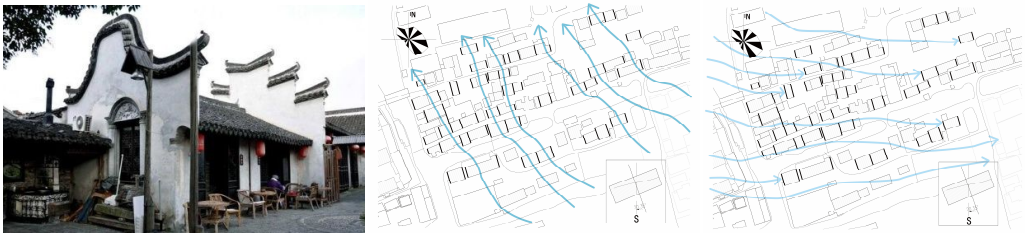

Figure 7: Kuan-Yin Dou and horse-head gable wall (left); summer wind pattern (mid); winter wind pattern (right)

The high gable wall (higher than the roof) is a typical aesthetic characteristic in South Yangtze River zones (Cao Yong-Pei, 1990). The horse-head type is very common, but Kuan-Yin Dou is unique to Feng Xian, differing from the well-known horse-head type. This might be because they used to be fishing villages and the fishermen preferred the more wave-like shape. Both shapes serve the same function: because a large amount of building material is timber, it is necessary to keep fire hazards down in a small region especially in a village or town when all the buildings are attached to each other.

In addition to the fire proof function, the gable wall is also called the “wind and fire wall”, indicating that it is also functional as a wind guide. According to our survey, locals say that their house is usually well ventilated in summer, but also blocks the westerly winter wind from penetrating their rooms and yards. We find these gable walls may take part in the seasonal wind guide. As the summer wind pattern shows in Figure 7, the summer prevailing winds usually comes from the eastern sea, mainly from a SSE direction. The building layout follows this direction, and these gable walls lie parallel to the wind guiding the sea wind through the residential area Figure 8 indicates the summer cross ventilation. Additionally, to encourage cross ventilation, there were lots of passageways found facing south to open up gaps for the wind to pass (Figure 8 right bottom photo). To the contrary, winter cold wind usually comes in from a WWN direction from Russia and the Chinese main land, and in the winter seasons, the cold wind is almost vertical to the gable walls, thus blocking the cold winter wind (Figure 8 winter wind block).

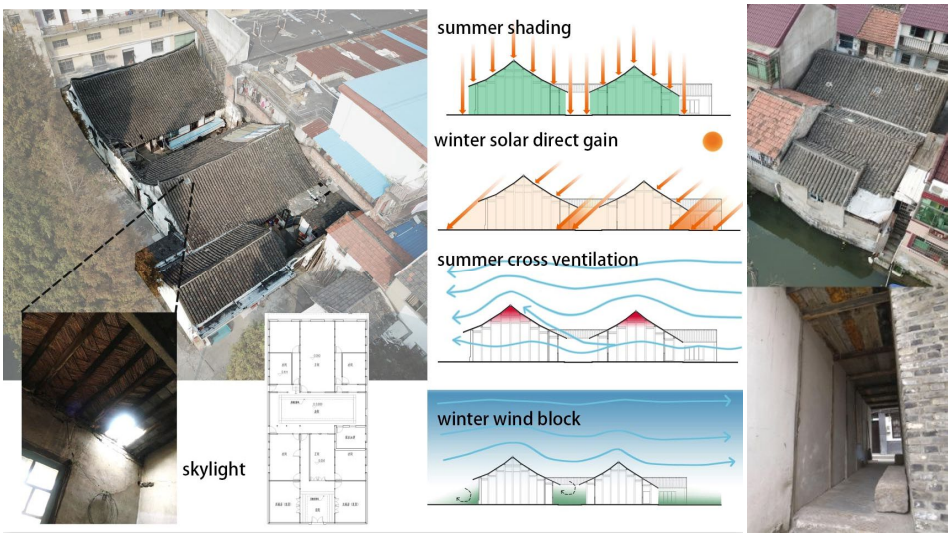

Figure 8: typical compound layout.

As Figure 8 shows, most of the local dwelling compounds were facing in the same direction, and we found skylights on the roofs serving the same purpose as we do today with light pipes. The extended roof provided sufficient shading in summer to the courtyard and the rooms, while in winter, the tilted roof encouraged sun light to be cast directly into rooms thanks to the south-facing layouts.

4. CONCLUSION

Local dwellings were born in a passive design era when resources and energy were not abundant. Local architects and master builders studied the local climate and learnt how to work with the environment. Local wisdom is something that we modern architects can learn from with their abilities to encourage and respect passive design principles. How to adapt to the environment and how to reduce resource use is an appropriate technology that “small is beautiful” (Schumacher, 1973) is still chasing.

Utilising passive design principles in Shanghai is difficult, but as our survey in Feng Xian indicated, even though it is hard, local citizen have already able to adapt their buildings to the environment and later generations still benefit from their design wisdom. They are able to say that their old house has almost zero energy consumption but still provides a high level of thermal comfort throughout the year, better than modern apartment buildings. In the case of building orientation and facade materials, they have found the best solution as well as being low cost, i.e. the rowlock wall functions very well in thermal performance in local condition. Meanwhile new building codes are still trying to add more thermal insulation material to facades (GB/T 50378-2014) while architects hundreds of years ago had already realised that thermal insulation does not really function well.

5. FURTHER RESEARCH RECOMMENDATION

Most of the thermal performance descriptions of local dwellings were based on interviews with the residents. More detailed internal environment monitoring should be carried out as a next step. Also the building facade thermal performance should be lab tested and verified. Through these studies, passive design in hot, high moisture summer and cold winter areas can reach more practical detailed guildlines.

6. REFERENCES

Bureau of Master Planning, Land use and Nature resource, Shanghai (2018) Shanghai rural survey report 2018

Cao Yong-Pei (1990) The Structure and Practice of the "Ma Tau Wall" of Huizhou Ancient Architecture. Ancient building garden technology magazine[J]

Ding Jun-qing (2008) Jiangnan residential. Shanghai Jiaotong University press.

GB/T 50378-2014 Assessment standard for green building

MA Zhan-yong, CHEN Dong-quan, HUO Liang.(2015) Research and application of clay tile roof design and construction technology. Construction Technology[J], 2015, 44(22): 94-96.

Schumacher, E.F. Small Is Beautiful: Economics as if People Mattered ISBN-13: 978-0061997761

Shanghai Gov Office (2018) Implementation Opinions on Promoting the Construction of Shanghai's "Four Good Rural Areas"

Shanghai Met Office (2018) weather data base

Shanghai Statistical Yearbook (2017) Households, population, population density and life expectancy of registered population (1978-2016)

#188: The effect of mean pressure on the performance of a single-stage heat-driven thermoacoustic cooler

Irna FARIKHAH[1], Ummi KALTSUM[2], Siti PATONAH[3], Joko SAEFAN[4], Harto NUROSO[1], Sigit RISTANTO[2], Nur KHOIRI[3], Choirul HUDA[8]

Department of Physics Education, Faculty of Mathematic Natural Sciences and Information Technology, Universitas PGRI Semarang, Jl.Dr.Cipto Semarang Indonesia.
[1]irnafarikha@gmail.com/irnafarikhah@upgris.co.id
[2]um_mik@yahoo.co.id
[3]sitifatonah@upgris.ac.id
[4] jokosaefan@upgris.ac.id
[5]hartonuroso@upgris.ac.id
[6]sigit.ristanto@gmail.com
[7]nurkhoiri@upgris.ac.id
[8]choirulhuda@upgris.ac.id

Waste heat is a global environmental issue. There are some technologies that can be used to recovery waste heat, one of which is thermoacoustic technology. Thermoacoustic technology can be divided into two parts; one is the thermoacoustic engine, and the other is the thermoacoustic heat pump. Using the combination of engine and heat pump, we can build a heat-driven thermoacoustic cooler. When an acoustic wave propagates in a narrow tube, a gas in the tube makes thermal interactions with the tube wall. As a result of these thermal interactions, an energy conversion between acoustical and thermal power take place. Then, the thermoacoustic engine which produces acoustical power drives the thermoacoustic heat pump to pump heat from the cold side to the ambient side. The cooler system consists of a looped tube, an engine regenerator and a heat pump regenerator. The acoustic wave spontaneously generates as the engine regenerator is heated. Afterwards, due to the energy conversion, acoustic power is generated. The acoustic wave travels along the looped tube then the acoustic power carried by the acoustic wave is consumed by the heat pump regenerator. There are some parameters that have impact on the performance of the thermoacoustic cooler system, one of which is the mean pressure. To design a cooler system having high efficiency and lower onset heating temperature, the effect of mean pressure is investigated. By increasing mean pressure, the onset heating temperature generating acoustic power can be decreased from 558°C to 307°C. Moreover, the efficiency of the engine regenerator reaches 73% of Carnot's efficiency, Efficiency of the cooler regenerator attain 43% of the upper limit values and 49% of the acoustical work generated by the engine regenerator as utilised in the cooler regenerator. As a result, 15% of the thermodynamic upper limit value of the whole cooler system is achieved.

Keywords: mean pressure; thermoacoustic; engine; cooler

1. INTRODUCTION

Thermoacoustic technology, which is a combination of acoustic and thermal energy, has attracted many scientists to conduct investigations related to energy conversion employing pistonless power (Ceperley, 1979; Swift, 1988; Swift, 1999; Yazaki, 2002; Sakamoto, 2004; Luo, 2006; De Blok, 2008; Kang, 2010; De Blok, 2012; Saechan, 2013; Zang, 2016; Farikhah, 2017). This power can be generated by many energy sources available in the world such as solar, geothermal, and waste heat energy (Twidel, 2006).

There are current issues around heat recovery following manufacturing processes in industry resulting in waste heat (Johnson, 2008) and it is important to properly tackle this problem. This waste heat has the range level below 400°C (De Blok, 2008). Using this technology, heat can be converted into acoustic power and this generated power can be used for applications such as driving a heat pump (De Blok, 2008; De Blok, 2012; Zang, 2016).

In the thermoacoustic field, there are two types of heat-driven cooler depending on the number of engine generators; one is a heat pump driven by a single engine i.e. single-stage engine (Yazaki, 2002; Sakamoto, 2004; Luo, 2006; Saechan, 2013; Kang, 2010) and another one is a heat pump driven by several engines, or a multi-stage engine (De Blok, 2012; Zhang, 2016).

Some researchers have been attracted to the multistage heat-driven cooler rather than the single heat-driven due to the ability to reach lower onset heating temperatures in the engine. However, this configuration is more complicated than the single-stage type, employing only one engine, where construction is simpler and has a high onset temperature (Yazaki, 2002; Sakamoto, 2004; Luo, 2006; Saechan, 2013; Kang, 2010, Farikhah, 2017). Furthermore, both types of the heat-driven cooler have low Carnot COP, particularly Carnot's COP of a single heat-driven cooler which has 2% of the Carnot's COP (Sakamoto, 2004; Saechan, 2013).

Some parameters have an impact on having low onset temperature and high performance. Zang et.al conducted an investigation related to multi-stage heat-driven coolers and found that by increasing mean pressure in this system, the onset temperature for generating acoustic power in the engine decreased (Zang, 2016). However, they needed more engine regenerators. To make it simpler, a single-stage heat-driven thermoacoustic cooler is investigated. In this study, we have numerically investigated the effect of mean pressure on the onset temperature of the engine by using the thermoacoustic theory proposed by Rott (1969, 1973) and advanced by Swift (2002) and Tominaga (1995, 1998).

2. METHOD

2.1. Calculation Model

Shown in Figure 1, the model of the thermoacoustic cooler consisted of two main parts of thermoacoustic components, namely engine regenerator and heat pump regenerator. The engine regenerator was sandwiched with cold and ambient hot exchanger. The temperature of ambient and cold heat exchanger is denoted as T_a and T_c, respectively. T_a is 28°C and T_c is -22°C.

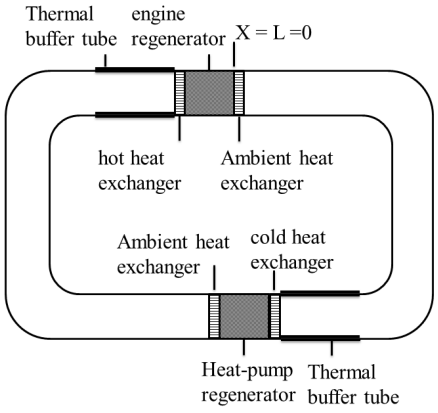

Figure 1: Schematics of the heat-driven cooler

The temperature of the heat exchanger was determined as a result of stability limit calculation (Ueda, 2008). Moreover, in the looped tube there were two thermal buffer tubes; the first was connected to the hot heat exchanger where the temperature changed gradually from hot temperature T_h to T_a and the other was the near cold heat exchanger where the temperature changed gradually from hot temperature T_c to T_a. The length of the regenerator was 40mm, and their porosity is set to 0.77. In addition, the radii and the position of those regenerators were chosen at the optimum values (Farikhah, 2017). All of these components were installed into a looped tube having a diameter of 40mm and length of 2.8m. These values were similar to those of Yazaki's experimental set up (Yazaki, 2002). The value of mean pressure P_m filled inside the looped tube was varied because it was used as a parameter to reveal the dependence of low onset temperature for generating the engine and the performance of the whole thermoacoustic cooler system.

2.2. Calculation Method

In the computation, we used the following two equations derived from Rott (Rott, 1969).

Equation 1: Momentum Equation.

$$\frac{dP}{dx} = -\frac{i\omega\rho_m}{1-\chi_\nu}U$$

Equation 2: Continuity Equation.

$$\frac{dU}{dx} = -\frac{i\omega[1+(\gamma-1)\chi_\alpha]}{\gamma P_m}P + \frac{\chi_\alpha - \chi_\nu}{(1-\chi_\nu)(1-\sigma)}\frac{1}{T_m}\frac{dT_m}{dx}U$$

Where:

- x = the axial coordinate along the looped tube (m)
- χ_α = spatially averaged thermal function
- χ_ν = spatially averaged viscous function
- σ = Prandtl number
- γ = ratio of isobaric to isochoric specific heats
- ρ_m= mean density of the working gas (kg/m^3)
- P = Oscillatory Pressure (Pa)
- U = Cross sectional Velocity (m/s)

The initial point of x was set at the ambient side of the engine regenerator (see Figure1).

Equation 1 and Equation 2 can be solved analytically if $dT_m/dx = 0$. However, if $dT_m/dx \neq 0$, the equations have to be computationally integrated (Ueda, 2008). In this integration, two temperature conditions were used. The first was dT_m/dx takes a constant value. Using this, value of T_h can be obtained. The second was dT_m/dx which was calculated with the assumption that the tube was insulated from its surroundings. Therefore, the enthalpy flow $\dot{H}$ along the regenerators must be set to be constant (Swift, 2002). Rott (1973) suggests $\dot{H}$ can be expressed as

Equation 3: Enthalpy flow along the regenerators.

$$\dot{H} = \dot{W} - \dot{Q}$$

Where:

- $\dot{H}$ = total energy flow (total power) (W)
- $\dot{W}$ = Acoustic Power (W)
- $\dot{Q}$ = heating power (W)

Substituting Equations 1 and 2 into Equation 3, we get

Equation 4: Temperature gradient along the regenerators.

$$\frac{dT_m}{dx} = \frac{\dot{H} - \frac{A}{2}Re\left[P\tilde{U}\left(1 - \frac{\tilde{\chi}_\nu - \chi_\alpha}{(1+\sigma)(1-\tilde{\chi}_\nu)}\right)\right]}{\frac{A\rho_m c_p|U|^2}{2\omega(1-\sigma^2)|1-\chi_\nu|^2}Im[\chi_\alpha + \sigma\tilde{\chi}_\nu]}$$

Where:

- $\dot{H}$ = total power (W)
- T_m = Mean Temperature (K)
- χ_α = spatially averaged thermal function
- χ_ν = spatially averaged viscous function
- x = t axial coordinate along the regenerators (m)

- $\widetilde{U}$ = Conjugate value of velocity (m/s)
- σ = Prandtl number
- A = Cross sectional area (m^2)
- ω = angular frequency (rad/s)

If the boundary conditions about P and U are given, by coupling Equation (1) – (4) $dT_m/dx \neq 0$, temperature gradient along the regenerators can be calculated. In our calculation, the acoustic streaming (Swift, 1999; Swift, 2002) and the thermal conduction along the x axis were neglected for simplicity.

In this calculation, the performance of the whole devices was verified. It included efficiency of the engine $\eta_{2,e}$, looped tube η_{tube} and heat pump $\eta_{2,c}$. First, to find the formula for the engine efficiency, acoustic power generated in the engine must be defined. The power can be expressed as

Equation 5: The gain of Acoustic Power.

$$\Delta\dot{W}_e = \dot{W}_{e,H} - \dot{W}_{e,A}$$

Where:

- $\Delta\dot{W}_e$ = gain of acoustic power in the engine (W)
- $\dot{W}_{e,H}$= acoustic power at the ambient end of the engine (W)
- $\dot{W}_{e,A}$= acoustic power at the hot end of the engine (W)

Then, the efficiency can be defined as

Equation 6: Efficiency of the engine.

$$\eta_{2,e} = \frac{\Delta\dot{W}_e/\dot{Q}_h}{\eta_{Carnot}}$$

Where:

- $\eta_{2,e}$ = Second law efficiency of the engine
- $\Delta\dot{W}_e$ = Gain of acoustic power (W)
- $\dot{Q}_h$ = heating power (W)

Here, $\dot{Q}_H$ is heating power of engine imposed by the hot temperature at hot side, and η_{Carnot} is thermodynamic upper limit of η_e as follow (Cengel, 2011).

Equation 7: Carnot efficiency of the engine.

$$\eta_{car} = 1 - \frac{T_a}{T_h}$$

Where:

- η_{car} = Carnot efficiency of the engine
- T_a = ambient temperature (K)
- T_h = heating temperature (K)

The second is the efficiency of the looped tube η_{tube}. It can be expressed as

Equation 8: Second law efficiency of the looped tube.

$$\eta_{tube} = \frac{\dot{W}_{hp,a} - \dot{W}_{hp,c}}{\Delta\dot{W}_e}$$

Where:

- η_{tube} = Efficiency of the looped tube
- $\dot{W}_{hp,a}$ = Acoustic power at the ambient end of the heat pump (W)
- $\dot{W}_{hp,c}$ = Acoustic power at the cold end of the heat pump (W)
- $\Delta\dot{W}_e$ = gain of acoustic power at the engine (W)

Finally, the efficiency of the heat pump can be defined as

$$\eta_{2,c} = \frac{\dot{Q}_c / \left(\dot{W}_{hp,a} - \dot{W}_{hp,c}\right)}{COP_{Carnot}}$$

Equation 9: Second law efficiency of the heat pump

Where:

- $\eta_{2,c}$ = Second law efficiency of the heat pump
- $\dot{Q}_c$ = cooling power (W)
- $\dot{W}_{hp,a}$ = Acoustic power at the ambient end of the heat pump (W)
- $\dot{W}_{hp,c}$ = Acoustic power at the cold end of the heat pump (W)
- COP_{Carnot} = Carnot Coefficient of Performance (COP) of the heat pump

COP_{Carnot} is the thermodynamic upper limit of the heat pump (Cengel, 2011).

It can be written as Equation 10

$$COP_{Carnot} = \frac{T_c}{T_a - T_c}$$

Equation 10: Carnot COP of the heat pump

Where:

- COP_{Carnot} = Carnot Coefficient of Performance (COP) of the heat pump
- T_c = cooling temperature (K)
- T_a = ambient temperature (K)

Thus, the second law thermodynamic of the total efficiency of this device is as follows

$$\eta_{2,total} = \frac{\dot{Q}_c / \dot{Q}_h}{\eta_{car}.COP_{carnot}}$$

Equation 11: Total efficiency of the whole cooler system.

Where:

- $\eta_{2,total}$ = Total efficiency of the whole cooler system
- $\dot{Q}_c$ = cooling power (W)
- $\dot{Q}_h$ = heating power (W)
- η_{car} = Carnot efficiency of the engine
- COP_{Carnot} = Carnot Coefficient of Performance (COP) of the heat pump

And it can also be written as

$$\eta_{2,total} = \eta_{2,e}.\eta_{2,hp}.\eta_{tube}$$

Equation 12: Total efficiency of the whole cooler system.

Where:

- $\eta_{2,total}$ = Total efficiency of the cooler system
- $\eta_{2,e}$ = Second law efficiency of the engine
- $\eta_{2,hp}$ = Second law efficiency of the heat pump
- η_{tube} = efficiency of the looped tube

3. RESULT AND DISCUSSION

Zang et. al. (2016) reported that there is a dependence of onset heating temperature on a multi-heat driven cooler. Therefore, we investigated the effect of mean pressure P_m on a single-stage heat-driven thermoacoustic cooler. Moreover, it is known that the design parameters of the regenerators, for instance, the ratio of narrow flow-channel

radii and the value of penetration depth, r/δ, have an impact on the performance of a cooler (Ueda, 2010; Farikhah, 2017). In this investigation, therefore, we selected the optimum r/δ at each variation of P_m. Thus, the result was not only low and medium onset heating temperature T_h of the single-stage engine, but also the high efficiency of the whole cooler system.

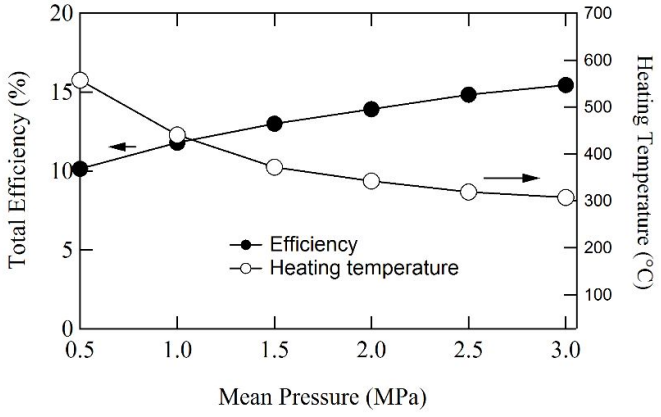

Figure 2: Total efficiency and heating temperature as a function of mean pressure

As shown in Figure 2, the total efficiency $\eta_{2,total}$ increased as P_m increased from 0.50 to 3.0 MPa. It can also be seen clearly in Figure 3 as P_m increased T_h decreased.

As mentioned above, in this calculation, we set $T_C = -22°C$. However, the value of T_h was varied as a result of stability limit calculation by variation of P_m.

It can be seen from Equation 13 that the cold constant temperature and the thermal relaxation dissipation power (namely, the second term in the fractional numerator on the right side) decreased as the mean pressure increased, resulting in a lower critical onset heating temperature difference.

Equation 13: Temperature difference on the engine.

$$\left[\frac{dT_m(x)}{dx}\right]_{crit} = \frac{\frac{1}{2}\omega\rho_m \frac{Im[-\chi_v]}{A|1-\chi_v|^2}|U|^2 + \frac{1}{2}\frac{\gamma-1}{\gamma P_m}\omega A_f Im[-f_k]|p_1|^2}{\beta\frac{1}{2}|p_1||U_1|[Re[g]cos\theta - Im[g]sin\theta]}$$

Where:

- T_m = mean temperature (K)
- x = the axial coordinate along the looped tube (m)
- ω = frequency angular (rad/s)
- ρ_m = mean density (kg/m^3)
- A = cross sectional area (m^2)
- χ_v = spatially averaged viscous function
- U = cross sectional velocity (m/s)
- p = oscillatory pressure (Pa)
- g = complex gain factor arising in continuity equation

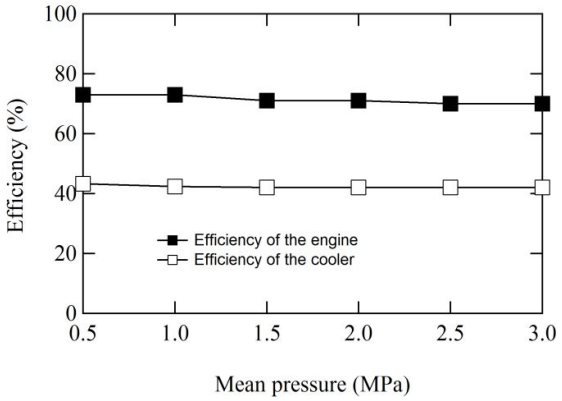

Figure 3: Efficiency of the engine as a function of mean pressure

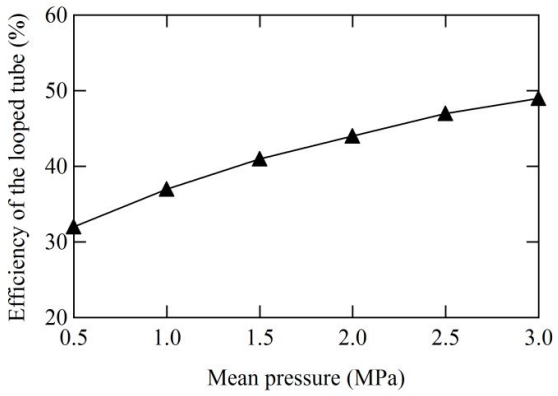

Figure 4: Efficiency of the looped tube as a function of mean pressure

As mentioned above, $\eta_{2,total}$ consists of efficiency of the engine $\eta_{2,e}$, efficiency of the heat pump $\eta_{2,c}$, and efficiency of the looped tube η_{tube}. Therefore, it was essential to know those values. Figure 3 shows that $\eta_{2,e}$ remained constant at a high value at about 73%. This value was comparable to the efficiency of the most efficient thermoacoustic engine constructed (Swift, 1999; Tijani, 2011). Like the value of $\eta_{2,c}$, this value also remained constant at about 43%. The value of $\eta_{2,total}$ was much higher than the value of that obtained in the previous research (Yazaki, 2002; Sakamoto, 2004; Luo, 2006; Saechan, 2013; Kang, 2010). The highest efficiency found in the previous research was below 2% (Sakamoto, 2004; Saechan, 2013). On the other hand, employing multi-stage engine for driving cooler, the construction was more complicated and the efficiency reaches 32% (De Blok, 2012). Therefore, compared to the other heat-driven coolers (Ceperley, 1979; Swift, 1988; Swift, 1999; Yazaki, 2002; Sakamoto, 2004; Luo, 2006; De Blok, 2008; Kang, 2010; De Blok, 2012; Saechan, 2013; Zang, 2016), we can say that the present result had high performance while keeping in the lower heating temperature using single stage type.

In this cooler, η_{tube} had a high impact on the value of $\eta_{2,total}$ as shown in Figure 4. Since the value of $\eta_{2,e}$ and $\eta_{2,c}$ remained constant at high values, the dependence of $\eta_{2,total}$ on P_m was influenced by η_{tube} as shown in Figure 5. Therefore, it was essential to reveal the reason of the dependence.

In Figure 4, as P_m rose, η_{tube} went up from 32% to 49%. This result can be attributed to the value of dissipation. The dissipation can be shown using a ratio of the value of intensity. In this device, there were two divisions of wave guide (looped tube). The first one was wave guide between the hot side of the engine and the ambient side of the heat pump regenerator, denoted as a ratio of the first acoustic intensity ratio $I_{out\,1}/I_{in1}$, representing a ratio of output intensity from the engine to input intensity of the heat-pump. The second one was the wave guide between the cold side of the heat-pump and the ambient side of the engine regenerator, denoted as the second acoustic intensity ratio I_{out2}/I_{in2} , representing the ratio of output intensity from heat-pump to input intensity of engine.

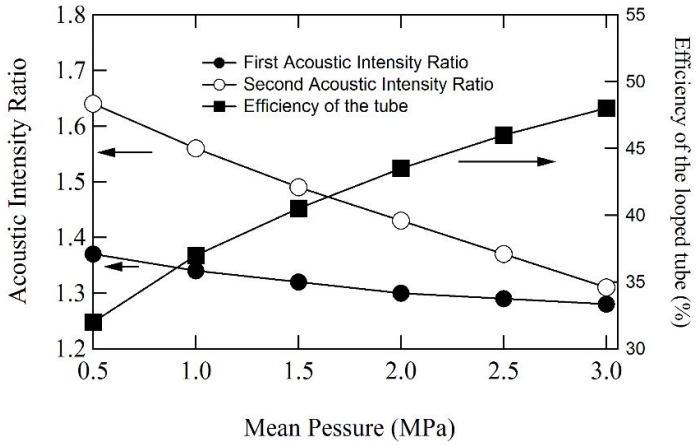

Figure 5: Acoustic Intensity ratio as a function of mean pressure

Figure 5 shows that $I_{out\,1}/I_{in1}$ and I_{out2}/I_{in2} decreased from 1.37 to 1.28 and 1.64 to 1.31, respectively. If the ratio of acoustic intensity decreased by approximately 1, the dissipation was almost 0. It was indicated with the increase of P_m as the dissipation decreased.

This result can also be explained using Equation 14 (Swift, 2002; Tijani, 2011).

$$E_{loss} = \frac{1}{4}\frac{|p|^2}{\gamma P_m}(\gamma - 1)\delta_k \omega$$

Equation 14: Energy dissipated by the thermal-relaxation dissipation.

Where:

- E_{loss} = energy dissipated by the thermal-relaxation dissipation (J)
- γ = ratio of isobaric to isochoric specific heats
- ω = angular frequency (rad/s)
- δ_k = penetration depth (m)
- p = oscillatory pressure (Pa)
- p_m = mean pressure (Pa)

It is shown in Equation14 that the value of E_{loss} was proportional to the value of $1/P_m$. Therefore, dissipation power decreased as the mean pressure increased.

4. CONCLUSION

Increasing P_m does not only decreased onset heating temperature to generate the engine from 558°C to 307°C, but also increased the performance. The efficiency of the tube considerably increased from 32% to 49% while keeping the high efficiency of the engine and heat-pump at 73% and 43%, respectively. Therefore, using only one engine regenerator it is possible to utilise lower waste heat for the engine while achieving high total efficiency of the heat-driven single-stage thermoacoustic cooler.

5. REFERENCES

Biwa, T, Tashihiro, Y, Ishigaki, M, Ueda, Y, Yazaki, T, 2007. Measurement of Acoustic Streaming in a looped tube thermoacoustic engine with a jet pump. *Journal of Applied Physics,* 110, 093519.

Cengel, Y.A, Boles, M.A, 2011. Thermodynamics. Seventh Edition. New York: McGraw-Hill.

Ceperley, P.H, 1979. A-Piston-less Stirling engine. *Journal Acoustic Society America,* 66, 1508-1513.

De Blok, K, 2012. Multi-stage travelling wave thermoacoustic in practice. The 19th International Congress of Sound and Vibration. Vilnius, Lithuania: International Institute of Acoustics and Vibration.

De Blok, K, 2008. Low operating temperature integral thermoacoustic device for solar cooling and waste heat recovery. The europian conference on noise control, euronoise,

Farikhah, I, Ueda, Y, 2017. Numerical Calculation of The Performance of a Thermoacoustic System with Engine and Cooler Stacks in a Looped tube. *Applied Sciences,* 51, 8, 403,408.

Johnson I, William T, 2008. Waste heat recovery: Technology and opportunities in U.S Industry US Department of Energy.

Kang, H, Zhou, G, Li, Q, 2010. Heat-driven thermoacoustic cooler based on the travelling-standing wave. *Energy Conversion and management*, 51, 2103-2108.

Luo, E.C, Dai, W, Zang, Y, Ling, H, 2006. Experimental investigation of a thermoacoustic-stirling refrigerator driven by a thermoacoustic-stirling heat engine. *Ultrasonics,* 44, e1531, e1533.

Rott, N, 1969. Damped and thermally driven acoustic oscillations in wide and narrow tubes. *Z.Angew.Math.Phys,* 20, 230-243.

Rott, N, 1973. Thermally driven acoustic ascillations part ii: stability limit for helium. *Z.Angew.Math.Phys.* 24, 54-72.

Swift, G.W, 1988. Thermoacoustic engines. *Journal Acoustical Society America*, 84 (4), 1145-1180.

Swift, G.W, 2002. Thermoacoustic: A unifying perspective for some engines and refrigerators. New York: Acoustical Society of America.

Swift, G.W, Gardner, D.L, Backhauss, S, 1999. A thermoacoustic Stirling Engine. *Nature,* 399, 335-338.

Saechan, P, Kang, H, Mao, X, Jaworski, A.J, 2013. Thermoacoustic refrigerator driven by a combustion-powered thermoacoustic engine-demonstrator of device for rural areas of developing countries, World congress on engineering, London, UK.

Twidel, J, Weir, T, 2006. Renewable energy resources. New York. USA: Tailor Francis.

Tijani, M.E.H, Spoelstra, S, 2011. A high performance engine. *Journal of Applied Physics*, 110, 093519.

Tominaga, A, 1995. Thermodynamic aspects of thermoacoustics theory. *Cryogenic,* 35, 427-440.

Tominaga, A, 1998. Fundamental thermoacoustic. Tokyo: Uchidarokakumo.

Ueda, Y, Bassem, MM, Tsuji, K, Akisawa, A, 2010. Optimization of the regenerator of a travelling wave thermoacoustic refrigerator. *Journal Applied Physics,* 107, 034901-1-5.

Ueda, Y, Kato, C, 2008. Stability analysis of thermally induced spontaneous gas oscillations in straight and looped tube.

Yazaki, T, Biwa, T, Tominaga, A, 2002. A Piston-less Stirling Cooler. *Applied Physics Letter,* 80, 157-159.

Zhang, X, Chang, J, Cai, S, Hu, J, 2016. A-multi-stage travelling wave thermoacoustic engine driven refrigerator and operation features for utilizing low grade energy. *Energy conversion and management,* 114, 224-233.

#189: Experimental investigation on window mini heat-pump air exchanger

Qi XU[1], Saffa RIFFAT[2], Shihao ZHANG[3]

[1] Department of Architecture and Built Environment, Faculty of Engineering, University of Nottingham, NG7 2RD University Park, Nottingham, UNITED KINGDOM, Qi.xu1@exmail.nottingham.ac.uk
[2] Department of Architecture and Built Environment, Faculty of Engineering, University of Nottingham, NG7 2RD University Park, Nottingham, UNITED KINGDOM, Saffa.Riffat@exmail.nottingham.ac.uk
[3] Department of Architecture and Built Environment, Faculty of Engineering, University of Nottingham, NG7 2RD University Park, Nottingham, UNITED KINGDOM, Shihao.zhang@exmail.nottingham.ac.uk

Normal ventilation without heat recovery in an air conditioned room would cause additional energy consumption. This study proposes a novel window mini heat-pump air exchanger (WMHPAE) unit which requires low power to operate. During its operation, the small-scale heat pump can cool the fresh hot outside air in the evaporator before sucking it into the room and cool the condenser by the indoor exhausted cold air in summer, which would achieve the ventilation as well as helping to increase COP of the micro-compressor heat pump. The prototype was built and tested under laboratory conditions with different parameter controls including power consumption, axial fan speed and temperature differences between indoor and outdoor. The results show that WMHPAE units could provide fresh air exchange with low energy consumption. The unit could also be retrofitted in residential buildings to contribute to better facades as it enjoys compact size to fit the widow frame. However, further real-life investigation and improvement are still needed for the WMHPAE unit.

Keywords: micro-compressor heat pump; air exchanger; performance; building applications

1. INTRODUCTION

Recently, the refrigeration compressor market has been growing rapidly around the world. Most refrigeration compression systems can provide thermal comfort and an acceptable indoor air quality (IAQ) for occupants (Yu *et al.*, 2009). But other key concerns for air conditioning systems are energy consumption and lack of fresh air exchange (Hsieh *et al.*, 2018); many similar air conditioning products ignore the function of fresh air exchange. As more and more modern buildings satisfy sound insulation requirements using airtight window, lower fresh air exchange rate, about 0.3 to 0.5 times per hour (Hsieh *et al.*, 2018), has occurred, which could influence indoor air quality.

Some studies have been carried out to explore ventilation issues. The total energy exchanger (also called “heat recovery ventilator”), (Liu *et al.*, 2010; Min and Duan, 2015) is the most popular energy-saving equipment for heat recovery in fresh air exchange. The heat recovery ventilator is used to recover the waste cold/heat of the exhaust room air to reduce power consumption of air conditioning equipment. However, the installation cost is high and needs a large amount of space (Hsieh *et al.*, 2018).

This study proposes a novel window mini heat-pump air exchanger (WMHPAE) unit which requires low power to operate. During its operation, the small-scale heat pump can cool the fresh outside hot air in the evaporator before sucking it into the room and cool the condenser by the indoor exhausted cold air in summer, which would achieve ventilation as well as helping to improve the energy efficiency of the mini heat pump. WMHPAE units can also be retrofitted in to residential buildings to contribute to better facades as it enjoys compact size to fit the widow frame.

2. DESIGN OF WINDOW MINI HEAT-PUMP AIR EXCHANGER (WMHPAE) SYSTEM

The proposed WMHPAE unit is an integrated window heat pump fresh air exchanger system which utilises a micro-compressor to cool the ambient hot fresh air in the evaporator before entering indoor and to cool the condenser using the exhaust cold air. It included five main components: a micro-compressor with display panel and controller; an evaporator; a condenser; an expansion valve and four axial fans for air supply and air exhaust. Table 1 shows the major features of the components.

Table 1: Major components of WMHPAE unit

Major components	Description
Micro-compressor	Type: GP2408C, from Guangdong Greatcool Compressor CO, LTD; Dimension: 54.7mm* height 101mm; Weight: 700g (1.5b) including lubricant oil; Power: 24V DC; Refrigerant: R134a.
Evaporator	1*Copper pipe with Aluminum fins (250mm*130mm*26mm)
Condenser	1*Copper pipe with Aluminum fins (265mm*130mm*40mm)
Expansion valve	1*Danfoss T2-X expansion valve 068Z3544
Axial fan	4*Sunon ME Series Axial Fan from RS No. 111-8182 (80mm*80mm*25mm)

As shown in Figure 1, the micro-compressor, evaporator, expansion valve, sight glass, dryer and condenser were connected by copper pipes to form a circle line. Two partitions divided the unit into three chambers to avoid air flow cross contamination. Axial fans were installed beside the evaporator and condenser separately to control the air flow directions. All the axial fans and micro-compressor display panel and controller were connected in parallel, which meant they employed the same power supply.

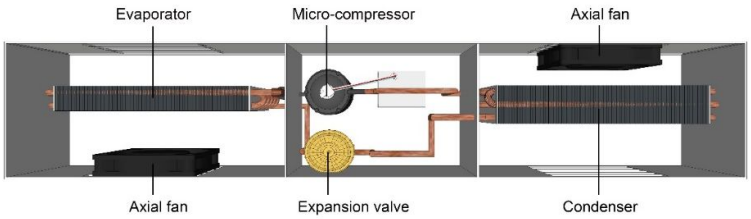

Figure 1: Schematic of the WMHPAE unit

During the operation in summer, the indoor cold exhaust air was sucked by the axial fans near to the condenser to cool the condenser and the ambient hot fresh air was sucked by the axial fans near to the evaporator and cooled before entering indoor, in spacing cooling. Figure 2 shows the operation of WMHPAE for cooling mode. The proposed WMHPAE unit could be retrofitted to a building / room window frame as its super compact size compars favourably to conventional window air conditioning.

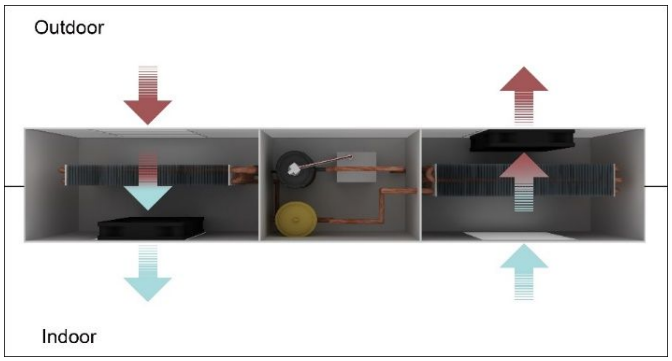

Figure 2: Operation of WMHPAE unit for cooling mode

In spacing cooling, the unit cooled the intake outdoor hot fresh air in the evaporator section. The condenser was cooled by the cold indoor exhaust air. Therefore, the evaporator temperature increased and the condenser temperature decreased. The whole system reduced the energy consumption of the heat pump since the pressure ration is reduced, while also achieving fresh air ventilation. Figure 3 shows the connection of WMHPAE unit.

Figure 3: Main components of WMHPAE unit

3. EXPERIMENTAL INVESTIGATION OF WMHPAE UNIT

3.1. Experiment set up

Table 2 summarises the measurement tools using during the whole testing.

Table 2: Major measurement tools

Measurement Tools	Details	Description
Datalogger	DT80 series 3 180mm x 137mm x 65mm 110/240Vac to 15Vdc, 800mA	Linearization errors < 0.1°C
Power supplier (for micro-compressor)	ETPS Limited compact DC power supply LAB/SM 270 482.6mm x 44.45mm x 440mm Output: 0-70VDC, 0-30A	Static regulation: ±0.05%+2mV ±0.1%+2mA
Power supplier (for linear fans)	MANSON Output DC Power Supply EP-603 145x150x200mm Multi-channel Output: 0-30VDC, 0-2.5A Continue voltage output: 12V DC/0.5A, 5V DC/0.5A	Output resolution: 1V 100mA
Anemometer	Testo 405i 200 x 30 x 41mm Maximum air velocity 30m/s	Air velocity resolution: 0.01m/s
Thermocouple	K-type 0.2mm diameter Operating temperature reaches up to 250°C	Accuracy: ±1.5°C

3.2. Experiment description

The experimental investigation of WMHPAE unit was carried out using an environmental chamber, located at the ground floor of the SRB building at the University of Nottingham, UK, to simulate the indoor and outdoor environment condition. The environment chamber, shown as Figure 4, comprised three components namely the metering box, the specimen panel and the cold box. Innovative heating and cooling elements were introduced in the design of the hot box using two separate units of thermoelectric (TEC) air to air heat pump at 102 W capacity, capable to achieve 5°C to 45°C in the cold and hot enclosure respectively. The cold box was chosen for our testing box and the size of the cold box part was 1.8m*1.8m*1.2m.

Figure 4: Image of environmental chamber

Figure 5 shows that half of the unit was positioned in the hot chamber acting as outdoor hot condition, the other half of the unit was positioned toward the laboratory assuming the indoor cold condition. Temperature, air flow velocity, power consumption for micro-compressors and instruments including axial fans and micro-compressor display panel and controller were measured.

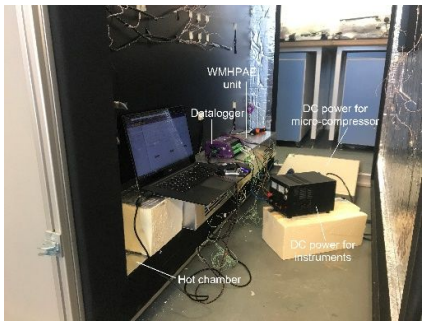

Figure 5: The testing set up

3.3. Data acquisition

The Data Taker DT80 Series 3 worked as an interface between a laptop and the temperature sensors (thermocouples). All the thermocouples (total 10 points) were K-type which were calibrated with the accuracy within 1.5°C. The temperature measurement system consisted of ten points, as shown in Figure 6.

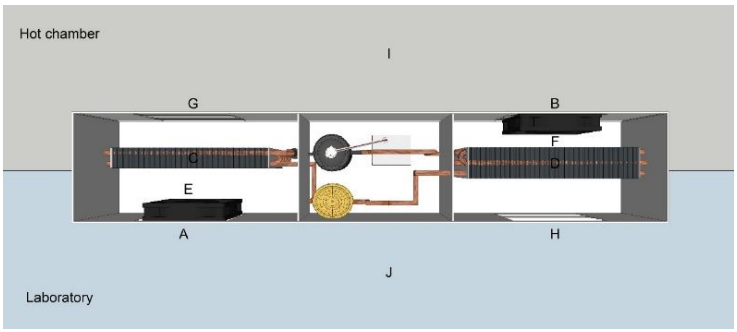

Figure 6: Diagram of thermocouple positions

Point A: Temperature of fresh air entering laboratory;
Point B: Temperature of exhaust air to hot chamber;
Point C: Temperature of fresh air reaching evaporator;
Point D: Temperature of exhaust air reaching condenser;
Point E: Temperature of fresh air after evaporator;
Point F: Temperature of exhaust air after condenser;
Point G: Temperature of fresh air from hot chamber;
Point H: Temperature of exhaust air from laboratory;
Point I: Hot chamber air temperature;
Point J: Laboratory air temperature.

In summer, for cooling operation, coefficient of performance (COP) of the micro-compressor heat pump can be calculated by the following equations:

Equation 1: Coefficient of performance.

$$COP = Q_c/(P + P_{ins})$$

Equation 2: Cooling capacity.

$$Q_c = C_{air} \cdot \dot{m} \cdot (T_{f-in} - T_{f-out})$$

Equation 3: Mass flow rate of air.

$$\dot{m} = \rho \cdot v \cdot A$$

Equation 4: Heat pump power consumption.

$$P = U \cdot I$$

Equation 5: Instruments power consumption.

$$P_{ins} = U_{ins} \cdot I_{ins}$$

Where:

- COP = coefficient of performance of the heat pump;
- Q_c = cooling capacity of the micro-compressor heat pump produced at evaporator;
- P = power supplied to micro-compressor;
- P_{ins} = power supplied to instruments;
- C_{air} = specific heat of air;
- $\dot{m}$ = mass flow rate of air;
- $T_{f\text{-}in}$ = temperature of fresh air from hot chamber;
- $T_{f\text{-}out}$ = temperature of supply air entering laboratory;
- ρ = mass density of air;
- v = air flow velocity;
- A = cross-sectional vector area;
- U, U_{ins}, I, I_{ins} = input voltage for micro-compressor, instruments and input current for micro-compressor, instruments separately.

4. TESTING RESULTS AND DISCUSSION

The first testing was investigated with 24V/1.4A to micro-compressor and 15V/0.8A to instruments and 1.12m/s air flow velocity measured by anemometer. Figure 7 shows the test results in cooling mode. The hot chamber temperature varied between 23.89°C and 25.74°C. The temperature of fresh air entering the laboratory was between 16.3°C and 17.2°C, while the laboratory temperature was maintained between 14.57°C and 15.57°C. It was seen that the temperature of the exhaust air reaching the condenser varied between 19.91°C and 24.28°C, which is lower than the hot chamber temperature (between 23.89°C and 25.74°C), with about 3°C average temperature difference. This verified that the recovery of waste cold air was achieved.

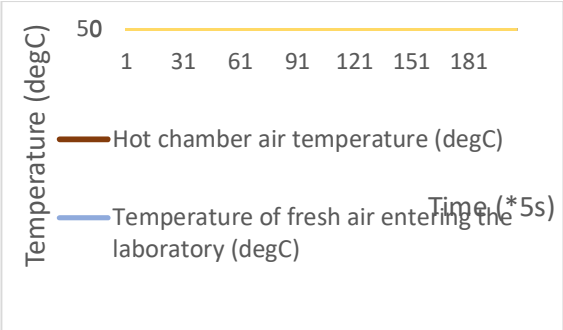

Figure 7: Temperature monitoring of hot chamber, laboratory, fresh air entering laboratory and exhaust air reaching condenser

The following testing was carried out under different modes: with different power supply to micro-compressor (24V/1.4A, 24V/2.1A, 24V/2.4A) to explore how the current supply for micro-compressor would affect the COP; with different power supply to axial fans to investigate the effect of air flow velocity to COP; with various temperature differences between the hot chamber and laboratory to observe the relationship between the temperature difference and COP.

4.1. Micro-compressor with different current

Table 3 summarises the results of WMHPAE unit performance under different power consumption (1.4A, 2.1A and 2.4A) of the micro-compressor. All the temperature figures were average valve during the testing.

Table 3: Performance test of WMHPAE unit with different current supply

	1	2	3
Hot chamber air temperature, T_{lab} °C	24.60	25.75	25.91
Temperature of fresh air from hot chamber, $T_{f\text{-}in}$ °C	26.62	26.47	26.71
Temperature of fresh air entering laboratory, $T_{f\text{-}out}$ °C	16.71	15.56	15.39
Temperature of fresh air reaching evaporator, T_{eva} °C	13.12	10.48	9.84
Temperature of exhaust air reaching condenser, T_{con} °C	21.36	23.46	23.81
Volumetric flowrate, m^3/s	0.010	0.010	0.010
Micro-compressor speed, rmp	2906	2956	2982
Cooling capacity at evaporator, Q_c W	120	132	137
Power consumption for micro-compressor, Q W	33.6	50.4	57.6
Power consumption for instruments, Q_{ins} W	12	12	12
COP	2.63	2.12	1.96

Figure 8 shows that with the DC current supply to micro-compressor, 1.4A, 2.1A and 2.4A, COP decreased with increasing micro-compressor power consumption. Further investigation is needed to explore how a bigger power consumption would affect COP as the maximum current of micro-compressor is 12A.

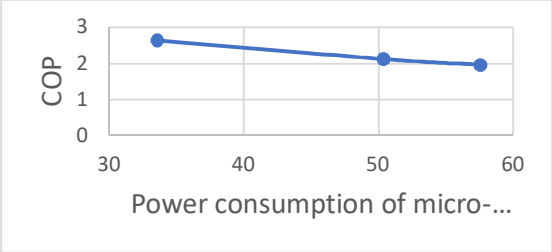

Figure 8: Variation of COP with micro-compressor power consumption

4.2. Operation with different air flow velocity

Table 4 shows the results of WMHPAE unit performance under different air flow velocity (0.84m/s, 0.93m/s, 1.12m/s and 1.26m/s) of micro-compressor. All the temperature figures were average valve during the testing.

Table 4: Performance test of WMCHP unit with different air flow velocity

	1	2	3	4
Hot chamber air temperature, T_{lab} °C	26.43	24.98	24.60	25.36
Temperature of fresh air from hot chamber, $T_{f\text{-}in}$ °C	26.83	26.36	26.62	26.10
Temperature of fresh air entering laboratory, $T_{f\text{-}out}$ °C	18.19	15.22	16.71	16.39
Temperature of fresh air reaching evaporator, T_{eva} °C	10.18	11.05	13.12	12.66
Temperature of exhaust air reaching condenser, T_{con} °C	27.34	23.59	21.36	22.85
Volumetric flowrate, m^3/s	0.008	0.009	0.010	0.012
Micro-compressor speed, rmp	2658	2658	2658	2658
Cooling capacity at evaporator, Q_c W	83.7	121.5	120	141.1
Power consumption for micro-compressor, Q W	33.6	33.6	33.6	33.6
Power consumption for instruments, Q_{ins} W	4	6	12	15.3
COP	2.23	3.06	2.63	2.89

From the above table, it is seen that the unit could achieve better COP when axial fans were working with its current rating (12VDC).

4.3. Performance at various hot chamber temperature

Table 5 describes the results of WMHPAE unit performance at various temperature differences between the hot chamber and laboratory (7.9°C, 9.66°C and 17.81°C) of micro-compressor. All the temperature figures were average valve during the testing.

Table 5: Performance test of WMCHP unit with various temperature difference between hot chamber and laboratory

	1	2	3
Hot chamber air temperature, T_{lab} °C	22.98	24.6	32.1
Temperature of fresh air from hot chamber, $T_{f\text{-}in}$ °C	23.96	26.62	31.58
Temperature of fresh air entering laboratory, $T_{f\text{-}out}$ °C	15.68	16.71	19.09
Temperature of fresh air reaching evaporator, T_{eva} °C	13.08	13.12	15.06
Temperature of exhaust air reaching condenser, T_{con} °C	21.22	21.36	19.44
Volumetric flowrate, m^3/s	0.010	0.010	0.010
Micro-compressor speed, rmp	2906	2906	2906
Cooling capacity at evaporator, Q_c W	100	120	151
Power consumption for micro-compressor, Q W	33.6	33.6	33.6
Power consumption for instruments, Q_{ins} W	12	12	12
COP	2.19	2.63	3.31

Figure 9 shows that COP increased with increasing temperature differences, $T_{hot} - T_{lab}$. The WMCHP unit introduced cold air from the laboratory to the condenser.

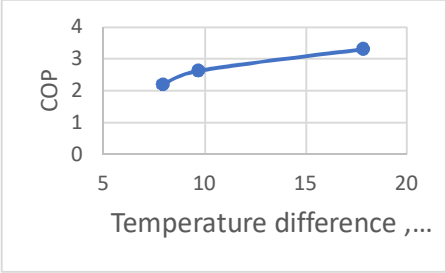

Figure 9: Variation of COP with temperature difference between the hot chamber and laboratory

5. SUMMARY AND FUTURE WORK

The design of the window mini heat-pump air exchanger (WMHPAE) unit was proposed to utilise a heat pump to cool the intake outdoor hot fresh air in the evaporator and to cool the condenser using the exhaust cold indoor air. The evaporator temperature of the heat pump increased and the condenser temperature decreased. This reduced the power consumption and increased COP of the heat pump. The fresh air entering the room could be 8.04°C to 12.49°C lower with a WMHPAE unit than normal ventilation without it in summer. During operation under laboratory condition, the micro-compressor achieved COP for cooling from 1,96 to 3.31, which was higher than traditional window air conditioning. Also the unit achieved a cooling capacity from 83.7W to 151W, much lower than window air conditioning. The present study showed that increasing temperature difference between outdoor and indoor improved the COP of the system.

However, the limitations of the testing are shown as following:

1. From the results under laboratory condition, the temperature of the evaporator (around 12°C) was much higher than normal conditions (7°C) and the temperature of the condenser (about 24°C) was much lower than normal conditions (45°C). The temperature difference between the evaporator and the condenser was rather low as a higher DC power supply was needed to support the micro-compressor. The maximum current of micro-compressor was 12A from the datasheet. However, the power supply in the laboratory could only provide 24V/2.5A to the unit which limited the running of the micro-compressor. Lower energy consumption caused higher COP at a certain degree. New DC power supply with higher current range is needed.

2. The amount of R134a refrigerant in the unit was 0.879kg. As the technicians could not find such a small receiver, the current unit was operated without the receiver which limited the working condition of the micro-compressor. The maximum speed of micro-compressor was 6000rmp from the datasheet. However, during the testing only 3000rmp speed was achieved as higher speeds caused strong vibration. The lack of the receiver also led to low temperature difference between the evaporator and the condenser. The improvement of adding a receiver with more refrigerant should be developed.

6. REFERENCES

Hsieh, Y.-Y. *et al.* (2018) 'A study of heat-pump fresh air exchanger', *Applied Thermal Engineering*, 132, pp. 708–718. doi: https://doi.org/10.1016/j.applthermaleng.2017.12.122.

Liu, Junjie *et al.* (2010) 'Efficiency of energy recovery ventilator with various weathers and its energy saving performance in a residential apartment', *Energy and Buildings*, 42(1), pp. 43–49. doi: https://doi.org/10.1016/j.enbuild.2009.07.009.

Min, J. and Duan, J. (2015) 'Membrane-type total heat exchanger performance with heat and moisture transferring in different directions across membranes', *Applied Thermal Engineering*, 91, pp. 1040–1047. doi: https://doi.org/10.1016/j.applthermaleng.2015.09.001.

Yu, B. F. *et al.* (2009) 'Review of research on air-conditioning systems and indoor air quality control for human health', *International Journal of Refrigeration*, 32(1), pp. 3–20. doi: https://doi.org/10.1016/j.ijrefrig.2008.05.004.

#190: Experimental investigation on bathroom straw heat exchanger

Qi XU[1], Shihao ZHANG[2], Saffa RIFFAT[3]

[1] Department of Architecture and Built Environment, Faculty of Engineering, University of Nottingham, University Park, Nottingham, NG7 2RD, UK, Qi.xu1@exmail.nottingham.ac.uk
[2] Department of Architecture and Built Environment, Faculty of Engineering, University of Nottingham, University Park, Nottingham, NG7 2RD, UK, Shihao.zhang@exmail.nottingham.ac.uk
[3] Department of Architecture and Built Environment, Faculty of Engineering, University of Nottingham, University Park, Nottingham, NG7 2RD, UK, Saffa.Riffat@exmail.nottingham.ac.uk

Hot wet air in bathrooms contain considerable amounts of thermal energy when we take a bath. Heat recovery ventilators could be an option to recover the waste heat in bathroom and create a better indoor environment. This study reports a novel bathroom straw heat exchanger (BSHE) unit which consisted of flexible plastic straws, PVC pipes and bathroom extractor fans. During its operation, the indoor exhausted hot air would be recovered through a cross flow pattern. The prototype was built and tested under laboratory conditions, exploring its sensible effectiveness and sensible recovered energy. The results showed that the BSHE unit could help to take advantage of waste thermal energy in bathrooms. The unit had advantages of low cost, easy installation and being energy-saving. However, investigations on latent energy effectiveness and different heat exchanger material choices for BSHE unit should be conducted, as well as real-life operation.

Keywords: bathroom heat exchanger; sensible effectiveness; thermal energy

1. INTRODUCTION

Nowadays, the building sector takes up nearly 1/3 of carbon emissions in the whole world (Buyle, Braet and Audenaert, 2013). It is necessary to reduce carbon emissions from buildings (Chau, Leung and Ng, 2015). The operation and maintenance of buildings could also be responsible for about 40% of global energy consumption (Pérez-Lombard, Ortiz and Pout, 2008).

Meanwhile, the need to improve indoor air quality has become a major concern worldwide (Paul, Sree and Aglan, 2010; Kosonen and Tan, 2004) requiring 100% fresh air in HVAC systems for certain buildings resulting in a significant increase in building cooling/heating loads (Nguyen, Kim and Shin, 2005; Zhang, 2006). For such systems, an energy recovery system could be utilised to reduce this load. During the operation, the system used the exhausted room air to pre-condition the ambient fresh air. As a result, a large amount of energy was recovered which in return reduced the overall HVAC energy requirement (Nasif *et al*., 2010).

In this research, the heat recovery unit under investigation was a bathroom straw heat exchanger (BSHE) utilising flexible plastic straws as the heat transfer core. BSHE provided a counter flow arrangement over most of the transfer surface. The application of BSHE can help to recovery waste heat in bathrooms.

2. DESIGN OF BATHROOM STRAW HEAT EXCHANGER (BSHE) SYSTEM

The proposed BSHE unit was a cross-flow heat exchanger, including five main components: two 4-inch inline extractor duct fans for the bathroom; 36Pcs flexible plastic straws; one 150mm round,350mm length PVC pipe; two 100mm round, 145mm length PVC pipe and four 5mm thickness wood hollow support frames to brace the pipes and fans. Table 1 shows the major figures of the components.

Table 1: Major components of BSHE unit

Major components	Description
Extractor duct fan	2*Kenley inline extractor duct fans
Flexible plastic straw	(Φ 100mm* L114mm) 220VAC,13W
PVC pipe A	36* Shuangtong flexible plastic straws
PVC pipe B	(Φ 6mm* L150mm)
Support frame	1*Manrose 61350 round PVC duct

The extractor fans, ducts and straws were constructed inline as shown in the Figure 1.

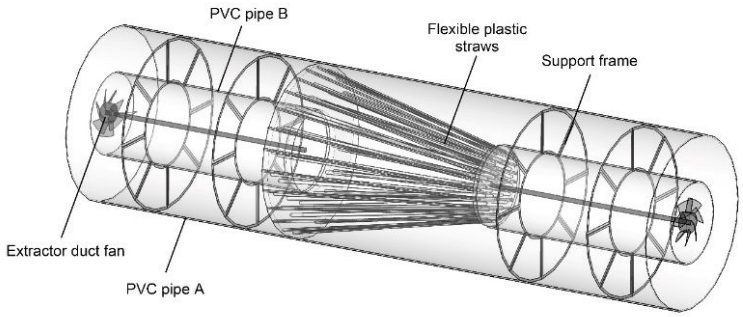

Figure 1: Schematic of the BSHE unit

The BSHE unit could provide fresh air ventilation for bathroom use. The major function of the BSHE unit was to minimise the heat loss during ventilation. During operation, the warm outdoor fresh air and indoor exhaust warm air were both sucked in by the extractor fans and the exhaust warm air warmed up the fresh air passing through the straws. Figure 2 presents the operation process of BSHE unit. In summary, BSHE unit allowed a heating fresh air supply into the bathroom whilst contributing to reducing domestic building energy consumption.

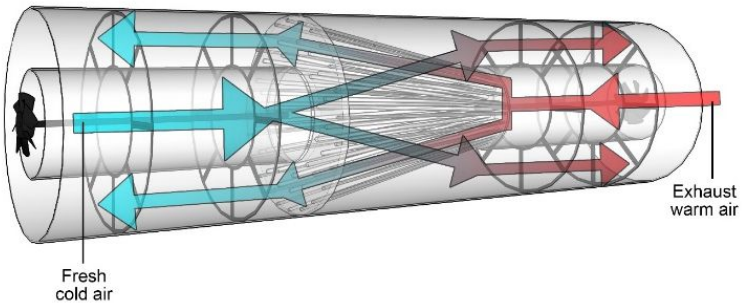

Figure 2: Diagram of BSHE unit operation

The proposed BSHE unit could be retrofitted to an existing bathroom, as its size is suitable for current bathroom ventilation holes (diameter 150mm). Figures 3 and 4 show the straw heat exchanger core and an image of the BSHE unit separately.

Figure 3: The straw heat exchanger core

Figure 4: Image of BSHE unit

3. EXPERIMENTAL INVESTIGATION OF BSHE UNIT

3.1. Experiment set up

Table 2 summarises the measurement tools using during the whole testing.

Table 2: Major measurement tools

Measurement Tools	Details	Description
Datalogger	DT80 series 3 180mm x 137mm x 65mm 110/240Vac to 15Vdc, 800mA	Linearization errors < 0.1°C
Anemometer	Testo 405i 200 x 30 x 41mm Maximum air velocity 30m/s	Air velocity resolution: 0.01m/s
Thermocouple	K-type 0.2mm diameter Operating temperature reaches up to 250°C	Accuracy: ±1.5°C

Figure 5 shows the schematic description of the testing set up.

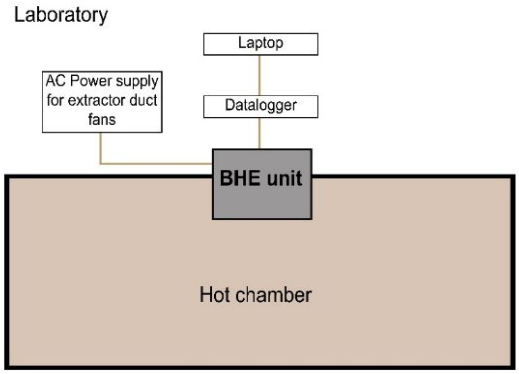

Figure 5: Testing rig

3.2. Experiment description

The experimental investigation of BSHE unit was carried out using an environmental chamber, located on the ground floor of the SRB building at the University of Nottingham, UK, to simulate the indoor and outdoor environmental conditions. The environment chamber, shown as Figure 6, comprised of three components namely; the metering box, the specimen panel and the cold box. Innovative heating and cooling elements were introduced in the design of the hot box using two separate units of thermoelectric (TEC) air to air heat pump at 102 W capacity, capable of achieving 5°C to 45°C in the cold and hot enclosure respectively. The cold box was chosen for our testing box and the size of the cold box part was 1.8m*1.8m*1.2m.

Figure 6: Image of environmental chamber

As Figure 7 shows, half of the unit was positioned in the chamber acting as bathroom conditions, the other half of unit was positioned toward the laboratory. Temperature and air flow speed were measured.

Figure 7: The testing set up

3.3. Data acquisition

Investigation of the efficiency of the heat exchanger unit required measurement of air temperatures and flow rates as all discussion in this report is about sensible effectiveness. The Data Taker DT80 Series 3 worked as an interface between a laptop and the temperature sensors (thermocouples). All the thermocouples (total of 10 points) were K-type which were calibrated with the accuracy within 1.5°C. Air temperature values outside the hot chamber, inside the hot chamber and in the supply and exhaust stream were measured. In order to determine the airflow measurements, a hand-held wireless anemometer was used to measure the velocity of the air stream at the supply and exhaust duct at the same locations as the temperature measurements.

The tests were carried out at laboratory temperature (outside temperature of hot chamber) of between 14°C and 15°C and hot chamber temperature at around 22°C. The temperature measurement system consisted of ten points, as shown in Figure 8:

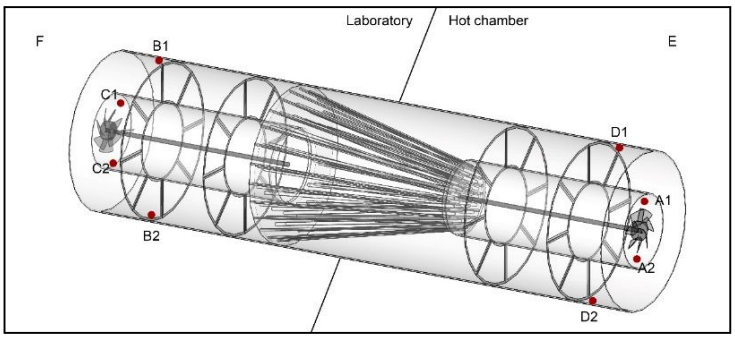

Figure 8: Diagram of thermocouple positions

Point A1, A2: Temperature of exhaust air inlet;
Point B1, B2: Temperature of exhaust air outlet;
Point C1, C2: Temperature of fresh air inlet;
Point D1, D2: Temperature of fresh air outlet;
Point E: Hot chamber air temperature;
Point F: Laboratory air temperature.

Sensible recovered energy, when heat or energy transfer through a casing by air leaks and heat conduction is not taken into account, is determined by the following expression:

Equation 1: sensible recovered energy.

$$Q_s = C_{air} \cdot \dot{m} \cdot (T_{ex-in} - T_{ex-out})$$

Equation 2: Mass flow rate of air.

$$\dot{m} = \rho \cdot v \cdot A$$

Where:

- Q_s = sensible recovered energy;
- C_{air} = specific heat of air;
- $\dot{m}$ = mass flow rate of air;
- T_{ex-in} = temperature of exhaust air inlet;
- T_{ex-out} = temperature of exhaust air outlet;
- ρ = mass density of air;
- v = air flow velocity
- A = cross-sectional vector area.

According to ASHRAE Standard sensible heat recovery efficiency or temperature efficiency is expressed by the temperature change of supply air to the temperature difference of the exhaust air and thus calculated by the following equation:

Equation 3: Sensible effectiveness.

$$\varepsilon = (T_{f-out} - T_{f-in})/(T_{ex-in} - T_{f-in})$$

Where:

- ε = sensible effectiveness/temperature efficiency,
- T_{f-out} = temperature of fresh air before the heat exchanger core,
- T_{f-in} = temperature of fresh air after the heat exchanger core,
- T_{ex-in} = temperature of exhaust air before the heat exchanger core.

4. TESTING RESULTS AND DISCUSSION

Testing was carried out three times under similar conditions at different times to investigate the performance of the prototype. The temperature difference across the heat recovery unit was recorded and the air velocity was measured at 1.04m/s during operation. Taking the first test as an example, Figure 9 shows the temperature variation of several setting points with times.

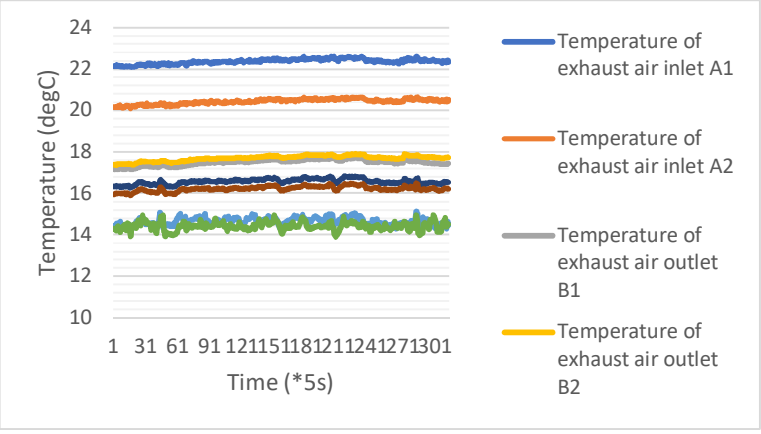

Figure 9: Temperature monitoring of setting points

Both exhaust air inlet (T_{ex-in}) and outlet (T_{ex-out}) temperature, and fresh air inlet (T_{f-in}) and outlet (T_{f-out}) temperature were average temperatures based on measured data under stable status. The efficiency of the crossflow heat recovery was evaluated using Equation1, 2 and 3 based on the measured data. Table 3 summarises all the three results of the calculation for airflows and temperature tested.

Table 3: Testing results

Testing	Mass flow rate (kg/s)	$T_{ex\text{-}in}$ (degC)	$T_{ex\text{-}out}$ (degC)	$T_{f\text{-}in}$ (degC)	$T_{f\text{-}out}$ (degC)	Q_s (W)	Sensible effectiveness (%)
1	0.010	21.40	17.59	14.53	16.39	41.90	27.07%
2	0.010	21.62	17.75	14.58	16.51	42.57	27.41%
3	0.010	22.04	17.98	14.51	16.59	45.65	27.62%

The measurements showed that at air velocity of 1.04m/s, indoor air temperature of around 22°C and outdoor air temperature of 21°C and 22°C, the sensible effectiveness was about 27%, and sensible recovered energy ranged from 41.90W to 45.56W. Temperature differences was about 3.81°C to 4.15°C.

5. SUMMARY AND FUTURE WORK

The heat recovery performance of a crossflow BSHE was investigated experimentally. The unit could achieve around 27% sensible effectiveness. However, humidity ratio measurements are missing as it is for a bathroom application. Also, based on the current studies, some improvements could be developed in the future:

1. The temperature differences between indoor and outdoor were too narrow. The effects of increasing temperature differences between indoor and outdoor with sensible effectiveness should be explored;

2. Another flexible straw arrangement might be considered to increase heat transfer area.

3. As plastic material enjoys rather poor heat transfer, changing the material of the straws, such as stainless-steel straws, could be further investigated.

6. REFERENCES

Buyle, M., Braet, J. and Audenaert, A. (2013) 'Life cycle assessment in the construction sector: A review', *Renewable and Sustainable Energy Reviews*, 26, pp. 379–388. doi: https://doi.org/10.1016/j.rser.2013.05.001.

Chau, C. K., Leung, T. M. and Ng, W. Y. (2015) 'A review on Life Cycle Assessment, Life Cycle Energy Assessment and Life Cycle Carbon Emissions Assessment on buildings', *Applied Energy*, 143, pp. 395–413. doi: https://doi.org/10.1016/j.apenergy.2015.01.023.

Kosonen, R. and Tan, F. (2004) 'The effect of perceived indoor air quality on productivity loss', *Energy and Buildings*, 36(10), pp. 981–986. doi: https://doi.org/10.1016/j.enbuild.2004.06.005.

Nasif, M. *et al.* (2010) 'Membrane heat exchanger in HVAC energy recovery systems, systems energy analysis', *Energy and Buildings*, 42(10), pp. 1833–1840. doi: https://doi.org/10.1016/j.enbuild.2010.05.020.

Nguyen, A., Kim, Y. and Shin, Y. (2005) 'Experimental study of sensible heat recovery of heat pump during heating and ventilation', *International Journal of Refrigeration*, 28(2), pp. 242–252. doi: https://doi.org/10.1016/j.ijrefrig.2004.07.022.

Paul, T., Sree, D. and Aglan, H. (2010) 'Effect of mechanically induced ventilation on the indoor air quality of building envelopes', *Energy and Buildings*, 42(3), pp. 326–332. doi: https://doi.org/10.1016/j.enbuild.2009.09.010.

Pérez-Lombard, L., Ortiz, J. and Pout, C. (2008) 'A review on buildings energy consumption information', *Energy and Buildings*, 40(3), pp. 394–398. doi: https://doi.org/10.1016/j.enbuild.2007.03.007.

Zhang, L. Z. (2006) 'Energy performance of independent air dehumidification systems with energy recovery measures', *Energy*, 31(8), pp. 1228–1242. doi: https://doi.org/10.1016/j.energy.2005.05.027.

#192: A steady-state experimental investigation of a bubble column solar desalination system for the humidification of air using direct solar thermal heating

Jianwei XIAO[1], Hongfei ZHENG[2], Rihui JIN[3], Shen LIANG[4]

[1] School of Mechanical Engineering, Beijing Institute of Technology, Beijing 100081, China. cauxjw@qq.com
[2] School of Mechanical Engineering, Beijing Institute of Technology, Beijing 100081, China. hongfeizh@bit.edu.cn
[3] School of Mechanical Engineering, Beijing Institute of Technology, Beijing 100081, China. 2808922112@qq.com
[4] School of Mechanical Engineering, Beijing Institute of Technology, Beijing 100081, China. liangshen09@163.com

In order to study in depth the influencing factors of water yield from solar desalination systems with direct heat bubbling humidification-dehumidification under actual weather conditions, the performance of the desalination system under steady-state conditions was experimentally studied. This paper introduces the structure of the device and its operation principle at steady state, tests the temperature and temperature characteristics of the system under the condition of stable energy supply at different powers, and studies the influence of input power, air temperature and water temperature, glass cover plate and air velocity in the tube on the water yield of the device. The experimental results show that the water temperature and air temperature of the evaporator and the condensing chamber have a linear relationship with the input power, and the water yield and power of the device have an approximate exponential relationship. Compared with the single-layer glass cover, the double-layer glass cover increased the water yield by 10.28%, 16.90% and 22.18% when the power was 1016.0w, 1221.6w and 1523.7w respectively. The higher the air velocity in the tube, the greater the water yield was. When the input power was 792.9w, 1016.0w and 1221.6w respectively, the air velocity in the tube increased from 11.6m/s to 14.9m/s, the water yield increased by 37.4%, 41.8% and 45.9% respectively, while the air velocity in the tube increased from 14.9m/s to 21.26m3/h, and the water yield increased by 9.9%, 15% and 19.3% respectively. The performance coefficient of the device was 0.91 when the device adopted double-layer glass cover, the air velocity in the tube was 21.26m3/h and the power was 1016.0w.The relative equations of heat and mass transfer of the device are listed and the related influencing factors of water yield and performance coefficient of the device and the influence of different power on water temperature and temperature are predicted theoretically by MATLAB calculation. It was found that the experimental results are basically consistent with the theoretical predictions.

Keywords: solar desalination, humidification-dehumidification, steady state, bubble column

1. INTRODUCTION

In recent decades, due to energy shortages and water scarcity, people have conducted a lot of research on solar desalination technology, but it has not been widely promoted. The main reasons are its low energy efficiency, poor economy and complex structure, which cannot be compared with traditional industrial desalination system.

Solar desalination technology can be divided into direct heating and indirect heating, indirect heating with solar desalination systems' components are built separately. Heat and mass transfer resistance between components results in the decrease of system efficiency, and also make the cost increase. But direct heating solar desalination technology reduce the heat and mass transfer resistance between components, improve the efficiency of the system, so we use the direct heating solar desalination technology.

In the solar desalination technology heated directly, the most mature is the basin solar distiller. It has the remarkable advantages of simple structure and low cost and easy material getting. However, the serious disadvantage of basin solar distiller is the low efficiency of water production. The main reasons for the low efficiency of water production are as follows: (1) there is no concentrated light, and the heat capacity of seawater to be evaporated is too large, which leads to the low operating temperature of the device, thus weakening the driving force of evaporation; (2) the natural convection heat transfer mode inside the device greatly limits the improvement of thermal performance of the distiller; (3) the latent heat of vaporisation in the process of water vapour condensation has not been reused.

In order to overcome these defects, a lot of work has been done to improve the efficiency of solar concentrator and receiver systems. In order to solve the problem of low operating temperature, it is necessary to combine solar high temperature concentrating technology with solar distiller to improve water production efficiency. Chaouchi (Chaouchi et al., 2007) and Omara (Omara and Eltawil, 2013) respectively designed different experimental devices combining basin paraboloid with traditional basin solar distiller. Pearce and Yadav (Y. P. Yadav, 2004) combined the compound paraboloid with the traditional distillation tray to improve the water production efficiency of the distillation tray. However, these devices are still based on the traditional solar distillation tray, the overall efficiency is low. At the same time, in order to reduce the heat transfer loss and improve the thermal energy utilisation efficiency of the water desalination device, Fresnel lens is used as the concentrator.

At present, solar desalination technologies mainly include multistage flash, reverse osmosis, vapour compression, multi-effect, humidification-dehumidification. However, multi-stage flash, reverse osmosis, vapour compression, multi-effect and other methods are only suitable for large capacity and medium capacity, and the cost is too high to apply to small capacity. The dehumidification method is suitable for small capacity desalination. The main ways to improve the efficiency of humidification-dehumidification device are to improve the efficiency of humidifying and dehumidifying and to reduce the loss of heat dissipation.

Commonly used humidifiers include spray towers (Houcine et al., 2006), bubble columns (El-Agouz, 2010), packed bed towers (Dai et al., 2002), etc. The research of Narayan (Narayan et al., 2010) shows that the packed bed towers can achieve higher water production efficiency by prolonged contact time between air and water and a larger area of air-water interface. The defect of this packing is that it is difficult to clean the packaging due to the precipitation of salt that accumulates on it, which leads to the complexity and cost of the equipment. Kabeel and Elsaid (Kabeel and El-Said, 2014) conducted an experimental study on humidification-dehumidification technology, a padded humidifier consisting of a polyvinyl chloride (PVC) rings with a diameter of 0.45m and a height of 0.8m was used. These fillers require frequent replacement and are costly, adding to the structural complexity of the device. Therefore, it is necessary to study a method of humidification-dehumidification technology with simpler structure and lower cost.

Recently, some scholars put forward a new idea of combining bubbling humidification technology and fresh water dehumidification technology in the solar desalination system. Ei-agouz (El-Agouz and Abugderah, 2008) and Rajaseenivasan (Rajaseenivasan and Srithar, 2017) studied the bubbling seawater desalination system, designed the experimental system respectively, and tested the water production efficiency of the bubbling seawater desalination system. The results show that although the technology of bubbling humidification-dehumidification is simple in structure, the effect of humidification-dehumidification is very obvious.

Hamed (Hamed et al., 2015) have established a theoretical model for predicting the water yield of the humidification-dehumidification devices and compared the calculated results with the experimental results. However, only a few variables, such as evaporation chamber temperature and water yield, were compared, and the theoretical calculation results were not comprehensively analysed, and the comparison with experimental results was not sufficient, and the influence of various influencing factors on the water yield performance of the device was not systematically studied.

Therefore, a new humidification-dehumidification device design scheme is proposed in this paper. This device adopts Fresnel lens to concentrate direct heat and combines solar energy collection system and heat transfer

system, reducing energy loss and heat and mass transfer resistance. At the same time, the wet saturated air through the bubbling horizontal pipe increases the surface area of the contact between water and air, and improves the evaporation efficiency of seawater and the condensation efficiency of fresh water. This will simplify the structure of the device and increased water yield. A theoretical model was established to study the water production performance of the device under the influence of different parameters.

2. EXPERIMENTAL SETUP AND WORKING PRINCIPLE

2.1. Device structure and experimental principle

In this experiment, the wet air in the humidification-dehumidification desalination device is forced to circulate by the fan, and the gas closed circulation mode is adopted. The main body of the desalination device is divided into two Chambers: the upper chamber is the evaporation chamber, and the heating tube is placed in the seawater of the evaporation chamber to promote the evaporation of seawater through heating. The lower chamber is a condensing chamber which has a cooling tube to promote the condensation of wet air. The condensing chamber also has the function of reheating and collecting fresh water. Figure 1 is a physical picture of the desalination device.

Figure 1: Photograph of the experimental equipment

The humidification-dehumidification desalination device is made of glass. It is 1.5m long, 30cm wide, 19cm high in front and 36cm high in back. The upper cover plate is inclined, with an Angle of 30 degrees with a width of 34.5cm.The length of front plate, back plate and upper cover plate is 1.5m.In order to make a comparison with the actual weather condition of the desalination device, in the steady state of the desalination device, except the upper cover, all the other surfaces are treated with insulation cotton.

The heating tube heats the seawater in the evaporation chamber, making the seawater evaporate. The seawater and circulating air exchange heat and moisture to form wet saturated steam. Wet saturated steam passes through the external pipe and bubble horizontal pipe and enters the condensing chamber to cool into fresh water. In the condensing chamber, the seawater of latent heat of gasification is absorbed, and then returns to the evaporating chamber for heating. There are bubble horizontal pipes in both evaporation and condensation cavities. On the one hand, bubble horizontal pipe is a part of all device pipe; On the other hand, the bubble pipe plays a role in promoting the evaporation of sea water in the evaporation chamber, and plays a role in promoting the condensation of wet saturated steam in the condensation chamber. Figure 2 shows the operation principle diagram of the dehumidifying and dehumidifying seawater desalination unit in steady state.

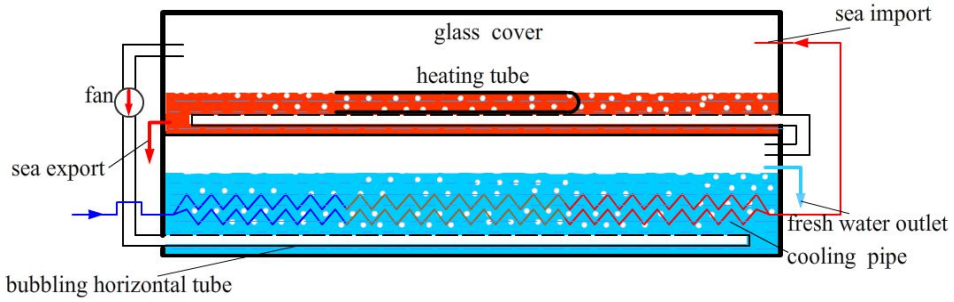

Figure 2: Schematic diagram of HDH system

2.2. The structure of evaporating and condensing cavities

Evaporation chamber and condensation chamber constitute the main chamber of the solar desalination unit. There is a glass plate between the evaporation chamber and the condensation chamber. In order to absorb heat effectively, the glass plate is made of 8mm thick black glass. The main chamber is 1.5m long, 30cm wide, the front side panel is 19cm high and the back side panel is 36cm high. Both sides are made of 8mm thick ordinary glass, and the left and right sides are made of 8mm thick inner mirror glass.

The upper cover plate of the evaporation chamber is inclined, with an angle of 30 degrees and a width of 34.5cm with the horizontal plane. It is made of ordinary transparent glass with a thickness of 4mm.Single-layer glass and double-layer glass are used in the test respectively. There is a closed air between the double-layer of glass, which can reduce the loss of heat dissipation. The condensing chamber is 12cm high.

The evaporation chamber contains black light absorbing material and PVC bubbling horizontal pipe. The light-absorbing material, namely the black cloth, is placed in the evaporation chamber, close to the bottom glass plate of the evaporation chamber, and absorbs the heat generated by the heating tube. Place two PVC pipes close to the light absorbing material. The two PVC pipes are 15cm apart and 7.5cm from the side wall respectively. PVC pipe with 100 holes, arranged symmetrically. Its geometric characteristic parameters are shown in table 1.These two PVC pipes connect the condensing cavity through the hole on the side wall and the external pipe. The wet air in the condensing cavity returns to the evaporation cavity through the small hole on the PVC pipe. By adjusting the water pump to control the flow of seawater, the water just overflows the bubbling horizontal pipe, so as to ensure the lower seawater heat capacity.

The condensing cavity contains PVC bubbling horizontal pipe and cooling pipe. Place two PVC pipes close to the bottom of the condensing cavity. The placement, processing and geometric characteristic parameters of the two PVC pipes are the same as those of the evaporation cavity. These two PVC pipes are connected to the fan through the hole on the side wall and the external pipe, and the fan is connected to the evaporation chamber through the pipe. The fan transfers the moist air from the evaporating chamber to the condensing chamber through the small holes in the external ventilation pipes and PVC pipes. Place the cooling pipe close to the top of the PVC pipe.

The cooling pipe is bellows, made of stainless steel, two pipes, each 5.5m long, 18mm outside diameter, S shaped spiral, placed on the condensation cavity bubbling horizontal pipe above. The cold seawater absorbs the latent heat of vaporisation in the condensing chamber through the cooling tube and then enters the evaporating chamber.

The thermocouple in the evaporation chamber is placed in the sea water and air 10cm above the sea water, while the thermocouple in the condensation chamber is placed in the fresh water and air 5cm above the fresh water.

Table 1: Geometric characteristics of PVC horizontal pipe

parameter	numerical
length	1.5m
diameter	20mm
hole spacing	3cm
pore diameter	2mm

2.3. Heating tube

In order to ensure adequate input power, two heating tube is adopted in experiment, the resistance of 56 Ω and 51 Ω respectively, put them together in parallel, the total resistance is 26.7 Ω. The input voltage is regulated by the voltage regulator to obtain different input power. If the maximum voltage is 220V, the maximum input power is 1812.7w, and the maximum instantaneous power of solar energy absorbed through the Fresnel lens concentrator is no more than 1500W, so the heating tube used in the test meets the requirements.

2.4. Auxiliary system and test system

Auxiliary systems and test systems mainly include ventilation ducts, cooling water ducts, cooling pipes, tracking systems, fans, pumps, frequency converters, voltage regulators and thermocouples. The experimental system is installed in accordance with Figure 3.The power consumption of electrical equipment is shown in table 2 below.

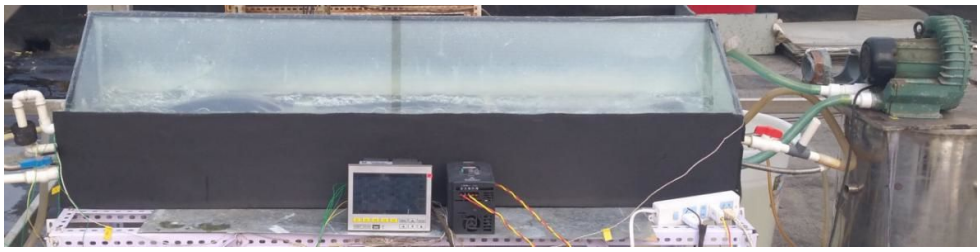

Figure 3: System parts installation diagram

Table 2: Power consumption of electrical equipment

equipment	parameter	number	power(W)
water pump	750L/h	1	7
fan	36m^3/h	1	260

The water temperature, air temperature, cooling water flow, fan wind speed and fresh water output of the evaporating chamber were measured and recorded in the steady-state experiment of the solar seawater desalination device with condensing direct heat bubble humidification-dehumidification. The temperature measured by the thermocouple is recorded by a 32-channel temperature patrol instrument. Before the test, the anemometer and thermocouple are measured and checked. The test was carried out in the vehicle experimental building of Beijing institute of technology on November 20, 2018, solstice on October 9, 2018. All the measurement instrument errors in the test were within the acceptable range. Table 3 shows the parameters of the experimental test equipment.

Table 3: Uncertainty of test instrument

instrument	measuring range	the uncertainty
32 way temperature patrol instrument	-200—1250•	1•
K thermocouple	-200—1250•	1•
anemometer	0.1—30m/s	0.1m/s
measuring cup	0—500ml	5ml

In order to verify the correctness of the theoretical model, a series of indoor steady-state experiments were carried out in the vehicle experimental building of Beijing institute of technology. In the experiment, heating tube with adjustable power is used to supply energy to the system instead of solar collector. In order to obtain accurate experimental data, the experimental data were collected half an hour after the system reached the steady state. The experiment was repeated three times in each working condition, and the average of different water yields was taken three times.

3. EXPERIMENTAL RESULTS AND DISCUSSION

3.1. The relationship between power and temperature

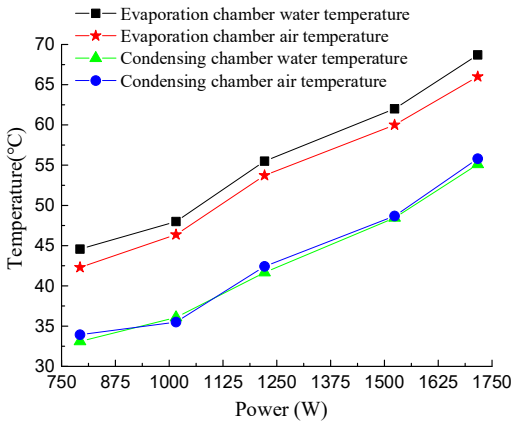

Figure 3: Curve of temperature with power

In order to study the influence of constant external input power on the water temperature and air temperature of evaporating chamber and condensing chamber, and the influence of stable water temperature and air temperature on the water yield of the unit, the steady-state test through heating tube was designed. In this steady-state test, a heating tube is used to provide a stable energy source for seawater in the evaporation chamber. The maximum power of the heating tube is 2kW, and the input voltage is adjusted with the voltage regulator to regulate the input power. Input the power of 792.9w, 1016.0w, 1221.6w, 1523.7w and 1716.8w respectively. After the system is stable, measure the air and water temperature of the evaporating and condensing cavities every 10min, collect and measure the water yield every 30min, and get the relationship curve as shown in Figure 3.

As can be seen from Figure 3, with the increase of power, the water temperature and air temperature of the evaporation chamber and the condensation chamber increase accordingly. Through curve fitting, it can be found that the water temperature and air temperature of evaporating cavity and condensing cavity have approximately linear relationship with power. This is due to the good insulation effect of the device, the input of electrical energy through the heating pipe into water and wet air heat energy. The water temperature in the evaporating chamber is slightly higher than the air temperature. This is because the heating tube is placed in the seawater and the seawater is heated first. The temperature in the condensing chamber is slightly higher than the water temperature, but the difference is very small. It can be considered that when the thermal equilibrium state is reached, the water temperature in the condensing chamber and the air temperature remain the same. The average temperature in the evaporation chamber is 9-12 degrees higher than that in the condensation chamber, with an average temperature of 11 degrees. The temperature difference is relatively stable. When the device reaches equilibrium, the cooling water condensation effect remains constant.

3.2. The effect of power on productivity and performance ratio

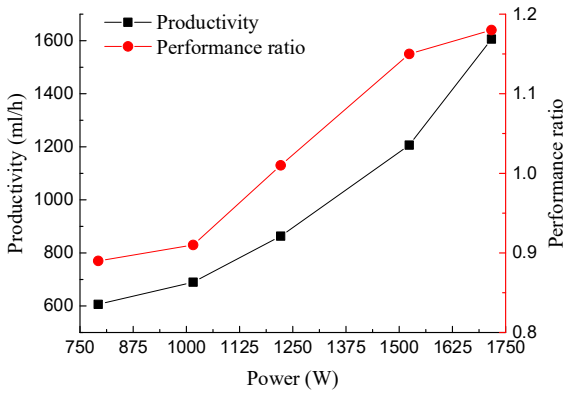

Figure 4: Curve of water yield and performance ratio with power

Figure 4 shows the curve of water yield and performance ratio of the device changing with input power when the wind speed of the fan is 18.8m/s with double glass cover. As can be seen from Figure 4, with the increase of power, the water yield increases slowly at first and then rapidly. Through curve fitting, it can be found that water yield and power have approximately exponential relationship, $y=244.55\exp(0.0011x)$, $R^2=0.9825$, where x is power, the unit is W and y are water yield, the unit is ml/h. This is because the water yield is equal to the moisture content of the air in the evaporation chamber minus the moisture content of the air in the condensation chamber, and the moisture content of the air has an exponential relationship with temperature, and the power has a linear relationship with temperature. By comparison with the figure above, it can be found that the relationship between temperature and water yield is also highly consistent with the exponential relationship. The higher the temperature is, the higher the water yield is. When the power reaches over 1100W, the water yield increases exponentially when the temperature rises to 60 degrees. Therefore, to improve the performance coefficient of the device and increase the fresh water output, the temperature and power must be increased.

The Performance ratio (PR) is an important index to characterise the system performance. The larger the Performance ratio is, the better the system performance will be.

According to the input/output relationship, the water-producing performance ratio of this device can be estimated by the following formula:

Equation 1: the equation of performance ratio.

$$PR = \frac{M_e h_{fg}}{Q_{in} + pt}$$

Where:

- M_e = total fresh water output of the unit over a given period of time (kg)
- h_{fg}= latent heat of vaporisation of water，approximate off for 2.3×10^6 (J/kg)
- Q_{in}= heat added to the system by a heating tube (J)
- pt= power consumption of fans, pumps and other equipment (J)

According to Equation 1, when the device adopts double glass cover plate, the wind speed of the fan is 18.8m/s, and the power is 792.9W, 1016.0W, 1221.6W, 1523.7W and 1716.8W, the PR of the device is 0.89, 0.91, 1.01, 1.15 and 1.18 respectively. The curves are shown in Figure 5.Therefore, the higher the power, the higher the temperature, the more the water yield, the higher the Performance ratio of the device. This is because there is an exponential relationship between the moisture content of air and temperature. The higher the temperature, the more the increase in water yield. At this time, most of the energy input into the system is used to directly produce fresh water, so the Performance ratio of the device is higher. Higher operating temperature can make the device have higher Performance ratio during operation, so in order to improve the performance of the device, it is necessary to find ways to improve the operating temperature of the device.

3.3. Effects of single and double glass plates on water temperature and water yield

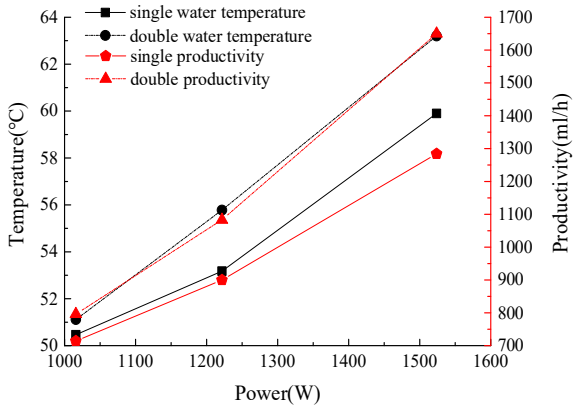

Figure 5: Comparison of water temperature and water yield between single and double layer glass plates

The water temperature in Figure 5 refers to the water temperature of the evaporating chamber. Figure 5 shows the comparison curves of water temperature and water yield of the evaporating chamber of single and double layer glass plates respectively with the increase of input power. As can be seen from Figure 5, with the increase of power, both water temperature and water yield of single and double layer glass plates increases. At the same time, when the input power is larger, the increase of water temperature and water yield is larger. The change of water temperature of double layer glass plate is almost consistent with the change of water yield. With the increase of power, the increase of water yield is lower than that of water temperature. Under the same input power, the water temperature of double glass is higher than that of single glass, and the water yield is higher than that of single glass. When the power is 1016.0 W, 1221.6 W and 1523.7 W respectively, the water yield of the double-layer glass plate increases by 10.28%, 16.90% and 22.18% respectively compared with the single-layer glass plate. The higher the power and the higher the temperature, the greater the increase of water yield of double glass. This is because monolayer glass dissipates heat more than double layer glass, so water temperature and water yield are lower than double layer glass.

When the input power is low, such as at 1016W, the water temperature of single and double glass plates varies little, while the water temperature of double glass plates is slightly higher. However, when the power is higher, such as higher than 1221.6w, the water temperature difference between the double glass plate and single glass plate begins to appear, and the temperature difference can reach 3-4 degrees. The larger the power, the higher the temperature, the greater the heat dissipation of single-layer glass plate. And relatively speaking, double glass board

insulation effect is better, so heat dissipation is smaller, higher temperature. It can be seen that double layer glass plate has obvious effect on improving water yield of the device.

3.4. The relationship between wind speed and water yield

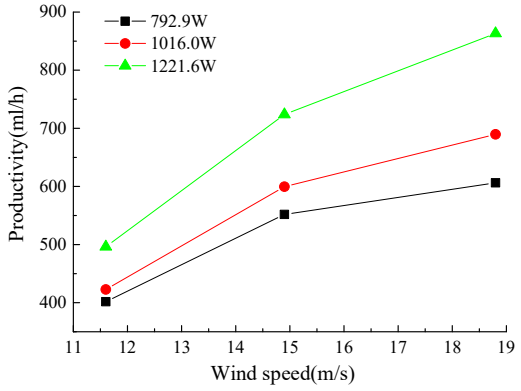

Figure 6: Curve of water yield with wind speed at different power

Figure 6 shows the curve of the water yield of the device changing with the wind speed of the fan under different input powers. When the input power is 792.9w, 1016.0w and 1221.6w respectively, the wind speed of the fan increases from 11.6m/s to 14.9m/s, and then increases to 18.8m/s, the water yield of the device is tested. It can be seen from Figure 6 that, with the same input power, the higher the wind speed of the fan, the higher the water yield of the device. This is because the higher the wind speed of the fan, the more circulating air through the device, the more wet air the condensing chamber condenses, and the higher the wind speed is conducive to the evaporation of sea water in the evaporating chamber, so the fresh water production increases.

When the input power is 792.9W, 1016.0W and 1221.6W respectively, the wind speed of the fan increases from 11.6m/s to 14.9m/s, and the water yield increases by 37.4%, 41.8% and 45.9% respectively, while the wind speed of the fan increases from 14.9m/s to 18.8m/s, and the water yield increases by 9.9%, 15% and 19.3% respectively. Thus, with the increase of wind speed, the increase of water production gradually decreases. That is, when wind speeds are higher, the amount of water produced increases less. This is because when the wind speed is higher, the evaporation rate of seawater in the evaporation chamber cannot keep up with the velocity of wet air, resulting in the unsaturated wet air in the evaporation chamber.

Due to the limitation of test conditions and time, we did not get the most sufficient data in the test to test the influence of wind speed on water yield. However, according to Figure 6 and theoretical analysis, we can still infer that, at the same power, the wind speed of the fan is bound to approach a limit value. When the wind speed of the fan is close to this limit value, increasing the wind speed has little impact on the fresh water production. Therefore, the appropriate wind speed value of the fan can be selected. In addition, we know that the higher the power, the higher the temperature, the faster the evaporation rate of seawater in the evaporation chamber, so the higher the limit wind speed value is. In other words, the higher the power, the higher the corresponding wind speed value, so that fresh water production can reach the maximum.

4. CONCLUSION

In this paper, a bubbling humidification-dehumidification type solar desalination device using Fresnel lens for direct heating is designed and produced. A comparison experimental study is conducted on the steady-state performance of the device, the influencing factors of water yield of the device are studied, and the performance ratio of the device is calculated. The main conclusions are as follows:

(1) the steady-state experimental results show that the water temperature and air temperature of the evaporating cavity and the condensing cavity increase with the increase of power, which is approximately linearly related to the power. The water yield of the device increases with the increase of power, which is approximately exponential.

(2) double layer glass plate has an obvious effect on improving the water yield of the device, especially when the input power is high. When the power is 1016.0 W, 1221.6 W and 1523.7 W respectively, the water yield of the double-layer glass plate increases by 10.28%, 16.90% and 22.18% respectively compared with the single-layer

glass plate. When the power is higher, such as higher than 1221.6w, the water temperature difference between the evaporation chamber of the double-layer glass plate and the single-layer glass plate can reach 3-4 degrees.

(3) the higher the wind speed of the fan, the greater the water yield, but when the wind speed is higher, the water yield changes less. When the input power is 792.9W, 1016.0W and 1221.6W respectively, the wind speed of the fan increases from 11.6m/s to 14.9m/s, and the water yield increases by 37.4%, 41.8% and 45.9% respectively, while the wind speed of the fan increases from 14.9m/s to 18.8m/s, and the water yield increases by 9.9%, 15% and 19.3% respectively.

(4) when the device adopts double glass cover, the wind speed of the fan is 18.8m/s, and the power is 792.9W, 1016.0W, 1221.6W, 1523.7W and 1716.8W, respectively, the PR of the device is 0.89, 0.91, 1.01, 1.15 and 1.18.The higher the power, the higher the PR of the device. In order to improve the performance of the device, the operating temperature of the device must be increased.

(5) In the following study, we will establish a theoretical model to calculate the productivity, and study the influence of cooling water flow rate, seawater inflow rate, cooling water temperature, environmental temperature and other factors on the productivity of the device. Methods to improve the water production performance of the device were studied.

5. REFERENCES

Chaouchi, B., A. Zrelli, and S. Gabsi, 2007, Desalination of brackish water by means of a parabolic solar concentrator: Desalination, v. 217, p. 118-126.

Dai, Y. J., R. Z. Wang, and H. F. Zhang, 2002, Parametric analysis to improve the performance of a solar desalination unit with humidification-dehumidification, p. 107-118.

El-Agouz, S. A., 2010, A new process of desalination by air passing through seawater based on humidification–dehumidification process: Energy, v. 35, p. 5108-5114.

El-Agouz, S. A., and M. Abugderah, 2008, Experimental analysis of humidification process by air passing through seawater: Energy Conversion and Management, v. 49, p. 3698-3703.

Hamed, M. H., A. E. Kabeel, Z. M. Omara, and S. W. Sharshir, 2015, Mathematical and experimental investigation of a solar humidification–dehumidification desalination unit: Desalination, v. 358, p. 9-17.

Houcine, I., M. BenAmara, A. Guizani, and M. Maâlej, 2006, Pilot device testing of a new solar desalination process by a multiple-effect-humidification technique: Desalination, v. 196, p. 105-124.

Kabeel, A. E., and E. M. S. El-Said, 2014, A hybrid solar desalination system of air humidification, dehumidification and water flashing evaporation: Part II. Experimental investigation: Desalination, v. 341, p. 50-60.

Narayan, G. P., M. H. Sharqawy, E. K. Summers, J. H. Lienhard, S. M. Zubair, and M. A. Antar, 2010, The potential of solar-driven humidification–dehumidification desalination for small-scale decentralized water production: Renewable and Sustainable Energy Reviews, v. 14, p. 1187-1201.

Omara, Z. M., and M. A. Eltawil, 2013, Hybrid of solar dish concentrator, new boiler and simple solar collector for brackish water desalination: Desalination, v. 326, p. 62-68.

Rajaseenivasan, T., and K. Srithar, 2017, An investigation into a laboratory scale bubble column humidification dehumidification desalination system powered by biomass energy: Energy Conversion and Management, v. 139, p. 232-244.

Yadav, Y. P., and Yadav, S. K., 2004, Parametric studies on the transient performance of a high- temperature solar distillation system.

#193: Biomass-based cogeneration systems and applications in Turkey

Fahriye Enda TOLON[1], Zafer UTLU[2]

[1]Department of Industrial Engineering, Faculty of Engineering, Istanbul Gedik University Istanbul, Turkey
enda.tolon@gedik.edu.tr
[2] Department of Mechanical Engineering, Faculty of Engineering, Istanbul Gedik University, Istanbul, Turkey
zafer.utlu@gedik.edu.tr

Although biomass resources are still used in traditional methods for heating and cooking in many countries around the world, it is becoming increasingly common to obtain heat and power from biomass by using modern technologies, contributing to regional sustainability through environmental and rural development programs. Cogeneration, namely the combined heat and power generation systems, is the most efficient way of producing heat and power from biomass source. Based on the fact that biomass has a pioneering role in the transition to a low carbon economy with its sustainable use in the energy field, this study provides information on the possibilities of cogeneration in energy production from biomass sources. Additionally, examples of combined heat and power generation applications in Turkey are discussed and this study aims to set out the requirements for combined biopower and bioheat applications in increasingly widespread use.

Keywords: biomass; biopower; bioheat; cogeneration; Turkey

1. INTRODUCTION

Energy, which is defined as the ability to do work, is one of the main requirements that improve the quality of life today. While producing and consuming, energy sources emit solid-liquid-gas pollutants to the atmosphere and affect greenhouse gas emissions and climate change. Thus, when producing a unit of power, it is necessary to use the available energy resources most efficiently.

Combined heat and power (CHP), also known as cogeneration, is the technology that enables the generation of electricity and heat simultaneously in order to use energy more efficiently. Unlike a gas turbine or engine that generates electricity, cogeneration systems can convert most of the heat energy to be discharged from the system into usable energy, and thus the total energy input can be evaluated at a rate of 85-95% (Annon, n.d). Typically, CHP plants are fuelled by any primary energy fuel source such as natural gas, coal, fuel oil biomass (Frangopoulos, 2017).

Biomass is any organic substance present in a biologically renewable form and is divided into four sub-categories based on their origin and source: woody biomass, herbaceous biomass, fruit biomass, biodegradable wastes, as well blends and mixtures of them all (Bracmort, 2009; Alakangas, 2010; Norton, 2003). With conversion methods, biomass raw materials can be converted into heat, electricity, fuel, chemicals, and materials. The most efficient use of biomass resources for heating and power can be possible by cogeneration systems.

The paper is arranged as follows: first, a literature review about combined heat and plants and biomass-based cogeneration systems given; then, the legal situation in Turkey is presented and, finally, the current situation of biomass-based cogeneration systems in the country is detailed with statistics. In this study, the aim is to reveal Turkey's current combined bioheat and biopower situation.

2. LITERATURE ON BIOMASS-BASED COMBINED HEAT AND POWER

In this chapter, previous research on combined and heat power plants and biomass-based combined heat and power is given.

2.1. Overview of Combined Heat and Power

The use of combined heat and power (CHP) dates to the beginning of this century when power plants were integrated to a community to provide district heating and hot water, and to process heating for residential and commercial buildings. CHP, also known as cogeneration, produces electricity while meeting heat needs of the processes simultaneously or sequentially from a single fuel source (Cengel, 2002).

In cogeneration systems, a high percentage of the generated or recovered heat comes from a thermal process as steam, hot air, hot water, etc. Moreover, it is imperative that a significant portion of the recovered heat be used in the thermal process. Therefore, the main prerequisite for an effective cogeneration process is a constant thermal energy demand (Meckler, 2010; Doty, 2004). The U.S Department of Energy states that with the integration of simultaneous, on-site electricity and heat generation, CHP applications operate at 65-75% efficiency. A CHP Process Flow Chart is shown in Figure 1.

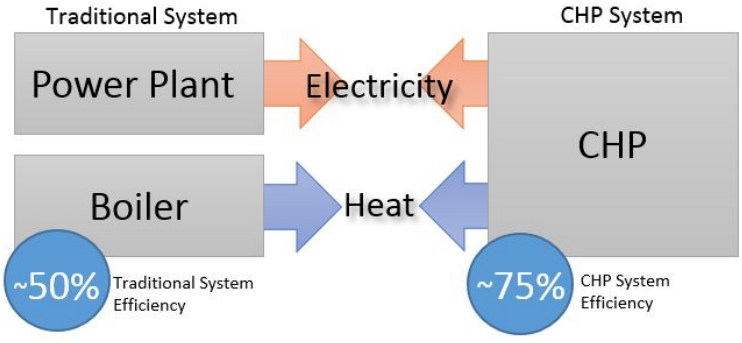

Figure 1: CHP Process Flow Chart

A cogeneration unit consists of three main components: a prime mover (turbines, engines, and fuel cells), an electrical generator, a heat recovery system, and an absorption cooling unit in the case of trigeneration. In prime movers, fuel energy is converted into mechanical and/or thermal energy; in an electrical generator the mechanical energy transformed into electricity; and a heat recovery system captures the rejected heat. For CHP production, two distinct operational modes are possible. Small CHP plants having low electrical efficiency are usually operated in a heat- controlled mode, while large CHP plants are operated in an electricity- controlled mode (Eksi, 2017).

Heat and power is produced in the CHP facilities from the combustion of fossil and/or biomass fuels, as well as from geothermal and solar thermal resources.

2.2. Biomass-Based Cogeneration Systems

Biomass resources can be used to co-generate electricity and heat via CHP systems, either on-site in buildings or distributed from larger production facilities via district energy systems, to provide heating to residential, commercial and industrial buildings.

Biomass-based CHP is realised through the biomass conversion to bioheat and biopower (thermochemical conversion, physical-chemical conversion, biochemical conversion) and the use of this fuel in a CHP system. The vast majority of the technical details of biomass-based CHP production is principally the same as ordinary fossil-based cogeneration. The utilisation of biofuel as feedstock and the appropriate utilisation of technologies differ in biomass-based CHP from ordinary CHP. However, for biomass-based cogeneration systems, there is new terminology called Combined Bioheat and Biopower (CBHBP) (Eksi, 2017) which emphasises that biofuel is used as the feedstock for the production of combined heat and power.

Because biomass resources come in different forms, its use as an energy source is divers so that many biomass resources can be transformed through various technologies for use in the energy sector. The success of any biomass-based CHP project is heavily dependent on the availability of a suitable biomass feedstock. For CBHBP, different resources like forest residues and wood wastes, energy crops and crop residues, manure biogas, wastewater treatment biogas, municipal solid waste, landfill gas, food processing residue can be used. On the other hand, various biomass resources can require different considerations regarding the conversion process and power generation technology. Because of that, other than stable thermal energy demand, the choice of biomass source, the design of a biomass supply chain network, the choice of appropriate conversion technologies are critical considerations for implementation (Eksi, 2017; Wickwire, 2007).

The major biomass conversion technologies are anaerobic digestion, direct combustion, gasification and associated prime mover technologies for CHP applications as given in Table 1 (Wickwire, 2007).

Table 1: Biomass Conversion Systems for Power and Heat Generation

Energy Conversion Technology	Integrated CHP Technology (Prime Mover)
Anaerobic Digestion	
Anaerobic digester (from animal feeding operations or wastewater treatment facilities)	Internal combustion engine Microturbine Gas turbine Fuel cell Stirling engine
Direct Combustion—Boilers	
Fixed bed boilers (stoker) Fluidized bed boilers Cofiring	Steam turbine
Modular direct combustion technology (Small, packaged, pre-engineered systems - smaller than 5 MW)	Small steam turbine Organic Rankine cycle "Entropic" cycle Hot air turbine
Gasification	
Fixed bed gasifiers Fluidized bed gasifiers	Gas turbines – simple cycle Gas turbines – combined cycle Large internal combustion (IC) engines IC engine
Modular gasification technology (Small, packaged, pre-engineered systems - smaller than 5 MW)	Microturbine Fuel cell Stirling engine
Modular hybrid gasification/combustion (Small, packaged, pre-engineered systems - smaller than 5 MW)	Small steam turbine

Investment in biomass-based cogeneration plants are increasing worldwide. According to the World Bioenergy Association statistics while 1.05 Exajoule (EJ) of biomass (Municipal Waste, Industrial Waste, Solid Biomass, Biogas, Liquid Biofuels) was used for heat and power generation in CHP plants in 2000, it was 1.56 EJ in 2005, 2.45 EJ in 2010, and 3.01 EJ in 2015 and finally 3.04 EJ of biomass used in CHP plants in 2016.

In the European Union (EU), bioelectricity is mostly produced in efficient CHP plants, but biopower-only installations are used in locations where the heat requirement is less, or not needed at all. 22 of the 28 EU Member States generate bioelectricity in CHP plants and the average of all members is 60% in 2017. Countries with less than 50% of their bioelectricity produced in CHP plants include Belgium, Spain, Hungary, Ireland and the United Kingdom. On the other hand, bioelectricity production in Czechia, France, Denmark, Cyprus, Finland, Lithuania, Latvia, Malta, Slovenia, Sweden, Slovakia is over than 90%. Additionally, six countries produce bioelectricity only in CHP plants (Calderón, 2019).

According to the U.S Department of Energy, in June 2019 in the USA there were 803 biomass-based CHP plant operating with the capacity range from 4 kilowatt (kW) to 136,000 kW in 38 different sector applications like agriculture (207 plant), wastewater treatment (184 plant), wood products (73 plant), solid waste facilities (54 plant), food processing (40 plant). For these plants, their prime movers were mostly reciprocating engines in 491 plants, with boiler/steam turbines in the 180 plants, micro turbines in the 69 plants, and combustion turbines in the 23 plants.

3. APPLICATIONS OF BIOMASS-BASED COGENERATION SYSTEMS IN TURKEY

Referring to the legislation in Turkey, cogeneration is defined in the Electricity Market Act (Law no: 6446) and, according to this law, micro-cogeneration plants whose facilities based on electrical energy have an installed capacity of 100 kilowatts or less, are provided with an efficiency value determined by the ministry of energy, and are exempt from the obligation of obtaining licenses and establishing a company.

In order to increase energy efficiency, the Energy Efficiency Act (Law no: 5627) provides investments as incentives. The annual average yield values depending on fuel types and technologies in cogeneration applications of industrial enterprises may benefit from investment incentives by the Under-secretariat of Treasury.

In the Utilization of Renewable Energy Resources for the Purpose of Generating Electrical Energy law (Law no. 5346), a purchase-guarantee with a feed-in tariff has been given to electricity generated from renewable resources for investments on electricity generation by the private sector. Within the scope of this Law, the feed-in tariff for biomass resource is 13.3 US$cent/ kWh. Also, depending on the local equipment technology additional prices added bioelectricity plant has local manufacturing cogeneration technology, feed-in tariff will be 13.7 US$cent/ kWh instead of 13.3 US$cent/ kWh (0.4 US$cent/ kWh comes from CHP technology).

The Turkish Cogeneration Association is the leading organisation actively working for the promotion of the wider use of cogeneration in Turkey for a sustainable energy future. The association is working to promote and encourage the use of “Combined Heat and Power” and also is contributing and facilitating suggestions to the legal infrastructure in order to support the implementation of the technology (Annon. n.d).

As of May 2019, according to the Electricity Market License Statistics, 131 licensed biomass facilities were operating with an installed power capacity of 770.06 Megawatt Electric (MWe). Moreover, according to Turkey’s Biomass Energy Potential Atlas, 43 different facilities were producing electricity from biomass resources such as animal waste, municipal waste, and agricultural waste without a license with the power of 42.54 MWe. However, only 11 of these biomass plants have combined heat and power plants with the total installed power capacity of 49.41 MWe. Biomass-based CHP plants operating in Turkey as of May 2019 are shown in Table 2 (Bozkurt, 2019).

Table 2: Biomass-based CHP plants operated in Turkey, as of May 2019

Facility Name (herein)	Province	Installed Capacity (MW_e)	License Status	Sector
Mavibayrak	Aydın	24	With License	Power Generation
Oltan & Köleoğlu	Çorum	5.00	With License	Power Generation
Tire	İzmir	4.80	With License	Power Generation
Seleda	Kırklareli	4.38	With License	Power Generation
Arel Çevre	Afyonkarahisar	3.81	With License	Power Generation
Bel-Ka	Ankara	3.20	With License	Power Generation
Biosun	Bilecik	1.60	With License	Power Generation
Kipaş	Kahramanmaraş	1.20	With License	Power Generation
Yapilcanlar	Aksaray	1.07	With License	Food
Cargill	Bursa	0.12	With License	Factory / Power Generation
Tigem	Bursa	0.23	Without License	Agricultural

4. CONCLUSION

For sustainable regional development and environmental protection, domestic energy resources should be used most efficiently in Turkey. Biomass is a strategic national renewable resource to meet the country's energy demand. As stated in the Turkey Biomass Energy Potential Atlas, the total energy equivalent of waste biomass (animal waste, agricultural waste, municipal solid waste) is 44.228.795 TOE/year. In the use of biomass as power, heat to ensure the high fuel utilisation efficiency CHP is the precondition. Suggestions for improvement in the wider biomass-based combined heat and power in Turkey include:

- Increasing energy efficiency by capturing waste heat in the traditional system,
- Meeting national energy requirements with domestic resources and increasing energy security,
- Reducing greenhouse gas emissions that cause climate change impact and the development of national environmental targets by utilising more energy per unit energy source,
- Reducing transmission losses through on-site production and distributed generation,
- Diversify the energy supply by further integration of locally produced and renewable fuels will be possible.

Consequently, it is necessary to increase the number of biomass-based combined power plants which currently contribute only 5.5% of the existing biomass power plants in Turkey.

5. REFERENCES

Alakangas, E. I. J. A., & Iii, E. (2010). New European Pellets Standard–EN 14961-1. vol, 5, 1-9.

Annon. (n.d) What is cogeneration *in Turkish* [online]. Available at: http://kojenturk.org/tr/kojenerasyon-nedir-15 [Accessed 8 July 2019].

Annon. (n.d) What we do? [online]. Available at: http://kojenturk.org/en/what-we-do-19

Bozkurt, Y. (2019) Private Communication

Bracmort, K., & Gorte, R. W. (2009). Biomass: Comparison of definitions in Legislation. Congressional Research Service, Library of Congress.

Calderón C., Colla M. (2019). Bioenergy Europe Statistical Report. Brussels, Belgium: Bioenergy Europe

Cengel, Y. A., & Boles, M. A. (2002). Thermodynamics: an engineering approach. Sea, 1000, 8862.

Doty, S., & Turner, W. C. (2004). Energy management handbook. Crc Press.

Eksi, G. (2017). Life cycle assessment of combined bioheat and biopower production and cost: simulated case studies based on combustion utilizing Turkish oak (Quercus cerris L.) coppices, Ph.D. Thesis. Istanbul Technical University.

Energy Market Regulatory Authority (n.d) Electricity Market License Statistics [online]. Available at: http://lisans.epdk.org.tr/epvys-web/faces/pages/lisans/elektrikUretim/elektrikUretimOzetSorgula.xhtml [Accessed 23 June 2019].

Frangopoulos, C. A. (Ed.). (2017). Cogeneration: Technologies, Optimization and Implementation IET (Vol. 87).

Meckler, M., & Hyman, L. B. (2010). Sustainable on-site CHP systems. McGraw-Hill.

Norton, G., Abraham, S., & Veneman, A. (2003). Memorandum of understanding on policy principles for woody biomass utilization for restoration and fuel treatments on forests, woodlands, and rangelands. US Forest Service and Bureau of Land Management, Washington, DC.

Republic of Turkey Ministry of Energy and Natural Resources (n.d) Turkey's Biomass Energy Potential Atlas, [online]. Available at: http://bepa.yegm.gov.tr/ [Accessed 23 June 2019].

U.S Department of Energy (n.d), Combined Heat and Power Installation Database [online]. Available at: Available at: https://doe.icfwebservices.com/chpdb/ [Accessed 23 July 2019].

U.S Department of Energy (n.d) Combined Heat and Power Basics [online]. Available at: https://www.energy.gov/eere/amo/combined-heat-and-power-basics [Accessed 4 July 2019].

World Bioenergy Association (2019). Global Bioenergy Statistics [online] Available at: https://worldbioenergy.org/uploads/181017%20WBA%20GBS%202018_Summary_hq.pdf [Accessed 20 July 2019].

Wickwire, S. (2007). Biomass Combined Heat and Power Catalog of Technologies. Washington DC.

#194: Multi-stage heat-pipe heat exchanger for improving energy efficiency of HVAC system in hospital operating room

Nandy PUTRA*, Imansyah Ibnu HAKIM, Ragil SUKARNO, Fadhil Fuad RACHMAN

Applied Heat Transfer Research Group, Department of Mechanical Engineering, Universitas Indonesia, Kampus UI, Depok, 16424, Indonesia

**Corresponding author: nandyputra@eng.ui.ac.id*

The demands of a room with specific requirements related to thermal comfort, such as the temperature, relative humidity, inside air exchange, and other factors required in a hospital operating room, have necessitated the development of energy-efficient heating, ventilation, and air conditioning (HVAC) systems. Energy recovery with a heat pipe that utilises cold air exhaust from a room in an HVAC system can enhance the efficiency and reduce emissions. In this study, experimental and theoretical analyses were performed to develop a more effective and efficient heat-recovery system using a heat-pipe heat exchanger (HPHE) for HVAC systems in hospital operating rooms. The experiment was conducted by using HPHEs having 3, 6, and 9 rows, with 4 heat pipes in each row arranged in a staggered configuration. The fresh-air inlet temperature in the evaporator section was varied between 30, 35, 40, and 45°C, and the air inlet velocity was varied between 1.5, 2.0, and 2.5 m/s. The theoretical analysis was conducted using the ε-NTU method for predicting the effectiveness, outlet temperature of the evaporator side, and energy recovery of the HPHE. The experimental results indicated that increasing the air inlet temperature in the evaporator section and the number of rows increased the HPHE effectiveness but increasing the air inlet velocity reduced the effectiveness. The highest effectiveness of 62.6% was obtained at an air inlet temperature of 45°C with an air inlet velocity of 2 m/s and a 9-row HPHE. The energy recovery of the HPHE increased with the number of rows, air inlet temperature, and air velocity in the evaporator section. The theoretical analysis results obtained using the ε-NTU method were similar to the experimental results. Thus, this technique can be used as a comparison method in the analysis of heat-recovery systems that apply HPHEs.

Keywords: heat-pipe heat exchanger; effectiveness; ε-NTU; energy recovery

1. INTRODUCTION

With the increasing price of fossil fuels and their environmental problems, renewable energy and energy efficiency have become major aspects of the energy strategies of several countries. Many countries are attempting to increase the percentage share use of renewable energy, e.g., in the transportation sector (Silitonga et al., 2018), in the residential sector (Aditya et al., 2017), and for electricity generation (Ismail et al., 2014). The main problem with renewable energy is its unstable supply; thus, renewable energy systems are always coupled with energy-storage equipment (usually batteries). Owing to the limitations of batteries, scientists are investigating alternative materials for energy storage (Amin et al., 2017, Putra et al., 2019, Mehrali et al., 2013). Energy-efficiency programs in all sectors are important strategies for many countries (Fournier et al., 2019, Han et al., 2018). Intensive efforts to reduce the energy growth on a global scale continues; however, dependency on fossil fuels as the main energy resource remains dominant. The increasing demand for facilities or new buildings that require maintenance of comfort levels will increase. Moreover, to provide comfortable rooms for occupants, buildings are usually equipped with heating, ventilation, and air conditioning (HVAC) systems (Ahmadzadehtalatapeh, 2013). In commercial buildings, HVAC systems account for a significant share of the total energy consumption (Papadopoulos et al., 2019), and has been determined at 40%–60% (Pérez-Lombard et al., 2008, Putra et al., 2017). The demand for rooms with special specifications related to the temperature, relative humidity, exchange of inside air, and other factors that are required in a hospital operating room under continuous use necessitates a more efficient HVAC system with low energy consumption.

According to ASHRAE, an operating room requires an inside air temperature that ranges from 20 to 24°C, a relative humidity that ranges from 30% to 60%, and 15 to 20 air changes per hour (ASHRAE, 2013, Hakim et al., 2018, Balaras et al., 2007, Teke and Timur, 2014). Further, the HVAC is often operated continuously for 24 h. Therefore, heat recovery from the waste heat of HVAC systems represents an effort to use energy efficiently (Cuce and Riffat, 2015). The use of a waste heat-recovery system with a heat pipe represents an excellent method for saving energy and reducing global-warming effects (Vakiloroaya et al., 2014, Srimuang and Amatachaya, 2012, Reay et al., 2013). In recent years, heat-pipe technology has been increasingly used in the building service industry to enhance energy savings and the thermal performance of heat exchangers in commercial HVAC systems (Jouhara and Merchant, 2012).

In HVAC systems, heat recovery can be applied by installing a heat-pipe heat exchanger (HPHE) on the air inlet and outlet of the ducting system through which air passes before reaching the cooling-coil device as a precooling device. Before air enters the cooling-coil device, the fresh-air temperature is reduced by recycling the cooled air from a room by using HPHEs. Thus, the energy consumption for cooling can be reduced, as well as the time needed to reach the dew-point temperature (Putra et al., 2017, Muhammaddiyah et al., 2018, Jadhav and Lele, 2015, Vakiloroaya et al., 2014, Abd El-Baky and Mohamed, 2007). Studies on the effects of different operating conditions and design parameters on thermal performance and energy saving, including both experimental and numerical analyses related to the development of the HPHE, have been performed by various researchers.

For example, Putra et al. (2017) investigated the use of an HPHE as a precooling device in an HVAC system. The HPHE consisted of several pipes arranged in staggered configurations with various numbers of rows, including 2, 4, and 6, with a total of 39 pipes in 6 rows, and with water serving as the working fluid. The incoming fresh-air temperature was varied from 30 to 45°C under 1, 1.5, and 2 m/s flows of fresh air. The largest heat recovery achieved was 1404.29 kJ/h, with an effectiveness of 0.15. The results indicated that increasing the number or rows of tubes increased the effectiveness of the HPHE, and energy savings could be achieved (Putra et al., 2017). Muhammaddiyah et al. (2018) added multi-wavy fins to the evaporator and condenser sections of the HPHE that were applied in the HVAC system. An HPHE consisting of 42 pipes was arranged in a staggered fashion with three rows. The results indicated that the highest effectiveness of 54.4% was obtained at an air inlet velocity and temperature of 1 m/s and 45°C, respectively (Muhammaddiyah et al., 2018). The use of theoretical analysis based on the NTU-effectiveness (ε-NTU) method for predicting the effectiveness of a thermosyphon HPHE has been reported (Noie, 2006, Yau and Ahmadzadehtalatapeh, 2015), and the effectiveness of the thermosyphon HPHE was compared between experimental and theoretical results.

The literature review indicates that the use of an HPHE reduces the energy consumption in HVAC systems, but new developments are needed to enhance the HPHE performance. Moreover, with the rapid growth of new hospitals, the number of operating rooms will increase. Hence, intensive efforts to save energy by recovering the waste heat from HVAC systems are important. The main objective of this study was to investigate the possible energy savings and effectiveness of an HPHE for heat recovery in the HVAC system used in hospital operating rooms. A performance analysis employing the ε-NTU method was conducted to predict the theoretical effectiveness of the HPHE. The results can be used provide guidance for continuing to the next steps of fabrication and experimental testing.

2. METHODOLOGY

2.1. Test facility design

This study was performed using an experimental test model comprising a simulation room with mini-chiller and ducting systems. The ducting system consisted of one inlet and two outlet channels on the two sides of the simulator room. The HPHE consisted of several heat-pipe rows that were arranged in a staggered configuration. The number of rows was varied between 3, 6, and 9, with 4 heat pipes in each row. The heat-pipe tubes were made of copper, and the inner surface of the tubes contained a wick structure of sintered copper. The tubes were filled with water as the working fluid at a filling ratio of

50% compared with the evaporator section. The outer diameter of the heat pipe was 10 mm, and the evaporator was 160 mm long. The length of the adiabatic section was 360 mm, and the length of the condenser section was 190 mm. To enhance the heat-transfer area, the HPHE was equipped with a continuous wavy fin made of aluminum with a thickness of 0.105 mm and a fin spacing of 2 mm, as shown in Figure 1.

The experimental test model was equipped with system control and a measurement device, as shown in Figure 2. The heat input involved a 4000-W heater equipped with a proportional–integral–derivative temperature controller that was placed before the axial fan inlet to customise the fresh-air inlet temperature in the evaporator section. The mini-chiller device consisted of a circulating thermostatic bath, a cooling coil, and a pump with a flow meter, which was used to deliver chilled water through the cooling coil that was mounted in the ducts of the air-handling unit.

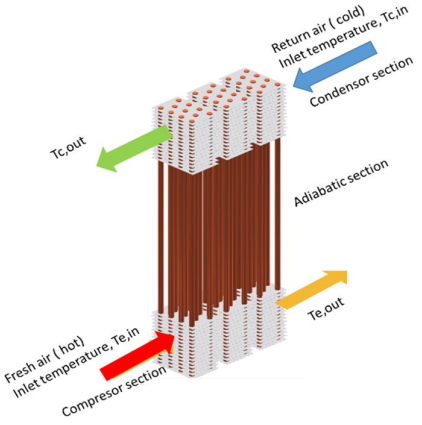

Figure 1: HPHE design

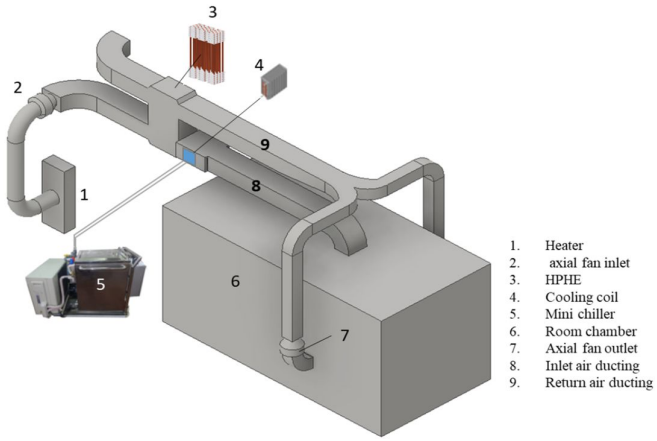

Figure 2: Experimental test model

2.2. Experimental setup

The performance of the HPHE is influenced by several parameters, including design and operation parameters.

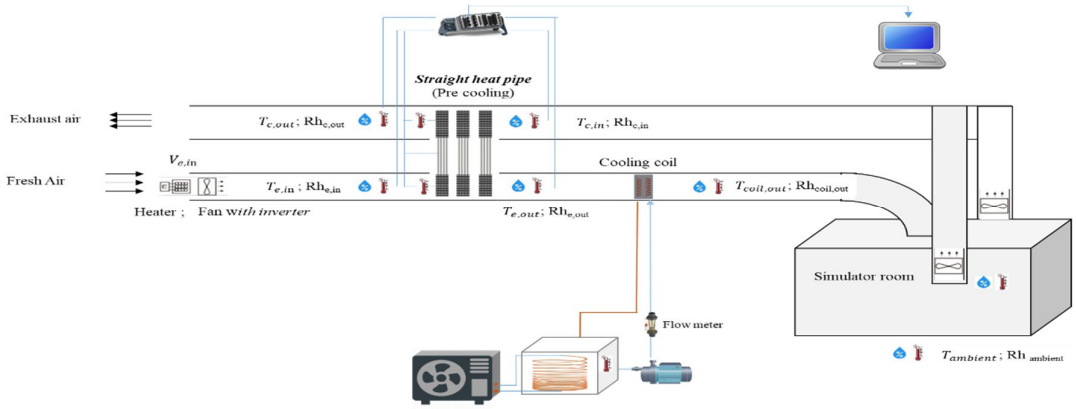

Figure 3: Experimental setup

The air temperatures at the inlet and outlet of the evaporator and condenser section were measured with type-K thermocouples which was connected to module NI 9214 with accuracy ±0,01°C, and the relative humidity at the same locations was measured using a humidity sensor (Autonic THD), which was connected in series to a data-acquisition device (NI cDAQ-9174). The measurement points on the HPHE shown in the experimental schematic are presented in Figure 3. The mass flow rate of the chilled water in the cooling coil in a constant guard was 4 L/min. The air inlet velocities of the evaporator and condenser sections were measured using hotwire anemometer Lutron AM-4204 sensor with accuracy ± (5 % + 0.1 m/s) at the centre of the duct.

2.3. Effectiveness

For describing the thermal performance of the HPHE, sensible effectiveness is a highly relevant parameter. Effectiveness is defined as the ratio of the actual heat transfer to the maximum heat transfer in a heat exchanger (Putra et al., 2017), which can be determined using Equation 1 for the test results obtained.

Equation 1: Temperature effectiveness

$$\varepsilon = \frac{Q_{act}}{Q_{\max}} \quad \text{(a)} \qquad \text{or} \qquad \varepsilon = \frac{T_{e,in} - T_{e,out}}{T_{e,in} - T_{c,in}} \quad \text{(b)}$$

2.4. Energy recovery

In HVAC systems, the evaporator side of the HPHE is installed on the inlet side of the ducting as a precooling device, while the condenser section is installed on the return side of the air ducting system.

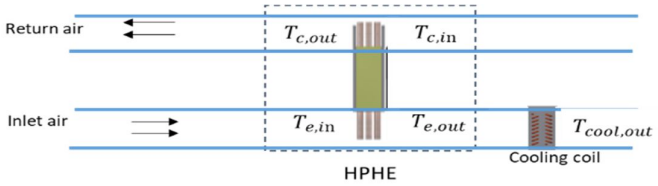

Figure 4: Installation of the HPHE in the ducting

In HVAC systems without heat pipes, the fresh air is typically overcooled from T_e to $T_{cool,\,out}$ until it reaches the dew-point temperature, and is subsequently reheated for the dehumidification process (Yau and Ahmadzadehtalatapeh, 2015). The cooling load is determined using Equation 2. By adding the HPHE as a precooling device, the cooling load of the cooling coil of the mini-chiller can be distributed, as indicated by Equation 3 (Yau and Ahmadzadehtalatapeh, 2015)

Equation 2: Cooling load

$$q_{load} = \dot{m} c_p (T_{e,in} - T_{coil,out})$$

Equation 3: Cooling load after added HPHE

$$q_{load} = q_{recovery} + q_{cooling\ coil}$$

Thus, the cooling load of the cooling coil ($q_{cooling\ coil}$) can be expressed as follows:

Equation 4: Cooling-coil load

$$q_{cooling\ coil} = \dot{m}\, c_p (T_{e,out} - T_{coil,out})$$

The energy recovery that can be achieved by applying the HPHE as a precooling device is given by Equation 5.

Equation 5: Energy recovery

$$q_{recovery} = \dot{m}\, c_p (T_{e,in} - T_{e,out})$$

2.5. ε-NTU effectiveness

The ε-NTU effectiveness approach has been used to investigate the performance of a thermosyphon HPHE (Jouhara and Merchant, 2012, Noie, 2006, Yau and Ahmadzadehtalatapeh, 2015). In an analysis using the ε-NTU approach, a thermosyphon HPHE is considered as two separate heat exchangers; i.e., the evaporator and condenser sections are associated with the working fluid in the heat pipe (Noie, 2006, Yau and Ahmadzadehtalatapeh, 2015). By determining the fresh-air inlet temperature in the evaporator, air inlet in the condenser, surface temperature of the heat pipes, and HPHE geometry, ε-NTU analysis can be used to predict the performance of the HPHE and can be very helpful in the design stage of the HPHE. The vapor inside the heat pipe is almost at a constant temperature; thus, the vapor capacity rate C_v is equal to infinity, corresponding to a heat-

capacity ratio, $C_e/C_v = C_c/C_v$, which is equal to zero. Assuming that $C_e/C_v = C_c/C_v = 0$, the ε-NTU of the HPHE at a single row of the evaporator and condenser can be expressed by Equation 6 (Jouhara and Merchant, 2012, Noie, 2006, Yau and Ahmadzadehtalatapeh, 2015).

Equation 6: ε-NTU *at single row* $\varepsilon_{e,1} = 1 - e^{(-NTU_e)}$ *(a)* and $\varepsilon_{c,1} = 1 - e^{(-NTU_c)}$ *(b)*

The number of transfer units (NTU) in the evaporator and condenser sections is determined using Equation 7.

Equation 7: NTU $NTU_e = \frac{U_e A_e}{C_e}$ *(a)* and $NTU_c = \frac{U_c A_c}{C_c}$ *(b)*

For the NTU calculation, the areas of an HPHE with a number of rows of heat pipes (denoted as A_e and A_c) are based on the total heat-transfer area in a row (Jouhara and Merchant, 2012). The HPHE developed in this study is equipped with a continuous wavy fin; thus, fins are considered in determining the heat-transfer area. For the evaporator and condenser sections, the heat capacity *C* is calculated using Equation 8.

Equation 8: Heat capacity $C_e = \dot{m}_e c_{p,e}$ *(a)* and $C_c = \dot{m}_c c_{p,c}$ *(b)*

The overall heat-transfer coefficient for the evaporator and condenser sections is calculated using the following equation (Jouhara and Merchant, 2012).

Equation 9 $\frac{1}{U_e A_e} = \frac{1}{\eta_{o,e} h_e A_{hp}} + R_{hp,e}$ *(a)* and $\frac{1}{U_c A_c} = \frac{1}{\eta_{o,c} h_c A_{hp}} + R_{hp,c}$ *(b)*

The overall fin surface efficiency η_{so} can be calculated using the following equation (Incropera et al., 2007, Wang et al., 1997).

Equation 10: Overall fin surface efficiency $\eta_{so} = 1 - \frac{A_f}{A_o}(1 - \eta_f)$

Equation 11: Single-fin efficiency (Wang et al., 1997) $\eta_f = \frac{\tanh(mr\phi)}{mr\phi}$, where: $m = \sqrt{\frac{2h}{kt}}$

For an HPHE with *n* rows, the ε-NTU effectiveness is given by Equation 12 (Noie, 2006, Yau and Ahmadzadehtalatapeh, 2015).

Equation 12: ε-NTU *for n rows*

In evaporator:

$$\varepsilon_{en} = \frac{\left[\frac{1 - \frac{C_e}{C_v}\varepsilon_{e,1}}{1 - \varepsilon_{e,1}}\right]^n - 1}{\left[\frac{1 - \frac{C_e}{C_v}\varepsilon_{e,1}}{1 - \varepsilon_{e,1}}\right]^n - \frac{C_e}{C_v}} \quad (a)$$

In condenser section:

$$\varepsilon_{en} = \frac{\left[\frac{1 - \frac{C_c}{C_v}\varepsilon_{c,1}}{1 - \varepsilon_{c,1}}\right]^n - 1}{\left[\frac{1 - \frac{C_c}{C_v}\varepsilon_{c,1}}{1 - \varepsilon_{c,1}}\right]^n - \frac{C_c}{C_v}} \quad (b)$$

Because $C_e/C_v = C_c/C_v = 0$, Equation 12 can be simplified as follows (Noie, 2006, Yau and Ahmadzadehtalatapeh, 2015):

Equation 13: ε-NTU *for n rows*

In evaporator section : $\varepsilon_{en} = 1 - (1 - \varepsilon_{e,1})$ *(a)*

In condenser section : $\varepsilon_{cn} = 1 - (1 - \varepsilon_{c,1})$ *(b)*

The overall effectiveness of the HPHE based on the ε-NTU can be defined as follows (Noie, 2006, Yau and Ahmadzadehtalatapeh, 2015):

Equation 14: Overall ε-NTU *If* $C_e > C_c$: $\varepsilon_o = \left[\frac{1}{\varepsilon_{c,n}} + \frac{\frac{C_c}{C_e}}{\varepsilon_{c,n}}\right]^{-1}$ (a) and *If* $C_c > C_e$: $\varepsilon_o = \left[\frac{1}{\varepsilon_{e,n}} + \frac{\frac{C_e}{C_c}}{\varepsilon_{c,n}}\right]^{-1}$ (b)

In this study, the mass flow rate of air at the inlet of the evaporator section is 0.056, 0.075, or 0.094 kg/s lower than that in the condenser section. Thus, the heat capacity is $C_c > C_e$. Accordingly, the HPHE effectiveness with 3, 6,

and 9 rows can be determined. After the effectiveness is obtained, the outlet air temperature in the evaporator section $T_{e,\,out}$ can be predicted, as follows:

Equation 15: Outlet air temperature in the evaporator section

$$T_{e,out} = T_{e,in} - \varepsilon_o \,(T_{e,in} - T_{c,in})$$

Determining the overall heat-transfer coefficient U requires the convection coefficients for the evaporator and condenser sections, i.e., h_e and h_c, respectively. The convection coefficients for the evaporator and condenser sections are obtained by considering the external cross flow in a bank of tubes. The thermal resistance of the heat pipe *R* is obtained from the measurements of 0.0041–0.0007 °C/W.

The bank of tubes of the HPHE applied in the HVAC system is shown in Figure 5.

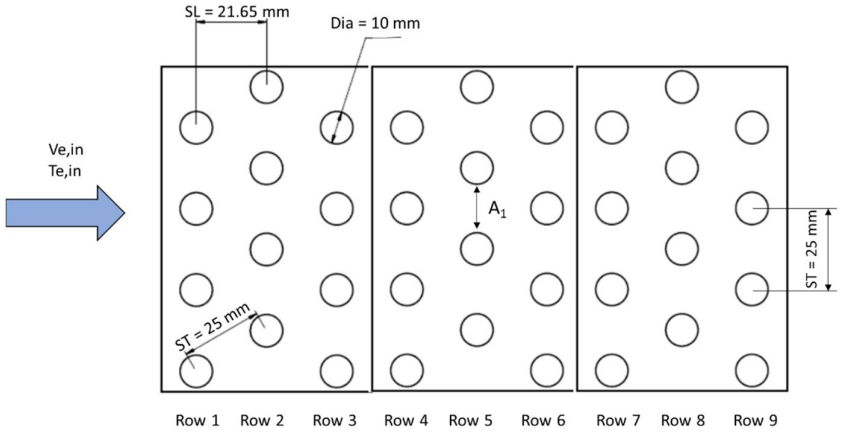

Figure 5: Schematic of tube arrangements in a bank with 9 rows in a staggered configuration

To determine the convection coefficients of the HPHE in the bank of tubes, the Zukauskas correlation can be used, as follows (Incropera et al., 2007):

Equation 16: Nusselt number

$$NU_D = C_1\, C_2\, \mathrm{Re}_{D,\max}^{m}\ \mathrm{Pr}^{0.36}\left(\frac{\mathrm{Pr}}{\mathrm{Pr}_s}\right)^{1/4}$$

The constant C_1 is the dimension that is associated with the configuration and the Reynolds number in the bank of tubes of the HPHE. C_2 is the correction constant for the heat exchanger with ≤20 rows of tubes. In this HPHE, the tube diameter *D* is 10 mm and is measured as the transverse pitch between tube centers. S_T is 25 mm, and the longitudinal pitch S_L is 21.65 mm. Thus, S_T/S_L < 2, and the constants C_1 = 0.36 and *m* = 0.6 are obtained. In contrast, the constant C_2 varies according to the number of rows of the HPHE (C_2 = 0.84 for 3 rows, C_2 = 0.94 for 6 rows, and C_2 = 0.96 for 9 rows).

The Reynolds number $\mathrm{R_{e,D}}$ used in Equation 16 is based on the maximum velocity that occurs in the evaporator and condenser sections. A staggered configuration on an external cross flow is shown in Figure 4, with $S_D = (S_T + d)/2$. The maximum velocity is determined using the following equation.

Equation 17: Maximum velocity

$$V_{\max} = \frac{S_T}{S_T - d} V_{e,in}$$

The convection coefficient is obtained from the Nusselt number through the following expression (Ramos et al., 2016, Incropera et al., 2007).

Equation 18: Heat-transfer coefficient

$$h = \frac{Nu.k}{d}$$

According to the temperature difference obtained from the experiment, the thermal resistance of the heat pipe can be obtained by dividing the temperature difference by the heat-transfer rate, as indicated by Equation 19 (Shabgard et al., 2015, Ramos et al., 2016).

Equation 19: Thermal resistance

$$R = \frac{T_{hp,e} - T_{hp,c}}{\dot{Q}}$$

3. RESULTS AND DISCUSSIONS

3.1. HPHE performance

A series of tests were conducted to investigate the performance of the HPHE arranged in a staggered fashion with 3, 6, and 9 rows. The fresh-air inlet temperature in the evaporator section was varied between 30, 35, 40, and 45°C, and the velocity of the inlet air in the evaporator section was varied between 1.5, 2.0, and 2.5 m/s. The reading for each variation was obtained at intervals of 30 min after steady-state conditions were achieved, and the steady-state conditions were achieved after the prototype was run for 10 min. Figure 6 displays the air-temperature profile on the inlet and outlet for the evaporator and condenser sections separately with an incoming air velocity of 1.5 m/s in the 9-row HPHE.

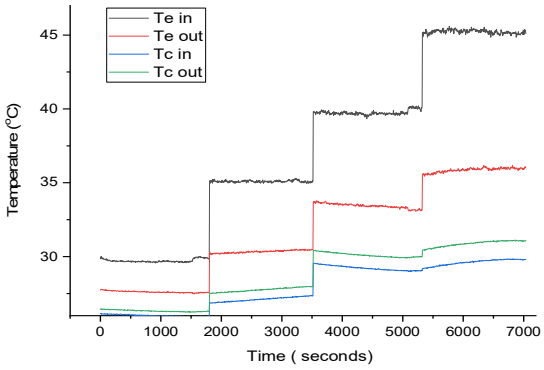

Figure 6: Temperature profile for an inlet air velocity of 1.5 m/s and 9 rows

Figure 6 shows that the application of the HPHE to the HVAC system was successful. The precooling media of the HPHE significantly absorbed the heat of the inlet air in the evaporator section, reducing the temperature before the air entered the cooling-coil devices. Heat release occurred through the cold air that passed through the condenser section of the HPHE. The air outlet temperature on the side of the condenser section was higher than with that in the inlet section. Figure 5 shows that with an increase in the fresh-air temperature in the evaporator section, the amount of heat absorbed by the heat pipe increased. This finding is indicated by the increased temperature difference between the inlet and outlet of the evaporator section.

The test results for investigating the effects of the fresh-air inlet temperature, air velocity, and number of rows on the effectiveness are shown in Figure 7. The results indicate that at the same velocity, increasing the fresh-air inlet temperature and number of rows increased the effectiveness. With the same number of rows, the effectiveness decreased with an increase in the air velocity. The highest effectiveness (62.6%) was obtained with an air inlet temperature of 45 °C, an air inlet velocity of 2 m/s, and 9 rows of the HPHE. The lowest effectiveness (43.1%) was obtained with an air inlet temperature of 30°C, an air inlet velocity of 2 m/s, and 3 rows of the HPHE.

Energy recovery indicates that heat is absorbed by the HPHE before it is cooled by the cooling-coil device. The largest temperature difference was 9.8°C, which was obtained with an air inlet temperature of 45°C, an air velocity of 2.5 m/s, and 9 rows of the HPHE. Under these conditions, the maximum energy recovery was 931.6 W. The smallest temperature difference in the evaporator section was 1.4°C, which was obtained with an air inlet temperature of 30°C, an air velocity of 1.5 m/s, and 3 rows of the HPHE. Under these conditions, 82.1 W of energy was recovered. The effects of the fresh-air inlet temperature, air velocity, and number of rows on the energy recovery are shown in Figure 8.

Figures 6 to 8 show that increasing the fresh-air inlet temperature increased the effectiveness and energy recovery. The ability of the heat pipe to absorb heat was affected by the boiling point of the working fluid in the heat pipe. As the temperature of the inlet fresh air entering the evaporator section increased, the rate of evaporation of the working fluid in the heat pipe increased, and the heat absorption increased.

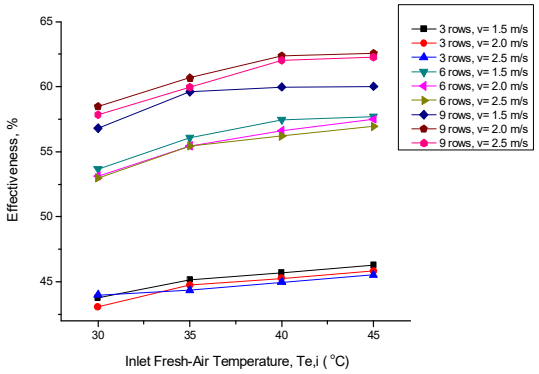

Figure 7: HPHE effectiveness profile with respect to the number of rows, air inlet temperature, and velocity

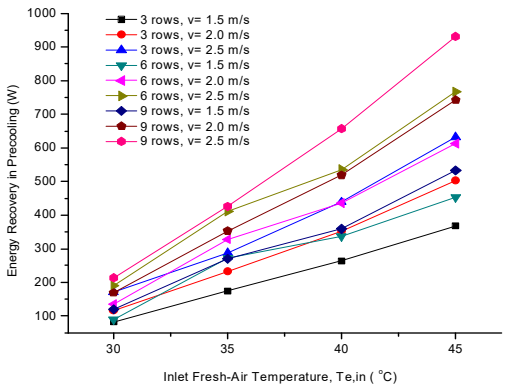

Figure 8: Energy-recovery profile with respect to the number of rows, air inlet temperature, and velocity

The effectiveness and energy recovery decreased with the increasing air velocity. This indicates that reducing the air velocity improved the heat absorption of the HPHE. Additionally, these results indicate that the precooling process of the fresh-air temperature in the evaporator occurred, and the temperature was significantly reduced before entering the cooling-coil device. Thus, the amount of energy needed to cool the air was reduced, and the dew point could be achieved more rapidly. The air returned from the room that was still cold was recycled and entered the condenser section to absorb heat, causing the working fluid to condense back into a liquid phase.

3.2. Performance comparison of experimental and ε-NTU effectiveness

Figure 9 shows a comparison between the experimental effectiveness and the predicted overall effectiveness obtained from the ε- NTU analysis for different fresh-air inlet temperatures, velocities, and row numbers.

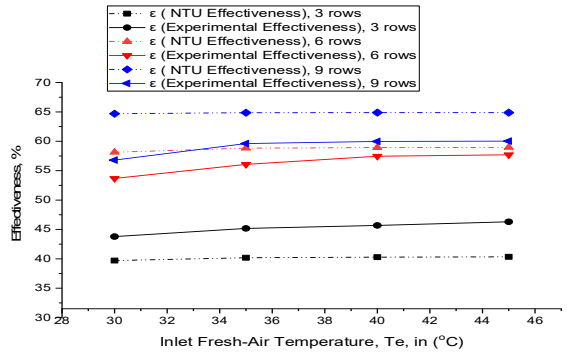

Figure 9: Comparison of the experimental effectiveness and ε-NTU analysis results for different fresh-air inlet temperatures and row numbers at a velocity of 1.5 m/s

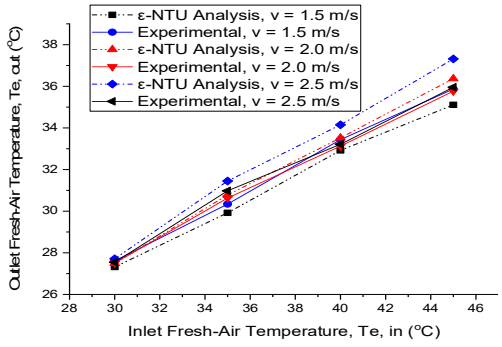

Figure 10: Comparison of the temperature profile in the evaporator section for 9 rows with different fresh-air inlet temperatures and velocities

After the effectiveness was obtained (and when the fresh-air inlet temperatures in the evaporator and condenser were known), the inlet air temperature in the evaporator section could be specified, as shown in Figure 10. For both of these methods, the theoretical predictions were similar to the experimental results. The effect of the heat load of the evaporator section on the thermal resistance of heat pipes is shown in Figure 11. The heat load and repeated energy recovery of the precooling process obtained by applying the HPHE were determined using Equation 5. With a heat load of 82.1 – 931.6 W, the thermal resistance decreased to 0.0041 – 0.0007°C/W. Increasing the heat load in the evaporator section reduced the thermal resistance of the heat pipe. Greater heat absorption was obtained when the air inlet temperature increased. Thus, increasing the air inlet temperature on the evaporator side reduced the thermal resistance, increasing the effectiveness of the HPHE.

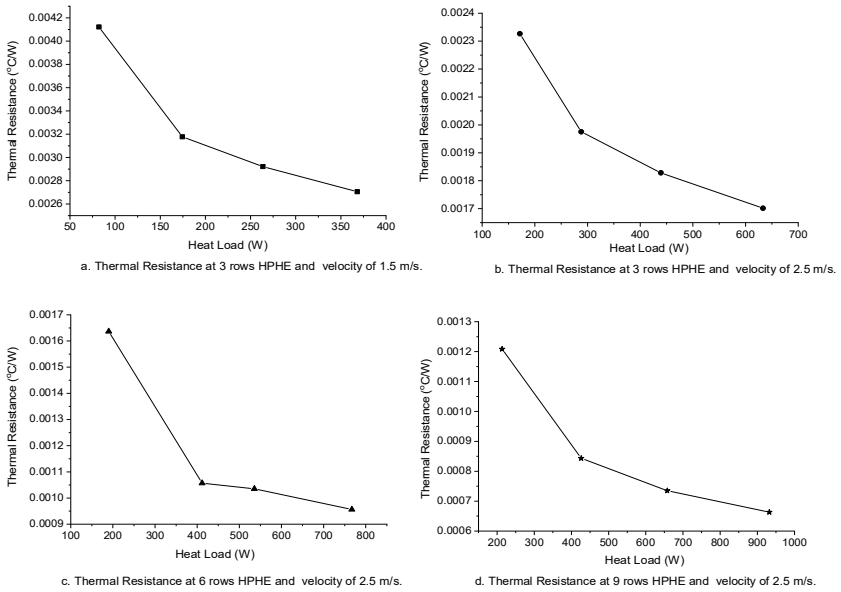

Figure 11: Effect of the heat load to thermal resistance of the HPHE

4. CONCLUSIONS

According to the results, the following conclusions are drawn.

- An increase in the air inlet temperature on the evaporator side and an increase in the number of rows increased the HPHE effectiveness, but an increase in the inlet air velocity reduced the effectiveness.
- The highest effectiveness of 62.6% was obtained with an air inlet temperature of 45°C, an air inlet velocity of 2 m/s, and 9 rows of the HPHE. The lowest effectiveness of 43.1% was obtained with an air inlet temperature of 30°C, an air inlet velocity of 2 m/s, and 3 rows of the HPHE.
- The energy recovery indicated that heat was absorbed by the HPHE before the air was cooled by the cooling-coil device. The largest temperature difference was 9.8 °C, which was obtained at an air inlet temperature of 45°C, an air velocity of 2.5 m/s, and 9 rows of the HPHE. Under these conditions, the maximum energy recovery was 931.6 W. The smallest temperature difference in the evaporator section was 1.4°C, which was obtained with an air inlet temperature of 30°C, an air velocity of 1.5 m/s, and 3 rows of the HPHE. Under these conditions, 82.1 W of energy was recovered.
- The ε-NTU method can be applied to HPHE systems for predicting the effectiveness of the HPHE. Theoretical analysis using the ε-NTU method provided results similar to those obtained via the experiment, and this method can be used as a comparison method for analysis of heat-recovery systems using an HPHE. Thus, the method can be used as an initial reference to predict the performance of an HPHE design before the design and manufacturing steps.
- Increasing the heat load in the evaporator section reduced the thermal resistance of the heat pipe. Increased heat absorption was obtained when the air inlet temperature was increased. These findings indicate that increasing the air inlet temperature on the evaporator side reduced the thermal resistance, hence increasing the HPHE effectiveness.

5. ACKNOWLEDGEMENT

The authors would like to thank for the financial support from Kemenristek Dikti through PPUPT Scheme 2019 with contract number NKB-1751/UN2.R3.1/HKP.05.00/2019.

6. NOMENCLATURE

ε	: Effectiveness	h	: Heat transfer coefficient, W/m^2-K
T	: Temperature, °C	k	: Thermal conductivity, W/m-K
η	: Efficiency	q	: Heat transfer rate, W
C	: Heat capacity rates, W/K	V	: Velocity, m/s
c_p	: Specific heat, kJ/kg-K	L	: Length of fin, m

NTU : Number of transfer unit
U : Overall heat transfer coefficient, W/m^2-K
A : Surface area, m^2
$\dot{m}$: Mass flow rate, kg/s
R : Thermal resistance, ^{o}C/W
Nu : Nusselt number
Re : Reynolds number
Pr : Prandtl number
Pr_s : Prandtl number in surface
ST : Transversal space of tube, m
SL : Longitudinal space of tube, m
SD : Diagonal space of tube, m
d : Diameter of heat pipe, m

Subscripts
e : Evaporator
c : Condenser
in : Inlet
out : Outlet
n : Number of rows
hp : Heat pipe
max : Maximum
o : Overall
f : Fin
t : Fin thickness
ø : Angle

7. REFERENCES

Abd El-Baky, M. A. & Mohamed, M. M. 2007. Heat pipe heat exchanger for heat recovery in air conditioning. *Applied Thermal Engineering,* 27**,** 795-801.

Aditya, L., Mahlia, T. M. I., Rismanchi, B., Ng, H. M., Hasan, M. H., Metselaar, H. S. C., Muraza, O. & Aditiya, H. B. 2017. A review on insulation materials for energy conservation in buildings. *Renewable & Sustainable Energy Reviews,* 73**,** 1352-1365.

Ahmadzadehtalatapeh, M. 2013. An air-conditioning system performance enhancement by using heat pipe based heat recovery technology. *Scientia Iranica,* 20**,** 329-336.

Amin, M., Putra, N., Kosasih, E. A., Prawiro, E., Luanto, R. A. & Mahlia, T. M. I. 2017. Thermal properties of beeswax/graphene phase change material as energy storage for building applications. *Applied Thermal Engineering,* 112**,** 273-280.

ASHRAE 2013. *HVAC Design Manual for Hospitals and Clinics.*

Balaras, C. A., Dascalaki, E. & Gaglia, A. 2007. HVAC and indoor thermal conditions in hospital operating rooms. *Energy and Buildings,* 39**,** 454-470.

Cuce, P. M. & Riffat, S. 2015. A comprehensive review of heat recovery systems for building applications. *Renewable and Sustainable Energy Reviews,* 47**,** 665-682.

Fournier, E. D., Federico, F., Porse, E. & Pincetl, S. 2019. Effects of building size growth on residential energy efficiency and conservation in California. *Applied Energy***,** 446-452.

Hakim, I. I., Putra, N., Marda, A. P., Alvaro, M. A. & Winarta, A. Experimental study on utilization of heat pipe heat exchanger for improving efficiency of clean room air system in hospitals. E3S Web of Conferences, 2018. EDP Sciences, 02056.

Han, L., Han, B., Shi, X., Su, B., Lv, X. & Lei, X. 2018. Energy efficiency convergence across countries in the context of China's Belt and Road initiative. *Applied Energy,* 213**,** 112-122.

Incropera, F. P., Lavine, A. S., Bergman, T. L. & Dewitt, D. P. 2007. *Fundamentals of heat and mass transfer*, Wiley.

Ismail, M. S., Moghavvemi, M. & Mahlia, T. M. I. 2014. Genetic algorithm based optimization on modeling and design of hybrid renewable energy systems. *Energy Conversion and Management,* 85**,** 120-130.

Jadhav, T. S. & Lele, M. M. 2015. Theoretical energy saving analysis of air conditioning system using heat pipe heat exchanger for Indian climatic zones. *Engineering Science and Technology, an International Journal,* 18**,** 669-673.

Jouhara, H. & Merchant, H. 2012. Experimental investigation of a thermosyphon based heat exchanger used in energy efficient air handling units. *Energy,* 39**,** 82-89.

Mehrali, M., Latibari, S. T., Mehrali, M., Mahlia, T. M. I., Metselaar, H. S. C., Naghavi, M. S., Sadeghinezhad, E. & Akhiani, A. R. 2013. Preparation and characterization of palmitic acid/graphene nanoplatelets composite with remarkable thermal conductivity as a novel shape-stabilized phase change material. *Applied Thermal Engineering,* 61**,** 633-640.

Muhammaddiyah, S., Winarta, A. & Putra, N. 2018. Experimental Study Of Multi-fin Heat Pipe Heat Exchanger For Energy Efficiency In Operating Room Air Systems. *International Journal of Technology,* 2**,** 422-429.

Noie, S. H. 2006. Investigation of thermal performance of an air-to-air thermosyphon heat exchanger using ε-NTU method. *Applied Thermal Engineering,* 26**,** 559-567.

Papadopoulos, S., Kontokosta, C. E., Vlachokostas, A. & Azar, E. 2019. Rethinking HVAC temperature setpoints in commercial buildings: The potential for zero-cost energy savings and comfort improvement in different climates. *Building and Environment,* 155**,** 350-359.

Pérez-Lombard, L., Ortiz, J. & Pout, C. 2008. A review on buildings energy consumption information. *Energy and Buildings,* 40**,** 394-398.

Putra, N., Anggoro, T. & Winarta, A. 2017. *Experimental Study of Heat Pipe Heat Exchanger in Hospital HVAC System for Energy Conservation*.

Putra, N., Rawi, S., Amin, M., Kusrini, E., Kosasih, E. A. & Mahlia, T. M. I. 2019. Preparation of beeswax/multi-walled carbon nanotubes as novel shape-stable nanocomposite phase-change material for thermal energy storage. *Journal of Energy Storage,* 21**,** 32-39.

Ramos, J., Chong, A. & Jouhara, H. 2016. Experimental and numerical investigation of a cross flow air-to-water heat pipe-based heat exchanger used in waste heat recovery. *International Journal of Heat and Mass Transfer,* 102**,** 1267-1281.

Reay, D., Mcglen, R. & Kew, P. 2013. *Heat pipes: theory, design and applications*, Butterworth-Heinemann.

Shabgard, H., Allen, M. J., Sharifi, N., Benn, S. P., Faghri, A. & Bergman, T. L. 2015. Heat pipe heat exchangers and heat sinks: Opportunities, challenges, applications, analysis, and state of the art. *International Journal of Heat and Mass Transfer,* 89**,** 138-158.

Silitonga, A. S., Masjuki, H. H., Ong, H. C., Sebayang, A. H., Dharma, S., Kusumo, F., Siswantoro, J., Milano, J., Daud, K., Mahlia, T. M. I., Chen, W. H. & Sugiyanto, B. 2018. Evaluation of the engine performance and exhaust emissions of biodiesel-bioethanol-diesel blends using kernel-based extreme learning machine. *Energy,* 159**,** 1075-1087.

Srimuang, W. & Amatachaya, P. 2012. A review of the applications of heat pipe heat exchangers for heat recovery. *Renewable and Sustainable Energy Reviews,* 16**,** 4303-4315.

Teke, A. & Timur, O. 2014. Assessing the energy efficiency improvement potentials of HVAC systems considering economic and environmental aspects at the hospitals. *Renewable and Sustainable Energy Reviews,* 33**,** 224-235.

Vakiloroaya, V., Samali, B., Fakhar, A. & Pishghadam, K. 2014. A review of different strategies for HVAC energy saving. *Energy conversion and management,* 77**,** 738-754.

Wang, C. C., Fu, W. L. & Chang, C. T. 1997. Heat transfer and friction characteristics of typical wavy fin-and-tube heat exchangers. *Experimental Thermal and Fluid Science,* 14**,** 174-186.

Yau, Y. H. & Ahmadzadehtalatapeh, M. J. T. S. 2015. Heat pipe heat exchanger and its potential to energy recovery in the tropics. 19.

#196: Effect of a spiral on the performance in a conical bubbling fluidized bed paddy dryer

Hirakh Jyoti DAS[1], Md Shoaib AAMIR[2], Rituraj SAIKIA[3], Pinakeswar MAHANTA[4,5]

[1] *Indian Institute of Technology Guwahati, Assam, India-781039, jyotihirakh@gmail.com*
[2] *Indian Institute of Technology Guwahati, Assam, India-781039, mdshoaibaamir@gmail.com*
[3] *Indian Institute of Technology Guwahati, Assam, India-781039, rsaikia@iitg.ac.in*
[4] *Indian Institute of Technology Guwahati, Assam, India-781039, pinak@iitg.ac.in*
[5] *National Institute of Technology Arunachal Pradesh, India-791110, pinak@iitg.ac.in*

The present work is the comparative study of drying characteristics between two conical bubbling fluidized bed dryers having cone angles of 5° and 10° and a conventional one with a cone angle of 0°. A series of experiments were carried out with a spiral inside the dryers to investigate the drying characteristics of paddy. Hydrodynamic behaviour, drying characteristics and energy consumption of the blower were investigated for these three dryers and results were compared. The experiments were performed with three different inlet velocities (1, 1.6 and 2.1 m/s), three different inlet temperatures (55°C, 60°C and 65°C) with 1-3 kg batch sizes of paddy as a bed inventory. It was observed that the time taken to reduce the moisture content in the conical bubbling fluidized dryer having a cone angle of 10° was less than the other two dryers. The drying rate was also found to be faster with the use of a spiral inside the dryers than without the spiral. The effect of the spiral was to exhibit better drying characteristics in terms of nutritional value and milling quality. Conical fluidized bed dryer saved more energy than conventional fluidized bed dryers. Both thermal and blower energy consumption was found to be reduced with the use of a spiral inside the dryers.

Keywords: Spiral; cone angle; energy consumption; drying; hydrodynamic

1. INTRODUCTION

Paddy rice is considered to be one of the most important basic staple foods in India. India is the 2nd largest rice producing country after China (Roy, Surje, & Mahato, 2013). In most of the tropical countries, paddy contains moisture content in the range of 24 to 28% immediately after harvesting (Beeny & Basil, 1970; Igathinathane, Chattopadhyay, & Pordesimo, 2008). This level of moisture content makes the paddy susceptible to fungi and pest attack which results in its damage and loss of nutritional values. Therefore, it is necessary for the paddy grains to be dried to reduce the moisture content to about 12-14% in order to have desired nutritional values and longer durability (Luthra, Sadaka, & Atungulu, 2018; Suherman, Djaeni, & Kumoro, 2017; Tirawanichakul, Prachayawarakorn, Varanyanond, & Soponronnarit, 2009).

Drying is a process to remove moisture content of solid particles. Nowadays, many types of drying techniques are available such as sun drying, solar drying and fluidized bed drying. Many researchers have conducted experiments on various types of drying methods with their own techniques. The sun drying technique is the oldest and easiest method, but the demerits of open sun drying are its dependency on weather and labour intensiveness (Fudholi, Othman, Ruslan, & Sopian, 2013; Palled, Desai, & Anantachar, 2014). Solar dryers also depend on the weather where the paddy due to its direct exposure to the sun, loses protein and other nutritional values (Yahya, 2016). Hence, numerous studies are carried out with conventional fluidized bed drying techniques. (Thant, Robi, & Mahanta, 2018) reported the drying characteristics in conventional bubbling fluidized bed dryer and observed that the non-uniform mixing of paddy particles in the radial direction is improved when the dryer is inclined at an angle 15°. (Firouzi, Alizadeh, & Haghtalab, 2017) compared two types of the dryer (IBBD) and observed that the Industrial horizontal rotatory dryer is advantageous over industrial batch type bed dryer in terms of energy saving and quality of milled rice. (Yahya, 2016) reported that the drying characteristics of paddy are improved with the incorporation of solar assisted fluidized bed dryer rather than conventional solar dryers. Apart from these, a group of researchers are involved with the study of operating parameters on drying characteristics. (Darvishi, Khoshtaghaza, & Minaei, 2015) investigated the effect of inlet air temperature and velocity on drying characteristics. They observed that the drying time is reduced with an increase in inlet air velocity and temperature. (Khanali, Khakpour Giglou, & Rafiee, 2018) observed that the moisture content decreases with increases in drying temperature and weir height. However, the moisture content was found to be increasing with inlet dry mass flow rate of particles. Effect of operating parameters on drying characteristics was also studied by (Xia, Zhang, Wang, Yu, & Fan, 2017). (Pourbagher, Rahmati, & Alizadeh, 2016) investigated the effect of heaters on drying characteristics and milling quality and observed that cracking involved with conventional heating is reduced with infrared heating.

The literatures discussed above addressed the various aspects of conventional fluidized bed dryer and other drying techniques. But the major shortcoming encountered with conventional fluidized bed dryer is consumption of more energy and longer drying time. Conical fluidized bed when used for drying has the potential of tackling these shortcomings. Moreover, none of the literatures has been found to discuss the effect of the spiral on the performance of drying characteristics in conical bubbling fluidized bed dryer. Hence, the present work deals with the study of the effect of a spiral on hydrodynamic behaviour and drying characteristics in two conical bubbling fluidized bed dryers and results were compared with a conventional fluidized bed dryer. Effect of operating parameters such as bed inventory, intake air temperature and velocity on the same has been investigated on these three dryers.

2. MATERIAL AND METHODS

The schematic diagram of a conical bubbling fluidized bed dryer is shown in Figure 1.

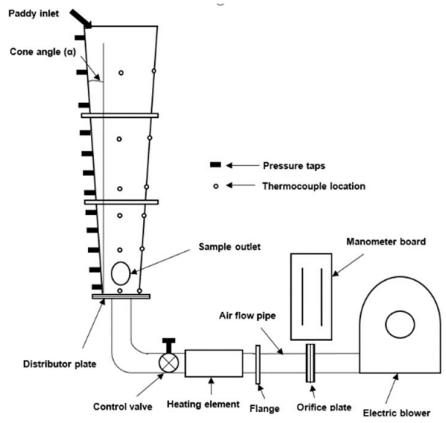

Figure 1: Schematic diagram of experimental setup

Figure 2: Spiral

The two conical dryers having taper angles 5° and 10° and a conventional dryer having taper angle 0° are considered for the present study and their dimensions are given in Table 1. The bottom diameter of both these dryers is taken as 15 cm. The area of cross-section is increasing along the height of the riser to maintain the desired cone angle as 5° and 10°. A couple of experiments are conducted on these two conical bubbling fluidized bed dryers' units by using paddy as a bed of batch material and air as the fluidizing medium. The initial moisture content of the paddy was 24% (WB). The paddy was boiled to increase the moisture content to approx. 42% (W.B.) which was measured by digital grain moisture tester with an accuracy of $\pm$0.5. The experiments were carried out for varying bed inventory between 1 to 3 kg with three different inlet air flow velocities such as 1.1, 1.6 and 2.1 m/s and three inlet drying temperatures (55°, 60° and 65°C). An experiment was started by switching on the high-pressure high discharge blower. Once it is on, the airflows from the blower and passes through the airflow pipes. The airflow rate was regulated by an adjustable gate valve installed on the flow pipes. A conventional heating coil was wrapped over the inlet airflow pipe which was covered by a layer of ceramic wool for thermal insulation. Electrical power was supplied to the heating coil and regulated by an autotransformer to heat the air and maintain the air intake temperature as 55°, 60° and 65°C respectively. The paddy particles were fed to the fluidized bed dryer in different amounts of batch sizes. The inlet air velocity was set to 2 or 2.5 times above the minimum fluidization velocity to maintain the bubbling regimes. A set of pressure tapings were inserted along the height of the dryer and were connected to a water-filled U-tube differential manometer. The difference of two consecutive pressure taps provides the pressure drop between two subsequent locations along the dryer. These difference of pressure drops give the information of hydrodynamic behaviour of the dryers. In order to study the effect of introducing a spiral inside the dryer column, a spiral fabricated out of MS was installed inside the conical dryer has been shown in figure 2. A small amount of paddy grain was taken out after every 5-minute interval to check the moisture content until it has arrived at 12-14% (W.B.) and results were noted down.

Table 1. Dimensions of conical bubbling fluidized bed dryers

Sl. No.	Cone angle (degree)	Inlet diameter (cm)	Outlet diameter (cm)	Height of riser (cm)
1	0°	15	15	120
2	5^0	15	25.74	120
3	10^0	15	36	120

The superficial velocity (U) is defined as the volume flow rate of air per unit cross-section of the bed and it can be written as:

Equation 1: $$U = \frac{Volume\ flow\ rate\ of\ air\ through\ the\ bed}{cross-sectional\ area\ of\ the\ bed} = \frac{Q}{A}$$

Where:

- A = cross-sectional area of bed (mm^2)
- *Q* = discharge through orifice meter (m^3/s)

Equation 2: $$Q = \frac{Ca\left(2\rho_s g \Delta h\right)^{\frac{1}{2}}}{\left\{\rho_g\left(1-\beta^4\right)\right\}^{\frac{1}{2}}} = 0.035\sqrt{\Delta h}$$

Where:

- C = discharge coefficient = 0.6082
- a = cross-section area of orifice = 0.004417
- β = diameter ratio = d/D = 0.5
- Δh = difference between pressure head (cm)

Non- dimensional particle velocity u^* and size d_p^* were calculated from the following equations:

Equation 3: $$d_p^* = d_p\left[\frac{\rho_g\left(\rho_s-\rho_g\right)g}{\mu^2}\right]^{\frac{1}{3}}$$

Equation 4: $$U = u^* \left[\frac{\mu\left(\rho_s - \rho_g\right) g}{\rho_g^2} \right]^{\frac{1}{3}}$$

Where:

- d_p = mean particle diameter
- ρ_g = density of air
- ρ_s = density of paddy
- μ = viscosity of air

The mean particle size and density were calculated by given formula as above. Substituting these values in the above equations and computing the value of d_p^* and u^*, a relationship between non-dimensional velocity and velocity of air is obtained as follows:

Equation 5: $$U = 0.4184\,\mathrm{u}^*$$

From the general flow regime curve given by Kuni and Levenspiel (Kunii & Levenspiel, 1991), the inlet air velocity for bubbling flow regimes has been determined.
Energy is consumed in the dryer as heat for removing the moisture content of paddy as well as electrical energy for driving the blower. Hence, energy consumption is calculated as both heat input and energy consumption by the blower. The heat input to the dryer is (Thant et al., 2018)

Equation 6: $$Q = V i t \times P.F. \times 60 \times 10^{-6}$$

Where:

- Q = heat input (MJ/kg)
- V = input voltage (V)
- i = current (A)
- t = drying time (m)
- P.F = power factor.

3. RESULTS AND DISCUSSIONS

3.1. Variation of pressure drop

The variation of pressure drop along the height of the two conical fluidized bed dryers has been shown in Figures 3 and 4. As observed in the figure, the pressure drops increase with the use of a spiral for both the dryers.

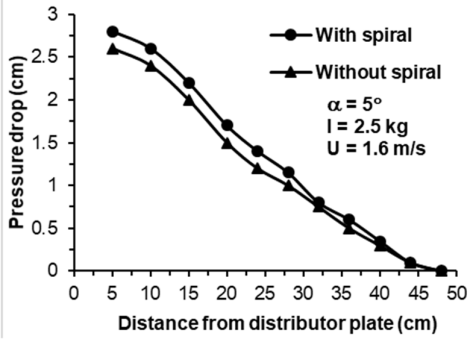

Figure 3: Pressure drop along the height of the dryer at 5° cone angle

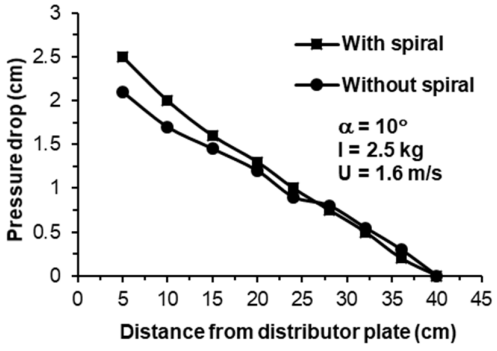

Figure 4: Pressure drop along the height of the dryer at 10° cone angle

It may be due to the vigorous agitation of particles along the height of dryers. Effect of cone angle on the variation of pressure drops with spiral is also investigated in Figure 5. It is observed that the pressure drops decrease with increase in cone angle. For the same amount of bed inventory and inlet air velocity, when the cone angle increases,

the cross-sectional area also increases and because of that, there is a more uniform distribution of particles. This may be the reason for the observation.

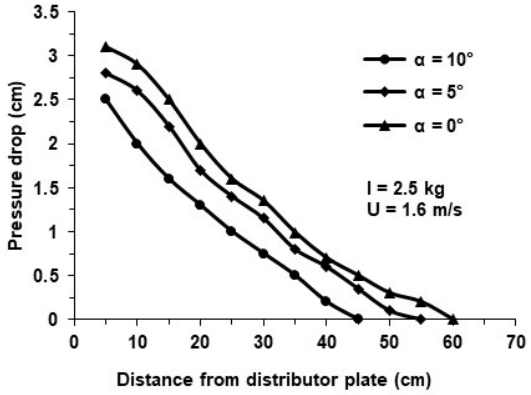

Figure 5: Effect of cone angle on pressure drop with spiral

3.2. Drying characteristics

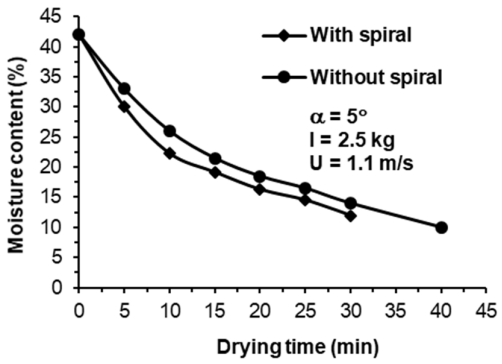

Figure 6: Drying characteristics in the conical dryer of 5° cone angle

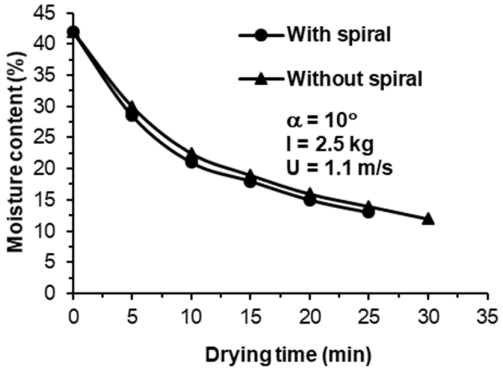

Figure 7: Drying characteristics in the conical dryer of 10° cone angle

The drying characteristics plots in terms of moisture content vs drying time graph with spiral and without spiral are presented in Figures 6 and 7. The results show that the spiral provides better drying characteristics than without spiral for both the dryers. Incorporation of spiral inside the dryer has direct contact with the particles. Due to the direct contact between particles and spiral, an unsteady state heat conduction takes place. Apart from that, the air also gets heated and transfer heat to the particles. However, for conventional dryer where the heater is placed on the wall surface of the inlet pipe of the dryer, heat transfer takes place between particles and heated air only. On top of that, the spiral enhances the turbulence of mixtures and make the heat transfer rate faster. Hence drying time is reduced in case of the dryer with spiral.

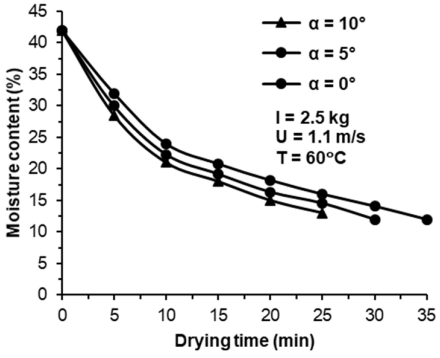

Figure 8: Effect of cone angle on drying characteristics with spiral

Effect of cone angle on drying characteristics with spiral is demonstrated in Figure 8. As indicated in the figure, the dying time is lesser for conical dryer having a larger cone angle. The higher is the cone angle at the same superficial velocity, the lesser will be the air volume fraction. Also, vigorous mixing of particles and air may be the reason for the observation. It is observed that for a higher degree of cone angle, the required drying time is approx. 25 mins. However, for conical dryer having smaller cone angle takes almost 30 mins for drying which is 20% more than that of larger cone angle of the conical dryer and the conventional dryer takes almost 34 mins to get the desired moisture content.

3.3. Thermal energy consumption

Thermal energy consumption between two conical dryers for heater without spiral and with a spiral at U = 1.1 m/s and I = 2.5 kg is illustrated in Figures 9 and 10. It can be concluded that the thermal energy consumption is higher for the conventional heater without spiral than with spiral.

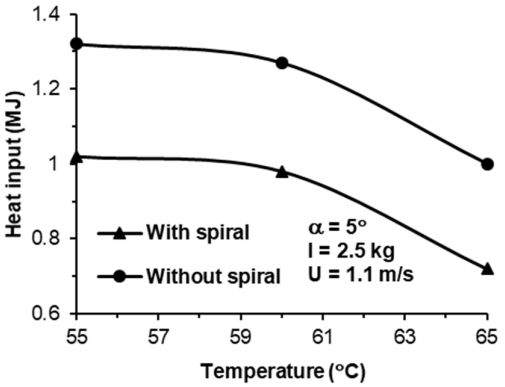

Figure 9: Thermal energy consumption at different temperature in conical dryer having 5° cone angle

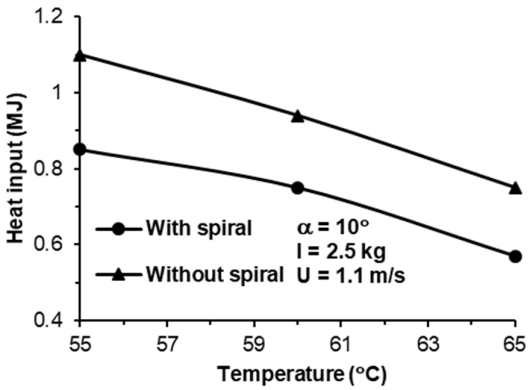

Figure 10: Thermal energy consumption at different temperature in conical dryer having 10° cone angle

Due to the higher heat transfer inside the bed, the time needed for removing moisture content is less for the dryer with spiral. Since the thermal energy consumption is directly related to the time required for drying, hence, it is found to be higher for the heater without spiral.

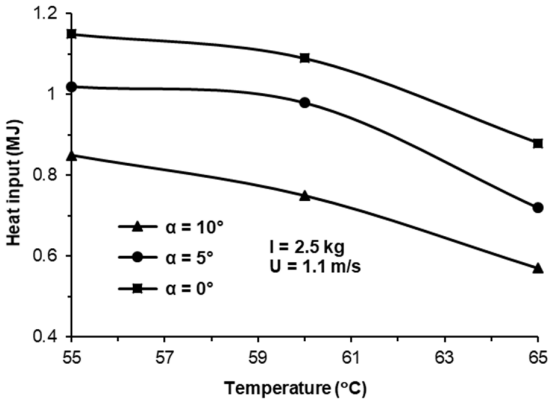

Figure 11: Effect of cone angle on thermal energy consumption at different temperature with spiral

Figure 11 also reveals the effect of cone angle on thermal energy consumption for the heater with a spiral. As shown in the figure, the thermal energy consumption is lower in the case of 10° cone angle of the conical dryer. This may be due to the lesser amount of drying time. It is found that nearly 19.26% of energy consumption is reduced for a higher degree of cone angle.

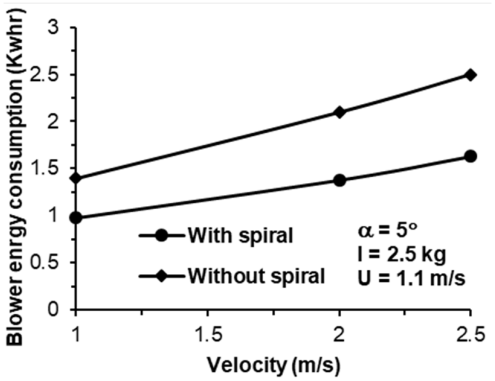

Figure 12: Thermal energy consumption at different inlet air velocity in conical dryer having 5° cone angle

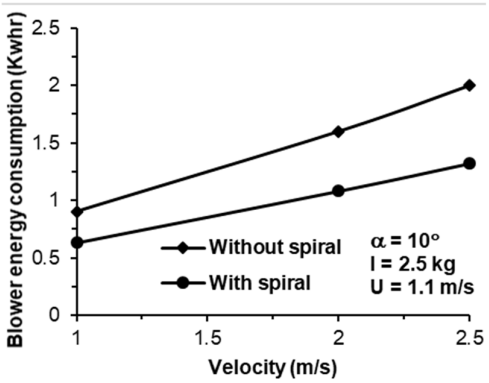

Figure 13: Thermal energy consumption at different inlet air velocity in conical dryer having 10° cone angle

The thermal energy consumption is also investigated for T = 65°C and I = 2.5 kg in Figures 12 and 13. The same trend is observed as in the previous case. Thermal energy consumption is higher for the heater without spiral than with spiral. Impact of cone angle on thermal energy consumption at T = 65°C and I = 2.5 kg is also explained in Figure 14. A similar result has been found as observed in Figure 11 that the thermal energy consumption decreases with an increase in cone angle.

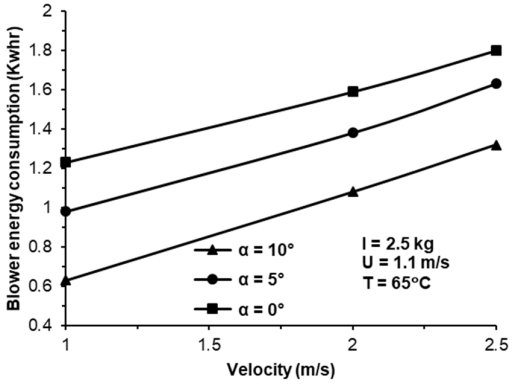

Figure 14: Effect of cone angle on thermal energy consumption at different inlet air velocity with spiral

3.4. Blower energy consumption

The blower energy consumption for these two conical dryers for the heater with spiral and without spiral at u = 1.1 m/s and I = 2.5 kg is explained in Figures 15 and 16. As shown in the figures, the blower energy consumption is higher for the heater without spiral than with spiral. The blower energy consumption is dependent upon drying -

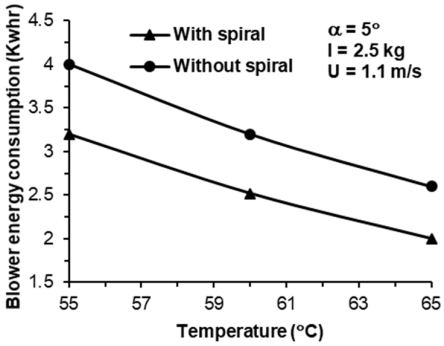

Figure 15: Blower energy consumption at different temperature of a conical dryer having 5° cone angle

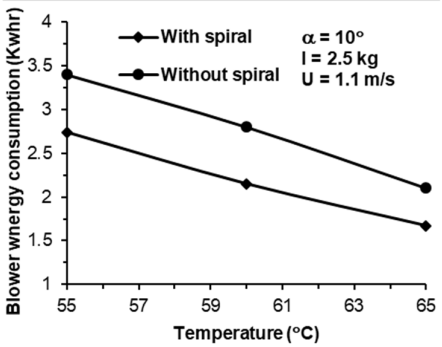

Figure 16: Blower energy consumption at different temperature of a conical dryer having 10° cone angle

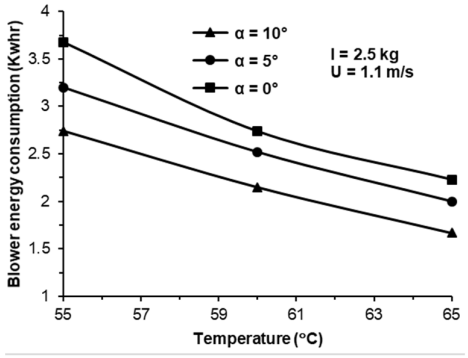

Figure 17: Effect of cone angle on blower energy consumption at different temperature with spiral

time and heat transfer characteristics. The more is the heat transfer between two phases, lesser will be the drying time. With the incorporation of the spiral, the interphase heat transfer is enhanced. Hence, the blower energy consumption is lesser. Figures 18 and 19 also explain the blower energy consumption at l = 2.5 kg and T = 65^0C for the two conical dryers. The blower energy consumption is found to be decreasing with the incorporation of the spiral inside both dryers. Effect of scale-up on blower energy consumption at different operating conditions is explained in Figures 17 and 19. As explained in the previous section, drying time is less for a conical dryer with a higher degree of cone angle. Hence, blower energy consumption is found to be decreasing with increase in cone angle. However, the difference in blower energy consumption between spiral and without spiral is found to be more prominent when the air velocity is increased.

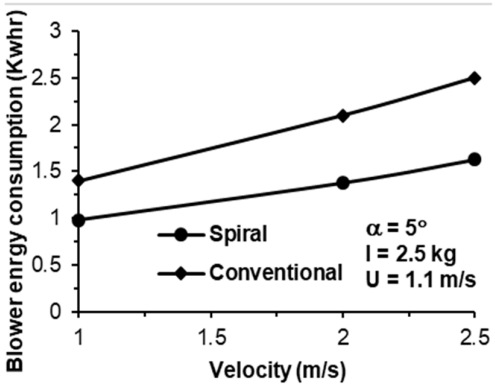

Figure 18: Blower energy consumption at a different velocity in the conical dryer of 5° cone angle

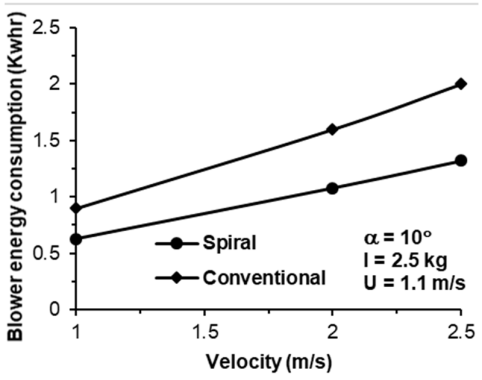

Figure 19: Blower energy consumption at a different velocity in the conical dryer of 10° cone angle

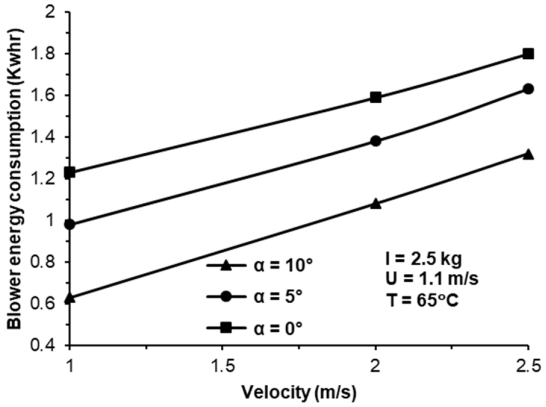

Figure 20: Effect of cone angle on blower energy consumption at different velocity with spiral

4. CONCLUSIONS

Hydrodynamic behaviour and drying characteristics are investigated in two conical bubbling fluidized bed dryers having 5° and 10° with and without spiral inside the dryer and results are compared with a conventional dryer. Effect of cone angle on the same is also investigated at different operating conditions. For all cases, the drying time is found to be lesser with the use of spiral. The maximum drying time is found to be 34, 30 and 25 mins respectively, for 0°, 5° and 10° cone angle of dryers with spiral. It is also observed that with the increase in cone angle the drying time decreases. The thermal energy consumption and blower energy consumption are also investigated for these two types of heater. The thermal and blower energy consumption associated with the spiral type is found to be lesser than dryer without spiral. The thermal energy consumption, as well as blower energy consumption, are also found to be lesser for a conical dryer with a higher degree of cone angle. The bed pressure drop in higher degree cone angle of the dryer was found to be lesser. However, the pressure drop tends to increase with the use of a spiral in both the dryers. The drying rate was also found to be faster with the use of a spiral than a conventional heater. Effect of spiral exhibits better drying characteristics in terms of nutritional value and milling quality. Conical fluidized bed dryer saves more energy consumption than straight bed fluidized bed dryer. The higher is the cone angle; the lower will be the energy consumption. Both thermal and blower energy consumption is reduced with the use of a spiral inside the dryers.

5. REFERENCES

Beeny, J. M., & Basil, C. S. N. (1970). Multipass drying of paddy (rice) in the humid tropics. *Journal of Agricultural Engineering Research*, *15*(4), 364–374. https://doi.org/10.1016/0021-8634(70)90096-X

Darvishi, H., Khoshtaghaza, M. H., & Minaei, S. (2015). Effects of fluidized bed drying on the quality of soybean kernels. *Journal of the Saudi Society of Agricultural Sciences*, *14*(2), 134–139. https://doi.org/10.1016/j.jssas.2013.09.002

Firouzi, S., Alizadeh, M. R., & Haghtalab, D. (2017). Energy consumption and rice milling quality upon drying paddy with a newly-designed horizontal rotary dryer. *Energy*, *119*, 629–636. https://doi.org/10.1016/j.energy.2016.11.026

Fudholi, A., Othman, M. Y., Ruslan, M. H., & Sopian, K. (2013). Drying of Malaysian Capsicum annuum L. (Red Chili) Dried by Open and Solar Drying. *International Journal of Photoenergy*, *2013*, 1–9. https://doi.org/10.1155/2013/167895

Igathinathane, C., Chattopadhyay, P. K., & Pordesimo, L. O. (2008). Moisture diffusion modeling of parboiled paddy accelerated tempering process with extended application to multi-pass drying simulation. *Journal of Food Engineering*, *88*(2), 239–253. https://doi.org/10.1016/j.jfoodeng.2008.02.014

Khanali, M., Khakpour Giglou, A., & Rafiee, S. (2018). Model development for shelled corn drying in a plug flow fluidized bed dryer. *Engineering in Agriculture, Environment and Food*, *11*(1), 1–8. https://doi.org/10.1016/j.eaef.2017.09.002

Kunii, D., & Levenspiel, O. (1991). Fluidization and Mapping of Regimes. In *Fluidization Engineering* (pp. 61–94). https://doi.org/10.1016/B978-0-08-050664-7.50009-3

Luthra, K., Sadaka, S., & Atungulu, G. G. (2018). Exploration of Rough Rice Head Yield Subjected to Drying and Retention Durations in a Fluidized Bed System. *Applied Engineering in Agriculture*, *34*(5), 877–885. https://doi.org/10.13031/aea.12925

Palled, V., Desai, S. R., & Anantachar, M. (2014). Field evaluation of solar tunnel dryer for grapes drying. *Ecology, Environment and Conservation*, *20*(4), 1665–1668.

Pourbagher, R., Rahmati, M. H., & Alizadeh, M. R. (2016). Air temperature and final grain moisture effects on drying time and milling quality in two types of fluidized bed dryer. *Agricultural Engineering International: CIGR Journal*, *18*(2).

Roy, B., Surje, D. T., & Mahato, S. (2013). Biodiversity of farmers' varities of rice (ORYZA SATIVA L.). *Int. Conf. Harmon. with Nat. Context Ecotechnological Interv. Clim. Chang*.

Suherman, S., Djaeni, M., & Kumoro, A. C. (2017). Drying Kinetics of Paddy in Fluidized Bed with Immersed Heating Element. *Advanced Science Letters*, *23*(3), 2364–2366. https://doi.org/10.1166/asl.2017.8672

Thant, P. P., Robi, P. S., & Mahanta, P. (2018). Inclined Fluidized Bed Dryer Performance in Energy Saving Option. *International Journal of Science, Engineering and Technology Research (IJSETR)*, *7*(4), 230–237.

Tirawanichakul, S., Prachayawarakorn, S., Varanyanond, W., & Soponronnarit, S. (2009). Drying Strategies for Fluidized-Bed Drying of Paddy. *International Journal of Food Engineering*, *5*(2). https://doi.org/10.2202/1556-3758.1401

Xia, L., Zhang, H., Wang, B., Yu, C., & Fan, X. (2017). Experimental and numerical analysis of oil shale drying in fluidized bed. *Drying Technology*, *35*(7), 802–814. https://doi.org/10.1080/07373937.2016.1218345

Yahya, M. (2016). Performance Analysis of Solar Assisted Fluidized Bed Dryer Integrated Biomass Furnace with and without Heat Pump for Drying of Paddy. *International Journal of Photoenergy*, *2016*, 1–17. https://doi.org/10.1155/2016/3801918

#197: The performance analysis of ground source heat pump using spiral coil energy piles with seepage in different climates of cold regions

Tian YOU[1], Hongxing YANG[2]

[1]*Renewable Energy Research Group, Department of Building Services Engineering, The Hong Kong Polytechnic University, Hong Kong, China, tian.you@polyu.edu.hk*
[2]*Renewable Energy Research Group, Department of Building Services Engineering, The Hong Kong Polytechnic University, Hong Kong, China, hong-xing.yang@polyu.edu.hk*

Ground source heat pump (GSHP) is an energy saving and efficient air conditioning technology. Energy piles group is an economic and efficient ground heat exchanger of the system to extract heat in winter and inject heat in summer for space heating and cooling of the buildings. However, for heating dominant buildings in cold regions, the annual soil thermal imbalance causes the cold accumulation in soil and heating deficiency of the building. To simulate the system performance, the system model is established, involving the model of energy piles group with seepage, the heat pump model, the water pump model, and the building model. An office building is selected as the objective and applied in three typical cities (Harbin, Changchun, and Shenyang) of cold regions in China for simulation. The summer in Harbin, Changchun, and Shenyang is not hot. Harbin has the coldest winter and its minimum monthly average air temperature is -18.8ºC. The building loads in different cities are simulated by transient software. The maximum monthly heating loads are -120.91 MWh in Harbin, -111.91 MWh in Changchun and -98.63 MWh in Shenyang. The soil thermal condition, the COP of heat pump and heating effect in the buildings of different cities are analysed. In Harbin, Changchun and Shenyang, the annually accumulated soil heat extraction decreases from -314.06 MWh, -303.74 MWh and -247.15 MWh in the first year to -223.70 MWh, -226.97 MWh and -229.47 MWh in the tenth year; the minimum COP decreases from 2.61, 2.85 and 3.46 in the first year to 1.99, 2.13 and 2.88 in the tenth year; the maximum heating deficiency is 51.9 kW, 44.4kW and 4.9kW in the tenth year. This work contributes to the performance prediction of GSHP system using spiral coil energy pile in different climates of cold regions.

Keywords: ground source heat pump; energy pile; soil thermal imbalance; different climates; cold regions

1. INTRODUCTION

Ground source heat pump (GSHP) is an energy saving and efficient air conditioning technology (Spitler 2005, Self et al. 2013). It uses ground heat exchanger to extract heat in winter and to inject heat in summer for space heating and cooling of the buildings (Omer 2008). As an important component in the system, ground heat exchanger has many different styles (Florides and Kalogirou 2007), of which the spiral coil energy pile saves the drilling cost and has good performance in heat transfer, drawing more attention and being applied in many projects. The system performance of GSHP using spiral coil energy piles is influenced seriously by the climates (Morrone et al. 2014, You et al. 2018). In cold regions, the large heat extraction causes the cold accumulation in soil and heating deficiency of the building. The accurate heat transfer model of energy piles group with seepage should be adopted to design the GSHP system and predict the system performance in different climates.

Liu et al. (2017) analysed the feasibility and performance of GSHP using boreholes as the ground heat exchanger in heating dominated areas. The numerical model of a single energy pile was established by Lee and Lam (2013). The model of energy piles group was developed and the soil thermal imbalance of a project was analysed for optimum design in our previous study (You et al. 2018, Zhang et al. 2015). However, there is no research on the GSHP performance influenced by different climates using the energy piles group model and considering the influential factors, like seepage and the thermal influences among different piles, on the heat transfer. The applicability of this system in different climates should be further investigated.

In this paper, the system model of GSHP using spiral coil energy piles is set up. An office building is selected as the objective and applied in three typical cities of cold regions in China for simulation. The building loads in different cities are simulated by a transient software. The soil thermal condition, the COP of heat pump and heating effect of the buildings in different cities are analysed. This work contributes to the performance prediction and application guidance of GSHP system using spiral coil energy pile in different climates.

2. GROUND SOURCE HEAT PUMP SYSTEM USING SPIRAL COIL ENERGY PILES WITH SEEPAGE

The system is mainly composed of spiral coil energy piles, heat pump, water pump, and the building. The pile foundations with spiral coil buried inside are considered as the soil heat exchanger. In winter, the cooled fluid flowing from the evaporator of the heat pump goes into the energy piles to extract heat from the surrounding soil and then is pumped back to the evaporator, composing a circulation in the soil side. It causes the temperature decrease and cold accumulation in the soil. Meanwhile, the heat from the evaporator is released to the water flowing past the condenser by the refrigeration cycle inside the heat pump. Then, the heated water is pumped into the building for space heating. After the heat is released in the building, the water flows back to the condenser of heat pump for absorbing heat, composing a circulation in the user side. In summer, the heated fluid flowing from the condenser of the heat pump goes into the energy piles to inject heat into the surrounding soil and then is pumped back to the condenser, composing a circulation in the soil side. It causes the temperature increase and heat accumulation in the soil. Meanwhile, the water flowing past the evaporator releases heat to the heat pump and then is pumped to the building for space cooling. After the heat is absorbed by flowing water in the building, the heated water flows back to the evaporator of the heat pump for releasing heat, composing a circulation in the user side. Besides, the underground seepage can increase the heat exchange around energy piles effectively and the thermal interaction among different energy piles makes the underground heat exchange in a pile group different from that around a single pile.

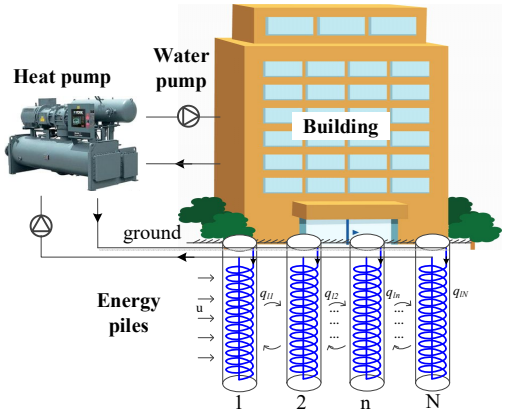

Figure 1: The schematic of Ground source heat pump system using spiral coil energy piles with seepage

3. METHODOLOGY

Combining the energy pile model, the heat pump model, the water pump model, and the building load model, the system model is set up. It can simulate the monthly system performance in the long-term. Different from other ground source heat pump models, this system model adopts the energy pile group model with seepage to simulate the heat transfer of energy piles. It accurately considers the practical geometry of spiral coil energy piles, the underground water flow and thermal interaction among energy piles group.

3.1. The Energy pile model and validation

The model of energy pile group with seepage is shown in Equation1 (You et al. 2018). In Equation 1, the heat fluxes of each energy pile at one moment can be calculated by the matrix if the inlet fluid temperature of each energy pile is input.

Equation 1: $$Q_l = A^{-1} \times B$$

Equation 1a: $$Q_l = \left[q_{l,1}(j\Delta\tau) \quad q_{l,2}(j\Delta\tau) \quad \ldots \quad q_{l,n}(j\Delta\tau) \quad \ldots \quad q_{l,N}(j\Delta\tau) \right]^T$$

Equation 1b:

$$A = \begin{bmatrix} \frac{R_p \times H}{L_{pipe}} + \frac{H}{2c_f m_f} + \frac{\Theta_{1,1}(\Delta\tau)}{\lambda_s} & \frac{\Theta_{2,1}(\Delta\tau)}{\lambda_s} & \cdots & \frac{\Theta_{n,1}(\Delta\tau)}{\lambda_s} & \cdots & \frac{\Theta_{N,1}(\Delta\tau)}{\lambda_s} \\ \frac{\Theta_{1,2}(\Delta\tau)}{\lambda_s} & \frac{R_p \times H}{L_{pipe}} + \frac{H}{2c_f m_f} + \frac{\Theta_{2,2}(\Delta\tau)}{\lambda_s} & \cdots & \frac{\Theta_{n,2}(\Delta\tau)}{\lambda_s} & \cdots & \frac{\Theta_{N,2}(\Delta\tau)}{\lambda_s} \\ \cdots & \cdots & & \cdots & & \cdots \\ \frac{\Theta_{1,n}(\Delta\tau)}{\lambda_s} & \frac{\Theta_{2,n}(\Delta\tau)}{\lambda_s} & \cdots & \frac{R_p \times H}{L_{pipe}} + \frac{H}{2c_f m_f} + \frac{\Theta_{n,n}(\Delta\tau)}{\lambda_s} & \cdots & \frac{\Theta_{N,n}(\Delta\tau)}{\lambda_s} \\ \cdots & \cdots & & \cdots & & \cdots \\ \frac{\Theta_{1,N}(\Delta\tau)}{\lambda_s} & \frac{\Theta_{2,N}(\Delta\tau)}{\lambda_s} & \cdots & \frac{\Theta_{n,N}(\Delta\tau)}{\lambda_s} & \cdots & \frac{R_p \times H}{L_{pipe}} + \frac{H}{2c_f m_f} + \frac{\Theta_{N,N}(\Delta\tau)}{\lambda_s} \end{bmatrix}$$

Equation 1c:

$$B = \begin{bmatrix} t_{in}(j\Delta\tau) - t_0 + \sum_{ni=1}^{N} \left\{ q_{l,ni}((j-1)\Delta\tau) \times \Theta_{ni,1}(\Delta\tau) - \sum_{i=2}^{j-1} \left[q_{l,ni}(i\Delta\tau) - q_{l,ni}((i-1)\Delta\tau) \right] \times \Theta_{ni,1}((j-i+1)\Delta\tau) - q_{l,ni}(\Delta\tau) \times \Theta_{ni,1}(j\Delta\tau) \right\} \Big/ \lambda_s \\ t_{in}(j\Delta\tau) - t_0 + \sum_{ni=1}^{N} \left\{ q_{l,ni}((j-1)\Delta\tau) \times \Theta_{ni,2}(\Delta\tau) - \sum_{i=2}^{j-1} \left[q_{l,ni}(i\Delta\tau) - q_{l,ni}((i-1)\Delta\tau) \right] \times \Theta_{ni,2}((j-i+1)\Delta\tau) - q_{l,ni}(\Delta\tau) \times \Theta_{ni,2}(j\Delta\tau) \right\} \Big/ \lambda_s \\ \cdots \\ t_{in}(j\Delta\tau) - t_0 + \sum_{ni=1}^{N} \left\{ q_{l,ni}((j-1)\Delta\tau) \times \Theta_{ni,n}(\Delta\tau) - \sum_{i=2}^{j-1} \left[q_{l,ni}(i\Delta\tau) - q_{l,ni}((i-1)\Delta\tau) \right] \times \Theta_{ni,n}((j-i+1)\Delta\tau) - q_{l,ni}(\Delta\tau) \times \Theta_{ni,n}(j\Delta\tau) \right\} \Big/ \lambda_s \\ \cdots \\ t_{in}(j\Delta\tau) - t_0 + \sum_{ni=1}^{N} \left\{ q_{l,ni}((j-1)\Delta\tau) \times \Theta_{ni,N}(\Delta\tau) - \sum_{i=2}^{j-1} \left[q_{l,ni}(i\Delta\tau) - q_{l,ni}((i-1)\Delta\tau) \right] \times \Theta_{ni,N}((j-i+1)\Delta\tau) - q_{l,ni}(\Delta\tau) \times \Theta_{ni,N}(j\Delta\tau) \right\} \Big/ \lambda_s \end{bmatrix}$$

where, q is the heat flux of each energy pile, W/m; R_p is the thermal resistance of pipe, (m·K)/W; H is the depth of the energy pile, m; L is the length of the spiral coil pipe, m; c is the specific heat capacity, J/(kg·K); λ is the heat conductivity coefficient, W/(m·K); t is the temperature, ºC; τ is the time, s; m is the mass flow rate, kg/s; Θ is the dimensionless temperature of a single energy pile with seepage (Zhang et al. 2015); Q_l is the matrix of heat fluxes of different energy piles.

To validate the energy pile group model, the sandbox experiment is set up. The sandbox has a size of 1m×1m×1m, and filled with sand. Five heat exchange pipes are buried inside and the water flowing inside the pipes is from the water bath with a constant water temperature. Four thermocouples are buried in the sand in the middle depth of the sandbox. The photo and schematic diagram of the sandbox experiment are shown in Figure 2. When the excess

temperature of the pipe inlet is 10ºC, the soil temperatures of 4 positions tested by the experiment and simulated by the analytical energy piles model (Equation 1) are shown in Figure 3. Results show that the temperatures of these two different methods match well. The analytical model has good accuracy.

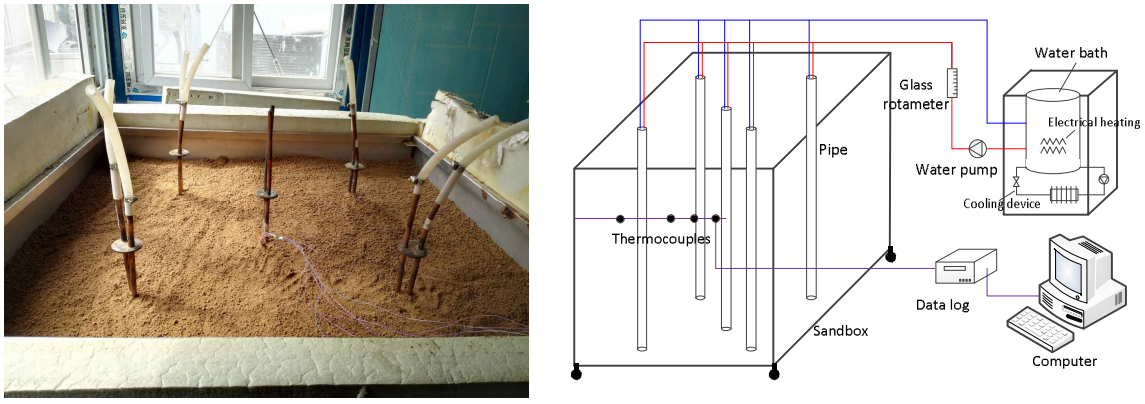

(a) Photos of experiment *(b) Schematic diagram*

Figure 2: Sandbox experiment

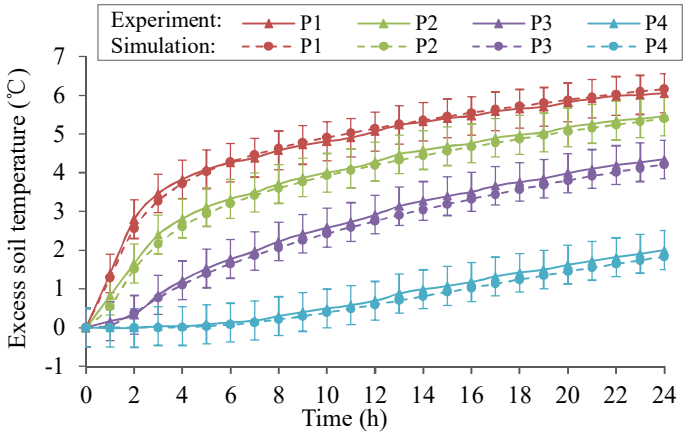

Figure 3: The soil temperature variations obtained by experiment and simulation (You et al. 2018)

3.2. The system model

Building model is set up in the dynamic building simulation software named DeST (Yan et al. 2008). The building layout should be drawn in this software. Besides, the information of hvac system operating strategy, the indoor equipment and people should be input for simulation. After the detailed setting as the practical operation, the heating and cooling load of each room and the whole building can be calculated.

The heat pump model is using the typical performance curves of practical products in the market, as shown in Equation 2. The heating and cooling capacity and power consumption are the functions of water temperatures of evaporator and condenser.

Equation 2a: $Q_h = 5.91T_{ei} - 1.24T_{co} + 162.99 \quad R^2 = 0.9943$

Equation 2b: $P_h = 0.46T_{ei} + 0.64T_{co} + 5.78 \quad R^2 = 0.9815$

Equation 2c: $Q_c = -1.64T_{ci} + 201.21 \quad R^2 = 0.9956$

Equation 2d: $P_c = 0.65T_{ci} + 22.40 \quad R^2 = 0.9973$

where Q is the heating or cooling capacity of heat pump, kW; P is the power consumption of heat pump, kW; T is the temperature, ºC; the subscript h and c mean heating and cooling modes, respectively; ei, ci, and co are the fluid temperatures at the evaporator inlet, condenser inlet, and condenser outlet, respectively.

The water pump model is shown in Equation 3. The power consumption of water pump can be calculated by the flow rate, water head and pump efficiency.

Equation 3:

$$P_{wp} = \frac{G_{wp} \times H_{wp}}{\eta}$$

Where G_{wp} is flow rate of water pump, m^3/s; H_{wp} is water head of water pump, kPa; η is efficiency of water pump, 0.6.

By coding in the MATLAB based on the component models, the system model is established, as shown in Table 1. To analyse the influence of different climates on the system performance of ground source heat pump with seepage, three cities in cold region of China are selected, which are Harbin, Changchun, and Shenyang. Besides, an office building with $7000m^2$ is selected as the objective. 25 energy piles with the depth of 50m are adopted in the project and arranged in a matrix. The velocity of groundwater flow is 3×10^{-7} m/s.

Table 1: Models of main components in the system

Component models	Specific methods
Building model	Hourly building load simulation using DeST software
Energy piles model	Analytical energy piles group model considering various practical factors (Equation 1)
Heat pump model	Typical performance curves of practical products in the market (Equation 2)
Water pump model	Equation 3 based on flow rate, water head and water pump efficiency

4. RESULTS AND ANALYSES

Based on the proposed system model, the system performance is simulated and the influence of different climates is analysed. The typical climates in three cities, the building loads, the heat exchanges with the soil, heating COPs of heat pumps and the unsatisfied heating loads are investigated in this part.

4.1. The typical climates in three cities

The monthly average air temperatures in three cities are shown in Figure 4. The minimum monthly average air temperature is -18.8ºC in Harbin, -15.4ºC in Changchun and -11.5ºC in Shenyang. And the maximum air temperature is 22.9ºC in Harbin, 22.9ºC in Changchun and 25.7ºC in Shenyang. It shows that Harbin has the coldest winter and the summer in all three cities is not hot.

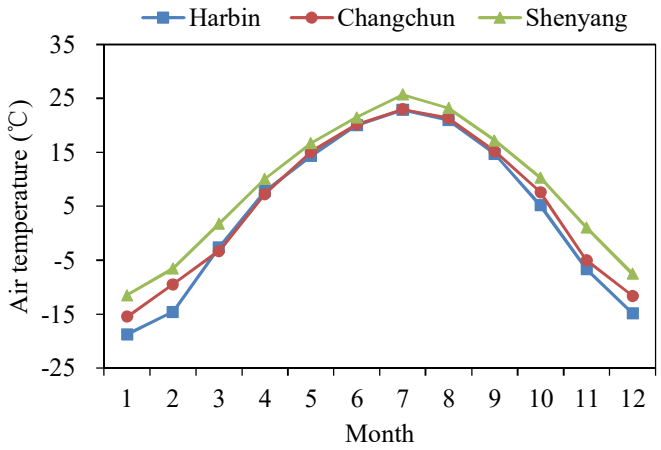

Figure 4: The monthly average air temperature of Harbin, Changchun and Shenyang

4.2. The building loads

The hourly building loads in different cities are simulated by a transient software named DeST and the monthly accumulated loads of three cities are shown in Figure 5. The maximum monthly heating loads are -120.91 MWh in Harbin, -111.91 MWh in Changchun and -98.63 MWh in Shenyang. The maximum monthly cooling loads are 33.47 MWh in Harbin, 33.71 MWh in Changchun and 59.23 MWh in Shenyang. It demonstrates that the buildings in these three cities are heating dominant. Harbin has the highest heating load and the lowest cooling load compared to other cities. Shenyang has the lowest heating load and the highest cooling load.

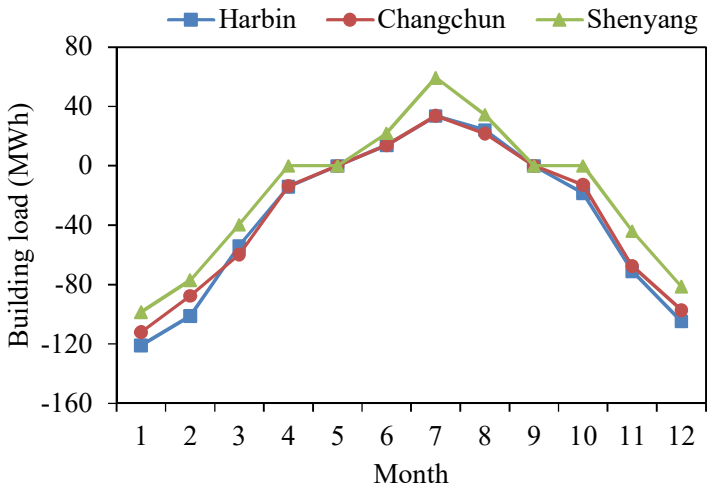

Figure 5: The monthly building load of an office building in Harbin, Changchun, and Shenyang

4.3. Heat extraction and injection

The monthly soil heat extraction and injection in ten years of three cities are shown in Figure 6.

The yearly accumulated soil heat extraction and injection are shown in Figure 6. In the first year, the accumulated heat extraction from the soil is -314.06 MWh and heat injection into the soil is 80.73 MWh in Harbin (Figure 6a). It has a serious soil thermal imbalance and the cold is accumulated in the soil. Since the soil temperature decreases yearly, the extracted heat driven by the heat pump decreases, causing the heating deficiency. Meanwhile, the soil thermal imbalance becomes gentle. The accumulated heat extraction is -223.70 MWh and heat injection is 79.28 MWh in the 10^{th} year. As shown in Figure 6b, the trend of yearly heat extraction and injection in Changchun is similar to that in Harbin. The accumulated heat extraction is -303.74 MWh and heat injection in Changchun is 78.55 MWh in the first year. In the 10^{th} year, they become -226.97 MWh and 76.97 MWh. Figure 6c shows that the decrease in yearly heat extraction in Shenyang is not that serious due to the relatively high soil temperature compared to the other two cities. The accumulated heat extraction and heat injection are -247.15 MWh and 135.12 MWh in Shenyang in the first year. They are -229.47 MWh and 132.99 MWh in the 10^{th} year.

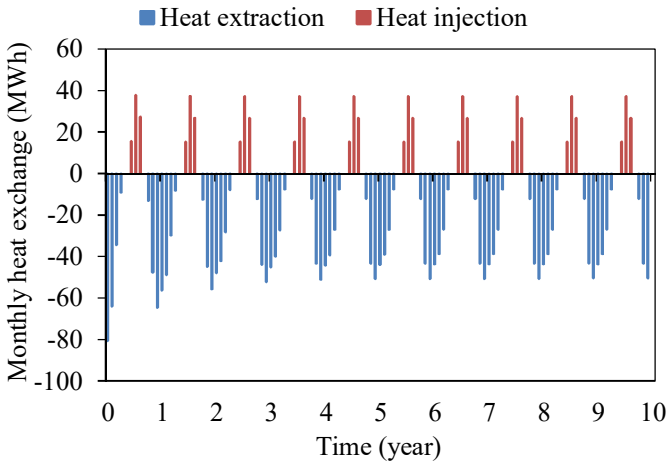

(a) Harbin

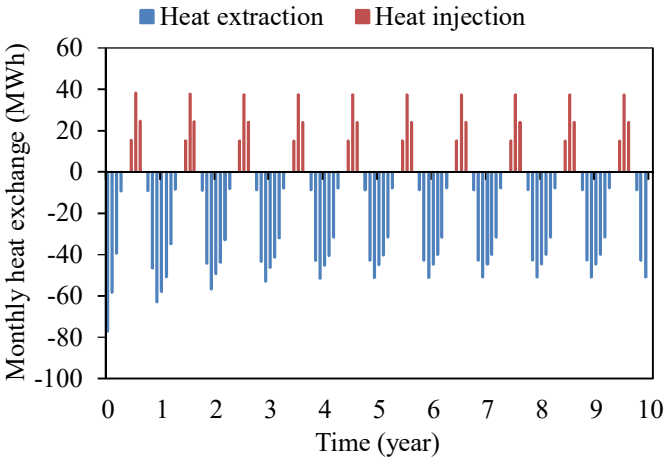

(b) Changchun

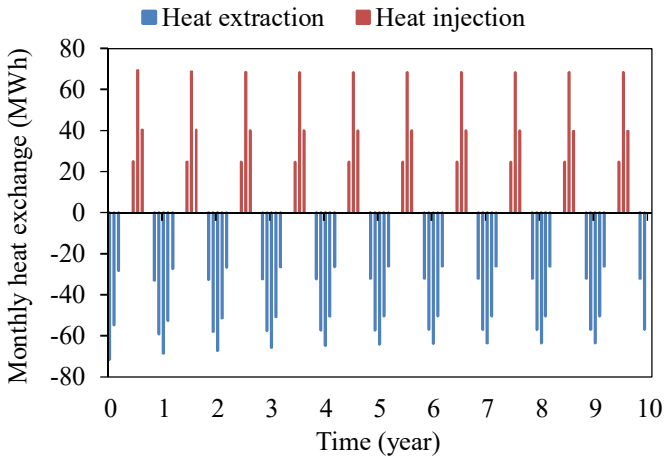

(c) Shenyang

Figure 6: The monthly accumulated heat extraction and injection in Harbin, Changchun, and Shenyang

4.4. Heating COP of heat pump

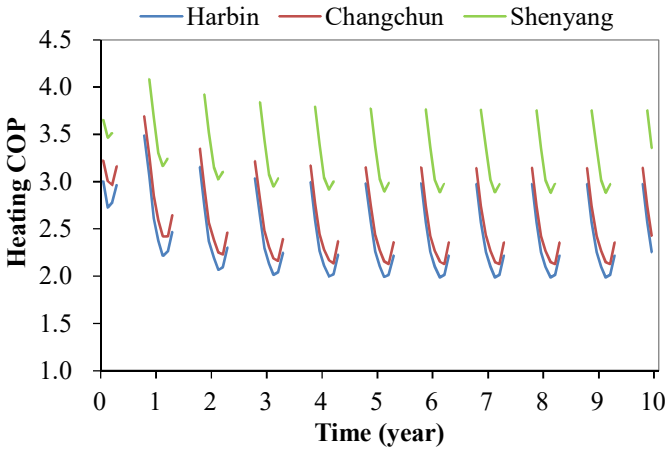

Figure 7: The monthly heating COP of heat pump in Harbin, Changchun, and Shenyang

The heating COP of heat pump is shown in Figure 7. Due to the dominant heating load and the cold accumulation in soil, the heating COP in three cities decreases yearly. The minimum COP in Harbin decreases from 2.61 in the first year to 1.99 in the tenth year. The minimum COP in Changchun decreases from 2.85 in the first year to 2.13 in the tenth year. The minimum COP in Shenyang decreases from 3.46 in the first year to 2.88 in the tenth year.

4.5. Unsatisfied heating load

The heating deficiency means that heat produced by the heat pump is less than the heating load. The monthly heating deficiencies of three cities are shown in Figure 8. All the cities have no heating deficiency in the first year. However, as the heat extraction from the soil decreases yearly, the heating deficiency increases yearly in these three cities. In Harbin, the maximum monthly heating deficiency is 23.9 MWh in the second year and 37.4 MWh in the tenth year, and the annually accumulated heating deficiency is 43.9 MWh in the second year and 74.0 MWh in the tenth year. In Changchun, the maximum monthly heating deficiency is 17.6 MWh in the second year and 32.0 MWh in the tenth year. In Shenyang, the maximum monthly heating deficiency is 0 in the 2nd year and 3.5 MWh in the 10th year.

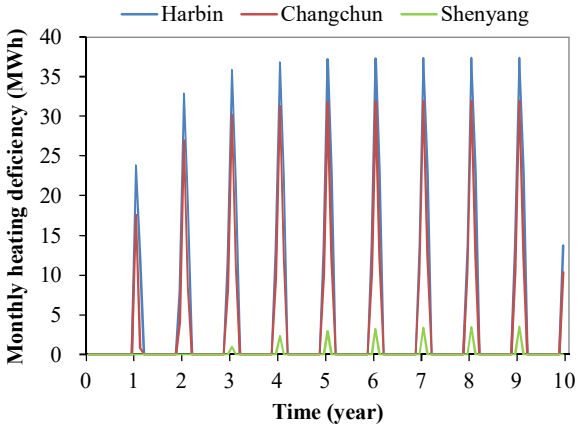

Figure 8: The monthly heating deficiency of Harbin, Changchun, and Shenyang

5. CONCLUSION

Annual soil thermal imbalance of ground source heat pump system in cold regions causes the cold accumulation in soil and heating deficiency of the building. To simulate the system performance, the system model is established, including the model of energy piles group with seepage, the heat pump model, the water pump model and the

building model. The influence of different climates on the system performance is investigated in this paper. Some conclusions are as follows.

The summer in Harbin, Changchun, and Shenyang is not hot. Harbin has the coldest winter, of which the minimum monthly average air temperature is -18.8 ºC. The buildings in these three cities are heating dominant. The maximum monthly heating loads are -120.91 MWh in Harbin, -111.91 MWh in Changchun and -98.63 MWh in Shenyang.

The soil heat extraction is obviously larger than heat injection in Harbin, Changchun, and Shenyang. The heat extraction decreases yearly because the soil temperature reduces. In Harbin, Changchun, and Shenyang, the annually accumulated soil heat extraction decreases from -314.06 MWh, -303.74 MWh and -247.15 MWh in the first year to -223.70 MWh, -226.97 MWh and -229.47 MWh in the tenth year; the minimum COP decreases from 2.61, 2.85 and 3.46 in the first year to 1.99, 2.13 and 2.88 in the tenth year; the maximum monthly heating deficiency is 37.4 MWh, 32.0MWh and 3.5MWh in the tenth year.

6. REFERENCES

Florides G, Kalogirou S, 2007. Ground heat exchangers—A review of systems, models and applications. *Renewable energy*, 32(15): 2461-2478.

Lee CK and Lam HN. 2013. A simplified model of energy pile for ground-source heat pump systems. *Energy*, 55: 838-845.

Liu Z, Xu W, Zhai X, et al. 2017. Feasibility and performance study of the hybrid ground-source heat pump system for one office building in Chinese heating dominated areas. *Renewable Energy*, 101: 1131-1140.

Morrone B, Coppola G, Raucci V. 2014. Energy and economic savings using geothermal heat pumps in different climates. *Energy Conversion and Management*, 88: 189–198.

Omer A M, 2008. Ground-source heat pumps systems and applications. *Renewable and sustainable energy reviews*, 12(2): 344-371.

Self SJ, Reddy BV, Rosen MA. 2013. Geothermal heat pump systems: status review and comparison with other heating options. *Applied Energy*, 101: 341–348.

Spitler JD. 2005. Editorial: ground-source heat pump system research—past, present, and future. *HVAC & R Research*, 11 (2):165–167.

Yan D, Xia J, Tang W, et al, 2008. DeST—An integrated building simulation toolkit Part I: Fundamentals, *Building Simulation*. Tsinghua Press, 1(2): 95-110.

You T, Li X, Cao S, et al. 2018. Soil thermal imbalance of ground source heat pump systems with spiral-coil energy pile groups under seepage conditions and various influential factors. *Energy conversion and management*, 178: 123-136.

Zhang W, Yang H, Lu L, et al. 2015. Study on spiral source models revealing groundwater transfusion effects on pile foundation ground heat exchangers. *International Journal of Heat and Mass Transfer*, 84: 119-129.

#198: Development of 3-D steady state thermal model of solar PV/T collector with sheet and tube heat exchanger

Anandhi PARTHIBAN[1], K.S. REDDY[1], Bala PESALA[2], T.K. MALLICK[3]

[1]*Heat Transfer and Thermal Power Laboratory, Department of Mechanical Engineering, Indian Institute of Technology Madras, Chennai 600 036, India*
[2]*Council of Scientific and Industrial Research - Central Electronics Engineering Research Institute, Chennai, 600113, India*
[3]*Environment and Sustainability Institute, University of Exeter Penryn Campus, Penryn TR10 9FE, UK*

This work involves the development of 3-D, steady state thermal model of PV with sheet and tube heat exchanger and aims to obtain the three-dimensional temperature distribution of various layers in the PV/T panel for various mass flow rates to identify the areas of hotspots in the PV surface. The computational domain of PV/T simulated for thermal analysis consists of glass cover, EVA, solar cell, EVA, Tedlar, absorber plate and cooling tube. The absorbed solar energy which is dissipated in the form of heat is used as volumetric heat generation boundary condition to solve the heat transfer equations and obtained the average temperature of the PV cell from which the temperature-dependent solar cell efficiency is obtained. Initial simulation is done by considering the volumetric heat generation at 15% cell efficiency from which the average efficiency of the cell is obtained and the governing equations are solved iteratively to obtain the temperature profiles. Simulations are performed for a range of mass flow rates at incident radiation of 1000 W/m^2 and 35°C ambient temperature. Results indicate a decrease in the panel temperature along the length with increase in mass flow rate due to increase convective heat transfer coefficient. At a mass flow rate of 55 LPH, the electrical efficiency and thermal efficiency are 18.16% and 49.09% respectively. Based on the analysis, it is recommended to cool the PV panel at high mass flow rates to obtain high efficiency and to reduce thermal stresses.

Keywords: photovoltaic; sheet and tube heat exchanger; thermal model; absorber plate

1. INTRODUCTION

Solar PV/T collector allows simultaneous production of heat and electricity. Solar PV converts the energy incident on it into electricity and the thermal collector placed at the bottom of the PV absorbs the heat from PV to decrease panel temperature and provides additional thermal output thereby increasing the overall output of the system.The performance of the PV module depends upon solar radiation available at the site and the temperature of the module. The solar radiation has a positive effect on the performance of the PV module and it can be increased by concentrating mirrors or by tracking. On the other hand, temperature has a negative effect and it decreases the power output from the PV panel. For every 1ºC rise in temperature there is 0.5% decrease in efficiency (Zsiborács et al., 2016). The energy that an electron receives from the incident photon is dissipated by flowing through the external circuit. But when the temperature of the PV panel is very high, the electron dissipates this energy by colliding with other atoms before it manages to get out of the cell and hence the absorbed photon energy is dissipated as heat instead of electricity. With the increase in cell temperature, the reverse saturation current increases which reduces the open circuit voltage (Suresh et al., 2013). Thus the decrease in open circuit voltage and increase in short circuit current due to temperature increase causes the efficiency of the panel to drop. The conversion efficiency of PV can be improved by reducing its operating temperature. Operating PV at high temperatures produces thermal stress which in the long run causes permanent damage to solar cell (Siddiqui and Arif, 2013) and reduces the payback period. In this work, a three-dimensional steady state thermal model for the water cooled PV/T collector with sheet and tube heat exchanger is developed. The PV/T collector with twelve tube configuration is considered in this study. For simplicity only one cooling tube with all its layers are considered for analysis. The modelling is done for different mass flow rates and the three-dimensional temperature distribution is obtained for all the layers. The results of the 3-D model are compared with the 1-D model obtained by solving energy balance equations.

1.1. Solar PV/T collector

There are various methods to cool the PV using air, water, PCM, fins etc. Among the cooling methods, water cooling is one of the efficient methods because of high heat transfer coefficients. The flow can be single pass or double pass. The heat exchangers are classified based on the flow pattern as direct flow, spiral and web flow (Fudholi et al., 2014). The different direct flow absorber-exchangers are sheet and tube, roll bond, box channel, V-groove and honey comb (Aste et al., 2014 and Ibrahim et al., 2009). The sheet and tube heat exchanger is commonly used because of better thermal performance, low temperature gradient along the length of collector and ease of fabrication. The sheet and tube heat exchanger is fabricated by soldering cooling tubes to absorber plate and are arranged in parallel under the PV panel. Herrando et al. (2019) studied the performance of sheet and tube exchanger for different number of risers considering thermal performance, cost and weight. It was reported that with the increase in the number of risers (n), the electrical and thermal efficiency increases. Beyond n=30, the efficiency asymptotes with additional increase in weight and cost of the system.The PV/T collector analysed in this work has 12 risers with tube pitch 78 mm. The aim of this work is to obtain 3-D temperature distribution of various layers in the PV/T panel for various mass flow rates/flux to identify the areas of hotspots in the PV surface.

2. PV/T COLLECTOR SYSTEM CONFIGURATION

The PV/T collector has solar PV module on top converting the incident radiation into electricity and thermal absorber plate with cooling ducts placed at the bottom of the PV to recover waste heat from PV. The PV/T configuration that is analysed in this work is depicted in Figure 1.

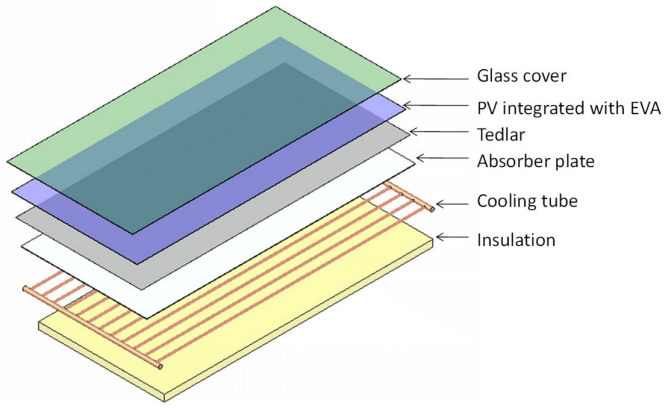

Figure 1: Exploded view of PV/T collector with sheet and tube heat exchanger.

As shown the various layers that constitutes PV/T collector are glass cover, PV integrated with EVA, Tedlar, absorber plate, cooling tube and insulation and enclosed in aluminium casing. The glass cover used has low iron content which allows short wavelength radiation to pass through it and blocks the long wavelength radiation reradiated from the PV surface. The semiconductor material is sandwiched between the layers of EVA to prevent PV from penetration of moisture and dust. The absorber plate is made of aluminium to which the copper cooling tubes are attached. Copper has high thermal conductivity and low specific heat capacity. The backside of the PV/T collector is insulated with rock wool to prevent any heat loss to the surroundings. The collector is subjected to convection and radiation loss at the top and bottom of the collector. The PV/T collector performance depends on number of cooling tubes, diameter of cooling tube, inlet water temperature and inlet mass flow rate The heat exchanger consists of parallel cooling tubes made of copper attached to the absorber plate called sheet and tube heat exchanger. There are totally twelve cooling tube attached to the absorber plate with tube pitch 78 mm.

3. NUMERICAL MODELLING

Thermal modelling of solar PV/T is performed to obtain the heat losses occurring in the collector and to optimise the flow rate in view of attaining maximum electrical and thermal yield from the collector. The modelling is done for the incident radiation of 1000 W/m^2 and the system is analysed for three mass flow rates - 11 LPH, 33 LPH and 55 LPH. The modelling involves both heat transfer and fluid flow analysis. Both three-dimensional modelling and one-dimensional modelling are performed to study the heat loss in PV/T collector.

3.1. Three-dimensional CFD Model

The steady state, three-dimensional modelling was developed using ANSYS 18.2. The PV/T collector is simulated to obtain its temperature distribution across various layers. The PV/T collector is analysed for laminar flow. In order to reduce the computational cost, the PV/T layers around one cooling tube is taken for modelling since the flow distribution among all the risers is expected to be uniform because of low pressure drops associated with single-phase flow for the range of flow rates considered in the current study.

Computational domain

The computational domain consists of PV semiconductor layer with its insulating and protective layers- glass cover, EVA, PV, EVA, Tedlar/back sheet, absorber plate, cooling tube and insulation. The computational domain is depicted in Figure 2. The thickness of various layers and its thermo-physical properties are detailed in Table 1. The optical properties of glass cover, solar cell and EVA are given in Table 2. The three-dimensional computational domain was generated using ANSYS DesignModeler. The geometric model is then meshed with structured hexahedral elements.

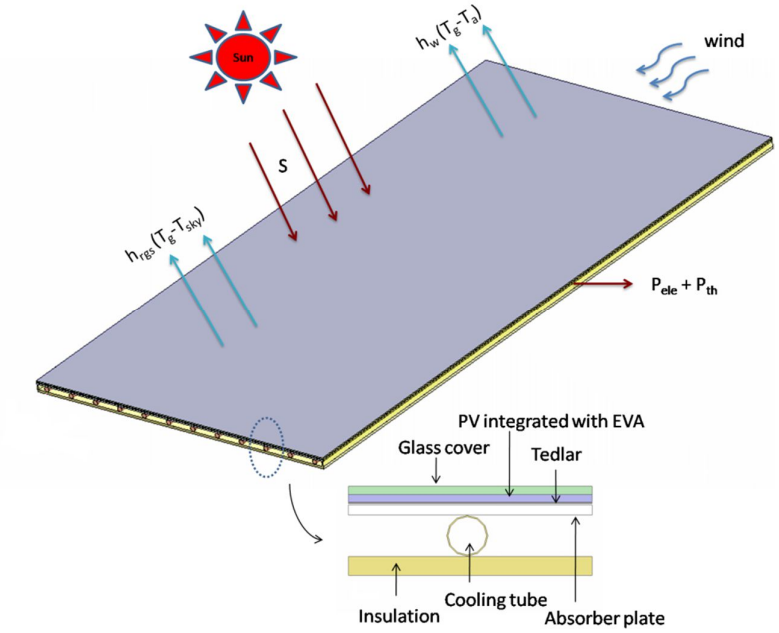

Figure 2: Solar PV/T collector with sheet and tube heat exchanger.

Table 1: Thermo-physical properties of various layers of PV/T collector (Baig et al., 2018)

Layer	Thickness (mm)	Thermal conductivity (W/m K)	Density (kg/m³)	Specific heat capacity (J/kg K)
Glass cover	3.2	1.8	3000	500
EVA top layer	0.5	0.35	960	2090
PV	2	148	2330	677
EVA bottom layer	0.5	0.35	960	2090
Tedlar	0.33	0.2	1200	1250
Absorber plate (Aluminium)	4	204	2710	910
Cooling tube (Copper)	1	386	8940	390
Water	-	0.63	998.2	4183
Insulation	50	0.05	180	1515

Table 2: Optical properties of various layers of PV/T (Zhou et al., 2015)

Layer	Transmissivity	Absorptivity	Reflectivity	Emissivity
Glass cover	0.92	0.04	0.04	0.85
EVA	0.90	0.08	0.02	-
PV	0.02	0.90	0.08	-

Methodology

The solar PV converts only a small amount of incident radiation into electricity and a significant amount is dissipated as waste heat. The generated heat is accounted in the numerical model by setting a volumetric heat source in the PV cell, top EVA and glass cover portions, while heat generation in EVA and glass cover remains constant that in PV varies with average temperature of the PV cell. The volumetric heat generation of PV as a function of PV average temperature is given by (Siddiqui et al., 2012)

Equation 1: Internal heat generation.

$$Q_{PV} = \frac{S\tau_g\tau_{EVA}\alpha_c(1-\eta_c)A_c}{V_c}$$

$$Q_{EVA} = \frac{S\tau_g\alpha_{EVA}A_{EVA}}{V_{EVA}}$$

$$Q_g = \frac{S\alpha_g A_g}{V_g}$$

Where:

- A_c = area of PV (m^2)
- A_{EVA} = area of top EVA (m^2)
- A_g= area of glass (m^2)
- Q_{EVA} = heat generation in top EVA (W/m^3)
- Q_g= heat generation in glass cover(W/m^3)
- Q_{PV} = PV heat generation (W/m^3)
- S = incident radiation (W/m^2)
- V_c = volume of PV (m^3)
- V_{EVA}= volume of top EVA (m^3)
- V_g= volume of glass cover (m^3)
- α_c = absorptivity of cell
- α_{EVA} = absorptivity of EVA
- α_g = absorptivity of glass cover
- η_c = solar cell efficiency
- τ_{EVA} = transmissivity of top EVA
- τ_g = transmissivity of glass cover

The efficiency of solar cell is function of average cell temperature (T_c) and is given by (Evans, 1981).

Equation 2: Electrical efficiency of solar cell as function of average PV temperature.

$$\eta_c = \eta_{ref}\ [1 - \beta\ (T_c - T_{ref})]$$

Where:

- T_c = solar PV cell temperature (K)
- T_{ref} = reference temperature (298 K)
- β = temperature coefficient (0.0045/ºC)
- η_{ref}= reference cell efficiency (20 %)

An iterative procedure is used to calculate the exact value of PV volumetric heat generation. Initial iteration is done by calculating PV heat generation at 15% of solar cell efficiency. The model is then solved to obtain the average temperature of PV and is substituted in equation 2 to obtain the cell efficiency. The iteration is repeated with internal heat generation value corresponding to new cell efficiency. The iterations are repeated until the error in temperature falls below 0.01°C. For any value of internal heat generation, the numerical model is solved by solving the continuity, momentum and energy equations and the behind-the-screen numerical procedure is detailed in ANSYS Theory Guide. The pressure-velocity coupling is solved by SIMPLE algorithm. The convergence criterion for the continuity, velocity and energy equations is 10^{-5}. Once the temperature distribution is obtained, the efficiency and power output are calculated. The various efficiencies are given by the following equations:

Equation 3: Electrical efficiency of module.

$$\eta_{ele} = \eta_c A_m \beta_c$$

Equation 4: Thermal efficiency of solar cell.

$$\eta_{th} = \frac{\dot{m} c_p (T_{out} - T_{in})}{S A_m}$$

Equation 5: Combined total efficiency of PV/T system.

$$\eta_{tot} = \eta_{th} + \frac{\eta_{ele}}{P}$$

Where:

- A_m= area of module (m^2)
- c_p = specific heat of water (4178 J/kgK)
- $\dot{m}$ = fluid mass flow rate (kg/s)
- P = Rankine power-plant efficiency (0.38)
- T_{in} = inlet water temperature (K)
- T_{out} = outlet water temperature (K}
- β_c= packing factor
- η_{ele}= electrical efficiency of module
- η_{tot}= combined total efficiency of PV/T
- η_{th}= thermal efficiency

Boundary conditions

The numerical model involves solving both heat transfer and fluid flow equations. The thermal and fluid flow boundary conditions applied to the computational domain are given separately in Table 3 and Table 4. The conversion efficiency of solar cell is a function of PV average temperature. A major fraction of the incident radiation is converted to heat due to low electrical conversion efficiency of the PV cell. The converted heat is accounted in the numerical model by setting a volumetric heat source in the PV cell portion which varies with average temperature of the PV cell. The amount of heat generated at 1000 W/m^2 of incident radiation and 15% of PV efficiency is calculated to be 320 kW/m^3. The glass cover on top is subjected to convection and radiation to the atmosphere. The wind velocity is taken to be 2.5 m/s, assuming ambient temperature of 35°C. The fluid flow problem is solved by specifying the velocity of the fluid entering the collector.

Table 3: Thermal boundary conditions

Region	Boundary Condition
Top surface of PV/T	Convection and radiation
Bottom surface of PV/T	Convection
PV	Heat source
Glass Cover	Heat source
EVA top	Heat source
Water Inlet	Fluid inlet temperature

Table 4: Fluid flow boundary conditions

Region	Boundary Condition
Water inlet	Fluid velocity
Water outlet	Pressure outlet
Cooling tube wall	No slip

Grid independence study

Grid independence study is performed by varying the element size for the conditions - 11 LPH flow rate, 1000 W/m^2 incident radiation and 15% solar cell efficiency – and monitoring the outlet water temperature and PV average temperature. With initial element size of 2.86x10^{-4} m, the outlet water temperature obtained is 56.73°C. On further reduction in element size, there is a change in outlet water temperature due to increase in number of elements and number of nodes. Further refinement in element size resulted in increased water temperature and the increase in element size is continued till the outlet water temperature stabilizes with element size. The variation of outlet water temperature with number of elements is depicted in Figure 3. For element size of 7.15x10^{-4} m, it is found that the outlet water temperature and the PV average temperature stabilize; with number of elements generated around 4 million.

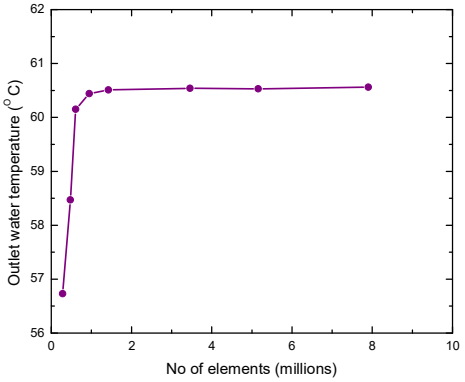

Figure 3: Grid independence study-variation of outlet water temperature with number of elements.

3.2. One-dimensional analytical model

The thermal model used for the determination of temperature of PV/T collector is shown. The model consists of PV with all its layers placed over conventional solar thermal collector. The steady state thermal model was developed by applying energy balance to various layers of the PV/T collector. The energy balance equation for the glass cover, PV, absorber plate, and the fluid is given below. The energy balance equations are arrived with following assumptions.

- one dimensional and steady state heat transfer is assumed
- The convection loss coefficient both at the top and bottom of the collector is the same
- The fluid is assumed to divide equally on all the riser tubes
- The heat capacity of various layers of the PV are neglected
- The properties of materials are assumed to be constant with temperature
- The attenuation of incident radiation by dust accumulation on glass cover is ignored
- There is no heat exchange from the collector to the manifold of the heat exchanger

The energy balance for the glazing, PV layer, absorber plate, water in cooling tube and back case of the collector yields following equations:

Equation 6: Energy balance for the glass cover.

$$S\,\alpha_g + h_{c\text{-}g}(T_c\text{-}T_g) = h_w(T_g\text{-}T_a) + h_{rgs}(T_g\text{-}T_{sky})$$

Equation 7: Energy balance for solar cell.

$$S\tau_g\tau_{eva}\alpha_c = S\,\tau_g\tau_{eva}\eta_c + h_{c\text{-}g}(T_c\text{-}T_g) + h_{c\text{-}p}(T_c\text{-}T_p)$$

Equation 8: Energy balance for absorber plate.

$$h_{c\text{-}p}(T_c\text{-}T_p) = F'\,h_f(T_p\text{-}T_f) + h_{p\text{-}b}(T_p\text{-}T_b)$$

Equation 9: Energy balance for the fluid domain.

$$F'\,h_f(T_p\text{-}T_f) = \frac{\dot{m}C_p}{B}\frac{dT_f}{dx}$$

Equation 10: Energy balance for the back case.

$$h_{p\text{-}b}(T_p\text{-}T_b) = h_w(T_b\text{-}T_a)$$

Where:

- B = width of the collector (m)
- F' = fin efficiency factor
- $h_{c\text{-}g}$ = conduction loss coefficient from cell to glass cover(W/m^{2}K)
- $h_{c\text{-}p}$ = conduction loss coefficient from cell to absorber plate
- h_f = fluid convection coefficient (W/m^{2}K)
- $h_{p\text{-}b}$ = conduction loss coefficient from absorber plate to back case through back insulation (W/m^{2}K)
- h_w = wind convection coefficient (W/m^2 K)
- h_{rgs} = radiation from glass cover to sky (W/m^{2}K)
- T_a = ambient temperature (K)
- T_b = back case temperature (K)
- T_f = fluid temperature (K)
- T_g = glass cover temperature (K)
- T_p = absorber plate temperature (K)
- T_{sky} = sky temperature (K), T_a-6

The PV/T collector is subjected to convection and radiation at the top and convection at the bottom of the collector. The heat transfer coefficients and fin factors are given by the following equations:

Equation 11: Correlation for wind convection coefficient for wind velocity 'V'.

$$h_w = 5.7 + 3.8\,V$$

Equation 12: Radiation heat transfer coefficient from glass cover to ambient.

$$h_{rgs} = \sigma\varepsilon_g({T_g}^2 + {T_{sky}}^2)(T_g + T_{sky})$$

Equation 13: Conduction loss coefficient from solar cell to glass covers.

$$h_{c\text{-}g} = \left(\frac{\delta_g}{K_g} + \frac{\delta_{EVA}}{K_{EVA}}\right)^{-1}$$

Equation 14: Conduction loss coefficient from cell to absorber plate.

$$h_{c\text{-}p} = \left(\frac{\delta_c}{K_c} + \frac{\delta_{EVA}}{K_{EVA}} + \frac{\delta_t}{K_t}\right)^{-1}$$

Equation 15: Conduction loss coefficient through back insulation from absorber plate to back case.

$$h_{p\text{-}b} = \frac{K_{in}}{\delta_{in}}$$

Equation 16: Fin efficiency factor.

$$F' = \frac{\frac{1}{U_L}}{W\left(\frac{1}{U_{L[(W-D)F+D]}} + \frac{1}{\pi D h_f} + \frac{1}{C_b}\right)}$$

Equation 17: Fin factor.

$$F = \frac{\tanh m\left(\frac{W-D}{2}\right)}{m\left(\frac{W-D}{2}\right)}$$

Equation 18: Fin parameter.

$$m = \sqrt{\frac{U_L}{K_{abs}\delta_{abs}}}$$

Where:

- C_b = bond conductance (W/mK)
- D = diameter of the tube (m)
- F = fin factor
- K_{abs} = thermal conductivity of absorber plate material (W/mK)
- K_c = thermal conductivity of solar cell material (W/mK)
- K_{EVA} = thermal conductivity of EVA (W/mK)
- K_g = thermal conductivity of glass cover (W/mK)
- K_{in} = thermal conductivity of insulator (W/mK)
- K_t = thermal conductivity of Tedlar (W/mK)
- m = fin parameter
- U_L = overall heat loss coefficient (W/m^2K)
- W = width of the fin (m)
- δ_{abs}= absorber plate thickness (m)
- δ_c = solar cell thickness (m)
- δ_{EVA} = EVA thickness (m)
- δ_g= glass cover thickness (m)
- δ_{in}= insulation thickness (m)
- δ_t= Tedlar thickness (m)
- ε_g = emissivity of glass cover
- σ = Stefan-Boltzmann constant (5.67×10^{-8} W/ m^2 K^4)

Details of PV/T modelling can be found from (Tiwari and Sodha 2006).The energy balance for various layers is solved using MATLAB to obtain the temperature distribution.

3.3. Validation

The developed 1-D and 3-D thermal models were validated against experimental results obtained from (Sakellariou and Axaopoulos, 2018). Details of module dimensions and testing conditions can be found in Sakellariou and Axaopoulos, 2018. Figure 4 shows outlet water temperature variation with radiation obtained using 1-D model, 3-D model and experiment for the input conditions-mass flow rate 95.43 LPH, inlet water temperature 24.58 ºC, ambient temperature 24.50ºC and wind velocity 1.45 m/s. One-dimensional modelling is done using MATLAB. A MATLAB code was written to solve energy balance equations across various material layers of PV/T to obtain the temperature distribution. The 3-D model was solved iteratively by considering PV as source of heat generation. The deviation in outlet water temperature between the experiments and that obtained from the developed models is less than 5%.

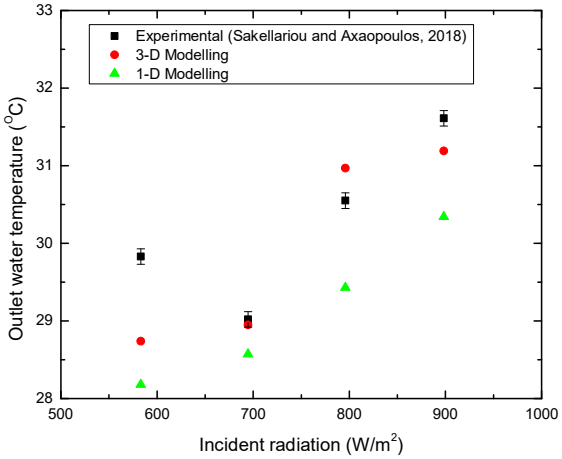

Figure 4: Validation for outlet water temperature obtained using 3-D model, 1-D model and experimental results

4. RESULTS AND DISCUSSION

Numerical modelling is done for incident radiation of 1000 W/m^2 and 35ºC of ambient temperature. The wind velocity was taken to be 2.5 m/s. The thermal model is analysed for three mass flow rates - 11 LPH, 33 LPH and 55 LPH. The temperature variation along the length of collector for all the flow rates is given in Figure 5. It can be seen that for any flow rate the solar PV cell has the highest temperature, as its conversion efficiency is very low and it dissipates most of the energy incident on the cell into heat. The temperature of Tedlar and glazing are very

close to cell temperature because of heat conduction from the solar cell and its small thickness. For flow rate of 55 LPH, the average temperature of PV was found to be 44.39ºC. The heat dissipated by the solar cell is effectively carried to the absorber plate through conduction. The difference between the solar cell temperature and the absorber plate temperature decreases along the length of the collector. Water enters the collector at inlet temperature of 30ºC and it reaches a maximum of 63ºC at outlet for 11 LPH, 49ºC for 33 LPH and 42ºC for 55 LPH. The bottom side of the PV/T collector is exposed to the ambient where heat loss occurs through insulation by conduction and subsequent convection.

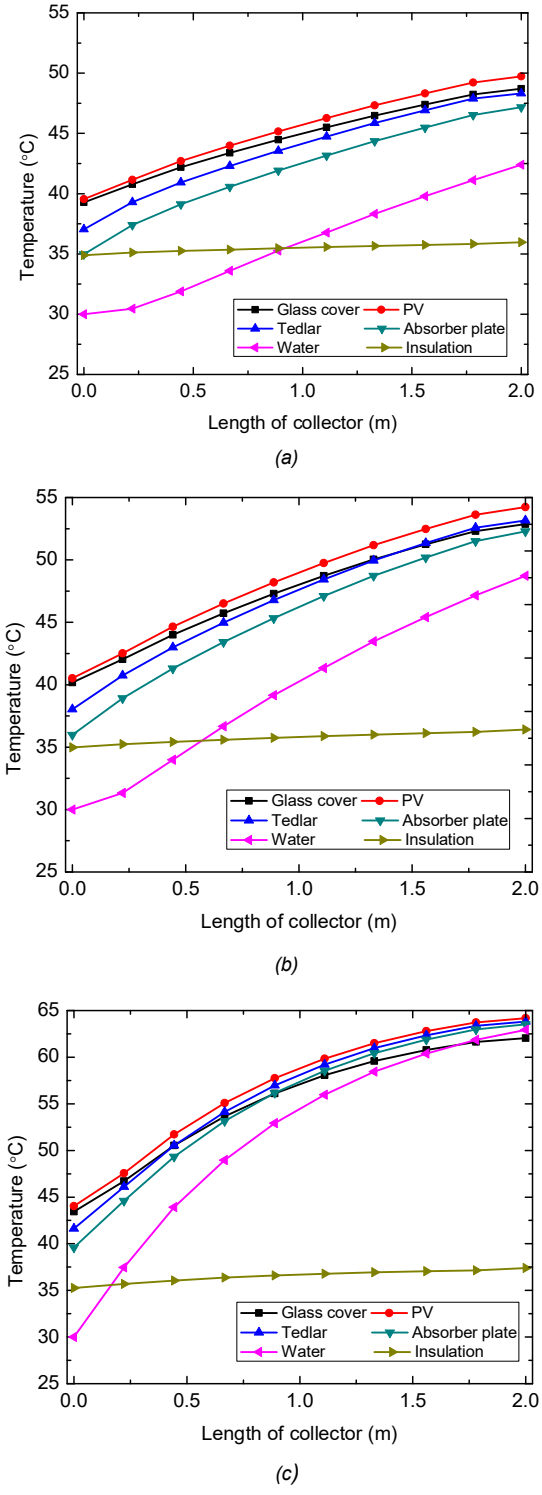

Figure 5: Temperature profile along length of collector for the flow rate (a) 55 LPH (b) 33 LPH (c) 11 LPH.

The temperature of the back case remains almost constant along the length which is due to poor thermal conductivity of glass wool. The temperature of water increases steadily along the length of the collector. The fluid temperature gain obtained for the flow rate of 11 LPH is 33ºC and 12ºC for 55 LPH, indicating the potential of PV/T for low temperature thermal applications. As the water removes the heat from the absorber plate, the temperature of PV along its length is reduced which improve its conversion efficiency. For the range of flow rate considered, the flow is found to be laminar. The temperature contours of glass cover, solar cell, absorber plate and water obtained for the flow rate of 55 LPH are shown in Figure 6. The variation of mass flow rate shows that the performance of the collector increases with increase in mass flow rate. The efficiency increase with increase in mass flow rate is given in Figure 7. At higher flow rates, the convection heat transfer coefficient is more due to high fluid velocity. Thus the temperature decreases with increase in flow rate. The average temperature of PV for the flow rate of 11 LPH is 57.15ºC indicating that the PV is operating at the efficiency of 17.11%. Similarly at 33 LPH, the average temperature of PV is 48.51ºC and at 55 LPH it is 44.39ºC.

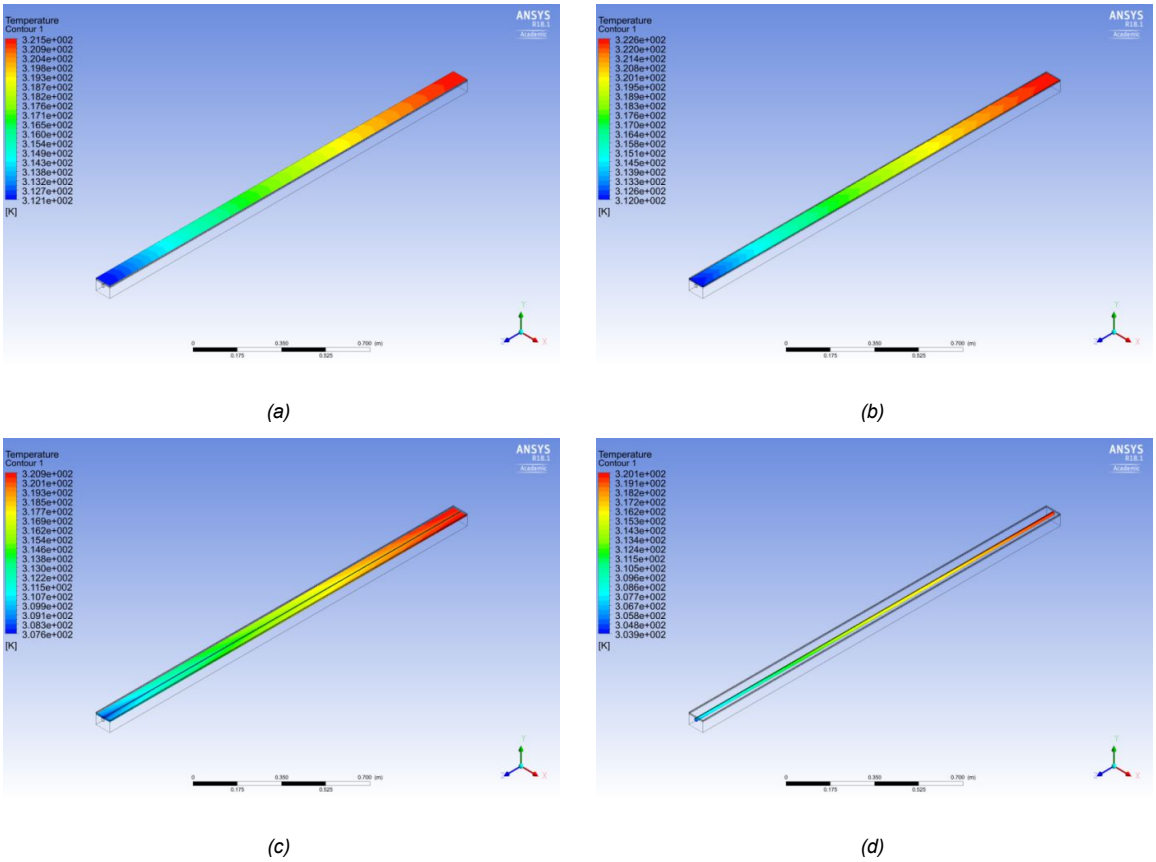

Figure 6: Temperature contours at 55 LPH flow rate for (a) Glass cover (b) solar cell (c) absorber plate (d) water domain.

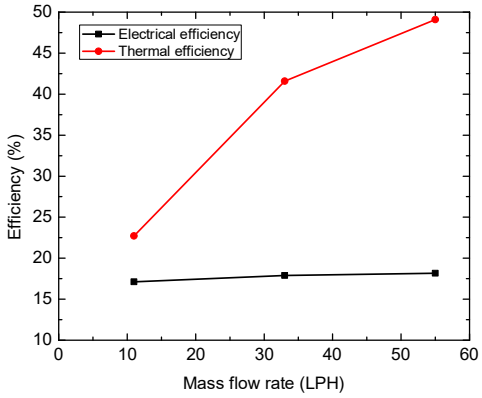

Figure 7: Electrical and thermal efficiency versus flow rate.

5. CONCLUSION

In this work, three-dimensional steady state numerical modelling was done for the PV/T collector. The equations governing heat transfer and fluid flow are solved using ANSYS FLUENT. The PV/T collector analysed is the water cooled PV with sheet and tube heat exchanger. The absorber plate is made of aluminium with copper cooling tubes welded to it. The numerical modelling is done for various mass flow rates - 11 LPH, 33 LPH and 55 LPH. The performance of collector is found to increase with increase in mass flow rate. At flow rate of 55 LPH, the combined electrical and thermal efficiency of PV/T collector was found to be 96% with 18.16% electrical efficiency and 49.09% thermal efficiency. The 3-D model is validated against the 1-D model which was validated against experimental results.

6. REFERENCES

ANSYS FLUENT Theory Guide Release 14.0, 2011

Aste, N., del Pero, C. and Leonforte, F., 2014. Water flat plate PV–thermal collectors: a review. *Solar Energy*, *102*, pp.98-115.

Baig, H., Jani, R., Markam, B.K., Maiti, S. and Mallick, T.K., 2018. Modelling and experimental analysis of a seasonally tracked V-trough PV/T system in India. Solar Energy, 170, pp.618-632. Evans, D.L., 1981. Simplified method for predicting photovoltaic array output. Solar energy, 27(6), pp.555-560.

Fudholi, A., Sopian, K., Yazdi, M.H., Ruslan, M.H., Ibrahim, A. and Kazem, H.A., 2014. Performance analysis of photovoltaic thermal (PVT) water collectors. *Energy conversion and management*, *78*, pp.641-651.

Herrando, M., Ramos, A., Zabalza, I. and Markides, C.N., 2019. A comprehensive assessment of alternative absorber-exchanger designs for hybrid PVT-water collectors. *Applied energy*, *235*, pp.1583-1602.

Ibrahim, A., Othman, M.Y., Ruslan, M.H., Alghoul, M., Yahya, M., Zaharim, A. and Sopian, K., 2009. Performance of photovoltaic thermal collector (PVT) with different absorbers design. *WSEAS Transactions on Environment and Development*, *5*(3), pp.321-330.

Sakellariou, E. and Axaopoulos, P., 2018. An experimentally validated, transient model for sheet and tube PVT collector. *Solar Energy*, *174*, pp.709-718.

Siddiqui, M.U. and Arif, A.F.M., 2013. Electrical, thermal and structural performance of a cooled PV module: Transient analysis using a multiphysics model. *Applied energy*, *112*, pp.300-312.

Siddiqui, M.U., Arif, A.F., Kelley, L. and Dubowsky, S., 2012. Three-dimensional thermal modeling of a photovoltaic module under varying conditions. *Solar energy*, *86*(9), pp.2620-2631.

Suresh, V., Naviynkumar, S. and Kirubakaran, V., 2013, December. Improved power output of PV system by low cost evaporative cooling technology. In *2013 International Conference on Green Computing, Communication and Conservation of Energy (ICGCE)* (pp. 640-643). IEEE.

Tiwari, A. and Sodha, M.S., 2006. Performance evaluation of solar PV/T system: an experimental validation. *Solar energy*, *80*(7), pp.751-759.

Zhou, J., Yi, Q., Wang, Y. and Ye, Z., 2015. Temperature distribution of photovoltaic module based on finite element simulation. Solar Energy, 111, pp.97-103.

Zsiborács, H., Pályi, B., Pintér, G., Popp, J., Balogh, P., Gabnai, Z., Pető, K., Farkas, I., Baranyai, N.H. and Bai, A., 2016. Technical-economic study of cooled crystalline solar modules. *Solar Energy*, *140*, pp.227-235.

#200: A comparative model study on forecasting energy efficiency of the cryogenic liquefaction system in the meaning of sustainability perspective

Elif ALTINTAS[1], Mert TOLON [2], Arif KARABUGA[3], Zafer UTLU[4]

[1]*Istanbul Gedik University, Department of Computer Engineering, Istanbul, Turkey, elif.altintas@gedik.edu.tr*
[2]*Istanbul Gedik University, Department of Civil Engineering, Istanbul, Turkey, mert.tolon@gedik.edu.tr*
[3]*Istanbul Gedik University, Energy Technologies Application and Research Center, Istanbul, Turkey, arif.karabuga@gedik.edu.tr*
[4]*Istanbul Gedik University, Department of Mechanical Engineering, Istanbul, Turkey, zafer.utlu@gedik.edu.tr*

Due to the lack of energy all over the world, the importance of sustainable energy resources and new energy technologies is a consideration for both practitioners and also academicians. Nowadays, the application of thermal engineering is at the top of the sustainable approaches that focus on energy efficiency. Also, as a necessity for improving the efficiency of all of the engineering research fields, the Artificial Neural Network (ANN) model is used to forecast different types of energy efficiency problems in thermodynamic literature. In this paper, the ANN model for thermodynamic evaluation of nitrogen that is obtained by cryogenic liquefaction method in refrigeration systems is applied by two different software programmes. The Engineering Equation Solver (EES) program is used to obtain 441 experimental measurements of the liquefaction. Then, both toolboxes were evaluated with artificial neural networks. This study aims to forecast the exergy efficiency of the cryogenic liquefaction system by applying different neural network architecture types (back propagation, general regression, etc.) in two different developed model. This ANN has been trained using temperature, pressure, enthalpy, and entropy data as inputs for both models. The results obtained from the two models were also compared with the input-output model estimates with reasonable accuracy. This study presents a new procedure for identifying the structure and parameters of hidden layers in ANN models with a higher accuracy ratio and can make predictions in terms of thermodynamic results. Finally, the results of user-friendly and interoperable programs in the package programs based on ANN are compared and meaningful comparative results found.

Keywords: sustainability; cryogenic liquefaction system; neural networks; MATLAB neural network toolbox

1. INTRODUCTION

Energy is vitally important to sustain life on Earth and is needed for economic, social, and environmental development. Energy resources and energy efficiency play a significant role in each country's economic growth and development in the industrial sector (Razmjoo, 2019). It is essential that all governments identify sustainable energy alternatives and define their own policies based on current energy approaches. In this context, numerous studies are being carried out for energy efficiency in response to environmental, economic and social problems in line with sustainable engineering solutions. In this regard, in terms of the energy sector, in addition to developing technologies of renewable energy sources, predicting the level of efficiency is also in the foreground in sustainable engineering approaches. Energy use is of paramount importance in all areas of the industrial sector. In particular, low temperature requirements in the cryogenic applications used in many fields of the sector such as Steel, Cast irons, Non-ferrous metals, Alloys, Carbides, Plastics and Ceramics require high energy consumption. As an example, Cryogenic Liquefaction System has taken its place in the literature in terms of efficient use of energy. Nitrogen used in the petrochemical and paint industries, material manufacturing sector, food freezing, and particle physics are obtained through cryogenic liquefaction which is one of the methods of industrial separation.

Cryogenic applications can be categorised into several categories;

i. separation and liquefaction of gases,
ii. storage and transport of gases,
iii. medical and health science
iv. particle physics
v. sports activities (oxygen tube and diving clothing)
vi. material science (iron forge, steel forge, semiconductive and superconductive technology)
vii. food, agricultural, chemical, and manufacturing technology.

Cryogenic separation and cryogenic liquefaction have a high energy consumption. In this context, the biggest cost of cryogenic air separation facilities is electricity. The cost of annual electricity consumption by these industrial gas producers reaches over 1$ billion per year. Significant economic profits can be provided with the help of measures in this field to reduce electricity consumption and cost (Chen et al., 2010). When the total final energy is taken into consideration in many countries, the industrial sector is responsible for two-fifths of the energy consumed (Utlu et al., 2013). Energy modelling is created based on current technology and analysis methods to minimise system costs while improving system efficiency (Ozturk et al. 2004). Nowadays, one of the methods used to determine energy efficiency is an Artificial Neural Network (ANN). ANN has been promised as a more effective method compared to the more traditional energy modelling methods for interpreting energy efficiency by finding quick solutions and speeding up data analysis. When the literature is examined, some works about the use of ANN in energy systems have been published. Azadbakht et al. used the ANN method for predicting osmotic pretreatment based on the energy and exergy analyses in microwave drying of orange slices (Azadbakht et al., 2018). Demirezen et al. found a novel ANN model to predict the outdoor temperature that could potentially replace smart sensors with a data-driven model utilising weather station data at time resolutions of 2 minutes and 1 hour with 0.95 R error in average (Demirezen et al., 2019).

2. MATERIAL AND METHODS

This section discusses cryogenic nitrogen liquefaction system descriptions, thermodynamic analysis, and construction of ANN architecture.

2.1. Liquefaction System Description

The analysis of the cryogenic liquefaction system is based on the following main assumptions:

- The system works under steady state conditions
- The changes in kinetic and potential energies are neglected
- The pressure drops and heat losses in the connecting pipes are neglected
- The compressor works with the adiabatic compression process
- The system operates at the atmospheric condition of T_0= 25 ºC and P_0=1 bar as the reference state.

In Figure 1, a flow diagram of a liquefaction system is introduced. When the literature is examined, the nitrogen liquefaction system was investigated by using a cryogenic method which is integrated into a real air separation unit was carried out below 120 K of the cryogen (Karabuga et al., 2018; Weisend et al., 1998).

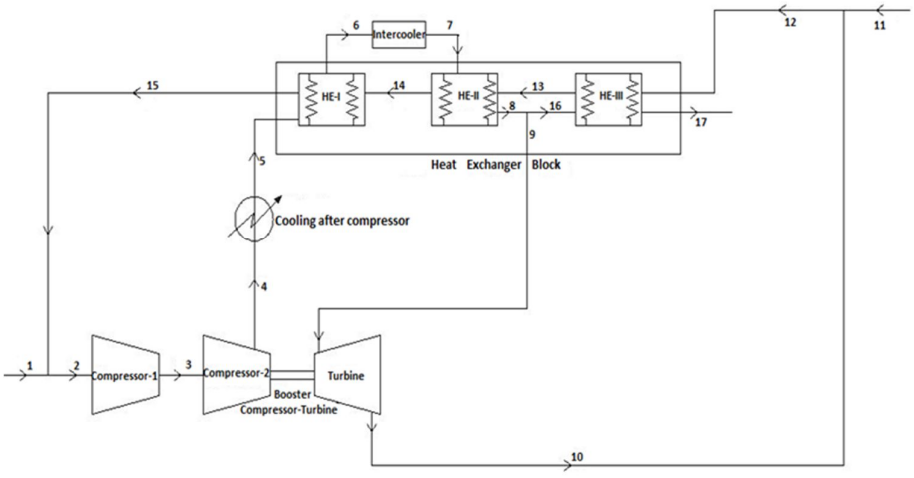

Figure 1: Double column internal flows by Linde Group

2.2. Thermodynamic Analysis

The first law of thermodynamics (FLT) defines the conservation of energy. The energy contained in all input streams of a process must be taken into account in the output streams accumulated in the system from the same process or in which the transaction takes place (Utlu et al., 2010). Exergy is an important concept to understand with the sustainability of energy, environmental effects, and utilising of energy (Utlu et al., 2006). There are many explanations of the Exergy concept. In general, exergy is identified as a form of energy or a measure of its usefulness or the quality or potential to cause change. Unlike energy, exergy is converted only during ideal operations and is destroyed by irreversibility in actual operations. Exergy is a measure of the maximum capacity of the system to do useful work when it reaches a certain final state in equilibrium with its environment (Utlu et al., 2007).

This section covers some of the key aspects of thermodynamics in terms of the energy and exergy equations used in the cryogenic liquefaction system. For a steady-flow process, the four balance equations are applied to find the work and heat change, the rate of exergy change, the rate of irreversibility, the energy and exergy efficiencies. The exergy is the utilisable, quality of energy, or the potential of the capability to the work. To calculate the exergy, mass balance and energy balance are firstly established when analysing the first law of thermodynamics. The thermodynamic analysis of the cryogenic liquefaction system was investigated by using the Engineering Equation Solver (EES) program.

Table 1: The thermodynamic analysis of the cryogenic liquefaction system

Temperature (K)	Pressure (Bar)	Enthalpy (kJ/kg)	Entropy (kJ/kgK)	Specific Volume (m3/kg)	Exergy (kJ/kg)
64	0.5	-149	2.452	0.001158	836.6
⋮	⋮	⋮	⋮	⋮	⋮
71	0.5	-134.9	2.661	0.001199	789.1
64	1	-149	2.452	0.001158	836.7
⋮	⋮	⋮	⋮	⋮	⋮
77	1	-122.7	2.825	0.001238	752.9
64	2	-148.9	2.451	0.001157	836.9
⋮	⋮	⋮	⋮	⋮	⋮
83	2	-110.3	2.978	0.001282	720
64	3	-148.8	2.451	0.001157	837.2
⋮	⋮	⋮	⋮	⋮	⋮
87	3	-101.9	3.076	0.001315	699.6
64	4	-148.7	2.45	0.001157	837.4
⋮	⋮	⋮	⋮	⋮	⋮
91	4	-93.35	3.171	0.001352	680.2
64	5	-148.6	2.45	0.001157	837.7
⋮	⋮	⋮	⋮	⋮	⋮
93	5	-88.98	3.217	0.001371	670.9

Temperature (K)	Pressure (Bar)	Enthalpy (kJ/kg)	Entropy (kJ/kgK)	Specific Volume (m3/kg)	Exergy (kJ/kg)
64	10	-148.2	2.447	0.001155	838.9
⋮	⋮	⋮	⋮	⋮	⋮
103	10	-66.13	3.443	0.00149	627.1
64	15	-147.8	2.444	0.001154	840.1
⋮	⋮	⋮	⋮	⋮	⋮
110	15	-48.52	3.601	0.001608	598.1
64	20	-147.4	2.442	0.001153	841.3
⋮	⋮	⋮	⋮	⋮	⋮
115	20	-34.53	3.718	0.001724	577.6
64	25	-147	2.439	0.001152	842.5
⋮	⋮	⋮	⋮	⋮	⋮
119	25	-22.01	3.817	0.001852	560.8
64	30	-146.6	2.436	0.001151	843.7
⋮	⋮	⋮	⋮	⋮	⋮
123	30	-6.615	3.936	0.002065	541
64	33	-146.4	2.435	0.00115	844.4
⋮	⋮	⋮	⋮	⋮	⋮
125	33	2.877	4.007	0.002236	529.4

When Table 1 is examined, the temperature and the pressure values of the 441 data change between 64 - 125 K, 0.5 - 33 Bar, respectively.

2.3. Artificial Neural Networks

Machine learning is a concept where a machine can decide how to perform a task without specific instruction having learnt from data submitted through computer programs, algorithms and mathematical formulations. Artificial neural networks are one of the applications developed in the field of machine learning. Data is given to the network in the computer, and it is requested that the learning process of the network is performed by looking at the results of these samples without any other information. The network performs learning using its system, and then it produces solutions or results by using the information that it has never seen.

In short, the ANN architectures have been developed to cope with problems which are practical. In any kind of problem in any kind of sector, while the input parameters represent the problem presented to the network, while the parameters in the output processing section give the calculation results obtained by the neural network (Tolon, 2007). Moreover, the ANN learns the given data and aims to change the information similar to the human brain. The architecture of the ANN model consists of the network architecture, the number of hidden layers, and the number of hidden neurons. Inputs which are obtained from given data send a signal to the neurons to process the signals regionally through a transfer function and an activation function by processing inputs and convert to the output of the particular neuron (Demirezen et al., 2019). The general view of ANN is expressed in Figure 2.

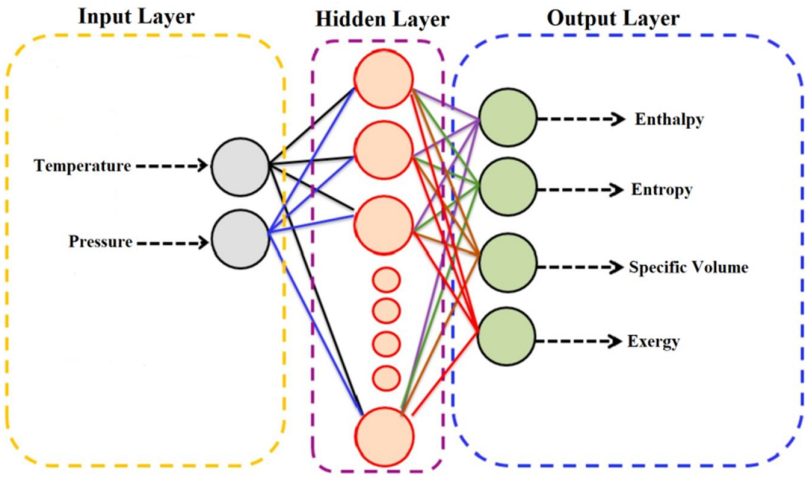

Figure 2: Schematic diagram of an artificial neural network.

ANN model consists of inputs (x_i), weights (w_i), transfer function (NET), activation function (f) and outputs (y_i). It can be given as follows:

Equation 1: Transfer function of Artificial Neural Network: $NET = \sum_{i=1}^{n} x_i . w_i$

Equation 2: Outputs of Network Architecture: $y_i = f(NET)$

Where:

- $x_i = Inputs$
- $w_i = Weights$
- $NET = Transfer\ function$
- $f = Activation\ function$
- $y_i = Outputs$

In the literature, there are many learning rules that can be used in artificial neural networks. These learning rules vary according to the structure of the problem and the purpose of use. Learning rules used in the literature can be given as follows (Haykin, 1998):

- Error-Correction Learning
- Memory-Based Learning
- Hebbian Learning
- Competitive Learning
- Boltzman Learning
- Hopfield Learning
- Widrow and ADALINE
- Kohenen Network

In this study, Error-Correction that is learning a rule to compare the system output with the actual output and to direct the error to the training is processed. Error values are used to adjust weights by an algorithm which is a back propagation algorithm (Haykin, 1998).

Equation 3: Error value of Network Architecture: $e = d - y$

Where:

- $e = error$
- $d = expected\ output\ of\ system$
- $y = output\ of\ system$

Error-Correction Learning algorithms try to minimise error value in each training iteration. It is important that the functions and algorithms to be used during this training should be chosen to give the best results. In this work, training algorithms used are Levenberg-Marquardt, Bayesian Regularization, and Scaled Conjugate Gradient in MATLAB Neural Network Toolbox. The developed model allows us to choose which variables will be used as network inputs and outputs, and to either specify or compute the minimum and maximum value for each variable. According to this, Temperature (K) and Pressure (Bar) are taken into consideration as input parameters. Enthalpy (kJ/kg), Entropy (kJ/kgK), Specific Volume (m3/kg) and the Exergy (kJ/kg) of the system are the output parameters that are used in the developed ANN model. Data classification is performed to present data to the network. Which variables are independent or dependent, how much of the data should be used for verification or testing should be introduced to the network. In this work, the data set is divided into three sections: training validation and testing. This classification is processed as 70% training, 15% testing, 15% validation or 80% training, 10% testing, 10% validation in literature (Hamzacebi, 2011). 70% training, 15% testing, 15% validation classification was preferred. Table 2 shows the classification of the data set.

Table 2: Data set classification

Number of rows in training set	309
Number of rows in the test set	66
Number of rows in the validation	66

One of the most important issue to be determined is how many hidden neurons will be in the artificial neural network layers. There are no certain rules for determining the number of hidden neurons. There are several equations of

hidden neuron determination supported by the literature. According to Tang and Fishwick, the equations of hidden neuron determination is as follow (Tang et al., 1993).

$$Equation\ 4: Determination\ of\ hidden\ neuron \qquad n = number\ of\ input\ neuron \rightarrow n = hidden\ neuron$$

Wong working on the same subject has determined the number of hidden neurons as follows (Wong, 1991).

$$Equation\ 5: Determination\ of\ hidden\ neuron = hidden\ neuron \qquad n = number\ of\ input\ neuron \rightarrow 2n$$

According to Masters who consider the number of output neurons (Masters, 1993),

$$Equation\ 6: Determination\ of\ hidden\ neuron \qquad \sqrt{n.m} = hidden\ neuron, \quad \begin{matrix} n = number\ of\ input\ neuron \\ m = number\ of\ output\ neuron \end{matrix}$$

When writing code or using Toolbox, the number of preferred hidden neurons is written to the relevant parts, and these numbers can be changed until the expected results are obtained.

If the difference between the actual value and the values obtained from the model is defined as an error, then if this error value is small for which model; it will be preferred. Some statistical criteria to be used to determine the error in an established model are as follow:

$$Equation\ 7: Mean\ Absolute\ Deviation - MAD \qquad MAD = \frac{1}{n}\sum_{t=1}^{n}|Y_t - F_t|$$

$$Equation\ 8: Sum\ of\ Squared\ Error - SSE \qquad SSE = \sum_{t=1}^{n}(Y_t - F_t)^2$$

$$Equation\ 9: Mean\ Square\ Error - MSE \qquad MSE = \frac{1}{n}\sum_{t=1}^{n}(Y_t - F_t)^2$$

$$Equation\ 10: Root\ Mean\ Square\ Error - RMSE \qquad RMSE = \sqrt{\frac{1}{n}\sum_{t=1}^{n}(Y_t - F_t)^2}$$

Where:

- $Y_t = Actual\ value$
- $F_t = Output\ obtained\ from\ ANN\ model$
- $n = Number\ of\ data\ set$

3. RESULTS AND DISCUSSION

In this study, to forecast the energy efficiency of the cryogenic liquefaction system in the meaning of sustainability perspective, artificial neural network models are developed by comparing different ANN architectures. The developed ANN model is constructed to evaluate thermodynamic results of nitrogen, energy efficiency, and sustainability through different computer programs. Best results are obtained in MATLAB Neural Network Toolbox by implementing Levenberg-Marquardt, Bayesian Regularization, and Scaled Conjugate Gradient learning algorithms which are based on the criteria of the mean square error and the coefficient of correlation. The error rate was determined to be minimised by choosing appropriate algorithms, a number of data, and hidden neurons. The employed algorithms are presented in Table 3, Table 4, and Table 5.

Table 3: Implementation on Levenberg-Marquardt on nitrogen liquefaction exergy analysis dataset

Case	Samples	MSE	R
70% Training	309	5.84896	0.999973
15% Testing	66	4.39313	0.999980
15% Validation	66	4.47911	0.999979

Table 4: Implementation on Bayesian Regularization on nitrogen liquefaction exergy analysis dataset

Case	Samples	MSE	R
70% Training	309	0.991590	0.999995
15% Testing	66	0	0
15% Validation	66	1.13744	0.999994

Table 5: Implementation on Scaled Conjugate Gradient on nitrogen liquefaction exergy analysis dataset

Case	Samples	MSE	R
70% Training	309	10.54984	0.999951
15% Testing	66	13.90688	0.999934
15% Validation	66	14.58499	0.999933

Based on the results, Levenberg-Marquardt, Bayesian Regularization, and Scaled Conjugate Gradient learning algorithms reach 22 epochs, 171 epochs and 63 epochs, respectively. It is observed that all algorithms can predict with an acceptable level of error, and the ANN models is a powerful tool in predicting exergy analysis.

4. CONCLUSION

This study found ANN models were able to accurately predict thermodynamic results of nitrogen using data which is obtained by cryogenic liquefaction method in refrigeration systems by applying the Engineering Equation Solver (EES) program. The specific exergy values of a cryogenic liquefaction system were estimated depending on the temperature and pressure each point values as an input by using ANNs. The network of the ANN was constructed using Levenberg-Marquardt, Bayesian Regularization and Scaled Conjugate Gradient learning algorithms with the observed data for future estimation and also successfully applied to determine the specific exergy values of the system working with nitrogen elements. This study is expected to contribute to existing literature in terms of energy planning, sustainability, determination of energy policies, and energy efficiency. The main conclusions that can be drawn from the present study are summarised as follows:

a) Especially in the industrial sector Steel, Cast iron, Non-ferrous metals, Alloys, Carbides, Plastics and Ceramics are used in many areas such as cryogical applications for low temperature requirements of large energy consumption is required.
b) The modelling of the cryogenic system with different approaches based on the results of thermodynamic analysis is a guide for energy efficiency and sustainability.
c) When the ANN model that examined was evaluated using various standard statistical performance evaluation criteria and mathematical formulations is trained, for the R squared value and correlation coefficient, the best is obtained from a network with 2 hidden layers.
d) The ANN network which is constructed with Levenberg-Marquardt algorithm: R-value is equal to 0.99998, and it reaches the best result at epoch 16.
e) The ANN network which is constructed with Bayesian Regularization algorithm: R-value is equal to 1, and it reaches the best result at epoch 168.
f) The ANN network which is constructed with Scaled Conjugate Gradient algorithm: R-value is equal to 0.99995, and it reaches the best result at epoch 57.
g) In this study, it is understood that the estimation of the energy efficiency of the cryogenic liquefaction system can be obtained with artificial neural network models in a very precise and rapid manner if there are sufficient and quality data.
h) In addition, it is thus understood that in terms of energy efficiency, it is possible to foresee the changes in the relevant input parameters and the conditions in which the arrangements will be made. And, this is very positive in terms of sustainable engineering approaches.

5. REFERENCES

Azadbakht, M., Torshizi, M. V., Noshad, F. & Rokhbin, A., 2018, Application of artificial neural network method for prediction of osmotic pretreatment based on the energy and exergy analyses in microwave drying of orange slices, *Energy*, 165, 836-845.

Chen, Z., Henson, M.A., Belanger, P. & Megan, L., 2010, Nonlinear Model Predictive Control of High Purity Distillation Columns for Cryogenic Air Separation. *IEEE Transactions on Control Systems Technology*, 18 (4), 811-820.

Demirezen, G., Fung, S.A., 2018, Application of artificial neural network in the prediction of ambient temperature for a cloud-based smart dual fuel switching system, *Energy Procedia*, 158 (2019) 3070–3075.

Hamzacebi C., 2011, Yapay Sinir Ağları Tahmin Amaçlı Kullanımı Matlab ve Neurosolutions Uygulamalı, Ekin Publisher, ISBN 6055431822.

Haykin, S., 1998, Neural Networks - A Comprehensive Foundation, Pearson Prentice Hall, ISBN 81-7808-300-0.

Karabuga, A., Utlu, Z., Selbas, A. 2019, Examination of the liquefaction system for the use of different cryogenics in terms of thermodynamic analysis International Journal of Exergy 29 (1), 1-21.

Masters, T., 1993, Practical Neural Network Recipes in C++, *Academic Press*, 25-50.

Ozturk, H.K, Ceylan, H., Hepbasli A. , Utlu Z., 2004, Estimating petroleum exergy production andconsumption using vehicle ownership and GDP based on genetic algorithm approach, *Renewable and Sustainable Energy Reviews*, 8, 289–302.

Razmjoo, A. A., Sumper, A., Davarpanah, A., 2019, Development of sustainable energy indexes by the utilization of new indicators: A comparative study, *Energy Reports,* 5, 375-383.

Tang., Z., Fishwick, P.A., 1993, Feedforward Neural Nets as Models for Time Series Forecasting*, ORSA Journal on Computing,* 5(4), 374-385.

Tolon, M., 2007, A neural network approach for slope stability during Earthquake, *Master's thesis*, Faculty of Civil Engineering, Istanbul Technical University, Istanbul, Turkey.

Utlu, Z., Hepbasli, A., 2007, Parametrical investigation of the effect of dead (reference) state on energy and exergy utilization efficiencies of residential–commercial sectors: A review and an application, *Renewable and Sustainable Energy Reviews,* 11, 603–634.

Utlu, Z., Hepbasli, A., 2010, Comparison of Turkey's Sectoral Energy Utilization Efficiencies between 1990 and 2000, Part 1: Utility and Industrial Sectors, *Energy Sources,* 26(14), 1331-1344.

Utlu, Z., Parali U., 2013, Investigation of the potential of thermophotovoltaic heat recovery for the Turkish industrial sector, *Energy Conversion and Management*, 74, 308–322.

Weisend, J.G., 1998, Handbook of Crygoenic Engineering, 504, Taylor&Francis, USA.

Wong F.S., 1991, Time series forecasting using backpropagation neural networks, *Neurocomputing,* 2(4), 147-159.

#202: Review of strategy for assessing the thermal performance of institutional building form in hot dry climate of Nigeria

Aminu Adamu BENA[1,2], Mark GILLOTT[1], Rabah BOUKHANOUF[1]

[1]*Department of Architecture and Built Environment, Faculty of Engineering, University of Nottingham, NG7 2RD University Park, Nottingham, UNITED KINGDOM*

[2]*Department of Architecture, Faculty of Environmental Science, Federal University Birnin Kebbi, Kebbi, NIGERIA*

Achieving comfortable indoor environment in buildings in hot climates requires enormous amounts of cooling energy specifically if passive design techniques were not considered from the outset of the construction process. For instance, overheating in building experienced in tropical climates of Nigeria impacts severely on occupants' productivity and well-being. This paper reviews existing construction and technological strategies of improving energy efficiency in hot climates with a focus on institutional buildings. The review covers in particular design of building form/shape, passive cooling techniques, thermal comfort and building performance assessment tools. The paper provides also a critical reflection on the effectiveness and suitability of each strategy to address the wider issues of sustainability of the building sector.

Keywords: energy efficiency; thermal comfort; institutional buildings; sustainability; passive cooling; hot climates

1. INTRODUCTION

In recent years, Nigerian government has invested much in financing the construction and upgrading of public facilities in its higher institutions across all levels. Higher educational institutions and universities across the states of the federation were funded towards provision of ideal teaching and learning environment, (Douglas, 2018). Educational institution buildings are places for teaching, learning, research, these activities are offered in many built facilities such as academic/administrative offices, classrooms, workshops, laboratories, theatres/studios, sports facilities, arenas, accommodation facilities etc. In many developed countries of the world, such as UK, USA and Europe, University environment is part of the urban city setting, where urban services are shared as a common facility, a purposeful energy efficiency plan with technical and behavioural improvement measures is required for a higher education building to achieve sustainable energy performance (Nelson, 2015).

According to Chryso and Aimilios (2018), Educational buildings in developed countries are responsible for extensive consumption of energy. Energy is required to provide thermal comfort to occupants, its reduction is recognized as an essential need for implementing greenhouse strategies by many governments, as such policies and targets are therefore set at certain periods. Thermal comfort perception affects all manner of building occupants; it is determined by climates, building type, form materials used in constructing building and user perception factors. For achieving desired quality indoor environment devoid of any health risk and improved users productivity, buildings should be monitored for performance across all stages of its development. Knowledge about energy use in building, thermal comfort, building forms energy consumption and assessment, are essential but sometimes actual consumption may differ from the estimated in terms of buildings parameters, physical characteristics and occupant's use of building. (Mishra et al, 2017; Shide and Amin, 2019). Globally the building sector accounts for more electricity use than any other sectors, offices buildings accounts for 48-68% of electricity consumption, 13-37% lighting and 12- 25%, equipment load, according to Nigeria Building Energy Efficiency Guideline the nation's electricity demand exceeds the supply and even the supply remains unreliable.

The available power supply in Nigeria is less than 41% of the total installed capacity. Energy sources used in buildings in Nigeria amounts to 0.4% hydro, 17% oil and gas and 82% biofuels and waste. Electrical energy consumption by offices buildings is majorly for cooling and lighting; 40-60% used for air condition, 13-37% lighting and12-25% office equipment (BEEG, 2017).

Building envelope refers to the roof, walls, windows, doors, floors and foundations of a building. The envelope is the building structure that is exposed to the environment which design, and construction affects internal temperature and heat loss. The smaller the external area of a building the less opportunity there is for heat to escape. While, building geometry refers to measurements relating to building configuration and arrangements, in broader sense it relate with building components, its envelope interact with interior and mediate the difference between outdoor and desired indoor conditions. Forms play the leading role in achieving energy efficiency of a structure and must be considered in design planning and construction. Good design of form can minimize and downsize heating and cooling requirement or eliminate need for them all (Gerhard et al, 2012; Hanan, 2014; Zero Carbon Hub, 2016).

According to Chryso and Aimilios (2018), assessment of institutions (education) buildings on forms for thermal performance is an essential measure of reducing CO_2 emission to the environment. In order to ensure thermal comfort, reduce the phenomena of overheating good indoor environmental quality is desired. Indoor environmental quality (IEQ) is the conditions inside a building, air quality, lighting, thermal conditions, ergonomics and their effects on occupants. Strategies for addressing IEQ include those that protect human health, improve quality of life, reduction in stress and potential injuries. It can enhance the lives of building occupants and increase the resale value of building. (Zero carbon Hub, 2016). In UK, there has been increase evidence of overheating in buildings in homes retrofitted to satisfy more demanding energy efficient standards. Overheating has serious health consequences on occupants of building, and it can lead to discomfort or loss of life. Andy and Micheal (2012) reported that summer heat in 2013 in Europe alone has caused the death of 35,000 people and 2000 in UK, due to daytime temperature rise between 26 - 37^0C and 19^0C.

Several studies were conducted on passive cooling design techniques of different buildings and forms in hot climates, majority from Middle East and North/West Africa (Hanan, 2014; Marwa et al., 2015; Abbas, 2015; Fahad and Steve, 2017; Maryam and Ahmad, 2017; Alshenaifi and Sharples, 2018; Farshad, 2018; Mahamood et al., 2018). Most global research that reviewed offices buildings are largely on context of commercial offices not institutional education buildings. Notable among these studies are work of Hanan (2014), Fahad and Steve, (2017) that offered useful guides on application of passive principle on multi storey high rise commercial offices buildings and the use of integrated environmental solution (IES) tool for assessments. The application of this strategy on low rise buildings in hot-dry climates is vast on residential buildings alone even in Nigeria by researchers, (Maryam, and Ahmad, 2017; Mahmood, 2018). Research specifically on educational institution and low-rise buildings with complex shape, varying geometry and multi-functional utility spaces (offices, studios, classes) are rarely reported. The National Energy Support Programme in Nigeria has clearly affirmed that there is the absence of relevant information on Building Energy Efficiency guidelines codes and energy use index for Educational Institutional offices and buildings (National Energy Support Programme, 2017; BEEG, 2017).

1.1. Aim and objectives

This paper reviews key variables for assessing the thermal performance of institution building in hot dry climates of Nigeria. The purpose is to achieve provision of thermally, comfortable indoor environment quality to the users. The review focus on climate, Forms/ shape parameter, thermal comfort and indoor environmental quality and simulation tool required for assessment of performance and sustainable energy reduction. Specifically, the paper reviews passive design techniques and approach in hot dry climates, identify processes and solutions of overheating in office buildings and process of optimising form energy efficiency. Technical data of an institutional building is presented, discussed and analysed in the paper as a base case study in order to create understanding of processes involved and explain the assessment strategies of building type in the climate.

Good literature can provide tangible guidelines to answer the following research questions: Does literature on passive techniques provide effective guide on achieving energy efficiency for buildings form in hot dry climate of Nigeria? What specific literature explains solutions to the phenomena of overheating in building interiors? How does knowledge of using simulation tools help in achieving sustainable assessment process? And how does literature on building form/shape influences buildings performance optimization?

2. STUDY AREA BIRNIN KEBBI

2.1. Location and climate

Birnin Kebbi is 235 m above sea level. It is located along latitude 12.45°N, and longitude 4.20°E. A Sudan savannah region of hot and dry climate zone. The Institution, Federal university Birnin Kebbi is 15km from the city centre close to Kalgo town. Wet season is hot and mostly cloudy, it lasts for 2.1 months while dry season is sweltering and partly cloudy. The cool season lasts for 2.4 months in a year.

Figure 1: Map of Nigeria showing Birnin Kebbi town

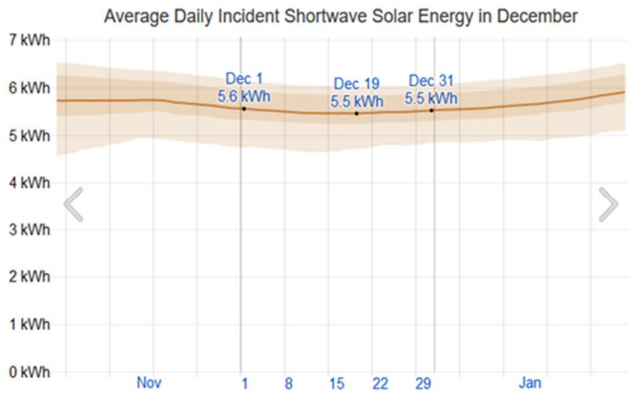

Figure 2: Average solar energy of B/ Kebbi town for December

Solar energy reaching the surface of the ground in December averaged 5.5 kWh while its lowest average is 5.5 kWh. Figures, (2 and 3), are graphical illustrations of monthly solar energy and time in various periods of the year. Average hourly wind speed is 3.8 m/s, the wind temperature and moisture determine humidity for comfort levels. Lower dew points make body drier and higher more humid. See Figure 4, for monthly temperature distribution.

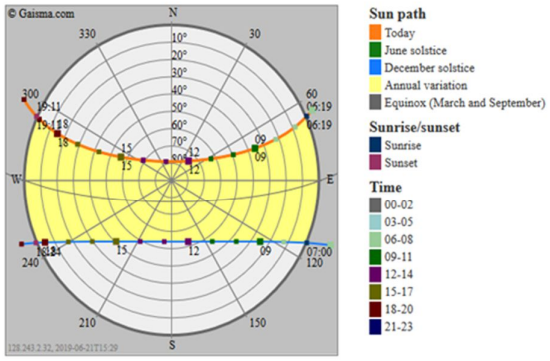

***Figure 3**: The Yearly Solar energy sun path of B/Kebbi town*

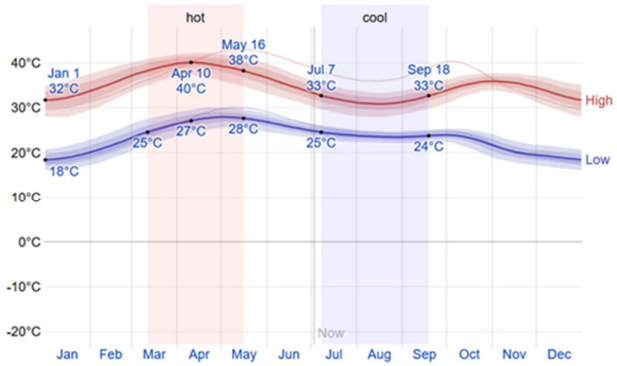

***Figure 4**: Monthly Temperature distribution of B/Kebbi town*

The shortest day of the year in Birnin Kebbi is December 22 with 11 hours, 24 minutes and the longest day is June 21, with 12 hours, 51 minutes of daylight. Sun rises early as, 6:16am and sets at 6:14pm. In November 19, sunset at 7:12pm. Windier part of the year lasts for 7.3 months, with average wind speeds of more than 2.8 m/s, February 9. (www.weathersparks.& gaisma.com).

2.2. Case study building

The Faculty of Environmental Science building of Federal university Birnin Kebbi is situated along Kalgo districts area of Birnin Kebbi, Kebbi state of Nigeria. This faculty building was completed and occupied in March 2016. It is an education institutional building complex that accommodates staff (academics/non-academics) and students offering built environment courses, (see Figure 6). The facility accommodates 3 departments; Architecture, Building and Quantity Surveying. Among other adjoining structure within the site layout are the 2-unit blocks of female students' hostels, library, 100 capacity lecture theatre, 4-unit blocks of classrooms, 1-storey lecture studios and 3-unit blocks of staff offices all located within the site layout as in Figure 5.

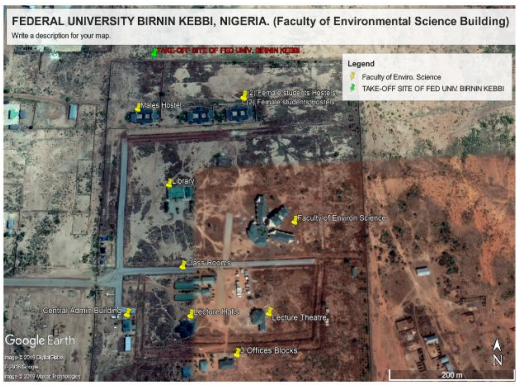

Figure 5: Aerial view of the University taken off site

Figure 6: Faculty of Environmental science building aerial view

Table 1: Building Physical Data

Name of Building	Photo	Basic Building Information
Faculty of Environmental Sciences, Federal University Birnin Kebbi, Nigeria		Category: Main Building Case study. Building Type: Education Institutional Faculty Building with Staff Offices Location: Kalgo, Birnin Kebbi, Nigeria. Floor Area: GFA: 2003.19m^2, 1st Floor: 371.79m^2. Number of floors: 2 Construction year: 2015. Cooling source: mechanical ventilation with using air conditioning systems Heating source: Natural sunlight, Ventilation: Windows fenestrations

Table 2: Ground Floor: Functional Spaces and Building Technical Data, Faculty of Environmental Science, FUB/K.

S/No	Functional Spaces	Number Required	Unit Area (m^2)	Total(m^2)
1.	Offices	45	23.13	1040.85
2.	Design Studio	1	125.31	125.31
3.	Workshop	1	125.31	125.31
4.	Lecture Hall	1	125.31	125.31
5.	Common Rooms	3	26.43	79.29
6.	Reception Hall	3	28.43	85.29
7.	Toilets for offices	47	1.87	87.89
8.	Toilets spaces for Students (m & f)	2	12.43	24.86
9.	stores	3	6.45	19.35
10.	Data Room	3	26.45	79.35
11.	Veranda	1	100,23	100.23
12.	Paved Walkway	1	30.00	30.00
13.	Central Offices Walkway	1	80.15	80.15
	TOTAL			**2003.19m^2**

Table 3: 1st Floor Plan spaces

S/No	Functional Spaces	Number Required	Unit Area (m^2)	Total(m^2)
1.	Offices	5	23.13	115.65
2.	Faculty Conference Hall	1	125.31	125.31
3.	Reception Hall	1	28.43	28.43
4	Toilets for offices	5	1.87	9.35
5	stores	1	6.45	6.45
6	Data Room	1	26.45	26.45
7	Staircase area	1	60.15	60.15
	TOTAL			**371.79m^2**

(Total floor space area in (m^2), from table 3 and 4 is 2374.98m^2. To calculate the roof area, minus 10% of roof deck.)

Table 4: Table indicates the ratio of natural lighting/ventilation provision and number of air conditioning units.

S/No	Functional Spaces	Provision spaces/units	Windows Natural lighting(m^2)	Ventilation area (m^2)	Air Condition units
1	Offices	50	0.72	1.44	50
2	Studio & Lect. hall	3	77.76	25.92	12
2	Faculty Conference H.	1	25.92	8.64	6
3	Reception Halls	3	12.98	4.32	6
4	Toilets for offices	50	72.00	36.00	-
5	stores	4	2.88	1.44	-
6	Data Room	4	25.92	8.64	8
7	Central walkway	4	5.76	2.88	-
8	Toilets for offices	8	11.52	5.76	-
	TOTAL	**127**	**235.46**	**95.04**	**82**

3. METHODOLOGY

A total of 35 publications, peer reviewed journal papers/ articles, books and website pages were consulted on relevant areas of the research topic; assessment of thermal performance of institutional building form in hot dry climate of Nigeria, from the context of indoor environmental quality (IEQ), which discusses the phenomena of overheating in buildings. 8 papers on passive cooling principles in hot/dry climates. 7, institutional building and form Energy characteristic, 8, other climates, 7, thermal comfort and 5 on IES VE simulation tool. All selected publications sited are within 2010-2019, are chosen form Elsevier (Buildings and Energy, Renewable & sustainable Energy Reviews, Science Direct, Energy & Buildings, and Energies, etc.), Buildings journal, Emeralds journals, International journals, SET, PLEA, conferences and policy documents such as CIBSE, CARBON Hub, ASHRAE, and BEEG. Expressing general literature on strategies, methodologies, parameters and guidelines for sustainable improvement of buildings in hot dry climates of Nigeria.

Table 5: Number of Publications Reviewed

S/No	Publications	Number
1.	Passive Cooling	8
2.	Climates	8
3.	Institutional Buildings/ Forms	7
4.	Thermal Comfort	7
5.	IES Simulation Tool	5
TOTAL		**35**

(Five to seven items in each strategy were highlighted in the case key headlines of this literature.)

3.1. Literature review strategy for buildings in hot climates

Reviewing literature on passive cooling techniques in hot dry climates is important because it offer some viable solutions for achieving minimum thermal comfort standard requirement for occupants of buildings, Table 6, gives information on building design approach and provide explanations on passive design strategy (Hanan, 2014; BEEG, 2017; Douglas, 2018).

Table 6: Summary of key passive design strategies in hot dry climates

S/No	Key passive Strategies	Hot and Dry Climate
1	Climatic conditions	• High ambient temperature, solar radiation levels, direct/reflected sunlight and dust storms.
2	Microclimate design approach	• Compact forms, shade and shelter for public spaces, glare control; roughness/ low reflective colours, evaporative cooling: by strategic inclusion of vegetation, windward location close to water bodies, protected urban edges from hot winds, narrow roads/ alleys, and mixed building heights.
3.	Building design approach	•Orientation: Windows facing mainly north and south with overhangs or external shading •Building form: Compact geometry reducing skin area, buffer zones and thermal zoning, day lighting, night cooled mass systems and evaporative cooling towers • Materials: Roof with high solar roof index (SRI), example; cool roof exhibits a combination of high reflectivity and high emissivity. High thermal mass, exterior insulation for reducing heat gains during the day and windows, visible light transmission (VLT) > 60% is ideal for good day lighting in offices, classroom and design studios for visual clarity.

3.2. Building forms/shape strategy

Energy saving strategy on building and increase supply in operation are many and comes in different dimensions apart from changes to its mechanical and electrical operations or system, building form (roof, walls, floors and windows/openings) may also provide savings using passive techniques by preventing outdoor heat into building interiors, keeping indoor heat out and controlling the flow of heat from building fabric surfaces. (Nick, 2016). In consideration to form energy performance, manipulation of form shape and characterization can considerably influence the building energy performance (Rashdi and Embi, 2014; Farshad, 2018; Tergu and Gadi 2018). Other form requirements include:

- Determining the types of form for assessment, (institutional, industrial or residential) and consider them under, case studies and main studied building.
- Set time frame for the conduct of building survey, inventories and investigations. Example, (1) year time frame to be taken for field survey visit, case study and simulation work.
- Obtaining and collecting general data for Input in simulation software as primary and secondary source; data such as building physical data, design and measured survey data.
- Case studies and base study building shall be chosen within area or the climatic zone in institutions on varying form shapes (Linea, (L) geometric and Courtyard shape plans.
- Adherence to the provision of Building Code, regulations/ byelaws for Nigeria/Kebbi state.

3.3. Passive Cooling Techniques

Literature review will offer guides on:

- Passive cooling processes entails the removal of an undesired heat substituting cool air, ventilation, blockage of heat passages and provision/ retention of cold air in the building interiors.
- Note the methods of form assessment and procedures for passive and active energy conservation.
- Utilize a passive cooling strategy like; voiding direct or indirect solar gain, isolation of solar gain, Heat storage, shading, insulation of form elements and glazing.
- Note that passive design techniques are easy to be applied on design and new buildings. Existing buildings can be adapted or "retrofitted".
- Passive solar technologies convert sunlight into renewable energy, knowledge/ literature will give good guide on exploration of alternative energies technology and its integration on building.
- Identify literature on variables (dependent and independent) on form character, elements, configurations thermal comfort perception and climatic elements.
- Identify literature on forms passive shading methodologies; self-form shading, external and shading using vegetation that are proven significant for performance improvement at design, construction and maintenance stages (Hanan, 2014; Building Bulletin 101, 2018).

3.4. Thermal comfort review of strategy

Thermal comfort is a state of mind in respond to perception of the physical environment. It is further defined by the American Society of Heating, Refrigerating and Air Conditioning Engineers-ASHRAE Standard 55, (2013), document as “condition of mind that expresses satisfaction with the thermal environment which can be assessed by subjective evaluation processes”. Climatic factors associated with thermal comfort are air temperature, air

speed, mean radiant temperature and relative humidity. Activities and clothing's are personal factors involved in human thermal perception. The implications of thermal comfort on human activities are increasingly considered in various energy management literature (Meshak and Ola, 2014, Diana, 2017; Building Bulletin 101, 2018).

Human beings have different form of cold and heat perception in indoors of buildings, there are factors that and this has to do with the perception of thermal comfort on occupants inside buildings which also depends on the heat balance of the body. According to Marwa et al, (2015), in hot climates where overheating is experienced and energy consumed is used for powering air conditioning sets for cooling in the summer, passive cooling strategy is convenient to remove or balance the heated interiors.

Certain factors should be considered in the assessment of thermal comfort as a strategy:

- Identification of literature on thermal comfort concepts, human comfort, indicators and standards.
- Aim to achieve; thermal control, optimization methods, practical and scientific method of assessments.
- Desire to check heat admission and emission from, lights, electrical appliances, outside sources through the walls, windows and roofs of the buildings.
- Learn from literature technologies for measuring and evaluating heat in buildings without the need for mechanical cooling. Relate the literature with climate of the study area, hot dry climate,
- Identify literature on processes of determining personal perception parameters for thermal control, mechanism for adaptive thermal comfort in ascertaining thermal comfort and thermal sensation.
- Note the following thermal comfort indices such as: Predicted Mean Vote (PMV), Predictive index (PI), Actual Mean Vote (AMV), and the Predicted Percentage Dissatisfied (PPD), with their modifications and variants, indicating standard applications to different situations in indoor environment assessment.
- Note the human thermal indices: Thermal neutral temperature (Tn), indoor resultant air temperature (Tm), transfer function of human physiology, thermal sensation, physical stimuli, psychological/ behavioural impact coefficient and adaptive clothing insulation coefficient.
- Knowledge of IEQ control strategies using models, such as parametric, statistical and hybrid models.
- Identifying the U-Value, V-Value and G-Value in specific case for necessary considerations in the building form assessment processes. (Gerhard, et al, 2012).

3.5. Building simulation tool

These are tools, models and computer software's widely used for analysing built infrastructure and providing guides in design, engineering construction, maintenance and retrofitting of buildings. Thermal models are now being developed by professionals for specific parametric assessment, investigation of specific natural and physical phenomena associated with buildings and users. These tools can be software's, models, added plug-ins that can serve as integrated or standalone models (Ncube and Riffat, 2014). The IES VE is an Architect and Engineering tool used in investigation and comprehensive analysis of bioclimatic strategies even before design starts. It can be connected to many BIM interphases; used in processing varieties of sustainable application tasks indicated in Table 8. The advantages of using this simulation tool are; ease in transfer/export of files, enhanced visual graphics, brilliant colour codes, sorting, flexible interfacing and has single platform for modelling, prediction and evaluation. Also good for thermal performance assessment because it is well recognised as a solution for existing building assessments. This informed the reason for its review in the literature. (www.iesve.com/webinar).

Table 8: The IES VE Tools and Task:

S/no	SIMULATION TASK	IES VE TOOLS
1.	Weather Data	Weather shift
2.	BIM Data	Revit and Excel
3.	Project Communication	IESVE Navigation
4.	Thermal comfort Analysis	Psych-chart & Micro Flo-CFD
5.	HVAC System Optimization	Apache HVAC
6.	HVAC System Sizing	ASHRAE Loads
7.	Import Meter Schedules	Ergon (IES Cloud)
8.	Climatic Analysis	VE Gaia
9.	Lighting Design	Light Pro & Flux Pro
10.	Day lighting Glare	Radiance IES
11.	Solar Simulation	Sun cast on IESVE Cloud
12.	Natural ventilation Design	Macro Flo & Apache Sim
13.	Envelope Simulation	Parametric Batch Processor
14.	Energy Modelling & Renewable	Apache Sim
15.	Geometric Master Planning Tools	Model IT & OSM
16.	Geometric Components	Sketch Up
17.	Compliance for ASHRAE Standard 55	ASHRAE 91.55 Navigator

Source: IESVE, Limited, Webinar@iesve.com., Glasgow, UK.

Added enhancement to IESVE tool include; model IT enhancement, high concentration photovoltaic renewable options, shading control and python script/easy copying & pasting of data. As such, valid simulation tool is required to achieve actual assessment of building form for energy performance with respect to climatic parameter.

3.6. Sustainable improvement & assessment guidelines

Technical improvement sourced literature from diverse studies regardless of climates, building type, form type, passive techniques and established building rating systems they are worthy in achieving sustainable improvement and desired goal. Some of the literature are: Rashdi and Embi (2014) and Teguh and Gadi (2018) discuses form manipulation and characterization of different shapes geometry and composition on energy performance in conservation and reduction. Salwa et al. (2017) and Rami, et al. (2019) utilizes solar advantage by using PV films and panels and integrating same on building to increase the electricity supply. Research by Adrian et al. (2015), suggested space cooling, using air desiccant materials and solar energy to reduce energy consumption, which offers good reliability and comfort control level, and a viable low carbon alternative. Lucelia et al., (2015), studied on mitigating overheating effects of insulated timber building using plaster board and comparing against concrete element in the UK climate. The study demonstrates high level of assessment techniques on timber material. All the research offers a useful guide towards providing reliable literature for sustainable performance improvement on energy after right assessment.

4. ANALYSIS

4.1. Analysis of main case study building

This analysis describes the base case study building and its surrounding built environment where this facility is located. It is ideal to analyse the physical environment and building physical structure that will guarantee development of idea for viable passive cooling strategy towards insuring provision of thermal comfort to users of building. Utility spaces will be match with standard provision of the building code/ user in studio, lecture hall and offices spaces. Interior spaces measured; Table 2, 3, and 4 will provide useful information on building technical data for accomplishing any required simulation task using valid tool. Accordingly, improvement in the final study will focus on influential form element (roof, floor or walls) that demonstrate potentials in reducing interior overheating and improving energy efficiency.

Passive solar technology literature emphasizes on using renewable energy alternatives, such as sunlight without having to use active mechanical systems, such technologies convert sunlight into renewable energy. The technologies include direct and indirect solar gain for space heating, solar water heating systems based on the thermosiphon, use of thermal mass and phase-change materials for slowing indoor air temperature swings, solar cookers, the solar chimney for enhancing natural ventilation, and earth sheltering. This approach is fundamental to the energy performance of a building (Carbon trust, 2018).

Figure 5 and 6 shows the faculty building is situated at the take-off site campus of the university together with other buildings to support teaching and learning activities. The overall area designated for the faculty building is (950 x 985m). Built on evenly plain land, with no proper landscaping, scarce/isolated trees that cannot provide any reasonable shading to the building. The entire building shape makes it difficult to achieve good orientation. The entrance main to the building was not properly located, it is positioned in-between the studio and lecture hall, see Table1. The studios have large window panel that persistently allow direct admittance of solar radiation. Building form is curvilinear in geometry, a combination of circular and axial transition of 3-linea forms are the departments offices buildings attached from the circular central courtyard axis at an inclined angle of 600 between each another, Figure 6, however, there were no defined exits ways. External walls along the offices are recessed around the window area, but difficulty in achieving desired orientation makes this insignificant. The roof has a parapet wall and roof gutter the gutter expansions is supposed to provide shading specifically along the studio's façade at the large glazed panel's windows, but substantial solar radiation gained direct access through the glazing to the interiors affecting occupants and creating discomfort.

Improving and maintaining the building fabric offers many advantages and opportunities, the low rise buildings in hot dry climates receives enormous heat impact on roof element more than any other form element, the case study building has 235.46 m^2 of glazing, (Table 4), the large glazing panel from the west side (façade area), creates an aperture for solar heat admittance into studios, classrooms and workshop, these are important learning spaces. Ventilation is half (0.5) of the glazing this makes the building at disadvantage position. Heat from the (coloured) roof covering and critical form shape all added to the overall overheating. About 82 Air conditioning units are installed these is economically unsustainable. IES VE tool, in Table 6, provides ranges of simulation task to guide on nature of maintenance required. The building from this angle has failed in performance and require passive sustainable maintenance.

The hot dry climate is known with high temperature, average 40^0C as a result of year-round solar radiation in the region, Figure 4. This effect is a useful guide for possible utilizing of passive strategy that can focus on tapping

from solar radiation endowment and integrated photovoltaic system technology for desired building improvement. The overheating phenomena required removal/control along the roofing element since it receives the highest solar radiation impact. Some strategic roof improvement from literature are; having roof covering material with low U-value, good choice of roof colour/material, lamination of roofing sheet, shading of roof with roof or PV panels and insulation of the gaps in-between ceiling. The faculty building can accommodate some of these improvements techniques considering the nature of its roof structure (Nigerian Energy Sector Programme, 2015).

5. CONCLUSION

Literature review offer strategic guide on any form of building improvement techniques the performance of form in any climate is a requirement to fulfil for achieving sustainable energy efficiency. The paper discuses literature on assessment guidelines outlined methodology of using passive design techniques and simulation tool IES VE, for institutional education building on form/shape. It is evident this subject has been globally discussed extensively on issues, policies of global warming and ways to reduce CO_2 emission in buildings. Literature guide discussed on methods of reducing overheating in buildings, ensuring minimum standard provision of thermal comfort, reducing cooling energy cost, improving the indoor environmental quality of the occupant and users in hot dry climate of Nigeria. It will also strengthen the research development by revealing step by step guidelines for assessing performance of offices building for sustainable development of the built environment sector. It's however, clearly evident that assessing the thermal performance of institutional building in developing countries have not yet received a research attention.

6. REFERENCES

Abbas, I. M. (2015). Sustainable Design Strategy: Assessment of the Impact of Design Variables on Energy Consumption of Office Buildings in Abuja, Nigeria. PhD. Thesis Doctor of Philosophy Degree of the University of Portsmouth School of Architecture, University of Portsmouth, UK.

Adrian, R. K., Rabah, B., and Robin W., (2015). Space cooling in building in hot humid climate: A review of the effect of humidity on the applicability of existing cooling techniques. 14th International Conference on Sustainable Energy Technologies. Sustainable Technology for a Resilient Future. (SET, 2015) 25th to 27th.Vol. 1. pp 550-558, Nottingham, UK.

Alshenaifi, M., Sharples, S. (2018). Investigating the Impact of Architectural Form and Wind Direction on the Performance of a Passive Downdraught Evaporative Cooling Tower in Saudi Arabia. Smart and Healthy within Two Degree Limit, PLEA. Proceeding of the 34rd International Conference. NCEUB. Hongkong. ISBN 978-0-9928957-5-4

Andy, D & Michael, S. (2012). Overheating in new homes: A review of the evidence. NHBC Foundation IHS BRE Press. P8-16. http://nhbcfoundation.org, UK. ISBN 978-1-84806-306-8

ANSI/ASHRAE Standard 55 (2013) Handbook of Fundamentals: Thermal Environmental Conditions for Human Occupancy, American Society of Heating, Refrigerating and Air Conditioning Engineers: Atlanta, GA, USA.

Buildings are here to stay, http://www.enquiries@iesve.com.acessed;12;32pm,26-04-2019 IESVE, Limited, Glasgow, UK.

Building Bulletin 101 (2018) – Guidelines on ventilation, thermal comfort and indoor air quality in schools, Issue 1, Education & Skills Funding Agency, Crown, (https://www.gov.uk/government/building-bulletin-101-ventilation-forschool- buildings)

Building Energy Efficiency Guideline for Nigeria (BEEGN), (2017). Federal Ministry of Power, Works and Housing (Housing) Shehu Yar'adua Way, Mabushi Abuja, Nigeria.

Carbon trust (2018) Building fabric; Energy saving techniques to improve the energy performance of buildings https://www.carbontrust.com/resources/guides/energy-efficiency/buildings-energy-efficiency/ Published in the UK, Office at: 4th Floor, Dorset House, 27 - 45 Stamford Street, London SE1 9NT.

Chryso, H. Aimilios M., (2018). Assessment of overheating risk and the impact of natural ventilation in educational buildings of Southern Europe under current and future climatic conditions. Energy 165. Pp, 1228e1239. https://doi.org/10.1016/j.energy.2018.10.051

Diana E. (2017). A review of thermal comfort models and indicators for indoor environments. Renewable and Sustainable Energy Reviews, 79, 1353-1379. http://dx.doi.org/10.1016/j.rser. 2017.05.175

Douglas, O. A. Taiwo Fadeke, A., Emmanuel I. A. Oluwaseyi A. A. (2018), Challenges of Sustainable Construction: A Study of Educational Buildings in Nigeria. International Journal of Built Environment and Sustainability. FBE, UTM Malaysia. IJBES 5(1), 33-46. DOI: 10.11113/ijbes.v5.n1.244

Fahad, A. and Steve, S. (2017). Envelope Design and Thermal Comfort Performance in a High-Rise Office Building in Saudi Arabia. Design to Thrive, PLEA. Proceeding of the 33rd International Conference. NCEUB. Edinburgh. ISBN 978-0-9928957-5-4

Farshad, K. (2018). A review on optimization methods applied in energy-efficient building geometry and envelope design. Renewable and Sustainable Energy Reviews 92. 897–920, https://doi.org/10.1016/j.rser.2018.04.080

Gerhard, H., Petra L, and Mike, S., (2012), Building to Suit the Climate A Handbook. Birkhäuser, Basel Printed in Germany. ISBN 978-3-0346-0728-5

Hanan, M. T., (2014). Using Passive Cooling Strategy to Improve Thermal Performance and Reduce Energy Consumption of Residential Buildings in UAE Buildings. Science Direct, Frontiers of Architectural Research No,3, pp,154–165 http://dx.doi.org/10.1016/j.foar.2014.01.002

Lucelia, R., Vaseleiso, S., and Mark, G. (2015). Investigating the potential of adding thermal mass to mitigate overheating in a Super-insulated Low-energy timber house. International Journal of Low carbon Technologies. https//www.researchgate.net/publication Doi:10.1093/ijlct/ctv003.

Mahmood, A., Sura A. and Malcolm C. (2018). Remodelling façade design for improving daylighting and the thermal environment in Abuja's low-income housing. Renewable and Sustainable Energy Reviews. 82.2820-2833. http://dx.doi.org/10.1016/j.rser.2017.10.010

Maryam, A. and Ahmad, T. (2017) Passive Design Strategies for Energy Efficient Housing in Nigeria. Design to Thrive, PLEA. Proceeding of the 33rd International Conference. NCEUB. Edinburgh. ISBN 978-0-9928957-5-4

Marwa, D., Omar, W., Mohamed, A. H., and Erik, J., (2015). Reducing cooling demands in a hot dry climate: A simulation study for non-insulated passive cool roof thermal performance in residential buildings. Elsevier, Energy and Buildings 89 (2015) 142–152. http://dx.doi.org/10.1016/j.enbuild.2014.12.034

Meshak, O.E. and Ola, U. (2014). Assessing Thermal Comfort and Energy efficiency in Tropical African Offices Using Adaptive Approach. Emerald Structural survey, Vol. 32 No. 5, pp, 396-412. Emerald Group Publishing. Doi: 10.1108/SS-03-2014-005

Mishra, A.K., Derks, MTH, Kooi L, Loomans, MGLC, and Kort HSM. (2017). Analysing thermal comfort perception of students through the class hour, during heating season, in a university classroom. Elsevier, Building and Environment. https://doi.org/10.1016/j.buildenv.2017.09.016

Ncube, M. and Riffat, S. (2015). Developing an Indoor Environmental Quality tool for Assessment of Mechanically Ventilated Office Building in the UK- A Preliminary Study. Building & Environment Journal 53, Pp26-33. doi: 10.1016/j. buildenv2015

Nelson, S., Luísa, D. P., João, F. Pedro, C., and Patrícia, P.S, (2015),"Energy efficiency of higher education buildings: a case study", International Journal of Sustainability in Higher Education, Vol. 16 Iss 5 pp. 669 – 691. Emerald Group Publishing Limited 1467-6370. DOI 10.1108/IJSHE-11-2013-0147.

Nick, R. (2016), NHBC. The challenge of shape and form Understanding the benefits of efficient design Published by the NHBC Foundation ISBN 978-0-9935574-2-2

Nigerian Energy Sector Programme (NESP), (2017). Recommendations on minimum energy requirements for Buildings (BEEC) Federal Ministry of Power, Works and Housing Shehu Yar'adua Way, Mabushi Abuja, Nigeria, Sponsored by, European Union & the German Federal Ministry for Economic Cooperation and Development (BMZ)

Rami, Z. Siddiq O., and Guohui, G. (2019). Experimental performance of latent thermal energy storage for sustainable cooling of buildings in hot-arid regions. Energy & Buildings 186 (2019) 169–185. https://doi.org/10.1016/j.enbuild.2019.01.013

Rashdi, W.S.S.W. M and Embi, M.R (2016). Analysing Optimum Building Form in Relation to Lower Cooling Load. Elsevier, Procedia - Social and Behavioural Sciences 222, pp, 782 – 790. doi: 10.1016/j.sbspro.2016.05.161

Salwa, El-G., Ahmed R.A., and Ayman, H., (2017). Building Integrated Photovoltaic Retrofitting in Office Building. International conference Alternative and Renewable Energy Quest (AREQ). Energy Procedia, 115. Pp239-252. 10.1016/j.egypro.2017.05.022.

Shady, A. and Salvatore, C. (2015). Impact of Using Different Thermal Comfort Model on Zero Energy Residential Building in Hot Climates. Elsevier, Energy and Buildings. 102, 117-128 http://dx.doi.org/10.1016/j.enbuild.2015.05.017

Shide, S. and Amin, H. (2019). Critical review and research roadmap of office building energy management based on occupancy monitoring. Energy & Buildings 182, pp, 214–241. https://doi.org/10.1016/j.enbuild.2018.10.007

Teguh, P. A. and Mohamad G., (2018). Investigation on performance of diverse innovative prismatic building models and establishment of form indicator. Applied Energy Symposium and Forum 2018: Low carbon cities and urban energy systems, Shanghai, China. Elsevier, Energy Procedia, 152, pp, 407-412. 10.1016/j.egypro.2018.09.165

Weather of Birnin Kebbi https://www.weathersparks.com/location/bk. Accessed; 10;52pm; 08-05-2019.

Weather of Birnin kebbi, solar path at https://www.gaisma.com/en/location/birnin-kebbi.html. Accessed; 10;52pm; 08-05-2019.

Zero Carbon Hub (2016), Overheating and Ventilation in Homes. www.zerocarbonhub.org. Leyden House, London, UK.

#205: Modelling of energy and exergy analysis of ORC integrated systems in terms of sustainability by applying artificial neural network

Zafer UTLU[1], Mert TOLON [2], Arif KARABUGA[3]

[1]Istanbul Gedik University, Department of Mechanical Engineering, Istanbul, Turkey, zafer.utlu@gedik.edu.tr
[2]Istanbul Gedik University, Department of Civil Engineering, Istanbul, Turkey, mert.tolon@gedik.edu.tr
[3]Istanbul Gedik University, Energy Technologies Application and Research Center, Istanbul, Turkey, arif.karabuga@gedik.edu.tr

The present study focuses upon the Organic Rankine Cycle integrated into Evacuated Tube Heat Pipe (ETHP), which systems are an alternative solar energy system to low-efficiency planary collectors. In this work, a detailed thermodynamic and artificial neural networks (ANN) analysis was conducted to evaluate the solar energy system. One of the key parameters of sustainable approaches focused on exergy efficiency is applying to thermal engineering. In addition to this nowadays, sustainable engineering approaches is a necessity for improving the efficiency of all of the engineering researches areas. For this reason, the Artificial Neural Network (ANN) model is used to forecast different types of energy efficiency problems in thermodynamic literature. Within the scope of this study, the exergy efficiency was evaluated on the developed Artificial Neural Network algorithm. The effect rates of parameters such as pressure, temperature, and ambient temperature affecting the exergy efficiency of ORC integrated ETHP were calculated. Finally, significant findings obtained were evaluated in terms of thermodynamics rules.

Keywords: energy and exergy analysis; sustainability; artificial neural network; ORC system

1. INTRODUCTION

The global energy and climate problem arise due to the increasing energy consumption, the decrease in the life of fossil fuels, and the inevitable increase in environmental pollution. According to the World Bank report, energy consumption from fossil fuels has declined dramatically after 1970, but today energy consumption from fossil fuels is still nearly 80% (Yilmaz, 2018; Utlu and Onal, 2018; Hoffmann, 2019). Global warming and environmental waste problems associated with the consumption of fossil fuels will have an impact over the coming centuries.

Restrictions on the use of fossil fuels known to be non-environmental have been adopted and signed by the Kyoto protocol and the Paris agreement by more than 150 countries. Because of governments adopted a decarbonisation policy in energy use, it made it necessary to provide alternative solutions to existing fossil resources. For this reason, renewable energy sources have been a rising trend in recent years. Multi-generation (electricity production, hot water use, heating, cooling, and clean water production) from solar energy makes solar energy stand out compared to other renewable energy sources (Erten et al., 2019). Also, solar-based multi-generation systems reduce carbon-based energy production due to environmental factors and become more attractive for sustainability and applicable to apply at buildings.

A sustainable structure is the result of a design that focuses on increasing the efficiency of resource use, especially energy. For this reason, it seems very significant to consider sustainable building practices in meeting energy demand. To this end, much effort is being made worldwide to implement renewable energy sources in buildings to use energy efficiently and reduce carbon footprint. Therefore, solar energy systems stand out as applicability in terms of sustainable structures.

As known, solar energy systems can convert solar energy into thermal, mechanical, and power energy. According to the International Energy Agency, renewable energy technologies can be divided into three different generations. The first generation is advanced technologies such as hydropower, biomass, and geothermal energy. The second generation, which is now rapidly developing technologies such as wind, solar, and hydrogen energy. The third generation is technologies that are in development, such as concentrated solar energy, ocean energy, and integrated energy systems (International Energy Agency, 2006). Evacuated tube heat pipe (ETHP) collectors operate at medium temperature and have better performance than planar solar collectors due to it can prevent convection and conduction heat losses (because of the vacuum inside the tube) (Huang et al., 2019; Tong et al., 2015). In ETHP systems, water is generally used as the working fluid for economic purposes. Although water is economical as a working fluid and thermodynamic properties are well known, the most significant disadvantage is that it causes corrosion and freezing of pipes (Huang et al., 2019; Ersoz, 2016). When the current literature on ETHP systems is examined, the researches on this subject are generally focused on experimental studies.

Jowzi et al. 2019, analysed the modified vacuum tube heat pipe system. In this study, both the thermal performance of the system and CFD modelling was performed. At the end of the study, the thermal efficiency of a typical evacuated tube solar collectors system was increased by 25% compared to the thermal efficiency of the modified system. Elsheniti et al., 2019, examined the thermal performance of a vacuum tube heat pipe collector at high inlet temperature. As a result of the study, it is assumed that collector efficiency decreases at higher inlet temperatures and more series connected tubes. Ghritlahre and Prasad, 2018, evaluated the application of the ANN technique to predict the performance of solar collector systems. The evaluations presented in this study show that the ANN technique is a very suitable tool for estimating the performance of solar collector systems. Daghigh & Zandi, 2019, studied the vacuum tube heat pipe system supported by nanofluids and auxiliary gas system. In this study, a hybrid solar-gas system was designed and manufactured. MWCNT, CuO, and TiO2 nanofluids have higher performance than water. MWCNT, CuO and TiO2 nanofluids efficiencies increased by 25%, 12%, and 10% respectively in August and 25%, 15% and 7% in October respectively.

This study aims to model the experimentally established evacuated tube heat pipe collector integrate Organic Rankine Cycle (ORC) system with Artificial Neural Networks (ANN) by calculating exergy efficiency separately. At the end of the study, the effect rates of parameters such as temperature, mass, and radiation on system efficiency were calculated.

2. MATERIAL AND METHODS

This section consists of solar-based power generation system description, the parameters affecting the exergy efficiencies of both ETHP system and ORC system in terms of thermodynamics thermodynamic analysis and construction of ANN architecture.

2.1. ETHP system description

The ETHP system consists of an evacuated tube heat pipe collector, a hot storage tank, two circulating pumps, a heat exchanger, an ORC turbine. A schematic diagram of the complete ETHP is illustrated in Figure 1. The analysis of the Evacuated Tube Heat Pipe (ETHP) system is based on the following main assumptions:

- The system works under steady state conditions
- The changes in kinetic and potential energies are neglected
- The pressure drops and heat losses in the connecting pipes are neglected
- The compressor works with the adiabatic compression process
- The system operates at the atmospheric condition of T_0= 25 ºC and P_0=1 bar as the reference state.

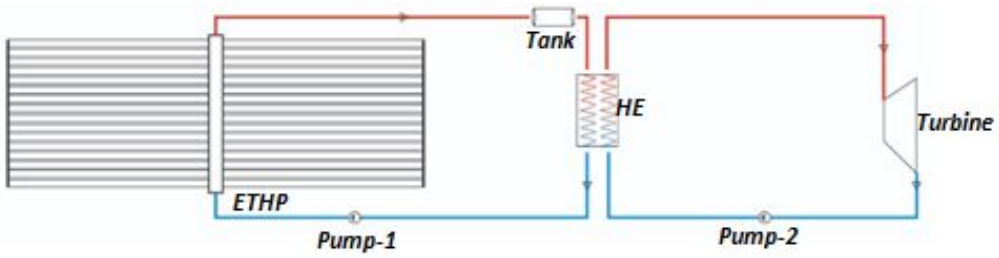

Figure 1: The schematic diagram of Evacuated Tube Heat Pipe (ETHP) system

The ETHP system has 108 heat pipes, and each tube consists of two intertwined tubes. The diameter of the outer tube is 47 mm, the outer diameter of the copper tube is 10 mm, and the length of the tube is 1800 mm. The copper tube is vacuumed between the glass tube. The evacuated between the copper tube and the glass tube. Therefore, the solar radiation coming into the glass pipe is absorbed, and the heat transfers its energy to the water as the working fluid in the pipe, and the rest is emitted again. The thermal energy obtained is transferred to the heat exchanger. By heat exchanger, thermal energy is transferred to the working fluid R134a in the ORC system. The working fluid is heated up to about 85 °C with heat exchanger and passes through to Turbine-I for power generation. A schematic shows the internal structure of ETHP is illustrated in Figure 2 and Figure 3. The shows of the ETHP system is illustrated in Figure 4.

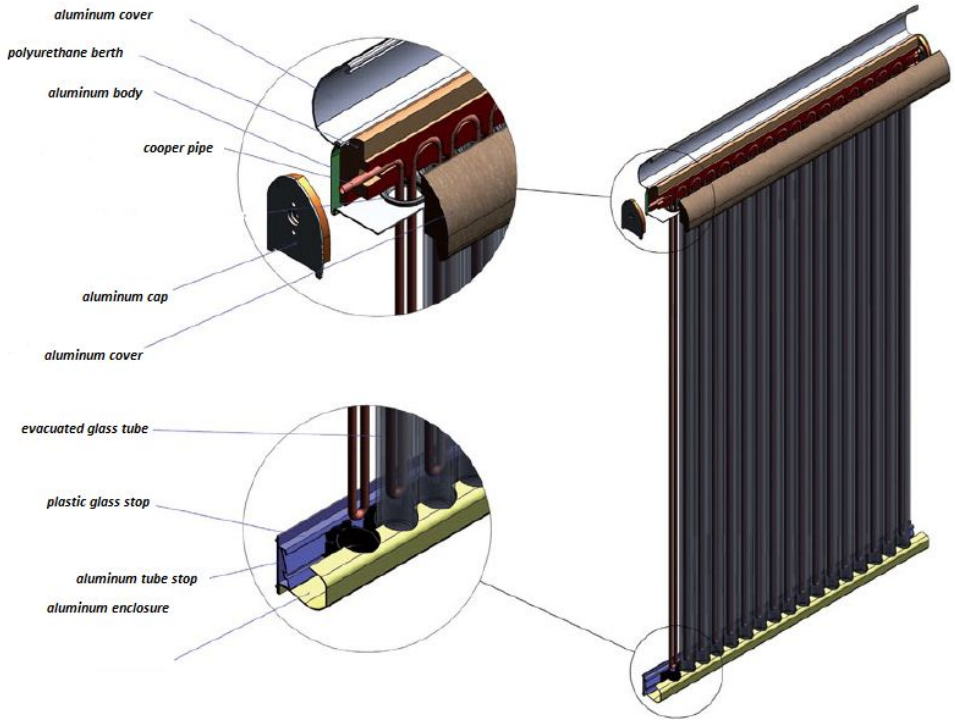

Figure 2: The schematic shows the internal structure of ETHP

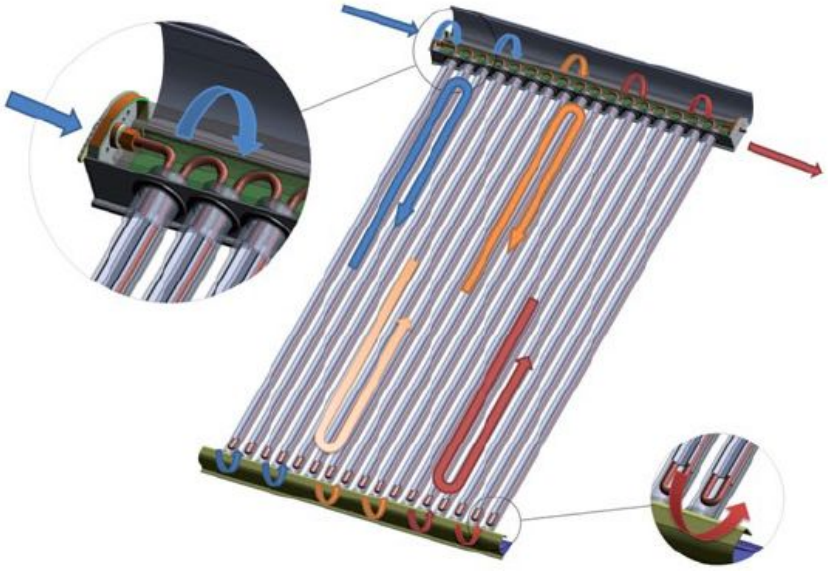

Figure 3: The schematic shows of the ETHP collector

Figure 4: The ETHP system

2.2. Thermodynamic analysis

Energy analysis is related to the first law of thermodynamics, and it examines the energy balance, energy conservation, and energy efficiency of systems. However, energy analysis is not enough to know all aspects of energy use in the system. Because we cannot calculate the usefulness and quality of energy with the first law. For this reason, to find the real efficiency of the system, exergy analysis, which is related to the second law of thermodynamics, should be done. Exergy analysis calculates exergy losses, exergy destruction, and exergy efficiency. Otherwise, exergy is a critical concept to understand the sustainability of energy, environmental effects, and utilising of energy well (Utlu and Hepbasli, 2007; Utlu and Hepbasli, 2010; Ersoz, 2016).

This section covers some of the critical aspects of thermodynamics in terms of the energy and exergy equations used in the ETHP system. For a steady-flow process, the four balance equations are applied to find the work and heat change, the rate of exergy change, the rate of irreversibility, the energy and exergy efficiencies. The exergy is a form, utilisable, quality of energy or potential of the capability to the work. To calculate the exergy, mass balance and energy balance firstly are established when analysing the first law of thermodynamics. The thermodynamic analysis of the ETHP system was investigated by using the Engineering Equation Solver (EES) program. Energy and exergy analysis of the system was performed according to the following formulas.

Equation 1: Total mass balance of the system

$$\sum \dot{m}_i = \sum \dot{m}_e$$

Where $\dot{m}_i$ and $\dot{m}_e$ are mass flow rate of the working fluid at inlet and outlet of the control volume, respectively.

Equation 2: The energy balance of the system

$$\dot{Q} - \dot{W} = \sum \dot{m}_e h_e - \sum \dot{m}_i h_i$$

Where $\dot{Q}$, $\dot{W}$ and h are the heat, work and enthalpy rate of the control volume, respectively.

Equation 3: The exergy balance of the system

$$\sum \dot{m}_i \varepsilon_i + \dot{E}x_Q = \sum \dot{m}_e \varepsilon_e + \dot{E}x_W + \dot{E}x_D$$

In equation 3, ε is specific exergy rate, $\dot{E}x_Q$ is exergy rate of the heat, $\dot{E}x_W$ is exergy of the work, and $\dot{E}x_D$ is exergy destruction. The rate of solar energy delivered by ETHP working fluid can be found using Eq. 4:

Equation 4: The solar energy

$$\dot{E}n_{solar} = I * \rho_{ref} * \rho_{rec} * \varepsilon_{rec} * A$$

Where I is solar radiation, ρ_{ref} is the reflection coefficient of mirrors, ρ_{rec} is absorber of the receiver, ε_{rec} is emissivity of the receiver, A is reflector area. The rate of solar exergy input can be found using Eq. 5:

Equation 5: The solar exergy

$$\dot{E}x_{solar} = \dot{E}n_{solar}\left(1 + \frac{1}{3}\left(\frac{T_{air}}{T_{sun}}\right)^4 - \frac{4}{3}\left(\frac{T_{air}}{T_{sun}}\right)\right)$$

Where T_{air} is ambient temperature, and T_{sun} is sun temperature. The net exergy change of water is writer using Eq. 6:

Equation 6: The exergy change of water

$$\dot{E}x_{water} = \dot{E}x_{out} - \dot{E}x_{in}$$

Where $\dot{E}x_{out}$ and $\dot{E}x_{in}$ are the output water exergy rate and the input water exergy rate, respectively.

Equation 7: The exergy of output water

$$\dot{E}x_{water,output} = \dot{m} * C_p * \left(\frac{T_{out}}{T_{air}}\right) - T_{air}\left(\ln\frac{T_{out}}{T_{air}}\right)$$

Where T_{out} is output water exergy rate.

Equation 8: The exergy of input water

$$\dot{E}x_{water,input} = \dot{m} * C_p * \left(\frac{T_{in}}{T_{air}}\right) - T_{air}\left(\ln\frac{T_{in}}{T_{air}}\right)$$

Where T_{in} is output water exergy rate. The exergy efficiency rate of the ETHP system calculated using Eq. 9:

Equation 9: The exergy efficiency of the ETHP system

$$\eta_{II} = \frac{\dot{E}x_{water}}{\dot{E}x_{solar}}$$

The exergy efficiency rate of the ORC system found using Eq. 10:

Equation 10: The exergy efficiency of the ORC system

$$\eta_{II} = \frac{\dot{W}_{Turbine}}{\dot{E}x_{HE}^{Q}}$$

Where $\dot{W}_{Turbine}$ is turbine work in ORC system.

2.3. Artificial neural networks

Computer systems that model human intelligence and decision-making processes are called artificial intelligence. As artificial intelligence is developed in electronic systems, it is used in many fields such as banking, agriculture,

and engineering applications. Artificial intelligence consists of two basic structures: expert systems and artificial neural networks. Artificial intelligence applications which have developed rapidly in the last decade give good results in solving many problems in engineering. Especially in neural networks with incomplete data sets or fuzzy logic applications, the accurate modelling and the establishment of the right structures provide a high success rate (Tolon et al., 2019; Keskinbora, 2019; Al-Mufti, et al., 2019). In the ANN model, the inputs of the system represent the problem given to the model, while the parameters in the output processing section give the calculation results obtained by the neural network (Figure 5). The structure of the model of artificial neural networks is basically composed of three parts. The first one is the network structure of the selected model, the second is the number of hidden layers, and the third is the number of neurons. The most commonly used architectures are General Regression Neural Networks (GRNN), Probabilistic Neural Networks are (PNN), Back Propagation Neural Network (BPNN) and the Group Method of Data Handling (GMDH). The BPNN has been applied with great success to model many phenomena in the field of engineering. Artificial neural networks (ANNs) each neuron in one layer receives inputs from the neurons in the previous layer (a specified or random number) and initiates a training process to adjust the weights of the interconnections between the neurons. It then processes its output through connections to neurons on the other layer. If the value obtained at the output is known, the training will be audited. Therefore, each link is assigned a weight, which is a numerical estimate of the link force (Tolon, 2007; Marugan et al., 2018; Demirezen et al., 2019).

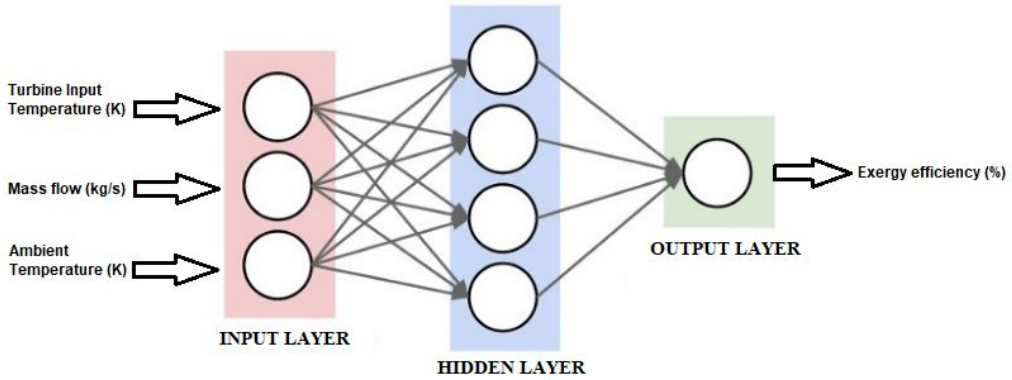

Figure 5: Schematic diagram of an artificial neural network.

3. RESULTS AND DISCUSSION

In this study, exergy analysis of ORC power system integrated to ETHP system, which is one of the solar energy systems, was performed. The values obtained as a result of the analysis are given in Table 1. Also, these results are modeled with ANN in terms of the sustainability concept.

Table 1: The result of the thermodynamic analysis of the ETHP system

Turbine Input Temperature (K)	Mass flow (kg/s)	Ambient Temperature (K)	Exergy efficiency (%)
323	0.36	294	0.2096
⋮	⋮	⋮	⋮
372	0.36	294	0.2406
358	0.25	294	0.3195
⋮	⋮	⋮	⋮
358	0.397	294	0.2147
358	0.36	280	0.1746
⋮	⋮	⋮	⋮
358	0.36	305	0.3187

The developed ANN model is constructed to evaluate thermodynamic results of ORC power system integrated to ETHP system, exergy efficiency, and sustainability. The Backpropagation, General Regression neural network architectures are developed. As the GRNN model did not succeed, only the BPNN model's properties and results are given below. The Turbine Input Temperature (K), the Mass flow (kg/s) and the Ambient Temperature (K) are taken as input parameters, and the Exergy efficiency (%) is considered as an output parameter in the developed models. In all the developed BPNN models which are BPNN with each layer connected to only the previous layer (standard nets), BPNN with recurrent networks with dampened feedback (Jordan-Elman nets), BPNN with multiple hidden slabs with different activation functions (Ward nets) and BPNN with each layer connected to every previous layer (Jumped

connection nets) in the learning phase, trainings and the testing are calculated according to the minimum and last average errors. Last average error from BPNN algorithm reaches almost zero (0.00006) after approximately 4664 learning epochs (Figure 6).

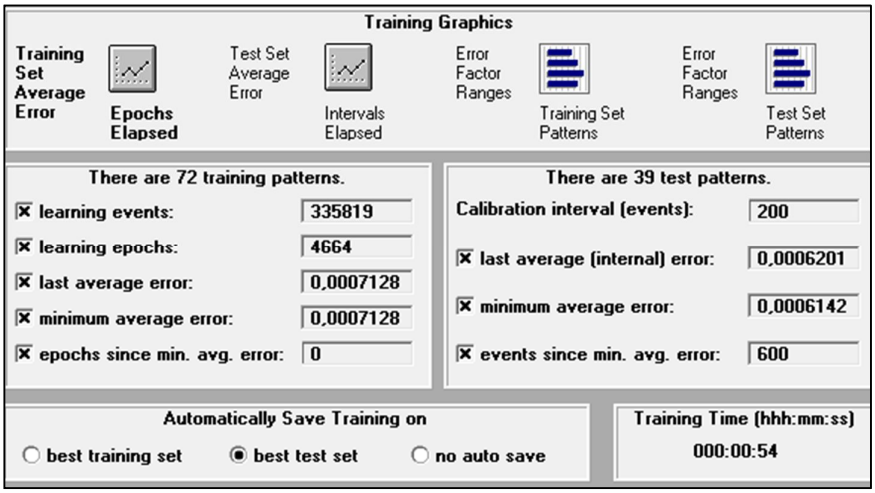

Figure 6: The training and learning criteria in the developed BPNN models.

Different activation functions tried in these model too. Best results are taken in the Logistic (Sigmoid logistic) activation function. In the hidden neurons, two neurons participate in the hidden slabs. Pattern selection is rotational and 72 patterns (55% of the dataset) processed for training, 39 patterns (30% of the dataset) processed for testing and 19 patterns (15% of the dataset) processed for forecasting. The learning rates are 0,2; momentum is 0,3 in all the hidden layers.

In this study, when the ANN model that examined was evaluated using various standard statistical performance evaluation criteria and mathematical formulations is trained, in BPNN training cycle, for the R squared value and correlation coefficient, the best is obtained from and BPNN with each layer connected to every previous layer (Jumped connection nets) (Figure 7).

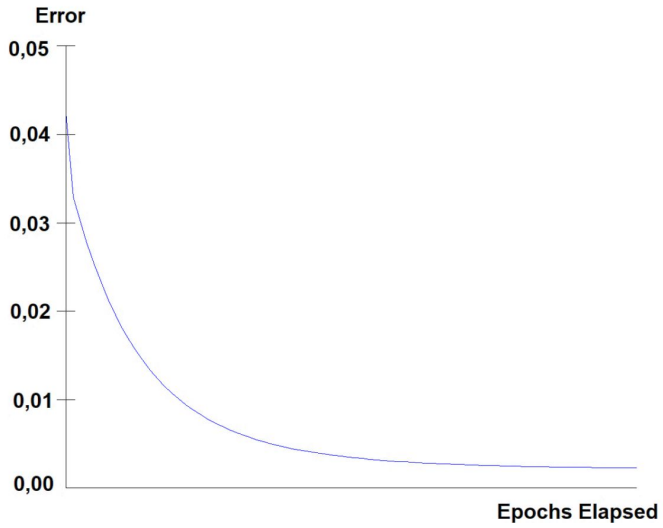

Figure 7: The Epochs – Errors graph of the developed BPNN (Jumped connection nets)

All the BPNN success rates are higher than %95 (0,95) but only at the BPNN with recurrent networks with dampened feedback (Jordan-Elman nets) an over-learning occurs so that the Relative contribution (strength) factors results did not become meaningful. On the other hand, according to the model 4 which is BPNN with each layer connected to every previous layer (Jumped connection nets), the relative contribution (strength) factors of input parameters on the output parameter are so meaningful (Table 2).

Table 2: Relative contribution (strength) factors of input parameters on the output parameter according to Model 4.

Input Parameters	Strength Factors on Exergy Efficiency
Turbine Input Temperature (K)	0,25102
Mass flow (kg/s)	0,44422
Ambient Temperature (K)	0,50969

4. CONCLUSION

In this study, exergy analysis of the ORC system integrated into ETHP system, which is one of the methods of utilisation of solar energy, was modelled with ANN. Equilibrium equations for thermodynamic results are solved by the Engineering Equation Solver (EES) program. The thermophysical results were successfully predicted by ANN with meaningful errors.
The exergy efficiency value of the ORC system integrated into ETHP was estimated depending on the turbine inlet temperature, mass flow, and ambient temperature system values as an input by using ANNs. ANN approach, which is developed, demonstrated to be a meaningful forecast tool. In this sense, It is understood that ANN can be successfully implemented for modelling and forecast in energy systems. This study is expected to contribute to the literature in terms of energy and exergy planning, sustainability, determination of energy policies, and exergy efficiency. Some outstanding results of the obtained from this study can be expressed as below;

- In this study, it is understood that the estimation of the exergy efficiency of the ETHP system can be obtained with artificial neural network models in highly successful results if there are sufficient data.
- The exergy efficiency of the ORC system integrated into ETHP was calculated as 23.39%.
- Ambient temperature was found to be the most influential parameter on exergy efficiency.
- The success rate of the developed BPNN model is %95,4.
- The most suitable BPNN architecture for this case study is recurrent networks with dampened feedback (Jordan-Elman nets).
- It is seen that BPNN is an applicable neural network algorithm to forecast the exergy efficiency of the ORC system integrated into ETHP.
- For future works, better results can be obtained by extending the training and testing datasets.
- This study is expected to contribute to the literature in terms of sustainability and to encourage authorities to apply solar systems to sustainable buildings.

5. REFERENCES

Al-Mufti, F., Dodson, V., Lee, J., Wajswol, E., Gandhi, C., Scurlock, C., Cole, C., Lee, K. & Mayer, S. A., 2019, Artificial intelligence in neurocritical care, Journal of the Neurological Sciences, (In Press), https://doi.org/10.1016/j.jns.2019.06.024

Daghigh, R. & Zandi, P., 2019, Improving the performance of heat pipe embedded evacuated tube collector with nanofluids and auxiliary gas system, Renewable Energy, 134, 888-901.

Demirezen, G., Fung, S.A., 2018, Application of artificial neural network in the prediction of ambient temperature for a cloud-based smart dual fuel switching system, *Energy Procedia*, 158 (2019) 3070–3075.

Elsheniti, M.B., Kotb, A. & Elsamni, O. 2019, Thermal performance of a heat-pipe evacuated-tube solar collector at high inlet temperatures, Applied Thermal Engineering, 154, 315-325.

Ersoz, M.A., 2016, Effects of different working fluid use on the energy and exergy performance for evacuated tube solar collector with thermosyphon heat pipe, Renewable Energy, 96, 244-256.

Erten, B., Utlu, Z. & Karabuga, A., 2019, Assessment of the hydrogen production system for domestic type use, 4th International Hydrogen Technologies Congress (IHTEC-2019), June20-23, 2019, Edirne, Turkey.

Ghritlahre, H.K. & Prasad R.K., 2018, Application of ANN technique to predict the performance of solar collector systems - A review. Renewable and Sustainable Energy Reviews, 84, 75-88.

Hoffmann, J.E., 2019, On the outlook for solar thermal hydrogen production in South Africa, International Journal of Hydrogen Energy, 44 (2), 629-640.

Huang, X., Wang, Q., Yang, H., Zhong, S., Jiao, D., Zhang, K., Li, M. & Pei, G., 2019, Theoretical and experimental studies of impacts of heat shields on heat pipe evacuated tube solar collector, Renewable Energy, 138, 999-1009.

International Energy Agency, 2006, Renewable Energy; RD&D Priorities, Insights from the IEA Technology Programmes, IAE, Paris.

Jowzi, M., Veysi, F. & Sadeghi, G., 2019, Experimental and numerical investigations on the thermal performance of a modified evacuated tube solar collector: Effect of the bypass tube, Solar Energy, 183, 725-737.

Keskinbora, K.H., 2019, Medical ethics considerations on artificial intelligence, Journal of Clinical Neuroscience, 64, 277-282.

Marugan, A.P., Marguez, F.P.G., Perez, J.M.P. & Ruiz-Hernandez, D., 20118, A survey of artificial neural network in wind energy systems, Applied Energy, 228, 1822-1836.

Tolon, F. E., Karabuga, A., Tolon, M. & Utlu, Z., 2019, Evaluation of thermodynamic analysis of solar energy systems integrated into sustainable buildings with artificial neural network: A case study, 3rd World Conference on Technology, Innovation and Entrepreneurship (WOCTINE), June 21-23, 2019, Istanbul, Turkey.

Tolon, M., 2007, A neural network approach for slope stability during Earthquake, *Master's thesis*, Faculty of Civil Engineering, Istanbul Technical University, Istanbul, Turkey.

Tong, Y., Kim, J. & Cho, H., 2015, Effects of thermal performance of enclosed-type evacuated U-tube solar collector with multi-walled carbon nanotube/water nanofluid, Renewable Energy, 83, 463-473.

Utlu, Z. & Hepbasli, A., 2007, Parametrical investigation of the effect of dead (reference) state on energy and exergy utilization efficiencies of residential–commercial sectors: A review and an application, *Renewable and Sustainable Energy Reviews,* 11, 603–634.

Utlu, Z. & Hepbasli, A., 2010, Comparison of Turkey's sectoral energy utilization efficiencies between 1990 and 2000, Part 1: Utility and industrial sectors, Energy Sources, 26 (14), 1331-1344.

Utlu, Z. & Onal, B.S., 2018, Thermodynamic analysis of thermophotovoltaic systems used in waste heat recovery systems: an application, International Journal of Low-Carbon Technologies, 13, 52-60.

Yilmaz, F., 2018, Thermodynamic performance evaluation of a novel solar energy based multigeneration system, Applied Thermal Engineering, 143, 429-437.

#208: A novel mathematical model of the solar assisted dehumidification and regeneration systems

Yousef Golizadeh AKHLAGHI [1], Ali BADIEI [2], Xudong ZHAO [3]

[1] Department of Engineering, University of Hull, Hull, HU6 7RX, UK, Y.Golizade-Akhlagi@2017.hull.ac.uk
[2] Department of Engineering, University of Hull, Hull, HU6 7RX, UK, A.Badiei@hull.ac.uk
[3] Department of Engineering, University of Hull, Hull, HU6 7RX, UK, Xudong.Zhao@hull.ac.uk

This paper introduces a state-of-the-art modelling technique to investigate the performance of solar assisted dehumidification and regeneration cycles. The dehumidification/regeneration system investigated in this study employs a solid adsorbent bed and enables use of both solar energy and returning warm air to deliver efficient dehumidification and regeneration of the treated air. Study of literature revealed a huge gap between model results and industrial performance of such systems. Hence, the modelling work presented in this paper employs Gaussian Process Regression (GPR) technique to close the gap between model outputs and real-life operation parameters of the system. An extensive amount of laboratory tests were also carried out on the dehumidification/regeneration system and model predictions were validated through comparison with experimental results. The model predictions were found to be in good agreement with experimental results, with maximum error not exceeding 10%.

The GPR technique enables simultaneous analysis of a vast quantity of key system parameters derived from mathematical models and laboratory tests. The system parameters investigated in this study include: temperature, relative humidity and flow rate of process air, and temperature of regeneration air, solar radiation intensity, operating time, moisture extraction efficiency of the dehumidification cycle and moisture removal efficiency of the regeneration cycle. Investigation of both modelling and experimental results revealed that efficiencies of the both dehumidification and regeneration cycles decrease as relative humidity of the process air increases. The increase in regeneration temperature leads to an increase in regeneration efficiency whereas; it does not have a significant impact on the dehumidification efficiency. A similar trend was also observed when solar intensity were increased.

The proposed technique reduced the complexity of model by eliminating the need for heat and mass transfer calculations; reduced the performance gap between model results and real-life performance data, and increased the reliability of model outputs by showing a good agreement with experimental results. The GPR based mathematical model delivers an effective design and performance evaluation tool for the solar assisted dehumidification and regeneration systems and provides an unprecedented opportunity for commercialising such systems.

Keywords: *Gaussian process regression, mathematical model, solar assisted, efficiency, dehumidification*

1. INTRODUCTION

Air humidity is an important factor in both residential and industrial buildings which generally is controlled by air conditioning systems. Excessive amount of humidity can either have a negative effect on the habitants or the electronic instruments of residential and industrial buildings. Furthermore, it is a key aspect for increasing durability of products as dry air is used for improving the quality of products in large industries such as food production, pharmaceutical production, and industrial chemicals production. It is also required in goods storage, packaging rooms, organic plants, organic products and hygroscopic raw materials storage (Yadav, 2012).

The air with relative humidity (RH) between 40% and 60% is the most convenient indoor air for various purposes (Dai et al., 2017). Mechanical vapour compression refrigeration air conditioning systems are the main devices that are used to provide a comfortable residential and industrial air environment by controlling the temperature and humidity of the air. Due to their energy intensive process and low COP (Bi et al., 2018), energy efficient desiccant cooling and air-conditioning systems have attracted the attentions in past decades. In such systems, the dehumidification is done by solar energy or waste heat recovery instead of energy intensive devices (Safizadeh et al., 2014). Desiccant cooling and air-conditioning systems with solid or liquid desiccant are potential substitutes to electrically driven vapour compression cooling systems (Xiao et al., 2011; Calise et al., 2014; Ge et al., 2011).

Analysis of the desiccant systems are commonly classified into numerical, experimental and mathematical models. Literatures have investigated the heat and mass transfer processes occurring in the sorption systems in order to study the suitability of different desiccant materials for the absorbent, system configurations, component dimensions, operating conditions, and regeneration heat sources. Furthermore, development of components such as absorbers and solar regenerators and systems for air conditioning and drying applications, comparative assessment of the liquid sorbents properties and the performance comparison between indirect and direct solar regeneration unit have been carried out over the past years (Yin et al., 2014; Rafique et al., 2016; Misha et al., 2012; Gomez-castro et al., 2018; Daou, 2006). The above-mentioned literatures have led to great achievements in optimisation, characterisation and design of the desiccant systems.

Comprehensive overview of the conducted literature for the desiccant systems (Yang et al., 2017; Li et al., 2015; Das et al., 2015; Yamaguchi & Saito, 2013) , which only few of them are listed in this paper, has revealed there is an apparent gap between the research findings and engineering application of this energy efficient technology. This paper pioneers in developing the Gaussian Process Regression (GPR) as a predictive mathematical model for the novel solar/waste energy driven dehumidification/ regeneration cycle to fill the outstanding gaps.

Gaussian process regression (GPR) is a powerful predictive tool to model, explore and predict the performance of the system. The GPR, as a non-parametric Bayesian approach towards regression problems, explores various considered operating scenarios in a huge dataset for the proposed system and then predicts the behaviour of the system for unforeseen scenarios by a fitting function. The GPR is non-parametric as the form of the fitted function depends on the number of data points in the dataset. The GPR has been applied to a wide range of fields such as engineering, finance, education, medicine, and law (Li et al., 2018; Shepero et al., 2018; Wang et al., 2008). For instance, Gray et al. (2016) analysed the suitability of Gaussian processes for thermal building modelling by comparing the day-ahead prediction error of the internal air temperature with a grey-box model. Wu et al. (2018) presented a new application of Gaussian process regression methods for the modelling and forecasting of human mortality rates. Liu et al. (2018) presented an accurate Gaussian process regression soft sensor with the sum of squared-exponential covariance function and periodic covariance function to capture the time varying and periodic characteristics in the subway IAQ data. Yuan et al. (2018) employed the Gaussian process regression to predict the ship fuel consumption for different scenarios.

An extensive literature review of the desiccant based dehumidification systems has disclosed the outstanding gap between the research findings and engineering application of the desiccant systems, since the current numerical and experimental models are limited to the narrow data scales. This situation has significantly obstructed the wide and rational application of the desiccant based dehumidification systems in practical engineering in which key operating parameters vary simultaneously during the different operational conditions. Additionally, the experimental models are slow and cost intensive, and the numerical models are cumbersome as the energy balance and mass transfer phenomenon must be simulated and lots of iterations makes the modelling time consuming. Lack of one by one and direct correlations between the main operating and performance parameters in the previously proposed models has apparently obstructed the analysis of the dehumidifier systems.

To fill the above mentioned gaps between the research findings and practical engineering application of the desiccant technology, this paper has pioneered in bringing the Gaussian Process Regression (GPR) into a solar/waste energy driven dehumidification/regeneration system which bridges the identified gap by enabling the performance analysis of the system by using the key parameters only. The GPR has been employed to convert thousands of numerical and experimental data to a practical engineering equation which enables the engineering scale and characterisation of the solar/waste energy driven dehumidification/regeneration cycle. The equation

correlates the key operating parameters with the performance parameters, and thus enables the performance analysis of the system by predicting the unforeseen operating conditions. The outstanding features of the GPR based mathematical model for the solar/waste energy driven dehumidification/regeneration cycle are:

- Directly correlates the main operating parameters i.e. temperature, relative humidity and flow rate of process air, temperature of regeneration air, length of the desiccant bed, solar radiation intensity and operating time with performance parameters i.e. moisture extraction efficiency for the dehumidification cycle and moisture removal efficiency for the regeneration cycle.
- Needless of the energy and mass balance equations, and associated initial and boundary conditions and iteration processes.
- Practical, swift, accurate and cost-effective method that make it suitable for studying any critical operating conditions without any danger and is appropriate for commercialising.
- Valid to predict system performance for any unforeseen operating conditions within the real operating ranges.

2. METHODS: GAUSSIAN PROCESS REGRESSION

Gaussian process regression (GPR) is a vigorous method to predict the value of the unforeseen points by observing some known data. Practically, GPR goes through the collected inputs (independent variables) and outputs (dependent variables) and accurately predicts the value of outputs for any new possible inputs by a fitted function and correspondent coefficients. The objective of this function is to find the accurate value of the output as quickly and accurately as possible. Moreover, the function can express and explore the direct and one by one relationship between any inputs and outputs. A detailed description of the GPR has been presented in (Rasmussen, 2004). Here a brief review of the fundamentals is provided.

In Equation 1, f denotes the unknown function, y represents the dependent variable, x represents the independent variable, and ϵ represents the measurement error.

Equation 1: Error, dependent and independent parameters function

$$y = f(x) + \epsilon$$

Gaussian process describes the distribution over functions and it needs a covariance or kernel function and mean function as shown in Equation 2 to be fully specified.

Equation 2: Covariance, kernel function and mean function

$$f(x) \sim GPR(m(x), k(x, \acute{x}))$$

Generally, the covariance function, defines the degree of correlation between the outputs of two input sets (x and $\acute{x}$), and plays a key role as the backbone on which the relationships between input variables are found. The mean covariance and the kernel functions can be defined as Equations 3 and 4 respectively:

Equation 3: Mean function

$$m(x) = E\,[\,f(x)\,]$$

Equation 4: Covariance function

$$k(x, \acute{x}) = E\,[\,\big(f(X) - m(x)\big)\big(f(\acute{x}) - m(\acute{x})\big)\,]$$

Where $E\,[\,f(x)\,]$ means expected value of $f(x)$.

An appropriate kernel is chosen on basis of the assumptions such as smoothness and likely patterns to be expected in the data. One common kernel function is the radial basis function kernel, which can be defined as:

Equation 5: Radial basis function kernel

$$k(x, \acute{x}) = \sigma_f^2 \exp\left(-\sum_{i=1}^{i=n} \frac{\|x(i) - \acute{x}(i)\|^2}{2\Theta(i)^2}\right)$$

Where σ_f^2 is called the signal variance and Θ is called the length-scale.

The covariance matrix for any two matrices (X = $[x_1, \ldots, x_n]$ and $\acute{X}$ = $[\acute{x}_1, \ldots, \acute{x}_n]$) is defined as:

Equation 6: Covariance matrix

$$K(\mathrm{X}, \acute{X}) = \begin{bmatrix} k(x_1, \acute{x}_1) & k(x_1, \acute{x}_2) & \cdots & k(x_1, \acute{x}_n) \\ k(x_2, \acute{x}_1) & k(x_2, \acute{x}_2) & & k(x_2, \acute{x}_n) \\ & \vdots & \ddots & \vdots \\ k(x_n, \acute{x}_1) & k(x_n, \acute{x}_2) & \cdots & k(x_n, \acute{x}_n) \end{bmatrix}$$

Once the prior kernel and mean functions are chosen, the GPR can be implemented to update the kernel and mean functions using the observed new data points to obtain the posterior estimation function.

3. DESCRIPTION OF THE DEHUMIDIFICATION/REGENERATION CYCLE

Schematic of the solar/waste energy driven dehumidification/regeneration cycle is shown in Figure 1. In such system, a desiccant bed which is illustrated in Figure 2, is located inside a channel and is constructed by a porous and visible-light LiCl-Sillicon-Gels material.

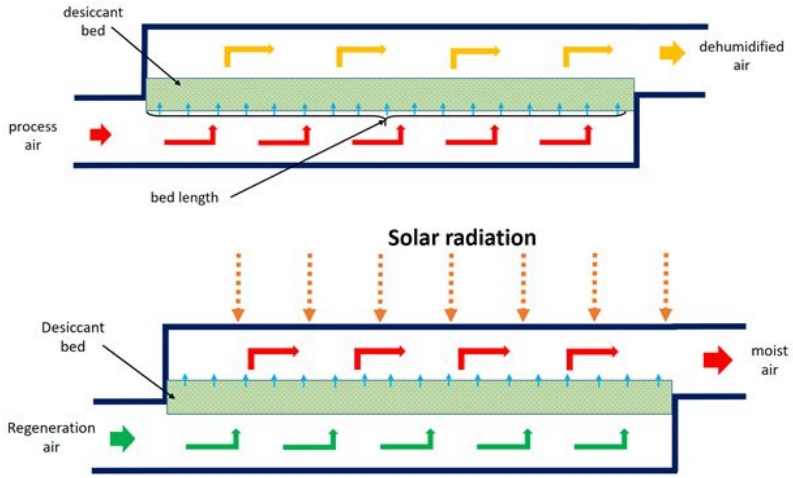

Figure 1: Solar/waste energy driven dehumidification and regeneration cycle: (upper) dehumidification process; (lower) regeneration process.

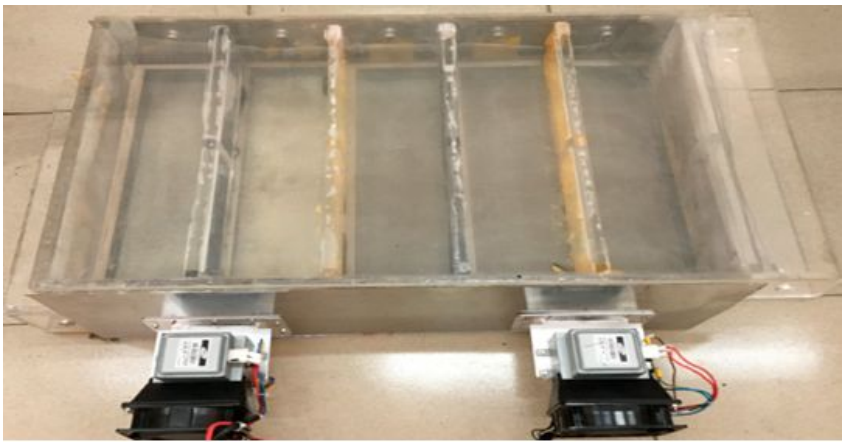

Figure 2: Image of the solar solid dehumidification/regeneration bed.

The bed specifications such as its dimensions and material play a key role in the performance of both dehumidification and regeneration cycles. The size of the bed for the selected system in this study is 700 mm × 500 mm × 250 mm and the thickness of the silica gel layer was chosen at 50 mm. In the dehumidification process, the humid air which is called process air, flows inside the channel and passes through the bed. The moisture of the process air is absorbed by the absorbent material in the desiccant bed owing to the vapour partial pressure difference between the solid absorbent surface of the bed and the process air. By passing the process air through

the desiccant bed, the absorbent material gradually will reach its saturation state and regeneration process must be started to regenerate the saturated absorbent material for the next dehumidification cycle.

During the regeneration process, either a warm regeneration air with a temperature more than 70°C or a low temperature regeneration air with the solar radiation, which is brought into the channel through the upper side solar-visible glasses, passes through the saturated absorbent. As the regeneration air passes through the channel, the heat is transferred from the regeneration air to the water sorted inside the absorbent voids and get the water evaporated. Eventually, the evaporated water is taken out by the regeneration air and the regenerated absorbent is ready for another dehumidification cycle. When the solar radiation is not available, the regeneration air is firstly heated by an available waste heat sources as the heat play a key role in evaporating the water that is sorted in the absorbent bed.

Moisture extraction efficiency is the ratio of the inlet humidity ratio of the process air as a performance parameter of dehumidification cycle can be expressed as:

Equation 7: Moisture extraction efficiency

$$\eta_{me} = \frac{d_{p,in} - d_{p,out}}{d_{p,in}}$$

Where $d_{p,in}$ is moisture content of inlet air and $d_{p,out}$ is the moisture content of outlet air.

The moisture removal efficiency for the regeneration cycle is given as:

Equation 8: Moisture removal efficiency

$$\eta_{mr} = \frac{W_0 - W}{W_0}$$

Where W_0 is initial water content of desiccant and W is the final water content of desiccant.

4. MATHEMATICAL MODEL

In order to develop the mathematical model, a comprehensive data points comprising the key operating parameters and corresponding performance parameters have been provided. These data points have constructed a single comprehensive dataset which has been analysed by Gaussian process regression in R programing language. The Gaussian process regression (GPR) has been presented by an applicable engineering equation. In this section model development process which is divided into three main sub-sections, is explained.

4.1. Determination of the dependent and independent variables

To carry out the mathematical model, the solar/waste energy driven dehumidification/regeneration cycle's main operating parameters, which are also called independent variables, and proper operating parameters, which are also called dependent variables, have been identified. In this study, seven main operating parameters as shown in Figure 3, including three main flow characteristics i.e., temperature, relative humidity and flow rate which can change continually during the system operation, have been selected for both dehumidification and regeneration cycles. Additionally, based on the previous numerical and experimental models, length of the desiccant has been selected as the main geometric characteristics because it has the dominant effect on the performance of the system among other geometric characteristics. Solar radiation intensity for the regeneration cycle and operating time of both dehumidification and regeneration cycle are considered as the operating parameters. For dependent variables, moisture extraction efficiency as a performance factor of dehumidification process and moisture removal efficiency as a performance factor of regeneration process have been selected to fulfil the performance analysis of the desiccant system.

To make the model more concentrated on the real operating conditions of the described system in section 2, and also to avoid the model from considering the unrealistic operating conditions, proper ranges for each independent variables are defined and thus the values of each variable has been narrowed to real operating conditions. Appropriate ranges have been set by a meticulous investigation of real operating conditions, numerical and experimental literatures as listed in Table 1. Flow rate and relative humidity of the air stream in both cycles are considered to be same.

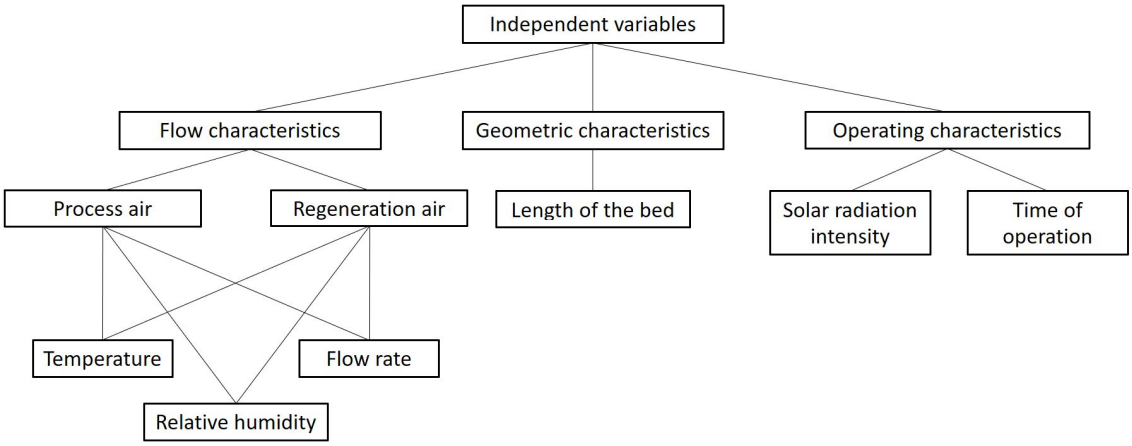

Figure 3: Independent variables diagram

Table 1: Range of operating parameters

Operating parameters	**Ranges**
Temperature of the process air, ^oC	25 – 40
Relative humidity of the process air, -	0.6 – 0.9
Temperature of the regeneration air, ^oC	70 – 80
Flow rate air stream, m/s	1 – 4
Length of the desiccant bed, m	1 – 5
Solar radiation intensity, W/m^2	0 – 1800
Operating time of each cycle, hr	1 – 5

A comprehensive dataset as a principal of statistical modelling which must be created to trigger the data exploration. The dataset is composed of two parts: 1) Independent variables 2) Dependent variables. To construct the independent (operating parameters) section, firstly, discrete values for each independent variable are chosen by considering the defined ranges listed in Table 2. Different discrete values could have been selected because the values in Table 2 are randomly chosen to construct the dataset only and validity of the model are not restricted to these specific values.

Table 2: Discrete values for operating parameters

T_p [^oC]	RH_p [-]	T_r [^oC]	U [m/s]	L_d [m]	I [W/m^2]	t [hr]
25	0.6	20	1	1	0	1
27.5	0.7	70	2	2	300	2
30	0.8	80	3	3	600	3
32.5	0.9	90	4	4	900	4
35	0.99	-	-	5	1200	5
37.5	-	-	-	-	1500	-
40	-	-	-	-	1800	-

Having identified the discrete values, to finalise the construction of the independent section of dataset, all possible combinations of the discrete values are created. All possible combinations allow the GPR model to be aware of all possible operating conditions of the system and thus accredits the model under any random operating conditions. Figure 4 illustrates three operating conditions out of n possible conditions. In each condition, single values for each independent variable is selected and then a set of all selected values is located in the independent part of the dataset as one operating condition. Once all possible sets are selected, the model will be aware of all possible combinations during the data analysis process.

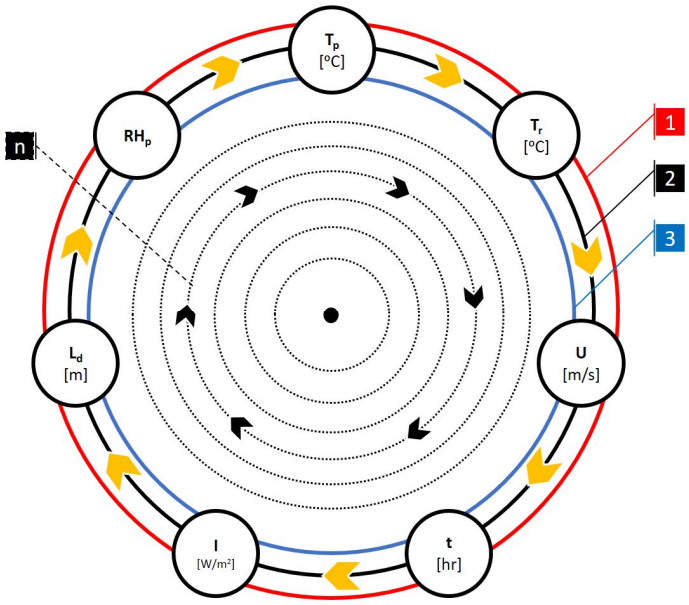

Figure 4: Illustration of three operating conditions out of n operating conditions

To build the dependent part of the dataset, all corresponding performance parameters for each created operating condition have been calculated through an experiment and constructed the comprehensive dataset as shown in Table 3. In this study, 4320 set of operating conditions are analysed by a GPR based mathematical model to provide the generalised model.

Table 3: Comprehensive dataset

Operating conditions	T_p [°C]	RH_p [-]	T_r [°C]	U [m/s]	L_d [m]	I [W/m²]	[hr]	η_{sorp}	η_{desorp}
1	25	0.6	20	1	1	600	2	0.277561778	0.518653866
2	25	0.6	1	3	20	600	1	0.368264439	0.692065835
3	25	0.6	20	1	1	1800	2	0.277561778	0.936875303
4	25	0.6	20	1	3	600	2	0.275255819	0.903544548
5	25	0.6	1	3	20	1200	2	0.275255819	0.999996842
⋮	⋮	⋮	⋮	⋮	⋮	⋮	⋮	⋮	⋮
4325	40	0.9	4	3	80	0	5	0.01325928	0.999999932
4326	40	0.9	4	3	90	0	5	0.01325928	1
4327	40	0.9	4	5	70	0	5	0.013555742	0.999972234
4328	40	0.9	4	5	80	0	5	0.013555742	0.999999935
4320	40	0.9	4	5	90	0	5	0.013555742	1

4.2. Gaussian process regression model

The GPR analysis has been carried out in R programing tool 3.5.1 using the DiceKriging package. The detailed information about the DiceKriging package can be found in (Roustant, 2012). The Gaussian covariance kernel has been selected in GPR because it is the standard choice for obtaining a smooth interpolating function.

The analysis is done in four major steps:

i. The constructed comprehensive dataset is imported.
ii. The GPR analysis is carried out by a fitted function for the imported dataset.
iii. Report of the analysis is printed with all calculated coefficients.
iv. Final exponential equation is produced.

5. RESULTS AND DISCUSSION

In this section, the model is firstly validated in model verification subsection and then generalised in order to accredit the model validity for any operating conditions within the defined ranges. Eventually, the constructed equation and its correspondent coefficients are presented for both dehumidification and regeneration processes. Finally, to illustrate the applicability and contribution of the model to the proposed system, effect of four operating parameters are discussed.

5.1. Model verification

The developed mathematical model by GPR have been verified by experimental results. Figure 5 gives the dehumidification efficiency for both experiment and GPR based mathematical models. The comparison has been done with listed values in Table 4 and for five hours of system operation for each cycle. Dehumidification efficiency decreases as the cycle continues and the desiccant bed absorbs more water. It can be seen that the results are almost overlapped where the maximum relative error is 9.7%.

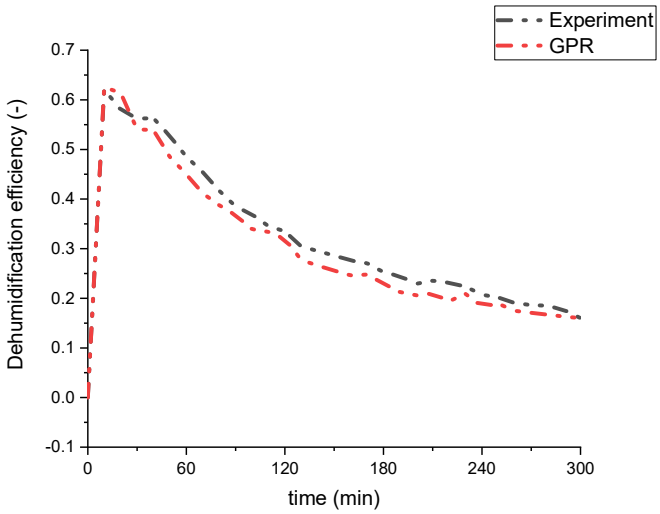

Figure 5: Validation of the mathematical model

Table 4: Parameters value for model verification

Parameters	Values
Relative humidity of the process air, -	0.81
Temperature of the regeneration air, ^{o}C	27.69
Flow rate air stream, m/s	0.62
Length of the desiccant bed, m	0.7
Solar radiation intensity, W/m^2	300
Relative humidity of the process air, -	0.81

5.2. Model generalisation

Once the model was verified, the cross verification is conducted to generalised the model and to show the independency of the model to the created dataset in Table 3 and thus to express the validity of the proposed model for any new operating condition within the defined ranges. For this purpose, ten unforeseen operating conditions are chosen to investigate the generalisation of the model as shown in Table 5. Figure 6 shows the comparison results for both experimental and GPR based mathematical models which indicates the good agreement of both models for random operating conditions in which the maximum relative errors for dehumidification and regeneration cycles are 2.14% and 9.96% respectively.

Table 5: New random independent parameters

Random operating conditions	T_p [°C]	RH_p [-]	T_r [°C]	U [m/s]	L_d [m]	I [W/m²]	t [hr]
1	26.9	0.7	3.7	1.4	20	600	1
2	26.9	0.87	3.7	4.6	20	600	1
3	33.2	0.65	1.25	4.6	20	600	1
4	33.2	0.7	1.25	4.6	20	600	1
5	38.5	0.65	2.85	4.6	20	600	1
6	38.5	0.7	1.25	4.6	20	600	1
7	38.5	0.87	3.7	4.6	20	600	1
8	26.9	0.7	1.25	1.4	90	0	1
9	26.9	0.87	3.7	4.6	90	0	1
10	33.2	0.65	3.7	4.6	90	0	1

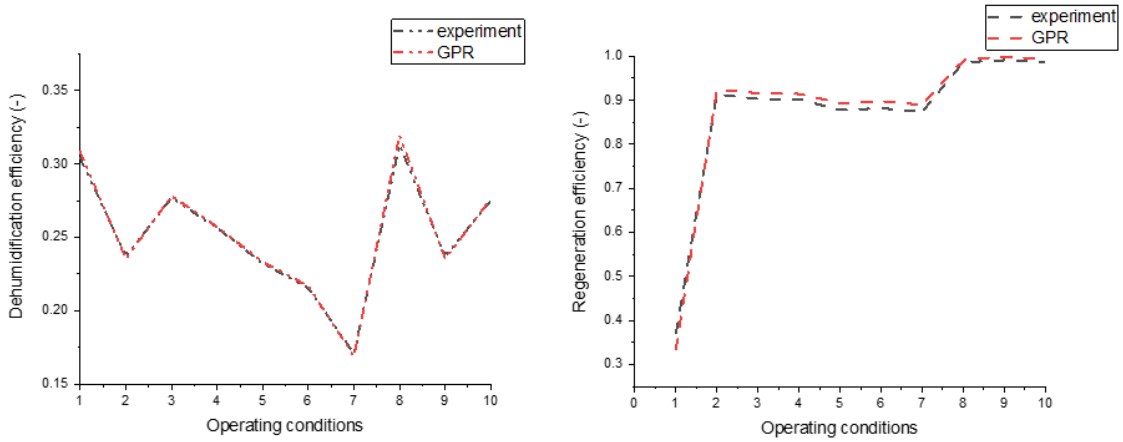

Figure 6: Cross validation of the mathematical model: (left) dehumidification efficiency (right) regeneration efficiency

6. CONCLUSION

A new application of Gaussian Process Regression (GPR) is presented in this paper which enables the performance analysis of the novel solar/waste energy driven dehumidification/ - regeneration cycle. Such effort adds important scientific values to the characterisation and engineering design of the solar/waste energy driven dehumidification/regeneration cycle by correlating the main parameters of the system. The existed gap in previous literatures between the research and engineering application of the system is now filled as the engineering scale design and characterisation of the desiccant system is now achievable. This approach offers an invaluable contribution to the commercialisation and market viability of the novel solar/waste energy driven dehumidification/regeneration cycle technology, and thus makes the analysis process of the system environmentally friendly.

The GPR based mathematical model has been developed by exploring thousands of numerical and experimental data into an exponential equation which directly correlates the main operating parameters of the desiccant system i.e. temperature, relative humidity and flow rate of process air, temperature of the regeneration air, length of the desiccant bed, solar radiation intensity and operating time of the system to the performance parameters, i.e. moisture extraction efficiency for the dehumidification cycle and moisture removal efficiency for the regeneration cycle. Additionally, the model enables analysis of the parameters and their effects on the performance of the system directly. The extraction process of the equation has been carried out in R programing language using the Dice Kriging package, and then the model is validated by experimental data with maximum relative error of 9.7%. Furthermore, the cross validation has been presented to illustrate the validity of the model for any new operating parameter with maximum relative errors of 2.14% and 9.96% for dehumidification and regeneration cycles respectively.

The presented GPR based mathematical model is simple, practical, accurate and swift in operation as no iteration, energy or mass transfer equations are needed to analyse the system. Thus, the GPR based mathematical model provides an effective design and performance evaluation tool for the solar/waste energy driven dehumidification/regeneration cycle to commercialise and explore the product.

7. REFERENCES

Bi, Y., W. Yang, and X. Zhao, Numerical investigation of a solar/waste energy driven sorption/desorption cycle employing a novel adsorbent bed. Energy, 2018. **149**: p. 84-97.

Calise, F., et al., Desiccant-based AHU interacting with a CPVT collector: Simulation of energy and environmental performance. Solar energy, 2014. **103**: p. 574-594.

Dai, L., et al., Sorption and regeneration performance of novel solid desiccant based on PVA-LiCl electrospun nanofibrous membrane. Polymer Testing, 2017. **64**: p. 242-249.

Daou, K., R. Wang, and Z. Xia, Desiccant cooling air conditioning: a review. Renewable and Sustainable Energy Reviews, 2006. **10**(2): p. 55-77.

Das, R.S. and S. Jain, Performance characteristics of cross-flow membrane contactors for liquid desiccant systems. Applied Energy, 2015. **141**: p. 1-11.

Ge, G., F. Xiao, and X. Xu, Model-based optimal control of a dedicated outdoor air-chilled ceiling system using liquid desiccant and membrane-based total heat recovery. Applied energy, 2011. **88**(11): p. 4180-4190.

Gómez-Castro, F.M., et al., Review of indirect and direct solar thermal regeneration for liquid desiccant systems. Renewable and Sustainable Energy Reviews, 2018. **82**: p. 545-575.

Gray, F.M. and M. Schmidt, Thermal building modelling using Gaussian processes. Energy and Buildings, 2016. **119**: p. 119-128.

Li, Z., S. Michiyuki, and F. Takeshi, Experimental study on heat and mass transfer characteristics for a desiccant-coated fin-tube heat exchanger. International Journal of Heat and Mass Transfer, 2015. **89**: p. 641-651.

Li, Y., S. Liu, and L. Shu, Wind turbine fault diagnosis based on Gaussian process classifiers applied to operational data. Renewable Energy, 2018.

Liu, H., et al., Modeling of subway indoor air quality using Gaussian process regression. Journal of hazardous materials, 2018. **359**: p. 266-273.

Misha, S., et al., Review of solid/liquid desiccant in the drying applications and its regeneration methods. Renewable and Sustainable Energy Reviews, 2012. **16**(7): p. 4686-4707.

Rafique, M.M., P. Gandhidasan, and H.M. Bahaidarah, Liquid desiccant materials and dehumidifiers–A review. Renewable and Sustainable Energy Reviews, 2016. **56**: p. 179-195.

Rasmussen, C.E., Gaussian processes in machine learning, in Advanced lectures on machine learning. 2004, Springer. p. 63-71.

Roustant, O., D. Ginsbourger, and Y. Deville, DiceKriging, DiceOptim: Two R packages for the analysis of computer experiments by kriging-based metamodeling and optimization. 2012.

Safizadeh, M.R., et al., Two-stage Air-dehumidification System for the Tropics--Experimental and Theoretical Analysis of a Lab System. Energy Procedia, 2014. **48**: p. 982-990.

Shepero, M., et al., Residential probabilistic load forecasting: A method using Gaussian process designed for electric load data. Applied Energy, 2018. **218**: p. 159-172.

Wang, J.M., D.J. Fleet, and A. Hertzmann, Gaussian process dynamical models for human motion. IEEE transactions on pattern analysis and machine intelligence, 2008. **30**(2): p. 283-298.

Wu, R. and B. Wang, Gaussian process regression method for forecasting of mortality rates. Neurocomputing, 2018. **316**: p. 232-239.

Xiao, F., G. Ge, and X. Niu, Control performance of a dedicated outdoor air system adopting liquid desiccant dehumidification. Applied Energy, 2011. **88**(1): p. 143-149.

Yadav, A., Experimental and numerical investigation of solar powered solid desiccant dehumidifier. 2012, National Institute of Technology.

Yamaguchi, S. and K. Saito, Numerical and experimental performance analysis of rotary desiccant wheels. International Journal of Heat and Mass Transfer, 2013. **60**: p. 51-60.

Yang, W., et al., Performance Study of a Novel Solar Solid Dehumidification/Regeneration Bed for Use in Buildings Air Conditioning Systems. Energies, 2017. **10**(9): p. 1335.

Yin, Y., J. Qian, and X. Zhang, Recent advancements in liquid desiccant dehumidification technology. Renewable and Sustainable Energy Reviews, 2014. **31**: p. 38-52.

Yuan, J. and V. Nian, Ship Energy Consumption Prediction with Gaussian Process Metamodel. Energy Procedia, 2018. **152**: p. 655-660.

#209: Research on the performance of multi-stage bubble column humidification-dehumidification solar desalination system

Rihui JIN[1], Jianwei XIAO[2], Xinglong MA[3], Hongfei ZHENG[4]

[1] Beijing Institute of Technology, Beijing 100081, China, 3120160249@bit.edu.cn
[2] Beijing Institute of Technology, Beijing 100081, China, 3120170267@bit.edu.cn
[3] Beijing Institute of Technology, Beijing 100081, China, baalxmxl@yeah.net
[4] Beijing Institute of Technology, Beijing 100081, China, hongfeizh@bit.edu.cn

To enhance the humidification and dehumidification process by bubbling, we designed a multi-stage bubble column (BC) solar desalination system, composing a humidifier and a condenser that are both M-*layers. The air is circulated by the air pump inside the device, which generates a lot of bubbles after passing through the perforated plate, so that the device has a huge heat and mass transfer area. In order to enable the system to operate stably within the selected working conditions and increase the heat transfer coefficient, the structural parameters of the condensing coil and the perforated plate were designed. A steady-state heat transfer model of the system involving a stepwise diversion of seawater was developed to explore an effective method to increase the system's performance ratio (*PR*). Based on the structural design and analysis of the calculation results, a "4-layers+4-layers" BC was fabricated and tested. The experimental results show that the system has a productivity of 27.2 kg/h and a* PR *of 1.38 at an operating temperature of 65.6°C. The theoretical model was verified by comparison with experimental values. Based on the theoretical model, further analysis found that: 1) under given flow rate of seawater and air, adjusting the seawater inlet temperature can make the* PR *reach a local maximum value (*PR_{max}*); 2) by selecting a smaller seawater flow rate, reducing the air flow rate and preheating the imported seawater to a specific temperature can further improve* PR_{max}*; 3) The effect of seawater diversion on increasing* PR_{max} *is more pronounced, a diversion at the final layer of the condenser can increase the* PR_{max} *by 25.2% relative to no diversion.*

Keywords: multi-stage bubble column; humidification-dehumidification; stepwise diversion of seawater

1. INTRODUCTION

Solar energy and seawater are abundant natural resources on the earth. However, fresh water is scarce in many areas so it is meaningful to use solar energy for seawater desalination. The current solar desalination is mainly divided into two categories: photovoltaic driving and photo-thermal driving. Photovoltaic solar desalination system is mainly composed of solar photovoltaic panels and reverse osmosis seawater desalination system, which has good advantages in application to large-scale systems. Its main disadvantage is the need for strict seawater pre-treatment and precise control. Therefore, the distributed small-scale solar desalination system mainly uses photo-thermal driving, especially air humidification and dehumidification (HDH) technology. Air HDH technologies operate particularly stably, adapt to the intermittence of solar energy, and do not require strict seawater pre-treatment. However, the economics of the current air HDH desalination system is still not good enough. This is mainly due to the fact that the heat and mass transfer coefficient inside the system is not high or the energy reuse is insufficient, resulting in a low water production rate of the system. In order to strengthen the heat and mass transfer process inside the thermal solar desalination system and achieve sufficient heat recovery, scholars have proposed a variety of new air HDH structures and operation modes. For example, Wu et al. (2016) proposed a vertical tandem structure with a system gain output ratio (GOR) of 2.6 at 80°C. Bourouni et al. (2001) analysed and discussed the process of air HDH desalination technology, and pointed out the development direction of the technology. Miller and Zhani analysed and summarised the main factors affecting air HDH desalination technology, and established a theoretical model to provide a theoretical basis for improving system performance (Zhani et al., 2011, Miller and Lienhard, 2013). In order to study the method of fully recovering the latent heat of the system, Zamen et al. (2014) designed a two-stage HDH desalination system, and carried out experimental research, and obtained a 20% increase in water production rate compared to a single-stage system. Conventional HDH desalination systems generally use a humidifying packing as an evaporator and a conventional heat exchanger as a condenser, but the heat and mass transfer coefficient when they are combined is not high. Recently, some scholars have proposed a new idea of using bubbling humidification technology and fresh water dehumidification technology in HDH desalination system. El-Agouz and Abugderah (2008) and Rajaseenivasan & Srithar (2017) both designed and tested experimental scale bubbling humidification systems. They gave the relationship between the orifice diameter, the air flow rate, the operating temperature and the humidification efficiency, and gave a general conclusion that the effects of single-stage bubbling humidification and multi-stage spray humidification are comparable. Liu et al. (2012) also designed a multi-stage bubbling humidification desalination system, which achieved a GOR of 2.88 at 89 °C. These results all show that although the bubbling HDH technology is simple in structure, the HDH efficiency is considerably high, so it is necessary to carry out more in-depth research.

In this paper, we designed a multi-stage bubble column (BC) HDH desalination system. The combination of bubbling humidification and fresh water absorption dehumidification greatly enhances the heat and mass transfer process in this system and has a good development prospect.

2. SYSTEM STRUCTURE AND OPERATION PRINCIPLE

2.1. Experimental setup

The multi-stage BC HDH desalination system described in this paper consists of a BC and other auxiliary components, including air pump, water pump and electric heating tank. The BC includes a humidification zone (H-zone), a dehumidification zone (DH-zone) and a water storage ventilation layer, as shown in Figure 1, and the H-zone and DH-zone are both 4-stages. The basic structure of each layer is the same, consisting of a perforated plate, a cylinder wall and two flanges. Each layer is 10mm high and is made entirely of Polycarbonate (PC). In the H-zone, in order to enable the seawater in the upper layer to flow into the lower layer, a bigger vertical pipe is penetrated through the perforated plate; in the DH-zone, the copper coil is immersed in fresh water for heat exchange. Flanges and seals are used to connect the layers and prevent water and gas from escaping. On the perforated plate with a diameter of 594 mm, 625 small orifices having a diameter of 2 mm were evenly distributed. The inner and outer diameters of the copper coil are 11.3 mm and 12.7 mm, respectively, and the length in each layer is about 8 m. The air pump used has a power of 1100 W and a maximum blowing pressure and suction pressure of 24 and 22 kPa, respectively. The pump used has a rated power of 370W, a rated flow of 2.0 t/h and a head of 22 m. The electric heating water tank has a capacity of 0.4 m^3 and a maximum power of 15 kW, and its power is adjustable. The multi-stage stacked structure makes the device have the advantages of compact space and simple internal piping structure.

2.2. Operation principle

Figure 2 is a schematic diagram of the operating principle of the system, which can be introduced from the following three aspects: seawater circulation, air circulation and seawater diversion. The pre-heated cooling seawater flows through the DH-zone from top to bottom in the cooper coil heat exchanger and recovers the latent heat of vaporisation, so that the DH-zone are maintained at a lower temperature, and a top-down temperature gradient is formed in the DH-zone. After recovering the latent heat, the seawater is further heated up in an electric heating

tank and then pumped into the first layer of the H-zone. Within each layer, hot seawater above a certain level will flow from the standpipe to the next layer until it reaches the lowest layer and then exits the outlet. In the above process, seawater continuously transfers heat to the bubbles and evaporates on the bubble surface, so that the air is heated and humidified, and a bottom-up temperature gradient is formed in the H-zone. The air is enclosed in the BC for circulation, and after being pressurised by the air pump, it passes through the H-zone, the water storage ventilation layer and the DH-zone, and is then sucked back to the air pump again. A large amount of bubbles are formed during the passage of air through the perforated plates of each layer and a large amount of water vapor is carried by the bubbles to the DH-zone to condense. During the cycle, the air is saturated or nearly saturated at all locations except the air pump outlet. The counter-current heat transfer during seawater and air circulation reduces the irreversibility of the heat exchange process. Based on the pinch analysis, when the number of system layers cannot be changed, the heat transfer efficiency can be improved by changing the flow rate of seawater at each layer to reduce the pinch temperature difference. Therefore, a seawater diversion strategy can be used during the experiment to increase the system *PR*.

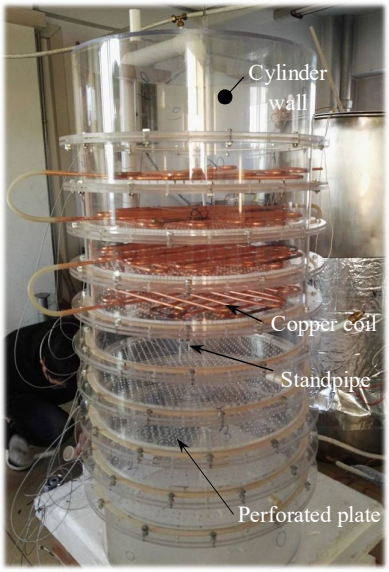

Figure 1: Structures of multi-stage bubble column HDH desalination system.

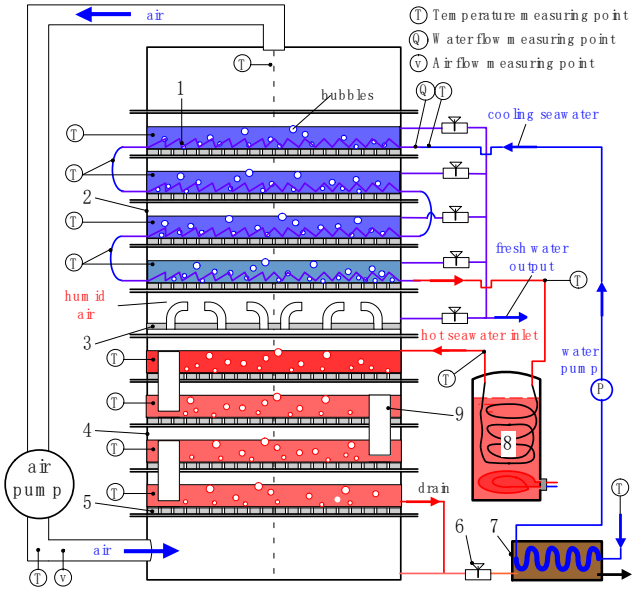

Figure 2: Schematic diagram of system operation.

(1-cooling coil, 2-condenser layer, 3-water storage ventilation plate, 4-humidifier layer, 5-perforated plate, 6-valve, 7-heat exchanger, 8-electric heating water tank, 9-standpipe.)

3. STRUCTURAL DESIGN OF BUBBLE COLUMN

The main parameters that determine the BC structure include the diameter of the cylinder wall, the height of each layer, the pore size of perforated plates, and the inner diameter of the copper coil. In order to reduce the influence of the boundary effect, a larger diameter of the cylinder wall is selected, which is determined by the mold; The height of each layer is required to be greater than twice the water level of each layer to prevent water of the lower layer from being carried into the upper layer by air bubbles or air current.

3.1. Diameter of the orifice on the perforated plate

At a given flow rate, the smaller the orifice on the perforated plate, the greater the pressure drop generated by the flow of air through the perforated plate, thus requiring a higher pump boosting capacity. And no bubbles are generated when the air pump power is insufficient. Increasing the orifice diameter can reduce the requirement for the pump's boosting capacity, but it increases the possibility of water leakage at all layers. At the same time, the increase in the diameter of the bubble reduces the specific surface area, which reduces the heat exchange efficiency. The design of the orifice diameter on the perforated plate, D_o, is discussed below from the aspects of pressure drop. Figure 3 is a cross-sectional view of an orifice on the perforated plate, including the water level above. The pressure drop between cross-section 1 and cross-section 3 is derived from a variety of energy losses, including the one caused by the

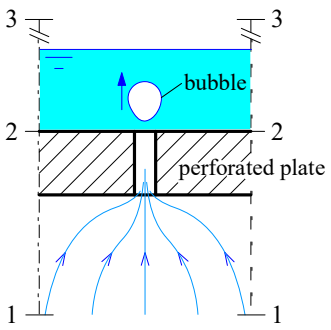

Figure 3: Cross-sectional view of an orifice.

flow of air through the sudden contraction structure, $e_{1\text{-}2}$, and energy loss during bubble generation, e_2, energy loss due to viscous drag when the bubble moves in water, $e_{2\text{-}3}$, and energy loss when the bubble breaks in the water surface, e_3.

$e_{1\text{-}2}$ can be easily obtained according to the J.C.Bordas's formula.

In the case of a high flow rate, the bubble generation process can be divided into two stages of formation and coalescence (Xie et al., 2013). In the formation stage, the bubbles overcome the pressure and surface tension of the water and increase in volume; in the coalescence stage, one or more smaller bubbles are quickly produced shortly after the previous bubble is detached, and then catch up with and merge with the previous bubble. The energy loss e_2 in this process is not considered in this paper.

Under the action of buoyancy, viscous drag and gravity, the bubbles moving under water will eventually enter a stable period, and the aspect ratio is close to 1 and hardly fluctuates (Xie et al., 2013). At this time, the bubbles are considered to be spherical. According to the force balance, the bubble will finally reach a maximum rising speed as calculated by Equation 1. Considering the rise of the liquid level caused by the bubble volume and taking bubbles as research objects, Equation 2 can be obtained according to the conservation of mechanical energy. Many literatures have been studied and summarised on the size of the newly detached bubbles (Jamialahmadi et al., 2001, Kulkarni and Joshi, 2005, Shen et al., 2008, Xie et al., 2013) . Equation 3 derived from Jamialahmadi et al. (2001) is used herein.

Equation 1: the maximum rising speed of bubble.

$$v_{b,max} = \sqrt{\frac{4g}{3C_D}\left(1-\frac{\rho_a}{\rho_w}\right)} \cdot D_b^{0.5}$$

Where:

- $v_{b,max}$= the maximum underwater rising speed of bubble (m/s)
- ρ_a = the density of the air (kg/m^3)
- ρ_w = the density of water (kg/s)
- g = the gravitational acceleration (kg/m/s^2)
- D_b= the equivalent diameter of the bubble (m)
- C_D= the drag coefficient, which is taken as 0.4 (Incropera et al., 2007) in this paper

Equation 2: the conservation of mechanical energy of bubbles from cross-section 2 to 3.

$$e_{2-3} + e_3 = \left(\frac{\rho_w}{\rho_a} - 1\right) g \left(H\left(1 + \frac{\dot{m}_a/\rho_a}{v_{b,max} D_1^2 - \dot{m}_a/\rho_a}\right) - \frac{D_b}{2}\right) - \frac{v_3^2}{2}$$

Equation 3: the size of the newly detached bubbles.

$$\frac{D_b}{D_o} = \left[\frac{5}{Bo^{1.08}} + \frac{9.261 Fr^{0.36}}{Ga^{0.39}} + 2.147 Fr^{0.51}\right]^{1/3}$$

Where:

- H = the initial liquid level (m)
- v_3 = the air flow rate at the cross-section 3 (m/s)
- D_o = the diameter of a orifice (m)
- $Bo = \rho_w g D_o^2 \sigma^{-1}$, Bond number
- $Ga = \rho_w^2 g D_o^3 \mu_w^{-2}$, Galileo number
- $Fr = v_o^2 (D_o g)^{-1}$, Froude number
- σ = the surface tension coefficient of water-air (N/m)

Let $\Delta p = \rho_a (e_{1-2} + e_{2-3} + e_3)$, which is used to indicate the pressure drop generated when air flows through the single dehumidification/humidification layer. Figure 4 is a plot of $8 \times \Delta p$ versus orifice diameter D_o. It can be seen that when D_o is small, the total pressure drop increases sharply with the decrease of D_o, and the change of air flow rate has a significant influence on the pressure drop.

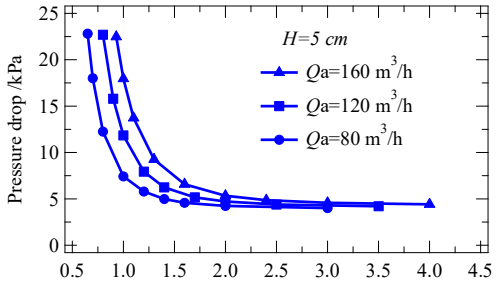

Figure 4: Relationship between pressure drop and orifice size.

3.2. Inner diameter of the copper coil

The smaller the inner diameter ($d_{c,i}$) of the copper coil, the greater the pressure loss caused by friction during the flow of seawater, especially when the flow rate is large. As the pump head is limited, in order to ensure that the

seawater flow can meet the experimental requirements, the frictional head loss when the seawater flows through the copper coil is analysed. The frictional head loss is calculated by Equation 4. The calculation of the friction factor of the copper coil is based on the correction to the straight tube condition. The critical Reynolds number Re_c of the coil is calculated by Equation 5.

Equation 4: the frictional head loss.

$$h_f = f\frac{L}{d_{c,i}}\frac{u^2}{2g}$$

Equation 5: the critical Reynolds number of the coil.

$$Re_c = 2100 \cdot \left[1 + \left(\frac{d_{c,i}}{2R}\right)^{0.5}\right]$$

Where:

- f = the wall friction factor
- L= the total length of the copper coil (m)
- u= the seawater velocity inside the tube (m/s)
- R= the curvature radius of the copper coil (m)
- $d_{c,i}$= the inner diameter of the copper coil (m)

According to the value of the Reynolds number, the correction of the friction factor of the copper coil is shown in Table 1, in which f_0 is the friction factor of the straight tube. f_0 is calculated by the C.F.Colebrook's formula when in the turbulent smooth/rough tube zone.

Table 1: Correction of the copper coil friction factor (Yao and Wang, 2007)

$Re \gtrsim Re_c$	$\frac{f}{f_0} = 1 + 0.075Re^{0.25}\left(\frac{d_{c,i}}{2R}\right)^{0.5}$
$Re_c \gtrsim Re \gtrsim 40\left(\frac{2R}{d_{c,i}}\right)^{0.5}$	$\frac{f}{f_0} = 0.288Re^{0.36}\left(\frac{d_{c,i}}{2R}\right)^{0.18}$
$Re \lesssim 40\left(\frac{2R}{d_{c,i}}\right)^{0.5}$	$\frac{f}{f_0} = 1$

For the coil shown in Figure 5, the relationship between the frictional head loss and the flow rate under different $d_{c,i}$ is shown in Figure 6. It can be seen that the frictional head loss increases almost exponentially with the increase in flow. The copper coil with a total length of L=7.48m has a frictional head loss of up to 10m at a flow rate of 8L/min and an $d_{c,i}$ of 8mm. Therefore, if the selected tube diameter is too small, the flow demand required for the experiment cannot be met.

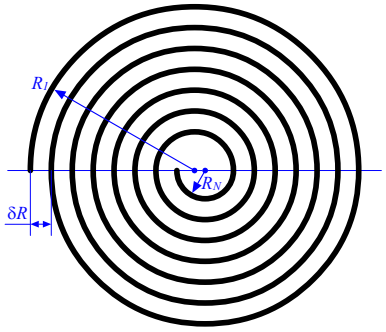

Figure 5: Structure parameters of the copper coil.

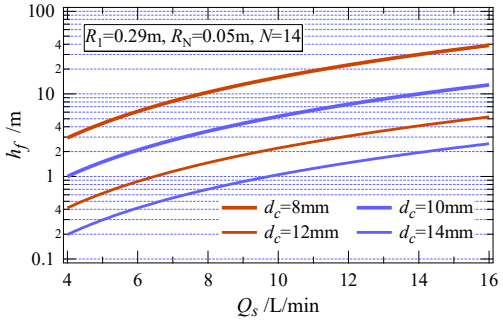

Figure 6: Frictional head loss of one coil under different $d_{c,i}$.

4. STEADY STATE CALCULATION MODEL OF BUBBLE COLUMN

For a bubble column in which both the DH-zone and the H-zone are M-layers, its internal energy conversion relationship is shown in Figure 7. Ignoring the change of seawater flow in the H-zone, the governing equations describing the operating state of the system include: energy conservation equations and heat transfer relationships.

4.1. Energy conservation equations

The following Equation 6 to Equation 8 are based on the following assumptions: 1) The water temperature in each layer is uniform; 2) The humid air in each layer is saturated; 3) The heat dissipation from the BC to the environment is negligible; 4) The pressure drop generated by the flow of air through each layer is the same.

(i) m^{th} floor ($m \in [2, M] \cup [M+2, 2M-1]$)

Equation 6: energy conservation equation in mth floor.

$$\dot{Q}(m) - \dot{Q}(m-1) = \dot{m}_s(m) \cdot \Delta h_s(m) + \dot{m}_a \cdot \Delta h_a(m)$$

Equation 7: the specific enthalpy changes of seawater.

$$\Delta h_s(m) = \int_{T_s(m-1)}^{T_s(m)} c_s \cdot dT_s$$

Equation 8: the specific enthalpy changes of humid air.

$$\Delta h_a(m) = \int_{T_w(m+1)}^{T_w(m)} c_{air} \cdot \mathrm{d}T_w + d(m) \cdot h_v(m) - d(m+1) \cdot h_v(m+1)$$

Where:

- $\dot{Q}(m)$ = the heat transfer power to the m^{th} layer via the perforated plate (W)
- $\dot{m}_s$, $\dot{m}_a$= the mass flow rates of seawater and dry air (kg/s)
- $\Delta h_s(m)$, $\Delta h_a(m)$ = the specific enthalpy changes of seawater and humid air in the mth layer (J/kg)
- c_s, c_{air} = the specific heat of seawater and humid air (J/kg/K)
- $T_s(m)$ = the temperature of the seawater flowing out from the mth layer (℃)
- $T_w(m)$ = the temperature of the fresh water in the mth layer (℃)
- $d(m)$ = the specific humidity of dry air in the mth layer ($kg_{(vapour)}/kg_{(air)}$)
- $h_v(m)$ = the specific enthalpy of water vapour in the mth layer (J/kg)

(ii) The difference in the remaining floors

The temperature of the seawater flowing into the 1st floor of DH-zone and the 1st floor H-zone is $T_{sc,i}$ and $T_{sh,i}$, respectively. The humid air entering the M^{th} floor is not saturated and has the same specific humidity as the 1st floor.

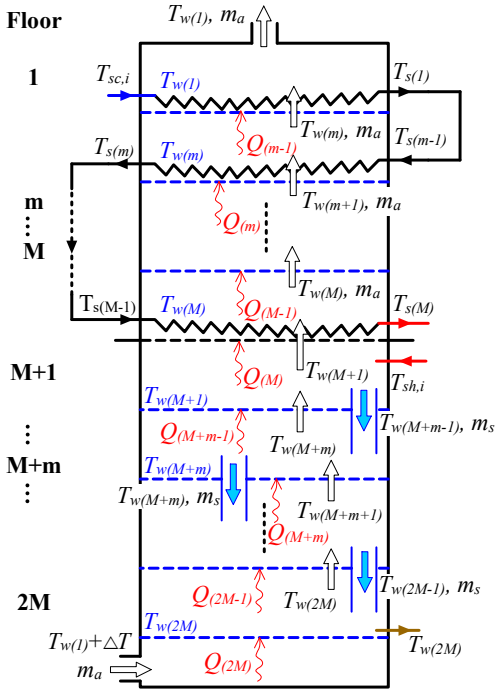

Figure 7: Internal energy conversion diagram of an M+M layers BC.

4.2. Heat transfer relationships

First, assume that the bubbles in each layer are uniformly generated. Tow and Lienhard (2014) summarised some of the thermal resistance model on the bubble side and found that mixing length of 4-5 cm is enough to achieve perfect mixing. In this case, the heat transfer resistance between the bubbles and the water is negligible. Therefore, the main heat transfer process in the DH-zone ($m \in [1, M]$) can be simplified to the heat transfer from the freshwater-bubble mixture to the cooling seawater in the copper coil as show in Equation 9. The distribution of seawater temperature along the copper coil (T_{sm}) can be solved by the following differential Equation 10.

Equation 9: the heat transfer from the freshwater-bubble mixture to the cooling seawater in the coil.

$$\dot{m}_s(m) \cdot \Delta h_s(m) = \int_0^L \frac{T_w(m) - T_{sm}(x)}{R_{w\_c}(m) + R_{c\_s}(x)} \mathrm{d}x$$

Where:

- L= the length of the copper coils of each layer (m)

- $T_{sm}(x)$= the seawater temperature at the *x* meters from the inlet of the coil of the m^{th} layer (℃)
- R_{w_c}, R_{c_s}= the thermal resistance per unit length between the freshwater-bubble mixture and the outer wall of the coil and between the inner wall of the coil and the seawater (K·m/W)

Equation 10: first-order differential equation for $T_{sm}(x)$.

$$\dot{m}_s(m) \cdot c_s \cdot \frac{\mathrm{d}T_{sm}(x)}{\mathrm{d}x} = \frac{T_w(m) - T_{sm}(x)}{R_{w\_c}(m) + R_{c\_s}(x)}$$

Boundary conditions:

$$T_{sm}(0) = \begin{cases} T_{sc,i}, & m = 1 \\ T_s(m-1), & m \neq 1 \end{cases}, T_{sm}(L) = T_s(m)$$

Secondary, consider the heat transfer between the layers via the perforated plate described by Equation 11. In the H-zone ($m \in [M+1, 2M]$), since the thermal resistance between the bubble and the water is neglected, only the heat transfer processes between the layers via the perforated plates are considered, which are also described by the Equation 11.

Equation 11: the heat transfer between the layers via the perforated plate.

$$\dot{Q}(m) = \frac{T_w(m+1) - T_w(m)}{R_{conv}(m) + R_{cond}(m)} \cdot \frac{\pi D_{BC}^2}{4}$$

Where:

- R_{conv}, R_{cond}= the thermal resistance of convection and conduction per unit area (K·m²/W)
- D_{BC}= the inner diameter of the bubble column (m)

4.3. Seawater diversion control model

Based on the pinch analysis method, the seawater flow rate should be gradually reduced from top to bottom in the DH-zone; conversely, it should be increased in the H-zone. Layer-by-layer control of seawater flow can be expressed by Equation 12. For example, $k(m)$=1 indicates that the upper seawater flows directly into the m^{th} layer without diversion. The seawater flowing out from the DH-zone is returned to the H-zone according to the rule of the Equation 13, so that the thermal energy can still be sufficiently recovered, and Figure 8 is a schematic view thereof.

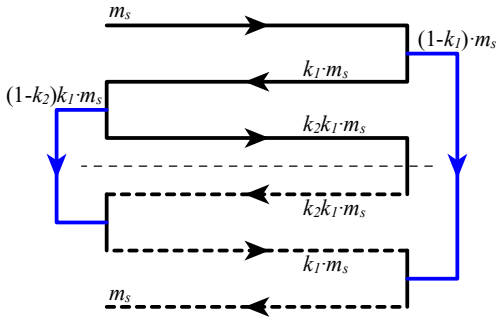

Figure 8: Schematic diagram of seawater diversion of the "3+3 layers" BC.

Equation 12: Seawater flow control of DH-zone.

$$\dot{m}_s(m) = k(m) \cdot \dot{m}_s(m-1),\ 2 \leq m \leq M$$

Equation 13: Seawater flow control of H-zone.

$$\dot{m}_s(M+m) = \dot{m}_s(M+1-m),\ 2 \leq m \leq M$$

Where:

- $k(m) \leq 1$, the proportion of seawater flowing into the m^{th} layer from the m-1^{th} layer

4.4. Convective heat transfer experimental correlation

For the heat transfer between the freshwater-bubble mixture and the outer wall of the copper coil during bubbling dehumidification, Tow and Lienhard (2014) reviews some relevant experimental correlations. In this paper, Equation 14 is derived from the equation of Deckwer (1980).

Equation 14: convective heat transfer coefficient between the freshwater-bubble mixture and the wall.

$$h_{w\_c} = 0.1 \cdot \left(\lambda_f \rho_f c_f\right)^{0.5} \nu_f^{-0.25} (u_a \mathrm{g})^{0.25}$$

Where:

- λ_f = the thermal conductivity of water (W/m/K)

- ρ_f= the density of water (kg/m^3)
- c_f= the specific heat of water (J/kg/K)
- ν_f= the kinematic viscosity of water (m^2/s)
- u_a= the ratio of air volume flow rate to column cross-sectional area (m/s)

The flow regime of seawater in the coil depends on its flow rate and temperature. It is known that $d_{c,i}$=11.3mm, and it can be determined that the seawater flow rate and its temperature during the experiment are 0.5-18 L/min and 15-80 °C, respectively. Therefore, the Reynolds number is calculated to be 800<*Re*< 2×10^5. It is assumed that the Nusselt number under laminar flow can be calculated under uniform wall temperature condition of the copper coil. The convection heat transfer equations used in different flow regimes are listed in Table 2. In Table 2, μ_c and Pr_c are the dynamic viscosity and the Prandtl number of seawater at the wall temperature of the copper coil, respectively, and *f* is the wall friction factor. Considering the secondary flow in the coil and the change in the friction factor shown in Table 1, the equations in Table 2 was corrected before application.

Table 2: Convection heat transfer equations used in different flow regimes.(Incropera et al., 2007, Yao and Wang, 2007)

Laminar flow: $Re \lesssim Re_c$	$\begin{cases} Nu(x) = 3.66 + \dfrac{0.00178(d_{c,i}/x)RePr}{\left(1 + 0.04\left[(d_{c,i}/x)RePr\right]^{2/3}\right)^2}, & Pr \gtrsim 5 \\ Nu(x) = \max\left\{1.24\left(\dfrac{RePr}{x/d_{c,i}}\right)^{1/3}\left(\dfrac{\mu}{\mu_c}\right)^{0.14},\ 3.66\right\}, & 0.6 \lesssim Pr \lesssim 5 \end{cases}$
Transitional flow: $Re_c \lesssim Re \lesssim 10^4$	$Nu = 0.012(Re^{0.87} - 280)Pr^{0.4}\left(\dfrac{Pr}{Pr_c}\right)^{0.11}, 1.5 \lesssim Pr \lesssim 500$
Turbulent smooth tube zone: $10^4 \lesssim Re \lesssim 10^6$	$Nu = \dfrac{(f/8)\cdot Re\cdot Pr}{1.07 + 12.7(f/8)^{0.5}\cdot(Pr^{2/3} - 1)}\left(\dfrac{\mu}{\mu_c}\right)^{0.11}$ $f = (1.82\cdot \lg Re - 1.64)^{-2}, 2300 \lesssim Re \lesssim 10^6$

The convective heat transfer coefficient between the layers via the perforated plate is estimated by Equation 15, which is the experimental correlation formula at the front stagnation point for gas flowing around a cylinder.

Equation 15: convective heat transfer coefficient between the layers via the perforated plate.

$$Nu_{conv} = 1.15 \cdot Re^{1/2} Pr^{1/3}$$

5. RESULTS COMPARISON AND ANALYSIS

5.1. Model verification

The experiment was carried out without the seawater diversion, and the system was tested under different seawater flow rates and air flow rates. As important indicators, operating temperatures ($T_{w,5}$) and *PR* were obtained for different seawater and air flow rates, respectively. The calculations were performed according to the theoretical model under the same conditions, and the results of the experiments and calculations are shown in Figures 9 and 10. It can be seen that the calculated value has a consistent trend with the experimental value, but slightly higher than the experimental value, their maximum deviation and average deviation are 13% and 9.5%, respectively. The fact that hot humid air isn't saturated, the selected bubble-water-wall heat transfer experimental correlations and the leakage of humid air and fresh water out of the BC are the main cause of the deviation.

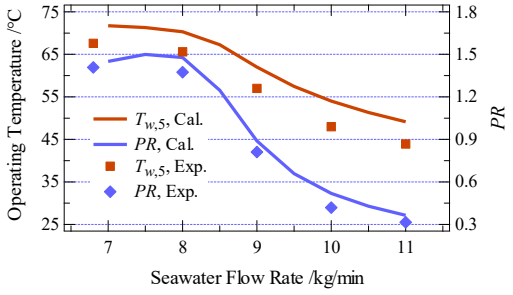

Figure 9: Operating temperature and PR at different seawater flows.

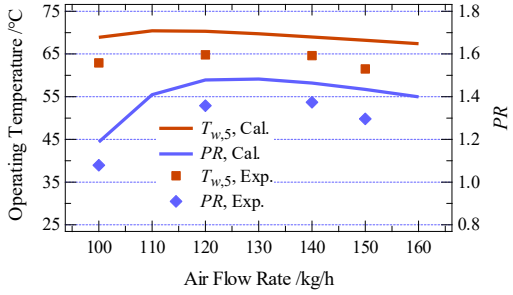

Figure 10: Operating temperature and PR at different air flows.

5.2. Calculation results and analysis

Seawater flow, air flow and seawater inlet temperature are all important factors influencing the performance of the system. Firstly, keeping the heating power constant, the variation of the *PR* with the seawater inlet temperature under different seawater flow rates and air flow rates was studied, as shown in Figures 11 and 12. These figures show that under certain seawater flow or air flow, the system *PR* increases rapidly with the increase of inlet seawater temperature and then decreases slowly. Therefore, when the heating power, seawater and air flow rate are constant, the *PR* can reach a local maximum value (PR_{max}) by adjusting the inlet seawater temperature. In Figure 11, the increase of seawater flow rate increases the optimum inlet seawater temperature corresponding to PR_{max}, and after $\dot{m}_s \gtrsim 8$ kg/min, PR_{max} decreases slightly with the increase of seawater flow rate. In Figure 12, the increase in the air flow rate causes the optimum inlet seawater temperature corresponding to PR_{max} to decrease, and the PR_{max} also decreases as the air flow rate increases. By comparing Figures 11 and 12, it can be found that the change in seawater flow within the adjustable range has a smaller effect on PR_{max} than the air flow.

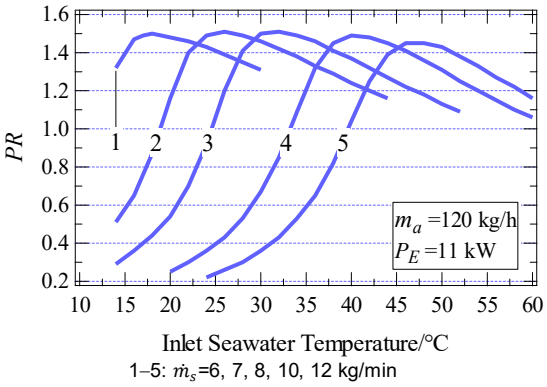

1–5: $\dot{m}_s$=6, 7, 8, 10, 12 kg/min

Figure 11: The PR under different seawater flows.

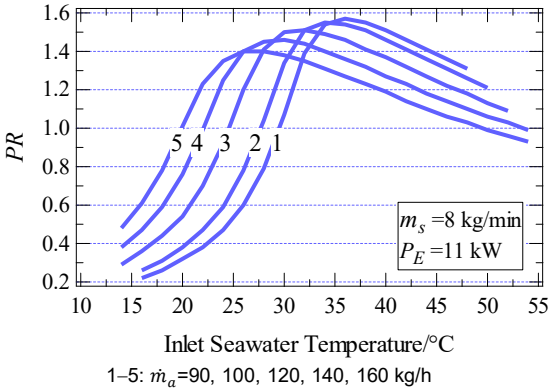

1–5: $\dot{m}_a$=90, 100, 120, 140, 160 kg/h

Figure 10: The PR under different air flows.

Then, keeping the seawater flow and the air flow constant, the influence of the heating power on *PR* is studied. From the calculation results shown in Figure 13, it can be found that the increase in heating power causes the temperature of the inlet seawater corresponding to PR_{max} to decrease, but has no significant effect on PR_{max}.

In summary, we can find that by selecting a smaller seawater flow, reducing the air flow and preheating the imported seawater, a larger PR_{max} can be obtained. When the heating power is 15 kW, the parameters were adjusted based on the above rules to increase PR_{max}, and the process is shown in Figure 14. By reducing the air flow from 140 kg/h to 90 kg/h, PR_{max} is increased by 5.5%. However, reducing the air flow rate and seawater flow rate increases the possibility of water leakage from the perforated plate and makes the operating temperature approach the boiling point of water. Therefore, this method has a limited improvement on the *PR*.

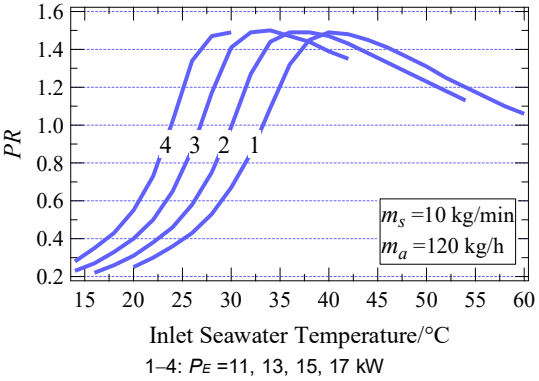

1–4: P_E =11, 13, 15, 17 kW

Figure 13: The PR under different heating power.

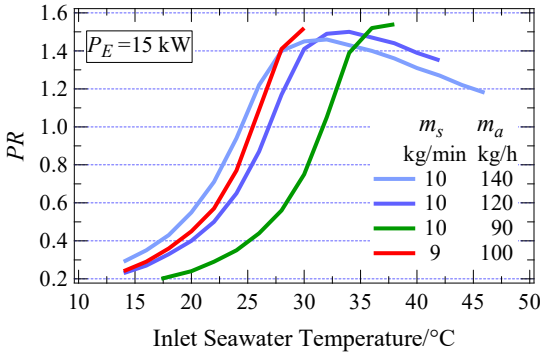

Figure 14: Exploration of a higher PR_{max} at a heating power of 15kW.

The above analysis was carried out for the case without seawater diversion. Depending on the pinch analysis of heat transfer or from the point of view of energy grading, high quality energy should be used to increase the temperature of the seawater in the high temperature range to the highest possible temperature. Therefore, in order to obtain a higher operating temperature while fully recovering energy, a stepwise diversion of seawater is necessary. The case of no diversion can be considered as the case where the diversion is performed before the first layer (k= [0.5, 1, 1, 1]). This paper only compares the single diversion at different layers, as shown in Figure 15, for exploring the effect of seawater diversion. The seawater flow before the diversion is 16 kg/min. In Figure 15, the PR_{max} of the seawater diversion at the 2rd, 3rd, and 4th layers are increased by 5.2%, 11.6%, and 25.2%, respectively, compared with the case of no diversion. Obviously, the effect of the diversion on the PR_{max} is greater than the adjustment of the seawater flow and the air flow, and the effect of diversion at the final layer of the DH-zone is most significant.

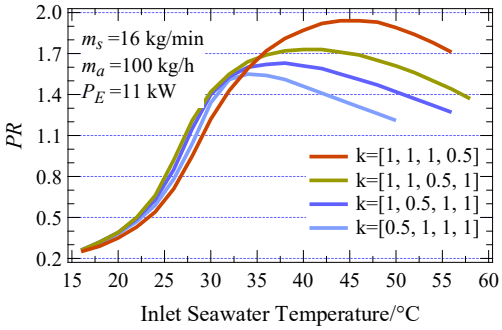

Figure 15: The effect of single seawater diversion.

6. CONCLUSIONS

In this paper, we have designed the main structural parameters of a multi-stage BC. A steady-state heat transfer model of the system involving a stepwise diversion of seawater was established, and then validated by experiments. The main conclusions are listed below:

1) Under the case of no seawater diversion, the experimental results showed a productivity of 27.2 kg/h and a *PR* of 1.38 at an operating temperature of 65.6°C;
2) A comparison of the calculated results with the experimental results shows an average deviation of 9.5% and a maximum deviation of 13%, which indicates that the theoretical model is suitable;
3) By selecting a smaller seawater flow rate, reducing the air flow rate and preheating the inlet seawater to a specific temperature can improve PR_{max} by a limited extent;
4) The effect of seawater diversion on improving PR_{max} is more pronounced, especially the diversion performed at the final layer of the DH-zone, which increases the PR_{max} by 25.2% compared to no diversion.

7. REFERENCES

Bourouni, K., Chaibi, M. T. & Tadrist, L. 2001. Water desalination by humidification and dehumidification of air: state of the art. *Desalination,* 137**,** 167-176.

Deckwer, W. D. 1980. On the mechanism of heat transfer in bubble column reactors. *Chemical Engineering Science,* 35**,** 1341-1346.

El-Agouz, S. A. & Abugderah, M. 2008. Experimental analysis of humidification process by air passing through seawater. *Energy Conversion and Management,* 49**,** 3698-3703.

Incropera, F. P., Dewitt, D. P., Bergman, T. L. & Lavine, A. S. 2007. *Fundamentals of Heat and Mass Transfer,* New York, John Wiley & Sons.

Jamialahmadi, M., Zehtaban, M. R., Müller-Steinhagen, H., Sarrafi, A. & Smith, J. M. 2001. Study of Bubble Formation Under Constant Flow Conditions. *Chemical Engineering Research and Design,* 79**,** 523-532.

Kulkarni, A. A. & Joshi, J. B. 2005. Bubble formation and bubble rise velocity in gas-liquid systems: A review. *Industrial & Engineering Chemistry Research,* 44**,** 5873-5931.

Liu, Z., Zeng, S., Cheng, T. T. & Jin, T. 2012. Steady experimental study on a solar distillation plant characterized with multi-effect bubbling evaporator. *Acta Energiae Solaris Sinica,* 33**,** 380-385.

Miller, J. A. & Lienhard, J. H. 2013. Impact of extraction on a humidification-dehumidification desalination system. *Desalination,* 313**,** 87-96.

Rajaseenivasan, T. & Srithar, K. 2017. An investigation into a laboratory scale bubble column humidification dehumidification desalination system powered by biomass energy. *Energy Conversion and Management,* 139**,** 232-244.

Shen, X. S., Shen, X. Y., Li, G. & Dai, G. C. 2008. Bubble formation from large submerged single orifice at high gas velocity. *Journal of Chemical Industry and Engineering (China),* 59**,** 2220-2225.

Tow, E. W. & Lienhard, J. H. 2014. Experiments and modeling of bubble column dehumidifier performance. *International Journal of Thermal Sciences,* 80**,** 65-75.

Wu, G., Zheng, H. F., Kang, H. F., Yang, Y. J., Cheng, P. & Chang, Z. H. 2016. Experimental investigation of a multi-effect isothermal heat with tandem solar desalination system based on humidification-dehumidification processes. *Desalination,* 378**,** 100-107.

Xie, J., Zhu, X., Wang, H., Liao, Q. & Ding, Y. D. 2013. Bubble formation and movement from a submerged micro-orifice. *Journal of Engineering Thermophysics,* 34**,** 282-285.

Yao, Z. P. & Wang, R. J. 2007. *Heat Transfer* Beijing, Beijing Institute of Technology Press.

Zamen, M., Soufari, S. M., Vahdat, S. A., Amidpour, M., Zeinali, M. A., Izanloo, H. & Aghababaie, H. 2014. Experimental investigation of a two-stage solar humidification-dehumidification desalination process. *Desalination,* 332**,** 1-6.

Zhani, K., Ben Bacha, H. & Damak, T. 2011. Modeling and experimental validation of a humidification-dehumidification desalination unit solar part. *Energy,* 36**,** 3159-3169.

#211: End-of-the-line urbanism: reprogramming the FEW-nexus of the city-region for a post-carbon society

Sean CULLEN[1], Greg KEEFFE[2], Emma CAMPBELL[3], Kevin LOGAN[4]

[1]Queen's University Belfast, School of Natural and Built Environment, sean.cullen@qub.ac.uk
[2]Queen's University Belfast, School of Natural and Built Environment, g.keeffe@qub.ac.uk
[3]Queen's University Belfast, School of Natural and Built Environment, ecampbell34@qub.ac.uk
[4]Maccreanor Lavington Architects, Vijverhofstraat 47 3032 SB Rotterdam, kl@maccreanorlavington.com

Northern Ireland is at the end of resource flows which have a significant environmental impact and situate the region in a vulnerable, insecure position. The techno-socio challenge of moving towards a post-carbon culture takes place in a post-industrial, post-conflict context, posing difficulties and opportunities in equal measure. Through an analysis of the food-energy-water (FEW) print of the region and the process of actor network mapping, the paper examines how the FEW-nexus can be radically reprogrammed through speculative intervention. Stocks and flows of food and energy are hacked to enhance urban and environmental resilience in highly globalised systems and networks. A specific focus is placed on transitions to sustainable: (1) forms of food and animal feed production and consumption; and, (2) shared, distributed forms of private transportation based on renewables fuel sources. Current attitudes to food production rely heavily on livestock due to poor soil quality while residents consume greater quantities of meat compared to the rest of the United Kingdom, posing significant environmental and health issues. Similarly, individual transportation is the largest form of energy consumption in Northern Ireland, almost entirely made up of petroleum products. Energy intensive, carbon-reliant flows of materials are reimagined to produce a nested, multi-scalar urbanism, imagining the new typologies of production, supply and generation. The paper proposes new paradigms for how regions precariously located at the end of resource flows, can pioneer alternative, cyclical forms of production and consumption, centred on and informed by place. The case study offers a framework for a highly contextual method of studying the FEW-print and multi-scalar design urbanism which can be applied elsewhere to produce healthy, vibrant and economically viable transitions to post-carbon societies.

Keywords: post-carbon cities; sustainable urbanism; food-water-energy nexus

1. INTRODUCTION

Northern Ireland (N.I.) sits at the periphery of the European continent – with little natural resources itself, the region is viewed as one at the end of resource flows. Electricity and gas interconnectors to the island of Ireland evidence the infrastructure that is the last stop. Approaching this design challenge through an analysis of stocks and flows, consumption and actor network mapping, new possibilities can be visualised for how a post-carbon society might be realised. Actor network mapping applies a systems thinking approach to urbanism, giving equal importance to people (agents engaged in the system), policy (the framework defining boundaries and rules) and place (the spaces shaped by people and policy). Historians and theorists have long believed in a systematic view of the city because of the burgeoning nature of complexity and the orbits of influence it now effects over a larger region. Mumford (1961) and Gottmann (1961) emphasise the importance of viewing the urban network as an exploded and disparate set of agents, organisations, institutions over a landscape beyond the perceived limits of the city – particularly true for N.I. where devolved powers of structure give regional governments influence in agriculture, energy and production. The context is a dispersed, hyper low-density region with the population of a large city with a history of conflict and significant deindustrialisation. The social and economic legacies of the region are constantly viewed through product, spatial-based initiatives aimed at rejuvenating industry and to segregate people. To challenge this approach, this paper views urban planning at a regional scale from a product-based approach, set with objectives relating to physical interventions and structures, to a tools-based approach, embedded in complex systems ecology, where intervention has wider network impacts in policy and the physical realm. Each new intervention into the actor network has spatial implications for the city from the scale of the home to the region. End consumption relies heavily of these flows of resources to the end of the line and the intention is to re-centre these stocks and flows in Northern Ireland. While the landscapes of production, storage, processing and generation exist in the 'terminal architecture', as Pawley (1998) describes it, located in the peri-urban industrial estates of the region, the aim of this paper is not to reform the architecture and planning of such locales. Instead, altering the rules around which each agent (people, space and policy) engages with the urban ecosystem, its orbit can be shifted around reimagined paradigms and goals. Through actor network mapping and speculative statements convening the FEW-nexus, the paper outlines a methodology for reprogramming regions for a post-carbon where resource stocks and flows emerge from its centre.

2. VISUALISATION OF COMPLEXITY

Viewing urbanism through the lens of constructed ecology represents a recent attitude to applying theories of systems thinking and cybernetics to new forms of discipline. Geddes was the first to applying ecological thinking to planning and architecture. Now commonly referred to as 'Ecological Urbanism', this paradigm shift in attitude has shifted design from product, or form, led practice to one of process, systems-based operation (Waldheim, 2006). The importance of inter-relational thinking in urbanism today still requires a framework for operation, visualisation and manipulation – one offered by Actor Network Theory. Pioneered by sociologists Latour, Callon and Law, Actor Network Theory depicts the relationship and influence of human and non-human agents in shaping the urban environment (Farias and Bender, 2010; Thun et al., 2015). The method of isolation, deconstruction and overlaying, as argued by Corner in his essay *The Agency of Mapping*, signifies relationship between pats where, "the resulting structure is a complex fabric, without centre, hierarchy or single organising principle" (1999; p. 235). As such, it flattens the agency of each actor in a manner that evidences a point of acupuncture to effect change. For the purposes of this paper, the focus is on the actors active in the food-water-energy nexus in N.I. (Figures 1-6).

Each are drawn stratified which have vertical connections indicating relationships which transcend or straddle different layers. Incorporated in the stratified networks are ideas relating to stocks and flows: market shares for suppliers; potential of generators; consumer base; import/export capacities. Flows of materials, information – through feedback loops – and knowledge are critical to systems thinking as they open a space in which to intervene. Energy has been translated to coal, gas, electricity and petroleum products – all reliant of carbon systems which are connected to N.I. through interconnectors, either via the Republic of Ireland or the rest of the United Kingdom. Water and food are single systems but all, including energy, encompass services relating to production, generation, transmission, distribution, storage, supply and regulation. The edges of these networks are boundless and frequently vague for commercial and security reasons. Therefore, the question of framing is critical; an act, as Cosgrove argues in *Mappings* (1999), that defines boundaries and limits are viewed by the designer, maker or cartographer, laced with devices for signposting and identification. Consequently, the actor network maps are transience, of a time and place, and framed by the author. Similarly, each is simplified in an attempt to flatten the priorities of actors within the process.

3. ACUPUNCTURE POINTS

The foundation of contemporary urbanism lies in systems thinking methods which requires an attitude to system leverage with the aim of altering the network effectively despite its complexity to understand. Leverage points, as described by Meadows (1999) in her manifesto “Leverage Points: Places to Intervene in a System”, are small interventions which produce system-wide reprogramming. A systems-based approach to urban planning is far more effective than the modernist ambition of comprehensively envisioning of urban futures that is programmatic. Thun et al. (2015), in *Infra Eco Logi Urbanism,* utilised this methodology in an attempt to apply speculative narratives to alter the *goals* and *paradigms* of the network – leverage points as identified by Meadows (1999) – which have tangible spatial implications to the complex urban system of the Greater Lakes Megaregion. Leverage points with the greatest effectiveness, in ascending order, according to Meadow (1999: p.3), are: the goals of the system; the mindset or paradigm out of which the system—its goals, structure, rules, delays, parameters—arises; the power to transcend paradigms. “Paradigms are the sources of systems” (Meadows, 1999: p.18). Thun et al. (2015) envisage new political, social and economic paradigms – acting as feedback loops – to operate beyond the realm of current orthodoxy to create alternative circumstance and opportunities. Within these methods, design moves beyond spatial proposition related to problem solving, to one which is tools-based and systematic in nature to deal with the complexity of actors which shape cities and regions. Livestock production and private transportation informed the hyper low-density urbanism formed around limited intensity; it shapes the infrastructure and landscape of the region immensely.

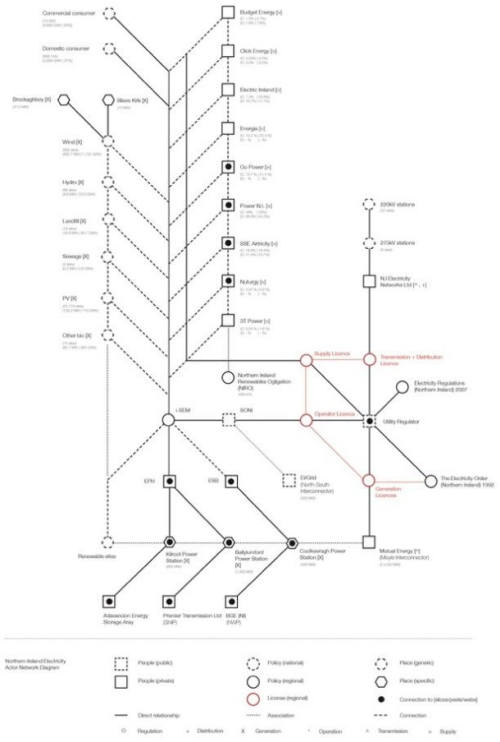

Figure 1: Electricity actor network diagram

The N.I. electricity market operates in tandem with the Republic of Ireland through the Integrated Single Energy Market (i-SEM). This allows trading on an all island basis, with one major interconnector between the north and south. In 2017, N.I. consumed 7,807GWh. Generation came through three power plants in N.I. (73.3%) and from renewables (25.3%) (DfE, 2018). Kilroot Power Station, on Belfast Lough, is one of the last remaining coal fired power stations still operating in the U.K. and Ireland. The Moyle Interconnector connects the N.I. electricity grid with Great Britain. Licenses, managed by the Utility Regulator, cover areas relating to generation, operation, supply, transmission and distribution. N.I. aims to produce 45-60% of its energy from renewables by 2035 but currently has new renewable incentives scheme since the end of the N.I. Renewables Obligation (NIRO) in 2015 (CCC, 2019).

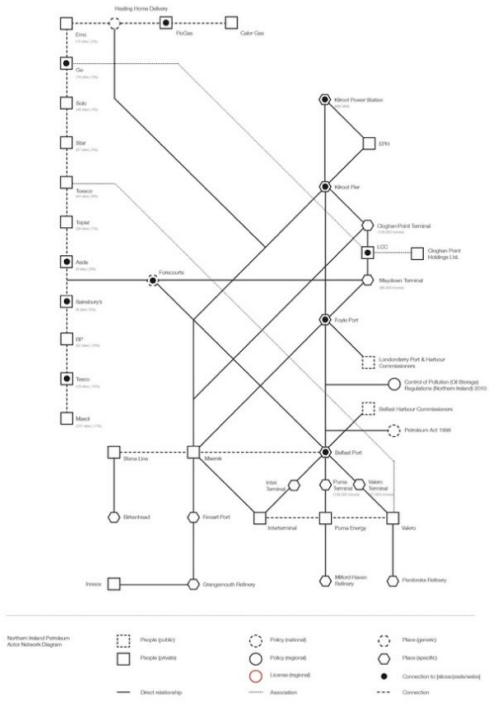

Figure 2: Petroleum actor network diagram

The largest source of energy in N.I. comes from petroleum products (Figure 2). In 2015, N.I. consumed 27,646 GWh of energy from petroleum products. 53% for transportation – private and commercial – while the remaining 47% for home heating systems (DfE, 2018). Due to the limited gas infrastructure in N.I., 68% of all households use oil for home heating. As such, the home and the forecourt are main typologies of consumption in a highly distributed system. Only four terminals import and store petroleum in N.I. with refined products coming predominantly from G.B.

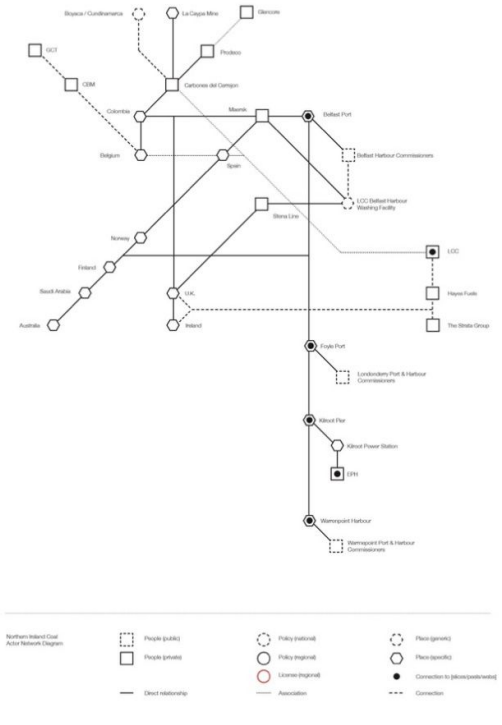

Figure 3: Coal actor network diagram

Coal is used on one of the three power stations in N.I. – the 660 MW Kilroot Power Station (Figure 3). While this is due to be phased out by 2025, coal accounts for 23% of electricity generation (DfE, 2018). In 2018, 1.66 million tonnes of coal and other solid fuels where shipped into Northern Ireland, one third for Kilroot and two-thirds for domestic and commercial use (NISRA, 2018). Significant domestic and commercial coal use arises because of the limited nature of gas infrastructure in N.I. One company, LCC imports coal from Colombia and washes it in Belfast Harbour before exporting it to Australia, Norway, Saudi Arabia and Spain.

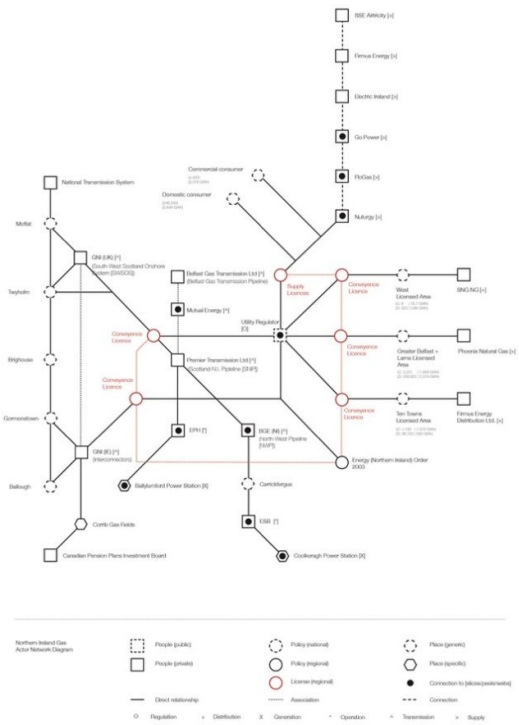

Figure 4: Gas actor network diagram

Gas arrives into N.I. through the Scotland-Northern Ireland Pipeline (SNIP), extracted from the National Transmission System (NTS) in G.B. at Moffat, Scotland. Gas only accounts for 24% of home heating in N.I. because of the limited nature of infrastructure. Three areas of transmission are currently operational, with the West Licensed Area commissioned only recently and hence the low number of customers. Gas accounts for approximately 50% of total electricity generation through the Ballylumford Power Station (1,400MW) and the Coolkeragh Power Station (450MW). An interconnector to the Republic of Ireland connects N.I. to the recently discovered Corrib Gas Field off the west coast of Ireland (DfE, 2018).

Agricultural production in N.I. is heavily reliant on livestock production. Farmland accounts for 68% of all land use in N.I., 83% of which is used for livestock purposes – compared to 43% across the U.K. – while 75% of all farms are in less favourable areas (LFA) which entitle businesses to additional payments under the Common Agriculture Policy (CAP) (DAERA, 2019a; CCC, 2019). Consequently, the agriculture sector is the biggest source of carbon emissions in N.I each year, accounting for 5.4 $MtCO_2e$ (27% of total) in 2017 (DAERA, 2019b). This attitude to land use is also reflected in the typical diet of the average N.I. resident. Compared to the rest of the U.K., someone in N.I. consumes 17% more non-carcase meat and meats products (including twice as much takeaway meats), 38% more carcase meats (including 63% more beef and veal) and 72% more potatoes (ONS, 2018). While these have significant health implications, the environmental impact of such a diet is also significant. The emissions based on per capita consumption are 1.71 tCO_2e every year, requiring an area of 3,160m^2 to sequester through forestry. Similarly, the land use required to produce food based on PCC is 3,295m^2 per person annually (Cullen and Keeffe, 2019). Currently, only 8% of N.I. land use is forestry and land use, land-use change and forestry (LULUCF) is a net contributor to emissions rather than a net sink (CEH, 2015; CCC, 2019). Changing cultural attitudes to food is challenging because of the embedded social and economic contexts that shape consumption. However, N.I. requires radical new approaches to rethinking land use and agriculture to not only reduce emissions through sequestration in line with carbon targets set by the U.K. government, but also to complement and enhance contributions to FEW nexus approaches.

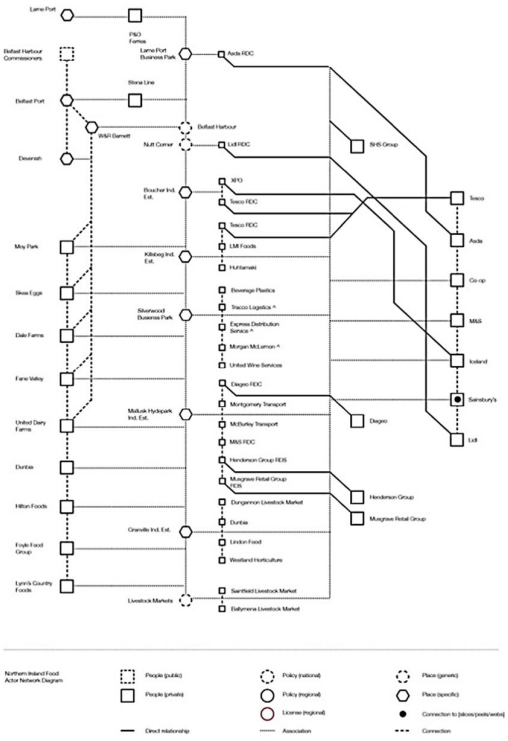

Figure 5: Food actor network diagram

Food production in N.I. reflects the embedded nature of agriculture in the economy and landscape. Dairy and livestock production are evident throughout the supply chain with notable inflows of grain to N.I. through the largest private sector company in the country – W&R Barnett. Finished products for supermarkets predominantly travel to N.I. through Ro-Ro ferry terminals. Tesco, Asda and Lidl are the only major U.K. supermarkets with regional distribution centres (RDCs) in N.I. As such, franchise and food service companies, including Henderson Group and Musgrave Retail Group, have a significant market share. The most significant location of storage, production and distribution is at Mallusk Hydebank Industrial Estate, situated between Belfast and the major Ro-Ro port of Larne.

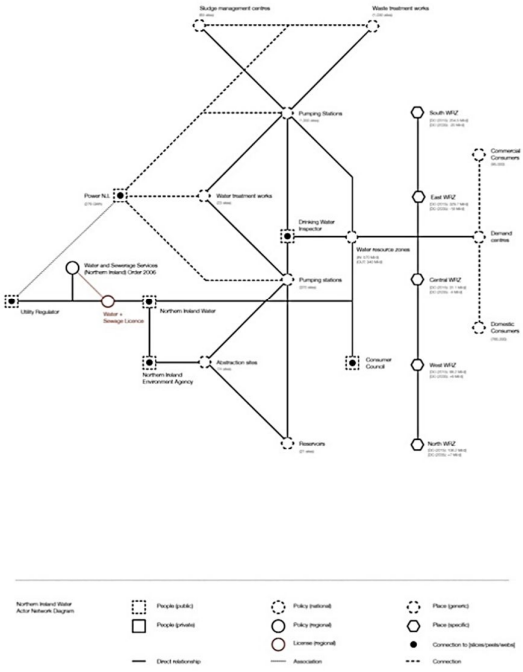

Figure 6: Water actor network diagram

N.I. Water, the sole licensed distributer and supplier in the region, distributes 570 million litres of treated water and collects 340 million litres of wastewater every day. This equates to approximately 150 litres per person daily. Split into five water resource zones (WRZs), a total of 24 abstraction sites and 21 reservoirs supply water to 765,000 domestic and 95,000 commercial customers. N.I. Water is the single largest energy customer in N.I, using 276GWh (3%) of total N.I. consumption. Electricity is used in water treatment centres (27%), pumping stations (19%), wastewater treatment works (25%) and sludge management centres (8%) (N.I. Water, 2018).

Transportation contributed 4.5 $MtCO_2e$ emissions (23% of total) in 2017 (DAERA, 2019b). Individual transport in N.I. is a significant energy user in the region, primarily through petroleum products. The reliance on this form of omni-nodal mobility for many reasons. Firstly, it is sited in a post-conflict context which saw urban flight during the Troubles. Secondly, its true modern development, after the signing of the Good Friday Agreement in 1998, occurred in post-Fordist years which relied on post-industrial services away from major ports. Vehicles consume 53% of all petroleum products in N.I. each year. There are 1,131,411 vehicles registered commercial (24.2%) and private (75.8%) in N.I. (DfE, 2018). Each year vehicle oil consumption totals 1.23 million tonnes of oil equivalent – 932,173 tonnes for private and 297,451 tonnes for commercial transportation. Therefore, each private vehicle consumes approximately 0.958 tonnes of oil equivalent per annum. Assuming an average fuel consumption of 5.5 litres per 100km, the typical car in N.I. travels 17,418 km (10,823 miles) every year. As of 2017, there were an average of 1.28 cars per household. The car is the dominant mode of transport, accounting for 77% of all journeys taken, with the average distance of 7.5 miles (as driver) and totalling 439 journeys each year. The difference between this survey – suggesting a total of 3,292 miles per annum – and the fuel consumption calculation – 10,823 miles per annum – suggests fuel consumption average per car is significantly different; or an apathy from residents as to how much they actually drive. It could be attributed to the time spent in congestion rather than based on travelling at a constant speed. The average journey time is approximately 18.9 minutes. Based on these figures, it suggests that each car completes 16.4 journeys per week totalling 309.2 minutes per week. Therefore, cars in N.I. are

stationary for 96.93% of the time. To compound this, research has suggested that owners spend £453 each month – or 22% of income – on cars (Moneybarn, 2018). Combined, N.I. residents spend £5.1 billion annually on running private vehicles. These staggering figures suggest the need for a new paradigm shift in terms of rethinking mobility in the region.

However, the identification of the acupuncture points must arrive with three important elements to examine the cause and effect. First is the action – the 'what-if' statement which shifts economic, social and environmental attitude. Second is enabler – what stocks and flows are reconstituted to allow for the action to take place. Third is the effect – the spatial impact evidenced at various scales from the home right up to the regional level. As such, the product is a nested, multi-scalar solution to visualising a post-carbon region at the end of resource flow. Offering a design-led approach to re-centering resource flows in a place is aimed at making the region more secure, economically and environmentally, to challenge paradigms and cultural attitudes to the ways people currently live and how new forms of production and infrastructure can be deployed.

4. KELPIC CONNECTIONS: MULTI-SCALAR, SPATIAL EFFECTS

The food and mobility acupuncture points require new paradigms in support of an action and an enabler. The following speculates about the spatial and system implications of design-led interventions within the actor networks, specifically: 'what-if' N.I. produces all necessary livestock feed itself; 'what-if' N.I. consumed similar amounts of meat to the rest of the U.K.; and, 'what-if' shared autonomous electric vehicles were deployed across the province. Visualised holistically as 'Kelpic Connections' (Figure 7), the project addresses the acupuncture points through a series of productive and infrastructural interventions which have economic and health benefits while attempting to re-centre resource flows in the region. The multi-scalar implications and effects on the systems are relational but not sequential.

The first reprogramming considers food production and consumption in N.I. as a key acupuncture point in order to produce a new economy and landscape which reduces environmental impact while also providing healthier diets to residents from local sources. The system is leveraged by speculating how N.I. might produce all of the livestock feed it currently imports through W&R Barnett into the province. For example, on any given day, N.I. has 17.6 million broiler chickens on farms (DAERA, 2019a). Considered through the lens of nutrients in the stocks and flows of imported grains, broiler chickens consume more calories (5.4 billion kCal) every day than the recommended calorie intake for the entire population (4.2 billion kCal). When considering the other livestock fed each day, cattle and sheep for example, the reliance on global grain supply chains is significant and illogical when viewed as nutrients. To compound the reliance on imports is the fact that 75% of farms are in LFAs, signifying poor soil quality for cereal growth. 'Kelpic Connections' proposes a use of N.I. coasts for intensive kelp farming. Kelp reconfigures the system in a number of ways. Firstly, it produces a food and feed locally with less methane produced by animals as a consequence, reducing agriculture emissions. Secondly, kelp sequesters carbon effectively and continuously. Lastly, such an industry produces new economic value for local coastal communities. Once reliant on small to medium scale fishing businesses, these coastal town now suffer from underinvestment and brain drain. Strengthening new coastal and rural economies through livestock feed growth and production with farming provides new cyclical economic value within the province.

Similarly, if N.I. were to reduce per capita consumption of beef (163 g / week) to match the level across the rest of the U.K. (100 g / week), the annual demand for beef would reduce by 6.13 million kilograms of processed meat product (ONS, 2018). When equated to land use – 23m^2 to produce 1kg of beef – it totals 14,098 ha of farmland for cattle (Williams et al., 2006). In order to convert LULUCF in N.I. to a net sink –currently a contributor to net emissions of 0.5 $MtCO_2e$ (DAERA, 2019b) – the annual afforestation rate requires 1,700ha of new woodland per annum to convert forest land coverage from the 8% to 12% by 2056 (DARD, 2006; CCC, 2019). If 14,098ha of former farmland in LFAs were converted to new forestry, N.I. could sequester a total of 0.186 $MtCO_2e$ per annum – at a rate of 3.6tC / ha per annum when planting Sitka Spruce YC16 (Byrne and Black, 2003) – and reduce N.I. LULUCF contributions by 37.2% every year. This does not take into account the reduce carbon emissions associated with agricultural production which would no longer contribute to emissions or the increased sequestration rate thanks to coastal kelp farming. New woodland forestry on former LFA livestock farms, located in rural regions, produces small, networked green infrastructure which can facilitate forest migration naturally as the climate changes. Patches and stepping stones could be planned and deployed utilising a space syntax methodology which enables natural seed dispersal agents to facilitate natural forest migration (Han and Keeffe, 2019). These spatial impacts require new paradigms relating to food consumption and production, but ones that create new environmental and economic opportunities. Economies centred on a farmer to forester model and in industries reimagining livestock feed production.

The starting point for reprogramming mobility in N.I. envisages a new paradigm of personal transportation that is predicated on leveraging the collective, annual cost of car ownership in N.I. to deploy autonomous, electric vehicles. Two major infrastructures integrated into 'Kelpic Connections' imagines new offshore wind farms, located at the end of kelp farms, connected to the already important interfaces of car fuel supply, the forecourt. While offshore wind energy in N.I. is significant (currently accounting for 83% of all renewable generation), intermittent weather

requires new storage systems (DfE, 2018). As such, the typology of the forecourt is reinterpreted, operating as an electrical hub. *Forecourt battery parks* store energy for the electrical grid at times of low electric vehicle demand and low energy demand – mainly at night. The new mobility typology of the *forecourt battery park* is located in the conduit infrastructure of the region, a low-density city. It is distributed and localised, co-operatively owned by the population, bought and paid for through annual mobility payments otherwise diverted to private transportation. Stored energy in the new *forecourt battery park* system is sold to the Ireland and G.B. market, dividends to investors and money flowing into local economies which would otherwise be sent it in the opposite direction. These capital inflows could reform new, citizen-led renewable incentive scheme to replace the NIRO which was discontinued in 2015 (CCC, 2019). These incentives would encourage communities to build renewable energy sources for localised *forecourt battery parks* and support new inter-seasonal home energy storage, decarbonising the energy system further. The removal of petroleum and coal from the energy system would transform local environments for residents in N.I. Road currently cluttered with parked vehicles would become spaces for new, low carbon forms of last-mile mobility, like bicycles and scooters. These corridors – in most cases two parked bays wide, 4.8 meters – could also accommodate green, networked infrastructure that would add financial value to the street let along health and environmental value.

These 'what-if' propositions, visualised through 'Kelpic Connections', are not intended to be predictive, rather they act as guiding principles for reprogramming a system that needs fundamental recalibrating. Viewing collective financial expenditure differently and imagining new consumptive behaviour, global benefits to the environment become possible through reduced emissions, while transforming economies to serve the post-carbon society. The need to design our cities and neighbourhoods for a decarbonisation of the energy system and reduction in emissions from the agriculture sector need new attitudes to consumption and collective economic bargaining.

5. CONCLUSION: EVAPORATED URBANITY

The emergence of a postmodern cultural attitude to urbanism is witnessing the vaporization of collective, intensive forms of urban development. A consequence is the proliferation of infrastructural networks and, as Thun et al. (2015) characterise, 'conduit urbanism'. The distributed networks of the post-Fordist industrial systems, set in motion globalised trading systems and neoliberal economic policies that relied on just-in time delivery from decentralised, dispersed agents in disparate locations; referred to by Harvey in *The Condition of Postmodern* (1989) as "flexible accumulation." Despite the evolving role of logistics in global capital flows, as clearly predicted by Snyder and Wall (1998), N.I. currently lacks the intensity and density to drive urban form along corridors of mobility because it is at the end of FEW resource flows. As such, a new epoch of urbanism faces N.I. It must bypass postmodernity to arrive at Evaporated Urbanity. Form making is forfeited to become a by-product of a service or utility that finds functions in the products of the neoliberal systems of production, consumption and associated networks. It distributes wealth and risk to the collective in an attempt to provide new, shared services that form the basis of new urban form making. It still relies on the infrastructure language of modernity, the ports, highways and rail lines, but serviced by adapted typologies which offer additional function to the system.

The intention of this paper has been to explore ways in which cities can plan for post-carbon societies and speculate about reprogramming FEW networks. It requires the identification for key acupuncture points and the testing of new paradigm. For N.I., the points of acupuncture focused on challenges that have emerged as a result of low intensity, hyper low-density urbanism supported by an agriculture-based economy. Inefficiencies in this system are exposed in the flow of nutrients throughout the province and the reliance on private vehicles using petroleum. Viewing these actor networks through the FEW nexus, exposes place specific points of acupuncture, exposing new interventions and accumulative possibilities for post-carbon infrastructures and typologies. The spatial consequences for buildings, the neighbourhoods and cities can be speculated but serve as the by-product of shift the design paradigms of urbanism from form related to system-orientated.

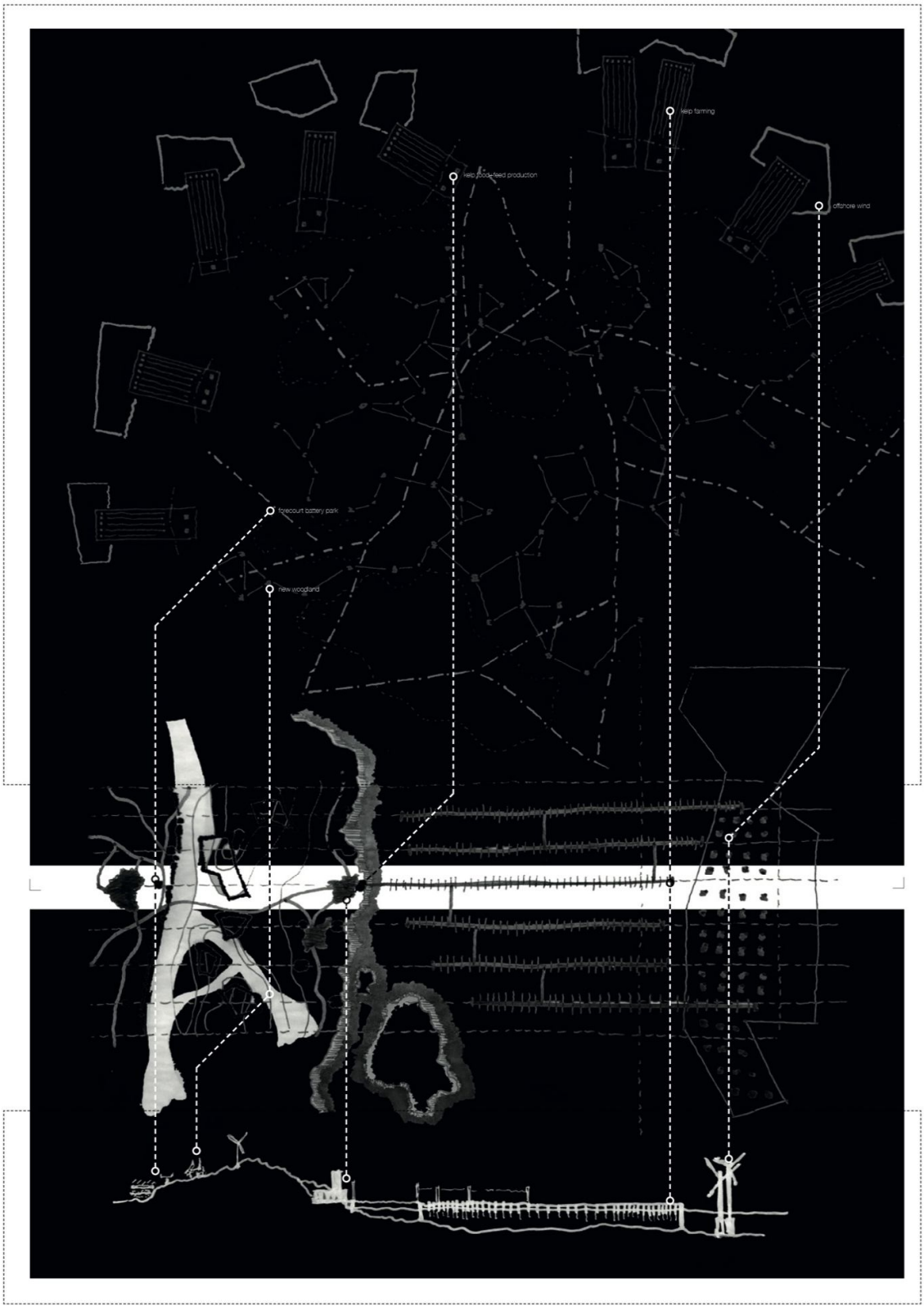

Figure 7: 'Kelpic connections'

6. REFERENCES

Byrne, K. and Black, K., 2003. Carbon Sequestration in Irish Forests. Dublin, Ireland: COFORD Connects.

Centre for Ecology & Hydrology (CEH), 2015. Land Cover Map 2015 Statistics. Natural Environment Research Council.

Committee on Climate Change, 2019. Reducing emissions in Northern Ireland. London, U.K.

Corner, J., 1999. The Agency of Mapping. In: D.E. COSGROVE, ed, Mappings. London: Reaktion, pp. 253-268.

Cosgrove, D.E., 1999. Mappings. London: Reaktion.

Cullen, S. and Keeffe, G., 2019. Quantification and visualisation of food impact in Northern Ireland.

Department for the Economy (DfE), 2018. Energy in Northern Ireland 2018. Belfast, U.K.: Analytical Services Division.

Department of Agriculture and Rural Development, (DARD), 2006. Northern Ireland Forestry: a strategy for sustainability and growth. Belfast, U.K.: Forestry Service, DARD.

Department of Agriculture, Environment and Rural Affairs (DAERA), 2019a. Animal farm populations. Belfast, U.K.

Department of Agriculture, Environment and Rural Affairs (DAERA), 2019b. Northern Ireland greenhouse gas inventory 1990-2017. Belfast, U.K.: Statistics and Analytical Services Branch, DAERA.

Farias, I. and Bender, T., 2010. Urban assemblages: how actor-network theory changes urban studies. Abingdon; 4: Routledge.

Gottmann, J., 1961. Megalopolis: the urbanized northeastern seaboard of the United States. New York: Twentieth Century Fund.

Han, Q. and Keeffe, G., 2019. Stepping-stone city: process-oriented infrastructure to aid forest migration in a changing climate. Contemporary Urban Design Thinking: Nature-Based Urbanism (accecpted).

Harvey, D., 1989. The Condition of Postmodernity: An Enquiry into the Origins of Cultural Change. Cambridge, U.S.A.: Blackwell Publishers.

Meadows, D., ed, 2009. Thinking in systems: a primer. London: Earthscan.

Moneybarn, 2018. The Cost of Car Ownership.

Mumford, L., 1961. The city in history: its origins, its transformations, and its prospects. San Diego; 4: Harcourt, Inc.

Northern Ireland Statistics and Research Agency, (NISRA), 2018. Northern Ireland Annual Coal Inquiry. Belfast, U.K.: Economic & Labour Market Statistics Branch, NISRA.

Northern Ireland Water Limited, 2018. Annual Report & Accounts 2017/18. Belfast, U.K.

Office for National Statistics, 2018. Family Food Survey 2016/2017. London, U.K.: Department for Environment, Food and Rural Affairs.

Pawley, M., 1998. Terminal architecture. London: Reaktion.

Snyder, S. and Wall, A., 1998. Emerging Landscape of Movement and Logistics. Architectural Design, 68(7/8), pp. 16-21.

Thun, G., Velikov, K., Ripley, C. and Mctavish, D., 2015. Infra Eco Logi Urbanism: a project for the Great Lakes Megaregion. Zurich, Switzerland: Park Books.

Waldheim, C., 2016. Landscape Urbanism. Oxford, U.K.: Princeton University Press.

Williams, A., Audsley, E. and Sandars, D., 2006. Determining the environmental burdens and resource use in the production of agricultural and horticultural commodities. London, U.K.: Department for Environment, Food and Rural Affairs (DEFRA).

#212: Techno-economic evaluation of solar water heating applications in dairy farms in the Eastern Cape Province of South Africa

Russel MHUNDWA[1], Michael SIMON[2], Stephen Loh TANGWE[3]

[1] *Fort Hare Institute of Technology, University of Fort Hare, P. Bag X1314, Alice 5700, South Africa, rmhundwa@gmail.com*
[2] *Fort Hare Institute of Technology, University of Fort Hare, P. Bag X1314, Alice 5700, South Africa, msimon@ufh.ac.za*
[3] *Fort Hare Institute of Technology, University of Fort Hare, P. Bag X1314, Alice 5700, South Africa, stangwe@ufh.ac.za*

There are variations in electricity usage in dairy farms with milk cooling and water heating being the major energy intensive processes. Hot water at a temperature of 40°C and 70°C is required for cleaning of the cow udder and sterilizing of the bulk milk cooler and all milk contact surfaces respectively. Optimizing these processes can lead to substantial electricity savings. Though the technical feasibility of solar water heating systems has been established, their financial viability in dairy farms need to be ascertained. This paper presents an economic analysis of solar water heating applications in dairy farms. An analysis of hot water demand and usage was done through an energy audit methodology on a dairy farm in the Eastern Cape Province of South Africa. A techno-economic evaluation and the feasibility of implementing such a system on a dairy farm is discussed and the payback period is evaluated. Beside this, other economic and environmental benefits to the dairy farmers by using solar energy systems are discussed. The results indicated that annual savings of 12,097 kWh can be realised through the installation of solar water heating systems on the dairy farm. The payback period was 3.84 years.

Keywords: techno-economic; dairy; payback period; solar water heating

1. INTRODUCTION

Dairy farming can be regarded as an energy intensive enterprise. The processes involved in dairy farming include milking, water heating, milk cooling and ventilation amongst other processes which use electrical energy (Ludington et al., 2003; 2004). However, since the sector deals with milk and dairy products which can be prone to high levels of contamination, it is imperative that the sanitary hot water system in place be reliable and efficient. Due to the increase in the global energy prices, most sectors are in the process of trying to use an energy mix whereby there is integration of the conventional energy supply and renewable energy technologies in an effort to address the current problem. Milk cooling accounts for the most energy consumption on the dairy farm followed by water heating. Worldwide, the dairy farm has to meet with high hygienic standards, as highlighted by Beardmore and Veitch (2008), the largest enforced use of hot water in the dairy is the twice-daily hot washing of the milk contact and internal surfaces of equipment after each milking. Typically, dairy farms use both hot water and cold water to clean the milk contact surfaces, however, the use of hot water helps in the removal of fats as well as kill bacteria that might have accumulated during the milking cycles. In addition, washing of the cow's udder and the milking cups is also an important practice to maintain the quality of the milk. After every milking cycle, it is commended that the milking equipment and other contact surfaces be cleaned and/or sterilised in preparation for the next milking cycle. Modern dairy farms have automatic systems which deliver water to the BMC for cleaning and upon completion, exhaustive cleaning and rinsing of the BMC commences. Also, other surfaces which might get into contact with milk are also cleaned hence the facilities are also equipped with sanitary hot water systems. Mainly, the sanitary hot water is heated by conventional electric geysers of which in most cases they are a series of 150 L/ 3 kW systems. Clearly, two methods of cleaning can be employed on dairy farm namely; the acidified boiling water (ABW), which involves the use of water close to 100ºC for once off cleaning. The other system makes use of recirculation under vacuum and it is typically used at a slightly lower temperature of 70ºC. Coupled to that, there is also need to warm water at approximately 40ºC for cleaning the teats and udder of the cows-in-milking before the milking commences though it is not a requirement (Ludington et al., 2003; 2004). Energy savings in water heating is viable if energy efficiency initiatives are implemented and these involve management practices and technology upgrades which can reduce energy consumption (Pressman, 2010; Mhundwa et al., 2017). In addition, some studies have focused on the direct consumption of electricity and thermal energy by identifying the energy users and their impact on the dairy farm's energy consumption. These studies have revealed that the highest consumer of electrical energy is the cooling process (43%) followed by sanitary hot water production (27%) (Rasmussen and Pedersen, 2004). However, similar studies have established the electrical consumption of the milk tank, water heaters and the vacuum pump. According to Shine et al. (2018), on average 7.42 L of water per litre of milk is consumed on average and there exists a relationship between electricity and water consumption with a change in milk production. South Africa has, in recent years, experienced high economic growth as well as a rapid expansion in the electric power consumer base (Ijumba & Sebitosi, 2001). The annual 24-hour global solar radiation average is about 220 W/m^2 for South Africa. Most areas in South Africa average more than 2 500 hours of sunshine per year, and average solar-radiation levels range between 4.5 and 6.5kWh/m^2 in one day (www.energy.gov.za). This makes so lucrative for solar energy utilisation for both domestic and commercial purposes. Though the technical feasibility of solar water heating systems has been established, their financial viability in dairy farms need to be ascertained. It is against this background that this paper presents a techno-economic evaluation and the feasibility of implementing solar water heating system on a dairy farm.

2. MATERIALS AND METHODS

The study was conducted on an existing dairy farm in the Eastern Cape Province of South Africa. The farm had a maximum of 800 cows in milking during the time of the experiment where a twice a day milking system was in place. An Energy audit was conducted in an existing dairy farm (Fort Hare Dairy Trust) and power and energy meters were installed to measure the energy consumption for the electric geysers on the facility and the temperature of the cold water was measured using a temperature sensor. Also, the overall water consumption was determined from the installed flow meters within the dairy farm. Quantifying of hot water demand on the Farm was done through some on the farm record sheets and the annual energy consumption due to water heating was deduced. Based on the results from the sizing of a solar water heater system for the dairy farm was done through a simulation application and the economic analysis of the system was done. Only the high pressure flat plate solar water heating systems was considered for the purposes of this study due to availability of empirical models and ease for retrofit to the existing geyser systems. The farm had everyday milking for the whole year and measurements were considered for the period April – December 2017. The peak milking season and the off-peak milking season was split into April – August and September – December respectively. Water usage on the farm was extracted from the farm records. A Data acquisition system comprising of relative humidity and ambient temperature sensor were used to record the weather parameters, moreover the radiation data was extracted from PVGIS. A simulation of the performance of the solar collectors was done through a mathematical model which was developed for the area by Ndlovu et al. (2015), which predicts the outlet water temperature from a solar collector located in Alice where the dairy farm is also located. This was then used to predict the solar contribution for the heating of water on the dairy farm and subsequently the energy savings, emissions reduction and the payback period from a conservative approach. Figure 1 shows the probe that was used to measure the weather parameters

Figure 21: HOBO Pro V2 Relative humidity and ambient temperature sensor and optical pipe

The HOBO Pro V2 data logger is a weatherproof logger that provided high accuracy temperature and relative humidity measurement for a broad range of outdoor measurements. The logger could measure ambient temperature, relative humidity (RH) and dew point. The Pro V2 used the optical foot pipe for fast download of data and configuration of the sensor. Its memory capacity could accommodate 42,000 measurements and can be configured to measure from one-second to 18 hour intervals as a fixed rate or multiple logging intervals (Onset, 2019). The option considered in this study is retrofitting the solar system to the existing geysers that are on the dairy farm, the geysers are shown in Figure 2.

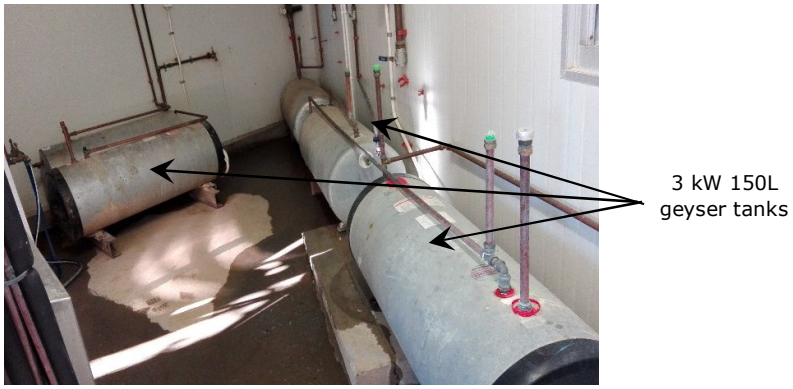

Figure 2: Electric geysers on the dairy farm

2.3. Calculations and theory

The energy required to heat up water was calculated using the following formula

Equation 1: Energy required to heat water.

$$Q = m_w C_p (T_o - T_i) / 3600$$

Where:

- Q = quantity of heating energy used to heat the water (kWh)
- m_w = mass of water (kg)
- C_p = specific heat capacity of water (4200 J/kg ºC)
- T_o = Outlet temperature required (ºC)
- T_i = Inlet temperature of water (ºC)

Equation 2: Simple payback Period (SPB).

$$SPB = \frac{Initial \quad Investment}{Yearly \quad Energy \quad Cost \quad Savings}$$

Equation 3: Solar collector performance model.

$$T_{co} = 1.167 + 0.44\,S_R + 0.669\,T_a + 0.056\,R_h + 0.33\,T_{ci}$$

Where:

- T_{co} = Collector outlet temperature (ºC)
- S_R = Solar radiation (W/m^2)
- T_a = Ambient temperature (ºC)
- $T_{c\,l}$ = Collector outlet temperature (ºC)
- R_h = Relative humidity (%)

2.4. Layout of the dairy system

Figure 3 illustrates the schematic layout of the dairy farm's cooling system.

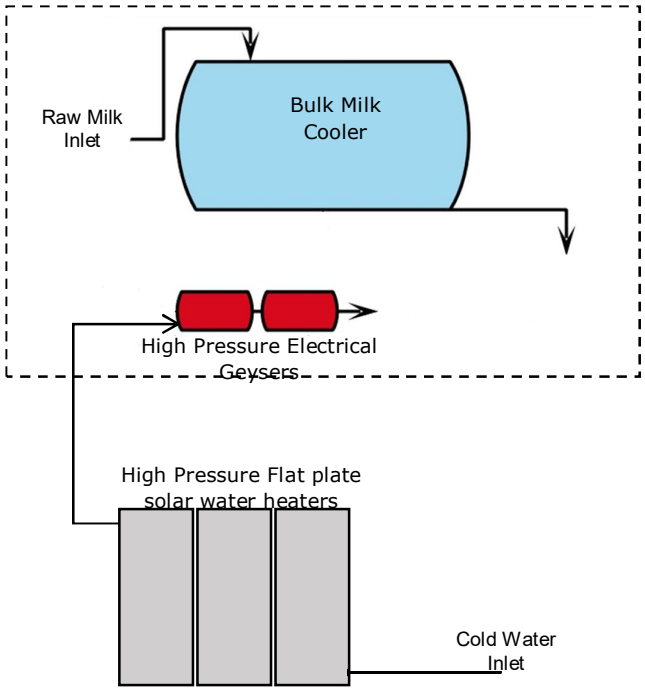

Figure 3: Electric geysers on the dairy farm

3. RESULTS AND DISCUSSION

3.1. Water and energy demand analysis

The water requirement for the dairy farm during the peak and off-peak season are presented in Figure 4 below. It can be deduced that seasonal change in cows in milking had a direct impact on the total water consumption.

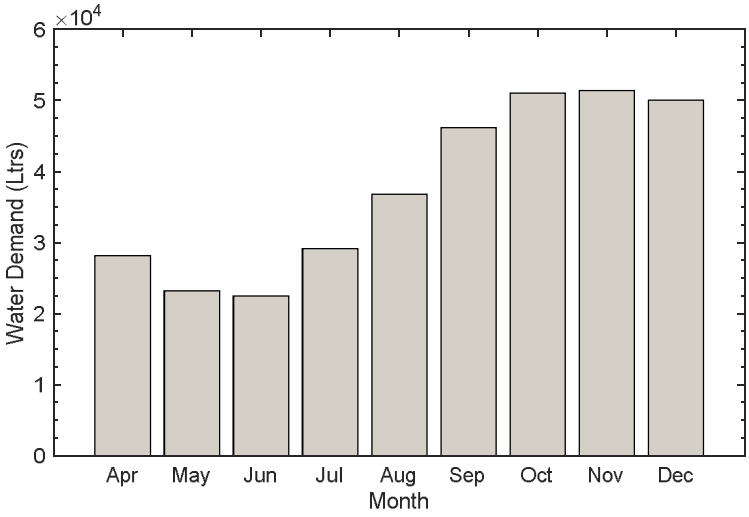

Figure 4: Water Usage in the dairy farm

The off-peak had an average of 27,970 litres of water was used as opposed to the peak period had 49,660 litres. There was an increase of 44% in the use of water within the dairy farm, this was as a result of increase in the herd size from 467 to 829 cows in milking (Mhundwa et al., 2017). The maximum water consumption for the whole duration was 51,366 litres. Table 1 shows the daily variation of hot and cold-water usage across the period of monitoring. The trend depicted in Table 1 reveal that there was also an increase in the average daily water consumption for both hot and cold as highlighted earlier on.

Table 1: Daily demand of hot and cold water on the dairy farm

Month	Av Daily Water Demand	Hot Water	Cold Water
April	940	536	404
May	749	427	322
June	748	427	322
July	940	536	404
August	1,188	677	511
September	1,539	877	662
October	1,647	939	708
November	1,712	976	736
December	1,614	920	694

One way ANOVA test indicated that there was no significant different difference between the hot and cold water demand as depicted by a p-value = 0.0891. It can be alluded that approximately 57% of water usage was hot water which translated to an annual hot water demand of 266,065 litres since the use of hot water in the farm is required for the cleaning of all mill contact surfaces and cold water is just used for rinsing and basic cleaning. Thus for all the two milking shifts there is need for cleaning of all mil contact surfaces leading to high usage of hot water. An analysis of the energy consumption due to water heating was done and is presented in Figure 5.

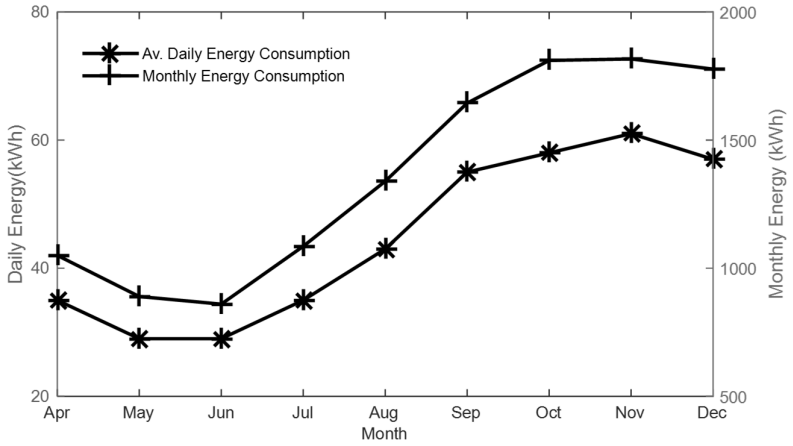

Figure 5: Average Daily Energy and Monthly Energy Consumption

As shown in Figure 5, the energy consumption for water heating in the dairy farm increased with an increase in the cows in the milking. On average for the off-peak period and peak period daily energy consumption was 1,044.82 kWh and 1,762.11 kWh respectively. There was a 26% increase in the energy consumption as the season changed from off-peak to peak. Cumulatively, the total energy for the period April – December was 16,290 kWh/year which translates to R37, 466. This made water heating to be the second energy intensive process after milk cooling.

3.2. Solar water heating

Based on the demand analysis presented earlier in 3.1, the solar water system was sized to be 30m^2 this was based on the ease to retrofit with the existing storage of 200 litre cascaded geysers as shown in Figure 2. This however resulted in considering the high-pressure flat plate collectors. The performance of the high-pressure flat plate collectors was reported by Ndlovu et al. (2015) where an empirical model was developed to predict the outlet water temperature from the collector. For the purposes of this study, the inlet water temperature was held constant at 20ºC since the times considered were between 09:00 – 17:00 where there is considerable radiation reaching the collector. The model related the ambient temperature, relative humidity, solar radiation and inlet water temperature as shown in Table 2.

Table 2: Performance of the flat plate solar system

Month	Solar Radiation (W/m^2)	Ambient Temperature (ºC)	Relative Humidity (%)	Water Inlet Temperature (ºC)	Collector Outlet Temperature (ºC)
April	820.18	16	69	20.00	58.42
May	779.24	14	57	20.00	54.61
June	736.84	12	49	20.00	50.96
July	790.94	12	48	20.00	53.28
August	866.96	11	59	20.00	56.58
September	937.13	14	60	20.00	61.73
October	913.74	21	62	20.00	65.49
November	893.27	21	70	20.00	65.04
December	852.34	23	76	20.00	64.91

It can be deduced from Table 2 that the average collector outlet temperature of 59ºC is achievable between April and December, with the peak season averaging 64.29ºC as opposed to 54.77ºC for the off-peak season. There was a significant difference between the collector outlet temperature for the peak and off-peak season as depicted by a p-value = 0.0002. It is interesting to note that for both off-peak and peak seasons the predicted temperature of water does not reach the required 70ºC for sanitary purposes of the dairy farm. Figure 6 illustrates the remaining temperature lift for the water to reach the required temperature level.

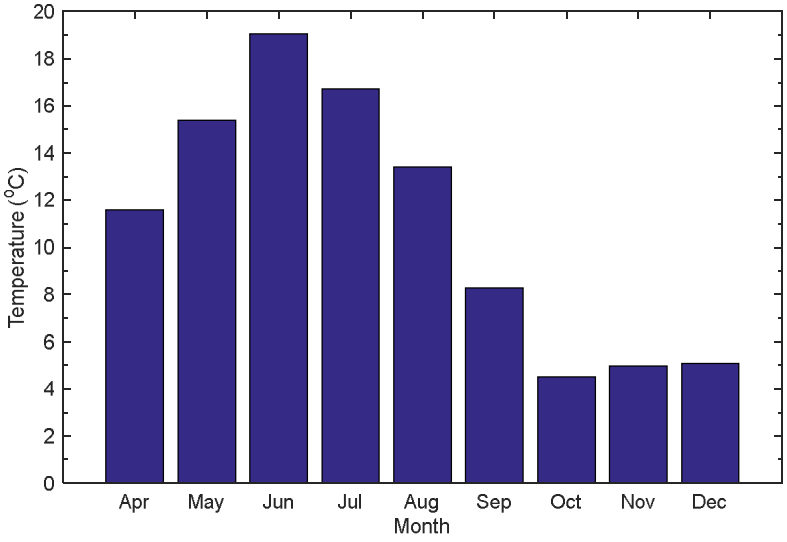

Figure 6: Temperature lift of water to 70 °C

As indicated in the Figure 6, an average temperature lift for the water was predicted to be 11ºC and the highest being 19.04ºC for the month of June. It can be alluded that the performance of the collector is seasonal as evidenced by higher temperature lift for the water to reach the required level in the winter months April – August as opposed to the summer months September – December. This however suggest that solar water heaters cannot be used as stand-alone systems hence there is need for electrical backup, hence the solar water heaters will work as preheaters. Table 4 shows the amount of energy that will be required to further heat up the water to 70ºC.

Table 3: Energy consumption for heating water to 70°C

Month	Energy (kWh)
April	216.03
May	236.55
June	282.87
July	322.52
August	327.07
September	252.71
October	152.32
November	168.60
December	168.49

For the duration April – December a total of 2,127.16 kWh would be required to further heat up the water to a threshold of 70ºC which translates to 2,836.21 kWh at a cost of R6,523.28. The trend shown in the table depict that there is high contribution from the grid during the off-peak months even though it is characterised by a small herd size as compared to the peak months. Furthermore, the inclusion of solar water heating at the dairy farm will result in some savings on the cost of electricity as well as environmental benefits such as reduction in emissions hence retard the global warming phenomenon. On average the solar energy contribution was 84% being complemented by 16% from the grid. An analysis of the savings and emissions reduction is shown in Table 5.

Table 4: Savings due to Solar Water heating on a dairy farm

Month	Energy Savings (kWh)	CO_2 Reduction (kg)	NO_X Reduction (kg)	SO_X Reduction (kg)	H_2O Saved (Ltrs)
April	716.97	709.80	3.00	5.69	0.96
May	532.04	526.72	2.23	4.22	0.71
June	459.97	455.37	1.93	3.65	0.62
July	642.19	635.76	2.69	5.09	0.86
August	891.19	882.27	3.73	7.07	1.19
September	1,274.57	1,261.83	5.34	10.11	1.71
October	1,537.39	1,522.02	6.44	12.19	2.06
November	1,531.02	1,515.71	6.41	12.14	2.05
December	1,487.55	1,472.68	6.23	11.80	1.99
Total	9,072.89	8,982.16	38.02	71.95	12.16

The average energy savings for the monitoring period amounted to 1,008.10 kWh and a total of 9,072.89 kWh. Huge savings were recorded during the peak milking period from September to December 64.26% as opposed to 35.74% for the off-peak period of April to August. Also, there was 55% increase in the energy savings as the season changed from off-peak to peak milking season, this can be explained from the fact that the summer season is from September to March within the country. This was also directly related to the reduction in emissions

3.3. Investment appraisal

Installation of the solar system was evaluated for its financial benefits and the payback period using the simple payback period. This is to assess the viability of implementing the technology on the farm with respect to its initial capital investment. It should be noted that any technology is considered viable if the life span and the payback period is favourable, generally the payback must be in few years while the life span must be longer. Considering the solar water heaters, the life span is estimated at approximately 15 years. The payback analysis for the system was done using the Eskom tariff of R2.30/kWh and also using an estimated 15% increase in tariff per year. The initial cost of the solar water heater including installation (panels only) was estimated at R3,560/m^2 making the total investment cost for this initiative to be R106,800. The annual energy savings for the solar water heating system was 12,097 kWh with a cost savings of R27,823.50. From the simple payback analysis, the system will be able to payback itself in 3.84 years. Considering a tariff increase of 15% per year the payback period for the system will be 3.34 years. This makes the investment viable for the dairy farms within the country.

4. CONCLUSION

In conclusion the study revealed that solar water heaters can be of benefit in the dairy farm since substantial savings can be realised. Also, the shorter payback period for the system makes it viable for investment. The solar contribution to water heating was high in the peak period and directly correlated to the change of season which coincided with the summer months. However, depending on solar water heaters alone to provide the hot water will make the collector area large and will impact on the cost involved, hence the use of the backup element connected to a timer switch is strongly recommended to cater for the winter periods where radiation is low. In this case solar water heaters will act as preheaters for the backup elements.

5. REFERENCES

Beardmore, J, Veitch, T, 2008. Solar Water Heating and Dairy Farming Potential in the Peak District National Park. T4 Sustainability Limited Version.

Ijumba, P, Sebitosi, A. B., (2010). Evaluating the Impact of Consumer Behaviour on the Performance of Domestic Solar Water Heating Systems in South Africa. Journal of Energy in Southern Africa, Vol. 21, No 1.

Kablan, M.M., 2004. Techno-economic analysis of the Jordanian solar water heating system. Energy, 29(7), pp.1069-1079.

Ludington, D, Johnson, E, 2003. Dairy Farm Energy Audit Summary. Energy Research and Development Autority. New York State Energy Research and Development Autority.

Ludington, D, Johnson E, Kowalski J, Anne M, Peterson, R, 2004. Dairy Farm Energy Efficiency Guide. Ithaca, NY: DLTech, Inc.

Mhundwa, R, Simon, M, Tangwe, S, 2017, August. Comparative analysis of the coefficient of performance of an on-farm direct expansion bulk milk cooler. In 2017 International Conference on the Industrial and Commercial Use of Energy (ICUE) (pp. 1-7). IEEE.

Ndlovu, N, Simon, M, Tangwe, S, 2015, January. Evaluation of an empirical model for a flat plat solar collector. In 2015 Southern African Universities of Power Engineering (SAUPEC)

Onset Computer Corporation www.onsetcomp.com.

Pressman, A, 2010. Dairy farm energy efficiency. ATTRA.

PVGIS http://re.jrc.ec.europa.eu/pvgis/apps4/pvest.php?lang=en&map=africa

Rasmussen, J.B, Pedersen, J, 2004. Electricity and water consumption at milking. Danish Agricultural Advisory Service, National Centre.

Shine, P, Scully, T, Upton, J, Murphy, M.D., 2018. Multiple linear regression modelling of on-farm direct water and electricity consumption on pasture based dairy farms. Computers and Electronics in Agriculture, 148, pp.337-346.

Shine, P, Scully, T, Upton, J, Shalloo, L, Murphy, M.D, 2018. Electricity & direct water consumption on Irish pasture based dairy farms: a statistical analysis. Appl. Energy 210, 529–537. http://dx.doi.org/10.1016/j.apenergy.2017.07.029.

www.energy.gov.za

Yohanis, Y.G, Popel, O, Frid, S.E, Norton, B, 2006. The annual number of days that solar heated water satisfies a specified demand temperature. Solar Energy, 80(8), pp.1021-1030.

#216: Review article: toward future particulate matter situations in Thailand from supporting policy, network and economy

Jitiporn WONGWATCHARAPAIBOON

Design Business and Technology Management Program, Faculty of Architecture and Planning, Thammasat University, 12121 Thailand, jjpinx4391@gmail.com

In the era of climate uncertainty in 2019, PM2.5 situations in Thailand are considered as big impacts to local livings in terms of health and well-being. This paper aims to investigate policies to decrease PM2.5 levels and to examine reliable networking systems. International and domestic policies are literally found for controlling traffic emission, open burning activities, public health and industrial zoning, when strong satellite networks can be proved by the reliability and accuracy of PM2.5 data collections, sources and chemicals identifications. Turning to financial loss during the PM2.5 situation, cost estimations have been accounted in terms of environmental tax, pollution footprint, health mortality, public air cleaning payment, GDP and uncertainty cost of air pollution. The results related to policy can affect local social interventions, if policies match correctly to suitable techniques in this research series. Also real-time prospective warning of local PM2.5 exceeding is required with accuracy, while all applicable methods are financially comparing in different contexts.

Keywords: PM2.5 in Thailand; supporting policies; economic effects; PM2.5 networking; cost estimation of PM2.5

1. INTRODUCTION

During the 5-year period of air pollution research in Thailand, Particulate Matter sized 2.5 micron (PM2.5) has been studied as environmental threats especially in middle and north land. The components of PM2.5 can be various chemical depending on types of source, geographic locations and activity contexts. There are several common sources of PM2.5 which include 1) the United State source: secondary sulphate, secondary nitrate, spark-ignition emissions, diesel emissions, road dust, biomass burning, pyrolyzed organic (OP) rich (Squizzato et al, 2018), 2) Asian source: secondary carbon (only in Asia), water soluble transition metals (Cr and Zn) (Park et al, 2018) and 3) European source: potassium (K), brown coal, black coal and oil (Pokorná et al, 2018). Within Thailand context, biomass burning and road dust provide black carbon and transportation chemicals to ambient environment.

Based on PM2.5 threats in the middle and north Thailand, there are resulted from the same type of open agricultural burning sources and traffic situations. However, different incidences are showed in receiving locations. For example, Chiang Mai province has a trough location which is blocked ventilation by natural pressure in winter season; while Bangkok has open basin near the coaster which ventilation is somehow blocked from ocean wind. In every winter season, PM2.5 concentrations exceed National Ambient Air Quality standards (NAAQs) and World Health Organization (WHO) at 35 and 25 $\mu g/m^3$ respectively. For example, the average intensity of PM2.5 levels is higher than 60 $\mu g/m^3$ for nearly a month in 2018 (Pardthaisong et al, 2018). Then the exceeding of PM2.5 has returned again in early 2019 which provide serious effects to sensitive group of people in symptoms of bloody cough, respiratory irritation and lung infection.

As a result, brainstorm solutions are called for emergency situations and research suggestions pointed out resilience city and well participants can mitigate PM2.5 level. Also well communication to rural residents and higher education organizations possibly protect people from future exceeding situation. Moreover, air cleaning application and network technology can support individual unit, project future situation and analyse relational factor etc. For example, satellite data analysis can find interrelation between PM2.5 source and mortality of local people which helps to navigate policy development (Shi et al, 2018). Therefore, this research paper aims to investigate example policies, satellite network systems and financial estimations.

2. SUPPORTING POLICY

From the dynamic of environmental change, all countries have been accounted to predict and avoid harmful situations as well as protecting themselves from PM2.5 threats. The difference in economic and social policy can result directly in challenges of sustainable urban development and implementation. Within these challenges, criteria and sustainability indicators should be set up clearly for all contributors and participants (Verma & Raghubanshi, 2018). The effectiveness of air quality policies for the Pacific Islands region was building up collaboration among land users. Also most successful policies resulted from promoting leadership and empower of air quality control by raising awareness, informing more alternatives, financial support and well cooperation from authorities to action facilitating. Noticed awareness of this policy was one-side focus on economic change without balancing of resources, well supports of guideline and facilitating factors. Ambiguous purpose of application and unplanned process of action could lead to misunderstanding and conflicts in government system (Isley & Taylor, 2018). Then clear messages of enforcements will be easy to implement to local people. This section includes all case studies and policies within top-down and bottom-up policies, air quality control and methodology and implementation.

2.1. Top-down and bottom-up policies

Throughout the strongest action on environmental concern, Extended Producer Responsibility (EPR) legislations were revealed command and control (CAC) and market-based incentive (MBI). The reactive environmental strategy (RES) responded significantly both side of actions and enterprise economics performance, while the proactive environmental strategy (PES) linked significantly to only MBI action and both economic and environmental performances. Top-down policies should well support the coordination of industrial operation, implementation, monitoring observation and feasible environmental regulations (Peng et al, 2018). It can be seen that top-down policy is suitable for business and government sectors which have organiser or leaders.

Turning to bottom-up policy, social interventions are always from group of users who can point out environmental gap and provide participation for policy improvement. Throughout three case studies from London, Hong Kong and San Francisco, air quality action plans (AQAPs) can reflect how sociotechnical imaginaries affect important air cleaning environment policy by a striking uniformity pattern .Also five planning policies of urban future need to be delimited within the topics of 1) the government up front, 2) economy for cleaning air, 3) technologies for air problems, 4) admiring 'good' citizen, and 5) science policy interaction (Gross, Buchanan & Sané, 2019). Also this example can examines how the requirement of street people can improve direction of policy. According to transportation policy, promoting pathway can support healthy behaviours by increase in physical activities and social interactions. However, these activities allow sensitive group of street people suffering easier from PM2.5 exposures (Frank et al, 2018). From 31 representative cities in China, 22 cities have needed policy to improve

efficiently air cleaning during the period of 2013-2016 which the study pointed to government supports and industrial cooperation (Li, Chiu & Lu, 2018). The positions of participants and contributors will affect future action of policy. Social intervention is supposed to be more sustainable development since people provides higher willingness of participation.

2.2. Air quality and burning control

Focusing on activities of burning control, outdoor burning is popular throughout rural areas in developing country because it is the lowest cost to eliminate all stuffs even body. Over 40 crematoriums in Mexico are identified being sources of PM2.5 exposures .To reduce effects of air pollution, longer times of combustion in 120 minutes is claimed to emit less PM2.5 at 11-59 mg /m^3, while those shorter times in 70 minutes provides more than double level of PM2.5 at 25-205 mg/m^3 (González-Cardoso et al, 2018). This finding links normally to regulation and policy controlling crematorium burning to have better oxidation of combustion .Oxidation is the same point to coal burning since it cannot reach high quality of combustion. From 2017 to 2030, simulating results of PM2.5 concentrations have been projected based on energy saving and adding control technology policies. If applying both policies, polluted areas of Sichuan Basin, Middle Yangtze and North China, it will reduce dramatically PM2.5 levels from residential combustion, opening burning and transportation .Coal combustion will be only one activity being threat of air quality in China in 2030 (Cai et al, 2018). This result is supported by research of coal substitution policy evaluation in 2019 .The coal replacement policy by gas or electricity is found to still emit high concentrations of air pollutions such as CO_2, SO_2, NO_x and PM2.5 .Then alternative energy and social welfare policies are recommended to further considerations (Chen & Chen, 2019).

Turning to mobility combustion, for the modelling development purpose, US Environmental Protection Agency's Motor Vehicle Emissions Simulator (MOVES) is used to predict six air pollution emissions in particular CO, CO2, NO2, PM10, PM2.5, and SO2. Other factors of morning peak-hour traffic period and rapid growing population in Texas are applied in this model. Dominant finding points to awareness of physical sensitivities resulted from policy decisions relied mostly on regional emission producers. The length of travel is reflecting speed of traffic through overall case simulations (Shah, Nezamuddin & Levin, 2018). It is supported by modelling study of road grade related to vehicle speed, PM2.5 emission and dispersion on freeways. 9.5 miles freeway provides impacts on PM2.5 dispersions along the road which indicates possible bias from results of the National Ambient Air Quality Standards (NAAQs) ignored different grade of road (Liu, Rodgers & Guensler, 2019). Secondary dust along the street canyon of Krasinski Avenue in the centre of Krakow has been collected from local station to improve Operational Street Pollution Model (OSPM) data since 2019 (Rzeszutek et al, 2018).

Furthermore, from international mega-events in China for examples, the 2008 summer Olympic Games, the 2014 APEC summit, and the G20 summit in 2016, top-down campaign under the name of 'Blue Sky' demonstrated well collaboration between local government enforcement and scientists monitoring air quality over functional region. This could be based –case study for sustainable development in science-policy integration and implementation for air pollution control (Shen & Ahlers, 2019). Then this integrative methodology was promoted again in 2019 because of the returning of air pollution crisis. The conclusion of policy guideline led to integrating technology with the key success of energy, top-down policy initiatives and people engagement (Tilt, 2019). Energy and air pollution crisis suggested to providing feasible and implementable policies, while the internet of things (IoTs) is also suggested to share and improve weakness of monitoring, predicting network. The detections of those monitoring were argued to be responded by local contributors in terms of environmental and carbon emission taxes. While, higher value in taxation showed in promoting renewable energy. These aspects of taxation should be applied to modelling policy and policy decision for the future (Wang et al, 2018).

After lunching policies, later situations and feedbacks should be monitored for transforming to more effective policies. For example, due to China's climate change action plans in 2014, there are some aspects needed to be improved in particular urban data, cross disciplinary assessment and policy transformation to develop system mechanism (Ng & Ren, 2018). Another suggestion indicates human behaviour which should be matched to enforcement policies. Theory of Planned Behaviour (TPB) was studied the relation to PM2.5 controlling policies in China. The study focused on transportation users' behaviour to take public transportation and to purchase electronic vehicles in intensive hazardous areas. It was assured that PM2.5 intensity was positively affected by attitude, subjective and moral norms, while perceived control affected indirectly intention by subjective norm (Shi, Wang & Zhao, 2017). The development of air pollution control has been mostly exemplified from China because their large industrial developments led them facing widely air pollution before other developing countries.

2.3. Methodology and implementation

The policy actions related to Internet of things (IoTs) do possibly provide convenient services and facilities, for example, transportations, energy healthcare, education and public safety .This smart transformation can be academically developed in four directions of conducting technological and theoretical studies, integrating

implementations and evaluating technologies, focusing current challenges and solutions, expanding existing technological research (Kankanhalli, Charalabidis & Mellouli, 2019).

For the conduction and theory, the comparisons of PM2.5 components and emission level were studied from agricultural fuel and coal resources. Biomass fuel provides higher PM2.5 level, carbon fraction emission and anionic and cationic chemicals in particular K+, Cl- to atmosphere. The oxidation in charcoal, briquette and wood branches burning can save 775-1,354 kiloton per year, 427-765 kiloton per year and 644-1,155 kiloton per year of PM2.5 emission (Sun et al, 2019).

To implement IoTs to local user, they may need to understand and apply all instruction by themselves. One forecast technique from cyberinfrastructure is merged well to international networks in Romania by artificial intelligent algorithms .This adding technical detector can pre-inform people to avoid PM2.5 exceeding from their children (Dunea et al, 2017). Also satellite data should be calibrated and validated to the real data collections. Based on Air Quality in Major Incidents (AQinMI) service, Osiris laser light scattering monitors are settled throughout 23 major incident industrial fires for testing accuracies of particulate matter (PM2.5 and PM10) collections in different ranges of exposure time (Griffiths et al, 2018).

Moreover, PM2.5 level was proved linking to 1.2 million premature deaths (42% higher) during the 10-year satellite observations between 2000 and 2010, while Henan, Anhui and Sichuan were monitored to be high population density areas. Then this could be the first rationale to improve air quality in China by relocation of intensive industries. Also government policies should promote emission control technologies in industrial areas (Xie et al, 2016). Then premature mortality in 1 square kilometre was proved to correlate sensing-geostatistical monitoring results of PM2.5 concentrations which were possibly parameter to report the trend of air quality in China .For result examples, nearly 20 $\mu g/m^3$ reduction of PM2.5 could save approximately 150,000 local people lives and save USD 210 billion in the 5-year period from 2013. From this application test, some second priority locations along with Harbin-Changchun Metropolitan Region, Central Henan City Belt and Yangtze-Huaihe City Belt always demonstrate noticed PM2.5 exceeding and high rate of mortality over 28,000 people per year (Zou et al, 2019). Premature mortality reduction relied on PM2.5 levels has been similar to the Air Pollution Prevention and Control Action Plan in Pearl River Delta region of China. The mortality reduction was estimated from four reducing admissions of stroke, ischemic heart disease (IHD), chronic obstructive pulmonary disease and lung cancer which related directly to 13% reduction of ambient PM2.5 and could save approximately USD 1300 million between 2013 and 2015 (Lu, 2018). The Action Plan could play important role to reduce PM2.5 emissions in top-down authorized country.

The challenges and solutions are depended on current pain points. For example, the policy to reduce air nitrogen pollution under the project of Ten Cities, Ten Thousand New Energy Vehicles (NEVs) has been reduced its important action to be optional plan because improvement of modern car could emit less nitrogen level (Tan, Tang & Lin, 2018). What's more, for the purpose of urban mobility, Sustainable Urban Mobility Plans (SUMPs) frameworks were applied among 642 cities in Europe which pointed out first priority to reduce PM2.5 and NO2 emissions. The effectiveness is positive when promoting low-cost measures of energy consumption and greenhouse gas emission. While introducing electro-mobility would increase the impact of air quality (Pisoni et al, 2019). Or even specific challenge subject can be met the requirement of people or standard. One methodology of the National Health Interview Survey, suitable compulsory in European countries, is following the input information of air pollution (PM2.5 and NO_2) exposure values and the outcomes are monitored within mortality and hospital admissions rate .These promoting values provide well networking of air quality modelling data within environmental and system diversities (Gandini et al, 2019).

In case of expanding research, it could be a part of policy or large project. For example, at Changping district in Beijing, the policy of 'Coal-To-Gas' has been promoted to respond PM2.5 situation since 2015 which premature death could be one of criteria. Increase by 40% of premature death needed 1.2 billion CNY affording before those death reduced to 13.3% and 26% in two years later. This is because PM2.5 level dropped continually to 2015 (Xi et al, 2019). With regard to air pollution concern, the Long-Range Energy Alternatives Planning System (LEAP) model was used to project total coal consumption in Shandong province. Coal substitution and used efficiency are dominant actions from three optional plans which could reduce coal consumption by 37 and 36 million tons respectively. Air quality improvement can decrease only 3.4 million ton of coal consumption. Four industrial areas of Binzhou, Jining, Linyi and Zibo need to be mainly monitored coal consumption (Zhang et al, 2018b). It is more clear and well understanding in this kind of research because it was shaped by the scope of main project.

3. NETWORK

To follow timeline of PM2.5 satellite monitor, the first period in 1998-2016 focused on improving higher quality of data resolution. Then during the period of 2015-2017, data collection and processing system were affected to rely on the Chinese "Air Pollution Prevention and Control Action Plan "launched in 2014. After well enforced policy, PM2.5 concentrations decreased by 6.5 μg/m3 especially in Central, North, Northeast and East China (Bai et al,

2019). On the other hand, in the same period, there was PM2.5 satellite monitor development by navigation following the urban Sustainable Development Goal which concerned mainly the effects of long-term pollution exposure on human health and environmental ecosystem (Beloconi et al, 2018) and the accuracy of data (Bhardwaj & Pruthi, 2019). While European countries concentrated firstly a multi-objective problems and solutions from air quality control policies within different motors plan depended on location (Carnevale et al, 2018a).

One of networking improvement is mapping data by adding specific approaches to the main model. For example, after applying a random forests-based geo-statistical approach, the accuracy and effectiveness of dataset increased and supported more real situation by providing brightness and night-time lights data (Liu et al, 2018). Dark target and deep blue (DB_DT) in aerosol optical depth (AOD) and Multi-Angle Implementation of Atmospheric Correction (MAIAC) in AOD could develop PM2.5 prediction model in Tehran, Iran. Data set of DB_DT model with random forest (RF) is similar to real time monitor of ambient PM2.5 (Nabavi, Haimberger & Abbasi, 2018). In developing country, low-cost sensors have been developed for the purpose of air quality monitoring (AQM) network and pollution policy and regulation developments. Only awareness of using low cost development is reliability and creditability of data collection process (Amegah, 2018).

Moreover, the Multi-angle Imaging Spectro Radiometer (MISR) from NASA's satellite is another approach supporting PM2.5 data to aerosol optical depth (AOD) approach. This provided more convenient for validation and reliability with allow other special data linking common collected data (Meng et al, 2018a). To observe PM2.5 level by real data collections in three different Chinese areas, AOD approach is used to investigate high correlation coefficient between those areas. This means ambient PM2.5 level affected other nearly region by suspension exposure (Kong et al, 2016). The comparison of mortalities between short-term and long-term exposure of PM2.5 pointed to those PM2.5 level in long-term condition provided stronger effects to Beijing people (Liang et al, 2018).

Then, in the period of 2005-2015, US estimation of PM2.5 has become error and machine learning approach called spatio-temporal distributions of PM2.5 constituents. This approach provided beneficial estimated outcome as assessment of economic cost of exposure, degradation and regional people health (Meng et al, 2018a).This spatio-temporal distribution has been developed in Southwest China within the random–forest sub models. The result shows more complete data set which helps reducing more than 30% of old error (Zhang et al, 2018a). This distribution is suitable for transportation assumption with chemical transport model (CTMs). It was found that population density could affect PM2.5 concentration to increase by 2.10 μg/m3/year during 2000–2007 (Xue et al, 2019). Throughout 178 network stations n Yangtze River Delta (YRD) of China, a weight of mobility in clustering algorithm of simulation was suggested to be higher ranking referred to meteorological conditions of local wind speed and direction, geographic distance and PM2.5 concentrations (Wang, Wang & Zhang, 2018).From the study of traffic density and smog pollution, traffic registrations and policies should be more restrict in high traffic density city; while household registration and restriction should be more flexible because of insignificant relation to ambient PM2.5 concentrations (Xie et al, 2018).

For the purpose of predicting open burning spot in China, the spots are normally higher and expand wider in winter and autumn season in Northeast part from 2014 to 2015. Middle-east parts' spot are high during summer season; however, those are less than spot number in Northeast. The number of crop burning spot correlates significantly to PM2.5 situation in each region (Yin et al, 2017). In case of uncertainty context of PM2.5 sources, an uncertain Gaussian diffusion model (UGD) should be applied to production-emission system (PES) for mitigating pressure on atmospheric control and managing multiplex data from industries, emission and period context (Zhu et al, 2019). The main purpose of network is sharing techniques and data to complete well policy simulation. To reach highest benefit, main standardised program and platform should be internationally agreed to apply for all users.

4. ECONOMY

Throughout the period of 11-year (2005-2016) data collection, public investment in environmental awareness in low developed country has more beneficial effects on the quality and policy related to environment (Chen, Huang & Lin, 2019). By statistical analysis model in the period of 1999-2011, there were 6 socioeconomic factors studied influencing PM2.5 concentrations in 12 regions of China. It can be seen that proportion of secondary economic sector influences first priority to PM2.5 increase. GDP and other economic calculations are negatively affected from air pollution within specific case. Urbanization can support or obstruct PM2.5 reduction depending on regions, weather and local people (Luo et al, 2018). According to promote PM2.5 policy to multi-region in China, it is found that main self-generated areas of PM2.5 indicate Central, Northwest, Northeast and Southwest China which loss amount of economic benefit and environmental cost (Etchie et al, 2018). Structural equation model (SEM) in 2014 and 2015 indicated industrial area caused mainly to PM2.5 pollution level and other supporting socioeconomic factors affected significantly air pollution especially city size, weather condition, outdoor situation of PM2.5 and people activities (Jiang et al, 2018). However PM2.5 level was negligibly concerned when customers made their decision to buy residences in Shanghai (Lu, 2018).

One commuting policy promoting active mobility was calculated financial cost based on different travels. By bike, users may reduce 3,000-3,800 million kilometre per year and may save institutional communication costs by 48-76 thousand Euro per year compared to travel by urban diesel car. Also this affects directly to 80% reduction of air pollution from gasoline and diesel combustions in Europe (Carnevale et al, 2018b). Between 1991 and 2014, the

transformation of biomass energy to commercial energy is significant reduced because of high price and poor mechanic function. To limit residential energy consumption per capita (RECPC), national energy strategy should be included rural energy and improved in facilitating transition process of energy and educating local residents (Han & Wu, 2018).

Within the condition of high population, health impact from PM2.5 situation in China could be summarized to consume 0.3% of GDP from PM2.5 protection as external cost and the impact could count economic loss from premature deaths equal 80% of overall external cost (Yin, Pizzol & Xu, 2017). In 2005, it was proved that ambient PM2.5 reduction in only one unit (microgram per cubic meter) could call up to USD 8.83 billion from all residences in China (Freeman et al, 2019). Form these cost and taxation, it is evident that high society people are willingness to pay for environmental protection, while increasing people income can reduce that willingness. Also people, who live in more polluted cities, have strong willingness to pay for environment (Shao, Tian & Fan, 2018). Last but not least, throughout 9 Japanese cities in the period of 2002-2008, it was found that only 10 $\mu g/m^3$ increase in PM2.5 could lead to 0.52% increase in risk of mortality or possibly loss profit at YEN 0.4-1.5 trillion (Seposo et al, 2018). According to PM2.5 suffering experiences, people are now willing to participate and pay for air quality improvement.

5. CONCLUSION

In summary, air pollution has become more severe in industrial developing Asian countries. There are two directions solving PM2.5 situations in Thailand which one is technological purifier and another methodology focuses on policy making. This research paper aims to review systematically literatures related to PM2.5 controlling plans which can be top-down or bottom-up policy. Top-down plan seems to be suitable for business and governmental organisations which have a few leaders to take action, while bottom-up policy is appropriated for sustainable social interventions. Then burning controls should be considered separately depended on activities such as open burning, mobility or industrial burning. The main purpose of open burning points suitably to better oxidation combustion linked directly to engine combustion too. For traffic and industrial activities, it is suitable to plan their zoning and monitor effectively PM2.5 in density zone. Also policy reflection and feedback are important for future transformations. The implementations of policy can divided into 4 states of 1) conducting application and theoretical study, 2) integrating and evaluating implementation, 3) focusing current challenges and solutions and 4) expanding research.

The network is a part of policy modelling which can be shared tactic and error to more complete simulation. The popular model is aerosol optical depth (AOD) which can be applied variety of algorithm included spatiotemporal approach, specific meteorological data, geographic data and specific existing situation of PM2.5. Last concern of economy, big amount of government loss in the past for reducing PM2.5 level leads us to improve well policy and social intervention to predict and avoid air pollution and to protect themselves from PM2.5 threats. Also suffering people have well known PM2.5 situation and they are willing to pay for environmental cost and taxation.

This research is one part of review article of concerning PM2.5 situations in Thailand. Optional policies and networking plan can provide firstly basic information to all participating sectors such as governmental, private business, public organization and academic institutes. More basic information related to PM2.5 controlling in building scale will be continually offered as the next research series.

6. REFERENCES

Air Quality and Noise Management Bureau. 2019. Thailand's air quality and situation reports. *In:* Air Quality and Noise Management Bureau. (ed.). Bangkok, Thailand.

Amegah, A. K. 2018. Proliferation of low-cost sensors. What prospects for air pollution epidemiologic research in Sub-Saharan Africa? Environmental Pollution, 241, 1132-1137.

Bai, K., MA, M., Chang, N.-B. & Gao, W. 2019. Spatiotemporal trend analysis for fine particulate matter concentrations in China using high-resolution satellite-derived and ground-measured PM2.5 data. Journal of Environmental Management, 233, 530-542.

Beloconi, A., Chrysoulakis, N., Lyapustin, A., Utzinger, J. & Vounatsou, P. 2018. Bayesian geostatistical modelling of PM10 and PM2.5 surface level concentrations in Europe using high-resolution satellite-derived products. Environment International, 121, 57-70.

Bhardwaj, R. & Pruthi, D. 2019. Variability analysis in PM2.5 monitoring. Data in Brief, 103774.

Cai, S., Ma, Q., Wang, S., Zhao, B., Brauer, M., Cohen, A., Martin, R. V., Zhang, Q., Li, Q., Wang, Y., Hao, J., Frostad, J., Forouzanfar, M. H. & Burnett, R. T. 2018. Impact of air pollution control policies on future PM2.5 concentrations and their source contributions in China. Journal of Environmental Management, 227, 124-133.

Carnevale, C., Angelis, E. D., Finzi, G., Pisoni, E., Turrini, E. & Volta, M. 2018a. Coupling European data and local air pollution models for integrated assessment. IFAC-PapersOnLine, 51, 67-72.

Carnevale, C., Angelis, E. D., Finzi, G., Turrini, E. & Volta, M. 2018b. Evaluating economic and health impacts of active mobility through an integrated assessment model. IFAC-PapersOnLine, 51, 49-54.

Chen, H. & Chen, W. 2019. Potential impact of shifting coal to gas and electricity for building sectors in 28 major northern cities of China. Applied Energy, 236, 1049-1061.

Chen, X., Huang, B. & Lin, C.-T. 2019. Environmental awareness and environmental Kuznets curve. Economic Modelling.

Dunea, D., Iordache, S., Pohoata, A., Bohler, T. & Savu, T. 2017. Towards a Better Protection of Children's Respiratory Health against Particulate Matter Pollution in Urban Areas – ROkidAIR Project. Procedia Engineering, 198, 283-292.

Etchie, T. O., Etchie, A. T., Adewuyi, G. O., Pillarisetti, A., Sivanesan, S., Krishnamurthi, K. & Arora, N. K. 2018. The gains in life expectancy by ambient PM2.5 pollution reductions in localities in Nigeria. Environmental Pollution, 236, 146-157.

Frank, L. D., Iroz-elardo, N., Macleod, K. E. & Hong, A. 2019. Pathways from built environment to health: A conceptual framework linking behavior and exposure-based impacts. Journal of Transport & Health, 12, 319-335.

Freeman, R., Liang, W., Song, R. & Timmins, C. 2019. Willingness to pay for clean air in China. Journal of Environmental Economics and Management, 94, 188-216.

Gandini, M., Scarinzi, C., Bande, S., Berti, G., Ciancarella, L., Costa, G., Demaria, M., Ghigo, S., Marinacci, C., Piersanti, A., Sebastiani, G. & Cadum, E. 2019. Life Med Hiss: An innovative cohort design for public health. MethodsX, 6, 82-91.

González-Cardoso, G., Hernández-Contreras, J. M., Santiago-Delarosa, N., Gutiérrez, M. & Mugica-Alvaréz, V. 2018. PM2.5 emissions from urban crematoriums. Energy Procedia, 153, 359-363.

Griffiths, S. D., Chappell, P., Entwistle, J. A., Kelly, F. J. & Deary, M. E. 2018. A study of particulate emissions during 23 major industrial fires: Implications for human health. Environment International, 112, 310-323.

Gross, P. L., Buchanan, N. & Sané, S. 2019. Blue skies in the making: Air quality action plans and urban imaginaries in London, Hong Kong, and San Francisco. Energy Research & Social Science, 48, 85-95.

Han, H. & Wu, S. 2018. Rural residential energy transition and energy consumption intensity in China. *Energy Economics,* 74**,** 523-534.

Isley, C. F. & Taylor, M. P. 2018. Air quality management in the Pacific Islands: A review of past performance and implications for future directions. Environmental Science & Policy, 84, 26-33.

Jiang, P., Yang, J., Huang, C. & Liu, H. 2018. The contribution of socioeconomic factors to PM2.5 pollution in urban China. *Environmental Pollution,* 233**,** 977-985.

Kankanhalli, A., Charalabidis, Y. & Mellouli, S. 2019. IoT and AI for Smart Government: A Research Agenda. Government Information Quarterly, 36, 304-309.

Kong, L., Xin, J., Zhang, W. & Wang, Y. 2016. The empirical correlations between PM2.5, PM10 and AOD in the Beijing metropolitan region and the PM2.5, PM10 distributions retrieved by MODIS. Environmental Pollution, 216, 350-360.

Li, J., Zhu, Y., Kelly, J. T., Jang, C. J., Wang, S., Hanna, A., Xing, J., Lin, C.-J., Long, S. & Yu, L. 2019. Health benefit assessment of PM2.5 reduction in Pearl River Delta region of China using a model-monitor data fusion approach. Journal of Environmental Management, 233, 489-498.

Li, Y., Chiu, Y.-H. & Lu, L. C. 2018. Energy and AQI performance of 31 cities in China. Energy Policy, 122, 194-202.

Liang, F., Xiao, Q., Gu, D., Xu, M., Tian, L., Guo, Q., Wu, Z., Pan, X. & Liu, Y. 2018. Satellite-based short- and long-term exposure to PM2.5 and adult mortality in urban Beijing, China. *Environmental Pollution,* 242**,** 492-499.

Liu, H., Rodgers, M. O. & Guensler, R. 2019. Impact of road grade on vehicle speed-acceleration distribution, emissions and dispersion modeling on freeways. *Transportation Research Part D: Transport and Environment,* 69**,** 107-122.

Liu, Y., Cao, G., Zhao, N., Mulligan, K. & Ye, X. 2018. Improve ground-level PM2.5 concentration mapping using a random forests-based geostatistical approach. Environmental Pollution, 235, 272-282.

Lu, J. 2018. The value of a south-facing orientation: A hedonic pricing analysis of the Shanghai housing market. Habitat International, 81, 24-32.

Luo, K., Li, G., Fang, C. & Sun, S. 2018. PM2.5 mitigation in China: Socioeconomic determinants of concentrations and differential control policies. Journal of Environmental Management, 213, 47-55.

Meng, X., Garay, M. J., Diner, D. J., Kalashnikova, O. V., Xu, J. & Liu, Y. 2018a. Estimating PM2.5 speciation concentrations using prototype 4.4 km-resolution MISR aerosol properties over Southern California. Atmospheric Environment, 181, 70-81.

Meng, X., Hand, J. L., Schichtel, B. A. & Liu, Y. 2018b. Space-time trends of PM2.5 constituents in the conterminous United States estimated by a machine learning approach, 2005–2015. Environment International, 121, 1137-1147.

Nabavi, S. O., Haimberger, L. & Abbasi, E. 2018. Assessing PM2.5 concentrations in Tehran, Iran, from space using MAIAC, deep blue, and dark target AOD and machine learning algorithms. Atmospheric Pollution Research.

Ng, E. & Ren, C. 2018. China's adaptation to climate & urban climatic changes: A critical review. Urban Climate, 23, 352-372.

Pardthaisong, L., Sin-Ampol, P., Suwanprasit, C. & Charoenpanyanet, A. 2018. Haze Pollution in Chiang Mai, Thailand: A Road to Resilience. Procedia Engineering, 212, 85-92.

Park, J., Park, E. H., Schauer, J. J., Yi, S.-M. & Heo, J. 2018. Reactive oxygen species (ROS) activity of ambient fine particles (PM2.5) measured in Seoul, Korea. Environment International, 117, 276-283.

Peng, B., Tu, Y., Elahi, E. & Wei, G. 2018. Extended Producer Responsibility and corporate performance: Effects of environmental regulation and environmental strategy. Journal of Environmental Management, 218, 181-189.

Pisoni, E., Christidis, P., Thunis, P. & Trombetti, M. 2019. Evaluating the impact of “Sustainable Urban Mobility Plans” on urban background air quality. Journal of Environmental Management, 231, 249-255.

Pokorná, P., Schwarz, J., Krejci, R., Swietlicki, E., Havránek, V. & Ždímal, V. 2018. Comparison of PM2.5 chemical composition and sources at a rural background site in Central Europe between 1993/1994/1995 and 2009/2010: Effect of legislative regulations and economic transformation on the air quality. Environmental Pollution, 241, 841-851.

Rzeszutek, M., Bogacki, M., Bździuch, P. & Szulecka, A. 2019. Improvement assessment of the OSPM model performance by considering the secondary road dust emissions. Transportation Research Part D: Transport and Environment, 68, 137-149.

Seposo, X., Kondo, M., Ueda, K., Honda, Y., Michikawa, T., Yamazaki, S. & Nitta, H. 2018. Health impact assessment of PM2.5-related mitigation scenarios using local risk coefficient estimates in 9 Japanese cities. Environment International, 120, 525-534.

Shah, R., Nezamuddin, N. & Levin, M. W. 2018. Supply-side network effects on mobile-source emissions. Transport Policy.

Shao, S., Tian, Z. & Fan, M. 2018. Do the rich have stronger willingness to pay for environmental protection? New evidence from a survey in China. World Development, 105, 83-94.

Shen, Y. & Ahlers, A. L. 2019. Blue sky fabrication in China: Science-policy integration in air pollution regulation campaigns for mega-events. Environmental Science & Policy, 94, 135-142.

Shi, H., Wang, S. & Zhao, D. 2017. Exploring urban resident’s vehicular PM2.5 reduction behavior intention: An application of the extended theory of planned behavior. Journal of Cleaner Production, 147, 603-613.

Shi, Y., Zhao, A., Matsunaga, T., Yamaguchi, Y., Zang, S., Li, Z., Yu, T. & Gu, X. 2018. Underlying causes of PM2.5-induced premature mortality and potential health benefits of air pollution control in South and Southeast Asia from 1999 to 2014. *Environment International,* 121**,** 814-823.

Squizzato, S., Masiol, M., Rich, D. Q. & Hopke, P. K. 2018. A long-term source apportionment of PM2.5 in New York State during 2005–2016. Atmospheric Environment, 192, 35-47.

Sun, J., Shen, Z., Zhang, Y., Zhang, Q., Wang, F., Wang, T., Chang, X., Lei, Y., Xu, H., Cao, J., Zhang, N., Liu, S. & Li, X. 2019. Effects of biomass briquetting and carbonization on PM2.5 emission from residential burning in Guanzhong Plain, China. Fuel, 244, 379-387.

Tan, R., Tang, D. & Lin, B. 2018. Policy impact of new energy vehicles promotion on air quality in Chinese cities. Energy Policy, 118, 33-40.

Tilt, B. 2019. China's air pollution crisis: Science and policy perspectives. Environmental Science & Policy, 92, 275-280.

Verma, P. & Raghubanshi, A. S. 2018. Urban sustainability indicators: Challenges and opportunities. Ecological Indicators, 93, 282-291.

Wang, B., Liu, L., Huang, G. H., Li, W. & Xie, Y. L. 2018. Effects of carbon and environmental tax on power mix planning - A case study of Hebei Province, China. Energy, 143, 645-657.

Wang, Y., Wang, H. & Zhang, S. 2018. A weighted higher-order network analysis of fine particulate matter (PM2.5) transport in Yangtze River Delta. Physica A: Statistical Mechanics and its Applications, 496, 654-662.

Xi, X., Li, H., Wallin, F., Avelin, A., Yang, X. & Yu, Z. 2019. Air pollution related externality of district heating – a case study of Changping, Beijing. Energy Procedia, 158, 4323-4330.

Xie, R., Sabel, C. E., Lu, X., Zhu, W., Kan, H., Nielsen, C. P. & Wang, H. 2016. Long-term trend and spatial pattern of PM2.5 induced premature mortality in China. Environment International, 97, 180-186.

Xie, R., Wei, D., Han, F., Lu, Y., Fang, J., Liu, Y. & Wang, J. 2018. The effect of traffic density on smog pollution: Evidence from Chinese cities. *Technological Forecasting and Social Change*.

Xue, T., Zheng, Y., Tong, D., Zheng, B., Li, X., Zhu, T. & Zhang, Q. 2019. Spatiotemporal continuous estimates of PM2.5 concentrations in China, 2000–2016: A machine learning method with inputs from satellites, chemical transport model, and ground observations. Environment International, 123, 345-357.

Yin, H., Pizzol, M. & Xu, L. 2017. External costs of PM2.5 pollution in Beijing, China: Uncertainty analysis of multiple health impacts and costs. Environmental Pollution, 226, 356-369.

Yin, S., Wang, X., Xiao, Y., Tani, H., Zhong, G. & Sun, Z. 2017. Study on spatial distribution of crop residue burning and PM2.5 change in China. Environmental Pollution, 220, 204-221.

Zhang, R., Di, B., Luo, Y., Deng, X., Grieneisen, M. L., Wang, Z., Yao, G. & Zhan, Y. 2018a. A nonparametric approach to filling gaps in satellite-retrieved aerosol optical depth for estimating ambient PM2.5 levels. Environmental Pollution, 243, 998-1007.

Zhang, Y., Liu, C., Li, K. & Zhou, Y. 2018b. Strategy on China's regional coal consumption control: A case study of Shandong province. Energy Policy, 112, 316-327.

Zhu, Y., Tong, Q. L., Yan, X. X. & Li, Y. X. 2019. Development of an uncertain Gaussian diffusion model with its application to production-emission system management in coal-dependent city- a case study of Yulin, China. *Energy Procedia,* 158**,** 3253-3258.

Zou, B., You, J., Lin, Y., Duan, X., Zhao, X., Fang, X., Campen, M. J. & Li, S. 2019. Air pollution intervention and life-saving effect in China. Environment International, 125, 529-541.

#218: Thermal performance evaluation of residential buildings in Makkah, Saudi Arabia

Mosaab ALABOUD [1,2], Mohamed GADI[1]

[1]Department of Architecture and Built Environment, Faculty of Engineering, University of Nottingham, Nottingham, NG7 2RD, United Kingdom
[2] Department of Architectural Engineering, Faculty of Engineering, Taibah University, Medina, Saudi Arabia.

Buildings consume huge amounts of electrical energy in the Kingdom of Saudi Arabia, particularly during the summer months because of enormous air conditioning demands due to the very hot outdoor temperatures. Residential buildings consume more than half of the electricity in Saudi Arabia, with the air conditioning load making up 70% of the use. The main aim of this study is to evaluate the thermal performance of two residential buildings in Makkah, Saudi Arabia. The two buildings are six stories and have the same orientation, but the first building is thermally insulated, while the second building is not. To investigate indoor thermal performance of the two buildings, environmental site monitoring was undertaken in May 2019. The data provided consisted of indoor air temperature values that were recorded every fifteen minutes for a period of sixty-eight hours for two chosen rooms in each building. Analysis of site monitoring data was conducted, and the results obtained to have a better idea of the effectiveness of the existing building fabric characteristics, in particular external walls and roof, in relation to indoor thermal performance. Then this was calibrated with the simulated results taken from thermal analysis software (TAS) to validate them, and finally to quantify the cooling load in the case study buildings. The outcome illustrates similarity between the measured and simulated results and also indicates that thermal insulation can decrease the cooling load to 50%.

Keywords: thermal performance evaluation; residential buildings; thermal insulation

1. INTRODUCTION

Buildings in Saudi Arabia are characterised by a severe excess of electrical usage, as buildings consume 80% of the electricity produced in Saudi Arabia, with air conditioning representing 50% of this consumption (SEEC, 2019). Building design is one of the many ways to reduce air conditioning use in buildings (Pacheco *et al*., 2012). Minimising the cooling load of buildings by architectural design means minimising the solar and envelope heat gain (Givoni, 1994). Nicole *et al.* (2012) state that poor quality of a building creates the most deep-rooted energy wastage problem. Taleb and Sharples (2011) demonstrate how a few design and operational changes could have had a significant impact on the thermal performance of the building. In terms of thermal insulation, 70% of residential buildings in Saudi Arabia lack thermal insulation (SEEC, 2019). Kharseh and Al-Khawaja (2016) investigate the impact of different retrofitting measures in reducing cooling requirements of buildings in Qatar. An hourly analysis program (HAP) model was used to simulate the cooling load for a residential house chosen as a case study. The result shows adding less than 2 cm of polyurethane to the external walls can reduce the cooling requirements of the building by 27%. Heravi and Qaemi (2014) determine the most effective design and construction measures concerning building energy efficiency in Iran. The measures were simulated independently by Design Builder software. The result illustrates that roof and wall thermal isolation is identified as the most effective measure with respect to building energy consumption. It shows that improving the opaque materials of the roof and wall can reduce the building energy consumption by 13.8% and 12.16% respectively. That can be done by using suitable roof and wall thermal resistance paint or a green roof, and adding thermal insulation materials. According to Alaidroos and Krarti (2015), maximum energy savings of up to 35% can be achieved from adding thermal insulation for both walls and roof. A few studies dealing with the calibration of thermal models are presented in Leong and Essah (2017), Saleh (2015) and Alves *et al.* (2016). The aim of the monitoring was to calibrate the computational model for local climate conditions. This study is designed to evaluate and improve indoor thermal performance of mid-rise residential buildings in Saudi Arabia, with Makkah as a case study.

Figure 1: The location of Makkah (Maps Saudi Arabia, 2019).

The case study buildings investigated are located in Makkah, Saudi Arabia (latitude 21.4° N and longitude 39.8° E). Makkah city is in the Makkah Province of Saudi Arabia (Figure 1). The city is around 45 miles east of Jeddah, the Red Sea's major sea port, and is surrounded by the Sarawat Mountains. The temperatures are warm to hot all year round (Nayebare *et al.,* 2018). The case study buildings are located in a district called Shisha, east of Makkah. They are six-storey residential buildings with the same orientation, as they are in the same street and so are close to each other.

2. METHOD

The two case study buildings are identical and both are on the same main street with the exact orientation. After an initial site visit to the site, these two buildings were chosen to evaluate their indoor thermal environment as the first case study building complies with the new Saudi building standard regarding the use of thermal insulation in external walls, roof and windows, while the second case study building was built in the late 1990s, with no insulation at all. The chosen zones for each building are a bedroom on the middle floor and a bedroom on the top floor with different orientations. The middle floor room has one external wall orientated north-east with one window, and the top floor room has one external wall orientated south-west with one window (Figure 2). The instruments used for the fieldwork are two data loggers (Elitech (UK) USB Temperature Data logger URC-5), mainly used for temperature recording, that were placed in the four different zones mentioned above to evaluate the building's performance over 68 hours from 4 May 2019 to 6 May 2019 (Table 1) (Elitech, 2019). The case study buildings are modelled using thermal analysis software (EDSL TAS version 9.4.2) (EDSL TAS, 2019). Thermal simulation results are compared to recorded indoor temperature data. The external temperature for the simulation is a historical result obtained from Meteonorm (Meteonorm, 2019), while the other external temperature used in graphs four and five is from the nearest weather station to the site (World Weather Online, 2019). Finally, building fabrics for the case study buildings are shown (Table 2 and 3).

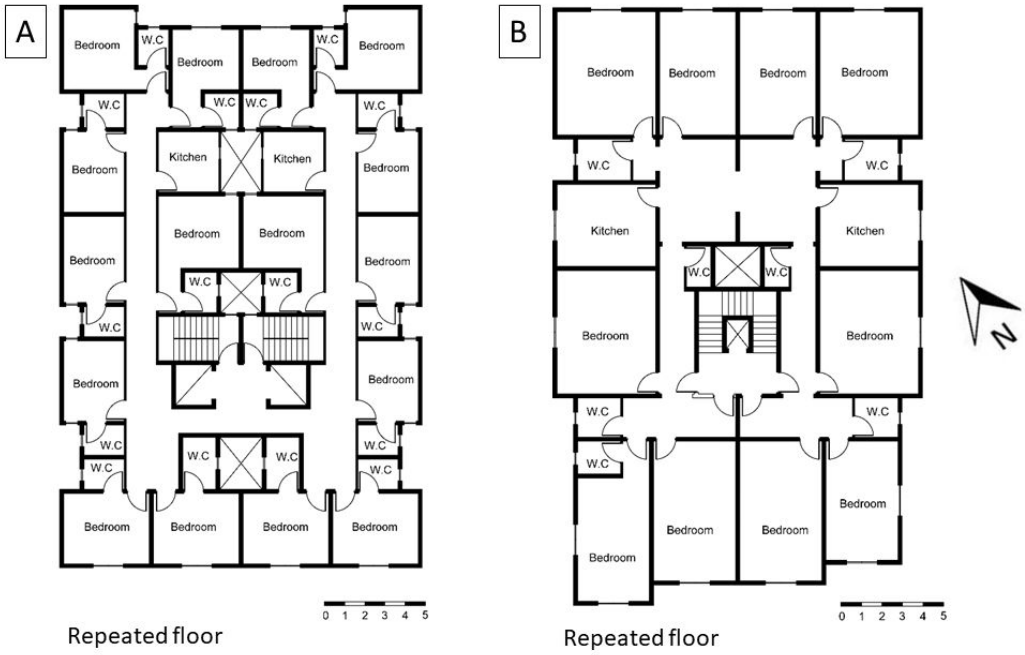

Figure 2: A. Architectural drawing of the repeated floor in first case study building. B. Architectural drawing of the repeated floor in second case study building.

Table 1: Instrument data

Name	Type	Parameter	Range	Accuracy	Note
Temperature data logger	Elitech URC5	Indoor air temperature	-30°C~+70°C	±0.5°C (-20°C ~+40°C); others, +1°C	Continuous test

Table 2: Building fabrics for the first case study building

Element	Description	Thickness/mm	U-value w/m2.K
External wall (main elevation)	Marble stone, cement mortar, insulated red hollow brick, cement mortar, white paint	300	0.52
External walls	Beige paint, cement mortar, insulated red hollow brick, cement mortar, white paint	250	0.53
Internal walls	White paint, cement mortar, red hollow brick, cement mortar, white paint	250	2.30
Internal floors	Tile, soil, reinforced concrete, air cavity, gypsum board	987	1.0
Roof	Tile, soil, insulation, reinforced concrete, air cavity, gypsum board	1027	0.26
Windows	Double glazing	22	1.6

Table 3: Building fabrics for the second case study building

Element	Description	Thickness/mm	U-value w/m2.K
External wall (main elevation)	Stone, cement mortar, red hollow brick, cement mortar, white paint	280	2.9
External walls and internal walls	Beige paint, cement mortar, concrete block, cement mortar, white paint	250	3
Roof and internal floors	Tiles, soil, reinforced concrete, cement mortar, white paint	355	2.23
Windows	Single glazing	10	5.5

3. RESULTS

An analysis of the fieldwork result was done to have perceptive insight of the existing building state regarding its thermal performance. For the fieldwork, in-site monitoring of indoor air temperature was conducted to have better understanding of the thermal performance of one building in Makkah. Indoor air temperature values were recorded every 15 minutes for nearly three days (4 May – 6 May 2019). The data is used to analyse indoor air temperature regarding building fabric features. A middle floor room and top floor room are chosen in both buildings (Figure 3 and 4).

Figure 3: A. The chosen room for the fieldwork on the middle floor of the first case study building. B. The chosen room for the fieldwork on top floor for the first case study building.

Figure 4: A. The chosen room for the fieldwork on the middle floor of the second case study building. B. The chosen room for the fieldwork on top floor for the second case study building.

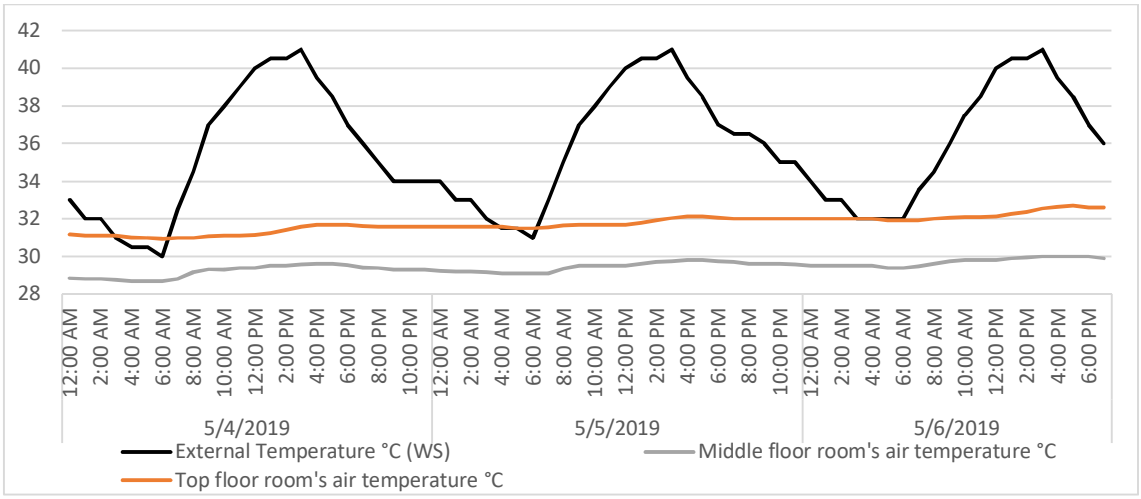

Figure 5: Outdoor and indoor temperature profiles for the two rooms on the middle floor and the top floor in the first case study building.

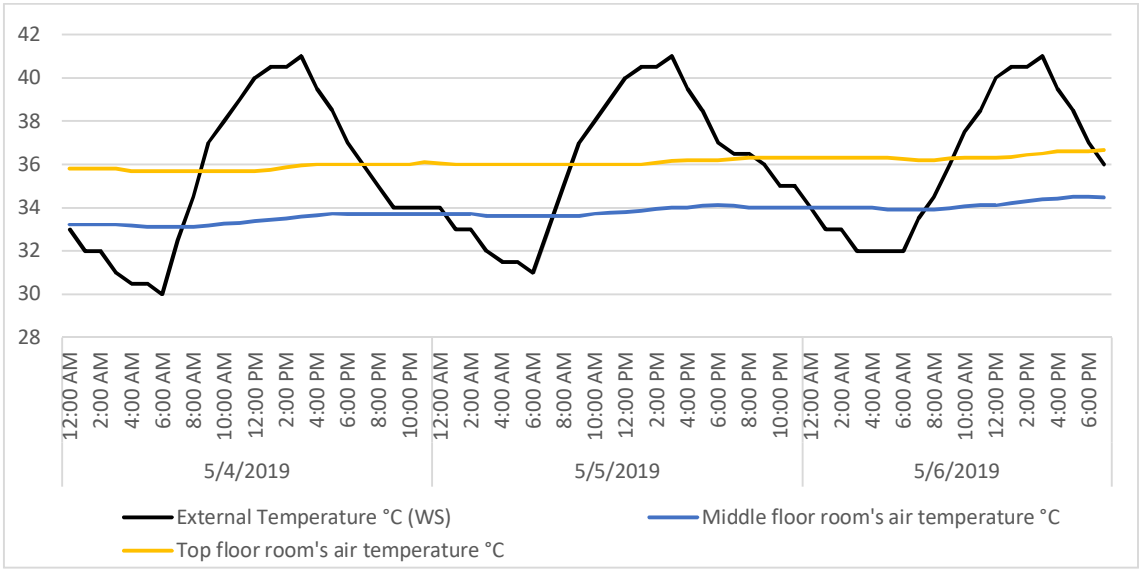

Figure 6: Outdoor and indoor temperature profiles for the two rooms on the middle floor and the top floor in the second case study building.

The analysis of indoor air temperature recorded result is given in regard to indoor thermal performance of the case study building (Figures 5 and 6). Outdoor air temperature (OAT) values were between 30°C and 41°C. OAT peaked during the day (11:00 - 17:00), while the lowest temperature values occurred in the morning times (3:00 - 7:00). Further, diurnal OAT ranges were found to be up to 11°C. For the first case study building, the temperatures indoor ranged between 28.7°C and 32.7°C (Figure 5). Constant status was noticed in both rooms that had daily temperature fluctuation of less than 1°C. The monitored temperature results stated that the air temperature on the middle floor room was 2.5°C less than the top floor room. This is mainly because the top floor room is exposed to solar radiation from the roof and also because it's external wall is orientated to the south-west. It can be seen that the indoor air temperature in both rooms is less than the OAT most of the time.

For the second case study building, the temperatures indoor ranged between 33.1°C and 36.6°C (Figure 6). Constant status was noticed in both rooms that had a daily temperature fluctuation of less than 1°C. The monitored temperature results stated that the air temperature on the middle floor room was around 2°C less than the top floor room. This is mainly because the top floor room is exposed to solar radiation from the roof and also because its external wall is orientated to the south-west. It can be seen that the indoor air temperature in both rooms in the second case study building is 4 to 5°C higher than the rooms in the first case study building. This is because the first case study building is well insulated externally.

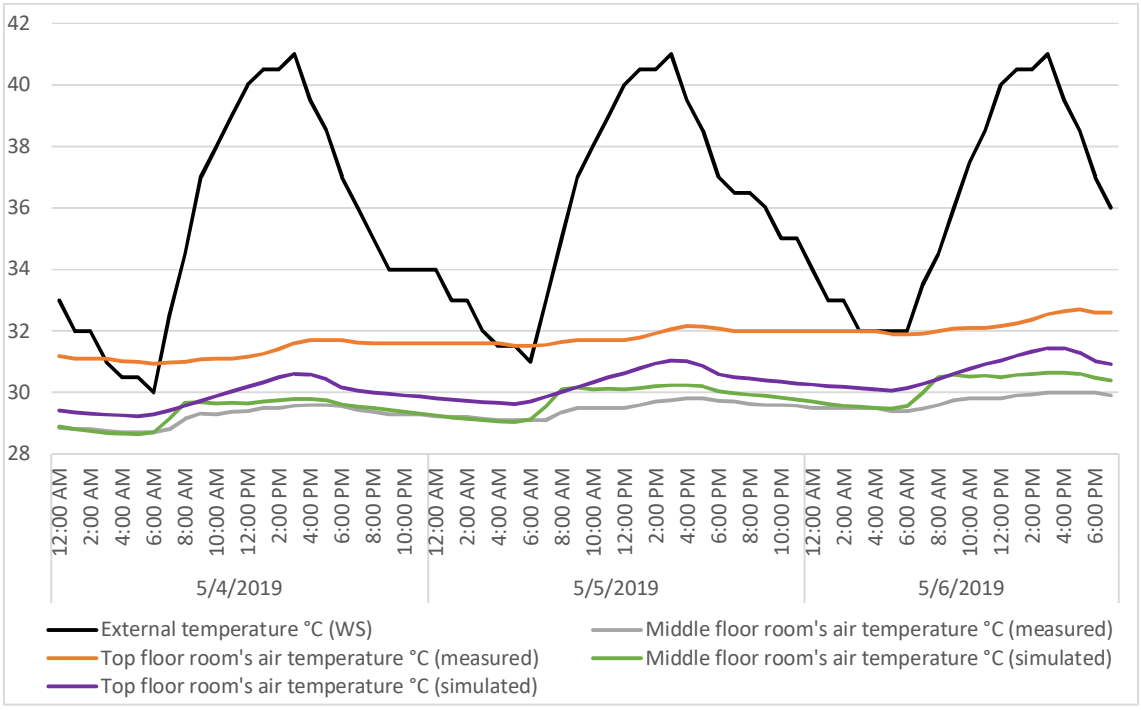

Figure 7: Measured and simulated data for outdoor and indoor temperature profiles for the two rooms on the middle floor and the top floor in the first case study building.

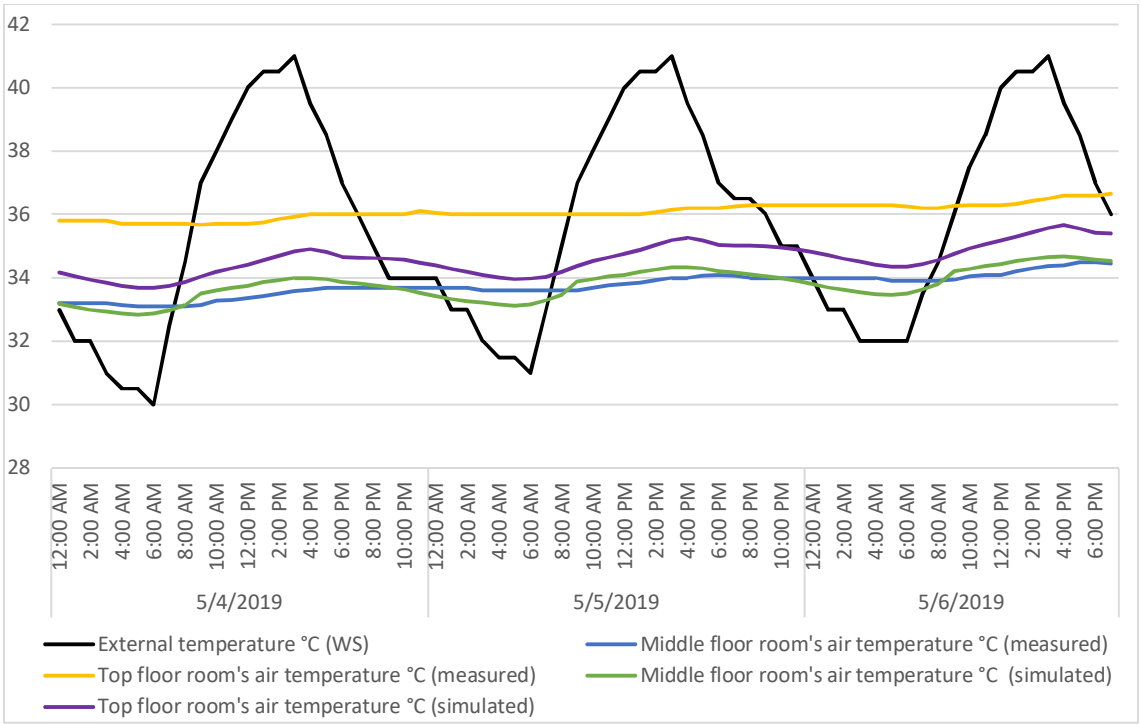

Figure 8: Measured and simulated data for outdoor and indoor temperature profiles for the two rooms on the middle floor and the top floor in the second case study building.

Table 4: Calibration result between the measured and simulated values

Case studies	Selected rooms	NMBE	CVRMSE
First building	Middle floor room	-0.6	2.4
	Top floor room	3.1	12.2
Second building	Middle floor room	-0.03	0.15
	Top floor room	2.7	12.2

The simulated result for the two case studies shows a very similar indoor air temperature result compared with the measured result for the two chosen rooms (Figure 7 and 8). The reason for plotting the simulated result is to verify and calibrate the analytic work. Simulated temperatures follow closely the recorded temperatures in the middle floor room but for the top floor room the difference is around 2K. For a simulated energy model to be acceptable based on ASHRAE guidelines (ASHRAE, 2002), the calculated normalised mean bias error (NMBE) and the coefficient of variation of the root mean square error (CVRMSE) should be 10% and 30%, respectively, for a model that deals with hourly figures. This study monitored hourly temperature and both the NMBE and the CVRMSE are calculated based on the values of the entire recorded temperature during the 68 monitored hours (Table 4). It can be seen the NMBE is also lower than the 10% set limit and the CVRMSE is lower than the 30% set limit by ASHRAE. Therefore, it is safe to consider the simulated results within acceptable range.

The cooling load is introduced at a set thermostat point of 25°C as recommended by the Saudi Energy Efficiency Centre (SEEC, 2019), and it is available all year around to quantify the effect of thermal insulation on cooling load in both buildings. The middle floor room and top floor room in the first case study building has an annual cooling load of 86 and 102 kWh/m2/y respectively, while the middle floor room and top floor room in the second case study building have annual cooling loads of 152 and 204 kWh/m2/y respectively. It can be seen that cooling load in the first case study building is reduced to up to half compared with the second case study building, especially in the top floor room. That is mainly because of lack of thermal insulation in the external walls, the roof in the second case study building, and the single glazing window.

4. CONCLUSION

The paper contains fieldwork data collection conducted in May 2019 to investigate the indoor thermal performance of two mid-rise residential buildings in Makkah, Saudi Arabia. Indoor air temperatures values were calculated for 68 hours in two zones in each building. To verify and calibrate the analytic work, thermal analysis software (TAS) was used. The simulated results were compared to the measured results and are in the range for the model to be acceptable. The result shows that building envelopes have a significant effect on the indoor air temperature. It can be seen that cooling load in the 1st case study building is reduced to up to half comparing the 2nd case study building especially in the top floor room. That mainly because of lack of thermal insulation in the external walls, roof in the 2nd case study building along with the single glazing window.

5. REFERENCES

Alaidroos, A. & Krarti, M., 2015. Optimal design of residential building envelope systems in the Kingdom of Saudi Arabia. Energy and Buildings, 86, pp.104–117. Available at: http://dx.doi.org/10.1016/j.enbuild.2014.09.083.

Alves, C.A., *et al.,* 2016. Residential buildings' thermal performance and comfort for the elderly under climate changes context in the city of São Paulo, Brazil. Energy and Buildings, 114, pp.62–71. Available at: http://dx.doi.org/10.1016/j.enbuild.2015.06.044.

ASHRAE. 2002. ASHRAE Guideline 14-2002: Measurement of Energy and Demand Savings. Available at: http://www.eeperformance.org/uploads/8/6/5/0/8650231/ashrae_guideline_14-2002_measurement_of_energy_and_demand_saving.pdf.

EDSL TAS. 2019. EDSL TAS. Available at: https://www.edsl.net/.

Elitech. 2019. Elitech. Available at: https://www.elitech.uk.com/temperature_logger/Elitech_UK_USB_Temperature_Data_logger_URC_5_147.html

Givoni, B. 1994. The Passive and Low Energy Cooling of Buildings. Milton, John Wiley & Sons Australia Ltd.

Heravi, G. and Qaemi, M., 2014. Energy performance of buildings: The evaluation of design and construction measures concerning building energy efficiency in Iran. Energy and Buildings, 75, pp.456–464. Available at: http://dx.doi.org/10.1016/j.enbuild.2014.02.035.

Kharseh, M. and Al-Khawaja, M., 2016. Retrofitting measures for reducing buildings cooling requirements in cooling-dominated environment: Residential house. Applied Thermal Engineering, 98, pp.352–356. Available at: http://dx.doi.org/10.1016/j.applthermaleng.2015.12.063.

Leong, X.W. and Essah, E.A., 2017. Bridging the gap between energy consumption and the indoor environmental quality of a 1960s educational building. Energy Procedia, 132, pp.87–92. Available at: http://dx.doi.org/10.1016/j.egypro.2017.09.643.

Maps Saudi Arabia. 2019. Mecca Saudi Arabia map. Available at: http://maps-saudi-arabia.com/mecca-saudi-arabia-map.

Meteonorm. 2019. Meteonorm. Available at: https://meteonorm.com/en/download.

Nayebare, S.R. *et al*., 2018. Ambient air quality in the holy city of Makkah: A source apportionment with elemental enrichment factors (EFs) and factor analysis (PMF). Environmental Pollution, 243, pp.1791–1801. Available at: http://dx.doi.org/10.1016/j.envpol.2018.09.086.

Nicol, F., *et al.,* 2012. Adaptive Thermal Comfort: Principles and Practice. Oxon, Routledge. 2012.

Pacheco, R., *et al*., 2012. Energy efficient design of building: A review. *Renewable and Sustainable Energy Reviews*, *16*(6), pp.3559-3573. Available at: https://doi.org/10.1016/j.rser.2012.03.045.

Saleh, P. H. 2015. Thermal performance of glazed balconies within heavy weight/thermal mass buildings in Beirut, Lebanon's hot climate. Energy and Buildings, 108, pp.291–303. Available at: https://doi.org/10.1016/j.enbuild.2015.09.009.

SEEC. 2018. Saudi Energy Efficiency Centre. Available at: https://www.seec.gov.sa/en/blog/buildings.

Taleb, H.M. & Sharples, S., 2011. Developing sustainable residential buildings in Saudi Arabia: A case study. Applied Energy, 88(1), pp.383–391. Available at: http://dx.doi.org/10.1016/j.apenergy.2010.07.029.

World weather online. 2019. World weather online. Available at: https://www.worldweatheronline.com/mecca-weather/makkah/sa.aspx.

#221: The drying kinetics of para rubber wood in kiln drying

Malisa CHANPET[1], Nirattisai RAKMAK[1], Nirandorn MATAN[1], Chairat SIRIPATTANA[1,2*]

[1] School of Engineering and Resources, Walailak University, 80161, Nakhon Si Thammarat, Thailand.
[2] Biomass and Oil-Palm Excellence Center, Walailak University, 80161, Nakhon Si Thammarat, Thailand.
*Corresponding author: schairat@wu.ac.th, schairat61@gmail.com

Kiln drying of para rubber wood lumbers is a complex transport phenomena for realistic modelling and simulation. To decouple this complexity, researchers normally divide their research into two parts, namely: one-lumber drying kinetics to describe how a wood lumber response to its surface conditions, and then combine this drying kinetic with lumped transport model or dispersion model or computational fluid dynamics. The mathematical models are then solved numerically to predict the industrial kiln drying behaviours. This work focuses on the drying kinetic of para rubber wood lumber using hot air having different %RH (6 – 67% RH) and different air temperatures (60-100°C). It was found that the drying kinetics follows conventional drying theory where there are two distinct drying periods, namely: constant and falling rate period. From the drying data analysis, it was not easy to predict the fibre saturation point because it was greatly influenced by wood microstructure which was not uniform. However, in general drying rate and overall moisture transfer coefficient increase with increasing drying temperature. RH directly affects the driving force of moisture transfer rate such that high RH reduced mass transfer rate and so do the EMC. A simple drying model was also developed which can describe the drying kinetics satisfactory. Furthermore, it can be used to predict the overall mass transfer coefficient in the falling rate period. These transport parameters will be used in more complex models in future research.

Apart from the analysis of kiln drying kinetics of para rubber wood lumber, this work attempts to describe the mechanisms and dynamics of batch industrial drying processes using the engineering principles, including the laws of mass and energy conservation, heat and mass transfer as well as the phenomenon of dispersion in moisture in air. Both lumped-parameter and dispersive distributed models will be developed in this work.

One unique feature of this work is the development and application of the so-called "the volumetric dispersion model (VDM)" to describe and predict the moisture distribution in wood lumber and air at various positions in kiln dryer when lumped-parameter (well-mixed) models are not applicable. This model is expected to simplify the model formulation, numerical computation and interpretation of three-dimensional nature of the chamber space inside the kiln dryers. Finally, the model will be used to predict the effect of air recycle ratio, temperature-humidity and the process interruption during kiln drying process.

Keywords: kiln drying, drying kinetics, energy cost saving, mass transfer coefficient, para rubber wood lumber

1. INTRODUCTION

Presently, there is very high competition in export-oriented rubber wood industry. In order to survive, a wood processing factory must operate at its best efficiency, reducing energy costs, waste and if possible turn waste into value-added products. In 2016, Thailand exported approximately 22 million cubic metres of rubber wood and earned more than 40 billion Thai baht (more than 1 billion US-dollars) excluding rubber wood products of various types. In normal rubber wood processing, the wood logs are sawn, pressurised in chemical solutions and dried in hot-air kilns. Currently, there are more than a hundred para-rubber wood lumber factories around Thailand (Department of Industrial Works, 2560) some of which have been operated for more than ten years. All of them know how to produce high quality lumber products matched with the market demand but are still struggling to reduce the total production costs in order to be more profitable in highly competitive markets where the buyers have increasing bargaining power.

In this kind of industry, energy costs are very high comprising of more than 15% of operating costs (Theppaya, 2002) and traditionally wood drying process consume more than 60% of total energy usage, mainly in the forms of heat and electricity.

Although para rubber wood industry is very significant for Southern Thailand and provides a main export earnings for the local industry, research activities and publications are scattered and limited. In-house research has not been a tradition of Thai Industrialists particularly for small-and-medium-size companies. As such, local para-rubber wood industry operates the factory at a sub-optimal condition simply just to be on the safe side. Consequently, a lot of energy used is wasted and long drying time (up to 7 days) is not necessary and makes it less competitive because of high cost per unit product. Although energy usage is the key competitive factor at the current status of this industry, there are very limited articles published so far. There are, however, a few published researches in which the authors investigated how raw material, kiln drier design and operational conditions affect the quality of rubber wood lumbers (Diawanich, Matan, & Kyokong, 2010).

Kiln drying process optimisation, particularly in a commercial scale, is very costly and sometimes not practical and disruptive. A better approach is to study drying kinetics of single or uniform wood lumber with specific physical characteristics (eg. dimensions, orientation, macro and micro-structure of wood, density etc) exposed to series of well-defined external environment (eg. air velocity, temperature, relative humidity). Then, the resulting drying curves are analysed to obtain key process parameters such as moisture sorption isotherm, specific drying rate, fibre saturation point (FSP), overall mass transfer coefficient for each drying regime, moisture diffusivity. These key parameters, in turn, are used in more complex mathematical models, which also incorporate kiln air-flow pattern, wood stack arrangement, inlet-air temperature-humidity profile and hot-air recycle ratio to predict how each wood lumber responses to the imposed environment. This approach has many advantages, namely minimal research and development cost, shortening the experiment time, infinite scenarios can be generated, minimum process disruption, and so on. However, the approach requires accurate parameter estimation and realistic, most of the time sophisticated and distributed, mathematical models.

One of the most important parameter of wood drying, which is difficult to predict theoretically, is the overall mass transfer coefficient (K) for all drying periods: initial period, constant drying rate and falling rate period. Special attention has been emphasised on K in falling rate period (after moisture content is lower than FSP) because this period is normally the longest period in kiln drying process, contributing to the largest portion of the process energy cost.

This study is to characterise the drying kinetics of para rubber wood lumbers. Special attention is paid on factors affecting the drying rate in constant rate period and overall mass transfer coefficient in falling rate period. As mentioned earlier these parameters are fundamental ones for more complex, realistic, practical modelling and simulation of kiln drying process.

1.1. Wood drying kinetics

According to the definition, the drying rate is related to the derivative of the wood moisture content as follows

$$\ln K = \ln A - \frac{Ea}{RT} \quad (1)$$

Where M_0 is wood dry mass (kg) and is external mass transfer area of wood (m^2)

This can also be written by referring to transfer resistance of the gas phase.

$$\Phi = K_G(P_i - P_v) \quad (2)$$

Chrusciel et al. (1999) show that K can be represented by two partial mass transfer coefficients, Kg for gas phase (air) and Ks for solid phase (wood). So the moisture vapor transfer rate at air-wood interface is estimated by:

$$\Phi = K_g A\,(H_S - H) = K_s A\,(X_C - X_S) \quad (3)$$

Where H_s -H is the difference of specific humidity between the air interface that is in equilibrium with wood surface and X_c -X_s is the difference between the wood moisture content at the wood-core and at the wood surface.

It can be shown that from Equation 3 we can write

$$\frac{1}{K} = \frac{1}{K_S} + \frac{1}{mK_G} \text{ or } \frac{1}{K} = R_I + R_E \quad (4)$$

Approximately, the internal resistance R_1 is proportional to wood thickness and the external resistance R_E is related to air velocity in the form of $R_E \propto \upsilon^{-n}$, where varies between 0.5 and 1.0. Furthermore, Chrusciel, Mougel, Zoulalian, & Meunier (1999) shows that 1/K is a decreasing exponential function of the residual air desiccation ratio z, where z = 1 – RH/100.

Ananias et al. (2011) discussed the influence of various factors on the overall resistance to moisture transfer in wood lumbers and proposed a general correlation for the global mass transfer resistance as follow.

$$\frac{1}{K} = \alpha + \beta \exp\left(\frac{-z}{X_{exp} - X^*}\right) \quad (5)$$

Where:

$$\alpha = a_0 \exp\left(\frac{c_0}{T_K}\right)e \text{ and } \beta = b_0 \exp\left(\frac{c_0}{T_K}\right)\upsilon^{-p} \quad (6)$$

In Equation 5 $X_{FSP} - X^*$ is the gap between the fibre saturation point and the equilibrium moisture content at a specific air temperature and relative humidity. T_K is air temperature in Kelvin (K) and is the lumber thickness (mm). Equation 5 is valid as long as z is not zero (so when RH tends to 100%). However Babiak & Kúdela (1995) underline that the fibre saturation point is not well-defined as the value of X^* at RH = 100 %.

Ananias et al. (2011) determined the parameters of Equations 5 and 6 for Spruce (Picea abies) and beech (Fagus sylvatica) during a whole kiln-drying schedule and gave the following values: X_{FSP} = 0.3 (kg moisture/kg dry wood), P = 0.8, a_0= 0.12 (m.s.kg-1), b_0 =23.9 (m.s.kg-1) and c_0 = 2683 (K). After substituting these parameters into Equations 5 and 6 we have

$$\frac{1}{K} = 0.12 \exp\left(\frac{2683}{T_K}\right)e + 23.9 \exp\left(\frac{2683}{T_K}\right)\upsilon^{-0.8} \exp\left(\frac{\frac{RH}{100} - 1}{X_{FSP} - X^*}\right) \quad (7)$$

2. MODEL DEVOLOPMENT

2.1. Equations

Sorption Isotherm of wood lumbers

The following sorption isotherm has been established for wood lumber and was verified for para rubber wood lumbers by Suchat Tomad (2011).

$$X^* = EMC(\%) = \frac{1200}{W}\left[\frac{Kh}{1-Kh} + \frac{K_1 Kh + 2K_1 K_2 K^2 h^2}{1 + K_1 Kh + K_1 K_2 K^2 h^2}\right] \quad (8)$$

where h is the relative humidity (decimal) and the parameters W, K, K1, and K2 depend on temperature (T) is in °C in Equation 8 from Bettina Franke, Steffen Franke, Marcus Schiere, & Andreas Müller (2016)

$$W = 349 + 1.29T + 0.0135T^2$$
$$K = 0.805 + 0.000736T - 0.00000273T^2$$
$$K_1 = 6.27 - 0.00938T - 0.000303T^2$$
$$K_2 = 1.91 + 0.0407T - 0.000293T^2$$

This relation will used to estimate the equilibrium moisture content (X*) in the following development.

For the constant rate period,

$$\frac{dX}{dt} = - k_1 \quad (9)$$

$$X = X_0 - k_1 t \quad (10)$$

And we propose that a constant mass transfer coefficient is valid to describe the drying rate in the falling rate period.

$$\frac{dX}{dt} = - k_2 A(X - X^*) = - KA(X - X^*) \quad , X < Xs \quad (11)$$

Or $$X = X^* + (X_0 - X^*)\exp(-k_2 t) = X^* + (X_0 - X^*)\exp(-\frac{K}{A}t) \quad (12)$$

Combining Equation 4 and Equation 5 and after inserting a suitable (and flexible) switching function we obtain the following drying equation covering both constant and falling rate periods.

$$X = \left[\frac{1}{2} + \frac{1}{\pi}\tan^{-1}\left(\kappa(t_s - t)\right)\right]\left(X_0 - k_1 t\right) + \left[\frac{1}{2} + \frac{1}{\pi}\tan^{-1}\left(\kappa(t - t_s)\right)\right]\left[X^* + \left(Xs - X^*\right)\exp\left(-k_2(t - t_s)\right)\right] \quad (13)$$

In order to obtain parameters in Equation 6 we may compare it with a complete drying curves and estimate the model parameters (κ ,t_s,k_1,k_2) using least square fitting algorithms.

Calculation of overall mass transfer coefficients: (K)

Can be calculated from basic definition. (Chairat Siripatana, 1997)

$$K = - \frac{1}{A(X - X^*)}\left(\frac{dX}{dt}\right) \quad (14)$$

Or for the model $$K_{model} = - \frac{1}{A(X - X^*)}\left(\frac{dX}{dt}\right)_{model} \quad (15)$$

And experimental $$K_{exp} = - \frac{1}{A(X - X^*)}\left(\frac{dX}{dt}\right)_{exp} \quad (16)$$

Lamped parameter drying model

This model states that the drying rate is linearly proportional to its driving force: drying potential which is $\bar{X} - X^*$, and the overall mass transfer coefficient. In addition, the model assumes that the mass and energy transfer occurs only in one direction, uniform moisture content in wood at drying starting time, the air in the dryer is well-mixed (uniformly distributed). The heat losses and temperature change at different stack position is negligible. From the moisture/water balance in drying air:

$$G\left(W - W_{in}\right) = KA\left(\bar{X} - X^*\right) \quad (17)$$

The moisture balance in the wood,

$$-M_0 \frac{d\bar{X}}{dt} = KA\left(\bar{X} - X^*\right) \quad (18)$$

or

$$\frac{d\bar{X}}{dt} = -\frac{KA}{M_0}\left(\bar{X} - X^*\right) \quad (19)$$

The air enthalpy balance,

$$G[(c_{pa}T+W(\Delta h_0+c_{pv}T))-(c_{pa}T_{in}+W_{in}(\Delta h_0+c_{pv}T_{in}))]= \quad KA\Delta h_V(\overline{X}-X^*)-hA(T-T_w) \tag{20}$$

And the enthalpy balance for the wood,

$$M_0\left(c_{pS}+c_{pL}\overline{X}\right)\frac{dT_w}{dt}= G[c_{pa}(T-T_{in})-(c_{pL}T_w)(W-W_{in})+c_{pv}(WT-W_{in}T_{in})-\Delta h_0(W-W_{in})] \tag{21}$$

Or

$$\frac{dT_w}{dt}= G'[c_{pa}(T-T_{in})-(c_{pL}T_w)(W-W_{in})+c_{pv}(WT-W_{in}T_{in})-\Delta h_0(W-W_{in})] \tag{22}$$

and

$$G'=\frac{G}{M_0(c_{pS}+c_{pL}\overline{X})} \tag{23}$$

$$\frac{dW}{dt}=\frac{KA}{M_a}(X-X^*)+\frac{G}{M_a}(W_{in}-W) \tag{24}$$

The moisture balance in the wood,

$$\frac{dX}{dt}=-\frac{KA}{M_0}(X-X^*) \tag{24}$$

The air enthalpy balance,

$$\frac{dT}{dt}=\frac{1}{M_a\left(c_{pa}+Wc_{pv}\right)}\left[G\left(H_{ain}-H_a\right)-M_a\Delta h_0\frac{dW}{d}-hA\left(T-T_W\right)\right] \tag{25}$$

Here, the enthalpy of

And the enthalpy balance for the wood,

$$\frac{dT_w}{dt}=\frac{1}{M_0\left(c_{pS}+c_{pL}X\right)}\left[hA\left(T-T_w\right)-M_0\Delta h_v\frac{dX}{dt}\right] \tag{26}$$

Recycle ratio

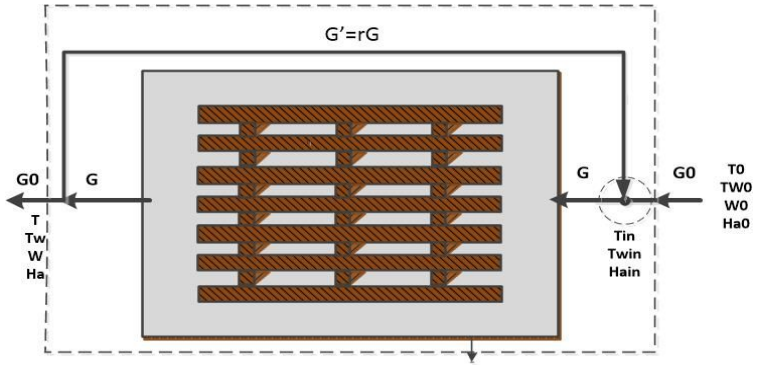

Figure 1: Recycle ratio in kiln drying.

$$G_0 = (1-r)G,\ r = \frac{G'}{G}, G' = rG \tag{27}$$

$$G = rG + G_0 \tag{28}$$

Moisture:

$$GW_{in} = rGW + G_0 W_0 \tag{29}$$

$$W_{in} = rW + \frac{G_0}{G} W_0 \tag{30}$$

Enthalpy:

$$GH_{ain} = rGH_a + G_0 H_{a0} \tag{31}$$

$$H_{ain} = rGH_a + \frac{G_0}{G} H_{a0} \tag{32}$$

3. EXPERIMENTAL METHOD

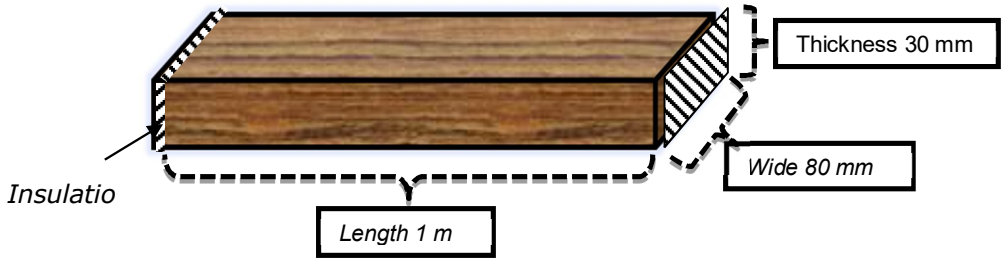

Figure 2: Dimensions of Para rubber wood.

The lumber in these experiments were prepared by sawing rubber-wood logs into lumber having dimensions of 1 m length × 80 mm width × 30 mm thickness. The lumber were on top of each other, forming stack of 7 layers. Each layer contained 6 boards with sticks (and used the sticks with dimensions 1 m length and 30 mm thickness) separating each layer of lumber. Before drying, the lumber were impregnated with boron solution. The average moisture content of lumber after the impregnation process was 110±5%.

Drying kiln (Eurasia, Singapore) have 15m^3 of volume, 4m/s of a fan speed, and fan was reversed at 4-hour intervals. The hot air for drying come from heat exchanger by using air and steam from boiler. LabView (National Instruments, USA) was used for the drying kiln control system.

The drying kinetics of para rubber wood in a kiln drier was studied in two cases. The first case was to investigate the effect of drying temperature in 60-100°C range (T1-T5) with controlled equilibrium moisture content (EMC) of wood lumbers (3.3%). The other case was to study the effect of relative humidity at a constant temperature (90°C) by varying wet bulb temperature in the range of 40-80°C (H1-H5). All experimental setups were shown in Table1.

Table 1: Experimental setups for studying the effect of temperature and relative humidity of air in kiln drying.

Treatment	Dry-bulb (°C)	Wet-bulb (°C)	RH (%)	EMC (%)
T1	60	34	12	3.3
T2	70	42	18	3.3
T3	80	51	24	3.3
T4	90	60	26	3.3
T5	100	71	29	3.3
H1	90	40	6	1.0
H2	90	50	14	2.0
H3	90	60	26	3.3
H4	90	70	43	4.9
H5	90	80	67	8.1

4. RESULTS AND DISCUSSION

The following experimental data were taken from (Suchat Tomad, 2011). Using Equation 13 to fit the data by least square algorithm, the evaporation rate (k_1) and the mass transfer coefficient (k_2) were obtained as tabulated in Table 2.

Table 2: The parameter estimate from wood drying kinetics model.

Treatment	*X_s (%)*	*k_1 (h^{-1})*	*k_2 (h^{-1})*	*R^2 (%)*
T1(60°C)	*37*	*3.574*	*0.041*	*0.999*
T2(70°C)	*43*	*4.171*	*0.037*	*0.981*
T3(80°C)	*38*	*6.161*	*0.054*	*0.998*
T4(90°C)	*25*	*5.656*	*0.043*	*0.993*
T5(100°C)	*21*	*5.150*	*0.024*	*0.990*
H1(90°C, 6% RH)	*45*	*12.932*	*0.035*	*0.993*
H2(90°C, 14% RH)	*42*	*11.622*	*0.026*	*0.989*
H3(90°C, 26% RH)	*25*	*5.657*	*0.041*	*0.996*
H4(90°C, 43% RH)	*55*	*7.352*	*0.029*	*0.997*
H5(90°C, 67% RH)	*44*	*3.448*	*0.032*	*0.998*

4.1. The effect on drying kinetics

In the constant drying period (MC > X_s), it was observed that, at fixed EMC (X* = 3.3) as air temperature increased from 60°C to 80°C, the drying rate (k_1) got higher from 3.574 h^{-1} to 6.161 h^{-1}. Further increase in air temperature beyond 80°C caused slightly decrease in k_2. This may be a result of wood excessive shrinkage occurring at high temperature, causing surface hardening, thus lowering the evaporation rate.

Similarly, in the falling rate period (after the MC passed through FSP), increasing air temperature from 60°C to 80°C also resulted in higher mass transfer coefficient (k_2) where as father temperature increase beyond 80°C resulted in sharply decrease in k_2. The same explanation should be applied for falling rate period.

It is interesting to notice that high temperature will generally shorter the total drying time because higher temperature was associated with lower fiber saturation point (X_s) as shown in Table 2.

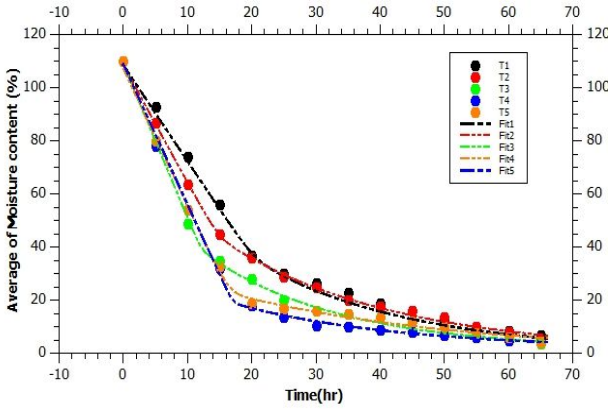

Figure 3: Relation between average of moisture content (%) and time (hr.) of drying temperature in 60-100°C range (T1-T5)

The effect of relative humidity on drying kinetics (at 90°C)

At constant temperature (90°C), generally high RH was associated with lower overall drying rate and high EMC although the experimental time was not sufficient for the moisture content to reach EMC. This can be explained by the driving force for moisture transfer ($X-X^*$) which is directly related to RH by Equation 13.

It was also noticed that there was a considerable fluctuation in X_s, indicating non-uniform structure of wood samples, making more difficult to interpret drying kinetics conclusively.

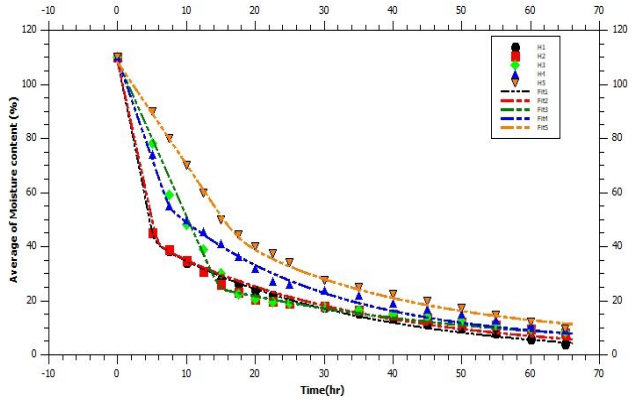

Figure 4: Relation between average of moisture content (%) and time (hr.) of wet bulb temperature in the range of 40-80°C (H1-H5).

The overall mass transfer coefficient (K) in falling rate period: comparison between experimental data, calculated from Ananias et al. (2011) and the current work

To evaluate the applicability of Equation 7 Ananias et al. (2011) for estimating K in para rubber wood drying, we compared the K from experimental data to that estimated by Equation 7 and that calculated from our kinetic model (Equations 15 and 16). The comparative results were shown in Table 3 and Figure 4.

Table 3: The parameters estimate from wood drying kinetics model (Equations 7, 15 & 16).

Wood Species	e (mm)	V (m/s)	T (Dry-bulb) (◦C)	Tw (wet-bulb) (°C)	RH (%)	K experimental Tomat (2011) (kg/m^2.s)	K from Eq. 8 and Eq. 9 (kg/m^2.s)	K Ananias et al. (2011) (kg/m^2.s)	K from Arrhenius equation. (kg/m^2.s)
			60	34	12	1.358e-04	1.315e-04	1.3367e-04	1.3266e-04
			70	42	18	1.5336 e-04	1.530e-04	1.4365e-04	1.643e-04
Para			80	51	24	2.1538e-04	1.988e-04	1.8708e-04	2.0103e-04
rubber			90	60	26	2.38e-04	2.89e-04	1.920e-04	2.4326e-04
wood	15	4	100	71	29	2.569e-04	2.496e-04	2.3991e-04	2.9136e-04

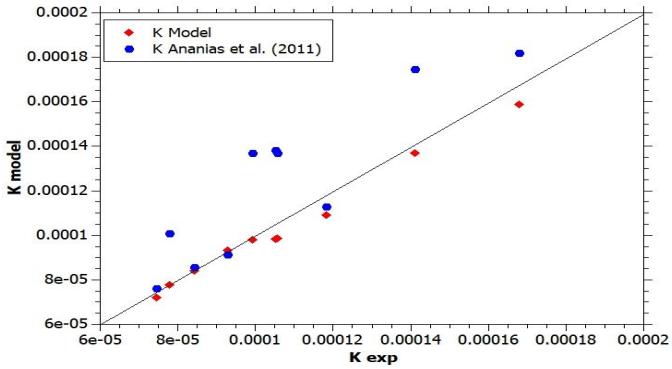

Figure 5: comparison between mass transfer coefficient (K) of experimental and modelling.

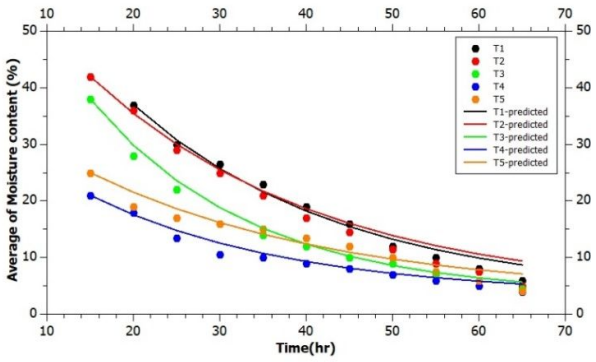

Figure 6: comparison between experimental drying data in falling rate period and the corresponding prediction of Equation 12

Lamped parameter drying model

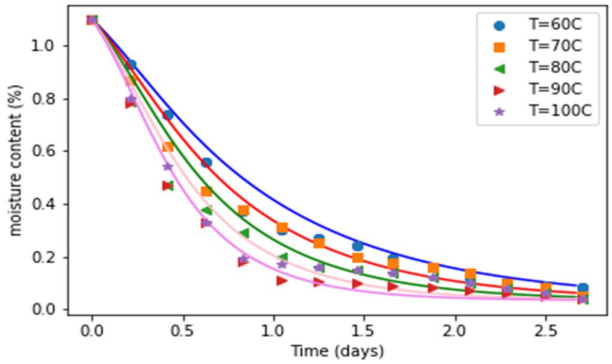

Figure 7: Relation between average of moisture content (%) and time (hr.) of drying temperature in 60-100°C range (T1-T5)

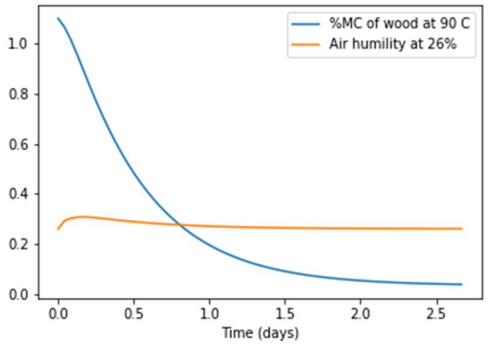

Figure 8: Relation between average of moisture content (%) and time (hr.) of drying temperature at 90°C

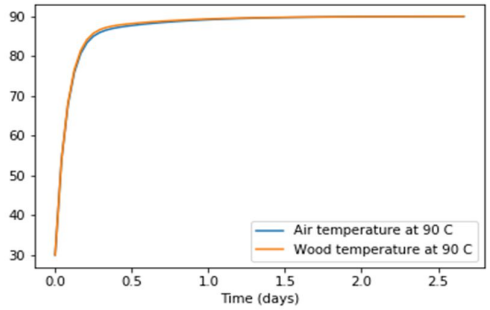

Figure 9: Relation between average of moisture content (%) and time (hr.) of drying temperature at 90°C

5. CONCLUSION

Kinetics of para rubber wood lumber drying is essential tool to estimate the design and operational parameters which are accurate and fundamental enough to be used as a representation of wood lumber in response to different flow and psychometric environments. This work concludes that it is possible and desirable to characterise the drying kinetic in constant and falling rate period with four parameters (and other physical wood characteristics), namely: evaporation rate in constant rate period, overall mass transfer coefficient in falling rate period, fibre saturation point and EMC.

6. ACKNOWLEDGEMENT

The authors would like to thank Walailak University Fund (Contact no. 11/59), Biomass and Oil-Palm Excellence Center Walailak University for financial support.

7. REFERENCES

Babiak, M., & Kúdela, J. (1995). A contribution to the definition of the fiber saturation point. *Wood Science and Technology*, *29*(3), 217–226. https://doi.org/10.1007/BF00204589

Bettina Franke, Steffen Franke, Marcus Schiere, & Andreas Müller. (2016). Moisture diffusion in wood – Experimental and numerical investigations (Vol. 2016). Presented at the World Conference on Timber Engineering, Vienna, Austria.

Chairat Siripatana. (1997). Solute diffusion in fruit, vegetable and cereal processing I: Simplified solutions for diffusion in anomalous shapes. *Songklanakarin Journal of Science and Technology*, *19*(1), 77–78.

Chrusciel, L., Mougel, E., Zoulalian, A., & Meunier, T. (1999). Characterisation of water transfer in a low temperature convective wood drier: influence of the operating parameters on the mass transfer coefficient. *Holz Als Roh- Und Werkstoff*, *57*(6), 439–445. https://doi.org/10.1007/s001070050070

Department of Industrial Works. (2560). Retrieved from http://www.diw.go.th

Diawanich, P., Matan, N., & Kyokong, B. (2010). Evolution of internal stress during drying, cooling and conditioning of rubberwood lumber. *European Journal of Wood and Wood Products*, *68*(1), 1–12. https://doi.org/10.1007/s00107-009-0343-z

Rube´n A. Ananias, William Broche, Mara Alvear, Carlos Salinas, & Roger B. Keey. (2009). Using an overall mass-transfer coefficient for prediction of drying of chilean coigue. *Wood Fiber Sci*, *41*, 426–432.

Rubén A. Ananias. (2011). Overall Mass Transfer Coefficient for Wood Drying Curves Predictions. In Laurent Chrusciel (Ed.), Carlos Salinas-Lira (Trans.), *Mass Transfer in Multiphase Systems and its Applications* (p. Ch. 14). Rijeka: IntechOpen. https://doi.org/10.5772/14242

Suchat Tomad. (2011). *Effects of Temperature and relative Humidity According to Various Drying Strategies on Internal Stress Generation during the Drying of Rubberwood Lumber*. Walailuk University.

T. Theppaya. (2002). Parameters Influencing drying behavior of rubber wood (hevea brazilliensis) as determined from desorption experiment. *Drying Technology*.

#222: Review of wind effect on measurement of building airtightness

Yun-Sheng HSU[1], Xiaofeng ZHENG[2], Mark GILLOTT[3], Christopher J WOOD[4]

[1]Department of Architecture and Built Environment, Faculty of Engineering, University of Nottingham, NG7 2RD University Park, Nottingham, UNITED KINGDOM
[1]Yunsheng.Hsu@nottingham.ac.uk
[2]Xiaofeng.Zheng@nottingham.ac.uk
[3]Mark.gillott@nottingham.ac.uk
[4]Christopher.wood@nottingham.ac.uk

A dramatic rise in the global energy demand has been noted, with its growth coming from the emerging economies, higher living standard and comfort levels. Research shows that building infiltration could account for 30-50% of energy consumption for space heating, including ventilation in a leaky house (i.e.10ach at 50Pa). Building airtightness is regarded as the fundamental building property that impacts infiltration and exfiltration, and is a crucial factor to be concerned with in order to improve the energy performance of buildings. The influence of poor airtightness on the built environment has brought about wide concern since the 1970s, citing negative impacts on building energy consumption, building durability, indoor air quality and noise transmission. Generally, the common method to quantify the building airtightness is implemented by pressurising or depressurising the building to achieve a pressure difference between the inside and the outside of the building and record the corresponding airflow rate. At present, the blower door is the most popular approach, and the Pulse technique is another promising technology for building airtightness measurement. Extensive studies on building airtightness measurements have been conducted using blower door and Pulse technique, and researchers have pointed out that the uncertainty of measurement could be caused by various factors under different weather conditions. In this study, a comprehensive review of the literature is presented regarding the wind effect on building airtightness measurement. The review indicates that limited investigations have been carried out to clarify the effect of unsteady wind condition on the building airtightness measurement both through blower door and Pulse testing and to provide a precise assessment of building airtightness under variable wind conditions. Requirements on the testing weather condition have been set in the national and international standards for fan pressurisation method to determine building airtightness. However, the wind speed limits for different national standards vary, which also indicates the necessity of defining more practical wind speed limit for building airtightness measurement. On the other hand, as no regulations for the Pulse testing have been found in the standards, there is a need of protocols that can be used to characterise building airtightness measurement for the Pulse technique.

Keywords: building airtightness; infiltration; wind effect; pulse technique; blower door

1. INTRODUCTION

In recent years, energy saving has attracted more and more attention globally. Its main purpose is to utilise the energy required for the building rationally and minimise its consumption to sustainable limits. Figure 1 shows the changes in each sector share of energy consumption since 1970. Transportation accounted for the largest proportion of final consumption in 2017 at 40% and followed by the domestic sector (i.e. 28%), industry (i.e. 17%) and the service sector (i.e.15%). It has been noted that domestic energy consumption is dominated by several factors, including household characteristics, building energy performance and electrical appliances. Compared to most European countries, the UK housing stock is old, with many houses dating back to the Victorian era. Many houses have poor energy performance as additional consumption is needed to maintain the required thermal comfort.

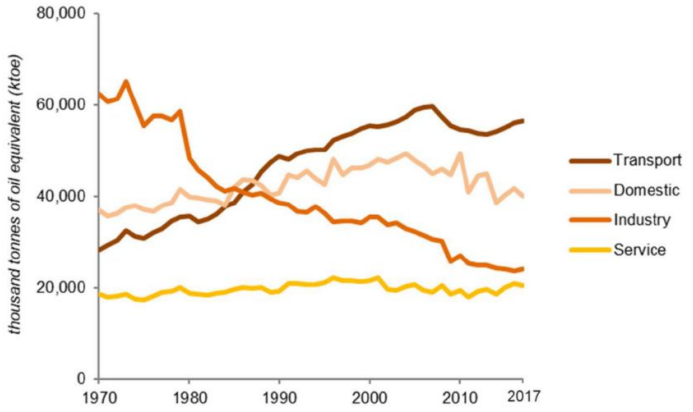

Figure 1: UK final energy consumption by sector (Department for Business, 2018)

It is noteworthy that a large amount of energy consumption in the building sector results in massive greenhouse gas emissions. To address it, energy-efficient building design needs to be adopted to reduce the energy losses, which could be realised through novel designs of the building construction. It has been noted that heat losses from the building envelope are mainly attributed to heat transfer and ventilation including infiltration (Lerma et al., 2018). Researchers revealed that building energy performance and indoor air quality are significantly dependent upon ventilation, which is also influenced by uncontrolled air leakage (i.e. air infiltration) across the building exterior (Wang et al., 2018). Airtightness is regarded as the fundamental building property that impacts infiltration and exfiltration (Han et al., 2015). The airtightness of buildings is a crucial factor that should be addressed to improve the energy performance of buildings. Many countries have issued the minimum requirements in terms of the building airtightness, as listed in Table 1. Different countries use different ways to express the airtightness requirement, which makes it not straightforward to make a direct comparison across different countries.

Table 1: Existing airtightness requirements in different countries (Erhorn-Kluttig et al., 2009, Charrier et al., 2015)

Country	Building Airtightness Requirement	
UK	New dwellings, commercial and public buildings over 500m^2: 10m^3/h/m^2 at 50Pa	
France	Single-family buildings: 0.6m^3/h/m^2 at 4Pa	
	Multi-family buildings: 1m^3/h/m^2 at 4Pa	
	Non-residential buildings: 1.7m^3/h/m^2 or 3m^3/h/m^2 depending on building type	
Netherland	Dwellings: 200dm^3/s at 10Pa	
	Non-residential buildings: 200dm^3/s per 500m^3 at 10Pa	
Belgium	Dwellings with balanced mechanical ventilation: <3ach at 50Pa	
	Dwelling with heat recovery: <1ach at 50Pa	
Norway	Detached and undetected houses: 4ach at 50Pa	
	Buildings with two storeys high or less: 3ach at 50Pa	
	Building with more than two storeys: 1.5ach at 50Pa	
Sweden	0.8 l/m^{2}s at 50Pa	
Switzerland	New buildings: 0.75m^3/h/m^2 at 4Pa (recommendation at 0.5m^3/h/m^2)	
	Refurbished buildings: 1.5m^3/h/m^2 at 4Pa (recommendation at 1m^3/h/m^2)	
Demark	1.5 l/s per m^2 floor area at 50Pa	
Czech Republic	Buildings with natural ventilation: 4.5ach at 50Pa	
	Buildings with mechanical ventilation	With heat recovery: 1.5ach at 50Pa
		Without heat recovery: 1ach at 50Pa
Germany	Buildings with natural ventilation: 3ach at 50Pa	
	Buildings with mechanical ventilation: 1.5ach at 50Pa	
USA	1.6ach at 4Pa	

The influence of poor airtightness on the built environment has aroused wide concern since the 1970s, for example, the impacts on building energy consumption, building damage, indoor air quality and noise transmission (Carrié and Rosenthal, 2008). To measure the building airtightness, the steady pressurisation method, which has been widely accepted, can be used. The most common steady pressurisation method to quantify the building airtightness is through a blower door test, which can be implemented by pressurising the building to a range of pressure differences, typically in 10–60Pa (British Standards Institute, 2015). Another novel testing method of building airtightness is the Pulse technique involving a low-pressure process, typically around 4Pa, with which the building airtightness can be determined by releasing a 1.5-second pulse of air from a pressurised vessel. Based on the investigations, researchers have pointed out that the measurement of building airtightness can be influenced by various factors, so uncertainty has been the key concern in many regions over the past few years. Airtightness of buildings under various wind conditions and environmental conditions is a complex process, which would be strongly influenced by the turbulent nature of the wind (Haghighat et al., 2000). For instance, the outdoor wind would cause a variation in the indoor pressure as different outdoor wind speeds would lead to different infiltration rates and thus affect indoor pressure accordingly (Wu et al., 2018). Likewise, during the measurement process, the outdoor wind could result in an impact on the accuracy of airtightness measurement of the building envelope. A number of researches have been conducted to evaluate the wind effect on the measurement of building airtightness and address the uncertainties of building airtightness measurement associated with wind effect. This paper presents a review of the literature of studies conducted in recent years investigating the wind effect on building airtightness measurement from different aspects.

2. BUILDING AIRTIGHTNESS AND THE IMPACT

In general, building airtightness is defined as the resistance to inward or outward air leakage through unintentional leakage cracks or gaps in the building envelope, which indicates how well the building envelope is sealed (Guyot et al., 2010). Air infiltration fundamentally determined by building airtightness not only changes the amount of air entering the building but also distorts the expected airflow pattern, thereby the overall indoor air quality and thermal comfort could be affected. It has been found that excessive infiltration leads to unnecessary heat loss and discomfort to the occupants in cold weather (Santamouris and Wouters, 2006). Additionally, excessive infiltration could interfere with the normal operation of the mechanical ventilation system, which results in poor indoor air quality, moisture damage and more energy consumption of building envelope components (Lstiburek et al., 2002). As air or pollutants could be drawn in from contaminated areas owing to poor airtightness, the indoor air quality is reduced accordingly. The places that could be regarded as contaminated areas include the attic, crawlspace and outdoor. Even the building envelope may be a source of contamination, which is attributed to mould or toxic materials. Evidence has been provided that the transport of fungal spores takes place through a crawl space into the indoor environment. Besides, poor building airtightness allows damp air to enter and be in contact with cool surfaces, which subsequently results in the growth of microorganisms. For cold regions, ice could be formed in and on exterior envelope components owing to poor building airtightness. The moisture convection due to the poor airtightness causes more moisture loads on the building structure and structural deterioration (Janssens and Hens, 2003). Basically, in order to achieve “Build tight–ventilate right”, buildings should not be too air-tight but should be ventilated with dedicated vents to ensure proper ventilation for thermal comfort.

3. BUILDING AIRTIGHTNESS MEASUREMENT METHODS

Airtightness of the building envelope needs to be measured because visual observations are difficult to detect gaps and cracks that do exist in building envelope. Also, leakage paths into the building envelope may be tortuous, and gaps are commonly obscured by internal architectural facings or external cladding (Vinha et al., 2015). The best way to demonstrate the airtightness of the building envelope is to measure the leakages of the entire building envelope. In terms of building measurement, the air leakage can be quantified as air permeability, which means the leakage of air in or out from the building under a given pressure difference normalised by building envelope area (Hunt et al., 1980). In terms of the building envelope, the assessment of air leakage involves the establishment of a pressure difference across the enclosure and measurement of the airflow required to achieve the pressure difference. The most common reference pressures are 50Pa for a blower door test and 4Pa with the Pulse technique, whereas other reference pressures also are available, such as 1Pa, 10Pa, 25Pa and 75Pa.

3.1. Blower door

The blower door is a common device for measuring the building airtightness. It can also be used to measure airflows between building areas, test duct tightness and help physically locate leaks in the building envelope. Basically, the blower door consists of three main components, a calibrated variable speed fan, pressure measuring instrument and a blower door mounting opening. The calibrated variable speed fan is capable of generating airflows in a wide speed range, which could be sufficient to pressurise and depressurise various building sizes to the desired range. In practical, the blower door unit, together with its fan, should be installed to a building opening such as a door or a window. The blower door test results provide measurements of air flow rate and pressure difference of the building indoor and outdoor, consequently building leakage and energy performance can be revealed (Chen et

al., 2012). For the sake of easily identifying air leakage, a smoke puffer could be utilised to reveal and trace air movement while conducting the blower door testing (Stabile et al., 2016).

3.2. Pulse technique

Generally, the Pulse technique measures the building airtightness at low pressure by rapidly releasing a known volume of air into the test building and thereby creating an instant pressure rise that quickly reaches "quasi-steady" condition (Cooper and Etheridge, 2007). A novel nozzle pulse pressurisation technique determines the adventitious building leakage at the low pressure around 4Pa, which has been regarded as a more accurate indicator than the conventional steady-state measurement at 50Pa (Cooper et al., 2014). The technique is based on the "quasi-steady pulse" concept, with which a pressure pulse inside the building is produced with a certain amount of air being introduced to the building in a very short time through an air compressor, a solenoid valve, a nozzle and a control unit. Due to the short-time operation, the technique minimises the effects of wind and buoyancy force and has been proven to be highly repeatable (Zheng et al., 2017). Instead of installing a fan into a doorway for blower door testing, the Pulse technique enables easy operation without the need of long-time setup and the entire testing process could be implemented in only 11 to 15 seconds (Cooper et al., 2014).

4. CURRENT RESEARCH ON ADDRESSING MEASUREMENT UNCERTAINTIES CAUSED BY WIND

The uncertainty of building airtightness measurement has been an important concern. The sources of uncertainty for the airtightness testing mainly include: building preparation for testing, tester behaviour, measurement error, uncertainties of measurement instrument, weather effect, thermal draft impact, seasonal variation of building airtightness, leaks with different flow exponents and linear regression (Sherman and Palmiter, 1995, Andrews, 1997, Geissler, 1999, Kraniotis et al., 2013, Kraniotis et al., 2014b, Leprince et al., 2017, Leprince and Carrié, 2018, Zheng et al., 2019b, Zheng et al., 2019a). For instance, the pressure difference between the building interior and the exterior environment could be affected in accordance with the indefinite nature of the wind and buoyancy effect, resulting in the imprecise measurement of the building airtightness. Through both numerical and experimental work, researchers have noted the impact of outdoor weather condition on building airtightness measurement. Therefore, requirements on the testing weather condition have been set in the standards for fan pressurisation method to determine building airtightness. Table 2 lists meteorological requirements for standards of EN13829, ASTM 779-03 and ISO 9972.

Table 2: EN13829, ASTM 779-03 and ISO 9972 requirements regarding the meteorological condition

	EN13829	ISO 9972	ASTM E779-03
Wind speed	The wind speed must be Beaufort scale 3 or less. If measured, should be 6m/s or less	The strong wind shall be avoided; Recommendations: wind speed near the ground ≤ 3 m/s meteorological wind speed ≤ 6 m/s or ≤ 3 on the Beaufort scale	Low-wind pressure conditions: the wind speed is to be part of the measurement record, use a wind-measuring device or obtain readings from a nearby weather bureau. Preferred test conditions: 0-2 m/s and outside temperature from 5-35°C (41 to 95°F).
Temperature	The product of the absolute value of the indoor/outdoor air temperature difference multiplied by the building height must be lower than 500 m.K	Large indoor-outdoor temperature difference shall be avoided; The product of the indoor/outdoor air temperature difference by the height of the building ≤ 250 m.K	Outside temperature: 5-35°C or 41-95°F. The product of the indoor/outdoor air temperature difference by the height of the building shall be ≤ 200 m.°C
Zero-flow pressure	The static pressure difference between the inside and outside of the building with the envelope closed up, but with no test equipment running, must be less than 5 Pa over a 30-second average.	The test is not valid if one zero low-pressure average (in absolute) ≥ 5 Pa	To create a single zone for the test procedure, all interconnecting doors, except for closets which should be closed in the conditioned space, should be opened such that a uniform pressure will be maintained within the conditioned space to within ±10 % of the measured inside/outside pressure difference.

The air leakage across the building envelope is mainly driven by a pressure gradient across the building envelope, including wind-induced pressures, buoyancy pressures and additional driving pressures for mechanical ventilation systems (Etheridge and Sandberg, 1996). The wind pressures are influenced by the wind characteristics, such as the velocity and direction, the shape of the building envelope and the topography of building location and surrounding environment (Kraniotis, 2014). In such a way, measurements are commonly recommended to be performed in low or steady wind speed conditions are assumed for simulation. Based on ISO 9972 standard, the overall uncertainty of the blower door testing can be estimated using error propagation calculation, which is lower than 10% in calm conditions, while it could reach up to ±20% in windy conditions (ISO, 2015). Based on the review

of the literature, both simulation (numerical modelling and CFD transient modelling) and experimental testing have been conducted, and several aspects are focused for considering wind effect, including test method, reference pressure and zero-flow pressure measurement, wind speed and wind fluctuations.

4.1. Test method

In general, there are three different test methods for the building airtightness measurement, namely one-point, two-point and multi-point test methods, which are illustrated respectively in Figure 2. For standards, like ASTM 779-03 and ISO 9972 multi-point test method is preferred for building airtightness measurement. Walker et al. (2013) used a one-point test method, in which a default value for the flow exponent (i.e. n=0.65) has been taken into account. The illustration of the one-point test method is shown in Figure 15(a). The uncertainty of the testing results has been assessed, and comparisons based on 6000 tests for six houses have been conducted with results obtained from a multi-point testing. They identified that the one-point test method is comparatively less sensitive to wind pressure fluctuation when wind speed is above 6m/s as an error related to n approximation is less notable than that of the wind. Additionally, they also suggested that the multi-point test would be better performed when the wind speeds lower than 6m/s. On the other hand, a numerical evaluation of the wind effect on testing uncertainties has been conducted by Carrié and Leprince (2016) using both one-point and two-point methods. Their simulation results imply the maximum combined uncertainty at a reference pressure of 4Pa is worse for the two-point method than in one-point with a full range of leakage distribution. It can be pointed out that the selection of the test method for measuring building airtightness depends on wind condition, so it is critical to choose a proper method in order to minimise uncertainties owing to wind effect.

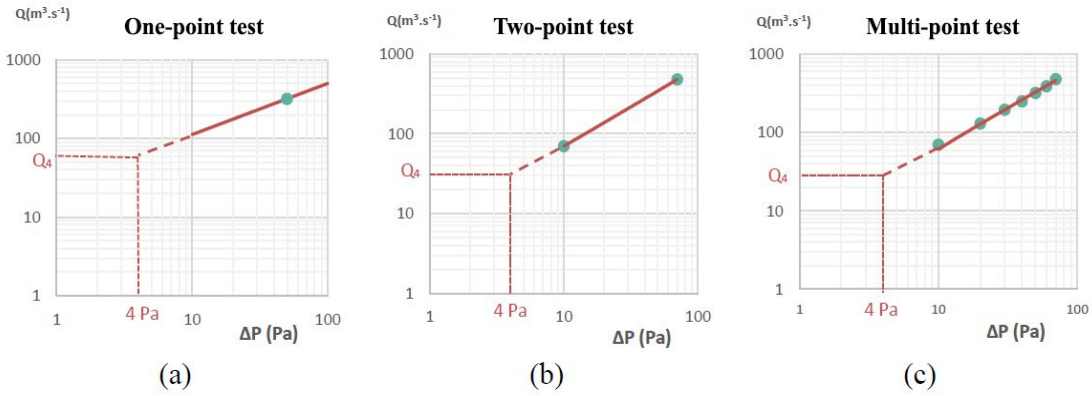

Figure 2: (a) One-point, (b) Two-point and (c) Multi-point test methods (Mélois et al., 2018)

4.2. Reference pressure and zero-flow pressure measurement

Due to the fact that the wind pressure induced on the upwind façade and the other building façades are not identical, the position of the installed pressure probe also affects the testing results (Holøs and Relander, 2010). It has been proved that the pressure uncertainty caused by the wind and by instrumentation inaccuracies is one of the major sources of uncertainty for fan pressurisation measurements of effective leakage area. Modera and Wilson (1990) proposed a methodology to reduce the effect of wind on the fan pressurisation measurement, by using multiple fan pressurisation measurements at a single site and employing four-surface pressure averaging and time averaging of pressure and flow data. The data evidently showed that the combined surface-averaging and time averaging technique significantly reduce the uncertainty at the calm condition and the uncertainty remains below 11% when wind speed increases up to 5m/s. Therefore, they recommended using surface-pressure averaging for more accurate building airtightness measurement. On the other hand, based on the simulation using single-zone building under isothermal condition, Leprince and Carrié (2018) suggested that it is necessary either to have a constraint on wind speed with maximum of 6m/s or to have a constraint on zero-flow pressure at maximum pressure of 5Pa to address the uncertainty caused by steady wind on building airtightness measurement.

4.3. Wind speed measurement

A number of researches have been conducted to find a precise prediction or estimation of the building permeability in order to accurately assess the airtightness level and calculate the permeable energy footprint. Through both numerical and experimental work, researchers have noted the impact of the outdoor condition on building airtightness measurement. Requirements on the testing weather condition have been set in the standards for fan pressurisation method to determine building airtightness. The influence of the weather condition leads to specific

recommendations for the wind velocity. For instance, the outdoor wind velocity for measuring building airtightness have been suggested not higher than 8m/s in the literature (Nevander, 1978). On the other hand, Kronvall (1978) adopted "static wind loads and simplified load distribution models" and suggested a lower outdoor wind speed limit of 5m/s for building airtightness measurement. The limit was defined as the wind velocity for the static wind load model, and a pressure difference of 5Pa with the simplified load distribution model. Standards specify various wind speed limits for both pressurisation and depressurisation methods, and as presented in Table 8, the wind speed limits for different national standards vary. For instance, Swedish standard SS 02 15 51, Norwegian standard NS 8200, American standard ASTM E779-81/ ASTM E779-03, Canadian General Standard (which is limited to depressurisation testing) and European Standard EN 13829.

Table 3: Provisions regarding wind speed limit in five tests standards

Standard (Year)	Wind Speed Limit
American standard ASTM E779-03 (2003)	< 2.0 m/s (ground wind speed)
American standard ASTM E779-81 (1981)	< 4.4 m/s (ground wind speed)
Canadian standard (1983)	< 5.5 m/s (meteorological wind speed)
Norwegian standard NS 8200 (1981)	< 6.0 m/s (meteorological wind speed)
European standard EN 13829 (2001)	≤ 6.0 m/s (meteorological wind speed)
Swedish standard SS 02 15 51 (1980)	< 10.0 m/s (meteorological wind speed)
International standard ISO 9972 (2015)	< 3.0 m/s (ground wind speed)
	< 6.0 m/s (meteorological wind speed)

It has been noted that a proper definition of wind speed is hard to find in the existing literature. Typically, there are two different definitions of wind speed, namely the meteorological wind speed, which represents wind speed at 10m from the ground and the local wind speed representing the wind speed at the height of the building. Additionally, ISO 9972 provides another wind speed reference, which is the wind speed near the ground. Due to different wind speed references, confusions might take place, and significant differences can be noticed for measuring or calculating wind speed (Mao et al., 2015). It is found that researchers employed different definitions of wind speed for investigating the wind effect on building airtightness measurement, and sometimes the wind speed was not clearly indicated. For instance, Walker et al. (2013) directly employed wind speed and direction taken from meteorological towers at the test site. In the numerical study conducted by Bailly et al. (2012), the wind speed at the height of the wall was defined depending on the wind speed at 10m. Based on their simulation results, they claimed that the measurement of building airtightness could be valid when wind speed is lower than 8m/s, which has not been well stated in ISO 9972 standard. Another issue is that the wind speed is usually measured only before and after the test, while the variation in wind speed during testing is ignored. The wind blowing directly at the blower door during the test could also cause the error in measurement results. Mean wind velocity is commonly used for investigating the effect of wind condition on building airtightness measurement. For example, Kraniotis et al. (2014a) used an ultrasonic anemometer to monitor outdoor wind characteristics, such as the direction angle and the instantaneous velocity and they carried out seven measurements with mean wind speed ranging from 2.9m/s to 5.3m/s. Carrié and Leprince (2016) studied the uncertainties in building pressurisation tests by focusing on only steady wind model error stemming from the heterogeneous pressure distribution around the building. They used mean wind speed at the building level ranging from 0 to 10m/s for simulation with both one-point and two-point methods. The results demonstrated that the uncertainty caused by wind effect on the estimated airflow rate is relatively small at the high-pressure point, but significant big at a low-pressure point.

Most of the investigations addressing wind impact on building airtightness measurement have been conducted for fan pressurisation testing, while limited studies related to the test performance of the Pulse technique under different wind conditions have been found in the literature. It was reported by Cooper et al. (2016) that seasonal changes in the environmental conditions produced testing repeatability of ±8% in repeated tests to a detached house over a year time. On the other hand, Zheng et al. (2018) conducted a repeatability assessment to the Pulse testing by using a multi-gear portable trailer fan to provide various artificially imposed steady wind conditions. They found that a small uncertainty (within ±3%) was obtained when the wind speed was below 3.5m/s. However, the uncertainty increased up to ±25.6% as the wind speed in the range of 4.5-9m/s. Furthermore, currently no relevant standards or regulations concerning wind condition for the Pulse test are in place.

4.4. Wind fluctuations

It has been noted in natural ventilation studies that unsteady wind is identified as a factor of uncertainty towards an accurate estimation of air exchanges (Etheridge, 1999). Researches have been found in the literature to assess the associated impact of wind fluctuations on natural ventilation. Table 4 presents a list of some research work with their main findings. For most of the existing literature in the field of building airtightness, a steady wind condition has been commonly considered or assumed in the numerical studies, and low wind speed condition is preferred for experimental work. In addition, wind fluctuations, for instance, gust frequency have not been widely considered for evaluation. In practice, building airtightness measurements could be conducted under unsteady wind condition, rather than only at very low wind speed in the same direction. It has been found that the wind fluctuations could result in noticeable uncertainties because the measured pressure and airflow vary during the testing period.

Kraniotis (2014) developed a multivariate model considering the wind speed, direction, gustiness and gust strength to estimate the infiltration rates of a building and to provide a better understanding of the wind effect. His results demonstrate that the steady-state wind characteristics are not precise enough to describe neither the dynamic behaviour of air infiltration nor the dynamics of indoors airflow. He found that wind gustiness has a key role in calculating the air infiltration rate. Along with other wind characteristics, like speed and direction, gusts have the potential of governing the resultant air exchanges that take place across the leakage paths of the building envelope. The research is limited to low-rise buildings. The leakage distribution and rate that correlates with unsteady wind phenomena have not been identified, and more measurements of leakage rates in buildings could be conducted to provide a better understanding of air infiltration under natural conditions. Kraniotis et al. (2013) studied numerically the impact of wind direction and wind gust frequency in a cross-infiltrated single-compartment building. A parametrical study of the external leakage distribution was carried out and finally linked to wind gustiness based on CFD transient analysis. It has been seen that high wind gust frequency increases the estimation uncertainty of the building infiltration rate. In addition, when the gust frequency is high, even the oblique angles could result in relatively high leakage rates. They also pointed out that the location of leakage paths and distribution on the building envelope is another factor causing air exchange rate variations, especially under more severe wind gust conditions. However, the study only accounts for two scenarios of wind gust frequency (i.e. Ω_{high}=0.5Hz and Ω_{low}=0.1Hz) and five angles of wind direction; it may not be precise enough to reflect the exact climatic condition. In another study conducted by Kraniotis et al. (2014a), tracer gas techniques were employed to calculate the infiltration rates of a room and the dynamic wind characteristics were analysed in the frequency domain (i.e. spectral analysis and Fast Fourier Transform). A good agreement was observed with the numerical simulation of Kraniotis et al. (2013), that high wind fluctuations frequency leads to the potential of higher air change rate. Based on the review, it can be noted that studies on the effect of wind fluctuations are still needed; for instance, comprehensive investigations on various wind conditions using both blower door and Pulse testing.

Table 4: Researches on the impact of wind fluctuations on natural ventilation

Authors	Key Findings
Cockroft and Robertson (1976)	The ventilation of an enclosure with a single opening subjected to a turbulent impinging airstream was studied through a theoretical pulsation flow model. The simulation provided an indication of the magnitudes of ventilating airflows, which may be generated by turbulent wind. They mentioned that the turbulent nature of wind causes diffusion of air through openings and cracks in the building envelope.
Phaff and De Gidds (1980)	An empirical correlation to predict the ventilation rate across an opening or a crack was provided by considering both buoyancy forces and wind phenomena. Their results imply that the fluctuating wind is only represented by an additional pressure drop as a function of the flow exponent *n*.
Ethridge and Alexander (1980)	An air infiltration predictive model for multi-cell buildings was developed to evaluate the impact of wind fluctuation. Based on their obtained data, they thought that additional ventilation resulted from turbulence only occurs when the fluctuations are large enough to cause flow reversal, and they also proposed an additional term to quantify the occurrences of large mean pressures.
Sasaki et al. (1987)	Their results indicate that the fluctuation of the airflow through the cracks could be influenced not only by the static resistance of the crack but also by the crack depth, the air volume behind the crack, and the wind fluctuations. However, the computation requirement for solving linear differential equations might restrict the practical application of the model.
Crommelin and Vrins (1988)	Work was conducted using a scale model in a wind tunnel to predict the ventilation rate through a single opening using N_2O as a tracer gas. Empirical coefficients to calculate the isothermal ventilation caused by the wind and the turbulence in the tunnel were derived.
Haghighat et al. (1991)	A power spectrum analysis linearization technique was adopted to model pulsating airflow due to turbulent wind-induced pressures. The concept of aerodynamic admittance functions was employed to modify the wind pressure spectra for deriving the average fluctuating wind pressure over an opening.
Dascalaki et al. (1995)	A correction factor for enhancing the existing ventilation work was proposed on the basis of the Grashof and Reynolds numbers, by taking into account the dynamic characteristics of wind.
Etheridge (2000b), (Etheridge, 2000a)	They presented numerical results of the effect of unsteady wind pressures on the instantaneous flow rates in certain types of purpose-designed naturally ventilated buildings. Their data show that inertia reduces the occurrence of flow reversal and may impede the reestablishment of the correct flow when a reversal is formed by some hysteresis effect.
Miguel et al. (2001)	Details were described for air infiltration in enclosed space. The momentum equation was established for a mathematical model to characterise air infiltration induced by fluctuating pressures. It is proved that their method can be used for simulating enclosures with a porous material (ventilation filters or screens) and apertures. Their experimental data validated the developed method.
Wang and Chen (2012)	An empirical model was developed for estimating the mean and the fluctuating ventilation rate of wind-driven natural ventilation. The simulation data show that the ventilation rate and wind velocity are linearly correlated.
Ai and Mak (2014)	A large eddy simulation (LES) model combined with the tracer gas concentration decay method was used to assess the fluctuating ventilation characteristics through a single opening under different wind directions. Based on their results, they pointed out that for windward ventilation, the velocity and pressure fields around the opening are relatively stable in terms of windward ventilation, which limits turbulence diffusion across the opening, while for lateral ventilation, the velocity and pressure fields are very unsteady. It indicates that wind direction greatly affects the airflow exchange at a single opening.

Authors	Key Findings
Mahrt et al. (2015)	The dependence of turbulence quantities on the wind speed and stability was examined with nocturnal data. A good agreement with previous studies was found, the turbulent velocities increase slowly with wind speed until the wind speed increases to a transition and then increase more rapidly with further increase in wind speed. The data also show that the impact of stratification is relatively small for the weakest winds. Owing to the influence of stratification and site-dependent non-stationarity in the weak-wind regime, the relationship between the turbulence and the wind speed cannot be regarded as universal.
Antoniou et al. (2017)	New ventilation indicated, namely, air delay was introduced to describe the outdoor urban ventilation. CFD simulations using Reynolds-Averaged Navier-Stokes (RANS) and Large Eddy Simulation (LES) approaches were conducted for ventilation simulation in a dense district and comparison was given between two approaches. Simulation results demonstrate that the LES is more capable of accurately predicting the mean wind speed and turbulence intensity in a complex urban area.

5. CONCLUSION

As building infiltration accounts a significant amount of total building consumption, airtightness is a critical aspect to consider for energy efficient buildings. In many countries, building airtightness testing has been mandatory for building standards. Extensive studies on building airtightness measurement have been carried out either through experimental or numerical work, from different perspectives, such as improvement in the measurement technique with associated accuracy, and addressing uncertainties resulting from various sources. The fact is that air infiltration of a building is a complex process under variable climatic conditions, and the building airtightness could be influenced by the outdoor wind condition. A number of studies have been found in the literature considering the wind effect on measuring building airtightness and solutions have been proposed to minimise the wind effect. Most studies focus on calm or steady wind characteristics, which may be inadequate to fully describe the dynamic behaviour of air infiltration or the dynamics of indoors airflow. In such a way, an incomplete image of the real energy consumption of a building may be provided by neglecting the dynamic characteristics of wind and infiltration. On the other hand, the effect of the unsteady wind condition has been discussed through simulation and experimental tests. However, there is still a need to clarify the role of the wind fluctuations with investigations of the local building dynamic phenomena to find the leakage magnitude and distribution. In terms of test methods, more considerations have been given to pressurisation tests using a blower door, while limited attention has been paid to the novel Pulse technique. It is of necessity to investigate the wind effect on building airtightness measurement more comprehensively using both blower door and Pulse technique and under variable wind conditions. Furthermore, this could contribute to a more comprehensive evaluation of the uncertainty of measurement of building airtightness with blower door and Pulse testing. Improvements in protocols that are used to characterise building airtightness measurement can also be realised with the inclusion of consideration of wind effect.

6. REFERENCES

Ai, Z. & Mak, C. 2014. Analysis of fluctuating characteristics of wind-induced airflow through a single opening using LES modeling and the tracer gas technique. *Building and environment,* 80**,** 249-258.

Andrews, J. 1997. Error analysis for duct leakage tests in ASHRAE Standard 152P. Brookhaven National Lab., Upton, NY (United States).

Antoniou, N., Montazeri, H., Wigo, H., Neophytou, M. K. A., Blocken, B. & Sandberg, M. 2017. CFD and wind-tunnel analysis of outdoor ventilation in a real compact heterogeneous urban area: Evaluation using “air delay”. *Building and Environment,* 126**,** 355-372.

Bailly, A., Leprince, V., Guyot, G., Carrié, F. & El Mankibi, M. Numerical evaluation of airtightness measurement protocols. 33rd AIVC Conference" Optimising Ventilative Cooling and Airtightness for [Nearly] Zero-Energy Buildings, IAQ and Comfort", Copenhagen, Denmark, 2012. 252-255.

British Standards Institute 2015. *BS EN ISO 9972: Thermal performance of buildings - Determination of air permeability of buildings - Fan pressurization method*, British Standards Institute.

Carrié, F. R. & Leprince, V. 2016. Uncertainties in building pressurisation tests due to steady wind. *Energy and Buildings,* 116**,** 656-665.

Carrié, F. R. & Rosenthal, B. 2008. An overview of national trends in envelope and ductwork airtightness. *Ventilation Information Paper,* 29.

Charrier, S., Bailly, A. & Carrié, F. R. 2015. Building airtightness in france: Regulatory context, control procedures, results France: Qualicheck.

Chen, S., Levine, M. D., Li, H., Yowargana, P. & Xie, L. 2012. Measured air tightness performance of residential buildings in North China and its influence on district space heating energy use. *Energy and buildings,* 51**,** 157-164.

Cockroft, J. & Robertson, P. 1976. Ventilation of an enclosure through a single opening. *Building and Environment,* 11**,** 29-35.

Cooper, E. & Etheridge, D. 2007. Determining the adventitious leakage of buildings at low pressure. Part 1: uncertainties. *Building Services Engineering Research and Technology,* 28**,** 71-80.

Cooper, E., Zheng, X., Gillot, M., Riffat, S. & Zu, Y. A nozzle pulse pressurisation technique for measurement of building leakage at low pressure. 35th AIVC conference, Poznan, September 2014, 2014.

Cooper, E., Zheng, X., Wood, C., Gillot, M., Tetlow, D., Riffat, S. & De Simon, L. 2016. Field trialling of a pulse airtightness tester in a range of UK homes. *International Journal of Ventilation***,** 1-18.

Crommelin, R. & Vrins, E. 1988. Ventilation through a single opening in a scale model. *Air Infiltration Review,* 9**,** 11-15.

Dascalaki, E., Santamouris, M., Argiriou, A., Helmis, C., Asimakopoulos, D., Papadopoulos, K. & Soilemes, A. 1995. Predicting single sided natural ventilation rates in buildings. *Solar Energy,* 55**,** 327-341.

Department for Business, E.I.S. 2018. Energy Consumption in the UK. *In:* Department for Business, E.I.S. (ed.).

Erhorn-Kluttig, H., Erhorn, H., Lahmidi, H. & Anderson, R. 2009. Airtightness requirements for high performance building envelopes. *ASIEPI European Project, Report P,* 157**,** 05.03.

Etheridge, D. Unsteady wind effects in natural ventilation design. Proceedings of the CIBSE National Conference, Harrogate, UK, 1999. 4-5.

Etheridge, D. 2000a. Unsteady flow effects due to fluctuating wind pressures in natural ventilation design—instantaneous flow rates. *Building and Environment,* 35**,** 321-337.

Etheridge, D. 2000b. Unsteady flow effects due to fluctuating wind pressures in natural ventilation design—mean flow rates. *Building and Environment,* 35**,** 111-133.

Etheridge, D. W. & Sandberg, M. 1996. *Building ventilation: theory and measurement*, John Wiley & Sons Chichester, UK.

Ethridge, D. & Alexander, D. 1980. British Gas multi-cell model for calculating ventilation. *ASHRAE Trans.;(United States),* 86.

Geissler, A. Error Estimation of blower door measurements by computer simulation. The 8th International Conference on Indoor Air Quality and Climate, 1999.

Guyot, G., Carrié, R., Schild, P., Thomsen, K. E., Rose, J. & Aggerholm, S. 2010. Stimulation of good building and ductwork airtightness through EPBD.

Haghighat, F., Brohus, H. & Rao, J. 2000. Modelling air infiltration due to wind fluctuations—a review. *Building and Environment,* 35**,** 377-385.

Haghighat, F., Rao, J. & Fazio, P. 1991. The influence of turbulent wind on air change rates—a modelling approach. *Building and environment,* 26**,** 95-109.

Han, G., Srebric, J. & Enache-Pommer, E. 2015. Different modeling strategies of infiltration rates for an office building to improve accuracy of building energy simulations. *Energy and Buildings,* 86**,** 288-295.

Holøs, S. B. & Relander, T.-O. Airtightness measurements of wood frame low energy row houses. Proceedings: BEST conference. Portland, 2010.

Hunt, C. M., King, J. & Trechsel, H. R. 1980. *Building air change rate and infiltration measurements*, ASTM International.

ISO 2015. *BS EN ISO 9972: Thermal performance of buildings - Determination of air permeability of buildings - Fan pressurization method*, British Standards Institute.

Janssens, A. & Hens, H. 2003. Interstitial condensation due to air leakage: a sensitivity analysis. *Journal of Thermal Envelope and Building Science,* 27**,** 15-29.

Kraniotis, D. 2014. *Dynamic characteristics of wind-driven air infiltration in buildings. The impact of wind gusts under unsteady wind conditions.* Norwegian University of Life Sciences.

Kraniotis, D., Aurlien, T. & Thiis, T. 2014a. Investigating instantaneous wind-driven infiltration rates using the CO2 concentration decay method. *International Journal of Ventilation,* 13**,** 111-124.

Kraniotis, D., Thiis, T. K. & Aurlien, T. Wind direction and leakage distribution in buildings. A CFD transient analysis of their impact on air exchange rates under unsteady wind conditions. 6th European-African conference on wind engineering (EACWE 2013), 2013.

Kraniotis, D., Thiis, T. K. & Aurlien, T. 2014b. A numerical study on the impact of wind gust frequency on air exchanges in buildings with variable external and internal leakages. *Buildings,* 4**,** 27-42.

Kronvall, J. 1978. Testing of houses for air leakage using a pressure method. *ASHRAE transactions,* 84**,** 72-9.

Leprince, V. & Carrié, F. R. 2018. Uncertainties due to steady wind in building pressurisation tests. *REHVA Journal,* 03**,** 53-57.

Leprince, V., Moujalled, B. & Litvak, A. 2017. *Durability of building airtightness, review and analysis of existing studies*.

Lerma, C., Barreira, E. & Almeida, R. M. S. F. 2018. A discussion concerning active infrared thermography in the evaluation of buildings air infiltration. *Energy and Buildings,* 168**,** 56-66.

Lstiburek, J., Pressnail, K. & Timusk, J. 2002. Air pressure and building envelopes. *Journal of Thermal Envelope and Building Science,* 26**,** 53-91.

Mahrt, L., Sun, J. & Stauffer, D. 2015. Dependence of turbulent velocities on wind speed and stratification. *Boundary-Layer Meteorology,* 155**,** 55-71.

Mao, J., Yang, W. & Gao, N. 2015. The transport of gaseous pollutants due to stack and wind effect in high-rise residential buildings. *Building and Environment,* 94**,** 543-557.

Mélois, A. B., Carrié, F. R., Mankibi, M. E. & Moujalled, B. 2018. Wind Speed in Building Airtightness Test Protocols: A Review. *39th AIVC - 7th TightVent & 5th venticool Conference Smart ventilation for buildings.* Antibes Juan-Les-Pins, France.

Miguel, A., Van De Braak, N., Silva, A. & Bot, G. 2001. Wind-induced airflow through permeable materials part I: the motion equation. *Journal of wind engineering and industrial aerodynamics,* 89**,** 45-57.

Modera, M. P. & Wilson, D. J. 1990. The effects of wind on residential building leakage measurements. *Air change rate and airtightness in buildings.* ASTM International.

Nevander, L. E. K., J. 1978. Airtightness of buildings - Research in Sweden. *IEA Seminar on R&D projects in the area of infiltration in buildings.* Paris, France.

Phaff, H. & De Gidds, W. 1980. Building ventilation, investigation of the consequence of opening one window on the internal climate of a room. *IMG-TNO Report C,* 448.

Santamouris, M. & Wouters, P. 2006. *Building ventilation: the state of the art*, Routledge.

Sasaki, T., Hayashi, M. & Aratani, N. On the ventilating characteristics of the space under the fluctuating wind pressure. Proceedings of ROOMVENT, 1987.

Sherman, M. & Palmiter, L. 1995. Uncertainties in fan pressurization measurements. *Airflow performance of building envelopes, components, and systems.* ASTM International.

Stabile, L., Dell'isola, M., Frattolillo, A., Massimo, A. & Russi, A. 2016. Effect of natural ventilation and manual airing on indoor air quality in naturally ventilated Italian classrooms. *Building and Environment,* 98**,** 180-189.

Vinha, J., Manelius, E., Korpi, M., Salminen, K., Kurnitski, J., Kiviste, M. & Laukkarinen, A. 2015. Airtightness of residential buildings in Finland. *Building and Environment,* 93**,** 128-140.

Walker, I., Sherman, M. H., Joh, J. & Chan, W. 2013. Applying Large Datasets to Developing a Better Understanding of Air Leakage Measurement in Homes. *International Journal of Ventilation,* 11**,** 323-338.

Wang, H. & Chen, Q. 2012. A new empirical model for predicting single-sided, wind-driven natural ventilation in buildings. *Energy and Buildings,* 54**,** 386-394.

Wang, Z., Xue, Q., Ji, Y. & Yu, Z. 2018. Indoor environment quality in a low-energy residential building in winter in Harbin. *Building and Environment,* 135**,** 194-201.

Wu, Y., Niu, J. & Liu, X. Air infiltration induced inter-unit dispersion and infectious risk assessment in a high-rise residential building. Building Simulation, 2018. Springer, 193-202.

Zheng, X., Cooper, E., Mazzon, J., Wallis, I. & Wood, C. J. A comparison study of the blower door and novel pulse technique on measuring enclosure airtightness in a controlled environment. 38th AIVC - 6th TightVent & 4th venticool Conference, 2017, 13-14 Sept 2017 Nottingham, UK.

Zheng, X., Cooper, E., Mazzon, J., Wallis, I. & Wood, C. J. 2019a. Experimental insights into the airtightness measurement of a house-sized chamber in a sheltered environment using blower door and pulse methods. *Building and Environment*.

Zheng, X., Mazzon, J., Wallis, I. & WooD, C. J. Experimental study of enclosure airtightness of an outdoor chamber using the pulse technique and blower door method under various leakage and wind conditions. 39th AIVC - 7th TightVent & 5th venticool Conference, 18-19 September 2018 2018 Antibes Juan-Les-Pins. 352-362.

Zheng, X. F., Cooper, E., Zu, Y. Q., Gillott, M., Tetlow, D., Riffat, S. & WooD, C. J. 2019b. Experimental Studies of a Pulse Pressurisation Technique for Measuring Building Airtightness. *Future Cities and Environment,* 5(1)**,** 10.

#224: Matching Gompertz and Logistic models to Monod single substrate model

Khunakon PHAYUNGPHAN[1,2], Laddawan NOYNOO[1], Chairat SIRIPATANA[1,2], Nirattisai RAKMAK[1,2] AND Archw PROMRAKSA[*,1,2]

[1] School of Engineering and Resources, Walailak University, 80161, Nakhon Si Thammarat, Thailand.
[2] Biomass and Oil-Palm Excellence Center, Walailak University, 80161, Nakhon Si Thammarat, Thailand.
*Corresponding author: archw.pr@wu.ac.th

In anaerobic digestion, many experimental results are represented by traditional form of kinetic models such as Gompertz and Logistic equations. They are derived to use as empirical representation of biogas/methane/hydrogen accumulation data. These models normally fit the anaerobic biogas evolution (ABE) curve very well. However, these parameters cannot be used directly for design operation and optimisation of the processes. Most researchers and biochemical engineers prefer to use the Monod approach to deal with designed problems because of its flexibility and well-proven industrial practices. The purpose of this work is to utilise large amount of biogas data which has been represented in Gompertz-type models for design, operation and optimisation purposes. However, it is difficult to match Gompertz or Logistic models to Monod single substrate model because their parameters have complicated interpretation and each parameter can affect more than one shape characteristic of the curve. Secondly, fitting the ABE data to the original or modified form of Gompertz and Logistic models will create initial value error that is at zero-time biogas is not zero. Thirdly, although we can avoid initial value error by using their corresponding corrected forms, the fitting process becomes more complicated because of extra-model parameter. The problem can be solved by using the corrected form of unified Gompertz (U-Gompertz) model or unified Logistic (U-Logistic) model. Therefore, in this work we propose to use U-Gompertz and U-Logistic models, and match them to a Monod-type models so that Gompertz-type parameters are converted to Monod-type parameters. We illustrated that U-Gompertz and U-Logistic models facilitate parameters matching because each parameter in these unified models affects only one shape characteristic of the curve. In this way, it is easy to choose four fixed points based on these U-form parameters and the curve fitting process is simplified. We illustrated the matching process with some published data successfully. This article shows that it is possible to use large amount of ABE data published in the literatures by this matching approach.

Keywords: Gompertz-Monod matching; accumulative biogas evolution; unified Gompertz and unified logistic models; Monod-type models; modified Gompertz and modified logistic models

1. INTRODUCTION

Gompertz-type or Logistic-type are empirical models to represent biogas/methane/hydrogen accumulation data which then extended or generalised/unified by many authors. Tsoularis and Wallace (2002) reviewed and compared many growth models and proposed a generalised form of logistic model with its several properties. This unified model covers many sigmoid models including exponential, generalised von Bertalanffy, Richards, Smith, Blumberg, hyperbolic and Gompertz growth models. Richards model is one of a unified Gompertz-type which has received special interest by many researchers (Tjørve and Tjørve, 2010). It covers the negative exponential, logistic, Bertalanffy and Gompertz models. Recently, Tjørve and Tjørve (2017) developed a family of Unified growth models (called U-models) which includes U-versions of the logistic, Gompertz and von Bertalanffy models. They claimed that the unified model uses the same set of three parameters, making comparison between the sub-models directly possible and easy. In addition, they presented the model in two forms: the first where one parameter describes the time of inflection and the second where one parameter indicates the starting point of the curves. Fitting the ABE data to any the original or modified forms of Gompertz and Logistic models will create initial value error that is at zero-time biogas is not zero. We can avoid initial value error by using their corresponding corrected forms. However, the fitting process becomes more complicated because an extra-model parameter introduced to satisfy the initial condition. In this article we propose a corrected form of Gompertz-type model which did not increase the number of parameter while solving the initial value problem.

Traditionally, in biochemical methane potential (BMP), specific methane acitivity (SMA) assays or similar batch experiments many researchers tended to represent accumulative biogas (ABE) (or methane, H_2) using some forms of Gompertz-type equation, most probably “the modified Gompertz equation”. This practice helps to estimate BMP or SMA in less subjective manner. However, Gompertz-type kinetic models are limited to batch AD and cannot be easily adapted or extended to different configurations. For the purposes of design, operation, control and optimisation of AD processes, Monod-type kinetics are normally used in practices. Therefore it is desirable to convert Gompertz-type parameters into the corresponding Monod-type parameters if large amount of BMP data available in the literature is to be available for AD design and operational purposes. Due to some difficulties to match Gompertz or Logistic models to Monod single substrate model. In this article, we propose to use parameters matching between U-Gompertz or U-Logistic models and Monod single substrate model that is more directly interpretation and easier than the use of the traditional models. In the following section, unified forms of Gompertz and Logistic models will be developed to point out weakness of the traditional forms in parameter matching and how the U-forms will be more effective way for matching to Monod single substrate.

2. MODEL DEVOLOPMENT

2.1. The Gompertz-type models

The modified form of Gompertz model which takes the following form.

Equation 1:

$$P_0' = \left(P_\infty + P_0'\right)\exp\left(-\exp\left(\left(R_m e / \left(P_\infty + P_0'\right)\right)\lambda + 1\right)\right)$$

Where: $\lambda = \alpha^{-1}\ln(\delta - 1)$, $R_m = P_\infty \alpha / e$ and $\delta = \mu_0 / \alpha$

Here P and P_∞ are accumulated methane and a specific time and at sufficiently long time respectively. R_m is a maximum methane production rate (mL/day) in a specific batch AD. lag time (λ) in lag phase (day). μ_0 and α are the initial (t = 0) specific growth rate (day^{-1}) and rate of growth rate reduction (day^{-1}) respectively. Unfortunately, Equation 1 does not valid for t = 0 because $\lim_{t\to 0} P \neq 0$ (Siripatana et al., 2016; Zhu, 2017) and in fact

Equation 2:

$$\lim_{t\to 0} P = P_\infty \exp(-\delta) \neq 0 \text{ or } P_0 / P_\infty = \exp(-\delta)$$

Where: P_0 is the equivalent (non-observable) biogas generated before starting digestion process (t < 0). To solve invalid initial condition, Siripatana et al. (2016) reformulate Schnute postulation and arrived at a corrected form of Gompertz equation as follows.

Equation 3:

$$\left(P + P_0'\right) / \left(P_\infty + P_0'\right) = \exp\left(-\exp\left(\left(R_m e / \left(P_\infty + P_0'\right)\right)(\lambda - t)\right) + 1\right)$$

Equation 4:

$$\lambda = \alpha^{-1}\ln(\delta - 1),\ R_m = \left(P_\infty + P_0'\right)\alpha / e,\ \alpha = R_m e / \left(P_\infty + P_0'\right) \text{ and } \delta = 1 + \exp(\lambda\alpha)$$

P_0' is hypothetical amount of biogas associated with the initial inoculum-substrate pair which was generated before starting the new digestion process (t < 0). It is related to the initial amount of active microorganisms involved in the AD process. However, as in most BMP tests, the initial amount of active microbes is not assayed and only ABE curves are the complete one. The other variable such as initial and final COD, VS, VFA, pH, alkalinity are supplementary albeit essential ones. If the biomass and product (biogas) yield coefficients (Y_{XS}, Y_{PS}) can be assumed constant, the initial cell biomass can be estimated from the following relation.

Equation 5:

$$X_0 = Y_{XS}P_0' / Y_{PS} \text{ and } X=P'/Y_{PX} = (P+P_0')/Y_{PX} \text{ or } P = P_0' + Y_{PX}X$$

Here, the equivalent biogas generated by X is defined as $P = P + P_0'$. However, although very useful for interpretation, this relation is only hypothetical because we did not observe how microbial consortia had evolved before we start the batch AD experiments. Thus, P_0 or the estimated X_0 should be interpreted as initial microbial activity rather than the actual microbial density at the initial time of AD process. In general, high P_0 (or high X_0) indicates high initial microbial activity which can be translated as relatively high microbial density and vice versa.

The corrected Gompertz model are still three since P_0 is related to P_∞ by the following relation.

Equation 6:

$$P_0' = (P_\infty + P_0')\exp\left(-\exp\left((R_m e/(P_\infty + P_0'))\lambda + 1\right)\right)$$

Unfortunately, the Equation (6) is not explicit in either P_0' or P_∞. Later in this article we will show that in original form the relationship between P_0' and P_∞ is explicit (Equation 7 – 8) and we recommend using that original form. If R_m and λ are required, it can be calculated by Equation 8.

One complaint about modified forms of Gompertz equation (e.g. Equation 1 and 3) is related to the time lag which appear frequently to have slightly negative values when the biogas is produced immediately without a lag period (Zhu, 2017). Negative time-lag in these cases is not abnormal or invalidate the models but it indicates that there is an initial imbalance between the highly active microbes and insufficient amount of substrate available when the AD process starts. Negative time-lag thus implies overuse of inoculum/seed which is intended in normal BMP assay to ensure the maximum possible biogas-generation rate to occur. This maximum possible biogas-generation rate is one important aspect of BMP tests particularly if the design parameters are to be estimated.

According to the authors' opinion, the corrected form of the modified Gompertz model is parsimonious and should be used for representing normal ABE curves obtained from batch AD experiments. All of four parameters has direct physical/biological meaning and easily estimated

Gompertz model as a special case of Schnute model

Follow the famous Schnute's postulates (Schnute, 2011), corrected and explicit form of Gompertz can be written as follows to have the Gompertz equation which satisfies the condition (t=0 then P=0).

Equation 7:

$$P' = P + P_0' = P_\infty' \exp\left[-\exp\left((R_m.e/P_\infty')(\lambda - t) + 1\right)\right]$$

And the maximum biogas production rate (R_m) and the lag-time (λ) can be calculated from the following equations.

Equation 8:

$$R_m = \left(P_\infty \alpha / e\right)\left(1 + \left[1/\left(\exp(\delta) - 1\right)\right]\right) \text{ and } \lambda = \left(1/\alpha\right)\ln(\delta - 1)$$

Logistic model as a special case of Schnute model

Recently, there have been many interests to use the logistic model (Noynoo et al., n.d.; Zaher et al., 2009). In this article we prefer to describe ABE data and to predict BMP of each set of batch data by using Equation 9 as follows because it provides the easily interpretative parameters like P_∞, Rm, λ and P_0.

Equation 9:

$$P'(t) = P + P_0' = \left(P_\infty + P_0'\right)/\left[1 + \exp\left(\left(4R_m/(P_\infty + P_0')\right)(\lambda - t) + 2\right)\right]$$

Terms of R_m and λ were re-parameterised as given by (Zwietering et al., 1990) to have the following relations:

Equation 10: $$\alpha = 4R_m / P'_\infty, R_m = \alpha P'_\infty / 4, \gamma = \exp\left[\left(4R_m\lambda / P'_\infty\right) + 2\right] \text{ and } \lambda = \left(P'_\infty / 4R_m\right)(\ln(\gamma) - 2)$$

Gompertz and logistic models in recently-developed unified forms

The U-family or Unified-family models are other ways to look at the traditional sigmoidal models (e.g. Gompertz, logistic, Schnute and von Bertallanffy models). Most of traditional sigmoidal models have been re-parameterised into different forms. However, many of these re-parameterizations are not very useful because their parameters affect more than one shape characteristics, resulting in the difficulty to compare the same parameters in different models. Moreover, each parameter cannot be interpreted explicitly because of its compounded nature (Tjørve and Tjørve, 2017). Many researches realised this problem and they tried to solve it by re-parameterization. Recently, Tjørve and Tjørve (2017) proposed an efficient re-parameterization of Richards model called Unified-Richards (U-Richards) model which is written as

Equation 11: $$W = A\left(1 + (d-1)\exp\left(-k_U(t - T_i) / d^{d/(1-d)}\right)\right)^{1/(1-d)}$$

Where: k_u is the relative maximum growth rate and other nomenclatures are summarised in Table 1.

Table 1: Symbols used in the U-family model (Tjørve and Tjørve, 2017) in the context of anaerobic digestion

Symbol	Meaning and interpretation
W	Variable representing growth, accumulative product $P' = P + P'_0$
t	Time variable, specific digestion time
A	Upper asymptote of W value, $W = P'_\infty$ in the context of anaerobic digestion
T_i	Time of inflection (t at which the reflection point occurs). It is a location parameter.
W_0	Starting value of W (initial condition). In the context of AD, $W_0 = P'_0$
k_u	Relative maximum growth rate. In the context of AD, it is the relative maximum biogas production rate.
d	Exponent of part of exponent which control the inflection value (d≠1 for Unified-Richards model; d→1, d ≠1 for Gompertz model; d ≠ -1 for Logistic model

From the unified-Richards model (Equation 11), setting d = -1, the following Unified-Logistic model is obtained.

Equation 12: $$P' = P + P'_0 = P'_\infty / \left[1 + \exp(-4k_U(t - T_i))\right]$$

And we can write P'_0 in terms of P_∞, k_u and T_i or T_i in terms of P_∞, k_u and P'_0as follow.

Equation 13: $$\theta = P'_0 / P_\infty = 1 / \exp(4k_U T_i) \text{ and } T_i = \left[\ln(1/\theta)\right] / 4k_U$$

In addition, comparing Equation 9 to Equation 12, the following relations are obtained.

Equation 14: $$k_U = R_m / (1+\theta)P_\infty \text{ and } T_i = R_m\lambda / (1+\theta)P_\infty + 0.5$$

In practice P'_0 is not observable whereas P_∞ is normally observed in batch AD experiments. Rewriting, Equation 12 in term of P_∞ instead of P'_∞, we obtain.

Equation 15: $$P = P' - P'_0 = P_\infty\left[(1+\theta) / (1 + \exp(-4k_U(t - T_i))) - \theta\right]$$

Equation 15 is a corrected and explicit forms of logistic model. for fitting ABE curves in term of P_∞ which is normally observable or can be projected from the data.

Again, from the unified-Richards model (Equation 11), by setting d → 1 resulting in the U-Gompertz model. That is,

Equation 16: $$P' = P + P'_0 = P'_\infty \exp(-\exp(-e\,k_U(t - T_i)))$$

Similarly, we can write P_0' in terms of P_∞, k_u and T_i or T_i in terms of P_∞, k_u and P_0' as follow.

Equation 17:
$$\theta = P_0'/P_\infty = 1/\left[\exp(\exp(e.k_U T_i)) - 1\right] \text{ and } T_i = \left[\ln\left(\ln\left((1+\theta)/\theta\right)\right)\right]/e.k_U$$

Equation 18:
$$P = P_\infty[(1+\theta)\exp(-\exp(-e.k_U(t-T_i))) - \theta]$$

Where:
$$k_U = R_m/P_\infty' = R_m/(1+\theta)P_\infty, T_i = \lambda + (1/e.k_U), R_m = k_U(1-\theta)P_\infty \text{ and } \lambda = T_i - (1/e.k_U)$$

In the context of fitting ABE curves, Equation 18 is most useful because it is a corrected form and P_0' does not appear in the model.

2.2. The Monod single substrate model

Monod kinetics was first proposed to describe the microbial growth. It was based on one-limiting-substrate assumption and sigmoidal growth-rate as a function of the concentration of the substrate. In the following sections, Monod-type models are referred to the class of mathematical model describing the microbial kinetics which make use of Monod's approach. However, in this section we will only one of the simplest cases of Monod-type model having only one limiting substrate without any kind of inhibition (or other effects do not show up explicitly in the model formulation). Based on assumption that cell yield and product yield are constant, we can write the following system of ordinary differential equations.

Equation 19:
$$dX'/dt = \mu X = \left[\mu_m S/(K_S + S)\right]X$$

Equation 20:
$$dX/dt = (\mu - k_d)X = \left[\left(\mu_m S/(K_S + S)\right) - k_d\right]X = \left[\left(\mu_m(S_0 Y_{PS} - P)/(K_S + S_0 Y_{PS} - P)\right) - k_d\right]X$$

The prime notation in X′ referred to the total accumulative microbes due to growth if there were no death. X is the concentration of active microbes (cell biomass) at a specific time. μ_m, μ are the maximum and the specific growth rate at a particular substrate concentration, k_d is the specific death rate, K_s is the Monod saturation constant. If we assume that all yield coefficients are constant and using the following definitions,

Equation 21:
$$Y_{PS} = \Delta P/\Delta S, Y_{X'S} = \Delta X'/\Delta S, Y_{PX'} = \Delta P/\Delta X' = PS/X'S \text{ and } P_0'/Y_{PS} = X_0'/Y_{X'S}$$

We can write the rate of substrate consumption and product formation as follow

Equation 22:
$$dS/dt = -(1/Y_{X'S})dX'/dt = -(\mu/Y_{X'S})X = -(1/Y_{X'S})\left[\mu_m S/(K_S + S)\right]X$$

Equation 23:
$$dP/dt = -Y_{PS}(dS/dt) = Y_{PX'}X\mu = Y_{PX'}X\left(\mu_m S/(K_S + S)\right) = Y_{PS}X\left[\mu_m(P_\infty - P)/(K_S Y_{PS} + P_\infty - P)\right]/Y_{X'S}$$

If no microbial death occurs during the AD process, solving Equation 20 to Equation 23, to obtain the following solution

Equation 24:
$$t = \left[(K_S/C)\ln(S_0(C-S)/S(C-S_0)) + \ln\left((C-S)/(C-S_0)\right)\right]/\mu_m$$

Where: $C = (X_0/Y_{X'S}) + S_0 = (X_0/Y_{X'S}) + (P_\infty/Y_{PS}) = (P_0' + P_\infty)/Y_{PS} = (P_\infty'/Y_{YS})$ or in term of P.

Equation 25:
$$t = \left[\left[K_S Y_{PS}/(P_\infty + P_0')\right]\ln\left(\left(P_\infty(P_0' + P)/P_0'(P_\infty - P)\right)\right) + \ln\left((P_0' + P)/P_0'\right)\right]/\mu_m$$

Notice that both analytical solutions are explicit in t but implicit in P, making more difficult to estimate the model parameters. However, if it appears that the cell biomass changes insignificantly as when the initial cell biomass is very high or growth rate and death rate are in balance, we can assume that the cell biomass is constant. In this case, the solution can be arranged explicitly in both t and P.

Equation 26:
$$t = Y_{XS}\left[K_S\ln(S_0/S) + S_0 - S\right]/\mu_m X_0 = Y_{PS}\left[K_S\ln\left(P_\infty/(P_\infty - P)\right) + (P/Y_{PS})\right]/\mu_m P_0'$$

Equation 27:
$$S = K_s W\left[(S_0/K_S)((-K_1 t + S_0)/K_S)\right]$$

Equation 28:

$$P = P_\infty - K_S Y_{PS} W\left[\left(P_\infty / K_S Y_{PS}\right)\exp\left(-\left(K_1 t - \left(P_\infty / Y_{PS}\right)\right)/K_S\right)\right]$$

Where: W is Lambert function and $K_1 = \mu_m X_0 / Y_{XS} = \mu_m P'_0 / Y_{PS}$

2.3. Contois models

Monod kinetics does not take into account the hindrance for substrate consumption due to high cell biomass concentration which suffer from mass transfer limitation. There are a few of models were proposed to address this problem and Contois models has been in a special attention. By using the same assumptions as the Monod model, the Contois model can be developed as following procedure.

Equation 29:

$$\mu = \mu_m S / \left[K_C\left(P + P'_0\right) + S\right] = \mu_m\left(P_\infty - P\right) / \left[K_C Y_{PS}\left(P + P'_0\right) + P_\infty - P\right]$$

Equation 30:

$$dP/dt = \mu_m\left(P_\infty - P\right)\left(P + P'_0\right) / \left[K_C Y_{PS}\left(P + P'_0\right) + P_\infty - P\right] = \mu_m / \left[\left(K_C Y_{PS} / \left(P_\infty - P\right)\right) + \left(1/\left(P + P'_0\right)\right)\right]$$

We obtain, after integration from (P = 0) to any P and arrangement.

Equation 31:

$$\left(K_C Y_{PS} / \mu_m\right)\ln\left(P_\infty / \left(P_\infty - P\right)\right) + \ln\left(\left(P + P'_0\right) / P'_0\right) / \mu_m = t$$

The prime notation in X is the concentration of active microbes (cell biomass) at a specific time. μ_m, μ are the maximum and the specific growth rate at a particular substrate concentration, K_c is the Contois saturation constant. If we assume that all yield coefficients are constant and using the following definitions,

Equation 32:

$$Y_{PS} = \Delta P / \Delta S, Y_{X'S} = \Delta X' / \Delta S, Y_{PX'} = \Delta P / \Delta X' = Y_{PS} / Y_{X'S} \text{ and } P'_0 / Y_{PS} = X'_0 / Y_{X'S}$$

3. METHODOLOGY

3.1. Matching Gompertz and logistic models to Monod-type single substrate model

Matching Gompertz or logistic models in their original form is possible but could be tricky for a few reasons. Firstly, fitting the ABE data to the original form of the modified forms of Gompertz and Logistic models will create initial value error (P(0) ≠ 0). Secondly, to avoid initial-value error their corresponding corrected forms (Equation 3 and Equation 9) must be used. However, we cannot write P'_∞ in term P_∞ explicitly. Thus, the curve fitting will become more complicated with one extra parameter (P'_0) unnecessarily. Alternatively, we can use Gompertz and Logistic models in their unified forms (Equation 12 and Equation 16). Consequently, we propose to use U-Gompertz and U-logistic model to perform parameter-matching with the Monod-family one-substrate model. Noting that Monod-family in this context includes Monod, Andrew, Haldane, many other extended forms as well as Contois kinetics.

It is important to note that simple Monod kinetics only fit well with logistic model, but, in general, fitting is not optimal for Gompertz model. Furthermore, we will illustrate that when the initial cell biomass concentration is high (indicated by no lag time of slightly negative time-lag (λ) when fitting ABE data with modified Gompertz model) Contois kinetics is preferred to describe AD kinetics in batch. However, no extensive investigation has not been performed and reported in the literature. So, this is not intended to be conclusive.

Matching U-Logistic models to the Monod model and U-Gompertz models to the Contois model

Firstly, we must make sure that U-Logistic model or U-Gompertz model does fit the ABE data well. In case that ABE data can fit Gompertz model well but not with Logistic model, it is better to try matching the resulting best-fit Gompertz parameters to Contois kinetics. In another case, ABE data can fit Logistic model well but not with Gompertz model, it is better to try matching the resulting best-fit Logistic parameters to Monod kinetics. The following steps are how the matching process proceeds in parallel of the two pair matching processes. Differences of utilised equations and parameters will be specified at some steps for different pair of matching.

1. Substituting Equation 13 for U-Logistic or Equation 17 for U-Gompertz, for θ to write θ in term of k_u and T_i. Then, the set of ABE data is fitted with U-Logistic or U-Gompertz model and the best-fit parameters (P_∞, k_u, T_i) of U-Logistic or U-Gompertz model are obtained.
2. Calculate θ from Equation (13) for U-Logistic or Equation 17 for U-Gompertz, and P'_0 is then calculated from $P'_0 = \theta P_\infty$.

3. Calculate Y_{PS} from P_∞ and $\Delta S_\infty = S_0 - S_\infty$ where S_0 and S_∞ are initial and final substrate concentration based on COD or VS. ($Y_{PS} = P_\infty/\Delta S_\infty$)
4. Choose a proper range of P for matching (eg. $0.5P_\infty < P < 0.95P_\infty$) and calculate time step (t_i) corresponding to the P-range.
5. Rewrite Equation 26 for U-Logistic or Equation (32) for U-Gompertz in the following form and solve for K_i

Equation 33:
$$t_i = K_i A_i + B_i / \mu_m$$

Equation 34:
$$\text{For i=1 to i=n; } K_i = (t_i - B_i / \mu_m)$$

Where: $A_i = 1/(P_\infty + P_0')\ln(P_\infty(P_0' + P_i)/P_0'(P_\infty - P_i))$, $B_i = \ln[(P_0' + P_i)/P_0']$ and $K_i = K_{S_i} Y_{PS} / \mu_m$ are defined for U-Logistic to Monod matching process or where: $A_i = \ln(P_\infty/(P_\infty - P_i))$, $B_i = \ln[(P_0' + P_i)/P_0']$ and $K_i = K_{S_i} Y_{PS} / \mu_m$ are defined for U-Gompertz to Contois matching process.

6. Searching for μ_m which satisfies the following criterion.

Equation 35:
$$\text{Relative difference } (\%) = \left|2(100)\left[(K_n - K_1)/(K_n + K_1)\right]\right| < 1$$

And a good estimated of K is $K_{est} = (K_n + K_1)/2$ and K_S is then calculated from $K_S = K_{est} Y_{PS}/\mu_m$

7. Substituting μ_m and K into Equation 33 for U-Logistic or U-Gompertz and, plotting P versus t using both U-Logistic and the corresponding matched Monod model on the same graph or plotting P versus t using both U-Gompertz and the corresponding matched Contois model on the same graph. The comparison of each two models matching process used to be satisfactory before the matched Monod or Contois model to be used for the design purpose.

4. RESULTS AND DISCUSSION

In this section, we use a data set obtained from anaerobic of palm oil mill effluent (POME). The experiments were carried out in batch mode. The inoculum/effluent ratio was 1:4. The physico-chemical characteristics of the effluents are summarised by Sangsri et al. (2019). In Figure 1, Unified Gompertz model was used to fit to biogas accumulation data from experiments by different amounts of POME. It is seen that the model is strongly represent all sets of the experimental data with very high accuracies. The fitting parameters are summarised in Table 2. Parameter matching between U-Gompertz model and Contois model (Monod single substrate model) had been done successfully in Figure 2. It is no doubt that converting parameters between the two different concepts are well accomplished due to overlapping of fitting lines from different models so we can use converted parameters summarised in Table 3 in the purposes of design and operation by Gompertz-Monod matching technique as well.

For more example to verify the matching model, the fitting parameters from U-Gompertz model were determined for methane accumulation data those were done by Sangsri et al. (2019) then summarised in Table 4 and the fitting parameters from U-Gompertz-Contois and Monod matching model are summarised in Table 5.

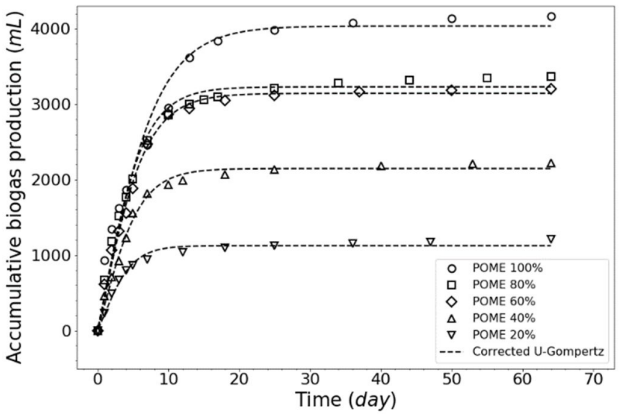

Figure 1: Biogas accumulation for Unified Gompertz model

Table 2: Parameters and the best-fit parameter (R^2) of cumulative biogas production for Unified Gompertz model

POME (%)	Parameter						
	P_∞ (mL)	T_i (d^{-1})	k_u (d^{-1})	α (d^{-1})	λ (d)	R_m (mL/d)	R^2
100	4037.5318	1	0.0813	0.22	0.97	195.83	0.9640
80	3230.7226	1	0.1115	0.30	0.96	234.91	0.9862
60	3144.1411	1	0.1051	0.28	0.96	211.72	0.9926
40	2147.0065	1	0.1212	0.33	0.95	173.86	0.9905
20	1125.6907	1	0.1578	0.43	0.94	128.85	0.9800

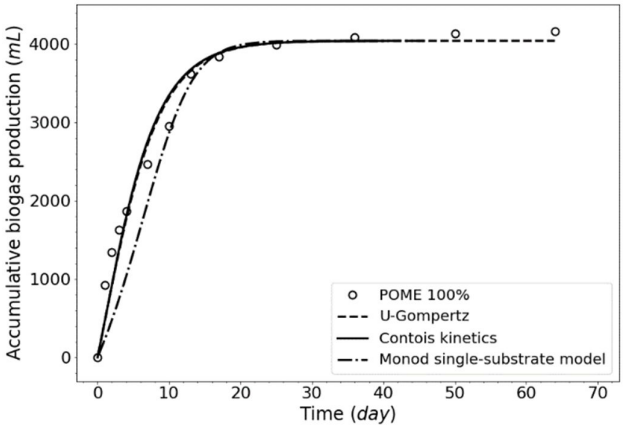

Figure 2: The fitting of Gompertz, Contois and Monod Matching

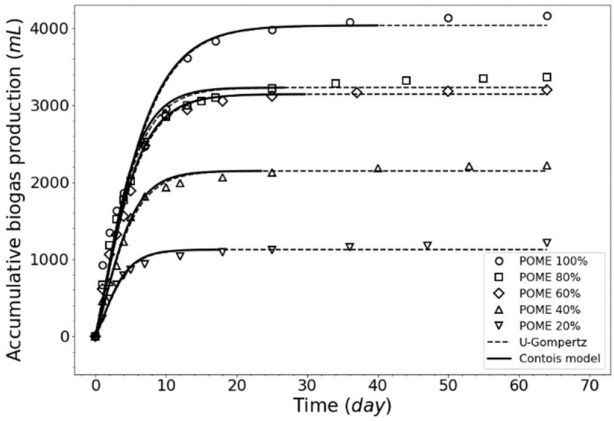

Figure 3: U-Gompertz and Contois matching

Table 3: Parameters of cumulative biogas production for U-Gompertz, Contois and Monod matching model

POME (%)	Parameter							
	θ	μ_0 (d)	P_0' (mL)	Y_{PS} (mL/ (mg_{COD}/L))	μ_{mc} (d^{-1})	K_C (mg/L)	μ_{ms} (d^{-1})	K_S (mg/L)
100	0.40	0.27	1627.44	0.0517	0.55	48.4081	0.27	14.5067
80	0.35	0.41	1124.05	0.0574	0.68	36.1267	0.39	13.0662
60	0.36	0.38	1129.52	0.0655	0.70	36.8204	0.35	11.4503
40	0.33	0.45	712.10	0.0490	0.75	43.1164	0.42	15.3061
20	0.27	0.65	308.65	0.0767	1.1	32.9140	0.55	9.7783

Table 4: Parameters and the best-fit parameter (R^2) of cumulative methane production for Unified Gompertz model

POME (%)	Parameter						
	P_∞ (mL)	T_i (d^{-1})	k_u (d^{-1})	α (d^{-1})	λ (d)	R_m (mL/d)	R^2
100	2104.7268	3.28	0.0622	0.16	0.97	103.33	0.9915
80	1524.6333	2.58	0.0872	0.23	0.96	107.90	0.9958
60	1657.1943	2.5	0.0927	0.25	0.96	125.99	0.9922
40	1122.1640	2.6	0.1239	0.34	0.95	125.13	0.9894
20	520.5838	0.42	0.1104	0.3	0.96	30.27	0.9833

Table 5: Parameters of cumulative methane production for U-Gompertz, Contois and Monod matching model

POME (%)	Parameter							
	θ	μ_0 (d)	P_0' (mL)	Y_{PS} (mL/ (mg_{COD}/L))	μ_{mc} (d^{-1})	K_C (mg/L)	μ_{ms} (d^{-1})	K_S (mg/L)
100	0.21	0.29	445.38	0.0270	0.55	138.2826	0.23	27.7778
80	0.19	0.43	286.54	0.0271	0.68	109.4471	0.32	27.6752
60	0.18	0.47	298.93	0.0345	0.7	79.8820	0.35	21.7391
40	0.1	0.81	111.93	0.0256	1.07	128.7236	0.51	29.2968
20	0.47	0.34	246.38	0.0355	1.1	119.1997	0.35	21.1267

In the same way, if we need to check that the biogas accumulation data from experiments by different amounts of POME from the same work (Sangsri et al., 2019) can also represent by Unified Logistic model. From the result Figure 4, successfully model fitting was done due to high accuracies for all different amounts of POME used. Fitting parameters from Unified Logistic model are summarised in Table 6. Parameters converting between U-Logistic model and Monod single substrate model was conducted by matching between the two models as shown in Figure 5. It is seen that the two models matching gives an excellent result as same as the Gompertz-Monod matching. The converted parameters in this match are summarised in Table 7 and they cloud be used in further AD process design problems.

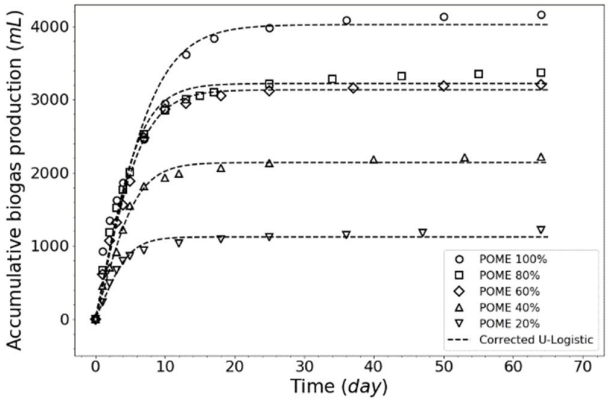

Figure 4: Biogas accumulation for Unified Logistic model

Table 6: Parameters and the best-fit parameter (R^2) of cumulative biogas production for Unified Logistic model

POME (%)	Parameter						
	P_∞ (mL)	T_i (d^{-1})	k_u (d^{-1})	α (d^{-1})	λ (d)	R_m (mL/d)	R^2
100	4024.2734	1	0.0623	0.38	16.06	445.93	0.9595
80	3219.0406	1	0.0863	0.34	11.59	474.33	0.9835
60	3133.9415	1	0.0811	0.32	12.33	437.89	0.9918
40	2139.1785	1	0.0938	0.38	10.67	338.37	0.9897
20	1122.8056	1	0.1218	0.49	8.22	220.56	0.9772

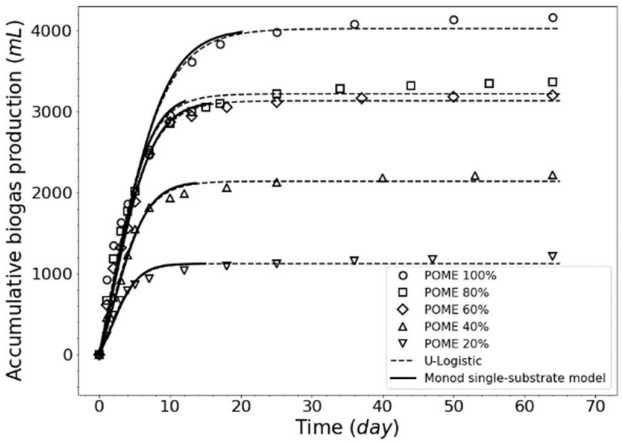

Figure 5: U-Logistic - Monod single substrate Matching

Table 7: Parameters of cumulative biogas production for U-Logistic - Monod single substrate Matching model

POME (%)	Parameter					
	θ	μ_0 (d)	P_0' (mL)	Y_{PS} (mL/ (mgCOD/L))	μ_{ms} (d^{-1})	K_S (mg/L)
100	0.78	0.39	3136.72	0.0515	0.7	14.5631
80	0.71	0.35	2279.63	0.0572	0.72	13.1119
60	0.72	0.33	2264.83	0.0652	0.80	11.5031
40	0.68	0.38	1470.09	0.0488	0.85	15.3689
20	0.61	0.49	689.40	0.0765	1.15	9.8039

For more example to verify the matching model, the fitting parameters from U-Logistic model were determined for methane accumulation data those were done by Sangsri et al. (2019) then summarised in Table 8 and the fitting parameters from U-Logistic-Monod matching model are summarised in Table 9.

Table 8: Parameters and the best-fit parameter (R^2) of cumulative methane production for Unified Logistic model

POME (%)	Parameter						
	P_∞ (mL)	T_i (d^{-1})	k_u (d^{-1})	α (d^{-1})	λ (d)	R_m (mL/d)	R^2
100	2096.2007	3.53	0.0488	0.19	72.31	153.74	0.9925
80	1522.6128	2.15	0.0637	0.25	33.81	153.13	0.9952
60	1637.3783	3.99	0.0946	0.38	42.15	189.23	0.9956
40	1110.4352	3.51	0.1215	0.48	28.91	159.40	0.9891
20	519.5496	0	0.0816	0.33	0.005	84.85	0.9841

Table 9: Parameters of cumulative methane production for U-Logistic - Monod single substrate Matching model

POME (%)	Parameter					
	θ	μ_0 (d)	P_0' (mL)	Y_{PS} (mL/ (mgCOD/L))	μ_{ms} (d^{-1})	K_S (mg/L)
100	0.50	0.19	1051.35	0.0268	0.75	27.9851
80	0.58	0.25	1522.61	0.0270	0.72	27.7778
60	0.22	0.35	361.31	0.0341	0.95	21.9941
40	0.18	0.39	201.39	0.0253	0.97	29.64
20	1.0	0.38	519.55	0.0354	1.15	21.1864

5. CONCLUSION

The matching techniques can be used effectively to convert the Gompertz-type and Logistic-type parameters into their corresponding Monod-type parameters. And the matched Monod-type parameters (using Contois model) can be used to design a completely-mixed continuous AD process using simulation. Thus, large amount of BMP data which were condensed in the form of Gompertz-type models and parameters, become more valuable not only for representing the results in batch AD specifically but also for being used directly in AD process design. However, these illustrations are over-simplified that in practice we must take into account other significant factors in AD-system design and operation.

6. ACKNOWLEDGEMENT

All supports from Walailak University Fund (Contact no. 05/60) and BOP Excellence Center are acknowledged.

7. REFERENCES

Noynoo, L., Jijai, S., Phayunphan, K., Rakmak, N., Siripatana, C., n.d. Gompertz-Type Two-Substrate Models for Batch Anaerobic Co-Digestion, in: Applied and Industrial Mathematics, MALTESAS CONFERENCE. Presented at the 2018 3rd Applied Mathematics in Science and Engineering International Conference (APPEMSE), International Journal of Engineering and Technology (UAE), Langkawi Island, Malaysia.

Sangsri, S., Siripatana, C., Rakmak, N., Wadchasit, P., Jijai, S., 2019. Evaluating Biomethane Potential of Inocula from Different Active Biogas Digesters for Palm Oil Mill Effluent by BMP and SMA: Effect of Dilution and Sources. Presented at the International Conference on the 4th Industrial Revolution and Its Impact (IC4ir), Walailak University.

Schnute, J., 2011. A Versatile Growth Model with Statistically Stable Parameters. Can. J. Fish. Aquat. Sci. 38, 1128–1140. https://doi.org/10.1139/f81-153

Siripatana, C., Jijai, S., Kongjan, P., 2016. Analysis and extension of Gompertz-type and Monod-type equations for estimation of design parameters from batch anaerobic digestion experiments, in: AIP Conference Proceedings. p. 030079. https://doi.org/10.1063/1.4965199

Tjørve, E., Tjørve, K., 2010. A unified approach to the Richards-model family for use in growth analyses: Why we need only two model forms. J. Theor. Biol. 267, 417–25. https://doi.org/10.1016/j.jtbi.2010.09.008

Tjørve, K., Tjørve, E., 2017. A proposed family of Unified models for sigmoidal growth. Ecol. Model. 359, 117–127. https://doi.org/10.1016/j.ecolmodel.2017.05.008

Tsoularis, A., Wallace, J., 2002. Analysis of Logistic Growth Models. Math. Biosci. 179, 21–55. https://doi.org/10.1016/S0025-5564(02)00096-2

Zaher, U., Li, R., Jeppsson, U., Steyer, J.-P., Shulin, C., 2009. GISCOD: General Integrated Solid Waste Co-Digestion model. Water Res. 43, 2717–2727. https://doi.org/10.1016/j.watres.2009.03.018

Zhu, J., 2017. Development of General Gompertz Models and Their Simplified Two-Parameter Forms Based on Specific Microbial Growth Rate for Microbial Growth, Bio-Products and Substrate Consumption. Adv. Biotechnol. Microbiol. 4. https://doi.org/10.19080/AIBM.2017.04.555640

Zwietering, M., Jongenburger, I., Rombouts, F.M., Van, T., 1990. Modeling of Bacterial Growth Curve. Appl. Environ. Microbiol. 56, 1875–81.

#225: Anaerobic digestion of synthetic wastewater (acetate): effect of COD and C/N ratio in batch mode

Laddawan NOYNOO[1], Hathaikarn THONGPAN[2], Sunwanee JIJAI[3], Norli ISMAIL[4], Chairat SIRIPATANA[5] and Nirattisai RAKMAK[6]

[1] School of Engineering and Resources, Walailak University, Nakhon Si Thammarat, Thailand 80160, ladda1995.ln@gmail.com.
[2] School of Engineering and Resources, Walailak University, Nakhon Si Thammarat, Thailand 80160, hathaikarn_thpn@hotmail.com.
[3] Faculty of Science Technology and Agriculture, Yala Rajabhat University, Yala, Thailand 95000, sunwanee.j@yru.ac.th.
[4] School of Industrial Technology, Universiti Sains Malaysia 11800, Pulau Pinang, Malaysia, norlii@usm.my.
[5] Biomass and Oil-Palm Excellence Center and School of Engineering and Resources, Walailak University, Nakhon Si Thammarat, Thailand 80160, schairat61@gmail.com.
[6] Biomass and Oil-Palm Excellence Center and School of Engineering and Resources, Walailak University, Nakhon Si Thammarat, Thailand 80160, nirattisai.ra@wu.ac.th.

This paper attempts to understand the effect of the main operating variables, find an optimized operating condition, and develop a model for biogas production from Palm Oil Mill Effluent (POME). However, POME is a complex substrate with mixed sources of carbon and nitrogen as well as other essential nutrients that makes it difficult to understand clearly how the C/N ratio and volatile fatty acid (VFA) affect the efficiency of the anaerobic digestion (AD) process. In order to clarify the effects of the main variables and be able to develop a deeper and more realistic mathematical model from focused/basic experimental data, the author chose to optimize the biogas production using a synthetic wastewater (acetate with nutrient supplements instead of POME) digested in batch mode. The effects of C/N ratio (for 10/1 to 50/1) and COD (in range of 1,000-12,000 mg/L) were studied in 1000 mL-reactors containing synthetic wastewater and inoculum (sludge of POME). The results of this study were as follows: the optimal for batch mode and COD (as acetate) was 1,000 mg/l of COD with gave %CH4 greater than 50, CH4 yield was 72.90 mg CH4/g CODremoval and 80.62% of CODremoval. The optimal C/N ratio was 30/1 with %CH4 around 35% and 44.49 of %COD removal. Moreover, all of the experiment data fitted well with both Gompertz and Monod models. Furthermore, it gave a corrected prediction of steady state performance of the biogas both qualitatively and quantitatively. In this work, a model to predict the composition of biogas production from the substrate composition was also preliminarily developed which predicted the biogas composition with a correct trend.

Keywords: C/N ratio; COD; synthetic wastewater; mathematic model; anaerobic digestion

1. INTRODUCTION

The palm oil industry is the biggest agro-industry in Southern Thailand, contributing over 45,000 million Baht each year (2.74 million tons of crude palm oil annually). Palm oil mills are wet factories, producing huge amounts of wastewater which are used for biogas production through anaerobic digestion (AD) processes. A number of

published articles on various aspects of AD of palm-oil mill effluents have been reported, increasingly its co-digestion with other nutrient sources has been investigated (Soh Kheang Loh, 2019). However, POME and other agro-industrial wastes are too complex to understand how the main parameters (such as C/N ratio) affect the AD process performance in a clear manner. For example, there are at least two approaches to understand the effect of C/N ratio on methane yield and its evolution rate. The simplest way is to design experiments such that varying C/N substrates (by adding ammonium nitrogen or by co-digesting with high-nitrogen substrates) are tested for biological methane potential (BMP) and then applying statistical methods to find how C/N ratio affect the AD performance. This approach potentially has a large degree of ambiguity because of complex interactions between various factors which obscure the contribution of the C/N ratio. Experimental design would also be more involved because many variables have an influence in the process at the same time while we are focusing on only 1 or 2 factors. Consequently, excessive resources would be needed to clarify the effect of C/N whereas predictive power of the resulting statistical models is limited; they are restricted to specific cases. Since the interaction between multi-substrate and microbial consortium are too complex to be described by moderate kinetic models, kinetic modelling has not been popular or very meaningful.

In this work, a different approach called “the approach of increasing complexity” (called PIC, in short) was used to understand the effect of C/N ratio on AD process in a fundamental way. By looking at main metabolic pathways of the AD process, one would find that acetate is the intermediate to be directly converted to methane and carbon dioxide in the final step of methanogenesis (Enzmann et al, 2018). How much methane produced through this route depends on the substrate compositions and physico-chemical condition surrounding the microbes. However, in most practical AD process, more than 60% of methane produced was derived from acetate. (CU Welte, 2018)

Here we still used the microbial sludge (seed) from an existing POME anaerobic digester in BMP tests. However, instead of using POME and other co-substrates we prepared a synthetic wastewater from sodium acetate (adjusted to different C/N ratios) and essential nutrients for the growth of methanogens. This synthetic wastewater has only acetate as its carbon source. By this way we expected to understand how C/N affects the kinetic of methane production without too many carbon sources getting involved at the same time. We also tried to find out that how far this simple AD system follows Monod and Gompertz kinetics given its inherent simplicity.

2. KINETIC OF BIOGAS

Monod and Gompertz kinetics were proposed to study the effect of biogas production, concentration of substrate and microbial biomass (Tongpan et al., 2016). It was based on one-limiting-substrate assumption and sigmoidal growth-rate as a function of the substrate concentration (Monod, 1949). If no microbial death occurs during the fermentation/AD process and all yield coefficients is constant, we can write the following system of differential equations.

Equation 1:
$$\frac{dX}{dt} = \mu X = \frac{\mu_m S}{K_S + S} X$$

Equation 2:
$$\frac{dS}{dt} = \left(-\frac{1}{Y_{X'/S}} \right) \mu X$$

Equation 3:
$$\frac{dS}{dt} = \left(-\frac{Y_{P/S}}{Y_{X/S}} \right) \mu X$$

Substituting the equation below into Equations (1) – (3),

$$Y_{PS} = \Delta P / \Delta S, Y_{X'S} = \Delta X' / \Delta S, Y_{PX'} = \Delta P / \Delta X' = Y_{PS} / Y_{X'S} \text{ and } P'_0 / Y_{PS} = X'_0 / Y_{X'S}$$

we obtain the following:

Equation 4:
$$\frac{dS}{dt} = \mu \left(S - S_0 - \frac{X_0}{Y_{X/S}} \right)$$

Equation 5:
$$\frac{dP}{dt} = Y_{P/S} \mu \left(\frac{P}{Y_{P/S}} - \frac{P_0}{Y_{P/S}} - \frac{X_0}{Y_{X/S}} \right) = \mu P$$

Solving Equations (1)-(5), one obtains the following analytical solution

Equation 6:
$$t = \left[\left(K_S / C \right) ln \left(S_0 (C - S) / S (C - S_0) \right) + ln \left(\left(C - S \right) / \left(C - S_0 \right) \right) \right] / \mu_m$$

Where $C=\left(X_0/Y_{X'S}\right)+S_0=\left(X_0/Y_{X'S}\right)+\left(P_\infty/Y_{PS}\right)=\left(P'_0+P_\infty\right)/Y_{PS}=\left(P'_\infty/Y_{YS}\right)$

The prime notation in X′ referred to the total accumulative microbes due to growth if there were no deaths.

Where:

- X = concentration of active microbes (cell biomass) at a specific time
- μm = maximum growth rate at a particular substrate concentration
- μ = specific growth rate at a particular substrate concentration
- k_d = specific death rate
- K_s = Monod saturation constant

The equivalent biogas generated by X is defined as P′=P+ P'_0 However, although very useful for interpretation, this relation is only hypothetical because we did not observe how microbial consortia had evolved before we start the batch AcoD experiments. Thus, P'_0 or the estimated X_0 should be interpreted as initial microbial activity rather than the actual microbial density at the initial time of AcoD process. In general, high P'_0 (or high X_0) indicates high initial microbial activity which can be translated as relatively high microbial density and vice versa.

3. MATERIALS AND METHODS

3.1. Experimental set-up

AD was carried out using the synthetic wastewater that consisted of mixture of 5 chemicals and acetate at different ratio as in Table 1 to give the COD values of 1000-12,000 mg/L.

Table 1: Composition of the synthetic wastewater

Chemicals (g/l)	Concentration of COD (mg/l)				
	1,000	3,000	6,000	9,000	12,000
Sodium Acetate)g/l)	2.09	6.27	12.54	18.81	25.08
Sodium dihydrogen phosphate)g/l)	0.2083	0.625	1.25	1.875	2.5
Ammonium Chloride)g/l)	0.083	0.25	0.5	0.75	1
Hydrochloric acid)ml/l)	0.083	0.25	0.5	0.75	1
Nickel (II) chloride)mg/l)	0.083	0.25	0.5	0.75	1
Ferric chloride)mg/l)	0.083	0.25	0.5	0.75	1

The inoculum was collected from an anaerobic sludge at the bottom of the active anaerobic pond in POME waste treatment plants in Nakhon Si Thammarat province. The inoculum was kept at 40°C for 3 days to completely consume the residue nutrients. The AD was performed under room temperature using 1 L volume of serum bottles. A working volume of 850 ml was used in all experiments. The serum bottles were covered with the rubber stoppers and sealed with aluminium caps. The volume of biogas was measured daily by using water displacement method. The experiment setup is shown in Figure 1.

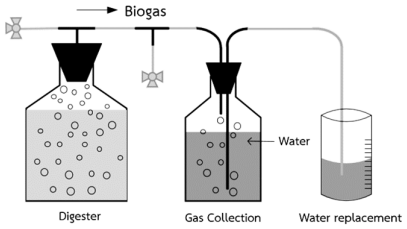

Figure 1: The experiment set-up for biogas production in batch mode

3.2. Analytical methods

Digestate was sampled from reactors and was performed every two days. In all experiments, pH, Chemical oxygen demand (COD), Total solid (TS), Total volatile solid (TVS), Suspended Solid (SS), Volatile Suspended Solid (VSS),

Mixed Liquor Suspended Solid (MLSS), Mixed Liquor Volatile Suspended Solids (MLVSS), Alkalinity and Volatile Fatty Acid (VFA) were evaluated according to standard methods for the examination of water and wastewater (APHA, 2017). Daily biogas production was settled by a water displacement method. The composition of biogas was analysed using Gas Chromatography.

3.3. Experiment design

Activity 1: Study the effect of COD on AD system

The inoculum for this study was treated before using as seed in batch experiments by daily adding 10% (by volume of inoculum) of synthetic wastewater into digester until 100% of volume. AD batch system was set up in 5 different conditions including mixing of synthetic wastewater at 1,000, 3,000, 6,000, 9,000 and 12,000 mg/l of COD and inoculum at fixed 28/1 of C/N ratio. The experiments were conducted at 35ºC until batch completion. The experiments were duplicated in all digesters. A flowchart of this experiment designed for study the effect of COD on the maximum biogas production in batch mode was shown in Figure 2.

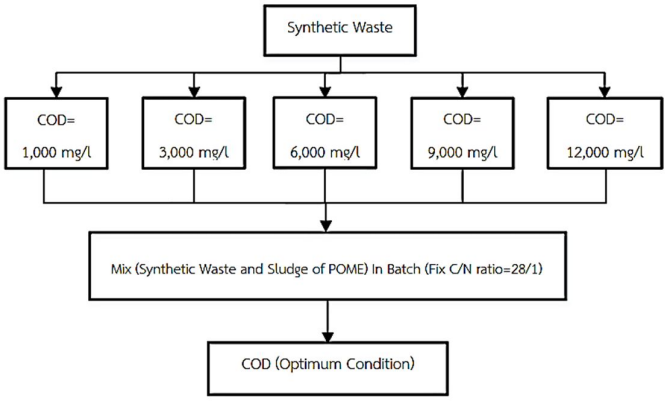

Figure 2: Experiment designed for study the effect of COD on AD system.

Activity 2: Study the effect of C/N ratio on AD system

The optimum COD value from Activity 1 that gave highest biogas yield was used to study the effect of C/N ratio on AD system. The synthetic wastewater and inoculum were prepared at difference C/N ratio including 10/1, 20/1, 30/1, 40/1 and 50/1. The experiments were conducted at 35ºC until batch completion and were duplicated in all digesters. A flowchart of the experiment designed for study the effect of C/N on the maximum biogas production in batch mode is shown in Figure 3.

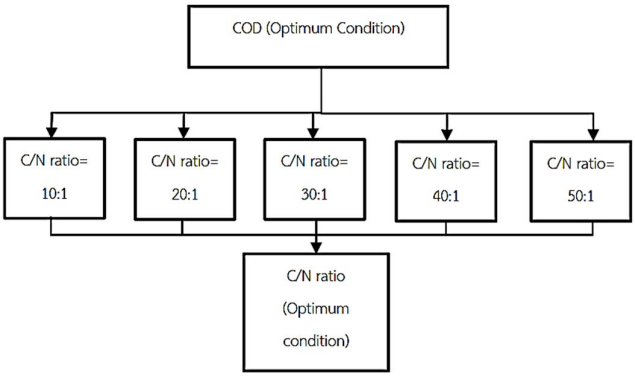

Figure 3: Experiments designed for investigating the effect of C/N on the performance batch AD system.

4. RESULTS AND DISCUSSION

4.1. The effect of COD on AD system

Physico-chemical characterisation of substrate (mixing of synthetic wastewater and inoculum) at the beginning of the anaerobic digestion process was performed. Chemical characterisation of substrate used in this study is showed in Table 2.

Table 2: Characteristics of substrate (mixture of synthetic wastewater and inoculum) used in the digestion experiments.

Parameter	Synthetic wastewater at difference of COD)mg/l)					Inoculum
	1000	3000	6000	9000	12000	
pH	5.82	5.84	5.85	5.90	5.85	6.60
TS, mg/l	1,555	3,890	7,195	11,405	13,641	-
TVS, mg/l	1,050	1,695	2,580	3,790	5,674	-
SS, mg/l	110	130	160	150	260	-
VSS, mg/l	580	845	840	680	565	-
MLSS, mg/l	-	-	-	-	-	28,530
MLVSS, mg/l	-	-	-	-	-	25,730
C/N ratio	25.58	25.58	25.58	25.58	25.58	-

Table 3: Characteristics of substrate (mixing of synthetic wastewater and inoculum) used in the digestion experiments.

	COD	ALK (mg/l)	VFA (mg/L)	VFA/ALK	COD (mg/L)	MLVSS (mg/l)	Methane yield (ml CH_4/g COD removal)
1,000	run system	4,875	4,225	0.87	9,677	20,755	72.90
	close system	4,375	3,000	0.39	1,875	39,669	
	%COD removal				80.63		
3,000	run system	5,338	4,263	0.8	10,101	21,259	70.06
	close system	4,925	2,313	0.47	3,279	39,669	
	%COD removal				67.54		
6,000	run system	7,475	6,850	0.92	19,355	18,004	65.05
	close system	6,575	2,313	0.42	3,279	21,980	
	%COD removal				49.18		
9,000	run system	8,175	7,538	0.92	25,806	14,630	53.34
	close system	8,500	3,138	0.37	13,125	15,561	
	%COD removal				49.14		
12,000	run system	9,313	8,500	0.91	19,355	21,224	47.33
	close system	7,475	2,625	0.35	10,625	22,631	
	%COD removal				45.10		

Initial and final characteristics of the digestates from synthetic wastewater and inoculum with different COD levels are shown in Table 3. The cumulative biogas production and %CH_4 of difference COD initial levels in batch digestion of mixed synthetic wastewater and inoculum are shown in Figure 4 and Figure 5. For the COD levels in the range of 1,000-12,000 mg/L, the cumulative biogas production fell in the range of 761-1,711 mL and %CH_4 was more than 50% in all experiments. During the first 5 days, yield of cumulative biogas production in all experiments was low because the pH of synthesis wastewater at the beginning of anaerobic digestion was lower than 6 and methanogens need to adjust to this slightly acidic environment. The higher the COD input value, the longer time for the microbes to produce biogas because microorganisms in inoculum needed to adapt before becoming stronger to produce biogas after 5 days.

It was found that 1,000 mg/L of COD input gave the highest methane yield of 72.90 ml CH_4/g COD removed because the VFA/ALK at this condition was in the suitable range of 0.1-0.4 which was non-inhibitive (Nabarlatz, 2013). From results tabulated in Table 3, 1,000 mg/L of COD input value gave maximum %COD removal of 80.62% following by the input COD of 3,000-12,000 mg/L (67.54-45.10). Moreover at the input COD of 1,000 mg/L the AD process gave the maximum MLVSS too. From the results, the optimal input COD was 1,000 mg/L was the optimum condition on for anaerobic digestion of synthetic wastewater and the inoculum based on the maximum cumulative biogas production at day 10 of batch AD, %COD removal and amount of microbial sludge after batch completion.

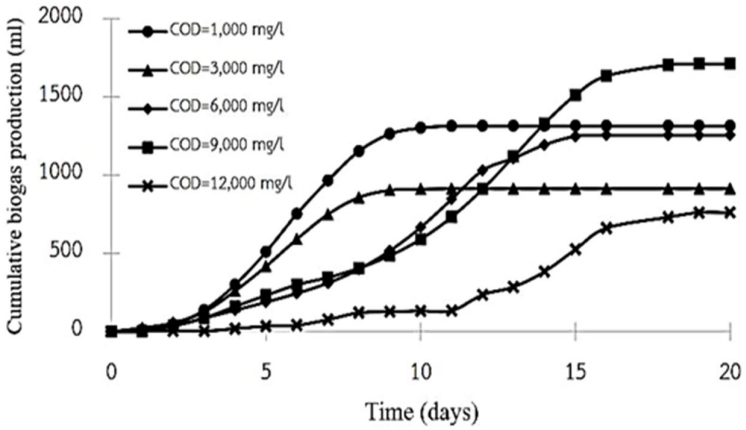

Figure 4: Cumulative biogas production at difference input COD. (at C/N ratio of 25.58)

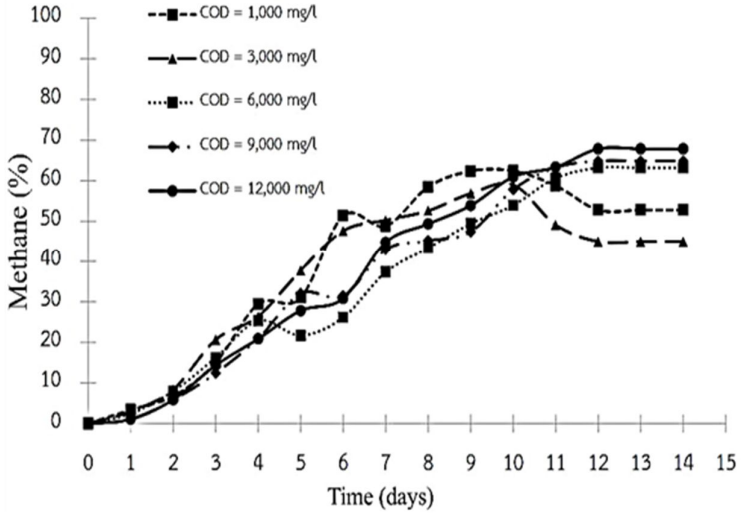

Figure 5: %CH4 of the biogas versus time for different input COD.

4.2. The effect of C/N ratio on the performance of AD system

The results of anaerobic digestion of acetate synthetic wastewater having 1,000 mg/L input COD and inoculum from POME sludge at different C/N ratios (10/1-50/1) are shown in Table 4. Figure 6 and Figure 7 show cumulative biogas production and %CH4 produced at difference C/N ratio of digestates after 30 days of batch AD experiments. From the result, during the first 5 days, yields of cumulative biogas production in all experiments were low because the microorganisms needed some time to adjust in the early stages of digestion. In all batch tests, yield of biogas production were very low in the first 10 days of the batch AD because VFA/ALKs of all experiments were out of the suitable range (0.1-0.4). At C/N ratio of 40/1 and 50/1 VFA/ALK were 0.94 and 0.95 respectively, which is too high for biogas production thus giving low %COD removal in the range of 26.38-28.22%. This was because a high proportion of acetate appeared in prepared synthetic wastewater to adjust C/N ratio. Interestingly, C/N ratio 10/1 gave minimum %COD removal (while producing highest accumulative biogas) as compared to 20/1 and 30/1 C/N ratios. This could be due to a high proportion of nitrogen in these substrates which was converted to toxic ammonia and inhibited the microbial growth. In addition, the anaerobic digestion requires a suitable carbon to nitrogen (C/N) ratio (about 15.6) for the substrate. The substrate with low or high C/N would inhibit the hydrogen producing bacteria to efficiently produce fermentative hydrogen (Xia et al., 2014). Whereas, the C/N ratio of microalgae biomass was too low due to the high protein content and relatively low carbohydrate content. Hence, flocculants with high carbon content could be used to improve the C/N ratio and the mixture could be used as the substrate for later energy conversion. From the result, C/N at 30/1 was the optimum condition to produce biogas at maximum accumulated biogas production and $\%CH_4$. (Xia et al., 2014).

Table 4: Characteristics of substrate (mixture of synthetic wastewater and inoculum) used in the digestion experiments.

COD		ALK (mg/l)	VFA (mg/L)	VFA/ALK	COD (mg/L)	MLVSS (mg/l)	Methane yield (ml CH_4/g COD removal)
1,000	run system	4,875	4,225	0.87	9,677	20,755	72.90
	close system	4,375	3,000	0.39	1,875	39,669	
	%COD removal				80.63		
3,000	run system	5,338	4,263	0.8	10,101	21,259	70.06
	close system	4,925	2,313	0.47	3,279	39,669	
	%COD removal				67.54		
6,000	run system	7,475	6,850	0.92	19,355	18,004	65.05
	close system	6,575	2,313	0.42	3,279	21,980	
	%COD removal				49.18		
9,000	run system	8,175	7,538	0.92	25,806	14,630	53.34
	close system	8,500	3,138	0.37	13,125	15,561	
	%COD removal				49.14		
12,000	run system	9,313	8,500	0.91	19,355	21,224	47.33
	close system	7,475	2,625	0.35	10,625	22,631	
	%COD removal				45.10		

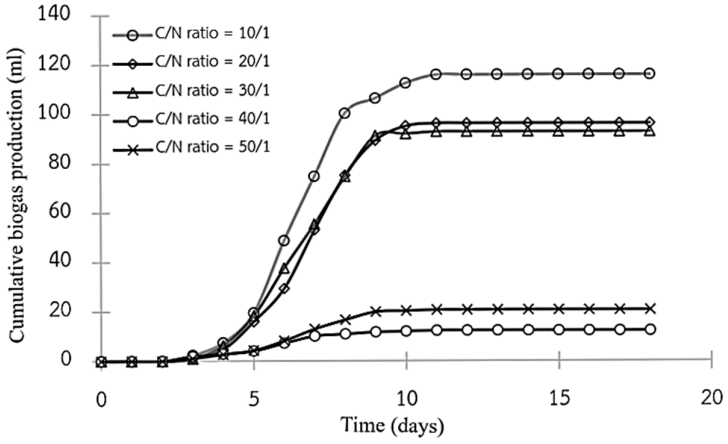

Figure 6: Cumulative biogas production at difference C/N ratio.

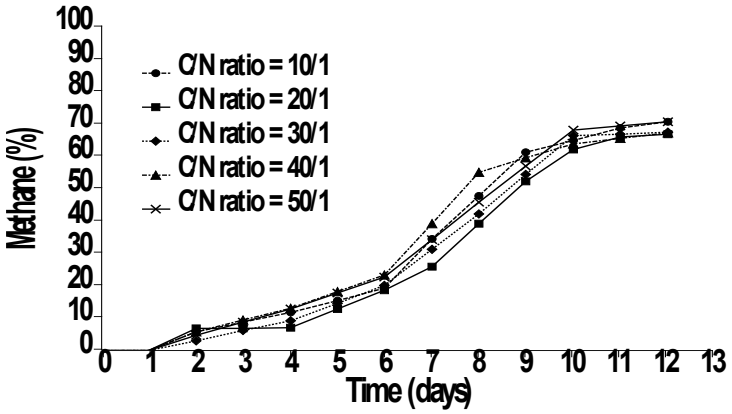

Figure 7: %CH_4 production at difference C/N ratio.

4.3. Fitting the data set to Gompertz models

The results of curve-fitting for Gompertz and Monod models are presented in Figure 8 and Figure 9. The best estimated parameters including those of the corresponding original models are summarised in Table 5.

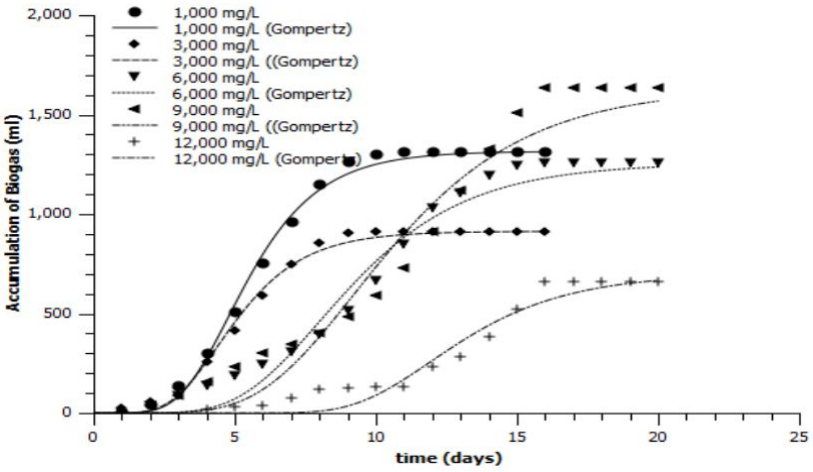

Figure 8: Biogas accumulation for Gompertz model.

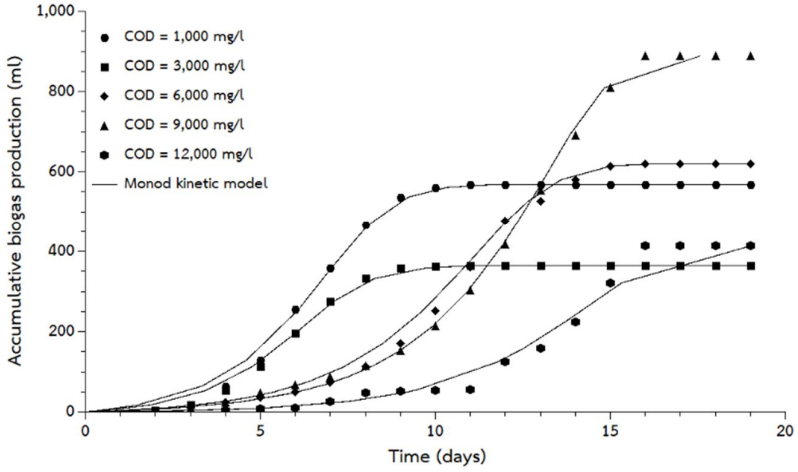

Figure 9: Biogas accumulation for Monod kinetic model.

Table 5: Parameters and the best-fit parameter (R^2) of accumulative biogas production for Gompertz and Monod model.

Model	Parameter	COD concentration (mg/l)				
		1,000	3,000	6,000	9,000	12,000
Gompertz equation $P' = \left(P_\infty + P_0\right)\left[\exp\left(-\frac{\gamma_0}{\alpha}\exp\left(-\alpha t\right)\right) - \exp\left(-\frac{\gamma_0}{\alpha}\right)\right]$	$\gamma_0\left(d^{-1}\right)$	8.7541	8.5404	5.8172	4.6106	9.0661
	$\alpha\left(d^{-1}\right)$	0.5708	0.6026	0.3503	0.2965	0.2834
	Fitted $P_\infty\left(ml\right)$	1,315	913	1,255	1,634	785
	R^2	0.99	0.99	0.98	0.96	0.96
Monod kinetic of producing biogas $t = \left(\frac{1}{\mu_m}\right)\left(\left(\frac{K_S Y_{PS}}{P_\infty + P_0'}\right)\ln\left(\left(\frac{P_\infty}{P_\infty - P}\right)\left(\frac{P_0' + P}{P_0'}\right)\right) + \ln\left(\frac{P_0' + P}{P_0'}\right)\right)$	$K_S\left(mg/l\right)$	5,000	5,000	5,000	5,000	5,000
	$Y_{PS}(ml/mgCOD)$	0.0729	0.0701	0.0651	0.0533	0.0473
	$P_\infty\left(ml\right)$	570	365	625	890	415
	$P_0'\left(ml\right)$	15	9	7	6	1.6
	$\mu_m\left(d^{-1}\right)$	0.85	1.16	0.6	0.48	0.6
	R^2	0.99	0.99	0.99	0.98	0.97

The model fitting clearly shows that corrected Gompertz model represented all data sets very well. These results confirm that the Gompertz model is highly suitable for describing batch AD data for simple-(single-) substrate surrounded by a high density of active microbial biomass which is true in these cases. Monod kinetics on the other hand is more suitable for the cases of relatively low biomass concentration.

5. CONCLUSION

In summary, this work, to some extent, has clarified the effect of COD levels of purely volatile fatty acid (acetate) and the C/N ratio on the performance of batch AD systems for this simplest system. This work almost confirm the usability of the Gompertz model for single-substrate surrounded by excessive microbial mass.

6. REFERENCES

Abdel-Hadi, M. (2008). A simple apparatus for biogas quality determination. Misr Journal of Agricultural Engineering, 25 (3), 1055-1066.

APHA, AWWA, & WPCF. (2017). Standard Methods for Examination of Water and Wastewater (19 ed.). New York: American Public Health Association, Washington D.C.

Badroldin, N. A. B. (2010). Treatment of palm oil mill effluent (POME) using hybrid up flow anaerobic sludge blanket (HUASB) reactor. Degree of Master, Universiti Tun Hussein Onn Malaysia, Malaysia.

Barnett, A., Pyle, L., & Subramanian, S. K. (1978). Biogas technology in the third world: a multidisciplinary review: International Development Research Center, Ottawa, Canada.

Bonvin, D. (1998). Optimal operation of batch reactors—a personal view. Journal of process control, 8 (5), 355-368.

Bryant, M. (1979). Microbial methane production—theoretical aspects. Journal of Animal Science, 48 (1), 193-201.

Buswell, A., & Mueller, H. (1952). Mechanism of methane fermentation. Industrial & Engineering Chemistry, 44 (3), 550-552.

Chaisri, R., Boonsawang, P., Prasertsan, P., & Chaiprapat, S. (2007). Effect of organic loading rate on methane and volatile fatty acids productions from anaerobic treatment of palm oil mill effluent in UASB and UFAF reactors. Songklanakarin J. Sci. Technol, 2, 311-323.

Chen, Y., Rößler, B., Zielonka, S., Wonneberger, A.-M., & Lemmer, A. (2014). Effects of organic loading rate on the performance of a pressurized anaerobic filter in two-phase anaerobic digestion. Energies, 7 (2), 736-750.

Childers, R. W. (1999). Continuous-operation, closed loop decontamination system and method: Google Patents.

Corman, A., & Pave, A. (1983). On parameter estimation of Monod's bacterial growth model from batch culture data. The Journal of General and Applied Microbiology, 29 (2), 91-101.

De Bere, L. (2000). Anaerobic digestion of solid waste: state-of-the-art. W ater science and technology, 41 (3), 283-290.

Deepanraj, B., Sivasubramanian, V., & Jayaraj, S. (2015). Kinetic study on the effect of temperature on biogas production using a lab scale batch reactor. Ecotoxicology and Environmental Safety. doi: 10.1016/j.ecoenv.2015.04.051i Eslami, A., &

Enzmann, F., Mayer, F., Rother, M., & Holtmann, D. (2018). Methanogens: biochemical background and biotechnological applications. AMB Express, 8(1), 1. doi:10.1186/s13568-017-0531-x

Takdastan, A. (2013). Using of powdered activated carbon as coagulant aid in Total organic carbon removal in Koot Amir Water treatment plant. Jundishapur Journal of Health Sciences, 5 (2), 117-128.

Gerardi, M. H. (2003). The Microbiology of Anaerobic Digesters. New Jersey: John Wiley & Son

Grady Jr, C. L., Daigger, G. T., Love, N. G., & Filipe, C. D. (2011). Biological wastewater treatment: CRC press.

Grady, R. M., Grange, R. W., Lau, K. S., Maimone, M. M., Nichol, M. C., Stull, J. T., & Sanes, J. R. (1999). Role for [alpha]-dystrobrevin in the pathogenesis of dystrophin-dependent muscular dystrophies. [10.1038/12034]. Nat Cell Biol, 1 (4), 215-220.

Hayes, T. D., & Theis, T. L. (1978). The distribution of heavy metals in anaerobic digestion. Journal (Water Pollution Control Federation), 61-72.

Igwe, J., & Onyegbado, C. (2007). A review of palm oil mill effluent (POME) water treatment. Global Journal of Environmental Research, 1 (2), 54-62.

Kardos, L., Juhasz, A., Palko, G., Olah, J., Barkacs, K., & Zaray, G. (2011). Comparing of mesophilic and thermophilic anaerobic fermented sewage sludge based on chemical and biochemical tests. Applie d Ecology and Environmental Research, 9 (3), 293-302.

Kim, M., Ahn, Y.-H., & Speece, R. (2002). Comparative process stability and efficiency of anaerobic digestion; mesophilic vs. thermophilic. Water research, 36 (17), 4369-4385.

Ling, Y. L. (2007). Treatability of palm oil mill effluent (POME) using black liquor in an anaerobic treatment process. USM.

Marchaim, U., & Krause, C. (1993). Propionic to acetic acid ratios in overloaded anaerobic digestion. Bioresource Technology, 43 (3), 195-203.

McCarty, P. L. (1964). Anaerobic waste treatment fundamentals.

Monod, J. (1949). The growth of bacterial cultures. Annual Reviews in Microbiology, 3 (1), 371-394.

Nabarlatz, D.-A., Arenas-Beltrán, L.-P., Herrera-Soracá, D.-M., & Niño-Bonilla, D.-A. (2013). Biogas production by anaerobic digestion of wastewater from palm oil mill industry. CT&F-Ciencia, Tecnología y Futuro, 5 (2), 73-83.

Nachaiyasit, S., & Stuckey, D. C. (1997). The effect of shock loads on the performance of an anaerobic baffled reactor (ABR). 1. Step changes in feed concentration at constant retention time. Water Research, 3 1 (11), 2737-2746.

Neves, L., Oliveira, R., & Alves, M. M. (2006). Anaerobic co-digestion of coffee waste and sewage sludge. Waste Management, 26 (2), 176-181.

Novak, J. T., Sadler, M. E., & Murthy, S. N. (2003). Mechanisms of floc destruction during anaerobic and aerobic digestion and the effect on conditioning and dewatering of biosolids. Water Research, 37 (13), 3136-3144.

Poh, P. E., & Chong, M. F. (2009). Development of anaerobic digestion methods for palm oil mill effluent (POME) treatment. Bioresource Technology, 100 (1), 1-9. doi: 10.1016/j.biortech.2008.06.022

Poulsen, T. G. (2003). Solid waste management. Chapter 5 Anaerobic digestion, Aalborg University. Denmark.

Puah, C. W., Choo, Y. M., & Ong, S. H. (2013). Production of palm oil with methane avoidance at palm oil mill: a case study of cradle-to-gate life cycle assessment. American Journal of Applied Sciences, 10 (11), 1351-1355.

Rittmann, B. E., & McCarty, P. L. (2001). Environmental biotechnology: principles and applications. McGraw-Hill. Boston.

Schnute, J. (1981). A versatile growth model with statistically stable parameters. Canadian Journal of Fisheries and Aquatic Sciences, 38 (9), 1128-1140.

Shanmugam, P., & Horan, N. J. (2009). Optimising the biogas production from leather fleshing waste by co-digestion with MSW. Bioresource Technology, 100 (18), 4117-4120. doi: 10.1016/j.biortech.2009.03.052

Siddiqui, Z., Horan, N. J., & Anaman, K. (2011). Optimisation of C: N Ratio for CoDigested Processed Industrial Food Waste and Sewage Sludge Using the BMP Test. International Journal of Chemical Reactor Engineering, 9.

Soh Kheang Loh, Mei Ee Lai, Muzzammil Ngatiman (2019). Vegetative growth enhancement of organic fertilizer from anaerobically-treated palm oil mill effluent (POME) supplemented with chicken manure in food-energy-water nexus challenge. Food and Bioproducts Processing, 117, 95-104.

Sreela-or, c., Sittijunda, S., & Reungsang, A. (2014). Methane Production from Acidic Effluent Obtained from Hydrogen Fermentation Process of Food Waste Using Continuous Stirred Tank Reactor. Chiang Mai Journal of Science, 42 (3), 578-587.

Tanimu, M. I., Ghazi, T. I. M., Harun, R. M., & Idris, A. (2014). Effect of carbon to nitrogen ratio of food waste on biogas methane production in a batch mesophilic anaerobic digester. International Journal of Innovation, Management and Technology, 5 (2), 116.

Tchobanoglous, G., & Burton, F. L. (1991). Wastewater engineering. Management, 7, 1-4

Thongpan, H., Thongnan, R., Rakmak, N., & Siripatana, C. (2016). Modeling of batch and continuous anaerobic digestion of palm oil mill effluent: the effect of wastewater-sludge ratio. Jurnal Teknologi, 78 (5-6), 125-U122.

Wang, X., Yang, G., Feng, Y., Ren, G., & Han, X. (2012). Optimizing feeding composition and carbon–nitrogen ratios for improved methane yield during anaerobic co-digestion of dairy, chicken manure and wheat straw. Bioresource Technology, 120, 78-83.

Wen, C., Huang, X., & Qian, Y. (1999). Domestic wastewater treatment using an anaerobic bioreactor coupled with membrane filtration. Process Biochemistry, 35 (3), 335-340.

Welte C. U. (2018). Revival of Archaeal Methane Microbiology. mSystems, 3(2), e00181-17. doi:10.1128/mSystems.00181-17

Wu, T. Y., Mohammad, A. W., Jahim, J. M., & Anuar, N. (2010). Pollution control technologies for the treatment of palm oil mill effluent (POME) through end of-pipe processes Journal of Environmental Management, 91(7),1467-1490.

Xia, A., Cheng, J., Ding, L., Lin, R., Song, W., Zhou, J., Cen, K. Enhancement of energy production efficiency from mixed biomass of Chlorella pyrenoidosa and cassava starch through combined hydrogen fermentation and methanogenesis Appl. Energy, 120 (120) (2014), pp. 23-30

Yadvika, Santosh, Sreekrishnan, T. R., Kohli, S., & Rana, V. (2004). Enhancement of biogas production from solid substrates using different techniques—a review. Bioresourc e T e c h n olo g y, 9 5 (1), 1-10.

Yen, H., & Brune, D. (2007). Anaerobic co-digestion of algal sludge and wastepaper to produce methane. Bioresource Technology, 9 8 (1), 130-134.

Zwietering, M., Jongenburger, I., Rombouts, F., & Van't Riet, K. (1990). Modeling of the bacterial growth curve. Applied and environmental microbiology, 56 (6), 1875-1881.

#227: Passive intervention for optimising day-lighting in a selected reading room of the Department of Architecture, Ahmadu Bello University, Zaria

Rukayyatu Bashiru TUKUR*, Yunus Yusuf BADIRU

Department of Architecture, Ahmadu Bello University, Zaria, Nigeria
**Corresponding author: rukkytukur@gmail.com*

Visual discomfort is one of the main triggers for making reading an uncomfortable exercise. Even though daylight is an abundant commodity in the tropics, the abundance of this within spatially deep planned areas hampers the efficacy of conventional windows in reading rooms to allow for visual comfort. This study assesses the fenestration type and material use in a selected reading room in the department. The room was selected based on its position with respect to other reading areas. The readings are observed and recorded with a light meter and were compared with simulated readings of the same room with a view to recommending suitable retrofitting of fenestration and light devices so as to optimise illumination whilst having minimum discomfort from glare etc. Simulations show that there can be a significant increase in illumination with the change in fenestration type. The data room of the Department of Architecture which doubles up as a library for the department, is taken as a case study to see how passive lighting techniques can be used to improve visual comfort in the chosen area. It is discovered that the windows on the southern side are prone to allowing excessive light into the room, thereby causing a problem of glare. Readers on that side of the room were only able to use that section of the library satisfactorily at certain parts of the day. Computer simulations indicate that there is sufficient illumination all through the study area with 70% of the study area having illumination values of a minimum of 100 lux and up to 2000 lux. This indicates a level of illumination that is sufficient and thus does not require artificial lighting. Visual discomfort such as glare can be reduced through the retrofitting of horizontal shading devices which will aid in curbing excess light.

Keywords: daylight, efficacy, passive intervention, retrofitting

1. INTRODUCTION

Daylight is an abundant commodity in the tropics, and developing countries are heavily dependent on it due to the lingering issue of power shortages and persistent outages. Therefore, there is a lot of dependence of natural lighting with all its attendant positives and negatives. Lighting is one of the most important of all building systems (Yuksek, Gorgulu, Kocabey and Dursun, 2015). Daylight is defined as 'the combination of the diffused light from the sky and sunlight. Classrooms in particular are subject to being over-heated from excessive exposure to too much light, as well as the occupants experiencing glare. Every school relies on lighting to provide an effective learning environment, which is one of the most critical physical characteristics of the classroom. The modern classroom is a space where a wide range of teaching/learning activities take place, and the most suitable directions for natural lighting are from the south and the north (Yuksek et al, 2015).

The careful introduction of daylight into educational buildings reduces operating costs, improves students' vision and perception, and contributes to students' health, comfort and productivity (Dahlan & Mahmoud, 2015). In developing countries, the need for day lighting is more fundamental in that there is mostly no alternative to it, especially in the rural and peri-urban areas. (Okotete, Salisu and Batagarawa, 2018). For countries like Nigeria with falling income from crude oil sales, poor power infrastructure, further complicated with an explosion in school age population, the need for good day lighting in classroom design is not an alternative, but a necessity (Salisu, 2015).

The most common source of lighting in the selected reading room is the clerestory of windows on both the northern and southern facades. Given the immense level of glazing that is used in the reading room, this comes with the attendant cost of overheating. For this reason, the northern façade of the building is heavily shaded with tall trees. These trees providing the needed cooling and shading which now brings about the problem of obstruction of the source of daylight.

There are several daylighting systems: a daylighting system is a device located near to or in the openings of the building envelope whose primary function is to redirect a significant part of the incoming natural light flux to improve interior lighting conditions. There are two simple daylighting systems, namely, side-lighting and top-lighting. Side-lighting, which is more commonly observed, is simply a window opening. Top-lighting is an opening in the ceiling or roof element of the building. The following devices as seen in Figures 1 - 4 have been identified in being able to help in carry light through either the top (light pipe in Figure 1) or the side (laser cut panels in Figures 2, 3 and 4).

Figure 1: A Typical light pipe (Source Kim J.T., Kim, G. 2009)

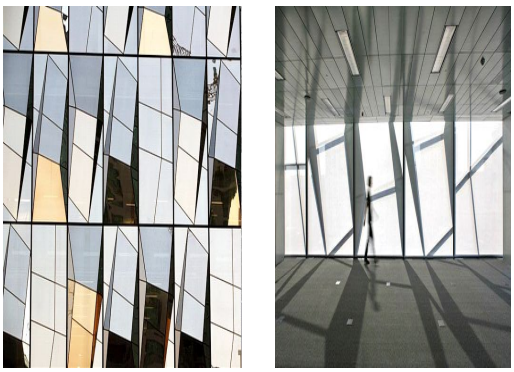

Figure 2: Exterior Laser Cut Panels

Figure 3: Horizontal & Vertical Louvers (Raven Industries, 2003 and Vollay Systems, 2013 respectively).

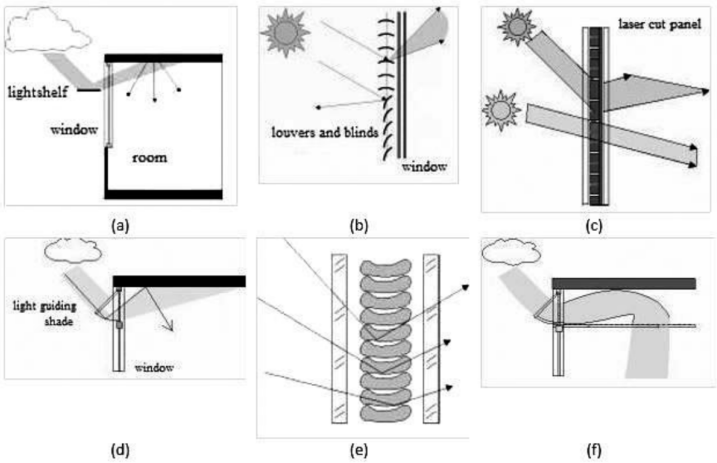

Figure 4: Daylighting systems using direct sunlight (a) Light shelf system (b) Window shade and blind system (c) Laser cut panels (d) Light guiding shade (e) Light guiding glass (f) Anidolic ceiling (Source Yuksek et al, 2015)

2. AIM

The aim of this paper is to study the illuminance levels in the southern side of a select reading room and identify the play of light in the room. The paper also aims to show the quality and depth of light in the tropical countries on an unobstructed southern façade. It is noted that the building already has existing shading devices which have helped in the reduction of glare, however the glare value is still above 20%. Thus, this paper also aims at identifying the best means of optimising the lighting in the room through the proposal of an alternative shading device.

3. MATERIALS AND METHODS

The entire reading room has an area of 167m^2, however, for the purpose of this study, the area under consideration is limited to only the southern façade with an area of 65m^2 approximately as seen in the floor plan in Figure 5. The twelve light metres (sensors) were simultaneously placed in the mapped out positions as seen in Figure 5 in the reading room and the data was taken over a period of approximately 1 hour for 3 consecutive days at exactly the same time; the average of which was collated. The light sensors/light meters were placed 600mm away from the wall and window opening at a work plane of 900mm above the ground.

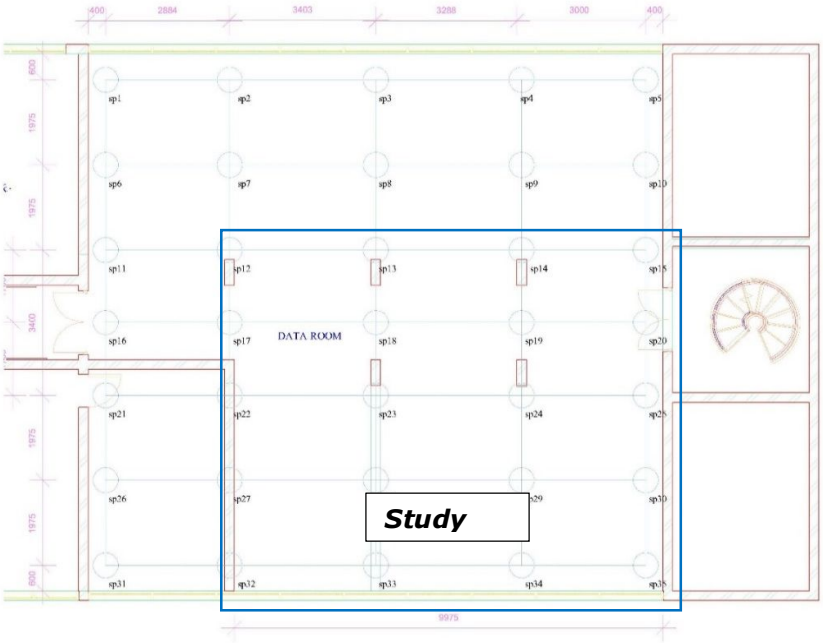

Figure 5: Floor plan of the selected reading room (Author's Fieldwork 2018)

Figures 1 and 2 show the view of the interior of the reading room capturing the light shelves which have hindered the illumination as well as height of the reading tables

Figure 1.

Figure 2.

Showing Interior view of the selected reading room/Study area. (Author's Fieldwork 2018)

Table 1 shows the average measured illuminance over the three days and this was simulated using the Diva (Rhinoceros) software. The results show that the values obtained from the simulation validate the measurements taken as the values are similar for most of the sensor positions.

Table 1: Measured average illuminance over the given period and simulated illuminance over the same period

SENSOR POINT	MEASURED (lux)	SIMULATED (lux)	PERCENTAGE difference between measured and simulated (%)
1 (22)	331	365	- 9.3
2 (23)	497	403	+23.3
3 (24)	621	584	+6.3
4 (25)	527	615	-14.3
5 (27)	854	855	-0.12
6 (28)	1074	995	+7.4
7 (29)	1737	1779	-2.4
8 (30)	1200	1061	+11.6
9 (32)	2230	2331	-4.5
10 (33)	2571	2681	-4.3
11 (34)	2679	2950	-10
12 (35)	2790	2724	+2.4

Source: Field work, Author (2018)

4. RESULTS AND DISCUSSIONS

The data collected was used to carry out the simulations which are graphically represented in Figures 6 to 9. For simulation data to be acceptable as reliable, the values of percentage difference have to fall within a range of -10% to 10%. (Reinhart, 2009 and Fisher, 1992). Only 3 sets of the readings (sensor positions 2, 4 & 8) fall outside that range giving an indication that 75% of the readings are within the acceptable range.

4.1. Simulation results

The simulation was undertaken with the *Diva for Rhinoceros* software employing data weather files for that same location and time. The overall daylight autonomy is 79.45%, and indicates that the quality of lighting is of sufficient quantity. Approximately 70% of the mapped out area recorded over 100 lux but ≤ 2000 lux. Only 8.35% of the mapped out area illuminance fell below 100 lux. The simulations also indicate that up to, but not above 22% of the mapped out area recorded an illumination of 2000 lux.

Table 2: Daylight Autonomy and illuminance Values

METRIC	Value (%)
Daylight autonomy (DA)	79.45
Useful daylight illuminance <100 lux (UDI<100)	8.35
Useful daylight illuminance 100-2000 lux (UDI 100-2000)	69.89
Useful daylight illuminance >2000 lux (UDI2000)	22.04

Source: Author (2018)

Figure 6: Useful Daylight Illuminance < 100 lux (8%)

Figure 7: Daylight Autonomy of 500 lux (73%)

Figure 8: Useful Daylight illuminance 100-2000 lux (75%)

Figure 9: Useful Day Light Illuminance >2000lux (16%)

Legend:

1. >100 lux
2. 100 - 2000 lux
3. < 500 lux

These results show that there is sufficient illuminance through most part of the selected area. The recommended required day-to-day illuminance for tasks is between 400-600 lux (Vergara-Salvat, 2011). However, some parts of the room experience glare and thus may require shading devices to be retrofitted on the openings on the southern façade as seen in Figure 9.

4.2. Passive intervention employed

Simulation tests were carried out to test the building without any of the in-built shading devices and as well as with employing the use of alternative horizontal shading devices. Results obtained (as seen on Table 3 show that with

the absence of the shading devices, the daylight autonomy had an insignificance increase of about 3% whilst the useful daylight illuminance (UDI) of <100lux was basically the same. For UDI of 100-2000 lux dropped by 13%. However, there was a higher possibility of users experiencing glare when the shading devices were removed and the indices rose from 22% (with existing shading shading devices) to 35% (without any for of shading). Therefore, to reach an optimised lighting capacity, a new type of horizontal shading device is proposed. This shading device in placed on the exterior and it projects by 900mm. this caused the Daylight autonomy to drop to 60%. However, the UDI of 100-2000 lux recorded 79% 22% higher than without shading devices and 10% higher than the existing shading device. This therefore implies that there is a better quality of lighting and this shading device had the least possibility of glare with just a probability of 13%. Table 3 shows the comparisons for all the light scenerios for with existing shading device, without shading device and propsed horizontal shading device.

Table 3: Indices for Existing, Without and Proposed Shading Device

METRIC	With Existing Shading Device	Without Shading Device	With Horizontal Shading Device
Daylight autonomy (DA)	79.45%	82.5%	60.7%
Useful daylight illuminance<100 (UDI<100)	8.35%	8.08%	8.59%
Useful daylight illuminance 100-2000 (UDI 100-2000)	69.89%	56.86%	78.77%
Useful daylight illuminance>2000 (UDI>2000)	22.04%	35.07%	12.64%

Source: Authors Fieldwork and Simulation Studies (2019)

5. CONCLUSION

The results indicate and strengthen the premise that there is abundant daylight given the orientation. The was optimisation of daylight properties and immense reduction of glare with the introduction of a proposed horizontal device. Given the geographical location, and where there is a clerestory of windows as that in the study area, there is therefore the need to introduce further exterior shading device so as to reduce the effect of glare. For further studies, there may be a need to provide light pipes (top light) in the centre of the room where the illuminance levels is low (<100 lux). The light that will be obtained through the employment of the light pipe can be softened by attaching a diffuser at the end of the light pipe. Book shelves also acted as obstructive elements towards the centre of the room, thus it is at that point that it will be best to introduce the use of the light pipes.

6. REFERENCES

Fisher, A. (1992). Tolerances in lighting design. *Proceedings of the CIE seminar on computer programs for light and lighting.* Vienna, Austria: CIE.

Okotete, A. O., Salisu, A. S. and Batagarawa, A (2018). Assessment of Lecture Rooms in Faculty of Environmental Design, Ahmadu Bello University Zaria Using Climate Based Daylight Modeling. AARCHES National Conference, Ahmadu Bello University, Zaria | Trends in 21st Century Architecture and Sustainable Built Environment, 21st - 23rd February, 2018, Ahmadu Bello University School of Post Graduate Studies, 91-102.

Reinhart, C. F., Mardaljevic, J., & Rogers, Z. (2006). *Dynamic daylight performance metrics for sustainable building design.* Leukos 3.

Salisu, A. S. (2015). *Optimising Fenestration For Daylight Provision In The Architecture Of Secondary Schools In Nigeria Using Climate-Based Daylight Modelling.* Zaria: Ahmadu Bello University, Zaria.

Tukur, R.B. (2013). Daylighting as a Tool for Visual and Thermal Comfort in Residential Buildings. Unpublished PhD Thesis, University of Nottingham.

Vergara-Salvat, M. (2011). Comfort Vs Efficiency or Comfort with Efficiency? M.Sc Thesis University of Nottingham.

Yuksek, I., Gorgulu, S., Kocabey S., Tuna, M., and Dursun, B. (2015). Assesment of Daylighting Performances of Classrooms: A Case Study in Kirklareli University, Turkey. *Light & Engineering Vol. 23, No.1, pp.15-24, 2015.* Znack Publishing House, Moscow ISSN 0236-2945.

#228: Effect of pretreatment of rice husk with $KMnO_4$ on biogas production from the co-digestion of Thai rice noodle wastewater, animal manures and rice husk

Tammathat BOONKAMNERD[1], Chairat SIRIPATANA[2], Laddawan NOYNOO[3], Nirattisai RAKMAK[4], Norli ISMAIL[5], Sunwanee JIJAI[6]

[1] School of Engineering and Resources, Walailak University, Nakhon Si Thammarat, Thailand 80160 Thailand. tammathat9@gmail.com.
[2] Biomass and Oil-Palm Excellence Center and School of Engineering and Resources, Walailak University, Nakhon Si Thammarat, Thailand 80160, schairat61@gmail.com.
[3] School of Engineering and Resources, Walailak University, Nakhon Si Thammarat, Thailand 80160, ladda1995.ln@gmail.com.
[4] Biomass and Oil-Palm Excellence Center and School of Engineering and Resources, Walailak University, Nakhon Si Thammarat, Thailand 80160, nirattisai.ra@wu.ac.th.
[5] School of Industrial Technology, Universiti Sains Malaysia 11800, Pulau Pinang, Malaysia, norlii@usm.my.
[6] Faculty of Science Technology and Agriculture, Yala Rajabhat University, Yala, Thailand 95000, sunwanee.j@yru.ac.th.

The objectives of this research were two-folds: firstly, to study the biogas production from anaerobic co-digestion of Thai rice noodle wastewater (TRW) with rice husk and different types of animal manure (cow manure, quail manure, and chicken manure); secondly, to obtain kinetic parameters for the purpose of designing continuous systems. The main focus of the research was to study the effect of pretreatment of rice husk with potassium permanganate (KMnO4) solution for 24 hours on the biochemical methane potential (BMP). The experiments were divided into 6 digesters including: the digesters 1-3 in which rice husk was pre-treated with potassium permanganate, adjusting the pH to 10 and then being soaked in the solution for the retention time of 24 hr. The digesters 4-5 which used untreated rice husk as a co-substrate. In each digester, 10 g of manure, 10 g of rice husk and 200 mL of TRW were used as co-substrates. The results show that the digester 1 which used pre-treated rice husk co-digested with cow manure and TRW gave the highest cumulative biogas (average value of 1,375 mL, 426.0 mL biogas/gCODadded) as well as the biochemical methane potential (215 mL CH_4 /$gCOD_{added}$) , followed by digester 2 which used pre-treated rice husk co-digested with quail manure and TRW (1,144 mL biogas, 221.7 mL biogas/gCODadded and 112 mL CH_4 /$gCOD_{added}$), and digester number 3 (pre-treated rice husk co-digested with chicken manure and TRW, 862 mL biogas, 186.3 mL biogas/gCODadded and 94.1 mL CH_4 /$gCOD_{added}$). The results show that pretreatment of rice husk with KMnO4 increased the co-substrate biodigestibility greatly (almost double for digest 2 and 3) which could be a result of the destruction of lignin and hemicellulose structures, helping the microorganisms to digest more substrate and thus produce more biogas. Furthermore, due to the complexity of substrate and accumulative biogas evolution (ABE) curves, the conventional the Gompertz model did not represent the ABE data very well. We also showed how Gompertz-type models and parameters can be converted to Monod-type (in this case Contois model) parameters and become more valuable not only for representing the results in batch AD specifically but also for being used directly in AD process design.

Keywords: Thai rice noodle wastewater; animal manure; pretreatment of rice husk; anaerobic co-digestion; matching model

1. INTRODUCTION

Demand for energy is increasing enormously due to a steady increase in world population and our quality of life. In Thailand, fossil fuel is the number one imported commodity in the country. Thus Ministry of Energy is seeking ways for renewable alternatives to reduce imported-energy consumption. Currently, biogas is the most frequently used renewable energy source. In the quest for new (and renewable) raw materials for biogas production, it is found that animal waste, agricultural waste and wastewater have become valuable assets and are mostly used as substrates for biogas production by anaerobic co-digestion. Thailand is the largest producer of rice in the world, and rice husks is one of the most abundant by-products to be used. Thai rice noodle is a popular product produced by many local factories across the country. The factories use large amounts of water which is finally released into the environment as wastewater. Without being properly treated, it will cause considerable environmental problems. Aerobic treatment is energy intensive thus the anaerobic co-digestion of wastewater with animal waste and rice husk have recently been considered as a promising alternative due to its low cost, energy generation and being less odorous.

Rice husk is yellow, light yellow or light brown in colour depending on the variety of rice. The chemical composition of raw rice husk has been reported to contain both organic (74%) and inorganic constituents (26%) (Xiaofei Zhao, 2018). The major organic component is cellulose 43.3 wt% and lignin 22 wt% and the major inorganic component is SiO_2 (80%). Ligno-cellulosic structure of rice husk is very difficult for microbes to digest. Thus, suitable pretreatment of raw rice husk is required to destroy its ligno-cellulosic structure so that it can be further degraded by microorganisms and finally consumed in AD process to produce biogas.

The animal manures are normally used as fertilizer. Farms use water to spray over this manure in order to clean the animals' stalls. When this waste enters the river without pre-treatment, it may create severe problems due to its high chemical oxygen demand (COD). So, AD not only has a potential to produce biogas but also to decrease environmental pollution.

Thai noodle wastewater (TRW) is translucent and white opaque in colour. If exposed in an ambient environment for seven days, it will turn into more acidic pH (lower pH) and have a spoiled odour, mostly as a result of a hydrolysis process which converts long-chain carbohydrate (Dahunsi, 2018) into sugar and finally be consumed by acidogenes to produce VFA. Thus, the anaerobic co-digestion of Thai noodle wastewater would balance nutrients and increase the buffer capacity. Numerous studies confirm that TRW has a biochemical oxygen demand (BOD) range of 3,060-28,300 mg/L and a chemical oxygen demand (COD) range of 5,568-33,969 mg/L. It is suitable for being used to produce biogas by AD.

The first objective of this research was to study the biogas production from co-digestion of TRW with rice husk and different types of manure (cow manure, quail manure, and chicken manure) as well as the effect of rice husk pretreatment with potassium permanganate. Secondly, the authors wanted to obtain kinetic parameters for the purpose of designing continuous systems. Traditionally, many authors represented concisely their accumulative biogas evolution data (ABE data) in the forms of parameters of Gompertz-type equations which many times resulted in poor representations particularly when the substrate composition was complex. However, these representations are very useful for BMP estimation but not for digester design and scale-up. In this work we illustrate the necessity for developing or extending these Gompertz-type models such that they can represent or describe the ABE curves adequately when dealing with complex substrates such as in many AD co-digestion practices. Then we try to make use of their concise representation by attempting to deduce the Monod parameters (design parameters) from Gompertz parameters. We do this by proposing what we call "Gompertz-Contois parameter matching".

2. THE GOMPERTZ-TYPE MODELS

In this paper, the Gompertz-type models are referred are to those parameterised sigmoid-shape models original pioneered by Gompertz (Syaichurrozi, 2013), then extended or generalised/unified by many authors. Tsoularis and Wallace (Van, 2018) reviewed and compared many growth models and proposed a generalised form of Gompertz-type model with its several properties. The unified model covers many sigmoid models including exponential, generalised von Bertalanffy, Richards, Smith, Blumberg, hyperbolic and Gompertz growth models. Richards' model is one of a unified Gompertz-type models which has received special interest by many researchers (Van, 2018). It covers the negative exponential, logistic, Bertalanffy and Gompertz models. Recently, Tjørve and Tjørve have developed a family of Unified growth models (called U-models) (Jha and Schmidt, 2017). They claimed that the unified models use the same set of three parameters, making comparison between the sub-models directly possible and easy. In addition, they presented the model in two forms: the first where one parameter describes the time of inflection and the second where one parameter indicates the starting point of the curves.

In the remaining sections of this paper, we will refer to different types of ABE curves (Noynoo et al., 2018) which are type I refers to the ABE curves obtained from AD with only one substrate entity. Type II, III refers to those obtained from AD with two substrate entities where they are consumed in parallel and sequential manners respectively. Type IV represents those obtained by the consumption of complex substrates by the microbial consortium.

3. GOMPERTZ MODEL IN RECENTLY DEVELOPED UNIFIED FORMS

The U-family models are other ways to look at the traditional sigmoidal models. Most of traditional sigmoidal models have been re-parameterised into different forms. However, many of these re-parameterizations are not very useful because their parameters affect more than one shape characteristics, resulting in the difficulty to compare the same parameters in different models. Moreover, each parameter cannot be interpreted explicitly because of its coupling nature (Tjørve and Tjørve, 2017). Richards (1959) proposed a model which is a generalisation of a family of models which was later called "Richards model". The model has the following form:

$$W(t) = A/(1+exp(-(b+kt)/d))^{d} \quad (1)$$

where W(t) and t are dependent variable representing growth, or accumulative product ($P'=P+\mathbf{P}_0^{'}$) and independent variable, specific digestion time respectively. A, b, k and d are the model parameters to be determined by curve-fitting. However, this form of Richards model is not very useful because of several parameters affect one shape characteristics of the curve. This parameter-shape multiple dependency makes all these parameters difficult to interpret.

Many researches realised this problem and they tried to solve it by re-parameterization. Recently, Tjørve and Tjørve (2017). Proposed an efficient re-parameterization of Richards model called Unified-Richards (U-Richards) model which is written as

$$W = A\left(1+(d-1)exp\left(-k_U(t-T_i)/d^{d/(1-d)}\right)\right)^{1/(1-d)} \quad (2)$$

Where:

- k_u = relative maximum growth rate
- Ti = time of inflection (t at which the reflection point occurs). It is a location parameter.
- A = Upper asymptote of W value,
- W = $\mathbf{P}_{\infty}^{'}$ in the context of anaerobic digestion

When t=0, W=W_0, W_0 is starting value of W (initial condition). In the context of AD, $W_0 = \mathbf{P}_0^{'}$. From the unified-Richards model (Eq. (1)), where d is exponent of part of exponent which control the inflection value, setting $d \rightarrow 1$, $d \neq 1$, the resulting in the unified-Gompertz model. That is,

$$P' = P + P_0' = P_\infty' \, exp(-exp(-e\,k_U(t-T_i))) \quad (3)$$

Similarly, we can write $\mathbf{P}_0^{'}$ in terms of P_∞, k_u and T_i or T_i in terms of P_∞, k_u and $\mathbf{P}_0^{'}$ as follow.

$$\theta = P_0'/P_\infty = 1/\left[exp(exp(e.k_U T_i)) - 1\right] and \; T_i = \left[ln\left(ln\left((1+\theta)/\theta\right)\right)\right]/e.k_U \quad (4)$$

Or writing in term of P_∞ instead of P_∞' and $\mathbf{P}_0^{'}$ that is

$$P = P_\infty[(1+\theta)exp(-exp(-e.k_U(t-T_i))) - \theta] \quad (5)$$

Similarly, comparing a corrected modified Gompertz form (Siripatana et al., 2016) to Eq. (3), the following relations are obtained.

$$k_U = R_m/P_\infty' = R_m/(1+\theta)P_\infty, T_i = \lambda + \left(1/e.k_U\right), R_m = k_U(1-\theta)P_\infty \; and \; \lambda = T_i - \left(1/e.k_U\right)$$

In the context of fitting ABE curves, Eq. (3) is most useful because it is a corrected form and P_0' does not appear in the model.

4. CONTOIS MODEL

Monod kinetics does not take into account the hindrance for substrate consumption due to high cell biomass concentration which suffers from mass transfer limitation. There are a few of models were proposed to address this problem and Contois models has been in a special attention.

Firstly, we will describe the Contois model for batch AD. In doing so, we impose the following assumptions:

1. The specific growth rate of the microorganisms involved in the AD process follows Contois kinetics without any (explicit) inhibition.
2. The biogas (biomethane and biohydrogen) production is growth associated.
3. The cell yield and product (biogas) yield are constant

The Contois model is based on the following kinetic function.

$$\mu = \mu_m S / \left[K_C \left(P + P_0' \right) + S \right] = \mu_m \left(P_\infty - P \right) / \left[K_C Y_{PS} \left(P + P_0' \right) + P_\infty - P \right] \quad (6)$$

$$dP/dt = \mu_m \left(P_\infty - P \right) \left(P + P_0' \right) / \left[K_C Y_{PS} \left(P + P_0' \right) + P_\infty - P \right] = \mu_m / \left[\left(K_C Y_{PS} / \left(P_\infty - P \right) \right) + \left(1 / \left(P + P_0' \right) \right) \right] \quad (7)$$

Upon integration

$$K_C Y_{PS} \int_0^P dP / \left(P_\infty - P \right) + \int_0^P dP / \left(P + P_0' \right) = \mu_m t \quad (8)$$

We obtain, after arrangement.

$$\left(K_C Y_{PS} / \mu_m \right) \ln \left(P_\infty / \left(P_\infty - P \right) \right) + \ln \left(\left(P + P_0' \right) / P_0' \right) / \mu_m = t \quad (9)$$

or

$$t = K \cdot ln \left(P_\infty / \left(P_\infty - P \right) \right) + ln \left(\left(P + P_0' \right) / P_0' \right) / \mu_m, \; K = \left(K_C Y_{PS} / \mu_m \right) \quad (10)$$

The prime notation in X is the concentration of active microbes (cell biomass) at a specific time. μ_m, μ are the maximum and the specific growth rate at a particular substrate concentration, K_c is the Contois saturation constant. If we assume that all yield coefficients are constant and using the following definitions,

$$Y_{PS} = \Delta P / \Delta S, Y_{XS} = \Delta X' / \Delta S, Y_{PX'} = \Delta P / \Delta X' = Y_{PS} / Y_{X'S} \text{ and } P_0' / Y_{PS} = X_0' / Y_{XS} \quad (11)$$

5. MATERIALS AND METHODS

5.1. Analytical characteristics of wastewater and substrates

1. The rice husk samples were collected from rice mills. The samples were kept at room temperature until used in the experiment.

2. Animal manures (Chicken, cow and quail) were freshly collected from the farm of Yala Rajabhat University, Mae Lan Campus. Prior to use in the experiment, the animal manures were dried by sunlight at ambient temperature.

3. The Thai rice noodle wastewater sample was collected from the community in Yala province. It was kept at 0-4°C until used in the experiments.

The physical and chemical characteristics of rice husk, animal manures and wastewater were analysed before starting the experiments. The parameters were measured according to the standard methods.

5.2. Experimental set-up

The BMP test was conducted using the method of Owen et al. (1979). The experiments were conducted at room temperature (28-30ºC) until batch completion. The 325-ml-volume serum bottles were used as reactors and a working volume of 20 ml was used in all experiments. The serum bottles were covered with the rubber stoppers and sealed with aluminum caps. The volume of biogas was measured daily by using water displacement method. The experiment setup is shown in Figure 1.

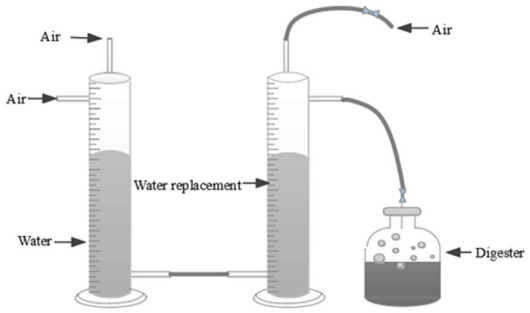

Figure 1: Schematic diagram of water displacement method system for biogas volume quantification during anaerobic digestion tests.

5.3. Experimental design

All experiments were operated in batch mode. Each reactor contains different type of manure and rice husk (non-pretreatment and pretreatment with potassium permanganate ($KMnO_4$). The anaerobic co-digester having a total working volume of 200 ml. The rice husk was pretreatment by soaking in the potassium permanganate solution prepared by adjusting the pH to alkaline of 10. After 24 hours of soaking, they were dried at 105°C and kept at desiccator for use as the co-digestion of anaerobic co-digestion (AcoD) test. The AcoD experiment of this study was divided in 6 designs with digesters 1-3 using TRW with pretreatment of rice husk and different types of animal manure and digesters 4-6 using TRW with non-pretreatment of rice husk and different types of animal manure. Each of digester used 10g of manure, added 10g of rice husk and 200 mL of TRW. Six different types of animal manure were used: digesters 1 and 4 used cow manure (CM), digesters 2 and 5 used quail manure (QM) and digesters 3 and 6 used chicken manure (ChM). Initial pH for all digesters was adjusted to 6.8-7.2 by addition of NaOH (1 N) solution. The experiments were duplicated in all digesters.

5.4. Analytical procedures

In all experiments, pH, Chemical Oxygen Demand (COD), Volatile Solids (VS), Alkalinity and Volatile Fatty Acids (VFA) were evaluated according to standard methods for the examination of water and wastewater (APHA, 2017). Daily biogas production was settled by a water displacement method. The potential of biogas production can be calculated by maximum accumulative biogas divided by gCODadded or maximum accumulative biogas divided by gVS_{added} .

6. RESULTS AND DISCUSSION

6.1. Properties of wastewater and substrates

Table 1: The results of experiment

Digester	pH		Alkalinity (mg/L as$CaCO_3$)		VFA (mg/L asCH_3COOH)		VFA/ALK		COD (mg/L)	VS (mg/L)
	before	after	before	after	before	after	before	after		
1	7.05±0.07	4.40±0.88	680	1635	720	4358	1.06	2.67	39394.14	24,933
2	7.05±0.07	5.71±0.10	1490	2470	2595	4778	1.74	1.93	19432.42	12,299
3	7.20±0.28	5.15±0.21	1670	1870	1530	5010	0.92	2.68	16138.12	10,214
4	7.00±0.00	6.16±0.48	1050	910	1335	5663	1.27	6.22	21032.96	13,312
5	7.10±0.14	5.49±0.50	780	875	1020	5850	1.31	6.69	34170.66	21,627
6	7.05±0.07	5.73±0.12	1600	1885	2340	7083	1.46	3.76	45856.34	29,023

Note: Calculate COD by factor of VS

Digester 1: Cow manure of Rice husk by pretreatment with $KMnO_4$
Digester 2: Quail manure of Rice husk by pretreatment with $KMnO_4$
Digester 3: Chicken manure of Rice husk by pretreatment with $KMnO_4$
Digester 4: Cow manure of Rice husk by non-pretreatment
Digester 5: Quail manure of Rice husk by non-pretreatment
Digester 6: Chicken manure of Rice husk by non-pretreatment

The characterisation of substrates before and after the AcoD test are shown in Table 1. The pH and VFA are important indicators of anaerobic digestion because their dynamics reflect the changing conditions. As shown in Table 1, the pH of all fermentation that co-digested with pretreated and non-pretreated of rice husk at the end of the digestion period (30 days) remained <7. The decrease of pH may have been associated with the variation in VFA concentration because the VFAs produced during AcoD reduce the pH. The highly concentrated acids in the manure led to a noticeable drop in pH. The pH decreased dramatically during the initial stage of the co-digestion of TRW, manure and rice husk (with pre-treated and non-pre-treated) likely due to the production of various organic acids from the degradation of cellulose, hemicellulose, and lignin after pretreatment (Guo and Mochidzuki, 2011). Methanogens are active at pH between 6.2 and 8, with an optimal range of 7.0 – 7.2 (Poliafico, 2007). Anaerobic digestion mainly includes 3 steps including hydrolysis, acidogenesis and methanogenesis. During the first two stages the production of a large amount of VFA leads to the decrease of solution pH. Non-methanogenic microorganisms can act to lower pH while, in this condition, methanogenic activities will be significantly inhibited. Since the pH trend is tightly linked to the variation of VFA concentration in the reactor, it was assumed to be an indicator of the process stress (L.Björnsson, 2000).

VFAs are intermediate organic acid products and the total VFA concentration is an important indicator of metabolic status (aside from influencing the pH) during anaerobic digestion (AD) (Fernández 2005). Table 2 shows that VFA/ALK after the experiment was higher than before the experiment. Therefore, when high VFA occurred, the pH in the system was rapidly reduced. Digester 2 showed the highest alkalinity at 2,470 mg/L as CaCO3 followed by digesters 6, 3, 1, 4 and 5 (1,885-875 mg/L as CaCO3). The high alkalinity was good for this system because it made a high buffer and stable biogas production. Digester 6 showed the highest COD.at 45856.34 mg/L followed by digesters 1, 2, 3, 4 and 5 with 39394.14, 19432.42, 16138.12, 21032.96 and 34170.66 mg/L respectively. Biodegradability improvement means that not only is more substrate used but also more biogas produced (Pang, Y, 2008)

7. BIOGAS PRODUCTION

The accumulative and biogas production of all experiments is shown in Table 2 whilst Figure 5 shows the total accumulated biogas volume for all experiments. The results show that digesters 1-3 that used pre-treated rice husk in the AcoD test showed more accumulated biogas than digesters 4-6 that used non-pre-treated rice husk after more than 20 days of experiment. Digester 1 (pre-treated rice husk co-digested with cow manure and TRW) gave the highest cumulative biogas (average value of 1,375 mL, 426.0 mL biogas/gCODadded) as well as the most biochemical methane potential (215 mL CH_4 /$gCOD_{added}$) , followed by digester 2 (pre-treated rice husk co-digested with quail manure and TRW) (1,144 mL biogas, 221.7 mL biogas/gCODadded and 112 mL CH_4

/$gCOD_{added}$), and digester number 3 (pre-treated rice husk co-digested with chicken manure and TRW, 862 mL biogas,186.3 mL biogas/gCODadded and 94.1 mL CH_4 /$gCOD_{added}$). From these results, the pretreatment of rice husk with KMnO4 increased the co-substrate biodigestibility greatly (almost double for digest 2 and 3) which could be a result of the destruction of lignin and hemicellulose structures, helping the microorganisms to digest more substrate and thus produce more biogas.

Table 2: Accumulative and biogas production of all experiment

Digester	Substrate	Maximum accumulative of biogas production (mL)	Potential of biogas production ($mL/gCOD_{added}$)	BMP based on 50.5 * $\%CH_4$ ($mL\ CH_4/gCOD_{added}$)
1	CM + RP	1,375	426.0	215.2
2	QM + RP	861.5	221.7	112.0
3	ChM + RP	783.5	186.3	94.1
4	CM + R	649.5	95.0	48.0
5	QM + R	1144	145.2	73.3
6	ChM + R	334	36.4	18.4

Note: CM = Cow manure, QM = Quail manure, ChM = Chicken manure
TRW = Thai rice noodle wastewater
R = Rice husk by non-pretreatment
RP = Rice husk by pretreatment with KMnO4
*Based on average value obtained from similar sets of experiments (Jijai *et al.* 2017)

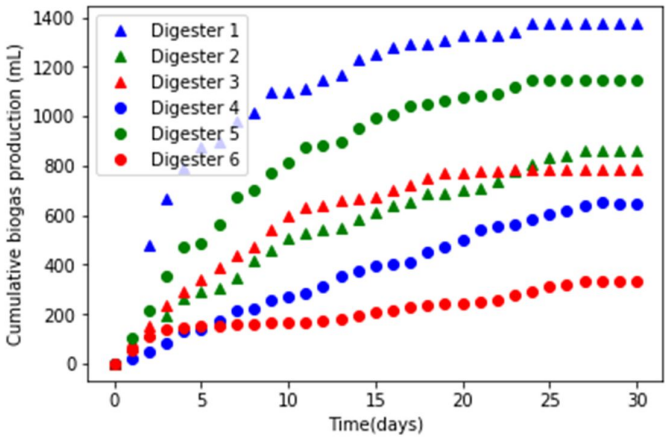

Figure 2: The total accumulated biogas volume for all experiments.

8. THE EFFECT OF RICE HUSK BY PRETREATMENT ON BIOGAS PRODUCTION

The effect of rice husk pre-treated with potassium permanganate ($KMnO_4$) had an adjusted pH of 10 and the retention time of 24 hours added to the potential of biogas production, with anaerobic co-digestion of Thai rice noodle wastewater and different type of manure (cow manure, quail manure, and chicken manure). The results depicts the comparison that the digesters used pretreatment of rice husk with potassium permanganate and adjusted the pH to alkaline of 10 at same type of manure gave a higher potential of biogas production than the digesters using non-pretreatment of rice husk. Schmidt (2017) reported that the substrates pretreatment with alkaline hydrolysis such as Sodium hydroxide (NaOH) can break down biomass in pretreatment and facilitates hydrolysis by disrupting cell wall structures, driving modification of the lignin structure and reducing cellulose crystallinity and chain length. Therefore, bacteria in the digester transformed these organic materials easily into biogas. GuangyinChen (2015) studied the effect of using concentrated NaOH as a pretreatment for substrate. The results showed that as the concentration of NaOH increased, the cellulose was higher. When the quantity of hemicellulose and lignin decreased, the efficiency of the biomass digestion was higher.

The environment of the anaerobic co-digestion process of Thai rice noodle wastewater with rice husk and different types of manure (cow manure, quail manure, and chicken manure) gave an average pH in the range of 4.40 – 6.16. It was observed that, at the end of experiment, the pH was higher than at the start of the experiment. The resulting pH is summarised in Table. 2. The initial anaerobic digestion was consumed by acidogenes to produce VFA and then was consumed by methanogenes to produce methane. Thus, as VFA increased, the efficiency of the biomass digestion is higher while the pH is decreased and can lower the methanogenic bacteria activity. Schmidt (2017) reported that Methanogenic bacteria having an average pH7 affects the highest production of biogas. Thus, the activity of biogas production depends on various parameters like pH, alkalinity (ALK), VFA which are summarised in Table 2. The presence of volatile fatty acids (VFAs) tends to decrease the pH and can lower the methanogenic bacteria activity and hence the biogas production in agreement with Patil & Deshmukh (2015) and Jijai et al. (2017) who studied the effect of biogas production from wastewater and residue wastes.

9. FITTING THE DATA SET TO U-GOMPERTZ MODEL

The results of curve-fitting for U-Gompertz model are presented in Figure 2. The best estimated parameters including those of the corresponding original models are summarised in Table 3. This is as expected because usually Gompertz can fit well when the biomass density is high. Since this is the BMP test (Yingthavorn N, 2019). where high biomass density was intended, thus U-Gompertz (or its original form) fits the data well.

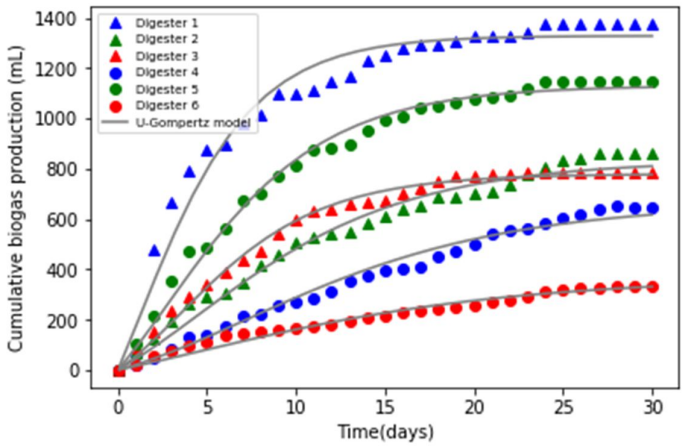

Figure 3: Biogas accumulation for Unified Gompertz model

Table 3: Parameters and the best-fit parameter (R^2) of cumulative biogas production for Unified Gompertz model

Digester	Parameter						
	P_∞(mL)	T_i(d^{-1})	k_u(d^{-1})	R^2	α(d^{-1})	λ(d)	R_m(mL/d)
1	1328.91	1.27	0.1006	0.967	0.2734	-2.3872	90.80
2	833.97	4.45	0.0536	0.9776	0.1734	-2.4141	36.95
3	779.6	3.51	0.0816	0.9918	0.1277	-0.9988	55.49
4	665.28	7.24	0.0437	0.9832	0.1039	-1.1792	26.05
5	1130.7	2.87	0.073	0.9911	0.2059	-2.1699	65.534
6	368.89	4.58	0.0359	0.9671	0.0976	-5.6684	9.7353

10. MATCHING U-GOMPERTZ MODEL TO THE CONTOIS MODEL

First, we must make sure that the U-Gompertz model does fit the ABE data well. If so, this is how the matching process proceeds.

1. Substituting Eq. (5) for θ to write θ in term of k_u and T_i. Then, the set of ABE data is fitted with U-Gompertz model and the best-fit parameters (P_∞, k_u, T_i) of the model are obtained.
2. Calculate θ from Eq. (4), and P_0' is then calculated from $P_0'=\theta P_\infty$.
3. Calculate Y_{PS} from P_∞ and $\Delta S_\infty = S_0 - S_\infty$ where S_0 and S_∞ are initial and final substrate concentration based on COD or VS. ($Y_{PS} = P_\infty/\Delta S_\infty$)
4. Choose a proper range of P for matching (eg. $0.5P_\infty < P < 0.95P_\infty$) and calculate time step (t_i) corresponding to the P-range.
5. Rewrite Eq. (10) in the following form and solve for K_i

$$t_i = K_i A_i + B_i / \mu_m \tag{12}$$

$$For\ i = 1\ to\ i = n;\ K_i = \left(t_i - B_i / \mu_m\right) / A_i \tag{13}$$

Where: $A_i = ln\left(P_\infty / \left(P_\infty - P\right)\right), B_i = ln\left[\left(P_0' + P_i\right) / P_0'\right]\ and\ K_i = K_{C_i} Y_{PS} / \mu_m$

6. Searching for μ_m which satisfies the following criterion.

$$Relative\ difference\ (\%) = \left|2\ (100)\left[\left(K_n - K_1\right) / \left(K_n + K_1\right)\right]\right| < 1 \tag{14}$$

A good estimate of K_i is $K_{i(est)} = (K_n + K_1)/2$ and K_C is then calculated from $K_C = K_{i(est)}\mu_m/Y_{PS}$

Substituting μ_m and K_C into Equation (9) and plotting P versus t using both U-Gompertz model and the corresponding matched Contois model on the same graph. The comparison used to be satisfactory before the matched Contois model to be used for the design propose.

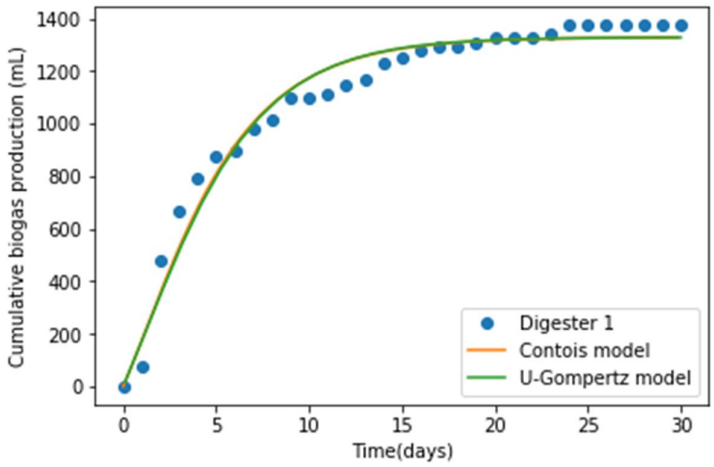

Figure 4: The best example for fitting of Gompertz-Contois Matching

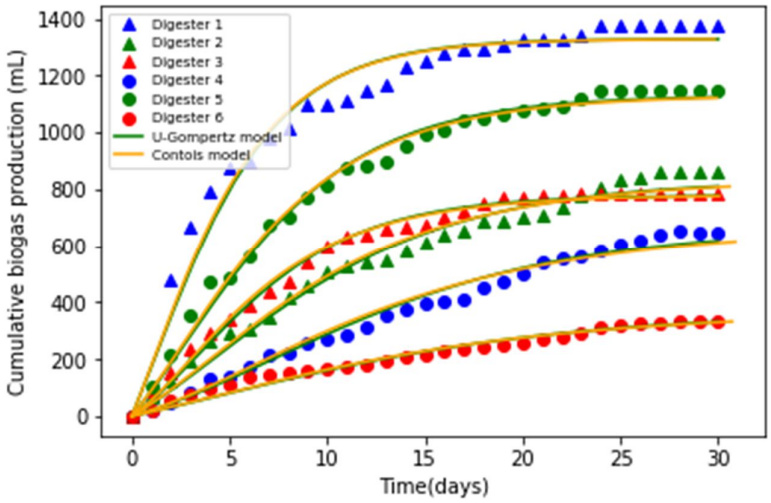

Figure 5: U-Gompertz-Contois Matching

Table 4: Parameters and the best-fit parameter (R^2) of cumulative biogas production for U-Gompertz-Contois and Monod matching model

Digester	Parameter					
	θ	μ_0 (d)	P_0' (mL)	Y_{PS} (mL/ (mgCOD/L))	μ_{mc} (d^{-1})	K_C (mg/L)
1	0.3207	0.387	426.31	0.0426	0.76	68.47
2	0.1734	0.2786	144.57	0.0222	0.44	146.81
3	0.1277	0.4831	99.57	0.0186	0.72	194.57
4	0.1039	0.2807	69.13	0.0095	0.4	409.88
5	0.2059	0.3537	232.89	0.0145	0.61	233.78
6	0.2649	0.1526	97.71	0.0036	0.28	858.76

We have chosen the cases of single and co-digestion to illustrate the necessity for developing or extending these Gompertz-type models such that they can represent or describe the ABE curves adequately when dealing with complex substrates such as in many AD co-digestion practices. Large amounts of ABE data has accumulated in the literature and has been represented concisely by Gompertz-type models and their best estimated parameters. We try to make use of their concise representation by attempting to deduce the Monod parameters (design parameters) from Gompertz parameters. The result that as the matching techniques can be used effectively to convert the Gompertz-type parameters into their corresponding Monod-type parameters and we attempted to bridge the gap between this data and their practical uses effective in design and operation of biogas systems rather than going back to look for the original data.

11. CONCLUSIONS

The matching techniques can be used effectively to convert the Gompertz-type parameters into their corresponding Monod-type parameters. The matched Monod-type parameters (using Contois model) can be used to design a

completely-mixed continuous AD process using simulation. Thus, a large amount of BMP, BHP and SMA data which was condensed in the form of Gompertz-type models and parameters, become more valuable not only for representing the results in batch AD specifically but also for being used directly in AD process design. However, these illustrations are over-simplified and in practice we must take into account other significant factors in AD-system design and operation.

12. ACKNOWLEDGEMENT

The arthor would like to thank Yala Rjabhat University and Walailak University grants for the financial support.

13. REFERENCES

Angelidaki I., Alves M., Bolzonella D., Borzacconi L., Campos J. L., Guwy A. J., Kalyuzhnyi S., Jenicek P. and van Lier JB. Defining the biomethane potential (BMP) of solid organic wastes and energy crops: a proposed protocol for batch assays. Water science and technology.2009, 59(5):927-34.

Anthony Njuguna Matheri. (2016). Modelling the Kinetic of Biogas Productionfrom Co-digestion of Pig Waste and Grass Clippings sewage sludge.Bioresour.Technol. 244, 996–1005

APHA, AWWA, & WPCF. (2017). Standard Methods for Examination of Water and Wastewater (19 ed.). New York: American Public Health Association, Washington D.C.

Cerrillo, M., Viñas, M., Bonmatí, A., 2018. Anaerobic digestion and electromethanogenic microbial electrolysis cell integrated system: Increased stability and recovery of ammonia and methane. Renew. Energy 120, 178–189.

Cook, S.M., Skerlos, S.J., Raskin, L., Love, N.G., 2017. A stability assessment tool for anaerobic codigestion. Water Res. 112, 19–28.

Dahunsi (2018). Mechanical pretreatment of lignocelluloses for enhanced biogas production: Methane yield prediction from biomass structural components.

Deepanraj B. (2015). Kinetic study on the effect of temperature on biogas production using a lab scale batch reactor

Fernández, A., Sanchez, A., Font, X., 2005. Anaerobic co-digestion of a simulated organic fraction of municipal solid wastes and fats of animal and vegetable origin. Biochem. Eng. J. 26, 22–28.

Gompertz, B. (1825). On the Nature of the Function Expressive of the Law of Human Mortality, and on a New Mode of Determining the Value of Life Contingencies, 115(0), 513–583.

Guo, P., Mochidzuki, K., Cheng, W., Zhou, M., Gao, H., Zheng, D., Wang, X.F., Cui, Z.J., 2011. Effects of different pretreatment strategies on corn stalk acidogenic fermentation using a microbial consortium. Bioresour. Technol. 102, 7526– 7531.

Iqbal Syaichurrozi. (2013). Predicting kinetic model of biogas production and biodegradability organic materials: Biogas production from vinasse at variation of COD/N ratio.

Björnsson, L., Murto, M., Mattiasson, B. Evaluation of parameters for monitoring an anaerobic co-digestion process, Appl. Microbiol. Biotechnol. 54(2000) 844–849.

Pang, Y., Liu, Y., Li, X., Wang, K., Yuan, H., 2008. Improving biodegradability and biogas production of corn stover through sodium hydroxide solid state pretreatment. Energy Fuel 22 (4), 2761–2766.

Pham Van. (2018). A new kinetic model for biogas production from co-digestion by batch mode

Poliafico, M., 2007. Anaerobic digestion: Decision support software. Masters Thesis, Department of Civil, Structural and Environmental Engineering, Cork Institute of Technology, Cork, Ireland.

TingLiu. (2018) Effects of liquid digestate pretreatment on biogas production for anaerobic digestion of wheat straw

Tjørve, E., & Tjørve, K. (2010). A unified approach to the Richards-model family for use in growth analyses: Why we need only two model forms. Journal of Theoretical Biology, 267, 417–425.

Tjørve, K., & Tjørve, E. (2017). A proposed family of Unified models for sigmoidal growth. Ecological Modelling, 359, 117– 127

Tsoularis, A., & Wallace, J. (2002). Analysis of Logistic Growth Models. Mathematical Biosciences, 179, 21–55.

Hagos, K., Zong, J., Li, D., Liu, C., Lu, X., 2017. Anaerobic co-digestion process for biogas production: Progress, challenges and perspectives. Renew. Sustain. Energy Rev. 76, 1485–1496.

Jha, P., Schmidt, S., 2017. Reappraisal of chemical interference in anaerobic digestion processes. Renew. Sustain. Energy Rev. 75, 954–971

Noynoo L., Siripatana C., Jijai S., Rakmak N. and Phayunphan K., "Gompertz-Type Two-Substrate Models for Batch Anaerobic Co-Digestion," submitted for publication.

Ma, J., Amjad Bashir, M., Pan, J., Qiu, L., Liu, H., Zhai, L., Rehim, A., 2018. Enhancing performance and stability of anaerobic digestion of chicken manure using thermally modified bentonite. J. Clean. Prod. 183, 11–19.

Ma, J., Bashir, M., Pan, J., Qiu, L., Liu, H., Zhai, L., & Rehim, A. (2018). Enhancing performance and stability of anaerobic digestion of chicken manure using thermally modified bentonite. Journal of Cleaner Production, 183.

Ghatak, M.D. (2017). Kinetic Model Development for Biogas Production from Lignocellulosic Biomass

Uddin, M.K. (2017). A study on the potential applications of rice husk derivatives as useful adsorptive material.

Sharma, R. (2014). Effect of Pretreatment of Rice Husk for the Production of Biogas

Richards, F. J. (1959). A Flexible Growth Model for Empirical Use. Journal of Experimental Botany - J EXP BOT, 10, 290–301.

Salimi M N & Yusoff A H M. (2017). Conversion of rice husk into fermentable sugar by two stage Hydrolysis

Schnute, J. (2011). A Versatile Growth Model with Statistically Stable Parameters. Canadian Journal of Fisheries and Aquatic Sciences, 38, 1128–1140.

Siripatana, C., Jijai, S., & Kongjan, P. (2016). Analysis and extension of Gompertz-type and Monod-type equations for estimation of design parameters from batch anaerobic digestion experiments. In AIP Conference Proceedings (Vol. 1775, p. 030079).

Shitophyta and Maryudi. (2018). Comparison of kinetic model for biogas production fromcorn cob

Jijai, S., and Siripatana, C. "Kinetic Model of Biogas Production from Co-digestion of Thai Rice Noodle Wastewater (Khanomjeen) with Chicken Manure," Energy Procedia, vol. 138, pp. 386–392, 2017.

Xiaofei Zhao, LeiLi DiWu, Taihui Xiao, Yao Ma., 2018. Modified Anaerobic Digestion Model No. 1 for modeling methane production from food waste in batch and semi-continuous anaerobic digestions

Yingthavorn N., Noynoo L., Boonkamnerd T., Rakmak N. and Siripatana C., "Biochemical Methane Potential of Palm Oil Mill Effluent (POME) Co-Digested with Rubber Latex Effluent (LTE): Effect of POME/LTE Ratio and Temperature," submitted for publication

#230: Harnessing low-grade waste heat by a thermomagnetic engine in conjunction with a hybrid generator system

Yeongmin KIM[1], Young Soo LEE[2], Rahate AHMED[3], Wongee CHUN[4]

[1] Department of Nuclear and Energy Engineering, Jeju National University, Jeju 63243, Republic of Korea, km820426@jejunu.ac.kr
[2]Thermal Energy Conversion Laboratory, Korea Institute of Energy Research, Daejeon 34129, Republic of Korea, yslee@kier.re.kr
[3]Department of Nuclear and Energy Engineering, Jeju National University, Jeju 63243, Republic of Korea, rahat@jejunu.ac.kr
[4]Department of Nuclear and Energy Engineering, Jeju National University, Jeju 63243, Republic of Korea, wgchun@jejunu.ac.kr

Conversion of low-grade thermal energy into electrical energy was explored with the application of a hybrid generator system driven by a thermomagnetic heat engine. The hybrid generator system consists of an electromagnetic generator (EMG) and flexible piezoelectric films, which was designed to draw electric power as much as possible from the rotating shaft of the thermomagnetic engine. The major components of the engine are Gadolinium (Gd) blocks and a bar shaped permanent magnet, where their interaction develops the rotational motion of the engine thanks to the magneto-caloric effect of Gadolinium (Gd). Gadolinium is one of the distinct materials whose transition temperature (Curie temperature) of magnetic property from ferromagnetic to paramagnetic takes place near room temperature facilitating the use of low–grade waste heat. The conventional electromagnetic generator (EMG) has an excellent performance with an open circuit voltage of 2 V, a short-circuit current of 6 mA under the rotational speed of 130 rpm, when the temperature difference between hot and cold water jets was around 6.5°C. Under the same conditions piezoelectric generator produced an open circuit voltage and short circuit current of 8 V and 8.2 μA, respectively.

Keywords: Gadolinium; hybrid generator system; thermomagnetic heat engine; electromagnetic generator; piezoelectric generator

1. INTRODUCTION

Due to growing challenges of environmental pollution and the worldwide energy crisis, strenuous efforts have been carried out by researchers and engineers to reclaim various forms of energies around us such as wind, solar, tide, waste heat, etc. so as to exploit the exergy contents that they possess which would otherwise go to waste. Of these, enormous amount of waste heat is produced from various industrial processes every day and it has great potential to be utilised more competitively as compared to other forms of energy readily available to us. Sources of waste heat include hot combustion gases, heated effluents from power plants and industrial processes, and heat transfer from various hot surfaces. It is estimated that 20 to 50% of industrial energy consumption remains unused and released as waste heat into the atmosphere. This wasted heat can be used to generate power by using a well-established technology.

Gadolinium is one of the rare-earth ferromagnetic materials, which is often used in the thermomagnetic engines based on transition materials displaying a sharp change in its magnetic property with temperature. Gadolinium has the transition temperature (Curie temperature) of 293.2 K, which makes it an attractable candidate to design a heat engine to harness low-grade waste heat not far above room temperature. By heating and cooling the gadolinium above and below its curie temperature and changing its magnetic property, it can be effectively applied to convert thermal energy into mechanical and, eventually into electrical energy.

These days, flexible piezoelectric materials are widely used to convert mechanical power into electricity (mechanical energy harvesters) in various configurations, especially with very high frequency response. They can effectively harvest mechanical energy from wind, respiration, rain-fall, footsteps, etc. Although piezoelectric materials have several advantages such as high frequency response, self-power generating, small physical dimensions and large measuring ranges, developing a piezoelectric generator is not simple due to their poor performance characteristics (low current, high impedance) and relatively low power output. To cope with the inherent technical issues related to piezoelectric materials, many attempts were made to combine a piezoelectric generator with some other types of energy converter like electromagnetic generator, photovoltaic resulting in an increase in the gross power generation. There are quite a number of research papers reporting the use of conventional electromagnetic generators in conjunction with piezoelectric materials. Especially, the efforts to design hybrid energy harvesters applying PV technology and piezoelectricity drew much attention as they appear to be practical and energy-efficient by allowing power generation by wind and solar at the same time without undue difficulties. It has been shown that these types of hybrid generators are capable of producing high power output.

This paper introduces an energy harvester to harness low temperature waste heat, where the above mentioned transition material, Gd, was extensively used to convert thermal energy into mechanical energy. A heat engine, thermomagnetic engine, was designed and built to exploit the change in its magnetic property with temperature. The engine readily converts thermal energy into mechanical engine and eventually into electrical energy with the help of a hybrid generator connected to the rotating axis of the engine. The hybrid generator is made by integrating an electromagnetic generator (EMG) with a number of piezoelectric generators. When the thermomagnetic engine comes into motion, power develops by EMG and piezoelectric generators. It produces a change in magnetic flux through stationary coils inducing AC currents in them as directed by the classical electromagnetic theory. Meanwhile, a magnet affixed on the tip of each piezo strip interacts with the magnets that rotate with the operation of the thermomagnetic engine, which results in the rumbling motion of piezo strips and develop power.

2. DESIGN OF A THERMOMAGNETIC ENGINE WITH GADOLINIUM

A schematic diagram of gadolinium based thermomagnetic engine is shown in Figure. 1. Proposed design comprises with 16 equally spaced gadolinium blocks, and a bar shaped permanent magnet, which makes the rotor part of the engine. Three water nozzles, 120° apart from each other, drives the thermomagnetic engine by delivering jets of hot and cold water. As shown in Figure 1, one hot jet was placed in the vicinity of the aforementioned bar magnet whereas the two cold jets were arranged on its opposite end. When hit by the cold jet, Gd becomes ferromagnetic below its Curie temperature and is attracted by the bat magnet. Meanwhile exposed to a hot water jet, its temperature gets raised above the Curie temperature and eventually becomes paramagnetic and pulled away towards the cold water jets developing a rotational motion. Of course, Gd regains its ferromagnetic nature when it returns to be hit by the cold water jet and is attracted by the permanent magnet. This cyclic motion repeats to continuously drive the thermomagnetic engine and thus produce electric power by the hybrid generator composed of EMG and piezoelectric generators.

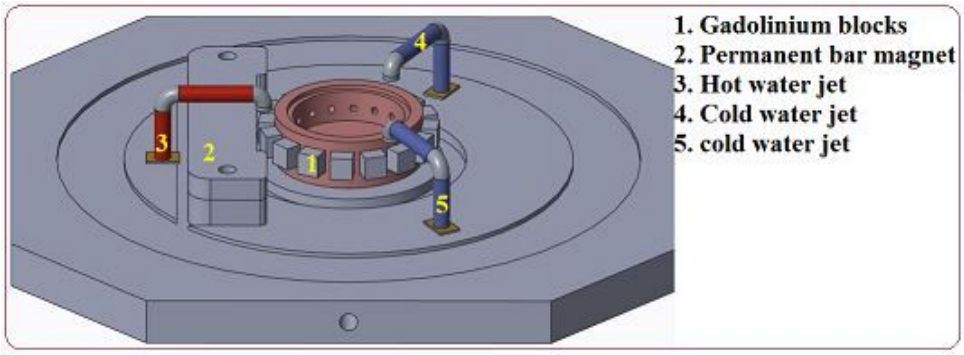

Figure 1: Schematic diagram of a thermomagnetic engine

3. DESIGN OF HYBRID GENERATOR SYSTEM

Figures 2 and 3 show some respective images of EMG and piezoelectric generators, which are the major components of the present hybrid energy harvester. As shown in Figure 2, the EMG consists of two circular structures one with cylindrical shaped magnets (a) and the other with coils (b). The former makes the rotor part and the latter makes the stator part of the present EMG. Twelve stator coils are connected in series, which develops the most power output from the hybrid generator.

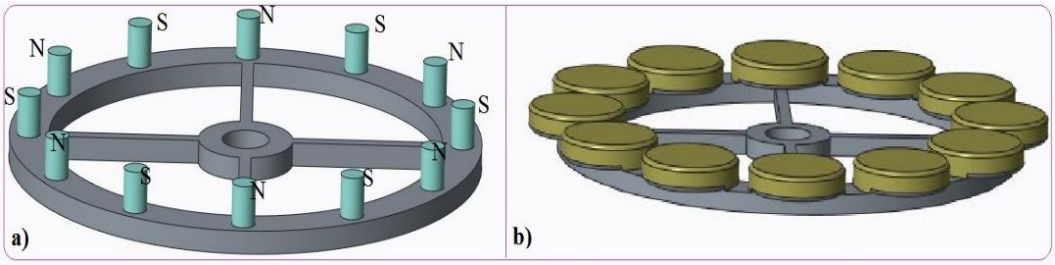

Figure 2: Electromagnetic generator (a) rotor part of EMG (b) stator part of EMG

As the engine runs, rumbling motions develop in the piezoelectric strips (films) generating electric power. Although minor, the combined power output from the piezoelectric generators still contributes in increasing the gross power output of the hybrid generator. There were 16 flexible LDT4-028K/L piezo strips used to generate power from the rotating motion of the engine. The piezo films are placed such that the rotating EMG magnets interact with the magnets affixed on the tips of piezo films. Figure 4 shows the actual energy harvester equipped with EMG and the piezoelectric generators.

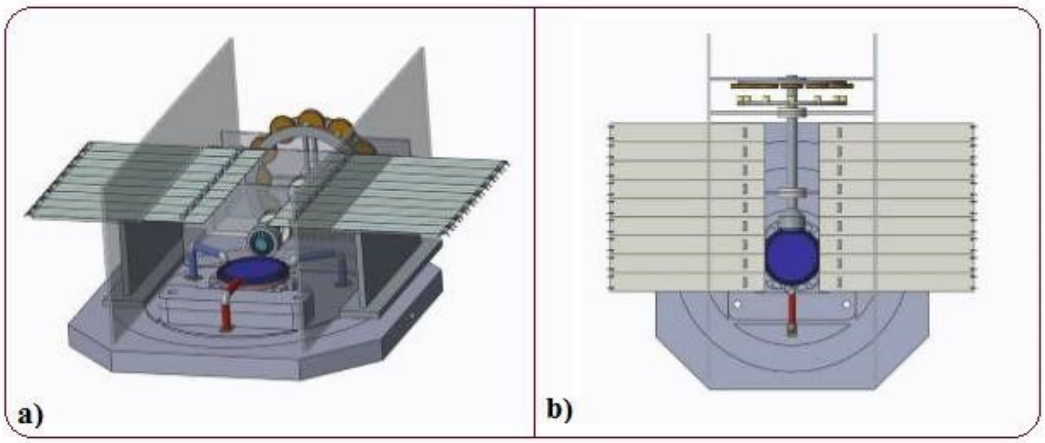

Figure 3: a) Schematic diagram of hybrid generator (EMG-Piezo) run by a thermomagnetic engine; b) Top view of the system

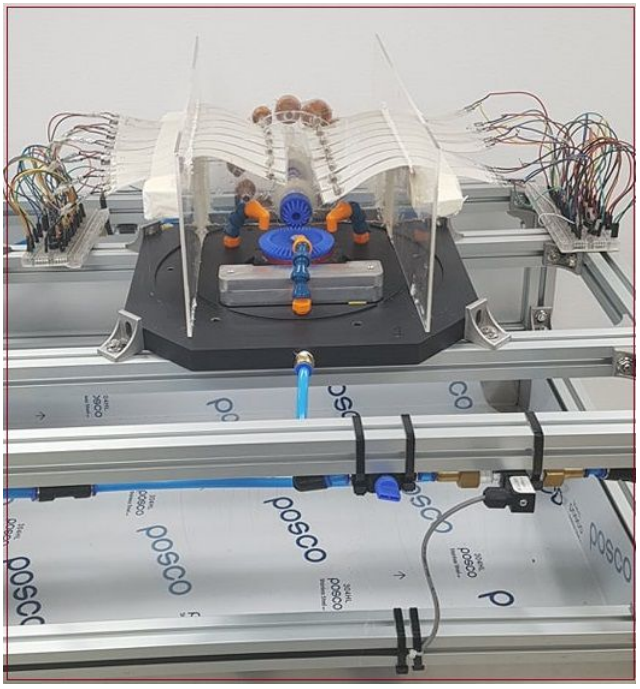

Figure 4: Hybrid generator (EMG-Piezo) integrated with a thermomagnetic engine

4. EXPERIMENTAL RESULTS

The output performance of the hybrid generator system has been analysed for its application with the operation of the thermomagnetic engine. The engine was run at different temperature differences between hot and cold water jets. The temperature of the cold water jet was kept constant at 18.5°C, while the hot water temperature was varied to different values. The gadolinium based thermomagnetic engine started to work when the temperature difference was as low as 4°C (the hot water jet at 22.5°C and the cold water jet at 18.5°C) with a rotational speed of 70 rpm. The maximum rotational speed of 228 rpm was observed when the temperature difference reached 45°C (the hot water jet at 63.5°C and the cold water jet at 18.5°C) as shown in Figure 5. The maximum amplitude of the swaying piezo films was observed at a temperature difference of 6.5°C between the hot and cold water jets when the thermomagnetic engine was rotating at speed of 130 rpm. At speeds lower than 130 rpm, the rambling motion of the piezo strips became jerky and hindered the generation of a smooth output. On the other hand, at speeds higher than 130 rpm, the amplitude of an oscillating piezo film decreased and eventually damped out. To measure its power output, each of the sixteen sheets of piezo films was connected separately with a rectifier. Measurements were made when the rotational speed of the thermomagnetic engine was maintained at 130 rpm. The AC voltage from each piezo film were subsequently rectified and integrated to produce an open circuit voltage of 8 V and a short circuit current of 8.2 µA, as shown in Figure 6. The performance of the EMG was also monitored at this test condition, where it recorded 2V and 6mA, respectively. Figure 7 shows the power output of the EMG.

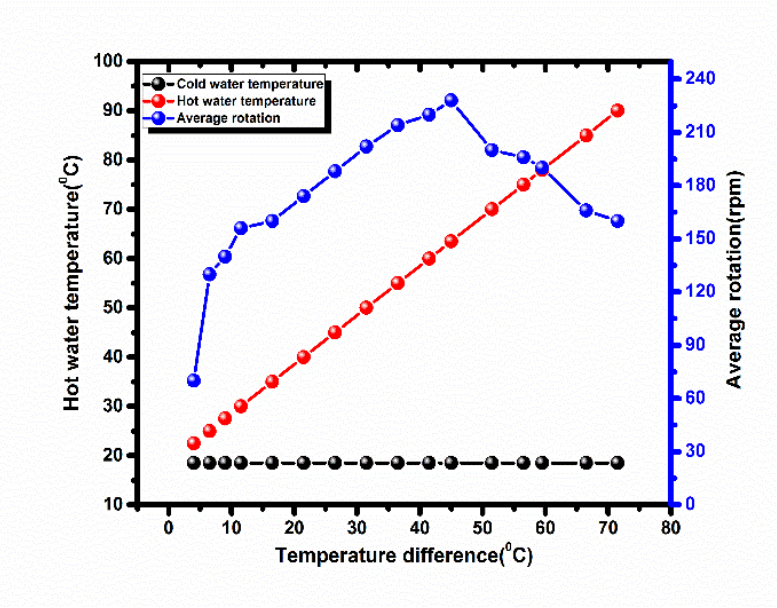

Figure 5: Variation rotational speed with temperature differences

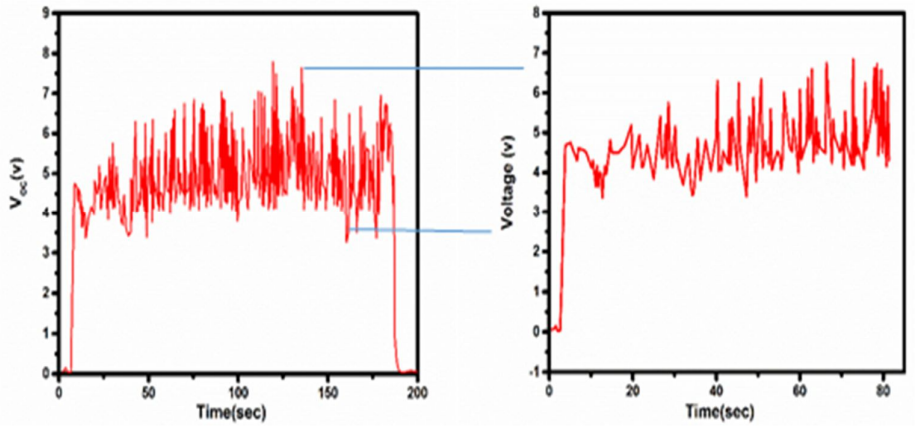

(a)

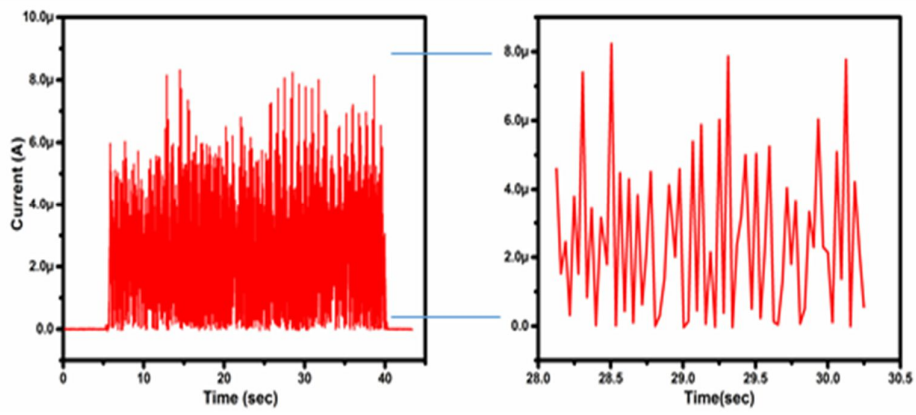

(b)

Figure 6: Power output by sixteen sheets of piezo films; a) rectified open circuit voltage produced by piezo films; b) rectified short circuit current produced by piezo films

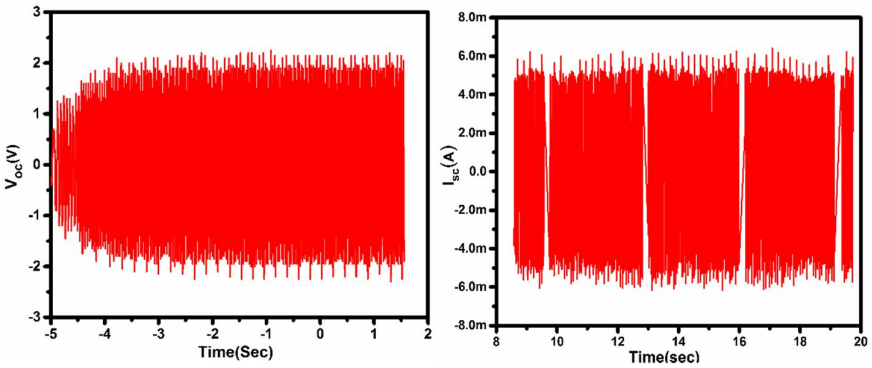

(a) *(b)*

Figure 7: Power output by electromagnetic generator (EMG) a) Open circuit voltage produced by EMG; b) Short circuit current produced by EMG

5. CONCLUSIONS

A thermomagnetic engine driven by resulting magnetic forces developed between Gd blocks and a permanent magnet was designed, fabricated and tested to analyse its applicability in harvesting low-temperature heat sources. To effectively convert the mechanical power of the engine into electrical power, a hybrid generator was developed which consists of an electromagnetic generator (EMG) and 16 strips of piezoelectric materials. The engine was operated at different temperatures between hot and cold water jets and its power output was monitored. It was observed that the maximum power could be produced by piezoelectric generators when the engine recorded its rotational speed of 130 rpm at a temperature difference of 6.5°C between the hot and cold water jets. However, more work is needed to find an operating condition where the combined power output of the EMG and piezoelectric generators could reach its maximum.

6. ACKNOWLEDGEMENT

The authors would like to acknowledge support from the National Research Foundation of Korea through the Ministry of Science, ICT & Future Planning (Grant Number 2017R1A2A1A05001461).

7. REFERENCES

Challa V.R., Prasad M.G., Fisher F.T., 2009. Coupled piezoelectric-electromagnetic energy harvesting technique for achieving increased power output through damping matching, *Smart Materials and Structures,* 18 (9), pp.95029-11.

Meyar-Naimi H., Vaez-Zadeh S., 2012. Sustainable Development Based Energy Policy Making Frameworks, a Critical Review, *Energy Policy,* 43, pp.351−361.

Tadesse Y., Zhang S., Priya S., 2008. Multimodal Energy Harvesting System: Piezoelectric and Electromagnetic. *Journal of Intelligent Material Systems and Structures,* 20 (5), pp.625–632.

Taufik T., Thornton J., Dolan D., 2012. 2012 Ninth International Conference on Information Technology - New Generations/Piezoelectric Converter for Wind Energy Harvesting. Las Vegas: IEEE.

Viola F., Romano P., Miceli R., Acciari G., 2013. 2013 International Conference on Clean Electrical Power/Harvesting rainfall energy by means of piezoelectric transducer. Alghero: IEEE.

Wang J. J., Su H. H., Hsu C. I., Su Y. C., 2014. Composite Piezoelectric Rubber Band for Energy Harvesting from Breathing and Limb Motion, *Journal of Physics: Conference Series,* 557, pp.18-21.

Yang B., Lee C., Kee W. L., Lim S. P., 2010. Hybrid energy harvester based on piezoelectric and electromagnetic mechanisms, *Journal of Micro/Nanolithography,* 9 (2), pp.023002.

#237: Evaluating the effects of excessive use of fuelwood on the environment in Northern Nigerian arid zones: a case study of Jigawa State

Rukaiyatu U. AHMED[1], Bahijjatu ABUBAKAR[2], Sulaiman.I. MUHAMMAD[3], Umar UJI[4]

[1]Department of Environmental Management and Toxicology, Federal University Dutse, Jigawa State, Nigeria Rukaiyatu.a@fud.edu.ng
[2]Federal Ministry of Environment, Department of pollution Control and Environmental Health, Maitama Abuja, bahijjah@gmail.com
[5]Biological Sciences Department, Federal University Dutse, Jigawa State, Nigeria sulaiman.muhd@yahoo.com
[4]Department of Environmental Management and Toxicology, Federal University Dutse, Jigawa State, Nigeria, umar.ujih@fud.edu.ng

The use of wood fuel in traditional cookstoves and heat stoves by almost 3 billion people across the globe has been a major source of profound concern to the global community because of its adverse effect on the environment as well as human life. Wood fuel, which can also be referred to as 'fuelwood' includes such biomasses like firewood, charcoal, wood chips, pellets, sheets, shavings and sawdust. The fuel is commonly used as a source of energy among rural dwellers, and it has remained the major source of fuel for over half the population of the world (FAO, 2011).

This study set out to examine the environmental effects of fuelwood usage in rural areas of Jigawa State as the main source of energy and reasons for over-dependency on it while exploring alternative safer fuel. Primary and secondary data were collected analysed and used in the study. Primary data was through questionnaires, survey and observations. The secondary data was form existing literature, results from previous studies and various reports including online resources.

The results show that in rural areas in Jigawa state, indeed like most parts of Nigeria and Africa, there is still a heavy reliance and exploitation of firewood as the major energy source for domestic cooking, heating, lighting, as well as commercial activities like blacksmith, roadside eateries, tea cafes and small scale bakeries. The study also found that cost and availability are the most important factors in the choice of fuelwood. People showed willingness to switch to alternatives if they are made available and affordable. Northern Nigeria communities are mainly agrarian and the potential for using agricultural wastes as cooking briquettes and pellets are quite encouraging. The pilot project was a big success that ticked all the boxes, reducing the need to cut down mature trees, reducing methane in agricultural fields, eliminating black carbon from bush burning, providing a sustainable and economically viable energy source, and creating a new enterprise of the pellets value chain. This has been tried with much success in other African countries too like Ghana.

Keywords: Dutse; energy; fuelwood, deforestation, briquettes

1. INTRODUCTION

Fuelwood is the major source of energy for rural and some urban populations in Nigeria. It serves as energy for cooking, heating, hot water production and other energy requirements. As the population grows, increasing depletion of forests has resulted in reductions in the energy resource available for cooking, shortages of wood for manufacturing, and ecological hazards due to southward encroachment of the Sahara Desert. The relatively high cost of other energy sources such as gas, kerosene and petrol influences the over-reliance on the fuelwood as the main source of energy.

The impact of current traditional cooking and heating practices contribute to overall environmental degradation in rural and urban communities as well as continuous deforestation and desert encroachment that contribute to forced migration and regional insecurity.

The use of wood fuel in traditional cookstoves and heat stoves by almost 3 billion people across the globe has been of profound concern to the global community because of its adverse effect on the environment as well as human health. Wood fuel, which can also be referred to as 'fuelwood' includes such biomasses like firewood, charcoal, wood chips, pellets, sheets, shavings and sawdust. The fuel is commonly used as a source of energy among rural dwellers and it has remained the major source of fuel for over half the population of the world (FAO, 2011). This practice has also in recent years become common amongst urban dwellers due to the rising cost of gas and kerosene. It was also observed that many small industries like bakeries and burnt bricks manufacturing have resorted to the use of fuelwood to save on energy costs, which is a very worrying trend, given the amount used daily. The form that is particularly used by an individual or household depends on the quality, quantity, source and application (Mead, 2005).

This study aims to assess how the excessive use of fuelwood affects the environment. It also helps to proffer possible means of controlling the negative implications of such excessive usage in areas such as the study area of Jigawa State, Nigeria.

2. LITERATURE REVIEW

Nigeria, according to the Food and Agriculture Organization (FAO) of the United Nations had the highest rate of deforestation in the world as at 2005 with the loss of 55.7% of its primary forests between 2000 and 2005. During that period its forest coverage reduced from 17 million hectares to 9 million hectares. One of the main drivers of deforestation in the nation is said to be the increasingly unsustainable fuelwood consumption of Nigerian households in both rural and urban areas.

Fuelwood consumption has grown from about 50 million m^3 per year in 1990 to about 70 million m^3 per year in 2010, which constitutes a higher proportion when compared with other competitive use such as logging (ECN and UNDP, 2018). Poverty is the most significant parameter driving the extensive and inherent traditional habit of utilising fuelwood and residues to fulfil different energy requirements in households and communities (UNDP, 2002). Fuelwood is consumed in diverse ways and at different levels; the life of most rural dwellers depends either directly or indirectly on fuelwood.

Meeting rural household wood fuel energy needs in the country has always been a major problem due to the enormous quantity of wood required. The daily consumption of firewood by Nigerian rural communities is estimated at 27.5 million kg/day (Ogunsawa, 2002). This data was corroborated by another data published by The Solar Cooking Archive in 2011, which put the estimate of Nigeria's fuelwood consumption as a percentage of energy at about 87%. The implication of this is that a huge number of the country's households are using and will continuously use dried biomasses for energy. The rise in consumption rate has also continued to grow with the population.

Démurger and Fournier (2011), have opined that heavy reliance on biomass fuels in developing countries has raised global concerns over environmental consequences such as forest degradation, deforestation and soil erosion. In a few years to come, unless something drastic is done to curb the situation and cause a decline in over-dependence of such households on biomass fuels, there will be serious repercussions. Deforestation in many parts of the world is said to continue at an alarming rate. Deforestation worldwide has resulted from factors which include: agricultural expansion; livestock ranching; logging; infrastructure expansion; overpopulation; overgrazing and fuelwood exploitation with one of these dominating in different parts of the world (Al-min, 2014).

Closely associated to deforestation is forest degradation which leads to gradual losses of biodiversity, forest structure, ecological functioning, which along with some other factors lessens the capacity of forest landscapes to provide the environmental goods and services that underpin food security and other basic human needs (Parrotta et al, 2016).

Firewood collection has a significant impact on the forest and that the dependence on firewood as a source of domestic fuel is linked to the nature of the livelihood of the household. Thus, the level of fuelwood consumption can be traced to the livelihood system of the consumer. This may be attributed to the traditional affiliations of such households (Momodu, 2013). In Africa, fuelwood exploitation is regarded as a major driver of deforestation that led Miltiadis to define deforestation as "the consequence of the imbalance between the (limited) rate of fuelwood production and the (excess) rate of fuelwood consumption" (Miltiadis et al, 2010). Nigeria's annual forest loss is put at a rate of 3.7%, which translates to about 410,000 hectares a year.

There are certain driving forces that make the households that depend mainly on biomass fuels for their energy needs to do so. These can be either economic or non-economic in nature. The economic factors may include the availability and market price of fuel, household income and expenditure. Its relatively low prices and easy accessibility top the chart. Other reasons are constraints in the supply of conventional fuels and the growing population, with a larger segment in the lower income brackets which make them unable to afford the cost of conventional fuels (Adedayo, 2005). Non-economic factors include characteristics like household size, age or gender composition, level of education of the household head, whether or not the household owns the dwelling unit, location of household, the type of food or the taste of food cooked with wood fuel, distance to fuel source and access to electricity (Osiolo, 2009).

3. STATE AND COUNTRY OF REVIEW

Nigeria is a former British colony, which came into existence as a result of the amalgamation of Northern and Southern protectorates, empires and smaller territories (Bello, 2007). Today, Nigeria is made up of 36 states and the Federal Capital Territory (FCT). Nigeria extends from latitude 4°N to 14°N and from longitude 3°E to 15°E (Macmillan Nigeria Secondary Atlas, 2006). Nigeria has a total area of 923,769km^2 (National Bureau of Statistics, 2009) and its relief is generally divided into lowlands and highlands. Nigeria is drained by many rivers, the major ones being Rivers Niger and Benue. The vegetation is also grouped into two main categories - forest and savanna (Bello, 2007). Nigeria's population is currently 200,993,000, about 2.6% of the entire world population (UNDP July 2019).

This study was conducted in Jigawa State, which is one of the 36 states that constitute the Federal Republic of Nigeria, and it is situated in the north-central part of the country. The state has a total land area of approximately 22,410 square kilometres. Its topography is characterised by undulating land, with sand dunes of various sizes spanning several kilometres in parts of the state. The southern part of Jigawa comprises the basement complex while the northeast is made up of sedimentary rocks of the Chad Formation. About 3.6 million people inhabit Jigawa State. Life expectancy as at 2001 was about 52 years with a total fertility rate of about 6.2 children per woman of childbearing age (a little above the national average) (National Human Development Report, 2018). Although the population of the state is predominantly rural (90%), the distribution in terms of sex is almost equal between male (50.8%) and female (49.2%). This pattern of population distribution is the same across various constituencies and between urban and rural areas (National Population Commission, 2006).

As mentioned previously, Nigeria has the third-highest rate of deforestation in the world. Desertification is the extension of the desert-like condition to areas which are not of desert origin. The United Nations Conference on Environment and Development has defined desertification as "land degradation in arid, semi-arid and dry sub-humid areas resulting from various factors including climatic variations and human activities. Northern Nigeria is prone to desertification mostly due to its proximity to the Sahara Desert. Nigeria is losing about 351, 000 km^2 to the desert representing 38% of its total landmass. It is also estimated that more than 30 million people in Nigeria live under the hardship of desertification (Ayuba and Dami, 2011).

Jigawa State to the east lies between latitude 10.00N to 13.00N and Longitude 8.00E to 10.15E. Kano and Katsina border Jigawa to the west, Bauchi to the east and Yobe to the northeast. To the north, Jigawa State shares an international border with the Niger Republic.

Jigawa state is one of the front-line arid zone states of North Central Nigeria. There is already evidence of desert encroachment with parts of the state especially bordering the Niger Republic becoming a semi-desert with devastating effects of desertification very evident. Illegal felling of trees has also been partly blamed, with recent statistics from the state government indicating that wood usage in the state has exceeded one ton per person per year.

4. METHODOLOGY

This study was conducted in July 2019 in Dutse (Figure 1), Jigawa State, Nigeria. Dutse, meaning ‘rock' in the local (Hausa) language, is the capital of Jigawa State in Northern Nigeria. Most of its inhabitants engage in small scale farming and other anthropogenic activities such as grazing and woodcutting for cooking, bakery use and other domestic usages.

The data utilised in this study are from both primary and secondary sources. The secondary data and information on the implication of usage of fuelwood and other biomasses were obtained from online resource journals and national statistics database including the National Population Commission and National Bureau of Statistics. The primary data is from questionnaires surveys and observations.

5. DATA COLLECTION

Four villages were selected for data collection, Madobi, Kacci, Fatarah and Shuwarin from the east, west and north of Dutse town respectively (Figure 2). Data were collected using questionnaires and observation methods. The questionnaires were randomly distributed in the selected villages. One hundred (100) questionnaires were distributed in each of the community and a total of four hundred (four) questionnaires were administered. All filled questionnaires were collected and entered and analysed in Excel.

Three of the four areas are in rural settings while the fourth is just on the outskirt of the city inhabited mostly by elites, to enable comparison.

Figure 1: Map of Nigeria showing the 36 states and Federal capital territory.

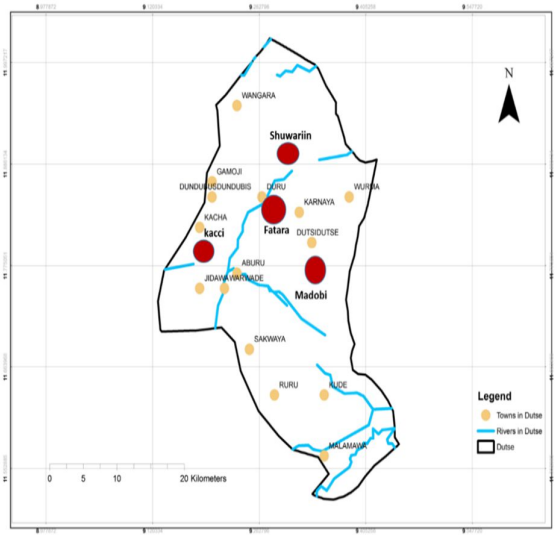

Figure 2: Jigawa State showing study areas: Madobi. Kacci, Shuwarin and Fatarah.

6. RESULTS FROM QUESTIONNAIRES SURVEY

Most of the respondent earn around 1000 to 18000 Naira monthly (Figure 3). Firewood is mostly used for cooking in most of the houses (see Figure 5).

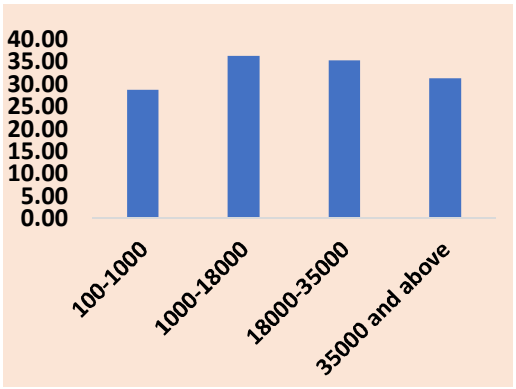

Figure 3: Monthly household income

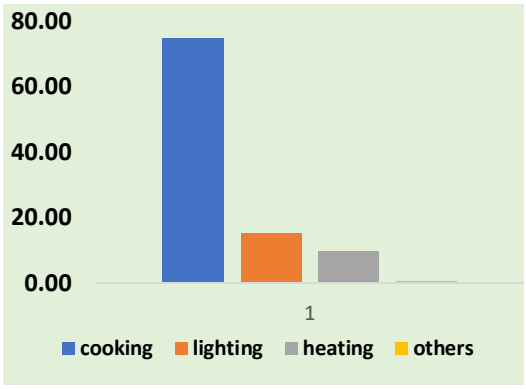

Figure 4: Major energy uses

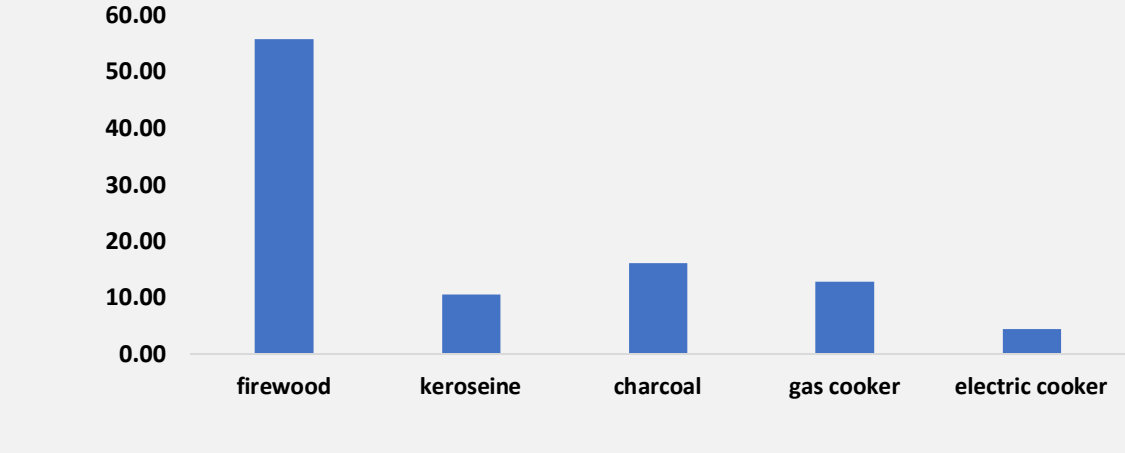

Figure 5: Source of energy of most people in the study area

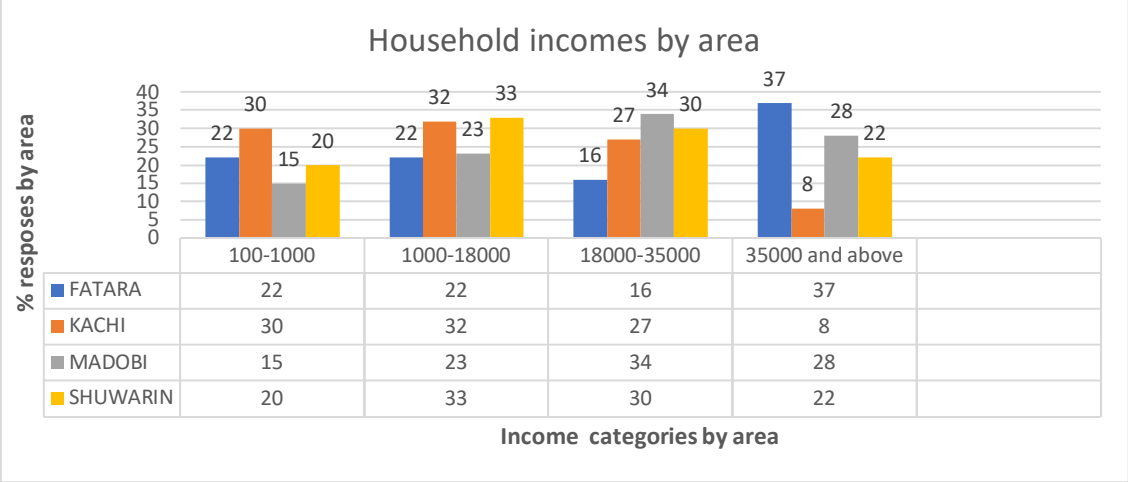

Figure 6: Household Incomes levels by area.

Table 1: Summary of responses to some of the questions asked in the four villages in Dutse, Jigawa State Nigeria.

QUESTIONS	OPTIONS	FATARA	KACHI	MADOBI	SHUWARIN	SUM	%
Firewood source	Market	45	19	33	33	130	35.23
	Tree cutting	10	18	20	25	73	19.78
	Local wood seller	43	60	41	22	166	44.99
Cost of wood per week	#10-50	50	8	41	45	144	36.55
	#50-100	24	43	33	29	129	32.74
	#100 & above	23	46	26	26	121	30.71

QUESTIONS	OPTIONS	FATARA	KACHI	MADOBI	SHUWARIN	SUM	%
Cost of kerosene per week	#100-250	14	12	66	50	142	36.04
	#250-500	27	25	2	28	103	26.14
	#500-above	56	60	11	22	149	37.82
	others	24				24	6.06
Barrier of preferred source	Availability cost	72	8	31	12	51	12.88
			92	69	88	321	81.06
Aware firewood from cutting trees	Yes	81	81	72	67	301	77.58
	No	16	16	22	33	87	22.42
Awareness of consequences of wood felling	Yes	78	94	52	71	295	75.45
	No	16	3	48	29	96	24.55
Conserve them?	Yes	55	72	60	53	240	69.36
	No	34	28	22	22	106	30.64
Consider alternative energy	Yes	82	13	69	86	250	74.40
	No	15	34	25	12	86	25.60
Willingness to participate in tree planting	Yes	88	12	72	82	254	67.37
	No	9	88	13	13	123	32.63

6.1. Photographic evidence of observed practices in the study areas

Figures 7 & 8: Newly felled trees being prepared for sell


Figures 9 & 10: Daily household cooking activities in all study areas using firewood


Figures 11 & 12: Fuelwood being used for blacksmith business in one of the study areas


Figures 13 & 14: Fuelwood used at a local village breakfast spot for tea and snacks

7. DISCUSSIONS

As shown above, the field data collection was via questionnaire administered in four communities: rural settlements of Madobi, Kacci and Shuwarin, and Abubakar Rimi Estate in Fattarah, an elitist settlement just at the outskirts of Dutse Emirate. This was a representative fraction of Jigawa State in order to share the views of the rural poor and elite class on the problems associated with the use of firewood vis-à-vis the environmental consequences. These include deforestation and resultant effects including flooding, windstorms, dunes, droughts, desertification, food insecurity, hunger, deaths, malnutrition and other climatic change crises which are human induced.

The results of the study as shown in Figures 3, 4, 5 and 6 above speak volumes of the number of people and households who use fuelwood energy for cooking daily. That is to say about 55% to 60% (Source of energy of most people in the study area) and 70%-80% (Major energy requirement of most people in the study area) and 70% of the population make use of firewood for their central energy needs (Figures 4 and 5) and all these environmental ills are attributable to the level of poverty.

It is encouraging that the results from the table also show that majority of the respondents (77.5%) are aware that their demand for firewood results in the degradation of the environment with some serious consequences. A majority (67.37%) have also expressed a willingness to participate in tree planting exercises to sustain their demand for firewood. A few, however, do not see the connection and have the attitude that the natural resources will not finish or be depleted.

Also, the income levels of the population ranged between 1000-18,000, at the very low end, indicating lack of affordability for using alternative and more costly energy sources such as gas and kerosene stove for their domestic and commercial energy requirements. Daily household cooking and heating during cold harmattan seasons and lighting in the nights for studies by pupils/students of Sanjaya schools (Quranic/Islamiyya lessons) in parts of Nigeria is an inevitability. Therefore, the cutting of trees to meet the demand will remain high for the foreseeable future, and unless something is done to curb the demand, the environment and its inhabitants will suffer the consequences.

8. CONCLUSION AND RECOMMENDATIONS

From all indications, it is evident that there are no cheaper alternatives to be found for the use of wood as fuel, and this is why the cheapest source of fuel for most rural and peri-urban communities (wood and other biomass residues) are still being used on a large scale.

The environmental and natural resources of Nigeria are becoming depleted especially the vegetation because of indiscriminate and uncoordinated exploitation of these resources for human use. Wood, flowers, herbs, grasses, stems, roots, leaves as well as fruits are on the decline due to non-replacement of trees and shrubs. There is an urgent need for environmental resuscitation, restoration, renewal and protection to prevent the depletion of these resources.

8.1. Sustainable management of forest resources

Strategies and initiatives, which can enhance sustainable means of managing these forest resources, the environment and human health, remain a high priority for the government and the people. Sustainable usage of wood for energy generation should be decisively investigated by the state, national and world leaders to curb the menace of environmental degradation associated with the high demand of and indiscriminate use of biomass fuels for energy. Initiatives such as the development of woodlots mainly for firewood production, which could be harvested and replaced sustainably, should be encouraged.

Strengthening and enforcement of existing forestry laws and imposing hefty penalties for noncompliance, especially in areas designated as forest reserves must be the way forward. Intensifying advocacy and sensitisation of the communities on dangers of indiscriminate tree cutting on both the environment and its inhabitants should be embarked upon through community leaders such as Emirs, Mai Aguwas, Dakachis, Bulamas, Ulama councils, Women associations/groups, youths, and Schools/colleges.

Adequate provision of free trees seedlings to all communities to establish woodlots to use and harvest at maturity and replace sustainably should be adopted. The results showed that most people are willing to participate in tree planting activities to ensure their demand for fuelwood is sustained and their environment is protected against storm and floods.

8.2. Facilitating alternatives source of energy

More funding should be made available to local researchers to develop alternatives that are accessible and affordable in rural areas. For instance, Northern Nigerian communities are mainly agrarian and the potential for using agricultural wastes, as cooking briquettes and pellets are quite encouraging. The pilot project was a big success that ticked all the boxes, reducing the need to cut down mature trees, reducing methane in agricultural fields, eliminating black carbon from bush burning, providing a sustainable and economically viable energy source, and creating a new enterprise of the pellets value chain. This has been tried with much success in other African countries like Ghana. The briquette pilot project in Nigeria should be rolled out on a bigger scale to benefit rural and urban low-income households.

Government subsidy on kerosene and gas appliances for the low-income households as part of the social investment programme should be provided. Most of the rural dwellers interviewed have alluded to the fact that they will switch if affordable alternatives were made available.

9. REFERENCES

Adedayo A.G (2005). Gender roles in forest resources utilization and its impact on rural environment in Kwara State, Nigeria. In: Environmental sustainability and conservation in Nigeria Ayars, G. H. (1997).

Al-Amin, M. (2014). "Domestic Energy Crisis and Deforestation Challenges in Nigeria". J of Environment and Earth Science, Vol.4, No.2. Pp.74-91

Ayars, G. H. (1997): Barnes, D. and Floor, W. (1999). "Biomass Energy and the Poor in the Developing Countries". Journal of International Affairs, 53(1): 237-259.

Bello, A.O. (2007). Regional Geography of Nigeria. In Eno J. Effeh (ed). Perspective of Geography. First Published in 2007 by Tamaza Publishing Co. ltd. Pg122.

Bruce, N., Perez-Padilla, R. and Albalak R. (2002). The Health Effects of Indoor Air Pollution Exposure in Developing Countries. Protection of the Human Environment.

CCAC (2016). Household Energy: Reducing short-lived climate pollutants from domestic cooking, heating and lighting; Available at https://ccacoalition.org/en/initiatives/household-energy.

ECN and UNDP (2018). Assessment of fuelwood availability and consumption in selected rural communities in Kaduna State; Submitted to Energy Commission of Nigeria and United Nations Development Programme by New Frontier Developments Ltd.

Edokpa, D. A. and Ikelegbe O. O. (2012): Ambient air quality and human health in oil producing rural communities of Edo state. Nigerian Meteorological Society (NMetS) Conference Proceedings of the 2012. Theme: Climate change and variability: saving our tomorrow today pp 180-185

Ezzati, M., Saleh, H. And Kamman, D. (2002). The Contributions of Emissions and Spatial Microenvironments to Exposure to Indoor Air Pollution from Biomass Combustion in Kenya. Environmental Health Perspectives, 108,833-839.

FAO (2011). State of the World's Forests (9th Ed.), Food and Agriculture Organization of the United States, Rome. 2011

Jones, A.P. (1999): Indoor Air Quality and Health. Atmosphere. Environment.33, 4535-4564.

Macmillan Nigeria Secondary Atlas (2006). First Published by Macmillan Nigeria Publishers Ltd. Pg 11 and 12.

Maloni, E., Vousta, D. and Samara, C. (2002): Chemical characteristics and Source identification apportionment of fine and coarse air particles in Thessalonik, Greece. Atmospheric Environment. 36 (6), 949-961.

Mead, D.J. (2005). Forests for Energy and the Role of Planted Trees Crit. Rev. Plant Sci., 24 (2005), pp. 407-421

National Bureau of Statistics. (2017). Demographic Statistics Bulletin (May, 2018). Pdf available and downloadable online at www.nigerianstat.gov.ng/download/775

National Bureau of Statistics (2009). Annual Abstract of Statistics. Published by the Federal Republic of Nigeria. Pg.1, 2, 14 and 64.

National Human Development Report. (2018). Jigawa State, Nigeria; Written by the Editors of Encyclopaedia Britannica. Available online at https://www.britannica.com/place/Jigawa

Ndamase, Z. (2012). "The Implication of Fuel-Wood Use and Governance to the Local Environment: A Case Study of Ward Seven of Port St John's Municipality in the Eastern Cape". A Master's Dissertation Submitted to the University of Fort Hare.

Ogunsawa O.Y. and Ajala O.O. (2002). Firewood crises in Lagos- implication on the suburban and rural ecosystem management. In: JE Abu, PO Onoja, A.O. and Idoko, O. (2012). "Econometric Analysis of Factors Influencing Fuel Wood Demand in Rural and Peri-Urban Farm Households of Kogi State." Journal of Sustainable Development Vol. 2(8). Pp.67-77

Smith, K.R., Mehta, S. and Maeusezahl-Feuz, M. (2004): Indoor smoke from household solid fuels. In:M. Ezzati, A. Lopez, A. Rodgers, S. Vander Ho

Straif, K. and IARC Monograph Working Group (2006). Carcinogenicity of some indoor pollutants: emissions from household combustion of coal, household combustion of biomass fuel, and high-temperature frying. Lancet Oncology. Assessment of Respiratory Health Impact of Fuel-Wood Utilization on Exposed Rural Women in Odeda, Southwestern, Nigeria

The Solar Cooking Archive (2011). Fuelwood as percentage of energy consumption in developing countries. Retrieved on 23th August, 2012 from: http://solarcooking.org/fuelwood.htm.http://solarcooking.org/fuelwood.htm.

UNDP (2002). World Energy Assessment Al-Amin, M. (2014). "Domestic Energy Crisis and Deforestation Challenges in Nigeria". J of Environment and Earth Science, Vol.4, No.2. Pp.74-91

WHO (2005). Indoor Air Pollution and Health. Fact Sheet, No. 292.Children's Health and the Environment. A Global Perspective. A Resource Guide for the Health Sector.

WHO (1997): Health and Environment in Sustainable Development: Five years after the Earth Summit. p. 87

#239: Waste vegetable oil-based organic solvent for liquid-liquid extraction of methyl violet from aqueous solutions

Amir TALEBI[1], Lain Joan ANN[2], Ismail NORLI[3], Norhashimah MORAD[4]

[1]*Environmental Technology Division, School of Industrial Technology, Universiti Sains Malaysia, 11800 Penang Malaysia, amirtalebi@usm.my*
[2]*Environmental Technology Division, School of Industrial Technology, Universiti Sains Malaysia, 11800 Penang Malaysia, lainjoanann@hotmail.com*
[3]*Environmental Technology Division, School of Industrial Technology, Universiti Sains Malaysia, 11800 Penang, norlii@usm.my*
[4]*Environmental Technology Division, School of Industrial Technology, Universiti Sains Malaysia, 11800 Penang, nhashima@usm.my*

The possibility of using two waste vegetable oil (residue oil from palm oil mill effluent (POME) and waste palm cooking oil (WPCO)) as a renewable and green organic solvent for methyl violet (MV) extraction from synthetic wastewater was investigated. Four factors (equilibrium pH, diluent. Di-2- ethylhexylphosphoric acid (D2EHPA) concentration, Tributylphosphate (TBP) concentration, and operating temperature) were screened by full factorial design. Central composite design (CCD) and response surface methodology (RSM) were used for optimisation study. Liquid-Liquid Extraction (LLE) results showed that equilibrium pH, carrier concentration, phase modifier concentration was significant. The optimum condition for using residue oil from POME as the organic solvent was: pH of 4.0, 124.92 mM of D2EHPA, 51.24 mM of TBP and operating temperature of 75˚C leading to extraction of 97.20% MV under the optimum condition. Slope analysis showed that one monomer of D2EHPA is attached to one MV molecule to form MV-D2EHPA complex.

Keywords: solvent extraction; methyl violet; D2EHPA; POME, waste oil

1. INTRODUCTION

Dye removal from textile wastewater has been an issue of high interest due to environmental laws and the large amount of wastewater that is discharged (Ueda et al., 2011). Dyes are usually removed from wastewater by physical-chemical treatment processes because most dyes are resistant to biological degradation (Sonawane et al., 2017). Examples of the physical-chemical methods for removal of dyes are precipitation, flocculation, adsorption, advanced oxidation process, ozonation process, and electrokinetic coagulation. Each of the physical-chemical treatment methods to remove dye has their disadvantages in terms of feasibility, environmental impact, practicability, production of toxic by-products, destruction of expensive dyes and sludge production (Pang and Abdullah, 2013; Sharma and Kaur, 2018).

Liquid-liquid extraction (LLE), also known as solvent extraction, is a non-destructive separation technique that has received much attention by researchers due to its definite advantages. The advantages of LLE include rapid and selective separation, ease of operation and high purification (Yang et al., 2003). LLE denotes the transfer of a solute (contaminant) from one liquid phase (aqueous phase) into another liquid phase (organic phase). The basic principle of LLE involves the distribution of contaminant (solute) between two immiscible solvents known as aqueous phase and solvent phase in a correct ratio, and the extraction efficiency depends on its mass transfer rate (Soniya and Muthuraman, 2015). The removal of dye using LLE has been studied by various researchers (Ueda et al., 2011; Othman et al., 2017). Talebi et al. (2013) studied the removal of methyl violet by LLE using a vegetable oil-based organic solvent. Under optimized condition, 84.7% of dye was extracted from aqueous solution. LLE was also used on synthetic dyes such as methyl violet, methylene blue, and rhodamine B by Muthuraman and Teng (2009).

Organic solvents in LLE plays a vital role in the extraction of dyes (Löfström Engdahl et al., 2010). Generally, organic solvents are liquids used in organic phase which consist of diluent, carrier(s) and phase modifier and they are used for the separation of solute from aqueous phase (Clement and Hao, 2012). According to Löfström Engdahl et al. (2010), the most important aspects of a successful LLE process is the selection of diluent. Talebi et al. (2013) reported that 84.7% of MV dye was extracted when palm oil-based organic solvent was used while only 74.3% of MV dye was extracted using soybean oil-based organic solvent.

Methyl violet (MV) is categorised under the group of basic dyes because of the presence of a positive charge on the amino group. The molecular formula of MV is $C_{24}H_{28}N_3Cl$, and it has a molecular weight of 393.95 g/mol. MV is a triphenylmethane dye, a class of intensely colored organic compounds, due to the presence of three aryl groups, each of which is bonded to a nitrogen atom that interacts with methyl groups and it is soluble in water and organic solvent (Sargin and Ünlü, 2013). Also, the presence of three aromatic rings attached to a central carbon and delocalisation of the double bond electrons account for its maximum absorbance of visible light at a wavelength of 584 nm (Sargin and Ünlü, 2013). MV is widely applied as a purple dye in the textile industry for dyeing materials such as silk, cotton, paper, bamboo, and leather. However, MV is a mutagen and mitotic poison in the environment because it can absorb and reflect sunlight, thereby affecting bacterial growth and photosynthesis in aquatic environments (Hashemian et al., 2012). According to Chen et al. (2010), MV may be harmful by ingestion, inhalation, and skin contact, and long term exposure can cause eye and skin damage.

In this article, the author has shown the extraction efficiency of LLE on MV removal using waste vegetable oil-based organic solvent which consists of carrier and phase modifier. The effect of operating temperature, equilibrium pH, D2EHPA concentration and concentration of TBP on the extraction of MV by using the waste vegetable oil-based organic solvent and the interaction effect of these factors on the MV extraction efficiency were determined. Also, the significant parameters were optimised in this study.

2. EXPERIMENTAL

2.1. Materials

Residue oil from POME (100% purity) collected from United Oil Palm Industries Sdn. Bhd., Malaysia, and waste palm cooking oil (WPCO) collected from a local restaurant, were used as diluent. Di-2- ethylhexylphosphoric acid (D2EHPA) (≥95%) purchased from Merck(M) Sdn. Bhd., Malaysia, was used as the carrier and Tributylphosphate ($(C_4H_9O)_3PO$) (≥97%), Merck(M) Sdn. Bhd., Malaysia was used as phase modifier. For aqueous phase preparation, Methyl Violet Dye (C24H28N3Cl), CI42535 ≥99% R&M chemicals, used as methyl violet dye source, sulphuric acid (H2SO4) ≥98% and sodium hydroxide (NaOH) ≥99%, Merck(M) Sdn. Bhd., Malaysia were used for pH adjustment. Silicone fluid, 50 mPa.s - Brookfield Engineering Laboratories Inc., USA, was used in viscosity standard solution for viscometer calibration.

UV Spectrophotometer, HACH, DR2800 used for measure dye concentration color point) before and after LLE; thermostated magnetic stirrer (WiseStir, MSH-20D) was used to Homogenize the dye solution, mix organic phase and aqueous phase and provide constant heating in the aqueous-organic system. Digital Viscometer (Brookfield, DV-E Viscometer) was used to measure the viscosity of waste vegetable oil samples, calibrated with silicone fluid,

50mPa.s. All experiments were carried out in duplicate or triplicate, and the percentage of relative standard deviation (%RSD) of the replicates were calculated according to Andersen et al. (2008).

2.2. Setup and procedure

There are two types of waste vegetable oil used in this study, which are residue oil from POME and waste palm cooking oil (WPCO). The residue oil of POME was collected, according to the method stated by Ainie et al. (1995), by scooping it from the effluent pond and stored in glass bottles with tight-fitting caps which was then kept in the dark and dry place. The sample was then heated up to 120°C for two hours to evaporate the water as according to the method, as stated by Manurung et al. (2017). Another waste oil which is WPCO was collected from a local restaurant and stored in PET bottles with tight-fitting caps, which was then kept in the dark and dry place as stated by Grujić et al. (2011). The sample was then pre-treated by heating the oil sample to 120°C to remove excessive water (Brown, 1987; Chang, 2016). The organic phase, which consists of waste vegetable oil loaded with various concentrations of TBP (5–150 mM) and various concentrations of D2EHPA (5-200 mM), was prepared.

Initially, the colour and pH of the aqueous solvent was measured by using a UV spectrophotometer and a pH meter, respectively. The MV dye extraction percentage (%E) was calculated based on:

Equation 1: MV extraction calculation

$$\text{MV extraction (\%)} = ([MV]_{ini}-[MV]_{aq}) / [MV]_{aq} \times 100$$

Where:

$[MV]_{ini}$ = initial MV dye concentration in the aqueous feed phase before extraction (Pt-Co)
$[MV]_{aq}$ = MV dye concentration in the aqueous phase after extraction (Pt-Co)

The determination of a suitable organic solvent method in this study was done, according to Chang (2014) and Wang et al. (2016). There are five different conditions of waste vegetable oil-based organic solvent studied on their potentiality to extract methyl violet (MV). The two different waste vegetable oil applied are residue oil from POME and WPCO while the aqueous phase contains 200 ppm of MV dye. Initially, the effect of equilibrium pH (pH) on MV dye extraction using with 200 mM D2EHPA and 5 mM TBP in both the waste vegetable oil were investigated. All experiments were carried out by using operating temperature of 65˚C and pH 4 aqueous solutions, except for the study of extraction pH isotherm of MV dye where pH from 2 to 11 was applied. Also, the physical-chemical characteristic of both the waste vegetable oil was determined.

Table 1 shows the screening factors studied in the two-levels design for four factors, also known as 2^4 factorial design and also three center points have been added to the base design. The fixed factors of screening studies were: Dye concentration: 200 ppm, mixing speed at 120 rpm and mixing time of 5 minutes. The chosen range for each factor was selected based on literature. According to Othman et al. (2017), the maximum dye removal by LLE is achieved in the alkaline range. However, Muthuraman and Teng (2009) reported that maximum dye removal was achieved in the acidic range. Thus, both the alkaline and acidic range of pH were examined in the screening experiment in this study. It was found that the small amount of TBP can improve extraction efficiency; however, the excess amount of TBP may influence the extractability of D2EHPA. Besides that, Vander Hoogerstraete et al. (2013) found that the operating temperature in solvent extraction is an important factor because it can increase the mass transfer and also reduce the time to obtain equilibrium. The range of operating temperature in this study was selected according to Vander Hoogerstraete et al. (2013). Next, the fixed factor in this study such as the concentration of dye was selected based on the highest dye concentration discharged from the textile industry as stated by Brown (1987) in literature while mixing speed and mixing time was selected according to Talebi et al. (2013). In LLE experiments, several factors were examined to determine the highest MV extraction. For this purpose, initially a volume (10–50 mL) of the prepared organic phase was mixed with the prepared aqueous phase (containing MV loaded by sodium sulfate) at a specific organic to aqueous phase of kerosene and D2EHPA (with and without TBP) ratio in a conical flask. An orbital shaker shook the bottles (Talebi et al., 2015). Samples were taken every 3 minutes from the aqueous phase to determine the shortest shaking time that the system required to reach equilibrium. The aqueous phase pH was measured before and after each run with a pH meter.

Table 1: 2^4 Factorial design applied in the screening experiment

Factor	Low level	High level
Equilibrium pH	2	11
D2EHPA concentration (mM)	5	200
TBP concentration (mM)	5	150
Operating Temperature (˚C)	65	90
Equilibrium pH	2	11

3. RESULTS AND DISCUSSION

The extraction pH isotherms of MV dye investigated with two different types of waste vegetable oil (residue oil from POME and WPCO) loaded with 200 mM of D2EHPA and 5 mM of TBP. The aqueous pH is important in selecting appropriate extraction condition because the proper utilisation of aqueous phase pH can determine the success of LLE. The change in pH of aqueous solution in LLE can drastically alter the distribution coefficient, thereby pulling the solute to be extracted from the aqueous phase into the organic phase. The high pH-dependency of D2EHPA in MV dye extraction could be deduced from the equation of reaction between D2EHPA (carrier) molecules and the dye ion and which, in the case of MV dye cation, is expressed as (Talebi et al., 2013):

Equation 2: MV extraction complexation

$$MV^{+}_{(aq)} + HA_{(carrier)} \rightleftharpoons MVA_{(org)} + H^{+}_{(aq)}$$

According to Equation 2, as the equilibrium pH increases from pH: 2 to pH: 4 (H^+ decreases), the position of equilibrium shifts to the right and, thereby giving rise to the percentage of MV dye extraction (Vahidi et al., 2009). However, at strongly acidic pH (pH 5 and pH6), D2EHPA is protonated and becomes unable to react with the MV (Galaction et al., 2016). Therefore, due to these phenomena, the optimum pH-value for the extraction with D2EHPA was found to be at pH 4.

3.1. Physical-chemical properties of waste vegetable oils

Table 2 summarises the physical-chemical properties of different waste vegetable oil sample obtained from this study.

Table 2: Physical-chemical properties of waste vegetable oils obtained in this study

Physical-chemical properties	Residue Oil from POME	Waste Palm Cooking Oil (WPCO)
Specific gravity at 65°C (g cm^{-3})	0.83 ± 0.01	0.89 ± 0.02
Viscosity at 65°C (cP)	22 ± 0.58	50 ± 1.73
FFA (%))	8.32 ± 0.01	3.69 ± 0.01
Acid Value	16.56 ± 0.02	7.34 ± 0.01

The screening experiment revealed that the percentage of MV extraction ranged from 9.32% to 80.75% and the evaluation of the significant effect of each screening factor on the percentage of MV extraction was done by plotting a half-normal probability plot of standardised effects at a significance level of 5% using. Figure 1 depicts the significant effect of equilibrium pH (A), [D2EHPA] (B), and [TBP] (C).

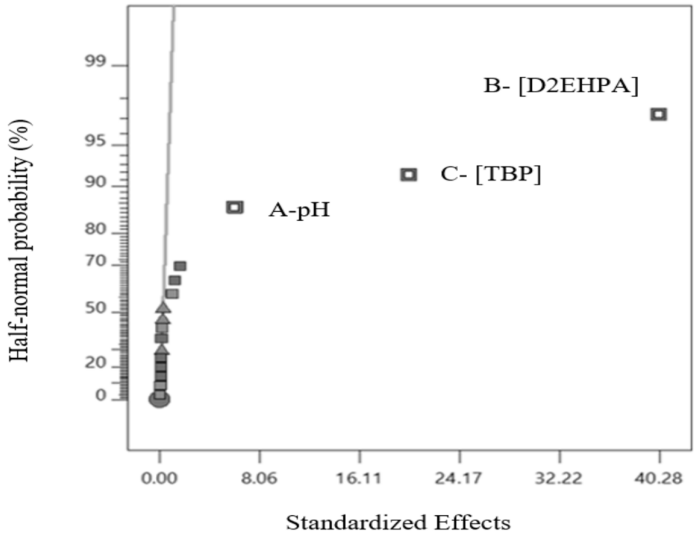

Figure 1: Half-normal probability plot of standardised effects for the percentage of MV dye extraction

Table 3 shows the estimated regression coefficients, along with the corresponding standard deviation, P values and the interaction terms of a regression model for a percentage of MV dye extraction (Equation 3) obtained from the regression analysis. Regression analysis of the optimisation experiment data was carried out, and a quadratic polynomial regression equation at 5% significance level was fitted as the following:

Equation 3: % MV dye extraction = 87.57-7.40A + 2.43B – 0.6252C + 0.9338AB + 0.2338AC+ 0.0788BC – 1.87A² – 0.6588B² – 0.0559C²

In Equation 3, the positive signs of coefficients for main effects B, AB, AC, and BC indicate their synergistic effects on the percentage of MV dye extraction while negative signs of coefficients for A, C, A^2, B^2 and C^2 denote their antagonistic effects. The order according to decreasing significance of each variable term with respect to its effect in % MV dye extraction is A > B > A^2 > AB > B^2 > C > AC > BC > C^2. This shows that the main effects A (pH) and B ([D2EHPA]) were the primary factors that influenced the % MV dye extraction relative to other factors.

Table 3: Estimated coefficient of the regression model for % MV dye extraction

Term[a]	Coefficient	SD	t-stat	*P-value*
Constant	87.57	0.1873	472.00	< 0.0001
A	-7.40	0.1242	3549.85	< 0.0001
B	2.43	0.1242	381.39	< 0.0001
C	-0.6252	0.1242	25.2	0.0005
AB	0.9338	0.1623	33.08	0.0002
AC	0.2338	0.1623	2.07	0.1805
BC	0.0788	0.1623	0.2353	0.6381
A²	-1.87	0.1210	238.50	< 0.0001
B²	-0.6588	0.1210	29.66	0.0003
C²	-0.0559	0.1210	0.2140	0.6536

3.2. Optimum conditions for MV dye extraction

Table 4 presents the optimum operating variables of equilibrium pH, D2EHPA concentration, and TBP concentration to achieve the highest MV dye extraction. From Table 4, it can be seen that the small deviation (1.24%) between the experimental (97.20%) and predicted (95.96%) values of percentage MV extraction indicates that the model was sufficient to predict the percentage of MV extraction in the range of factors studied. The three-dimensional response surface plot of MV dye extraction versus equilibrium pH and concentration of D2EHPA at a fixed TBP concentration of 50mM is illustrated in Figure 2. From Figure 2, it can be seen that the highest percentage of MV extracted was 95.96% when a high level of D2EHPA concentration (125 mM) and low level of equilibrium pH (4) was applied.

Table 4: Optimum conditions and model validation

MV Dye Extraction Efficiency (%)						
pH	[D2EHPA] (mM)	[TBP]	Temperature (˚C)	Predicted	Measured	% deviation
4	124.92	51.24	75	95.96	97.20	1.24

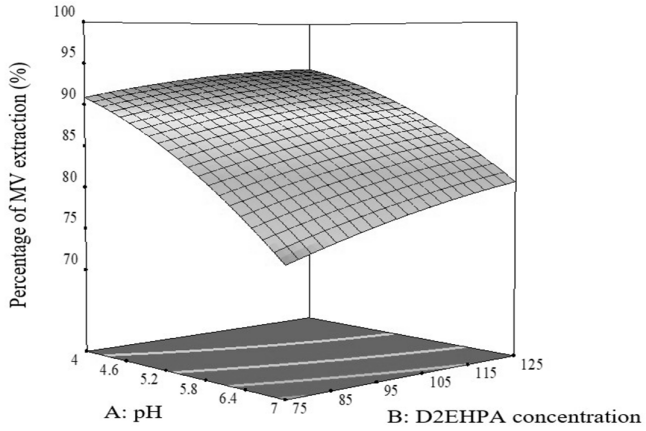

Figure 2: 3D surface plot showing the effect of equilibrium pH (A) and D2EHPA concentration (B) on the MV dye extraction efficiency when TBP concentration was kept at 50 mM

The effects of the variable factors on the MV dye extraction are investigated. Also, the effect of the interaction between pH and concentration of D2EHPA on the extraction efficiency of MV dye is outlined. The effect of equilibrium pH ranged from 4.0 to 7.0 on the extraction of cationic methyl violet (MV) dye from aqueous solution is shown in Figure 3. The organic phase consists of residue oil from POME loaded with 100 mM D2EHPA and 70 mM TBP while the aqueous phase contains 200 ppm of MW dye sample. The pH of the aqueous phase is an important factor to study on dye removal because dye wastewater is often discharged at different pH (Othman et al., 2017). According to Muthuraman et al. (2012), dye behavior may change at different pH condition due to hydrolysis or aggregation. The result shown in Figure 3 indicates that when the equilibrium pH increases from pH 4 to 7, MV dye extraction decreases from 93% to 78%. This may be because D2EHPA is protonated and unable to form an ion-pair complex with the cationic MV dye at pH above 4 (Galaction et al., 2016). According to Talebi et al. (2013), extraction of dye in liquid-liquid extraction depends on whether the dye can form an ion-pair complex with the carrier. When no ion-pair complex is formed between carrier and dye, dyes cannot be transported from the aqueous phase to the organic phase (Galaction et al., 2016). It can be predicted that if the equilibrium pH were adjusted to pH8, the percentage of MV removal would be lesser than 78% compared to pH 7 (78%) under the same condition (100 mM D2EHPA and 70 mM TBP). Therefore, a further increase in equilibrium pH beyond pH4 reduces the efficiency for extraction of MV.

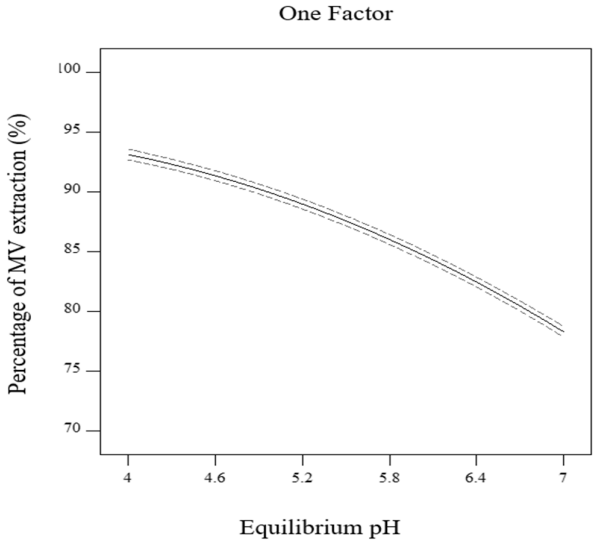

Figure 3: Effect of equilibrium pH on the MV dye extraction efficiency (%) with 100 mM D2EHPA and 70 mM TBP

The effect of concentration of TBP (phase modifier) from 50 mM to 90 mM loaded in residue oil from POME on the extraction of MV dye from aqueous solution was investigated. The operating condition of 200 ppm of MV dye, a pH of 5.5, 70 mM of D2EHPA was employed. It was observed the extraction of MV is high (88%) at low TBP

concentration (50 mM) as compared to high TBP concentration (90 mM) which results in lower extraction of MV (86%). The role of TBP as a phase modifier is well established in liquid-liquid extraction due to its phased modification characteristic that can reduce the formation of the emulsion by reducing the tension, interfacial viscosity as well as the elasticity of the organic-aqueous interface (Chagnes et al., 2012). However, high concentration of TBP (relative to D2EHPA concentration) reduces the extraction efficiency due to the formation of intermolecular connections between TBP and D2EHPA compound in the organic phase (Guezzen and Didi, 2012). The formation of hydrogen bonds between D2EHPA and TBP in the organic phase may be the reason for this negative synergism (Krea and Khalaf, 2000). The cation exchange is the principal mode of action of D2EHPA during the extraction reaction (Cox, 2004). The reduction in the percentage of MV in this study may be because some D2EHPA molecules are polymerised through hydrogen bonds with TBP, which affects the reaction of dye with D2EHPA and thus reduces the extraction of MV. It could be predicted that the percentage of MV removal will reduce to less than 86% if more than 90 mM of TBP were to be used under the same condition (200 ppm of MV dye, pH of 5.5, 70 mM of D2EHPA). Therefore, TBP concentration is a significant factor that affects the extraction of MV dye, where a higher concentration of TBP relative to D2EHPA concentration, reduces the extraction of MV.

The plot of log D (logarithmic distribution ratio of MV dye in diluent) versus log [D2EHPA] (logarithmic D2EHPA concentration) shown in Figure 4, where the condition employed in aqueous phase was 200 ppm of MV dye and equilibrium pH of 4, while the organic phase contains residue oil from POME with 50 mM of TBP. The slope of the log D against log [D2EHPA] was used to determine the number of molecules engaged in dye-carrier complexation. A linear correlation with a slope value of 1.0405 (close to 1) indicating the association of 1 mole of carrier per mole of MV dye ion in the extracted species. Therefore, the equation below can be used to represent the extraction equation between the cationic MV dye and D2EHPA molecules:

Equation 4: MV stoichiometric complexation

$$MV^{+}_{(Dye)} + HA_{(carrier)} \rightarrow MVA + H^{+}$$

Where:

- HA = is D2EHPA in the residue oil from POME (organic solvent)

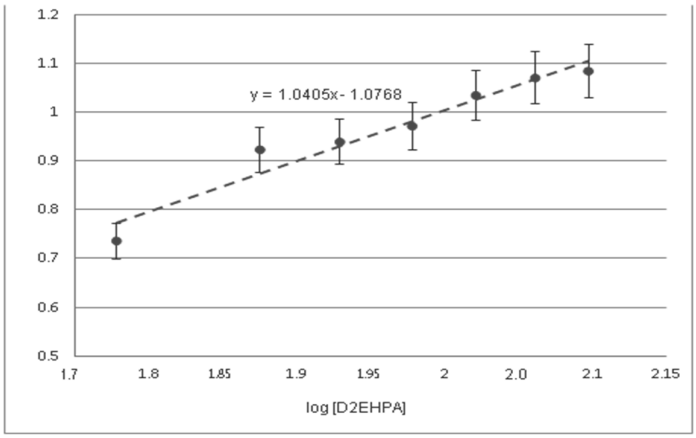

Figure 4: Effect of equilibrium pH on the MV dye extraction efficiency (%) with 100 mM D2EHPA and 70 mM TBP

4. CONCLUSION

Residue oil from Palm Oil Mill Effluent (POME) was selected as the most suitable organic solvent due to its high efficiency (90.06%) with 200mM of D2EHPA (carrier) and 5mM of TBP (phase modifier) and it has favorable physical-chemical characteristic such as higher FFA (32%±0.01), higher acid value (16.56%±0.02), lower viscosity (22cP±0.58) and lower specific gravity (0.83 g cm-3 ±0.01) for the methyl violet (MV) extraction process. Also, the results show residue oil from POME can be claimed to function as both diluent and extractant in this study. The four factors (equilibrium pH, the concentration of D2EHPA, the concentration of TBP, and operating temperature) were screened by building a 2^4 full factorial design to evaluate their significance. The results show that equilibrium pH, the concentration of D2EHPA, and concentration of TBP were the significant individual factors affecting MV extraction, whereas operating temperature was less significant. A regression model was developed to capture the correlation between the response (% MV extraction) and the significant factors (pH, [D2EHPA] and [TBP]) and also the regression model adequacy was checked. The adequacy in predicting the response over the whole uncertainty range of factors was satisfied. A regression model was developed for per cent extraction, while R^2_{adj} (0.9955) and R^2 (0.9977) were determined. The optimum condition obtained was: pH of 4.0, 124.92 mM of D2EHPA, 51.24 mM of TBP, and operating temperature of 75˚C, and the highest MV extraction of 97.20% was attained. LLE results

show that the extraction of MV increases from 78% to 93% when pH decreases from 7 to 4. Besides that, when D2EHPA concentration increases from 75 mM to 125 mM, the extraction of MV increases from 85% to 90%. In this study, the interaction of factors affecting MV extraction was determined. RSM results show that the interaction of equilibrium pH and D2EHPA concentration on MV extraction was significant. It was confirmed that H^+ cations and MV-D2EHPA complex replace methyl violet cation is formed. Slope analysis suggests that one monomer of D2EHPA are attached to one MV molecule to form MV-D2EHPA complex.

5. ACKNOWLEDGEMENT

This work was supported in part by the Ministry of Energy, Science, Technology, Environment & Climate Change (MESTECC) Malaysia under the MESTECC Research & Development Fund (MESTECC R&D Fund) Project No: 03-01-05-SF0847

6. REFERENCES

Ainie, K., Siew, W., Tan, Y. and Ma, A. (1995). Characterization of a by-product of palm oil milling. *Elaeis* **7**(2), 162-170.

Andersen, W.C., Turnipseed, S.B., Karbiwnyk, C.M., Clark, S.B., Madson, M.R., Gieseker, C.M., Miller, R.A., Rummel, N.G. and Reimschuessel, R. (2008) "Determination and confirmation of melamine residues in catfish, trout, tilapia, salmon, and shrimp by liquid chromatography with tandem mass spectrometry." *Journal of Agricultural and Food Chemistry* **56**, 4340-4347. 10.1021/jf800295z.

Brown, D. (1987) "Effects of colorants in the aquatic environment." *Ecotoxicology and Environmental Safety* **13**, 139-147. 10.1016/0147-6513(87)90001-7.

Chagnes, A., Courtaud, B., Thiry, J., Bayardon, J., Jugé, S. and Cote, G. (2012) "Influence of phase modifiers on the degradation of tri-n-octylamine/dodecane extracting mixture by an acidic solution of vanadium (V)." *Solvent Extraction and Ion Exchange* **30**, 67-76. 10.1080/07366299.2011.566524.

Chang, S.H. (2014) "Vegetable oil as organic solvent for wastewater treatment in liquid membrane processes." *Desalination and Water Treatment* **52**, 88-101. 10.1080/19443994.2013.782829.

Chang, S.H. (2014) "Vegetable oil as organic solvent for wastewater treatment in liquid membrane processes." *Desalination and Water Treatment* **52**, 88-101. 10.1080/19443994.2013.782829.

Chang, S.H. (2016) "Waste Cooking Oil-Based Organic Solvent as A Potential Green and Low-Cost Solvent for Metal Extraction." *International Journal of Research in Chemical, Metallurgical and Civil Engineering* **3**. 10.15242/IJRCMCE.ER0116021.

Chang, S.H., Wahab, A.A.A. and Som, A.M. (2016) "Extraction Behaviour of Cu 2 Ions with Used Cooking Oil-Based Organic Solvent." *International Proceedings of Chemical, Biological and Environmental Engineering* **96**. 10.7763/IPCBEE. 2016. V96. 4.

Chen, S., Zhang, J., Zhang, C., Yue, Q., Li, Y. and Li, C. (2010) "Equilibrium and kinetic studies of methyl orange and methyl violet adsorption on activated carbon derived from Phragmites australis." *Desalination* **252**, 149-156. 10.1016/j.desal.2009.10.010.

Clement, R. and Hao, C. (2012) "Liquid–Liquid Extraction: Basic Principles and Automation." 51-63. 10.1016/B978-0-12-381373-2.00063-6.

Galaction, A.-I., Poştaru, M., Bompa, A.-S. and Caşcaval, D. (2016) "Synergic Extraction of Pantothenic Acid with Two Different Extractants." *Brazilian Journal of Chemical Engineering* **33**, 1031-1040. 10.1590/0104-6632.20160334s20150265.

Grujić, S., Aleksić, V., Vukić, M. and Petrović, Z. (2011) "The effect of packing material on storage stability of sunflower oil." *Quality of life* **4**. 10.7251/QOL1102075G.

Guezzen, B. and Didi, M.A. (2012) "Removal of Zn (II) from aqueous acetate solution using di (2-ethylhexyl) phosphoric acid & tributylphosphate." *International Journal of Chemistry* **4**, 32. 10.5539/ijc.v4n3p32.

Hashemian, S., Tabatabaee, M. and Gafari, M. (2012) "Fenton oxidation of methyl violet in aqueous solution." *Journal of Chemistry* **2013**. 10.1155/2013/509097.

Krea, M. and Khalaf, H. (2000) "Liquid–liquid extraction of uranium and lanthanides from phosphoric acid using a synergistic DOPPA–TOPO mixture." *Hydrometallurgy* **58**, 215-225 DOI: 10.1016/S0304-386X(00)00129-8.

Löfström Engdahl, E., Aneheim, E., Ekberg, C. and Skarnemark, G. (2010). *Diluent effects in solvent extraction*. Proceedings of the First ACSEPT International Workshop Lisbon, Portugal, 31 March–2 April 2010.

Manurung, R., Ramadhani, D.A. and Maisarah, S. (2017). *One step transesterification process of sludge palm oil (SPO) by using deep eutectic solvent (DES) in biodiesel production*. AIP Conference Proceedings, AIP Publishing.

Muthuraman, G. and Teng, T.T. (2009) "Extraction and recovery of rhodamine B, methyl violet and methylene blue from industrial wastewater using D2EHPA as an extractant." *Journal of industrial and engineering chemistry* **15**, 841-846. 10.1016/j.jiec.2009.09.010.

Muthuraman, G., Teng, T.T., Leh, C.P. and Norli, I. (2009) "Extraction and recovery of methylene blue from industrial wastewater using benzoic acid as an extractant." *Journal of Hazardous Materials* **163**, 363-369. 10.1016/j.jhazmat.2008.06.122.

Othman, N., Noah, N.F.M., Yi, O.Z., Rosly, M.B., Rahman, H.A. and Rashid, R. (2017) "Kinetic extraction of basic dye using vegetable oil as a solvent." *Malaysian Journal of Fundamental and Applied Sciences* **13**, 685-689. 10.11113/mjfas.v13n4.927.

Pang, Y.L. and Abdullah, A.Z. (2013) "Current status of textile industry wastewater management and research progress in Malaysia: a review." *Clean–Soil, Air, Water* **41**, 751-764. 10.1002/clen.201000318

Sargin, İ. and Ünlü, N. (2013) "Insights into cationic methyl violet 6B dye–kaolinite interactions: kinetic, equilibrium and thermodynamic studies." *Clay Minerals* **48**, 85-95. 10.1180/claymin.2013.048.4.05.

Sharma, S. and Kaur, A. (2018) "Various Methods for Removal of Dyes from Industrial Effluents-A Review." *Indian Journal of Science and Technology* **11**. 10.17485/ijst/2018/v11i12/120847.

Sonawane, P.R., Bhostekar, H.G., Moharir, S.R., Suryawanshi, M.A. and Mane, V.B. (2017) "Experimental study on Solvent Extraction of Crystal Violet dye." *International Journal of Advance Engineering and Research Development* **4**, 1074-1077. 10.1016/j.biortech.2007.02.011.

Soniya, M. and Muthuraman, G. (2015) "Recovery of methylene blue from aqueous solution by liquid–liquid extraction." *Desalination and Water Treatment* **53**, 2501-2509. 10.1080/19443994.2013.866055.

Talebi, A., Teng, T.T., Alkarkhi, A.F.M and Su, Y. (2013) "Methyl violet removal from synthetic wastewater by liquid-liquid extraction using vegetable oils as solvent." *International Journal of Scientific Research in Environmental Sciences* **1**, 357. 10.12983/ijsres-2013-p357-364.

Talebi, A., Teng, T.T., Alkarkhi, A.F.M. and Norli, I. (2015). Nickel ion coupled counter complexation and decomplexation through a modified supported liquid membrane system. RSC Advances, 5, 38424-3843.

Ueda, A.C., de Oliveira, L.H., Hioka, N. and Aznar, M. (2011) "Liquid− liquid extraction of basic yellow 28, basic blue 41, and basic red 46 dyes from aqueous solutions with reverse micelles." *Journal of Chemical & Engineering Data* **56**, 652-657. 10.1021/je1008558.

Vahidi, E., Rashchi, F. and Moradkhani, D. (2009) "Recovery of zinc from an industrial zinc leach residue by solvent extraction using D2EHPA." *Minerals Engineering* **22**, 204-206. 10.1016/j.mineng.2008.05.002.

Vander Hoogerstraete, T., Onghena, B. and Binnemans, K. (2013) "Homogeneous liquid–liquid extraction of rare earths with the betaine—betainium bis (trifluoromethylsulfonyl) imide ionic liquid system." *International Journal of Molecular Sciences* **14**, 21353-21377. 10.3390/ijms141121353.

Wang, J., Mohd, R., Norhashimah, M. and Kaizar, H. (2016) "Extraction of Toxic Rhodamine B Dye by Using Organic Solvent: A Statistical Analysis." *Research Journal of Environmental Toxicology,* **10**, 152-158. 10.3923/rjet.2016.152.158.

Yang, X., Fane, A. and Soldenhoff, K. (2003) "Comparison of liquid membrane processes for metal separations: permeability, stability, and selectivity." *Industrial & engineering chemistry research* **42**, 392-403 10.1021/ie011044z.

#240: Thermochemical heat storage systems with salt impregnated honeycomb filter with different pore volumes

Behiye YÜKSEL[1], Devrim AYDIN[2], Zafer UTLU[3], Saffa RIFFAT[4]

[1]Department of Mechanical Engineering, Engineering Faculty, İstanbul Gedik University, 34876 İstanbul TURKEY, behiye.yuksel@gedik.edu.tr
[2]The Eastern Mediterranean University, Gazimagusa, CYPRUS, devrim.aydin@emu.edu.tr
[31]Department of Mechanical Engineering, Engineering Faculty, İstanbul Gedik University, 34876 İstanbul TURKEY, zafer.utlu@gedik.edu.tr
[4]Department of Architecture and Built Environment, Faculty of Engineering, University of Nottingham, NG7 2RD

Development of the thermal energy storage systems which are driven by low temperature heat attracts increasing interest day by day. Storage of low temperature heat as well as studies about this subject have shown great potential in thermal energy storage field. Due to the limitations of the conventional porous host materials such as natural porous rock currently used, research has focused on new materials for these systems. In this study anodic alumina oxide (AAO) templates were used as a porous host material. Aluminium oxide pores were fabricated on aluminium by using a two-step anodisation method. AAO templates with three different pore sizes were filled with 4 different salts as $CaCl_2$, LiCl, $MgCl_2$ and $LiNO_3$ via a vacuum impregnation method obtained using the same experimental parameters for thermal energy storage system. The aim of this study was to investigate the effect on the heat storage capacity when changing the salt type in the AAO templates with different pore volumes. Thermal storage capacities were determined using DSC (Differential scanning calorimetry). The results from DSC were compared and the most suitable salt for use in thermal energy storage systems selected by determining the energy storage capacities of the obtained templates.

Keywords: AAO templates, heat storage, salt-impregnation

1. INTRODUCTION

Developments in the industrial world, rapid population growth and urbanisation have increased the importance of more effective energy use and energy efficiency day by day (Grekova *et al.,* 2016). One of the most important factors to consider in energy efficiency enhancement efforts is the recovery of waste heat. Today, housing and domestic buildings are responsible for the significant increase in energy consumption (Hongois *et al.,* 2011; Rammelberg *et al.,* 2016; Posern & Kaps*,* 2010). In recent years, insulation in buildings, energy saving applications, and heat storage applications have become important to increase efficiency and reduce energy consumption (Henninger *et al.,* 2016; Aristov, 2015; Liu *et al.,* 2013). Heat storage systems are recognised as a promising technology in renewable energy systems due to their low cost and high efficiency (Aydin, 2015; Roßkopf *et al.,* 2015). Development of new advanced heat storage systems could allow a reduction of the fossil fuel consumption while enhancing the utilisation of renewable energies. Today, a significant amount of low-temperature (<100°C) heat from buildings and industrial plant is discharged directly to the atmosphere. Therefore, low temperature advanced heat recovery technology needs to be promoted to reduce fossil fuel consumption, negative impacts of fossil fuels on the environment and to enhance the utility of renewables (Liu, 2014). Thermal energy storage (TES) is an advanced technology suitable for providing supply–demand balance in building heating and air-conditioning systems. Currently, there are three main types of TES systems known: sensible heat storage (SHS) systems, latent heat storage (LHS) systems and thermochemical heat storage (THS) systems (Tatsidjodoung *et al.,* 2013; Sharma *et al.,* 2009). Nowadays, there are several candidate systems used to provide domestic thermal energy storage (TES) such as electric storage heaters, air heating system, hot water tanks and phase change materials (PCM) (Casey *et al.,* 2014).

Materials used up to now in THS systems are usually natural materials such as zeolite, silica gel or activated carbon. Also, some salt impregnated porous spongy materials have been developed for use in THS applications (Zhang *et al.,* 2016; Pasaoglu, 2011; Masuda & Fukuda, 1995). However, some of the limiting features of such materials such as high charging temperature, limited cyclic performance and poor heat and mass transfer characteristics have led to the search for alternative materials. The studies about this subject in literature are limited. For these reasons, this study aims to develop a new high thermal storage capacity composite THS material that uses anodic aluminum oxide (AAO) templates as an alternative to the other THS materials.

In this study honeycombs with three different pore sizes were formed on AAO templates by two-step anodisation method and these pores were impregnated with four different salts ($CaCl_2$, LiCl, $MgCl_2$, $LiNO_3$) under vacuum for obtaining high thermal storage capacity.

2. EXPERIMENTAL

The aluminum templates with purity of 99.99% were used as a base material in this study. Before anodising, the aluminum template surfaces were ultrasonically and chemically cleaned until the surfaces of the aluminum sheet were ready for anodising. First of all, the aim was to create high ordered and homogeneous aluminum oxide templates to obtain nanoscale honeycomb structures. Anodic aluminium oxide (AAO) pores were fabricated on aluminium by using a two-step anodisation method. Following the surface cleaning prosess, the first anodisation was performed at oxalic acid ($C_2H_2O_4$) solution (0.6 M) at an anodising voltage of 40 V for 30 min. After the first anodisation, the pre-prepared AAO pores were left in a chromate solution for 15 min at 60°C for chemical polish. The sample was further anodised under the same conditions as the second anodisation, for 30 min and highly ordered AAO template was formed. At the end of the second anodisation, anodised surfaces of the templates were immersed in NaOH solution for pore expanding for 5, 10 and 15 min. Then these samples were kept in an oven for 24 hours at 110°C to dry.

At the end of 24 hours, the samples whose nemesis has been completely removed were ready for the salt impregnation process. AAO templates were submerged into the solutions placed in separate containers, with the AAO templates fully penetrating. The specimens thus placed in the oven were allowed to stand in salt solutions at 30°C for 48 hours under 0.1 MPa vacuum. In this environment, capillary action is provided to fill the pores with the salt solution.

The morphology of nanopores on AAO templates were scanned by Scanning Electron Microscope (SEM). Besides the energy storage density, E_d (kJ/kg) of the materials were investigated, which is one of the most important material properties for thermochemical heat storage. Following the synthesis of the salt in matrix composites, differential scanning calorimetry (DSC) of DSC Q2000 was used to determine the E_d. Using the data obtained from the instrument, the value of the E_d was calculated using excel software. During the testing, variable rates of heat was applied to saturated salt impregnated Al_2O_3 matrices within the temperature range of 30 < T < 140°C and a ramp rate of 1.00°C/min.

3. RESULTS AND DISCUSSION

In this study, all anodised samples were examined with a JSM-6335F model JEOL field emission scanning electron microscope (FESEM). The aluminium templates were anodised at 40V and voltage was kept steady during anodising. The results show that the average pore diameter of AAO film was about 30±5 nm as shown in Figure 1. The pores were regular and high ordered. The thickness of the oxide wall between two pores in the SEM image of the samples after the anodisation is about 65±10 nm.

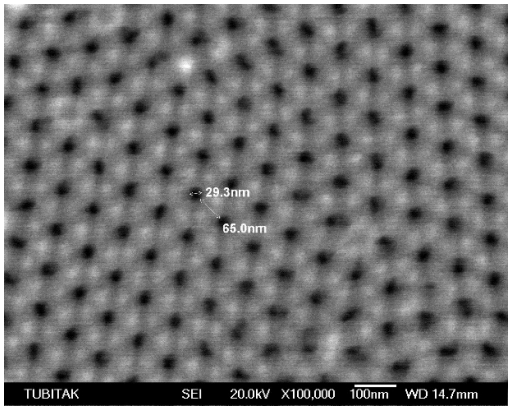

Figure 1: Image of nanopores on AAO templates after two-step anodising process

After two-step anodisation, the pore diameters were opened by immersion in 3.5% NaOH solution for 5, 10 and 15 minutes. The pore diameter was extended by approximately 40 ± 5 nm after 5 minutes given in Figure 2a. The distance between the two adjacent pore centres was about 100 ± 5 nm and the distance between the outer surfaces of the pores was 50 ± 5 nm after 5 minutes immersion time. As the pore expansion time in the NaOH solution increased, the nanotubes were dissolved from the inner surfaces and the wall thickness decreased. As seen in Figures 2b and 2c, the pore diameter increased to 55± 5 nm and 85± 5 nm respectively as the dipping time increased. In other words, it was observed that the wall thickness of the nanotubes decreased and the pore volume increased with the increasing pore diameter.

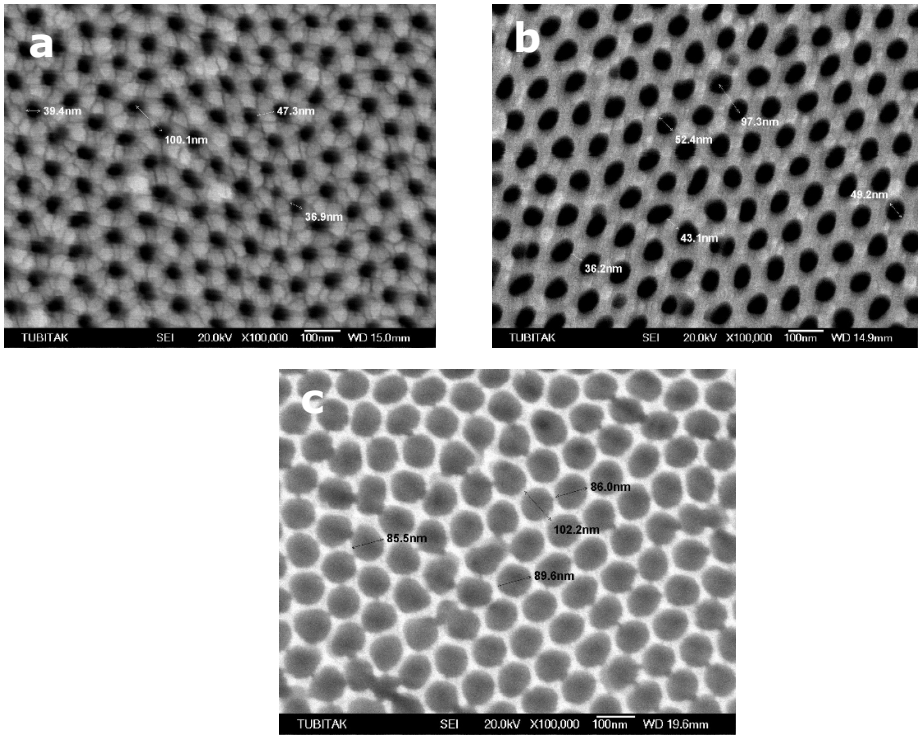

Figure 2: FESEM image from top of AAO templates after (a) 5 minutes, (b) 10 minutes and (c) 15 minutes of the pore expansion process.

Figure 3 shows a cross-sectional view of the AAO templates. The average length of the nanotubes is approximately 5 µm. The increase of the lengths of the nanotubes depends on the increase of the anodisation period. The lengths of the nanotubes are directly proportional to the duration of second step of the two-step anodising.

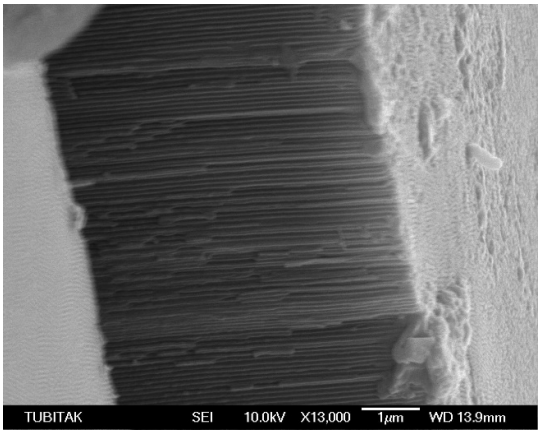

Figure 3: Cross-section view of the obtained nanotubes

Following the pore expansion process, AAO templates were immersed in 4 different fully saturated salts as LiCl, $LiNO_3$, $MgCl_2$ and $CaCl_2$. Table 1 shows the pore expansion times of the composite materials obtained in the NaOH solution affecting the pore diameter of the AAO structure and the salts impregnated in AAO plates for fabrication of 12 different samples.

Table 1: Pore expansion times of AAO templates and impregnated salts

Sample No	Pore Expansion Time (min.)	Impregnated Salts
1	5	LiCl
2	5	$LiNO_3$
3	5	$MgCl_2$
4	5	CaCl
5	10	LiCl
6	10	$LiNO_3$
7	10	$MgCl_2$
8	10	CaCl
9	15	LiCl
10	15	$LiNO_3$
11	15	$MgCl_2$
12	15	CaCl

Following the synthesis of the salt impregnated AAO composites, energy storage density, Ed (kJ/kg or kW h /m^3) of the materials were investigated, which is one of the most important material properties for THS. According to the BS EN ISO 11357-4 standards, Ed determination was made using TA Instrument SDT Q600 model differential scanning calorimeter (DSC). Using the data obtained from the instrument, the value of the Ed is calculated using Excel software.

In the DSC studies, the specific heat capacity (Cp, J/kg K) was calculated and the composite density of the composite (Ed) was calculated according to Equation (1) by integrating the area under the desorption heat–Cp curve.

Equation 1: $$Cp = \Delta Q/(m.\Delta T)$$

Where:

Q = the amount of heat supplied to the system,
m = sample weight,
T = temperature range.

Therefore, total energy values are obtained from the derivative according to the temperature change of Cp values. Theoretically, it can be assumed that the total energy absorbed by the material during desorption is equal to the energy it could produce during the sorption process. Accordingly, the ratio of the desorption energy to the sample weight tested yields the energy storage density (Ed).

Figure 4 shows the energy density for the samples (1, 2, 3 and 4). The material with the highest Ed value was found as sample #2 with an Ed of 251.6 kJ/kg. Sample #4 has the second highest value with an energy density of 242.2 kJ/kg. The expected performance from samples #3 (231.6 kJ/kg) and #1 (220.8 kJ / kg) could not be obtained. Based on the data obtained, $LiNO_3$ and CaCl salts were found to be good candidates.

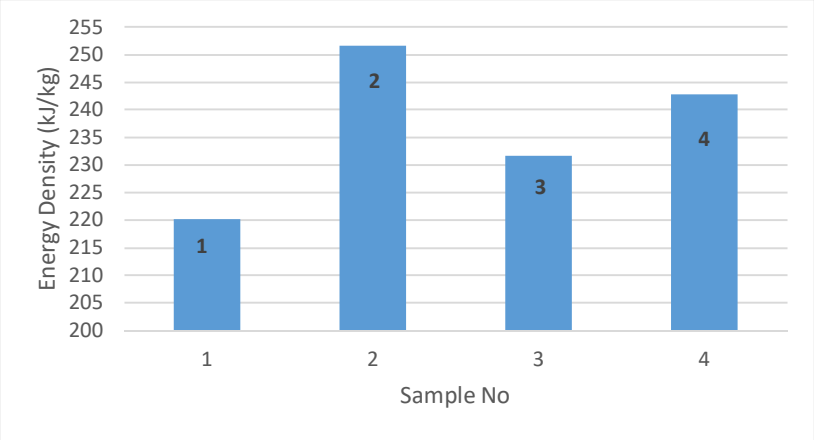

Figure 4: Ed values of samples prepared by impregnation

After the second anodisation in the production of AAO templates, some of samples produced were subjected to pore expanding for 10 minutes and 15 minutes with NaOH solution. In this process, pore diameters and corresponding nanotube volumes were obtained. Here, it is aimed to investigate the change in the amount of salt solution that the pores can absorb due to the increased pore volume and the change in the amount of energy that the sample can store.

The Ed values of the AAO templates of different diameters impregnated with saturated salts given in Figures 5 and 6 also supported this information. Sample #6 impregnated with $LiNO_3$ has an energy density of 491.3 kJ/kg, while sample #10 impregnated with $LiNO_3$ has an energy density of 646.4 kJ/kg. Sample #10 with pore diameter wider than the other gave better results.

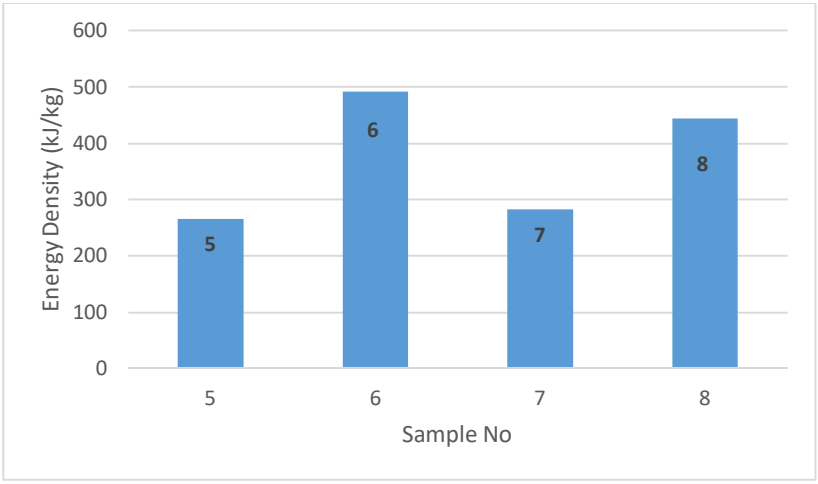

Figure 5: Ed values of samples immersed in NaOH solution for 10 min.

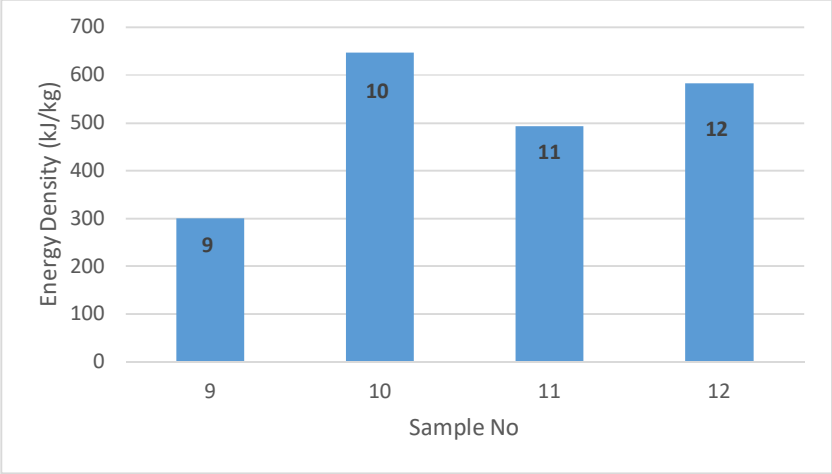

Figure 6: Ed values of samples immersed in NaOH solution for 15 min.

4. CONCLUSION

According to the experimental parameters used, the samples for thermal storage were obtained in accordance with the desired pore diameter by the anodisation process. It is possible to change the pore diameter by using different parameters. The samples with $LiNO_3$ salt impregnated (sample #10) was found to give better results in terms of energy density compared to others.

The parameters used in this work provided promising results in terms of energy density when compared with previous studies investigating natural materials (168–406 kJ/kg) (Tatsidjodoung *et al.,* 2013; Tay *et al.,* 2017). This work is the first step of studies investigating the characteristics of salt impregnated AAO plates as an alternative composite sorbent for low temperature THS applications. Development of efficient, low cost Salt-AAO composites could be used for different purposes in the future such as residential solar heat storage or industrial waste heat recovery, which could lead to considerable energy savings and reduction in fossil fuel consumption.

5. ACKNOWLEDGEMENT

This study was supported by the Scientific and Technological Research Council of Turkey (TUBİTAK) (Project No: 119M073)

6. REFERENCES

Aristov Y.I., Current progress in adsorption technologies for low-energy buildings, Future Cities & Environment 1 (1) (2015) 171.

Aydin D., Casey S.P., Riffat S., The latest advancements on thermochemical heat storage systems, Renewable & Sustainable Energy Review. 41 (2015) 356-367.

Casey, S. P., Elvins, J., Riffat, S., Robinson, A., (2014) Salt impregnated dessicant matrices for 'open' thermochemical energy storage-Selection, synthesis and characterisation of candidate materials. Energy and Buildings, 84, 412-425.

Grekova, A., Gordeeva, L., Aristov, Y., (2016) Composite sorbents "Li/Ca halogenides inside Multi-wall Carbon Nano-tubes" for Thermal Energy Storage. Solar Energy Materials & Solar Cells. 155, 176-183

Henninger, S., Ernst, S., Gordeeva, L., Bendix, P., Fröhlich, D., Grekova, A., Bonaccorsi, L., Aristov, Y., Jaenchen, J., (2016). New Materials for Absorption Heat Transformation and Storage. Renewable Energy, Energy 115, 1-10

Hongois, S., Kuznik, F., Stevens, P., Roux, J. J., (2011) Development and characterisation of a new MgSO4-zeolite composite for long-term thermal energy storage. Solar Energy Materials & Solar Cells, 95, 1831-1837

Liu, H., Nagano, K., Sugiyama, D., Togawa, J., Nakamura, M., (2013) Honeycomb filters made from mesoporous composite material for an open sorption thermal energy storage system to store low-temperature industrial waste heat. International Journal of Heat and Mass Transfer 65, 471-480

Liu, H. (2014) Study on Open and Closed Chemical Thermal Energy Storage Technology with Low-regeneration Temperature, Hokkaido University Collection of Scholarly and Academic Papers: HUSCAP Page 2.

Masuda H., Fukuda K., (1995), "Ordered metal nano-hole arrays made by a two-step replication of honeycomb structures of anodic alumina", Science, 268, 1466.

Pasaoglu, D., I., 2011, Electrodeposition and Characterization of Ni-W Nanowires on Anodized Aluminium Oxide Templates, , M.Sc. Thesis, Istanbul Technical University , Istanbul, TURKEY

Posern, K.; Kaps, C. Calorimetric studies of thermochemical heat storage materials based on mixtures of MgSO4 and MgCl2. Thermochimica Acta 2010, 502, 73–76.

Rammelberg, H., O., Osterland, T., Priehs, B., Opel, O., Ruck, W., (2016) Thermochemical heat storage materials – Performance of mixed salt hydrates. Solar Energy 136, 571-589

Roßkopf, C., Afflerbach, S., Schmidt, M., Görtz, B., Kowald, T., Linder, M., Trettin, R., (2015) Investigations of nano coated calcium hydroxide cycled in a thermochemical heat storage. Energy Conversion and Management 97, 94-102

Sharma, A., Tyagi, V. V., Chen, C. R., & Buddhi, D. (2009). Review on thermal energy storage with phase change materials and applications. Renewable and Sustainable Energy Reviews, 13(2), 318–345.

Tatsidjodoung, P., Le Pierrès, N., & Luo, L. (2013). A review of potential materials for thermal energy storage in building applications. Renewable and Sustainable Energy Reviews, 18, 327–349.

Tay, N. H. S., Liu, M., Belusko, M., & Bruno, F. (2017). Review on transportable phase change material in thermal energy storage systems. Renewable and Sustainable Energy Reviews, 75, 264–277.

Zhang, Y. N., Wang, R. Z., Zhao Y. J., Li, T. X., Riffat, S. B., Wajid, N. M.,(2016). Development and thermochemical characterizations of vermiculite/SrBr2 composite sorbents for low-temperature heat storage. Elsevier, Energy 115, 120-128

#243: An edifying strategy for sustainable building information modelling integration to higher education

Yunusa Yusuf BADIRU[1], Ruqayyatul Bashir TUKUR[2], Abubakar Daroda ABUDULAZEEZ[3]

[1] *Department of Architecture, Faculty of Environment Design, Ahmadu Bello University, Zaria, Nigeria.*
[2] *Department of Architecture, Faculty of Environment Design, Ahmadu Bello University, Zaria, Nigeria.*
[3] *Department of Building, Faculty of Environment Design, Ahmadu Bello University, Zaria, Nigeria.*

Building Information Modelling (BIM) is a project delivery development in the construction industry that has a growing need for competent workforce and its production. The literature confirms that only a small fraction of stakeholders in the construction industry are aware of BIM and are willing to adopt its culture, despite its relevance and benefits. Also, the appraisal of higher education, its globalisation and challenges of technology integration to higher education is overriding, this explains the inadequacy of BIM-competent workforce for employment in the industry. In order to have a constant supply of adequate BIM workforce for the construction industry, knowledge and skills of BIM must be integrated into higher education academic programs. This study researched educational theories that might facilitate a sustainable BIM integration to education. Some of the theories reviewed include: Problem Based Learning (PBL); Didactic Transposition (DT); Zone of Proximal Development (ZPD) and 21st Century Learning and Skills Frameworks (P21). The relevance of each of these theories for the integration were discussed and therefrom a theoretical framework for the integration of BIM to higher education was developed.

Keywords: u strategy; building information modelling; sustainable; education; integration; theories

1. INTRODUCTION

The importance of education cannot be over emphasised to humans and resource development. Montessori (1976) acknowledged that education plays essential roles in the process of human resources development. In this millennium the role and responsibility of human resources in the professional development have changed radically from the traditional approach and the competencies needed to fulfil a successful human resources development is knowledge and training (Ulrich *et al.*, 1995). Thus, the inadequacy or lack of knowledge and skills are challenges that must be tackled for a successful competence optimisation in any professional, business organisation, and at national level for economy benefits (Jajri and Ismail, 2007). Building Information Modelling (BIM) is the digital documentation, a process of holistic data about the sequential phases of construction project that is made apparent at the design stages. BIM bring about collaboration of persons and various constructions stages such as; construction planning, project construction, facility management and operations (Yusuf *et al.*, 2015). It is an era of BIM where construction project standards are measured and benchmarked for evaluating efficiency in Architectural, Engineering, Construction and Operations (AECO) (Yusuf *et al.*, 2015; Yusuf *et al.*, 2017). A sustainable strategy is a necessity for education to cope with rapid changes in this millennium. And in order to keep abreast with the twenty-first century technological innovations, it imperative that education research and theories are necessary ingredient to achieve a seemly integration of education and technology. Hence, educational innovations are imperative, and its effectiveness would be based on technology of education as regards systematic approach to the teaching-learning process (Singh, 1991).

Building Information Modelling (BIM) is a project delivery development in the construction industry that has a growing need for competent workforce and its production (Badiru *et al.*, 2016). However, the primary goal of this study is to explore and identify educational theories that best fit for sustainable BIM integration to higher education. It is on this premise that this paper focuses on understanding the higher education setting in Malaysia and its educational readiness for BIM integration. Consequently, four research underpinning theories were assessed and their relevant to BIM knowledge integration to higher education were under studied. Among the theories are: Didactic Transposition (DT), Zone of proximal Development (ZPD), Problem Based Learning (PBL) and 21st Century learning and skills (P21). Focusing on the characteristic of higher education, its global influence, and the technological innovation and integration. Altbach (2004) is of the views that the influence of globalisation on higher education cannot be over stressed. And the argument further stressed that globalisation, internet, sciences and technology are moulding new sets of knowledge that are interdependence. This has created contemporary pressures on higher education which is leading to many changes experiencing in academic world globally. It is also worth of note that the influence of globalisation on higher education in developing countries calls for concerns. This is because there evolve new sets of academic needs to accommodate the innovative breakthrough

2. BUILDING INFORMATION MODELLING AND EDUCATION

BIM is a contemporary method of delivering construction project and many countries around the world are adopting it for projects of certain magnitude especially government projects (Badiru *et al.*, 2016). It is apparent that technology improve learning and this must be included in the education curriculum for the training of students in order to enhance their knowledge and skills for societal benefits (Davies and Harty, 2013). BIM is a component of Information Technology (IT) and it is an effective means for widening educational opportunities. Education institutions and many governments have recognised the importance of integrating modern technology into education. Bauer and Kenton (2005) observed that, the use of technology as an instructional delivery system that have come to stay, but he noted that it integration to academic curriculum still remain a barrier. In order to deal with higher education technological integration challenges, academic delivery should employ technology through a practical oriented system that will enables problems solving as the need arises (Bauer and Kenton, 2005).

3. EDUCATION RESPONSE TO BIM INTEGRATION

BIM is a global phenomenal that have come to stay for construction industry, but one may as “of what need is the BIM integrating to education”. Dean (2007) conducts a research and the outcome made him to conclude that BIM education is needed among AEC academics students. His conclusion was derived from the fact that about 75% of respondents prefers the employment of BIM graduate applicant to those without BIM knowledge and skills (Dean, 2007). In another argument, adequate BIM integrated to education stands to provide industry required knowledge and experts for the construction industry market needs (Woo, 2006). This a strong ground for advocating for the teaching of BIM on a collaborative platform among.

Achieving competent BIM knowledge is a function of adequate support from professional trained BIM experts, but the unfortunate story is that this support is has been lacking. The global development trends in the construction industry is that BIM incorporation into higher education will not only services the growing needs for BIM competent professionals but it would also create new prospects for students to be developed in their professional careers, thus enabling them to deal with new occupational challenges with high efficiency achieved by applying BIM (Woo,

2006). Based on Vintage human capital models, Weinberg (2004) noted that young workers are more technological and computer friendly, fast adopters and beneficiaries of the new computer technologies.

Incorporating this new technology to education is a great challenge. Therefore, a number of approaches have been employed in the introduction of BIM in the academic curricula. Some institution directly integrate BIM into their curriculum, while others prefers to teach BIM as a standalone courses or match the approaches (Sacks and Barak, 2010). The preference of the approach to be adopted should favour the construction industry requirements this is because the industry seeks to engage professionals who can apply knowledge to practical situations and this can better be achieve when BIM integrated teaching approach is adopted (Wong (Wong *et al.*, 2011; Barison and Santos, 2011).

Traditionally, academic institutions are found to always need more time to come to teams with new technology changes especially when such changes are frequently coming. The university curricular changes take longer time which serve as an impediment to build environment academic disciplines to match the pace at which the construction industry is advancing in this sector, also in addition, there tend to be reluctance in the adoption of digital and computational approached (Sharag-Eldin *et al.*, 2010). Sharag-Eldin *et al.* (2010), further note that academic exercises tend to confront the technology with new needs, applications, and new possibilities. This tend to delimits full integration of information technologies into curricular which is a problem that affects both the practices and the academic sector of the industry, thus, making them to miss opportunities for developing the industry as a whole. It obvious that the construction industry needs BIM experts to fill the market gaps (Gardner et al., 2014). It is on this note that the professionals or software vendor educators are making efforts to provide the elementary BIM knowledge for newly graduates for their admission into the labour market of the industry (Wu and Issa, 2013; Wu and Luo, 2016; Gardner *et al.*, 2014). However, the danger of recruiting BIM experts without an established education standard may relegated the BIM expert training to just a part-time or graduate levels course. Hence, delimiting research and development (R&D) as well as it theoretical and academic pursuit, while reduce BIM to vocational training. Macdonald (2011) also noted that BIM is a new technology that is still struggling to be integrated to the academic, and where this seem to have happened, students are still been educated in their isolated departments with no integration or collaborations among the specialisations. Technology integration into education should be cross-curricular rather than become a separate isolated course or topic in itself (Flanagan and Jacobsen, 2003).

BIM is an all-encompassing building delivery process, and therefore education and training should follow suite. BIM education should be taught among all academic specialisation in construction industry in form of departments, faculties, schools and colleges in an interactive and collective teaching module system among their students. This will aid the spirit of working collaboratively and inter-transfer of knowledge can be enhanced. Worldwide the construction industry is encourages collaboration among various specialisations in the industry, through the application of BIM tools and process; whereas HEIs are finding it difficult to embrace the change. It is expected that the higher education will follow suit the industry for undergoing a paradigm shift from the traditional approach to integration and information sharing (Macdonald, 2012).

3.1. Challenges to technology integration to Higher Education

For higher education to remain competitive in this millennium, effort must be geared toward the development of knowledge and skills with provision of adequate learning and technical support that would aid technological integration into various AEC industry academic disciplines (Rogers, 2000). Training and technical support is critical and there had always been little to complete absence on the effective use of IT resources for instructional and scholarly work(Rogers *et al.*, 2015). This has led to poor education amenities for ICT skills and training of institutional faculties. Hence, higher education is still lagging behind the industry.

Kim *et al.* (2013) identify and classified the barriers that are often encountered in the technology integration to curriculum into two classifications: the First-Order which is external barrier and Second-Order called internal barriers. The external barriers referred to as the first order barriers, these includes the needed resources for integration such as equipment, time, training and other supports; these are either inadequate or completely missing in the academic implementation environment. The external barriers are relatively easy to be eliminated, because it financial resource that are needed (Kopcha, 2012). In the other hand, the internal barriers impede fundamental changes due to the fact that it is personal and inert to the teachers and are not easily noticeable. Dede (2010); Fisher *et al.* (1996) admit that these barriers causes more hitches than the first-order barriers. Teaching, learning and knowledge methods also constitute a major impeding factor to technological integration to education when they are not standardised (Ritchie and Wiburg, 1994; Tondeur *et al.*, 2013; Kopcha, 2012).

Kiviniemi (2013) noted that higher education is not island and that there exist a strong linkage with the construction industry. He further noted that there exist a number of impedance to BIM integration to education. These factors includes:

i. Understanding and management of expectations
ii. Education of the educator
iii. Education Curriculum
iv. Resistance to change old mode of doing things
v. Accreditation requirements.
vi. BIM education is not just technology, software training nor learning to use tools
vii. Securing platform for integration of professionals in practice and academic educators

3.2. Academic readiness to imbibe the new technology

The significant lack of the understanding of BIM and industry readiness for it adoption has been identified as a major hindrance, this has led to a growing demand for tertiary institutions to integrate BIM into their curricula, in order to equip new graduates with such knowledge (Kriengsak *et al.*, 2013). With the growing awareness coupled with the realisation of the importance and the potentials benefits stands to be gain for the adoption of BIM, several governments globally are now making efforts in actualising BIM adoption in the construction industry sector. The need for a framework for BIM application has also been considered as a fundamental prerequisite to guarantee optimal usage. Many government around the world has put forward strategies for BIM application and adoption. Many governments such as USA, Australia, UK, Finland, Norway, Denmark and many others, have established organs to develop standards and best practices guideline for BIM adoption (Monteiro and Poças Martins, 2013).

4. EDUCATION INTEGRATION THEORIES AND APPLICATION

Theories are set of interrelated concepts, definitions, and propositions that explains or predicts events or situations by specifying relations among variables. Most of our decisions and actions are based on our predictions of their possible consequences and those prediction are based on established or personal theories about social life (Glanz, 2013). In the field of social research, a bulk of evidence suggests that interventions developed with an explicit theoretical foundation or foundations are more operational than those without a theoretical base, it is also acknowledge that some strategies that combine multiple theories and concepts have larger effects (Glanz, 2013). However, the research seeks to consider the guiding principles in the extension of knowledge and proffering solution toward the research problems. With the rapid development of BIM as emerging technology, the integration of Information and Communication Technology (ICT) has increasingly attracts the attention of academia. BIM is a complementary part of ICT in the construction industry. Though, the simple combination of hardware and software will not make integration naturally follow, likewise the adoption of BIM in education will not naturally followed no matter the level of ICT integration into the academic disciplines instruction structures (Earle W. Kennett, 2010).Therefore, there is need for conscious effort of academies and researchers to come up with integration strategies that will facilitate integration of BIM knowledge into education. Numerous instructional design models are currently available to help in the integration of BIM education curricula but with little or no consideration to academic readiness. Hence, to achieve the above, the research will explore some relevant and effective learning models; in order for the postulation of criteria necessary for integration of BIM in to construction industry academic disciplines of higher education. The following learning models will be exploited for the study, these includes:

i. The Problem Based Learning (PBL)
ii. The Didactic Transposition (DT)
iii. The Zone Of Proximal Development (ZPD)
iv. 21st Century Learning and Skills Frameworks (P21)

4.1. Problem-based learning (PBL)

The PBL model is important in the learning process. It is touted to be the approach and means to achieve the 21st century skills. Moving away from traditional learning style, Project-based Learning (PBL) builds on individual strengths, and allows individuals to explore their interests, it also incorporates the principles of providing challenging and complex work, interdisciplinary and encourages cooperative learning. Blumenfeld et al. (1991) explains, that PBL lends authenticity to learning. While in practice, practitioners plan, implement and evaluate projects in real-world situations beyond the classrooms. PBL experiences are often designed to address real-world problems and issues, which is complex, interconnecting, and ambiguous, sometime project-based learning may be called inquiry-based learning or learning by doing, since the learning process is integral to the knowledge and skills students acquire (Savery, 2006; Bell, 2010; Monson; Christopher Monson). Bartels and Beil (2017) made use of Figure 1 to demonstrate the difference between tradition learning method and PBL. While the tradition learning involves been told what need to be known, memorise it and assigned problem to illustrate it intangibly. PBL in other is a learning style that assigned real life problem, identify the needed solutions which is then learn and applied. The implementation of inquiry-based science learning is to develop students to have an integrated understanding of task before them and this availed them with opportunity to achieve three interrelated learning objectives: the development of general inquiry abilities, the acquisition of specific investigation skills, and the under-standing of

science concepts and principles (Edelson *et al.*, 1999). Computing and networking technologies offers new opportunities to support inquiry-based learning.

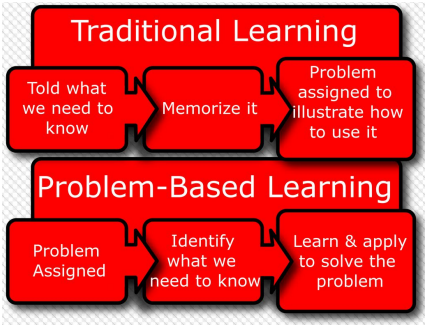

Figure 1: Traditional learning versus problem-based learning (Bartels and Beil, 2017)

Blumenfeld et al. (1991) identifies six contributions that technology can make to the learning process, these are: a) Enhancing interest and motivation; b) Providing access to information; c) Allowing active, manipulable representations; d) Structuring the process with tactical and strategic support; e) Diagnosing and correcting errors; f) Managing complexity and aiding production. In academic setting, the knowledge transfer of BIM needs interest and motivation which are of great importance; this is to provide access to information which will enable students to be active through a process of tactical and strategic support. The aspect of conflict detection and resolution using models at design stage is made possible for the management of complex projects for all project team members, in order to deliver the project to the best practise standards. Edelson *et al.* (1999) explains that computing technologies offer benefits for inquiry-based learning for large data storage and manipulate of information both in visual and audio formats; it also supports complex computations for communication and expression with the ability to respond rapidly among project team members. These qualities of PBL in the knowledge transfer made it suitable and promising technologies developed for learners, which makes it applicable for the integration of BIM to education and to enhance ability of virtual appreciation of digital project before real life reproduction (Edelson *et al.*, 1999).

4.2. Didactic transposition (DT)

The DT theory raises awareness for understanding of knowledge transformation to occur with constraints. To tackle the constraint two main steps of transpositions emerges. The first is the reference knowledge or practical knowledge to the curriculum, while the second is the transposition of knowledge from curriculum to the classroom, which is the main obligation of teacher and curriculum designers (Tiberghien and Sensevy, 2014). Furthermore, DT is an analytical process of transposing (or transforming) human knowledge such as domain specific knowledge into knowledge for education (Duit, 2014). It is a scientific process of knowledge transformation from practical to a teachable knowledge. The concept of DT was first introduced by Chevallard (1988) in 1985, this was in the context of mathematics education. From the works of Bosch and Gascón (2006); Duit (2014) and Achiam (2014) they all observed that for certain knowledge to be taught at school, transformation process needed to be carried out so that elements that were not made for school are made to changes into elements that may be reconstructed inside school. Hazzan *et al.* (2010) points out that DT is the process by which professional content becomes school content, and this goes beyond simplifying or eliminating difficult or abstract features, but rather by means of transposition process that adapts and shapes the professional knowledge to fit the school environment. The development of BIM knowledge into education involves all the stakeholders in the industry, but may not be easily transferable. Hence, for the integration of BIM to education instruction manual (i.e. curriculum), a DT processes can be adopted. Figure 2 show that the knowledge development in the construction industry can only be integrated to HEIs through pedagogical and cognitive processes of didactic. Therefore, BIM knowledge is an emerging body of knowledge that need to be transposed and diffused to the AEC industry society. BIM can be subjected to a scientific study (and the knowledge resulting therefrom) of the innumerable actions taken to provoke the diffusion of knowledge in the AEC industry. In another argument, there should exist a relationship between knowledge and teaching, this enables a teaching process to be established and determined (Shulman, 1987). Therefore, teaching of BIM in higher institution should have a semblance of the way the knowledge is been practices in the real construction industry setting. DT is a phenomenal that is a theoretical construct for knowledge diffusion to institutions or society.

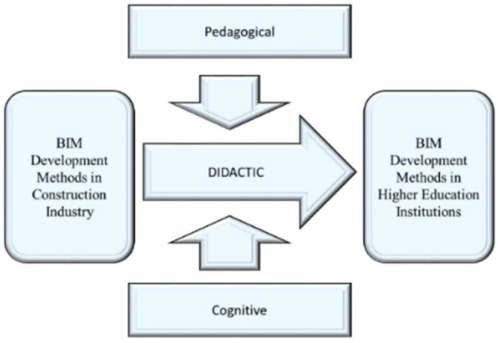

Figure 2: Didactic Transposition of BIM development (adopted from Hazzan et al. (2010a))

4.3. Zone of proximal development (ZPD)

Wass and Golding (2014) presents Vygotsky's ZPD, a theory that was introduces in Russia in the 1920s by Vygotsky, but the works was translated and made available to the Western World in late 1950s. Vygotsky is of the views that interaction with peers as an effective way of developing skills and strategies. However, Vygotsky defined the ZPD as 'the distance between the actual developmental level as determined by independent problem solving and the level of potential development as determined through problem solving under adult guidance or in collaboration with more capable peers" (Wertsch, 1984). He recommends that teachers use cooperative learning exercises where less competent peers develop with aid from more skilful peers - within the ZPD. This is applicable to BIM competent professionals or BIM software vendors to pair with higher education as scaffolding till enough boost in BIM knowledge and skills is achieved, then the scaffolding can be removed. Furthermore Vygotsky's theory also encourages collaborative learning, where group members should have different levels of ability so more advanced peers can help less advanced members operate within their ZPD (Golding, 2013; Wass and Golding, 2014). Knowledge is a social process that also follows the principle of osmosis, where diffusion of fluid take place from higher concentration to lower one through membrane. ZPD employ the concept of osmosis where knowledge is transfer from higher knowledge level is drawn to the low level knowledge for an equilibrium level to be attained. The common zone of equilibrium between high and low level knowledge is ZPD as illustrated in Figure 3 This principle is applicable to BIM knowledge spread in the construction industry between the practices and the academics. Chaiklin (2003b) notes that the common conception of the ZPD is a two-way scenario of interaction between a more competent person and a less competent person on a task, in such a way that the less competent person becomes independently proficient at what was initially a jointly-accomplished task. ZPD is an education model that provides a distinctive perspective for conceptualising the relation between human learning and development, this perspective is of fundamental differences compare to many of the currently predominant views about this relation (Chaiklin, 2003b). The adoption of BIM in the construction industry practices is far ahead of the education sector of the industry, but with constant interaction of the two side, there is every possibilities that rate of adoption will pick up rapidly, though other impeding factors will be eased out with serious awareness campaign of the level of development at the practices and what is required of young graduates. Figure 3.3 illustrated that knowledge and experience are contributed from the professional experts, while intellectual capabilities development are from HEIs educators to a common zone of proximal development (ZPD). This ZPD facilitates competent delivery of standard workforce that is needed in work life.

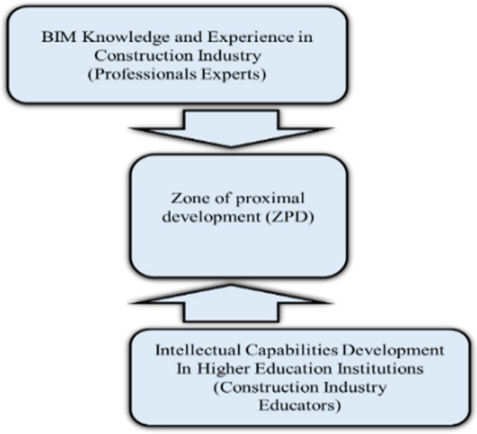

Figure 3: Zone of Proximal Development (Roth and Radford, 2010)

4.4. 21st Century learning and skills (P21)

Trilling and Fadel (2009) note that there is monumental shift from Industrial Age production to Knowledge Age Economy, information-driven, and global networks, which is life-altering in a changing world. This is similar to the shift from the Agrarian to the Industrial Age of three and half centuries ago. Noss (2012) also observes that 21st century knowledge is qualitatively different from the preceding centuries knowledge, which gave birth to existing curricula, thus, this calls for careful consideration for the design of digital technologies for knowledge learning and accessibility (Noss, 2012). The core subjects and interdisciplinary 21st century themes are surrounded by the three sets of skills most in demand in the 21st century: Learning and innovation skills; Information, media, and technology skills; and Life and career skills. Trilling and Fadel (2009) note that P21's Framework for 21st Century Learning was developed with input from teachers, education experts, and business leaders to define and illustrate the skills and knowledge students need to succeed in work life and citizenship, as well as the support systems necessary for 21st century learning outcomes. It has been used by thousands of educators and hundreds of schools in the U.S. and abroad to put 21st century skills at the centre of learning. Similar to P21 are: The United Kingdom's 21st Century Learning Alliance; France's National Ministry of Education's socle commun; New Zealand's Council for Educational Research and the twenty-one-member Asia-Pacific Economic Cooperation (APEC) forum of which Malaysia is a member (Trilling and Fadel, 2009; Noss, 2012) . They have common agenda of knowledge empowerment with technological updates for students under training so as to make them successful in their work life and a be technological updated. Figure 4 presents 21st Century Learning Framework that help to define and illustrate the skills and knowledge students need to succeed in work, life and citizenship, as well as the support systems necessary for 21st century learning outcomes. The expected student outcomes is represented by the arches of the rainbow and these are: life and career skills; learning and innovation skills 4Cs (critical thinking, communication, collaboration and creativity); information, media and technology skills. While the systems to support realisation of these outcomes were depicted by the pools at the bottom; these includes: standards and assessment; curriculum and instruction; professional development and learning environments. The framework has been found useful and adopted in order to put 21st century skills at the centre of learning.

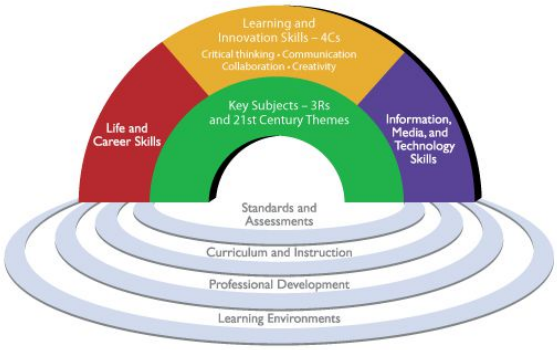

Figure 4: 21st Century Learning Framework (Trilling and Fadel, 2009)

The 21st century comes with its own uniqueness that is quite different from the 20th century, due to the capabilities people need for work, citizenship, and self-actualisation. These differences are in the emergence of very sophisticated information and communications technologies that characterised the 21st century. It is evident that in the immediate past century works done by people are now done by machines and with computers and ICT continually shifting and expanding capabilities to accomplish human tasks (Dede, 2010). This made many organisational groups to call for 21st century skills and thus, further evolve frameworks for the new millennium contents and process of teaching of students with the aim to facilitate practitioners integrates skills into the teaching of core academic subjects as presented in Figure 4 Partnership for 21st Century Skills (P21) is one such an organisation that has developed a unified, collective vision for learning known as the Framework for 21st Century Learning. Dede (2009) presents the five critical support systems identified by the 21st Century Learning Partnership which is to ensure student mastery of 21st century skills: (a) 21st Century Standards; (b) Assessments of 21st Century Skills; (c) 21st Century Curriculum and Instruction; (d) 21st Century Professional Development and (e) 21st Century Learning Environments.

5. RELEVANCE OF DT, ZPD, P21 AND PBL ADOPTED APPROACH

Theories and models help explain behaviour, as well as suggest how to develop more effective ways to influence and change behaviour (Glanz, 2013). However, the above theories are set of interventions that is meant to influence higher education to integrate BIM into their academic programs. ZPD is a theory that recognise knowledge as a social process where awareness are transferred and diffused among two different level of knowledge till an equilibrium level of understanding is attained; this principle is also applicable to BIM knowledge spread in the

construction industry between the practices and the academics (Chaiklin, 2003b). In most countries of the world, construction industry have bodies of professional practitioners (consultants, contractors and other stakeholders) that have adopted BIM in their practise with a level of competence, whereas, education institution are have not begins to competent BIM graduates to march with the global BIM requirement. The education sector are characterised with lack of risk taking in venturing into new technology adoption and this is due to academic bureaucracy and curriculum rigidity, which is a limiting factor.

DT is an analytical process of transposing (or transforming) theory of human knowledge such as domain specific knowledge into knowledge for education (Duit, 2014; Duit et al., 2012). It is a scientific process of knowledge transformation from practical to a teachable knowledge. Therefore, a practical knowledge has wider experiences, application and in the service of larger population, so more information about the phenomenal in question will be rich and reachable in data which can only be tap with a quantitative data mining technique. In other hand, a teachable knowledge that is restrictive has limited information to offer.

Moreover, PBL is education processes that lends authenticity to learning and in practice, practitioners plan, implement and evaluate projects in real-world situations beyond the classrooms. In Malaysia industrial working experience is part of student training, where students are exposed to real life working environment during their training. Industry-Based Learning (IBL) is a renowned programme which allows undergraduate students the opportunity to undertake full-time, paid employment in an area relevant to their studies. PBL experiences are often designed to address real-world problems and issues, which is complex, interconnecting, and ambiguous, sometime it is been referred to as: inquiry-based learning or learning by doing, since the learning process is integral to the knowledge and skills students acquire (Savery, 2015). Construction industry is very notable for its practical skills for construction project delivery; this practical skill must be learned formally or in an informal setting.

Furthermore, P21 Framework describes the skills, knowledge and expertise students must master to succeed in work and life; it is a blend of content knowledge, specific skills, expertise and literacies. The P21 frameworks advocated that at 21st century learning requires more than identifying specific skills, content knowledge, expertise and literacies. They are of the opinions that an innovative support system must be created to help students master the multi-dimensional abilities that will be required of them in their daily life after school (Dede, 2009). In 2014, Malaysia Education Ministry adopted and launched the Pendidikan Abad Ke-21 (PA21) program to Malaysia government funded schools which is an extension of P21. The Pendidikan Abad Ke-21 (PA21) is a new paradigm shift in the 21st century learning and skills meat for the advancement of learning and skills needed for work life of present day students (Baki, 2017).With BIM technology that have been widely identified as improving project delivery and has becoming construction industry standards; thus, it teaching and learning are skills computing and networking technologies that offers new opportunities to support inquiry-based learning (Blumenfeld et al., 1991) . Problem PBL is a teaching method in which students' gains knowledge and skills by working for an extended period of time to investigate and respond to an engaging and complex question, problem, or challenge.

6. CONCEPTUAL FRAMEWORK FOR BIM KNOWLEDGE INTEGRATION

Knowledge is a process that offers an understanding of the manner in which organisations create new knowledge, maintain existing knowledge and discard 'old' knowledge (Fombad et al., 2009; Hargreaves, 1996; Fombad, 2008). This is basically the call by 21st century learning and skills frameworks (P21) and PBL which believe that old knowledge should be replaced with the new way of doing things in this millennium. In addition, DT and ZPD are applicable for this study because of its relevance and frequent adoption for many areas of human devious. Thus, BIM is a process, tools and technology that is of international acceptance and which is fast becoming the global standard, and its adoption in the higher education is inevitable and the earlier the education sector acknowledged the better (Macdonald, 2012a; Shelbourn et al., 2016). This is the main task of this research to establish strategies (a framework) for the inclusion of BIM in the education delivery manual of higher education for the would-be professional in the construction industry.

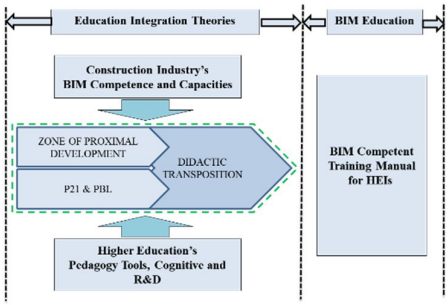

Figure 5: Conceptual Framework for BIM Knowledge Integration

7. CONCLUSION

The conceptual framework for BIM knowledge integration as presented in the Figure 5 has two phases, the first is referred to as education integration theories and the second is BIM education. At the education integration theories phase, considerations are given to activities and responsibilities of construction industry at one hand and the higher education in the delivery of BIM competent workforce to the industry in Malaysia. Considering the fact that theories are adopted to effectively influence and change behaviour among variables (Glanz, 2013). Thus, the industry and the higher education are to be influence for effective BIM integration to higher education in Malaysia. This is by the adoption of ZPD, PBL and P21 to create a zone of activities, responsibilities and competent overlap among the industry and higher education. The items in the zone of competent overlap among the dual is push forward for adoption as BIM competent training manual using DT theories which states that professional content should be made school content without simplify nor eliminates difficult or abstract features. The items from the zone of competent overlap is to be made a pedagogical and cognitive tools (that is BIM education curriculum) for the delivery of BIM competent training.

8. REFERENCES

Achiam, M. (2014). Didactic Transposition; From Theoretical Notion to Research Programme. *In:* Copenhagen, U. O. (ed.) *ESERA Summerschool.*

Altbach, P.G. (2004). Globalisation and the university: Myths and realities in an unequal world. *Tertiary Education & Management.* 10(1)**,** 3-25.

Badiru, Y.Y., Ali, K.N. and Embi, M.R. (2016). Building Information Modeling as a Process of Systemic Changes for Collaborative Education in Higher Education. *ScienceDirect.* 219**,** 820-827.

Barison, M.B. and Santos, E.T. (2011). The Competencies of BIM Specialists: a Comparative Analysis of the Literature Review and Job Ad Descriptions. *ASCE.*

Bartels, L. and Beil, J. 2017. *What is Problem-Based Learning (PBL)?* [Online]. Southern Illinois University Edwardsville: Center for Faculty Development and Innovation. Available: http://www.siue.edu/facultycenter/services_resources/teaching/pbl.shtml [Accessed 29 December, 2017 2017].

Bauer, J. and Kenton, J. (2005). Toward Technology Integration in the Schools: Why It Isn't Happening. *Jl. of Technology and Teacher Education.* 13(4)**,** 28.

Bell, S. (2010). Project-Based Learning for the 21st Century: Skills for the Future. *The Clearing House: A Journal of Educational Strategies, Issues and Ideas.* 83(2)**,** 39-43.

Bosch, M. and Gascón, J. (2006). Twenty-five years of the didactic transposition. *ICMI Bulletin.* 58**,** 51-65.

Chevallard, Y. (1988). On Didactic Transposition Theory: Some Introductory Notes.

Christopher Monson, R. Student Collaboration as The Foundation for Learning Bim Software- Ideas from Project-Based Introduction.

Davies, R. and Harty, C. (2013). Implementing 'Site BIM': A case study of ICT innovation on a large hospital project. *Automation in Construction.* 30**,** 15-24.

Dede, C. (2010). Comparing frameworks for 21st century skills. *21st century skills: Rethinking how students learn.* 20**,** 51-76.

Duit, R. (2014). Teaching and Learning the Physics Energy Concept. *Teaching and Learning of Energy in K–12 Education.*

Earle W. Kennett (2010). The VA-BIM-Guide. *In:* Stubbs, S. (ed.) *Department of Veterans Affairs.*

Edelson, D.C., Gordin, D.N. and Pea, R.D. (1999). Addressing the Challenges of Inquiry-Based Learning Through Technology and Curriculum Design. *Journal of the Learning Sciences.* 8(3-4)**,** 391-450.

Fisher, C., Dwyer, D.C. and Yocam, K. (1996). *Education & Technology: Reflections on Computing in Classrooms.* ERIC.

Flanagan, L. and Jacobsen, M. (2003). Technology leadership for the twenty-first century principal. *Journal of Educational Administration.* 41(2)**,** 124-142.

Gardner, J.C.H., Hosseini, M.R., Rameezdeen, R. and Chileshe, N. (2014). Building Information Modelling (BIM) Education in South Australia: Industry Needs. *International Conference On Engineering, Project, And Production Management*. Port Elizabeth 6031, South Africa, 293-302.

Glanz, K. (2013). Social and Behavioral Theories. *e-source Behavioral and Social Sciences Research.* National Institutes of Health.

Hazzan, O., Dubinsky, Y. and Meerbaum-Salant, O. (2010). Didactic Transposition in Computer Science Education. *standard articles.* 1(4).

Jajri, I. and Ismail, R. (2007). Technical Efficiency, Technological Change and Total Factor Productivity Growth in Malaysian Manufacturing Sector. *Journal of Industrial Economices.*

Kim, C., Kim, M.K., Lee, C., Spector, J.M. and Demeester, K. (2013). Teacher beliefs and technology integration. *Teaching and Teacher Education.* 29**,** 76-85.

Kiviniemi, A. (2013). Challenges and opportunities in the BIM education: How to include BIM in the future curricula of AEC professionals?

Kopcha, T.J. (2012). Teachers' perceptions of the barriers to technology integration and practices with technology under situated professional development. *Computers & Education.* 59(4)**,** 1109-1121.

Kriengsak, P., Wong, M.L., Doh, J.H., Stewart, R.A. and Mccarthy, T.J. (2013). Integrating building information modelling (BIM) into Engineering education: an exploratory study of industry perceptions using social network data. *University of Wollongong, Research Online.*

Macdonald, J.A. (2011). Bim – Adding Value By Assisting Collaboration.

Macdonald, J.A. (2012). A Framework For Collaborative Bim Education Acros The Aec Disciplines.

Monson, C. Student Collaboration As The Foundation For Learning Bim Software: Ideas From A Project-Based Introduction. *Building Construction Science Program.*

Monteiro, A. and Poças Martins, J. (2013). A survey on modeling guidelines for quantity takeoff-oriented BIM-based design. *Automation in Construction.* 35**,** 238-253.

Ritchie, D. and Wiburg, K. (1994). Educational variables influencing technology integration. *Journal of Technology and Teacher Education.* 2(2)**,** 143-153.

Rogers, J., Chong, H.-Y. and Preece, C. (2015). Adoption of building information modelling technology (BIM) perspectives from Malaysian engineering consulting services firms. *Engineering, Construction and Architectural Management.* 22(4)**,** 424-445.

Sacks, R. and Barak, R. (2010). Teaching Building Information Modeling as an Integral Part of Freshman Year Civil Engineering Education. *JOURNAL OF PROFESSIONAL ISSUES IN ENGINEERING EDUCATION AND PRACTICE.*

Savery, J.R. (2006). Overview of Problem-based Learning: Definitions and Distinctions. *Interdisciplinary Journal of Problem-Based Learning.* 1(1).

Sharag-Eldin, A., A.P., L. and Nawari, N.O. (2010). BIM in AEC Education. *ASCE 2010.*

Singh, R.R. (1991). *Education for the Twenty-First Century Ry: Asia-Pacific Perspectives.* Printed in Thailand, UNESCO Principal Regional Office for Asia and the Pacific.

Tiberghien, A. and Sensevy, G. (2014). *Transposition Didactique*. *Encyclopedia of Science Education.* (pp. 1-4). Springer.

Tondeur, J., Kershaw, L.H., Vanderlinde, R. and Braak, J.V. (2013). Getting inside the black box of technology integration in education: Teachers' stimulated recall of classroom observations. *Australasian Journal of Educational Technology.* 29(3).

Ulrich, D., Brockbank, W., Yeung, A.K. and Lake, D.G. (1995). Human resource competencies: An empirical assessment. *Human Resource Management.* 34(4)**,** 473-495.

Weinberg, B.A. (2004). Experience and technology adoption.

Wong, K.A., Wong, K.F. and Nadeem, A. (2011). Building Information Modelling For Tertiary Construction Education In Hong Kong. *Journal of Information Technology in Construction.*

Woo, J.H. (2006). BIM (Building Information Modeling) and Pedagogical Challenges. *43rd ASC National Annual*.

Wu, W. and Issa, R.R.A. (2013). BIM-education-for-new-career-options_an-initial-investigation. *BIM Academic Workshop*. Washington, DC.

Wu, W. and Luo, Y. (2016). Pedagogy and assessment of student learning in BIM and sustainable design and construction. *JOURNAL OF INFORMATION TECHNOLOGY IN CONSTRUCTION.* 21**,** 218-232.

Yusuf, B.Y., Ali, K.N. and Embi, M.R. (2015). Building Information Modeling (BIM): A Potential for Effective Building Industry Practice in Malaysia. *Jurnal Teknologi.* 77(15)**,** 55-62.

Yusuf, B.Y., Embi, M.R. and Ali, K.N. (2017). Academic Readiness for Building Information Modelling (BIM) Integration to Higher Education Institutions (HEIs) in Malaysia. *IEEE.* 3(17).

#245: Energy performance and indoor climate assessment of 150 UK school buildings from 1873 to present

Sara MOHAMED [1], Richard SMITH[2], Lucelia RODRIGUES[3], Siddig OMER[4], John CALAUTIT[5]

[1] *Sara Mohamed, Department of Architecture and Built Environment, Faculty of Engineering, the University of Nottingham, University Park, Nottingham NG7 2RD, UK*
[2] *Richard Smith, School Energy Efficiency CIC, Chair of Governors - FHA Ladybrook,UK, www.schoolenergyefficiency.co.uk*
[3]*Lucelia Rodriguesc, Department of Architecture and Built Environment, Faculty of Engineering, the University of Nottingham, University Park, Nottingham NG7 2RD, UK*
[4]*Dr Siddig Omer Department of Architecture and Built Environment, Faculty of Engineering, the University of Nottingham, University Park, Nottingham NG7 2RD, UK*
[5]*Dr John Calautit Department of Architecture and Built Environment, Faculty of Engineering, the University of Nottingham, University Park, Nottingham NG7 2RD, UK.*

School energy efficiency measures, such as adoption of several energy efficiency measurements, represent a driver for increasing the risk of overheating hence has a significant impact on the student learning and health. In order to deal with the problem realistically, it is essential to investigate energy audits based on extensive case studies. Analysis data of 150 energy audit of schools building stock were conducted, to examine the energy consumption performance and internal environment of the schools constructed in different periods from 1873 to 1901. Energy audit techniques were carried out to identify any energy conservation opportunities (ECOs). Level 1 (walk-through assessment), level 2 (survey and data analysis) audits and thermal images data for interiors were conducted over all building zones.

Results of 150 schools case studies showed an increased on the pattern of the energy used and most of the internal environment experience overheating, this highlight the issues of the reduction of fresh air flow rates

Keywords: Energy audit; School energy efficient; overheating

1. INTRODUCTION

The construction and operation of buildings contribute a large proportion of the total energy used in the world (DOE, 2010, Asadi et al., 2012, Ma et al., 2012) As the replacement rate of existing buildings by new builds is only around 1.0%-3.0% per annum (Barlow and Fiala, 2007, Roberts, 2008, DOE, 2018), the enhancement of energy efficiency in existing buildings is essential for the timely reduction of global energy use and increase in environmental sustainability.

A study by the Carbon Trust found that retrofitting UK schools could reduce energy costs by around £44 million per year and also prevent 625,000 tonnes of CO2 from entering the atmosphere (Carbon Trust, 2018).

As the government squeezes school budgets, it has never been more significant for local authorities to identify low-cost solutions to deliver large financial savings. Reducing energy consumption is one of the quickest and simplest ways to provide direct savings and could help the average secondary school save £21,500 in energy bills almost equal to the annual salary of a newly qualified teacher (Rugg, 2011).

At the same time, many international organisations and governments have made significant efforts towards energy efficiency improvement in existing buildings. For instance, in the United States (DOE, 2018), the government has provided significant financial assistance to support existing building retrofit. In Australia (DOCC&EE, 2018), from 1st November 2010, the Commercial Building Disclosure (CBD) programme has obliged the owners of Australia's commercial and office buildings to deliver energy efficiency information to potential buyers or occupants. In the UK, in 2010 the UK government made a significant commitment to advancing and upgrading the energy efficiency of more than 6 million British homes by 2020, aiming to reduce carbon emissions by 29% (GOV.UK, 2018).

In parallel, a significant amount of research has been carried out to develop and investigate different energy efficiency opportunities to enhance the energy performance of existing buildings (Flourentzou and Roulet, 2002, Xing et al., 2011). The results have shown that energy use in existing buildings could be reduced considerably through proper retrofitting or refurbishment (Hestnes and Kofoed, 2002, Ardente et al., 2011, Chidiac et al., 2011, Mahlia et al., 2011). School building retrofitting or refurbishment is one of the main approaches to achieve energy consumption and greenhouse gas emissions reduction.

Retrofitting and reducing the energy use of existing UK school buildings faces many challenges. The main challenge faced is that there are many uncertainties, such as climate change, human behaviour change, government policy change, etc. Other challenges may include financial limitations and barriers, perceived long payback periods and interruptions to operations (Ma et al., 2012). The willingness of the school management is another challenge if there is no financial support from the government. Alternatively, retrofitting of school buildings offers great opportunities for enhanced energy efficiency, improved and increased student productivity, reduced maintenance costs and better thermal comfort in the classroom. As a consequence, it can also assist in community/social responsibilities, reduce exposure to energy price growth and more importantly make school buildings more liveable.

School buildings in the UK include various functional spaces, however classroom are still the most commonly-used space as most children particularly in the primary level spend most of the day there. Classrooms or the cluster learning are the largest occupied area for every school building design, and host the largest part of the daily school student's activities. Primary school buildings cluster learning start from the early years to 11 year old, as this is the most dominated features of it is occupancy density and internal gains. This results in very large values of internal heat sources, besides internal emission of the body, odours, water vapour and CO_2, causing an increasing concern with regards to overheating and internal air quality for the pupils which they are exposed to and spend long periods of time in (Besler and Besler, 2000, Ellis, 2003).

An energy audit is widely considered as one of the most cost-effective ways to improve energy by investigating the energy flows within the building (Trianni et al., 2014, Kluczek and Olszewski, 2017). Energy audit (survey) methods have studied energy use in school buildings in the West and Midlands of the UK. They enable identification of energy use and cost, from which energy cost and consumption control measures can be implemented and reviewed (Australia, 2000). An energy audit plays an essential role in an energy retrofit programme to identify areas with energy-saving potential, identify issues regarding thermal comfort of occupants of the school buildings and provide information needed in the school buildings' performance assessment.

The potential retrofit opportunities (after identifying the problem) can be determined based on the information collected during the energy audit (Jaggs and Palmer, 2000, Santamouris and Dascalaki, 2002). To reliably predict energy saving and identify issues regarding school buildings from a huge number of energy reports, considerations of the design and parameters of the simulation model can be calibrated with the energy audit data. In this paper, energy audit of 150 exciting schools constructed in different periods were examined. These energy audits will be used to examine the existing energy performance internal environment condition of the school buildings.

2. METHODOLOGY

This study used detailed/audit report of energy consumption of end users collected from School Energy Efficient (SEE) data. This provided deeper insight into how energy was used and explained the underlying factors. The methodology comprised of five phases of analysis which provided a complete understanding of the patterns of energy use in UK schools and the factors that influenced their energy demand. Assessment of the latest trends of energy use in UK school buildings involved understanding the influence of building construction periods and operational features on their energy performance. The insights required to address the research questions and gaps are difficult to obtain without employing empirically observed data.

The study extensively used empirical/observed data which was vital for interpreting the energy consumption data in the context of benchmarking. Descriptive analysis of the data allowed the latest and historical patterns of energy use in various building construction periods to be examined, to assess the factors that determine the effect of most energy consumption periods, as well as to address the critical research problems. The hierarchical structure of the analysis of the school data means that each of the reports became gradually focused on elements that were more specific. Below are descriptions of the aims of each analysis.

The initial analysis focused on improving the understanding of the latest trends in the energy performance of school buildings that have lodged energy performance data. It also involved the data for two years and assessments of the energy benchmarks; the scope covered school buildings for which data are available. The next phase was analysing the data down to the primary and secondary school stock, date of build, energy, energy performance operating rating, and annual and typical energy use. Having a narrower focus meant that the analysis was able to delve deeper into the data. This phase involved not only description of the data but also testing of various hypotheses to examine the implications of classifications and school building characteristics. It also allowed additional data to be combined with the existing data of each construction period to enrich the picture.

In the third analysis, the focus shifted towards assessing the correlations between the intrinsic features of buildings and school construction periods that determine the demand for energy and the energy performance of schools. There was, however, currently no existing data that describe the built forms/materials of schools. This phase, therefore, involved a massive data collection exercise to gather descriptions of buildings, including the built form and design, to further enhance the analysis of the dataset that was developed in the previous analysis.

The last analysis focused on detailed information obtained from site visits, thermal images and energy audits of school buildings. At this stage, more exceptional detail, such as specifications of building fabric and equipment, were introduced in the following section. This very detailed information provided insights into the breakdown of overall energy use in schools and why some schools were more intensive energy users than others. The data on the built period, which were comparable to the data developed in the previous analysis, also allowed correlations between building characteristics and various end uses to be examined. A flow chart representing the process is shown in Figure 1.

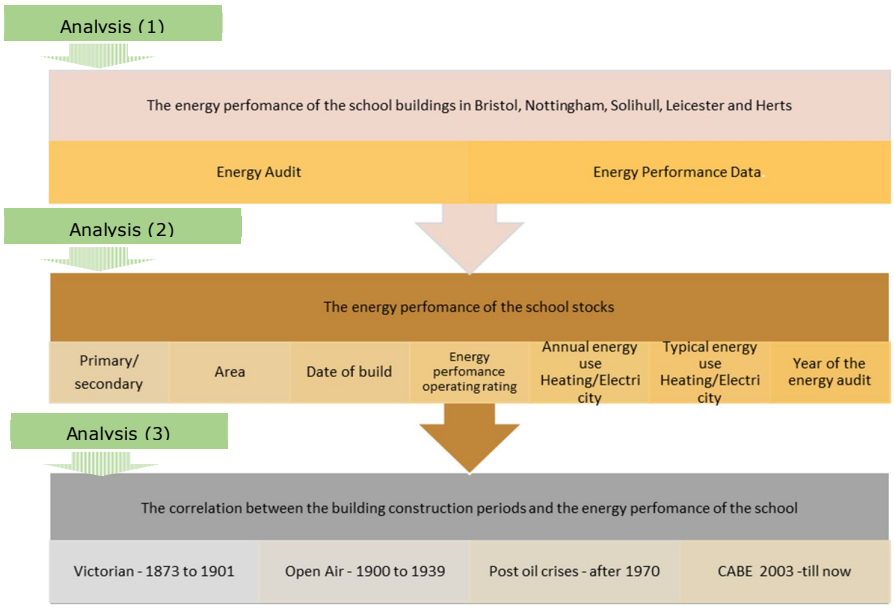

Figure 1: Description of the methods for analysing the school energy audit data.

3. RESULTS AND DISCUSSION

3.1. Energy consumption in schools

The dataset described in the figures below was analysed to observe changes in the patterns of energy use of school buildings in the UK over five periods: Victorian (1873-1901), Open air (1900-1939), Post-war (1945-1970), Post-oil crisis (1970-2003) and CABE (2003 until now). The data analysis was carried out based on those cases where there are more than 100 school buildings in any given benchmark category. This was to ensure that the results derived from the analyses were representative of the stock. The changes in the energy performance of buildings in different construction periods were assessed using a clustered column graph. The average movement of the trend lines was taken as the typical pattern of energy use of the school buildings in the construction periods.

The energy performance data over two years meant that it was possible to examine how the patterns of energy use in school buildings in different construction types changed over the period. A significant feature of the database created for the data analysis was that it tracked the energy performance of the school buildings over these years and different construction periods. Figure 2 below shows that there is considerable variation in the pattern of energy use in the case of the data/study school, despite similarity in the activity. The chart shows that there were five main school construction periods. Schools built in the in post-war construction periods (1945-1970) Commission for Architect and Build Environment (CABE) 2003-2010 period were all found to be significantly more intensive in energy use for heating. However, schools dating from (1945-1970) were found to use more energy one is about 212 kWh/m2 – due to their high ceilings and large windows. These factors will be explored further in the following section.

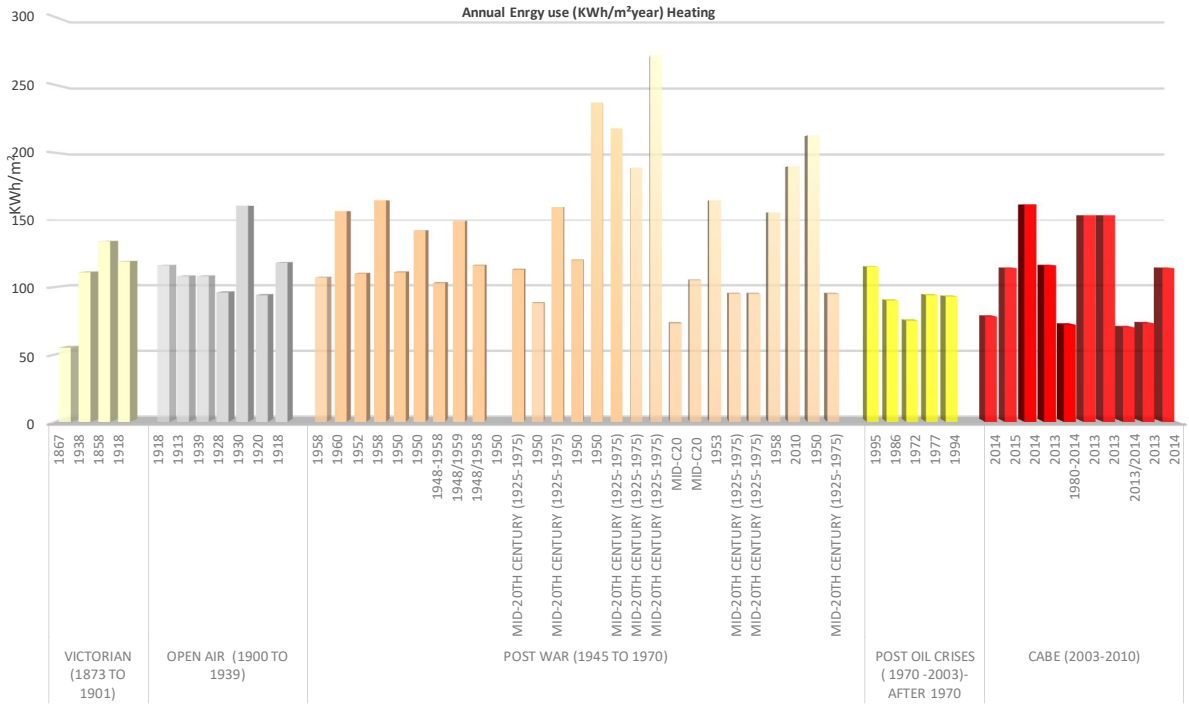

Figure 2: variations in the patterns of heating energy use in the case study schools in five different construction periods

Comparing energy consumption in Figure 3, which is plotted against typical values for school building (ref), it is clear that the values presented for heating energy were higher than expected in all school constructed in different periods. The post war experience consumed more energy due to the light weight construction and prefabrication technology that was applied in that period to increase the speed of construction. As a result, many of these schools suffer from poor insulation.

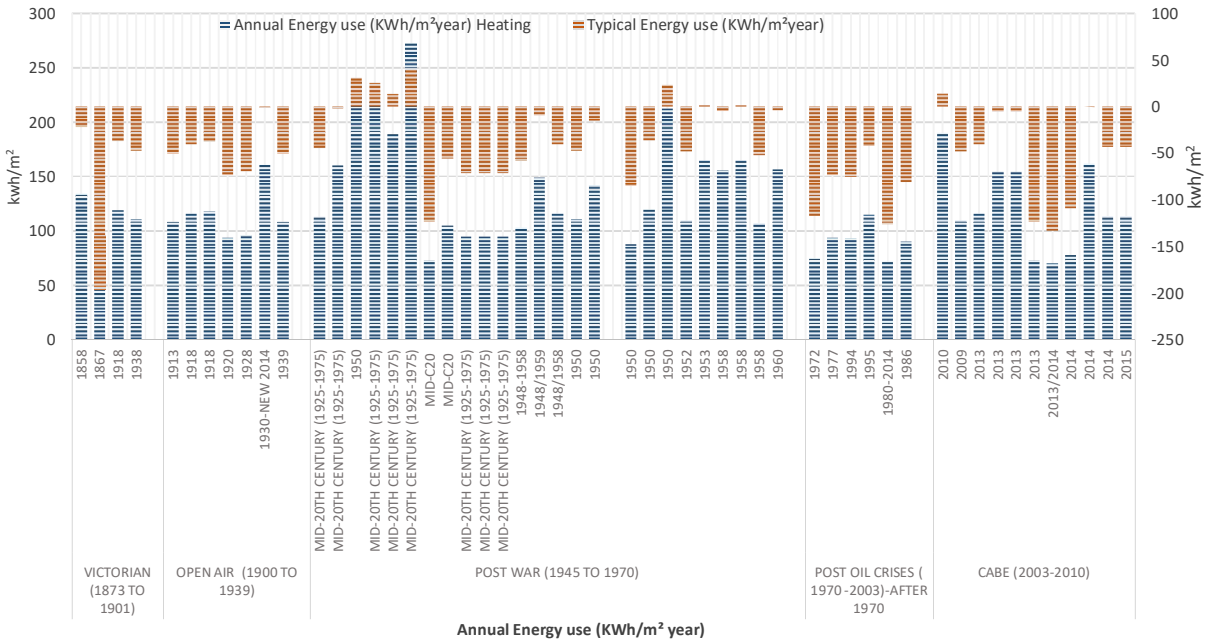

Figure 3: the results from the cross-sectional / data analysis of the DEC-Display Energy Certificate records. The results show the patterns of energy use of school buildings in different construction period categories.

Figure 4 demonstrates the annual electricity consumption in UK school buildings compared with typical energy used built in different periods. Figure 5 displays the electricity consumption compared with the floor area for each school constructed in different periods. This typical energy consumption is plotted against the annual energy use for specific school. As can be seen, schools constructed in CABE (2003-2010), new built in 2013 and 2013 total energy consumption is more than 42% higher than those compared with typical energy used. The data on electricity use in the case study of schools in the figures below shows that the electricity consumption is considerably higher than typical energy consumption benchmarks in different school construction periods. The figure records trends in the energy consumption of the schools. What is more, the maximum consumption in recently constructed schools was found to be more than twice that of a typical older school, taking into consideration that these were built in 2003 or later, compared with the open air (1945-1970) and post-oil crises (1970-2003) periods. The difference indicates how electricity-intensive modern schools are becoming, despite the effort to design low-energy schools. It can be seen that electricity consumption has gradually increased. This trend reflects the increasing occurrence of virtual learning environments that involve the use of electrical technologies, such as ICT equipment. The increases in the intensity of electricity use suggest that schools are likely to have continued their uptake of ICT and electrical equipment and that the trend has continued up to the present (Global Action Plan 2006; Ofsted 2011).

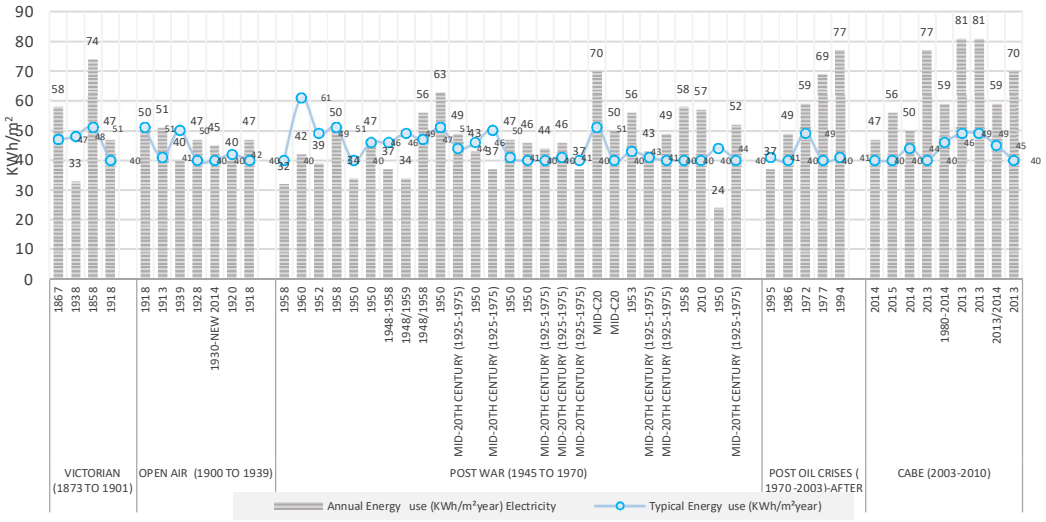

Figure 4: Annual Energy use in school building constructed in different periods comparing with typical use for the present school

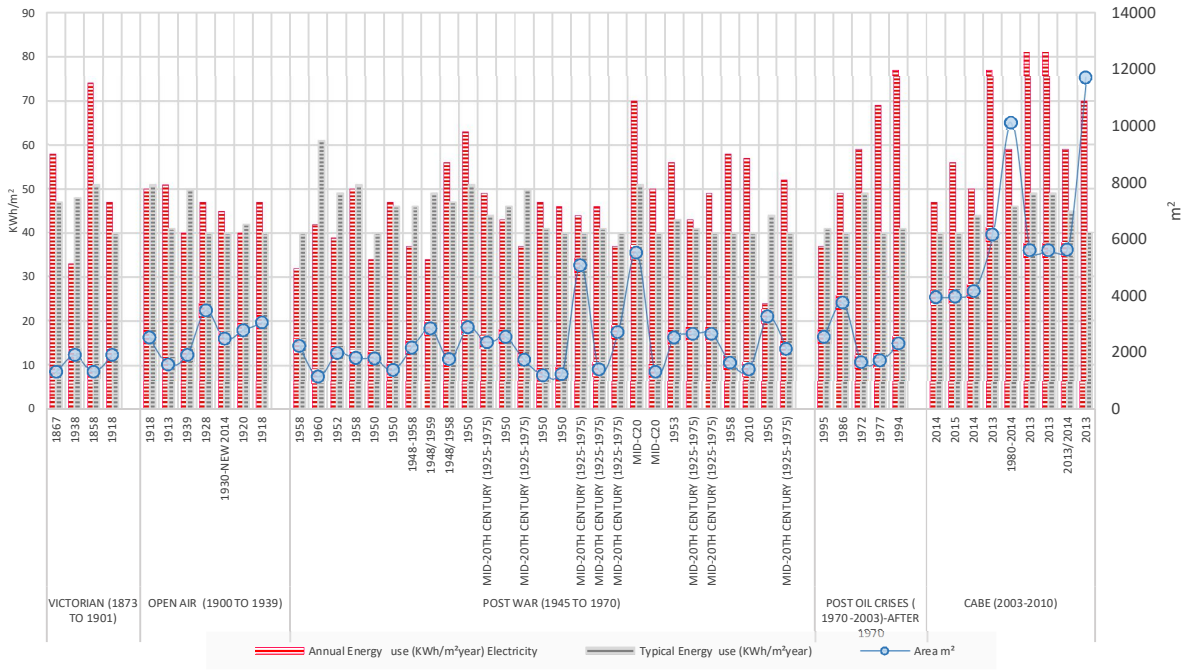

Figure 5: Annual electricity consumption per floor area for each school constructed in different periods

Figure 6 shows the changes in the energy performance of schools buildings from different construction periods using a clustered column graph. The results displayed the monitoring total energy consumption annually and the energy performance operating for each school constructed in different periods compared with the energy consumption monitored and operating rating for the following year for each building, which vary from 2015-2016 to 2016-2017. The results showed a significant increasing in most of the schools in year 2 comparison with year 1. Also the results demonstrate a significant rise in Energy performance operating rating in year 2 in post oil crises (1970-2003), post war(1945 to 1970) and CABE(2003-till now).

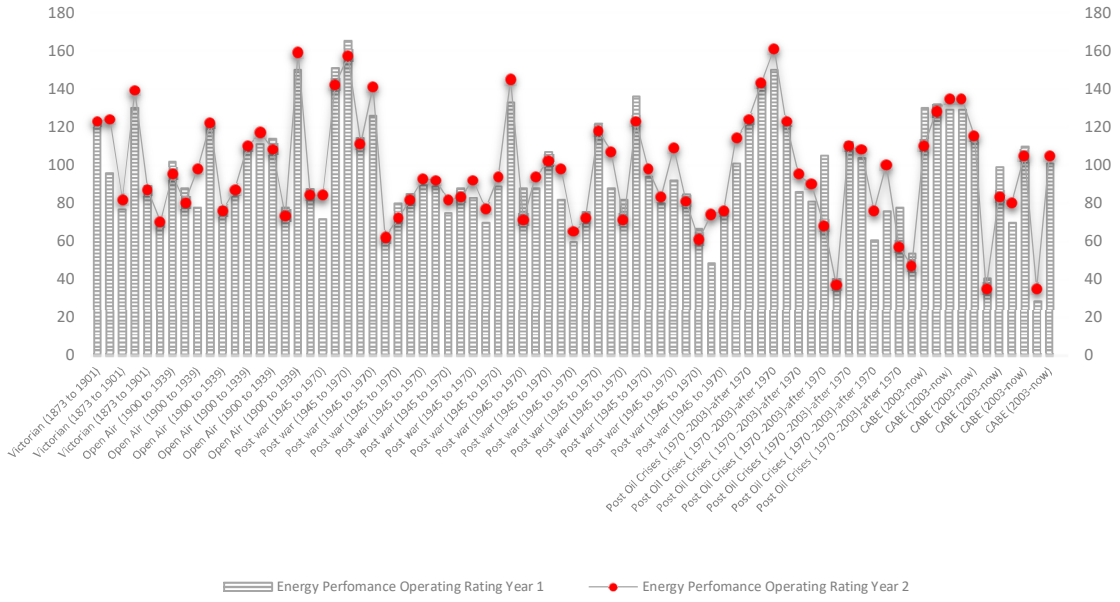

Figure 6: variation in the patterns of energy use in schools, in the Victorian school, Post war, Post oil crises and CABE

3.2. Environmental design in Victorian/Edwardian school (1873-1901)

Victorian schools fall into two categories: schools constructed before and after the 1870 Education Act. This Act made local authorities accountable for providing education and constructing schools. The second generation of Victorian schools is still in use. The most major influence on the design of schools throughout England was that of E.R. Robson, the architect and surveyor appointed by the London School Board in 1871. In accordance with his proposals, classrooms were arranged around a long central hallway with high ceilings, making the depth of buildings greater than 20 metres. These brick schools are often two or three storeys high with large windows and high ceilings. Today, Victorian schools are found to be thermally comfortable during summer (with low cooling demand and stable indoor temperatures) but not in winter. Due to their sash windows and high ceilings, these schools can utilise the stack effect to maintain IAQ and comfortable temperatures during the summer (Montazami et al., 2015).

Furthermore, the main elevations of the classrooms are generally towards the north, which results in a lower level of solar gain. Heavy thermal mass surfaces have a significant impact on maintaining indoor temperatures as they can absorb any direct solar energy that is received. However, the occupants of these schools suffer from a high level of echo and reverberation and consequently from a higher level of background noise due to the high ceilings Bridget Shield and Dockrell (2004) suggested that acoustic tiles could be added to decrease echo and reverberation in Victorian schools. The heavy thermal mass surfaces in Victorian schools play an important role in creating stable and acceptable indoor temperatures as they can absorb direct solar energy. In addition, heavy thermal mass surfaces have a significant influence in terms of controlling and potentially decreasing the indoor temperature during summer. The majority of Victorian schools are now listed buildings and their façades are therefore required to be preserved unaltered. Sash windows with single glazing are a part of the historical heritage of Victorian schools. These windows can be a source of heat loss during the heating season with the concomitant impact on heat demand. Following the Primary Capital Programme (PCP), some of the old single-glazed windows were replaced with trickle-vented double-glazed units. In order to study the implication of such replacements, two similar Victorian primary schools in north London (one with and one without double glazing) were analysed by Montazami et al. (2015). IAQ, overheating, and student health and satisfaction were investigated, illustrated in Figure 8. This study shows that although Victorian schools with double-glazed windows save annually on heating energy bills, the double glazing increases overheating, mould growth and CO_2 due to a reduction in the infiltration rate. As a result, there is conflict between thermal comfort during heating and cooling seasons. In addition, there is conflict between thermal comfort and air quality during the heating season. Understanding design issues in Victorian schools is valuable as these schools are part of UK heritage and continue to be used. They also have the potential to be less vulnerable to projected changes to the future climate due to their high level of thermal mass, as shown in Figure 7.

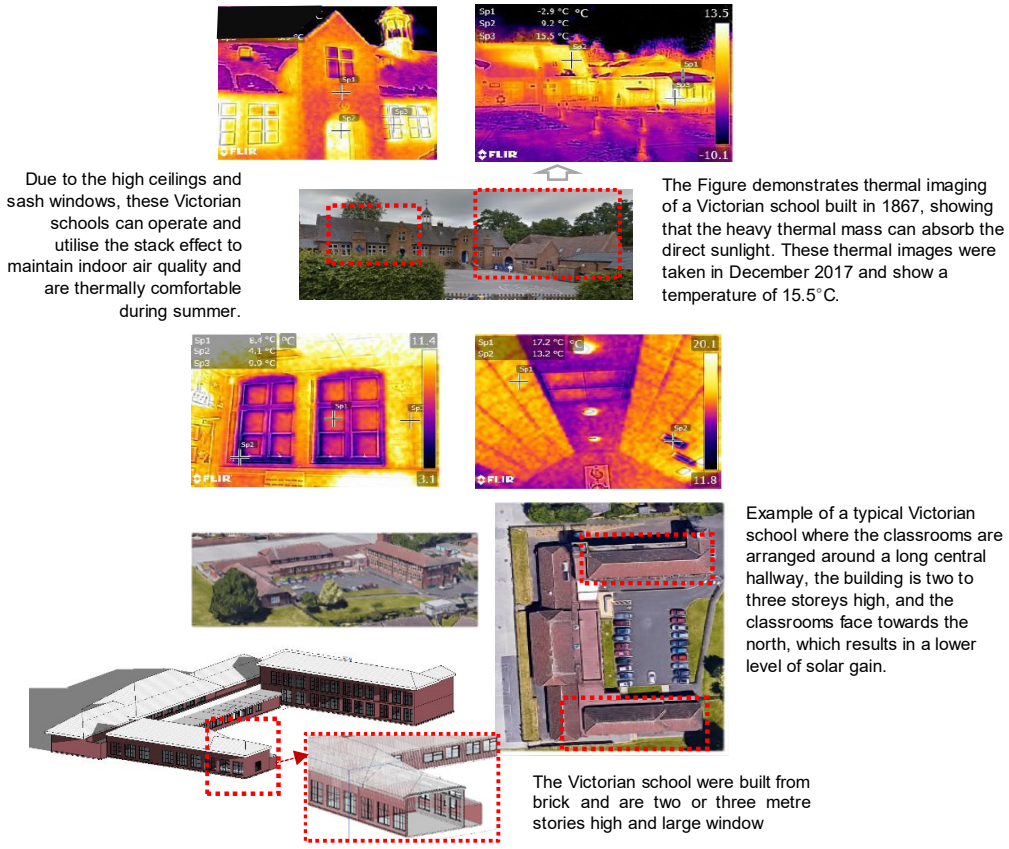

Figure 7: Environmental performance of case school -Victorian School (1873-1901), source SEE, 2018 School

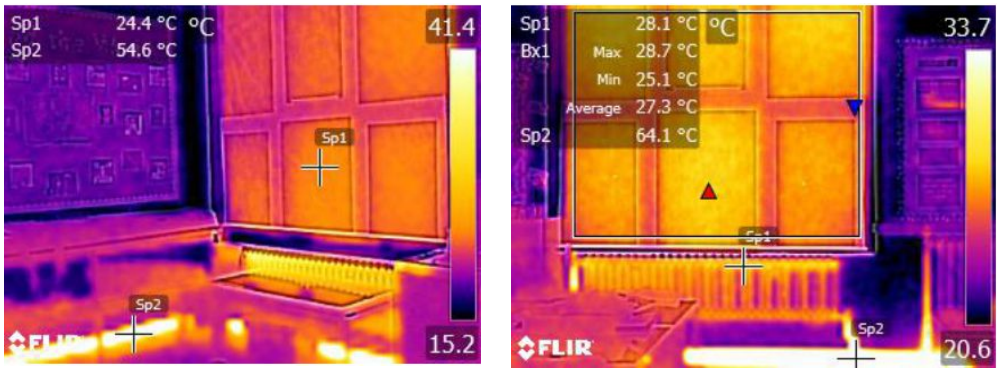

Figure 8: The thermal images demonstrated classroom overheating inside the Victorian school. Although Victorian schools with double glazing save on annual heating bills, this increases overheating due to reduced infiltration.

3.3. Environment of open-air schools (1900-1939)

Because of concerns over the spread of tuberculosis in this period, the needs of children in education were targeted with particular reference to their wellbeing and health. As a result, schools were designed with much more open space, and greater importance was placed on natural light and ventilation from both sides of the classrooms, which were placed around courtyards. At that time, antibiotics were not available to fight tuberculosis and therefore a high level of ventilation was needed. Even during the winter, windows were left open while the heating system was left on. Due to the impact of natural cross ventilation, these school buildings were thermally comfortable during summer. However, during the winter providing thermal comfort with natural ventilation required consuming a significant amount of energy. Therefore, there was conflict between thermal comfort and air quality during the winter or heating season. Once antibiotics became available, schools did not have to operate cross ventilation during winter and this conflict was removed in that period. Montazami et al. (2015) stated that currently there is a risk of overheating in these schools during summer, as most of them no longer have cross ventilation since one side has been covered by a closed corridor to provide better environmental conditions and to save energy during the winter. The end of the need for disease control led to the closing off corridors, as can be seen in Figure 9 and 10. This has led to a risk of overheating during summer as most of these school contractions have no longer have cross ventilation since one side has been covered by closed corridor to provide better environmental conditions during winter to save energy. Figure 10 demonstrates the view of a classroom in a school built in 1939, of which one side has been covered by a closed corridor. Thermal images were taken in December 2015 and show the temperature variation.

The thermal images displays the risk of overheating and the classroom covered by a closed corridor.

Figure 9:The figures shows the open-air schools was built in 1913, the thermal images displays the conflict between the thermal comfort and air quality during the heating season required consuming significant amour of energy, the figure displays the temperature on the heating between 35 to 54.5 CO while in the temperature at windows 5 to 12CO

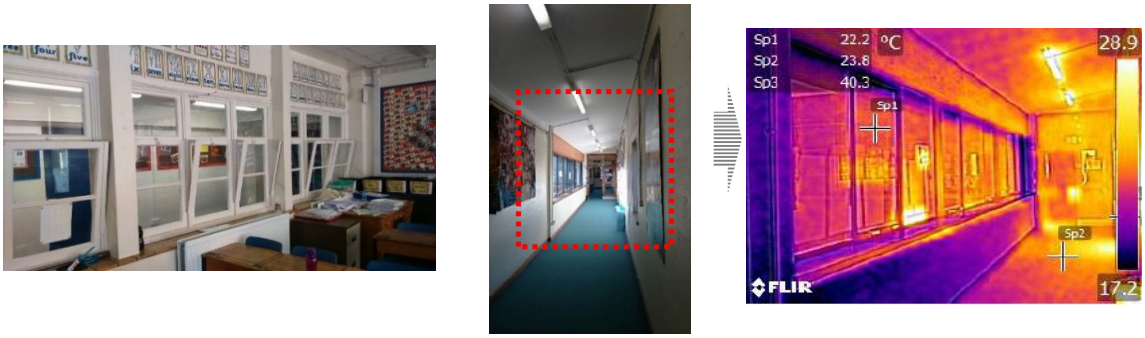

Figure 10: View of a classroom in a school built in 1939, of which one side has been covered by a closed corridor. Thermal images were taken in December 2015 and show the temperature variation.

3.4. Environmental design issues in BSF and CABE (2003 till now)

Three schemes were proposed after the post-oil crises period. The PCP and Building Schools for Future (BSF) were proposed in 2003 and 2006, respectively, BSF 2003, and with CABE 2010 they resulted in a guide for school communities, local authorities, funders and design and construction teams involved in the school building process. Its ten case studies provide examples of efficient involvement across a range of school building projects as stated in the previous chapter. However, one of the aims and targets of constructing these schools was to provide the best environmental conditions for schools and classrooms. For a variety of reasons, some of the schools constructed during this time failed to provide an acceptable indoor environment. Mumvic et al. (2010) examined the winter IAQ and thermal comfort performance of newly-built secondary schools in England following the BSF investment programme in 2009 and stated that there was a conflict between air quality and thermal comfort. Mechanical ventilation was installed to provide good air quality by delivering 8 l/s fresh air per person. Although mechanical ventilation delivered the required fresh air, it also produced cold draughts that had a negative impact on thermal comfort during winter. Hence, although the schools had recently been built based on the BSF programme, they did not deliver a comfortable environment as the comfort factors conflicted and interacted with each other. Another reason that schools constructed under the PCP and BSF programmes do not provide comfortable environments (for example, thermal comfort) is the lack of understanding regarding occupants' perceptions about comfort factors in the design outline. Moreover, Jenkins *et al.* (2009) stated that several schools built according to the BSF programme experienced overheating, Figures 11, 12 and 13.

According to Montazami and Nicol (2015), one reason that BSF schools experienced overheating was due to these schools being designed based on Building Bulletin 101 [12] which was too 'lenient'. This leniency was due to deficiencies in terms of ventilation design as well as in terms of understanding the occupants' perceptions regarding thermal comfort. The UK climate is predicted to experience further increases of 2°C every year and more than 7°C by the end of this century. Meeting the thermal and internal air quality standard for schools built in this period can be very difficult for buildings that (traditionally in the UK) have not used mechanical ventilation and air conditioning. With climate change and the predicted significantly increased temperatures, this issue is becoming more problematic. In particular, low carbon schools can produce excessive thermal insulation in the walls and underfloor heating as well as air tightness of the building envelope.

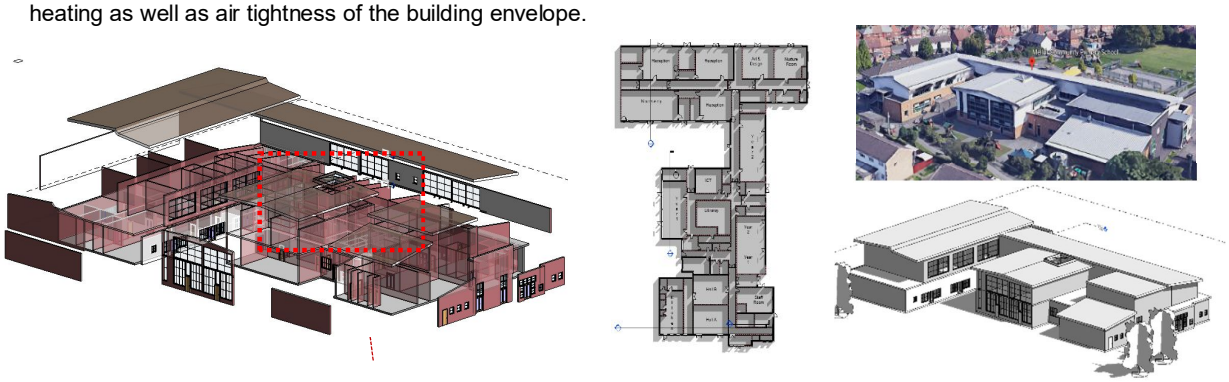

An Example of primary school build in 2010 and the typical feature of BSF School is the Atrium

An Example of primary school build in 2010 and the typical feature of BSF School is the Atrium

Typical primary school of BSF and CABE School Revit 2 010 (drawn by author S.MOH.)

Figure 11: typical example of CABE and Building school for Future-BSF School

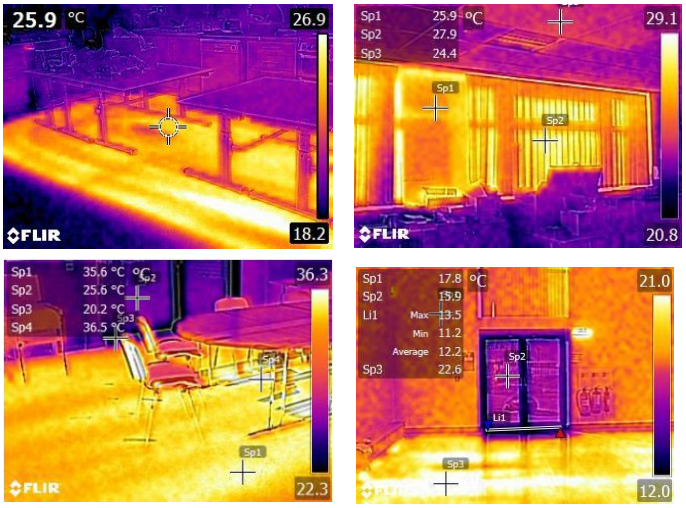

Figure 12: Thermal images display the internal environment of the classrooms and the level of overheating due to the extreme thermal insulation and air tightness, particularly at the window.

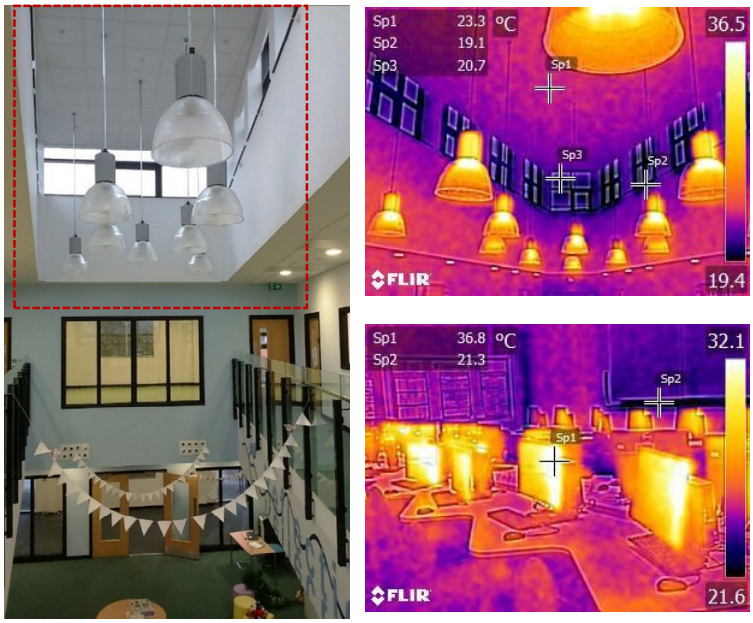

Thermal images display the atrium in a school constructed in the BSF programme.

Thermal images display internal heat gain due to the use of IT equipment and the temperatures reaching more than 36.8°C.

Figure 13: The figures show a BSF school and a typical feature is its atrium. The image shows some of the classrooms around the atrium. Although the atrium space benefits from natural light, it can also be a source of heat loss as well as consume more heating energy, School, built in 2010.

4. CONCLUSION

This paper investigated and studied the energy performance for 150 school buildings case studies. Detailed auditing were done to the school building constructed in different periods. Thermal images for internal environment in different zones were generated and studied heat loss and temperatures distribution into the occupied space,

The proposed integrated approach for energy performance and indoor climate assessment provides the information that school buildings operation managers need to identify energy consumption patterns and major energy consumers, and document indoor climate conditions. The proposed methodology has the potential to help achieve the goals of sustainable energy consumption contributing towards inadequate environments in a relevant segment of the building sector (schools) and could be applied to other typologies of buildings to help managers identify opportunities for reducing energy costs.

Access to the data of DECs over the two years made it possible to examine how patterns of energy use in school buildings in different construction types have changed over time. The internal classroom in the schools experience large internal heat sources, which usually found in the classroom during the school hours, this lead to prevent achieving thermal comfort in both winter and summer.

This paper is concerned with how to save heating and cooling energy in UK schools and the overheating risk in the classroom, in particular during summer as at this time of year pupils have assessments and exams. This is discussed in the preceding chapters with the analyses of 150 school buildings in Nottingham, Solihull, Leicestershire, Bristol and elsewhere. In general, school buildings were designed to provide comfort during the heating season. Rising summer temperatures have occurred in recent decades, and predictions of a future warmer climate require recognition of the need to reduce overheating when considering a building's thermal performance.

5. REFERENCES

Ardente, F., Beccali, M., Cellura, M. & Mistretta, M. 2011. Energy and Environmental Benefits in Public Buildings As A Result Of Retrofit Actions. Renewable and Sustainable Energy Reviews, 15, 460-470.

Asadi, E., Da Silva, M. G., Antunes, C. H. & Dias, L. 2012. Multi-Objective Optimization for Building Retrofit Strategies: A Model and an Application. Energy and Buildings, 44, 81-87.

Australia, S. 2000. Australian/New Zealand Standard: Energy Audits (As/Nzs 3598:2000), Standards Australia International Ltd and Standards, New Zealand (2000).

Barlow, S. & Fiala, D. 2007. Occupant Comfort In UK Offices-How Adaptive Comfort Theories Might Influence Future Low Energy Office Refurbishment Strategies. Energy and Buildings, 39, 837-846.

Besler, G. J. & Besler, M. 2000. Towards Healthy Microclimate of Closed Spaces and Habitats. Environment Protection Engineering, 26, 23-38.

Bridget Shield & Dockrell, J. E. 2004. External and Internal Noise Surveys of London Primary Schools. Acoustical Society of America.

Chidiac, S. E., Catania, E. J. C., Morofsky, E. & Foo, S. 2011. Effectiveness of Single and Multiple Energy Retrofit Measures On The Energy Consumption Of Office Buildings. Energy, 36, 5037-5052.

Docc & Ee. 2018. Commercial Buildings in Australia, Department Of Climate Change and Energy Efficiency, Australian Government [Online]. Available: Http://Www.Climatechange.Gov.Au/What-You-Need-To-Know/Buildings/Commercial.Aspx [Accessed 13/8 2018].

Doe 2010. Buildings Energy Data Book. Washington, Dc, USA: Office Of Energy Efficiency And Renewable Energy, U.S. Department Of Energy.

Doe. 2018. Doe to Fund Up To $454 Million for Retrofit Ramp-Ups In Energy Efficiency [Online]. Available: Http://Energy.Gov/Articles/Doe-Fund-454-Million-Retrofit-Ramp-Ups-Energy-Efficiency [Accessed 13/08 2018].

Ellis, R. 2003. Commissioning For Indoor Air Quality. Engineered Systems, 20, 30.

Flourentzou, F. & Roulet, C. A. 2002. Elaboration of Retrofit Scenarios. Energy and Buildings, 34, 185-192.

Gov.Uk. 2018. Warmer Homes, Greener Homes: A Strategy for Household Energy Management, UK Department Of Energy And Climate Change [Online]. Available: Http://www.Decc.Gov.UK/ [Accessed 15 2018].

Hestnes, A. G. & Kofoed, N. U. 2002. Effective Retrofitting Scenarios for Energy Efficiency And Comfort: Results Of The Design And Evaluation Activities Within The Office Project. Building and Environment, 37, 569-574.

Jaggs, M. & Palmer, J. 2000. Energy Performance Indoor Environmental Quality Retrofit - A European Diagnosis and Decision Making Method For Building Refurbishment. Energy and Buildings, 31, 97-101.

Kluczek, A. & Olszewski, P. 2017. Energy Audits In Industrial Processes. Journal Of Cleaner Production, 142, 3437-3453.

Ma, Z., Cooper, P., Daly, D. & Ledo, L. 2012. Existing Building Retrofits: Methodology And State-Of-The-Art. Energy And Buildings, 55, 889-902.

Mahlia, T. M. I., Razak, H. A. & Nursahida, M. A. 2011. Life Cycle Cost Analysis And Payback Period Of Lighting Retrofit At The University Of Malaya. Renewable And Sustainable Energy Reviews, 15, 1125-1132.

Montazami, A., Gaterell, M. & Nicol, F. 2015. A Comprehensive Review Of Environmental Design In Uk Schools: History, Conflicts And Solutions. Renewable And Sustainable Energy Reviews, 46, 249-264.

Roberts, S. 2008. Altering Existing Buildings In The Uk. Energy Policy, 36, 4482-4486.

Rugg, R. 2011. Benefits Of Driving Energy Efficiency In Schools [Online]. Carbon Trust. Available: Https://Www.Carbontrust.Com/News/2011/10/Benefits-Of-Driving-Energy-Efficiency-In-Schools/ [Accessed 18/8/ 2018].

Santamouris, M. & Dascalaki, E. 2002. Passive Retrofitting Of Office Buildings To Improve Their Energy Performance And Indoor Environment: The Office Project. Building And Environment, 37, 575-578.

Trianni, A., Cagno, E. & De Donatis, A. 2014. A Framework To Characterize Energy Efficiency Measures. Applied Energy, 118, 207-220.

Trust, C. 2018. Energy Efficiency And Carbon Saving Advice For Schools [Online]. Available: Https://Www.Carbontrust.Com/Resources/Guides/Sector-Based-Advice/Schools/ [Accessed 18/8 2018].

Xing, Y., Hewitt, N. & Griffiths, P. 2011. Zero Carbon Buildings Refurbishment - A Hierarchical Pathway. Renewable And Sustainable Energy Reviews, 15, 3229-3236.

#246: Laser scribing for simultaneous nitrogen doping and reduction of graphene oxide films for flexible high energy/power density supercapacitors

Aya HAMED[1], Amr HUSSEIN [2], Ahmed Abd EL-MONEIM [3]

[1] Department of Materials Science and Engineering, Egypt-Japan University of Science and Technology, New Borg El-Arab, Alexandria 21934, Egypt, aya.kadi@ejust.edu.eg
[2] Department of Mathematical and Physical Engineering, Faculty of Engineering (Shoubra), Benha University, Cairo, Egypt
[3] School of Basic and Applied Science, Egypt-Japan University of Science and Technology, New Borg El-Arab, Alexandria 21934, Egypt

Major research efforts have been aimed at replacing traditional fossil fuels with green energy sources to meet the current energy crisis and environmental concerns. In this work, a low cost, fast processing technique is proposed for simultaneous doping, reduction and patterning of graphene oxide films supported on flexible poly-(ethylene terephthalate) PET substrate. Both reduced graphene oxide (rGO), and nitrogen doped reduced GO (N-rGO) films are successfully synthesized from GO dispersion in one single step using laser scribing technique. The rGO, and N-rGO films are examined as electrodes for supercapacitor (SC) application. The aim of this work is to develop, lightweight, thin, flexible, and environmentally friendly supercapacitor with potential for application in wearable electronics and flexible displays, using a simple technique. The films are found to depict high electrical conductivity of 325, and 1539 Sm^{-1} for rGO, and N-rGO respectively. The performance of the assembled N-rGO based SC is compared to the undoped based SC. The electrochemical performance is estimated by means of cyclic voltammetry (CV), Galvanic constant current charge-discharge (GCCD) and electrochemical impedance spectroscopy (EIS) measurements via two electrodes configuration. The fabricated rGO, and N-rGO devices exhibit specific capacitance of 344, and 2995 mFg^{-1}, respectively at a current of 0.2 mA. Nitrogen doping is found to have positive effect on the behaviour of SC. N-rGO based SC reveals high energy and power densities. The prepared films represent a potential material for flexible high-performance supercapacitors. Moreover, the devised technique represents a convenient method for large scale fabrication of flexible functionalized graphene films.

Keywords: supercapacitors; graphene; flexible substrates (PET); chemical doping; laser reduction and patterning

1. INTRODUCTION

Energy storage has become one of the substantial focuses of leading world powers and scientific research. There has been growing interest in developing more efficient energy storage devices to conform to the current trend towards producing clean, sustainable energy. Confronting the depletion of fossil fuels and their negative effects on climate and environment requires a change towards sustainable energy sources. Renewable technologies, such as wind power, solar power, hydropower, and bioenergy are intermittent in nature and completely reliable on weather conditions, making them less controllable and less predictable. Integrating renewable energy technologies with efficient energy storage devices makes it possible to supply stable power at demand and to increase the power transmitted to the grid, through storing excessive energy when the demand is low and provide more energy when the demand is high. Recently, there has been a growing interest in high power and energy density storage systems. Conventional charge storage devices such as batteries are limited by their low power density, low charge-discharge rates, short cycle life and expensive cost. Supercapacitors (SCs) have drawn great attention because of their high charge/discharge rate, long life cycle, low maintenance, and outstanding power density. SCs have several applications in power electronics, memory protection, battery enhancement, portable energy sources, hybrid electric vehicles, and military and aerospace applications. Development of flexible, lightweight, low-cost and environmentally friendly energy storage devices has become inevitable. Prominent attention has been given to flexible supercapacitors for their potential applications in flexible displays, wearable devices, mobile phones, and computers (Shi *et al.*, 2013; Hassan *et al.*, 2014; Khosrozadeh, Xing and Wang, 2014; Chee *et al.*, 2016; Salanne *et al.*, 2016).

Electrode material plays a decisive role on the performance of supercapacitors. Graphene has some fascinating properties including high electrical and thermal conductivity, excellent mechanical strength, and high specific surface area. All these properties made graphene an exemplary material for supercapacitor electrodes (Chee *et al.*, 2016). Graphene can be synthesized using different methods such as chemical vapor deposition, epitaxial growth, and liquid-phase exfoliation electro-chemical exfoliation. Although the harsh conditions these methods require, they are also known to be of low productivity. Large-scale production of graphene can be achieved through the reduction of graphene oxide (GO) by chemical, thermal and photothermal means (Liu *et al.*, 2010; Gamil *et al.*, 2014; González *et al.*, 2016; M. and Paul, 2017)

Chemical doping modulate**s** the electrical properties of graphene. The doping enables modifying graphene intrinsically, tailoring its electronic properties, enriching free charge-carrier densities and promoting its electrical or thermal conductivities. Nitrogen is considered an excellent element for the chemical doping of carbon materials because it is of comparable atomic size. Nitrogen contains five valence electrons available to form strong valence bonds with carbon atoms, so it can be introduced into the graphene structure in the form of quaternary N (graphitic nitrogen), pyridinic N and pyrrolic N (Li *et al.*, 2009, 2016; Wang and Shi, 2015)**.** Fabrication of Nitrogen doped graphene can either be through direct synthesis or post synthesis methods. For direct-synthesis, N-doping is performed during the growth of graphene for example chemical vapor deposition(Wei et al., 2009), arc discharge of carbon electrodes in the presence of H2/ammonia (Panchakarla et al., 2009). For post-synthesis, N-doping is performed by post-treating the previously prepared graphene or graphene oxide with N-precursors like thermal treatment of graphene with ammonia (NH3) (Li *et al.*, 2009; Lv *et al.*, 2012), electrothermal reaction with ammonia, hydrothermal(Zhang et al., 2017), nitrogen plasma treatment of graphene(Wang et al., 2010), and solvothermal method (Deng et al., 2011).Post-synthesis methods for nitrogen doping of graphene can achieve high-quality N-G which is enriched in graphitic-N and contain small amounts of defects (Li et al., 2016). Unfortunately, these methods consist of many steps and require many sophisticated processing procedures that consume time. Therefore, it became essential to develop new and simple synthesis techniques that can reduce fabrication time and promote mass production.

In this work, we propose a new single step, low cost, and fast processing method for simultaneous doping, reduction and patterning of large area of graphene oxide film drop-casted on flexible PET substrate using laser scribing. This technique requires no additional post processing or sophisticated procedures. Contrary to reduced graphene oxide (rGO), graphene oxide (GO) is easily dispersed in distilled water and can be easily drop casted on the PET substrate to give a uniform and homogeneous film. Nitrogen doped reduced GO film was successfully synthesized from GO/ ammonia dispersion in one single step. The films were patterned into the desired shape of the electrode. The prepared films were examined as electrodes for supercapacitor application. The SC device was assembled from 2 electrodes in the conventional sandwich structure. The performances of both devices were measured using electrochemical test unit and their performances were compared. The N-rGO SC device shows high capacitance behaviour compared to the undoped rGO device. As it gives higher capacitance, energy and power densities in contrast to the rGO device.

2. EXPERIMENTAL

2.1. Preparation of GO and GO/NH3 films on PET

Graphite oxide sheets were synthesized from graphite using modified Hummer's method (Hummers and Offeman, 1958; Wojtoniszak *et al.*, 2012). Graphite oxide was dispersed in distilled water with an initial concentration 4 mg ml-1 by magnetic stirring. The nitrogen doping process was performed by adding ammonia solution (33%) dropwise to the graphite oxide solution until its pH reached 10. The graphite oxide dispersion is the exfoliated into of graphene oxide (GO) through ultrasonication 1 hour using ultrasonic bath followed by probe sonication for 2 hours. The obtained GO solution was centrifuged at 3000 rpm for 20 min to remove the non-exfoliated graphite oxide particles. Flexible PET substrate with dimensions 10 cm ×10 cm was first cleaned for 20 min by ultrasonication in ethanol and then rinsed with water. After drying at room temperature, the cleaned PET substrate was subjected to plasma treatment with an oxygen flow at 75W for 10 min in order to enhance the adhesion of GO to the substrate. The previously GO solution was then drop-casted onto the PET substrate then it is left to dry naturally at ambient conditions.

2.2. Fabrication of N-rGO electrode

The dried GO film was then reduced and patterned into the required design of the electrode using a high-powered CO2 laser machine (VersaLASER, VLS 3.50) (El-Kady *et al.*, 2012; Strong *et al.*, 2012; Ghoniem, Mori and Abdel-moniem, 2016; Tran *et al.*, 2018; Wan *et al.*, 2019). The optimized laser parameters for our film were 3.5 W for power, and 18% of maximum laser speed. The ultrasonication effect together with the localized heating induced by laser reduction leads to nitrogen to be introduced into reduced graphene oxide lattice structure and (N-rGO) is produced. A detailed illustration of the fabrication process of the electrodes is shown in Figure 1a. Drop-casting of the film is performed on a glass sheet to make sure of a complete level balancing. The undoped-rGO film was produced with similar procedure but without the addition of ammonia solution.

2.3. Assembly of the supercapacitor device

Potassium hydroxide of single molarity (1M KOH) was used as an electrolyte for the supercapacitor device. A filter paper was immersed in the prepared electrolyte to be used as a separator the supercapacitor device was assembled in a conventional manner (sandwich structure) where two electrodes were brought together face to face with a wet filter paper in between as shown in Figure 1b. The assembled supercapacitor device was left for 5-6 h at ambient conditions to ensure that the electrolyte completely wets the electrode. A copper tape is used to ensure good electrical contact between the supercapacitor electrodes and the potentiostat electrodes.

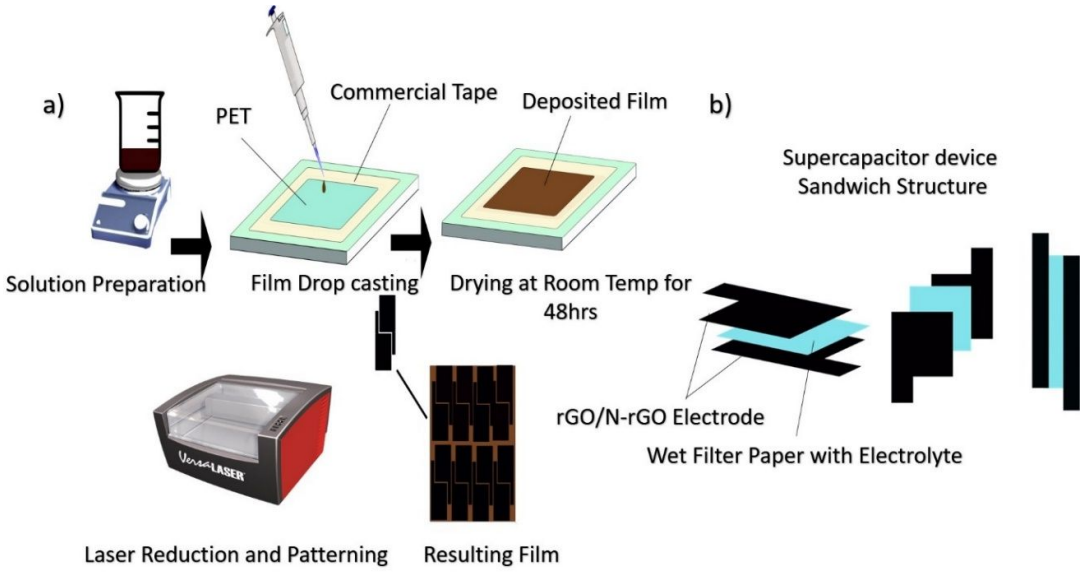

Figure 1: a) Schematic for the steps of fabrication process of the electrode drop-casting, laser reduction and patterning. b) Assembly of supercapacitor device sandwich structure.

2.4. Material characterization

The morphology of rGO and N-rGO films was determined using Scanning Electron Microscopy "SEM" (JEOL JSM-6010LV), and Transmission Electron Microscopy "TEM" (JEOL JEM-2010F). X-ray diffraction was performed with (Shimadzu XRD-6100). The electrical conductivity of the produced films was measured employing 2-probe configuration using source meter unit (Keithley 2400). Conductivity is calculated from Equation 1

Equation 1: Conductivity of the produced film material in Sm-1

$$\sigma = \frac{L}{RA}$$

Where:

- σ = Conductivity of the film material (Sm^{-1})
- L = length of the film (m)
- *R* = resistance of the film equals to inverse of the slope of IV curve (Ω)
- *A* = cross sectional area of the film equals to width* thickness (m^2)

2.5. Electrochemical performance

The electrochemical performances of the assembled supercapacitor devices were assessed using cyclic voltammetry (CV), galvanostatic charge-discharge (GCCD), in addition to electrochemical impedance spectroscopy (EIS) electrochemical characterization tools by means of VersaSTAT4 potentiostat using two-electrode configuration. The CV behaviour of the electrodes was studied within a potential window of 0 – 1 V at scan rates of 10 – 100 mVs^{-1}. GCD measurements were carried out at constant current in the range of 0.1 – 0.6 mA. The specific capacitance was calculated from GCD according to Equation 2 (Zhang and Zhao, 2012; Zhang and Pan, 2015).

Equation 2: Specific Capacitance of assembled SC device calculated from GCD data

$$\mathrm{C}_{sp} = \frac{\mathrm{I}}{\mathrm{m}\ \mathrm{dV/dt}}$$

Where:

- C_{sp} = specific capacitance of SC device (Fg^{-1})
- *I* = constant charge-discharge current (A)
- *dV/dt* = slope of the discharge curve (Vs^{-1})
- *m* = mass of active material of the two electrodes of SC device (g)

The mass of the active electrode material rGO/N-rGO was calculated by subtracting the mass of the empty PET substrate from the mass of the substrate after deposition by means of a micro balance. Energy density and power density of the assembled supercapacitor devices were calculated using Equation 2 and Equation 3, respectively.

Equation 3: Energy density of assembled SC device

$$E_{max} = \frac{\frac{1}{2} C_{sp} V^2}{3600}$$

Where:

- E_{max}= maximum energy stored per unit mass SC device (Wh kg^{-1})
- C_{sp} = specific capacitance calculated from Equation 1 (Fkg^{-1})
- *V* = potential window of SC device (V)

Equation 4: Maximum power delivered by the assembled SC device

$$P_{max} = \frac{V^2}{4 R_S m}$$

Where:

- P_{max} = maximum delivered power (Wkg^{-1})
- C_{sp} = specific capacitance calculated from Equation 1 (Fg^{-1})
- V = potential window of SC device which is determined by the electrolyte's thermodynamic stability
- m = mass of active material of the two electrodes of SC device (kg)
- R_s = equivalent series resistance (ESR) and can be found from either EIS analysis or Equation 5 (Ω)

Equation 5: equivalent series resistance of SC device

$$R_S = \frac{V_{drop}}{2\,I}$$

Where:

- R_s = equivalent series resistance (ESR) of SC device (Ω)
- V_{drop} = voltage IR drop (V)
- *I = constant charge/discharge current (A)*

3. RESULTS AND DISCUSSION

The Plasma treatment of the PET substrate lead to improved adhesion which is extremely crucial for the mechanical integrity and flexibility of the electrode

3.1. Structure and morphology

The SEM images shown in Figure 2 of the produced films display a 3D network structure of rGO flakes with good accessible surface area, and consequently facilitates ion transport and diffusion through the films. Doping resulted in no apparent change on the morphology of the films.

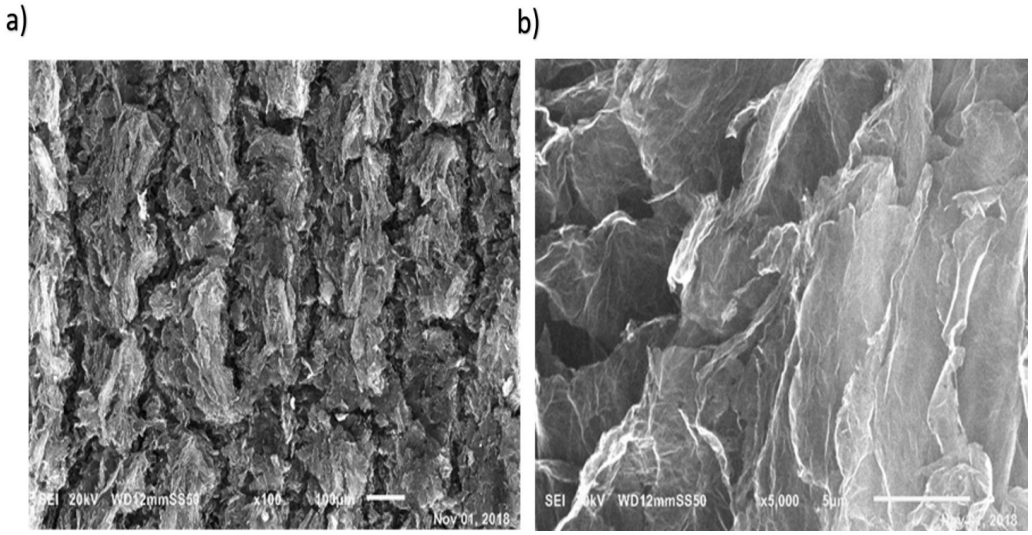

Figure 2: (a-b) SEM images of rGO film

As can been seen from Figure 3, few graphene planar sheets are observed in both rGO and N-rGO TEM images, this is due to non-complete reduction of GO. Full reduction of GO is not advantageous for supercapacitor application as it results in removal of additional oxygen functional groups that contribute to pseudo-capacitance (Tran *et al.*, 2018; Wan *et al.*, 2018).Thus non-complete removal of oxygen functional groups has good impact on the supercapacitor performance. However, full reduction of GO films can be beneficial for other applications and can be achieved using laser scribing technique through tuning of the laser reduction parameters. Also, it can be observed that the nitrogen doped film exhibited larger number of graphene sheets indicating higher surface to volume ratio than the undoped film. Therefore, N-rGO film possesses larger accessible surface area compared to rGO film.

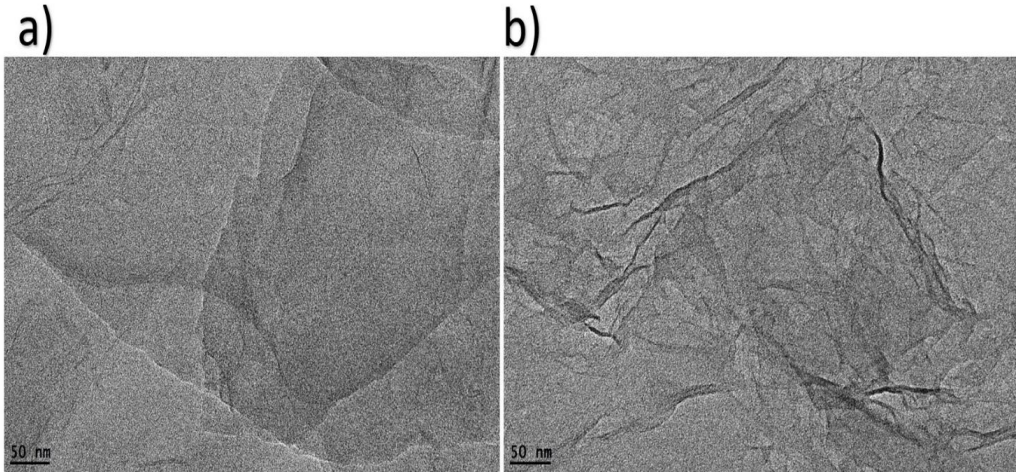

Figure 3: a) TEM image of rGO film, b) N-rGO

Figure 4 demonstrates the XRD patterns of the films before and after reduction and doping process. The GO is distinguished by a sharp peak at 9.7°, corresponding to an interlay distance of 0.91 nm. This peak was greatly reduced, and another broad peak appeared centred at around 23.7° (d= 0.375 nm) for rGO while for N-rGO the peak was found at 25.6° corresponding to (d=0.3475 nm). It can be seen that the interlayer spacing of graphene and N-graphene are larger than that of graphite (0.335 nm), and the size of crystallite for N-graphene has decreased compared with graphene, maybe due to ammonia corrosion and defects resulted from nitrogen doping (Geng *et al.*, 2011). Hence, XRD results conform the successful reduction process and the recovery of graphitic crystal structure where the graphene oxides are almost completely reduced. Additionally, the presence of some oxygen functional groups is expected to be positively reflected on the supercapacitor performance, as the presence of some oxygen functional groups will contribute to pseudo capacitance in addition to the electric double-layer capacitance. Since the reduction process consists of two adjustable fundamental subprocesses depending on laser power and scanning speed: the conversion of sp^3 carbon to sp^2 carbon and the removal of oxygen functional groups. At low fluence (mJ cm^{-2}), there is clear conversion of sp^3 carbon to sp^2 carbon, while the percentage of oxygen containing groups only decreases by a small amount. Increasing laser fluence on film (through increasing power and decreasing scanning speed) results in noticeable reduction in oxygen containing groups, together with the distinctive conversion of sp^3 carbon to sp^2 carbon (Wan *et al.*, 2018)

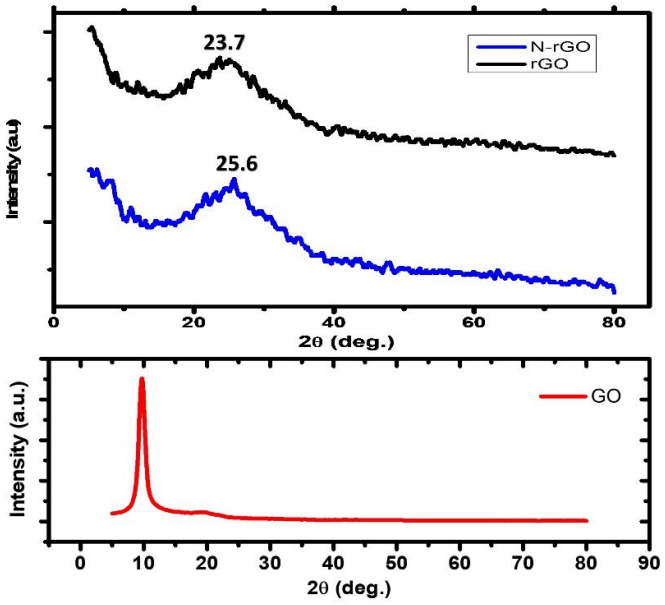

Figure 4: XRD patterns for rGO, and N-rGO films

3.2. Conductivity measurements

The electrical conductivity of the material of the produced films was measured employing 2-probe configuration using (Keithley 2400) source meter. The Conductivity of the films was determined from I-V curve (Figure 5) as 325 and 1539 Sm^{-1} for rGo and N-rGO films respectively. The result shows an evident improvement in the conductivity of the doped film where the conductivity of the doped film is approximately 5 times that of the undoped film. Chemical doping enhance the conductivity of the electrodes as it enriches free charge-carrier densities and enhances the electrical or thermal conductivities (Wang *et al*., 2010).

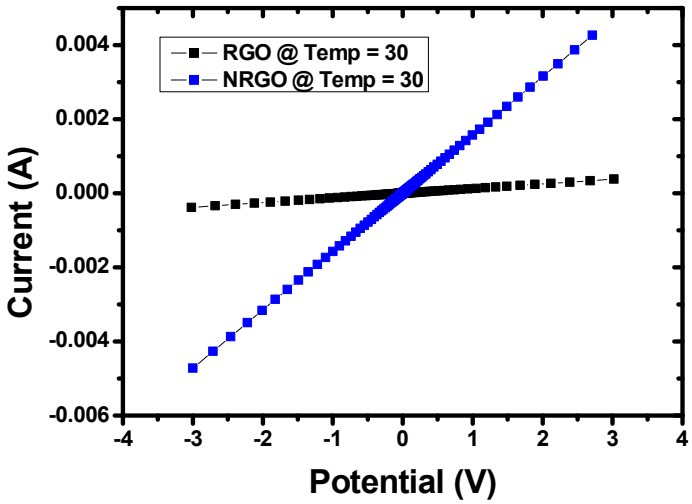

Figure 5: IV curve of both doped and undoped films material

3.3. Electrochemical measurements

The cyclic voltammograms for the two supercapacitor devices fabricated with N-rGO and rGO electrodes were measured at scan rate 50 mVs^{-1} are shown in Figure 6a. Clearly seen from the figure that, the CV profiles of both devices take the shape of an ellipsoid. This result can be attributed to the pseudo capacitance effect resulting from the presence of oxygen functional groups remaining after laser reduction (Ghoniem, Mori and Abdel-moniem, 2016). Also, the CV of N-rGO device attained a larger enclosed integration area compared to the rGO device indicating a higher capacitance. The enclosed area in the CV curve corresponding to N-rGO device is more than twice that of rGO curve.

The performances of the two assembled devices were also examined by GCCD at a constant current 0.2 mA and the obtained data are presented in Figure 6b. The IR drop is a measure of the overall resistance of the electrode and its value is proportional to the applied discharge current density. The IR drop for N-rGO SC device is smaller than that of rGO SC, indicating that the resistance of the N-rGO electrode is much lower than that of the undoped electrode. Hence, the smaller IR drop denotes higher conductivity of the N-rGO film due to the free charge-carriers enrichment by N-doping (M. and Paul, 2017). The specific capacitance was calculated using Equation 1 as 344 and 2995 mFg^{-1} for rGO and N-rGO SCs, respectively. The specific capacitance of N-rGO device reveals an eight-fold enhancement resulting from the doping effect.

In order to demonstrate the overall performance evaluation of the supercapacitor devices, energy (E) and power (P) densities of the fabricated devices were also calculated from Equations (2-4) at applied current of 0.2 mA and the obtained results are summarized in Table 1. The data reveals a remarkable high energy and power densities for N-rGO SC device in comparison with those of the rGO device. N-rGO SC showed higher energy and power density compared to rGO based SC.

R_{ESR} of the two devices was calculated from the EIS analysis shown in Figure 5c via linear interpolation of the low-frequency part of Nyquist plot to Im(Z) = 0 or by taking the real part of the complex impedance corresponding to 1kHz (Zhang and Pan, 2015). The rGO based device showed R_{ESR} of 573Ω, while the N-rGO device exhibited only 282 Ω. R_{ESR} can also be calculated from CCCD curves using Equation 5. The result of EIS analysis verifies that the doped based device has better charge transfer characteristics.

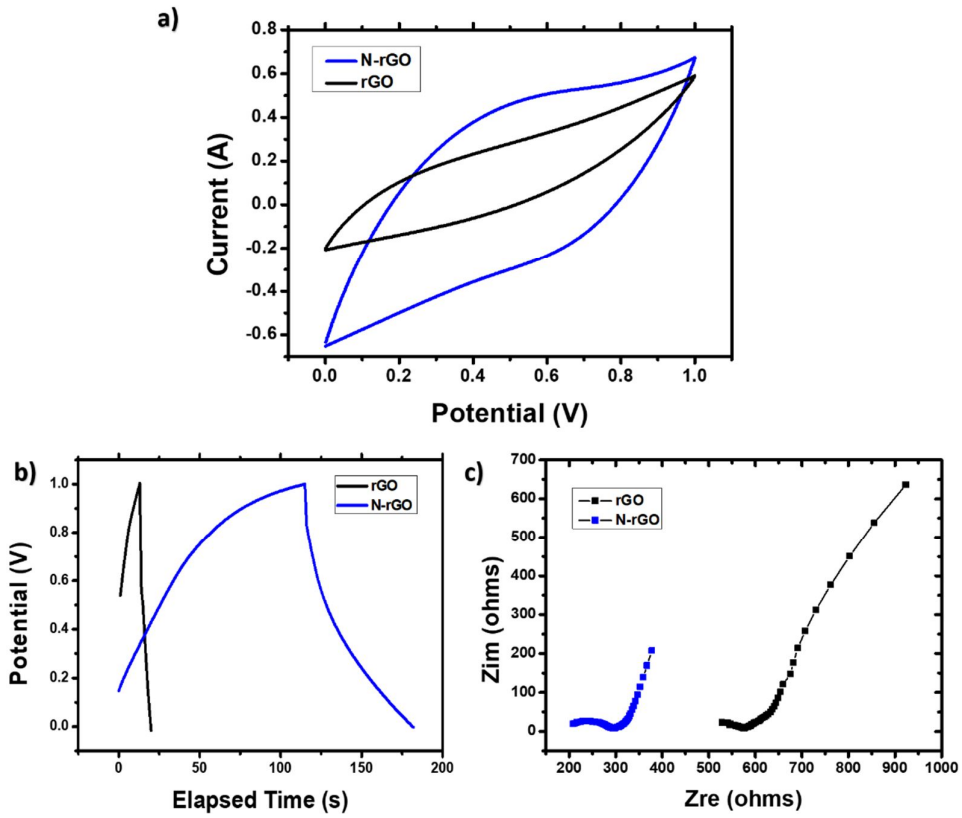

Figure 6: Electrochemical performance of rGO and N-rGO a) CV profiles b) Charge/discharge curves at current density 0.2mA, and c) EIS.

Table 1: Summary of calculated conductivity, capacitance, energy density, power density, and ESR of the assembled rGO and N-rGO SC devices using KOH electrolyte

SC type	Undoped rGO based SC	N-rGo based SC
Electrode material conductivity	325 Sm^{-1}	1539 Sm^{-1}
Capacitance	344 mFg^{-1}	2995mFg^{-1}
ESR	573 Ω	282 Ω
Energy density	15.76 mWh kg^{-1}	286 mWh kg^{-1}
Power density	12.65 W kg^{-1}	66 W kg^{-1}

4. CONCLUSION

In summary, we succeeded to produce high quality rGO and N-rGO films supported over flexible PET substrate using a low-cost single-step fabrication technique. The devised technique can be easily applied to other dopant sources to induce reduced graphene doping with different heteroatoms other than nitrogen (e.g. B, S, and P). This can lead to a potential advancement in the fabrication technology for electrochemical storage devices. The resulting films displayed high conductivity, flexibility, mechanical stability, and crack-free. Both films were examined as potential electrodes for SC application. The N-rGo film revealed fourfold increase in conductivity compared to undoped rGO. Both rGO and N-rGO based SCs exhibited reasonable specific capacitances of 344 and 2995 mF g^{-1} and an ESR of 573, and 282 Ω respectively. The capacitance of doped SC was significantly higher that of the r-GO based SC. NRGO based supercapacitor achieved both higher energy and power density compared to the rGO device. Energy density of N-rGO based SC almost increased by one order of magnitude compared to rGO SC. Also, the power density N-rGO SC recorded more than a fivefold increase, where, it increased significantly from 12 to 66 Wkg^{-1} in case of r-GO and N-rGO respectively. These results confirm that the produced N-rGO film represents a promising material for supercapacitors' electrodes. The ease of manufacture and simplicity of the

procedures, together with adequate performance makes the suggested technique attractive, besides the capability for mass production.

5. REFERENCES

Chee, W. K. *et al.* (2016) 'Flexible Graphene-Based Supercapacitors: A Review', *The Journal of Physical Chemistry C*, 120(8), pp. 4153–4172. doi: 10.1021/acs.jpcc.5b10187.

Deng, D. *et al.* (2011) 'Toward N-Doped Graphene via Solvothermal Synthesis', *Chemistry of Materials*, 23, pp. 1188–1193. doi: 10.1021/cm102666r.

El-Kady, M. F. *et al.* (2012) 'Laser Scribing of High-Performance and Flexible Graphene-Based Electrochemical Capacitors', *Science*, 335(6074), pp. 1326–1330. doi: 10.1126/science.1216744.

Gamil, M. *et al.* (2014) 'Graphene-Based Strain Gauge on a Flexible Substrate', *Sensors and Materials*, 26(9), p. 699. doi: 10.18494/sam.2014.1030.

Geng, D. *et al.* (2011) 'Nitrogen doping effects on the structure of graphene', *Applied Surface Science*, 257(21), pp. 9193–9198. doi: 10.1016/j.apsusc.2011.05.131.

Ghoniem, E., Mori, S. and Abdel-moniem, A. (2016) 'Low-cost fl exible supercapacitors based on laser reduced graphene oxide supported on polyethylene terephthalate substrate', *Journal of Power Sources*. Elsevier B.V, 324, pp. 272–281. doi: 10.1016/j.jpowsour.2016.05.069.

González, A. *et al.* (2016) 'Review on supercapacitors: Technologies and materials', *Renewable and Sustainable Energy Reviews*, 58, pp. 1189–1206. doi: 10.1016/j.rser.2015.12.249.

Hassan, S. *et al.* (2014) 'MnO 2 /carbon nanowall electrode for future energy storage application: Effect of carbon nanowall growth period and MnO 2 mass loading', *RSC Advances*, 4(39), pp. 20479–20488. doi: 10.1039/c4ra01132e.

Hummers, W. S. and Offeman, R. E. (1958) 'Preparation of Graphitic Oxide', *Journal of the American Chemical Society*, 80(6), pp. 1339–1339. doi: 10.1021/ja01539a017.

Khosrozadeh, A., Xing, M. and Wang, Q. (2014) 'A high-capacitance solid-state supercapacitor based on free-standing film of polyaniline and carbon particles', *APPLIED ENERGY*. Elsevier Ltd, 153, pp. 87–93. doi: 10.1016/j.apenergy.2014.08.046.

Li, X. *et al.* (2009) 'Simultaneous Nitrogen Doping and Reduction of Graphene Oxide', *J. Am. Chem. Soc.*, 131(43), pp. 15939–15944. doi: 10.1021/ja907098f.

Li, X. *et al.* (2016) 'Unraveling the formation mechanism of graphitic nitrogen- doping in thermally treated graphene with ammonia', *Nature Publishing Group*. Nature Publishing Group, (March), pp. 1–10. doi: 10.1038/srep23495.

Liu, C. *et al.* (2010) 'Graphene-Based Supercapacitor with an Ultrahigh Energy Density', *Nano Letters*, 10(12), pp. 4863–4868. doi: 10.1021/nl102661q.

Lv, R. *et al.* (2012) 'Nitrogen-doped graphene: beyond single substitution and enhanced molecular sensing', *Scientific Reports*, 2(1), p. 586. doi: 10.1038/srep00586.

M., A. and Paul, A. (2017) 'Importance of Electrode Preparation Methodologies in Supercapacitor Applications', *ACS Omega*, 2(11), pp. 8039–8050. doi: 10.1021/acsomega.7b01275.

Panchakarla, L. S. *et al.* (2009) 'Synthesis, Structure, and Properties of Boron- and Nitrogen-Doped Graphene', *Advanced Materials*, 21(46), pp. 4726–4730. doi: 10.1002/adma.200901285.

Salanne, M. *et al.* (2016) 'Efficient storage mechanisms for building better supercapacitors', *Nature Energy*, 1(6), p. 16070. doi: 10.1038/nenergy.2016.70.

Shi, S. *et al.* (2013) 'Flexible supercapacitors', *Particuology*. Chinese Society of Particuology, 11(4), pp. 371–377. doi: 10.1016/j.partic.2012.12.004.

Strong, V. *et al.* (2012) 'Patterning and Electronic Tuning of Laser Scribed Graphene for Flexible All-Carbon Devices', *ACS Nano*, 6(2), pp. 1395–1403. doi: 10.1021/nn204200w.

Tran, T. X. *et al.* (2018) 'Laser-Induced Reduction of Graphene Oxide by Intensity-Modulated Line Beam for Supercapacitor Applications', *ACS Applied Materials & Interfaces*, 10(46), pp. 39777–39784. doi: 10.1021/acsami.8b14678.

Wan, Z. *et al.* (2018) 'Tuning the sub-processes in laser reduction of graphene oxide by adjusting the power and scanning speed of laser Tuning the sub-processes in laser reduction of graphene oxide by adjusting the power and scanning speed of laser', *Carbon*. Elsevier Ltd, 141(2019), pp. 83–91. doi: 10.1016/j.carbon.2018.09.030.

Wan, Z. *et al.* (2019) 'Tuning the sub-processes in laser reduction of graphene oxide by adjusting the power and scanning speed of laser', *Carbon*. Elsevier Ltd, 141(January 2019), pp. 83–91. doi: 10.1016/j.carbon.2018.09.030.

Wang, X. and Shi, G. (2015) 'An introduction to the chemistry of graphene', *Physical Chemistry Chemical Physics*. Royal Society of Chemistry, 17(43), pp. 28484–28504. doi: 10.1039/C5CP05212B.

Wang, Y. *et al.* (2010) 'Nitrogen-Doped Graphene and Its Biosensing', *ACS Nano*, 4(4), pp. 1790–1798.

Wei, D. *et al.* (2009) 'Synthesis of N-Doped Graphene by Chemical Vapor Deposition and Its Electrical Properties', *Nano Letters*, 9(5), pp. 1752–1758. doi: 10.1021/nl803279t.

Wojtoniszak, M. *et al.* (2012) 'Synthesis, dispersion, and cytocompatibility of graphene oxide and reduced graphene oxide', *Colloids and Surfaces B: Biointerfaces*. Elsevier B.V., 89, pp. 79–85. doi: 10.1016/j.colsurfb.2011.08.026.

Zhang, J. and Zhao, X. S. (2012) 'On the Configuration of Supercapacitors for Maximizing Electrochemical Performance', *ChemSusChem*, 5(5), pp. 818–841. doi: 10.1002/cssc.201100571.

Zhang, S. *et al.* (2017) 'One-step hydrothermal synthesis of nitrogen doping graphene based cobalt oxide and its supercapacitive properties', *Journal of Alloys and Compounds*. Elsevier B.V, 705, pp. 801–805. doi: 10.1016/j.jallcom.2017.02.169.

Zhang, S. and Pan, N. (2015) 'Supercapacitors Performance Evaluation', *Advanced Energy Materials*, 5(6), p. 1401401. doi: 10.1002/aenm.201401401.

#247: A comparative techno-economic analysis of solar water heating systems with thermal battery

Mohammad Sajad NAGHAVI[1]*, Behnam RAHMANIAN[1], Ong Kok SENG[2], Hendrik Simon Cornelis METSELAAR[1], Ang Bee CHIN[1,3]

[1] *Centre of Advance Materials (CAM), Department of Mechanical Engineering, Faculty of Engineering, University of Malaya, Kuala Lumpur, Malaysia*
[2] *Department of Industrial Engineering, Faculty of Engineering and Green Technology, Universiti Tunku Abdul Rahman, Kampar, Malaysia*
[3] *Department of Chemical Engineering, Faculty of Engineering, University of Malaya, Kuala Lumpur, Malaysia*
Corresponding author: Sajad.naghavi@um.edu.my

One of the most successful applications in renewable energy is the utilisation of solar energy for domestic water heating systems. Depending on the location, about 70% of consumed energy in the residential sector is for space heating/cooling, hot water usage and appliances in cold climates. However, the full deployment of solar energy in domestic water heating is only possible when a good performance energy storage system at an acceptable price is available. Within the past decade, various types of systems deploying phase change materials as an energy storage unit or part of it were introduced. Some of these designs offer several advantages including high storage capacity, low storage volume, and isothermal operation during the charging and discharging phases. In this paper, the technical specifications and economic viability of some of the introduced designs are compared to each other under specific circumstances. This study is important and indicative to facilitate and pave the way for future research and developments of these products.

Keywords: solar water heater; phase change material; heat storage; thermal battery; CAPEX

1. INTRODUCTION

Several models of solar water heaters (SWH) are on the market. The oldest and first generation of SWH is recorded in the U.S. date to before 1900, involving a black-painted tank mounted on a roof. The second generation of SWHs is flat-plate heat collectors used for the first time in Florida and Southern California in the 1920s. In this system a network of pipes was attached to the back of the black flat plate and transferred the solar heat to the water pipe. The third generation of SWHs was evacuated tube solar collectors in different forms of U-shape pipe, thermosiphon and heat pipe. It can be anticipated that the fourth generation of SWH systems will be some sort of combined thermal energy storage system utilising sensible heat and latent heat storage. The best candidate for latent heat storage is phase change materials (PCM).

There are some potential fields of investigation in SWH systems to improve their performance and efficiency. Some problems are heat loss during pick time, less heat gain in early morning or late evening, stratification effect in hot water tank, energy collection ratio, maintenance, infrastructure, cost-benefit and health issues.

This paper aims to compare some of the introduced SWH systems integrated with PCM as latent heat storage (SWH-PCM), according to a series of essential technical parameters and followed by a cost-effectiveness analysis.

2. LITERATURE REVIEW

Since the first solar water heating system was developed, extensive studies on its theoretical investigations, practical applications and demonstration tests have been conducted. Although the technology has become technically and economically mature, solar water heating technology continues to be a crucial area of research. Numerous research projects covering various aspects of the technology, e.g., (1) integrated structure and individual components layout, sizing and optimisation, (2) thermal performance simulation and prediction, (3) laboratory based measurement compared against the modelling prediction, (4) dynamic performance evaluation through real time and onsite measurement, (5) energy saving, economic and environmental performance assessment and social acceptance analyses, and (6) dissemination, marketing and exploitation strategies, have been developed.

Studies related to theory, application, marketing and research activities to determine the performance of SWH-PCM systems were conducted by Kaygusuz (1995). An improved low-cost large solar heating system design suitable for applications in mild sunny climates was proposed by Tsilingiris (1997), where the prospects for the promotion of solar heating technology were favourable. Theoretical analysis was developed which allowed design and operational behaviour predictions of the physical system. Long-term efficiency and typical input-output performance was investigated based on statistically processed long-term meteorological measurements for Athens, Greece. Derived results indicated that substantial performance would be expected for the proposed fractional cost system design.

The characteristics and performance of horizontal mantle heat exchangers for application in thermosiphon SWHs was theoretically and experimentally investigated by Morrison et al. (1998). The results indicated that configurations of mantle heat exchangers used in current solar water heater applications degraded thermal stratification in the inner tank.

The long-term performance of thermosiphon type domestic SWHs was predicted by Kalogirou and Panteliou (2000) using an artificial neural network method that 30 systems have been tested and modelled according to the procedures outlined in the standard ISO 9459-2 at three locations in Greece. From these, data from 27 of the systems were used for training and testing the network while data from the remaining three were used for validation. Results indicated that the proposed method can successfully be used for the prediction of the solar energy output of the system.

The cost benefit analysis for evaluating solar water heating systems in comparison with competitive conventional technologies in Greece was presented by Diakoulaki et al. (2001), as well as energy saving, environmental impact and job creation influences. The multi-tank liquid-water system for storing low-temperature solar-derived heat was experimentally and analytically compared with a single-tank system by Mather *et al.* (2002) due to the perceived economic advantage of the proposed system over the single-tank system in solar heating systems where the required total volume of water was rather large, e.g., 2000 litre.

According to the minimum annual backup energy supplied to the system to meet an annual load, the design approach by using one absorber plate and a smaller and better insulated tank to maximise solar contribution and minimise material usage in the construction of solar water heating system was described by Mills and Morrison (2003). Two new designs were shown which allowed the solar fraction of systems to be increased to approximately 80–90% in Sydney, Australia using a standard model of domestic hot water usage specified in Australian Standard AS4234. Pollution from fuel use dropped to as little as 40% of that of conventional flat plate solar water heaters.

The methodology for synthesis, analysis, and optimisation of solar water heating systems was proposed by Kulkarni *et al.* (2007) by identifying the minimum and maximum collector area and storage volume of solar water heating system for a given solar fraction. Based on the identified figures, the solar water heating system was optimised by minimising annual life cycle cost.

The simple and inexpensive test method to determine the thermal behaviour of domestic SWH system was proposed by García-Valladares *et al.* (2008). The tests were carried out independently of the configuration between the solar collector and the storage tank, the way the fluid circulates and the type of thermal exchange.

The effect of water replenishment on the system sizing was studied, and a novel strategy for water replenishment to improve the design and performance of solar water heating systems was proposed by Kulkarni *et al.* (2009). For the cost-optimal system configuration, a reduction of 12.7% in the collector area and 10.2% reduction in the storage volume were observed with the novel strategy.

3. SELECTED SWH-PCM SYSTEMS

By having a look at all of the SWH-PCM systems introduced by researchers, three types of the systems could be categorised, as PCM integrated to solar collector plate, PCM integrated into the hot water storage tank and PCM as an intermediate storage layer between solar collector and cold water. Four of the experimental tested systems were selected and briefly explained in the following. These systems have considerable differences in design, operation mechanism and heat transfer processes.

3.1. SWH with a back layer of PCM

Several researchers worked on integrated PCM-flat plate solar collector, theoretically and experimentally *(Khan et al.,* 2018). The experimental study of this model performed by Khalifa *et al.* (2013) and Lin *et al.* (2012). They carried out outdoor experiments to demonstrate the potential of the storage solar system for water heating. In this model, a storage solar collector that consists of six copper pipes connected in series is integrated with a back container of paraffin wax as a PCM thermal storage media. Six 80-mm-outside diameter copper tubes, 1-mm-thick, and 1500 mm long each are used to construct the storage collector with a centre-to-centre distance of 120-mm. Ordinary black mat paint was used on the tubes. The copper tubes are connected by 15-mm-outer diameter, 1-mm-thick pipes to form a series flow pattern. The connecting pipes are welded to connect the upper part of one tube to the lower part of the following tube. A layer of wax that contained in a rigid enclosure at the back of the solar hot water storage system is employed to act as a thermal storage media, as shown in Figure 1.

3.2. SWH with hot water tank filled with packed bed PCM capsules

Nallusamy *et al.* (2007) investigated experimentally on thermal behaviour of a packed bed of combined sensible and latent heat thermal energy storage (TES) unit. A TES unit was constructed with a solar collector to study the performance of the TES unit, filled with paraffin in spherical capsules, which are packed in an insulated cylindrical storage tank. The water used as heat transfer fluid (HTF) to transfer heat from the solar collector to the TES tank also acts as sensible heat storage (SHS) material. The stainless-steel TES tank has a capacity of 47 litre to supply hot water for a family of 5–6 persons. The total number of capsules in the TES tank is 264 and the spherical capsules are uniformly packed in eight layers and each layer is supported by wire mesh. The PCM capsules occupy the 50% of the total volume of storage tank and the remaining volume is occupied by SHS material. The paraffin is used as PCM that has a melting temperature of 60°C and water is used as both SHS material and HTF. The system is built and tested in India. A schematic diagram of the experimental setup is shown in Figure 2.

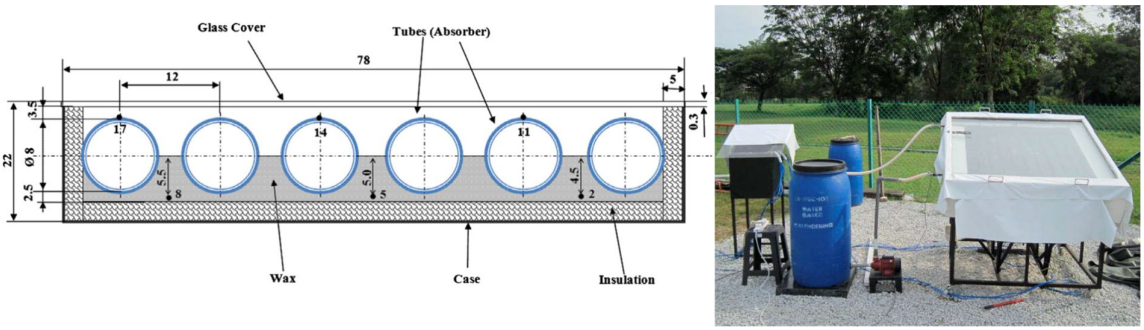

Figure 3: Integrated PCM-flat plate solar collector

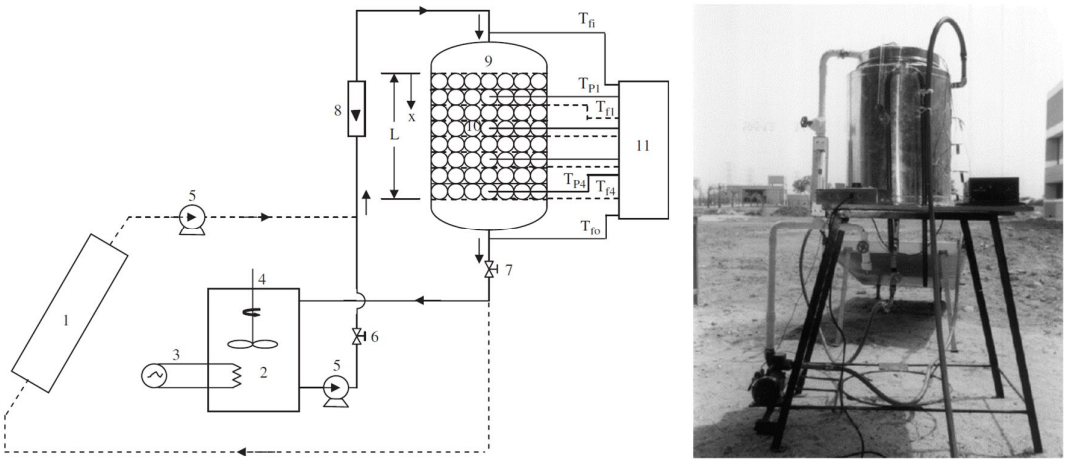

Figure 2: TES tank integrated with varying inlet heat source solar flat

3.3. SWH with hot water tank with an internal surrounding layer of PCM

Gürtürk *et al.* (2017) and Kılıçkap *et al.* (2018) experimentally built and tested a flat plate SWH with hot water storage tank which PCM is placed in a middle layer of a double-glazed water tanks. The heat storage tank of the system was modified to fill PCM between insulation and hot water part. The PCM section was filled with 43 kg of mixture of Aluminium Ammonium Sulphate (40%) and Sodium Hydrogen Phosphate (60%). Solar water heater system consists of two flat plate collectors, cold water tank automation unit and heat storage tank. Trapezoidal shape of steel plate which was placed between water and the PCM is to increase heat transfer from surface between hot water and the PCM. The heat storage tank has two inlets and two outlets. These are inlet and outlet of heat exchanger pipe which passed heat transfer fluid from inside and others are cold water inlet and hot water outlet for domestic use. In fact, the tank used both as a heat exchanger and also for the storage of water and PCM. The experiments were performed in Turkey in November when solar radiation was weak due to cloudy sky. The schematic and set-up of the system showed in Figure 3.

3.4. SWH with attached PCM filled TES tank

Naghavi *et al.* (2017) developed a SWH employing evacuated tube heat pipe solar collectors (HPSCs) and PCM based latent heat storage tank (LHS) as thermal battery. In this design, solar energy incident on the HPSC is collected and stored in the LHS tank via a heat pipe with fins attached to the condenser ends. The stored solar heat is then transferred to the domestic hot water supply via another set of finned tube heat exchangers located inside the LHS tank. This system introduces a compact heat pipe solar collector with connected rechargeable thermal battery. This unique design of thermal battery is based on using latent heat storage by PCM. The system is tested in sunny and cloudy days in Malaysia. The schematic and set-up of the system showed in Figure 4.

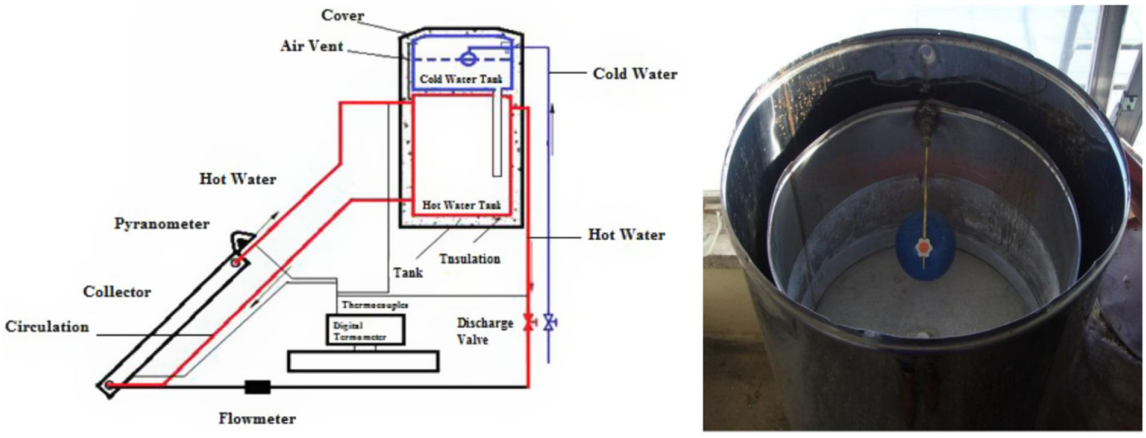

Figure 3: Schematic of Open loop system and inside of the tank with PCM

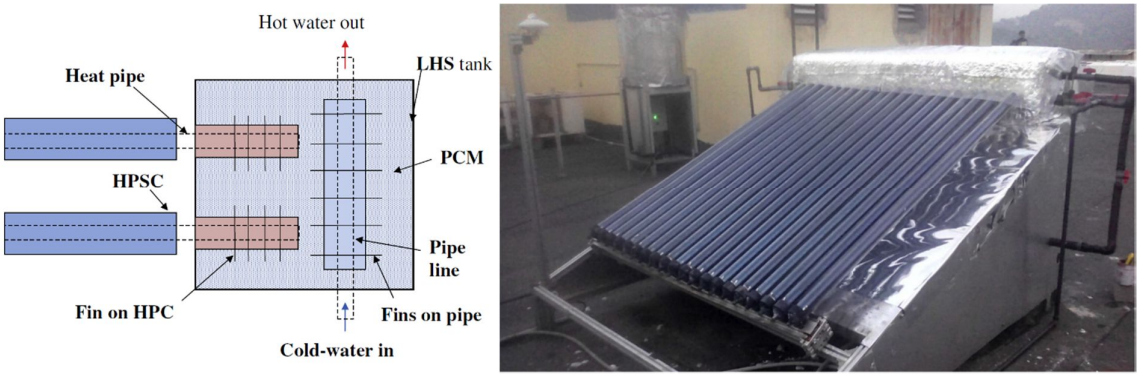

Figure 6: Schematic of system and experimental setup

4. METHODOLOGY

To be able to compare the above-mentioned systems, parameters related to the performance, structure, economic and heath were defined and the experimental results provided by researchers are used to examine the parameters. Parameters to consider of selection of SWH-PCM systems are defined as following:

1. Performance

a. Efficiency

Overall efficiency of the system is according to the total heat transfer to the water over solar heat absorption.

b. Hot water production volume

Depend to the size of solar collector area and hot water production volume at operating temperature could be defined. Armstrong et al. (2014) defined usable hot water volume as equal to the volume of fluid from a tank that can be mixed to a useful final operating temperature, T_u. The usable hot water volume could be computed by:

$$V_u(t) = m_w \times \sum_{hr=1}^{12} \frac{T_{w.t.o}(t) - T_u}{T_u - T_{w.t.i}(t)}$$

Therefore, the fraction of V_u/A_s, where V_u is daily hot water volume in operation temperature (39°C) and A_s is the total solar absorber area. This value could be used to be able to compare the hot water production of systems.

c. Hot water temperature

The temperature of hot water from solar system varies during the day. Therefore, instead of direct comparison, an approximate average and/or maximum temperature of inlet/outlet water are considered.

d. Steadily of performance in early morning

Depend to the design of the storage unit, existence of PCM may cause a delay in hot water production ability in early morning.

e. Steadily of performance in high and low solar radiation intensity days

Impact of solar radiation strength intensity play the most important role in performance of every solar system. Therefore, knowing the ability of the system in different weather condition or climatic situation helps to have better understanding of the system performance.

f. Stratification effect in the storage tank

One of the important problems in current hot water tank is stratification problem, which causes to lots of heat loss in the system. One of aim of using PCM is to minimise this effect.

g. Heat absorption in midday

The maximum solar radiation intensity happens in midday. Depend to the heat absorption mechanism of the SWH, there are several design parameters that might amplitude heat absorption.

h. Heat absorption in low intensity times of day

Depend to the design of the heat absorption mechanism, the system may not be able to pick up the absorbable solar heat from the absorber plate, it may cause of the negative temperature difference between solar plate and heat storage unit.

i. Heat loss
Heat loss occur even with good insulation materials. Total area exposing to the surrounding environment play important role in heat loss, mainly from piping and heat storage tank.

j. PCM thermal storage capacity
The latent heat capacity of the PCM play the most important role in performance of the system. Therefore, the potential latent and sensible heat storage proportional to the solar collector size is determined.

2. Structural

a. Direct and indirect systems
Based on whether or not they require a heat exchanger, solar water heating systems could be categorised into direct and indirect systems.

b. Passive and active systems
Based on whether or not they require pumps to function, solar water heating systems could be grouped into two basic configurations, namely passive and active systems

c. Infrastructure
Depend to the design of the TES unit it might be installed in the rooftop or on the ground, addition of mounting structure, piping and water pump.

d. Hot water tank
TES may be a combination of hot water tank and PCM in one tank or separate tanks.

e. Type of PCM
Type and thermal properties of the PCM plays significant role in performance of design of TES unit.

f. Weight of thermal energy storage (TES) unit
TES unit mainly contains of PCM, enclosure, and pipes. Weight of TES could be an important issue for fabrication and installation. To be able to compare TES of different systems the weight of the TES divided by solar collector size.

g. Piping system
Design of the system may need to use lots of piping, which cause to extra costs, heat loss and pressure drop.

3. Economic

a. Estimated cost of the system
The approximate overall cost of manufacturing of system should be estimated based on the size of the introduced experimental system.

b. Installation cost
Depend to the design of the system, installation cost may vary for different models.

c. Lifecycle cost
Periodic costs related to maintenance, cleaning hot water tank and water pipe repairing should be considered here.

4. Health

a. Contaminant mixture with water and growing legionella bacteria
Legionnaires' disease is normally acquired by inhalation or aspiration of legionellae from a contaminated environmental source (Paola et al., 2004). One of the environments that it legionella bacteria can grow is the hot water tanks.

b. PCM and accessibility to water side
Most of PCM have chemical basis and in case of accessibility to hot water, there is risk of affecting the water safety.

5. RESULTS AND DISCUSSION

One difficulty to compare the mentioned system in section 3 is that the researchers used different size of collector and storages, flowrate, method of heat transfer and different terms to address their findings. Therefore, the parameters need to be somehow explained and adjusted to be able to provide a platform to compare systems, which is prepared in section 4.

Table 1 presents the parametric comparison of the studied system according to their claims.

Table 1: Parametric comparison of four SWH-PCM systems

Parameter	Design 1	Design 2	Design 3	Design 4
Daily Efficiency	About 43%	Estimated value is about >36%	About 45%	About 43%
Hot water production volume in operating temp. per square meter of solar collector	Averagely 55 litres	Averagely 70 litres	Averagely 95 litres	Averagely 85 litres
Inlet/Outlet water temp.	Averagely inlet water temp. in midday is 20°C Averagely, hot water temp. in midday is 50°C in flowrate of 0.15 l/min	Averagely inlet water temp. in midday is 32°C Averagely, hot water temp. in midday is 70°C in flowrate of 2 l/min	Averagely inlet water temp. in midday is 30°C Averagely, hot water temp. in midday is 65°C in flowrate of 0.32 l/min	Averagely inlet water temp. in midday is 29°C Averagely, hot water temp. in early discharge time is 50°C in flowrate of 1.1 l/min
Steadily of performance in early morning	Not able to provide	Depend to discharge level in previous day, TES is able to provide hot water in early morning	Depend to discharge level in previous day, TES is able to provide hot water in early morning	Depend to discharge level in previous day, TES is able to provide hot water in early morning
Steadily of performance in high and low solar radiation intensity days	system provide steady efficiency in different climatic conditions	System looks to be able to provide steady performance to some extend	System looks to be able to provide steady performance to some extend	system provide steady efficiency in different climatic conditions
Stratification effect in the storage tank	no improvement	By using spherical PCM capsules, the stratification effect will be minimised.	By using outer layer of PCM in hot water tank, the stratification effect will be reduced	Due to elimination of hot water tank and instant heating of water, there is no stratification effect in the system
Heat absorption in midday	This configuration can amplitude the heat absorption in midday	This configuration can amplitude the heat absorption in midday	This configuration can amplitude the heat absorption in midday	Existence of fins and PCM with evacuated tube heat pipe solar collector, increase the heat absorption in midday by direct storage in TES tank
Heat absorption in low intensity times of day	Lack of potential due to partially absorption of heat by PCM	System is unable to pick up the low temperature hot water at afternoon	Due to indirect heating mechanism, the system may not be able to pick solar heat energy in afternoon	If there is no discharge in day time, system would not be able to pick up solar heat in late afternoon
Heat loss	due to the fact there is no insulation in top side, it could be expected that the heat loss percentage be considerable, mostly in night time	minimum heat loss	minimum heat loss	minimum heat loss
TES thermal storage capacity	About 7,000 kJ	up to 10,000 kJ	Up to 9,000 kJ	Up to 9,000 kJ

Table 2 presents the heat transfer mechanism of the system, in addition to the structural changes of the new SWH-PCM system in comparison with conventional system.

Table 2: Infrastructural comparison of the selected SWH-PCM systems

Parameter	Design 1	Design 2	Design 3	Design 4
Direct and indirect systems	Direct	Direct	Indirect	Direct
Passive and active systems	Passive	Passive	Passive	Active
Infrastructure	The solar collector requires stronger structure, due to	Due to the weight of the TES unit, it needs to be installed on the ground	Due to the weight of the TES unit, it needs to be installed on the ground	Elimination of hot water tank reduce the required infrastructure and piping

	the extra weight of PCM in solar collector.	and hot water needs to be pressurised by a pump and requires a stronger structure.	and hot water need to be pressurised by a pump and requires a stronger structure.	and pump. Replacement of the conventional heat transfer manifold with TES unit on rooftop, requires a stronger mounting structure
Hot water tank	It is required	it is merged with PCM and made the TES unit	It is merged with PCM and made the TES unit	Eliminated
Type of PCM	Paraffin Wax Melting point 46.7°C Latent heat 166.7 kJ/kg	Paraffin Wax Melting point 60.0°C Latent heat 213.0 kJ/kg	Calcium chloride hexahydrate Melting point 32°C Latent heat 188.4 kJ/kg	Paraffin Wax Melting point 55.0°C Latent heat 164.0 kJ/kg
Weight of TES unit	TES is actually the solar collector plate. Overall about 60kg; Paraffin wax (42kg) and solar collector (18kg)	The weight of TES tank is about 62kg, empty tank (15kg), Paraffin wax (20kg), HDPE spherical capsules (4kg), water (23kg)	The weight of TES tank is about 115kg, empty tank (8kg), Paraffin wax (42kg), water (65kg)	existing manifold replaced with TES. The weight of TES is about 105kg, TES structure (70kg) and Paraffin (35kg)
Piping system	This configuration does not need more piping in comparison with conventional system.	This configuration does not need more piping in comparison with conventional system.	This configuration needs more piping, due to the indirect passive system.	This configuration minimises the required piping, due to elimination of hot water storage tank and direct, active mechanism

Table 3 presents the cost related effects on the changes of systems in comparison with conventional system.

Table 3: Effect of innovation in design of SWH-PCM system on the capital and maintenance costs

Parameter	Design 1	Design 2	Design 3	Design 4
Estimated cost of the system	For this system, there will be 3 extra costs; for Paraffin wax, packing of Paraffin to prevent leaking, and redesigned housing for flat plate collector to have stronger structure for Paraffin wax	Larger storage tank and cost of capsulated PCMs are extra cost on the system.	This type of PCM is expensive, and due to the required mass of the PCM it will cause so much of the capital cost increment	Elimination of hot water tank, structure of that and required piping reduce the cost of the system in one side, but fabrication of an integrated TES tank to the solar collector, PCM and required structure for that has additional cost. Overall, the cost of the system may not vary to much from the conventional system
Installation cost	Similar cost of conventional system	Similar cost of conventional system	Similar cost of conventional system	Less than the conventional system
Maintenance cost	Over usual maintenance costs, there might be a requirement for PCM packed bed leaking problem	Over usual maintenance costs, there might be a requirement for capsulated PCM leaking problem	Due to the indirect passive system, two pumps are required for delivery of the hot water	due to the direct, active heat transfer mechanism, pump is not required and TES tank does not require maintenance

Some researchers reported health issues related to the hot water stored in the storage tank after period of time. Therefore, it brings up the questions about the effect of new design on health issues risks. Table 4 address these issues in situation of the SWH-PCM systems.

Table 4: Influence of the new design of SWH-PCM on health issues

Parameter	Design 1	Design 2	Design 3	Design 4
Contaminant mixture with water and growing legionella bacteria	Potential risk in hot water tank	Potential risk in hot water tank	Potential risk in hot water tank	By elimination of hot water tank, there would not be any risk of this problem.
PCM and accessibility to water side	would not be any problem	Potential risk if the capsulated PCMs does not sealed carefully	No risk	No risk

Although the efficiency of the Designs 1, 3 and 4 were in about the same level, the hot water production in Designs 3 and 4 were high enough to fulfill requirement of a domestic family. Influence of flowrates on hot water temperature is important. Providing enough high temperature water with a reasonable flowrate is one of the key elements of the power of the solar collector. Being able to utilise the pressure of domestic tap water, it become more important to provide a system with the ability to warm up the water in a faster process. Extension of time that the system is able to provide hot water is another key element on usability of the system for domestic application. All four reports claimed that their system is able to utilise the PCM storage capacity to produce hot water out of the pick time. Stratification occurs as a result of a density differential between two water layers and can arise as a result of the differences in salinity, temperature or a combination of both, which caused a loss of a portion of captured energy in the storage tank. Only Design 4 addressed this issue and claimed to solve this problem, however, Designs 2 and 3 can also reduce this effect in hot water tank.

Complexity of system, simplicity of installation, weight of TES, number and size of required equipment for infrastructure of the system, make the design more or less attractive. According to Table 2, Design 4 provides simplest system in terms of weight, equipment, piping and heat transfer process. Accordingly, the system design has direct effect on cost of the system, which Designs 2 and 4 looks to have lower initial and life cycle costs.

6. CONCLUSION

All of the reported SWH-PCM systems were used as the initial design with no optimisation applied to the design. Therefore, it would not be possible to conclude which one is the most suitable one. However, there are potential improvement for all systems. More importantly, all reports claimed improvement in the system performance with application of PCM in the TES unit.

It could be expected that the fourth generation of SWH systems will utilise advantages of TES unit, by using PCMs. However, still, there are potential improvements in SWH-PCM systems in the field related to optimisation of TES unit, infrastructure and cost of the system.

7. REFERENCES

Armstrong, P., Ager, D., Thompson, I. & Mcculloch, M. 2014. Domestic hot water storage: Balancing thermal and sanitary performance. *Energy Policy,* 68**,** 334-339.

Diakoulaki, D., Zervos, A., Sarafidis, J. & Mirasgedis, S. 2001. Cost benefit analysis for solar water heating systems. *Energy Conversion and Management,* 42**,** 1727-1739.

García-Valladares, O., Pilatowsky, I. & Ruíz, V. 2008. Outdoor test method to determine the thermal behavior of solar domestic water heating systems. *Solar Energy,* 82**,** 613-622.

Gürtürk, M., Koca, A., Öztop, H. F., Varol, Y. & Şekerci, M. 2017. Energy and exergy analysis of a heat storage tank with a novel eutectic phase change material layer of a solar heater system. *International Journal of Green Energy***,** 1-8.

Kalogirou, S. A. & Panteliou, S. 2000. Thermosiphon solar domestic water heating systems: long-term performance prediction using artificial neural networks. *Solar Energy,* 69**,** 163-174.

Kaygusuz, K. 1995. Experimental and theoretical investigation of latent heat storage for water based solar heating systems. *Energy Conversion and Management,* 36**,** 315-323.

Khalifa, A. J. N., Suffer, K. H. & Mahmoud, M. S. 2013. A storage domestic solar hot water system with a back layer of phase change material. *Experimental Thermal and Fluid Science,* 44**,** 174-181.

Khan, M. M. A., Ibrahim, N. I., Mahbubul, I. M., Muhammad. Ali, H., Saidur, R. & Al-Sulaiman, F. A. 2018. Evaluation of solar collector designs with integrated latent heat thermal energy storage: A review. *Solar Energy,* 166**,** 334-350.

Kılıçkap, S., EL, E. & Yıldız, C. 2018. Investigation of the effect on the efficiency of phase change material placed in solar collector tank. *Thermal Science and Engineering Progress,* 5**,** 25-31.

Kulkarni, G. N., Kedare, S. B. & Bandyopadhyay, S. 2007. Determination of design space and optimization of solar water heating systems. *Solar Energy,* 81**,** 958-968.

Kulkarni, G. N., Kedare, S. B. & Bandyopadhyay, S. 2009. Optimization of solar water heating systems through water replenishment. *Energy Conversion and Management,* 50**,** 837-846.

Lin, S. C., Al-Kayiem, H. H. & Aris, M. 2012. Experimental investigation on the performance enhancement of integrated PCM-flat plate solar collector. *Journal of Applied Sciences,* 12**,** 2390-2396.

Mather, D. W., Hollands, K. G. T. & Wright, J. L. 2002. Single- and multi-tank energy storage for solar heating systems: fundamentals. *Solar Energy,* 73**,** 3-13.

Mills, D. & Morrison, G. L. 2003. Optimisation of minimum backup solar water heating system. *Solar Energy,* 74**,** 505-511.

Morrison, G. L., Nasr, A., Behnia, M. & Rosengarten, G. 1998. Analysis of horizontal mantle heat exchangers in solar water heating systems. *Solar Energy,* 64**,** 19-31.

Naghavi, M. S., Ong, K. S., Badruddin, I. A., Mehrali, M. & Metselaar, H. S. C. 2017. Thermal performance of a compact design heat pipe solar collector with latent heat storage in charging/discharging modes. *Energy,* 127**,** 101-115.

Nallusamy, N., Sampath, S. & Velraj, R. 2007. Experimental investigation on a combined sensible and latent heat storage system integrated with constant/varying (solar) heat sources. *Renewable Energy,* 32**,** 1206-1227.

Paola, B., Montagna, M. T., Vincenzo, R.-S., Serena, S., Giovanna, S., Maria, T., Rachele, N., Isabella, M., Guglielmina, F., Daniela, T., Christian, N., Gianluigi, Q., Patrizia, L., Erica, L., Giovanna De, L., Cristina, O., Matteo, M. & Gabriella Ribera, D. A. 2004. Legionella Infection Risk from Domestic Hot Water. *Emerging Infectious Disease journal,* 10**,** 457.

Tsilingiris, P. T. 1997. Design, analysis and performance of low-cost plastic film large solar water heating systems. *Solar Energy,* 60**,** 245-256.

#248: An overview of carbon-based nanocomposites as efficient materials for hydrogen energy storage

Ali SALEHABADI, Mohammad Faisal UMAR, Akil AHMAD, Mardiana Idayu AHMAD, Mohd RAFATULLAH *

Environmental Technology Division, School of Industrial Technology, Universiti Sains Malaysia, 11800 Minden, Penang, Malaysia
**Corresponding author: mrafatullah@usm.my*

Research on hydrogen fuel generation as a renewable energy is becoming a hot topic among scientists searching for alternative energy sources. Hydrogen energy is considered as alternative source of energy which is eco-friendly, renewable and green source. To synthesise and develop highly potential materials for hydrogen energy is still a challenge for researcher which can be tackled to store hydrogen economically and efficiently. Various materials have been applied for this purpose, but carbon-based nanocomposites have gained more attention due to low processing cost, high surface area and light weight in nature. Due to functional groups present on the surface and edges, it is easy to modify with various metal oxides and other metal-organic frameworks to enhance the storage capacity of hydrogen. In addition, chemical adsorption is another way to enhance the hydrogen storage capacity of carbon based nanocomposites materials. In this review, we have discussed the success achieved so far and the challenges for the physical and chemical storage of hydrogen in various carbon based nanocomposites.

Keywords: nanocomposites; hydrogen; renewable energy; graphene oxide; carbon nanotubes

1. INTRODUCTION

Due to rapid industrialisation and population growth, human life is suffering from many environmental problems like climate change and global warming and demands for alternative green energy are increasing. Now our environment is facing two major issues namely energy and environmental pollution. Researchers are looking for alternative ways to produce renewable energy since traditional fossil fuels are reducing day by day and have serious environmental pollution. However, humans need more energy to fulfil their daily requirements and it is also required in many areas such as commercial, electricity, transportation, industrial activities which are met by energy consumption, manufacturing products to heating or cooling the buildings (Arto *et al.*; Wiedenhofer, 2013). Besides, there is a huge amount of energy required and it is further going to exceed in mid twenty first century (Vringer, 2016). Today's energy need is depends on the exhaustible energy source (Mesarić & Krajcar, 2015). These energy sources include coal, gaseous petrol, and oil that are exhausting quickly because of their enormous utilisation (Jacobson, 2009). In addition, these types of sources are the great cause of global warming for the increasing quantity of carbon dioxide in the environment associated with the emission of fossil fuel, is very unsafe for the condition (Kondratenko *et al.*, 2013).

Hydrogen fuel energy is considered as a green energy and have potential to use in vehicles and only produces water as by product. Hydrogen fuel is the sustainable energy that tend to reduce fossil fuel. The energy of hydrogen has good efficiency as compared to combustion of petrol or diesel (three times) and seven times of coal with corresponding mass (Nagpal & Kakkar, 2018). Whereas a limited quantity of hydrogen fuel also the same mileage like diesel or petrol for any vehicles (L. Zhou, 2005; Hosseini & Wahid, 2016; Balat, 2008; Baschuk & Li, 2009). Non-renewable energy sources and renewable energy sources are summarised in Table 1. Although hydrogen is unstable, there is a large barrier for active hydrogen storage fuel and interrupts the comprehensive utilisation. For example, the economic building (Assaf & Shabani, 2018; Khiareddine *et al.*, 2018) and infrastructure (Campíñez-Romero *et al.,* 2018) by produce stored energy from inexhaustible sources generating rely on hydrogen fuel. Hence, Proper hydrogen storage, should have a significant energy density, low energy waste, and excessive reliability (Xu *et al.,* 2018). Hydrogen fuel is exploitation possesses a great power that reduces greenhouse effect, and to complete the process of fossil fuel. As a potential strength source to attain zero efficiencies, it is necessary to have hydrogen storage fuel. Whereas, the biggest challenge of hydrogen fuel storage at now a concern for the valuable storage of hydrogen in a secure and cheap manner (Ma *et al*., 2017; Chattaraj *et al.*, 2017). Any hydrogen fuels such as compressed or liquefied hydrogen, it requires excessive maintenance cost, owing to which application and concerns cannot be met by various on-board (Ahmed *et al.,* 2016; S. Singh *et al.*, 2015; O'Malley *et al.,* 2015). According to the rules of the United States Department of Energy (DOE), by 2020 the gravimetric and volumetric stockpiling limits are required to meet the objective of 5.5 wt.% and 40 g/L, respectively at encompassing working conditions (Wang, 2017; Rather & Nahm, 2014). From now, existing innovations are not perfect to meet the DOE targets. For ideal utilisation of hydrogen, the foreseen gas stockpiling attributes are high gravimetric and volumetric densities, low sorption temperature and warmth move, and great reversibility, in addition to the fast rate of reaction and cost-effective (Verhelst, 2014; *(Brooks et al.,* 2014; Silambarasan, 2013; Langmi, 2014). No capacity (adsorbent) material at surrounding conditions could achieve this errand. In this way, over the globe, scientists are searching after the examination of strong materials for the capacity of hydrogen at the concentrated-on levels. It is a superb green fuel in which the higher significant aspect from other energy sources Provides renewal waste product i.e. water (Hamad *et al*., 2014a), Compatibility of hydrogen with fuel cell, Efficiency higher (65%) as contrasted to diesel (45%) or gasoline (22%),and richer energy content than gasoline or diesel respectively (Cipriani *et al.,* 2014). There is essential work to the storage of hydrogen for usage it feasible; Hence hydrogen is one of the most sustainable sources (Ramesh, 2015). It is a basic component and very rich on the earth's covering (Hu *et al.*, 2016) . It is present in almost all elements in combined form and vital for life (Abdul Mujeebu, 2016). Hydrogen controls the universe with its essence in stars where proton-proton responses happen (Kamikawa, 2003). It is amazingly combustible gas and goes about as a fuel in space transport motors (S. Singh *et al.,* 2015). Use of hydrogen is additionally accomplished for preparing of fossil fuel (Cormos, 2011). The researcher has given focus to two new indicators by which hydrogen storage can be done, one thing that, mass storage and other is volume storage densities. In the last decades, a lot of researchers has to be work vastly and thoroughly studies (Onishi, 2018; Muir & Yao, 2011). A graphical representation is shown as a trend for hydrogen storage research publications based on the Science direct search engine from 2010 to 2019. Although, one more branch also includes, which divided hydrogen storage based on material as physical adsorption (adsorption due to weak Vander wall force between the adsorbant and surface) and chemisorption (adsorption due to chemical formation between the adsorbant and absorbate molecules).

In this review, we discuss the hydrogen storage capacities of various types of only carbon-based nanocomposites by the above two adsorption phenomena. The structural architecture influences the selective uptake of hydrogen carbon-based nanocomposites. The importance of nanostructured metal/metal oxide doping on the surfaces of carbon-based nanocomposite substrates for improving the hydrogen storage capacity is still evaluated. The mechanisms for enhanced hydrogen storage are discussed to understand the chemistry carrying out the evolution of later hydrogen storage systems.

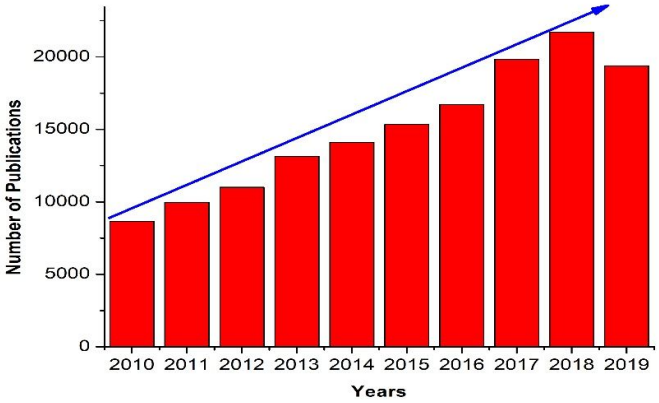

Figure 1: Research publication trends on hydrogen storage

Table 1: Non-renewable energy sources and renewable energy sources

Non-renewable energy sources	**Influence our environment**	**References**
Coal	Coal is a source of electricity which is manufactured by decay plant embedded under slightly earth surface, to assist generate the power generation. Carbon is combined with oxygen to produce carbon dioxide, which is responsible to greenhouse effect, that carbon is major production through coal.	(Chen *et al.* 2016) (Obara *et al.* 2015) (Hosseinzadeh *et al.* 2016) (Bjorkegren *et al*. 2015)
Oil	Oil are the powerful fuel utilise in the vehicle our world and is major contributor towards economy they occur almost in middle east countries like Iraq, Kuwait, Saudi Arabia, Iran and UAE. Whenever the stock oil is beneath the sand and mud that result not alive of plant and animal. While many people have been using this fuel, there result to create a very dangerous pollution our environment they have injurious our health. It is most important advantage to help transportation. Moreover, disadvantage when oil fall in the ocean during transportation create a lot of widespread destruction of flora and fauna.	(Liao *et al.* 2016) (Rahman *et al*. 2014) (Wu *et al.* 2012) (Lan *et al*. 2015) (A. Singh *et al.* 2015)
Natural Gas	Natural gas thoroughly burned without ashes, other aspect that no causes in air pollution. It is vast reserved area cover in Iraq and Iran. Natural gas become influence is an economical and environmentally beneficial source, other non-renewable sources.	(Lim *et al*., 2015) (Afgan *et al,* 2007) (Pascoli, Femia & Luzzati, 2001)
Nuclear Energy	Today's energy needs at all the world's people are drifting towards nuclear energy. Nuclear energy influences the world economy at government considerably. It is classified based on nuclear reactor named as thermal reactor. It is of two process going on one is nuclear fission other is nuclear fusion. Thermal power plant gets place nuclear reaction during these processes Out of this radioactive waste emerges, which radiates harmful emissions and hence should be dealt with perfectly. One more disadvantage they play important role in nuclear bomb.	(Norgate, Haque & Koltun, 2014) (Yan *et al,* 2011) (Zinkle & Busby, 2009) (van der Zwaan, 2002) (Stram, 2016)
Renewable energy sources	**Influence our environment**	**References**
Solar Energy	There are many technologies like photovoltaic, solar heating, solar energy, and solar process space heating and cooling is employed are to be affected by solar energy. Although the solar energy project is carrying out on in India and distinct part of countries, at now U.S alone 22.7 GW of the solar panel are in operation. The consumer is affection for these desire technologies of solar panel, because of cost-effective and fabrication.	(Kannan & Vakeesan 2016) (Kar, Sharma & Roy, 2016) (Li & Yi, 2014) (Eldin, Abd-Elhady & Kandil, 2016)
Bioenergy	Electricity generated is utilised by chemical energy which is stored in organic matter is bioenergy. Whenever biomass, biogas, biofuel is burned which emitted not clean source such as the gases like sulphurous oxide (SO_2), nitrous oxide (NO_2), and particulate matter (PM). They are harmful our environment,	(Krishnan & McCalley, 2016) (Birjandi *et al*, 2016) (Gupta, Rehman & Sarviya, 2010)

Geothermal Energy	It is known by the thermal energy assigned with many areas, such as preventing freezing on a stepped pathway, drying foods, power generation, and steaming buildings. While energy production by radioactive decomposition of minerals. Geothermal energy vast utilised in the U.S and annually earn pay $280 million.	(Rahmouni *et al.*, 2014) (Angrisani *et al.,* 2016) (Lund *et al.,*, 2011)
Hydrogen Energy	The trait of hydrogen energy carrying the widest energy between all other prevailing energy sources with low polluting fuel. Besides this, most enough and easily identified on earth. It is employed for transport, electrical power generation, and heating.	(Zhang *et al,* 2016) (Marchenko & Solomin, 2015)

2. HYDROGEN STORAGE THROUGH CARBON BASED NANOCOMPOSITES

Carbon content can create hydrogen storage in these materials since much as achievable, making hybrids with C-H bonds. Then, probable hydrogen energy in distinct types of carbon content such as carbon nanotube, carbon dots, carbon nanofiber, graphene, graphite carbon nitride, etc. can be storage (Yürüm, Taralp & Veziroglu, 2009).

2.1. Hydrogen storage through physisorption and chemisorption process.

Hydrogen energy can be stored in carbon based materials by two different ways: physisorption (or molecules are held by weak vander wall forces) and chemisorption (molecules held by strong chemical bond). The adsorption between hydrogen molecules and adsorbate molecules by weak Vander forces, arise in physisorption process. In a physisorption process, their many gas molecules a great interaction over the surface of the adsorbate. While the temperature of the physisorption process examined at very low temperature (<273k) and interaction energy between adsorbate and adsorbent is (1-10kj/mol), (Challenge, 2009) since weak interaction between adsorption surface and adsorbate. Examples of physisorption include the storing of hydrogen in carbon structures and organic or inorganic frameworks.

Graphene based nanocomposites

Carbon-containing material graphene is certainly appropriate for the hydrogen storage material since it is excess surface area and excellent chemical property. It's employed with a free metal catalyst provide stimulated to a fuel cell, due to graphene is a favourable electrochemical and chemical properties. However, it involves powerful physical-chemical properties like high carrier mobility, elasticity, and acceptable thermal conductivity (Fan, Chen & Dai, 2015). The hybridisation of a graphene is sp2, the structure of graphene covalent bonded honeycomb arrangement, which permits potential easily attach with hydrogen atoms (Ohashi, 2015). Due to being flexible, this graphene allows hydrogen to facilitate easy assimilation of the module. Both Adsorption process doing occurs either physisorption or chemisorption, to get adsorbed of hydrogen on the surfaces of graphene. In so far as graphene activity and doping of its hydrogen improves storage efficiency. Whenever this phenomenon occurs due to the spills of hydrogen, the separation of hydrogen molecules on the same surface of metal or metal oxide and afterwards transferred over that graphene surface where easy adsorption. Maryam Masjedi-Arania and Masoud Salavati-Niasari prepared novel Cd_2SiO_4 nanoparticle via sonochemical technique in the presence of different surfactants anionic (SDS), cationic (CTAB) and polymer (PVP)(Chatrou et al., 2009). The fine and uniform Cd_2SiO_4 mesoporous nanoparticle was prepared using PVP surfactant and ultrasonication. The synthesised nanoparticles were characterised by FTIR, XRD and EDAX. SEM and TEM were applied to confirm the particle size and surface morphology. After then Cd_2SiO_4 nanoparticle blend with graphene sheet to form the Cd_2SiO_4/graphene carbon nanocomposite by pre-graphenization method. First time, the electrochemical behaviour of these two materials namely Cd_2SiO_4 nanoparticle and Cd_2SiO_4/graphene have been carried out for hydrogen storage. From the results, the hydrogen storage capacity of Cd_2SiO_4 nanoparticle was found to be 1300 mAh/g which had lower hydrogen storage capacity as compare to Cd_2SiO_4/graphene nanocomposite (3300 mAh/g). This is because of good electrical properties and high surface area. Therefore, author concluded that Cd_2SiO_4/graphene nanocomposite may be better alternate and can be efficiently applied for the electrochemical hydrogen storage than Cd_2SiO_4 nanoparticle.

Graphene is considered as a very light weight material which attracted to researcher for H-storage application. Ngqalakwezi et al. synthesised a nanocomposites using alkaline Calcium metal with graphene through improved Tours method (Nkazi, Gotthard & Ntho, 2019). After that, they reduced it using L-Ascorbic acid and ammonia. To synthesise the graphite oxide, a precursor of graphite flakes (100 µm) was used. A small angle shift (11.3°) in GO was observed through XRD study which indicates the successful oxidation of graphite from graphite flakes (30°). However, L ascorbic acid is a better reducing agent as compared to ammonia which is converting the functionality of GO into rGO and this was proved from FTIR and Raman spectra. From the XRF study, it was confirmed that the presence of Ca onto the graphene surface and successfully synthesised the Ca/graphene nanocomposite which is also confirmed by TEM study. From the XRF results, Ca percentage increased from 0.516% in graphite clusters to 8.227% in case of ammonia reduction to form Ca/graphene composite. Calcium filler spread on the graphene matrix as shown by the TEM, and hydrogen capacity is investigated from the TGA and TPP equipped with a mass

spectrometer. The hydrogen uptake capacity was increase from 2% in graphene to 4.98 wt% and 3.99 wt% of Ca/graphene nanocomposite reduced from ammonia and L-ascorbic acid, respectively. From the results, it was concluded that ammonia has a tendency to increase the hydrogen storage in graphene, although it partially reduce graphite oxide. Eventually, they assess to establish that the uptake of hydrogen storage in Ca/graphene nanocomposite reduced by ammonia and L-Ascorbic acid.

Further, another group reported the addition of magnesium onto the rGO to synthesised the rGO-Mg composites (Cho *et al.,* 2016) and applied for electrochemical hydrogen storage. Although demand of hydrogen fuel is increasing rapidly for automated applications and now it is the scientific challenge to safe and dense of hydrogen storage(Cho et al., 2016). Metal hydride provides enough storage capacity and operation do not require cryogens or excessive high pressure. Authors developed new and ecofriendly magnesium nanocrystal encapsulated with fine and reduced graphene oxide (rGO) sheets and has been employed for the hydrogen storage. From the results, formation of GO-Mg multilaminates protect the rGO layer from oxygen and moisture and having the greatest hydrogen storage capacity (6.5 wt% and 0.105 kg hydrogen per litre in the total composite). This material has advantage to reduce inactive mass in the composite estimated indivisibility fine structure and protect the degradation of Mg nanocrystal and used as a catalyst, to increase the rate of hydrogen absorption and desorption. This material was characterised by XRD and TEM. To increase the energy density of nanaomaterial, nano composite material was synthesised by a facile method. Hence, rGO-Mg showed exceptional environmental stability and excellent hydrogen storage efficiency. From the results, this material can be efficiently used for solid hydrogen storage and indivisible fine 2D material can be employed together to protect nanomaterial from ambient condition.

Ravi Nivetha and Grace fabricated a Manganese and Zinc based graphene nanocomposites and applied for hydrogen evolution. Novel $MnFe_2O_4$/Graphene (MFG) and $ZnFe_2O_4$/Graphene nanocomposites were synthesised for evolution of hydrogen through solvothermal route (Nivetha, Grace & Grace, 2019). The morphology and structural of the prepared nanocomposites feature recognised by scanning electron microscopy (SEM) and XRD studies. Furthermore, the anatomy of nanocomposite is evidently observed by TEM from the illustrations of MFG and ZFG. Although all electrochemical activity is associated with linear Sweep Voltammetry (LSV), cyclic Voltammetry, Tafel polarisation and Electrochemical Impedance Spectroscopy (EIS) exhibited good performance activity towards HER by electrochemical nanocomposites. This shows the enhance catalytic activity of the changed electrode MFG and ZFG nanocomposite as compared bare electrode assigned electrochemical investigation such as Tafel slope (exchange current density value being 60.11 $mAcm^{-2}$ 47 $mAcm^{-2}$ with a Tafel slope of 106.4 $mVdec^{-1}$ and 114.3 mVdec-1 and with low over potential (313 mV and 315 mV) occur in acidic medium activity for hydrogen evolution reaction. However, TOF, electrochemical specific surface area, and less charge transfer resistance value for both nanocomposites (MFG, ZFG) was observed (1.47 H_2/s,1.09 H_2/s), (1.51 $mFcm^{-2}$,0.3 $mFcm^{-2}$) and (8.5Ω, 13.0Ω) respectively. During the hydrogen evolution reaction, electrode Tafel counters are working to perceive, that reaction progression from Volmer mechanism. Accordingly, prepared nanocomposite is assured high-performance electrocatalysts for hydrogen evolution reaction exist in a sour medium.

In another works, Tarasov *et al.* (2019) prepared a metal decorated nanocomposite (Ni/graphene like materials GLM) and applied in hydrogen storage. The prepared materials act as a good catalyst for hydrogenation and dehydrogenation process and showed good regeneration capacity. Composition and micro structure of materials are characterised by various techniques such as SEM, TEM and XRD which shows 2-5 nm particle size and homogeneous distribution of particles in composites. Ni/GLM with Mg showed high potential to store hydrogen which is more than 6.5 wt% and have good rates of adsorption and desorption of H-storage. Rate of reaction increases in case of Mg doped GLM and Ni/GLM and improved from 2 to 6.5 as compared to without addition of Mg. From the results, it was found that dehydrogenation rate constant increases 1.4 and 2.3 times. In case of Mg/MgH_2+Ni/GLM composite have higher dehydrogenation rate constant 15-37 times as compared to individual Mg/MgH_2 where both prepared in same conditions. Kinetics curves of hydrogen absorption and desorption of composites were analysed using the Eravami E. Aerofev approach and measured by Sievert's types laboratory. Although, cycle of re-hydrogenation in kinetics process are constant and stable up to 10 cycles without major loss of hydrogen absorption capacity. From the results, it was confirmed that Mg's composites with 5-10 wt% of Ni/GLM are efficient which have had high reversible hydrogen storage material capacity (>6.5 wt%).

Gholami, Salavati-Niasari, & Sabet (2018) prepared a novel $ZnAl_2O_4$ and ZnAl2O4/graphene nanocomposites materials by a green method using green tea and olive leaf extract and applied for electrochemical storage of hydrogen. This material was characterised by XRD, BET, EDS, FTIR, SEM and TEM to examined the phase and purity of composites, material porosity, composition, functional group on surface of composite, morphology and particle size. From the results, it was observed that green tea and olive leaf extract have great impact on the morphology and particle size of the product. Furthermore, in presence of electrolyte 6M KOH and 1mA, it shows better hydrogen storage capacity. $ZnAl_2O_4$/graphene and $ZnAl_2O_4$ nanocomposites samples show the highest of Coulombic efficiency (67.5%) and discharge capacity (3100mAh/g) respectively. From the results, it was concluded that it can be a good candidate for the hydrogen storage and have good coulombic efficiency.

The decoration of a graphene structure with a transition metal oxide gives excellent hydrogen storage. Liu, Zhang, & Hu (2018) prepared hierarchically porous 3D-graphene materials doped with TiO_2 through electrostatic assembly method and tested its efficiency for hydrogen adsorption. The obtained 3D-HPGT nanocomposites have great ability to store hydrogen energy because of enormous pore volume (0.41 cm^3/g), high surface area (705m^2/g) and maximum storage capacity. It showed the hierarchy structure of materials containing multi-level pores like macropores, mesopores and micropores. Nanocomposites showed high storage capacity of hydrogen 1.48 and 4.11 wt% at 298 and 77k, respectively at pressure 5 bar. Due to three dimensional structure of porous graphene and strong attachment of TiO2 nanoparticles with graphene nanosheets enhanced the storage capacity. This research enhances the practical application of 3D-porous graphene nanocomposites in area of hydrogen storage.

In another study, Du *et al.* (2019) investigated the hydrogen storage capacities using vanadium supported reduced graphene oxide nanocomposites and then combined with $Mg_{85}Al_{15}$ alloy. Nanocomposite was synthesised via an impregnation method and $Mg_{85}Al_{15}$ alloy was introduced through mechanical milling process. V_2O_3@rGO nanocomposites on H-storage of $Mg_{85}Al_{15}$ alloy has been characterised through various techniques such as DSC, PCT, TEM, XRD and FE-SEM and assessed the synergistic effect of rGO and V_2O_3 into hydrogen storage. From the results, it was found that V_2O_3 and rGO play crucial role to destabilising the stability of $Mg_{85}Al_{15}$ alloy hydrides. Temperature 220°C required with the rate of 2°C/min for hydrogen absorption of 1.0 wt% while temperature declines 181 °C and 192 °C respectively in case of V_2O_3 and rGO when separately used as a catalyst. A reversible process for hydrogenation and dehydrogenation were occurred for $Mg_{85}Al_{15}$+ V_2O_3 and $Mg_{85}Al_{15}$ + V_2O_3@rGO at 250 °C. From the results, hydrogen absorption/desorption decreases by the addition of V203@rGO to Mg due to hysteresis effect. Thereafter, the nanocomposite synthesis from $Mg_{85}Al_{15}$ and V_2O_3@rGO ($Mg_{85}Al_{15}$ + V_2O_3/rGO), the activation energy of hydrogen absorption/desorption diminishing as correlated to alloy from 80.1 $kJmol^{-1}$/ 173.2 kJ mol^{-1} to 61.6 kJ mol^{-1}/91.3 kJ mol^{-1} respectively.

A Palladium/graphene nanocomposites was synthesised by(C. Zhou & Szpunar, 2016) has been used for the hydrogen storage. The palladium is uniformly distributed over the matrix of graphene with size of 5-45 nm which is confirmed by TEM analysis. Pd nanoparticles are bound with graphene structure through Pd−C and Pd−O−C bonds. This system has favorable, characteristics for hydrogen storage like low temperature of hydrogen discharge, high storage capacity and ambient condition for uptake of hydrogen. From the results, it was found that hydrogen storage has attained a density of 6.7 % by taking 1% Pd/graphene at pressure of 50 bar. This study also revealed that uptake capacity reached up to 8.67 wt % in the 1% Pd/graphene nanocomposite by applying pressure of 60 bar and 7.16 wt % uptake capacity was achieved by taking 5% Pd/graphene nanocomposite. It was concluded that amount of hydrogen uptake exceeded than the gravimetric target given by the US department of energy (DOE).

Carbon nanotube (CNT)

Carbon nanotubes was first reported by Ijima in 1991 since then receiving the much attention in various application such as energy storage, biomedical, displays, optoelectronics etc. due to their chemical, structural, electronic and mechanical properties. CNTs acquired very exclusive physical properties such as electrical conductivity similar to copper but can flow more currents, better thermal conductivity except than pure diamond and tensile strength is 100 times better than steel. CNT is considered as an efficient materials for a quality hydrogen storage because of it has adequate porous structure (Pyle, Gray, & Webb, 2016).

CNTs are made up from sp^2 carbon-bonded hybridisation and made a hexagonal shape networks which are similar as graphene sheet (Merkoçi, 2006). It can be generally found in two forms: single-walled carbon nanotube (SWCNTs) and multiwalled carbon nanotubes (MWCNTs). SWCNTs is a seamless cylindrical which consist of only one layer graphene, composed of a single layer of graphene which forma of a cylindrical shape around 0.4–3nm observed by TEM and the Allotropes of sp^2 hybridises atom which is similar to fullerence and the structure form six carbon atom ring in a hexagonal shape, which is identical graphite (Balasubramanian & Burghard, 2008). Although MWCNTs is also cylindrical in shape, with multiple concentric layers of graphene composing it, but made of layer of graphene, which formed in a concentric pattern around the smallest nanotube and allotropes of MWCNTs involve several tubes which set in concentric layer in a cylindrical shaped .it also efficiency are significant better at working in the highly corrosive atmosphere (Ajayan, 1999). The MWCNTs show lowered loss or oxygen reduction when used as catalyst for fuel cell as compared to SWCNTs. Carbon nanotube has been a high percentage of pore volume and surface area because of them as a good adsorbent for hydrogen storage.

Varshoy, Khoshnevisan & Behpour (2019) prepared materials to improve hydrogen storage. An electrochemical deposition method was carried out to synthesise the Ni-Sn alloy/multi-walled carbon nanotube (MWCNT) nanocomposite and applied for efficient irreversible sodium and hydrogen storage. The crystallinity and group composition in the nanocomposite was examined using an X-ray diffraction analysis and Fourier transform infrared spectroscopies. However, the structural morphology and sphere like nanoparticle Ni-Sn alloy dispersed uniformly over the MWCNT with average size 190 nm was confirmed by scanning electron microscope. Hydrogen discharge capacity of Ni-Sn alloy/MWCNT nanocomposite electrode initially increases slightly 550 mAh g_{-1} under the current density 1000 mA g^{-1} and further increases the hydrogen discharge capacity 5200 mAh g^{-1} at current density 1100 mA g^{-1} and this capacity was retain up to 20 cycles which shows the high stability of Ni-Sn alloy/MWCNT

nanocomposite electrode. Afterwards, up to 40 cycles, coulombic efficiency was increases approximately 98% at current density between 1000 and 1100 mA g^{-1}. From the results, it was concluded that synthesised electrode materials can be efficiently use for the hydrogen capacity.

3. ADVANTAGE OF HYDROGEN ENERGY

Hydrogen is widely gas spread on the earth and is considered as a green fuel. It is a dull, odourless, and non-poisonous in nature. It is extensively found in nature but does not in free- state rather in combined form. It has an incredible arrangement of various procedures to separate it from the source element. Although, during preparing hydrogen, does not leave any types of poisonous emission and spoil material since hydrogen is environmentally friendly. Furthermore, we get reusable water as the side effect, which can be exploited significantly to create more hydrogen (Hamad et al., 2014b). Analysing the fuel cell used as a hydrogen fuel cell is much more powerful than the other fossil fuel cell sources. At initially cost estimate may be expensive of hydrogen fuel cell, while after that maintenance is cost effective. Its Commercial use in chemical industries makes it very much reliable for use in food, microelectronics, chemical and polymer synthesis industries, petrochemical and metallurgical process industries. There is an enormous advantage of hydrogen energy is a renewable source and easily synthesised. it is employed by various method for preparation with a large quantity such as which include electrolysis of water, photochemical process and other process like thermochemical decompositions (Kaur & Pal, 2019).

4. APPLICATION

- In the hydrogen fuel cell to generate energy assigned oxygen and hydrogen is blend, after that water is formed as a clean by product (Rodriguez, Puzenat, & Thivel, 2016). It carries fuel cell utilised as a fuel source in submarines, cars, space craft's (Belz, 2016) with electrochemical cells are environmentally friendly (Gadalla & Zafar, 2016).
- Non-renewable resource like coal, natural gas and diesel oil which is used in vehicle buses trucks, submarines, cars and rockets can be replace by hydrogen fuel source is employed in most of the vehicles (Köhler *et al*., 2010).
- Hydrogen used as a fuel source to different power plant for electricity generation (Fernandes *et al,* 2016).
- It is used as gas fuel in weather balloons to give information about weather forecast assigned meteorologist (Winter, 2009).
- It also used the preparation of various chemical compounds (Heng, Zhang & Xiao, 2016). Such as production of ammonia with large amount through the reaction of nitrogen and hydrogen (Frattini *et al*., 2016).
- Hydrogen are widely applicable in food and chemical industry (Kadier *et al.,* 2016), for making the hydrogenated vegetable oil (Jang et al., 2015), for refinement of crude oil (Elreedy & Tawfik, 2015) and metal extraction (Eatwell-Hall, Sharifi & Swithenbank, 2010).

5. CONCLUSION AND FUTURE PROSPECTS

The large scale consumption of the fossil fuel prompted researchers to search an alternative source of the green renewable energy with less toxic effect on environment. Therefore, we conclude that hydrogen can be the greatest sources of energy as compared to other non-conventional energy (solar energy, geothermal energy, and bioenergy), even conventional sources (coal, petrol), and has a great fuel cell. It also has a specific amount of energy compared to another source of energy. Nope effect of hydrogen fuel our environment which can be utilised in various transportation in trucks, buses and space craft because they are low polluting pollutant, eco-friendly, biocompatible and formed water. Various energy storage but hydrogen storage has been sustainable for researchers, industrialists, and scientists. Hydrogen storage have been taken more efforts and the same protection new comprehensive are still emerging. Different type of material has been employed of the hydrogen storage capacity such as alloy, metal oxide, polymers etc. In this review, we have reported decorated almost all composites of metal oxide, metal with MWCNT, Graphene oxide and reduce graphene oxide which is employed of hydrogen storage. However, all are porous is employed for hydrogen storage easily. Hydrogen easily provided by a different source of energy like biomass, water etc. and utilisation in various employed such that electricity, power supply, and electronics.

Furthermore, there are many advantages of hydrogen technology, hydrogen is react with oxygen to generate electricity in fuel cell and formation of water which is utilised again for hydrogen production. In future aspect novel material developed carbon-based nanocomposites MWCNT together with conducting polymers and reduce graphene oxide, its produce having a pores with large surface area for good hydrogen storage.

6. ACKNOWLEDGEMENT

The authors are grateful to the Universiti Sains Malaysia for supporting this work through RUI grant (1001/PTEKIND/8011044).

7. REFERENCES

Abdul Mujeebu, M. (2016). Hydrogen and syngas production by superadiabatic combustion – A review. *Applied Energy*, *173*, 210–224. https://doi.org/10.1016/j.apenergy.2016.04.018

Afgan, N. H., Carvalho, M. G., Pilavachi, P. A., & Martins, N. (2007). Evaluation of natural gas supply options for south east and central Europe. Part 1: Indicator definitions and single indicator analysis. *Energy Conversion and Management*, *48*(9), 2517–2524. https://doi.org/10.1016/j.enconman.2007.03.022

Ahmed, A., Al-Amin, A. Q., Ambrose, A. F., & Saidur, R. (2016). Hydrogen fuel and transport system: A sustainable and environmental future. *International Journal of Hydrogen Energy*, *41*(3), 1369–1380. https://doi.org/10.1016/j.ijhydene.2015.11.084

Ajayan, P. M. (1999). Nanotubes from Carbon. *Chemical Reviews*, *99*(7), 1787–1800. https://doi.org/10.1021/cr970102g

Angrisani, G., Diglio, G., Sasso, M., Calise, F., & Dentice d'Accadia, M. (2016). Design of a novel geothermal heating and cooling system: Energy and economic analysis. *Energy Conversion and Management*, *108*, 144–159. https://doi.org/10.1016/j.enconman.2015.11.001

Arto, I., Capellán-Pérez, I., Lago, R., Bueno, G., & Bermejo, R. (2016). The energy requirements of a developed world. *Energy for Sustainable Development*, *33*, 1–13. https://doi.org/10.1016/j.esd.2016.04.001

Assaf, J., & Shabani, B. (2018). Experimental study of a novel hybrid solar-thermal/PV-hydrogen system: Towards 100% renewable heat and power supply to standalone applications. *Energy*, *157*, 862–876. https://doi.org/10.1016/j.energy.2018.05.125

Balasubramanian, K., & Burghard, M. (2008). Electrochemically functionalized carbon nanotubes for device applications. *Journal of Materials Chemistry*, *18*(26), 3071. https://doi.org/10.1039/b718262g

Balat, M. (2008). Potential importance of hydrogen as a future solution to environmental and transportation problems. *International Journal of Hydrogen Energy*, *33*(15), 4013–4029. https://doi.org/10.1016/j.ijhydene.2008.05.047

Baschuk, J. J., & Li, X. (2009). A comprehensive, consistent and systematic mathematical model of PEM fuel cells. *Applied Energy*, *86*(2), 181–193. https://doi.org/10.1016/j.apenergy.2007.12.004

Belz, S. (2016). A synergetic use of hydrogen and fuel cells in human spaceflight power systems. *Acta Astronautica*, *121*, 323–331. https://doi.org/10.1016/j.actaastro.2015.05.031

Birjandi, N., Younesi, H., Ghoreyshi, A. A., & Rahimnejad, M. (2016). Electricity generation through degradation of organic matters in medicinal herbs wastewater using bio-electro-Fenton system. *Journal of Environmental Management*, *180*, 390–400. https://doi.org/10.1016/j.jenvman.2016.05.073

Bjorkegren, A. B., Grimmond, C. S. B., Kotthaus, S., & Malamud, B. D. (2015). CO 2 emission estimation in the urban environment: Measurement of the CO 2 storage term. *Atmospheric Environment*, *122*, 775–790. https://doi.org/10.1016/j.atmosenv.2015.10.012

Brooks, K. P., Semelsberger, T. A., Simmons, K. L., & van Hassel, B. (2014). Slurry-based chemical hydrogen storage systems for automotive fuel cell applications. *Journal of Power Sources*, *268*, 950–959. https://doi.org/10.1016/j.jpowsour.2014.05.145

Campíñez-Romero, S., Colmenar-Santos, A., Pérez-Molina, C., & Mur-Pérez, F. (2018). A hydrogen refuelling stations infrastructure deployment for cities supported on fuel cell taxi roll-out. *Energy*, *148*, 1018–1031. https://doi.org/10.1016/j.energy.2018.02.009

Challenge, E. (2009). Part Two Effi cient Energy Storage Nanostructured Materials for Hydrogen Storage. *Nanostructured Materials*.

Chatrou, L. W., Escribano, M. P., Viruel, M. A., Maas, J. W., James, E., & Hormaza, J. I. (2009). *Accepted Manuscript*. https://doi.org/10.1016/j.ympev.2009.07.024

Chattaraj, D., Kumar, N., Ghosh, P., Majumder, C., & Dash, S. (2017). Adsorption, dissociation and diffusion of hydrogen on the ZrCo surface and subsurface: A comprehensive study using first principles approach. *Applied Surface Science*, *422*, 394–405. https://doi.org/10.1016/j.apsusc.2017.06.012

Chen, X., Huang, X., Wang, T., Barwe, S., Xie, K., Kayran, Y. U., Masa, J. (2016). Traditional earth-abundant coal as new energy materials to catalyze the oxygen reduction reaction in alkaline solution. *Electrochimica Acta*, Vol. 211, pp. 568–575. https://doi.org/10.1016/j.electacta.2016.05.137

Cho, E. S., Ruminski, A. M., Aloni, S., Liu, Y. S., Guo, J., & Urban, J. J. (2016). Graphene oxide/metal nanocrystal multilaminates as the atomic limit for safe and selective hydrogen storage. *Nature Communications*, *7*, 1–8. https://doi.org/10.1038/ncomms10804

Cipriani, G., Di Dio, V., Genduso, F., La Cascia, D., Liga, R., Miceli, R., & Ricco Galluzzo, G. (2014). Perspective on hydrogen energy carrier and its automotive applications. *International Journal of Hydrogen Energy*, *39*(16), 8482–8494. https://doi.org/10.1016/j.ijhydene.2014.03.174

Cormos, C.-C. (2011). Hydrogen production from fossil fuels with carbon capture and storage based on chemical looping systems. *International Journal of Hydrogen Energy*, *36*(10), 5960–5971. https://doi.org/10.1016/j.ijhydene.2011.01.170

Du, J., Lan, Z., Zhang, H., Lü, S., Liu, H., & Guo, J. (2019). Catalytic enhanced hydrogen storage properties of Mg-based alloy by the addition of reduced graphene oxide supported V2O3 nanocomposite. *Journal of Alloys and Compounds*, *802*, 660–667. https://doi.org/10.1016/j.jallcom.2019.06.221

Eatwell-Hall, R. E. A., Sharifi, V. N., & Swithenbank, J. (2010). Hydrogen production from molten metal gasification. *International Journal of Hydrogen Energy*, *35*(24), 13168–13178. https://doi.org/10.1016/j.ijhydene.2010.09.003

Eldin, S. A. S., Abd-Elhady, M. S., & Kandil, H. A. (2016). Feasibility of solar tracking systems for PV panels in hot and cold regions. *Renewable Energy*, *85*, 228–233. https://doi.org/10.1016/j.renene.2015.06.051

Elreedy, A., & Tawfik, A. (2015). Effect of Hydraulic Retention Time on Hydrogen Production from the Dark Fermentation of Petrochemical Effluents Contaminated with Ethylene Glycol. *Energy Procedia*, *74*, 1071–1078. https://doi.org/10.1016/j.egypro.2015.07.746

Fan, X., Chen, X., & Dai, L. (2015). 3D graphene based materials for energy storage. *Current Opinion in Colloid & Interface Science*, *20*(5–6), 429–438. https://doi.org/10.1016/j.cocis.2015.11.005

Fernandes, A., Woudstra, T., van Wijk, A., Verhoef, L., & Aravind, P. V. (2016). Fuel cell electric vehicle as a power plant and SOFC as a natural gas reformer: An exergy analysis of different system designs. *Applied Energy*, *173*, 13–28. https://doi.org/10.1016/j.apenergy.2016.03.107

Frattini, D., Cinti, G., Bidini, G., Desideri, U., Cioffi, R., & Jannelli, E. (2016). A system approach in energy evaluation of different renewable energies sources integration in ammonia production plants. *Renewable Energy*, *99*, 472–482. https://doi.org/10.1016/j.renene.2016.07.040

Gadalla, M., & Zafar, S. (2016). Analysis of a hydrogen fuel cell-PV power system for small UAV. *International Journal of Hydrogen Energy*, *41*(15), 6422–6432. https://doi.org/10.1016/j.ijhydene.2016.02.129

Gholami, T., Salavati-Niasari, M., & Sabet, M. (2018). Novel green synthesis of ZnAl2O4 and ZnAl2O4/graphene nanocomposite and comparison of electrochemical hydrogen storage and Coulombic efficiency. *Journal of Cleaner Production*, *178*, 14–21. https://doi.org/10.1016/j.jclepro.2018.01.012

Gupta, K. K., Rehman, A., & Sarviya, R. M. (2010). Bio-fuels for the gas turbine: A review. *Renewable and Sustainable Energy Reviews*, *14*(9), 2946–2955. https://doi.org/10.1016/j.rser.2010.07.025

Hamad, T. A., Agll, A. A., Hamad, Y. M., Bapat, S., Thomas, M., Martin, K. B., & Sheffield, J. W. (2014a). Hydrogen recovery, cleaning, compression, storage, dispensing, distribution system and End-Uses on the university campus from combined heat, hydrogen and power system. *International Journal of Hydrogen Energy*, *39*(2), 647–653. https://doi.org/10.1016/j.ijhydene.2013.10.111

Hamad, T. A., Agll, A. A., Hamad, Y. M., Bapat, S., Thomas, M., Martin, K. B., & Sheffield, J. W. (2014b). Hydrogen recovery, cleaning, compression, storage, dispensing, distribution system and End-Uses on the university campus

from combined heat, hydrogen and power system. *International Journal of Hydrogen Energy*, Vol. 39, pp. 647–653. https://doi.org/10.1016/j.ijhydene.2013.10.111

Heng, L., Zhang, H., & Xiao, R. (2016). Hydrogen production from heavy fraction of bio-oil using iron-based chemical looping process: Thermodynamic simulation and performance analysis. *International Journal of Hydrogen Energy*, *41*(40), 17771–17783. https://doi.org/10.1016/j.ijhydene.2016.07.068

Hosseini, S. E., & Wahid, M. A. (2016). Hydrogen production from renewable and sustainable energy resources: Promising green energy carrier for clean development. *Renewable and Sustainable Energy Reviews*, *57*, 850–866. https://doi.org/10.1016/j.rser.2015.12.112

Hosseinzadeh, S., Norman, F., Verplaetsen, F., Berghmans, J., & Van den Bulck, E. (2016). A study on the effects of using different ignition sources on explosion severity characteristics of coals in oxy-fuel atmospheres. *Journal of Loss Prevention in the Process Industries*, *43*, 53–60. https://doi.org/10.1016/j.jlp.2016.04.011

Hu, Y., Lei, J., Wang, Z., Yang, S., Luo, X., Zhang, G., … Gu, H. (2016). Rapid response hydrogen sensor based on nanoporous Pd thin films. *International Journal of Hydrogen Energy*, *41*(25), 10986–10990. https://doi.org/10.1016/j.ijhydene.2016.04.101

Jacobson, M. Z. (2009). Review of solutions to global warming, air pollution, and energy security. *Energy Environ. Sci.*, *2*(2), 148–173. https://doi.org/10.1039/B809990C

Jang, S., Kim, D.-H., Yun, Y.-M., Lee, M.-K., Moon, C., Kang, W.-S., … Kim, M.-S. (2015). Hydrogen fermentation of food waste by alkali-shock pretreatment: Microbial community analysis and limitation of continuous operation. *Bioresource Technology*, *186*, 215–222. https://doi.org/10.1016/j.biortech.2015.03.031

Kadier, A., Kalil, M. S., Abdeshahian, P., Chandrasekhar, K., Mohamed, A., Azman, N. F., … Hamid, A. A. (2016). Recent advances and emerging challenges in microbial electrolysis cells (MECs) for microbial production of hydrogen and value-added chemicals. *Renewable and Sustainable Energy Reviews*, *61*, 501–525. https://doi.org/10.1016/j.rser.2016.04.017

Kamikawa, T., Hashimoto, M., & Arai, K. (2003). Formation of atoms, molecules and the first objects in the universe with a variable cosmological term. *Nuclear Physics A*, *718*, 668–670. https://doi.org/10.1016/S0375-9474(03)00883-2

Kannan, N., & Vakeesan, D. (2016). Solar energy for future world: - A review. *Renewable and Sustainable Energy Reviews*, *62*, 1092–1105. https://doi.org/10.1016/j.rser.2016.05.022

Kar, S. K., Sharma, A., & Roy, B. (2016). Solar energy market developments in India. *Renewable and Sustainable Energy Reviews*, *62*, 121–133. https://doi.org/10.1016/j.rser.2016.04.043

Kaur, M., & Pal, K. (2019). Review on hydrogen storage materials and methods from an electrochemical viewpoint. *Journal of Energy Storage*, *23*(February), 234–249. https://doi.org/10.1016/j.est.2019.03.020

Khiareddine, A., Ben Salah, C., Rekioua, D., & Mimouni, M. F. (2018). Sizing methodology for hybrid photovoltaic /wind/ hydrogen/battery integrated to energy management strategy for pumping system. *Energy*, *153*, 743–762. https://doi.org/10.1016/j.energy.2018.04.073

Köhler, J., Wietschel, M., Whitmarsh, L., Keles, D., & Schade, W. (2010). Infrastructure investment for a transition to hydrogen automobiles. *Technological Forecasting and Social Change*, *77*(8), 1237–1248. https://doi.org/10.1016/j.techfore.2010.03.010

Kondratenko, E. V., Mul, G., Baltrusaitis, J., Larrazábal, G. O., & Pérez-Ramírez, J. (2013). Status and perspectives of CO2 conversion into fuels and chemicals by catalytic, photocatalytic and electrocatalytic processes. *Energy & Environmental Science*, *6*(11), 3112. https://doi.org/10.1039/c3ee41272e

Krishnan, V., & McCalley, J. D. (2016). The role of bio-renewables in national energy and transportation systems portfolio planning for low carbon economy. *Renewable Energy*, *91*, 207–223. https://doi.org/10.1016/j.renene.2016.01.052

Lan, D., Liang, B., Bao, C., Ma, M., Xu, Y., & Yu, C. (2015). Marine oil spill risk mapping for accidental pollution and its application in a coastal city. *Marine Pollution Bulletin*, *96*(1–2), 220–225. https://doi.org/10.1016/j.marpolbul.2015.05.023

Langmi, H. W., Ren, J., North, B., Mathe, M., & Bessarabov, D. (2014). Hydrogen Storage in Metal-Organic Frameworks: A Review. *Electrochimica Acta*, *128*, 368–392. https://doi.org/10.1016/j.electacta.2013.10.190

Li, H., & Yi, H. (2014). Multilevel governance and deployment of solar PV panels in U.S. cities. *Energy Policy*, Vol. 69, pp. 19–27. https://doi.org/10.1016/j.enpol.2014.03.006

Liao, S., Wang, F., Wu, T., & Pan, W. (2016). Crude oil price decision under considering emergency and release of strategic petroleum reserves. *Energy*, *102*, 436–443. https://doi.org/10.1016/j.energy.2016.02.043

Lim, C., Kim, D., Song, C., Kim, J., Han, J., & Cha, J.-S. (2015). Performance and emission characteristics of a vehicle fueled with enriched biogas and natural gases. *Applied Energy*, *139*, 17–29. https://doi.org/10.1016/j.apenergy.2014.10.084

Liu, Y., Zhang, Z., & Hu, R. (2018). Synthesis of three-dimensional hierarchically porous reduced graphene oxide–TiO2 nanocomposite for enhanced hydrogen storage. *Ceramics International*, *44*(11), 12458–12465. https://doi.org/10.1016/j.ceramint.2018.04.036

Lund, J. W., Freeston, D. H., & Boyd, T. L. (2011). Direct utilization of geothermal energy 2010 worldwide review. *Geothermics*, *40*(3), 159–180. https://doi.org/10.1016/j.geothermics.2011.07.004

Ma, M., Ouyang, L., Liu, J., Wang, H., Shao, H., & Zhu, M. (2017). Air-stable hydrogen generation materials and enhanced hydrolysis performance of MgH 2 -LiNH 2 composites. *Journal of Power Sources*, *359*, 427–434. https://doi.org/10.1016/j.jpowsour.2017.05.087

Marchenko, O. V., & Solomin, S. V. (2015). The future energy: Hydrogen versus electricity. *International Journal of Hydrogen Energy*, *40*(10), 3801–3805. https://doi.org/10.1016/j.ijhydene.2015.01.132

Merkoçi, A. (2006). Carbon Nanotubes in Analytical Sciences. *Microchimica Acta*, *152*(3–4), 157–174. https://doi.org/10.1007/s00604-005-0439-z

Mesarić, P., & Krajcar, S. (2015). Home demand side management integrated with electric vehicles and renewable energy sources. *Energy and Buildings*, *108*, 1–9. https://doi.org/10.1016/j.enbuild.2015.09.001

Muir, S. S., & Yao, X. (2011). Progress in sodium borohydride as a hydrogen storage material: Development of hydrolysis catalysts and reaction systems. *International Journal of Hydrogen Energy*, *36*(10), 5983–5997. https://doi.org/10.1016/j.ijhydene.2011.02.032

Nagpal, M., & Kakkar, R. (2018). An evolving energy solution: Intermediate hydrogen storage. *International Journal of Hydrogen Energy*, *43*(27), 12168–12188. https://doi.org/10.1016/j.ijhydene.2018.04.103

Nivetha, R., Grace, A. N., & Grace, A. N. (2019). *AC SC*.

Nkazi, D., Gotthard, S., & Ntho, T. (2019). *SC*.

Norgate, T., Haque, N., & Koltun, P. (2014). The impact of uranium ore grade on the greenhouse gas footprint of nuclear power. *Journal of Cleaner Production*, *84*, 360–367. https://doi.org/10.1016/j.jclepro.2013.11.034

O'Malley, K., Ordaz, G., Adams, J., Randolph, K., Ahn, C. C., & Stetson, N. T. (2015). Applied hydrogen storage research and development: A perspective from the U.S. Department of Energy. *Journal of Alloys and Compounds*, *645*, S419–S422. https://doi.org/10.1016/j.jallcom.2014.12.090

Obara, S., Morel, J., Okada, M., & Kobayashi, K. (2015). Study on the dynamic characteristics of an integrated coal gasification fuel cell combined cycle. *International Journal of Hydrogen Energy*, *40*(43), 14996–15011. https://doi.org/10.1016/j.ijhydene.2015.09.009

Ohashi, T. (2015). Carbon Nanotubes. In *Carbon Nanomaterials for Advanced Energy Systems: Advances in Materials Synthesis and Device Applications*. https://doi.org/10.1002/9781118980989.ch2

Onishi, N., Laurenczy, G., Beller, M., & Himeda, Y. (2018). Recent progress for reversible homogeneous catalytic hydrogen storage in formic acid and in methanol. *Coordination Chemistry Reviews*, *373*, 317–332. https://doi.org/10.1016/j.ccr.2017.11.021

Pascoli, S. Di, Femia, A., & Luzzati, T. (2001). Natural gas, cars and the environment. A (relatively) 'clean' and cheap fuel looking for users. *Ecological Economics*, *38*(2), 179–189. https://doi.org/10.1016/S0921-8009(01)00174-4

Pyle, D. S., Gray, E. M. A., & Webb, C. J. (2016). Hydrogen storage in carbon nanostructures via spillover. *International Journal of Hydrogen Energy*, *41*(42), 19098–19113. https://doi.org/10.1016/j.ijhydene.2016.08.061

Rahman, M. M., B. Mostafiz, S., Paatero, J. V., & Lahdelma, R. (2014). Extension of energy crops on surplus agricultural lands: A potentially viable option in developing countries while fossil fuel reserves are diminishing. *Renewable and Sustainable Energy Reviews*, *29*, 108–119. https://doi.org/10.1016/j.rser.2013.08.092

Rahmouni, S., Settou, N., Chennouf, N., Negrou, B., & Houari, M. (2014). A Technical, Economic and Environmental Analysis of Combining Geothermal Energy with Carbon Sequestration for Hydrogen Production. *Energy Procedia*, *50*, 263–269. https://doi.org/10.1016/j.egypro.2014.06.032

Ramesh, T., Rajalakshmi, N., & Dhathathreyan, K. S. (2015). Activated carbons derived from tamarind seeds for hydrogen storage. *Journal of Energy Storage*, *4*, 89–95. https://doi.org/10.1016/j.est.2015.09.005

Rather, S., & Nahm, K. S. (2014). Hydrogen uptake of high-energy ball milled nickel-multiwalled carbon nanotube composites. *Materials Research Bulletin*, *49*, 525–530. https://doi.org/10.1016/j.materresbull.2013.09.022

Rodriguez, J., Puzenat, E., & Thivel, P.-X. (2016). From solar photocatalysis to fuel-cell: A hydrogen supply chain. *Journal of Environmental Chemical Engineering*, *4*(3), 3001–3005. https://doi.org/10.1016/j.jece.2016.06.011

Silambarasan, D., Surya, V. J., Vasu, V., & Iyakutti, K. (2013). Single Walled Carbon Nanotube–Metal Oxide Nanocomposites for Reversible and Reproducible Storage of Hydrogen. *ACS Applied Materials & Interfaces*, *5*(21), 11419–11426. https://doi.org/10.1021/am403662t

Singh, A., Asmath, H., Chee, C. L., & Darsan, J. (2015). Potential oil spill risk from shipping and the implications for management in the Caribbean Sea. *Marine Pollution Bulletin*, *93*(1–2), 217–227. https://doi.org/10.1016/j.marpolbul.2015.01.013

Singh, S., Jain, S., PS, V., Tiwari, A. K., Nouni, M. R., Pandey, J. K., & Goel, S. (2015). Hydrogen: A sustainable fuel for future of the transport sector. *Renewable and Sustainable Energy Reviews*, *51*, 623–633. https://doi.org/10.1016/j.rser.2015.06.040

Stram, B. N. (2016). Key challenges to expanding renewable energy. *Energy Policy*, *96*, 728–734. https://doi.org/10.1016/j.enpol.2016.05.034

Tarasov, B. P., Arbuzov, A. A., Mozhzhuhin, S. A., Volodin, A. A., Fursikov, P. V., Lototskyy, M. V., & Yartys, V. A. (2019). Hydrogen storage behavior of magnesium catalyzed by nickel-graphene nanocomposites. *International Journal of Hydrogen Energy*, (xxxx). https://doi.org/10.1016/j.ijhydene.2019.02.033

van der Zwaan, B. C. . (2002). Nuclear energy. *Technological Forecasting and Social Change*, *69*(3), 287–307. https://doi.org/10.1016/S0040-1625(01)00127-5

Varshoy, S., Khoshnevisan, B., & Behpour, M. (2019). The dual capacity of the Ni[sbnd]Sn alloy/MWCNT nanocomposite for sodium and hydrogen ions storage using porous Cu foam as a current collector. *International Journal of Hydrogen Energy*, *44*(13), 6674–6686. https://doi.org/10.1016/j.ijhydene.2019.01.085

Verhelst, S. (2014). Recent progress in the use of hydrogen as a fuel for internal combustion engines. *International Journal of Hydrogen Energy*, *39*(2), 1071–1085. https://doi.org/10.1016/j.ijhydene.2013.10.102

Vringer, K., van Middelkoop, M., & Hoogervorst, N. (2016). Saving energy is not easy. *Energy Policy*, *93*, 23–32. https://doi.org/10.1016/j.enpol.2016.02.047

Wang, H., Zhu, Q.-L., Zou, R., & Xu, Q. (2017). Metal-Organic Frameworks for Energy Applications. *Chem*, *2*(1), 52–80. https://doi.org/10.1016/j.chempr.2016.12.002

Wiedenhofer, D., Lenzen, M., & Steinberger, J. K. (2013). Energy requirements of consumption: Urban form, climatic and socio-economic factors, rebounds and their policy implications. *Energy Policy*, *63*, 696–707. https://doi.org/10.1016/j.enpol.2013.07.035

Winter, C.-J. (2009). Hydrogen energy — Abundant, efficient, clean: A debate over the energy-system-of-change☆. *International Journal of Hydrogen Energy*, *34*(14), S1–S52. https://doi.org/10.1016/j.ijhydene.2009.05.063

Wu, L. M., Zhou, C. H., Keeling, J., Tong, D. S., & Yu, W. H. (2012). Towards an understanding of the role of clay minerals in crude oil formation, migration and accumulation. *Earth-Science Reviews*, *115*(4), 373–386. https://doi.org/10.1016/j.earscirev.2012.10.001

Xu, T., Chen, J., Yuan, W., Li, B., Li, L., Wu, H., & Zhou, X. (2018). Preparation and Hydrogen Storage Characteristics of Surfactant-Modified Graphene. *Polymers*, *10*(11), 1220. https://doi.org/10.3390/polym10111220

Yan, Q., Wang, A., Wang, G., Yu, W., & Chen, Q. (2011). Nuclear power development in China and uranium demand forecast: Based on analysis of global current situation. *Progress in Nuclear Energy*, *53*(6), 742–747. https://doi.org/10.1016/j.pnucene.2010.09.001

Yürüm, Y., Taralp, A., & Veziroglu, T. N. (2009). Storage of hydrogen in nanostructured carbon materials. *International Journal of Hydrogen Energy*, *34*(9), 3784–3798. https://doi.org/10.1016/j.ijhydene.2009.03.001

Zhang, F., Zhao, P., Niu, M., & Maddy, J. (2016). The survey of key technologies in hydrogen energy storage. *International Journal of Hydrogen Energy*, *41*(33), 14535–14552. https://doi.org/10.1016/j.ijhydene.2016.05.293

Zhou, C., & Szpunar, J. A. (2016). Hydrogen Storage Performance in Pd/Graphene Nanocomposites. *ACS Applied Materials and Interfaces*, *8*(39), 25933–25940. https://doi.org/10.1021/acsami.6b07122

Zhou, L. (2005). Progress and problems in hydrogen storage methods. *Renewable and Sustainable Energy Reviews*, *9*(4), 395–408. https://doi.org/10.1016/j.rser.2004.05.005

Zinkle, S. J., & Busby, J. T. (2009). Structural materials for fission & fusion energy. *Materials Today*, *12*(11), 12–19. https://doi.org/10.1016/S1369-7021(09)70294-9

#249: Study on available energy of capillary heat exchanger in coastal areas

Zhenpeng BAI[1], Yanfeng LI[2], Hua ZHONG[3]*

[1]Beijing Key Laboratory of green built environment and energy efficient technology, Beijing University of Technology, Beijing, China. baiyi1056@126.com
[2]College of Architecture and Civil Engineering, Beijing University of Technology, Beijing, China. liyanfeng@bjut.edu.cn
[3]Nottingham Trent University, Nottingham, NG1 4FQ UK. hua.zhong@ntu.ac.uk,
*Corresponding author

This paper studies the available energy of capillary heat exchanger systems (CHEs) in coastal areas. Compared with conventional ground source heat pump systems (GSHPs) with horizontal and vertical pipes used for storage and utilising thermal energy, CHEs is proposed to have a good performance in energy storage. The local soil temperature changed during operating period of capillary. The Influence of different burial conditions were analysed by the available energy efficiency of CHEs in summer and winter respectively. Results showed that the change of ambient temperature had a significant effect on exergy increment in capillary. With the increase of buried depth, the power consumption of the pump was obviously increased. When buried depth of the capillary was larger than 1.0 m, it was not economic to improve available energy efficiency by increasing the burial depth. In addition, for evaluating the available energy efficiency of CHEs, exergy efficiency was put forward for making comparison between GSHPs with horizontal pipe and the GSHPs with capillary as front part to extract energy based on the same cooling and heating demand. The total energy utilisation efficiency of CHEs was more than 70% in both summer and winter conditions. The results would provide theoretical guidance to utilisation of CHEs in coastal areas rationally.

Keywords: capillary heat exchanger; available energy; energy efficiency

1. INTRODUCTION

People are paying attention to the research of energy storage technology (Lewis, 2016). Most of energy is stored after being converted to heat. Solar thermal storage is a representative low temperature thermal storage. The solar energy can be converted into fuel, heat, or electricity. Despite the costs of solar panels have dropped rapidly, however, technology gaps still exist for realising cost effective sustainable deployment, which could combine storage technologies to supply reliable, suitable energy (Lewis, 2016). Energy consumed in buildings by heating ventilation and air cconditioning (HVAC) systems could be reduced with proper implementation of a thermal storage system (TES). The reason is that TES allows the storage of thermal energy (heat and cold) for a later use (Navarro, 2016).

At present, the energy consumption of civil buildings accounts for more than 20% in the energy consumption. And energy consumption by heating and cooling accounts for 56%-58% in the total building energy consumption. In order to save energy, renewable energy utilisation technology has developed rapidly. In this research field, vertical and horizontal GSHPs have good energy storage effect (Omer, 2008). It uses shallow geothermal energy as heat source. GSHPs conducts heat extraction or injection into the soil through horizontal and vertical pipes. Vertical GSHPs uses deep holes to extract cool and heat, the tubes as heat exchanger take advantage of the constant ground temperature. The high excavation costs for these deep heat wells are reflected in the GSHPs cost. As for horizontal GSHPs, it requires large surface areas to install the heat exchanger, which is difficult in urban areas (Benli, 2013). Therefore, the thermal performance is mainly restricted by local environment conditions, which would affect the economy of GSHPs. This thermal storage system provides a good choice to keep thermal comfort environment for human life (Kharseh, 2008).

The performance of heat pumps has been studied in many previous studies. Z.C. Zeng set up a thermodynamic analysis model for the air source heat pump system in refrigerant direct floor radiant heating (Zeng, 2010.). The energy efficiency ratio of GSHPs and the exergy loss of GSHPs component were calculated and analysed in different outdoor environments. And the comprehensive thermodynamic performance of different heating systems were compared and evaluated. H. Zeng conducted three models for vertical ground heat exchangers to study the GSHPs efficiency (Zeng, 2003). Chen proposed the thermodynamic exergy analysis model in GSHPs with buried pipes (Chen, 2009). The exergy analysis of the heat exchanger system was carried out with buried pipes in different climatic regions and buried depths. Ozgener made the exergy analysis of solar assisted GSHPs (Ozgener, 2007). Esen combined artificial neural network (ANN) and adaptive neuro-fuzzy inference system (ANFIS) in the slinky (the slinky-loop configuration is also known as the coiled loop or spiral loop of flexible plastic pipe) type ground heat exchanger (GHE) (Esen, 2017). Balbay conducted the possibility of a GSHPs consisting of the vertical type single U-borehole heat exchangers for snow melting on pavements and bridge decks (Balbay, 2010). However, these studies did not take the capillary heat exchange system into account.

Capillary heat exchange is commonly used indoor air conditioning system. It consists of plastic capillary grids with the dimension of 3.4 x 0.55mm or 4.3 x 0.85 mm. The plastic capillary grid space ranges from 10mm to 40mm. The liquid flow velocity range is 0.05 to 0.2 m/s in the capillary. In recent years, capillary heat exchanger has also been used as a front energy extraction device in GSHPs. Therefore, GSHPs allows heat extraction and injection into the soil with CHEs. As for China, the shallow layer of offshore area is rich in geothermal energy, it is necessary to develop and utilise this kind of renewable energy. However, few studies have been made on thermodynamic analysis of shallow buried capillary heat exchange system in coastal area.

In this paper, the aim is to study the available energy of CHE in coastal areas. CHEs was designed with 12.5% aqueous solution of ethylene glycol as the working medium. The first law and the second law of thermodynamics were used to establish the thermal analysis model. The parameter such as outlet temperature of capillary was determined by numerical simulation. The capillary heat transfer process was analysed in detail. The energy conversion rate, the loss coefficient and commission efficiency of CHEs were determined. The energy comprehensive thermodynamic performance was evaluated for CHEs. This research could provide theoretical and practical basis on optimising the energy efficiency characteristics for CHEs.

2. METHOD

In CHEs, thermal energy is stored as available energy in the capillary. The theoretical analysis and numerical simulation are adopted to study the available energy of CHEs in coastal areas. The capillary outlet temperature is obtained by numerical simulation. The exergy analysis is conducted in capillary and exergy value of capillary is obtained. Then, the energy conservation effect of CHEs with different structural forms are investigated. Three different locations of CHEs are also considered for getting more shallow geothermal energy. Moreover, the equivalent efficiency of the capillary heat exchange system are calculated for winter and summer conditions respectively.

2.1. Thermal energy storage

In general, water is the most appropriate material for heat storage due to the high specific heat and inexpensive (Kant, 2016). In the sensible heat storage, thermal energy is stored by increasing the temperature of water. The water temperature changes in the capillary during the process of heat storage and heat release. The amount of heat storage depends on the specific heat of water, temperature difference and the numbers of capillary. The energy storage amount E is expressed by Equation 1.

Equation 1: The energy storage amount is decided by the temperature change value of the water.

$$E=m\int_{T_1}^{T_2} c_p dT = mc_p(T_2-T_1)$$

Where:

- m= the mass flow (kg/s)
- c_p = the specific heat at constant pressure (kJ/(kg K))
- T_1= the lower temperature in the storage operates (K)
- T_2 = the higher temperature in the capillary energy storage operates (K)

2.2. Exergy analysis of capillary

Exergy is defined as the part of energy that can be converted to useful work with the maximum extent, when the system reversibly changes from one state to another given state of phase equilibrium. During the process, there is no other heat source except the variation of environment temperature. All the actual thermodynamic processes are irreversible. The irreversible process is driven by heat and mass transfer, and these two factors ensure the process to continue. The irreversibility of the process leads to the work and energy loss. And the quality of energy is changed in the process of transmission. Exergy is not fully conserved in the actual process. Thus, the exergy of the input system is not equal to the exergy of output system. The main reason for exergy loss are the discharge of substance. Another reason causing exergy loss is energy from the system to the environment, and the exergy dissipation caused by energy irreversibility in the transition process. From the point of view of the total energy system, it is important to control the exergy dissipation at a certain optimum value, and to minimise the discharge of material and energy to the environment, for reducing the effective energy loss of the system (Ahmadi, 2011).

2.3. Calculation of exergy value

In the process of heat transfer between CHE and the local soil, the temperature of soil is T_1, which is assumed to be constant. Temperature of working medium with the glycol aqueous solution in capillary changes from T_2' to T_2''. For a finite process, the specific heat of working medium is constant (Ng, 2017). Then, the energy loss of soil and CHEs can be calculated by Equation 2.

Equation 2: The loss energy of soil and capillary heat exchange system Π

$$\Pi = QT_0(\ln\frac{T_2''}{T_2'})/(T_2''-T_2')$$

Where:

- Q= the rate of heat exchange between glycol solution and local soil (W)
- T_0 = the environment temperature (K)
- T_2' = the inlet temperature in capillary (K)
- T_2'' = the outlet temperature in capillary (K)

According to the thermodynamic principle, the useful work is done by the open system with steady flow from the initial state to the environmental state through reversible process. For 1 kg working medium flowing through the open system, the exergy can be expressed as Equation 3 (Zhao, 2009).

Equation 3: For the 1 kg working fluid flowing through the open system, the exergy expressed as ex.

$$ex = w_{max} = c_p(T-T_0) - T_0(c_p\ln\frac{T}{T_0})$$

Where:

- ex= exergy (kJ/kg)
- w_{max} = the maximum useful work of fluids (kJ /kg)
- T_0 = environment temperature (K)
- T= working temperature at initial state (K)
- c_p = the specific heat at constant pressure (kJ/(kg K))

Available energy efficiency in CHEs is defined as the ratio of heat loss to heat entering in Equation 4.

Equation 4: Available energy efficiency in CHE η .

$$\eta = \frac{\mathrm{Ex}_{dest}}{Ex_1} \times 100\%$$

Where:

- Ex_{dest}= the amount of available energy entering CHE.
- Ex_1 = the total energy absorbed by the CHE.

2.4. Numerical simulation method

The picture of CHE mat is shown in Figure 1. The CHE model was built by FLUENT software as in Figure 2. In order to solve the governing equations including momentum equation, energy equation, SIMPLE method are used in the second order upwind discrete scheme for velocity and pressure coupling problems (Su, 2017). Because the physical model is laminar flow, the laminar model is selected in FLUENT software (Ng, 2017). The working medium is a 12.5% aqueous solution of ethylene glycol in the capillary.

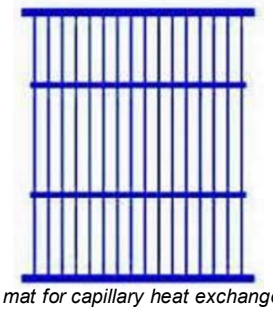

Figure 1: Picture of the mat for capillary heat exchanger with interval of 20 mm

According to actual operating conditions of CHEs, two different heat transfer conditions were simulated in winter and summer, respectively. CHEs were placed in the soil under different locations including seawater, coastal area and shoal beach area respectively. The CHEs buried in the soil has two boundary conditions. They are temperatures of the upper surface and the bottom surface of the surrounding soil. There is a fluctuation in the temperature on the upper surface of the surrounding soil. In comparison, the temperature of the lower surface is almost constant.

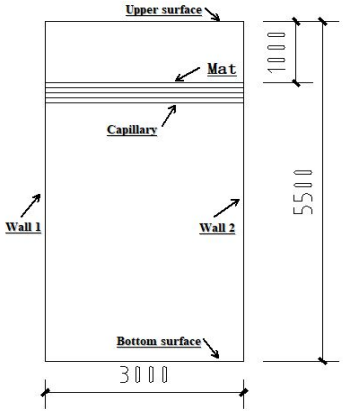

Figure 2: Physical model of capillary heat exchanger with 5 mats.

The front view of simulated CHEs with 5 mats is shown in Figure 2. CHEs with fixed structure has the length of capillary is 3000 mm, the spacing of mat is 160 mm. The interval of grids between capillaries in Figure 1 is 20mm. The five capillary mats are buried in the soil at 1000 mm under the ground surface. The distance from bottom surface to top surface of soil is 5500 mm.

The boundary conditions are given as follows: wall 1 and wall 2 are adiabatic boundary. The upper soil surface temperature varies with different seasons. The bottom surface temperature of soil is given as a constant. The CHEs is composed of surrounding soil and 12.5% ethylene glycol solution circulating in capillary (Lazaar, 2015). To facilitate theoretical analysis, the following assumptions are made (Hazami, 2004):

(1) The inlet velocity is set as 0.1m/s in the capillary. The flow is laminar. (2) The velocity of ethylene glycol is constant in the capillary. (3) The design inlet temperatures of the CHEs are -1℃ in winter and 37℃ in summer. (4) The indoor terminal load of building is constant. The supply water and return water temperature are constant. (5) Capillary is located in the shoal near the coast area. The temperature of upper soil surface follows the cosine function as Equation 5.

Equation 5: The temperature of upper surface t_s.

$$t_s = 14.4 + 10.1983\cos\left(\frac{\pi}{6}\tau + 2.023\right) + 0.8805\cos\left(\frac{\pi}{3}\tau + 2.6274\right)$$

Where:

- τ = the month

When the medium flows in the CHEs, it is considered as incompressible flow. The physical parameters are listed in Table 1. The temperatures of sea water are 3.7°C in winter, and 24.6°C in summer, respectively. It would influence the upper soil surface temperature t_s.

Table 1: Capillary heat exchanger system parameters.

Parameter	Glycol	Capillary	Seawater	Soil
Coefficient of thermal conductivity （$W/(m\cdot K)$）	0.53	0.24	0.56	1.6
The density （kg/m^3）	1015	900	1025	1600
Specific heat at constant pressure （$J/(kg\cdot K)$）	3980	2000	4217	2530
Pr	17.5			

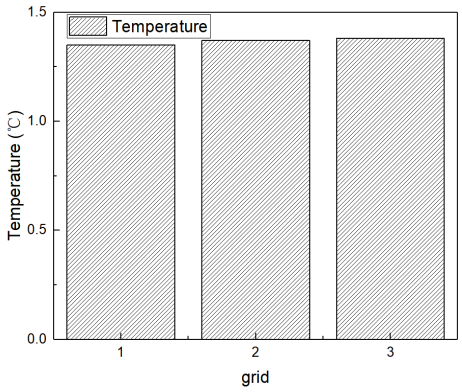

Figure 3: Capillary outlet temperature with different number grids in winter

In order to ensure the predicted results on heat transfer are plausible enough, it is necessary to conduct the analysis of mesh grid size sensitivity before numerical simulation. Different number mesh grids of capillary (grid 1 = 620,000, grid 2 = 1,240,000, grid 3 = 2,100,000) were selected. As shown in Figure 3, the capillary outlet temperature was obtained. When the number of grids changed from grid 1 to grid 3, the simulation results showed that the capillary outlet temperature was about 1.37°C in winter. And the influence error of different grids was less than 5% on the calculation results, which met the requirement of calculation accuracy. When grid 2 was used, it was noticed that the grid had nothing to do with the actual calculation accuracy and cost. Hence, grid 2 has been proved to be necessary to acquire accurate results.

3. RESULTS AND DISCUSSION

In this section, the effects of the CHEs are discussed. The GSHPs using capillary as front part to extract energy from the local soil was studied. The performance of GSHPs with capillary was compared with that of GSHPs with horizontal pipes based on the same cooling and heating demand. The total energy utilisation efficiency of these two system are determined in order to evaluate the performance of CHEs. Because the composition of the load side of the heat pump system is basically identical, the main difference lies in the heat recovery device at the front end of the heat pump. As shown in Figure 4, the principle diagram GSHPs with horizontal pipes and GSHPs with capillary. Therefore, the influence of capillary heat exchange parameters and boundary conditions, such as capillary length, burial depth, winter and summer conditions, on the yield increment is studied.

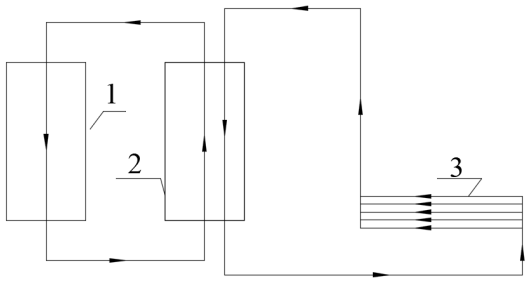

Figure 4: The principle diagram GSHPs with horizontal pipes and GSHPs with capillary.

1. Indoor room; 2. GSHPs 3. Horizontal pipes or capillary as front part to extract energy.

3.1. Comparison between GSHPs with horizontal pipes and GSHPs with capillary

Both conventional GSHPs with horizontal pipe and GSHPs with capillary have a steady flow. A fixed form of CHEs was selected as Figure 2. The numerical simulation was carried out for steady state.

For the conventional GSHPs with horizontal pipe ran in winter, water temperature was set as 12°C at the inlet and was 10°C at outlet. While in summer, the inlet temperature was 32 °C and outlet temperature was 25°C. The surrounding soil temperature was 3.7°C in winter and 25°C in summer. This parameters were commonly selected and adopted in design process of GSHPs with horizontal pipe as front part in China (Zeng, ZC, 2010.).

For the GSHPs with capillary, the CHE was buried in the sand. The buried depth was 1.0m. The capillary outlet average temperature after a week of operation was calculated by simulation. Thus, the exergy of capillary outlet was obtained by using Equation 3. Then, the energy saving efficiency of CHEs were computed by Equation 4 for the winter condition and summer condition.

Winter condition

As for the conventional GSHPs with horizontal pipe, the water exergy, ex_1, is 0.511 kJ/kg at inlet with temperature of 12°C .At outlet, water temperature is 10°C and water exergy, ex_2, is 0.296 kJ/kg.

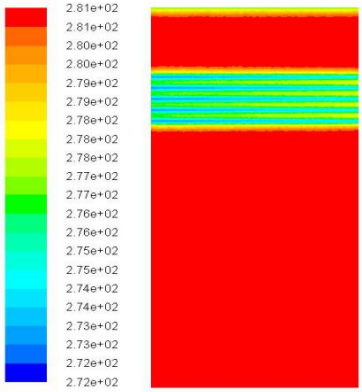

Figure 5: Temperature contours of capillary model in winter.

For CHEs, The capillary model temperature field was calculated with the FLUENT software in winter as shown in Figure 5. It could be found that the capillary outlet water temperature was 1.37°C in winter. The capillary outlet water temperature by numerical simulation results were in good agreement with the experimental results (Li, 2016).

For the GSHPs with capillary, when the inlet temperature was -1°C, the aqueous solution of ethylene glycol exergy, ex_3, is 0.169 KJ/kg. At the outlet, temperature was calculated as 1.37°C, the aqueous solution of ethylene glycol exergy, ex_4, is 0.041 kJ/kg according to Equation 3.

The mass flow ratio of the water in two systems can be obtained by the equation $Q=mc_p(T_2''-T_2')$. Based on the temperature difference of two system, the ratio of the conventional GSHPs mass, m_1, to the GSHPs with capillary mass, m_2, i.e, $m_1/m_2=0.213$.

When the temperatures at inlet and outlet were 12°C and 10°C, the unit loss of the area per unit time was: $\Delta E_1=m_1(ex_1-ex_2)=0.215m_1$ for the conventional GSHPs with horizontal pipe; for the GSHPs with capillary, the temperatures at inlet and outlet were -1°C and 1.37°C, the unit loss of the area per unit time was: $\Delta E_2=m_2(ex_3-ex_4)=0.218m_2$. When these two systems have the same heating effect, the energy saving of the GSHPs with capillary is $\eta=(\Delta E_1-\Delta E_2)/\Delta E_1\times100\%=87.3\%$

Summer condition

As for the conventional GSHPs with horizontal pipe, the water exergy, ex_5, is 0.379 kJ/kg at inlet with temperature of 32°C. At outlet, water temperature is 25°C and water exergy, ex_6, is 0.005 kJ/kg.

For CHEs, The capillary model temperature field was calculated with the FLUENT software in summer as shown in Figure 6. It could be found that the capillary outlet water temperature was 34°C in summer. The capillary outlet water temperature by numerical simulation results were in good agreement with the experimental results (Li, 2016).

For the GSHPs with capillary, when the inlet temperature was 37°C, the aqueous solution of ethylene glycol exergy, ex_7, is 1.053 KJ/kg. At outlet, temperature was calculated as 34°C, the aqueous solution of ethylene glycol exergy, ex_8, is 0.609 kJ/kg according to Equation 3.

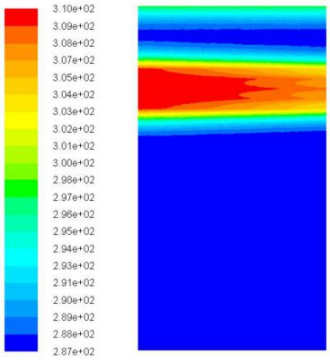

Figure 6: Capillary model temperature contours in summer.

The mass flow ratio of the water in two systems can be obtained by the equation $Q=mc_p(T_2''-T_2')$. Based on the temperature difference of two system, the ratio of the conventional GSHPs mass, m_1, to the GSHPs with capillary mass, m_2, i.e, $m_1/m_2=0.213$.

When the temperatures at inlet and outlet were 32°C and 25°C, The unit loss of the area per unit time was: $\Delta E_3=m_1(ex_5-ex_6)=0.374m_1$ for the conventional GSHPs with horizontal pipe; For the GSHPs with capillary, the temperatures at inlet and outlet were 37°C and 34°C, the unit loss of the area per unit time was: $\Delta E_4=m_2(ex_7-ex_8)=0.444m_2$; When these two systems have the same cooling effect, the energy saving of the GSHPs with capillary is $\eta=(\Delta E_3-\Delta E_4)/\Delta E_3\times100\%=74.7\%$.

It can be seen from the calculated results that GSHPs with capillary can save 87.3% in winter and 74.7% in summer compared with the GSHPs with conventional horizontal pipes, respectively. The CHEs can take the "quality" and "quantity" of energy into account. The capillary energy conservation is not only reflected in the quantity of energy, but also in the quality of energy.

3.2. Influence of capillary buried depth and capillary length

In order to study the energy conservation effect, the CHEs contained of different structural forms were analysed. Conditions with different length and depth were selected for CHEs in the coastal area. The average temperature of the capillary outlet was obtained by simulation. According to the exergy calculation formula, the exergy efficiency was calculated. The exergy values were calculated for winter and summer conditions.

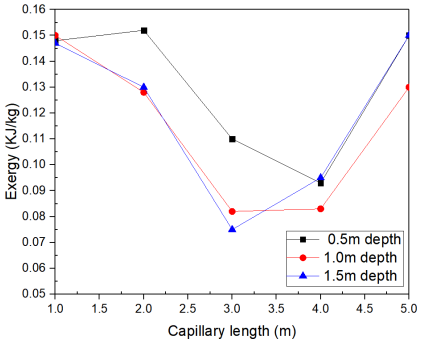

Figure 7: Capillary outlet water exergy with different length and depth in winter.

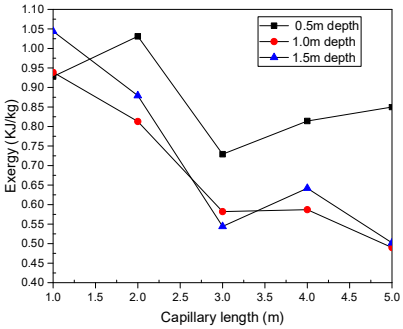

Figure 8: Capillary outlet water exergy with different length and depth in summer.

Effect of the capillary length

Figure 6 shows the water exergy at outlet for conditioning with different length and depth in winter. It can be found that when the capillary length is shorter than 3m, the output exergy value of the capillary shows a downward trend for three buried depths with increase of the capillary length. However, there is turning point of capillary length. For buried depths of 0.5m, 1.0 and 1.5m, the turning points length are 4.0m, 3.0m and 3.0m respectively. The reason is that the capillary has an optimum length in which it could sufficiently exchange heat with the surrounding environment. As for water exergy at outlet in summer in Figure 7, the optimum length of capillary is about 3m.

Effect of the buried depth

As shown in Figures 6 and 7, the water exergy at outlet for 0.5m depth is clearly higher those of conditions with depth of 1.0m and 1.5m. It can be explained that the atmosphere environment could influence the upper surface temperature. For a smaller buried depth, heat transfer process of capillary is clearly influenced by upper surface temperature and then outlet temperature would be lower. In addition, the trend of water exergy are almost same for conditions with depth of 1.0m and 1.5m. However, the trend for capillary with the buried depth of 1.0m is different from those of conditions with depth of 1.0m and 1.5m. The reason that heat transfer process of capillary is almost not influenced by upper surface temperature with depth of 1.0m.

3.3. The effect of buried locations

The CHEs was placed in three different locations. First, the capillary was installed in the seabed water as caissons. Second, the capillary was put in offshore seabed soil. Third, the capillary was set in the soil of shoal beach areas. Under steady conditions, results of average temperature were obtained at outlet of CHEs in winter and summer conditions by numerical simulation. Results are shown in Table 2.

When CHEs is placed at different locations in coastal area, the equivalent energy utilisation efficiencies are different. The equivalent efficiencies of CHEs are calculated in winter and summer, respectively.

In winter, the equivalent exergy values of capillary outlet fluids in seawater, offshore seabed soil and beach area were 0.054, 0.048 and 0.082, respectively. The equivalent exergy efficiencies of capillary outlet fluids in seawater, offshore seabed soil and beach area were 68.1%, 71.4%, 51.7%, respectively. In summer, the equivalent exergy values of capillary outlet fluids in seawater, offshore seabed soil and beach area were 0.795, 0.775 and 0.582, respectively. The equivalent exergy efficiency of capillary outlet fluids in seawater, offshore seabed soil and beach area were 19.2%, 21.4%, 8.0%, respectively.

Table 2: Capillary heat exchanger system parameters.

Temperature (℃)	Seabed water (℃)	offshore seabed soil (℃)	Beach area soil (℃)
Environment in winter	3.7	3.7	3.7/0.2
Capillary outlet in winter	1.04	1.18	0.43
Environment in Summer	25	25	25/31.5
Capillary outlet in summer	35.77	35.62	36.1

Among three different locations the exergy efficiency of CHEs in shallow buried beach area has the lowest value of 51.7%. The reason is that the upper surface temperature is lowest because there is a periodic contact between the upper surface and air. For the condition of offshore seabed soil, the equivalent exergy values is highest. The reason is the upper surface temperature is highest due to the influence of sea water on seabed soil. For the seabed water condition, the bottom surface of capillary is sea water, the exergy efficiency value is medium. Therefore, location of arrangement is an important factor for performance of CHEs. Offshore seabed soil is the best choice for burying for GSHPs with capillary in coastal area.

4. CONCLUSION

The selection of CHE as energy extraction device could improve the energy utilisation efficiency in coastal area. When CHEs is placed at the coastal area, the energy utilisation ratio is higher that of device located in inland. The available energy efficiency of capillary is large and the exergy loss rate is small because sea water has great thermal energy. Based on the same cooling and heating demand, the GSHP with capillary network can save energy 87.3% in winter and 74.7% in summer by comparison with the conventional GSHPs with horizontal pipe.

Energy utilisation efficiency increased with the capillary length less than 3m. This length is conducive to improve the available energy utilisation efficiency. Three locations of CHEs are compared for analysing the surrounding environment effect. The total energy utilisation efficiency for CHEs buried in coastal area is highest among three conditions. The value is higher than 70% in winter. The energy loss coefficient of system was also significantly smaller than the other two conditions. The offshore CHEs has a great potential for energy conservation and a high priority.

In the future work, operating conditions should be designed as much as possible to obtain more general applicable results. However, weather conditions are also the limit to the operation of CHEs. For example, supply water temperature needed to keep constant while the ambient soil temperature is floating. Another issue limits the performance of CHEs is the sensible heat loss, when it charges and discharges energy as a consequence of heating and cooling the water. Also, attention should be paid on area of building, yet with appropriate size than the numbers used CHEs.

5. ACKNOWLEDGEMENT

This work was supported by “the national natural science foundation of a major plan, and the thermal transfer and thermodynamic index system in the extreme heat and humid climate zone in China” (Project No 51590912).

6. REFERENCES

Ahmadi, P., Dincer, I., & Rosen, M. A., 2011. Exergy, exergoeconomic and environmental analyses and evolutionary algorithm based multi-objective optimization of combined cycle power plants. Energy, 36(10), 5886-5898.

Balbay, A., & Esen, M., 2010. Experimental investigation of using ground source heat pump system for snow melting on pavements and bridge decks. Scientific Research and Essays, 5(24), 3955-3966.

Benli, H., 2013. A performance comparison between a horizontal source and a vertical source heat pump systems for a greenhouse heating in the mild climate Elaziğ, Turkey. Applied Thermal Engineering, 50(1), 197-206.

Chen Y, Dai C S, Zhao J., 2009. Source-side exergy analysis of ground-source heat pump systems with buried pipes. Tianjin University Science, 42 (07): 567-573.

Esen, H., Esen, M., & Ozsolak, O., 2017. Modelling and experimental performance analysis of solar-assisted ground source heat pump system. Journal of Experimental & Theoretical Artificial Intelligence, 29(1), 1-17.

Hazami, M., Kooli, S., Lazaar, M., Farhat, A., Kerkani, C., & Belguith, A., 2004. Capillary polypropylene exchangers for conditioning of museum aquariums (Tunisia). Desalination, 166, 443-448.

Kant, K., Shukla, A., Sharma, A., Kumar, A., & Jain, A., 2016. Thermal energy storage based solar drying systems: A review. Innovative Food Science & Emerging Technologies, 34, 86-99.

Kharseh, M., & Nordell, B., 2008. Potential of ground-source heat pump systems for heating/cooling in Syria. Renewable Energy Group, Division of Architecture and Infrastructure, Luleå University of Technology (LTU), Luleå, Sweden.

Lazaar, M., Bouadila, S., Kooli, S., & Farhat, A., 2015. Comparative study of conventional and solar heating systems under tunnel Tunisian greenhouses: Thermal performance and economic analysis. Solar Energy, 120, 620-635.

Lewis, N. S., 2016. Research opportunities to advance solar energy utilization. Science, 351(6271), aad1920.

Li Z. Study on the operating characteristics of Coastal Shoal Capillary Heat pump system [D]. Qingdao University of Technology, 2016.

Navarro, L., De Gracia, A., Colclough, S., Browne, M., McCormack, S. J., Griffiths, P., & Cabeza, L. F., 2016. Thermal energy storage in building integrated thermal systems: A review. Part 1. Active storage systems. Renewable Energy, 88, 526-547.

Ng, K. C., Shahzad, M. W., Son, H. S., & Hamed, O. A., 2017. An exergy approach to efficiency evaluation of desalination. Applied Physics Letters, 110(18), 184101.

Omer, A. M., 2008. Ground-source heat pumps systems and applications. Renewable and sustainable energy reviews, 12(2), 344-371.

Ozgener, O., Hepbasli, A., & Ozgener, L., 2007. A parametric study on the exergoeconomic assessment of a vertical ground-coupled (geothermal) heat pump system. Building and Environment, 42(3), 1503-1509.

Su, M., Yin, J. X., & Wang, J., 2017. Comparative analysis of heat transfer performance of the smooth U-tube and finned U-tube in ground source heat pump. Chemical Engineering (China), (11), 8.

Zeng Z C., 2010. Research on energy efficiency and floor heat transfer of air source heat pump direct floor radiant heating. Zhengzhou University.

Zeng, H., Diao, N., & Fang, Z., 2003. Efficiency of vertical geothermal heat exchangers in the ground source heat pump system. Journal of Thermal Science, 12(1), 77-81.

Zhao J. W., 2009. Temperature field numerical simulation and technical and economic analysis of ground source heat pump ground heat exchanger. Hefei University of Technology.

#250: Humidification-dehumidification desalination system using a state of art hollow fibre membranes

Omar RAMADAN[1], Siddig OMER[2], Mahmoud SHATAT[3], Mona NAIM[4], Yasser DESSOUKY[5], Mahmoud ELEWA[6], Saffa RIFFAT[7]

[1] University of Nottingham, Nottingham, omar.ramadan@nottingham.ac.uk
[2] University of Nottingham, Nottingham, siddig.omer@nottingham.ac.uk
[3] Oxford Policy Management, UK, Mahmoodshatat@hotmail.com
[4] Alexandria University, Egypt, monanaim66@gmail.com
[5] Arab Academy for Science and Technology and Maritime Transport, Egypt, ygd@aast.edu
[6] Arab Academy for Science and Technology and Maritime Transport, Egypt, mahmoud.elewa@gmail.com
[7] University of Nottingham, Nottingham, saffa.riffat@nottingham.ac.uk

The increase in global population growth and population density has limited the ability of many nations to sustain fresh water supply. Sea or brackish water desalination provides a sustainable and nonconventional solution for the world's water scarcity and the rapid increase in fresh water demand. This article investigates humidification-dehumidification water desalination system, using a state of art hollow fibre membranes, which are employed in the humidification chamber of the experimental rig, to humidify and heat the ambient air. The humidified air is then cooled via heat transfer in dehumidification chamber resulting in condensation of the water vapour to produce fresh potable water. A number of experimental tests were carried out using the test rig to investigate its water production capacity. A synthetic seawater water solution was prepared in the lab and used for the tests and its total dissolved solids (TDS) and electrical conductivity were measured before and after the distillation process. The aim of this work is to investigate and evaluate the performance of hollow fibre membranes as a humidification medium for the ambient air and optimise the operational performance of the system, using different mass flow rates of saline water and air. A water quality analysis showed that levels were well within the World Health Organization guidelines for drinking water. Further research is being performed to improve the performance of the installation.

Keywords: Water desalination, humidification, dehumidification, sea water

1. INTRODUCTION

The rapid global growth in population has led to the increase in demand for fresh water, which reduced the ability of many local supplies to sustain fresh water (Lee et al, 2011). Where people are struggling to balance declining per capita water supplies with the rapid demands rising populations (Shatat et al, 2013). Even though over 71% of the earth's surface is covered with water, however around 97.5% of water on the earth is sea or brackish water, which contains large amounts of salt (Zhang et al 2017). It is forecasted that by the year 2025 water demand will exceed supply by 56%, due to persistent regional droughts, shifting of the population to urban coastal cities. In the next 50 years, water scarcity is expected to affect 2 to 7 billion people according to the United Nations (Teow et al, 2017). Water desalination system purifies brackish water or seawater, hence producing fresh water with total dissolved solids within the permissible limit of 500 ppm or less. Production of fresh water using desalination technologies driven by renewable energy presents a viable solution to the water scarcity at remote areas characterised by lack of potable water and conventional energy sources. However, conventional water desalination systems have some disadvantages, for example, electrodialysis, reverse osmosis and distillation are capital and energy intensive with hard maintenance regularly required (Wang et al, 2012, Welgemoeda et al, 2005, Yang et al, 2005). There are different types of water desalination systems, including thermal processes with phase change, membrane processes including Reverse osmosis (Gabelich et al, 2007), hybrid processes including phase change and membranes (Zhang et al 2017). However, such plants are not economically viable in remote areas, even those near a coast, and an electricity supply can also be lacking. The development of alternative, compact, small-scale water desalination systems is imperative for the population in such areas. In this article, experimental investigation is carried out for humidification-dehumidification based on water desalination system using hollow fibre membranes as a humidification medium under the ambient air conditions.

2. EXPERIMENTAL SETUP

Hollow fibre membrane bundles are used in the humidification chamber to humidify and heat the air, via heat and mass transfer with hot salty water. The resulting hot humid air is then cooled via heat exchange with cold salty water, in a shell and tube heat exchanger, leading to condensation of the air on the walls of the tube, and producing fresh potable water.

2.1. System Description

In the proposed system, a synthetic solution of sodium chloride with concentration of 35000 mg/l salinity is used to simulate the seawater, which is measured by Kern Salt Refractometer. The hollow fibre membrane bundles used in the humidification chamber are polypropylene with pore size of 0.1 × 0.5 µm. Air is blown from an environmental chamber under controlled conditions (temperature and humidity) using a fan. Heat and mass transfer occurs between the air on the shell side of the hollow fibre membrane humidifier and the hot salty water flowing on the inside of the fibre bundles. Under trans-membrane vapour partial pressure differences, water vapour from saline water inside the fibres can pass through the pores. The water vapour is absorbed by the air stream outside the fibre, resulting in the outlet air becoming hot and humid, while the outlet salty water becomes cooler with slightly higher salinity. The hot humid air then is condensed on the on the walls of the shell and tube heat exchanger dehumidification unit via heat transfer with the cold salty water, and the produced fresh water is collected in fresh water tank. The new hot salty water from the heat exchanger with the hot humid air in the dehumidification unit is pumped to a stainless steel tank where it is further heated using an immersion heater before it enters the humidification unit. The schematic diagram for the design is shown in Figure 1.

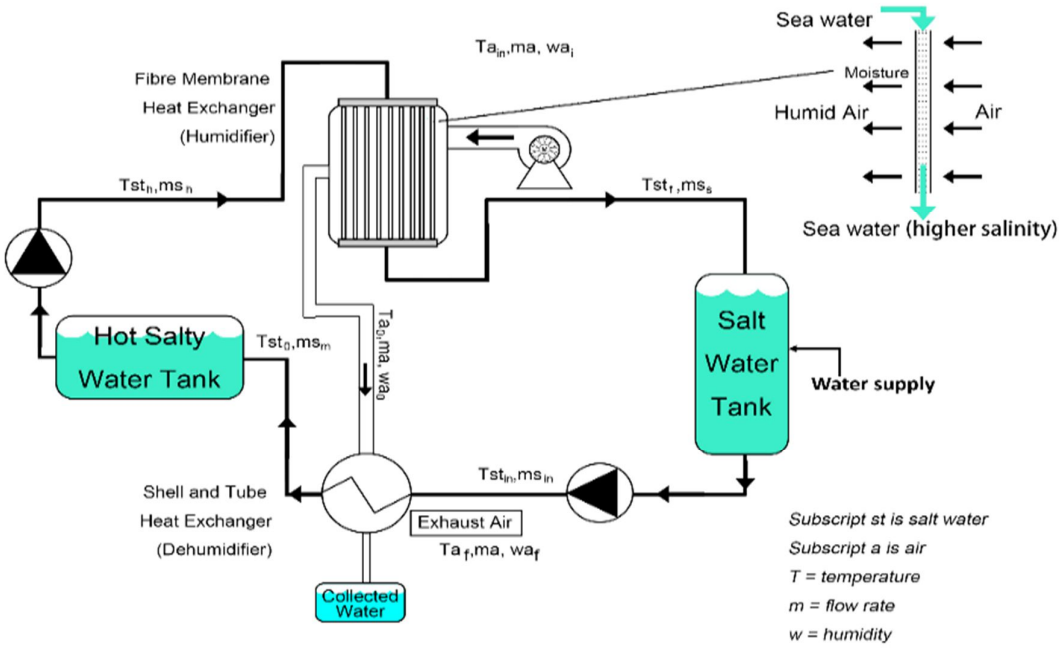

Figure 1: Schematic diagram of the proposed system process

2.2. Experimental Design

The aim of the experimental investigation is to optimise the system operation using different flow rates of the salty water and the air on the system's performance. The system components include the humidification chamber consisting of 18 bundles of hollow fibre membranes provided by Zena with 1385 fibres per bundle, while a shell and tube heat exchanger is used as the dehumidification chamber. An immersion heater is used to heat the salty water to the required temperature (after initial heating in the shell tube heat exchanger). Two Grundfos pumps are used to pump the salty water, the first circulating the salty water from the cold salty water storage tank to the shell and tube heat exchanger while the second pump is used to circulate the hot salty water from the storage tank with the immersion heater to the humidification unit. An in-line ducted fan integrated with a speed controller is used to circulate air at ambient temperature and humidity to the humidification chamber. Atrato Ultrasonic Flow Meter is used to monitor the liquid flow rates. Sensirion EK-H4 evaluation kit was used to monitor the humidity and temperature levels of the air at different locations of the system. Thermocouples were used to measure the temperature of the air and the salty water at different locations and the measured data was logged into a data logger (Data Taker DT85). The experimental rig developed is shown in Figure 2. Initially, the environmental chamber (source of air), is set to temperature of 26°C and 65% relative humidity for all the tests. The immersion heater temperature in the stainless steel tank is set to 60°C before starting the operation. The system was then operated for 1 hour for each flow rate of air and salty water. The air temperature and relative humidity levels were measured every second including controlled ambient temperature (from the environmental chamber) and at the outlet of the humidification chamber. While the salty water temperature was measured every second at the inlet to the dehumidification chamber (shell and tube heat exchanger), at the outlet of the stainless steel tank (with immersion heater) and at the outlet of the humidification chamber. The inlet ambient air speed was varied from 0.4m/sec to 1.4m/sec while maintaining the flow rate of the salty water at a constant value of 1litre/minute. Then the salty water flow rates were varied from 0.5litres/minute to 1.5litres/minute, while maintaining the air speed at a constant value of 0.9m/sec.

Figure 2: System experimental test rig

2.3. Experimental Results and Discussion

The results for the temperature and humidity levels investigated for the two tests carried out for variable flow rates for the salty water and variable speed of inlet air from the environmental chamber. The level of produced fresh water varied from 550ml/hour to 650ml/hour for the conducted tests. The produced water quality was measured, and showed electrical conductivity levels of 15 µs/m and 10 mg/l, which is close to the value of distilled water. The amount of produced fresh water was not compared in this study, because the temperature of the cold salty water flowing to the dehumidification chamber was not controlled at a constant temperature (even though a chiller was used to maintain the salty water in the cold tank at a lower temperature), due to the closed loop nature of the designed system, which allowed variable temperature of salty water leaving the humidification chamber, which is the inlet to the dehumidification unit. Therefore, a comparison of the freshly produced water would not have been accurate for the closed loop designed system.

Variation of flow rates of salty water

As the inlet temperature of air was controlled for all the conducted tests via the environmental chamber, it was set at 26°C. Figure 3, shows the impact of varying the flow rate of the salty water, on temperature drop of the salty water inside the humidification chamber, after heat and mass transfer with the incoming ambient air in the fibre membrane bundles. The figure shows that there is a temperature decrease of salty water in all the conducted tests. This means that, heat and mass transfer occurs with the ambient air inside the humidification chamber. Furthermore, lower the flow rate of the salty water, resulted in higher temperature drop, which means that there is more heat transfer with the incoming air. The reason is that, the salty at lower flow rate, has more time inside the fibre membranes in contact with the air, which allows for added heat exchange compared to the higher flow rates.

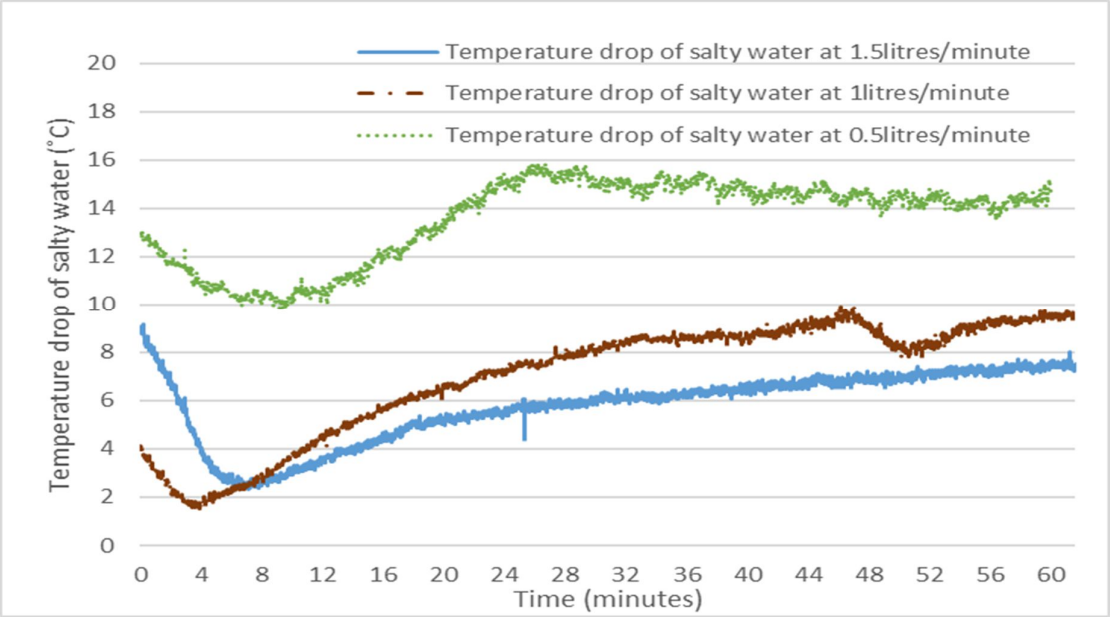

Figure 3: Effect of flow rates of salty water on temperature drop inside the humidification chamber

Figure 4 show the impact of varying the flow rates of the salty water, on the relative humidity of air at the outlet of the humidification chamber. The results show that the performance of the hollow fibre membrane as a humidification medium is very efficient, as the relative humidity levels after heat and mass transfer in the chamber varies from 95.5% to over 99%. Hence, the ambient air absorbs the moisture as it leaves the pores in the fibre membranes to increase its humidity levels. This means, that relative humidity has increased in the chamber by around 30% (from 65% set at the environmental chamber).On the other hand, higher flow rate resulted in higher relative humidity of air at the outlet of the humidification chamber.

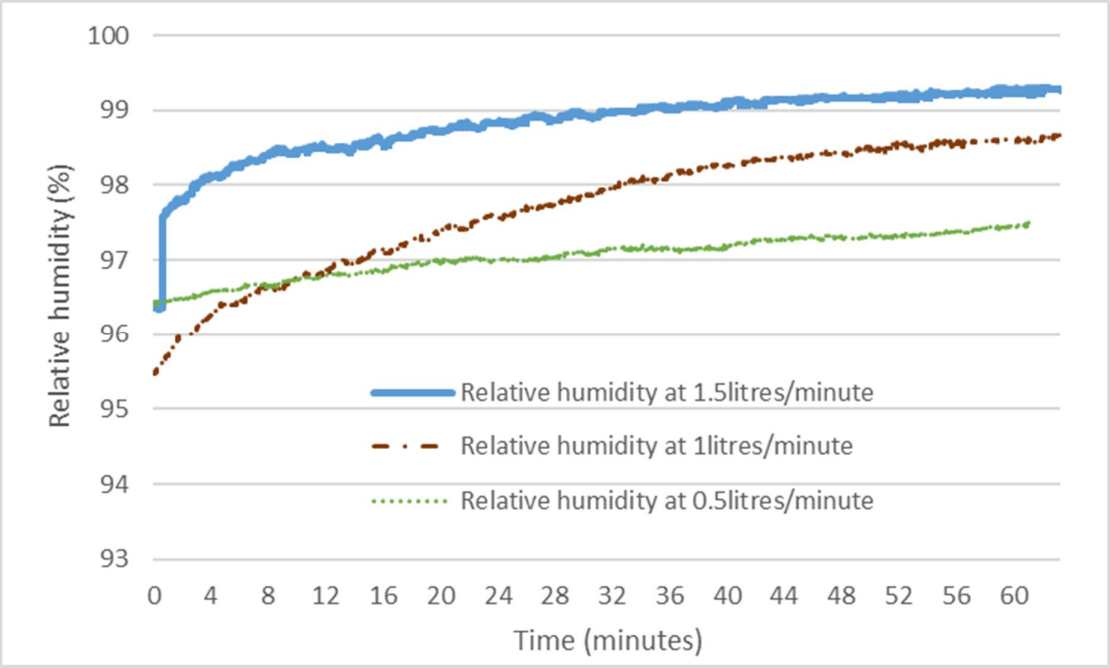

Figure 4: Effect of different flow rates of salty water on relative humidity of air

Variation of ambient air speeds

Figure 5 shows the effect of varying the inlet ambient air speed from 0.4m/sec to 1.4m/sec. The air inlet temperature was controlled at 26°C, hence the results indicate that there is an increase in the temperature of air at the outlet of the humidification chamber by 14°C -22°C (at the steady state of the system after 30 minutes of running), depending on the air speed, due to the heat transfer with the hot salty water. In addition, the results show that the air outlet temperature was highest when the inlet air speed was lowest (0.4m/sec). While, at the start of operation, at air speed of 0.9m/sec, the air outlet temperature was initially 30°C, however, the temperature of the air at the outlet increased to over 40°C at the steady state, hence becoming higher than that of the temperature of the outlet air at air speed of 1.4m/sec (compared to the start of the operation). These outcomes indicates that lower air speed leads to higher temperature gradient between the air temperature at the inlet and outlet of the humidification chamber. This reason is that, the air remains in the humidification for a longer time, leading to higher heat transfer with the hot salty water flowing through the fibre membrane bundles.

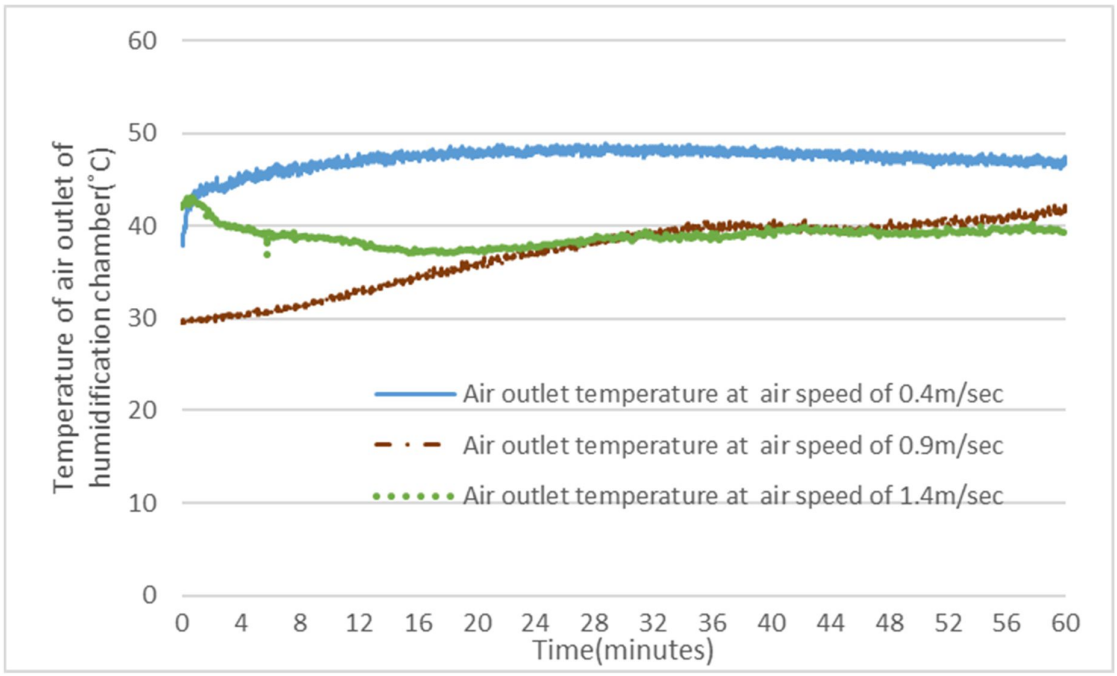

Figure 5: Effect of inlet air speeds on air outlet temperature from the humidification chamber

Figure 6, shows the effect of inlet air speeds on the relative humidity of the air at the outlet of the humidification chamber. The results indicate that the relative humidity was lowest at the highest air speed (1.4m/sec). On the other hand, relative humidity at air speeds of 0.4m/sec and 0.9m/sec, seem to produce similar relative humidity levels.

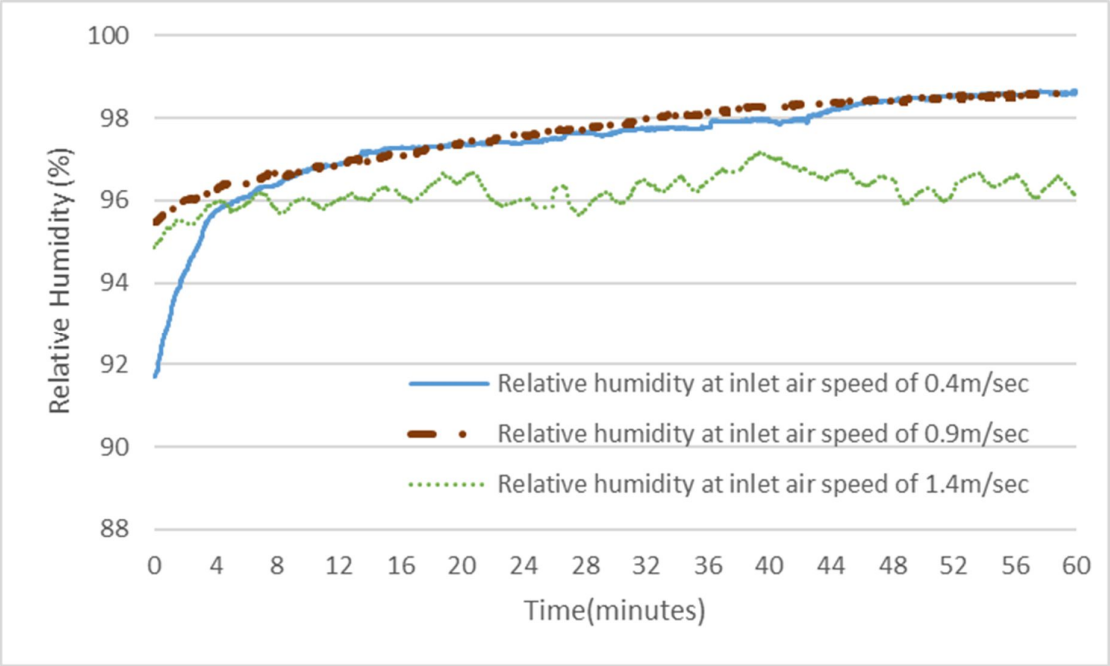

Figure 6: Effect of air speeds on relative outlet air humidity from the humidification chamber

3. CONCLUSION

This paper presented results of an experimental evaluation, which was carried out to investigate the performance of a humidification-dehumidification water desalination unit employing fibre membrane bundles as a humidification unit and a shell and tube heat exchanger as a dehumidification unit. The temperature of the salty water and humidity of the air were monitored at different locations in the experimental test rig. The purpose of the tests was to assess the impact of the input parameters including the flow rates for the salty water and the ambient inlet air speeds on the system performance. The tests demonstrated that the fibre membranes has significant potential to be used in the heat and mass transfer in humidification-dehumidification water desalination systems, as air relative humidity levels were increased significantly, reaching relative humidity of 99%, by absorbing the moisture which is leaked from the pores of the hollow fibre membrane bundles. Similar results in terms of temperature increase for the air were achieved when using different flow rates of salty water, while using lower flow rates of salty water resulted in higher temperature drop of the salty water in the humidification chamber; hence, it enhances heat transfer with the incoming inlet air. On the other hand, the lowest air speed used (0.4m/sec), led to the highest temperature of the air at the outlet of the humidification chamber, and displayed the highest value of relative humidity (98.5%).

4. ACKNOWLEDGEMENT

The authors would like to gratefully acknowledge that this work is funded by the Newton Fund Institutional Links (Award ref 261839879)

5. REFERENCES

Gabelich, C. J., Williams, M. D., Rahardianto, A., Franklin, J. C., & Cohen, Y. 2007. High-recovery reverse osmosis desalination using intermediate chemical demineralization. *Journal of Membrane Science*, Vol. 301(1), pp. 131-141

Geng, H., Wu, H., Li, P., He, Q., 2014. Study on a new air-gap membrane distillation module for desalination. *Desalination*, Vol. 334(1), pp. 29-38

Lee, K.P. Arnot, T.C., Mattia D., 2011. A review of reverse osmosis membrane materials for desalination—Development to date and future potential. *Journal of Membrane Science*, Vol. 370, pp. 1-22

Shatat M., Omer S., Riffat S., 2013. Theoretical simulation of small-scale psychometric solar water desalination system in semi-arid region. *Applied Thermal Engineering,* Vol 59 (1), pp. 232-242

Teow, Y. H., Mohammad, A.W., 2017. New generation nanomaterials for water desalination: A review, *Desalination*. In Press.

Wang, Z., Dou, B., Zheng, L., Zhang, G., Liu, Z., & Hao, Z., 2012. Effective desalination by capacitive deionization with functional graphene nanocomposite as novel electrode material. *Desalination*, Vol. 299, pp. 96-102

Welgemoeda, T.J., Schutte, C.F., 2005. Capacitive deionization technology: an alternative desalination solution, *Desalination,* Vol. 83, pp. 327–340.

Yang, C.M., Choi, W.H., Na, B.K., Cho, B.W., Cho W.I. 2005. Capacitive deionization of NaC1 solution with carbon aerogel–silica gel composite electrodes, *Desalination*, Vol. 174, pp. 125–133

Zhang, L.Z., Li, GP., 2017. Energy and economic analysis of a hollow fibre membrane-based desalination system driven by solar energy. *Desalination*, Vol. 404, pp. 200-214.

Water and Process Technology, http://www.gewater.com/what_we_do/water_scarcity/ desalination.jsp., Accessed on 30 May 2019.